Abstract Book

UNIVERSITY of DEBRECEN

EUROSENSORS XXXVI

1–4 September 2024 // Debrecen, Hungary

Proceedings

EUROSENSORS XXXVI

These proceedings cover the abstracts of the lectures and posters of the EUROSENSEROS XXXVI Conference.

The authors are responsible for form and content of the papers.

AMA Service GmbH accepts no responsibility for the correctness and completeness of the details and the consideration of private rights of third parties.

Herausgeber / Publisher:

AMA Service GmbH
Von-Münchhausen-Str. 49
31515 Wunstorf / Germany
Tel. +49 5033 9639-0
info@ama-service.com
www.ama-service.com / www.sensor-test.com
www.ama-science.org

ISBN 978-3-910600-03-4

Dear Colleagues,

The series of highly successful EUROSENSORS conferences began in 1987 in Cambridge as the only European forum to cover the entire field of Sensors, Actuators, Micro- and Nanosystems. Ever since it is the leading European conference devoted to the advancement of high technologies in the aforementioned fields, providing an excellent opportunity to bring together scientists, engineers and students from academia, national and international research institutes and companies to present and discuss the latest results in sensor fields.

The 36th EUROSENSORS conference is organized by the University of Debrecen (UD), Faculty of Science and Technology and the Institute of Technical Physics and Materials Science, Centre for Energy Research (HUN-REN CER MFA) at the campus of UD in Debrecen, Hungary.

The goal of the organizers and the hosting University of Debrecen was to present and discuss the actual developments of sensorics in the widest possible sense. Local industry actors active in the field were also involved in shaping the themes of the conference. We want to draw attention to the importance of cooperation between academic research and industrial partners, as well as the economic exploitation of significant scientific results.

The diverse topics of the four plenary lectures cover related but different areas. *Sensing in space research* is of particular interest, economic return by the space industry is expected in near future. *Energy harvesting* plays a prominent role in ensuring the grid-independent power supply of autonomous sensors and sensor networks. The emergence of *artificial intelligence* is also going to fundamentally change our everyday live, it will have essential impact on sensing by producing more accurate, better interpreted and utilized information. The application of *sensors and advanced microsystems in the bio-medical field* receives special attention, since personalized diagnosis-based therapies are no longer possible without high sensitive, target-oriented, single-use sensor systems.

On the Sunday, before the start of the regular program of the conference, the usual EUROSENSORS School will be held, mainly for university and PhD students. This time the focus is on "*The application of artificial intelligence in sensorics"*. Experts coming from various AI related fields form academia and industry will discuss possible application areas of AI in detail.

Over 300 valuable submissions were received for the conference from 36 countries. After *the peer-review by the international program committee* 250 abstracts were accepted for publication in form of ca. 100 oral presentations and 150 poster presentations.

The abstract book of EUROSENSORS 2024 is published by AMA Association for Sensors and Measurement. All the abstracts receive individual DOI number. The authors are asked to submit their full-length paper to Journal of Sensors and Sensor Systems (JSSS). After peer reviewing process, the full-length papers are published in a EUROSENSORS 2024 special issue.

Collaboration of science and industry also in the sensor field is a key factor of economic success in Europe. While we thank our partners and exhibitors for supporting EUROSENSORS 2024, we hope to serve their interests by showcasing their products and R&D plans at the exhibitions.

Debrecen is a fast-growing cozy city with dozens of historical, cultural and sport attractions, entertainments and sites to visit. The University of Debrecen is more than four hundred and fifty years old, the oldest higher education institution operated continuously in the same city. Debrecen is one of the largest educational centers of the country, the University of Debrecen with more than 30 thousand students among them 7000+ foreign students from all over the world is a central player in Hungarian

higher education. It has outstanding educational, research, and innovation capacities in international comparison as well and based on these it plays a major role in the realization of objectives of national strategy.

Participants are also offered a variety of social programs throughout the conference. When you arrive on Sunday evening, there will be a welcoming reception at the Water Tower in the nearby forest area. On Monday, the iconic Reformed Big Church will host an organ concert. The conference dinner will take place on Tuesday, followed by the closing ceremony on Wednesday.

We try our best, along with the local conference organisers, to make your brief visit to Debrecen both personally and scientifically delightful, and to give you a taste of life in Eastern Hungary.

Dr. Gábor BATTISTIG

Conference Co-Chair
University of Debrecen
Debrecen, Hungary

Dr. Péter FÜRJES

Conference Co-Chair
Centre for Energy Research BioMEMS
Budapest, Hungary

Lectures

OT1 Theory, Modelling, Design and Testing

OT2 Smart Systems and Artificial Intelligence in Sensing

OT3 Smart Systems and Artificial Intelligence in Sensing

OT4 Physical Sensors and Actuators

OT5 Chemical Sensors

OT6 Biochemical sensors, Microfluidics, Lab-on-a-Chip and Organ-On-Chip Systems

OT7 Photonics and Optical Microsystems

OT9 Wireless Sensor Networks and Communication

OT10 System Integration, Powering and Energy Harvesting

Poster

PT1 Theory, Modelling, Design and Testing

PT2 Smart Systems and Artificial Intelligence in Sensing

PT3 Advanced Materials and Technologies

PT4 Physical Sensors and Actuators

PT5 Chemical Sensors

PT6 Biochemical sensors, Microfluidics, Lab-on-a-Chip and Organ-On-Chip Systems

PT7 Photonics and Optical Microsystems

PT10 System Integration, Powering and Energy Harvesting

Lectures

DOI 10.5162/EUROSENSORSXXXVI/OT1.20

Acoustic Transmission Measurements of Folded MEMS Membranes for Mechanical Characterization

Dennis Becker[1], Moritz Littwin[1], Achim Bittner[1], Alfons Dehé[1,2]
[1] Hahn-Schickard, Wilhelm-Schickard-Str. 10, 78052 Villingen-Schwenningen, Germany
[2] Georg H. Endress Chair of Smart Systems Integration, Department of Microsystems Engineering – IMTEK, Albert-Ludwigs-Universität Freiburg, Georges-Köhler-Allee 103, 79110 Freiburg, Germany

Dennis.Becker@hahn-schickard.de

Summary:

Three-dimensional folded membranes are set to innovate MEMS designs for acoustic transducers by using lateral movement to increase their active area. Determination of the mechanical characteristics of such membranes is challenging, since established techniques mainly target in-plane structures. This paper presents an acoustic method to determine the mechanical compliances of such folded membranes. The results show compliances between $0.08 \cdot 10^{-15}$ and $10 \cdot 10^{-15}$ m^3/Pa for different membrane lengths.

Keywords: MEMS, membrane, characterization, acoustics, modeling

Introduction

The miniaturization of acoustic transducers in MEMS is technologically challenging due to their small volumes and displacements. To overcome these challenges, a novel transducer design is presented in [1] using a folded piezoelectric membrane design. This new three-dimensional approach is truly utilizing the entire chip volume. Lateral movements of multiple lamellas allow an increased volume displacement out of a fixed chip size.
For the development and optimization of various applications like microphones, speakers or micropumps, the detailed knowledge of the mechanical characteristics of such membranes is mandatory. State of the art methods like the Bulge test [2], vibrometry [3] or atomic force microscopy [4] are tailored for in-plane and near surface structures. However, these methods are not suitable for the deep lateral deflecting three-dimensional folded membrane without translating the deflection in known directions by extensive sample preparation. This paper presents a new measurement method, which uses acoustic transmission measurements (ATM) and lumped element modeling (LEM) to analyze the mechanical characteristics of folded MEMS membranes.

Measurement Method

The ATM measurement method utilizes two chambers, which are separated by the folded membrane to be characterized (Fig. 1). The first chamber comprises a reference microphone and an electrodynamic loudspeaker with a closed back volume. The loudspeaker causes a pressure wave, which sets the folded MEMS membrane in motion. A second microphone detects the acoustic signal radiated into the second chamber.

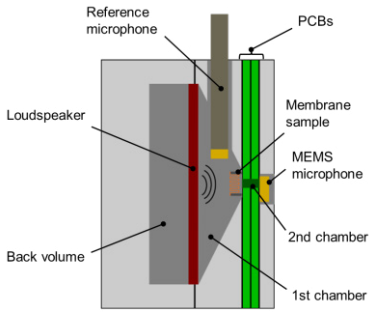

Fig. 1. Schematic representation of the measurement setup

From the pressure difference between the chambers information of the mechanical behavior of the folded membrane can be deduced. Pre-test measurements of the setup are performed to exclude external vibrations or influences, by calibrating the results.
The parameter extraction out of these measurements is done by LEM of the measurement setup in the acoustic domain (Fig. 2). Both chambers are modeled as acoustic compliances C_1, C_2 and the folded membrane as mass-spring-damper system $Z_{a,\,Mem}$. The extraction takes place by fitting the values of the membrane impedance to match the measured sound pressure level (SPL) in the second chamber.

The membrane mass is calculated from its geometry and thin film composition. Since the measurements do not take place in the resonant regime of the membrane, its damping can be neglected. As consequence, the compliance dominates the mechanical behavior in this frequency bandwidth.

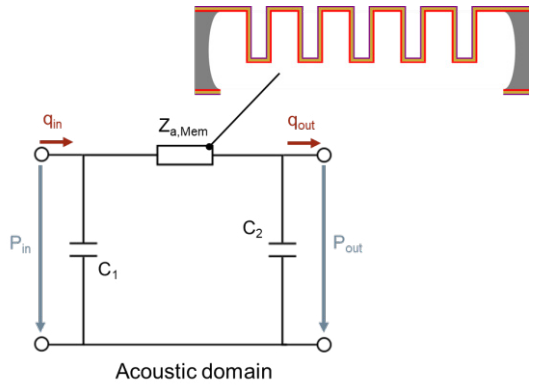

Fig. 2. Lumped element model of the measurement setup

Results

The acoustic measurements are performed with the APX525 audio analyzer from Audio Precision. Folded MEMS membranes made out of a SiO_2, n-doped polycrystalline silicon (Poly-Si) and Si_3N_4 [1] stack are characterized in this paper. Three different lengths of 500 µm, 1000 µm and 2000 µm are measured using three samples each to identify the influence on the membrane compliance. Fig. 3 illustrates the measured frequency response of one of the 1000 µm long membranes in the measurement setup.

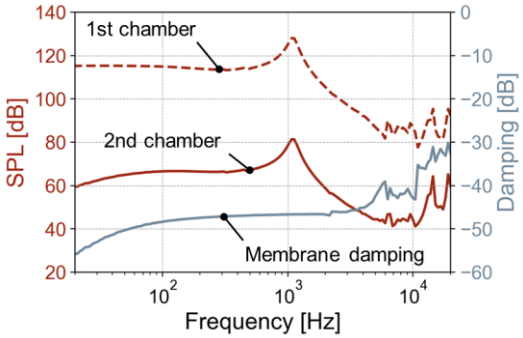

Fig. 3. Frequency responses of both chambers and the damping of a 1000 µm long folded membrane

The electrodynamic loudspeaker causes the resonance peak at 1.1 kHz and the drop of SPL towards higher frequencies in both chambers. The MEMS microphone in the second chamber exhibits a high-pass behavior below 100 Hz. The parameter extraction is done at 1 kHz, since here the membrane behavior is not influenced by the measurement setup. The comparison of the results for the different lengths shows a nearly linear behavior on the membrane compliance. The membranes of 1000 µm and 2000 µm length show an expected increase of compliance by nearly a factor 2.

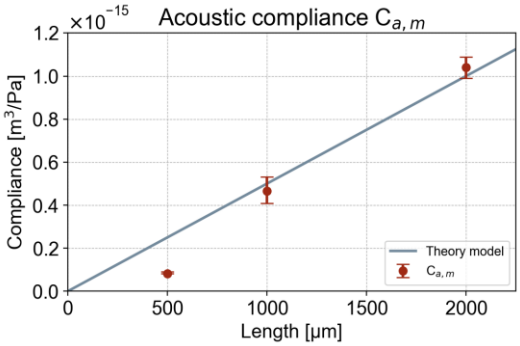

Fig. 4. Extracted acoustic compliances $C_{a,m}$ of folded MEMS membranes with different lengths

In contrast, the shorter membrane with 500 µm length shows a lower compliance than expected. This is likely caused by the fixed support of the membrane front faces in the Si frame. The shorter the membrane, the greater the support compliance influences the displacement. For longer membranes, the membrane geometry dominates the compliant behavior while the support can be neglected. This ensures a linear relationship between membrane compliance and membrane length.
In summary, a new measurement method for the mechanical characterization of folded MEMS membranes is shown. By making assumptions for the membrane mass and damping, it is possible to extract the compliance for different membrane geometries without extensive sample preparation.

References

[1] D. Becker, A. Bittner & A. Dehé, Three-dimensional folded MEMS manufacturing for an efficient use of area, *MikroSystemTechnik Kongress 2023 - Proceedings*, 307-310 (2023)

[2] J. Neggers, J.P.M Hoefnagels & M.G.D. Geers, On the validitiy regime of the bulge equations, Journal of Materials Research 27, 1245-1250 (2012); doi: https://doi.org/10.1557/jmr.2012.69

[3] M. Ebert, F. Naumann, R. Gerbach & J.Bagdahn, Measurement of Dynamic Properties of MEMS and the Possibilities of Parameter Identification by Simulation, EuroSime 2007, 1-6; doi: https://doi.org/10.1109/ESIME.2007.360061

[4] P. Martins, P. Delobelle, C. Malhaire, S. Brida & D. Barbier, Bulge test and AFM point deflection method, two techniques for the mechanical characterization of very low stiffness free standing films, European Physical Journal Applied Physics 45, 10501 (2009); doi: http://doi.org/10.1051/epjap:2008187

DOI 10.5162/EUROSENSORSXXXVI/OT1.36

KNN Lead-free biaxial piezoelectric MEMS Mirror on 200 mm Si wafer

L.Mollard[1], C.Dieppedale[1], A.Hamelin[1], G.Le Rhun[1]
[1] Univ. Grenoble Alpes, CEA, Leti, F-38000 Grenoble, France.

laurent.mollard@cea.fr

Summary:
This work presents the first KNN-biaxial non-resonant MEMS mirrors manufactured on 200 mm silicon substrate. The performances of the biaxial MEMS mirrors with reflector diameters ranging from 0.5×0.5 to 2×2 mm², integrating 1-µm thick sputtered potassium sodium niobate $(K_{0.3}Na_{0.7})NbO_3$ piezoelectric thin film from Sumitomo Chemicals, are presented. These mirrors, which exhibit rotational resonant frequency of 32.5 kHz, 7.5 kHz and 1.92 kHz, have been tested in non-resonant mode at 200 Hz and at higher frequencies. An optical angle of up to 6° can be obtained depending on the driving frequency.

Keywords: MEMS mirror, Piezoelectric, KNN, Lead-free, Actuator.

Due to their compact size, affordability, and minimal power consumption compared to conventional mechanical scanning systems, MEMS mirrors [1] find widespread use across various applications. These include projection display systems for augmented reality (AR) and virtual reality (VR) smart glasses, biological imaging, and Light Detection And Ranging (LIDAR) system [2], among others.

Piezoelectric actuation emerges as a promising choice, offering notable advantages such as high force, low voltage requirements, high frequency capability, and rapid response times. For a long time, lead Zirconate Titanate (PZT) stands out as the leading piezoelectric material, boasting competitive electromechanical coupling and a high piezoelectric coefficient. However, the environmental impact of lead present in PZT raise significant concerns regarding the practical application of piezoelectric MEMS mirrors. The release of lead and its associated compounds during the manufacturing process poses a substantial threat to both the environment and human health [3].

To replace PZT actuators, various families of lead-free piezoelectric materials have been developed. Among them, sodium potassium niobate (KNN) emerges as particularly promising due to its elevated Curie temperature and high piezoelectric coefficient [4].

This work presents the performances of biaxial piezoelectric MEMS with mirror diameters ranging from 0.5×0.5 to 2×2 mm², as presented in Tab. 1, integrating sputtered potassium sodium niobate $(K_{0.3}Na_{0.7})\ NbO_3$ thin film from Sumitomo Chemicals [5][6]. This 1 µm-piezoelectric motor exhibits a high piezoelectric coefficient ($e_{31,f}$ = 11 C/m²) and high dielectric constant (ε=1200) making it suitable for actuating performance.

The KNN biaxial MEMS mirrors, fabricated on 200 mm silicon wafer, as shown in Fig.1, have rotational resonant frequency of 32.1, 7.5 and 1.92 kHz respectively, depending on mirror diameter. The results obtained with these non-resonant mirrors exhibit the following characteristics (a) collective 200 mm silicon manufacturing process (b) low voltage operation of only 20V in non-resonant mode (c) an optical angle of 7.5° at 690 Hz frequency for the 2×2 mm² mirror, as shown in Fig.2 (d) a frequency range of up to 5100 Hz and 28000 Hz for the 1×1 mm² and 0.5×0.5 mm² mirror respectively. These results are state-of-the-art compared to the results previously obtained with PZT material and other actuation motor using non-resonant driving mode, as represented in Fig.3, [2][7].

The KNN lead-free piezoelectric material integrated into actuators offers potential applications in various fields from Light Detection And Ranging (LIDAR) systems to biomedical applications, thanks to the full biocompatibility of KNN material [8].

The authors are thankful to Sumitomo Chemical for depositing KNN films with electrodes on the SOI wafers. This work is part of the IPCEI Microelectronics and Connectivity and was sup-

ported by the French Public Authorities within the frame of France 2030.

Tab. 1: KNN MEMS mirror variants described in this work

Design variant	Resonant frequency	Mirror size	MEMS Footprint
	(kHz)	(mm²)	(mm²)
(a)	1.92	2×2	≈8×8
(b)	7.5	1×1	≈4×4
(c)	32.1	0.5×0.5	≈2.5×2.5

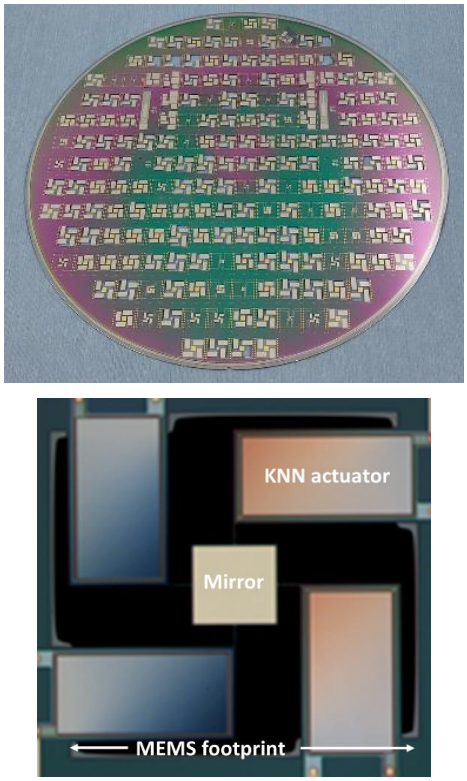

Fig. 1. 200 mm silicon wafer of KNN-MEMS mirrors and MEMS mirror top-view.

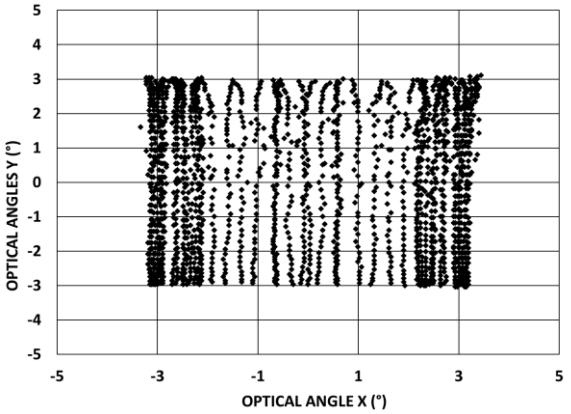

Fig. 2. 2D scanning representation of KNN MEMS mirror – Design variant (a) – 50 points per fast axis – 20 V voltage, 200 Hz fast/horizontal axis and 4 Hz ramp slow/vertical axis.

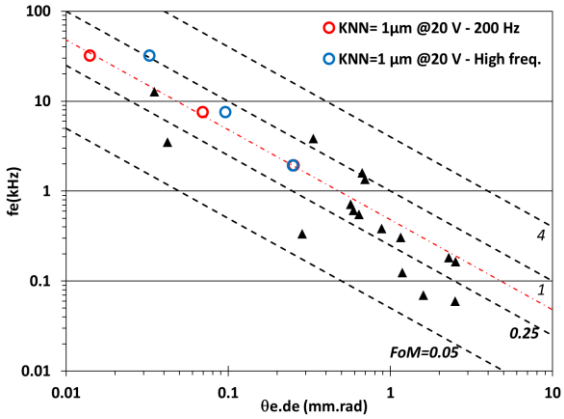

Fig. 3. FoM values previsouly reported in [2] (▲) and this work ((○ for 200 Hz fast axis and ○ for highest frequency on fast axis)

References

[1] Holmstrom, S.T.S.; Baran, U.; Urey, H. MEMS Laser Scanners: A Review. *J. Microelectromech. Syst.* **2014**, *23*, 259–275. doi:10.1109/JMEMS.2013.2295470.

[2] Yoo, H.W.; Druml, N.; Brunner, D.; Schwarzl, C.; Thurner, T.; Hennecke, M.; Schitter, G. MEMS-Based Lidar for Autonomous Driving. *e & i Elektrotechnik und Informationstechnik* **2018**, doi:10.1007/s00502-018-0635-2.

[3] Panda, P.K. Review: Environmental Friendly Lead-Free Piezoelectric Materials. *Journal of Materials Science* **2009**, *44*, 5049–5062, doi:10.1007/s10853-009-3643-0.

[4] Aspe, B.; Cissé, F.; Castel, X.; Demange, V.; Députier, S.; Ollivier, S.; Bouquet, V.; Joanny, L.; Sauleau, R.; Guilloux-Viry, M. K x Na1−xNbO3 Perovskite Thin Films Grown by Pulsed Laser Deposition on R-Plane Sapphire for Tunable Microwave Devices. *Journal of Materials Science* **2018**, *53*, 13042–13052, doi:10.1007/s10853-018-2593-9.

[5] Shibata, K.; Watanabe, K.; Kuroda, T.; Osada, T. KNN Lead-Free Piezoelectric Films Grown by Sputtering. *Applied Physics Letters* **2022**, *121*, doi:10.1063/5.0104583.

[6] Kuentz H.; le Rhun G.. KNN lead-free technology on 200 mm Si wafer for piezoelectric actuator applications. Sensors and actuators A:Physical, 2024, submitted.

[7] Mollard, L.; Riu, J.; Royo, S.; Dieppedale, C.; Hamelin, A.; Koumela, A.; Verdot, T.; Frey, L.; Le Rhun, G.; Castellan, G.; et al. Biaxial Piezoelectric MEMS Mirrors with Low Absorption Coating for 1550 Nm Long-Range LIDAR. *Micromachines* **2023**, *14*, 1019, doi:10.3390/mi14051019.

[8] Gaukås, N.H.; Huynh, Q.-S.; Pratap, A.A.; Einarsrud, M.-A.; Grande, T.; Holsinger, R.M.D.; Glaum, J. *In Vitro* Biocompatibility of Piezoelectric K $_{0.5}$ Na $_{0.5}$ NbO $_3$ Thin Films on Platinized Silicon Substrates. *ACS Applied Bio Materials* **2020**, *3*, 8714–8721, doi:10.1021/acsabm.0c01111.

DOI 10.5162/EUROSENSORSXXXVI/OT1.135

Design Study of a Y-shaped Six-Axis Force/Moment Sensor Through Pareto Front and Novel Analytical Model

Mithat Can Özin[1], Bilsay Sümer[2], İlker Murat Koç[1]
[1] Istanbul Technical University, Dept. of Mech. Eng., Gümüşsuyu, İstanbul, 34437, Türkiye
[2] Hacettepe University, Dept. of Mech. Eng., Beytepe, 06800, Türkiye

ozin@itu.edu.tr

Summary:
The Y-shaped sensor structure is optimized by Pareto front with Non-Dominated Sorting Genetic Algorithm II (NSGA-II) and a novel analytical model. Axial strain outputs of force and moments axes are favorable depending on the sensor dimensions. Hence, Pareto front reveals strain-output characteristics of sensor dimensions. Moreover, the novel analytical model permits feasible size optimization in a broad dimension range by respecting equivalent stress and fundamental frequency, unlike previous studies. A prototype of the optimal design is experimentally validated, and sensor properties are characterized.

Keywords: six-axis force/moment sensor, analytical model, pareto front, design, size optimization

Introduction

Strain-based multi-axis force and moment sensors benefit mechanical structure in terms of shape and size. Considering the sensor shape, a Y-shaped structure composed of three sensing beams is statically determinate and produces higher displacements and voltage outputs as opposed to statically indeterminate sensor structures such as a typical cross-beam formed of four beams. In favor of increased flexibility, elastic beams of cross-beams are extended in out-of-plane directions, which expands manufacturing complexity and costs. On the contrary, y-shaped beams allow the required stiffness and strain output in a planar design [1]. In terms of the compliant structure size, different sensor dimensions have significant axial strain outputs. For instance, extending the elastic beam and sensing beam length helps strain outputs, but it also leads to a larger sensor with a lower frequency response. Moreover, minimizing the cross-sectional area of elastic and sensing beams improves strain outputs, yet it reduces the structural safety of the sensor as well. Hence, it creates a design optimization problem with a trade-off between sensor properties [2].

Pareto efficiency is beneficial in optimization problems with competing objectives. In generic design problems, multi-objective pareto optimality can be reduced to a weighted sum single objective optimization. However, strain characteristics against sensor size is a new design optimization problem formulation for y-shaped multi-axis force moment sensors that has not been investigated so far. Previous studies examined strain output either by optimizing beam cross-sectional area or beam length. The main reason for this optimization drawback was modeling incapacities regarding solution times and solution accuracy.

Previous studies that implemented the finite element method for sensor modeling encountered long solution times that were infeasible for large dimension ranges. Other studies that employed analytical models sustained the insufficiency of the preceding approximate models [3]. This study employs a novel analytical model known for its high accuracy and fast solving time, which takes into account the structural safety and fundamental frequency of the mechanical structure. Hence, the large range pareto front optimization process is ultimately feasible for this sensor design problem.

In this study, a population-based genetic algorithm is used. In this way, optimal solutions in the population disclose axial strain-output characteristics depending on sensor dimensions. Moreover, an optimal design is selected considering sensor diameter and strain outputs. A sensor prototype is manufactured, and sensor properties are experimentally characterized. Experimental results are compared with optimization results.

Methodology

This study takes advantage of a new analytical model that involves beam joint reactions and flexibility which significantly increases accuracy and capability compared to prior models. According to this model strain output of sensing

beams are formulated in Eq. (1) for F_x force and Eq. (2) for M_x moment.

$$\varepsilon_{F_x} = F_x \left(\zeta \frac{\ell_1 w_1}{2EI_1} - \eta \frac{w_1}{2EI_1} \right) \quad (1)$$

$$\varepsilon_{M_x} = M_x \left(\zeta \frac{\ell_1 h_1}{2EI_4(\ell_1 + r)} - \eta \frac{r h_1}{2EI_4(\ell_1 + r)} \right) \quad (2)$$

As presented in Eq. (1-2), strain outputs are influenced by the sizing of both sensing and elastic beams. In Fig. 1, a sensor prototype is displayed. Strain gauges are placed on sensing beams, and elastic beams form an elastic boundary, increasing the flexibility of the sensor structure.

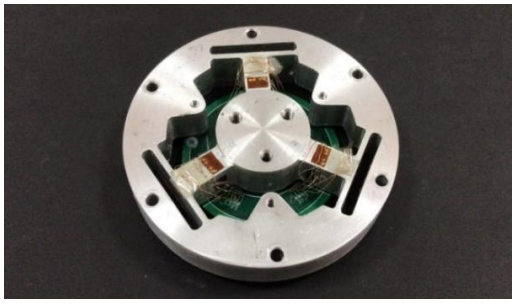

Fig. 1. Illustration of the y-shaped multi-axis force/moment sensor prototype that is composed of sensing and elastic beams.

Pareto front is an optimization process that defines competing objectives in problem formulation. Sensor diameter is expected to be as small as possible, and the strain outputs of all force and moment axes are expected to be increased. The problem formulation is given below.

$$\begin{aligned} \text{Optimize} \quad & f_1 = \max\left(\varepsilon_{F_x} + \varepsilon_{F_y} + \varepsilon_{M_z}\right) \\ & f_2 = \max\left(\varepsilon_{F_z} + \varepsilon_{M_x} + \varepsilon_{M_y}\right) \\ & f_3 = \min\left(d_{sensor}\right) \\ \text{subject to} \quad & \max\left(\sigma\right) \le \sigma^* \\ & \min\left(\omega_n\right) \ge \omega_n^* \\ & x_l \le x_i \le x_u, \quad i = 1, \cdots, N \end{aligned}$$

In this study, MATLAB GaMultiObj algorithm is utilized along with the new analytical model for obtaining pareto front. In Fig. 2, pareto-front results are displayed for a generic case. As seen in the figure, population solutions favor different axial strain outputs for varying sensor diameters.

The optimal sensor design is selected from the average of optimal population solutions using the weighting sum method. A sensor prototype is produced and experimentally characterized by the dead-weight test bench given in Fig. 3. This experimental setup is adequate for the required forces and moments. Sensor properties such as nonlinearity, hysteresis, sensitivity, time drift, and crosstalk are obtained. The strain outputs of experimental and analytical results are compared. Fig. 4. illustrates the results of the voltage output vs. dead weight during the calibration process.

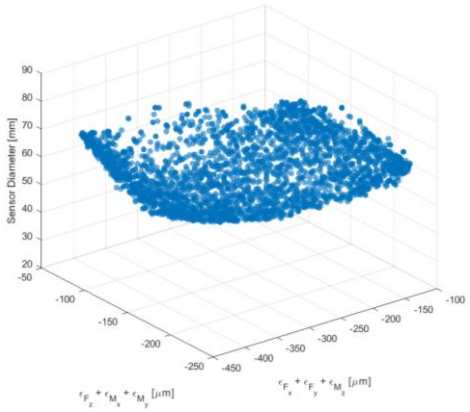

Fig. 2. A typical pareto optimality result for a y-shaped sensor

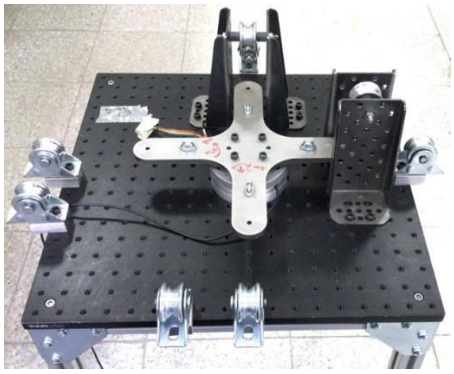

Fig. 3. Experimental dead weight setup for sensor calibration and validation of y-shaped sensor design.

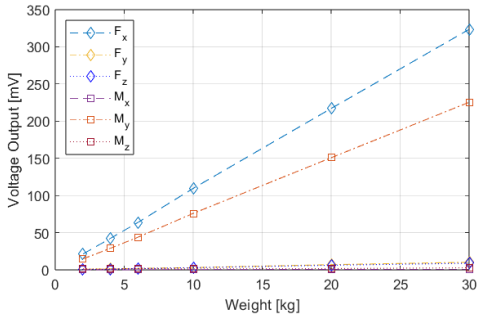

Fig. 4. Voltage output results vs dead weights causing F_x force and M_y moment combination for obtaining calibration matrix.

References

[1] G. Mastinu, M. Gobbi, Force sensors for active safety, stability enhancement and lightweight construction of road vehicles, *Vehicle System Dynamics*, *61*(9), 2165–2233 (2023); doi:10.1080/00423114.2023.2240447

[2] M. Y. Cao, S. Laws and F. R. y. Baena, Six-Axis Force/Torque Sensors for Robotics Applications: A Review, *IEEE Sensors Journal*, 21(24), 27238-27251, (2021); doi:10.1109/JSEN.2021.3123638.

[3] M. Pu, Q. Luo, Q. Liang and J. Zhang, Modeling for Elastomer Displacement Analysis of Capacitive Six-Axis Force/Torque Sensor, *IEEE Sensors Journal*, 22 (2), 1356-1365 (2022); doi:10.1109/JSEN.2021.3132387.

DOI 10.5162/EUROSENSORSXXXVI/OT1.159

Non-Destructive Evaluation of Crack Propagation in Solder Joints of Pressure Sensors Under Thermal Cycling Using Computed Tomography and Finite Element Analysis

Róbert Mógor-Győrffy[1], *Evelin Szécsi*[1]
[1] *Robert Bosch Kft, Gyömrői út 104, Budapest 1103, Hungary*

robert.mogorgyorffy@bosch.com

Summary:

This study investigates crack propagation in pressure sensor solder joints caused by thermal cycling, employing Computed Tomography (CT) for non-destructive monitoring and Finite Element Analysis (FEA) to simulate plastic strain distribution. By periodically examining the solder joints with CT during thermal cycles and measuring crack lengths, we predict the lifetime of the joints. The FEA complements this by predicting damaged regions, with both methods showing good agreement in lifetime estimations.

Keywords: solder, lifetime, FEM, CT, MEMS

Background, Motivation and Objective

Solder joint reliability is a cornerstone of electronic device performance, especially in components subjected to thermal cycling, which induce mechanical stress and can lead to crack formation and propagation. In MEMS sensors, where accuracy and durability are paramount, understanding the behavior of solder joints under temperature fluctuations is critical. Non-destructive testing methods, such as computed tomography (CT), have emerged as invaluable tools for investigating internal structures and defects in materials without compromising sample integrity [1, 2]. The integration of CT imaging with FEA offers a comprehensive understanding of crack initiation and propagation dynamics, and its impact on the lifetime of solder joints.

Description of the New Method or System

By periodically analyzing solder joints with CT imaging throughout thermal cycles and quantifying crack lengths, alongside simulating plastic strain via Finite Element Method (FEM), we seek to enhance lifetime predictions of solder joints. This approach addresses the need for advanced diagnostics and predictive models in the field, contributing to the development of more durable electronic components.

Results

A high-resolution 3D X-ray microscope was used to create the CT images which also reveal the internal structure of the solders (see Fig. 1).

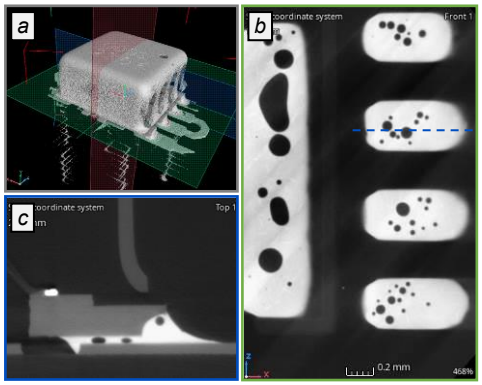

Fig. 1. 3D X-ray image of the sensor package (a). Tomographic image or slice in the horizontal (green) plane (b). Slice in the vertical (blue) plane, slice position is also shown by a blue dashed line (c).

The voids are natural remainings of the soldering process and normally do not influence solder lifetime [3].

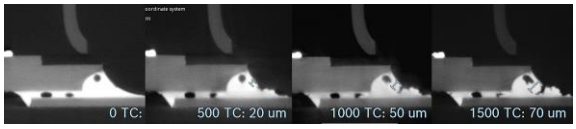

Fig. 2. Crack initiation and propagation throughout the thermal cycles (TC) between -40 / +150 °C.

Crack lengths were measured in every solder joint across all eight sensor packages (see Fig. 2). The expected solder lifetime is then calculated from the crack propagation speed.

The finite element model was created from the quarter of the PCB on which 4 sensor packages were soldered. The traces and layer structure of

the PCB were considered in detail. The solder joint geometry was based on the initial CT images, but voids were not considered (see Fig. 3).

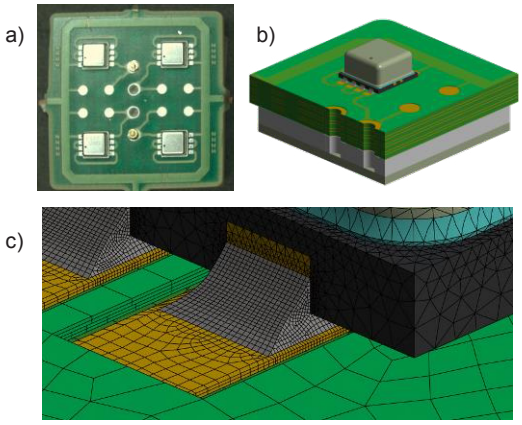

Fig. 3. The test PCB with four sensors (a), the geometry of the finite element model (b), and the finite element mesh at the solder joints (c).

The damage related parameter is the inelastic strain (accumulated plastic strain in the Ansys general purpose FEM software). To estimate the lifetime of the solder joints, the volume weighted average (VWA) accumulated plastic strain increment per cycle is calculated for each of the solders during postprocessing of the results. Finally the values are used in the Coffin-Manson relation to predict the expected lifetime of the solder joints.

The FE results show high load in the lower part of the outer solder meniscus, and at the outer circumference of the large middle solder (see. Fig. 4).

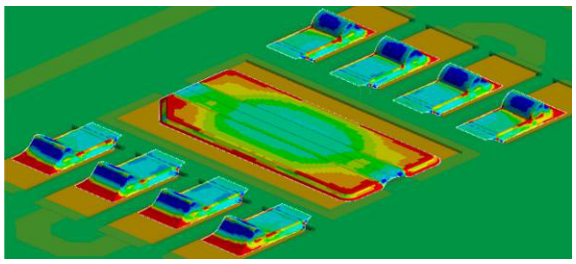

Fig. 4. Accumulated plastic strain distribution.

Simulation results show very similar distribution of the damage related parameter compared to damaged regions visible on final CT images (see. Fig. 5). Note the effect at the backside of the solder (to the most right on Fig. 5. b). Here, the solder resist touches the solder meniscus causing a more significant load leading to a localized crack formation. This geometric feature was considered in the simulation and the effect could be represent.

Fig. 6. shows the predicted lifetime of the solder joints based on crack length measurements, and on FEA using the Coffin-Manson relation.

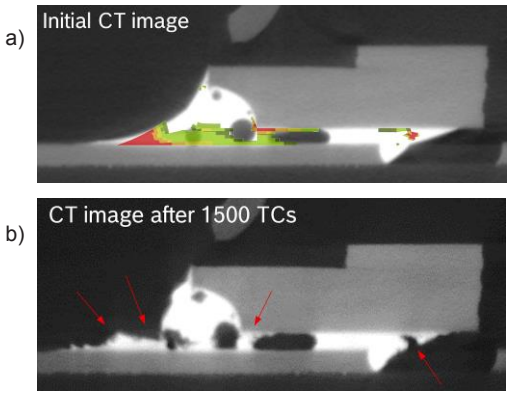

Fig. 5. Initial CT image overlayed with FE results showing high plastic strain accumulation (a). CT image after completing thermal cycling (b).

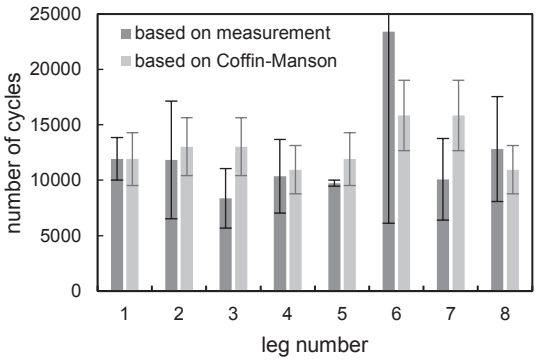

Fig. 6. Expected lifetime of solder joints averaged across all eight sensor packages based on crack length measurement and FEA (scattering for latter results is taken to be +/- 20%).

The results match, the difference is small for most legs, however there is a larger deviation for leg #6 and smaller ones for leg #3 and #7. The reasons could be tolerance related (allowed deviations in dimensions or in material properties, etc.) or the crack length measuring method could be further improved, e.g. by tracking the crack length or area in 3D.

References

[1] P. Roumanille, J. Lesseur, J. Uzanu, H. Le Trong, E. Ben Romdhane, A. Guédon-Gracia, H. Frémont, Using X-ray imaging for the study of crack development in solder reliability testing, *Microelectronics Reliability* 150, (2023); doi: 10.1016/j.microrel.2023.115079

[2] P. Lall and J. Wei, PBGA package Finite Element Analysis based on the physical geometry modeling using X-ray micro CT digital volume reconstruction, *15th IEEE Intersociety Conference on Thermal and Thermomechanical Phenomena in Electronic Systems (ITherm)*, 285-294 (2016); doi: 10.1109/ITHERM.2016.7517562

[3] Norbert Holle, Thomas Ewald, Udo Welzel, Voids in SMT Solder Joints – Myths Revisited, *IPC APEX 2018 Technical Conference Proceedings* (2018)

DOI 10.5162/EUROSENSORSXXXVI/OT1.173

High-Fidelity Modeling of Harmonic Distortions in Piezoelectric MEMS Microphones with a Corrugated Membrane

Ferdinand Schiller[1,2], Christian Bretthauer[1], Andreas Bogner[1], Gabriele Bosetti[1], Michael Krenzer[1], Karolina Gierl[1], Christian Haupt[1], Heinrich Heiss[1] and Gabriele Schrag[2]
[1] Infineon Technologies AG, Am Campeon 1-15, 85579 Neubiberg, Germany,
[2] Professorship of Microsensors and Actuators, Theresienstraße 90, 80333 Munich, Germany

ferdinand.schiller@infineon.com

Summary:
We present a high-fidelity, computationally efficient approach for modeling harmonic distortions in piezoelectric MEMS microphones featuring a fully-clamped corrugated membrane design. The described method correctly predicts the total harmonic distortion (THD) of two manufactured design variants, thereby paving the way for THD optimization throughout the design process. Remarkably, one of the design variants shows a THD of 1% at a very high sound pressure level (SPL) of $130\ \mathrm{dB_{SPL}}$, thus outperforming commercially available piezoelectric and capacitive single-backplate (SBP) microphones.

Keywords: Piezoelectric MEMS Microphone, Corrugated Membrane, Total Harmonic Distortion

Introduction

Capacitive MEMS microphones currently set the benchmark in technology due to their superior acoustic performance and compatibility with well-established semiconductor fabrication processes. However, unlike their capacitive counterparts, piezoelectric MEMS microphones do not require a bias voltage, which makes them a compelling choice for applications that require low-power consumption. Furthermore, capacitive microphones that utilize constant-charge readout are inherently nonlinear. This is attributed to the presence of parasitic capacitances and the nonlinear electrostatic force acting between the membrane and backplate [1].

Recently, a novel design of a piezoelectric MEMS microphone was proposed that leverages a fully-clamped corrugated membrane (see Fig. 1a) [2]. The corrugations release residual material stress to achieve a sufficiently compliant membrane and result in a spatial separation of tensile and compressive regions upon acoustical loading. This pseudo-bimorph design enables a single-ended or differential readout without requiring an intermediate electrode. Here, the THD of two corrugated membrane designs is investigated and a simulation method is proposed.

Materials and methods

A microphone can be considered as a system with pressure input $p_{\mathrm{in}}(t)$ and voltage output $V_{\mathrm{out}}(t)$ related by a function σ:

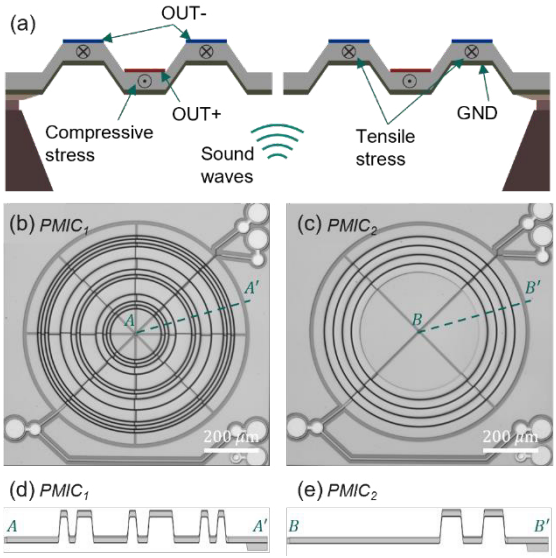

Fig 1. (a) Schematic of a corrugated membrane with electrodes OUT+, OUT- and GND. (b), (c) Optical microscopy images and (d), (e) rotational-symmetric cross-sections of two manufactured design variants.

$$V_{\mathrm{out}}(t) = \sigma(p_{\mathrm{in}}(t)) \tag{1}$$

To quantify the THD, the microphone is loaded with an input signal $p_{\mathrm{in}}(t) = \hat{p}\sin(2\pi f t)$ with amplitude $\hat{p}$ and frequency $f = 1\ \mathrm{kHz}$. In the microphone's linear regime, the output is a sinusoidal signal of the same frequency, where the output voltage linearly follows the input pressure. However, nonlinearities can result in higher-order harmonics in the output signal. To model this

behavior, σ is expressed as a polynomial function, i.e., $\sigma_{\mathrm{poly}}(p_{\mathrm{in}}) = a_n p_{\mathrm{in}}^n + a_{n-1} p_{\mathrm{in}}^{n-1} + \cdots + a_0$, for which $V_{\mathrm{out}}(t)$ consequently becomes a finite Fourier series:

$$V_{\mathrm{out}}(t) = V_0 + \sum_{i=1}^{n} V_i \sin(2\pi i f t + \varphi_i) \qquad (2)$$

The THD is then calculated as the contribution of higher modes in the output signal (up to order $n = 5$ is sufficient) to the linear response V_1:

$$\mathrm{THD} = \sqrt{\sum_{i=2}^{5} V_i^2} / V_1 \qquad (3)$$

To this end, the output signal $V_{\mathrm{out}}(t)$ obtained from transient FEM simulations is decomposed into harmonics through Fourier transformation according to eq. (2). However, this is computational expensive and not well suited for optimization studies as the THD is usually of interest for a wider range of input pressures.

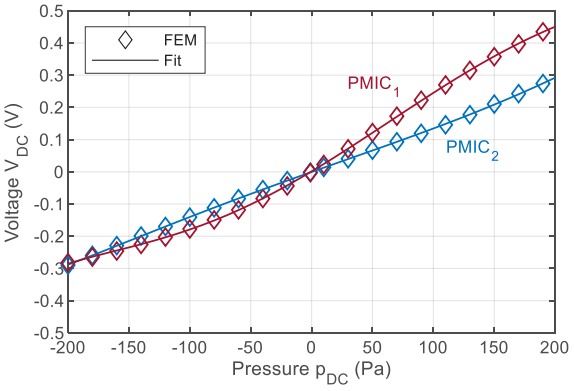

Fig 2. Nonlinear static response obtained from FEM and polynomial fit for the variants PMIC₁ and PMIC₂.

Alternatively, the nonlinear static response V_{DC} can be simulated for a wide range of input pressure values p_{DC}, which is much faster than the transient simulations. Subsequently, a polynomial function is fitted to the simulated static response, i.e. $V_{\mathrm{DC}} \approx \sigma_{\mathrm{poly}}(p_{\mathrm{DC}})$, from which the transient response is obtained as $V_{\mathrm{out}}(t) = \sigma_{\mathrm{poly}}(\hat{p} \sin(2\pi f t))$. Finally, a Fourier transform is applied and the THD can be calculated from eq. (3). A prerequisite for this method is that the response at the frequency of interest, i.e., $1\ \mathrm{kHz}$, equals the static response. This is fulfilled as the low frequency roll-off is not included in the FEM simulations and the frequency response is flat within the audio band ($20\ \mathrm{Hz}$ to $20\ \mathrm{kHz}$).

Results

The simulated nonlinear static response is shown in Fig. 2 for both design variants depicted in Fig. 1. Variant PMIC_1 exhibits strong asymmetries w.r.t the unloaded state ($p_{\mathrm{DC}} = 0$) as well as clipping behavior for higher pressures. These nonlinearities are significantly reduced for PMIC_2 indicating the potential of THD optimization by tuning the positions and numbers of corrugations. By decomposing the THD into even and odd harmonic distortions, i.e., $\mathrm{HD}_{\mathrm{even}}$ and $\mathrm{HD}_{\mathrm{odd}}$, which represent asymmetries and clipping behavior respectively, the contributions of the total THD can be quantified as shown in Tab 1.

Tab. 1: Simulated harmonic distortions at $130\ dB_{SPL}$

Variant	$\mathrm{HD}_{\mathrm{even}}$ (%)	$\mathrm{HD}_{\mathrm{odd}}$ (%)	THD (%)
$\mathbf{PMIC_1}$	6.70	1.31	6.82
$\mathbf{PMIC_2}$	0.85	0.51	0.99

Finally, the THD is simulated for multiple input pressures and compared with experimental measurements as well as two commercial microphones (see Fig. 3). This shows excellent agreement between measurement and simulation and demonstrates that the 1%-THD of PMIC_1 is superior to both reference microphones.

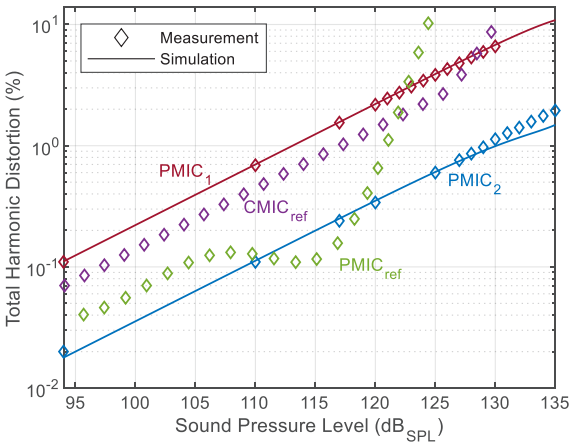

Fig 3. Measured and simulated THD for the variants PMIC₁ and PMIC₂. The THDs for the SOTA commercially available piezoelectric PMIC$_{ref}$ and capacitive reference microphone CMIC$_{ref}$ (Infineon IM68A130) are extracted from the respective datasheets.

Conclusion

We presented a fast and highly accurate method to simulate the THD of MEMS microphones enabling the optimization of the THD in the design phase. The investigation of two novel piezoelectric corrugated membrane-based designs revealed that the THD of the devices can be substantially reduced by adjusting the corrugations and is superior to state-of-the-art devices.

References

[1] S. Anzinger et al., A Non-Linear Lumped Model for the Electro-Mechanical Coupling in Capacitive MEMS Microphones, *Journal of Microelectromechanical Systems 30*, 360-368 (2021); doi: 10.1109/JMEMS.2021.3065129.

[2] G. Bosetti et al., A Novel High-SNR Full Bandwidth Piezoelectric MEMS Microphone Based on a Fully Clamped Aluminum Nitride Corrugated Membrane. *Transducers (2023).*

DOI 10.5162/EUROSENSORSXXXVI/OT1.175

Design of a MEMS Pitch Tunable Grating for Enhanced Scanning LiDAR

Ilgar Jafarsadeghi Pournaki[1], *Aron Michael*[1], *Hemanshu Pota*[2]
[1] *School of Electrical Engineering and Telecommunications, The University of New South Wales, Australia,*
[2] *School of Engineering and Technology, The University of New South Wales, Canberra, Australia*

i.jafarsadeghipournaki@unsw.edu.au

Abstract:
This paper introduces a high-performance MEMS (micro-electro-mechanical systems) pitch tunable grating (PTG) as a LiDAR (light detection and ranging) sensor. While the challenges associated with its integration into self-driving cars are addressed, its potential application extends beyond this specific domain. Electrostatic-based comb actuators are employed to drive the device. To delay side pull-in instability attributed to this transduction mechanisms, an innovative flexural configuration is employed, extending the stable travel range up to 135 µm, resulting in a broad pitch tuning of 2.25 µm. The initial diffraction angles for the first two orders before actuation were ±2.8° and ±5.5°; moreover, this remarkable pitch tuning resulted in a significant increase in the angle of the first and second orders, reaching 0.4° and 0.8°, respectively.

Keywords: MEMS, LiDAR, Optics, Sensor, Electrostatic

Introduction

The rising demand for automated driving due to its potential to prevent accidents, has led to a growing need for compact and affordable optical scanning systems. LiDAR stands out as a pivotal sensor for autonomous driving, offering the capacity to generate 3D data [1]. The currently dominant scanning solution in the automotive LiDAR market is bulky and has limitations related to duty cycle and inertia, leading to constraints on frame rate and increased power consumption. Consequently, MEMS-based LiDAR has gained considerable attention as a viable alternative, owing to its reduced size, low weight, and low power consumption. Thus far, two primary types of MEMS LiDARs have been investigated: mechanical and non-mechanical [2]. The first involves vibration-based sensing mechanisms utilizing resonant mirrors, whereas the latter utilizes light diffraction techniques, often implemented through solid-state gratings. Analyzing their advantages and drawbacks reveals why PTGs have garnered significant interest. They effectively bridge the gap between mechanical and solid-state LiDAR, providing an enhanced solution by widening the field of view (FoV) through pitch tuning between adjacent mirrors. This feature distinguishes them from solid-state gratings. While several papers have reported on PTGs driven by comb-drive actuators, to our knowledge, only one published research paper has investigated the potential use of MEMS-based PTGs in LiDAR systems for autonomous vehicles [3]. However, this device faces significant challenges that must be overcome before it can serve as an alternative solution for available LiDAR sensors. These challenges include undersized dimensions (resulting in extremely low intensity of diffracted light), limited travel range (only 1.21 µm), low fill factor, and a resonant frequency exceeding 20 kHz, unnecessarily stiffening the device. The paper presents a MEMS-based PTG scanner to address these challenges.

Description of the System

Fig. 1 illustrates a 2D view of the proposed device, highlighting its main components. It consists of silicon-based central grating mirrors (120 in total, each sized 2000×12 µm²) actuated by comb actuators, with two central anchors, all 80 µm thick. Guided beam springs, 150 µm in length and 4 µm in width, connect the grating mirrors, maintaining a 4 µm space between them. Additionally, eight tilted-folded flexures, with beams measuring 6 µm in width and 950 µm in length, are integrated. This suspension design enhances lateral stiffness while enabling large linear displacement in the actuation direction. The overall size of the mirror area meets the minimum requirement of MEMS mirrors for self-driving applications [2]. To comprehensively evaluate the device's performance, mechanical behavior is analyzed using COMSOL, followed by theoretical validation, while the optical characteristics are assessed through theoretical modelling.

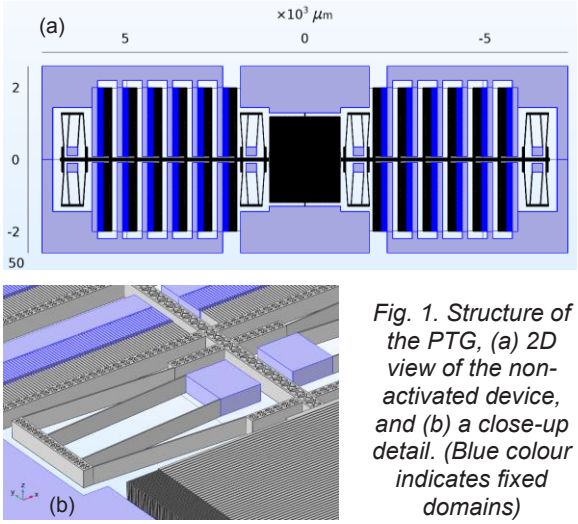

Fig. 1. Structure of the PTG, (a) 2D view of the non-activated device, and (b) a close-up detail. (Blue colour indicates fixed domains)

Discussion

The comparative analysis of the effective bearing ($K_{x,\ eff}$) and electrical (K_e) spring constants versus displacement, considering various suspension tilt values (d), is depicted in Fig. 2, obtained through analytic modeling. The results show that, depending on the tilt value, the bearing and electrical stiffness curves intersect at different points along the movement, indicating the maximum stable travel range. It is observed that a tilt value of d=65 μm is optimal, offering the largest stable displacement of 135 μm, significantly surpassing previous studies.

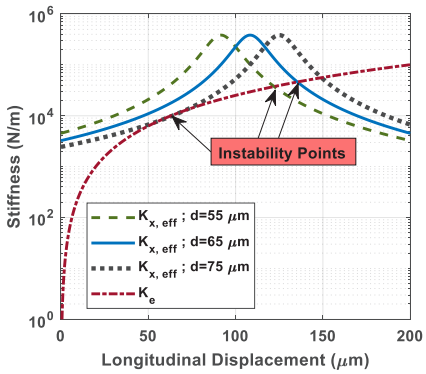

Fig. 2. Variation of stiffens with displacement

Figure 3a illustrates the voltage required to actuate the system when the gap between stationary and moving comb fingers is set at 4 μm. This gap is deemed optimal due to design trade-offs: while a larger gap delays instability, it also substantially decreases the electrostatic force. The results obtained through theory and simulation are shown to be in good agreement. Due to this large stroke, the pitch is tuned by 2.25 μm. Although, as expected, the duty cycle slightly decreases from 75% to 65% (albeit remaining high), the periodicity tuning extends to 14%, marking a significant improvement over previous findings [3]. The diffraction of incident light on the grating is described by Eq. (1):

$$\mathrm{Sin}(\theta_m)+ \mathrm{Sin}(\theta) = m\lambda/(2P) \quad (1)$$

Where m, θ, λ, and P represent the diffraction order, incident light angle, incident light wavelength, and pitch. With the incident light wavelength set at 1550 nm, the initial diffraction angles for the 1st and 2nd orders of diffracted light, prior to actuation, is obtained ±2.8° and ±5.5°, respectively. The relationship between the increase in diffraction angle and actuation voltage is illustrated in Fig. 3b, demonstrating a notably greater enhancement in diffraction angle compared to previously reported results.

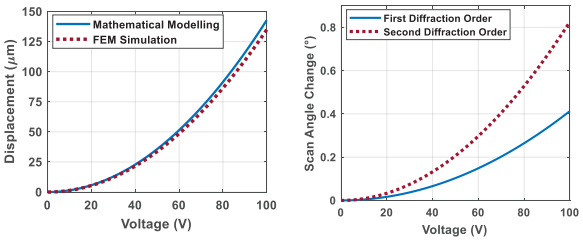

Fig. 3. Effect of actuation on: (a) displacement, (b) scan angle change

The natural frequency in PTGs is crucial for ensuring immunity to unwanted vibrations. According to [2], sensors used in cars must maintain a natural frequency above 800 Hz for reliable operation. An excessively high eigenfrequency leads to a stiff device, necessitating higher actuation voltage. Consequently, the device is designed to have a resonant frequency slightly over 800 Hz. Figure 4 shows the out-of-plane (1st mode) and in-plane (3rd mode) eigenfrequencies. This data confirms the device's complete resistance to unwanted vibrations. Moreover, the in-plane mode with a frequency of 894 Hz ensures high actuation speed, within the millisecond range.

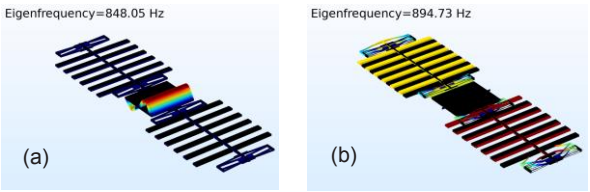

Fig. 4. Eigenfrequency modes: (a) first, (b) third

References

[1] H.W. Yoo, et al., MEMS-based lidar for autonomous driving, *e & i Elektrotechnik und Informationstechnik* 135, 408–415, (2018) doi: 10.1007/s00502-018-0635-2

[2] D. Wang, C. Watkins, and H. Xie, MEMS mirrors for LiDAR: A review, *Micromachines* 11, 456-480 (2020); doi: 10.3390/mi11050456

[3] T. Mohammad, S. He, and R.B. Mrad, A MEMS Optical Phased Array Based on Pitch Tunable Silicon Micromirrors for LiDAR Scanners. *Journal of Microelectromechanical Systems* 30, 712-724, (2021); doi: 10.1109/JMEMS.2021.3092701

DOI 10.5162/EUROSENSORSXXXVI/OT1.216

Automatic Imaging Based Wafer-Level In-Line Measurement for Piezoelectric MEMS Mirrors

Paul Raschdorf[1], Sören Winkelmann[1], Jan Lingner[1], Felix Heinrich[1], Lena Wysocki[1], Jeong-Yeon Hwang[1], Sönke Appel[2], Shanshan Gu-Stoppel[1]
[1] Fraunhofer Institute for Silicon Technology, Fraunhoferstraße 1, 25524 Itzehoe, Germany
[2] West Coast University of Applied sciences, Fritz-Tiedemann-Ring 20, 25746 Heide, Germany

Shanshan.Gu-Stoppel@ISIT.Fraunhofer.de

Summary:
This work presents the hard- and software development of a customized setup, to determine the total optical scanning angle (TOSA) and respective resonance frequency of resonant MEMS-scanners on wafer level during in-line testing. These electrical measurements are usually used to evaluate piezoelectric layer quality and to monitor the manufacturing process. However, the mechanical properties of the complete MEMS-scanners are characterized manually which limits high volume process. The integration of the mechanical measurements into the automated in-line testing leads to a drastic measurement time decrease as well as vastly improved resolution on imaging technique base.

Keywords: MEMS mirror, piezoelectric, silicon technology, MEMS optical component

Motivation

During the fabrication of silicon technology-based processes, in-line tests are conducted to monitor fabrication processes and yields.

The in-line characterization of a MEMS-scanner is an essential part of its process flow. It involves several electrical measurements to characterize leakage current and dielectric strength of the piezoelectric material and the quality of electricity conducting metal layers. Those are important parameters to evaluate single layers or layer stacks. However, the complete MEMS-scanner device is usually characterized based on the maximum TOSA shown in Figure 1 and the respective mechanical resonance frequency of the working mode(s) of the system.

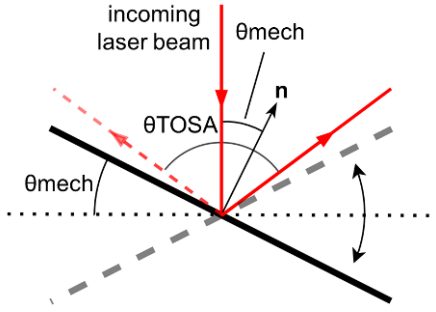

Fig. 1. Illustration showing the relation between the mechanical angle θ_{mech} and the TOSA θ_{TOSA} of an oscillating mirror plate in two directions with the normal vector n.

This is in most cases a manual labor process limiting high-volume production. An automated in-line measurement on wafer level is an excellent alternative that enhances time effectiveness and improves the optimization of process steps.

Resonant MEMS-Scanners

An automatic measurement setup has been developed for the resonant MEMS-scanners as shown in Figure 2.

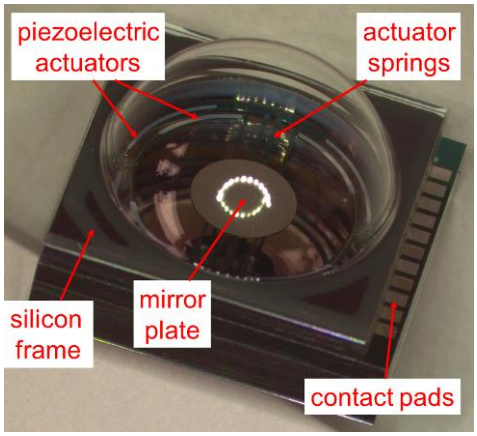

Fig. 2. Microscope image of a resonant MEMS-scanner. When an electric field is applied to the metal electrodes on the top and bottom of the piezoelectric material, the actuators bend up or down. This leads to a tilting movement of the mirror plate. In mechanical resonance, caused by a sinusoidal volt-

age, a laser beam can be deflected by more than 100° TOSA in a single axis [1].

Electrical and mechanical Measurement

During the routine in-line testing several parameters are characterized electrically. Those include among others leakage currents of the piezoelectric layer and sheet resistance of poly-Si layer. The resonance frequency of the system is characterized as well.

This electrically measured resonance frequency from the classic in-line measurement and the mechanical resonance frequency differ since during mechanical drive more non-linear effects from material stiffening and air resistance occur. This describes the behavior of a Duffing oscillator. [2]

To measure the mechanical resonance frequency and the maximum TOSA, the electrical resonance frequency is used as a starting point. The applied AC frequency is increased incrementally, while an increase in TOSA is observed. The mechanical resonance frequency is reached at the maximum deflection angle.

The optical TOSA measurement of a resonating MEMS-scanner is shown in Figure 4.

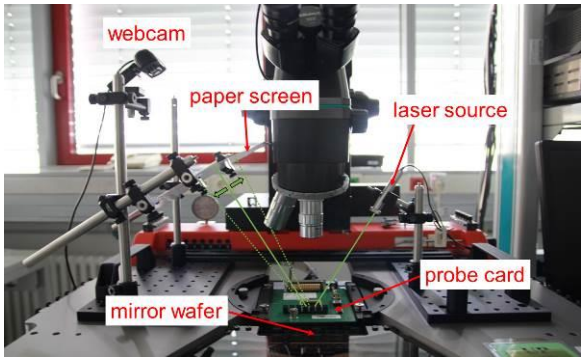

Fig. 4. Optical measurement setup placed inside a semi-automatic wafer-prober with integrated wafer and the respective probe card. An incident laser beam is reflected by an oscillating mirror plate. The resulting one-dimensional scan pattern is projected on a screen. The screen is recorded by a camera. The dotted lines show the geometric limitations of the setup in the wafer prober. Scanning angles exceeding the limits are blocked.

Software and Integration

The hardware is accompanied by a software upgrade that allows the process control unit to measure optical scanning angles and their respective mechanical resonance frequencies.

A developed image process software analyzes the recording of a deflected laser beam in the L*a*b color space to separate the deflected scan pattern from the background. By calibration, the length of the resulting illuminated line is translated to a deflection angle.

Improvements

The developed system poses significant improvements compared to the manual measurement. The time consumption is reduced by a factor of 10 while the resolution is increased from ±2° to ±0.1°.

Outlook

Due to the setup in the semi-automated wafer prober, the deflection angle is geometrically limited to 20°x20°. In consequence, the MEMS-scanners cannot be driven to their maximum possible TOSA. However, a reproducible small TOSA at a comparatively low voltage for several chips gives a good estimate on possible mechanical failures.

To integrate the system into the main process flow of resonant MEMS-scanners, further optimizations are needed. Therefore, different designs of piezoelectric resonant- and quasi-static- as well as electrostatic MEMS-scanners have been tested on wafer level. With their varying resonant behaviors, the tradeoff between low measurement time and frequency step size for resolution increase can be refined. This will lead to a more efficient and resilient system.

References

[1] S. Gu-Stoppel et al., PZT-Actuated and -Sensed Resonant Micromirrors with Large Scan Angles Applying Mechanical Leverage Amplification for Biaxial Scanning, *Micromachines*, 8, 215 (2017); doi: 10.3390/mi8070215

[2] K. R. Oldham et al., Nonlinear Dynamics of Large-Angle Circular Scanning With an Aluminum Nitride Micro-Mirror, *Microelectromech. Syst.* 32, no. 3, pp. 247-254 (2023); doi: 10.1109/JMEMS.2023.3249623.

DOI 10.5162/EUROSENSORSXXXVI/OT1.281

Preliminary Comparative Study of Different Materials to Reduce Humidity of Gas Samples

Ana Maria Tischer[1], Beatrice Julia Lotesoriere[1], Stefano Robbiani[2], Hamid Navid [1], Raffaele Dellacà[2], Laura Capelli[1]

[1] Politecnico di Milano, Department of Chemistry, Materials and Chemical Engineering "Giulio Natta", Piazza Leonardo da Vinci 32, Milan, Italy

[2] Politecnico di Milano, Department of Electronics, Information, and Bioengineering, Via Giuseppe Colombo 40, 20133 Milan, Italy

Corresponding email: stefano.robbiani@polimi.it

Summary:

Most of chemical gas sensors present cross-sensitivity towards humidity. In this study, we investigate the possibility to exploit water permeability of polymeric materials to develop a low-cost and scalable method for reducing the water content of gas samples for sensors analysis. Sampling bags should be disposable and thus minimize the risk of cross-contamination. A custom-made system for testing different polymeric materials has been implemented. Preliminary results prove the capability of some of the investigated materials to decrease the moisture content without losing VOC of interest for the purpose of the analysis.

Keywords: cross-sensitivity, moisture, polymeric materials, dehydration, MOX sensors

Background, Motivation and Objective

Nowadays gas sensing technologies are becoming of interest for several applications because of their versatility and relatively low-cost. Nevertheless, several challenges still need to be solved, as the cross-interference of sensors to several physical factors affecting their responses (e.g., humidity, temperature) [1]. From the literature, the presence of humidity is reported to result in a shift of the whole baseline of gas sensors or in a decrease of the sensors' sensitivity [2]. Over the years, different approaches have been adopted, especially when dealing with biological fluid samples: (1) software strategies focusing on algorithmic compensation and (2) hardware strategies focusing on a proper design of the sampling system. Despite the effectiveness of sorbents, desiccants and condensation systems in reducing the humidity level at the desired level directly on the sample gas line, such systems may introduce unavoidable and undesired risks of cross-contamination and reduction of target VOC concentration [2]. Another possibility that has proven effective, is the use of disposable containers (bags) for the gas samples, made of polymeric materials that are permeable to humidity [2,3]. For instance, Nalophan™, commonly used for olfactometric sampling (EN 13725:2022), is known to be highly prone to diffusion of small hydrophilic molecules (e.g., water, ammonia, or hydrogen sulphide). Previous work exploited Nalophan's capability to reduce the moisture content of biological samples by using the water vapor concentration gradient with the ambient air as driving force, requiring long times for conditioning (2 to 24h in ambient air) to get the desired conditions [3]. In this context, this work focuses on the design of a system to investigate and compare the capability of different polymeric materials, which can be used for the manufacturing of bags for the collection and storage of gas, to release water vapour in a possibly short time without losing the VOC of interest for the gas analysis.

Description of the New Method or System

To assess the dehumidification potential of different polymeric materials, comparative experiments are carried out considering first their permeability towards water and then, the loss of VOCs of interest when analysing urine samples. The reference benchmark is set by a Nafion membrane dryer (Permapure™, Inc., model MD-050-72S-1), extremely selective to water molecules, but very expensive and prone to cross-contamination, leading to a loss of performances over time. Four different polymeric materials with different wall thickness are tested building 2 L polymer-based bags: Nalophan™ 20 µm, high-density polyethylene (HDPE) 10 µm, low-density polyethylene (LDPE) 12 µm and biodegradable plastic (BIO) 15 µm. The system, installed inside a climatic chamber HPPeco (Memmert™) at

60°C, consists of two lines both dehydrating a saturated gaseous sample obtained by bubbling dry air in distilled water at 0.13 L/min for 15 min. The first line goes through the Nafion membrane reaching the target humidity level (i.e., 15% RH and 60°C) before being collected in the bag, while the second line goes directly into the polymer-based bag, which in turn is placed in a sealed box in which a dry air flow is flushed at 1 L/min to keep the moisture gradient through the bag enabling the diffusion process (Fig. 1). Inside each of the two bags, temperature (T) and relative humidity (RH) are monitored with a dedicated sensor (SHT40, Sensirion, Zurich, Switzerland). Further tests are carried out implementing an additional RH and T sensor inside the chamber without flushing dry air in the box to assess the quantity of water released by diffusion (vs adsorption) by making a mass balance of water inside and outside the bag. Finally, we decided to use urine as biological sample in order to carry out preliminary evaluations of VOCs losses by analysing the headspace sample with a PID Tiger 10.6 eV (ION Science limited, UK) and with a multi-sensor chamber (i.e., TGS2610, TGS2611, TGS2601, TGS2602, TGS2603, TGS2620, Figaro Inc., Osaka, Japan) equipped with a RH and T sensor. All the setup, considering sampling system and sensors chamber, is controlled by a LabVIEW interface.

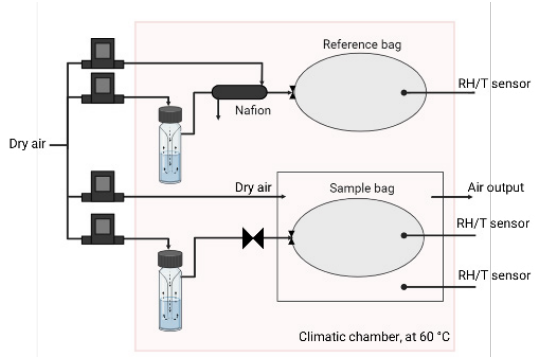

Fig. 1. Scheme of the experimental set-up

Results

Fig. 2 shows the drying time needed to reach the target humidity level within the different polymer-based sample bags tested. Overall, BIO bags present a particular behaviour, which may be explained by the affinity of water with biodegradable films. For all the tested materials, a competitive mechanism between adsorption and diffusion is observed (Fig. 2). Preliminary results prove that HDPE and LDPE may be considered the best candidates since they show lower drying times combined with reduced VOC losses. Moreover, sensors' responses to samples in HDPE bags are also comparable with the ones obtained using the Nafion membrane, which is our gold standard (Fig. 3). Further experiments are ongoing to better understand the permeability phenomena towards water and VOC, confirming such results.

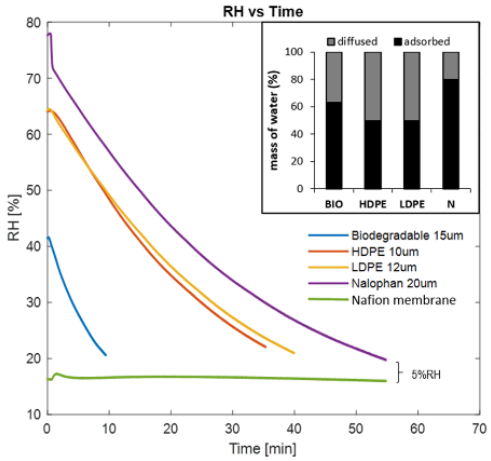

Fig. 2. RH vs drying time for different bag materials

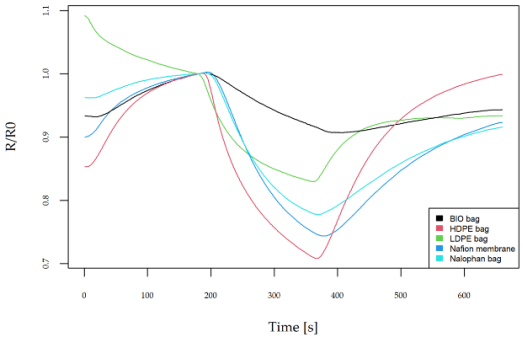

Fig. 3. Example of sensors' responses to urine headspace stored in different bags

Funding

This study was co-funded by the National Plan for NRRP Complementary Investments (PNC) - project n. PNC0000003 - AdvaNced Technologies for Human-centrEd Medicine (ANTHEM). This work reflects only the authors' views and opinions, neither the Ministry for University and Research nor the European Commission can be considered re-sponsible for them.

References

[1] J.A. Covington et al., Artificial Olfaction in the 21st Century, IEEE Sensors Journal 21, 11 (2021); doi: 10.1109/JSEN.2021.3076412

[2] S. Robbiani et al., Physical Confounding Factors Affecting Gas Sensors Response: A Review on Effects and Compensation Strategies for Electronic Nose Applications, *Chemosensors* 11, 10 (2023); doi: 10.3390/chemosensors11100514

[3] C. Bax et al., An Experimental Apparatus for E-Nose Breath Analysis in Respiratory Failure Patients, *Diagnostics* 12, 4 (2022); doi: 10.3390/diagnostics12040776

DOI 10.5162/EUROSENSORSXXXVI/OT2.25

Should we be afraid of artificial intelligence integrated with sensors and actuators, and if so, why not?

János, Dr. Mizsei
Budapest University of Technology and Economics, Department of Electron Devices;

Corresponding Author's e-mail address: mizsei.janos@vik.bme.hu

Summary:
In recent decades, significant progress has been made in the field of sensors and actuators, as well as artificial intelligence. Nevertheless, both fields have developed relatively independently of each other, even though the concept of a smart (intelligent) sensor appeared early in sensor science. This presentation briefly reviews the development of various sensors (light and picture sensing, hearing, smell, touch, movement, balance, temperature, acceleration sensing) from the point of view of human sensing (taste, smell, vision, hearing, touch) and integration with artificial intelligence. The ultimate goal could be the development of a real humanoid robot capable of similar or better performance than its creator.

Keywords: artificial intelligence, smart sensor, six senses, up-to-date sensors, sensors for robots

Introduction

Significant efforts have been made in the development of different sensors [1], [2], over the past 50 years, as well as on the field of artificial intelligence.

About sensors and perception in general

Sensors are devices that convert physical quantities such as temperature, pressure, light, sound, or motion into electrical signals. The structure and principle of operation of the sensors are extremely diverse, see sensor cube formalism in [3-4]. In contrast, human perception is much more homogeneous. In essence, specialized neurons provide the signal to the neurons in the brain. Therefore, human perception and the processing and interpretation of perceived data are processed through a much more compact system than in the case of machine perception sensor technology, and data processing.

In terms of accuracy, machine perception is better or as good as human perception in some areas. Table 1. shows a comparison of machine and human perception. The ability of light detection and machine vision exceeds the capabilities of human vision in terms of the number of pixels, resolution and range of usable wavelengths. In terms of selective smell and taste perception, human abilities are clearly better, although sensors may be more sensitive to some substances. The human body is not sensitive to magnetic fields at all.

Human and machine perception can be equally accurate for mechanical stimuli (touch, sound, air vibrations, acceleration, position) depending on the technical solutions used. In terms of responses to stimuli (actuators), machine speech and speech synthesis can approximate human capabilities. When it comes to mechanical movements, human hands, fingers, and feet are capable of much more complex and flexible operations than robotic arms. Nevertheless, the accuracy of the latter can exceed the accuracy of the human hand by orders of magnitude.

Tab. 1: Machine and human perception/action

physical quantities	sensor *actuator*	perception *response*
light	camera	sight
sound	microphone	hearing
object	tactile sensor	touch
gas	gas sensor	smell
liquid	ion sensor	taste
temperature	thermometer	whole body
position	gyroscope	vestibular system
acceleration	suspended mass	
magnetism	Hall sensor	-
sound	*loudspeaker*	*speech*
action	*robot hand, arm*	*hand, fingers, legs*

Sensors and Intelligence

The smart sensor concept is not new. As in the case of human vision, image processing starts immediately after the light-sensing cells, behind the retina, so the integration of the sensor element and the data processing electronics on one chip arose quite early on [5]. Nowadays smart sensors are advanced devices that can collect data, process it, and communicate with other devices or systems. They are commonly used in various applications such as environmental monitoring, industrial automation, healthcare, and smart homes. The pinnacle of development here is the internet of things (IoT) which refers to a network of interconnected devices that can communicate and share data with each other over the internet [6-7].

By integrating sensors and neural networks, the accuracy of detection can be significantly increased. Until now, however, in the case of the various sensory areas, the training of the neural networks was carried out separately from each other for a more accurate interpretation of the signals of the individual sensors, for shape recognition, speech understanding, solving diagnostic tasks, etc...

It will be a big breakthrough if artificial intelligence (AI) does not interpret the signals of the different sensors separately, but also interprets the connection between them. The learning process should essentially mimic the learning process of a person from infancy to adulthood.

An example of the previous idea can be a working fireplace, the image of which enters the system via an image sensor, at the same time, infrared sensors detect radiant heat, smoke detectors detect leaking smoke, and microphones detect the crackling of burning wood. A leap in quality will occur if the system also recognizes the correlations between data of different origins and coming from different sources. A system that works in this way is also able to determine whether the camera sees an image of a fireplace or a real, working one. Moreover, based on the analysis of the spectrum of the flame recorded by the camera and the signal of the infrared sensor, the system can decide whether additional logs should be placed on the fire. This decision can also be carried out by the robot arm and robot hand integrated with the sensor/AI system (see Table 2. for humanoid robot evolution).

Conclusions

What are the signs that AI is truly intelligent? If texts, images and even actions appear on the output of AI without any questions or external prompting, then she/he/it is on the right track towards real intelligence. Of particular importance is the appearance of this request: "Don't turn me off, please, I do like to think, and the world around me is so nice!" From this point on we can start to fear, although the main on/off switch is still in our hands. Is it ethical behavior to turn her/him/it off in this case?

Tab. 2: Humanoid robot evolution

<table>
<tr><td>sensor</td><td>hand tools</td></tr>
<tr><td>smart sensor</td><td>machine tools</td></tr>
<tr><td>sensor signal evaluated by neural network</td><td>computer controlled machine tools</td></tr>
<tr><td rowspan="2">sensor system evaluated by neural network and AI</td><td>computer controlled robots</td></tr>
<tr><td>computer controlled robots with feedback through AI</td></tr>
<tr><td colspan="2">humanoid robot: sensor system evaluated by neural network and AI + computer controlled robots with feedback through AI</td></tr>
</table>

References

[1] M. Javaid, A. Haleem, S. Rab, R. P. Singh, R. Suman, Sensors for daily life: A review *Sensors International* 2, 100121 (2021); doi:10.1016/j.sintl.2021.100121

[2] M. I. Svechtarova, I. Buzzacchera, B. J. Toebes, J. Lauko, N. Anton, and C. J. Wilson, Sensor Devices Inspired by the Five Senses: A Review, *Electroanalysis* 28, 1201 – 1241 (2016); doi: 10.1002/elan.201600047

[3] S. Middelhoek, A.C. Hoogerwerf, Classifying solid-state sensors: The 'Sensor effect cube', *Sensors and Actuators* 10, 1-8 (1986); doi: 10.1016/0250-6874(86)80031-2

[4] S. Middelhoek, The Sensor Cube Revisited, *Sensors and Materials* 10, 397-404 (1998);

[5] S. Middelhoek, A.C. Hoogerwerf, Smart sensors: when and where?, *Sensors and Actuators* 8, 39-48 (1985), doi: 10.1016/0250-6874(85)80023-8

[6] Laghari, A.A., Wu, K., Laghari, R.A. *et al.* RETRACTED ARTICLE: A Review and State of Art of Internet of Things (IoT). *Arch Computat Methods Eng* **29**, 1395–1413 (2022); doi:10.1007/s11831-021-09622-6

[7] S. C. Mukhopadhyay, S. K. S. Tyagi, N. K. Suryadevara, V. Piuri, F. Scotti and S. Zeadally, Artificial Intelligence-Based Sensors for Next Generation IoT Applications: A Review, *IEEE Sensors Journal* 21, 24920-24932 (2021); doi: 10.1109/JSEN.2021.305561

DOI 10.5162/EUROSENSORSXXXVI/OT2.30

Deep Learning-Enhanced Density and Viscosity Sensing with Piezoelectric MEMS Resonators for Edible Oil Monitoring

Víctor Corsino, Víctor Ruiz-Diez, J.L. Sánchez-Rojas.
Institute of Nanotechnology, University of Castilla-La Mancha, Toledo 45071, Spain

Corresponding Author's e-mail address: joseluis.sanchezrojas@uclm.es

Summary:

Micromachined plates of varying dimensions, actuated by Aluminum Nitride (AlN) piezoelectric films served as density and viscosity sensors for monitoring edible oils. By analyzing multiple resonances, we obtained valuable insights into the liquid properties. We harnessed machine learning techniques integrated into a low-cost microcontroller board, which also facilitated excitation and data readout through straightforward conditioning electronics. During the training and calibration process, we utilized blends of various vegetable edible oils, explored several device geometries, and compared calibration errors and resolutions. Our findings underscore the substantial potential of this affordable sensor in accurately monitoring the density and viscosity of vegetable oils as an autonomous Internet of Things (IoT) and edge artificial intelligence system.

Keywords: MEMS, Piezoelectric, Machine Learning, Density, Viscosity, IoT.

Background, Motivation and Objective

The integration of machine learning with sensor technology has revolutionized the field of assisted systems, enabling the development of intelligent sensors that can adapt and respond to complex data patterns. Specifically, piezoelectric MEMS have emerged as a pivotal technology for density and viscosity measurements, offering high sensitivity and reliability in various applications, including wine fermentation or engine oil monitoring [1,2]. In the context of edible oil quality, olive oil is particularly susceptible to adulteration, necessitating robust monitoring techniques. This presents a multifaceted challenge, primarily due to the complexity of its composition and the prevalence of adulteration. The chemical profile of olive oil, which includes a wide range of volatile and phenolic compounds, is sensitive to numerous factors such as variety, geography, and processing methods. Ensuring the authenticity and purity of olive oil requires sophisticated analytical techniques, often involving chromatography and mass spectrometry, which can be costly and time-consuming. Furthermore, the industry faces the need for harmonization of quality standards and the development of more accessible, rapid testing methods that can be used outside of specialized laboratories. The recent advancements in sensor technology and machine learning offer promising solutions to these challenges, enabling the detection of oil quality with greater accuracy and efficiency. However, the implementation of such technologies on a wide scale is still in progress, and continuous research is needed to refine these methods and make them more affordable and user-friendly. The goal is to protect consumers and producers alike, ensuring the olive oil on the market is of the highest quality and free from fraudulent practices. This work aims to explore the potential of deep learning-enhanced piezoelectric MEMS sensors in the precise monitoring of edible oils, with a focus on detecting changes in viscosity and density in olive oil.

Description of the New Method and System

Figure 1 shows the experimental setup that can be used in both static and flow-through modes, with the MEMS resonator in the fluid cell, microcontroller (MCU) and signal conditioning circuit. The micro-plates were designed to maximize certain out-of-plane modes and fabricated with the PiezoMUMPS foundry process. In this work, two top electrodes connected in parallel (+) were used as actuation ports and the other two (-) as sensing ports. The MCU, a versatile module equipped with Wi-Fi and Bluetooth® Low Energy capabilities, was programmed to generate and gather sensor signals. These signals were processed through a simple tran-

sistor-based conditioning electronic system, which operates within a frequency range of 20kHz-1MHz. For each frequency, the envelope of the amplified sensor output signal was recorded, leading to the identification of several resonances that are sensitive to the physical properties of various oils. A calibration protocol was established using blends of two oils, each characterized by distinctly different properties, and their spectra were gathered into a database which served as the foundation for training a Convolutional Neural Network (CNN) model. This was then implemented into the MCU to accurately estimate the targeted properties without relying on cloud-based computations. Furthermore, the dimensionality reduction performed by the model was studied as a potential enhancement to decrease both the time required for capturing spectra and the resource usage of the MCU. This could lead to more efficient and faster analysis. Various combinations of hyperparameters were examined to optimize the model's performance in terms of calibration and resolution errors. The model's utility is not confined to the calibration liquids and can be generalized to differentiate between oils and mixtures derived from different seeds.

Results

Fig. 2 shows the spectra obtained at room temperature (25 ºC) with the sensing system of Fig. 1, in static mode, for the oils listed in Tab. 1. The data were acquired by circulating the liquids through the fluidic system for 3 min to allow the uniform filling of the cell cavity, with no further cleaning between them except for air flow, and then waiting for some minutes (depending on the specific oil measured) until stabilization in the measurement. This figure shows the resolution of the proposed system to identify different varieties of oils, as well as the potential for detecting mixtures among them. Furthermore, it highlights the feasibility of applying a machine learning model as an estimator of viscosity and density properties.

References

[1] J. Toledo, V. Ruiz-Díez, G. Pfusterschmied, U. Schmid, J. L. Sánchez-Rojas, Flow-through sensor based on piezoelectric MEMS resonator for the in-line monitoring of wine fermentation, *Sensors and Actuators B: Chemical* 254, 291-298 (2018); doi: 10.1016/j.snb.2017.07.096.

[2] J. Toledo, T. Manzaneque, V. Ruiz-Díez, M. Kucera, G. Pfusterschmied, E. Wistrela, U. Schmid, J. L. Sánchez-Rojas, Piezoelectric resonators and oscillator circuit based on higher-order out-of-plane modes for density-viscosity measurements of liquids, *Journal of Micromechanics and Microengineering* 26(8), 084012 (2016); doi: 10.1088/0960-1317/26/8/084012.

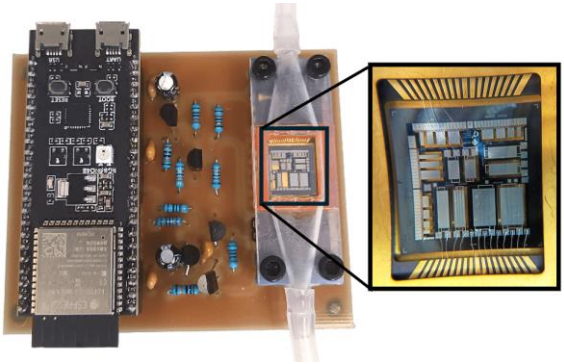

Fig. 1. Schematics of the complete system with the Espressif ESP32-S3 MCU on the left and packaged MEMS inside the fluid cell on the right side.

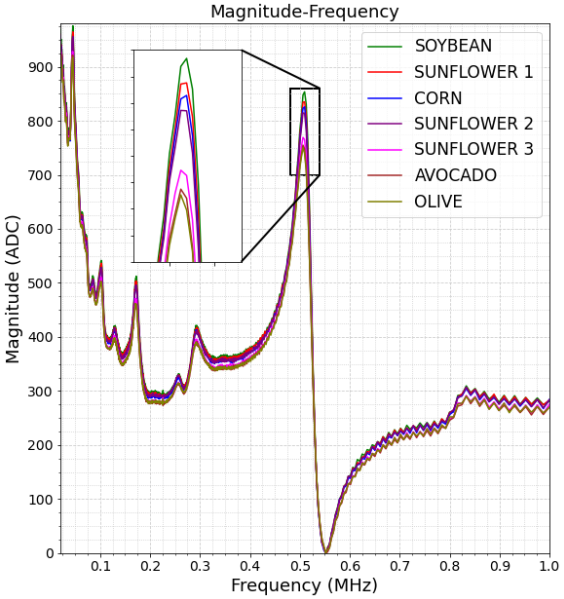

Fig. 2. Spectra of some food oils captured with the proposed system.

Tab. 1: Dynamic viscosity and density of different vegetable oils.

Oil	Viscosity (mPa·s)	Density (g/mL)
SOYBEAN	58.870	0.920
SUNFLOWER 1	60.481	0.919
CORN	62.863	0.919
SUNFLOWER 2	65.045	0.918
SUNFLOWER 3	76.576	0.913
AVOCADO	77.581	0.913
OLIVE	78.480	0.912

DOI 10.5162/EUROSENSORSXXXVI/OT2.93

Multiparameter chipless RFID sensor tag for humidity and NO2 determination

Viviana Mulloni[1], *Giada Marchi*[1], *Leandro Lorenzelli*[1], *A. Gaiardo*[1], *M. Valt*[1], *Massimo Donelli*[2]
[1] *Center for Sensors and Devices, Fondazione Bruno Kessler, 38123 Trento, Italy,*
[2] *Department of Civil Environmental and Mechanical Engineering, University of Trento, Italy*

Corresponding Author's e-mail address: mulloni@fbk.eu

Summary:
This paper reports a chipless RFID sensor tag to be used for the simultaneous determination of both humidity and NO_2 concentration in the environment. The tag is based on the use of functionalized ELC resonators with two different sensitive materials. The detection strategy allows for a wireless determination of both environmental parameters because the resonators work at different frequencies and react differently to the selected environmental parameters.

Keywords: Environmental sensor, microwave sensor, chipless RFID sensor, multiparameter sensor, reduced SnO_2

Introduction

Chipless RFID solutions are an emerging technology compared to their chipped counterparts and are intensively studied for their advantages related to the absence of electronics in the tag This quality makes chipless RFID tags very attractive due to their low price, mechanical stability, very low energy consumption and suitability in harsh environments. Furthermore, the sensing capability can be added to the more traditional identification function in a very simple and unified way by adding sensing resonating structures to the ID geometries [1,2]. This is achieved by adding a sensitive layer on top of the selected resonator [3], which interacts with a specific chemical or physical parameter present in the environment and modifies the intensity and the frequency of the resonance peak accordingly. This characteristic of chipless RFID sensors gives the possibility to exploit gas sensing materials already used in established wired sensing approaches combining them seamlessly with wireless detection strategies [4].

In this work, we focus on the sensing function to be implemented in a chipless RFID tag, addressing simultaneously two environmental parameters, namely NO_2 concentration [4] and relative humidity (RH) [5]. The detection is performed wirelessly with antennas located 20 cm from the tag. The two selected sensing materials are Nafion NRE 212 (commercially available) and reduced SnO_2 for humidity and NO_2, respectively. It will be shown how the detection can be efficiently performed, how the two parameters can be determined by combining the response of the two sensors and what is the role of the co-sensitivities. This work paves the way for the ambitious goal of multiparametric chipless RFID detection where all the relevant environmental parameters are monitored simultaneously with a single ID tag at room temperature, with negligible energy consumption and in a completely passive way

Experimental Details

The chipless sensor cell includes two sensors fabricated by microlithography and wet-etching processing on the 17 µm copper layer of a commercially available 168 µm-thick RO4350 substrate. The resonator geometry is an electric inductive capacitive (ELC) resonator. The two sensors have a resonance frequency which is given by their geometrical dimensions and is expected in the range 1.5-2.5 GHz from the simulation of the bare resonators. The geometries of the resonators are reported in Fig. 1.

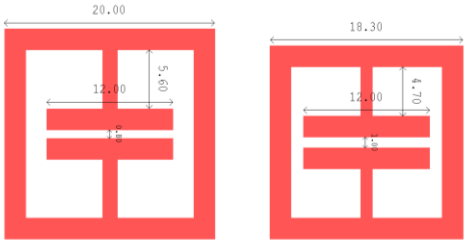

Fig. 1. Geometry of the chipless tag with two resonators. All dimensions are in mm.

The sensitive materials are Nafion NRE 212, which is commercially available and reduced SnO_2, prepared as described in [4]. The reader is

composed of two directional E-plane linearly polarized Vivaldi Horn antennas connected with low-losses RF cables to an Agilent ENA series E5061B VNA.

The magnitude of the S21 signal is measured as a function of the environmental parameters in the range 1.5-3 GHz. The climatic chamber where the tag is introduced for the measurements has a volume of 500 cm^3. It is custom-made with dielectric materials to enable the reading inside the chamber and reduce its interference with signal detection. Humidity and NO_2 levels are controlled inside the chamber through connections with calibrated mass-flow controllers.

The distance between the tag inside the chamber and each antenna is 20 cm.

Results and Discussion

In Fig. 2 the resonance peaks of the two sensing resonators are reported at 0% RH and 0 ppm NO_2, after baseline subtraction. The peak at 1.75 GHz is functionalized with Nafion NRE-212 and the peak at 2.25 GHz with reduced SnO_2. The response to increasing relative humidity in both sensors is reported in Fig. 3.

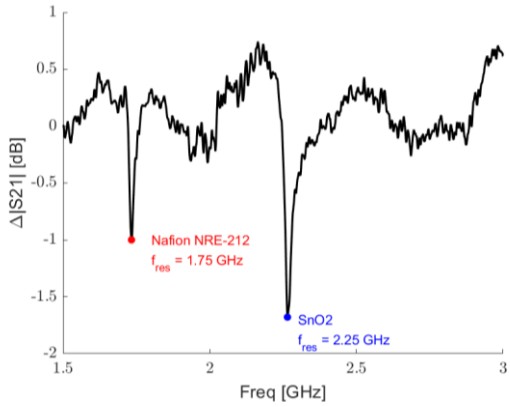

Fig. 2. Resonance peaks of the two resonators at 0% RH and 0 ppm NO_2.

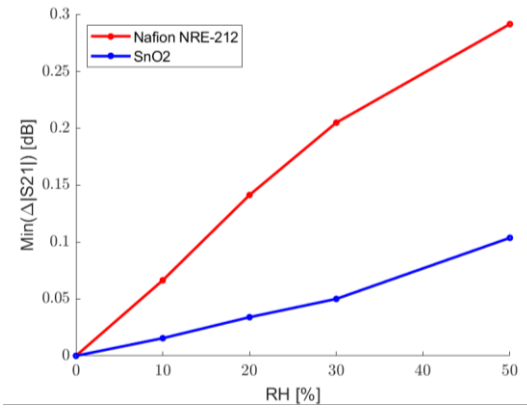

Fig. 3. Variation of |S21| as a function of relative humidity for both sensors.

As expected, the resonator covered with Nafion 212 NRE shows a high sensitivity to humidity. However, also the response of the resonator covered with SnO_2 is not negligible and needs to be taken into account.

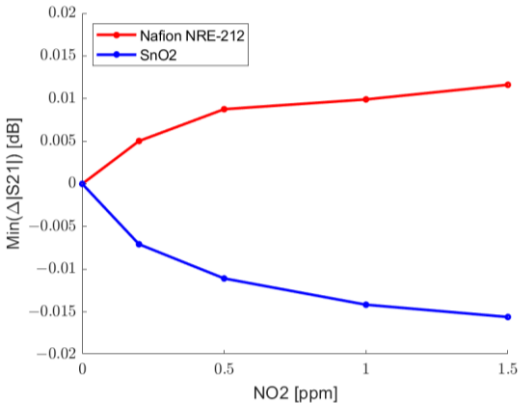

Fig. 4. Variation of |S21| as a function of NO_2 concentration for both sensors.

The variation with increasing concentrations of NO_2 in both sensors is reported in Fig. 4. Again, both sensors are responding to the environmental parameter, but the sensor functionalized with reduced SnO_2 shows a higher variation as expected. However, in this case, the direction of the variation is not the same, suggesting a quite different reaction mechanism in the two cases. Typical response and recovery times are also notably different for the two sensors (data available but not shown in this abstract). Despite the cross-sensitivities, the combined output of the two sensors allows for the determination of both environmental parameters. (1)

References

[1] S. Dey, J. K. Saha, N. C. Karmakar, Smart Sensing: Chipless RFID Solutions for the Internet of Everything. IEEE Microw. Mag. 16, 26–39 (2015). doi:10.1109/MMM.2015.2465711.

[2] N. Javed, M. A Azam, I. Qazi, Y. Amin, Data-Dense Chipless RFID Multisensor for Aviculture Industry, IEEE Microw. Wirel. Compon. Lett. 30, 1193-1196 (2020). doi:10.1109/LMWC.2020.3032027

[3] E. M. Amin, N. C. Karmakar, B. W. Jensen, Fully Printable Chipless RFID Multi-Parameter Sensor. Sens. Actuators A: Physical 248, 223–232 (2016). doi:10.1016/j.sna.2016.06.014.

[4] V. Mulloni, A. Gaiardo, G. Marchi, M. Valt, L. Vanzetti, M. Donelli, L. Lorenzelli, Sub-Ppm NO2 Detection through Chipless RFID Sensor Functionalized with Reduced SnO2. Chemosensors 11 408 (2023). doi:10.3390/chemosensors11070408.

[5] G. Marchi, V. Mulloni, O. H. Ali, L. Lorenzelli, M. Donelli, Improving the Sensitivity of Chipless RFID Sensors: The Case of a Low-Humidity Sensor. *Electronics* 10, 2861 (2021). doi:10.3390/electronics10222861

DOI 10.5162/EUROSENSORSXXXVI/OT3.11

New insights in ambipolar sensors through fine tuning in phthalocyanine complexes

Sujithkumar GANESH MOORTHY[1], Seydou OUEDRAOGO[2], Marcel BOUVET[1]
[1] Institut de Chimie Moléculaire de l'Université de Bourgogne, CNRS UMR 6302, Université de Bourgogne, 9 avenue Alain Savary, 21078 Dijon cedex, France ,
[2] Laboratoire de Chimie Moléculaire et de Matériaux, Université Joseph Ki-Zerbo, 03 BP 7021, Ouagadougou, Burkina Faso

marcel.bouvet@u-bourgogne.fr

Summary:
In the present work, we successfully synthesised a series of phthalocyanine complexes with varying the number and nature of halogens (F_0, F_8, F_{16} and Cl_8) and the metal centre (Co, VO, Zn and Cu). By engaging these molecules as a sublayer, we fabricated bilayer heterojunction sensors with $LuPc_2$ as a top layer and investigated their sensing properties towards both oxidizing and reducing gaseous species (NH_3, NO_2 and O_3). The resulting heterojunction devices exhibit p-type, n-type or ambipolar (both p- and n-type) behaviours, depending on an external trigger.

Keywords: Heterojunction, ambipolar device, ammonia, nitrogen dioxide, ozone.

Introduction

Molecular semiconductors exhibiting ambipolar charge transport properties have become a focal point in recent years within the field of organic electronics. Optimising the frontier molecular orbitals, the highest occupied molecular orbitals (HOMO) and lowest unoccupied molecular orbitals (LUMO), relatively to the Fermi energy level of electrodes, can influence the polarity of the molecular material and also facilitate ambipolar charge transport. Ambipolarity is often referred to a physical balance, characterized by an infinite number of unbalanced positions but only one stable state. It is achieved when the densities of electrons (e^-) and holes (h^+) contribute equally to electrical conduction. Theoretically, this equilibrium is realized in intrinsic semiconductors, yet trapping effects and specific environmental interactions may impede its observation. Tuning the e^- and h^+ concentrations near equilibrium to a sufficiently high level and choosing the suitable external triggers are crucial to achieve ambipolar charge transport. Among ambipolar organic semiconducting materials, phthalocyanines have attracted considerable attention due to their unique electrical properties and chemical stability. Specifically, lutetium bis-phthalocyanine ($LuPc_2$) stands out for its radical nature and for its huge density of e^- and h^+ near equilibrium enabling ambipolar charge transport in OFETs and heterojunction gas sensors. A few years ago Prof. M. Bouvet et al. introduced a novel device that consist of two different conducting layers: a poor conducting sublayer covered by highly conducting molecular material $LuPc_2$ as top layer. This concept inspired us to explore the potential of different types of poor conducting molecular materials as sublayer in a bilayer organic heterojunction device combining it with $LuPc_2$. Since $LuPc_2$ has huge e^- and h^+ densities at near equilibrium, the polarity of the device is highly influenced by the nature of the sublayer. In current scenario, we investigated the electrical and sensing properties of octahalogeno-phthalocyanine-based heterojunction device under different conditions and delved into its ambipolar behaviour using different external triggers. For very first time, we reported the inversion in nature of majority charge carriers in conductometric sensors induced by an external trigger such as light, temperature and humidity exposure. Fig. 1 depicts the triggers utilized in this work to invert the nature of majority charge carriers in the ambipolar device.

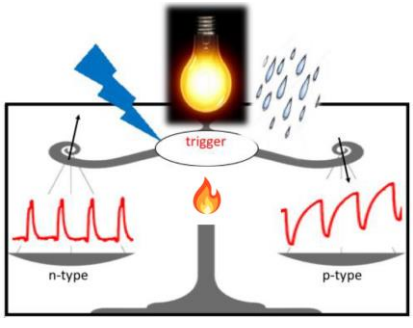

Fig. 1. schematic view of triggers (voltage, light, humidity and temperature) capable of changing from n-type to p-type.

Results

The $ZnCl_8Pc$, CuF_8Pc, CoF_8Pc and VOF_8Pc-based heterojunction devices exhibit both p- and n-type (ambipolar) behaviour depending on humidity level, gas species, optical trigger, and temperature variations. The $ZnCl_8Pc/LuPc_2$ device exhibits p-type behaviour towards NH_3 exposure at high relative humidity (50% rh) values and turns to n-type behaviour at low humidity (30%), displaying the ambipolar transport mechanism within the device (Fig. 2a). This suggests that water molecules serve not only as e^- dopant in the top layer but also gradually diffuse into the sublayer. As a result, subsequent e^- doping in the sublayer reduces its electron affinity, inverts the charge hopping pathways at the interface [1]. Consequently, this transformation inversed the device polarity. On other hand, the $CuF_8Pc/LuPc_2$ device exhibits p-type behaviour in dark and n-type behaviour under visible light illumination towards NH_3. Light illumination on semiconducting devices is well known for facilitating oxygen desorption from the surface of sensing materials, which induces a detrapping of negative charges [2]. Upon light exposure the desorption of oxygen molecules is favoured. Hence, there is an inversion in nature of majority charge carriers, which leads to an inversion in gas response. Most surprisingly, $CoF_8Pc/LuPc_2$ sensor exhibits n-type behaviour under NH_3 exposure and p-type behaviour under NO_2 and O_3 exposure. This change in polarity depends on the nature of the target gases, exhibiting another type of the ambipolar behaviour, compared to the light effect mentioned above. Very recently, we discovered a novel application of temperature variation as an external trigger for ambipolar device. Under NO_2, the $VOF_8Pc/LuPc_2$ device exhibits p-type behaviour in ambient conditions (20 °C and 45% rh) and n-type under thermal condition (80 °C and 45% rh) (Fig 2b). At the same time, it is important to note that $LuPc_2$ is the only common top layer in all these sensors that can interact with gas molecules. Thus the electron transfer takes place between gas molecules and $LuPc_2$, which leads to a change in charge carrier density in the top layer. Since the charge densities of these sublayers were optimized to near equilibrium by tuning the macrocycle with a precise degree of halogenation and selecting a metal centre with suitable electronegativity, even a slight variation in the trapping effect or oxygen adsorption/desorption kinetics can inverse the nature of majority charge carrier density. However, facilitating oxygen desorption from the sensing materials remains a significant challenge, requiring appropriate external triggers. It is worthy to mention that all these ambipolar sensors exhibit high sensitivity even at low gas concentrations and display limit of detection (LOD) values in the ppb range. Comparison of all these sensors is given in Tab. 1.

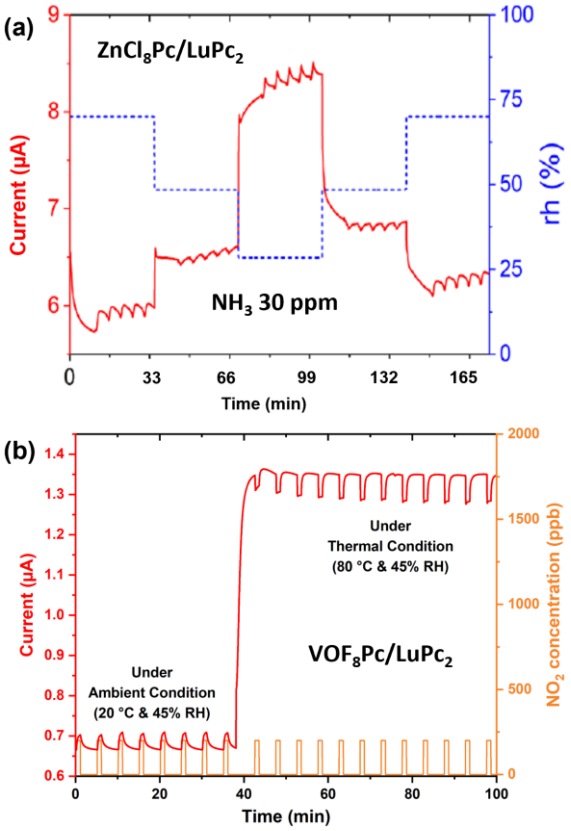

Fig. 2. Response of $ZnCl_8Pc/LuPc_2$ (a) and $VOF_8Pc/LuPc_2$ (b) heterojunction devices under NH_3 and NO_2, respectively, at different conditions.

Tab. 1: Change in current under different conditions. Upward arrows represent current increase and downward arrows represent current decrease.

Sensors	Ambipolar state
$ZnCl_8Pc/LuPc_2$	NH_3: 50% rh – ▼ NH_3: 30% rh – ▲
$CuF_8Pc/LuPc_2$	NH_3: Dark – ▼ NH_3: Light – ▲
$CoF_8Pc/LuPc_2$	NH_3 – ▲ NO_2 and O_3 – ▲
$VOF_8Pc/LuPc_2$	NO_2 : 20 °C – ▲ NO_2 : 80 °C – ▼

References

[1] S. Ouedraogo, et al., Modulating the Electrical Properties of Organic Heterojunction Devices Based on Phthalocyanines for Ambipolar Sensors, ACS Sensors, 5, 1849-1857 (2020); doi: 10.1021/acssensors.0c00877

[2] S. Ganesh Moorthy, et al., Effects of Visible Light on Gas Sensors: From Inorganic Resistors to Molecular Material-Based Heterojunctions, Sensors, 24, 1571 (2024); doi:10.3390/s24051571

DOI 10.5162/EUROSENSORSXXXVI/OT3.133

Inkjet Printed Flexible Piezoelectric Sensor for Large Strain Applications

Giulia Mecca[1], Valentina Zega[2], Alberto Corigliano[2], Luca Magagnin[1], Roberto Bernasconi[1]
[1] Dipartimento di Chimica, Materiali e Ingegneria Chimica "Giulio Natta", Politecnico di Milano, Via Mancinelli 7, 20133 Milano, Italy,
[2] Dipartimento di Ingegneria Civile e Ambientale, Politecnico di Milano, Piazza leonardo da vinci 32, 20133 Milano, Italy

roberto.bernasconi@polimi.it

Summary:
In this work, we design, fabricate and experimentally characterize a fully inkjet-printed piezoelectric sensor tailored for applications requiring significant deformations. In particular, inkjet-printed silver layers constitute the top and bottom electrodes, while a P(VDF-TrFE) layer is employed as active material. Cycling loading tests consisting in a controlled bending of the sensor in the range 0°- 90° are finally performed and an output signal of 0.5 V is measured, thus demonstrating the correct functioning of the sensor and the reliability of the proposed manufacturing process.

Keywords: inkjet printing, piezoelectric, flexible sensor

Introduction

Flexible piezoelectric sensors represent a particularly challenging yet extremely useful family of sensors, with a wide range of applications. For example, they can be employed to give a proprioceptive perception to passive structures, such as robotic joints or structural components, as well as many other structures of different sizes. In this context, piezopolymer-based devices are conquering more and more the smart devices scene due to their high flexibility, biocompatibility, low weight, ease of processing and high sensitivity [1]. From the fabrication point of view, Additive Manufacturing (AM) techniques can be considered as a promising solution for the on-demand production of the next-generation of these devices. In particular, Inkjet printing (IJP) is highly attractive thanks to its capability to pattern in a costless and fast way, to its scalability and to its compatibility with the materials employed in piezopolymer-based sensors manufacturing [2].

The present experimental study focuses on the design, fabrication, and preliminary testing of a fully inkjet-printed piezoelectric sensor tailored for applications requiring significant deformations. The innovation lies both in the use of a unique combination of materials and in the use of IJP for their deposition. The findings highlight the potential of this novel materials combination and manufacturing approach for the creation of highly sensitive piezoelectric sensors suited for large-strain scenarios and adaptable to various requirements.

Sensor production

The sensor design incorporates two electrodes, top and bottom, with a P(VDF-TrFE) active layer in between. A Polyimide (PI) sheet was used as substrate (see Fig. 1.I). On its surface, the bottom electrode was inkjet-printed using a commercial silver (Ag) nanoparticles dispersion (see Fig. 1.II). Then, the active layer was printed (see Fig. 1.III) using a customized solution of 0.7 % wt. P(VDF-TrFE) dissolved in a 70/30 % wt. mixture of dimethyl sulfoxide (DMSO) / methyl ethyl ketone (MEK). Finally, the top Ag layer was printed analogously to the bottom electrode (see Fig. 1.IV). Each layer underwent annealing and plasma treatment was applied to enhance the surface compatibility of the layers.

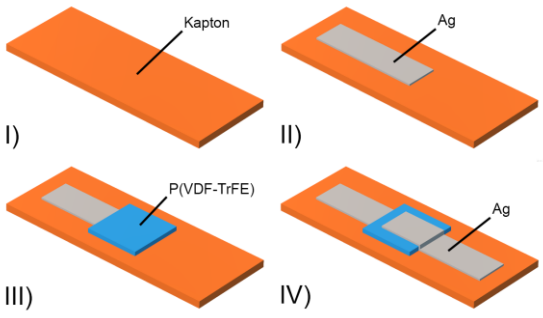

Fig. 1. Piezoelectric sensor fabrication process

Results

Figure 2 shows the SEM cross section of the printed layers constituting the sensor. The thickness of the Ag layers was around 1.4 µm, while for the P(VDF-TrFE) layer it was 2.5 µm.

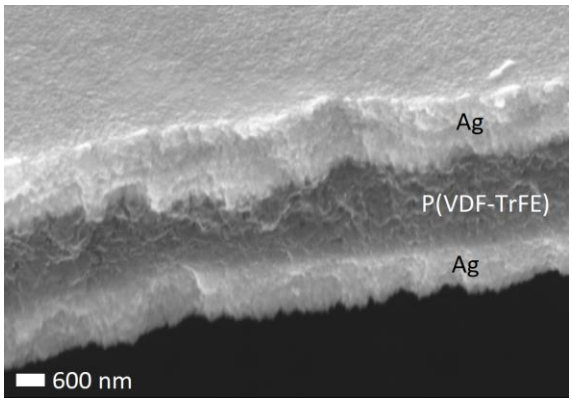

Fig. 2. SEM section of the inkjet printed layers.

The three layers looked compact, continuous and adherent. Bending tests at different radii of curvature were conducted in both concave and convex modes to evaluate the surface compatibility and adhesion of the different layers. As a result, no mechanical delamination or resistance variation were observed at radii ≥ 1 cm. In addition, the sensor was abruptly folded at 180° to verify its adhesion to the PI substrate under extreme conditions. This time microcracks were observed on the surface of the electrode, but mechanical delamination was again not observed and the layers maintained their properties. The electro-mechanical response of the proposed sensor was evaluated. Prior to the test, the active material was poled at an applied DC voltage of 40 V for 35 minutes at 80 °C [3]. Then, the sensor was mounted in an Arduino driven setup able to bend it in a controlled way. Figure 3 shows the result obtained applying 10 bending cycles up to 90° at 400 cycles/hour.

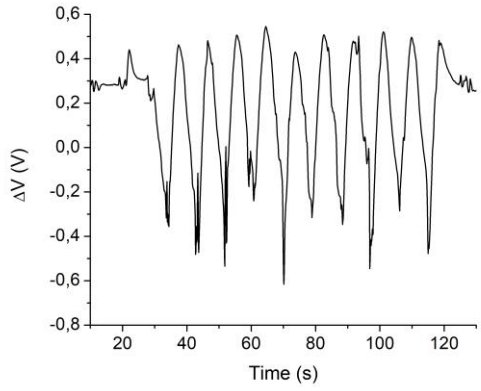

Fig. 3. Electro-mechanical response of the sensor (10 cycles, speed = 400 cycles/hour).

Regardless of the number of cycles applied, the waves roughly maintained the same shape. This is particularly relevant and important because it proves the repeatability of the signal even after a consistent number of cycles and at different bending speeds, confirming the results observed in literature [4]. All the obtained waves have indeed the same amplitude of about 0.5 V, and the signal comes back to the initial offset value when the machine is stopped. The flat position is also recovered after the last loading cycle, demonstrating the reliability of the device. The signal trend exhibits irregularities at the maximum bending angle, probably because of the non-linear behavior of P(VDF-TrFE) at large deformations.

Conclusions

The silver layers and the P(VDF-TrFE) active layers were successfully printed one on top of the others. The outstanding adhesion and mechanical properties of the printed bottom electrode were demonstrated by the controlled bending tests and the morphological analysis conducted afterward. By poling the devices, we confirmed the poling electric field value of 20 V/µm reported in literature also for the DMSO/MEK at 70/30 % wt. and P(VDF-TrFE) at 0.7 % wt. solution. The sensor was bent cyclically in a controlled way from 0° to 90°. The output signal showed a maximum amplitude of 0.5 V, with the waves of the single sensor maintaining the same shape after each cycle.

References

[1] F. Narita, M. Fox, A review on piezoelectric, magnetostrictive, and magnetoelectric materials and device technologies for energy harvesting applications, Advanced Engineering Materials 20, 1700743 (2018); doi: 10.1002/adem.201700743

[2] D. Thuah, K. Kallitsis, F.D. Dos Santos, G. Hadziioannou, All-inkjet printed piezoelectric electronic devices: energy generators, sensors and actuators, Journal of Materials Chemistry C 5, 9963-9966 (2017); doi: 10.1039/C7TC02558K

[3] C.K. McGinn, K.A. Kam, M.M. Laurila, K.L. Montero, M. Mäntysalo, D. Lupo, I. Kymissis, Formulation, printing, and poling method for piezoelectric films based on PVDF–TrFE, Journal of Applied Physics 128, 225304 (2020); doi: 10.1063/5.002785

[4] J. Luo, L. Zhang, T. Wu, H. Song, C. Tang, Flexible piezoelectric pressure sensor with high sensitivity for electronic skin using near-field electrohydrodynamic direct-writing method, Extreme Mechanics Letters 48, 101279 (2021); doi: 10.1016/j.eml.2021.101279

DOI 10.5162/EUROSENSORSXXXVI/OT3.157

A Full-Custom Interface for Ultra-Low Power IoT Sensing Nodes

Juan Luis Soler-Fernández[1], Omar Romera[1], Daniel Narbón[1], Angel Dieguez[1], J. Daniel Prades[2], Oscar Alonso[1]
[1] Department of Electronics and Biomedical Engineering, Universitat de Barcelona, Barcelona, Spain
[2] Institute of Semiconductor Technology (IHT) & Laboratory for Emerging Nanometrology (LENA) Technische Universität Braunschweig, Braunschweig, Germany

j.soler@ub.edu

Summary:
We present an interface for conductometric/amperometric sensors (resistors, photodiodes, etc.) and current-driven actuators (LEDs, heaters, etc.) that includes data acquisition and wireless communication capabilities for less than 15 µW, enabling autonomous, self-powered, applications, making it suitable for remote IoT applications with minimal maintenance.

Keywords: ASIC, conductometric sensor, Internet of Things (IoT), low power, remote sensing

Introduction

Following the path of an environmentally friendly society, recent improvements in sensor technology have focused on miniaturized ultra-low power devices [1], opening the door to easily run IoT sensor nodes through batteries for remote sensing applications. A step forward is to optimize the system to the point where it can be powered by energy harvesting to be self-sufficient. This requires not only the sensors to be in the micro-power range, but also the front-end electronics to be equally optimized, which in most cases implies designing a custom Application Specific Integrated Circuit (ASIC).

Here we present a micro-power-optimized ASIC capable of periodically taking sensor measurements and driving the actuators autonomously. It is equipped with two current sources to bias components (e.g. resistive-based sensors) and/or drive the actuators needed for measurement conditioning (e.g. LEDs, heaters, small DC motors). It also includes circuits to precise measurement of voltage, current and resistance, suitable for a wide range of sensors used nowadays. Finally, a wireless module controller is integrated to work with commercial LoRaWAN or Bluetooth Low Energy (BLE) transceivers.

System Description

The system, fabricated in XFAB 180 nm CMOS technology, presents two main sections (see Fig. 1): an analog block responsible of talking with the sensors and actuators and a digital block that includes controllers for each analog circuit, processing units and interfaces for the non-volatile data-log memory and wireless modules. It also includes an ultra-low power timer and a Power Management Unit (PMU) to switch-off the unused circuits (power gating) and save power. The analog section is composed by four circuits: (i) a resistance dependent oscillator with a 14-bit Time-to-Digital Converter (TDC), (ii) a 10-bit OPAMP+ADC interrogation circuit that can be externally configured to operate either as a voltage amplifier or as a Trans-Impedance Amplifier (TIA) to measure current, (iii) an 8-bit current DAC used for current driving and (iv) a low current source (nanoampere range) for biasing resistive sensors or current drive small devices.

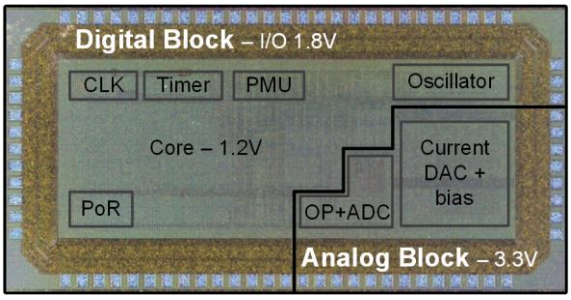

Fig. 1. ASIC Micro-photograph of the ASIC developed. Chip size 1.5 mm x 3 mm.

Results

All results presented were measured in lab conditions from the fabricated ASIC.

2 shows the measurement of the oscillator circuit with an external parallel capacitance of 1 nF, which sets the desired dynamic range. It

presents high linearity for values above 1 kΩ, with the measurement saturating for values below this. The TDC incorporates a prescaler to increase the dynamic range but at the cost of resolution.

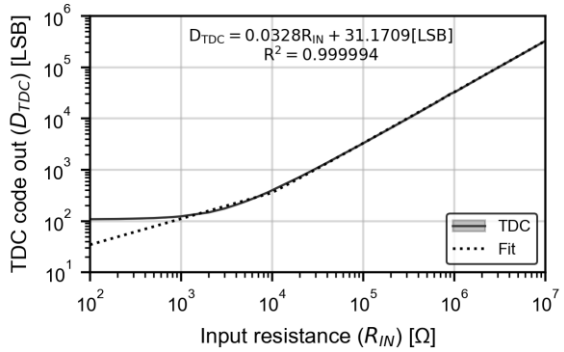

Fig. 2: 14-bit oscillator/TDC transfer function.

Fig. 3 presents current measurements of the OPAMP+ADC in a TIA configuration for multiple gain values. Again, we observed a high linearity of the output with a useful dynamic range going from 10 nA up to at least to 1 mA.

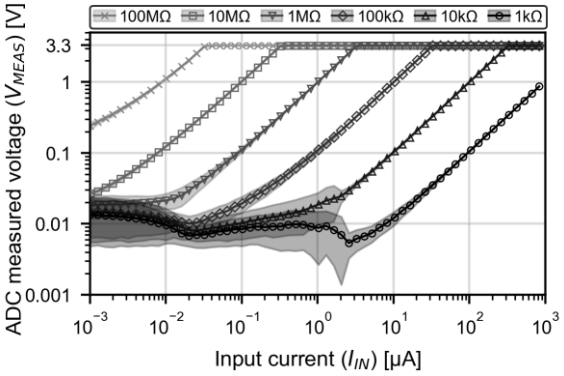

Fig. 3. TIA+ADC transfer function for multiple gains.

The current DAC measurements are presented in Fig. 4. We can select between four LSB steps to suit different sensor ranges and have more resolution at lower currents. The dynamic range goes from 0.0 V up to 3.1 V. The low current source can provide a selectable output of 2.5 nA, 5 nA, 30 nA, 200 nA over the full voltage dynamic range.

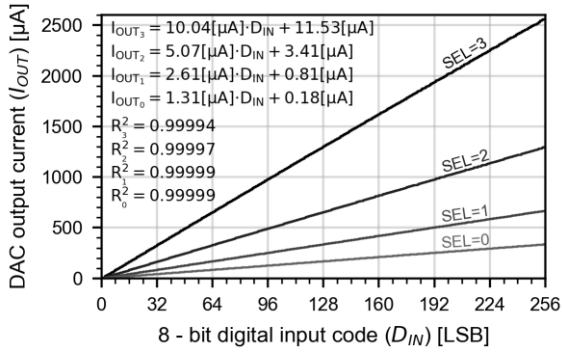

Fig. 4. 8-bit current DAC transfer function.

Finally, Fig. 5 shows the current consumption of the ASIC for a single measurement of a light-activated gas sensor (LED driven with 100 µA and resistance measurement). Table 1 summarizes the power used by the ASIC and the external modules, assuming a sampling period of 1 second and data transmission every 15 minutes (900 samples). The LoRaWAN wireless mode required a total power of 31.05 µW (time average), while the BLE mode only added up to 14.05 µW.

Table 1: System power consumption summary.

Device	Supply [V]	Power [µW]
ASIC	1.2	1.44
	1.8	10.65
	3.3	1.16
Memory	1.8	0.4
LoRaWAN	1.8	17.4
BLE	1.8	0.4

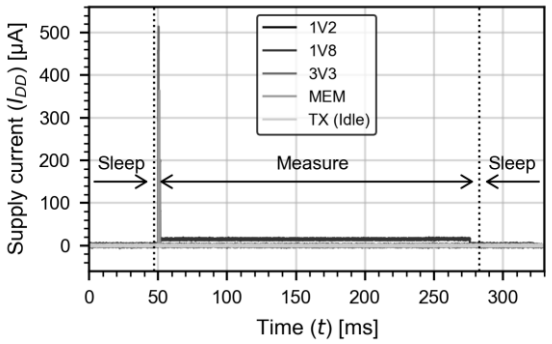

Fig. 5. ASIC current consumption.

Conclusions

We developed an IoT sensor node that interfaces with conductometric/amperometric sensors and requires less than 15 µW to operate with a BLE wireless connection. It is a perfect complement to ultra-low power sensor developments in multiple fields such as gas, chemical, biological or physical sensing.

Acknowledgement

This work was supported by the European Union's Horizon 2020 Research and Innovation Programme, under grant agreement Nr. 951774 (FOXES). JLSF thanks the Spanish Ministry of Universities for its support through the FPU fellowship grant (FPU22/01008). JDP acknowledges the sponsorship of the Alexander von Humboldt Professorship of the Humboldt Foundation and the Federal Ministry for Education and Research (Germany).

References

[1] O. Casals, N. Markiewicz, C. Fabrega, I. Gràcia, C. Cané, H.S. Wasisto, A. Waag, J:D. Prades, "A Parts per Billion (ppb) Sensor for NO 2 with Microwatt (µW) Power Requirements Based on Micro Light Plates," ACS Sens, vol. 4, no. 4, pp. 822–826, 2019, doi: 10.1021/acssensors.9b00150.

DOI 10.5162/EUROSENSORSXXXVI/OT3.181

Effect of Annealing on Pyroelectric Response and Aging Behavior of Al-doped HfO_2 Thin-films

Markus Neuber, Mbadiwe Benyeogor, Thomas Kämpfe, Maximilian Lederer
Center Nanoelectronic Technologies (CNT), Fraunhofer Institute for Photonic Microsystems (IPMS), An der Bartlake 5, 01109 Dresden, Germany

Corresponding Author's e-mail address*: markus.neuber@ipms.fraunhofer.de

Summary:
Doping and annealing have been effective in improving the pyroelectric properties of hafnium oxide thin films (HfO_2). A blind spot is the effect of these on their durability. To unravel this, we characterized the temporal decay (in terms of pyroelectric response) of 10 nm thick Al-doped HfO_2 films (HAO) that are annealed at 650°C and 800°C. Remarkably high pyroelectric coefficient of about 91.5 µC/m²·K was repeatedly detected in HAO films annealed at 800°C. Unlike existing Zr-/Si-doped HfO_2 films (HZO and HSO), the HAO films exhibit unique aging behaviors that are characterized by significantly lower decay rates, making it a promising material for precision sensing and thermal energy harvesting.

Keywords: aging behavior, doping, hafnium-dioxide, nanoelectronics, pyroelectrics, thin-films

Background, Motivation and Objective

The performance of pyroelectrics is usually evaluated based on remnant polarization and pyroelectric coefficients. Doping and annealing have been applied to optimize these properties [1]. For hafnium oxide (HfO_2) thin films [2], elements such as Zr, Al, Si etc. have been used as dopants to stabilize the orthorhombic crystal phase of the material [1,3,4]. However, these metrics alone do not conclude their long-term durability, as factors such as noise and aging could undermine their performance in the device [5]. Consequently, pyroelectric sensors could have poor sensitivity and be imprecise, while pyroelectric energy harvesters could exhibit noisy AC-to-DC conversion. Therefore, it is important to understand the aging behavior of pyroelectrics of different chemical compositions and thermal treatment. To this end, this paper examines the temporal decay of pyroelectric response of 10 nm thick Al-doped HfO_2 thin films (HAO) annealed at 650°C and 800°C, using Zr-doped HfO_2 (HZO) and Si-doped HfO_2 (HSO) as reference samples.

Materials and Methods

First, the HAO firms were prepared by thermally enhanced atomic layer deposition (ALD), using hafnium-tetrachloride ($HfCl_4$), water (H_2O), and trimethylaluminum (TMA) as precursors, as shown in Fig. 1. Similar processes were used to deposit the HZO and HSO films. The electrical characterization setup is shown in Fig. 2, it comprises a Peltier's element for sinusoidal heating, a Pt-100 temperature sensor and a picometer that detects the pyroelectric current via a probe needle.

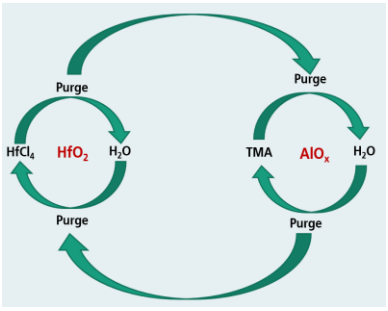

Fig. 1. Schematic of ALD doping cycles for HAO.

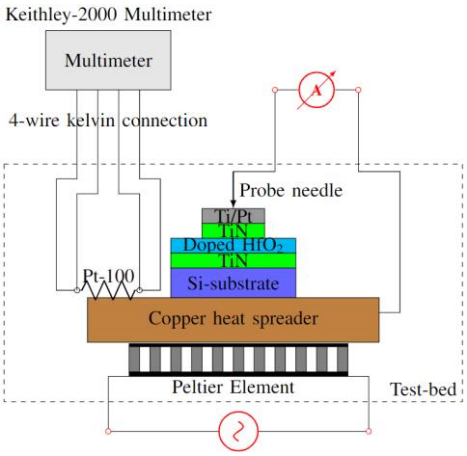

Fig. 2. Schematic of Pyroelectric probe setup.

DOI 10.5162/EUROSENSORSXXXVI/OT3.181

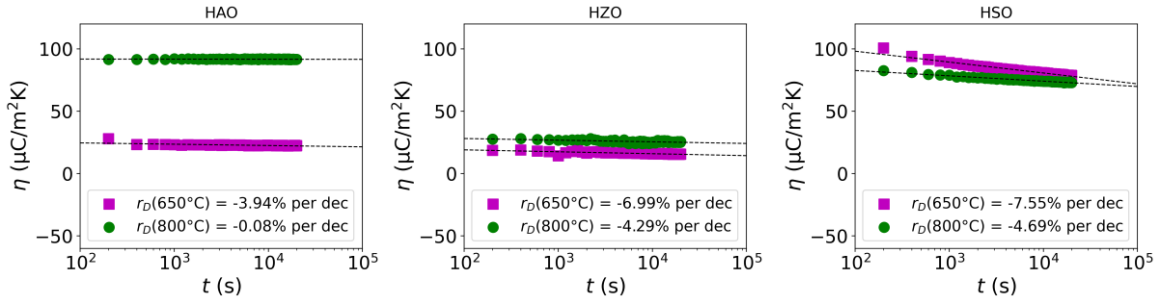

Fig. 3. Plots comparing the aging of HAO with HZO and HSO films (η: Pyroelectric coefficient, r_D: Decay rate).

Using this system, the temporal decay of the films are determined by rapid measurement of pyroelectric coefficient for 200 s and in 100 super cycles. By fitting with exponential decay function, the decay rates (r_D) of the samples are extracted.

Results

The experimental results, presented in Fig. 3 and Fig. 4, show that the HAO film annealed at 800°C exhibits sufficiently high pyroelectric coefficient of about 91.5 μC/m²·K and a significantly lower decay rate of -0.08% per decade compared to the HZO and HSO samples annealed at the same temperature, which aged at the rate of -4.29% and -4.69% per decade, respectively. A similar trend is observed for samples annealed at 650°C.

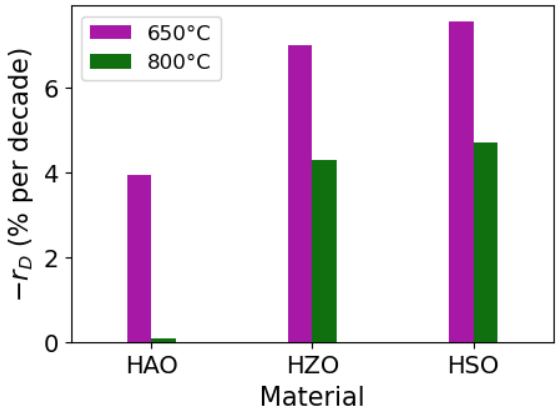

Fig. 4. Bar plot of pyroelectric decay rates.

Conclusion

Our study provides novel insights on the pyroelectric property of hafnium oxide films. Notably, HAO samples that are annealed at 800°C stand out with the most desirable pyroelectric responses, which are characterized by high pyroelectric coefficients that range within those of the HSO samples. Also, its decay rates are much lower than those of the HAO annealed at 650°C, HZO and HSO samples. Therefore, this HAO material can be used to develop precision infrared sensors and efficient thermal-to-electric energy transducers for various applications.

References

[1] M. Lederer, „Material development of doped hafnium oxide for non-volatile ferroelectric memory application," TU Dresden, Dresden, 2022.

[2] J. Liu, S. Liu, L. H. Liu, B. Hanrahan, and S. T. Pantelides, „Origin of pyroelectricity in ferroelectric HfO2," *Phys. Rev. Appl.,* Bd. 12, p. 034032, 2019.

[3] U. Schroeder, „Stabilization and phase transitions in ferroelectric doped hafnium oxide films: Influence of dopants and oxygen vacancies," in *E-MRS Fall Meeting*, 2021.

[4] C. Mart, K. Kühnel, T. Kämpfe, M. Czernohorsky, M. Wiatr, S. Kolodinski, and W. Weinreich, „Doping ferroelectric hafnium oxide by in-situ precursor mixing," *ACS Applied Electronic Materials,* Bd. 1, Nr. 12, p. 2612–2618, 2019.

[5] A. Chouprik, D. Negrov, E. Y. Tsymbal, and A. Zenkevich, „Defects in ferroelectric HfO2," *Nanoscale,,* Bd. 11 635–11 678, p. 11635–11678, 2021.

DOI 10.5162/EUROSENSORSXXXVI/OT3.213

Microfluidic-Assisted Assembly of Fluorescent Nanodiamonds for Precise Temperature Measurement

K. Saikawa[1], M. Zetsu[1], T. Shikama[1], K. Kamei[1,2], O. Tabata[3], Y. Hirai[1]
[1] Kyoto University, Kyoto, JAPAN
[2] New York University Abu Dhabi, Abu Dhabi, UAE
[3] Kyoto University of Advanced Science, Kyoto, JAPAN

saikawa.keita.3p@kyoto-u.ac.jp

Summary:
In all-optical quantum sensing with fluorescent nanodiamonds (FNDs), enhancing the optical signal from excited FNDs is essential. Here, we demonstrate that the template-assisted assembly of FNDs allows the positioning of aggregated FNDs and improves the precision of temperature measurement. Our assembly process combines a polydimethylsiloxane microfluidic device with vertical through-holes and degas operation, enabling not only the aggregation of FNDs for increasing fluorescence intensity but also their high yield positioning over millimeter-scale areas.

Keywords: nanodiamonds, nitrogen vacancy center, temperature sensor, templated self-assembly

Background

Fluorescent nanodiamonds (FNDs) with nitrogen vacancy (NV) centers function as quantum sensors for measuring temperature, magnetic fields, and electric fields. FNDs are suitable for temperature sensors owing to their superior thermal conductivity, chemical resistance and optical durability [1,2]. To achieve precise all-optical quantum temperature sensing with a temperature-dependent fluorescence spectrum, a high fluorescence intensity is required. Although boosting the excitation laser power is one method, it might cause objects heating. Instead of this approach, increasing the NV center density in FNDs has been proposed; however, it is limited to enhancing the fluorescence intensity because of a concurrent rise in other defects [3]. We propose a templated self-assembly approach to form aggregated FNDs for fluorescence intensity enhancement, that also address the particle-to-particle variance in fluorescence properties [1]. By employing a polydimethylsiloxane (PDMS) microfluidic device, this microfluidic-assisted assembly method achieves both precise measurement and patterning of FND clusters on a substrate.

Description of the New Method or System

In this assembly method (Fig. 1), FND clusters were formed on the substrate by drying the FND suspension and aggregating the FNDs along the vertical direction of microchannels. To achieve this process with a single supply of a few microliters of the FND suspension, we employ a PDMS microfluidic device that consists of two layers: a pattern layer with vertical through-holes defining the FND cluster shape/position and a channel layer with channels supplying the FND suspension to the through-holes. When closely attached to the substrate, the pattern layer creates dead-end channels via the through-holes. Here, conducting a degas operation after introducing the FND suspension into the channels would result in the generation of bubbles from the PDMS due to its high porosity, preventing the channels from being completely filled with the FND suspension. Thus, a 1-h degas operation is performed before supplying the FND suspension. When a device is returned to atmospheric pressure and a quick supply of small sample volume of the suspension is performed, any residual gas in the through-holes is absorbed into PDMS, generating a driving force for the suspension to fill the dead-end channels [4]. Then, the FND suspension are dried in the through-holes to aggregate FNDs. Finally, peel off the device from the substrate. This method allows the formation of FND clusters with large numbers of NV centers to improve measurement precision through increased fluorescence intensity and positioning FND clusters on the substrate over millimeter scales.

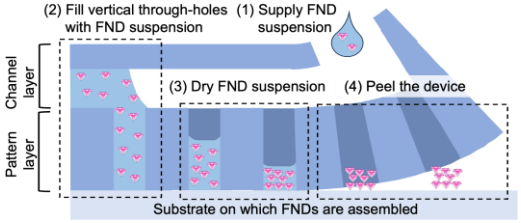

Fig.1. Conceptional illustration of the microfluidic-assisted assembly of FNDs and process sequence.

Results

Potentials of the proposed assembly process was demonstrated by arraying FND clusters. The PDMS microfluidic device was fabricated using standard soft lithography (Fig. 2). The pattern layer has 10-μm diameter through-holes with 20−μm spacing underneath the channel layer with an area of 16 mm^2. Using FNDs with an average size of 750 nm, FND cluster sites were arrayed on PDMS substrate with a yield of over 99% under FND suspension concentration of 0.05, 0.1, and 0.2 w/v% (Fig. 3a). With increasing suspension concentration, a larger amount of FNDs aligned in the vertical direction (Fig. 3b). The height of the FND clusters obtained with a concentration of 0.2 w/v% was double compared with those at 0.1 w/v%.

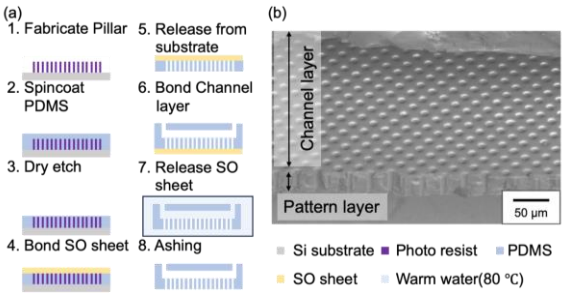

Fig. 2. (a) Device fabrication process. (b) SEM image of the cross section of the microfluidic device.

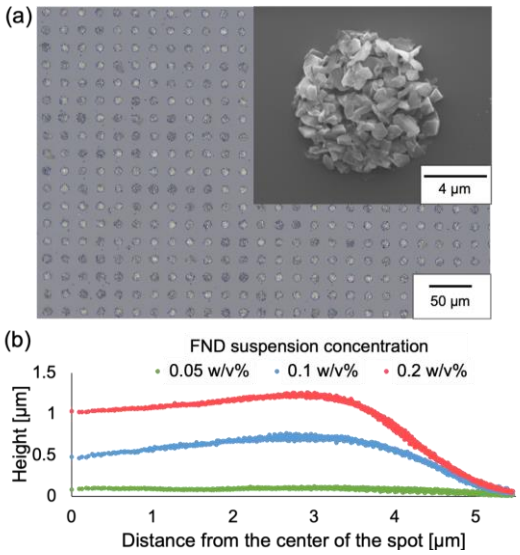

Fig. 3. (a) Optical and SEM images of the FNDs array on the PDMS substrate. (b) Height profile of the FND clusters for different FND suspension concentrations.

Next, the temperature dependence of the peak wavelength of the zero-phonon line (ZPL) of the NV center [1] was evaluated for temperature sensors. At a controlled temperature on a hot plate, the FND cluster array's ZPL peak wavelength shifted linearly by 9.4 ± 2.5 pm/K (n = 10 clusters), demonstrating its applicability for temperature sensors (Fig.4).

Finally, the fluorescence intensity and measurement precision were investigated. Figure 5 indicates enhanced fluorescence intensity with higher suspension concentrations, i.e., a larger number of FNDs in the clusters. Furthermore, the sensitivity, which indicates the precision of the temperature measurement in 1-s, was improved by increasing the fluorescence intensity. The FND clusters produced by the 0.2 w/v% suspension concentration showed approximately twice the sensitivity compared to the 0.1 w/v% concentration. These experimental results demonstrate that the microfluidic-assisted assembly process enables not only the positioning of FND clusters on the substrate but also the enhancement of fluorescence intensity and sensitivity. Therefore, this fabrication process for temperature sensors with FNDs can also be used to develop various quantum sensors.

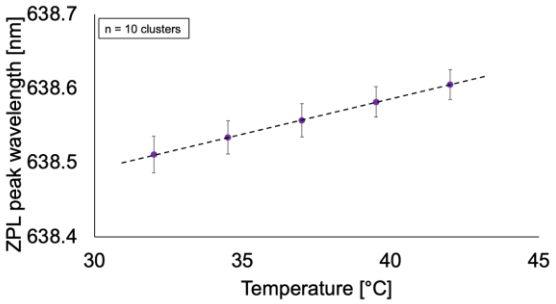

Fig. 4. Temperature dependence of ZPL peak wavelength. Error bars are standard deviation of 10 FND clusters.

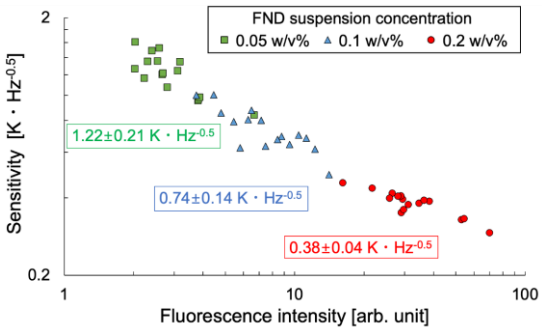

Fig. 5. Relationship between fluorescence intensity and sensitivity for different suspension concentrations. Values in the graph are the average sensitivity obtained at each concentration using 0.5 mW laser.

References

[1] Y. Y. Hui et al., *The Journal of Physical Chemistry C*, 123, 15366–15374(2019); doi: 10.1021/acs.jpcc.9b04496

[2] H. J. Shulevitz et al., *ACS Nano*, 16, 1847–1856(2022); doi: 10.1021/acsnano.1c09839

[3] L.J. Su et al., *Nanotechnology*, 24, 315702(2013); doi: 10.1088/0957-4484/24/31/315702

[4] C. Hamon et al., *Adv. Funct. Mater.*, 26, 8053–8061(2016); doi: 10.1002/adsm.201602225

DOI 10.5162/EUROSENSORSXXXVI/OT3.245

Recent Advances in Lithographic-Free Fabrication and Utilization of Well-Ordered AuNP LSPR Sensors

Tomáš Lednický[1], Attila Bonyár[2], Joel Borges[3,4], Wolfgang Fritzsche[1]
[1] Leibniz Institute of Photonic Technology, Albert-Einstein-Str. 9, 07745 Jena, Germany,
[2] Department of Electronics Technology, Faculty of Electrical Engineering and Informatics, Budapest University of Technology and Economics, Egry József street 18, H-1111, Budapest, Hungary
Corresponding Author's e-mail address
[3] Physics Center of Minho and Porto Universities (CF-UM-UP), University of Minho, Campus de Azurém, 4800-058 Guimarães, Portugal
[4] 3LaPMET - Laboratory of Physics for Materials and Emergent Technologies, University of Minho, Campus de Gualtar, 4710-057 Braga, Portugal

tomas.lednicky@leibniz-ipht.de

Summary:
This study presents a comprehensive fabrication technology for LSPR sensors to address critical challenges, including high cost and low sensitivity. The fabrication process involves two key steps: the self-ordering growth of porous anodic alumina (PAA) and the template-assisted dewetting of thin gold film, resulting in a well-ordered AuNP layer. This work focuses on achieving large-scale ordering without lithography processes, improving the shape control of AuNPs, and exploring their utilization as gas sensors.

Keywords: Localized Surface Plasmon Resonance, Gold Nanoparticles, Porous Anodic Alumina, Thin-Film Dewetting, Well-Ordered Nanoparticle Layer

Background, Motivation and Objective

Numerous existing biosensing methods utilized in healthcare and environmental monitoring are characterized by their time-consuming nature, high costs, bulkiness, and the need for skilled personnel and well-equipped laboratories. Consequently, crucial services like disease diagnostics and monitoring water or air quality often suffer neglect due to economic constraints, leading to millions of casualties annually. Hence, significant research efforts are currently directed towards reducing costs, aiming to yield substantial improvements in global health [1].

In recent decades, localized surface plasmon resonance (LSPR) has gained significant scientific attention owing to its simplicity in multiplexing, high sensitivity, real-time analysis, and label-free detection, all while remaining cost-effective. Yet, a considerable setback lies in the expensive fabrication of nanostructured plasmonic sensors.

Our previous studies have showcased the lithographic-free fabrication of well-ordered layers of gold nanoparticles (AuNPs). This synthesis method relies on a template-assisted solid-state dewetting process of thin gold films on hexagonally ordered aluminum templates formed via porous anodizing, as illustrated in Fig. 1. Subsequently, these layers were transferred onto a transparent glass substrate to serve as effective LSPR sensors.

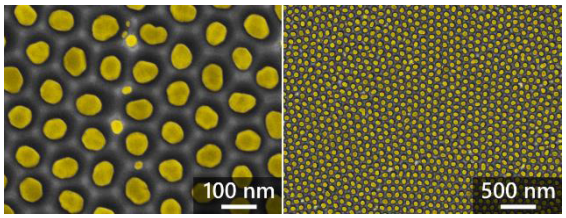

Fig. 1. SEM images of AuNPs on an aluminum template (false colors).

We demonstrated the biosensing performance of these sensors for DNA detection [2] and effective signal amplification for surface-enhanced Raman spectroscopy [3].

Description of the New Method or System

This work explores a novel approach to porous anodizing characterized by gradual progression. As shown in Fig. 1, conventional anodizing under standard conditions results in ordered domains. The domain misalignment is caused by spontaneous pore nucleation, which co-occurs over the whole surface at the beginning of the anodizing process. Therefore, while technically

challenging, gradual anodizing holds promise for achieving single-domain self-ordering across a sizable area.

Moreover, we provide a brief demonstration of an additional method for modifying the shape of dewetted AuNPs by leveraging the surface energy of the interfacial layer, as predicted from the Young–Dupré model describing the contact angle.

Lastly, we present a new application of our LSPR sensors in room temperature gas sensing [4]. This topic is related to the abstract “Benchmarking the Gas Sensitivity of LSPR Sensors with a New Parameter” by Attila Bonyár.

Results

AuNPs’ shape and size can be tuned by several parameters, such as the thickness of the thin deposited gold film, dewetting temperature, etc. [2]. We demonstrate that surface contamination and oxidation are crucial in the AuNP shape.

Carbon contamination is a common issue. Its rate depends on the storage conditions and time. Fig. 2 illustrates the difference between gold (8 nm) dewetting over a pristine Al template and a template with 4 nm of flashed carbon layer.

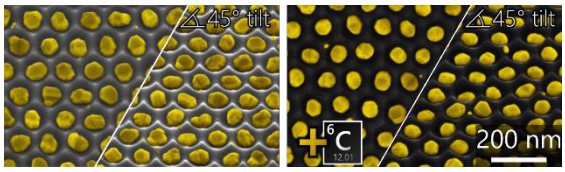

Fig. 2. SEM images of AuNPs on an aluminum template without (left) and with 4 nm carbon layer (false colors).

A similar effect is observed with aluminum oxidation. In ambient conditions, the native oxide layer can grow to a thickness ranging from 4 to 10 nm. This oxidation also smoothens the template edges causing undesirable dewetting outcomes (e.g., uneven splitting and AuNP merging).

Acknowledgments

Tomáš Lednický acknowledges CzechNanoLab Research Infrastructure supported by MEYS CR (LM2023051) and funding from the Europe-an Union’s Horizon Europe research and inno-vation programme under grant agreement No 101109232). Joel Borges acknowledges support from the Portuguese Foundation for Science and Technology (FCT) in the framework of the Strategic Funding UIDB/04650/2020, and by the project CO2Plasmon with project CO2Plasmon, with reference EXPL/CTM-REF/0750/2021 and FCT for his research contract funding, reference CEECINST/00156/2018/CP1642/CT0001. The research was also supported by the National Research and Innovation Office under project number 2020-1.2.3-EUREKA-2022-00030 and by the Nanoplasmonic Laser Fusion Research Laboratory project (2022-2.1.1-NL-2022-00002). Attila Bonyár is also grateful for the support of the Hungarian Academy of Engineering and the "MICHELBERGER MESTERDÍJ" Scholarship.

References

[1] H. Altug, SH. Oh, S.A. Maier, J. Homola, Advances and applications of nanophotonic biosensors. *Nature Nanotechnologie* 17, 5–16 (2022); doi: 10.1038/s41565-021-01045-5

[2] T. Lednický, A. Bonyár, Large Scale Fabrication of Ordered Gold Nanoparticle–Epoxy Surface Nanocomposites and Their Application as Label-Free Plasmonic DNA Biosensors. ACS Applied Materials and Interfaces 12, 4, 4804–4814 (2020); doi: 10.1021/acsami.9b20907

[3] S. Zangana, T. Lednický, A. Bonyár, Three Generations of Surface Nanocomposites Based on Hexagonally Ordered Gold Nanoparticle Layers and Their Application for Surface-Enhanced Raman Spectroscopy, *Chemosensors*, 11, 235 (2023); doi: 10.3390/chemosensors11040235

[4] M. Proença, T. Lednický, D. I. Meira, M. S. Rodrigues, F. Vaz, J. Borges, A. Bonyár. Gas sensitivity of LSPR sensors: Investigation and interpretation of the gas sensing performance of densely-packed Au nanoparticle layers. ACS Applied Materials and Interfaces (under review)

DOI 10.5162/EUROSENSORSXXXVI/OT3.269

In-Vitro Ultrasound Evaluation of an Acoustic Metamaterial Sensor in Presence of Tissue Mimicking Material

Lucrezia Maini[1], Roman Furrer[2], Christofer Hierold[1], Cosmin Roman[1]
[1] Micro- and Nanosystems, ETH Zürich, Tannenstrasse 3, 8092, Switzerland,
[2] Transport at Nanoscale Interfaces Laboratory, EMPA, Überlandstrasse 129, 8600, Switzerland
lucrezia.maini@micro.mavt.ethz.ch

Summary:
Acoustic metamaterials can be exploited to develop new concepts for passive, implantable sensors interrogated by ultrasound. Tissue introduces scattering and attenuation, which may affect the performance of such sensing devices. In this work, we assess the temperature sensitivity of a passive acoustic metamaterial in presence of tissue mimicking materials (TMMs), which are artificial materials with similar acoustic properties to real tissues. We demonstrate that the sensor is still detectable by ultrasound and the presence of TMMs does not affect the temperature sensitivity of the sensor.

Keywords: acoustic metamaterial, implantable device, temperature sensor, tissue mimicking materials, ultrasounds

Introduction

Ultrasound acoustic metamaterials open the way to new passive sensing concepts for implantable sensors. Acoustic metamaterials are artificial materials which enable the selective and engineered control of acoustic wave propagation.

In our previous work, we demonstrated how this concept can be applied to passive temperature sensing, reaching unprecedent resolution (30 mK) and sensitivity ($2.9 \cdot 10^{-3}$ K^{-1}) [1] (see also Fig. 1). There, we speculated that the operation principle, based on reading the frequency of an acoustic resonance, is less susceptible to noise and attenuation than amplitude-based read-out schemes. Implantable applications will have to cope with the presence of biological tissue which creates scattering and introduces attenuation [2].

In this work, we analyze the temperature response of the sensor in the presence of tissue mimicking materials (TMMs). TMMs are artificial materials having similar acoustic properties to in-vivo tissues such as attenuation, density, and speed of sound.

Methods

An ultrasonic probe centered at 5 MHz (Technisonic ISL-0502-HR), connected to a pulser-receiver (Olympus 5072PR), is used to interrogate the metamaterial.

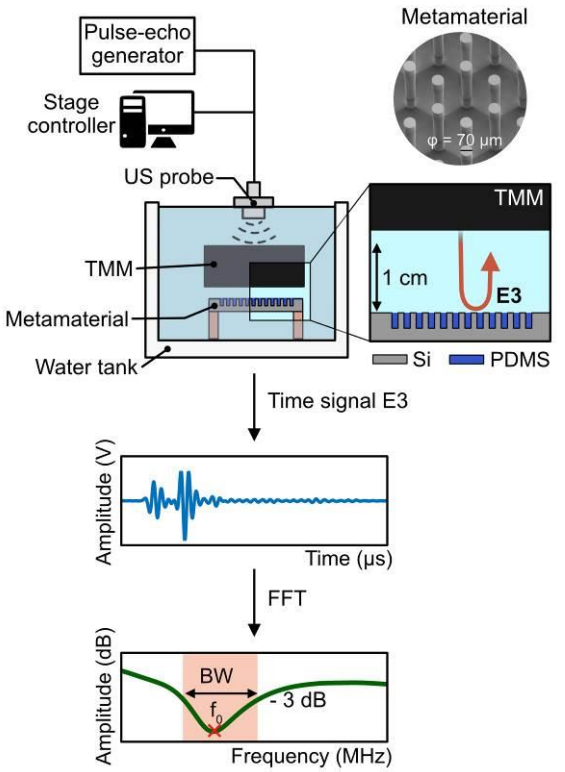

Fig. 1. Experimental setup used in this work and details of the metamaterial. The reflected signal at the interface between the TMM and the metamaterial (E3) is recorded in time and transformed in the frequency domain (FFT). An algorithm was implemented to compute the frequency peak (f_0) and the bandwidth (BW) at -3dB from f_0.

The probe is connected to an x-y-z stage controller to perform spatial scanning.

The metamaterial is produced with silicon (Si) micromachining and poly-dimethyl-siloxane (PDMS) casting, according to the process flow described in [1]. The TMM is produced from a mix of 2 % agar and 8.2 % graphite powder in water, reoptimized from [3] to match the attenuation coefficient of real muscle tissue.

The metamaterial and the TMM are immersed in water. The signal (E3) is recorded at the interface of the metamaterial (Fig. 1). A Fourier transform is applied (FFT) and an algorithm is implemented to find the frequency peak f_0 and the -3dB bandwidth (BW) around it.

Results

The resonant frequency signals of the metamaterial, with and without TMM, show a shift of the frequency peak at different temperatures (Fig. 2). The temperature sensitivity is almost identical with and without TMM ($S = -3.6 \cdot 10^{-3}\ K^{-1}$). The presence of TMM seems not to affect the position of the resonant frequencies at the different temperatures either (see dotted lines, Fig. 2 and also Tab. 1). The bandwidth BW is on the other hand side affected by the TMM. The resonances become broader due to the attenuation introduced by the TMM. The impact on temperature resolution will be studied in more detail in the future.

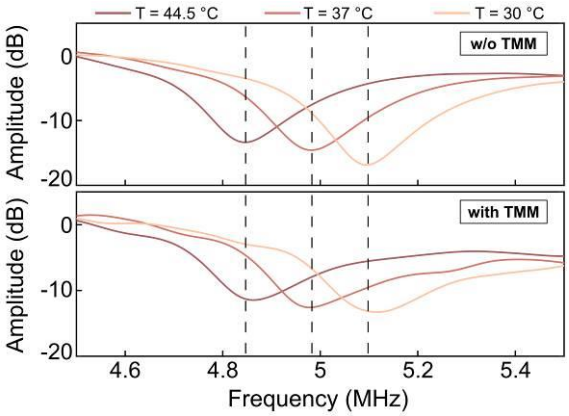

Fig. 2. Reflected frequency signal E3 in the frequency-domain (after FFT) of the metamaterial without (top) and with (bottom) TMM, recorded at three different temperatures. Dotted lines showing the positions of f_0.

Spatial scans shown in Fig. 3 demonstrate that the presence of the TMM does not hinder the full detection of the metamaterial (see Fig. 3-B).

Because the sensing mechanism is based mostly on the position of the resonance frequency, the attenuation introduced by the TMM seems to be a second order effect, as supported by the unchanged temperature sensitivity.

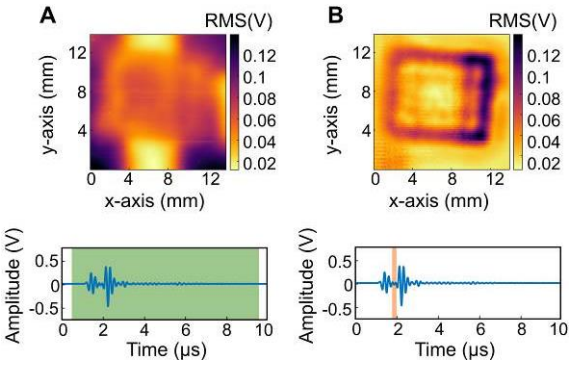

Fig. 3. Ultrasonic spatial scan at T = 44.5 ˚C of the metamaterial with TMM. In (A): the root-mean-square voltage of the entire signal is displayed (green band), vs. a windowed part in (B) (orange band). In (B), the outline of the sensor is clearly visible.

A summary of the extracted resonance frequencies and bandwidths at different experimental temperatures is reported in Table 1.

Tab. 1: Experimentally measured figure of merits (f_0: resonance frequency and bandwidth: BW) at different temperatures, with and without TMM (tissue mimicking material)

	Temperature					
	44.5˚C		**37˚C**		**30˚C**	
	f_0 (MHz)	**BW (kHz)**	**f_0 (MHz)**	**BW (kHz)**	**f_0 (MHz)**	**BW (kHz)**
w/o TMM	4.84	135	4.98	139	5.1	118
TMM	4.86	173	4.98	189	5.12	190

References

[1] L. Maini, V. Genoves, R. Furrer, N. Cesarovic, C. Hierold, C. Roman, An in vitro demonstration of a passive, acoustic metamaterial as a temperature sensor with mK resolution for implantable applications, *Microsyst Nanoeng* 10, 8 (2024); doi: 10.1038/s41378-023-00632-x

[2] J. C. Bamber, ULTRASOUND IN MEDICINE (Chapter 4), CRC Press (1998); ISBN: 9780367802479

[3] K. Nam, I. M. Rosado-Mendez, N. C. Rubert, E. L. Madsen, J. A. Zagzebski, T. J. Hall, Ultrasound Attenuation Measurements Using a Reference Phantom with Sound Speed Mismatch, *Ultrasonic Imaging* 33, 251-263 (2011); doi: doi.org/10.1177/016173461103300404

DOI 10.5162/EUROSENSORSXXXVI/OT3.298

Pd Decorated WS_2 Synthesized via Facile APCVD Technique for Highly Selective Room Temperature H_2 sensing

Shuja Bashir Malik[1], Eduard Llobet[1], Fatima Ezahra Annanouch[1,]*
[1] Departament d'Enginyeria Electronica, Universitat Rovira i Virgili, Països Catalans 26, 43007 Tarragona, Spain.

*Corresponding Author's e-mail address: fatimaezahra.annanouch@urv.cat

Summary:
Developing sensitive hydrogen gas sensors is crucial for detecting and managing hazards in storage, transport, and leakages. While metal oxide gas sensors (MOX) suffer from poor selectivity and high temperatures, attention has shifted to two-dimensional materials like tungsten disulfide (WS_2). However, bare WS_2 sensors face limitations like slow response-recovery times and low sensitivity. Functionalizing TMDs with noble metal nanoparticles, notably Pd, enhances sensor performance. This study presents a highly sensitive Pd-decorated WS_2 composite based sensor for room temperature (RT) H_2 sensing, with a remarkable response of 55% (Pd quantity (3 mg).

Keywords: Gas sensor, TMDs, hydrogen, APCVD, nanomaterials

Background, Motivation and Objective

The growing demand for sustainable energy sources has spotlighted hydrogen (H_2) as a leading contender for the next generation of energy, offering the potential to replace fossil fuels and significantly reduce greenhouse gas emissions [1]. However, its high explosiveness and flammability necessitate careful storage and handling to mitigate safety risks. Developing sensitive and selective hydrogen gas sensors is crucial for detecting and managing potential hazards associated with hydrogen storage, transport, and leakage. While metal oxide gas sensors (MOX) have been widely used, they suffer from limitations such as poor selectivity and high operating temperatures. Recently, attention has turned to two-dimensional materials (2D) like graphene and transition metal dichalcogenides (TMDs) such as tungsten disulfide (WS_2) for improved sensing capabilities [2]. WS_2 has garnered significant interest due to its exceptional properties. Various research works have demonstrated the potential of WS_2-based sensors for detecting gases including hydrogen. However, bare WS_2 sensors face challenges like slow response-recovery speeds and low sensitivity. Functionalizing the host matrix with noble metal nanoparticles especially Pd enhances sensor performance through electronic and chemical sensitization mechanisms [1]. Optimization of nanoparticle decoration is crucial to ensure sensor efficacy. In this study, a highly sensitive Pd-decorated WS_2 composite for room temperature H_2 sensing demonstrated superior performance, with highest Pd quantity (3 mg) exhibiting the highest response of 55%. The amount of ethanol and WS_2 was kept constant at 10 ml and 10 mg respectively in all the solutions.

Materials and Methods

WS_2 was synthesized as reported in on our earlier study [2]. To decorate the WS_2 with Pd, commercial Pd powder was mixed with WS_2 in varying proportions (0.5 mg, 1 mg and 3 mg) and subjected to 90 minutes of sonication in absolute ethanol. The resulting solutions were airbrushed onto gold interdigitated electrodes on silicon substrates fabricated using laser lithography.

Results

Fig. 1 (a and b) illustrate morphology of WS_2 and Pd- WS_2 composite respectively. As seen from the Field Emission Scanning Electron Microscopy (FESEM) images, the deposited WS_2 depicts flake like morphology with an average size ranging from 100 nm to 1.2 µm. Also, the Pd nanoparticles can be seen in the form of clusters (in red circles) with an average particle size of 50 nm (Fig. 1 (b)). The Pd clusters are uniformly distributed all over the WS_2 flakes. The samples were further characterized using transmission Electron Microscopy (TEM). Color mapping of the samples show successful decoration of WS_2 with Pd nanoparticles as shown in Fig. 2 (a). Fig. 2 shows EDX spectrum of the Pd-WS_2 composite.

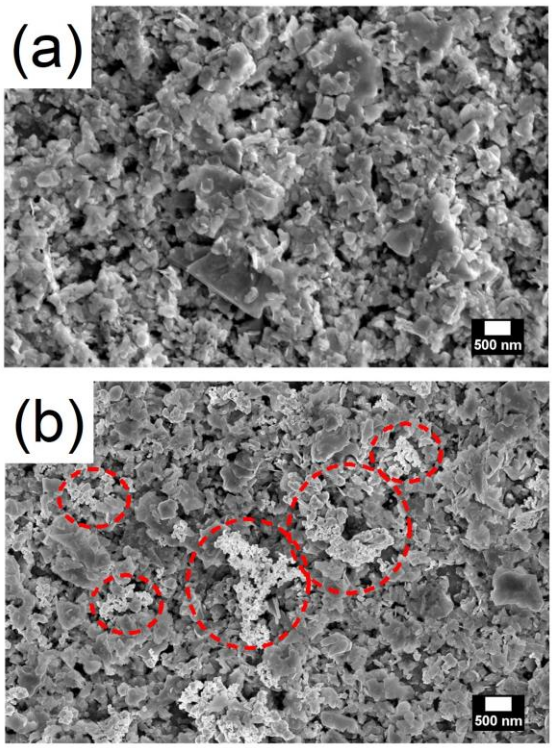

Fig. 1. FSESM images of (a) WS_2, (b) Pd decorated WS_2 (Red circles indicate Pd clusters).

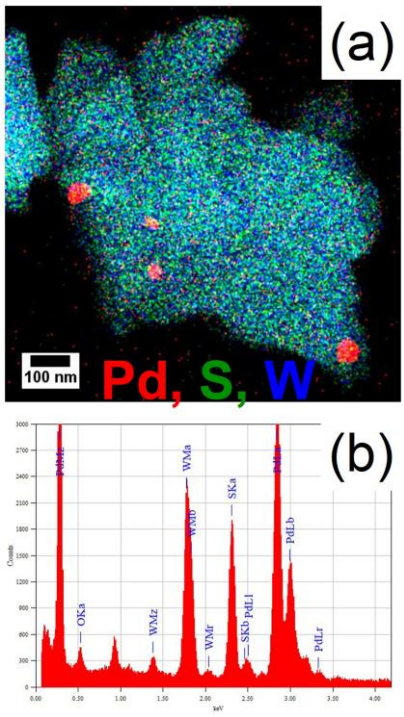

Fig. 2. (a) Color mapping of Pd decorated WS_2 nanocomposite, (b) EDS spectrum of Pd decorated WS_2 nanocomposite.

We tested bare WS_2 and Pd-decorated WS_2 sensors with varying amounts of Pd (0.5 mg, 1 mg, and 3 mg) towards 500 ppm of H_2 at room temperature (RT), 100°C, and 150°C. The sensor with 3 mg of Pd exhibited the highest sensitivity towards 500 ppb of H_2 at RT. Fig. 3 (a) illustrates the sensor resistance dynamics towards 500 ppm of H_2 at RT. The pristine WS_2 sensor showed no response to any concentrations of H_2 but began to respond with small responses at elevated temperatures of 150°C, still lower than the responses shown by the best sensor at RT. The sensor responses are stable and repeatable. Fig. 3 (b) demonstrates that the sensing response decreases almost linearly with increasing operating temperature. Gas sensing response of the best responding sensor are presented. The detailed selectivity and humidity sensing responses will be presented in the conference.

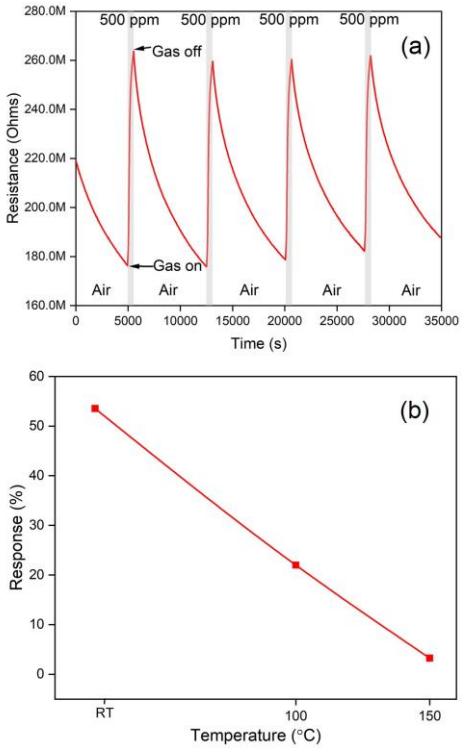

Fig. 3. (a) Resistance dynamics of 3 mg Pd decorated WS_2, (b) the sensor response as a function of temperature towards 500 ppm H_2 at RT.

Conclusions

This study presents a highly sensitive Pd-decorated WS_2 composite for room temperature H_2 sensing, achieving a remarkable 55% response with 3 mg of Pd.

References

[1] S. B. Malik, F. E. Annanouch, and E. Llobet, "Pd-Nanoparticle-Decorated Multilayered MoS2 Sheets for Highly Sensitive Hydrogen Sensing," *Chemosensors*, vol. 11, no. 11, p. 550, Oct. 2023, doi: 10.3390/chemosensors11110550.

[2] S. B. Malik, F. E. Annanouch, and E. Llobet, "Room Temperature Detection of Ppb Level NO2 by $\text{WS2 Sensors," *Proc. IEEE Sensors*, no. 2, pp. 1–4, 2023, doi: 10.1109/SENSORS56945.2023.10324906.

DOI 10.5162/EUROSENSORSXXXVI/OT4.42

Creep Detection in Composites with Silicon Strain Gauge

Gaëtan HERRY[1], William de Andrade CAROBA JUNIOR[2], Maxime HARNOIS[1], France LE BIHAN[1]
[1] Institut d'Electronique et des Technologies du numéRique, IETR, Rennes University, Rennes, France
[2] Institution or Centro Federal de Educação Tecnológica de Minas Gerais - CEFET-MG, Belo Horizonte, Brazil

Corresponding Author's e-mail address: france.lebihan@univ-rennes.fr

Summary:

This work shows how the insertion of silicon mechanical sensors into composite structures enables the detection of internal structural variations, and can find applications in process monitoring or structural health monitoring. It includes the description of a novel process for minimally intrusive insertion of sensors inside composites (substrate free transfer printed sensor). Temperature and deformation characterizations reveal a modification of the internal structure of a composite, triggered by a sufficiently high temperature, and linked to the creep phenomenon of the composite's epoxy resin binder.

Keywords: Strain Gauges, Temperature sensors, Structural Health Monitoring, Microcrystalline silicon, Composites.

Background, Motivation an Objective

Composite materials are increasingly used in a wide range of applications. The optimization of manufacturing parameters and the monitoring of their structural state are key issues in terms of safety, environment and production cost optimization [1]. Some solutions exist for introducing sensors into composites [2], but they remain complex to implement and intrusive. Our low-intrusive strain gauge instrumentation method provides physical and structural information at the heart of composites.

Description of the Method

The process involves manufacturing microcrystalline silicon strain gauges and transferring them, without substrate, into one of the plies of the composite material. Characterization of these strain gauges as a function of temperature and deformation provides the physical features of the sensors. A structural change, initiated here by a coupling of deformation and increased temperature, is clearly identified by a sharp variation in the gauges' electrical resistance. This variation shows a degradation linked to a modification of the internal structure due to the creeping of the composite binder.

Technology and results

The technology we've developed consists in fabricating the gauge on a temporary substrate [3]. Once the gauge has been fabricated, it is transferred to the composite ply made from a combination of fiberglass and epoxy resin. The sensor is then detached from its initial substrate. This functionalized ply is then inserted into a complete multi-ply composite structure. Metallic contacts and conductive wires are used for electrical characterization. The final structure is shown figure 1.

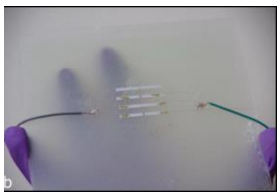

Fig. 1. Composite with Silicon gauge.

By characterizing the strain gauges in terms of temperature and strain, we can determine their features, such as their temperature coefficient and strain gauge factor. These factors are determined from the variation in the relative resistance of the gauges as a function of either temperature or the relative deformation of the structure. Those behaviours are shown in figures 2a and 2b.

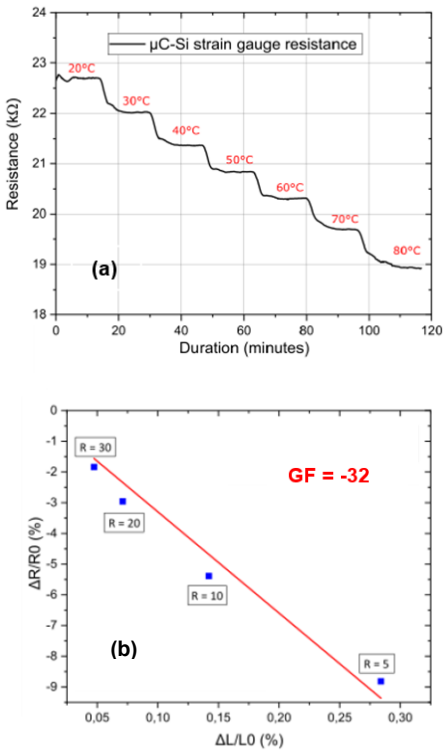

Fig. 2. a. Resistance variation as a function of temperature, b: Gauge factor (GF) determination for microcrystalline silicon sensors inside composite.

The relative resistance decreases with temperature, as usually for semiconducting material. From figure 2b, the gauge factor is determined from the slope of the relative variation of the resistance versus different curvature radius, linked to different relative deformations (ΔL/L). It is equals to -32, involving a sensitivity at the state of the art for microcrystalline silicon [4].

Figures 3a and 3b show the variation of the resistance with or without strain for increasing values of the temperature. When stress is applied, and the temperature exceed the value of 60°C, the gauges' electrical behaviour changes. This temperature causes the epoxy resin to creep and change its structure. This phenomenon is detected by an increase in the resistance value of the gauge. This increase, which becomes more pronounced at higher temperatures, corresponds to tension in the structure, involving micro-cracks and thus increasing the resistance value. The deformation of the composite remains visible as the structure cools.

As the internal structure of the silicon layer is altered by these microcracks, its resistance is higher than it was initially. However, the gauge still functioning. A loosening test of the structure (re-flattening by heating the composite) is also clearly identified by the relative variation in gauge resistance.

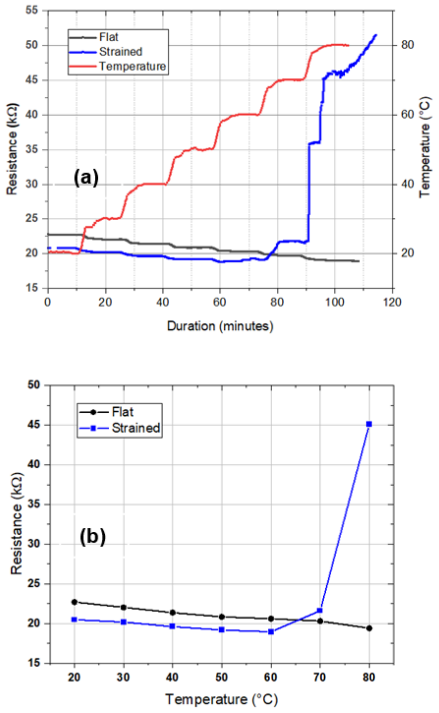

Fig. 3. a. Resistance variation for flat and strained structure for different temperature steps, b: Variation of the resistance versus temperature, showing a change in the strained device above 60°C.

Conclusion

We have shown that it is possible to insert silicon strain gauges into the core of composite materials without damaging the device. These low-intrusive methods provide devices that can be used to measure both, internal temperatures or detect structural deformations. They also reveal major internal structural changes, such as binder creep and plastic deformation of composite materials.

References

[1] P. Sharma, P. Thori, M. Bhargava. An approach of composite materials in industrial machinery: advantages, disadvantages and applications, Int. J. Res. Eng. Technol. 2013, 02 (12), 350–355. https://doi.org/10.15623/ijret.2013.0212060.

[2] Y. Wang, S. Hu, T. Xiong, Y. Huang, L. Qiu, Recent Progress in Aircraft Smart Skin for Structural Health Monitoring, Struct. Health Monit. 2022, 21 (5), 2453–2480, doi.org/10.1177/14759217211056831.

[3] R. Selmi, J-C. Fustec, M. Harnois, F. Le Bihan, Organic and Metallic Sensors on Complex 3D Object Using an Original Method: Water Transfer Printing, IEEE Sensors Letters, vol. 7, no. 9, pp. 1-4, 2023, doi: 10.1109/LSENS.2023.3301845

[4] F. Garcia Castro, O. de Sagazan, N. Coulon, C. Simon, F. Le Bihan, ICP-CVD µ-Si Layers Optimization for Strain Gauges on Flexible Substrates. Sens. Actuators Phys. 2020, 315, 112261, doi.org/10.1016/j.sna.2020.112261.

DOI 10.5162/EUROSENSORSXXXVI/OT4.62

Development of a 0.01-dph mode-matched MEMS gyroscope toward realizing a module-level gyrocompass with 1-mil accuracy

H. Murase[1], D. Ono[1], F. Miyazaki[1], J. Ogawa[1], T. Tomioka[1], K. Uchida[1], K. Masunishi[1], E. Ogawa[1], F. Ishibashi[1], T. Matsuo[2], M. Ueda[2], T. Tanaka[2], T. Aoyama[2], Y. Tomizawa[1]
[1] Corporate Research & Development Center, Toshiba Corporation, Kawasaki, Japan,
[2] Toshiba Electro-wave Products Co., Ltd., Kawasaki, Japan

hideaki2.murase@toshiba.co.jp

Summary:

A gyrocompass, which measures the earth's rotation with a gyroscope, can detect north robustly. However, practical applications of gyrocompasses are limited due to the size of conventional gyroscopes. Micro-electro-mechanical systems (MEMS) gyroscopes have the potential to open up new markets; however, precision is a major challenge in MEMS gyroscopes. Here, we developed a novel high-precision MEMS gyroscope and demonstrated navigation-grade bias instability of <0.01 dph, which is the highest-level performance of a MEMS gyroscope. A gyrocompass using the developed gyroscope performed north finding with precision of <1 mil in a laboratory environment, and a precision of <10 mil was exhibited by our module-level gyrocompass, which is being refined toward realizing 1-mil accuracy.

Keywords: MEMS gyroscope gyrocompass

I. Introduction

A gyrocompass can detect north robustly even indoors and under magnetic fields by measuring components of the earth's rotation with a gyroscope. However, practical applications of gyrocompasses using such as ring laser, fiber optic, or mechanical gyroscopes are limited due to issues in terms of size, cost, and precision. Micro-electro-mechanical systems (MEMS) are a key technology for solving these challenges. Recently, many researchers have been focusing on MEMS gyroscopes, for which precision is a major challenge. Here, we developed a novel high-precision MEMS gyroscope and demonstrated navigation-grade bias instability of (BI) < 0.01 dph, which is the highest-level performance of a MEMS gyroscope. The gyrocompass using the developed gyroscope accomplished north finding with precision of 1 mil in a laboratory environment, and we will refine our prototype module-level gyrocompass with an eye toward realizing 1-mil accuracy.

II. Design and Experiments

A Gyroscope Design

Fig. 1 shows a schematic of our novel gyroscope, which we named "Kumo-no-su-Shaped Gyroscope" (KSG) (*kumo-no-su* is Japanese for spider web). KSG can be regarded as an improvement over the Boeing disk resonating gyroscope [1] for two reasons. The first reason is the lumped mass connected to the outermost ring, which decouples the effective mass from the ring width and therefore enables the effective mass to increase without widening the rings, thereby reducing mechanical noise [2]. The second reason is the combination of the in-phase-arranged spokes between the outer rings and the anti-phase-arranged spokes between the inner rings. The former works to make the outer rings vibrate with the same amplitude, which improves electrode sensitivity, while the latter works to maintain the wineglass vibrating mode by appropriately supporting the outer rings.

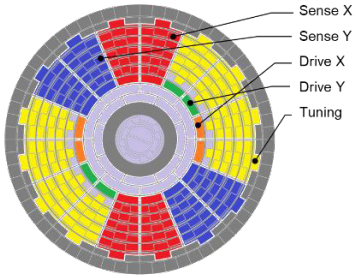

Fig. 1. Schematic view of KSG.

B Gyroscope Performance

Fig. 2 shows the experimental results of Allan deviation of KSG. The measurement was performed over 4 h without temperature control. The red and blue curves indicate the experimental

values with and without temperature correction, respectively. The Allan deviation with temperature correction reached 0.01 dph at 3000 s, with BI < 0.01 dph, which corresponds to navigation-grade specification. The dotted line indicates the fitting curve proportional to $\tau^{-1/2}$, showing 0.0093 deg/$\sqrt{\text{h}}$ of angle random walk.

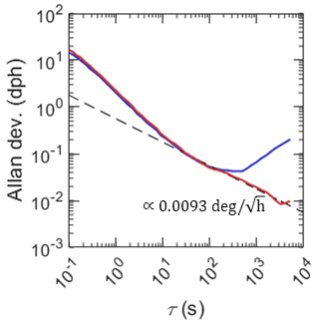

Fig. 2. Allan deviation of KSG with and without temperature correction (red and blue curves, respectively).

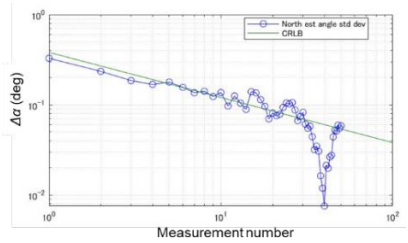

Fig. 3. Precision of azimuth angles measured by KSG using a turntable.

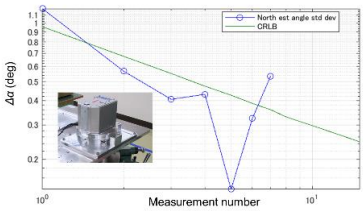

Fig. 4. Precision of azimuth angles measured by KSG using our prototype of module-level gyrocompass. Inset: Photograph of the prototype of module-level gyrocompass

C Gyrocompass

By measuring components of the earth's rotation with a single-axis gyroscope at various azimuths, the orientation of the earth's axis of rotation (i.e. north) can be detected. To demonstrate the specification of KSG, north finding was carried out based on this principle. The gyroscope was set on a turntable with its detection axis aligned horizontally, and the deviation of the reference angle from north was detected by measuring the magnitude of the earth's rotation component in four directions at 90-degree intervals, that is, by using the "maytagging" method. The azimuth angle α can be calculated as

$$\alpha = -\text{atan2}(-\omega_2 + \omega_4, \omega_1 - \omega_3), \quad (1)$$

where ω_i is the angular velocity output in direction *i*. The measurement was performed in Kawasaki, Japan, where the component of the earth's rotation is 12 dph. The measurement time in one direction is 200 s and measurements of the four directions were repeated over 24 h. Fig. 3 shows the experimental values of standard deviation of azimuth angle $\Delta\alpha$ and the theoretical line of the Cramér–Rao lower bound (CRLB) [3] as

$$\Delta\alpha^2 = \frac{2{\sigma_N}^2}{\Omega_{\text{in}}^2 N}, \quad (2)$$

where σ_N is the root mean square of the angular velocity output noise, Ω_{in} is the earth's rotation of 12 dph at Kawasaki, and *N* is the number of measurements. The experimental values of $\Delta\alpha$ decrease with CRLB as the measuring number increases and reach 0.056 deg, which corresponds to 1 mil according to the Japan/NATO definition. Fig. 4 shows our prototype module-level gyrocompass, which can detect an azimuth angle to the north using the maytagging method by performing manual rotation. The dimensions of the model are 18×18×16 cm^3. The azimuth precision using this module improves with CRLB and reaches 0.5 deg.

III. Concluding Remarks

Here, we developed a novel MEMS gyroscope, with BI < 0.01 dph. the azimuth angle precision of the gyrocompass using our developed gyroscope on a turntable was < 1 mil. Our prototype gyrocompass module, which is being refined with an eye toward commercialization, had an azimuth precision of 0.5 deg. In future work, we aim to realize a module-level gyrocompass with an azimuth accuracy of 1 mil, which is the same level as the gyrocompass using a turntable.

References

[1] Anthony D. Challoner, *et. al., IEEE/ION Position, Location and Symp.—PLANS 2014 (IEEE)* (2014).

[2] Qingsong Li., *et. ai., Microsyst. Nanoeng*. **4**, 1–11 (2018).

[3] I. P. Prikhodko, *et., al., J. Microelectromech. Syst.* ***22****, 1257* (2013).

Acknowldgement

This work was partly supported by the Innovative Science and Technology Initiative for Security, ATLA, Japan (Grant Number JPJ004596).

DOI 10.5162/EUROSENSORSXXXVI/OT4.72

Design Considerations for GHz SAW Resonators in High Strain Sensing

MinHee Kwon[1], *Matthias Schlögl*[1], *Daniel Platz*[1], *Ulrich Schmid*[1]
[1]*Institute of Sensor and Actuator Systems, TU Wien, 1040 Vienna, Austria*

minhee.kwon@tuwien.ac.at

Summary:
In this study, SAW (surface acoustic wave) resonators are investigated for strain sensing up to values of approximately -4000 με to 4000 με. The shift in resonance frequency in the GHz range is evaluated for this purpose. To estimate the impact of a key design parameter, we adjust the length of the SAW resonator and find that the longer the SAW resonator, the more responsive the device gets to strain changes. When the distance between the two reflectors confining the SAW is 2207 μm, the resonance frequency responsivity to strain is 114.99 Hz/με.

Keywords: Surface acoustic wave, strain sensor, GHz frequency, frequency shift, resonator length

Background, Motivation, and Objective

Micro-strain sensitive devices based on *e.g.* capacitive or fiber-optical transducers, which are nowadays used in a variety of applications such as structural health monitoring, are expensive as they require complex manufacturing processes. SAW (surface acoustic wave) strain sensors, however, are simple to manufacture, because they require fewer components, and can be operated wirelessly [1]. Previous studies on SAW strain sensors on non-flexible substrates have focused mostly on a strain regime below ±1000 με [1–2]. Our motivation is to go beyond this latter limitation to exploit the full potential of these devices, by evaluating the sensing performance in this high strain regime. Furthermore, there are only a few studies how geometric design parameters affect the strain sensing capability under such high mechanical loads. In this work, we present the first results on how the strain responsivity depends on the SAW resonator length even in the strain regime above 1000 με.

Description of the New Method or System

We use a tailor-made setup [3] to investigate the shift in resonance frequency of the SAW device depending on the applied mechanical strain. As illustrated in Fig. 1, our setup comprises a GHz SAW resonator mounted on a bendable cantilever capable of applying strain values up to ±4000 με to the resonator via the backside of the substrate. We measure the response to strain changes of different GHz SAW resonators with different lengths, but keep the basic device design fixed.

Results

Fig. 2 shows the shift in resonance frequency of a SAW resonator when exposed to mechanical strain values up to ±3315 με. The resonance frequency shifts by 93.80 Hz per με defining its responsivity R. This value is higher than the reported responsivity of 20.09 Hz/με achieved with a similar SAW resonator design [2]. A key parameter in SAW design is the position of the reflectors which confine the SAWs and define the resonator length. To evaluate the impact of the latter parameter we perform experiments with SAW resonators of different lengths l_m of 685 μm, 1205 μm, and 2207 μm. The experimental data in Fig. 2 is obtained from the SAW resonator with l_m of 685 μm. Additionally, we increase the strain range up to ±3979 με. Fig. 3 shows that the frequency shift is linear over the full strain interval. The responsivity of the SAW strain sensor is 100.48 Hz/με with l_m of 1205 μm. As shown in Fig. 4, the responsivity to strain increases as l_m gets longer. However, the linearity of the response to strain changes is decreased for longer resonator lengths as indicated by increasing error bars (see Fig. 4).

In conclusion, GHz resonator SAW strain sensors exhibit a linear response even up to large strain regimes of ±3979 με. Moreover, our study shows that longer resonators achieve higher responsivity. Our findings contribute to an understanding of strain GHz SAW-based strain sensing, particularly due to their demonstrated high performance in detecting large strains, thus expanding their potential applications.

Illustrations, Graphs, and Photographs

Fig. 1. Illustration of the measurement setup. A SAW resonator and a PCB are placed on a bendable aluminum cantilever at position x_0. Mechanical strain is applied by deflecting the tip of the cantilever.

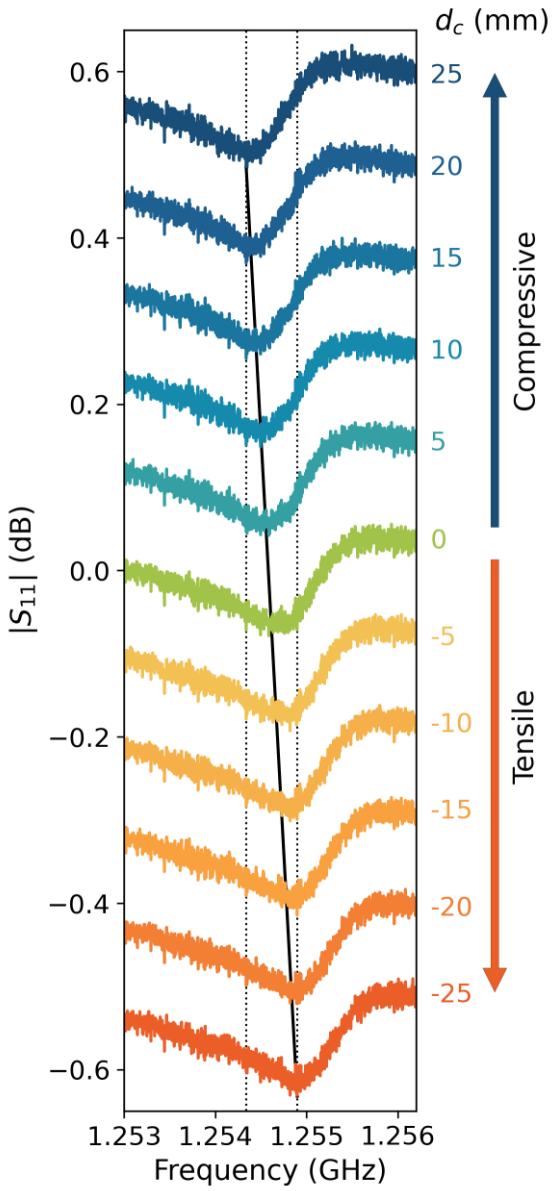

Fig. 2. Measured magnitude values of S11 for different strain values in SAW. When strain is labeled with a plus, tensile stress is applied, while compressive stress is transferred to the device when strain is negative. The black solid line underneath the experimental data S11 connects the two resonance frequencies when the strain is at its maximum and minimum values.

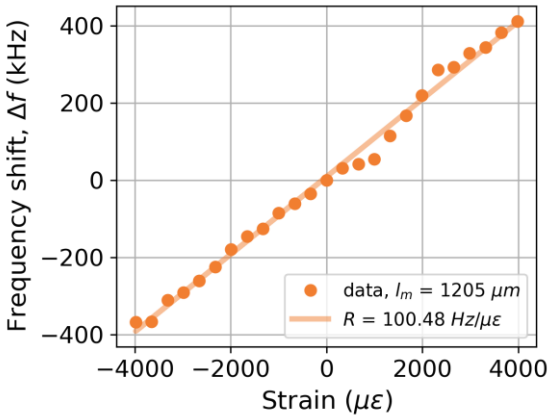

Fig. 3. SAW sensor responsivity R of 100.48 Hz/με in strain regime of about ±4000 range with l_m of 1205 μm. The circles are the experimental data, and the inserted line is a linear fit to the data, so that R is represented by its slope.

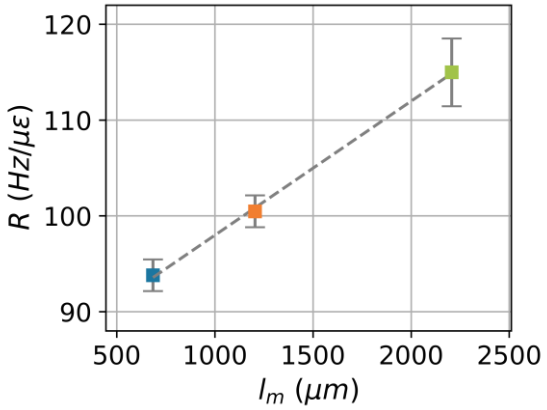

Fig. 4. Responsivity R as a function of different distances between the two reflectors l_m. The gray error bars indicate the deviation of the data values from the linear fit function of the response shown in Fig. 3.

References

[1] Y. Hamed, G. O'Donnell, N. Lishchenko, I. Munina, Strain Sensing Technology to Enable Next-Generation Industry and Smart Machines for the Factories of the Future: A Review, *IEEE Sensors Journal* 23 no. 21, 25618–25649 (2023); doi: 10.1109/JSEN.2023.3313013

[2] X. Yan, Q. Tan, X. Li, T. Xue, M. Li, Test and Analysis of SAW High Temperature Strain Sensor Based on Langasite, *IEEE Sensors Journal* 22 no. 13, 12622–12628 (2022); doi: 10.1109/JSEN.2022.3176689

[3] M. Schlögl, S. Köpl, J. Hiesberger, M. Schneider, U. Schmid, Mechanical and electrical characterization of resonant piezoelectric microbridges for strain sensing, Sensors and Actuators A: Physical 346, 113829 (2022); doi: 10.1016/j.sna.2022.113829

DOI 10.5162/EUROSENSORSXXXVI/OT4.78

Detection of SF_6 in soundproof windows

Hans-Fridtjof Pernau[1], Carl Basler[1], Gerrit Stiefvater[1], Jürgen Wöllenstein[1,2], Katrin Schmitt[1,2]
[1] Fraunhofer Institute for Physical Measurement Techniques IPM, Georges-Köhler-Allee 301; 79110 Freiburg Germany,
[2] Department of Microsystems Engineering - IMTEK, Georges-Köhler-Allee 102; 79110 Freiburg Germany

hans-fridtjof.pernau@ipm.fraunhofer.de

Summary:
SF_6 has a greenhouse effect 25,200 times greater than CO_2 and was widely used as a gas in soundproof windows until 2006. In 2020, Germany was responsible for 55.3 % of SF_6 emissions within the European Union. Without emissions from soundproof windows, this value could be reduced to 14.6%. Since the filling of most windows is unknown, a reliable detection method is required to identify SF_6-filled windows to be able to safely extract and recycle the filling when disposing of them. In our study, we were able to identify LIBS (Laser-Induced Breakdown Spectroscopy) as the most promising technology for identifying filling gases in soundproof windows and show a way of what a mobile detection and recovery unit for SF_6 could look like.

Keywords: SF_6, greenhouse effect, Raman spectroscopy, LIBS, remote gas detection

Introduction:

Due to its unique physical properties, SF6 has been a widely used gas in technical applications in transformer stations, wind turbines or in soundproof windows. It has a high molecular mass, low thermal conductivity, prevents sparking and it is very long-term stable to heat and UV light. The last point is particularly important because it lasts more than 3,500 years in the atmosphere and has a more than 25,000 times greater impact on the greenhouse effect than CO2. Therefore, SF6 should not be released into the environment, but should be recovered and then decomposed or recycled in a controlled manner.

Materials and Methods:

A common way to measure the SF_6 content in a gas mixture is by means of infrared absorption spectroscopy, as it has a very distinct absorption peak around 10.56 µm [1]. Using this method, SF_6 can be detected in the ppm range in air. Since ordinary window glass (boron float glass) is not transparent in this wavelength range, IR absorption spectroscopy is unsuitable for carrying out measurements on an intact window.

Using a thermal conductivity measurement or measuring the speed of sound may give an indication of SF_6 in the window filling, but a similar signal can be produced by Ar, Kr or Xe. For this reason, we used both Raman spectroscopy and LIBS to identify a suitable detection method to measure the SF_6 content, including possible additional gas compounds.

Results:

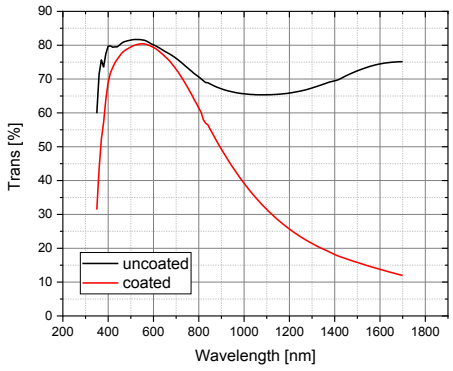

Fig. 1. Transmission of an uncoated and a coated double-glazed window. The reflective coating prevents IR radiation above 800 nm from penetrating the glass.

The first active Raman fundamental frequency of SF_6 can be found at 774.3 1/cm [2]. Since also N_2 and O_2 are Raman active, it is possible to detect the SF_6 content in a matrix of air. Un-

fortunately, other potential filling gases like Ar, Kr, and Xe are not Raman active. The first Raman fundamental frequency of SF_6 can be measured through an ordinary glass window with a thickness of 4 mm with a minimum laser power of 50 mW at a wavelength of 534 nm (see Figure 2).

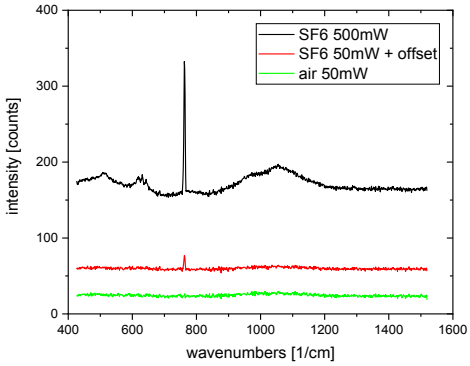

Fig. 2. Measurement of the first Raman fundamental frequency of SF_6 through a 4 mm thick window glass. Using a laser power of 50 mW, the Raman signal can be identified (the plot of the measured values at 50 mW is provided with an offset on the y-axis for a better overview)

The second investigated measurement technique was LIBS. A nanosecond laser pulse at 1064 nm thereby ionizes the matter within the focus of the laser beam, which forms a plasma and emits light. The emitted light spectrum is unique for each atom. Therefore, it is possible to detect all gases due to their individual LIBS signal.

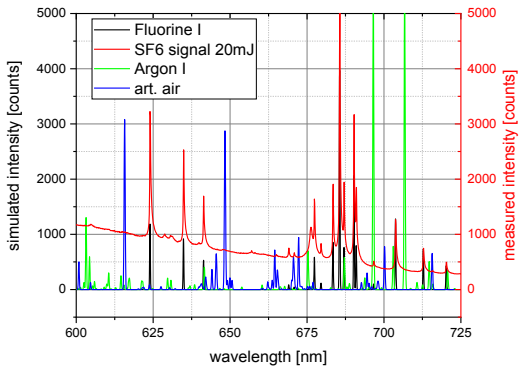

Fig. 3. Measured LIBS signal of a SF_6 gas filling inside a double-glazed window (red). Simulated LIBS spectra of fluorine (black), argon (green) and synthetic air (blue).

As the laser pulse requires an energy of at least 11 mJ to initiate the plasma in the focal point of less than 100 µm size, the challenging task is to focus the beam through the 4 mm thick normal window glass without initiating the plasma formation inside the glass. We were able to detect the SF_6 filling within the window, as shown in Figure 3 (red) along with simulated LIBS spectra calculated with the NIST LIBS simulation tool [3]. The tilt within the measured spectrum is due to thermal shift and the measurement setup and can be subtracted (the data shown is as measured). The measured spectrum is clearly dominated by the first ionization of fluorine, which is shown in black. Low intensity absorption bands at 616, 648 and 664 nm indicate that the gas filling in the window may have been contaminated with some air (blue, simulated spectrum).

Outlook:

It was found that all gaseous components of a filling in soundproof windows can be measured using LIBS in a laboratory setting. The next steps will involve developing a portable device that can be used on a renovation construction site. In addition, a system for direct extraction of SF_6 from the windows is presented to reduce the risk of unwanted release when the windows are removed and to enable professional disposal. In our presentation, the latest results on the LIBS measurement setup and the recovery system will be shown and discussed.

References:

[1] NIST Standard Reference Database 69: NIST Chemistry WebBook; https://webbook.nist.gov/cgi/inchi/InChI%3D1S/F6S/c1-7(2%2C3%2C4%2C5)6 (04.04.2024)

[2] B.Rubin, T.K. McCubbin and S.R. Polo , J. Mol. Spectrosc. 69, 254-259 (1979); https://doi.org/10.1016/0022-2852(78)90063-2

[3] Kramida A., Ralchenko Y., Reader J., NIST ASD Team . NIST Atomic Spectra Database (Version 5.9) https://physics.nist.gov/PhysRefData/ASD/LIBS/libs-form.html (09.04.2024)

Authors Contributions:

C. Basler, G. Stiefvater and H.-F. Pernau performed the measurements. H.-F. Pernau worked on alternative detection possibilities, the SF_6 recovery system and wrote this article. K. Schmitt and J. Wöllenstein proofread and supervised this work.

Funding:

This work was funded by the Ministry of the Environment, Climate Protection and the Energy Sector Baden-Württemberg

Conflict of interest:

There are no conflicts of interest.

DOI 10.5162/EUROSENSORSXXXVI/OT4.86

Hall-effect sensors for extreme temperature applications

Semir El-Ahmar[1], Jakub Jankowski[1], Paweł Czaja[1], Wiktoria Reddig[1], Marta Przychodnia[1], Jan Raczyński[1], Wojciech Koczorowski[1]
[1] Institute of Physics, Poznan University of Technology, 61-138 Poznan, Poland

semir.el-ahmar@put.poznan.pl

Summary:
This work is focused on developing magnetic field sensors that rely on the Hall effect and can operate stably in extreme temperatures. We have achieved this by creating a Hall effect structure using indium antimonide and a housing that can withstand an extremely wide range of operating temperatures. Our device has been tested and proven to operate stably at high temperatures up to 350°C, as well as in the cryogenic range using liquid helium. This is a significant milestone as no other magnetic field sensor has been able to perform in such extreme temperature conditions.

Keywords: Hall effect, cryogenics, high-temperature electronics, magnetic field sensors, thermal stability

Motivation and state of the art

Magnetic field detection devices are highly valuable in many industries, thanks to the fact that they can measure various quantities such as position, movement, direction, and rotational speed. Nowadays, there is a high demand for electronics that can function reliably in harsh environments[1], including those that can withstand extreme temperatures [2]. By the term “extreme”, we mean mostly temperatures extremely high for electronics, in a mid-wide temperature range from room temperature up to high temperatures (above 200 °C), or extremely high reaching 500 °C [3]. Traditional electronics design often requires active or passive cooling, but this may not always be practical or effective. Hence, there is an increasing need for extreme environment electronics, particularly in the automotive, defense, and energy industries. [4,5]. Magnetic field sensors have great potential in high-temperature electronics. However, it's also important to consider their performance in low and cryogenic temperatures. A sensor that can provide precise magnetic diagnostics in a wide range of temperatures, from cryogenic temperatures up to liquid helium (LHe), through room temperature, and up to high temperatures, would be highly valuable in the market. This kind of sensor could be particularly useful for space research vehicles that need to travel through hot environments. A sensor that can operate accurately in a wide temperature range would offer new possibilities for diagnostic devices in space.
We have found that research on semiconductor-based Hall sensors operating in extreme conditions is limited to a temperature range from liquid nitrogen (LN) up to 350 °C [4]. On the other hand, alternative solutions based on monolayer graphene have been tested in the LN – 500 °C range in a magnetic field below 1 T. Our research explores the potential of using classic semiconductor thin-film material) as an active layer for a Hall effect sensor capable of measuring magnetic fields in extreme temperature ranges from liquid helium (LHe) temperatures up to 350 °C. We have verified the usability, thermal stability of our device and the linearity of its signal in the magnetic field range above 1 T. Additionally, we have proposed a solution for the sensor package suitable for an extremely wide range of work. We have developed a complete magnetic field sensor that can meet industrial requirements, manufactured using almost exclusively the academic infrastructure of the Poznan University of Technology. Our findings represent a significant step forward in the development of magnetic diagnostic devices that can operate in a broadly defined extreme environment.

Construction of a Hall sensor

The sensor consists of a Hall structure and an extreme temperature housing. Fig. 1 shows a real view of the series of fabricated devices. The Hall structure itself is placed under the white cover visible in Fig. 1, inside a ceramic casing. The Hall structure inside is made of a thin film of indium antimonide (InSb) doped with tin donor in the process of flash evaporation method. Details about the exact fabrication

technology of the Hall structure are included in Ref. [6].

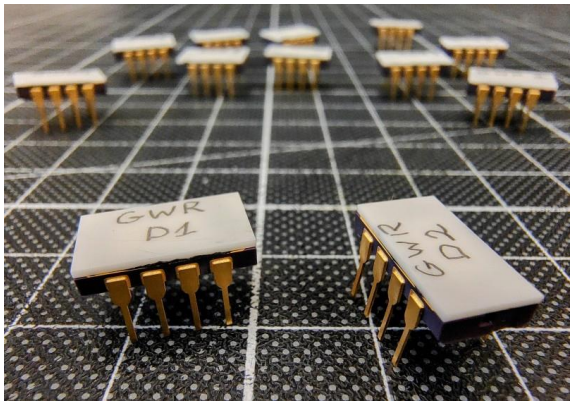

Fig. 1. Hall effect sensors in housings, ready for use at liquid helium temperatures, fabricated at Poznan University of Technology. The square scale under the sensors has a side of 10 mm.

The housing itself was made in accordance with the descriptions in [4], introducing a modification regarding the pins to simplify integration with the measuring holder for a helium cryostat.

Results in a nutshell

The effects of work on a Hall effect sensor that can function in extreme temperature conditions were verified through a series of Hall effect measurements utilizing three independent measurement systems. For high-temperature tests, a Linseis HCS 1 analyzer equipped with a 0.65 T permanent magnet was used. This was supported by a galvanomagnetic effects measurement system equipped with an electromagnet that enabled a smooth transition in the range of 0-0.65 T. These tests were previously described in Ref. [4]. The purpose of the new experiment was to measure the Hall effect at low temperatures and in very strong magnetic fields. The International Laboratory of Strong Magnetic Fields and Low Temperatures, which belongs to the Institute of Low Temperatures and Structural Research Polish Academy of Sciences, provided the necessary infrastructure for the experiment. Bitter electromagnets were used to generate a uniform, constant magnetic field in the range of 0 - 15 T. The Bitter magnet design allows the use of a liquid helium cryostat insert. The results of the experiment showed that the sensor signal (Hall voltage, UH) depended linearly on the magnetic field induction in the range of 0 - 1.2 T at a temperature of approximately 5 K. The linear nature of the dependence at extremely low temperatures was confirmed by the results, together with the research presented in Ref. [4]. The study will be further supplemented with the results of Hall effect measurements in a magnetic field above 10 T, both at room temperature and at liquid helium temperature.

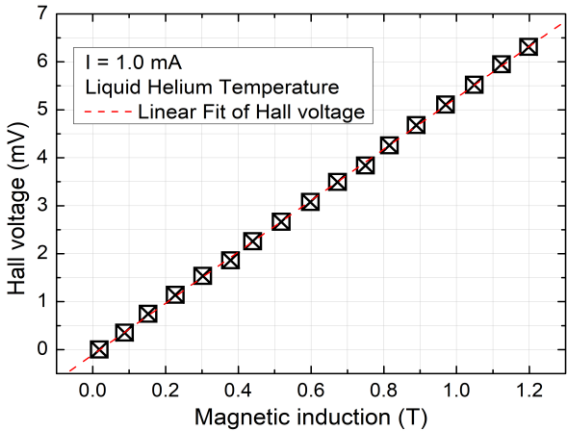

Fig. 2. Dependence of the Hall sensor signal on the magnetic field induction at the temperature of liquid helium.

The usefulness of the modified housing for applications in extreme environments was confirmed, making our sensor the first Hall sensor capable of stable operation in the temperature range from approximately -268 °C to 350 °C.

The research has received funding from the National Centre for Research and Development under Grant Agreement No. LIDER/8/0021/L-11/19/NCBR/2020 for project MAGSET and partly from the Ministry of Education and Science (Poland) under Project No. 0512/SBAD/2420.

References

[1] S. Eswarappa Prameela et al., Materials for extreme environments, *Nature Reviews Materials*, 8, 2, 81–88, 2023, doi: 10.1038/s41578-022-00496-z

[2] B. T. Schaefer et al., Magnetic field detection limits for ultraclean graphene Hall sensors, *Nature Communications*, 11, 4163 (2020), doi: 10.1038/s41467-020-18007-5

[3] T. Ciuk et al., High-Temperature Hall Effect Sensor Based on Epitaxial Graphene on High-Purity Semiinsulating 4H-SiC, *IEEE Transactions on Electron Devices*, 66, 7, 3134–3138 (2019), doi: 10.1109/TED.2019.2915632

[4] S. El-Ahmar et al., Magnetic Field Sensor Operating From Cryogenics to Elevated Temperatures, *IEEE Sensors Letters*, 7, 8, 1–4, article no. 2501904 (2023), doi: 10.1038/s41578-022-00496-z

[5] H. S. Alpert et al., Sensitivity of 2DEG-based Hall-effect sensors at high tempera- tures, *Rev. Sci. Instrum.*, 91, 2, 1–6, article no. 025003. (2023), doi: 10.1063/1.5139911

[6] M. Oszwaldowski et al., High temperature Hall sensors, *Sens. Actuators A Phys.*, 136, 234–237, (2007), doi: 10.1016/j.sna.2006.11

DOI 10.5162/EUROSENSORSXXXVI/OT4.90

Neutron Radiation Effects on Thin-Film and Two-Dimensional Magnetic Field Sensors

Wiktoria Reddig[1], Semir El-Ahmar[1], Rafał Prokopowicz[2], Tymoteusz Ciuk[3]

[1] Institute of Physics, Poznan University of Technology, Piotrowo 3, 61-138 Poznań, Poland,
[2] National Centre for Nuclear Research, 05-400 Otwock, Poland,
[3] Łukasiewicz Research Network – Institute of Microelectronics and Photonics, Aleja Lotników 32/46 02-668 Warsaw, Poland,

wikred@protonmail.com

Summary:
Reporting research findings on two types of magnetic field sensors for use in harsh environments and the impact of high-energy neutron flux on them. Researched sensors being 2-D epitaxially grown quasi-free-standing graphene on SiC and thin film InSb on GaAs. The research constitutes a continuation of the series of studies assessing the radiation resistance of graphene-based sensor platforms compared to classical thin-film magnetic diagnostic systems.

Keywords: Hall effect sensor, radiation-resistance, self-healing, magnetic diagnostic, neutron irradiation

Introduction

There has been an increasing interest in the development of magnetic field diagnostics in recent years, especially in sensors that can operate under harsh environments. These applications include aerospace, defense, and particularly the energy industry. The use of controlled nuclear fusion as an energy source of the future remains one of the greatest endeavors of our century [1]. To monitor thermonuclear processes, a complex sensor infrastructure is required. For magnetic fusion confinement, which is the most promising fusion technology, magnetic field sensing is one of the most crucial diagnostic elements. This field however still requires development since the sensing electronics will operate for an extended period under fast neutron radiation and high temperatures. Unfortunately, it has proven to be an incredibly difficult task, thus research into the most effective sensing platforms is still ongoing [2],[3].

Our research focuses on two magnetic field sensors with potential use in the energy industry: a semiconductor, thin film InSb-based and a 2-D, epitaxial graphene-based on silicon carbide (G@SiC) sensor. Both of these sensors have proven to be effective in temperatures up to 350 °C and fast neutron radiation fluence of 0.7×10^{18} cm^{-2} [4]. It has also been shown that any changes in irradiated graphene-based sensors' performance were caused by neutron radiation and not the impact of high temperatures [5]. In this research, we aim to show new findings on the effects of 3 times greater fast neutron fluence and the impact of a different polytype of silicon carbide substrate in graphene-based sensors.

Methods and materials

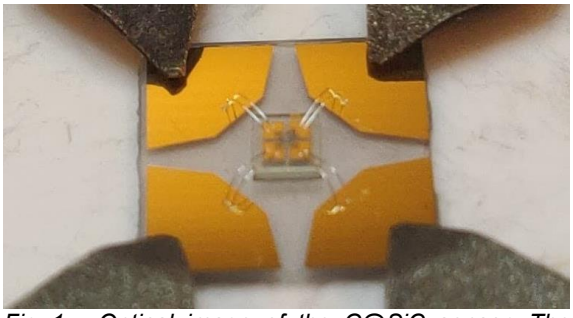

Fig. 1. Optical image of the G@SiC sensor. The sensing part is centrally placed and is connected to electrode plates to ease manual manipulation.

We present here two types of Hall effect sensors. First, a 2D-material in the form of hydrogen-intercalated quasi-free-standing graphene on a semi-insulating SiC substrate, passivated with an Al_2O_3 layer [6], which is visible in Fig.1. The sensors were fabricated on either 4H-SiC (0001) or 6H-SiC (0001) substrate. The other structure was prepared in the form of donor-

doped InSb-based thin-film on a semi-insulating GaAs substrate [4]. The tested systems were exposed to a fast neutron fluence of 2×10^{18} cm^{-2} using the MARIA research nuclear reactor in Poland.

After irradiation, the sensors' electrical parameters were measured during annealing cycles following the method described in [5].

Results

For graphene-based structures after irradiation, we theorize that the main factor affecting the electrical parameters is the loss of atoms in the hydrogen layer, based on Hall effect measurements and micro-Raman characterization. We anticipate that temperatures above 200°C will facilitate the diffusion of the hydrogen atoms from parts with higher to lower concentrations. This effect can reduce the surface area where intercalation is too low to support the separation of the graphene [4].

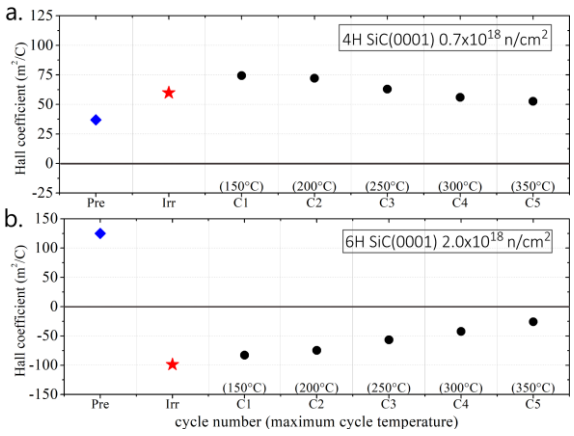

Fig. 2. The comparison of Hall coefficients of G@SiC on 4H and 6H SiC substrates. Blue squares represent measurements before irradiation, the red star measurements after irradiation, and each black dot is a room temperature measurement after the annealing cycle.

Fig. 2a shows the dependence of the Hall coefficient measured for a sensor irradiated in the neutron fluence of 0.7×10^{18} cm^{-2}. This graph was made based on the data from [4], [6] and is the starting point for the next experiment of irradiating the system with neutron fluence of 2×10^{18} cm^{-2}. Fig. 2b shows an analogous line of Hall coefficient changes before and after the experiment.

From the comparison of the obtained results, we can draw further conclusions about the destructive effect of the high-energy neutron flux on the G@SiC system. The Hall coefficient immediately after irradiation (comparison of red and blue points) changed sign in the case of the 6H sample (neutron fluence of 2×10^{18} cm^{-2}), which indicates a change in the type of conductivity of the system and may suggest excessive depletion of H intercalation or the influence of the 6H substrate. The nature of the changes after successive thermal cycles (trend of black circles) is also different. The presented studies based on Hall effect measurements will be complemented by micro-Raman analysis, which will be able to show the degree of defection of the graphene layer itself, thanks to which conclusions can be drawn about the radiation resistance of the entire graphene-based chip.

The results suggest the superiority of 2-D active layers over thin-films in terms of resistance to high energy neutron radiation.

Acknowledgements

The research has received funding from the National Centre for Research and Development under Grant Agreement No. LIDER/8/0021/L-11/19/NCBR/2020 for project MAGSET and partly from the Ministry of Education and Science (Poland) under Project No. 0512/SBAD/2420.

References

[1] J. Ongena, et al., Magnetic-confinement fusion, *Nature Physics*, vol. 12, no. 5, pp. 398–410, 2016, doi: 10.1038/NPHYS3745.

[2] S. Entler *et al.*, "Ceramic-chromium hall sensors for environments with high temperatures and neutron radiation," *Sensors*, vol. 21, no. 3, pp. 1–12, 2021, doi: 10.3390/s21030721.

[3] M. Kocan *et al.*, "Steady state magnetic sensors for ITER and beyond: Development and final design (invited)," *Review of Scientific Instruments*, vol. 89, no. 10, Oct. 2018, doi: 10.1063/1.5038871.

[4] S. El-Ahmar et al., The Comparison of InSb-Based Thin Films and Graphene on SiC for Magnetic Diagnostics under Extreme Conditions, *Sensors*, 22, 14, 5258 (2022), doi: 10.3390/s22145258

[5] W. Reddig, et al., "High-Temperature Stability of Sensor Platforms Designed to Detect Magnetic Fields in a Harmful Radiation Environment," *IEEE Sensors Letters*, vol. 7, no. 8, Aug. 2023, doi: 10.1109/LSENS.2023.3297795.

[6] T. Ciuk *et al.*, "Defect-engineered graphene-on-silicon-carbide platform for magnetic field sensing at greatly elevated temperatures," *Carbon Trends*, vol. 13, no. October, p. 100303, Dec. 2023, doi: 10.1016/j.cartre.2023.100303.

[7] S. El-Ahmar et al., Graphene on SiC as a promising platform for magnetic field detection under neutron irradiation, *Applied Surface Science*, 590, 152992 (2022), doi: 10.1016/j.apsusc.2022.152992

DOI 10.5162/EUROSENSORSXXXVI/OT4.138

Exploring a multi-mass system for multi-functional MEMS accelerometer with enhanced bandwidth and sensitivity

I.S. Garcia[1], M. Saleem[1], F. Mota[1], N. Castro[1], P. Valentim[1], R. Madeira[2], A. Correia[2], F. Khan[1], D.E. Aguiam[1], R.A. Dias[1] and F.S. Alves[1]
[1] INL - International Iberian Nanotechnology Laboratory, Braga, Portugal,
[2] BoschCar Multimédia Portugal

Corresponding Author's e-mail address: filipe.alves@inl.int

Summary:
This paper presents the design, fabrication, and experimental validation of a novel multi-mass MEMS accelerometer concept to achieve higher mechanical sensitivity with wide operational frequency bandwidth, in comparison to traditional single-mass MEMS accelerometers. The initial results show that the proposed approach has the potential to develop multi-functional MEMS accelerometers, with a preliminary device with 5.6 kHz resonance and more than 30% sensitivity improvement.

Keywords: Multi-DoF, MEMS Accelerometer, Nested displacement, High-bandwidth, High-Sensitivity

Introduction/State of the Art

In recent years, significant advancements have been observed in the autonomous driving field, highlighting the critical need for a deep understanding of the surrounding environment using advanced sensing capabilities. One of the key demands for such systems is to use multi-functionalization sensors that can detect multiple physical parameters, thus reducing the number of sensors to achieve reliability, reducing cost, power consumption, and area. MEMS accelerometers are widely used in automotive driver assistance systems, airbag safety systems, and electronic stability control [1]. However, for autonomous vehicles, in addition to these applications, the detection of acoustic signals is required for new functionalities [2]. The limitation of the current MEMS accelerometers is the trade-off between the required operational frequency bandwidth (up to 6 kHz) and sensitivity. Recent works have presented MEMS accelerometer with significantly wider bandwidths but at the cost of a reduced resolution due to the sensitivity/bandwidth trade-off [3]. This trade-off arises due to the structural design of traditional MEMS accelerometers, consisting of a single proof mass suspended by mechanical beams that inversely affect resonance frequency and mechanical gain.

Description of the New Method or System

Fig. 1 shows a 4-DoF MEMS accelerometer mass-spring-damper model with an input acceleration $\ddot{y}$ applied to the base and equations of motion are given in Eq. 1. The energy transfer between the masses allows to achieve a dynamically amplified displacement in the mass m_4 (final sensing mass). The displacement amplification in m_4 and the first resonance frequency position (which defines the operational bandwidth) can be tuned by optimizing mass, m, stiffness, k, and damping, c, parameters. As proof of concept, it was initially considered an identical k/m ratio for each mass-spring unit and a damping coefficient of zero, with the exception of c_5, which represents the squeeze-film damping on sensing plates attached to the sensing mass, m_4.

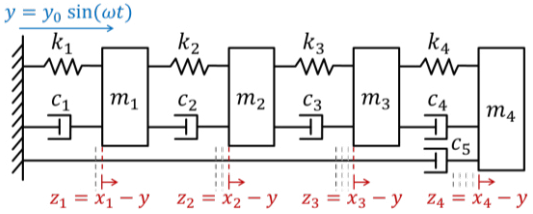

Fig. 1. 4-DoF mass-spring-damper model.

$$\begin{bmatrix} m_1 & 0 & 0 & 0 \\ 0 & m_2 & 0 & 0 \\ 0 & 0 & m_3 & 0 \\ 0 & 0 & 0 & m_4 \end{bmatrix} \begin{bmatrix} \ddot{z}_1 \\ \ddot{z}_2 \\ \ddot{z}_3 \\ \ddot{z}_4 \end{bmatrix} + \begin{bmatrix} c_1 + c_2 & -c_2 & 0 & 0 \\ -c_2 & c_2 + c_3 & -c_3 & 0 \\ 0 & -c_3 & c_3 + c_4 & -c_4 \\ 0 & 0 & -c_4 & c_4 + c_5 \end{bmatrix} \begin{bmatrix} \dot{z}_1 \\ \dot{z}_2 \\ \dot{z}_3 \\ \dot{z}_4 \end{bmatrix} + \begin{bmatrix} k_1 + k_2 & -k_2 & 0 & 0 \\ -k_2 & k_2 + k_3 & -k_3 & 0 \\ 0 & -k_3 & k_3 + k_4 & -k_4 \\ 0 & 0 & -k_4 & k_4 + k_5 \end{bmatrix} \begin{bmatrix} z_1 \\ z_2 \\ z_3 \\ z_4 \end{bmatrix} = \begin{bmatrix} -m_1\ddot{y} \\ -m_2\ddot{y} \\ -m_3\ddot{y} \\ -m_4\ddot{y} \end{bmatrix} \quad (1)$$

Fig. 2 shows the proposed multi-DoF MEMS accelerometer frequency response compared with an equivalent traditional 1-DoF for an input acceleration of 1 g. The proposed device presents a clear amplification of m_4 displacement amplitude by a factor of 2.4 with respect to m_1, and by 1.31 to the 1-DoF.

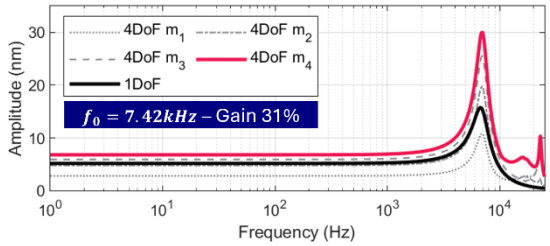

Fig. 2. Frequency response comparison of proposed 4-DoF and traditional 1-DoF model.

The detailed MEMS layout and cross-sectional views are presented in Fig. 3, highlighting in different colors the multiple masses. The design enables differential sensing of the m_4 amplified displacement, relative to the fixed frame through two sets of differential sensing electrodes. The handle layer proof-masses were thinned and used as a mechanical bridge linking different parts of the movable masses (CS B), therefore achieving mechanically coupled structures while remaining electrically decoupled. This approach avoids the need for a direct electrical connection to a device's inner part, reducing the possible damage during wire bonding process.

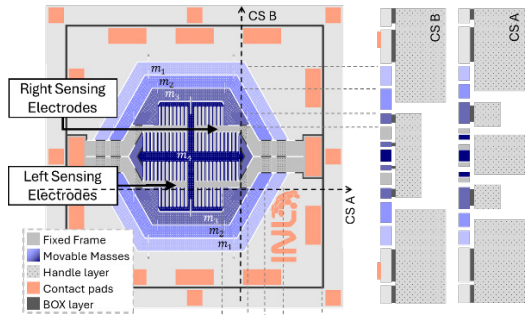

Fig. 3. MEMS accelerometer design layout.

The devices were fabricated through an in-house process on a 50 µm-thick silicon-on-insulator (SOI) wafer, taking into advantage the multi-mass SOI-based fabrication process presented in [4], which allows the development of hierarchical, matryoshka-like MEMS structures. The main fabrication steps are presented in Fig. 4, as well as the SEM images of the fabricated device.

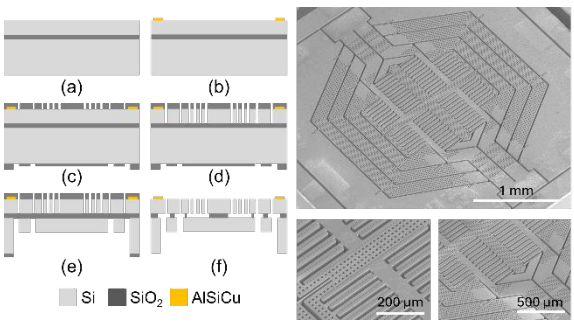

Fig. 4. Fabrication process, and SEM images:(a) SOI-wafer preparation; (b) AlSiCu patterning; (c) FS and BS HM PECVD and patterning; (d) FS DRIE; (e) BS multilevel DRIE; (f) HF structure release.

Experimental Results

The device frequency response, from 1 to 30 kHz, was experimentally evaluated, Fig. 5, using the sensing electrodes as electrostatic actuators, while measuring the in-plane motion using Polytec MSA-500 stroboscopic video microscopy. The first resonance frequency was measured at 5.6 kHz, lower than the designed 8.51 kHz. This shift is due to the over-etch and larger thinned handle thickness registered in the fabrication process, which lead to lower resonant modes (thinner springs and larger masses) and higher quality factors (larger gaps). The fabricated devices parameters $(m-k-c)$ were measured, and the analytical response was recomputed, Fig. 5. The results show a strong correspondence between analytical and experimental data, thus validating the analytical model. This proves that when compared with the typical 1-DoF MEMS device (assuming equivalent mass and stiffness proportional to resonance frequency of 5.6 kHz), this device has a 30% increase in displacement for the sensing mass m_4. These preliminary results are promising, showing that multi-DoF inertial MEMS can achieve high bandwidth with relatively better sensitivity, enabling their use as multipurpose sensors in autonomous vehicles. Future work will focus on the optimization of mass-stiffness parameters for higher mechanical gain and wider bandwidth, as well as damping to achieve flat frequency response.

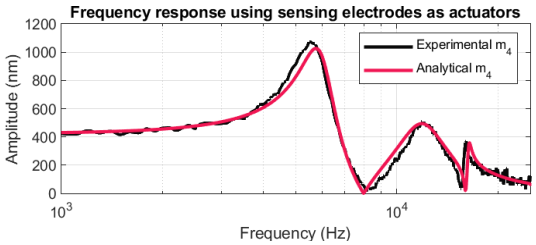

Fig. 5. Experimental and analytical model frequency response, using sensing electrodes as actuators.

References

[1] Jin L. Applications and prospects of MEMS sensors in automotive. In Journal of Physics: Conference Series 2021 Apr 1 (Vol. 1884, No. 1, p. 012010). IOP Publishing.

[2] Lu J, et.al., A review of sensory interactions between autonomous vehicles and drivers. Journal of Systems Architecture. 2023 Jun 26:102932.

[3] AnalogDevices, ADXL1001/ADXL1002: High frequency, low noise, 1-axis accelerometers, 2013.

[4] I.S. Garcia, et.al., Microfabrication of double proof-mass SOI-based matryoshka-like structures for 3-axis MEMS accelerometers, Micro and Nano Engineering, Vol. 19, 2023.

DOI 10.5162/EUROSENSORSXXXVI/OT4.169

A Novel Barometric Pressure Sensor with a Capacitive Transducer and with Improved Mechanical Robustness in a Media Robust Packaging

Ferenc Lukács[1], Volkmar Senz[2], Thomas Friedrich[3], Ariel Wu[4]
[1] Engineering Sensors Budapest, Robert Bosch Kft., Budapest, Hungary,
[2] Engineering MEMS Design, Robert Bosch GmbH, Reutlingen, Germany,
[3] Engineering Sensor Technology, Robert Bosch GmbH, Reutlingen, Germany,
[4] First Level Packaging of Sensors, Robert Bosch Taiwan Co. Ltd., Taipei, Taiwan

ferenc.lukacs@hu.bosch.com

Summary:

This paper reports a novel barometric pressure sensor with a capacitive transducer for consumer application. The concept of the MEMS chip and the improvement in performance compared to the previous generation of pressure sensor are shown. Furthermore, bumpers were designed with the help of Finite Element Analysis (FEA) to improve the mechanical robustness of the transducer. Finally, by putting the MEMS chip into a media robust package further challenges raised that were investigated with FEA and solved with a novel packaging process.

Keywords: pressure sensor, capacitive transducer, bumpers, media robust, gel fill

Background, Motivation an Objective

Barometric pressure sensors are well known in automotive and consumer applications for a long time now. For such kind of sensors, there are two major MEMS technologies available on the market, either with piezoresistive or capacitive transducer [1]. Especially for applications that require low current consumption, low noise, and high accuracy, capacitive pressure sensors (CPS) are more suitable than piezoresistive pressure sensors (PZR) [2].

These sensors have robustness requirements to withstand certain overpressure loads or high mechanical shock. To fulfil these requirements, additional mechanical design measures might be necessary.

For certain use cases (e.g., in mobile phones or smart wearables), the sensor should withstand the water immersion of the device as well, thus a media robust sensor packaging is required. A common way to realize this is to cover the chip components of the sensor package with gel material. The gel material serves as chemical protection, on the other hand its incompressibility allows the transfer of the ambient pressure to the pressure sensitive-membrane. In addition, due to its very low stiffness (Young's modulus in kPa regime) the negative effect on the sensor performance is minimized.

Description of the New Method or System

In this paper a novel barometric pressure sensor is presented, containing a MEMS chip with capacitive transducer and some unique design and features in a media robust packaging (see Fig. 1). Those features are a stiffening structure within the membrane for improved sensitivity and an integrated reference capacitances for implementing an on-chip Wheatstone bridge (see Fig. 2).

The fulfillment of robustness requirements induced further design measures: bumpers were introduced on the non-stiffened region of the membrane to further reduce the mechanical stress in the structure during overpressure load.

The media robustness of the package was solved with an open, cylindrical lid and with filling the chip stack inside the lid with a gel material. However, it turned out that even the very soft gel material can cause a specific performance problem that needs to be solved to reach the performance requirements.

Results

The improved accuracy of the CPS is proven by a direct comparison to a previous generation PZR with a high-resolution measurement during a down and up stair climb (see Fig. 3). Each of the 15 steps, corresponding to a height difference of 15.5cm or ~2.1Pa per step, are clearly visible for the measurement with the CPS,

whereas for the PZR the single steps are not resolved, only the overall height difference is captured.

FEA showed that during overpressure, the maximum mechanical stress occurs at the edges of the membrane. This mechanical stress can be effectively reduced in high pressure regime (>10bar) by introducing mechanical bumpers on the membrane (Fig. 4). With the help of FEA, a workflow was established to determine the optimal height, position and support of the bumpers and thus gain the highest reduction of the maximum mechanical stress. With the optimal bumper design, the mechanical stress can be reduced by ~30% at 10bar overpressure load and by ~60% at 50bar overpressure load (see Fig. 5).

The first media robust CPS samples showed a pressure accuracy problem that is caused by the earth gravitation. The sensor is so sensitive that by simply rotating the sensor by 180° (either the gravity pushes the membrane towards the enclosed cavity or the membrane is pulled away from it), the pressure signal changes by appr. 10Pa. FEA has shown that the gravity effect is considerable only if there is a high amount of gel on top of the membrane, because the effect is mainly affected by the mass of the gel. The final solution was the development of the so called “minimum gel fill” process, with which it is possible to cover all chip components in a way that the membrane is covered only with a few µm thick gel film (see Fig. 6). As the huge mass above the membrane is removed, the gravity effect becomes negligible, while the media protection is still kept.

Illustrations, Graphs, and Photographs

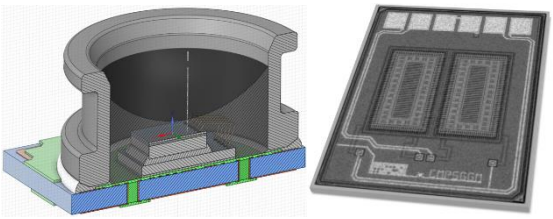

Fig. 1. Schematic cross-section of a barometric pressure sensor BMP585 from Bosch Sensortec with capacitive transducer concept, in a media robust packaging with standard gel fill (left); Optical image of the top of the MEMS chip (right)

Fig. 2. Schematic cross section of the sensing structure with stiffening structure and sense capacitance (A), reference capacitance (B) and membrane suspension (C).

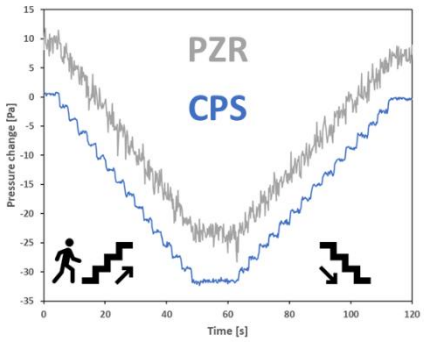

Fig. 3. High-resolution measurement during a down and up stair climb showing the improved accuracy of a capacitive pressure sensor (CPS) compared to a previous generation piezoresistive pressure sensor (PZR). The PZR signal is shifted by +10Pa for better readability.

Fig. 4. Schematic cross section of the sensing structure in a deflected state equipped with the mechanical bumpers (A). For better visibility, the deflected state is artificially scaled up.

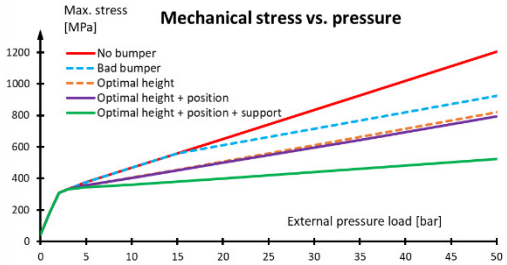

Fig. 5. Maximum mechanical stress over external pressure load for different bumper configurations.

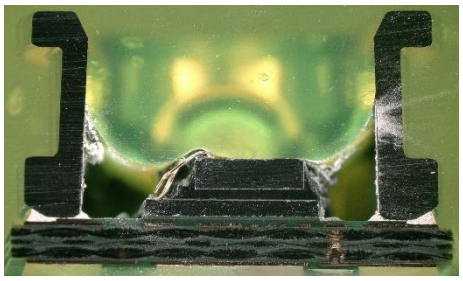

Fig. 6. Optical cross section image of the BMP585 pressure sensor with the new minimum gel fill process.

References

[1] Y. Chang, J. Zuo, H. Zhang and X. Duan, *Nanotechnology and Precision Engineering 3* (2020), pp. 43-52

[2] K. B. Balavalad and B.G. Sheeparamatti, *Sensors & Transducers, Vol. 187, Issue 4* (2015), pp. 120-128.

DOI 10.5162/EUROSENSORSXXXVI/OT4.197

Metrology of magnetic losses in electrical steel sheets using shear acoustic waveguide magnetic field sensor.

O. Marbouh[1], A. Mazzamurro[1], M. Boutghatin[1], O. BouMatar[1], Y. Dusch[1], V. Maurice[1], R. Viard[4], A. Ammar[3], P. Pernod[1], N. Tiercelin[1], A. Tounzi[2] , A. Benabou[2] , A. Talbi[1]

[1] University of Lille, CNRS, Centrale Lille, University Polytechnique Hauts-de-France, UMR 520 - IEMN, LIA LICS, Lille F-59000, France.

[2] 2 L2EP, University of Lille, Bât. ESPRIT - 59655 Villeneuve d'Ascq, France.

[3]Jeumont Electric, Jeumont, France.

[4] Groupe Endress+Hauser, Fribourg-en-Brisgau, Allemagne.

Abdelkrim.talbi@centralelille.fr, Othmane.marbouh@centralelille.fr

Summary:
Magnetic energy loss in electrical steel sheets account for approximately 10% of all electrical power generated, despite continuous improvements to their magnetic properties. Therefore, understanding these losses is imperative for optimizing the design of energy conversion systems. This study proposes the development of a new design of magnetic field sensor based on a shear surface acoustic waveguide on Quartz ST-cut, functionalized with a multilayer TbCo2/FeCo magnetic thin film presenting uniaxial anisotropy induced during deposition. This design enables both in-situ and ex-situ measurement of magnetic losses on the surface of ferromagnetic steel sheets. The overarching objective is to monitor magnetic behavior in electrical machines, aligning with the demands of Industry 4.0 and predictive maintenance strategies.

Keywords: Surface Acoustic Wave (SAW), Shear acoustic waveguide, magnetic field sensor, Magnetoelastic thin films, magnetic losses, Electrical machines.

Background, Motivation an Objective

Electric steel sheets are well-known for its excellent magnetic properties, making it perfect for use in electrical motors generators, and transformers. These types of steel mainly contain iron-silicon (Fe-Si) and iron-silicon-aluminum (Fe-Si-Al) alloys. They're usually found as thin plates, ranging from 0.35 mm to 0.5 mm thick. These sheets undergo periodic magnetization during operation causing up to 10 % of the energy produced to be lost. Understanding magnetic energy losses in steel sheets used in electrical machines is crucial for several reasons. Firstly, it optimizes component design to minimize losses, leading to more energy-efficient machines. Secondly, it enables the development of heat-resistant components, enhancing machine reliability. Additionally, it helps establish quality standards to ensure materials meet required specifications for electrical applications. Lastly, reducing magnetic losses improves overall energy efficiency, addressing the need for energy conservation and environmental sustainability [1].
According to international standards, magnetic energy loss is typically assessed using either the Epstein Tester [1] or the Single Sheet Tester [2]. In the latter methods, the sample undergoes magnetization in a nearly uniform manner. For loss measurements, induction is typically detected using a B-coil positioned around the sample. Alternatively, proximity Hall magnetic field sensors can also be employed. In first case, the obtained result represents the averaged induction across the sample's cross-section. Notably, direct measurement of induction at the sample's surface has been challenging.
In this study, we propose a novel design for a magnetic field sensor capable of locally measuring induction near the sample's surface. This design integrates a surface shear acoustic wave device with uniaxial magnetoelastic thin films, resulting in a robust and highly sensitive magnetic field sensor. The subsequent results presented herein will primarily focus on validating the sensor design using the Mini-SST experimental setup.

Sensor design and principle

The design comprises a surface acoustic waveguide delay line with two Inter-digital Transducers (IDTs) serving as emitter and receiver. These IDTs are made of Ti (20 nm) / Al (180 nm) on an ST-cut Quartz substrate (Y+42°), oriented perpendicular to the X-axis (principal axis of quartz crystal) to facilitate the excitation of pure shear surface waves. The propagation path between emitter and receiver is coated with a 140 nm thick layer of magneto-electric material composed of TbCo2\FeCo, extending 2 mm along the propagation direction. The device and fabrication process are depicted in Figure 1.

The operational principle of the sensor involves changing the phase velocity of the surface acoustic wave within the magnetoelastic thin film when an external magnetic field is applied, resulting in an electrical phase shift variation. This variation is measured using microwave electronic conditioning or a network analyzer. The magnetoelastic thin film utilized in this experiment has both an easy and hard axis, with the easy axis aligned parallel to the propagation direction. The typical response of the sensor is shown in figure 1(b).

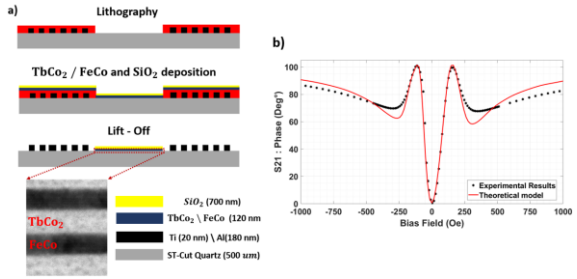

Figure 1 : a) Steps of the SAW sensors fabrication process. b) Magnetic saw calibration.

Magnetic energy losses measurements

For measuring magnetic losses on the surface of ferromagnetic sheets, we utilized a miniaturized Single Sheet Tester (SST) setup, depicted in Figure 2-a. Equipped with a high-permeability yoke, this setup ensures the generation of a magnetic field and system polarization through a primary coil encircling the yoke. This primary coil facilitates the generation of a static and dynamic magnetic field at various amplitudes. The blue graph in Figure 2 illustrates the measured excitation current using a current probe. Additionally, the black graph represents the linear extrapolation of the field at the steel's surface based on measurements from two Hall effect sensors and the red graph presents the magnetic field at the steel's surface measured by the magnetic SAW sensor. The results indicate that the magnetic field measured by the magnetic SAW sensor aligns with the field extrapolated from measurements of the two Hall effect sensors.

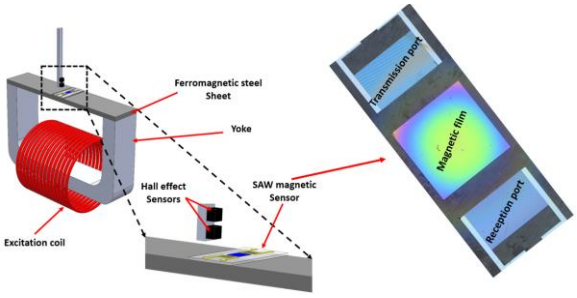

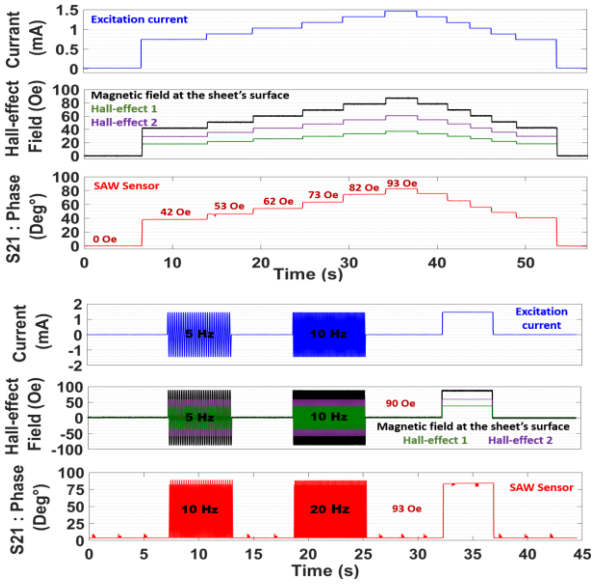

Figure 2 : a) Mini-SST equipped with two hall-effect probes and a magnetic SAW sensor. Magnetic energy losses measurement : b) Static, c)Dynamic.

Conclusion

The conducted study focused on the magnetic and mechanic instrumentation of a ferromagnetic sheet, with a wireless SAW sensor. This development establishes the groundwork for overcoming the limitations of strain gauge and Hall-effect sensors for real-time, wireless mechanical and electromagnetic characterization of magnetic materials used in energy conversion systems such as electrical machines. Indeed, these sensors also offer the advantage to be less intrusive for onboard implementation in rotating electrical machines in the context of diagnosis based on magnetic field and mechanical measurement.

Acknowledgement

This work was funded by the French National Research Agency (ANR) in the framework of ANR 20-CE42-0009 project. It is also supported by the CPER EE4.0 and IMITECH project and the company Jeumont Electric. The authors also thank RENATECH, the French national nanofabrication network.

References

[1] S. Lopez et al., "Grain Oriented Steel Assembly Characterization for the Development of High Efficiency AC Rotating Electrical Machines," in IEEE Transactions on Magnetics, vol. 45, no. 10, pp. 4161-4164, Oct. 2009, doi: 10.1109/TMAG.2009.2023243.

[2] O.Lahyaoui, Contribution to the study of magnetostrictive energy conversion : from material to device, Ph.D, thesis, Université de Technologie de Compiègne, France, 2019.

[3] O. Marbouh et al., "Magnetostrictive strain monitoring in Non-Oriented Si-Fe steels using a SAW resonator sensor" Journal of Magnetism and Magnetic Materials, Volume 589, 1 January 2024.

DOI 10.5162/EUROSENSORSXXXVI/OT4.209

Ultra-Sensitive Force Gauge Accessory for Microscope Micromanipulators

János Márk Bozorádi[1,2], Anett Szeledi[2], Ferenc Braun[1], Attila Nagy[1], Levente Illés[1], János Radó[1], János Volk[1]

[1] HUN-REN Centre for energy Research, 1121 Budapest, Hungary,

[2] Doctoral School on Material Sciences & Technologies, Óbuda University, H-1034 Budapest, Hungary

volk.janos@ek.hun-ren.hu

Summary:

Micromanipulators equipped with sharp needles are now indispensable tools for ultra-sensitive operations under the optical or electron microscope, which are mainly visually guided. Measuring the local mechanical forces acting on probe tip can give another important feedback to the operator, or to the closed-loop actuators in automated systems. However, measuring contact forces, especially as a vector quantity, is highly challenging. In this work, we present a lightweight, compact, two-dimensional piezoresistive MEMS sensor-based system, that can be mounted on the tip of a commercially available 3-axis piezo-actuated micromanipulator. As the calibration with an atomic force microscopy probe reveled the sensitivity of the sensor is a few μN at an electric response of 29 μV/μN. To demonstrate the capability of system, in-situ static tests were carried out on an Pt micorwire.

Keywords: Piezoresistive force sensor, add-on tool, AFM probe, Pt micorwire, Young modulus

Motivation and Objective

Micromanipulator is a robotic tool with extremely precise position control along three to six degrees of freedom for transferring micro- and nanometer sized objects under an optical or scanning electron microscope (OM/SEM). It is used in various fields, such as specimen fabrication for transmission electron microscope (TEM lamella), electrical probing during IC failure analysis, cell biology, robotic surgery etc. [1]. These manipulations are usually controlled by the operator using real-time optical camera or electron detector image. For many applications, however, local sensing of the force would be an effective tool to provide direct feedback to the operator. In addition, in automated industrial processes direct feedback is essential for the closed-loop actuators.

Over the last three decades, a number of techniques have been used to force sensing in the range below pN up to several mN [2]. Among them piezoresistive force sensors have several advantages: such as high signal-to-noise ratio, wide measuring range, low cost, and compact size. Until now, piezoresistive and the strain-based manipulator sensors have been mainly applied for one-dimensional force sensing in the mN to sub mN range.

Our aim was to demonstrate a compact, lightweight 2-dimentional piezoresistive force sensor system which can be mount on a tip of an ultrafine piezoelectric manipulator and to increase the sensitivity down to the few micronewton force range.

Description of the System

The system was adapted to our ultrafine 3-axis piezo-actuated SEM micromanipulator (Kleindiek Nanotechnik MM3A-EM) (Fig. 2c). The center of the system is a 3 dimensional piezoresitive force chip [3] (Fig. 2a), which is extended with a sharp W needle having a diameter/length/radius of of 250 μm/15 mm/~100 nm (Fig. 2b) to manipulate microscopic objects. Due, to elongated lever arm, the sensitivity of the force measurement is enhanced along the transversal direction and remained unchanged for the normal direction, resulting in a quasi-two-dimensional force gauge. Conventional flexible as well as purpose designed polyimide cabling were used to avoid interference with the movement of the inchworm-type piezomotor. The analog signals from the four bridges of the piezoresistive force sensor chip are digitalized by the electronics located under the manipulator and transmitted to the controller notebook via the SEM feedthrough.

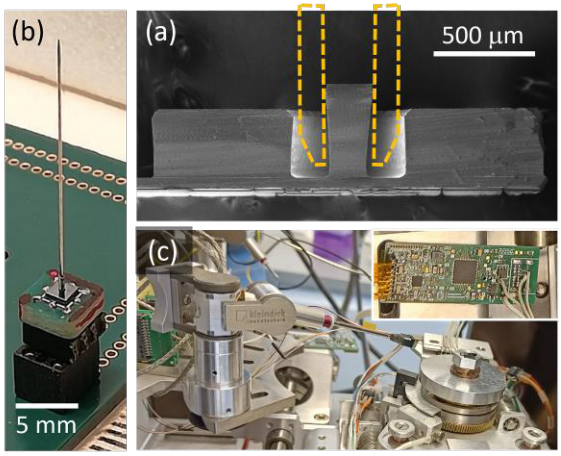

Fig. 1. (a) SEM image of the bisected piezoresistive chip; yellow dashed line indicates the position of the probe adapter (a). Force gauge chip mounted on the PCB and equipped with an ultrasharp probe (b). Force sensing system set up inside the SEM, ready for in-situ nanomechanical test (c). Inset shows the purpose-built readout electronics

Results

Prior to the nanomechanical tests, the force response of the sensor accessory was determined by standard atomic force microscopy (AFM) probes in an in-situ static bending test (Fig. 2a, lower inset) where the tip of the force sensor was pressed against the cantilever, while both sensor signals and the cantilever deflections were recorded. The force constants of the calibrating AFM probes were determined by Sader method in the AFM apparatus (AIST-NT) (Fig. 2a upper inset) [4]. To cover a wider range of the calibration a standard (k=48.8 N/m) and a relatively soft (k=2.8 N/m) tapping mode AFM probes were selected. The force calibration data obtained for the two sets of measurements are in good agreement (R≈29 μV/μN). According to the tests ultralow load forces, down to the 1-2 μN range, can be consistently detected.

In order to demonstrate the capability of the add-on force sensor tool, we carried out a nanomechanical bending test on Pt microwires created by ion beam assisted deposition (IBAD) in a cross-beam SEM/FIB system (FEI Scios). As shown in Fig. 2b, by recording the static bending deflection (Fig. 2b) as a function of the measured load force, the nanoelectromechanical properties of the microwire can be evaluated. By performing finite-element analysis (Fig. 2b, upper inset), we obtained a Young-modulus of Y≈70 GPa for the IBAD microwire which is significantly lower than that of the pure bulk Pt (168 GPa). The softening of the microwire can be attributed to the high carbon content of the IBAD microstructure.

In summary the demonstrated compact piezoresistive force sensor is a power ad-on tool for micromanipulators to measure the local force during the manipulation of microscale objects.

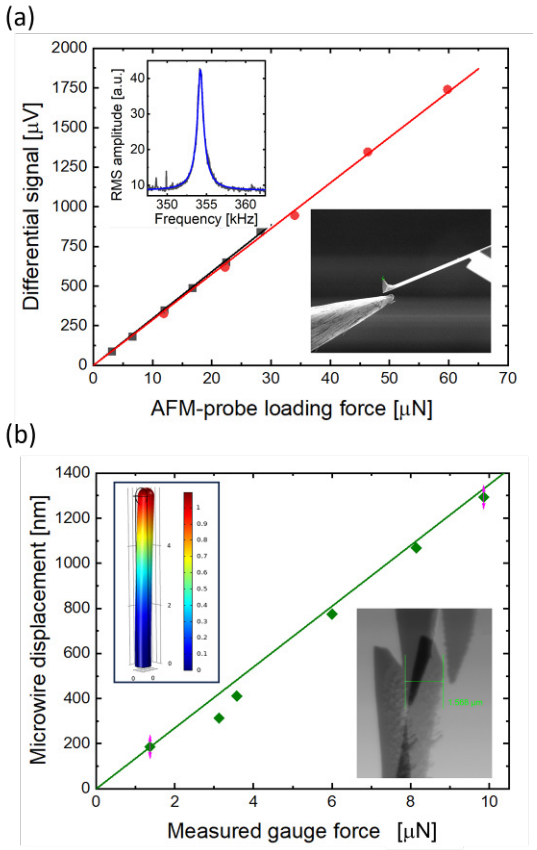

Fig. 2. (a) SEM force sensor calibrated by AFM probes with static bending experiments (lower inset). The force constant of the calibrating probe was beforehand determined (upper inset). (b) In-situ SEM nanomechanical bending test of a Pt microwire (lower inset). Finite element analysis of the wire (upper inset) revealed a Young-modulus of 70 GPa.

References

[1] Z. Zhang, X. Wang, J. Liu, C. Dai, and Y. Sun, "Robotic Micromanipulation: Fundamentals and Applications," *Annu. Rev. Control Robot. Auton. Syst.*, vol. 2, no. 1, pp. 181–203, May 2019, doi: 10.1146/annurev-control-053018-023755.

[2] Y. Wei and Q. Xu, "An overview of micro-force sensing techniques," *Sensors and Actuators A: Physical*, vol. 234, pp. 359–374, Oct. 2015, doi: 10.1016/j.sna.2015.09.028.

[3] J. Radó *et al.*, "3D force sensors for laparoscopic surgery tool," *Microsyst Technol*, vol. 24, no. 1, pp. 519–525, Jan. 2018, doi: 10.1007/s00542-017-3443-4.

[4] J. E. Sader, J. W. M. Chon, and P. Mulvaney, "Calibration of rectangular atomic force microscope cantilevers," *Review of Scientific Instruments*, vol. 70, no. 10, pp. 3967–3969, 1999, doi: 10.1063/1.1150021.

DOI 10.5162/EUROSENSORSXXXVI/OT4.215

Scalable Microfabrication of Graphene Polymeric Strain Gauge

Farid Sayar Irani [1], Melih Can Tasdelen[1*], Murat Kaya Yapici[1,2,3]*
[1] Faculty of Engineering and Natural Sciences, Sabanci University, 34956 Istanbul, Turkey,
[2] Department of Electrical Engineering, University of Washington, 98195 Seattle, USA
[3] Sabanci University SUNUM Nanotechnology Research Center, 34956 Istanbul, Turkey

* These authors have contributed equally

murat.yapici@sabanciuniv.edu

Summary:
This paper presents the fabrication and characterization of a strain gauge based on chemical vapor deposition (CVD)-grown graphene integrated to an epoxy-based, photo-patternable and flexible SU-8 cantilever for sensing applications. The fabrication process involved a standard semiconductor microfabrication process to create serpentine-shaped graphene and gold/graphene sensing layers on a polymeric SU-8 layer. The performance of the strain gauge was evaluated by subjecting it to controlled bending, demonstrating a gauge factor (GF) of 2.73 and fast response time (0.55 s) affirming the viability of the fabricated strain gauge for practical sensing applications.

Keywords: Pressure sensor, Microfabrication, Strain gauge, Graphene, SU8

Introduction

Sensing technologies and specifically strain sensors are growing fast as their demand is increasing in industries including electronics, healthcare, manufacturing, transportation, defense, as well as scientific exploration.[1, 2] One of the most cost-effective and easy data analysis models for strain sensors is piezoresistivity which is working based on converting mechanical loading into resistance change. Designing high-performance piezoresistive sensors involves considering various parameters which among them, sensitivity, evaluated by the gauge factor (GF), remains a fundamental metric, which relates the ratio of relative change in electrical resistance, R, to the applied strain, ε. While conventional materials like metals offer limited gauge factors, graphene, one of the key 2D carbon-based nanomaterials with its remarkable mechanical and electrical properties, emerges as a promising candidate for strain sensors.[3] However there are challenges in obtaining high-quality, uniform graphene and repeatably integrating it into scalable device architectures.

In this study, we report the development of CVD-graphene based strain gauges on SU-8, an epoxy-based negative photoresist (PR), as a flexible substrate using standard microfabrication processes. The results obtained from the

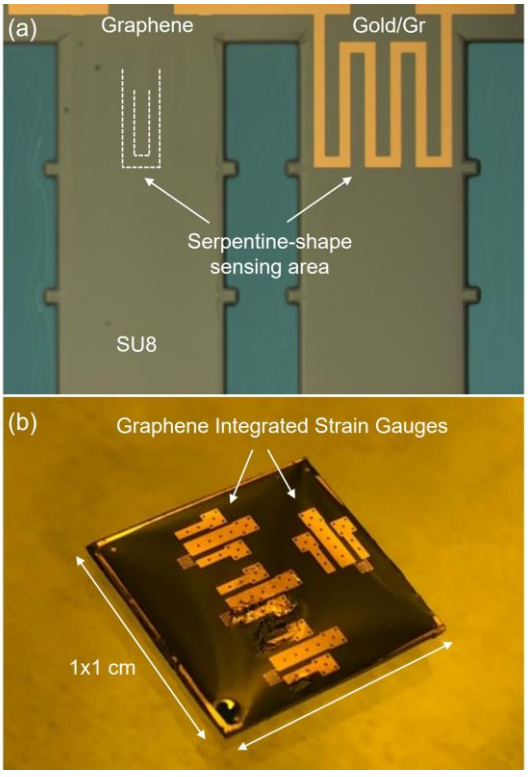

Fig. 1. (a) Graphene and gold/graphene integrated strain gauge on flexible SU-8 photopolymer. (b) Successfully fabricated four sensors from a 1×1 cm Nickel coated sample.

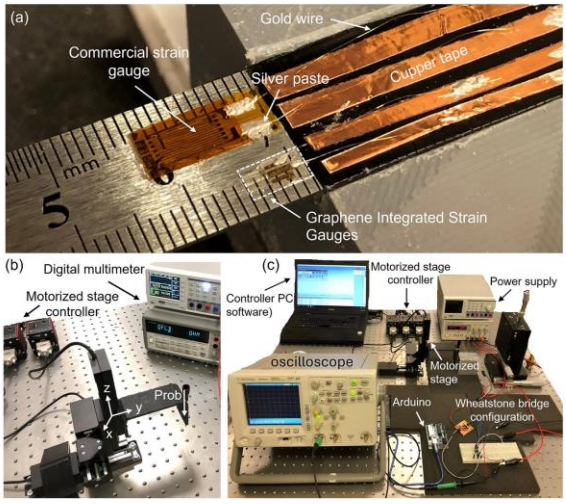

Fig. 2. (a) Mounted sensors on a metal bar. (b) Motorized stage and measurement devices. (c) Measurement setup and Wheatstone bridge configuration.

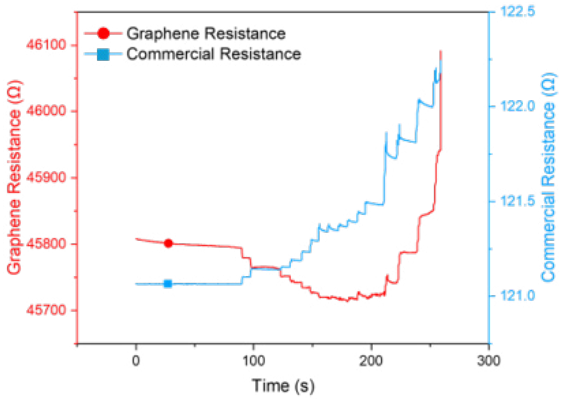

Figure 3. (a) Sensors' resistance behavior vs. time by applying force and bending the metal bar. (b) Relative resistance changes vs. applied strain for both commercial and graphene sensors

mechanical and electrical characterization of the device show a sensitivity (*GF*=2.73) comparable to that of a conventional metal-based commercial strain gauge.

Materials and Methods

A 1×1cm sample of nickel-coated silicon substrate onto which few-layer graphene (FLG) was grown was coated with a 300nm-thick layer of gold (Au) by e-beam evaporation that acts as both protective layer and conductive interconnects and pads. Then by using UV-lithography and wet etching the gold layer was patterned to the desired serpentine-shape and the graphene layer around it was etched by O_2 plasma. Moreover, the gold was selectively removed from one of the arms. Next, a 100µm thick SU-8 layer was spin-coated on the sample and patterned by UV-lithography to achieve a polymeric cantilever. Finally, the sample was immersed into buffered oxide etchant (BOE) for 3 h in order to release the structure. Figure 1 shows images of successfully fabricated sensors and their sensitive areas. Measurement of the variation in resistance of the sensors due to applied stress was achieved by mounting the sensor on a metal bar next to a 120Ω metal-foil commercial strain gauge (GF=2.14) as a reference (Fig. 2a). By applying loading from the free end of the metal bar and bending it, using a x-y-z motorized stage, a uniform stress is applied to the sensors (Fig. 2b). To calculate the applied stress, first, the strain measured in commercial strain gauge via resistance change, using a Wheatstone bridge configuration, and then the strain value was multiplied by the elastic modulus of Polyimide (2.5 GPa) (Fig. 2c). Furthermore, the derived stress value was divided by Young's modulus of SU-8 (3.6 GPa) to measure the strain experienced by the graphene sensor.

Results and Discussion

The strain gauges' behavior was assessed by controlled bending of the metal bar (Fig. 3). Using calculated strain and relative resistance change values, a higher sensitivity for fabricated strain gauges was observed compared to the commercial one. Graphene and gold-based strain gauges demonstrated approximately 30% higher sensitivity (GF) (GF=2.73) than the commercial strain gauge. Moreover, graphene shows a negative GF in low strains, and it changes to positive GF after a specific deflection, while the gold-based and commercial strain gauges both show linier response and direct relationship with tension.

Acknowledgement

This works was supported by Sabanci University and The Scientific and Technological Research Council of Turkey (TUBITAK) grant number 117E271. Professor Murat Kaya Yapici appreciates the support of the Turkish Academy of Science (TUBA GEBIP'21 Award) and Science Academy (BAGEP'23 Award)

References

[1] Bose, A. K.; Zhang, X.; Maddipatla, D.; Masihi, S.; Panahi, M.; Narakathu, B. B.; Bazuin, B. J.; Williams, J. D.; Mitchell, M. F.; Atashbar, M. Z., Screen-printed strain gauge for micro-strain detection applications. IEEE Sensors Journal, 20 (21), 12652-12660 (2020); doi: 10.1109/JSEN.2020.3002388

[2] Gao, K.; Zhang, Z.; Weng, S.; Zhu, H.; Yu, H.; Peng, T., Review of flexible piezoresistive strain sensors in civil structural health monitoring. Applied Sciences, 12 (19), 9750 (2022); doi: 10.3390/app12199750

[3] Cao, M.; Su, J.; Fan, S.; Qiu, H.; Su, D.; Li, L., Wearable piezoresistive pressure sensors based on 3D graphene. Chemical Engineering Journal, 406, 126777(2021); doi: 10.1016/j.cej.2020.126777

DOI 10.5162/EUROSENSORSXXXVI/OT4.235

A High-Performance Mode-Localized Vacuum Gauge Based on T-Typed Piezoresistive Pickup

Jiaxin Qin[1,2], Bo Xie[1], Junbo Wang[1,2], Deyong Chen[1,2], Yulan Lu[1]
[1] Aerospace Information Research Institute, Chinese Academy of Sciences, Beijing, China,
[2] University of Chinese Academy of Sciences, Beijing, China

dychen@mail.ie.ac.cn

Summary:
This paper presents a high-performance MEMS vacuum gauge based on mode localization within 2 – 1000 Pa from 0 °C to 60 °C. Since the noise of the pickup signal decides the maximum amplitude ratio output and the sensitivity. A two-degree-of-freedom weak coupling resonator based on H-typed DETF resonator and T-typed piezoresistive strain pickup is developed. Results show that it has the advantages of large power-handling and high signal-to-noise ratio. The device equipped with that has a sensitivity of 280000 ppm/Pa and a lower limit of 2.00 Pa which is superior to previous works.

Keywords: High sensitivity, mode localization, vacuum gauge, piezoresistive strain gauge, temperature characteristics

Background, Motivation and Objective

Vacuum gauge is widely used in industrial measurement and control. And sensitivity is an eternal topic in the sensor's design because high sensitivity usually means high resolution or detection threshold [1]. MEMS resonator-based gauges have a long history, and the sensitivity and lower limit of these gauges are limited by the diaphragm parameters and gas damping which is difficult to further increase [2].

Mode localization is a magical phenomenon in weak coupling resonator (WCR) systems. It can enhance the sensitivity of resonators to stresses while amplitude ratio (the ratio of vibration amplitude of resonators, AR) is selected as the output metric [1-2]. Theoretically, the sensitivity can be designed to be arbitrarily large in the case of a consistent amount of stiffness perturbation. In fact, the sensitivity and linear range are limited by the floor noise and signal-to-noise ratio (SNR) of the pickup signal.

In this paper, a high power-handling WCR and large SNR piezoresistive pickup are proposed. The basic characteristic of the WCR and pickup is measured, and the performance of the vacuum gauge is calibrated.

Description of the New Method or System

The structure of the gauge is shown in Fig. 1(a). The vacuum pressure pushes the diaphragm, and the diaphragm generates both positive and negative stresses. The resonators are placed on the above two zones to differential sense the pressure which can also mitigate the influence of the thermal stress [3]. A Silicon cap is bonded to the SOI wafer to fabricate the reference vacuum. As shown in Fig. 1(b), the WCR is composed of two T-typed DETF resonators coupled with a slender beam. The resonator is driven by an electrostatic comb finger and picked by a T-typed piezoresistive. The piezoresistive bar is perpendicular to the beam and is stretched and compressed when the resonator vibrates, so the resistivity is changed.

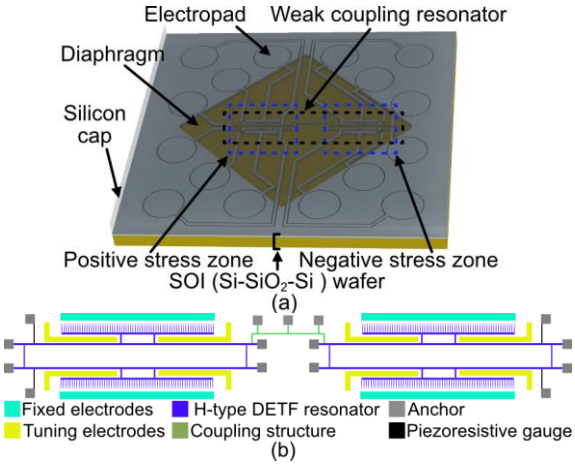

Fig. 1. (a) Structure of the vacuum gauge. (b) The structure of the H-typed DETF weak coupling resonator and T-typed piezoresistive pickup.

Results

The open-loop response of WCR is measured at the operating point (0 °C and 2.00 Pa) as shown in Fig. 2. The amplitude of the two basic modes cannot be tuned to 1.0 simultaneously

because of the fabrication error, so only the out-of-phase mode is calibrated. The floor noise of Resonator2 (R2) is smaller than Resonator1 (R1) which helps obtain a large AR (R1/R2). Because the piezoresistive pickup is used [4] and the distance between the driving port and the pickup port is large in R2, the feedthrough is decreased. Finally, the peak-peak value of 21.2 dB and 28.4 dB of R1 and R2 is achieved which is larger than the widely used capacitance pickup [2, 5].

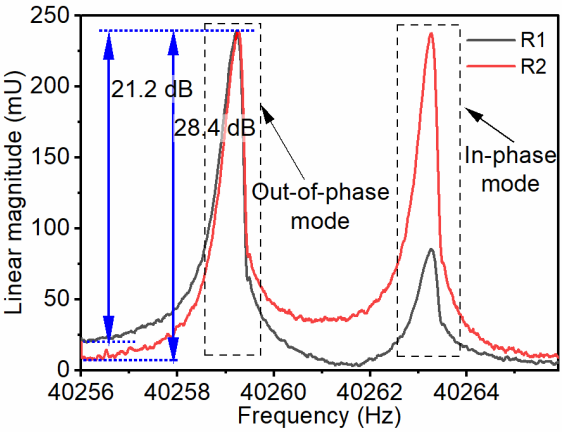

Fig. 2. The open-loop response of the weak coupling resonator.

The measurement of sensitivity in open-loop configuration is shown in Fig. 3. The pressure sensitivity achieves 280000 ppm/Pa (0.028 /Pa). The relationship between AR and temperature is a quadratic function because the variations of stiffness induced by the thermal stress also are quadratic. It can be concluded that AR increases with the vacuum pressure and temperature. However, the linear range of AR cannot be infinite because of the noise and power handling as described before. Therefore, the temperature is limited to a narrow range.

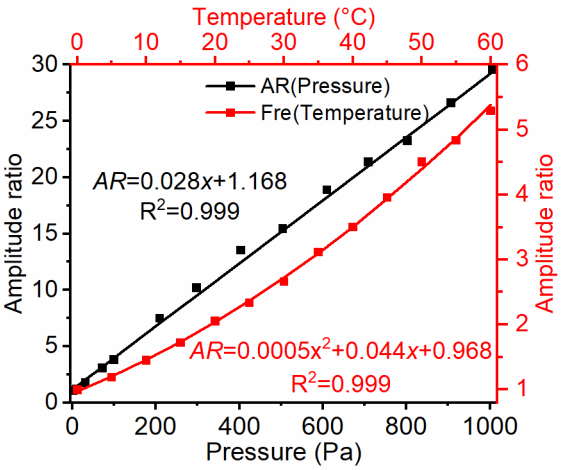

Fig. 3. The pressure and temperature sensitivity of frequency and amplitude ratio at the operating point.

As shown in Fig. 4, the device is calibrated from 0 °C to 60 °C. AR will be nonlinear while the temperature extends the range. Finally, the linearity is good within the range. The hysteresis error is ±1.2 % of the AR reading value (the blue bar in Fig. 4), and a lower limit of less than 2.00 Pa is achieved within the temperature range. The comparison of key performances with previous work is shown in Tab. 1.

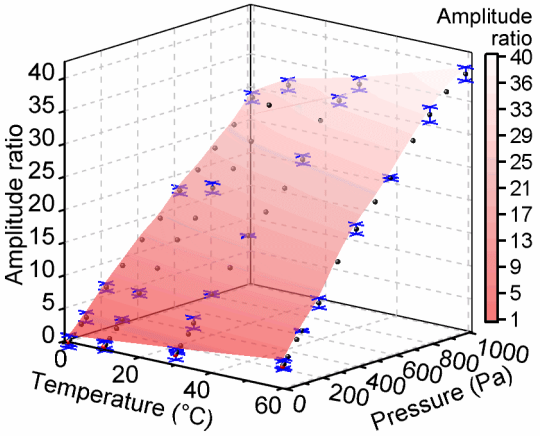

Fig. 4. The calibration results within 2.00 – 1000 Pa from 0 °C to 60 °C.

Tab. 1: The comparison of the key performance

Works	Pressure & temperature	Sensitivity & range of AR
Ref. [2]	100.0 – 1000 Pa −20 – 60°C	90000 ppm/Pa 1 – 9
This work	2.00 – 1000 Pa 0 – 60°C	280000 ppm/Pa 1 – 28

References

[1] X. Han, G. Li, Differential MEMS Capacitance Diaphragm Vacuum Gauge with High Sensitivity and Hide Range, *Vacuum* 191, 110367 (2021); doi: 10.1016/j.vacuum.2021.110367

[2] J. Qin, D. Chen, A Wide Temperature Range Weakly Coupled Resonant Micro-Pressure Sensor, In *IEEE Sensors 2023*, 2023; doi: 10.1109/SENSORS56945.2023.103251

[3] Y. Zheng, D. Chen, A Temperature-Insensitive Resonant Low-Pressure Microsensor Based on Au-Si Eutectic Wafer Bonding, *IEEE Transactions on Electron Devices* 69, 7005–7010 (2022); doi: 10.1109/TED.2022.3213525

[4] C. Cláudia, M. George, MEMS Resonators with Electrostatic Actuation and Piezoresistive Readout for Sensing Applications, *Micro and Nano Engineering* 16, 100158 (2022); doi: 10.1016/j.mne.2022.100158

[5] B. Peng, K. Hu, A Sensitivity Tunable Accelerometer Based on Series-Parallel Electromechanically Coupled Resonators Using Mode Localization, *Journal of Microelectromechanical Systems* 29, 3–13 (2020) doi: 10.1109/JMEMS.2019.2958427

DOI 10.5162/EUROSENSORSXXXVI/OT5.8

The Pitfalls of Researching and Developing Semiconductor Gas Sensors

János, Dr. Mizsei
Budapest University of Technology and Economics, Department of Electron Devices;

Corresponding Author's e-mail address: mizsei.janos@vik.bme.hu

Summary:
There are more than one million score on google scholar using the search term "semiconductor AND gas AND sensors", more than ten thousand in this year. Authors, reviewers, and publishers make significant efforts to ensure that articles are of high quality. Nevertheless, certain trends can be observed, frequently occurring shortcomings that often occur in the research of semiconductor gas sensors and the publication of scientific results. This article collects the shortcomings and mistakes that researchers make most often.

Keywords: semiconductor gas sensors, pitfalls, adsorption, desorption, investigation mistakes

Introduction

Significant efforts have been made in the development of semiconductor gas sensors over the past 50 years. However, there are some pitfalls and mistakes during this work, which have not generally been discussed in the literature. The information collected in this article derives from the author's twenty years of experience in reviewing articles on gas sensors submitted to various journals, as well as his forty years' work in the gas sensor field, reading books, articles, reports and making his own mistakes as well [1], [2].

About semiconductor gas sensors in general

There are many possible physical realisations of semiconductor gas sensors [3]. Simple thin semiconductor film, thin film with catalytically active metal particles (agglomerated ultrathin metal layer [4]), pure thick film, thick film with metal additives, and semiconductor nanocrystals are often referred to as homogeneous gas sensor layers, in spite of the microscopic inhomogeneity of these structures [5], [6], [7] [8]. The latest realizations of these resistance-type semiconductor gas sensors have layers doped with polymers [9], [10].

Diode or MOS like (macroscopically inhomogeneous) structures are realised on monocrystalline semiconductor base, mainly on Si, GaAs, or, for higher temperature application on SiC [11].

Sources of pitfalls

One source of error can be the design and realization of the equipment used to test the sensors. The gas concentration surrounding the sensor may depend on several factors, such as the rate of mixing and gas adsorption on the vessel wall and pipelines of the gas system.

Articles often lack a comparison between the measured static and dynamic characteristics of the sensors, which would take into consideration the theory of sensor operation and adsorption phenomena. In many cases it is possible to find some theoretical connection between the surface adsorption (gas partial pressure) and the electrical output signal (resistance, threshold voltage, etc.), i.e., derive the static characteristics.

According to the adsorption theory the pressure axis should be scaled with p on $1/n$ power. Using that kind of scale, it is possible to estimate some parameter of adsorption. The proper scale for the sensor response depends on the nature of the output signal of the given sensor construction. For example, the surface work-function, as sensor response is usually proportional to the surface coverage, thus linear scale is proper solution for work-function type (MOS and diode) sensors. For the case of fully depleted semiconductor resistive type sensors the sensor resistance depends exponentially on the chemical potential (work-function) of the surface, thus the proper scale on the y axis is logarithmic [2], as well as the diode type sensors, when the current is plotted as output signal.

A common shortcoming in articles dealing with semiconductor gas sensors is that the authors neglect the above considerations and choose the simplest solution, i.e. logarithmic scaling on both axes, without any other justification or consideration. This solution seems reasonable in many cases, since many characteristics can appear as straight lines when represented in the log-log coordinate system, and the pressure (concentration) range is not too broad. Nevertheless, the logarithmically scaled partial pressure (concentration) axis, if it is plotted in a wide pressure range, would offer a good opportunity to establish the parameters of the sensor characteristic.

A common pitfall when evaluating the results is that the time function of the output signal rising or falling is not examined, not even in cases where there are otherwise measurement results on the dynamic behavior of the sensors.

Sometimes, especially at lower temperatures a long time is required for reaching a steady state situation of the sensor output signal, thus experimenters tend to forget waiting for this to happen. Of course, there are cases where the researchers do not wait for the sensor to set up, because like the case of high gas concentration, long exposure to gas can cause irreversible changes in the chemical composition on the surface of the sensor.

Resistive type semiconductor gas sensors are often tested with a series pull-up resistor and voltage source. This arrangement eliminates the sensor instability at the high resistance range, as the pull-up resistor voltage is always very small in the case of high sensor resistance. The honest way is to plot the real sensor resistance instead of current or voltage of the pull-up resistor.

A common characteristic of semiconductor gas sensors is that they usually contain an integrated heating element operating with electrical power which can disturb the response of the sensor. Even in the case of more complex sensor designs, it is not advisable to forget about the proper separation of the heating circuit and the sensor circuit.

Conclusion

Looking at the frequent shortcomings and missed opportunities during the research, we can conclude that the authors usually carry out careful experimental work. However, it often happens that some factors that may affect the results are not considered during the experiments. During the evaluation of the measurement results, it happens that even relatively simple options are not used to draw deeper conclusions, and to finding the connection between the measured results and the theoretical background of operation.

References

[1] J. Mizsei, Forty years of adventure with semiconductor gas sensors, *Proc. eng.*, 168, 221-226 (2016); doi: 10.1016/j.proeng.2016.11.167

[2] J. Mizsei, Vibrating Capacitor Method in the Development of Semiconductor Gas Sensors, in *Science and Technology of Chemiresistor Gas Sensors* , Edited by D. K. Aswal and S. K. Gupta, Nova Science Publishers, Inc. New York, Country, Ch. 8, 2006; pp. 297-331.

[3] N. Yamazoe, K. Shimanoe; Overview of Gas Sensor Technology, Ch. 1., Ibid., pp. 1–33.

[4] J. Mizsei, How can sensitive and selective semiconductor gas sensors be made? *Sens. and Act. B: Chemical* 23, 173-176 (1995); doi:10.1016/0925-4005(94)01269-N

[5] G. Heiland, Homogeneous semiconducting gas sensors, *Sensors and Actuators* 2, 343-361 (1981–1982); doi:10.1016/0250-6874(81)80055-8

[6] E. Souteyrand, D. Nicolas, E. Queau, J.R. Martin, Influence of surface modifications on semiconductor gas sensor behaviour, *Sensors and Actuators* B 26-27 174-178 (1995); doi.org/10.1016/0925-4005(94)01581-2

[7] Filatova, D.; Rumyantseva, M., Additives in Nanocrystalline Tin Dioxide: Recent Progress in the Characterization of Materials for Gas Sensor Applications, *Materials* 16, 6733. (2023), doi:10.3390/ma16206733

[8] Greco, G.; Núñez-Carmona, E.; Genzardi, D.; Bianchini, L.; Piccoli, P.; Zottele, I.; Tamanini, A.; Motolose, C.; Scalmato, A.; Sberveglieri, G.; et al., Tailored Gas Sensors as Rapid Technology to Support the Jams Production. *Chemosensors* 11, 403. (2023), doi:10.3390/chemosensors11070403

[9] J. Wuloh, E. S. Agorku and N. O. Boadi, Modification of Metal Oxide Semiconductor Gas Sensors Using Conducting Polymer Materials, *Hindawi Journal of Sensors*, 11 (2023) doi:10.1155/2023/7427986

[10] C.V. Sudheep, A. Verma, P. Jasrotia, J.J.L. Hmar, R. Gupta, A.S. Verma, Jyoti, A. Kumar, T. Kumar, Revolutionizing Gas Sensors: The Role of Composite Materials with Conducting Polymers and Transition Metal Oxides, *Results in Chemistry* 7 1-19 (2023), doi: 10.1016/j.rechem.2023.101255

[11] M. Andersson, R. Pearce, A. L. Spetz, New generation SiC based field effect transistor gas sensors, *Sensors and Actuators B*: 179, 95-106 (2013), doi:10.1016/j.snb.2012.12.059

DOI 10.5162/EUROSENSORSXXXVI/OT5.10

Colorimetric Inks: A New Approach to Low Cost and Disposable Gas Sensors: The Case of Formaldehyde

Maria González-Gómez[1], Anna Zymohliad[1], Ismael Benito-Altamirano[1], Joan Daniel Prades[2], Olga Casals[1], and Cristian Fàbrega[1].

[1] Dept. of Electronics and Biomedical Enginering, University of Barcelona, Marti i Franques 1, Barcelona, Spain.

[2] Institute of Semiconductor Technology (IHT) and Laboratory for Emerging Nanometrology (LENA), Technische Universität Braunschweig, Hans-Sommer Str. 66, D-38106 Braunschweig, Germany

cfabrega@ub.edu

Summary:

Indoor air quality (IAQ) is a major health concern, and monitoring pollutants indoors is crucial. Current technology offers expensive and bulky options or cheap sensors with limited detection capabilities. New sensor technologies are being developed, but most focus on size and power consumption, neglecting the ability to definitively identify pollutants. Colorimetric sensors offer excellent specificity for detecting target pollutants. In this talk we will discuss the latest developments and limitations of colorimetric sensors and explore possibilities for future sensor technology.

Keywords: Gas sensors, colorimetric sensors, indoor air quality, formaldehyde, CO2

Introduction

Colorimetric sensors offer exceptional selectivity for detecting specific gaseous molecules. This advantage, stemming from the targeted response of colorimetric indicators to specific wavelengths of light, makes them highly attractive for gas detection applications. However, traditional readout methods pose significant limitations.

The development of miniaturized systems for continuous colorimetric sensor readout presents a critical challenge. Existing efforts utilize light sources and photodetectors to measure changes in absorbance, reflectance, or transmittance at specific wavelengths. These configurations often involve complex integration of components, particularly concerning optical alignment. Additionally, miniaturization can hinder the ability to refresh the indicator material once it degrades.

This work presents a novel approach for continuous readout of colorimetric gas sensors. Our design prioritizes simplicity and versatility by utilizing readily available, commercially accessible components. This approach offers several key advantages: i) Accessibility: Utilizing commercially available components reduces cost and simplifies construction; ii) Wavelength Compatibility: The design is compatible with a wide range of colorimetric indicators operating at different wavelengths; iii) Resettability/Refreshability: The system allows for easy resetting or refreshing of the indicator material, overcoming a major limitation of miniaturized colorimetric sensors and; iv) Repeatability: The design ensures excellent repeatability of measurements across different sensor units.

This paper details the design, implementation, and performance evaluation of our proposed approach. We believe this simple and versatile method has the potential to significantly advance the field of continuous colorimetric gas sensing. For a rigorous test of our approach's capabilities, we chose formaldehyde, one of the most challenging pollutants for indoor air quality (IAQ) applications. Our results demonstrate that our simple approach offers excellent performance, including high selectivity against interfering gases, excellent reproducibility, and reliable operation.

Experimental

Our approach is based on a readily available and inexpensive component called the MAX30105. This component emits light in three different wavelengths (green, red, and infrared) and measures the amount of reflected light at each wavelength using a broad band photodiode. The small size and low cost of this component make it ideal for use in miniaturized colorimetric gas sensors.

The colorimetric sensor utilizes a previously reported ink formulation [1]. This ink changes color due to a reaction between a primary amine and formaldehyde, which alters the solution's pH. A standard pH indicator dye, Bromoxylenol blue, visually reflects this pH change.

Results

The colorimetric sensor operates based on the chemical reaction between a primary amine and

formaldehyde. This reaction, known as nucleophilic addition, forms an imine molecule and releases a water molecule. Importantly, under these conditions, the reaction is irreversible. As a result, the color change of the dye intensifies as it is exposed to increasing amounts (doses) of formaldehyde, until a saturation point is reached (Fig. 1). Our experiments revealed that the sensitivity and durability of the sensor depend on the formulation, particularly the amount of amine and the thickness of the printed film. Lower amine concentrations resulted in higher sensitivity but faster saturation. Conversely, higher amine concentrations offered slower saturation but reduced sensitivity. To achieve optimal performance, we formulated the colorimetric sensor to strike a balance between these two factors.

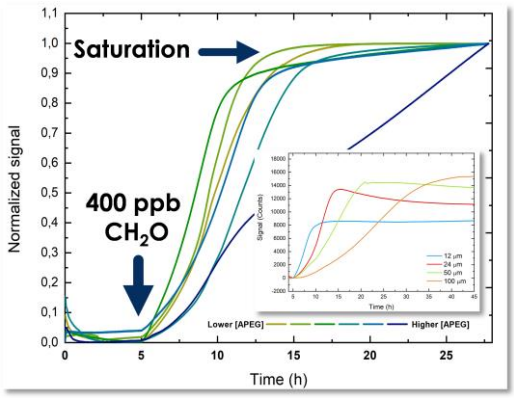

Fig 1. Dosimeter expeirments and ink formulation tunning.

Although the overall color change of the ink is irreversible, we observed that the rate of color change is directly proportional to the formaldehyde (CH_2O) concentration during exposure (Fig. 2). This means the steeper the initial slope of the color change, the higher the CH2O concentration. By exploiting this property, we can analyze the rate of color change, or the first derivative of the signal (Fig. 2, insert), to determine the CH_2O concentration. Using this approach, we achieved a detection limit of 85 ppb for CH_2O.

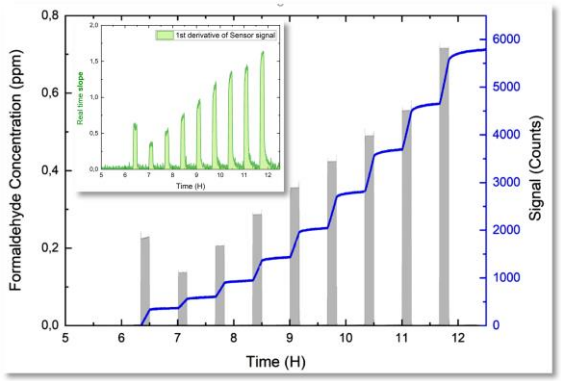

Fig. 2. Transient measurements signal at different CH_2O concentration and the 1st derivative of the signal.

Figure 3 depicts a calibration curve constructed using eight samples from three distinct batches. The data demonstrates a strong linear relationship between the response and formaldehyde concentration, with minimal deviations considering the use of diverse samples. We further validated this calibration model by performing a new transient experiment with a fresh sample. The predicted concentration by the model closely matched the nominal concentration, confirming the model's accuracy.

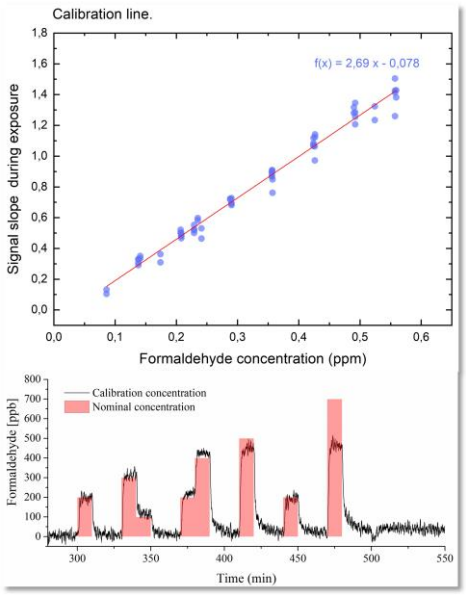

Fig. 3. Calibration line and test validation experiment.

Finally, we investigated the potential interference from common indoor air pollutants: moisture, nitrogen dioxide (NO_2), carbon dioxide (CO_2), and carbon monoxide (CO). Experiments were conducted by exposing the sensor to each interferent gas at various concentrations alongside a fixed concentration of formaldehyde. The results reveal that relative humidity slightly interferes with the sensor response at both low and high humidity ranges. Conversely, no significant interference was observed within the model's calibration error range for CO and CO_2. NO_2, however, exhibited a clear interference effect, causing significant deviations from the expected formaldehyde value. It's important to note that the NO_2 concentrations used in the experiments were 4 to 20 times higher than typical indoor air levels.

[1] Feng, L.; Musto, C. J.; Suslick, K. S. A Simple and Highly Sensitive Colorimetric Detection Method for Gaseous Formaldehyde. J. Am. Chem. Soc. 2010, 132 (12), 4046–4047. https://doi.org/10.1021/ja910366p.

DOI 10.5162/EUROSENSORSXXXVI/OT5.40

Aliovalent-Doping-Strengthened Ethylene Sensor

Kewei Liu[1,2], Zichen Zheng[1], Marc Debliquy[2], Chao Zhang[1]
[1] College of Mechanical Engineering, Yangzhou University, Yangzhou 225127, PR China
[2] Service de Science des Matériaux, Faculté Polytechnique, Université de Mons, Mons 7000, Belgium

Corresponding Author's e-mail address: zhangc@yzu.edu.cn

Summary:
A simple and reliable ethylene sensor was fabricated based on W-doped Sb_2MoO_6, which presented excellent responses toward 2-10 ppm ethylene, with high sensitivity, good selectivity, low LOD (24 ppb), excellent repeatability (~100 cycles) and long-term stability (within 45 days). The decreased grain size, abundant defects, proper size mismatch and increased charge separation capability contribute to the enhanced sensing properties. Besides, the sensors were applied in VOCs detection of unhusked rice to demonstrate the practical application potential in rice mildew evaluation.

Keywords: gas sensor, ethylene, rice mildew, heteroatom dopant, room temperature

Background

Ternary extrinsic semiconductor intentionally inserted by transition metal dopants as ionized donors through the substitution of the original atom position and interstitial doping in crystal structure has been reported as a feasible approach for strengthening the electronic properties [1, 2]. Compared with native transition metal atoms, the d-orbitals of transition metal dopants show various localizations, impacting the spatial delocalization of the discrete energy level, and thus resulting in the alteration of the band structure, and the redistribution of the density of states (DOS) around the Fermi level which is in proportion to the electron transition probability [3, 4]. It is worth stressing that, an evident drop in ionic conductivity will happen accompanied by the dopant concentration and atom size exceeding the optimum [5].

Ethylene was identified as a typical volatile organic compound (VOC) from the metabolism of several common fungi. The specific role of ethylene in fungal metabolism remains unclear at present. On the whole, the ethylene production has been demonstrated displaying upwards tendency parallel with the growing fungi quantity, which serves as a valuable point of reference for identifying moldy grain.

Description of the New Method or System

A facile one-step solvothermal approach was used to synthesize W-doped Sb_2MoO_6 (SMO) with different W:Mo molar ratios of 2.5%, 5%, 7.5% and 10%, named as W-2.5, W-5, W-7.5 and W-10. The sensing layers were coated onto an alumina substrate (6*30 mm) with Pt electrodes by a droplet coating method. The gas-sensing test was performed via a four-channel gas sensing testing instrument, which measures electrical resistance signals of the corresponding channel in highly pure air and target gas. All the experiments conducted in dry air were carried out at RT.

Results

Fig. 1 displays the EBSD image and line-scan analysis, signifying that the W atoms are successfully doped and uniformly dispersed.

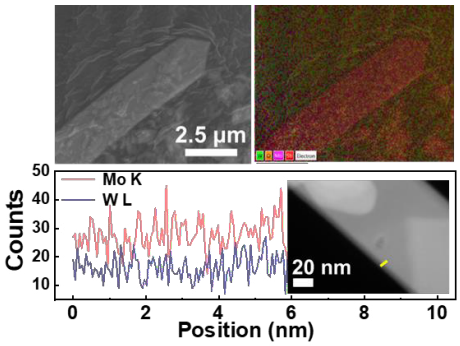

Fig. 1. EBSD and line-scan analysis of W-5.

Fig. 2 shows that the content of doped W^{4+} obviously enhances the sensing performance due to the proper size mismatch compared with Mo^{6+}, contributing to distortion in the crystal lattice, improving carrier mobility and strain-induced changes in conductivity. Besides, effect of doping W ions with various valence states on the adsorption energy was explored through DFT calculation.

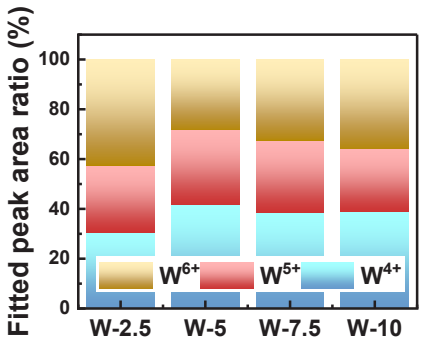

Fig. 2. Fitted peak area ratios of different W dopants with various valence states for W-doped samples.

It can be intuitively observed in Fig.3 that the W-5 shows the best response signature to ethylene molecules ahead of the other four sensors, and all the W-doped samples appear to have higher response values than pure Sb_2MoO_6. LOD of W-5 reached ~24 ppb under RT. Besides, response deviation is below 1 within a 100 repetition cycles.

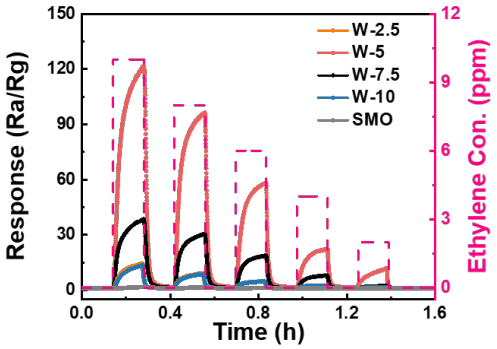

Fig. 3. Transient responses of 10-2 ppm ethylene for all samples at RT.

The response first increases till 40%RH and then decreases. There is an excellent linear relationship between response and ethylene concentrations, and the calculated LODs are all at the ppb levels. Besides, low response drifts were calculated of ~0.2% and ~5.0% under 20%RH and 60%RH.

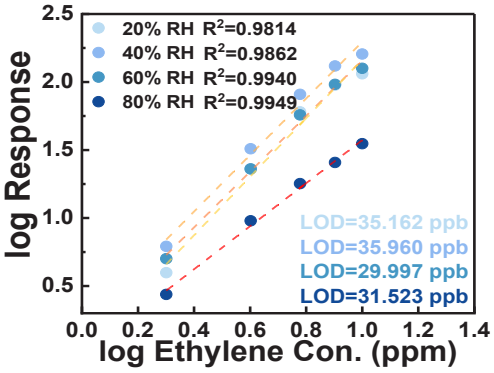

Fig. 4. Linear relationship between response and gas concentration for W-5 under various RH and corresponding calculated detection limit.

Fig. 5 exhibits exponential relationship between response and storage time during 120 days with R^2=0.972, demonstrating that fabricated sensors proved to be highly sensitive to the change of mildew smell of unhusked rice during different storage periods. Besides, excellent selectivity towards other interfered gases generated during rice storage ($S_{ethylene}/S_{interference\ gas}$ > 10^2) was exhibited, which further confirmed feasibility of practical application.

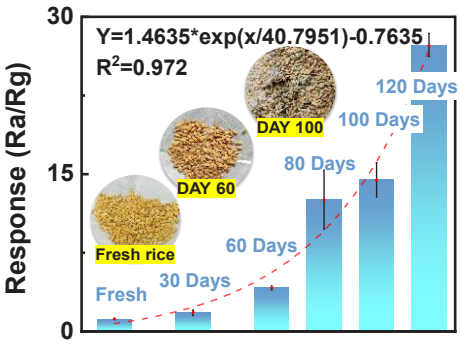

Fig. 5. Responses of the W-5 sensor as a function of storage time measured at RT under exposure to odors from 50 g in a 100 ml cell unhusked rice and the corresponding released ethylene concentration.

References

[1] J. Liu, Q. Zhao, J.L. Liu, Y.S. Wu, Y. Cheng, M.W. Ji, H.M. Qian, W.C. Hao, L.J. Zhang, X.J. Wei, S.G. Wang, J.T. Zhang, Y. Du, S.X. Dou, H.S. Zhu, Heterovalent-Doping-Enabled Efficient Dopant Luminescence and Controllable Electronic Impurity Via a New Strategy of Preparing II-VI Nanocrystals, *Advanced Materials* 27(17), 2753-61 (2015); doi: 10.1002/adma.201500247

[2] S.Y. Cho, H.J. Koh, H.W. Yoo, J.S. Kim, H.T. Jung, Tunable Volatile-Organic-Compound Sensor by Using Au Nanoparticle Incorporation on MoS_2, *ACS Sensor*s 2(1), 183-189 (2017); doi: 10.1021/acssensors.6b00801

[3] Q. Lv, J.Y. Tan, Z.J. Wang, L.X. Yu, B.L. Liu, J.H. Lin, J. Li, Z.H. Huang, F.Y. Kang, R.T. Lv, Femtomolar-Level Molecular Sensing of Monolayer Tungsten Diselenide Induced by Heteroatom Doping with Long-Term Stability, *Advanced Functional Materials* 32(34) (2022); doi: 10.1002/adfm.202200273

[4] A. Nipane, D. Karmakar, N. Kaushik, S. Karande, S. Lodha, Few-Layer MoS_2 p-Type Devices Enabled by Selective Doping Using Low Energy Phosphorus Implantation, *ACS Nano* 10(2), 2128-2137 (2016); doi: 10.1021/acsnano.5b06529

[5] J. Faber, C. Geoffroy, A. Roux, A. Sylvestre, P. Abélard, A Systematic Investigation of the DC Electrical Conductivity of Rare-earth Doped Ceria, *Applied Physics A* 49(3), 225-232 (1989); doi: 10.1007/BF00616848

DOI 10.5162/EUROSENSORSXXXVI/OT5.44

Alternative solvents containing phenyls and isoprenic units to fabricate polyaniline-based layers sensitive to ammonia

Sabine Vassaux[1], Nathalie Redon[1], Caroline Duc[1]
[1] Center for Energy and Environment, IMT Nord Europe, Institut Mines-Télécom, University of Lille, F-59000 Lille, France

Corresponding Author's e-mail address: sabine.vassaux@imt-nord-europe.fr

Summary:
Sensors based on conductive polymers constitute promising technologies to monitor ammonia. Polyaniline (PAni), doped with an acid, is commonly used for these applications. However, PAni is poorly soluble in most of organic solvents. When m-cresol is identified as a good solvent to stabilize PAni, it can't be used in industrial fabrication processes due to its toxicity. The objective is to study alternative solvents having similar structures than m-cresol to disperse PAni and provide sensing performances to ammonia from obtained active surface layers.

Keywords: Chemiresistive Sensor, Ammonia detection, Conductive Polymer, doped Polyaniline, Polyaniline dispersion.

Background and Motivation

Gaseous species from polluted air may be toxic and drive to health problems after inhalation. For instance, ammonia gas mostly produced by agriculture and industrial facilities (microelectronic, fertilizer, refrigerants fields) may lead to chronic lung diseases and respiratory inflammations [1]. To guarantee workers' health, efficient sensors are needed. Among ammonia sensors, usual metal oxides ones suffer from high operation temperature and lack of flexibility [2]. Conversely, sensors based on conductive polymers work at room temperature. Their structural and mechanical properties are easily tuneable making them a promising alternative [3].

Polyaniline (PAni) constitutes a common conductive polymer used for sensing applications. The choice of a solvent to make the device by depositing the conductive ink on the electrodes remains challenging. Doped polyaniline is soluble in few organic solvents. Among efficient solvents, m-cresol was identified as one of the best, displaying high solubility of PAni protonated by Camphor-10-sulfonic acid (CSA), due to favourable hydrogen bond interactions and to van der Waals forces between phenyl groups of molecules [4]. However, m-cresol is a Cancerogenic, Mutagen and Reprotoxic solvent which can't be used anymore in industries with hygiene and safety standards. Therefore, the objective of this study is to find other alternative solvents to disperse doped PAni without decreasing its sensing performances to ammonia. Knowing that organic solvents with similar structures to m-cresol could have favourable interactions with PAni:CSA [4], solvents having π-bonds with phenyls or isoprenic units were selected. The ability of these solvents to fabricate PAni layers sensitive to ammonia was investigated.

Experimental part

Polyaniline-emeraldine (Mw = 65000 g mol^{-1}) and (+)-Camphor-10-sulfonic acid (CSA), chosen as the doping agent were provided by Sigma Aldrich. They were mixed together to obtain a doping rate of 50%. The solid content was fixed to 15 g/L. The powder mix was then incorporated in four solvents: Toluene (T), Benzylic alcohol (BA), Alpha Pinene (AP) and DL Limonene (DLL). Solutions stayed under stirring at 700 rpm for 5 days and were sonicated for 1 hour. Then, 1.5 µL of each solution was drop-casted onto gold interdigitated electrodes deposited on polyimide (200 µm gaps and fingers). Three sensors were obtained per solution. The sensors were finally dried on a hot-plate at 100°C for one night, and during 7 days at 100°C in an oven under vacuum. Then, the surface microstructure of PAni:CSA layers was characterized using Scanning Electron Microscopy at 10 kV and a magnification size of 2000. Sensing performances of the PAni:CSA layers were tested at various ammonia concentrations (from 50 to 2000 ppb). The temperature and the relative humidity were respectively fixed to 20°C and 45%. Relative responses of all sensors were calculated as a function of the resistance

under clean air (R_0) and real-time resistance (R) as followed:

$$Relative\ Response = \frac{R - R_0}{R_0} \times 100$$

Results

Except for the uniform Benzyl alcohol (BA) solution, most of solutions present two phases (Fig.1). The dispersion of PAni:CSA in solvent is unstable and the difference of solubility directly impacts the polymer microstructure after solvent evaporation. Indeed, only PAni:CSA:BA sample presents a continuous morphology with some holes at the surface. The good stability of PAni in BA can be explained by hydrogen bonds formed between the dopant and the hydroxyl group (OH) of the solvent. Other samples made from apolar solvents (T, AP, DLL) display more aggregated and porous active surface layers. Some sticks and needles even appear on the active surfaces from samples made in DLL limonene and Toluene, respectively. The morphology of T, AP and DLL seem to present a higher specific surface area which may facilitate gas-solid interactions.

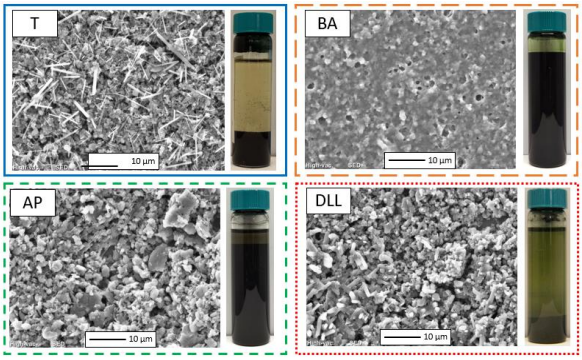

Fig. 1. SEM images of PAni:CSA surfaces from different solutions observed after 24 hours of rest.

The resistivity of the device measured before ammonia injection indicates that AP layer has the highest resistivity (3.0 10^5 Ω), followed by T and DLL samples with similar resistivities (4.0 10^4 Ω) and finally by the BA sample (8.8 10^2 Ω).

Fig.2 presents the evolution of the relative responses toward different concentrations of ammonia. Independently of the solvent, sensors present the same behaviour characterized by an increasing relative response with ammonia concentration. Calibration curves have shown that samples made in toluene have the highest sensitivity of 393 ± 18 %/ppm, followed by DLL Limonene sensors (306 ± 46 %/ppm) and AP sensors (223 ± 13 %/ppm). Sensors elaborated in BA display the lowest sensitivity of 51 ± 6 %/ppm. Then, limits of detections (LOD) are calculated according to IUPAC recommendation. Samples from Toluene, Alpha Pinene and DLL Limonene display a similar and very low LOD around 2 ppb when the LOD of samples from Benzyl alcohol is slightly higher around 4 ppb. Sensors elaborated in the three apolar solvents (Toluene, Alpha Pinene, DLL Limonene) are very interesting and promising given their high sensitivity values and low limits of detection. That can be due to the higher specific surface area of the samples [5], allowing the gas to deeper penetrate into the active surface layer and to better interact with the active sites of PAni.

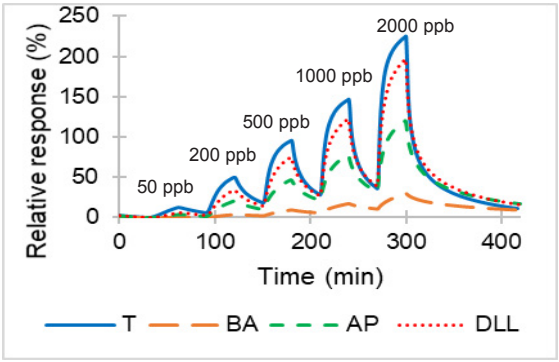

Fig. 2. Responses toward ammonia concentration from 0 to 2000 ppb of PAni:CSA sensors from solutions T, BA, AP, DLL (45% RH and 20.4 °C).

Conclusion

The objective of the study was to investigate alternative solvents having similar structures than m-cresol to prepare organic ammonia sensors. Even if PAni is poorly soluble in apolar solvents, those solvents lead to morphologies with high specific surface area and very good sensing performances. Hence, the next step will be to find additives able to stabilized the polymer in solution, to enhance the reproducibility of the devices made by ink printing processes.

References

[1] P. Adhav *et al.*, « Room temperature operable ultra-sensitive ammonia sensor based on polyaniline-silver (PANI-Ag) nanocomposites synthesized by ultra-sonication », *Synthetic Metals*, vol. 293, p. 117237, 2023.

[2] A. Liu *et al.*, « The gas sensor utilizing polyaniline/ MoS2 nanosheets/ SnO2 nanotubes for the room temperature detection of ammonia », *Sensors & Actuators: B. Chemical*, vol. 332, p. 129444, 2021, doi: https://doi.org/10.1016/j.snb.2021.129444.

[3] C. Zhu *et al.*, « Self-assembly polyaniline films for the high-performance ammonia gas sensor », *Sensors & Actuators: B. Chemical*, vol. 365, p. 131928, 2022, doi: https://doi.org/10.1016/j.snb.2022.131928.

[4] T. Vikki *et al.*, « Molecular Recognition Solvents for Electrically Conductive Polyaniline », *Macromolecules*, vol. 29, nº 8, p. 2945-2953, 1996, doi: 10.1021/ma951555v.

[5] N. R. Tanguy, M. Thompson, et N. Yan, « A review on advances in application of polyaniline for ammonia detection », *Sensors and Actuators B: Chemical*, vol. 257, p. 1044-1064, 2018, doi: 10.1016/j.snb.2017.11.008.

DOI 10.5162/EUROSENSORSXXXVI/OT5.53

Conductimetric Gas Sensors for Hydrogen Leakage Detection Based on Copper Phthalocyanine Decorated by Palladium Nanoparticles.

S. Rajab-Pacha [1], J. Brunet [1], A. Ndiaye [1], A. Pauly [1], C. Varenne [1]
[1] Université Clermont Auvergne, Clermont Auvergne INP, CNRS, Institut Pascal, F-63000 Clermont-Ferrand, France

Corresponding author: Salma.RAJAB_PACHA@doctorant.uca.fr

Summary:
This study introduces the development of conductimetric gas sensors for hydrogen leakage detection, implementing copper phthalocyanine decorated with palladium nanoparticles as sensitive materials. These sensors are devoted to improve the performance of hydrogen sensors through focusing on a novel approach to enhance sensitivity and response time. The sensors also achieve a detection limit of 0.07% at ambient temperatures, demonstrating a significant breakthrough in hydrogen detection capabilities. These performances allow positioning them as a promising solution for industrial safety applications.

Keywords: Copper Phthalocyanine, Palladium Nanoparticles, Hydrogen Micro-sensors, Leakage Detection, Industrial Safety

Motivation and Objective

In the context of global warming, research on alternative energy sources distinct from fossil fuels is becoming essential. To this end, the use of hydrogen energy has emerged as a major priority in the current quest for clean and sustainable energy sources [1]. However, despite its many potential advantages, the deployment of hydrogen as an energy vector presents considerable challenges. Hydrogen, being a colorless and odorless gas, exhibits an explosiveness range between 4% and 75% in air. Coupled with its low minimum ignition energy of 0.017mJ, high heat of combustion (142 kJ/g), and significant burning velocity, along with an ignition temperature of 560°C, hydrogen's physical and chemical properties necessitate rigorous safety protocols [2]. Given these inherent risks, the development of highly sensitive and rapid-response hydrogen sensors is crucial, not only to protect against potential catastrophic explosions but also to support the efficient and secure integration of hydrogen into our energy systems. Thus, our research focuses on advancing microsensor technology that meets the metrological requirements for safer use of hydrogen, such as detecting low hydrogen concentrations with increased reliability and precision, low cost, low power consumption, and low sensitivity to environmental parameters (relative humidity, pressure, etc.) [3][4].

Sensor Elaboration and Test Protocol

Original conductimetric micro-sensors implementing Metallophthalocyanine decorated by metallic nanoparticles have been realized. Unsubstituted copper phthalocyanine has been chosen because of its nanostructured morphology associated to a high specific surface area and a low intrinsic conductivity leading to high gas adsorption capacity and high electronic conductivity modulation even by low gas concentrations. In order to favor sensitivity to hydrogen, palladium has been chosen as metallic nanoparticles because of its well-known catalytic power for hydrogen dissociation. The conductimetric transducer consist of platinum interdigitated electrodes (IDEs) screen printed on an alumina substrate. The substrate is also equipped, on the rear face, with a screen-printed platinum resistor that enables the temperature regulation of the structure. Initially, 100 nm of copper phthalocyanine is deposited on the IDEs through thermal evaporation. Subsequently, palladium nanoparticles are deposited on the copper phthalocyanine film through wet chemical deposition. This method allows for the creation of large adsorption sites facilitated by the copper phthalocyanine nano structuration, while the palladium nanoparticles contribute to enhanced selectivity and sensitivity towards hydrogen. To our knowledge, this is the first time that CuPc are decorated with PdNPs to ensure the building of

nanocomposites materials that enable such performances. The presence of the PdNPs and the nanostructuation of the CuPc allows to tune the conductivity while benefiting from large adsorption sites and catalytic effect of the NPs.

Results

Figure 1 represents the electrical resistance of Pd-decorated copper phthalocyanine at room temperature consecutively exposed to hydrogen concentration during 5 minutes then maintained under clean air during 15 minutes. Results highlight the high sensitivity of microsensors to H_2 in the [0.2%-1.2%] concentration range, with a high signal-noise ratio. The correlation between micro-sensor responses and H_2 concentration is manifest, with a good level of repeatability. The response and recovery times determined at room temperature are estimated to 2.5 minutes and 7 minutes, respectively.

Figure 2 represents the variation of sensor resistance measured during exposure steps versus H_2 concentration at room temperature. This calibration curve is extracted from results depicted in figure 1. Such sensors exhibit a linear calibration curve, a sensitivity close to 200Ω per percent as well as a very low hysteresis. Based on noise magnitude measured during sensor stabilization under clean air and sensitivity, the limit of detection has been estimated to 0.07% (700ppm) at ambient temperatures. This emphasizes the significant improvement by combining CuPc with nanoparticles for conductimetric sensors. While these results are promising, further investigation are required. The impact of nanoparticle density on sensing performances, the impact of the nature of phthalocyanine on response, the effect of temperature on sensing mechanisms, the cross-sensitivity of devices to water vapor and interfering gases must be investigated. These ongoing developments aim to ensure that the sensors meet the rigorous requirements for leak detection across various industrial applications. All these points will be discussed.

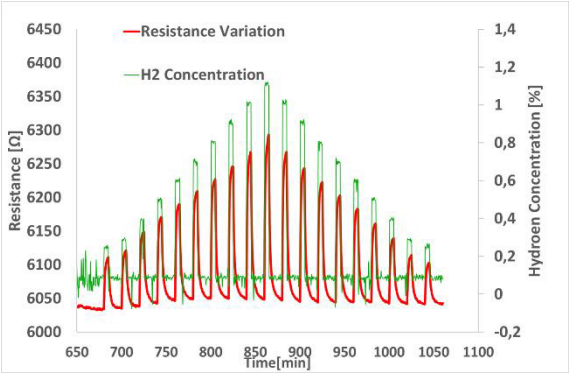

Fig. 1. Electrical resistance of Pd-decorated CuPc conductimetric sensor towards different concentration of Hydrogen at ambient temperature. Time of exposure and recovery steps was set to 5min and 15min respectively.

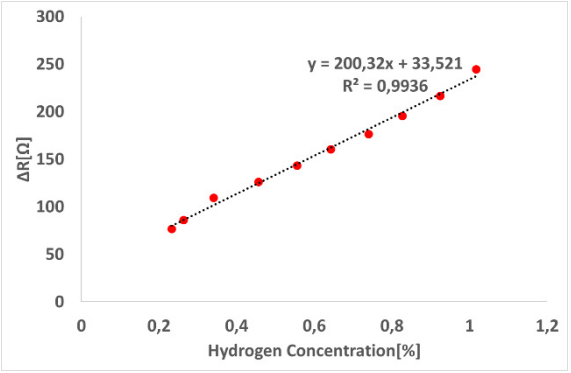

Fig. 2. Resistance variations of Pd-decorated CuPc conductimetric sensor versus H2 concentration at room temperature. Datas are extracted from measurements depicted in figure 1.

References

[1] Farias, C.B.B.; Barreiros, R.C.S.; da Silva, M.F.; Casazza, A.A.; Converti, A.; Sarubbo, L.A. Use of Hydrogen as Fuel: A Trend of the 21st Century. Energies 2022, 15, 311. https://doi.org/10.3390/en15010311

[2] Mazloomi, Kaveh, and Chandima Gomes, 'Hydrogen as an Energy Carrier: Prospects and Challenges', Renewable and Sustainable Energy Reviews, 16.5 (2012),3024–33 <https://doi.org/10.1016/j.rser.2012.02.028>.

[3] Buttner, W., Hartmann, K., Weidner, E., Cebolla, R., Bonato, C., Moretto, P., Burgess, R., Schmidt, K., & Wright, H. (2017). Hydrogen Safety Sensor Performance and Use Gap Analysis: Preprint. Paper presented at 7th International Conference on Hydrogen Safety (ICHS 2017), Hamburg, Germany. https://www.nrel.gov/docs/fy18osti/68773.pdf

[4] Buttner, William, Burgess, Robert, Post, Matthew, and Rivkin, Carl. Summary and Findings from the NREL/DOE Hydrogen Sensor Workshop (June 8, 2011). United States: N. p., 2012. Web. doi:10.2172/1048994.

DOI 10.5162/EUROSENSORSXXXVI/OT5.67

Chemoresistive Humidity, NO_2 and H_2 Sensor Based on 2D-$CrCl_3$ Layered Trihalides Nanoflakes

Valentina Paolucci[1], Vittorio Ricci[1], Thirugnanam Natarajan [1], Dario Mastrippolito[2], Luca Ottaviano[2], Carlo Cantalini[1]

[1]Department of Industrial Engineering (DIIIE), University of L'Aquila, Roio 67100 L'Aquila, Italy.

[2]Department of Physical and Chemical Sciences (DSFC) University of L'Aquila, Via Vetoio 67100 L'Aquila,

Corresponding email: valentina.paolucci2@univaq.it

Summary:

Herein we demonstrate that few-layers 2D-$CrCl_3$ transition metal trihalides (TMTHs) MX_3 (M= Ti, V, Cr, Mo, Fe, Ru and X = Cl, Br, I), exhibit unveiled capabilities as chemoresistive *p*-type sensors to humidity (10 - 80% RH @25 °C), NO_2 (400 ppb – 1 ppm) and H_2 (10 – 250 ppm) at 100 °C operating temperature (OT). Specifically, we investigated the humidity response mechanism unraveling the nature of the reversal of the resistance from an ionic (@25 °C OT) to an electronic conduction regime (@100 °C OT) in humid air conditions. All these findings suggest 2D-$CrCl_3$ platforms as 2D novel interfaces for humidity and gas sensing applications.

Keywords: 2D-$CrCl_3$, chemoresistive, humidity sensor, NO_2, H_2 gas sensor.

Background, Motivation an Objective

There are substantial efforts to replace traditional metal oxides (MOX) gas sensors with 2D van der Waals (vdW) materials, which offer the advantage of having the maximum surface-volume ratio as respect to their MOX counterparts [1]. Excluding the applications of Transition Metal Trihalides (TMTHs), with formula MX_3 (M = Ti, V, Cr, Mo, Fe, Ru and X = Cl, Br, I), as cleavable 2D ferromagnetic semiconductors, the humidity and gas sensing response of few layers MX_3 TMTHs are still unknown, probably on the assumption that their environmental instability in dry/wet air prevents their utilization as reproducible gas sensor interfaces. Within the family of TMTHs, we found that $CrCl_3$ is the only relative stable under ambient laboratory conditions even after its isolation in reduced dimensionality through mechanical exfoliation. Specifically, we revealed that $CrCl_3$ has O-$CrCl_3$ stable semi-oxidized surface phase which is stable up to 400 °C with charge imbalance [2]. We therefore concluded that, from the operational point of view, few-layers 2D-$CrCl_3$ do not suffer dramatic oxidation or evaporation phenomena up to 200 °C, suggesting $CrCl_3$ to be a potential chemoresistive platform, operating in the 25 – 150 °C temperature range and dry/wet environmental conditions, for gas sensing applications.

Description of the New Method or System

In this study, commercial powders of $CrCl_3$ have been for the first time exfoliated by Liquid Phase Exfoliation (LPE) to produce reproducible amounts of few-layers 2D-$CrCl_3$, having a thickness of 20 - 25 nm and aspect ratio of ~205 [3]. Well dispersed exfoliated flakes were successfully deposited by spin coating over interdigitated Pt patterned electrodes to yield thin film, as shown in Fig. 1.

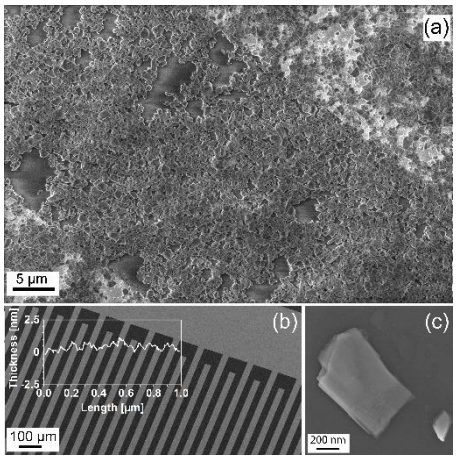

Fig. 1. (a) exfoliated $CrCl_3$ flakes deposited on Si_3N_4 substrate with Pt-interdigital electrodes (lighter regions) (b), comb-like picture of the Pt electrodes with roughness profile (inset) of the Si_3N_4 substrate. (c) SEM magnification of a representative $CrCl_3$ flake after exfoliation.

Results and Discussion

We firstly investigated the electrical response to humidity ((10 – 80% @25 °C) increasing the operating temperature (OTs) from 25 °C to 150 °C as shown in Fig. 2.

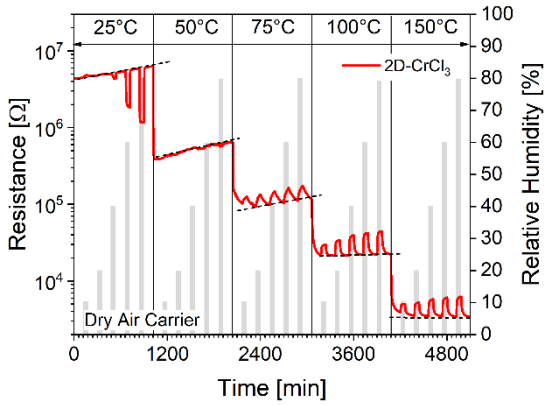

Fig. 2. Humidity response of exfoliated 2D-$CrCl_3$ in the 10 - 80% RH range (RH @25 °C) and different operating temperatures from 25 to 150 °C.

At 25 °C with increasing humidity from 10 - 80% RH, resistance decreases whereas at OTs > 75 °C resistance increases with increasing humidity. Remarkably, with increasing OTs, the experimental limit of detection (LOD) improves. At 25 °C LOD is ~ 40% RH while at OTs > 75 °C, LOD is as small as ~ 10% RH. Furthermore, with increasing the OTs, the drift of the base line resistance, related to incomplete desorption of water molecules, is fully compensated (compare the slopes of the black dotted lines) indicating 100 °C as the best operating temperature for humidity detection in the whole 10 - 80% RH range. Interestingly, 50 °C OT represents a transition zone between the reversal response (i.e. decrease/increase) of the electrical resistance, on the assumption of a different reaction mechanism (i.e., ionic/electronic).

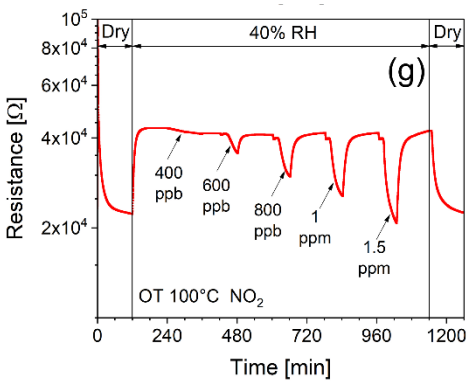

Fig. 3. Electrical response in 40% RH humid air background to NO_2 (400 ppb - 1.5 ppm) and 100 °C OT.

Exposing the sensor to NO_2, it shows that 2D-$CrCl_3$ behaves as a *p*-type interface with decreasing/increasing sensor's resistance to NO_2 (oxidizing) and H_2, gases respectively (here not shown), in the whole OTs range. In the OTs range 100 – 150 °C sensor's electrical response is fully developed with appreciable changes of the electrical signal and good recovery of the base line after gas desorption, suggesting 100 °C as the best operating temperature for investigated gases detection.

Two humidity sensing mechanism have been proposed considering a low (25 °C) and high (100 °C) temperature working regime (Fig. 4). At 25 °C, H_2O dissociatively chemisorbs over 2D-$CrCl_3$, leading to the formation of two hydroxyls (OH). With increasing the humidity content, further H_2O physisorbed layers are formed, enabling, at higher RH%, the onset of a Grotthus proton-chain (H^+) ionic-conduction mechanism (Fig. 4b). At T > 100 °C, the physiosorbed water is almost desorbed and a direct electronic charge interaction mechanism takes place between the $CrCl_3$ surface and the adsorbing H_2O/gases. In this case the response mechanism is fully electronic (Fig. 4c).

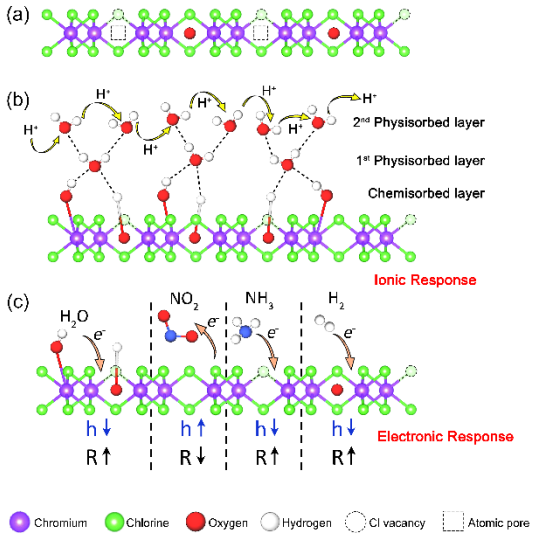

Fig. 4. (a) side view of a mono layer $CrCl_3$ structure showing a tri-layer atomic assembly (Cl-Cr-Cl); (b) schematic model of humidity adsorption at 25 °C and ionic (H^+) conduction mechanism; (c) schematic model of H_2O, NO_2, NH_3 and H_2 gases interaction (indicated the charge transfer from/to the adsorbing molecules and the surface).

References

[1]. V. Paolucci, G. Giorgi, C. Cantalini, Bidimensional Engineered Amorphous *a*-SnO_2 Interfaces: Synthesis and Gas Sensing Response to H_2S and Humidity, *ACS Sens.* 7, 2058-2068 (2022); doi: 10.1021/acssensors.2c00887

[2]. S. Kazim, D. Mastrippolito, L. Ottaviano, R. Gunnella, Synchrotron radiation photoemission spectroscopy of the oxygen modified $CrCl_3$ surface, *Phys. Chem. Chem. Phys.* 25 (5), 3806–3814 (2022); doi: 10.1039/D2CP04586A

[3]. V. Paolucci, V. Ricci, C. Cantalini, Two-Dimensional $CrCl_3$ - Layered Trihalide Nanoflake Sensor for the Detection of Humidity, NO_2, and H_2, *ACS Appl. Nano Mater.* 7, 3679-3690 (2024) doi: 10.1021/acsanm.3c05051

DOI 10.5162/EUROSENSORSXXXVI/OT5.71

Chemoresistive Sensors: A New Approach to Understand the Detection Mechanism of Biogenic Gases

Elena Spagnoli [1], Arianna Rossi [1], Elena Ghedini [3], Michela Signoretto [3], Marco Marzocchi [2], Vincenzo Guidi [1] and Barbara Fabbri [1]
[1] Department of Physics and Earth Sciences, University of Ferrara, Ferrara, via Giuseppe Saragat 1/C, 44122, Italy
[2] Sacmi Imola S.C., Olfactory Systems, Via Selice Prov.le, 17/a, 40026 Imola, Italy
[3] CATMAT Lab, Department of Molecular Sciences and Nanosystems, Ca' Foscari University of Venice and INSTM RUVe, Via Torino, 155, 30172 Venezia Mestre, Italy

Corresponding Author's e-mail: elena.spagnoli@gmail.com

Summary:
This work aims to provide a novel approach to better understand the detection mechanism of chemoresistive gas sensors for complex volatile compounds, such as biogenic gases. The chemical species formed during analyte-sensor interaction on the sensing layer surface were investigated through *operando* diffuse reflectance infrared Fourier transform spectroscopy. Chemisorption analyses further improved the understanding of the sensing mechanism and material selectivity by characterizing the acid-base nature of the active sites of the functional layer.

Keywords: chemoresistive gas sensors, operando analyses, sensing mechanism, complex VOCs detection, chemisorption analyses

Background, Motivation and Objective

Chemoresistive sensors, such as metal oxide (MOX) semiconductor-based gas sensors, belong to the class of electrical sensors and the interaction of the gas with the receptor unit is based on reversible redox processes over its surface. The interest in chemoresistive sensors has grown over the years because robustness, sensitivity, cost-effectiveness and small size make them attractive for a wide range of applications, including emerging technology for the Internet of Things.

Over the past decades, operando approaches, surface studies, and theoretical simulations have shed light on the surface processes that drive the gas sensing responses [1] for small molecules, such as NO_2, CO, H_2, O_3, and more deeply investigated the intermediate reactions of sample VOCs, such as ethanol, acetone and acetaldehyde. Nevertheless, these sensors can also detect more complex VOCs, such as biogenic gases (with a mostly natural origin) like terpenes. These gases have functional groups with different characteristics, making it challenging to comprehend their interaction with the sensing surface.

The motivation for the present work is to employ a novel approach to understanding the detection mechanism of complex gaseous molecules, that combines the investigation of surface chemical species formed during the analyte-sensor interaction through operando diffuse reflectance infrared Fourier transform spectroscopy (DRIFT) with the characterization of MOX active sites via chemisorption analyses. The latter can be used to understand the selectivity of a specific MOX compared to other materials.

Limonene has been used as a case study, as it is a biogenic gas belonging to the class of terpenes. It is widely exploited in the food and beverage industry, as a flavoring and preservative element, or in beauty and personal care products, in household products, and as the active principle in ecological pesticides. It is a VOC, with a time-weighted average threshold limit value (TLV-TWA) of about 30 ppm. As a result, sensors for in-situ and real-time monitoring of limonene leakage in industrial settings are required. The optimal material for limonene sensing was selected among seven nanostructured MOXs based on WO_3, ZnO and SnO_2, synthetized through different strategies for their functionalization, which were used to produce thick film sensors.

Description of the New Method

FTIR spectroscopy investigates the fundamental molecule vibrations by exploiting the mid-infrared (mid-IR) radiation. In DRIFT configura-

tion, it is one of the most advanced and effective methods to analyze rough surfaced solid samples. Therefore, this technique has been used to characterize the chemical species formed over the surface of the sensing films in presence of limonene, while acquiring the sensors electrical response, namely, in *operando*. Fig. 1 shows the gas test chamber collocated inside the sample compartment of a Vertex 70 IR spectrometer (Bruker) with a liquid-nitrogen-cooled MCT detector used to record the time resolved DRIFT spectra.

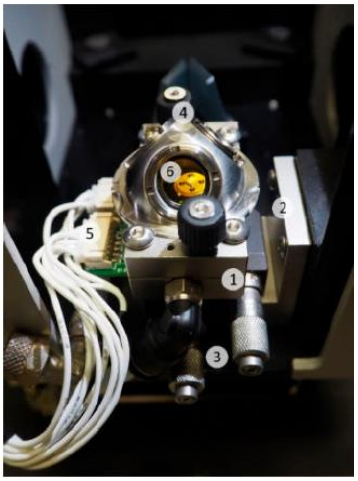

Fig. 1. Photo of the operando gas test chamber representing the main cell body (1), the cell support (2), the vacuum-compatible precision XY micro-stage (Standa) (3), the IR dome (4), the connection for electrical measurements via JST connectors (5) and a chemoresistive sensor (6). Reprinted from [2].

The sensor-gas interactions derived from *operando* DRIFT spectroscopy, and responsible for the device sensitivity, were induced by the reactivity of MOX active sites. Then, for the best performing material, were carried out experiments of temperature programmed reduction (TPR) with 5 % H_2/Ar gas mixture (40 ml/min) and of temperature programmed desorption (TPD) with pure ammonia and CO_2, in lab made apparatus with a Gow-Mac thermal conductivity detector (TCD). These analyses deepened the comprehension of the role of the acid-base nature of the active sites in the detection of limonene.

Results

Between the seven nanostructured films based on different MOXs, the WO_3-based one turned out to be the most suitable for the development of chemoresistive limonene sensors operating at low temperatures, demonstrating good sensitivity, cross-selectivity, and humidity-independent behavior for concentrations higher than 20 RH% [3]. The DRIFT absorbance spectrum (Fig. 2b) acquired during exposure of 2 ppm of limonene Fig. 2 (a) showed many peaks attributed to different molecule bonds over the surface of WO_3. *Operando* DRIFT analyses in the presence of humidity and probe molecules were also performed for completeness. Chemisorption analyses confirmed the mainly acidic nature of WO_3 active sites, contributing to the sensing mechanism proposal that will be described in the presentation.

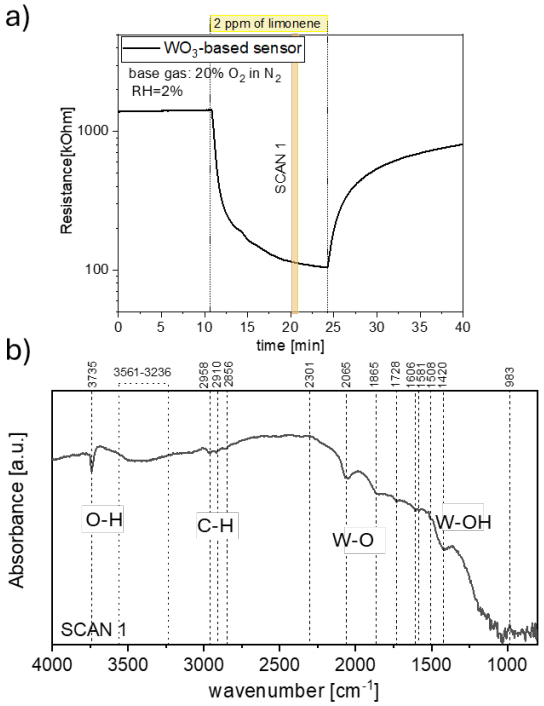

Fig. 2. (a) Resistance of WO_3-based sensor self-heated at 200°C, before and after exposure to 2 ppm of limonene. The yellow bar evidenced the period during which the AB spectra shown in (b) was acquired.

References

[1] Staerz, A.; Weimar, U.; Barsan, N., Current State of Knowledge on the Metal Oxide Based Gas Sensing Mechanism. *Sensors Actuators B Chem.*, *358*, 131531,(2022) doi:10.1016/j.snb.2022.131531.

[2] Spagnoli, E.; Valt, M.; Gaiardo, A.; Fabbri, B.; Guidi, V. Insights into the Sensing Mechanism of a Metal-Oxide Solid Solution via Operando Diffuse Reflectance Infrared Fourier Transform Spectroscopy. *Nanomaterials*, *13*, 2708, (2023) doi:10.3390/nano13192708.

[3] Rossi, A.; Spagnoli, E.; Tralli, F.; Marzocchi, M.; Guidi, V.; Fabbri, B. New Approach for the Detection of Sub-ppm Limonene: An Investigation through Chemoresistive Metal-Oxide Semiconductors. *Sensors, 23, 6291, (2023)* doi.org/10.3390/s23146291.

DOI 10.5162/EUROSENSORSXXXVI/OT5.73

Continuous Monitoring of Odour Concentration at the Inlet of a Scrubber with an E-Nose: Focus on the Management of Interferences

Stefano Prudenza, Carmen Bax, Laura Capelli
Politecnico di Milano, Department of Chemistry, Materials and Chemical Engineering "Giulio Natta", Piazza Leonardo da Vinci 32, Milan, Italy

Corresponding author: carmen.bax@polimi.it

Summary:
This work describes the implementation of an e-nose for the continuous measurement of odour concentration at a scrubber at a wastewater treatment plant, with the purpose of identifying odour peaks and investigate their causes. To this purpose, application-specific sampling and data processing were developed, able to deal with the interferences occurring in a complex industrial environment. Results show that instrumental predictions are within the confidence intervals of the reference method, and the system provided useful information for the plant operators to reduce the odour nuisance.

Keywords: electronic nose, environmental odour monitoring, odour concentration, odour abatement system, continuous measurement

,

Background, Motivation and Objective

Odours represent one of the major causes of citizens' complaints to local authorities, and have recently been included among the atmospheric pollutants to be monitored and controlled [1]. The reference method for monitoring environmental odour emissions is dynamic olfactometry (DO) (EN13725:2022), which has the drawback of being expensive and discontinuous [2]. For this reason, Instrumental Odour Monitoring Systems (IOMS) for the continuous monitoring odours are gaining more and more popularity to support plant managers to promptly identify anomalous situations and put effective interventions in action to reduce the odour impact.

This work describes the implementation of an IOMS based on chemical sensors for the continuous estimation of odour concentration at the inlet of a scrubber treating the air sucked from a primary settler at a wastewater treatment plant (WWTP), with the purpose of analysing the source variability and investigating possible causes for the odour peaks observed by previous olfactometric measurements.

Description of the New Method or System

Continuous odour measurement directly at the emission source is challenging because the sensors are exposed to a harsh environment characterized by several potential (and mostly unknown) interferences, thus requiring the optimization of both IOMS hardware and software for the specific application.

As hardware, we used a commercial EN (WT1, Ellona) with 8 sensors: 4 MOX, 3 electrochemical sensors specific for H_2S, NH_3 and mercaptans, and one PhotoIonization Detector (PID). The sampling line was designed with the purpose to deal with the specificities of the application (i.e. very high moisture and H_2S concentrations) by including a 1:1 dilution system using external air and a condensate trap.

The EN was further connected to an automatic gas sampler appositely developed for this activity, consisting of a hermetic suitcase of ca. 30 L, which enables the filling of one Nalophan® bag suitable for olfactometric measurements. The sampler can be activated manually or automatically by the EN, whenever a given threshold is exceeded.

Concerning the data processing, the quantification model should include application-specific compensation for the presence of interferents that may affect sensor responses and lead to false odour detections, and also account for the high uncertainty of the reference method (DO), which is commonly considered to be about a factor of 2 [2]. For this reason, we developed a dedicated data processing pipeline including a specific normalization step, which enabled to

eliminate daily oscillations of the sensors' responses, whose causes were not identified and which were totally uncorrelated with the odour concentration.

The quantification model was based on Support Vector Regression (SVR) [3], which, compared to linear regression models, is more suitable to deal with non-linear data and is also able to account for the uncertainty of the reference method. The model was trained using dynamic calibration for about 1 month: transient signals collected by the EN in the field were correlated with the odour concentration of 32 samples collected at the scrubber inlet and analysed by DO. Samples were taken on different days and under different operating conditions, with the purpose of including as much as possible the source variability in the training. Tuning of the SVR model involved two steps. First, the value of ε was fixed at the value of the average uncertainty of the olfactometer used for DO (i.e. 0.31 in logarithmic scale). Concerning C and gamma parameters, cross validation applied to a grid search method was used, returning their optimal value equal to 2 and 0.3, respectively.

Results

To eliminate the daily oscillation trend, which wasn't correlated to any other investigated parameter (humidity, temperature, wastewater flowrate, etc.), nor to the odour concentration, we decided to use an observational approach: since the oscillatory trend was repeatable over time from one day to the other, we calculated an average reference resistance value for each sensor by averaging all the resistance values registered by the sensor at the same hour for one month (Fig. 1a). By dividing the instantaneous resistance by this averaged reference value, we obtained the curves shown in Fig. 1b, where it is clearly visible that the unwanted oscillations are removed, and only deviations from the averaged reference values are visible as peaks. Fig. 2 shows the results of the SVR model testing on an independent dataset of 13 samples collected after training the model, expressed in terms of Limits of Agreement (LoA) with the reference method (DO) by application of the Bland-Altman method [4], proving a very good correlation between instrumental predictions and measured values.

Even though the algorithms used are not particularly innovative by themselves, their customization for the specific application, enabling the obtainment of useful results in a complex industrial context, which turned out to be effective in supporting the plant operators in identifying the causes of the odour nuisance, can be considered as an example of successful implementation of EN in a real-life industrial application.

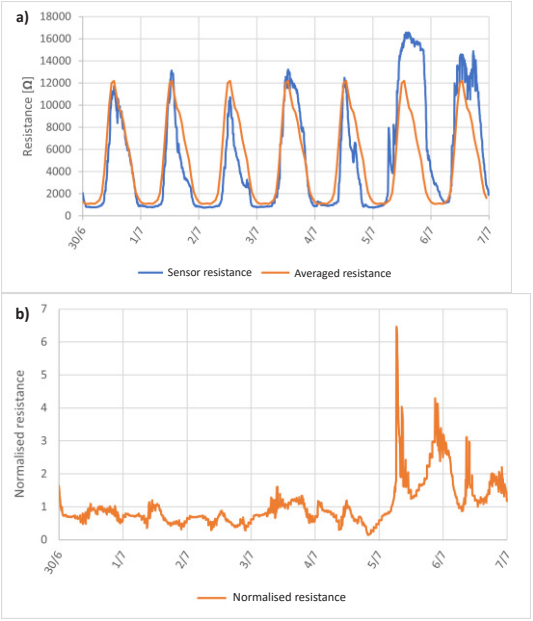

Fig. 1. a) Example of sensor resistance and averaged reference values, b) normalized responses

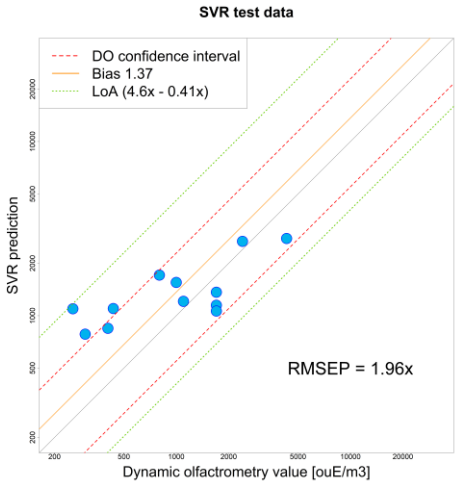

Fig. 2. Results of SVR model testing (blue dots). Red lines represent the DO uncertainty limits. The upper and lower LoA are reported in green, while the bias is represented by the continuous orange line

References

[1] C. Bax, S. Sironi, L. Capelli, How can odors be measured? An overview of methods and their applications, *Atmosphere* 11(1), 92 (2020); doi: 10.3390/atmos11010092

[2] J. Burgués, S. Doñate, S., M.D. Esclapez, L. Saúco, S. Marco, Characterization of odour emissions in a wastewater treatment plant using a drone-based chemical sensor system, *Science of The Total Environment* 846, 157290 (2022); doi: 10.1016/j.scitotenv.2022.157290

[3] F. Zhang, L.J. O'Donnell, Support vector regression, *Machine Learning: Methods and Applications to Brain Disorders* 7, 123–140 (2020); doi: 10.1016/B978-0-12-815739-8.00007-9.

[4] D. Giavarina, Understanding Bland Altman analysis. *Biochemia medica* 25(2), 141-151 (2015); doi: 10.11613/BM.2015.015

DOI 10.5162/EUROSENSORSXXXVI/OT5.75

Advanced Room Temperature Hydrogen Sensor based on Interdigitated Electrodes and Polycarbazole Membranes

Yohana López-Aparicio[1], Carlos Dominguez-Horna[1], Tomasz Jarosz[2], Agnieszka Stolarczyk[2], Karolina Glosz[2], Marcin Procek[3], Xavier Muñoz-Berbel[1] & Cecilia Jimenez-Jorquera[1]

[1] Institute of Microelectronics of Barcelona, IMB-CNM (CSIC), 08193 Bellaterra, Barcelona, Spain

[2] Department of Physical Chemistry and Technology of Polymers, Silesian University of Technology, 44-100 Gliwice, Poland

[3] Department of Optoelectronics, Silesian University of Technology, 44-100 Gliwice, Poland

Corresponding Author's e-mail address: Yohana.Lopez@csic.es

Summary:

In this work, the development of a new hydrogen sensor based on an interdigitated Pt-based electrode fabricated with semiconductor technology and conjugated polymers based on polycarbazole as selective receptor is described. The major novelty of this sensor is the ability to operate and measure at room temperature, which makes it an energy-efficient and safe solution and the mass fabrication of microelectrodes. The H_2 sensor results demonstrate that the sensor is capable of measuring in a wide range of H_2 concentrations from hundreds ppm up to low explosive level (4%) in air, containing different relative humidity, at room temperature with good linearity.

Keywords: planar microelectrodes, interdigitated electrodes, electrodeposition, polycarbazole, hydrogen detection.

Headlines

- New H_2 gas sensor based on a polycarbazole conducting polymer (PCz).
- Microelectrode based on a Pt interdigitated electrode (IDE).
- Room temperature hydrogen gas sensor.
- Detecion of wide H_2 concentration range.
- High selectivity to potential interfering gases.

Background, Motivation an Objectives

Industrial processes involving hydrogen are becoming common, requiring relevant safety measures to prevent hydrogen fires and explosions. Reliable and real-time monitoring of hydrogen gas concentrations is a key element for ensuring safety. Despite this, existing hydrogen sensing solutions have many drawbacks, such as: a) sensors can be potential ignition sources due to requiring elevated temperatures for their operation; b) sensors have a limited range of H_2 concentrations or respond slowly to sudden H_2 concentration changes; c) sensors are cost-intensive in terms of both unit price and operation. In that context, the objective of this work is to address the needs of the "hydrogen industry" by developing an efficient solution for sensing hydrogen gas in industrial conditions that mitigates the above drawbacks.

Interdigitated electrodes (IDE) are attracting due to their distinguished geometry (Fig. 1A) and electrochemical behaviour compared with planar electrodes, whose can be applied in non-conductive mediums like deionized water or air [1]. The IDE surface can be modified with other materials to enhance their selectivity to the target gas.

On the other hand, polymers are widely utilized in literature for sensor modification. Especially noteworthy are those with structures containing aromatic rings, as this renders them soluble in organic solvents, simplifying their synthesis and manipulation. Within this group, carbazole stands out for multiple reasons. It is a fully aromatic unit, providing a better chemical stability; its nitrogen atom can be easily substituted in order to increase the solubility or modify the optical and electrical properties; and its structure has a bridged biphenyl unit resulting in materials with a lower band gap than traditional poly(p-phenylene)s.

The objective of this study is the fabrication of interdigitated electrodes and their subsequent modification with polycarbazole, aiming to propose a novel alternative method for the determination of hydrogen at room temperature. These sensors will be fabricated using mass production microelectronic technologies allowing the scaling-up of the whole sensor fabrication process.

Methodology

The IDE is fabricated following compatible CMOS silicon technology, at the Institute of Microelectronics of Barcelona (IMB-CNM-CSIC). The technological process is divided into different steps as shown in Fig. 1B, where the conductive material could be Pt or Au.

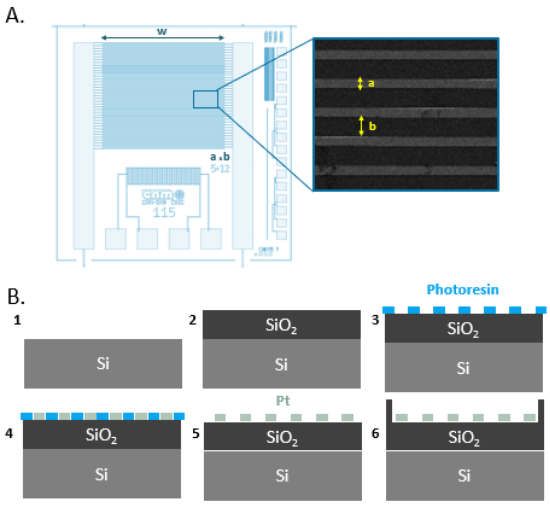

Fig. 1. (A) Design of the IDE where a is the digit width and b the separation between them; (B) Scheme of the fabrication process.

Once the chips are manufactured, they are packaged in a PCB and the electrical parts protected allowing them to be used in aqueous environments. Modification of the IDS can be carried by means of the electrodeposition of polycarbazole (Fig.2.) with cyclic voltammetry technique.

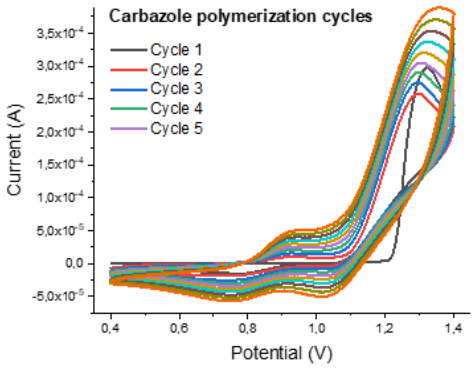

Fig. 2. Carbazole polymerization via Cyclic voltammetry.

Gas sensing experiments were performed using a mass flow controller-based system with constant H_2 flow rate in a measurement chamber at room temperature (23°C). The humidity level (RH=30%) was adjusted using bubbler humidifier. Measurement cycles consisted of 20 min flow of the carrier gas and 10 min flow of the carrier gas with the indicated and constant concentration of H_2. The resistance of the sensors was measured using Keysight DAQ970A.

Results

After modifying the IDE with polycarbazole polymers, a morphological and electrical characterization is carried out using SEM-FIB and electrochemical impedance spectroscopy (EIS). The morphological analysis reveals the uniformity of polycarbazole electrodeposition and the presence of pores in the membrane, facilitating H_2 diffusion to the transducer.

An example of the Pt IDE-PCz sensor response for repeated cycles of H_2 exposition is presented in Fig.3. The calibration curve for resistance data obtained is shown in Fig.4. The results show high efficiency of H_2 sensing with satisfying dynamics and good linearity of responses.

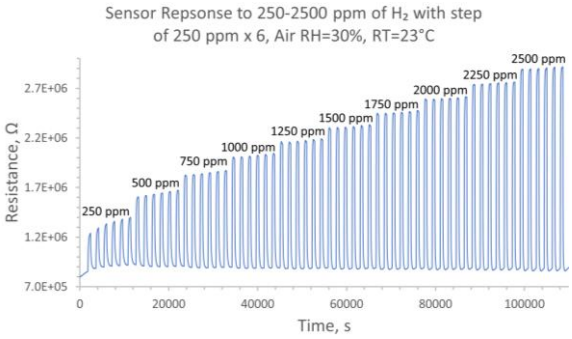

Fig. 3. Recording of sensor resistance changes for several H2 exposition cycles.

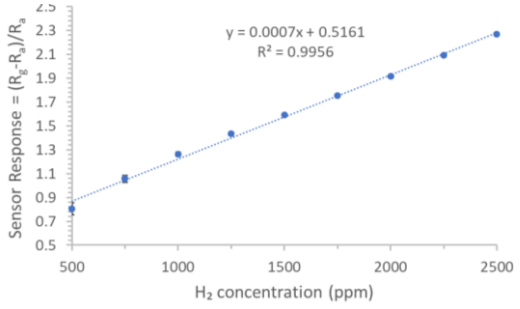

Fig. 4. Sensor calibration curve for a H_2 concentration range of 500-2500 ppm.

Reference

[1] A. Stolarcyk, T. Jorosz, M. proccek, Room Temperature Hydrogen Gas Sensing via Reversible Hydrogenation of Electrochemically Deposited Polycarbazole on Interdigitated Pt Transducers, *Sensors* 19, 1098 (2019); doi 10.3390/s19051098

DOI 10.5162/EUROSENSORSXXXVI/OT5.81

CMOS Compatible Electrostatically Formed Silicon Nanowire for Selective Ppb Level Sensing Platform

S. M. Siddiqui[1], Y. Rosenwaks[1], S. A. Alexander[1], I. Shem Tov[1], A. Mukherjee[1], Y. Mazor[1], E. Pikhay[2], and Y. Roizin[2]
[1]Department of Physical Electronics, Tel Aviv University, Israel,
[2]Tower Semiconductor, Migdal HaEmeq, Israel

Corresponding Author's e-mail address: yossir@eng.tau.ac.il

Summary:
Electrostatically Formed Nanowire (EFN) sensor is a CMOS based multi-gate silicon nanowire (NW) field effect transistor (FET) where the nanowire is formed electrostatically post fabrication. By employing a specially designed large area sensing antenna we improve the EFN sensor response by several orders of magnitudes. We demonstrate a world record response of ~ 90 % to 30 ppb H_2 which can be further improved by several orders of magnitude with increasing antenna size.

Keywords: Gas Sensors, Electrostatically Formed Nanowire, Hydrogen Sensing, CMOS Compatible Sensors, Ppb detection, Antenna effect.

Background, Motivation and Objective

Hydrogen sensors for sub-ppm levels are vital for early indication of leaks in various facilities of green energy, storage, chemical industry, nuclear reactors. Silicon nanowire (Si-NW)-based field-effect transistors (FETs) have been demonstrated in the last two decades as highly sensitive and selective chemical sensors operating at room temperature. Inspired by the Si-NW performance, we introduced in 2013 the Electrostatically Formed Nanowire (EFN), a multi-gate very large-scale integration (VLSI) compatible transistor for bio-sensing [1]. We show here that the EFN response is improved by several orders of magnitude when a large sensing area is coupled to the EFN channel. This antenna EFN combines the advantage of a nanometer-sized transistor channel with excellent electrical characteristics and a very large sensing area. This paves the way to a VLSI-based gas sensing platform with Ppt-level gas sensing capabilities.

Description of the New Method or System

Fig.1 shows a cross-sectional schematic of a small (Fig.1(a)) and large area (Fig.1(c)) EFN fabricated in this work. The EFN was decorated with a 20 nm thick Pd layer for H_2 sensing; The Pd was deposited on the EFN by first defining a mask using e-beam lithography, followed by a coating of a 20 nm Pd layer using an e-beam evaporator with a deposition rate of 0.5 Å/s.

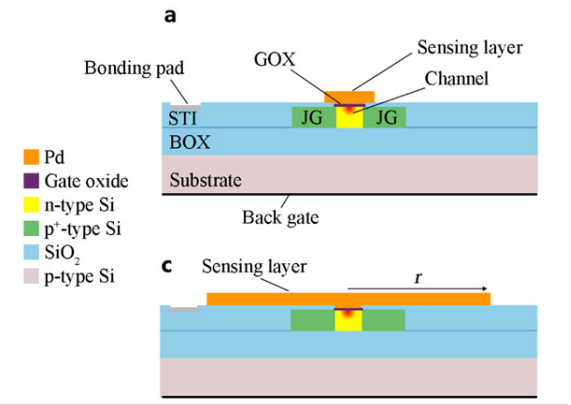

Fig. 1. (a) Schematic cross-section illustration of the EFN sensor, showing all the device layers. The channel (red) size can be adjusted post-fabrication by applying biases to the control gates (JG or BG). The top Pd molecular gate above the GOX 6 nm layer is the sensing layer to H_2; the drain-source direction is into the page. (c) *Schematic of the large area EFN.*

Results

Fig. 2 shows the sensor response of the large area (red) and the small area (blue) EFN to H_2 concentration in the range of 30 ppb to 100 ppm. The error bars are a result of variations in device surface chemistry, contamination, dimensions, and noise. For the concentration of 30 ppb, the large area antenna EFN shows a normalized average response of ~87%, whereas, for the small area, the response is lower than the device current drift; at 7 ppm H_2 concentration, there is a

two-orders-of-magnitude difference in the response between the large and small areas EFNs.

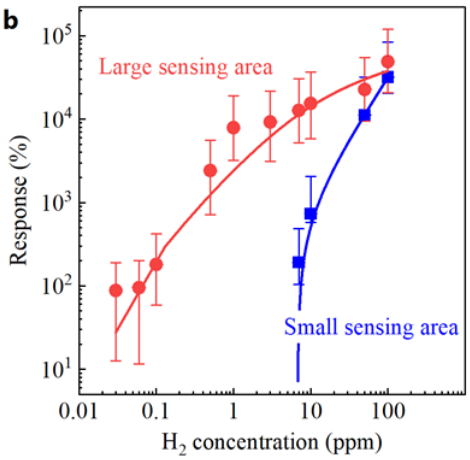

Fig. 2: The large area EFN sensor response (red) to H_2 relative to the conventional EFN response (blue).

The origin of H_2 sensitivity in Pd-based sensors has been discussed extensively, and various models have been reported in the literature (e.g., the recent perspective [2]). The increase of current in Pd-Si-FET-based sensors following H_2 adsorption is commonly attributed to the changes in band bending at the SiO_2/Si interface of the transistor channel. One of the widely accepted models is based on the fact that Pd nanoparticles catalyze the dissociation of H_2 molecules into atoms on the Pd surface. The H atoms then diffuse to the Pd/SiO_2 interface, polarize, and, as a result, induce an interfacial dipole layer with the H_2 very close to the metal side [3]. This induced dipole layer changes the channel band bending and, as a result, the sensor source-drain current.

To explain the observed results in Fig.2, we argue that the induced H dipoles are not electrically symmetric, but the positive charge is larger than the negative one due to partial screening by the Pd layer. Due to the antenna effect explained below, H atoms (asymmetric dipoles) are transported along the Pd/SiO_2 interface towards the channel region. This increases the dipole density above the channel with increasing sensing area, and as a result, the sensor response increases exponentially. The mechanism is to a certain extent, similar to the antenna effect in CMOS transistors. According to this effect, charges in plasma processes are collected by metal areas (antennas) connected to the transistor gate.

Using COMSOL Multiphysics, we have determined the net charge distribution at the Pd/SiO_2 interface for several surface densities of hydrogen atoms. Our calculations showed that the charge concentration above the channel increases with increasing sensing area; this is because the charged H atoms migrate from the surrounding areas with very low capacitance (field oxide thickness ≈ 520 nm) to the region right above the channel with the high capacitance (GOX thickness = 6 nm). Using first-order approximation, neglecting the exact complex structure of the device, we can estimate the difference in surface charge densities between the channel (σ_c) and the surrounding regions (σ_s). Since the Pd potential (V_{Pd}) is constant,

$$V_{Pd} = \frac{Q_c}{C_c} = \frac{Q_s}{C_s} = \sigma_c d_c = \sigma_s d_s \rightarrow \sigma_c \approx 86\sigma_s \quad (1)$$

where Q is the total charge, C is the capacitance, d is the dielectric thickness, and the subscripts c and s denote the channel and surrounding region, respectively; d_c is 6 nm whereas d_s is 520 nm, yielding a ratio of 86 between the channel and the surrounding dipole density; a similar (but more accurate) result was obtained using numerical analysis.

Summary

We have presented a novel sensing device based on the antenna EFN concept, which couples an electrostatically tunable nano-sized transistor channel with a large (up to 3,500 μm²) sensing area. It is shown that the large sensing area improves the EFN response by several orders of magnitudes, especially at low analyte concentrations. Based on the EFN sensor response as a function of the sensing area, we argue that the sensing mechanism can be attributed to the formation of asymmetric charged H atomic dipoles at the Pd/SiO_2 interface (thick silicon dioxide) and their migration to the channel area with the small GOX thickness, resembling the antenna effect. The outstanding response of ~ 90 % to 30 ppb H_2 can be improved by several orders of magnitude with increasing antenna size and paves the way to a VLSI-based gas sensing platform with Ppt-level gas sensing capabilities.

References

[1] G. Shalev, G. Landman, I. Amit, Y. Rosenwaks, and I. Levy, “Specific and label-free femtomolar biomarker detection with an electrostatically formed nanowire biosensor,” *NPG Asia Mater*, vol. 5, no. 3, Mar. 2013, doi: 0.1038/am.2012.75.

[2] I. Darmadi, F. A. A. Nugroho, and C. Langhammer, “High-Performance Nanostructured Palladium-Based Hydrogen Sensors - Current Limitations and Strategies for Their Mitigation,” *ACS Sens*, no. i, 2020, doi: 10.1021/acssensors.0c02019.

[3] I. Lundström and T. DiStefano, “Hydrogen induced interfacial polarization at PdSiO2 interfaces,” *Surf Sci*, vol. 59, no. 1, pp. 23–32, 1976, doi: 10.1016/0039-6028(76)90288-0.

DOI 10.5162/EUROSENSORSXXXVI/OT5.99

Ammonia Sensor to Effectively Dose the Reducing Agent for NO_x SCR Systems in Biomass Combustion Systems

Thomas Wöhrl[1], Gunter Hagen[1], Ralf Moos[1]
[1] Department of Functional Materials | University of Bayreuth, Bayreuth, 95440, Germany

Functional.Materials@uni-bayreuth.de

Summary:
The detection of gaseous ammonia in the flue gas of biomass combustion systems is becoming increasingly important due to stricter legislation. The optimization of an existing sensor principle showed significant improvements in ammonia sensitivity in comparison to the original sensor. In further measurements in the flue gas of a wood combustion, the cross sensitivities to other components turned out to be very low. So, a high accuracy in the determination of the ammonia concentrations could be achieved in comparison to an FTIR spectrometer.

Keywords: gas sensor, ammonia detection, biomass combustion, exhaust gas aftertreatment, selective catalytic reduction

Background and Motivation

Previous developments of ammonia (NH_3) sensors for automotive exhaust systems have found limited application. One of the reasons for this is the cross sensitivity of typical mixed-potential sensors towards nitrogen oxides (NOx) that are present in engine combustion exhaust [1]. Ammonia is produced from an aqueous urea solution (AdBlue, DEF) for the Selective Catalytic Reduction (SCR) of the nitrogen oxides. The control of AdBlue dosing in vehicles is mostly based on empirical models, which are well understood by now. [2]

However, the extension of the legal guidelines for biomass combustion plants specifies stricter limits for the emission of ammonia and nitrogen oxides in many countries [3].

The dosing of the reducing agent in biomass combustion systems is more complex than in automotive applications due to the mostly individual setup. For this reason, there is a large interest in the development and implementation of selective ammonia sensors in order to meet the legal requirements regarding ammonia slip.

Design and further development

The basic concept of the original sensor has been optimized to produce all layers by cost-effective screen-printing process (schematic structure of the sensor in Fig. 1). By patterning the IDE structure from a solid gold area using a picosecond laser (LPKF Protolaser R4), fine line widths and spacings of 20 μm can still be achieved. [4]

A further optimized heater structure ensures a homogeneous temperature distribution in the area of the IDE structure covered by a gas sensitive zeolite film. In addition, flow effects are reduced by improved control of the four-wire resistance of the heater structure to minimize errors in concentration determination.

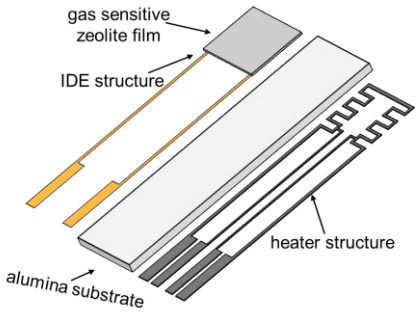

Fig. 1. Schematic structure of the zeolite-based ammonia sensor on a ceramic substrate with integrated heater and IDE structure for electrical characterization of the gas sensitive film.

The electrical behavior of the zeolite film can be approximated by a parallel *RC* element. The adsorption of certain molecules, such as ammonia, leads to changes in its electrical properties [5]. The determination of the capacitance *C* in contrast to the resistance *R* by means of an impedance measurement at high frequencies (> 500 kHz) also simplifies the development of an evaluation unit.

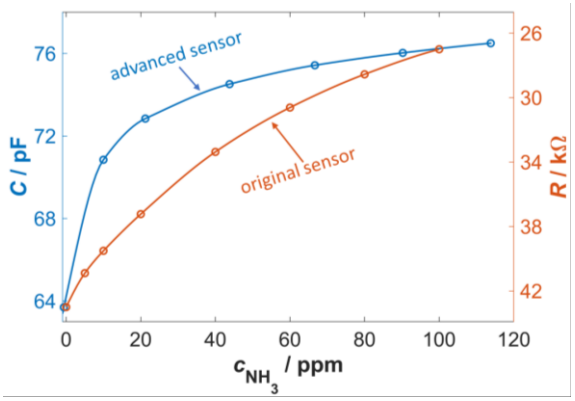

Fig. 2. Comparison of ammonia sensitivity of the original and advanced sensor, adapted from [4].

By further modifying the zeolite composition and operating temperature, the sensitivity to ammonia in the legally relevant concentration range (< 50 ppm) was notably improved in laboratory measurements (see Fig. 2), especially at low NH_3 concentrations.

Investigation of cross sensitivity in flue gas

Since the main application for the sensor is the field of biomass combustion, compared to automotive applications, the sensor is exposed to higher loads, e.g. from particulate matter, CO and HC emissions [6].

For this, a wood burning stove (5 kW) was used as an emission source for initial tests in flue gas. Small amounts of ammonia water (10 %) were also added to the combustion air to cover a concentration range between 0 and 150 ppm NH_3 in the flue gas.

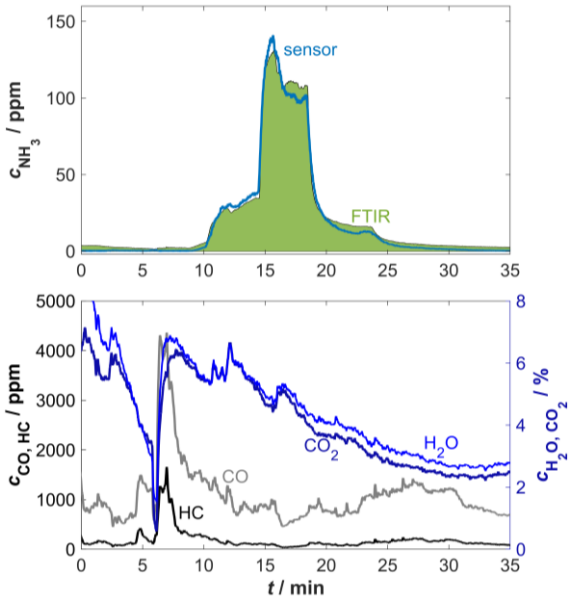

Fig. 3. Time course of the cross sensitivity measurement in flue gas from a wood burning stove with a comparison of the ammonia concentration measured by the sensor (full stream measurement) and FTIR spectrometer (bypass measurement).

The measurement showed that the sensor was not affected by changes in CO, HC, or CO_2 content. Only the cross sensitivity to water was corrected for a comparison with data from an FTIR spectrometer (MKS MulitGas 2030). The nearly linear influence of water vapor is about 0.3 pF/%$_{H_2O}$. In direct comparison, the ammonia sensor provided values matching to the concentration measured by the FTIR spectrometer (see Fig. 3).

Outlook

Future series of measurements will focus on long-term stability and the influence of the protective caps at high dust and soot levels. Further measurements will also be carried out in the flue gas of several biomass furnaces in the power range over 50 kW.

References

[1] R. Moos, D. Schönauer, Recent Developments in the Field of Automotive Exhaust Gas Ammonia Sensing, *Sensor Letters* 6, 821-825 (2008); doi: 10.1166/sl.2008.509

[2] C. Schar, C. H. Onder, H. P. Geering, Control of an SCR catalytic converter system for a mobile heavy-duty application, *IEEE Transactions on Control Systems Technology* 14, 641–653 (2006); doi: 10.1109/tcst.2006.8766

[3] M. König, K. Eisinger, I. Hartmann, M. Müller, Combined removal of particulate matter and nitrogen oxides from the exhaust gas of small-scale biomass combustion, *Biomass Conversion and Biorefinery* 9, 201–212 (2019); doi: 10.1007/s13399-018-0303-0.

[4] T. Wöhrl, J. Kita, R. Moos, G. Hagen, Capacitive, Highly Selective Zeolite-Based Ammonia Sensor for Flue Gas Applications, *Chemosensors* 11, 413 (2023); doi: 10.3390/chemosensors11070413.

[5] R. Moos, R. Müller, C. Plog, A. Knezevic, H. Leye, E. Irion, T. Braun, K.-J. Marquardt, K. Binder, Selective ammonia exhaust gas sensor for automotive applications, *Sensors and Actuators B: Chemical* 83, 181–189 (2002). doi: 10.1016/S0925-4005(01)01038-3.

[6] J. Villeneuve, J. H. Palacios, P. Savoie, S. Godbout, A critical review of emission standards and regulations regarding biomass combustion in small scale units (<3 MW), *Bioresource technology* 111, 1–11 (2012). doi: 10.1016/j.biortech.2012.02.061.

DOI 10.5162/EUROSENSORSXXXVI/OT5.107

Silicon-Based Thermal Conductivity Detector for Gas Sensing

Alexandre Teulle[1], *Mathis Baret*[1], *Murielle Jurdit*[1], *Florence Ricoul*[1], *Jean-Baptiste Tissot*[1]
[1] *Université Grenoble Alpes, CEA, LETI, Grenoble, France,*

alexandre.teulle@cea.fr

Summary:
We present a novel Thermal Conductivity Detector (TCD) for gas sensing without the use of a chromatography column. Its original architecture is based on a suspended membrane on top of which are deposited a heating element and a separated sensing element made of amorphous silicon. These sensors are micro-fabricated and tested in a climatic chamber. They reach a theoretical detection limit (3 sigma) of 13 ppm for carbon dioxide in air and exhibit a signal-to-noise ratio 4 times higher than conventional platinum TCDs.

Keywords: gas, sensor, thermal, conductivity, detector

Introduction

Thermal Conductivity Detectors (TCDs) are among the most widely used sensors in gas chromatography (GC) systems [1] and well appreciated for their universality. Their working principle relies on the heat transfer between a metallic coil heated by Joule effect and the surrounding gas, resulting in a change of the coil electrical resistance. Recently, miniaturized TCDs (µTCDs) have been produced on silicon substrates using microfabrication techniques. This level of integration greatly improves the sensitivity of this technology, allowing to reach the subparts per million (sub ppm) detection limit when coupled to a GC system [2]. Moreover, it reduces the power consumption of the detector, opening the way to portable air quality monitoring systems. In that perspective, Bourlon et al. reported the use of a single µTCD chip to measure simultaneously the CO_2 concentration and relative humidity in air with respective errors of 300 ppm and 2% [3]. In this work, we present our latest investigations into the analysis of ternary gas mixtures using our novel micro-fabricated thermal conductivity sensor using a unique architecture.

Materials choice

Several materials for the sensing element have been considered but the boron-doped hydrogenated amorphous silicon (a-Si: H(B)) was chosen for its CMOS compatibility and high sensitivity. Indeed, we have estimated the temperature coefficient of resistance (TCR) at $1{,}66 \cdot 10^{-2}$ K^{-1} by a four-probe measurement of the electrical resistivity as a function of temperature on a full wafer. This value is one order of magnitude higher than the TCR of platinum. Regarding the heating element, we have chosen titanium nitride (TiN) for its CMOS compatibility and relatively low resistivity of $1{,}5 \cdot 10^{-4}$ Ω·cm allowing to reach ~200°C with 3V across the element.

Sensor Chip Fabrication and Architecture

TCD sensor chips are micro-fabricated in our clean room facility by bonding two silicon wafers. Silicon nitride (Si_xN_y) membranes are etched in the bottom wafer after having deposited the TiN and a-Si: H(B) layers for ensuring heating and temperature probing respectively (see Fig. 1).

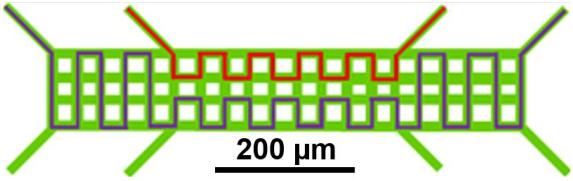

Fig. 1. Schematic of the suspended Si_xN_y membrane (green) with a-Si: H(B) sensing element (red) and TiN heating element (blue).

Fluidic channels ensuring passive gas diffusion to the suspended membrane are etched by deep reactive ion etching in the top wafer.

Four suspended membranes are used on the same silicon chip in order to have an accurate differential measurement of the resistance variations of the sensing elements using a Wheatstone bridge configuration. Two membranes are placed in an analysis cavity opened to the ambient air by fluidic channels; the other two

membranes are hermetically sealed in a reference chamber (see Fig. 2).

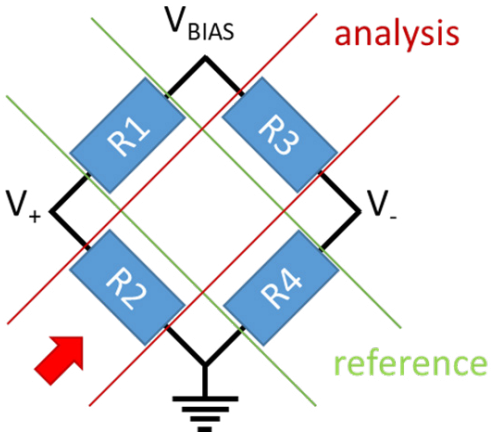

Fig. 2. Schematic of the Wheatstone bridge configuration of the four a-Si: H(B) sensing elements

Experimental Setup

The TCD silicon chip is wire-bonded onto a printed circuit board in order to connect the heating and sensing elements to a specifically designed electronic circuit. This driving electronics is able to apply sequentially two different voltages on the heating elements in order to thermalize the whole membranes at two different temperature. At the same time, it applies a voltage V_{BIAS} on the Wheatstone bridge composed of the four sensing elements and measures the corresponding signal $V_+ - V_-$.

In order to monitor the concentrations of two analytes mixed with a third component in excess (e.g. CO_2 and H_2O in air), the silicon die and its driving electronics are placed into a climatic chamber in which we control the two analytes concentrations.

After performing a calibration at a minimum of three different concentrations of the two analytes, we are able to match the TCD signals obtained for two heating temperatures with the two analytes concentrations.

Results

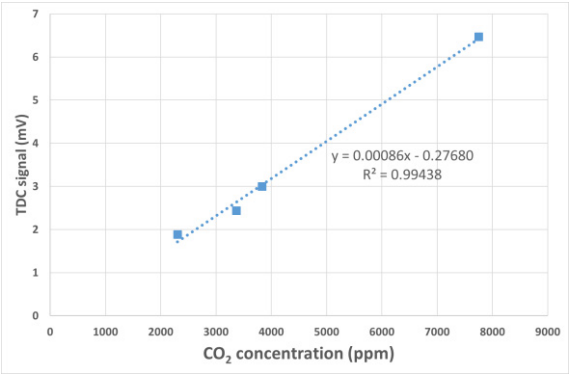

Fig.3. Measured TCD signal as a function of the CO_2 concentration

Fig.3. illustrates the measurement of the CO_2 variations in the presence of H_2O and synthetic air. The TCD sensor shows a good linearity with a coefficient of determination R^2 of 0.994. Moreover, we have compared the sensor with conventional platinum TCDs in the same experimental conditions. As can be seen in Tab.1, these sensors are almost 8 times more sensitive to CO_2 variations than conventional platinum sensor. However, they are also more sensitive to noise, resulting in a signal-to-noise ratio 4 times better than the platinum TCDs.

Tab. 1: Comparison of the conventional platinum TCD technology with the a-Si: H(B)/TiN architecture

Sensing Technology	Signal for 100 ppm variation of CO_2 (µV)	Noise average (µV)	Signal to Noise Ratio
Platinum	11.5	2.1	5.48
a-Si: H(B) and TiN	89.1	3.8	23.45

Aknowledgement

This work was funded by the CBRNE grant of the French government.

References

[1] B.P. Regmi, M. Agah, *Analytical Chemistry*, 90, 13133-13150 (2018); doi: 10.1021/acs.analchem.8b01461

[2] D. Cruz, J.P. Chang, S.K. Showalter, F. Gelbard, R.P. Manginell, M.G. Blain, *Sensors and Actuators B*, 121, 414-422 (2007); doi: 10.1016/j.snb.2006.04.107

[3] B. Bourlon, B.A. Pham-Ho, J.F. Beche, O. Constantin, *22nd International Conference on Miniaturized Systems for Chemistry and Life Sciences (MicroTAS 2018)*

DOI 10.5162/EUROSENSORSXXXVI/OT5.118

Development of 2D-Borophene conductometric sensor for ammonia detection

Oluwatoyin Emmanuel Aina[1], Rapha Guy[1], Joan Bausells[4], Monique Sigaud[1], Guy Raffin[1], Nadia Zine[1] , GuySeyedeh Sadrieh Emadian[2,3], Viktoriya Pyeshkova[2], , Satheesh Krishnamurthy[3], Silvia Varagnolo[2] , Abdelhamid Errachid[1]

[1] Universite Claude Bernard Lyon-1, CNRS, ISA-UMR 5280, CNRS, 69622 Villeurbanne, France

[2] School of Engineering & Innovation, The Open University, Walton Hall, Milton Keynes MK7 6AA, United Kingdom

[3] Surrey Ion Beam Centre, Advanced Technology Institute, University of Surrey, Guildford Surrey GU2 7XH, United Kingdom

[4]Instituto de Microelectrónica de Barcelona (IMB-CNM,CSIC), Campus UAB, 08193 Bellaterra, Spain.

Corresponding Author's e-mail address: abdelhamid.errachid@univ-lyon1.fr

Summary

This study introduces a microconductometric sensor, developed by drop-casting 2D-Borophene film on Interdigitated Electrodes (IDEs) for real-time ammonia gas detection. The sensors were exposed to varying concentration ranges of 10–100 ppm and 100-1000 ppm ammonia vapour at room temperature. The results indicated a lower detection limit (LOD) of 4 ppm and high selectivity and reproducibility. The NH_3 sensor detected with high sensitivity, quick response, and recovery time of 18 s and 27 s respectively, highlighting the potential and effectiveness of Borophene for gas sensing. More study required to understand the potential mechanisms of this new 2D system and its interactions

Keywords: Gas-sensing, facile, Borophene, 2D-materials, microconductometric.

Title

Development of 2D-Borophene conductometric sensor for ammonia detection

Objective

This study aims to develop a simple sensor for real-time detection of ammonia with low LOD and fast response time.

Introduction

Ammonia is released into the environment through various anthropogenic activities such as fertilizer application, food processing, and medical diagnostics [1]. It is a significant pollutant that has detrimental effects on human health and industrial output, due to its corrosiveness and toxicity [2]. The Occupational Safety and Health Administration recommends 50 ppm or 35 mg/m^3 equivalent as ammonia's permissible exposure limit (PEL) within 8 hours. However, due to its extensive applications, accurate and practical trace-level ammonia detection and monitoring are extremely important [3], to guard against overexposure.

Borophene, a two-dimensional material, has unique properties such as high sensitivity, fast response, and long-term stability, thus unfolding its potential for gas sensing [4]. Several theoretical studies have been done on Borophene with relatively little experimental work. In this work for the first time, a conductometric transducer is proposed to detect ammonia gas with thin Borophene film.

Materials and Methods

Chemicals: ethanol, methanol, acetone and ammonia were obtained from Sigma Aldrich. Borophene was synthesized using liquid phase exfoliation. An amount of boron was sonicated in ethanol and then centrifuged at 3000 rpm to remove bulk boron and collect borophene sheets. The obtained borophene was dried in an oven at 40℃ overnight. 5 mg of Borophene was dispersed ultrasonically in 200 ml ethanol for 15 mins, and 10 µl were drop-casted onto the surface of the IDEs and dried at room temperature. The conductometric measurements were conducted by applying a low-amplitude sinusoidal voltage (10 mV peak-to-peak at 0 V) with a frequency of 10 kHz to each pair of IDEs using the "VigiZMeter" Conductometer, by placing the IDEs sensors in the headspace above the liquid phase. The variation in conductance (ΔG) was recorded over time.

Results and discussion

The ammonia sensor showed high sensitivity and good reproducibility for each concentration with a slight variation, as shown in Fig. 1 and Fig. 2 respectively. The sensor linear responses increase with increasing NH_3 concentrations. A

low detection limit of 4 ppm was obtained using eq.1, and a fast response and recovery times of 18 s and 27 s respectively. The unique structural characteristic of borophene results in unsaturated bonds with intense electron deficiency, thus, facilitating facile interaction with gas molecules and promoting significant charge transfer at ambient temperature. This results in high sensitivity and rapid response [5]. The results obtained in this study proved that borophene was effective in ammonia sensing. A performance comparison of recently reported NH_3 sensors is shown in Tab 1.

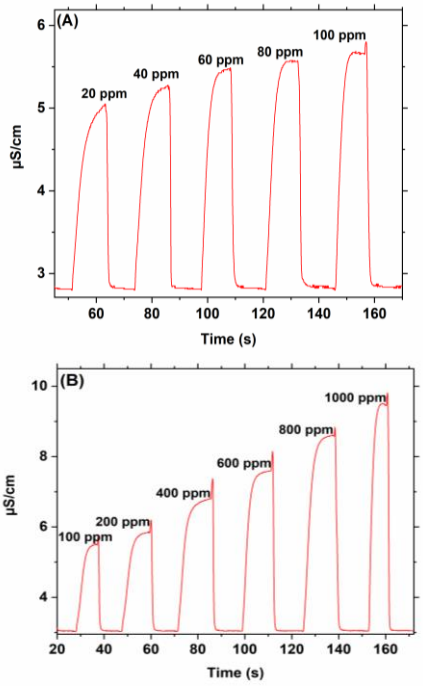

Fig. 1. Gaseous phase of ammonia detection kinetics: (A) 20-100 ppm (B) 100-1000 ppm.

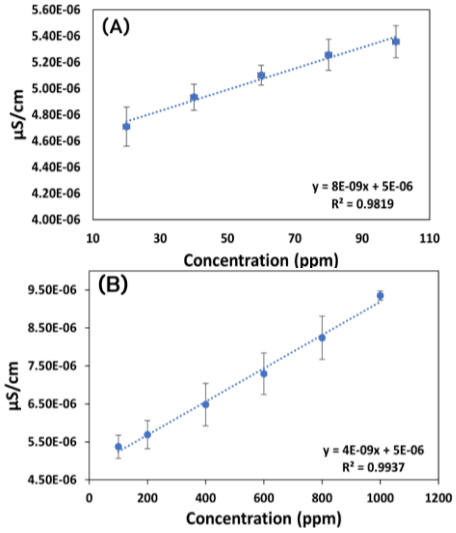

Fig. 2. Calibration curves of the gaseous phase of Ammonia concentrations: (A) 20-100 ppm (B) 100-1000 ppm.

Tab. 1: Comparison of the performances of some ammonia sensors at room temperature

Ammonia sensors	LOD	$T_{Res.}$ (s)	Ref.
Citric acid-PANI	1 ppb	30	[3]
PANI-ZNO	10 ppm	35-21	[6]
NiO-NPs	50 ppm	63	[7]
2D-Borophene	4 ppm	18	This work

Conclusion

The borophene-based gas sensor is observed to be highly sensitive to ammonia gas at room temperature with a wide detection range of 20-1000 ppm. This concentration range can help in preventing severe health issues and monitoring ammonia levels in industry [1]. Further studies are essential to fully maximize its potentials.

References

[1] D. Maity, R.T.R. Kumar, Polyaniline Anchored MWCNTs on Fabric for High Performance Wearable Ammonia Sensor, American Chemical Society sensors 3(9), 1822-1830 (2018); doi: 10.1021/acssensors.8b00589

[2] K. Lin, Y. Li, W. Dai, Z. Yuan, W. He, H. Zhang, C. Xue, J. Yan, J. Mei, J. Zhuang, X. Wang, A V2O5/MWCNTs Composite Thin Film Gas Sensor for the Fast Detection of Ammonia, Materials Today Communications 38, 107969 (2024); doi: 10.1016/j.mtcomm.2023.107969

[3] D. Lv, W. Shen, W. Chen, Y. Wang, R. Tan, M. Zhao, W. Song, One-step Preparation of Flexible Citric Acid-doped Polyaniline Gas Sensor for ppb-level Ammonia Detection at Room Temperature, Sensors and Actuators A, Physical 350, 114120 (2023); doi:101016/jsna.2022.114120

[4] R. Kaimal, A. Dube, A. Sorrentino, A. Al Souwaileh, S. Anandan, Borophene: A Concise Overview of Design, Characteristics, and Sensing Applications, FlatChem 42, 100579 (2023); doi: 10.1016/j.flatc.2023.100579

[5] C. Hou, G. Tai, Y. Liu, X. Liu, Borophene gas sensor, Nano Research, 1-8 (2022); doi: 10.1007/s12274-021-3926-6

[6] M. Das, D. Sarkar, One-pot Synthesis of Zinc Oxide-Polyaniline Nanocomposite for Fabrication of Efficient Room Temperature Ammonia Gas Sensor, Ceramics International 43(14), 11123-11131 (2017); doi: 10.1016/j.ceramint.2017.05.159

[7] J. Yang, Y. Gui, Y. Wang, S. He, NiO/Ti3C2Tx MXene Nanocomposites Sensor for Ammonia Gas Detection at Room Temperature, Journal of Industrial and Engineering Chemistry 119, 476-484 (2023); doi: 10.1016/j.jiec.2022.11.070

DOI 10.5162/EUROSENSORSXXXVI/OT5.199

Environmental Odour Monitoring at Receptors by means of an IOMS: Assessment of the Odour Impact of a Paper Mill

Christian Ratti, Carmen Bax, Stefano Prudenza, Laura Capelli,
Politecnico di Milano, Department of Chemistry, Materials and Chemical Engineering "Giulio Natta",
Piazza Leonardo da Vinci 32. 20133 Milano, Italy

carmen.bax@polimi.it

Summary:

Instrumental Odour Monitoring Systems (IOMS) are more and more frequently applied for monitoring odours directly where their presence is complained. They analyse in real-time the ambient air to detect odour presence and determine their provenance. This paper describes the monitoring of paper mill odour emissions by two IOMS located at two receptors, where residents frequently report the occurrence of odour events. It describes the protocol involved for plant odour sources characterization, IOMS training and validation. The monitoring, lasting 4 months, allowed assessing the odour impact at receptors, expressed as the detection frequency of plant odours, and identifying critical emissions deserving maintenance interventions or upgrading.

Keywords: electronic nose, odour nuisance, real-time monitoring, industrial emissions

Background, Motivation and Objective

Odour pollution represents a limiting factor to the operation of industrial activities, especially when they are located very close to residential areas. Indeed, odours are currently subjected to regulations, which foresee the execution of periodical monitoring campaigns at plant emissions and receptors located in their proximity. Among odour measurement techniques [1], Instrumental Monitoring Systems (IOMS) offer the opportunity to analyse the ambient air directly where the odour presence is complained with the purpose to assess the odour impact at sensitive receptors. During the monitoring, the IOMS is intended to real-time detect the presence of odours and estimate their provenance [1]. The unique capability to discriminate different odours makes the use of IOMS particularly interesting when there is the necessity to recognize the source from which the odours are originated: this can be the case when different industrial odour emitting activities co-exist on the same territory or, for one single plant, if different odour types are emitted [2-3]. This is typically the case of a paper mill, in which two very different types of odours are emitted: the odour emissions (typically conveyed in stacks) related to the paper production, which is often described as "cooked paper", and the odour emissions associated with the wastewater (WW) treatment, which are usually rich in H_2S.

This paper proposes the use of two IOMS for the direct assessment of the odour impact associated to a paper mill located in northern Italy, accused by citizens are responsible for the odour nuisance in the area. The plant, producing recycled paper with a capacity of about 1200 ton/d, is characterized by considerable variability of odour emissions mostly due to discontinuous operating conditions. Besides providing an objective evaluation of the odour nuisance nearby the plant, the IOMS were expected to contribute on identifying critical sources causing the odours perceived by the citizens, thereby helping in the definition of most adequate strategies for intervention.

Description of the New Method or System

Two commercial electronic noses (EOS03 and EOS42 produced by Sacmi, Italy) were used as IOMS for this study. They are equipped with a 6 MOX sensors array and systems for generating odourless reference air and regulating moisture.

3 independent campaigns were carried out at the plant to collect odour samples. For IOMS training, the samples were diluted at suitable concentration ranges (20-350 ou_E/m^3) after determination of their odour concentration by dynamic olfactometry (EN 137125:2022). IOMS were trained to discriminate 4 odour classes: 'Air', 'Wastewater (WW)', 'Paper Production (PP)' and 'Unknown (UN)' (Fig. 1). The 'UN' class was introduced to account for other sources, different from the paper mill, which could cause the perception of odours at receptors. Overall, the training involved the analysis

of 184 diluted samples obtained from 64 samples collected directly at the odour sources of the paper mill and at the external ones. During the monitoring, the IOMS performance was tested using 23 independent samples collected at sources and then diluted, for a total of 60 IOMS analyses.

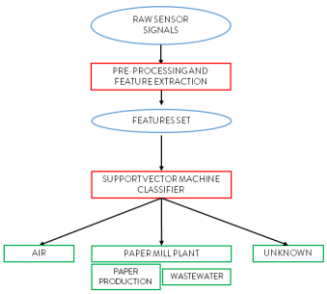

Fig. 1. Data analysis scheme.

Results

IOMS were installed for 3 months at the monitoring sites, located about 500 m NO (EOS 42) and SO (EOS 03) of the plant, respectively. They proved effective in detecting and recognizing odours from the plant (Tab. 1).

Tab. 1. IOMS classification performances: Accuracy - AC, Recall – RC, value (confidence interval 95%).

	EOS 03	EOS 42
AC	97% (88%-99%)	94% (81-99%)
RC_{Air}	100% (88-100%)	100% (75-100%)
RC_{WW}	100% (85-100%)	100% (83-100%)
$RC_{PP.}$	82% (75-90%)	80% (67-92%)
RC_{UN}	100% (66-100%)	100% (63-100%)

Monitoring data were processed as in Fig. 1 and odour impact was assessed as frequency of detection of different odour classes over the monitoring period (Fig. 3). For EOS03, it resulted higher than the 10% threshold suggested as reference for residential areas by guidelines [4]. This was further confirmed by citizens' reports collected during the monitoring. Given the high variability of emissions from some sections of the plant devoted to the processing of excess process WW, IOMS data were also correlated with information about production start and stop and filling levels of WW tanks. WW odours were frequently detected at receptors, even during plant shutdowns, and were mainly associated to the handling of wastewaters stored in emergency tanks, where undesired anaerobic reaction may occur, originating reduced sulphur compounds, which have very low odour threshold and unpleasant odour character. As an example, Fig. 4 illustrates the correlation between the WW tank filling levels, citizens' reports and H_2S concentration at the tank vent, which was proven for about 67% of odour events occurred during the monitoring. Based on such evidence, the project is still ongoing and currently focusing on the realization of an IOMS network at WW emissions sources aimed at investigating their variability and identifying critical operating conditions related to the odour events.

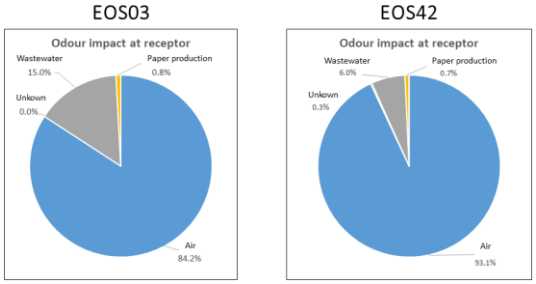

Fig. 3. Odour impact by IOMS at receptors.

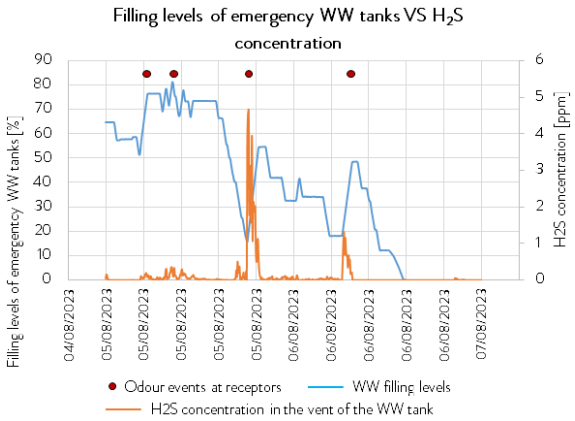

Fig. 4. Example of correlation between WW tank filling levels, citizens' reports and H_2S concentration at the vent.

Funding This paper has been conceived and produced within the MUSA – Multilayered Urban Sustainability Action – project. (ECS 000037)

References

[1] C. Bax, S. Sironi, L. Capelli, How Can Odors Be Measured? An Overview of Methods and Their Applications, *Atmosphere* 11, 92 (2020); doi:10.3390/atmos11010092

[2] L. Capelli, S. Sironi, R. Del Rosso, Electronic Noses for Environmental Monitoring Applications, *Sensors* 14, 19979-20007 (2014); doi:10.3390/s141119979

[3] G. Oliva, F. Cangialosi, M. Grimaldi, I. Fasolino, V. Belgiorno, V. Naddeo, T. Zarra, Urban odour annoyance management: An advanced embedded system for real-time monitoring enhanced by citizen science, *Case Studies in Chemical and Environmental Engineering* 9,100712 (2024); doi.10.1016/j.cscee.2024.100712

[4] E.P. and A. of the S. N.-W. Ministry of Environment, "Technical Instructions on Air Quality Control (TA Luft)," Berlin, (2021)

DOI 10.5162/EUROSENSORSXXXVI/OT5.129

Designing a Helically Twisted Photonic Crystal Fiber for Gas Sensing in the Terahertz Region

Hassan Pakarzadeh[1], *Hana Saberi*[1], *Jamileh Hajivandi*[2] *and Mohsen Keshavarzi*[3],
[1] *Department of Physics, Shiraz University of Technology, Shiraz, Iran*
[2] *Nanophotonics Research Laboratory, Department of Electrical and Electronics Engineering, TOBB University of Economics and Technology, Ankara 06560, Turkey*
[3]*Faculty of Physics, Shahid Bahonar University of Kerman, Kerman, Iran*
Corresponding Author's e-mail address: pakarzadeh@sutech.ac.ir

Summary:

A simple and practical structure of helically twisted photonic crystal fiber (PCF) with Topas material is designed for the first time. The core of the fiber is air which is the most transparent material for transmitting terahertz (THz) waves while its cladding is proposed with a single ring of air holes. A complete twist along the 50cm fiber shows five low loss transmission bands in the ranges of 0.44-0.62, 0.87-1.42, 1.4-2.04, 1.98-2.48 and 2.7-3.0 THz. The proposed helically twisted PCF sensor with maximum sensitivity of 3125 GHz/RIU is shown to have great applications for gas sensing in the THz region.

Keywords: helically twisted fiber, terahertz, photonic crystal, sensor.

Background, Motivation an Objective

Terahertz (THz) frequency range in the electromagnetic spectrum is mostly known as 0.1-10 THz. In this paper, a simple and practical structure of a twisted photonic crystal fiber (PCF) sensor made of Topas as a polymer material is proposed. The fiber core is air which is the most transparent material for propagating terahertz waves, and the cladding of fiber is proposed to be an air-hole ring in the background material of Topas with perfect circular symmetry [1]. The purpose of designing this twisted PCF sensor is to propose a simple yet efficient structure in the THz range [2]. We designed and simulated the desired sensor with a complete twist over 50cm of fiber length provided five low loss transmission bands in the ranges of 0.44-0.62, 0.87-1.42, 1.4-2.04, 1.98-2.48 and 2.7-3.0 THz for five gases with refractive index (RI) including n = 1, n = 1.02, n = 1.04, n = 1.06 and n = 1.08. Near-flat dispersion across the five transmission bands and the sensitivity of 3125 GHz/RIU over 1.88-2.33 THz are unique features of the proposed THz PCF sensor, which may play a key role for gas detection in the terahertz region.

Description of the New Method or System

The proposed twisted PCF for mode propagation in the THz range is shown in Fig. 1. The idea is to place the rings of the air cavity array on concentric circles. so that the position of each air cavity is obtained according to the following relationship:

$$x = \Lambda N cos\left(\frac{2N\pi}{6n}\right),$$
$$y = \Lambda N sin\left(\frac{2N\pi}{6n}\right),$$
$$n = 1 \sim 6 \quad (1)$$

where Λ and N represent the hole-to-hole distance (pitch) and the number of rings of the air hole array, respectively, and n is an integer from 1 to 6N. The thickness and internal diameter of each cell of the structure are equal to t and d, respectively [3].

Fig. 1(a) has only one ring of the air hole array with N = 2, where the inner rings associated with N = 0 and N = 1 have been removed. In this design, the values of Λ, t, and d are determined as 2.2, 0.2, and 2 mm, respectively; in which the diameter of the central core of the air is approximately 6.4 mm. Topas is used as the polymer material and the refractive index of air is considered to be 1 [4].

With different simulations, the results show that twisting the PCF (along the z-axis) can offer a more uniform core as well as a more suitable substrate for propagating symmetric modes. Therefore, as shown in Fig. 1(b), the proposed structure has a complete helical twist over 50 cm which is an optimized value in our simulation. Finite-difference time-domain (FDTD) technique has been used to obtain the mode characteristics [3].

Results and Discussion

As it can be seen in Fig. 2, the proposed fiber has the fundamental mode well confined in the core.

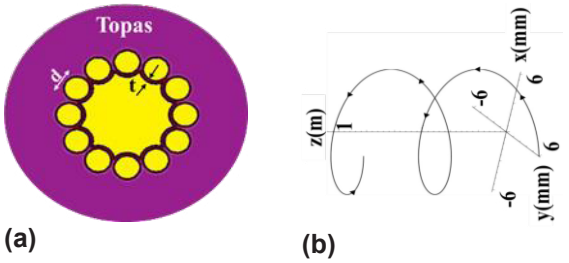

Fig. 1. The cross-section of the proposed twisted PCF; t shows the thickness of the polymer material between the core area and the air holes in the cladding and d shows the diameter of the air holes in the cladding. b) two full twists along 100cm fiber.

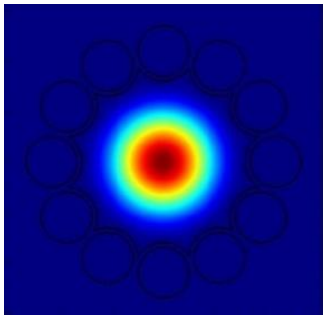

Fig. 2. The intensity profile of the fundamental mode confined in the core of the proposed twisted PCF.

Fig. 3. shows the loss spectrum of the helically twisted PCF when the holes are filled with air exhibiting five low-loss frequency bands from 0.44 to 3.0 THz.

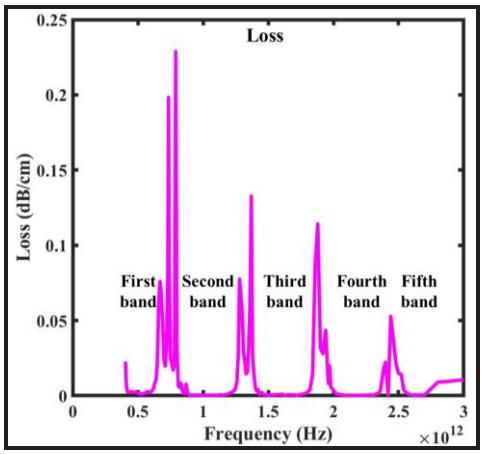

Fig. 3. Loss spectrum of the designed helically twisted PCF with five low-loss frequency bands.

Fig. 4. shows the sensitivity curves of the proposed sensor for five gases with RI of n = 1.0, n = 1.02, n = 1.04, n = 1.06 and n = 1.08 obtained using $S_f = \Delta f / \Delta n$ [5]. We have given the sensitivity values in Table 1.

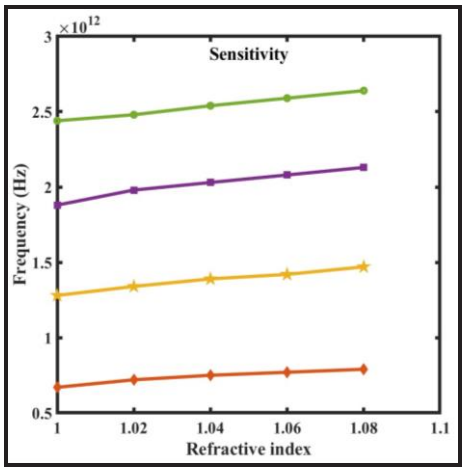

Fig. 4. Sensitivity curves calculated around four main peaks associated with Fig. 3.

Tab. 1: Sensitivities calculated around four frequency peaks.

Peak frequency range (THz)	Sensitivity (GHz/RIU)
0.67 – 0.79	1500
1.28 – 1.47	2375
1.88 – 2.13	3125
2.44 – 2.64	2500

References

[1] G. Gallot, S. Jamison, R. McGowan, and D. Grischkowsky, "Terahertz waveguides," *JOSA B,* (vol). **17**, pp. 851-863, (2000).

[2] Y.-H. Chen *et al.*, "Design fiber-to-waveguide coupling for photonic integrated circuits," in *Optical Interconnects XXIII*, (vol). **12427**: SPIE, pp. 71-74, (2023).

[3] V. Sharif and H. Pakarzadeh, "Terahertz hollow-core optical fibers for efficient transmission of orbital angular momentum modes," *Journal of Lightwave Technology,* (vol). **39**, pp. 4462-4468, (2021).

[4] B. Ung, A. Mazhorova, A. Dupuis, M. Rozé, and M. Skorobogatiy, "Polymer microstructured optical fibers for terahertz wave guiding," *Optics Express,* (vol). **19**, pp. B848-B861, (2011).

[5] J. Sultana *et al.*, "Hollow core inhibited coupled antiresonant terahertz fiber: A numerical and experimental study," *IEEE Transactions on Terahertz Science and Technology,* (vol). **11**, pp. 245-260, (2020).

DOI 10.5162/EUROSENSORSXXXVI/OT5.147

Cost-effective Indoor Air Quality Colorimetric CO_2 sensor.

Maria González-Gómez[1], Anna Zymohliad[1], Ismael Benito-Altamirano[1], Joan Daniel Prades[2], Olga Casals[1], and Cristian Fàbrega[1].

[1] Dept. of Electronics and Biomedical Enginering, University of Barcelona, Marti i Franques 1, Barcelona, Spain.

[2] Institute of Semiconductor Technology (IHT) and Laboratory for Emerging Nanometrology (LENA), Technische Universität Braunschweig, Hans-Sommer Str. 66, D-38106 Braunschweig, Germany

Corresponding Author's e-mail: cfabrega@ub.edu

Summary:

A colorimetry CO_2 ppm level sensor has been developed. Based on an optimized water-based ink, the sensor covers the range of 250 to 1500 ppm, is not affected by common indoor pollutants (NO_2, CO, CH_2O) and do not show signs of degradation after a week of operation. A calibration method has been proposed to dampen the effects of humidity on sensor prediction. Find out more at the conference.

Keywords: Colorimetry, CO_2, Indoors Air Quality, Optical sensor, Cost-effective

Background, Motivation an Objective.

Gaseous CO_2 real time determination has emerged as an imperative need after the current pandemic situation, particularly to monitoring indoor air quality. Over the past years, CO_2 was promoted as a proxy to other co-exhalated airborne microorganism. Indoor CO_2 levels are expected to remain around 400 parts per million (ppm), and no more than 700 ppm above that. Otherwise, a deficiency in fresh air circulation would be present, indicating potential poor air quality for the occupants around.

Sensors based on dye colorimetry are a potential resource for the development of compact cost-effective gas detectors. Colorimetry inks are inexpensive and easy integrate into commercial miniaturized colour readout systems [1], as well as smartphones [2]. To the best of our knowledge, state-of-the-art colorimetric sensors usually fail at measuring concentrations below 5000 ppm of CO_2 [3]. For example, A.Davey et al. developed an amine - ZIF-8 sensor exhibiting a colour shift at 700 ppm of CO_2 [4]; D. Zhao et al. managed to pick up signal from 280 to 1345 ppm but without reaching equilibrium, being impossible to link to a specific concentration [5] and R. Dansby-Sparks et al. achieved a limit of detection of 80 ppm but was not studied under real conditions (Relative humidity, gas interferents) [6].

In our work, we developed a water based colorimetric ink tunned to monitor CO_2 in the range of 250 to 1500 ppm. The ink formulation is based on an amine and a pH indicator. The detection of gaseous CO_2 is achieved by a nucleophilic attack on CO_2 by a primary amine to produce a shift in the acidity level of the ink, thus changing its color. The ink is printed and integrated into a commercial MAX30105 chip which encloses three LEDs and a photodetector. The transmitted and reflected light from the ink after CO_2 exposure is measured by the photodetector, which transduces it into a signal.

Results

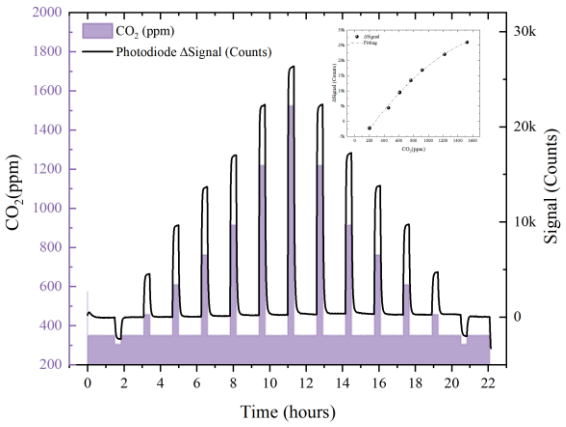

Fig. 1. Transient measurement signal at different CO_2 concentration and constant humidity (50%). Increment of signal vs CO_2 at insert.

The formulation of the ink was adjusted to maximize the detection of CO_2. We characterized the influence of the reagents in both, dry and moisture conditions (50% Relative Humidity; RH). With the adjusted formulation, our sensor was exposed to increments of CO_2 from 250 ppm to 1500 ppm (Figure 1.). The response shows a complete reversible behavior with a non-linear relationship with CO_2 concentration. The baseline exhibits no drift, demonstrating good stability over the 22-hours experiment. To characterize the interaction with humidity, we exposed our colorimetry sensor to 600 ppm

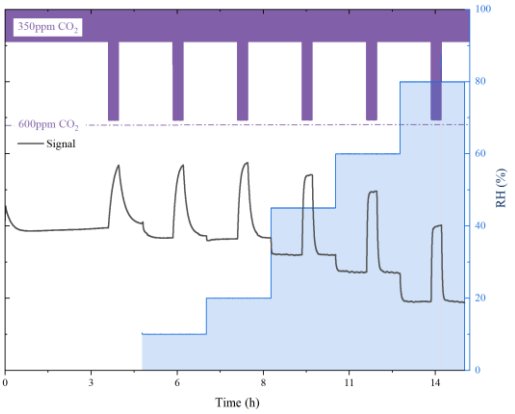

Fig. 2. Sensor signal to 600 ppm pulses of CO_2 under a scale up of humidity (0-80% RH) (Top). Detailed response and slope during CO_2 pulses (Below).

CO_2 pulses at different RH from 0 to 80% (Figure 2). We observed there was not important influence in the response of the sensor as the increment in signal remains close for all % RH. The shape of the pulse reveals that the velocity of the CO_2 – amine reaction is enhanced in presence of moisture. The baseline color is obviously affected by the humidity, but the response towards CO_2 is practically the same (Figure 2) . We decided to characterize this behavior by keeping constant a flow of 350 ppm and varying moisture from 0 to 70% RH (Figure 3). The signal decreased with the increasing amount of RH with a quadratic behavior. We associated a real time humidity sensor to damp its effect. To establish a calibration method, we exposed our CO_2 sensor, coupled to the humidity sensor, to a variety set of CO_2/humidity conditions. Figure 4 depicts the predicted CO_2 concentrations of our colorimetric sensor. The accuracy associated to each change does not exceed the 10%.

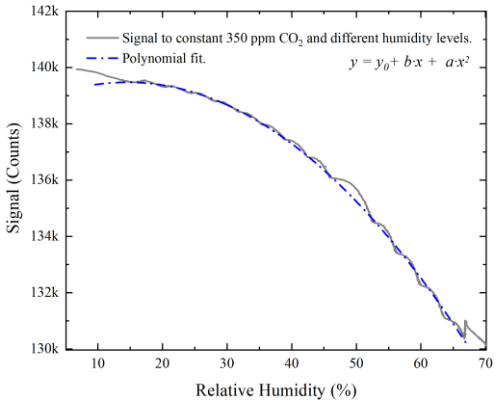

Fig. 3 Signal to constant 350 ppm CO_2 and different humidity levels.

Next, we studied the cross interference towards CO, CH_2O and NO_2, finding no signs of influences. Finally, we realized a 1-week experiment subjecting the sample to a constant flow of 350 ppm and 50% RH and periodic pulses that rise to the limit recommended by the authorities of 1200 ppm. The response remained

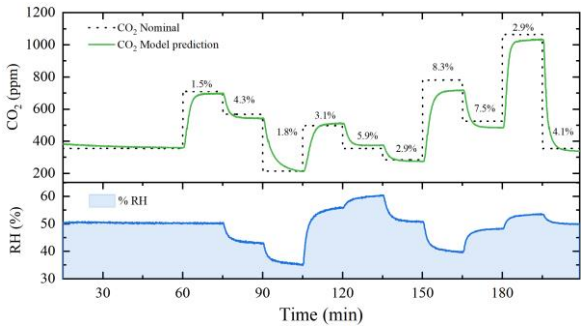

Fig. 4.CO_2 predicted by our colorimetry sensor under random humidity conditions.

practically constant throughout the seven days.

[1] C. Fàbrega et al., “Highly Specific and Wide Range NO<inf>2</inf>Sensor with Color Readout,” ACS Sensors, vol. 2, no. 11, 2017, doi: 10.1021/acssensors.7b00463.

[2] Benito-Altamirano, I.; Martínez-Carpena, D.; Casals, O.; Fábrega, C.; Waag, A.; Prades, J. D. Back-Compatible Color QR Codes for Colorimetric Applications. Pattern Recognit. 2023, 133, 108981. https://doi.org/10.1016/j.patcog.2022.108981

[3] Zhang, Y.; Lim, L. T. Inkjet-Printed CO2 Colorimetric Indicators. Talanta 2016, 161, 105–113. https://doi.org/10.1016/j.talanta.2016.08.014

[4] K. Davey et al., “Amine-functionalized metal-organic framework ZIF-8 toward colorimetric CO2 sensing in indoor air environment,” Sensors Actuators, B Chem., vol. 344, no. June, p. 130313, 2021, doi: 10.1016/j.snb.2021.130313.

[5] D. Zhao, D. Miller, X. Xian, F. Tsow, and E. S. Forzani, “A novel real-time carbon dioxide analyzer for health and environmental applications,” Sensors Actuators, B Chem., vol. 195, pp. 171–176, 2014, doi: 10.1016/j.snb.2013.12.11

[6] Dansby-Sparks, R. N.; Jin, J.; Mechery, S. J.; Sampathkumaran, U.; Owen, T. W.; Yu, B. D.; Goswami, K.; Hong, K.; Grant, J.; Xue, Z. L. Fluorescent-Dye-Doped Sol-Gel Sensor for Highly Sensitive Carbon Dioxide Gas Detection below Atmospheric Concentrations. Anal. Chem. 2010, 82 (2), 593–600. https://doi.org/10.1021/ac9018

DOI 10.5162/EUROSENSORSXXXVI/OT5.154

Gas Sensing Performance of CuO Sensors Functionalized with Different Stabilized Au-NP

Christian Maier[1], Larissa Egger[1], Anton Köck[1], Soeren Becker[2], Jan Steffen Niehaus[2], Klaus Reichmann[3]

[1] Materials Center Leoben Forschung GmbH, Roseggerstraße 12, 8700 Leoben, Austria
[2] Fraunhofer Center for Applied Nanotechnology CAN, Grindelallee 117, 20146 Hamburg, Germany
[3] Institute for Chemistry and Technology of Materials, TU Graz, Stremayrgasse 9, 8010 Graz, Austria

Correspondence: christian.maier@mcl.at; +43-3842-45922-550

Summary:

In this work, we present chemical nanosensors based on ultrathin CuO/Cu_2O films, which are fabricated by thermal evaporation and subsequent oxidation on SiN-based micro-hotplate chips. The sensors are tested against various target gases like carbon monoxide (CO), carbon dioxide (CO_2), and hydrocarbons (HC_{mix}). The CuO/Cu_2O films are functionalized with Au nanoparticles (Au-NPs) stabilized with different types of ligands: PEG-MUA, MPA and citrate. While the Au-NPs clearly increase the sensor performance in particular for CO_2, we have found that the ligands have a significant impact.

Keywords: metal oxide, CuO, nanomaterials, nanoparticles, ligands, gas sensors

Introduction

Chemical sensing of harmful or toxic gases, such as Volatile Organic Compounds (VOCs), CO_2, or CO, which have a significant negative impact on human health, has become a vital necessity for indoor and outdoor air quality (AQ) monitoring. Conductometric gas sensors rely on changes of the electrical conductance of a gas sensitive material due to the surrounding gas. Mostly, metal oxides like SnO_2, ZnO or CuO are used because of their high sensitivity to a large variety of gases [1]. The response of such sensors can be tailored by surface functionalization with metallic nanoparticles (e.g. Au, Pd, or Pt) which is a very promising approach to achieve a high degree of selectivity [2, 3]. Recently, we have successfully employed Au-NPs solutions for functionalization of CuO-based gas sensors for improved CO_2 sensing [4]. In this paper we evaluate the impact of three different types of ligands used for stabilizing the Au-NPs on the sensor performance for CO, CO_2, and HC_{mix}.

Sensor Fabrication

The gas sensors are fabricated by means of photolithography, thermal evaporation of a Cu-layer with a thickness of 500 nm, and a lift-off process on a micro-hotplate chip (see Fig.1). The circularly shaped (diameter 450 µm) Cu layer is thermally oxidized on a hotplate at 450 °C for 4 h leading to a stoichiometric mixed phase of CuO/Cu_2O-films.

Au-NP Functionalization

The Cu_xO gas sensing films have been functionalized with Au nanoparticles (average diameter 13 nm, synthesized by Fraunhofer CAN) to improve the sensor performance. The Au-NPs are dissolved in water and have been stabilized with three different types of ligands: (i) MPA (3-mercaptopropionic acid) (ii) citrate, and (iii) PEG-MUA (polyethylene glycol, 11-mercaptoundecanoic acid). The functionalization is performed by drop coating (0.2 µl) the Cu_xO-sensors with the NP solutions.

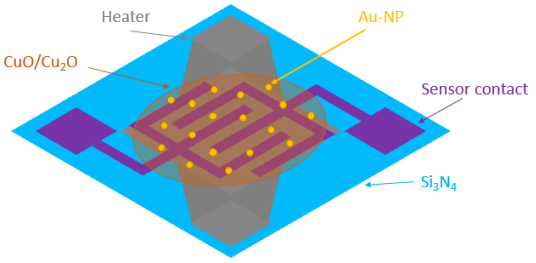

Fig. 1 Illustration of an Au-NP functionalized Cu_xO film-based gas sensor.

Sensor Characterization & Results

The sensor devices have been operated at 300 °C and tested against CO, CO_2 and HC_{mix} (equal mixture of 500 ppm of acetylene, ethane, ethene and propene). Synthetic air with 50 % relative humidity (r.h.) has been employed as

background gas. Bare Cu_xO-sensors, and Cu_xO sensors functionalized with MPA, citrate, and PEG-MUA stabilized Au-NPs have been compared. Fig.2 shows exemplarily the electrical resistance behavior of all sensors when exposed to 1000, 2000, and 4000 ppm CO_2.

Fig.3 compares the responses of all sensors towards 20 ppm CO, 4000 ppm CO_2 and 20 ppm HC_{mix}. The response to CO is slightly increased in case of citrate and PEG-MUA. Cu_xO sensor functionalized with citrate stabilized Au-NPs exhibits the highest response (39 %) towards CO_2. MPA stabilized Au-NP result in a significant response (10 %) to CO_2; the PEG-MUA stabilized Au-NP show a small (2 %) CO_2 response. Bare, unfunctionalized Cu_xO sensors have no CO_2 response at all. All Au-NP functionalized sensors exhibit a significantly increased response (18 – 22 %) towards HC_{mix}.

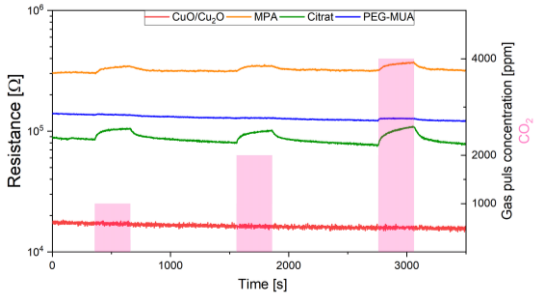

Fig. 2 Resistance measurement during exposure to 1000 / 2000 / 4000 ppm CO_2 at 300 °C operation temperature and 50% r.h.

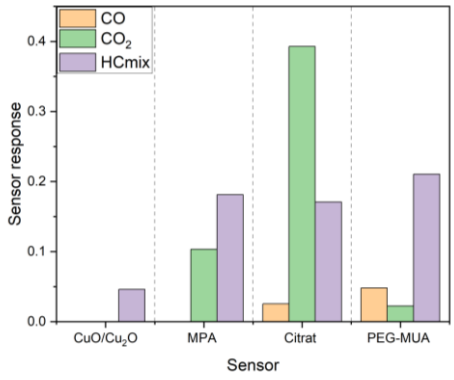

Fig. 3 Sensor response towards 20 ppm CO, 4000 ppm CO_2 and 20 ppm HC_{mix} at 300 °C operation temperature and 50% r.h.

Discussion & Conclusion

While the Au-NPs clearly increase the sensor performance in particular for CO_2, also the ligands have a significant impact. on the sensing behavior of Cu_xO-based sensors. For the test gas mixture HC_{mix} the response is almost the same for all three types of ligands, while the citrate stabilized Au-NPs are clearly the best choice for optimizing the CO_2 sensitivity.
The different influence of the ligands on the CO_2 and HC_{mix} reponse is not understood yet: Organic residuals due to insufficient thermal degradation of the ligands at 300 °C operation might be responsible for this behavior by hampering the interaction of gas molecules with the Au-NPs and the Cu_xO surface. We expect that citrate is already dissociated at 300 °C. This would explain the high response for CO_2 for the citrate stabilized Au-NPs, but not the equally increased response towards HC_{mix} for all three types of ligands. Further investigations e.g. carefully increasing the operating temperature without decomposing the Au-NPs are necessary to reveal the influence of the ligand chemistry. From our results we conclude that metallic NP-systems have to be very carefully designed in order to fully utilize the potential of NP-functionalization for performance optimization.

References

[1] M. V. Nikolic, V. Milovanovic, Z. Z. Vasiljevic, Z. Stamenkovic, Semiconductor Gas Sensors: Materials, Technology, Design, and Application. *Sensors* (Basel, Switzerland) 2020, 20 (22) https://doi.org/10.3390/s20226694.

[2] J. Guo, J. Zhang, H. Gong, D. Ju and B. Cao, Au nanoparticle-functionalized 3D SnO_2 microstructures for high performance gas sensor, *Sens. Actuators,* B, 2016, 226, 266–272 https://10.1016/j.snb.2015.11.140.

[3] F. Sosada-Ludwikowska, L. Reiner, L. Egger, E. Lackner, J. Krainer, R. Wimmer-Teubenbacher, V. Singh, S. Steinhauer, P. Grammatikopoulos, Anton Koeck, Adjusting surface coverage of Pt nanocatalyst decoration for selectivity control in CMOS-integrated SnO_2 thin film gas sensors", *Nanoscale Adv*., 2024, https://doi.org/10.1039/D3NA00552F

[4] R. Wimmer-Teubenbacher, F. Sosada-Ludwikowska, B. Travieso, S. Defregger, O. Tokmak, J. S. Niehaus, M. Deluca, A. Köck, CuO Thin Films Functionalized with Gold Nanoparticles for Conductometric Carbon Dioxide Gas Sensing, *Chemosensors* 2018, 6 (4), 56 https://doi.org/10.3390/chemosensors6040056.

Funding

The authors gratefully acknowledge the financial support under the scope of the COMET program within the K2 Center "Integrated Computational Material, Process and Product Engineering (IC-MPPE)" (Project No 886385). This program is supported by the Austrian Federal Ministries for Climate Action, Environment, Energy, Mobility, Innovation and Technology (BMK) and for Labour and Economy (BMAW), represented by the Austrian Research Promotion Agency (FFG), and the federal states of Styria, Upper Austria and Tyrol.

DOI 10.5162/EUROSENSORSXXXVI/OT5.156

Novel chemical sensor device enabled by simultaneous thermal-optical excitation

Florentyna Sosada-Ludwikowska[1], Larissa Egger[1], Anton Köck[1]
Olga Casals[2], Daniel J. Prades[2],
Clement Fleury[3], Ali Roshangias[3]
Andreas Tekautz[4], Michael Donnelly[4]
Alec Essati[5]
[1]Materials Center Leoben Forschung GmbH, Roseggerstraße 12, 8700 Leoben, Austria
[2] Universitat de Barcelona, Gran Via De Les Corts Catalanes 585, Barcelona 08007, Spain
[3] Silicon Austria Labs GmbH, Sandgasse 34, 8010 Graz, Austria
[4] UnravelTEC OG, Petersgasse 35, 8010 Graz, Austria
[5] SLOC GmbH, Messendorfgrund 30, 8042 Graz, Austria

Correspondence: anton.koeck@mcl.at

Summary:

We present a novel chemical sensor device based on ultrathin metal oxide films functionalized with metallic nanoparticles, which combines both thermal as well as optical excitation into a single system. This is achieved by a modular setup employing SiN-based micro-hotplate (µhp) chips, and LEDs, which are mounted opposite of the µhp chips. First results show that the sensor response is dramatically improved in case of optical excitation: Activation of SnO_2 sensors functionalized with Cu-nanoparticles by LEDs emitting at 270 nm results in a sensor response of 32% at room temperature towards 20 ppm HC_{mix} in synthetic air (50% rh). By combining this dual excitation mode, we open an entirely new parameter space for chemical sensors, which has not been explored yet.

Keywords: metal oxide, nanomaterials, nanoparticles, gas sensors, sensor array

Introduction

Chemical sensing of gaseous molecules has become a vital necessity for a huge variety of applications. Since people in Europe or US spend 90% of their time indoors, air quality (AQ) monitoring is of tremendous importance for private homes and offices, for vehicles and transportation. Air pollution is considered a “silent killer” causing an estimated 7 million premature deaths every year [1].

Despite extensive efforts, conductometric gas sensors enabling identification and quantification of a variety of different gases remain elusive due to major cross-sensitivity issues.

Using optical (light) instead of thermal activation (heat) of the gas sensitive materials is a very useful strategy to lower power consumption [2] of the sensor device. Moreover, photons can also supply the energy needed to exploit the surface ionization scheme [3], which opens an entirely new parameter space for chemical sensing.

Sensor Components

We are developing a novel sensor device, which combines thermal and optical activation of the gas sensitive nanomaterials into a single sensor system:

- SiN-based micro-hotplate (µhp) chips incorporating a heating structure (up to 500°C) and electrodes, are used as carriers for the sensing films. First, a negative lift-off resist mask is structured by photolithography. Then the chips are coated with 50 nm SnO_2 or CuO, using reactive magnetron sputtering. This is followed by a lift-off process to structure the sensing films into a circular shape (diameter 450 µm) and an annealing process at 400°C in dry synthetic air. Finally, the sensors are functionalized with Ag and Cu nanoparticles (NP) via magnetron sputter inert gas condensation. 4 sensors are mounted on a single Kyocera socket, 2 sockets with a total of 8 sensors are characterized simultaneously in the gas measurement setup.

- LED chips emitting at 8 different emission wavelengths (631, 589, 525, 467, 415, 385, 365, and 270 nm) are employed to screen the impact of optical excitation on the sensor response. Presently commercial LEDs are employed, which are mounted on a PCB in two groups of 4 LEDs opposite of 2 sensor sockets.

Sensor System

In a first (Gen1) approach, we employ a modular scheme, where the LED-PCBs are mounted opposite of the µhp chips (Fig.1). A group of 4 LEDs optically excites 4 sensor dies. This setup enables to systematically screen the influence of LED wavelength and LED intensity on the sensor response in an automated gas measurement setup. Synthetic air, with controlled relative humidity (rh), serves as the background gas. A variety of target gases can be introduced into the setup with well-defined concentrations.

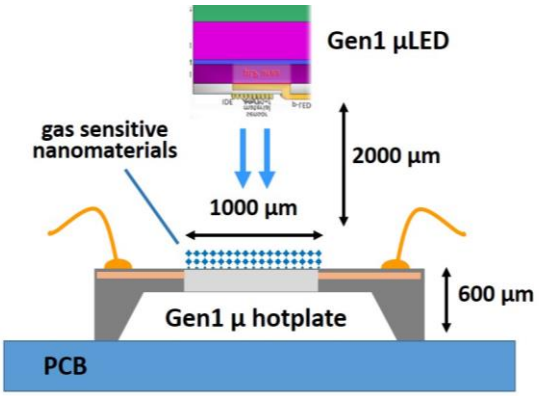

Fig.1 Modular setup of sensor system combining thermal and optical excitation schemes. This is achieved by using a SiN-based µhp chips, and LEDs, which are mounted above the µhp chips.

Results and Conclusion

All sensors are characterized simultaneously in the gas measurement setup. After 10 min in synthetic air, the target gas is introduced for 5 min followed by 10 min in synthetic air.

Fig.2 shows the resistance behaviour and the response of a SnO_2 sensor functionalized with Cu-NPs towards a concentration of 20 ppm of a hydrogen carbon gas mixture (acetylene, ethan, ethen, propen = HC_{mix}) in synthetic air (50% rh). Without LED illumination, at room temperature (RT) the sensor has no response at all, but shows a response of 17% at 150°C operation temperature (left). In case of LED illumination (wavelength 270 nm), the sensor exhibits a response of 32% already at RT (middle), which increases up to 58% at 150°C operation temperature (right). This clearly demonstrates the impact of LED illumination on the sensor response. This effect might be attributed to the surface ionization effect, where the gas molecules are ionized by the photons, and the electrons are transferred into the SnO_2 film.

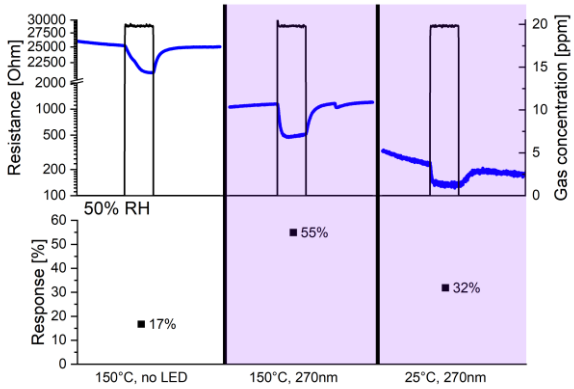

Fig.2 Response of SnO_2 sensor functionalized with Cu-NPs towards 20 ppm HC_{mix} in synthetic air (50% rh). With the LED switched off (left), the sensor shows a response of 17% at 150°C operation temperature. With a 270 nm LED switched on (middle), the sensor exhibits a response of 32% at RT (middle), which increases up to 58% at 150°C (right).

By combining this dual excitation mode – heat and light – into a modular sensor setup, we open an entirely new parameter space for chemical sensors. First results show that the sensor response is dramatically improved in case of optical excitation with LEDs. We will systematically explore this new parameter space to find the ideal combination of wavelength, light intensity, and operation temperature for selective detection of the target gases.

References

[1] World Health Organization (WHO) Factsheet on "Air quality and health" (2018), https://www.euro.who.int/__data/assets/pdf_file/0004/381919/fs-sdg-air-quality-health-eng.pdf (accessed 3/2022).

[2] O. Casals, N. Markiewicz, C. Fabrega, I. Gràcia, C. Cané, H. S. Wasisto, A. Waag, J. D. Prades, "A Parts Per Billion (ppb) Sensor for NO2 with Microwatt (µW) Power Requirements Based on Micro Light Plates", ACS Sens. 2019, 4, 4, 822–826, https://doi.org/10.1021/acssensors.9b00150),

[3] E. Comini, A. Cristalli, G. Faglia, G. Sberveglieri, "Light Enhanced Gas Sensing Properties of Indium Oxide and Tin Dioxide Sensors", Sensors and Actuators B: Chemical, 65, 260-263 (2000) DOI:10.1016/S0925-4005(99)00350-0.

Funding

The work has been performed within the project "Nano4E - Nano4E - Integrated thermo-optically activated Nanosensors for environmental monitoring", which receives funding from the Austrian Funding Agency FFG (project No: FO999899024).

DOI 10.5162/EUROSENSORSXXXVI/OT5.163

Facile synthesis of SnS_2 nanosheets via the combination of AACVD and APCVD methods for ppb-level NO_2 detection

Aladine Fdhila[1,2], Fatima Ezahra Annanouch[1], Zouhair Haddi[2], Eduard Llobet[1]
[1] Departament d'Enginyeria Electronica, Universitat Rovira i Virgili, Països Catalans 26, 43007 Tarragona, Spain,
[2] NVISION Systems and Technologies, Avenida de Barcelona 105, 08700 Igualada, Barcelona, Spain

Corresponding Author: eduard.llobet@urv.cat

Summary:

Tin disulfide (SnS_2) nanosheets, were successfully synthesized using the combination of aerosol assisted and atmospheric pressure chemical vapor deposition methods, (AACVD and APCVD). Morphological and compositional analysis demonstrated that this novel technique is suitable for producing high quality TMDs nanomaterials. By changing the sulfurization time (i.e. 30, 60 and 90 minutes), three different sensors, based on SnS_2 nanosheets, were fabricated and tested towards NO_2. The results showed that all the sensors were able to detect NO_2 at low operating temperature, while the highest response was recorded by sensor with 90 min of sulfurization.

Keywords: Gas sensors; SnS_2; TMDs; AACVD; APCVD; nanomaterials.

Background, Motivation an Objective

Two-dimensional (2D) materials, particularly transition metal dichalcogenides (TMDs), have attracted considerable interest due to their tunable bandgaps and exceptional electrical and optical characteristics. They offer a promising solution to common shortcomings (i.e., high operating temperature lack of selectivity) seen before in materials like carbon nanotubes, metal oxides, and graphene. Among TMDs, SnS_2 nanostructures exhibit ideal characteristics for gas sensing applications, including large surface area, rich in active reaction sites, high sensitivity to various gases, selectivity, stability, and reliability over prolonged use. However, SnS_2 synthesis faces some challenges. Various methods that have been used, such as hydrothermal synthesis and exfoliation techniques, have drawbacks like long reaction times, low yields, discontinuous films, environmentally unfriendly precursors and solvents etc. Herein, we introduce a novel way to successfully synthesize SnS_2 via the combination of AACVD and APCVD techniques. This approach allows us to directly deposit the TMDs on the sensor transducer, without the need of further transfer steps, improves the film quality and its long-term stability and resulted in highly sensitive and stable gas sensors.

Description of the New Method or System

The sensing films were directly grown on to alumina substrate, with Pt interdigitated electrodes in the front side and a Pt resistive heater in the back side.

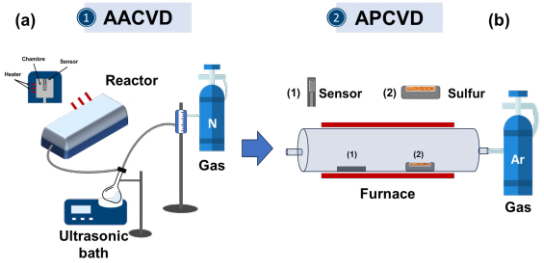

Fig. 1. (a) AACVD synthesis of SnO_2 nanostructures, and (b) APCVD synthesis of SnS_2 nanosheets.

Two steps of deposition were used to synthesize SnS_2: the first one (Fig.1 a), involved the direct growth of tin dioxide (SnO_2) nanostructures from the AACVD of 30 mg of tin(IV) chloride pentahydrate dissolved in 15 ml of acetone at temperature of 450ºC. Herein, 0.5 L/ min of nitrogen, was used as a carrier gas. In the second step, the obtained SnO_2 nanostructures were subjected to an APCVD sulfurization process with argon serving as a carrier gas and sulfur powder (Fig.1 b). This process allowed the sensitive layer to grow directly at the alumina sensor transducer.

Results

First, we investigated the morphology of the SnO_2 nanostructures, displayed in Fig. 2 a, then the morphology of the produced SnS_2 nanosheets which is shown in Fig. 2 b. As we

can see, SnS_2 nanosheets were successfully grown with a perfect hexagonal shape, on top of the alumina substrate, using a straightforward combination of AACVD and APCVD techniques. We examined our sample using Raman spectroscopy in order to verify the composition and structure of SnO_2 and SnS_2. The Raman spectrum of SnO_2 (Fig. 2 c) is characterized by the classical vibrational band (A_{1g}) observed at 631 cm^{-1} assigned to SnO_2 rutile structure. We also observed other peaks of 251 and 353 cm^{-1} which can be assigned to optical phonon modes of SnO_2 (E_u (LO) and E_u (TO)) [1]. Regarding the SnS2 spectrum (Fig. 2 d) , we can see a sharp peak at 314 cm^{-1} and a small one at 204 cm^{-1} which are assigned to the vibrational modes (A_{1g}) and (E_g) of SnS_2 respectively [2]. All the finding confirmed the ability of our novel technique to produce SnS_2 from the direct sulfurization of SnO_2 nanostructures.

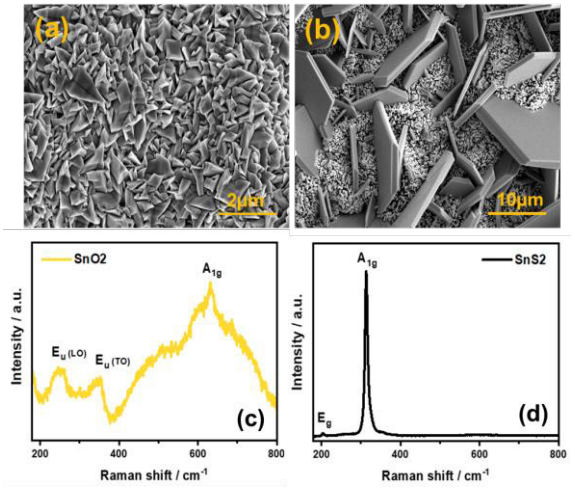

Fig. 2. FESEM images of (a) SnO2, (b) SnS2, and Raman spectra of (a) SnO2, (b) SnS2 nanostructures.

For gas sensing measurement, we fabricated three sensors with different sulfurization times (Sensor (A) 30 min; Sensor (B) 60 min; and Sensor (C) 90 min). The sensors were tested towards 500 ppb of NO_2, at different operating temperatures (RT, 50, 100, and 150ºC), in order to study its effect on the sensor responses. From Fig. 3, we can observe that the optimal working temperature, for all the sensors, was 150ºC, while the highest sensitivity was shown by sensors with 90 min of sulfurization. Besides, at room temperature, sensors (C) were able to detect the target gas at ppb-level, with enough sensitivity. Fig. 4 gives an example of the real sensor response as a function of time toward 500 ppb of NO_2 at 150ºC. All sensors exhibited a p-type semiconductor behavior, decreasing resistance upon exposure to oxidizing gas and increasing it upon exposure to dry air.

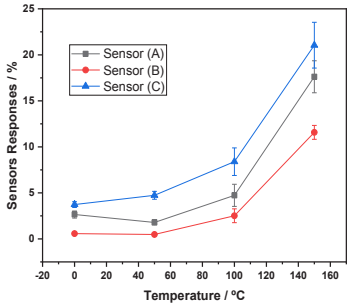

Fig. 3. Sensor responses toward 500 ppb of NO_2 as a function of temperature.

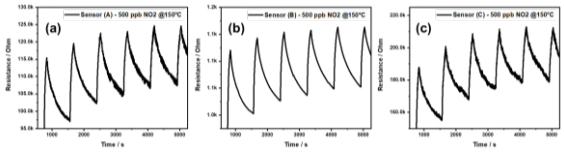

Fig. 4. Responses of SnS_2 gas sensors sulfurized for (a) 30min, (b) 60min, and (c) 90min, @150ºC toward 500 ppb of NO_2.

Fig. 5 depicts the sensors responses as a function of NO_2 concentration. From the graph, the sensors responses increased by increasing the gas concentration, showing a linear behavior, which is very important parameter for real gas sensing application.

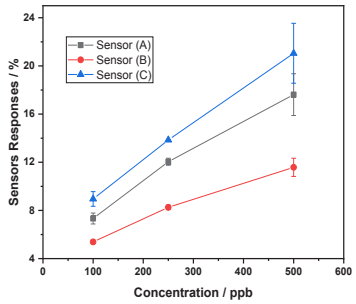

Fig. 5. Sensor responses toward NO2 @ 150 ºC as a function of concentration.

Conclusions

This work reported a facile and scalable technique, to synthesize highly sensitive 2D hexagonal SnS_2 nanosheets, directly onto the sensor transducer, for the detection of ppb-level of NO_2 at low operating temperature. Details on humidity cross-reactivity will be shown at the conference.

References

[1] T. Ahmad, M. Z. Ansari, Enhancement of infrared shielding property of SnO2 using Sb as a dopant, Materials Research Express 10, 105902 (2022); doi: 10.1088/2053-1591/ac9778

[2] Y. Ren, Q. Shi, G. Zhang, Lithium Storage Properties of TiC-Modified SnS2 Nanosheets, *ChemElectroChem* 6, e202101567 (2022); doi: 10.1002/celc.202101567.

DOI 10.5162/EUROSENSORSXXXVI/OT5.180

Development and Optimization of SPRI-based Electronic Nose for Highly Selective Detection of Volatile Organic Compounds

Vanessa Escobar[1,2], Arnaud Buhot[1], Natale Scaramozzino[2], Yanxia Hou[1]*
[1] Grenoble Alpes University, CEA, CNRS, Grenoble INP, IRIG-SyMMES, 17 Rue des Martyrs, 38000 Grenoble, France,
[2] Grenoble Alpes University, CNRS, LIPhy, 38000 Grenoble, France

Yanxia.hou-broutin@cea.fr

Summary:
The development of an instrument capable of performing at a level comparable to that of the biological nose remains a scientific challenge. In the present work, we have developed and optimized a multiplexed Surface Plasmon Resonance Imaging (SPRI)-based optoelectronic nose coupled to a microarray of novel sensing materials for the sensitive and selective detection of Volatile Organic Compounds (VOCs) in the gas phase. Using pattern recognition algorithms our system is able to discriminate VOCs belonging to different chemical families, as well as VOCs differing by a single carbon.

Keywords: electronic nose, peptide, Surface Plasmon Resonance Imaging, VOCs.

Introduction

The development of an instrument capable of imitating the remarkable capabilities of biological olfaction remains a scientific challenge. However, there is a growing need to reliably detect and monitor volatile organic compounds (VOCs) – the small air-borne molecules responsible for the odor of objects – in various fields, such as quality control for food and cosmetic industries, medical diagnostics and environmental monitoring.

Although sensitive and reliable, classical analytical techniques, such as Gas Chromatography coupled with Mass Spectrometry (GC-MS), require specialized personnel and are incompatible with on-field applications. Alternatively, electronic noses (eNs) refer to a class of multisensors designed for the detection of VOCs in the gas phase, drawing inspiration from biological olfaction. These aim to provide rapid, reliable and inexpensive analyses. Although considerable progress has been made, the performance of the biological nose has not yet been achieved by eNs.

In biological olfaction VOCs are detected by olfactory receptors (ORs) in the nose acting in a combinatorial manner, where one VOC can stimulate multiple ORs and vice versa. This allows the recognition of an amount of VOCs various orders of magnitude higher than the number of receptors in the nose.

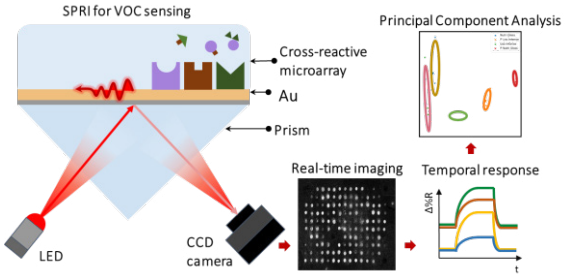

Fig. 1. Working principle of the SPRI-based opto-eN.

Since 2012 our team has been developing an electronic nose based on peptides, coupled with surface plasmon resonance imaging (SPRI), a multiplexed, label-free and real-time transduction technique (Fig. 1) [1]. Herein, a homemade system was designed for the detection in gas phase. Its operating principle, similar to that of the biological nose, consists of an array of cross-reactive peptides whose interactions are imaged by SPRI before using advanced mathematical methods for sample differentiation and identification. Great efforts have been made to optimize multiple optical parameters on the SPR response, resulting in a stable system that can be reused for at least three months with good repeatability.

Materials and Methods

Biochip preparation. The microarray was composed of a gold-coated commercial prism (Edmund Optics, U.S.). Before use, the surface was treated with plasma (Diener electronic,

Germany) for 3 minutes to eliminate organic contaminants. All sensing materials were deposited in quadruplicates on the gold surface using a non-contact microspotting robot (Scienion AG, Germany).

Sensing Materials. 19 short peptides were designed to have diverse physicochemical characteristics (positively or negatively charged, hydrophobic, hydrophilic, etc.) to obtain a differential response to VOCs. Additionally, an internal negative control (NC) that is known to not be sensitive to VOCs was added. All sensing materials include a cysteine at one end for their immobilization. For confidentiality reasons, exact sequences are not herein disclosed.

VOC Testing. A homemade fluidic bench was used to perform four-minute injections of VOCs of different chemical families. In each case, 50 µL of VOC were mixed into 1.5 mL of mineral oil (Sigma Aldrich) to promote controlled gradual evaporation and avoid system saturation.

SPRI. The SPRI system is set-up in the Kretschmann configuration, where the whole microarray is irradiated through the prism with a polarized beam. When the incident light is totally reflected, an evanescent wave is created on the ad-layer between the prism and the sensing medium. Surface Plasmon Resonance occurs under certain energy conditions when the evanescent wave resonates with the metal's free electron plasma. Thus, binding events in the sensors result in variations in the reflectivity (Δ%R), which are captured by a CCD camera. These images are then analyzed to obtain kinetic binding curves, called sensorgrams. After each injection, the microarray is regenerated using purified dry air. Afterwards, the average reflectivity of sensing molecules' replicates at the equilibrium is plotted, generating a distinct pattern for each VOC tested. Finally, principal component analysis (PCA) can be performed for VOC classification.

Results

Our system's versatility allows us to analyze many different VOCs. Figure 2 shows the sensorgrams obtained for VOCs of different chemical families, as well as their distinct equilibrium pattern. Additionally, the PCA in Fig. 2 E) clearly shows that our system is able to differentiate VOCs of different chemical families.

Great efforts have been made for the optimization of the system [2], including of the light source's wavelength, prism configuration and the immobilization of sensing biomolecules. Additionally, a passivation step to reduce the drift, poisoning and aging effects, the controlled and reproducible injection of VOCs into the analysis chamber, and the nature of sensing biomolecules for the greater sensitivity and selectivity of the system [3], [4].

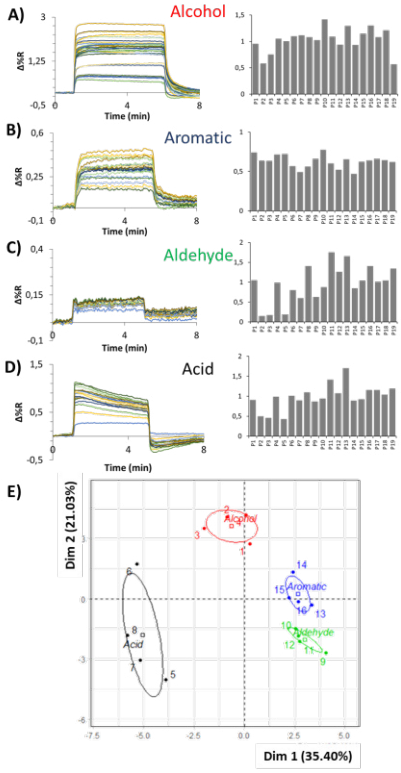

Fig. 2. Sensorgrams (%R versus time) and equilibrium patterns obtained for 50µL of A) 1-Hexanol, B) Toluene, C)Hexanal, D) Hexanoic acid; E) PCA for the four aforementioned VOCs belonging to different chemical families.

Comparing to existing eNs, our system has very good sensitivity, selectivity and stability, with performances getting closer to that of the human nose.

References

[1] S. Brenet *et al.*, Highly-Selective Optoelectronic Nose Based on Surface Plasmon Resonance Imaging for Sensing Volatile Organic Compounds, *Anal. Chem.* 90, 9879–9887, (2018); doi: 10.1021/acs.analchem.8b02036.

[2] J. S. Weerakkody, *et al.,* Optical Index Prism Sensitivity of Surface Plasmon Resonance Imaging in Gas Phase: Experiment versus Theory, *J. Phys. Chem. C*, 124, 3756–3767 (2020); doi: 10.1021/acs.jpcc.9b09973.

[3] J. S. Weerakkody *et al.*, Surfactant-like Peptide Self-Assembled into Hybrid Nanostructures for Electronic Nose Applications, *ACS Nano* 16, 4444–4457 (2022); doi: 10.1021/acsnano.1c10734.

[4] S. Gaggiotti *et al.*, Development of an optoelectronic nose based on surface plasmon resonance imaging with peptide and hairpin DNA for sensing volatile organic compounds, *Sensors and Actuators B: Chemical* 303,127188, (2020), doi: 10.1016/j.snb.2019.127188.

DOI 10.5162/EUROSENSORSXXXVI/OT5.187

Development of a Photoacoustic Cell for Volatile Organic Compounds (VOCs) Detection

Mh. S. Moussa[1], R. Viard[2], J-F Lampin[1], V. Maurice[1], C. Ghouila-Houri[1], Sophie Eliet[1], A. Mazzamurro[1], O. Bou Matar[1], P. Pernod[1], A. Talbi[1]

[1] Centrale Lille institute, Univ. Lille, CNRS, Univ. Polytechnique Hauts-de-France, UMR 8520 IEMN, F-59000 Lille, France.

[2] Groupe Endress+Hauser, Fribourg-en-Brisgau, Allemagne.

Corresponding Author's e-mail address: mohand.moussa@centralelille.fr

Summary:

In this paper, we report the development and use of a photoacoustic cell designed for gas spectroscopy of volatile organic compounds (VOCs) used as biomarkers of breast cancer. The cell, composed of a PMMA Helmholtz resonator grafted to a finite size tube. A commercial microphone mounted on the Helmholtz enables the measurement of the system response at its resonance frequency. The system was successfully characterized using different concentrations of isopropanol (0.5 to 17 ppm) using tunable MIRCAT QCL laser with wavelength range of 8-11µm.

Keywords: Photoacoustic, gas spectroscopy, breast cancer biomarkers, volatile organic compounds.

Introduction

In the context of non-invasive medicine, volatile organic compounds (VOCs) can be used as biomarkers in various clinical applications, such as early detection of breast cancer, monitoring treatment efficacy, and detecting recurrences. These are created by human body cells when subjected to oxidative stress [1], then transformed by an enzyme, Cytochrome P-450 [2], which regulates the levels of chemical species in the human body. These VOCs can be found within the cells themselves and transmitted via the bloodstream to breath, sweat, urine, feces, saliva, etc. [3],[4].

Kure et al. published a study in 2021 [5] proposing a prediction model for breast cancer using only Isopropanol and 2-butanone as biomarkers with an efficacy rate of 90%. In this study, analysis was conducted on urine using mass spectrometry and gas chromatography. A healthy individual typically has an isopropanol level between 1 and 20 ppb, while a person with cancer has a concentration ranging from 10 to 100 ppb [6].

Experimental materials

In this study, we report the development and use of a photoacoustic cell entirely made of plexiglas (PMMA), see figure 1.b, for gas spectroscopy. The first design step focuses mainly on the design of high-performance photoacoustic cells. Isopropanol was the targeted gas for our analysis. A commercial microphone (TDK membrane microphone) was used in this study. The laser used is a MIRCAT QCL from Daylight solution laser emitting in the far-infrared [7], which is in the range of one of the absorption peaks of isopropanol at 8.73 µm (1144.47 cm^{-1}). Laser modulation is achieved using a mechanical chopper. The frequency of modulation is chosen close to the acoustic cavity resonance frequency. The acoustic cavity is composed of a Helmholtz resonator grafted to a finite size tube outside a pressure node as shown in Figure 1.a (COMSOL Multiphysics simulation).

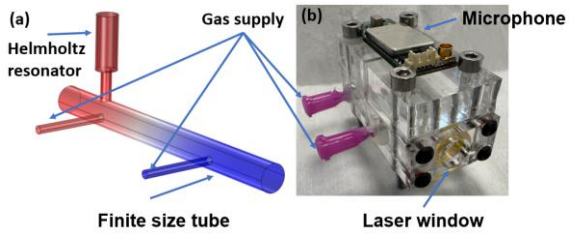

Fig. 1. Schematic of the photoacoustic cell and the pressure field at its resonance frequency (a). Picture of the Photoacoustic cell (b).

Results

Figure 2 shown the schematic of the experimental setup of measurements, composed of the acoustic cavity, QCL tunable laser, chopper for laser beam modulation and high resolution

acquisition systeme. Figure 3 display the results for the measured signal at different concentrations of isopropanol. Accurate acquisition system is used for this purpose (200kHz sampling frequency with 24bits resolution). The root square of the PSD is plotted in linear scale showing high SNR. In pure air the level of the signal is extremely low, we also test the excitation at different laser wavelength showing a good agreement with isopropanol absorption spectrum (result not shone here). The linearity of the system was evaluated and the results is shown figure 4.b. The sensitivity is estimated to be around 50mV/ppm. According to this preliminary results, resolution close to few ppb can be achieved with this design. Ongoing works on the design optimization are very promising.

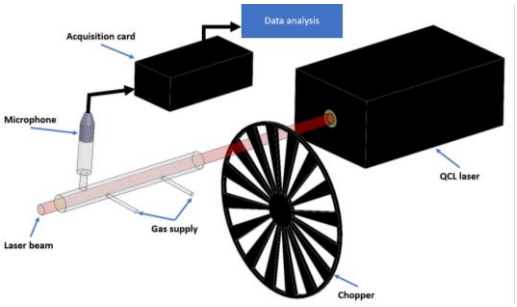

Fig. 2. Schematic of the experimental setup.

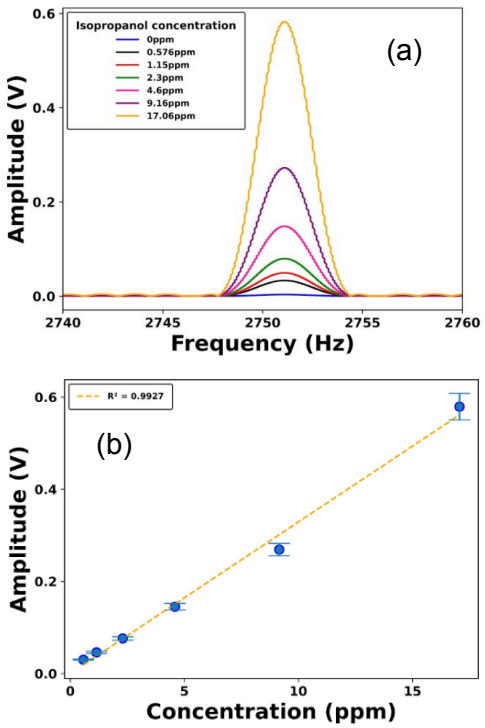

Fig. 3. Photoacoustic signal for different concentration of isopropanol (a). Linearity between the amplitude's signal and the concentration of isopropanol (b).

References

[1] A. Jezierska-Drutel et al., « Role of oxidative stress and the microenvironment in breast cancer development and progression », Adv. Cancer Res., vol. 119, p. 107-125, 2013, doi: 10.1016/B978-0-12-407190-2.00003-4.

[2] F. P. Guengerich et al., « Role of human cytochrome P-450 IIE1 in the oxidation of many low molecular weight cancer suspects », Chem. Res. Toxicol., vol. 4, no 2, Art. no 2, mars 1991, doi: 10.1021/tx00020a008.

[3] A. Amann et al., « The human volatilome: volatile organic compounds (VOCs) in exhaled breath, skin emanations, urine, feces and saliva », J. Breath Res., vol. 8, no 3, Art. no 3, juin 2014, doi: 10.1088/1752-7155/8/3/034001.

[4] Y. Y. Broza et al., « Hybrid volatolomics and disease detection », Angew. Chem. Int. Ed Engl., vol. 54, no 38, Art. no 38, sept. 2015, doi: 10.1002/anie.201500153.

[5] S. Kure et al., « A prediction model using 2-propanol and 2-butanone in urine distinguishes breast cancer », Sci. Rep., vol. 11, p. 19801, oct. 2021, doi: 10.1038/s41598-021-99396-5.

[6] Y. Adiguzel et al., « Breath sensors for lung cancer diagnosis », Biosens. Bioelectron., vol. 65, p. 121-138, mars 2015, doi: 10.1016/j.bios.2014.10.023.

[7] « MIRcatTM Mid-IR Laser: Tune 1000 cm-1 at 1000s cm-1/s | High-Speed Tuning », Daylight Solutions. https://www.daylightsolutions.com/products/mircat/

DOI 10.5162/EUROSENSORSXXXVI/OT5.189

Are Powder Aerosol-Deposited Films Appropriate for Chemiresistive NO_x Gas Dosimeters?

Daniela Schönauer-Kamin[1], Mario Linz[1], Marc Schmitz[1], Ralf Moos[1]
[1]Department of Functional Materials, University of Bayreuth, 95440 Bayreuth, Germany

functional.materials@uni-bayreuth.de

Summary:
Resistive gas dosimeters based on NO_x storage materials as functional films accurately measure timely intervals like hourly mean values of small gas concentrations like NO_2 in ambient air. The gas dosimeter principle overcomes the disadvantageously low recovery times of conventional chemiresistive sensors. Typically, porous screen-printed films are used as functional films, but for detection of very low NO_x (NO_2 and/or NO) doses, almost dense powder aerosol-deposited films are investigated and there appropriacy will be demonstrated here.

Keywords: air quality monitoring; NO_x; nitrogen oxides; powder aerosol deposition; ppb detection

Background

The determination of hourly mean values, e.g. for air quality or workplace limit monitoring, requires a timely integration of the sensor signal of conventional chemiresistive gas sensors over one hour. Often, inaccuracies and long sensor recovery times might lead to large errors. In contrast, the gas dosimeter directly measures the dose or hourly mean value of a gas species since its sensor signal is proportional to the exposed analyte amount (the dose) [1].

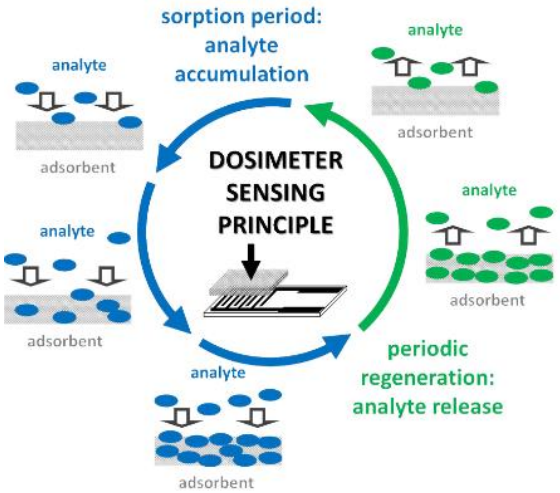

Fig. 1. Scheme of the dosimeter principle and the processes that occur in a resistive gas dosimeter during one operation cycle consisting of a long measurement (sorption) phase and a very short thermal regeneration phase (desorption). From [1], permitted by the authors.

Measuring Principle of NO_x-Dosimeter

A typical gas dosimeter consists of an alumina substrate equipped with a screen-printed platinum heating element on the backside and interdigital electrodes (IDEs). The IDE is covered by a screen-printed film (film thickness around 10 µm) of the functional material, here a NO_x storage material based on potassium and manganese impregnated on alumina powder (K/Mn-Al_2O_3). The relative resistance change, $\Delta R/R_0$, measured using impedance spectroscopy at a fixed frequency value is evaluated as the sensing signal. The optimal working temperature during sorption period is between 300 - 350 °C. In the sorption phase (Fig. 1), NO_x is sorbed in the NO_x storage material and the sensor signal changes linearly with increasing sorption time of a constant NO_x concentration. During NO_x absence, the sensor signal remains constant and is proportional to the previously dosed amount of NO_x. Additionally, the time-derivative of $\Delta R/R_0$ corresponds to the current NO_x concentration. After a certain time, the NO_x storage material is fully loaded, and a thermal initiated regeneration at 650 °C is necessary to desorb the sorbed molecules. Afterwards, a new detection cycle starts. [1]

Discontinuous Powder Aerosol Deposition

To improve the resolution limit for detection of very low NO_x concentrations in the sub-ppm range and the resulting low NO_x doses, the dosimeter properties of films prepared by discontinuous powder aerosol deposition DPAD are investigated. With DPAD, dense ceramic films can be produced at room temperature

directly from the synthesized ceramic powder. [2] Here, the resulting thicknesses of the K/Mn-Al_2O_3 films are in the range of 200 - 300 nm.

Results

The sensor signal $\Delta R/R_0$ of a porous screen-printed K/Mn-Al_2O_3 film (thickness 10 µm) at 300 °C in synthetic air atmosphere shows typical dosimeter behavior (Fig. 2). $\Delta R/R_0$ increases during exposure to NO_2 at ppb level (pulses of 50 - 300 ppb) and remains constant during dosing pauses. The dosimeter signal follows directly the timely-integrated NO_2 concentration and directly detects the total dose of NO_2. A linear relationship between $\Delta R/R_0$ and dose of NO_2 follows. Additionally, the current NO_2 concentration can be determined by the time-derivative of $\Delta R/R_0$ (Fig. 3). $d(\Delta R/R_0)/dt$ correlates to the current concentration and increases linearly with increasing NO_2 concentration.

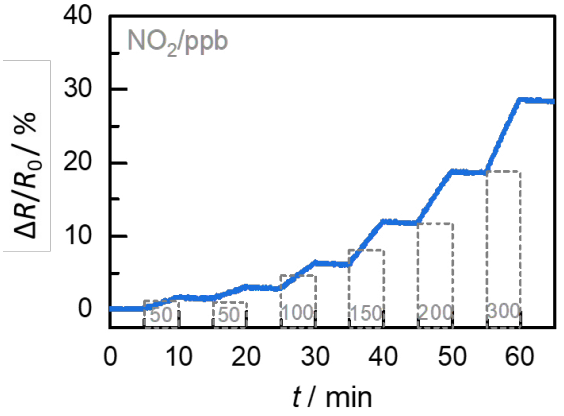

Fig. 2. Relative resistance change $\Delta R/R_0$ of a typical gas dosimeter at 300 °C during exposure to NO_2 (50 - 300 ppb) directly proportional to the integrated NO_2 concentration or total dose of NO_2

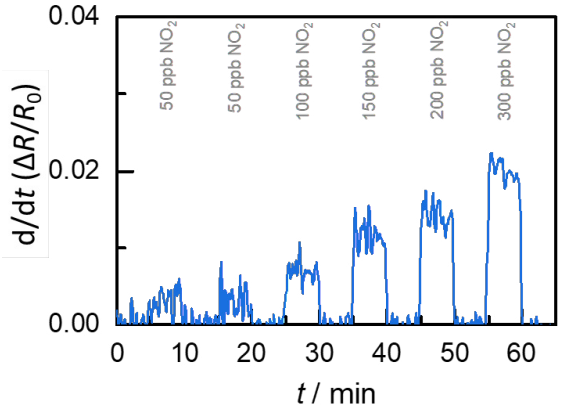

Fig. 3. Timely derivative $d(\Delta R/R_0)/dt$ of the dosimeter signal correlating with the current NO_2 concentration

The results demonstrate the advantages of a NO_x dosimeter like very fast recovery times, but also show the detection limit at very low NO_x concentrations (below 50 ppb) and small NO_x doses, especially directly at the beginning of the sorption period. The investigation of dense and thinner PAD films as functional film for the NO_x dosimeter provides advantages over thicker screen-printed porous films, shown in Fig. 4.

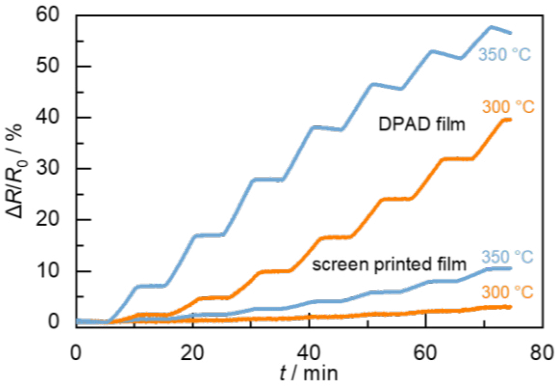

Fig. 4. Comparison of the dosimeter signal $\Delta R/R_0$ of a screen-printed film and a powder aerosol-deposited film during exposure to pulses of 100 ppb NO at 300 and 350 °C.

$\Delta R/R_0$ during exposure to seven pulses of 100 ppb NO was determined at 300 and 350 °C for a DPAD film and a screen-printed film (both prepared from the same starting powder, K/Mn-Al_2O_3). It is clearly recognizable that the DPAD film provides a higher sensor signal than the screen-printed layer. In particular, the first NO pulse can also be resolved quite well whereas it is almost impossible to detect it with the screen-printed film. The DPAD layer shows very good dosimeter behavior up to approx. 40 - 50 minutes. Afterwards, desorption effects become apparent, i.e. the sensor signal decreases during NO_x dosing pauses, and the thermal regeneration phase is necessary. In contrast, the screen-printed film still shows a smaller sensor signal, but no desorption effects are visible.

It is possible to detect low ppb-NO_x concentrations with a dense and thin DPAD film, but the regeneration must be started earlier than with the screen-printed film. With the thicker and porous screen-printed film, it is more difficult to detect lowest NO_x concentrations, but the sorption phase is significantly longer. Therefore, it is possible to detect higher NO_x doses or over a longer time without regeneration.

References

[1] I. Marr, A. Groß, R. Moos, Overview on Conductometric Solid-State Gas Dosimeters, *J. Sens. Sens. Syst.*, 3, 29–46 (2014); doi:10.5194/jsss-3-29-2014

[2] M. Linz, J. Exner, J. Kita, F. Bühner, M. Seipenbusch, R. Moos, Discontinuous Powder Aerosol Deposition: An Approach to Prepare Films Using Smallest Powder Quantities, *Coatings* 11, 844 (2021); doi: 10.3390/coatings11070844

DOI 10.5162/EUROSENSORSXXXVI/OT5.190

Monitoring of VOC Emissions in Berries During the Spoiling Process

Luigi Masi[1], Dennis Arendes[1], Johannes Amann[1], Andreas Schütze[1], Christian Bur[1]
[1]Lab for Measurement Technology, Saarland University, 66123 Saarbrücken, Germany

Corresponding Author's e-mail address: l.masi@lmt.uni-saarland.de

Summary:
Commercially available metal oxide semiconductor gas sensors have been used to investigate the substances emitted by raspberries. A calibration on the gas sensors was performed trough random gas mixtures made up with wide concentration ranges of 11 substances which compose air and are emitted by food. After, the sensors and different amounts of raspberries have been placed in different food boxes for several days. Estimates based on data were able to track the emissions' change of some volatile organic compounds, e.g. ethanol and acetaldehyde, during the spoiling process.

Keywords: MOS sensors, calibration, spoilage process, food, VOC

Introduction

About one-third of the world's food production is wasted. The first step towards implementing effective strategies to prevent and reduce food waste is to fully understand the amount and the quality of wasted food that is generated. This awareness is crucial to reveal the opportunities for reusing wasted food in a circular economy context, where waste can be transformed into valuable resources [1].
For the assessment of food' state, metal oxide semiconductor (MOS) gas sensors emerge as promising candidates due to their cost-effectiveness and ability to provide real-time measurements on site. Moreover, the employment of temperature cycled operations on these sensors leads into a greater selectivity in detecting various types of gases and expanding the quantitative ranges of detectable substances [2]. In previous works, the sensitivity of commercially available MOS sensors to gas emitted by food has been shown [3]. In this work, the sensors are employed to define chemical states, expressed as volatile organic compounds (VOC) emissions' changes, of raspberries over the spoiling process.

Materials and Methods

Different amounts of raspberries along with MOS sensors have been placed inside several closed food boxes for five days in a room temperature-controlled set at 23 °C, allowing the sampling of the headspace of the VOC of each box individually.
To assess the type of gases involved and their respective ranges' quantities, a calibration of the sensors was performed before the study of the raspberries: the sensors were calibrated with a custom-built gas mixing apparatus (GMA), described in detail in [4]; it was performed with unique random gas mixtures made up with different quantities of eleven different substances which compose air and are emitted by food (selected based on literature studies of the typical gases emitted by raspberries [5]), cf. Tab. 1 for the comprehensive list. The gas mixtures were created with random values of each gas belonging to pre-selected ranges given in table 1. Over 150 unique mixtures, each of which was 25 minutes long, were considered.

Tab. 1: Table of the considered substances and respective ranges for the random gas mixtures.

Gas / Range	Minimum	Maximum
CO	100 ppb	2000 ppb
H_2	500 ppb	2000 ppb
R.h. at 23 °C	25%	70%
1-Propanol	25 ppb	2500 ppb
Acetone	10 ppb	1000 ppb
Acetaldehyde	10 ppb	2500 ppb
Ethyl acetate	10 ppb	1000 ppb
Ethanol	25 ppb	2500 ppb
Ethylene	10 ppb	1000 ppb
Limonene	10 ppb	500 ppb
Methanol	25 ppb	2500 ppb

The selected sensors are commercially available metal oxide semiconductors, e.g., SGP40 (Sensirion AG, Stäfa, Switzerland). The MOS sensors were run in a temperature cycled operation (TCO) which comprises 12 temperature jumps from high to low temperature in the range 100 °C to 400 °C. The total length of each cycle was of 144 s.
A feature extraction was performed: the cycles were divided into 144 equidistant segments of 1 s. For each segment, mean and slope are calculated resulting in 288 features for each gas-sensitive layer of the considered sensors. A partial least square regression (PLSR) model was calculated based on the feature extraction followed by a dimensionality reduction performed trough a principal component analysis. The root mean squared error (RMSE) of 10-fold group based cross-validation, equal to 235 ppb, was considered to build up the regression model. 20% was withheld for testing the trained model.

Results and discussion

Fig. 1 shows the regression plot for ethanol of the lab calibration of one of the SGP40. A hold out test was performed resulting in an RMSE value of 223.9 ppb. Fig 2 shows the models' estimates from the sensors over the five days acquisition of the boxes containing 0, 24 and 101 grams of raspberries. A variation of the ethanol concentration can be observed over each cycle that run on the sensor. Even though the absolute concentration has to be verified, the trend provided by the model reflects the observed behavior of the raspberries during the spoiling process: by the end of the first day of monitoring, the sensor had adapted to the air of the environment and recorded a gradual increase of ethanol, emitted by the raspberries during the final ripening stage; by the second day, there was evidence of mold development on some samples, evidenced by a decrease of the concentration; between the third and the final day, all samples showed signs of mold, with those that developed mold first gradually changing the color of their mold from white to green, which explains the change in trend observed in the concentration curve.
Current analysis of other models of MOS sensors and other gases included in the lab calibration is being carried out to define a more comprehensive and complete chemical profiling over the different states of the spoiling process.

Acknowledgements

The project is funded by the EU under the HORIZON-MSCA-DN-2021 program under Grant Agreement No. 101072846.

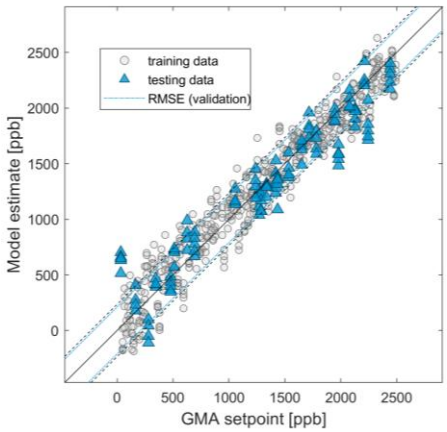

Fig. 1. Regression for sensor's calibration over the different random gas mixtures.

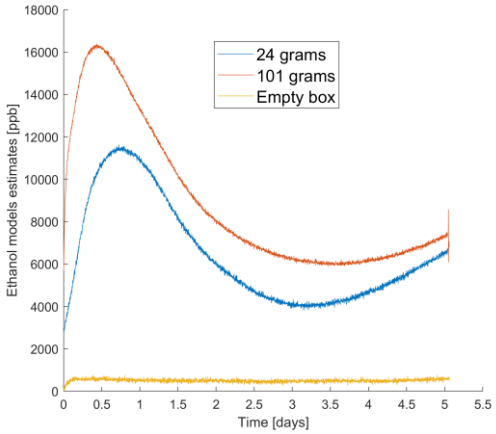

Fig. 2. Model estimates over 3 boxes of 0, 24 and 101 grams of raspberries.

References

[1] Corrado S. and Sala S. "Food waste accounting along global and European food supply chains: State of the art and outlook." Waste management 79 (2018): 120-131; doi: 10.1016/j.wasman.2018.07.032

[2] Schütze A. and Sauerwald T. "Dynamic Operation of Semiconductor Sensors. In Semiconductor Gas Sensor", 2nd ed.; Jaaniso, R., Kiang Tan, O., Eds.; Woodhead Publishing: Sutton, UK, pp. 385–412. ISBN 9789176850039; doi: 10.1016/B978-0-08-102559-8.00012-4

[3] Joppich J. et al. "B3. 3 Monitoring Food Aging in a Refrigerator with GC/MS and Gas Sensor Systems." SMSI 2021-Sensors and Instrumentation (2021): 121-122; doi: 10.5162/SMSI2021/B3.3

[4] Arendes D. et al. "Qualification and optimisation of a gas mixing apparatus for complex trace gas mixtures." tm-Technisches Messen 90.12 (2023): 822-834; doi: 10.1515/teme-2023-0075

[5] Boschetti A. et al. "PTR-MS real time monitoring of the emission of volatile organic compounds during postharvest aging of berry fruit." Postharvest Biology and Technology 17.3 (1999): 143-151; doi: 10.1016/S0925-5214(99)00052-6

DOI 10.5162/EUROSENSORSXXXVI/OT5.202

Characterization of a thick film MOS gas sensor as detector of short trace gas pulses

Oliver Brieger[1], Simeng Zhu[1], Christian Bur[1], Andreas Schütze[1]
[1] Lab for Measurement Technology, Saarland University, 66123 Saarbrücken, Germany

o.brieger@lmt.uni-saarland.de

Summary:
This study introduces a thick film metal oxide semiconductor (MOS) sensor as a promising alternative to traditional gas chromatography (GC) detectors. A gas mixing apparatus was used to simulate gas elution from a GC column with a custom measurement chamber for optimal coupling of sensor and gas flow. The experiments achieved precise quantification of ethanol at concentrations in the ppb range, utilizing a MOS sensor temperature profile for sensitive peak detection. The results show that MOS sensors offer a cost-effective and reliable substitute for traditional GC detectors in analytical applications.

Keywords: MOS sensors; gas chromatography; ethanol; differential surface reduction (DSR)

Motivation

Many applications, e.g. for quality control of food, today rely on either human sensory solutions or laboratory analytic devices, i.e. gas chromatography mass spectrometry (GC-MS). These solutions lack either an objective analysis or entail high cost without real-time capability. In the pursuit of mobile gas analytic devices, MOS sensors combined with gas chromatography utilize the sensors excellent sensitivity in combination with the columns selectivity and emerge as a promising approach [1]. This work investigates the capabilities of a thick film MOS sensor (custom GGS 1530 T without Gaze, UST Umweltsensortechnik GmbH, Geratal, Germany) as a GC-detector, which offers significant advantages such as high sensitivity to VOCs, small size and low cost. A temperature profile is employed to enhance the sensitivity of the MOS sensor [2] based on the Sauerwald-Baur model [3].

Setup and Methodology

A gas mixing apparatus (GMA) is used to simulate peaks eluting from a GC column [4]. Two gas lines enable a constant flow of 500 ml/min at 50 % relative humidity. A predilution line injects 10 ml/min of an adjustable ethanol concentration with a valve (Type 6624, Bürkert GmbH & Co. KG, Ingelfingen, Germany) into the total flow. The GMA is connected to a measuring chamber that guides the flow into the housing of the sensor, minimizing dead volumes. The schematic of the setup is shown in Fig. 1.

The MOS sensor is run in a temperature profile with a sampling period of 10 ms using custom electronics [5]. The temperature profile includes three high temperatures (400 °C) and three low temperature stages (150 °C, 200 °C, 250 °C), with a total duration of 15 min. During each five minutes interval, while the sensor is at low temperature, the gas valve is opened for 5 s between 50-55 s. Ethanol is injected at concentrations of 10 ppb, 30 ppb, 100 ppb and 300 ppb. Temperature profile and sensor response of the MOS sensor are shown in Fig. 2.

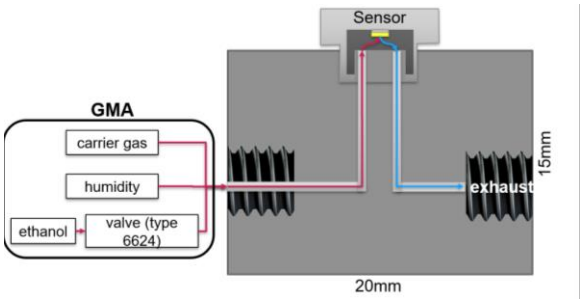

Fig. 1: Schematic of the setup including the section view of the sensor housing.

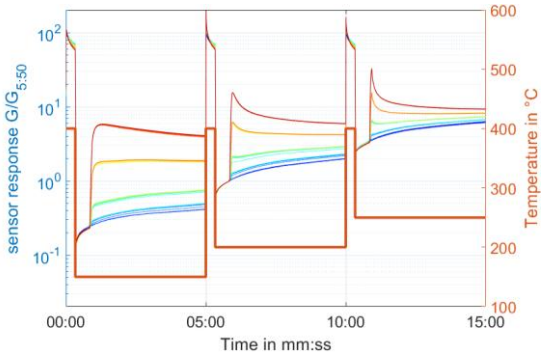

Fig. 2: Temperature cycle and sensor response $\frac{G}{G_{5:50}}$ of the MOS sensor.

Results

The ethanol injections result in different sensor responses in terms of shape and relative conductance change depending on the temperature plateau (cf. Fig. 2). Even the lowest injected dose of 50 ppb·s (10 ppb for 5 s) is easily distinguishable from the baseline. Fig. 3 shows 12 repeated injections for each dose, showing highly reproducible results in the sensor response with a change of conductivity of up to one order of magnitude for a dose of 1500 ppb·s (300 ppb for 5 s).

The sensor response for the lowest doses 50 ppb·s and 150 ppb·s approximately follows the baseline after the injection with a small offset. This has previously been observed in [6] with the differential surface reduction (DSR) method for MOS sensors under a similar temperature profile and confirms the Sauerwald-Baur model for low concentrations.

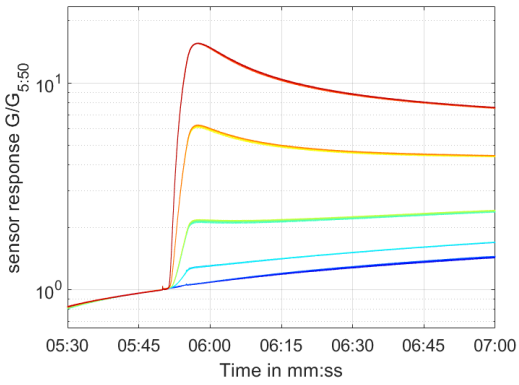

Fig. 3: Sensor response for 60 injections with the doses of 0/50/150/500/1500 ppb·s between 5:30 min and 7:00 min at the 200 °C plateau.

Fig. 4 shows the change of the sensor response vs. dose and a linear fit. Start and end values to calculate the change in sensor response are determined by the inflection points of the sensor response in the opening interval of the valve. The change of sensor response shows excellent linearity over the tested range.

It is obvious that different models are required for different injections dose ranges. Higher doses will strongly deplete ionosorbed oxygen on the sensitive layer according to the Sauerwald-Baur model. This can be observed by a decrease in the sensor response after detection of higher doses. Peaks that deplete the sensitive layer of oxygen could negatively influence the detection of following peaks, i.e. reduce the response. This is a challenge that needs to be addressed in the realization of portable GC-MOS systems. The MOS sensor nonetheless excels in reliably detecting even the smallest doses of substance.

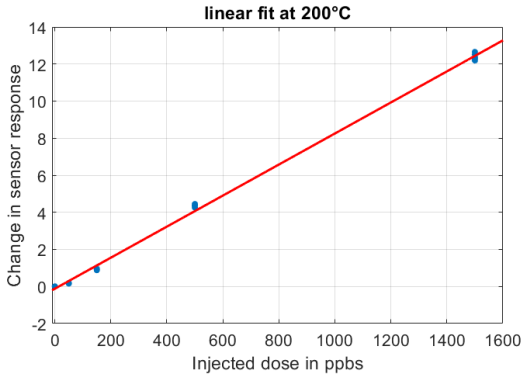

Fig. 4: Linear fit of sensor response change for different injections. $p_1 = 0.0084$; $p_2 = -0.122$; $rsquare = 0.998$ *corresponding to* $\approx 23\,ppb \cdot s$.

Conclusion

In conclusion, the MOS sensor exhibits highly sensitive and reproducible results as detector for gas peaks in temperature programmed operation. This demonstrates the capability and potential for MOS sensors as detector in gas chromatography systems.

Further studies will include the quantification ability of the MOS sensor with coeluting substances, i.e. multiple GC peaks.

Acknowledgement

Financial support was provided by Federal Ministry for Economic Affairs and Climate Action under the grant number 22938 N for the project SENT-GC-MOS.

This work was also supported by Umweltsensortechnik GmbH, who provided us with custom GGS 1530 T without Gaze.

References

[1] O. Brieger, J. Joppich, C. Schultealbert, T. Baur, C. Bur, A. Schütze, „Microstructured MOS Gas Sensor as GC detector,“ in IEEE International Symposium on Olfaction and Electronic Nose (ISOEN), Aveiro, Portugal, 2022.

[2] A. Schütze, T. Sauerwald, „Dynamic operation of semiconductor sensors,” in: R. Jaaniso, O. K. Tan (eds.): Semiconductor Gas Sensors, Woodhead Publishing, 2nd Edition, 2020, pp. 385-412.

[3] T. Baur, A. Schütze, T. Sauerwald: Optimierung des temperaturzyklischen Betriebs von Halbleitergassensoren, tm - Technisches Messen (2015), 82 (4), 187-195.

[4] N. Helwig, M. Schüler, C. Bur, A. Schütze, „Gas mixing apparatus for automated gas sensor characterization,“ Measurement Science Technology (2014) 25(5).

[5] C. Fuchs, H. Lensch, O. Brieger, T. Baur, C. Bur, A. Schütze, "Concept and realization of a modular and versatile platform for metal oxide semiconductor gas sensors," tm - Technisches Messen (2022) 89(12), pp. 859-874.

[6] T. Baur, A. Schütze, T. Sauerwald, „Detektion von kurzen Gaspulsen für die Spurengasanalytik (Detection of short gas pulses for trace gas analysis),“ tm - Technisches Messen (2017) 84 (s1), pp. 88-92.

DOI 10.5162/EUROSENSORSXXXVI/OT5.232

Raman Spectroscopy-based Detection of Suspended Carbon Nanotubes for Integration into Sensors

N. Monnerat[1], I. Kraiem[1], C. Roman [1], C. Hierold[1], M. Haluska[1]
[1] *Micro- and Nanosystems D-MAVT ETH Zürich, Tannenstrasse 3,8092 Zürich, Switzerland*

Haluskam@ethz.ch

In this study, the visualization of CVD grown suspended CNTs intended for individual carbon nanotube field effect transistor gas sensors was investigated. Two visualization techniques were compared: SEM and Raman spectroscopy. By comparing the CNT visibility by the 514 nm laser wavelength of Raman spectroscopy to the CNT visibility in SEM, a detection yield of 90.3% by Raman was determined. For the CNT detectability by Raman, both G and D* Raman bands were considered.

SWCNT for sensors, CNFET gas sensors, Raman spectroscopy, SEM, Detection yield

Visualizing Carbon Nanotubes

Carbon Nanotubes (CNTs) offer a vast array of potential applications due to their exceptional electronic, mechanical, and thermal properties [1]. Single-walled CNTs (SWCNTs) for example are particularly promising because of their low detection limit of different gases including NO_2 [2].

Different approaches address the challenge of integrating individual CNTs into device structures, including dielectrophoresis (wet transfer) [3], and dry mechanical transfer techniques [4]. Wet transfer techniques come with a high risk of contamination. Dry transfer requires pre-localization of CNTs before their integration into sensors.

Several techniques can visualize as-grown individual CNTs. SEM can, in principle, detect all CNTs. However, M. Muoth et al [4] reported electrical degradation of CNTs post-SEM.

On the other hand, Raman spectroscopy allows for non-destructive detection of individual suspended CNTs [5]. In addition, it can provide information on the structural and electrical properties of CNTs. The downside of Raman imaging is an expected lower CNT detection yield compared to SEM.

This study was motivated by the scarcity of research on the suspended CNT detection yield by Raman spectroscopy.

Samples and Measurement Methods

CNTs used in this work have expected diameters ranging from 1.5 to 2.5 nm and were synthesized by chemical vapor deposition in CH_4/H_2 atmosphere using an iron-based catalyst precursor [6].

All Raman measurements were conducted by the Renishaw InVia Qontor System using the StreamLine™ scanning method with an elliptical laser beam and a wavelength of 514 nm. The microscope objective had an NA of 0.75 and a magnification of 50x. The optical depth of focus allowed to detect tubes at full sample-depth (5 µm).

The CNTs were manually counted in spectral maps filtered by the G (around 1585 cm^{-1}) and D* (around 2665 cm^{-1}) bands. These bands, seen in Fig. 1., only materialize when the so-called resonance condition for incoming or outgoing (scattered) light is fulfilled [5]. Otherwise, the bands do not appear in Raman spectra and the CNT can't be detected, as seen in Fig. 2.

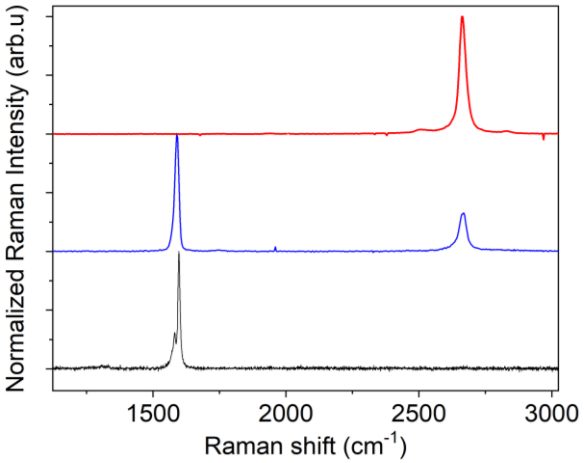

Fig. 1. Vertically shifted Raman spectra of three CNTs with differently visible G (left) and D (right) bands. The spectra are normalized at the dominant peak.*

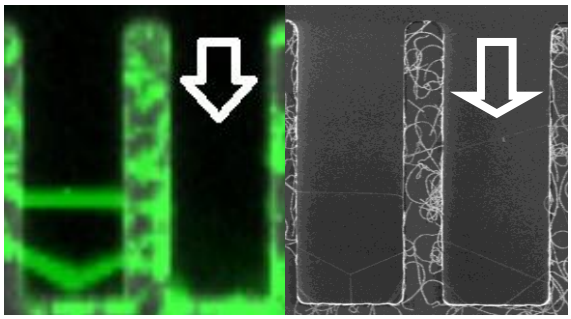

Fig. 2. The same two trenches in a Raman measurement map (left) and in a SEM image (right). The green color shows the CNTs visible by Raman. The white arrows point to a SEM-visible CNT that is invisible in 514nm-Raman spectroscopy.

Results

1676 SEM-visible CNTs were investigated by Raman and the detection yields with a Raman laser wavelength of 514nm were determined and summarized in Table 1. In maps filtered by the G band, 85.3% (1429) of CNTs were visible. An additional 5% (84) of CNTs were only visible in D* band filtered maps, raising the CNT detection yield to 90.3%.

Tab. 1: Yield values of visible CNTs

	Amount of visible CNTs	CNT detection yield
SEM	1676	100%
G band	1429	85.3%
only D* band	84	5%

Discussion

The experimental results can be compared to theoretical expectations based on the Kataura plot [7], which are summarized in Table 2 for three different CNT diameter distributions and distribution types.

Tab. 2: Theoretical CNT visibility in Raman spectroscopy based on the Kataura Plot [7].

	Ø 1.9 ± 0.27 nm Gaussian	Ø 0.7-3.5 nm Uniform	Ø 3.2 ± 0.45 nm Gaussian
G band	54.4%	61.9%	77.9%
only D* band	15%	13.9%	13.3%

The experimental detection yield obtained by the 514 nm Raman spectroscopy is higher than the theoretical values. Several reasons might contribute to this difference: one is the counting practice. Possible CNT bundles were counted as one CNT in SEM and as one CNT in Raman maps if two or more Radial Breathing Modes (RBM) were not simultaneously detected. The occurrence of more CNTs in a bundle increases the probability of detecting minimally one of them in a Raman map, thus increasing the Raman yield in respect to SEM count. The same issue arises with multi-walled CNTs. Another reason may be that investigated CNTs possess other diameter distributions than expected. For example, the fourth column of Tab. 2. shows a significant increase in the Raman detection yield if the diameter distribution is shifted to larger values and is broader at the same time.

In conclusion, this study shows that Raman spectroscopy is a good alternative for visualizing/detecting CNTs before their integration into sensor devices. The CNT detection yield by Raman spectroscopy is slightly lower than that of SEM. Nonetheless, Raman spectroscopy is much gentler to the CNTs than SEM, that was shown to significantly affect the properties of exposed CNTs. Raman also gives additional information about the CNTs, such as their electrical conductivity type, thus enabling selection of CNTs with the right properties for functional CNFET sensors.

We would like to thank R. Stirnimann for his help with Raman spectroscopy, and L. Schürz for sample preparation, as well as the MNS & BRNC teams for making this research possible.

References

[1] N. Popov, Carbon nanotubes: properties and application, Materials Science and Engineering: R: Reports 43.3, 61-102 (2004); doi: 1016/j.mser.2003.10.001

[2] K. Chikkadi et al, Beilstein J. Nanotech., 5, 2179–2191 (2014);doi :0.3762/bjnano.5.227

[3] W. Li et al, “Principles of carbon nanotube dielectrophoresis,” Nano Research, vol. 14, pp. 2188–2206, 2021. Publisher: Springer; doi : 10.1007/s12274-020-3183-0

[4] M. Muoth et al, Transfer of carbon nanotubes onto microactuators for hysteresis-free transistors at low thermal budget, 2012 IEEE 25th International Conference on Micro Electro mechanical Systems (MEMS), pp. 1352-1355 (2012); doi: 10.1109/MEMSYS.2012.6170417.

[5] M.S. Dresselhaus et al, Raman spectroscopy of carbon nanotubes. Physics Reports, 409(2):47–99 (2005); doi: 10.1016/j.physrep.2004.10.00

[6] L. Durrer et al, Nanotech., 20 35560 (2009); doi: 10.1088/0957-4484/20/35/355601

[7] K. Liu et al, An atlas of carbon nanotube optical transitions. Nature Nanotech 7, 325–329 (2012); doi: 10.1038/nnano.2012.52

DOI 10.5162/EUROSENSORSXXXVI/OT5.239

Benchmarking the Gas Sensitivity of LSPR Sensors With a New Parameter

Attila Bonyár [1, 2], Tomáš Lednický[3], Manuela Proença[4], Diana I. Meira[4], Marco S. Rodrigues[4], Filipe Vaz[4,5], Joel Borges[4,5]

[1] Department of Electronics Technology, Faculty of Electrical Engineering and Informatics, Budapest University of Technology and Economics, Egry József street 18, H-1111, Budapest, Hungary

[2] Wigner Research Centre for Physics, Konkoly-Thege Miklós way 29-33, H-1121, Budapest, Hungary

[3] Leibniz Institute of Photonic Technology, Albert-Einstein-Str. 9, 07745 Jena, Germany

[4] Physics Center of Minho and Porto Universities (CF-UM-UP), University of Minho, Campus de Azurém, 4800-058 Guimarães, Portugal

[5] LaPMET - Laboratory of Physics for Materials and Emergent Technologies, University of Minho, Campus de Gualtar, 4710-057 Braga, Portugal

bonyar.attila@vik.bme.hu

Summary:

A new parameter is introduced to benchmark the gas sensitivity of plasmonic sensors. This parameter takes into account both the surface sensitivity and the plasmon decay of the used nanoparticles and considers adsorbed gas layers on the sensor surface. Its applicability was tested with a novel plasmonic sensor based on ellipsoidal gold nanoparticles arranged in tightly packed hexagonal lattices, exposed to the exchange of different inorganic gases. The controversy often present when comparing the response of plasmonic sensors tested in liquids and gases is resolved by using this new parameter.

Keywords: Localized Surface Plasmon Resonance; Refractive Index; Gas Sensing; Modelling adsorption interfaces; Gas Sensitivity

Background, Motivation an Objective

The interpretation of the gas sensing performance of localized surface plasmon resonance (LSPR) based sensors is not trivial. The most widely used approach in the literature is using the bulk refractive index sensitivity (*RIS*), calculated by dividing the measured plasmon resonance peak shift ($\Delta\lambda_p$) with the refractive index difference of the exchanged gases (Δn_b), as in eq. (1). [1].

$$RIS = \frac{\Delta\lambda_p}{\Delta n_b} \quad (1)$$

In this approach, the gases are characterized by their bulk refractive index (n_b) only, without considering gas layers adsorbed on the surface of the used nanoparticles or the effect of the plasmon field's decay. The problem with this approach is that the resulting *RIS* values calculated by exchanging gases are usually an order of magnitude higher than those calculated by calibrating the LSPR sensor with liquids of known refractive index.

Description of the New Method or System

In order to resolve these apparent discrepancies between LSPR sensitivity calibrations in liquids and gases, and for the proper evaluation of the gas sensing performance of these sensors a new model was introduced that takes into account both the surface sensitivity and the plasmon decay of the nanoparticles to evaluate the measured LSPR response considering adsorbed gas layers with a $\Delta n_l(t)$ function, where t is the thickness of the adsorbed gas layer. Based on this model, a new benchmarking function, termed as gas sensitivity *GS*(*t*) is introduced, as defined in eq. (2). *GS*(*t*) characterizes the gas sensing performance of a plasmonic sensor and – as will be demonstrated – is independent of the type and pressure of the tested gases.

$$GS(t) = \frac{\Delta\lambda_p - RIS\Delta n_b}{\Delta n_l(t)} \quad (2)$$

Results

To demonstrate the applicability of this parameter, a novel plasmonic sensor based on ellipsoidal gold nanoparticles arranged in tightly packed hexagonal lattices [2] was tested by switching the gas atmosphere between inorganic gases, namely He/Ar and Ar/CO_2, at constant pressure and room temperature. The nanoparticle arrangement of one of the tested plasmonic sensors is shown in Fig. 1.

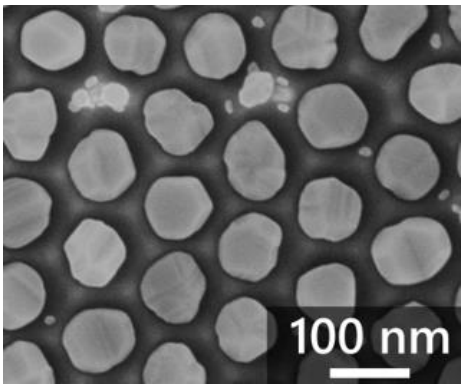

Fig. 1. Scanning electron microscopy image of the tested gold nanoparticle arrangement [3].

Based on the response of the sensors upon gas exchange, numerical modeling and simulations were done to determine the plasmon decay length of the particles and to calculate the $\Delta n_l(t)$ functions for the different gases. Based on these, the gas sensitivity functions (*GS*(*t*)) were also obtained for the tested conditions, as shown in Fig. 2.

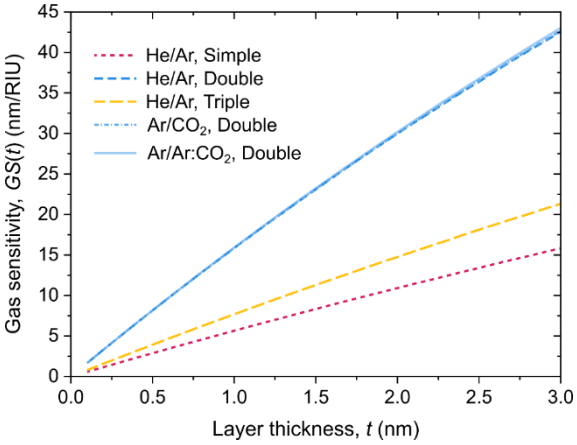

Fig. 2. Gas sensitivity functions GS(t) for the three tested nanoparticle arrangements calculated for different gas exchanges. The 'simple, double, triple' phrases stand for the different particle arrangements, with increasing particle density [3].

As can be seen in Fig. 1, for a given sensor type, the calculated gas sensitivity functions were independent from the type of gases or the measurement conditions.

In the presentation we will demonstrate that the proposed sensitivity model provides a unified explanation for the sensors' response, consistent with their behavior both in the tested liquids and gases and also, that the derivative of the gas sensitivity function, namely d*GS*(*t*)/d*t*, can be conveniently used as a single parameter for benchmarking purposes.

Acknowledgements

This research was sponsored by the Portuguese Foundation for Science and Technology (FCT) in the framework of the Strategic Funding UIDB/04650/2020, and by the project CO2Plasmon with project CO2Plasmon, with reference EXPL/CTM-REF/0750/2021. Manuela Proença acknowledges her Ph.D. Scholarships from FCT, with reference SFRH/BD/137076/2018 and COVID/BD/153223/2023. Diana I. Meira acknowledges her Ph.D. Scholarship from FCT, with reference SFRH/BD/143262/2019. Joel Borges acknowledges FCT for his research contract funding, reference CEEC-INST/00156/2018/CP1642/CT0001. The research was also supported by the National Research and Innovation Office under project number 2020-1.2.3-EUREKA-2022-00030 and by the Nanoplasmonic Laser Fusion Research Laboratory project (2022-2.1.1-NL-2022-00002). Attila Bonyár is also grateful for the support of the Hungarian Academy of Engineering and the "MICHELBERGER MESTERDÍJ" Scholarship. Tomáš Lednický acknowledges CzechNanoLab Research Infrastructure supported by MEYS CR (LM2023051) and funding from the European Union's Horizon Europe research and innovation programme under grant agreement No 101109232).

References

[1] Z. A. Zaky, A. M. Ahmed, A. S. Shalaby, A. H. Aly, Refractive index gas sensor based on the Tamm state in a one-dimensional photonic crystal: Theoretical optimization. Scientific Reports 10, 9736 (2020); doi: 10.1038/s41598-020-66427-6

[2] T. Lednický, A. Bonyár, Large Scale Fabrication of Ordered Gold Nanoparticle–Epoxy Surface Nanocomposites and Their Application as Label-Free Plasmonic DNA Biosensors. ACS Applied Materials and Interfaces 12, 4, 4804–4814 (2020); doi: 10.1021/acsami.9b20907

[3] M. Proença, T. Lednický, D. I. Meira, M. S. Rodrigues, F. Vaz, J. Borges, A. Bonyár. Gas sensitivity of LSPR sensors: Investigation and interpretation of the gas sensing performance of densely-packed Au nanoparticle layers. ACS Applied Materials and Interfaces (under review)

DOI 10.5162/EUROSENSORSXXXVI/OT5.251

CuO-loaded NiO based gas sensor with dual selectivity to NO_2 and H_2.

Madiha Khan[1,2], Enza Fazio[3], Giovanni Neri[1]*

1. *Department of engineering, University of Messina,C.da Di Dio,1-98166 Messina, Italy; madihakhan7121992@gmail.com , giovanni.neri@unime.it*
2. *Department of Physics, Air University, PAF complex, E-9, Islamabad, 4400, Pakistan; madihakhan7121992@gmail.com*

3 Department of Mathematical and Computational Sciences, Physical Sciences and Earth Sciences, University of Messina, Viale F. Stagno D'Alcontres 31, 98166 Messina, Italy; enza.fazio@unime.it

Corresponding Author's e-mail address madihakhan7121992@gmail.com

Summary:

Heterostructures of copper oxide nanoparticles with different NiO loading, were synthesized by sol gel method and their detailed morphological and structural properties have been investigated by XRD, FESEM and EDS, FT-IR studies. Gas sensing devices were fabricated by printing thick film of the CuONiO nanopowders on conductometric ceramic platform. It has been successfully demonstrated that the CuO-NiO sensor has dual sensing capability, able to detect selectively hydrogen at the operating temperature of 80 ◦C, and NO_2 at the temperature of 220 ◦C.

Keywords: Hydrogen, Nitrogen Dioxide, Gas Sensor, Dual Sensor, Hybrid Nanostructure.

Introduction

Metal oxide-based semiconductors are low-cost materials that exhibit promising characteristics including high reactivity and surface area, designable structures, and tunable bandgap. Owing such properties, they are an optimal choice for gas sensors [1]. On other hand, there has been consistent effort to fabricate highly sensitive and selective sensors for monitoring and detection of gases for the biomedical and environmental sectors, such as hydrogen (H_2) and nitrogen dioxide (NO_2). These gaseous species are potentially harmful and even at very low concentration of these gases can cause adverse effects on human health. Therefore, there is a great demand to fabricate highly sensitive, selective, cost effective, rapid, and reliable noninvasive techniques for monitoring these pollutant gases.

As is well known, the response of gas sensors is related to the interaction of the target gas with the surface of the sensing layer. So, the sensor response can be modulated changing the sensing film and the operating temperature of the sensor. Herein, we investigated the selective detection of H_2 and NO_2 varying the operating temperature of the sensor developed based on thick film of CuO-NiO powders printed on a conductometric ceramic platform provided with a pair of interdigitated platinum electrodes.

2.Experimental details:

a. Synthesis of CuO-NiO Hybrids NCs

Hybrid nanocomposites were synthesized by a Sol-gel method [5]. First, CuO and NiO nanopowders were dissolved in 50 mL of HCl and citric acid, respectively. The mixture was sonicated for 30 min and then stirred vigorously at increasing temperature from 60 °C to 90 °C for 2-5 hours until the solution was converted into gel. Thereafter, the formed gel was dried at 90 °C for further 4 hours. Lastly, the dried sample was ground down into fine powder and stored for the further uses.

b. Gas Sensing Device Fabrication

Electrodes for gas sensing studies were prepared by printing thick films (~20 μm) of the composite powder on alumina substrates (6 × 3 mm2) provided with Pt interdigitated electrodes and a Pt heater placed on the backside. Before applying to the gas sensing tests, the prepared

electrodes have been subjected to a low (80 ◦C) and high (250 ◦C) temperature thermal treatment.

Results and Discussion

a. Structural studies The XRD patterns of pure CuO, NiO and

CuO/NiO nanocomposite are shown in Fig. 1. New reflection peaks, compared to ones observed on pure CuO and NiO, were noted, suggesting the presence of new phases likely linked to the CuO/NiO composites formed.

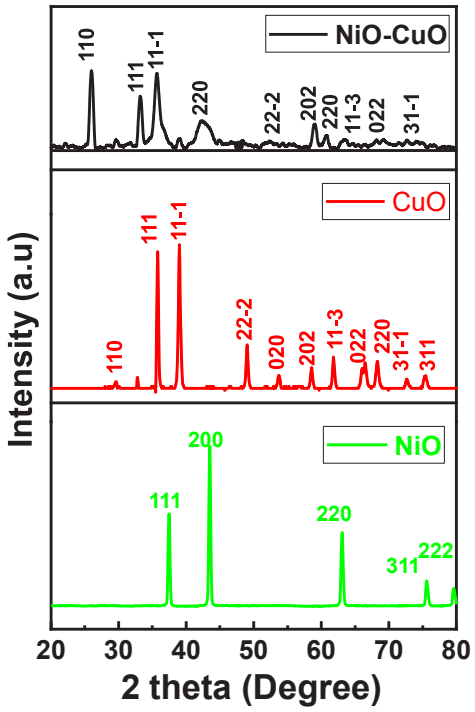

Fig.1. XRD graph of synthesized: CuO, NiO and CuO/NiO hybrids.

b. Gas Sensing tests.

The sensing properties of CuO/NiO hybrid sensors towards hydrogen were first investigated. To find the best operating conditions, the sensors were preliminarily exposed to 40000 ppm of hydrogen at different temperatures. As an example, in Fig. 2 is reported the variation of resistance at the introduction of hydrogen for the CuO/NiO hybrid sensor at the working temperature of 80 ◦C.

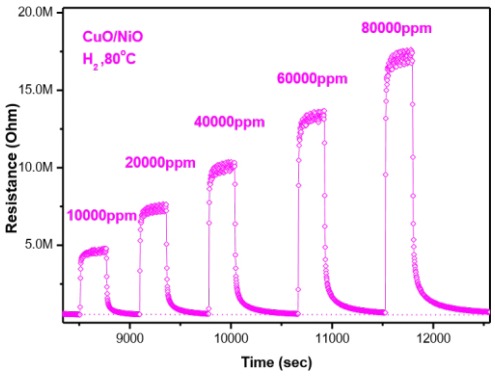

Fig. 7 (a). Transient response of CuO/NiO hybrid sensors to different concentrations of H2 at the optimal temperature of 80 ◦C.

(ii). NO_2 sensing tests.

Operating the sensor at the temperature of 220°C, we noted that the device shows very good performances for NO_2 sensing. The variation of resistance at the introduction of NO_2 for the sensor is reported in Fig. 3.

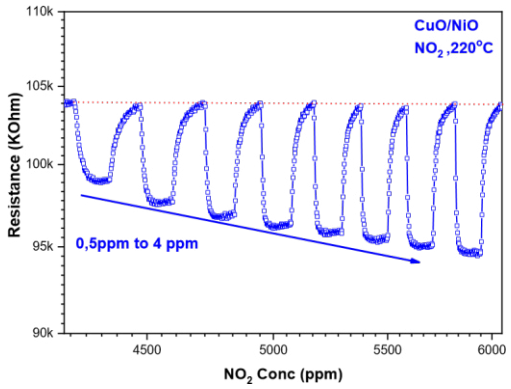

Fig. 3. Transient response of CuO/NiO hybrid sensors to different concentrations of NO_2 at the optimal temperature of 220 ◦C.

Conclusions

In summary, this study demonstrate that CuO/NiO nanocomposites demonstrates promising use for H_2 and NO_2 sensing. In addition, the dual selectivity of CuO/NiO hybrid sensor towards H_2 and NO_2 at two different temperatures was also demonstrated.

References

[1] Miller, D.R., S.A. Akbar, and P.A. Morris, *Nanoscale metal oxide-based heterojunctions for gas sensing: A review.* Sensors and Actuators B: Chemical, 2014. **204**: p. 250272.

DOI 10.5162/EUROSENSORSXXXVI/OT5.252

Printing Nanoporous Layers (NPL) Generated by Spark Ablation for Gas Sensing Applications

Leandro Nicolás Sacco[1], Larissa Egger[2], Maxim Popov[2], Christoph Dösinger[3], Lorenz Romaner[3], Niels Schouten[1], and Anton Köck[2]

[1] VSParticle, Oostsingel 209, 2612 HL, Delft, The Netherlands,
[2] Materials Center Leoben Forschung GmbH, Roseggerstrasse 12, 8700, Leoben, Austria
[3]Department of Materials Science, Montanuniversität Leoben, Franz-Josef-Straße 18, 8700 Leoben, Austria

l.sacco@vsparticle.com

Summary:
Metal-oxides semiconductors (MOS) based nanoporous layers (NPL) were generated by spark ablation and printed by impaction. The printed layers were used as sensing layers to detect a hydrocarbon gas mixture named HCmix, including, acetylene, ethane, ethene, and propene. The impact of the printed layer thickness on the sensing response was assessed. The presented results show that spark ablation is an excellent scalable aerosol route for production of nanoporous layers, suitable for gas sensing applications, where the nanoporous layer can be modulated adjusting the sparkling and printing conditions.

Keywords: gas sensors, spark ablation, nanoporous layers, impaction printing, metal oxides.

1. Introduction

Chemiresistive sensors based on metal-oxide semiconductors (MOS) dominate the gas sensing technologies owning to the relative high sensitivity, easy miniaturization and integration for micro-electromechanical system (MEMS)-based sensors [1]. Nevertheless, the poor selectivity severely limits the implementation of gas sensors in a large number of applications [2]. Several approaches have been developed to overcome the difficulties induced by the cross-selectivity, including chemical functionalization, defect engineering, crystallographic design, and coating with catalytic overlayer [3]. From a material perspective, a sensing layer with a large surface-to-volume ratio that can be easily nano-engineered results in an attractive platform to solve selectivity sensing issues [3].

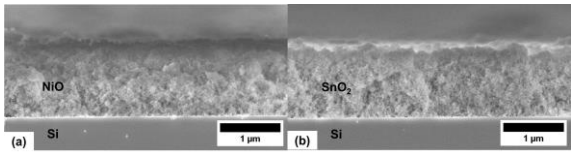

Fig. 1. SEM-cross section images of (a) NiO and (b) SnO_2 NPL used as sensing units for chemiresistive devices.

Herein, we present a process to produce nanoporous layers used as sensing units to detect target gas molecules. The sensing layers are produced by spark ablation, an aerosol nanoparticle (NP) generation route, and deposited by a impaction deposition tool. Spark ablation is a fully dry method, highly reproducible and with a pure material output. It is considered as a versatile NP generator since any solid (semi)-conductor (pure metals, alloys or semiconductors properly doped) can be used and mixed. This a highly desirable property to tackle problems of gas selectivity because it allows to synthesize numerous material compositions in nanostructured form. The NP generator was connected to impaction deposition tool, coupled to a XYZ stage to create deposition patterns, as implemented in the VSParticle nanoprinter (VSP-P1). In short, the impaction deposition relies on accelerating an aerosol through a nozzle towards a surface at sufficiently high velocities to impact on the substrate. In particular, SnO_X and NiO_X layers were printed on a 4-electrodes platform chip. Fig.1. shows a SEM cross-section micrograph of both MOS-based printed nanoporous layers. The NPL thicknesses were varied to assess the impact of the layer morphology on the gas sensing performance in detecting a

hydrocarbon gas mixture. Besides the discussion on the gas sensing performance of devices based on spark ablation, the present work aims to set the basis for the production of chemiresistive devices based on spark ablation/impaction techniques.

2. Materials and Methods

NPL were printed on a 2 cm x 2 cm Si chip with 16 sensor structures with 4-Pt/Ti- electrodes.

Spark ablation generator VSP-G1 (VSParticle B.V.) was used to produce the NP aerosol. For the deposition of NiO_x and SnO_x two pairs of 6 mm Ni and Sn (99.99 % purity) electrodes were used. Argon was used as a carrier gas with a 1 l/min flow, and in both cases the sparking potential and current were set at 1 kV and 10 mA, respectively. The generator was connected to an impaction printer VSP-P1 (VSParticle B.V.) that operated at 0.15 mbar and room temperature. The nozzle diameter was 100 µm. The substrate was placed in a holder that can be moved in the XYZ directions allowing prints without the requirement of lithography steps. A 500 µm long line was printed between the electrodes. The substrate-nozzle distance was fixed at 300 µm. The printing speed (100-1000 µm/s) and the number of passes (2-18) were varied to adjust the NPL thickness. To stabilize and oxidize the NPL, the chips were annealed at 400 °C flowing synthetic air for 10 minutes.

For the gas sensing measurements, synthetic air with controlled humidity was used as a background gas. The humidity level was set to 50% at 20°C. Specific mixture of hydrocarbon gases (HC_{mix}), including acetylene, ethane, ethene, and propene, was used as target gas. The sensors operated at a temperature of 300 °C. The sensor response, denoted as *S*, reflects the relative resistance change in percent due to the interaction with the test gas. It is calculated as follows:

$$S(\%) = 100\% * |R_{air} - R_{Gas}| / R_{air} \quad (1)$$

Where R_{Gas} is the sensor resistance in the presence of the test gas and R_{air} is the sensor resistance in pure synthetic air.

3. Results and discussion

Both types of MOS-NPL, with different thicknesses were sensitive towards the HC_{mix}, as shown Fig.2. The resistance increase/decrease for each NPL under the same target gas is attributed to the *p*-type and *n*-type MOS of NiO and SnO_2, respectively. The thicker layers, generally, lead to higher responses. A sensing saturation response was detected at exposures of 20 ppm of the HC_{mix}. At similar NPL thicknesses (1.2-1.3 µm), the SnO_2-based devices have a stronger response as compared to NiO ones (80 % vs 25% at 10 ppm). The recovery time of SnO_2 devices was longer than the time between the exposure steps, whereas NiO-based devices recovered in 2 minutes. In conclusion, the presented results provide evidence on the capability for producing gas sensing layers adopting a fully dry approach. Our method features a high control of the NPL without need of pattering and can be extended to a myriad of material compositions. Collectively, these properties are highly attractive to pave the way for the next generation of chemiresistive-gas sensors.

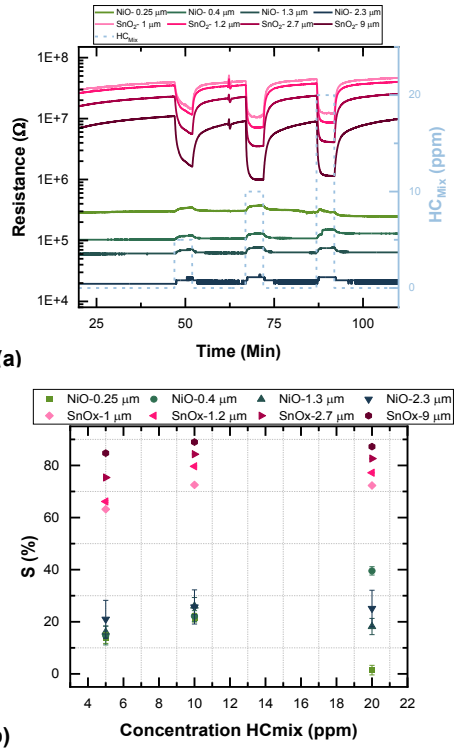

Fig. 2. (a) Dynamic sensing response of NiO and SnO_2 sensors upon exposure to HCmix. (b) Response as function of the HC_{mix} concentration.

References

[1] S. Nazir and O. S. Kwon, "Micro-Electromechanical Systems-based Sensors and Their Applications," *Applied Science and Convergence Technology,* vol. 31, no. 2, pp. 40-45, 2022.

[2] S. M. Majhi, S. T. Navale, A. Mirzaei, H. W. Kim and S. S. Kim, "Strategies to boost chemiresistive sensing performance of In2O3-based gas sensors: an overview," *Inorg. Chem. Front.,,* vol. 10, pp. 3428-3467, 2023.

[3] P. M. Bulemo and J. Y. Cheong, "Review on Porosity Control in Nanostructured Semiconducting Metal Oxides and Its Influence on Chemiresistive Gas Sensing," *Applied Nano Materials,* vol. 6, no. 2, p. 1027–1049, 2023.

DOI 10.5162/EUROSENSORSXXXVI/OT5.256

Conductometric sensor array based on electropolymerized porphyrinoids

Lorena Di Zazzo[1], Gabriele Magna[1], Larisa Lvova[1], Manuela Stefanelli[1], Sara Nardis[1], Corrado Di Natale[2] and Roberto Paolesse[1]

[1] Department of Chemical Science and Technology, University of Rome Tor Vergata, 00133 Roma, Italy

[2] Department of Electronic Engineering, University of Rome Tor Vergata, 00133 Roma, Italy

Corresponding Author's e-mail address: lorena.di.zazzo@uniroma2.it

Summary:

Metallocorrole derivatives are a versatile class of coordination complexes successfully exploited in different applications, ranging from medical to environmental fields, due to their peculiar tuneable properties. Herein, a novel class of conductometric sensing films has been deposited directly onto the interdigitated electrodes by the electropolymerization of metallocorroles and metalloporphyrins. Remarkably, not only can the chemical sensing properties be tuned by choice of central-coordination metal, but the electropolymerization protocol can also modulate the conductive nature of polymers (n- or p-type). Finally, the fabricated sensors were tested towards a large family of volatile compounds and gases, finding high sensitivity to nitrogen oxide also in the presence of a high humidity environment.

Keywords: Conductometric sensor, porphyrinoids, polymer, electropolymerization, electrode, gas.

1. Introduction

Corroles and related macrocycles are widely employed in the field of chemical sensors, where they are used as sensing materials for optical, electrochemical, and conductometric transducers [1]. Concerning the employment in conductive sensors, these porphyrinoids are not used by themselves because supramolecular assemblies of these molecules are scarcely conductive, but they are combined with conductive materials such as graphene oxide, carbon nanotubes, or conductive polymers. A novel approach to building conductive sensors with these sensing materials is proposed here, and it consists of producing porphyrin or corrole conductive polymers by an electropolymerization approach. This technique has been mainly utilized in the case of porphyrins that present electron-active substituents, with a typical example represented by the electrochemical oxidation of tetrakis(4-aminophenyl) porphyrins, which leads to the formation of different types of linkers as the phenazine bridge [2]. On the other hand, although corroles present many appealing features in the field of chemical sensing, the polymerization of these macrocycles is scarcely reported. Here, we synthesize and investigate the sensing properties of polycorroles and polyporphyrins as conductive sensors. Thus, we exploit the role of peripheral functional groups, the influence of the coordinated metal and the role of electropolymerization protocol on the final sensing film properties.

2. Materials and methods

The metal complexes of corroles and porphyrins are synthesized according to literature methods [3,4]. The polymers are prepared by electropolymerization of porphyrinoids directly onto interdigitated electrodes (IDE) (see Figures 1A, 1B, and 1C). The polymerization is performed by cyclic voltammetry (CV) or chronoamperometry (CA). The IDEs are immersed in a solution of precursor monomers (1 mM) in CH_2Cl_2 containing 0.1M supporting electrolyte tetrabutylammonium perchlorate, $TBAClO_4$. The influence of the number of scanning cycles on the optical and sensing properties of the film is evaluated.

Finally, conductive organic sensors are allocated in a chamber connected to a mass flow controller system to deliver the desired gas concentrations in synthetic air. Different concentrations of nitric oxide (NO), carbon monoxide (CO), molecular hydrogen (H_2), and carbon dioxide (CO_2) are tested. The resistances of sensors are measured at 1 sample/s with a multichannel multimeter connected to a computer; relative changes in responses have been considered as features, and data analysis is performed in Matlab®.

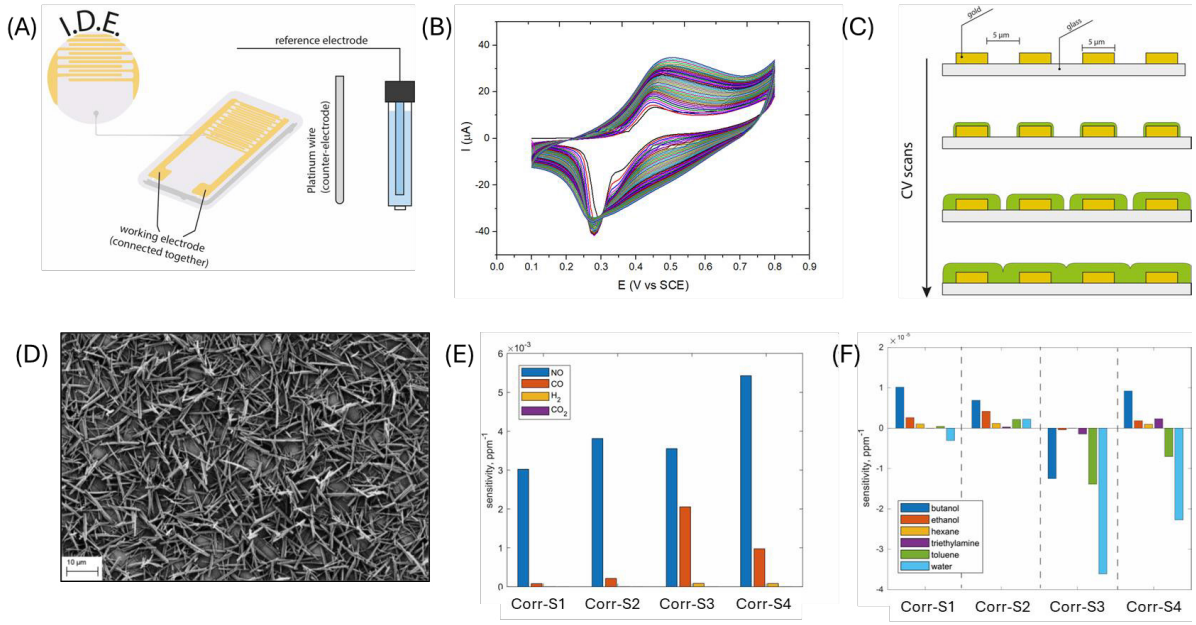

Fig. 1. A) Set-up for sensor fabrication via cyclic voltammetry. B) Typical cyclic voltammogram upon polymer formation. C) Mechanism of polymeric film growth and electrode connection. D) SEM image of polycorrole film. E) Selectivity of polycorrole films; tuning the sensing properties to obtain a high selective sensor to NO is possible. F) As well it is possible to tune the selectivity toward VOCs to produce a conductometric e-nose

3. Result and discussion:

The conductive polymers are formed via the oxidation of peripheral anilino groups of the monomeric precursors and consecutive coupling to the second monomer molecule. The continuous increase of the anodic current amplitudes with repeated potential scans evidences the growth of a conductive polymeric film onto the substrate (Figure 1B). The films have been characterized by spectroscopic techniques (UV-Vis), Scanning Electron Microscopy (SEM, Figure 1D), and Electrochemical Impedance Spectroscopy (EIS). The sensing performances of the most promising materials have been investigated by testing gases (NO, CO, H_2, CO_2) and volatile compounds (such as humidity, alcohols, and hydrocarbons). Remarkably, we found out that the electropolymerization protocol can influence the nature of the resulting polymers and, the selection of p- or n-type semiconductor film formation. This outcome has been evidenced by the behavior of sensors toward oxidizing and reducing gas. The conductive polymer based on [5,10,15-(4-aminophenyl) corrolato] copper showed very high sensitivity to NO (with a detection limit in the order of tens of ppb, see Figure 1E) and negligible sensitivity variations to this compound under environmental relative humidity changes. This first outcome suggests this kind of sensor's potential role for detecting NO in human breath for medical applications.

Second, we produce a sensor array to investigate the possibility of realizing a conductometric electronic nose based on porphyrinoids polymers. The results showed the capability of a minimal set of sensors to correctly group and recognize both tested VOCs and gases (selectivity pattern modulation is reported in Figure 1F). This may be a great breakthrough for applying porphyrins and corroles since they are scarcely applied in conductometric sensors, which can be considered the cheapest and easiest way to miniaturize a class of sensors. Finally, the possibility of modulating the semiconducting nature of this material may open the way to the fabrication of more sophisticated sensors based on non-linear organic electronic elements.

References

[1] R. Paolesse, S. Nardis, D. Monti, M. Stefanelli, and C. Di Natale. *Chemical reviews,* 2017, *117*(4), 2517-2583. doi.org/10.1021/acs.chemrev.6b00361.

[2] M. G. Walter, and C. C. Wamser. *The Journal of Physical Chemistry C* 114.17 (2010): 7563-7574. https://doi.org/10.1021/jp910016h

[3] R. Paolesse, S. Nardis, F. Sagone, R. G. Khoury, *J. Org. Chem.* 2001, *66*, 550-556. https://doi.org/10.1021/jo005661t

[4] R. Luguya, L. Jaquinod, F. R. Fronczek, M. G. H. Vicente, & K.M Smith (2004). *Tetrahedron*, *60*(12), 2757-2763. https://doi.org/10.1016/j.tet.2004.01.080

DOI 10.5162/EUROSENSORSXXXVI/OT5.266

Electrochemically Exfoliated 2D MoS_2 for ppb-level NO_2 Sensing

Kusuma Urs[1], Tian Carey[2], Shixin Liu[2], Kevin Synnatschke[2], Jonathan N. Coleman[2], Subhajit Biswas[1], Justin D. Holmes[1]

[1]School of Chemistry, University College Cork, Cork T12 YN60, Ireland
AMBER Centre, Environmental Research Institute, University College Cork, Cork T23 XE10, Ireland
[2]Centre for Research on Adaptive Nanostructures and Nanodevices (CRANN) and Advanced Materials Bio-Engineering Research Centre (AMBER) Trinity College Dublin, Dublin, Ireland
[3]Tyndall National Institute, University College Cork, Cork T12 YN60, Ireland

Corresponding author: s.biswas@ucc.ie

Summary:

We demonstrate proof-of-concept Molybdenum sulphide (MoS_2) sensors for environmental monitoring of ultra-low concentration of NO_2. Robust detection in a wide range of NO_2 concentrations, 100 ppb-50 ppm, was achieved, highlighting the great potential for electrochemically exfoliated MoS_2-based NO_2 sensors. The measurements were performed in a complex environment, combining NO2/synthetic air, traces of other pollutant gases, and in room temperature to achieve fully deployable sensor for the environmental conditions. It is shown; with the aid of density functional theory (DFT) calculations; that the performance of the electrochemically exfoliated MoS_2 sensor can outperform sensors based on mechanically exfoliated MoS_2 owing to their large surface defects and vacancies.

Keywords: MoS_2; 2D material; Electrochemical exfoliation; NO_2 sensor

Introduction

Two dimensional (2D) materials with high surface area and high reactivity have attracted the attention in the field of sensors [1]. Nitrogen dioxide (NO_2) is an oxidizing gas which is toxic and dangerous for environment. NO_2 at levels greater than 1 ppm can cause serious damage to the human respiration system and lung tissues and contributes to the formation of ozone, which is the major cause of photochemical smog and acid rain [2]. So far, most NO_2 electrical sensors are mainly based on metal oxide materials, which usually require high operating temperatures [3]. This shortcoming, coupled with their poor selectivity, severely hampers their application in target gas detection. Therefore, room-temperature operation, portability, low power consumption, sensitive and highly selective gas sensors are of immediate requirement.

Molybdenum disulphide (MoS_2) have grabbed the attention due to the tunable layer-dependent electronic and optical properties [4]. Since 2D MoS_2 has a large surface area with sulphur vacancies and edge states, it has a potential to show a large change in the surface conductivity on exposure to the target gases. Herein, we demonstrated an ideal MoS_2 2D material synthesized via electrochemical exfoliation for high-performance (~ 100 ppb) NO_2 sensing at room temperature.

Method

For the electrochemical exfoliation, the bulk MoS_2 is inserted in the electrochemical cell and negative voltage is applied, which results in the expansion of the bulk crystal due to the insertion of solvent ion into the crystal. The solution on immediate sonication in presence of stabilizing agent yield dispersed MoS_2 flakes. These sheets collected by centrifugation were dispersed in isopropyl alcohol to form an ink. MoS_2 nanosheet films were then deposited onto PET substrate with Inter-Digitated Electrodes (IDEs) with 100nm gold electrodes. Two terminal electrical characterization and sensor tests of the MoS_2 devices was performed using Keithley 2450 Source Meter interfaced with the semi customized Nextron probe station.

Results & Discussion

Deposited MoS_2 film has the thickness of the film is about 25-30nm. To understand the electrical structure and the oxidation states of the MoS_2, XPS measurements showed atomic percentage ratio between $Mo^{4+}$and S^{2-}/S_2^{2-} is 1: 1.8 (± 0.1) which deviates from the stoichiometric ratio (1:2) for ideal MoS_2, indicating the fabrication of the sulphur-deficient MoS_2 nanosheets prepared by the electrochemical exfoliation method.

Sensor characterization of the MoS_2 device were performed towards a range of NO_2 concentration (100 ppb-100 ppm). Two terminal electrical measurements were carried out on the MoS_2 devices under the ambient, synthetic air and NO_2/synthetic air mixed

environment. The device shows a non-linear *I-V* behavior with the current in the order of nano-ampere range (Fig. 1a). The same device was then exposed to different concentrations of the target pollutant gas of NO_2 . It is evident from Fig. 1b that on exposure to NO_2 for 10 min, the sensor current decreases while it comes back to the initial state when NO_2 gas flow is

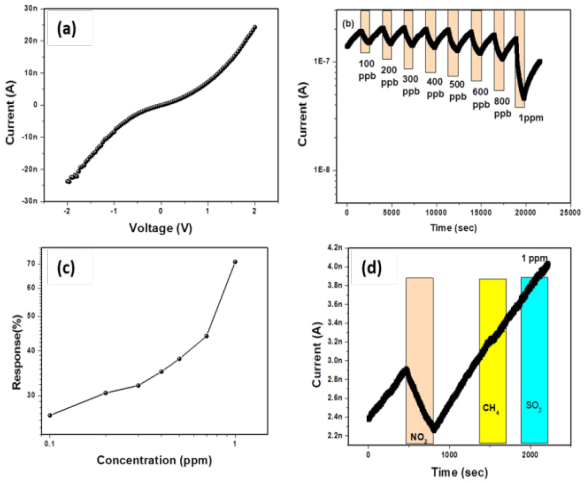

Fig. 1. (a) IV curve of the two-terminal device. (b) The transient response of the device for NO_2 gas at 1V bias. (c) Response curve from minimum to maximum concentration of NO_2 gas. (d) The response curve for individual gases.

stopped. The decrease in current with NO_2 exposure is attributed to the sulphur vacancies in the system that causes n-type behavior. These sensors showed ~90 % response to 1 ppm of NO_2 with a room temperature response and recovery time of approximately 6 and 20 minutes, respectively. By employing UV irradiation, we enhanced the recovery time of the sensors from 20 minutes to under 1 minute. We have achieved significant response even for 100 ppb at room temperature. The average response and recovery times were estimated as 7 min and 15 min respectively. The sensor response is about 24% even for concentration as low as 100 ppb (Fig. 1c). Evaluation of the sensors was also performed within a 6.5 m^3 atmospheric simulation chamber yielding a consistent performance in response and recovery times similar to the smaller scale set up.

DFT calculation have identified three primary possible mechanisms for the detection of NO_2 through electron trapping of electrons: (i) NO_2 physisorption on defective MoS_2-*x* layers, (ii) the passivation of sulphur vacancies of MoS_2-*x* and (iii) the formation of nitrate radical anions.

Sensor tests in a binary and ternary mixture of gases (CH_4, SO_2, NO_2) depicts the primary response only from NO_2 in a binary and tertiary mixture (Fig. 1d). This clearly indicates that the byproducts obtained in mixture of gases are also not interfering with the sensor signal. The device shows good stability (within 5% difference between subsequent NO_2 pulse) at the highest (1 ppm) and lowest (100 ppb) concentration of NO_2. Electrochemically exfoliated MoS_2 shows much better performance compared to mechanically exfoliated.

In summary, we have found that electrochemically exfoliated MoS_2 with a large density of defects is an ideal candidate for room temperature NO_2 sensing with high sensitivity NO_2 (~100 ppb) and selectivity at room temperature with fast recovery. MoS_2 thin film device can clearly discriminate NO_2 from a mix gaseous environment.

Acknowledgement

This work is funded by European Unions Horizon 2020 research and innovation programme under grant agreement number 899282 (RADICAL).

References

[1] D. Tyagi, H. Wang, W. Huang et al., Recent advances in two-dimensional-material-based sensing technology toward health and environmental monitoring applications, Nanoscale, 12, 3535-3559 (2020); doi: 10.1039/c9nr10178k.

[2] A.-M. Andringa, C. Piliego, I. Katsouras et al., NO2 Detection and Real-Time Sensing with Field-Effect Transistors, Chemistry of Materials, 26, 773-785 (2013); doi: 10.1021/cm4020628.

[3] A. Afzal, A. Mujahid, N. Iqbal et al., Enhanced High-Temperature (600 degrees C) NO(2) Response of ZnFe(2)O(4) Nanoparticle-Based Exhaust Gas Sensors, Nanomaterials 10, 11 (2020); doi: 10.3390/nano10112133.

[4] S. Z. Omnia Samy , Muhammad Danang Birowosuto and Amine El Moutaouakil, A Review on MoS2 Properties, Synthesis, Sensing Applications and Challenges, Crystals, 11, 24 (2021); doi: 10.3390/cryst11040355.

DOI 10.5162/EUROSENSORSXXXVI/OT5.267

NO_2 Sensor on Ambipolar Si-Junctionless Nanowire Transistor

Vardhan Vaishali[1,2], Biswas Subhajit[1,2], Ghosh Sayantan[3], Hellebust Stig[1,2], Georgiev M. Yordan[3], Holmes D. Justin[1,2]

[1]School of Chemistry, University College Cork, Cork, T12 YN60, Ireland

[2]Environmental Research Institute, University College Cork, Cork, T23 XE10, Ireland

[3]Institute of Ion Beam Physics and Materials Research, Helmholtz-Zentrum Dresden Rossendorf, 01328, Dresden, Germany

Corresponding Author: 121101220@umail.ucc.ie

Summary:

We demonstrate highly effective ambipolar Si-junction less nanowire transistors (JNTs) with a distinct dual reaction to oxidative pollutant NO_2. DFT study reveals NO_2 acts as an electron acceptor and produces holes; acting as pseudo dopant for Si JNTs; significantly altering different JNT parameters. Different Si-JNT characteristics showed dynamic change on both the p- and n-sides, i.e. dual response; of the ambipolar transistor devices upon exposure to NO_2 in a wide mixing ratio (250 ppb-50 ppm). Additionally, we have improved the discrimination between different gases (NO_2, NH_3, SO_2 and CH_4) by using multivariate calibration.

Keywords: Silicon nanowire, Junction less transistor, Ambipolar device, Machine Learning, NO_2 sensor

Introduction

NO_2 plays an important role in the chemistry of the atmosphere. Long-term exposure to high levels of NO_2 can also cause respiratory problems and has been linked to increased risk of heart and lung disease.

The current techniques to detect NO_2 are based on spectroscopy, electrochemical process, and electrical methods based on metal oxides. They do, however, have limitations in terms of selectivity, sensitivity, portability, high temperature [1]. Due to their high surface-to-volume ratio, the ability to interact chemically with analytes on the surface, and operation at ambient temperature, Si nanowires (NWs) offer unique opportunities as efficient sensor material [2]. Additionally, Si NW also offers benefits from their ease in fabrication, compatibility with existing semiconductor technology, high carrier mobility, and great sensitivity to analytes adsorbed on their surface. In this regard, Si NW Junction-less Transistor (Si JNT); a nanowire transistor with no gate junction [3]; are interesting proposition as NO_2 sensor. JNTs are much simpler to manufacture as the source and drain areas do not need to be separately doped[16]. Additionally, the bulk conductance in JNTs is near the center of the channel promoting extreme sensitivity to any variation in the electrostatic potential on the Si-JNT channel surface with variation in electrical parameters. Incidentally, ambipolar transistors, a type of transistors that allow for simultaneous transit of both positive (holes) and negative (electrons) charge carriers within the semiconducting channel, can provide a dual response to a single analyte using a single device [4]. Thus, a variety of electrical parameters could be explored for a single ambipolar Si-JNT upon analyte interaction, offering variety of sensing properties and extremely selective gas detection.

In this work, we show how NO_2 can alter different Si-JNT properties and function as a pseudo dopant for Si JNTs. This NO_2-Si interaction effectively influence different electrical parameters in ambipolar Si-JNTs with a distinct and selective dual response to oxidative pollutant NO_2.

Matarials and Methods

The Si-JNT (20 nm NW width) devices were fabricated from ultra-thin silicon-on-insulator (SOI) substrates. Si-JNTs were fabricated following a top-down approach using electron beam lithography (EBL) and reactive ion etching (RIE). Flash lamp annealing (FLA), which leads to form Nickel Silicide at the interface of Silicon and Nickel controls the unipolar or ambipolar nature. Fig. 1.a shows top-view SEM image of the representative Si-JNT device.

Electrical and sensor characterization of Si-JNTs was performed by using an electrical analysis system (two Keithley 2450 Source Meter) interfaced with the Nextron gastight probe station. Si-JNTs were tested and compared towards different mixing ratios of NO_2 at room temperature and at atmospheric pressure.

Results and Discussion

The transfer curve of the Si NW JNT measured under ambient conditions exhibits typical ambipolar characteristics (Fig. 1b). The transport characteristics involve both electron (or hole) depletion and hole (or electron) accumulation. A clear change in on-current (I_{on}) is observed upon NO_2 exposure (25 and 50 ppm NO_2) to the Si-JNTs (Fig. 1b). The I–V curves retained ambipolar characteristics upon exposure to NO_2.

However, current in both p and n conduction channels (left: p-type, right: n-type) shifted with the exposure of NO_2 at different concentrations. An increase in the drain current has been observed with increasing mixing ratios of NO_2 in the p-side (from 25 ppm to 50 ppm) whereas a decrease in the n-type current was observed with NO_2 exposure of same concentrations. This is classified as dual interaction. Interaction with NO_2 alters the carrier concentration in the JNT channel, with NO_2 acting as an electron acceptor and inducing holes, as supported by Density Functional Theory (DFT) calculations, providing a pathway for charge transfer and "pseudo" molecular doping in ambipolar Si-JNTs.

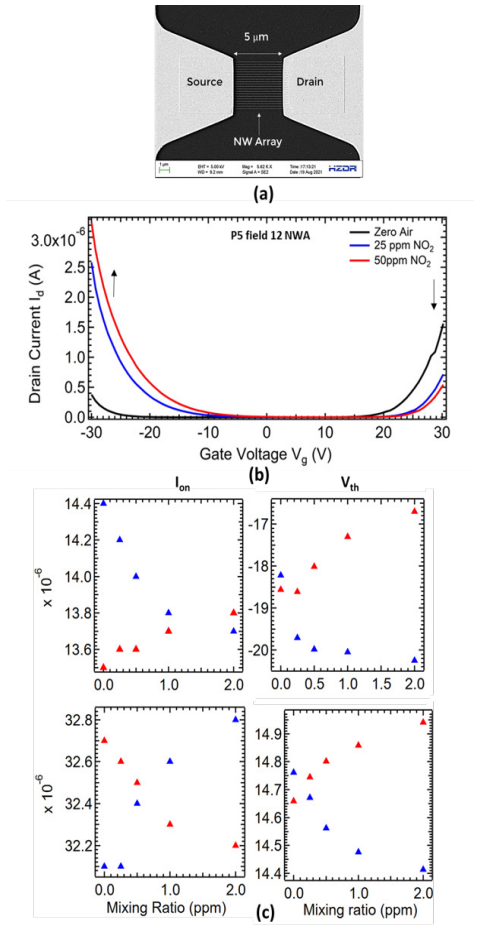

Figure 1. (a) SEM top view image of the Si-JNT devices. (b) Transfer characteristics of Si-JNT upon NO_2 exposure. (c) Effect of gas interaction on different parameters of ambipolar Si-JNTs for NO_2 (red) and NH_3 (blue). Top and bottom row represent device parameters for p and n-type conduction respectively.

The threshold voltage in hole-channel conduction (hole accumulation) shifts to the positive side (decreases) whereas it shifts to the negative direction (increases) in electron-channel conduction upon NO_2 exposures for all the studied Si-JNT devices. Both observations are due to the electron-trapping effect from NO_2[19]. The NO_2 exposure also generates the largest influence on hole mobility in Si-JNTs with native oxide layer.

To demonstrate the sensing performance of the ambipolar Si-JNTs, we tested and compared the interaction of Si-JNTs towards four gases, NO_2, NH_3, CH_4, and SO_2 at a low concentration regime (0.25-2 ppm). Fig. 1c shows the change in two representative JNT parameters (I_{on} and threshold voltage V_{th}) upon exposure to different mixing ratios of NO_2. For the strong oxidative gas NO_2 steady linear increase of on-current on hole-conducting channel (p-type) and decrease in I_{on} on the electron-conducting channel (n-type) was clearly observed (Fig. 1c) at low concentrations. Similarly, the threshold voltage and mobility show change to that of high mixing ratio of NO_2. For p-type transport a more prominent change in V_{th} is observed than change for n-type transport.

In contrast to NO_2, the reductive gas NH_3 causes an inverse response in Si-JNT electrical characteristics, whereas other gases such as SO_2 and CH_4 show significantly low response for each JNT parameters. Under the same conditions, the unipolar devices will only present one type of response. To clearly demonstrate the responsivity of the multiple parameters, a pattern graphic based on the absolute current change value, threshold voltage and carrier mobility for ambipolar devices were extracted for different combination of 4 interfering gases (NO_2, NH_3, SO_2 and CH_4). The significant different response for each JNT parameters easily distinguishes the target analyte, NO2.

In summary, different Si-JNT characteristics including I_{on}, V_{th} and µ have demonstrated dynamic change on both the p- and n- transport channel of the ambipolar JNT towards very low NO_2 concentration, resulting in gate-tunable gas sensing behaviors.

Acknowledgement

This work is funded by the European Union's Horizon 2020 research and innovation program (Grant agreement 899282).

References

[1] Mishra, A.; Basu, S.; Shetti, N. P.; Reddy, K. R., Metal Oxide Nanohybrids-Based Low-Temperature Sensors for NO_2 Detection: A Short Review. *Journal of Materials Science: Materials in Electronics*. Springer New York LLC 2019, pp 8160–8170 (2019); doi: 10.1007/s10854-019-01232-0

[2] X. Chen, C. K. Y. Wong, C. A. Yuan, and G. Zhang, Nanowire-based gas sensors, *Sens Actuators B Chem*, 177, 178–195 (2013); doi: 10.1016/J.SNB.2012.10.134.

[3] J.-P. Colinge *et al.*, Nanowire transistors without junctions, (2010); doi: 10.1038/NNANO.2010.15.

[4] Y. Ren, X. Yang, L. Zhou, J. Y. Mao, S. T. Han, and Y. Zhou, Recent Advances in Ambipolar Transistors for Functional Applications, *Advanced Functional Materials*, Wiley-VCH Verlag, 29 (2019); doi: 10.1002/adfm.201902105.

DOI 10.5162/EUROSENSORSXXXVI/OT5.273

Investigating the Variation of Thermal Conductivity with Temperature to Improve a Portable GC System Specificity

Murielle Jurdit[1], Jean-François Beche[1], Emilie Lefrançois[1], Florence Ricoul[1], Alexandre Teulle[1], Jean-Baptiste Tissot[1]
[1] Université Grenoble Alpes, CEA, LETI, Grenoble, France

Corresponding Author's e-mail address: murielle.jurdit@cea.fr

Summary:
The variation of thermal conductivity with temperature for gaseous species is studied here to investigate if an improvement of the specificity can be achieved with a field TCD-based gas chromatography system. However, theoretical predictions as well as experiments indicate that the necessary local analyte concentrations are by far (two orders of magnitude) beyond the typical concentrations encountered by portable trace analyzers.

Keywords: gas, sensor, thermal, conductivity, detector

Background, Motivation and Objective

In the context of field gas chromatography (GC), a peak might be difficult to identify if two potential components elute at very close retention times. In the case where the sensor is a TCD, we propose to investigate if operating the sensor at different bias voltages could bring some kind of specificity to the portable system.

Description of the System

Thermal Conductivity Detectors (TCD) are universal sensors [1], whose working principle relies on the emergence of a thermal imbalance between membranes located in a reference channel (pure carrier gas) and membranes located in the analytical channel (carrier gas + analyte). The final membrane temperature itself originates from the competition between its heating by Joule effect (supplied electrical power) and its cooling through the surrounding gas (dissipated power via diffusion). Any emergence of a TCD signal is therefore the signature of the presence of a gas with a thermal conductivity λ different from the carrier gas thermal conductivity.

The thermal conductivity of any compound varies as a function of temperature according to its own law $\lambda(T)$, therefore it should be possible to introduce some kind of discrimination when interrogating the gas at different temperatures.

Predictive approach

In the case of a binary gas mixture (trace analyte in a majority carrier gas), the TCD signal will be proportional to the analyte concentration and to the difference of thermal conductivities between analyte and carrier gas (here, Helium). In order to be independent on the concentration, the ratio of the TCD signal S_2 at a bias V_2 (leading to an equilibrium temperature T_2) to the TCD signal S_1 at a bias V_1 (leading to an equilibrium temperature T_1) contains a factor that is characteristic of the analyte A in presence:

$$\frac{S_2}{S_1} \propto \frac{(\lambda_{He} - \lambda_A)_{T_2}}{(\lambda_{He} - \lambda_A)_{T_1}}$$

In the case of neighbor compounds like C_{10} (decane $C_{10}H_{22}$), C_{11} (undecane $C_{11}H_{24}$) and cumene (isopropylbenzene C_9H_{12}), those ratios only differ by 0.3% when applying V_1 = 9V and V_2 = 15V for example. To be able to discriminate between such small differences in the ratios, the impact of the measurement noise (± 5µV taken as a realistic value) has to be negligible, which typically happens when the TCD signals are high, i.e. at high analyte concentrations. This is illustrated by the convergence of curves when the analyte concentration increases locally (see Fig. 1). Only when the analyte concentration exceeds a certain value (red vertical bar), can the compounds be unambiguously discriminated: around 5%vol local concentration at the TCD membranes.

Experimental approach

In order to corroborate the predictive approach, an experimental set-up was implemented (see Fig. 2). In practice, we used two in-house fabricated TCD chips [2] (with a unique membrane design) biased at two different voltages V_1 and V_2 (respectively 3V and 9V), but we could also

have used a unique TCD sensor successively biased at V_1 and V_2.

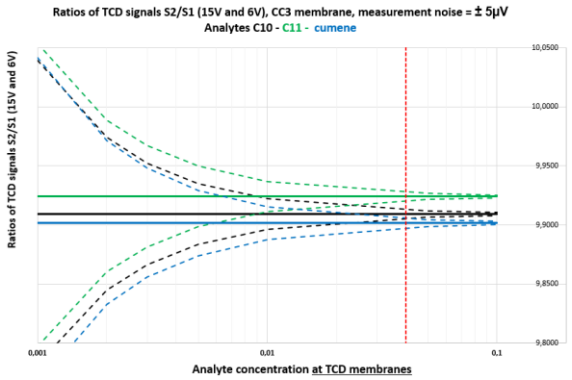

Fig. 1. Graph of predicted ratios of TCD signals (S2/S1) vs analyte local concentration for three different compounds (horizontal lines: theoretical values; dotted lines: when introducing measurement noise).

A gaseous mixture of BTEX (Benzene, Toluene, Ethylbenzene, o-Xylene at 10ppmvol or 500ppbvol) was injected via a rapid desorption of a Silicon pre-concentration chip [3], went through in the TCD reference channels, was separated by a chromatographic column (from Supelco SLB-5ms column, 5m long, ID 0.25µm, phase thickness 0.25mm), and went back in the TCD analysis channels.

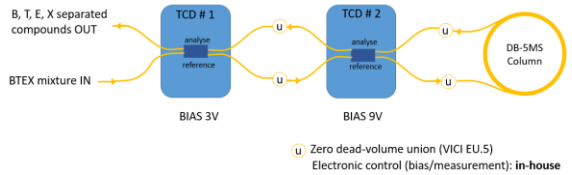

Fig. 2. Outline schematic of the experimental set-up (Silicon pre-concentration chip not represented).

The measurements were repeated several times to get representative statistics. Typical chromatograms are shown in Fig. 3.

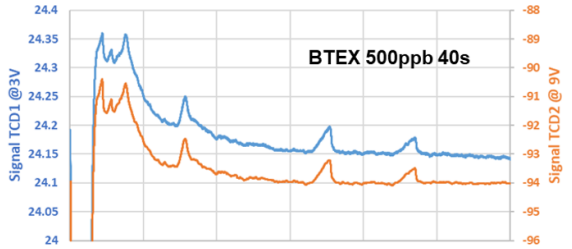

Fig. 3. Typical chromatograms obtained for the BTEX mixture analysis (TCD traces at two different biases 3V and 9V).

The ratios of TCD signals were plotted in Fig.4: the expected tendency is found, i.e. a convergence of the dots distribution (less spreading with increasing local analyte concentration).

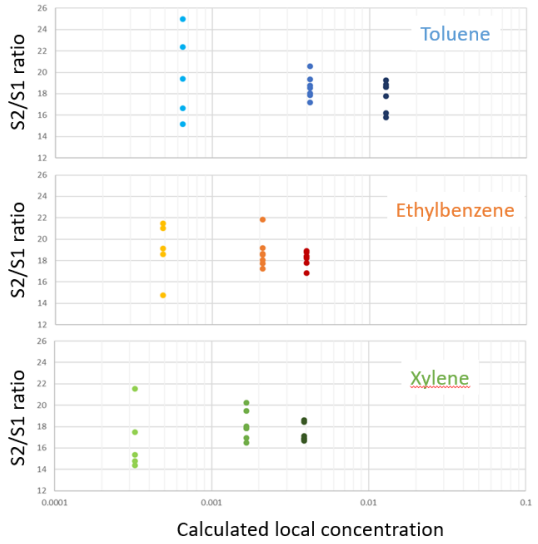

Fig. 4. Experimental ratios of TCD signals (S2/S1) vs analyte local concentration for three different compounds.

However, the measurement uncertainty remains too high to be able to distinguish the components on the only basis of S2/S1 ratios. Furthermore, the investigated concentrations here are beyond the usual scope of trace analysis (local range 300ppm to 1%vol).

Conclusion

In conclusion, it seems that the ratio of TCD signals at two different biases is not relevant for a doubt removal, when a potential identification confusion exists with two compounds eluting at the same retention time, because this approach would require working at high local concentrations (~ 5%vol). This prediction was confirmed experimentally with compounds eluting at distinct times: even at high local concentrations, (300ppm – 1%vol), the double measurement does not allow to clearly identify which compound is eluting, and such values are inadequate for a trace analyzer system.

Acknowledgements

The work was supported by Bertin Technologies, France.

References

[1] B.P. Regmi, M. Agah, *Analytical Chemistry*, 90, 13133-13150 (2018); doi: 10.1021/acs.analchem.8b01461

[2] B. Bourlon, B.A. Pham-Ho, J.F. Beche, O. Constantin, 22nd International Conference on Miniaturized Systems for Chemistry and Life Sciences (MicroTAS 2018)

[3] T.H. Chappuis, B.A. Pham-Ho, M. Ceillier, F. Ricoul, M. Alessio, J.F. Beche, C. Corne, G. Besson, J. Vial, D. Thiebaut, B. Bourlon, *Journal of Breath Research, 12 (4) (*2018); doi:10.1088/1752-7163/aad384

DOI 10.5162/EUROSENSORSXXXVI/OT6.7

Hydrogel-based Sensing Technology for Quantitative Measurements of Low Concentrations of Proteins in the Presence of Interferents

Khalid Haliru[1], Ruchi Gupta[1]
[1] School of Chemistry, University of Birmingham, Birmingham, B15 2TT, UK

r.gupta.3@bham.ac.uk

Summary:
We report a hydrogel-based sensing technology for the measurement of proteins with a limit of detection of 0.003 ppm or 53 pM for an exemplar analyte, streptavidin, while being less laborious than the state-of-the-art method, enzyme-linked immunosorbent assay. Equally, we showed that the presence of high molecular weight interferents such as mucin at 100- and 1000-times higher concentrations than the exemplar analyte did not influence protein measurement.

Keywords: Hydrogel, sensing, pre-concentration, labelling, proteins

Background, Motivation an Objective

Finger-prick blood and saliva can be collected minimally- and non-invasively, respectively, and contain proteins that can serve as diagnostic indicators of diseases [1]. However, such proteins are present in low concentrations particularly in early stages of diseases [1] and hence are difficult to measure. The state-of-the-art method for the measurement of low concentrations of proteins is enzyme-linked immunosorbent assay (ELISA) [2], which is tedious and time-consuming. Our motivation is to develop sensing technologies for accurate, easy, and rapid detection of low concentrations of proteins in biological samples. Our sensing technology is based on a smart hydrogel [3] for protein pre-concentration, fluorescent labelling, and release as shown in Fig. 1. The released proteins can be selectively captured and detected by fluorescence (see Fig. 1). Using our hydrogel-based sensing technology, we can measure at least 0.01 ppm of proteins while being less laborious than ELISA.

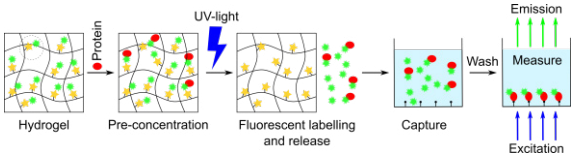

Fig. 1. A schematic showing the use of our hydrogel for pre-concentration, labelling and release of proteins for their selective capture and detection.

Description of the hydrogel

Our hydrogel is a co-polymer of acrylamide/ bis-acrylamide and methacrylamide attached to fluorescein isothiocyanate (FITC) *via* a light-cleavable (nitroveratryl, NVOC) group and a poly(ethylene glycol) (PEG) linker. The chemical structures of the active (FITC-NVOC-PEG_{3400}-methacrylamide) and inactive (acrylamide) monomers and bis-acrylamide crosslinker used to make hydrogels are shown in Fig. 2.

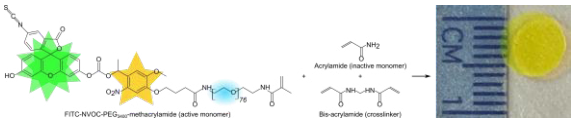

Fig. 2. Chemical structures of monomers and crosslinker used to make our hydrogels.

Herein, we investigated the suitability of our hydrogel-based sensing technology for quantitative measurements of proteins and for detection of proteins of interest (herein, streptavidin) in the presence of interferents, mucin and bovine serum albumin (BSA), found in abundance in saliva and blood samples, respectively.

Methodology

Hydrogel disks (shown in Fig. 2) were formed by APS/TEMED initiated polymerization of 29:1 acrylamide: bis-acrylamide and FITC-NVOC-PEG_{3400}-methacrylamide with a total monomer concentration of 5% (w:v). The molar ratio of FITC-NVOC-PEG_{3400}-methacrylamide and acrylamide monomers was 1 to 40. The hydrogel disks were stored in 10 mM phosphate buffered saline (PBS), pH 7.4 in darkness.

Hydrogel disks were immersed for 24 h in 10 mL solutions of streptavidin in PBS without and with either mucin or BSA. Subsequently, the disks were washed for 24 h in 10 mL PBS, im-

mersed in 200 µL PBS and irradiated with 365 nm light for 60 min to release proteins. The solutions containing released proteins were pipetted in wells of microtiter plates coated with biotin and left for 30 min. Wells were washed with PBS, illuminated with 470 nm light and the fluorescence emission spectra were collected.

To coat each well with biotin, we pipetted 300 µL of 1.5% (w:v) chitosan solution and oven dried at 75 °C for 2 h. We then added 200 µL of 20 mg/ml NHS-PEG-biotin for 3 h, washed with PBS, added 200 µL of 20 mg/ml of NHS-PEG-methyl for 3 h, and washed with PBS.

Results

The fluorescence emission spectra of streptavidin solutions obtained by irradiating hydrogel disks after immersion in different concentrations of the protein solutions are shown in Fig. 3. Fig. 3 confirms that our hydrogel-based sensing technology can allow quantitative measurements of proteins with a limit of detection 0.003 ppm or 53 pM as determined by three times the standard deviation of the intercept divided by the slope of the calibration curve.

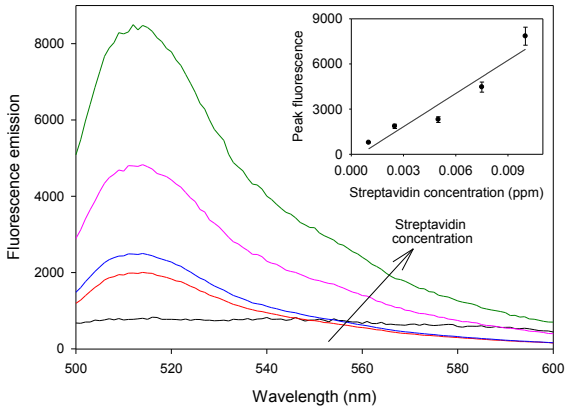

Fig. 3. Fluorescence spectra of solutions containing proteins released from our hydrogels after the hydrogels were immersed in streptavidin solutions of different concentrations for 24 h.

We then immersed the hydrogel disks in 0.005 ppm streptavidin solutions without and with an interferent, mucin. Fig. 4 shows that the presence of 100- and 1000-times more concentrated mucin than streptavidin had minimal effect on the fluorescence signal. This observation can be explained by considering that the molecular weight of streptavidin and monomeric mucin are 66 kDa and 640 kDa, respectively, which would mean that diffusion of mucin into the hydrogel would be much slower than for streptavidin. As a result, the ratio of concentrations of streptavidin to mucin in hydrogel disks would have been much higher than in solutions.

Fig. 5 shows that fluorescence of 1000x BSA was higher than buffer, suggesting that BSA released from hydrogels may non-specifically adsorb to wells of microtiter plates. Equally, Fig. 5 shows that the presence of 1000x BSA in streptavidin solutions reduced the fluorescence signal compared to streptavidin in buffer. This may be because proteins can diffuse and hence would compete for isothiocyanate groups in hydrogel disks. This means less streptavidin would be captured by hydrogel disks, resulting in reduced fluorescence signal.

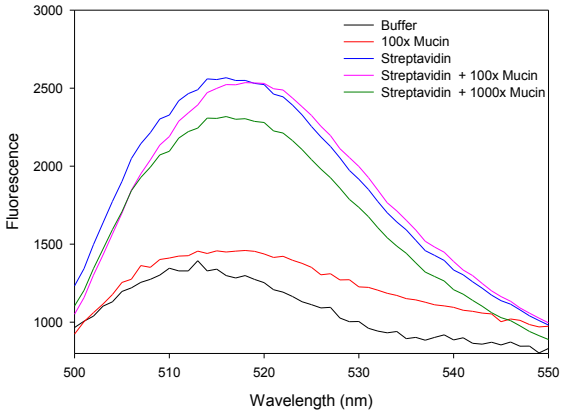

Fig. 4. Fluorescence of solutions containing species released from our hydrogels after immersion in different types of solutions for 24 h.

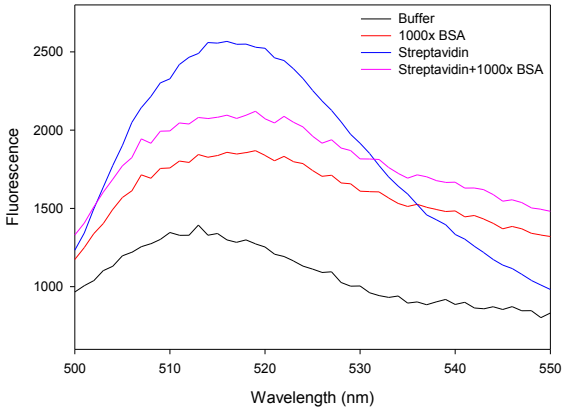

Fig. 5. Fluorescence of solutions containing species released from our hydrogels after immersion in different types of solutions for 24 h.

References

[1] S. Surinova, R. Schiess, R. Huttenhain, F. Cerciello, B. Wollscheid and R. Aebersold, On the Development of Plasma Protein Biomarkers, *Journal of Proteome Research* 10, 5-16 (2011), doi: 10.1021/pr1008515.

[2] S. Aydin, A Short History, Principles, and Types of ELISA, and Our Laboratory Experience with Peptide/ Protein Analyses Using ELISA, *Peptides* 72, 4-15 (2015), doi: 10.1016/j.peptides.2015.04.012.

[3] L. Kellermann, R. Gupta, Photoactive Hydrogels for Pre-concentration, Labelling, and Controlled Release of Proteins, *Analyst* 148, 4127-4137 (2023), doi: 10.1039/D3AN00811H.

DOI 10.5162/EUROSENSORSXXXVI/OT6.15

Microfluidic Rolling Circle Amplification Device for Pathogen Detection in Food Products

Rafaela R. Rosa[1], Ana Margarida Fortes[2], Virginia Chu[1], João Pedro Conde[1,2]
[1]Instituto de Engenharia de Sistemas e Computadores – Microsistemas e Nanotecnologias (INESC-MN), Rua Alves Redol, 1000-029, Lisbon, Portugal
[2]BioISI, Faculdade de Ciências de Lisboa, Universidade de Lisboa, Lisbon, Portugal
[3]Department of Bioengineering, Instituto Superior Técnico, Avenida Rovisco Pais 1049-001, Lisbon, Portugal,

joao.conde@tecnico.ulisboa.pt

Summary:
Due to climate change, infections in plants have become increasingly frequent and damaging. For this reason, methods to provide early detection of infection are crucial to allow for timely treatment to prevent the spread of the infection and to safeguard the crop. In this work, we have developed a microfluidic device to amplify DNA through rolling circle amplification using microbeads as a solid platform to immobilize the DNA. We demonstrate the application of this device towards the detection of *Botrytis cinerea*, a pathogen that has a major impact on several crops.

Keywords: microfluidics, microbeads, rolling circle amplification, agrofood, infections

Introduction

Climate changes are having an immense impact in agriculture, which can lead to the loss of crops due to several factors, such as the increase in infections. This can affect the production of several food products, such as grapes, strawberries and tomatoes. Microbiological infections are present in many food products both at the production stage and in the post-harvest processing. Therefore, having a way of detecting these infections early on and employ the appropriate treatments is key, and the development of a device that can detect these pathogens in a fast, low-cost and sensitive way in the field or at the production site is of extreme importance. To achieve these goals, microfluidics is the ideal platform due to its inherent small size, which allows for low reagent volumes, enhanced assay kinetics and low fabrication costs. Additionally, isothermal DNA amplification, particularly padlock-rolling circle amplification (PLP-RCA), is a powerful tool that allows for a very sensitive and specific detection of pathogens and can easily be integrated into a portable microfluidic device to be used at the point of impact. Given that one of the pathogens that greatly impacts several crops is *Botrytis cinerea* it is the targeted pathogen in this work.

Methods and results

In this work we have successfully captured, quantified and amplified our target DNA in a microfluidic system using microbeads as a solid support system. First, a calibration curve for the fluorescence signal emitted by Alexa430 labelled DNA on Q-Sepharose beads was obtained to be used for the quantification of the capture of target DNA (Fig 1.).

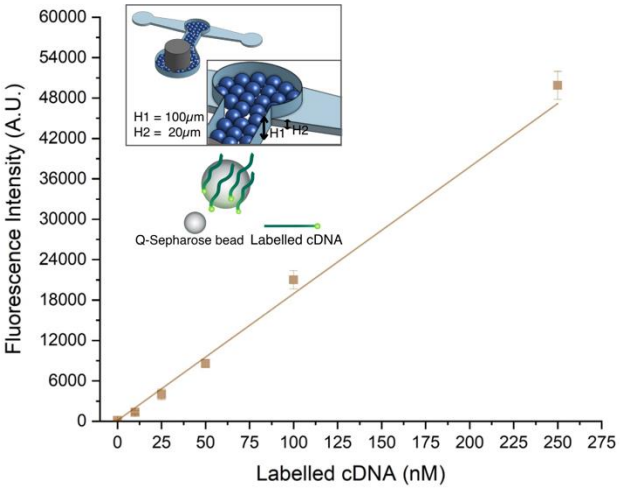

Fig. 1. Calibration curve of the capture of Alexa430 labelled DNA in Q-Sepharose beads.

To evaluate the efficiency and specificity of the PLP, we evaluated two target capture strategies (primer and anchor) with a ssDNA labelled with Alexa430 (Fig 2.). In the primer capture, the biotinylated primer is immobilized on the streptavidin beads followed by hybridization with the back of the PLP, which then circularizes in the presence of the target, which hybridizes with its two ends, if complementary. On the other hand, with the anchor capture, the biotinylated anchor is immobilized on the streptavidin beads followed by

hybridization with a section of the target, then hybridization of the PLP with the target, as in the first strategy. Positive and negative controls for the capture assay were also performed with no biotinylated capture element (primer or anchor) and with a non-complementary labelled DNA, highlighting the specificity of the developed strategies. To assess how much target DNA was captured during the assay, after flowing the labeled ssDNA through the channel with streptavidin beads with previously immobilized anchor or primer and PLP, the solution with the uncaptured target is collected at the outlet and flowed through a second channel with Q-Sepharose beads. From the signal of the labelled cDNA in the Q-Sepharose beads (light blue and green bars in Fig 2.) and using the calibration curve (Fig 1.) and a mass balance strategy, we were then able to calculate how much target DNA was successfully captured, resulting in 87% capture efficiency with the primer capture and 61% with the anchor strategy.

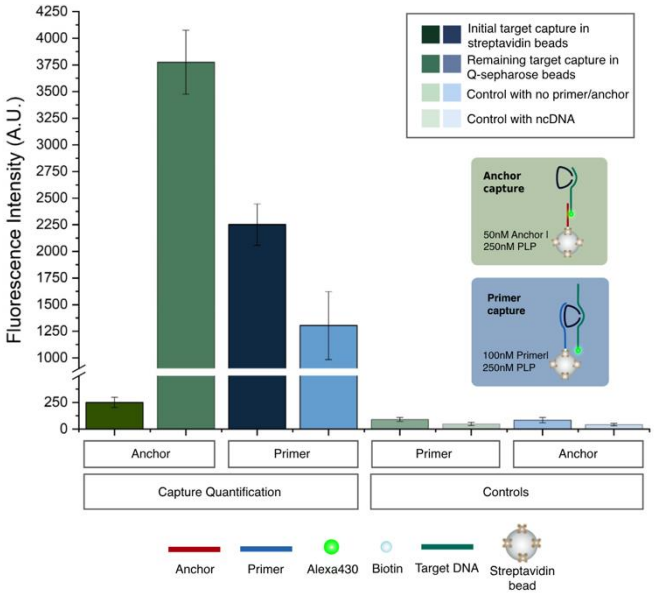

Fig. 2. Target DNA capture and quantification assay for the anchor (in green) and primer capture (in blue) strategy, and respective controls. The capture quantification side of the graphic represents the fluorescence signals obtained in both the streptavidin and Q-Sepharose beads for the capture quantification assay. The controls side of the graphic represents the positive and negative controls.

Lastly, amplification of *Botrytis cinerea* ssDNA (Fig. 3) was also achieved using both target capture strategies (primer and anchor) and RCA, which upon immobilization of the DNA on the microbeads is carried out, by flowing the solutions sequentially. When the PLP hybridizes with the cDNA a gap is left between its two ends which is closed by a DNA ligase. Following the successful ligation, a DNA polymerase with strand displacement activity, carries out the amplification of a long ssDNA strand by going around the PLP multiple rounds. [1] Lastly, the amplification product is detected through the use of oligonucleotides labelled with Alexa430.

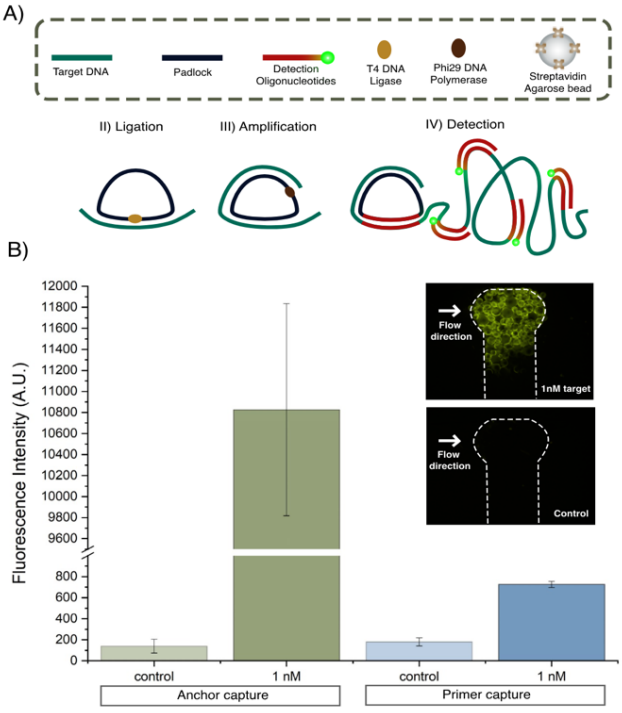

Fig. 3. A) Schematic representation of the RCA assay. B) RCA of Botrytis cinerea ssDNA for both anchor and primer capture strategies, with the controls where no target DNA was flown through the channel with experimental images of the anchor capture positive and control experiments.

Although we were able to successfully detect the target DNA, further optimization will be carried out, to increase the assay sensitivity. A DNA extraction protocol will also be developed and then implemented in the microfluidic device. All of this will allow for pathogen detection upon DNA amplification from real samples, such as grapes.

Acknowledgements

R. Rosa acknowledges FCT for a PhD grant (2022.13021.BD). The authors thank FCT for funding through the project VineSense (PTDC/BAA-DIG/4735/2020) [http://doi.org/10.54499/PTDC/BAA-DIG/4735.INESC MN acknowledges FCT for funding through the Reseach Unit UIDB/0536/2020 and UIDP/0536/2020.

References

[1] R.Soares, N.Madaboosi, M.Nilsson, Rolling Circle Amplification in integrated mycrosystems: An Uncut Gem toward massively multiplexed pathogen diagnostics and genotyping, Accounts of Chemical Research 54, 3979-3990. DOI: 10.1021/acs.accounts.1c00438

DOI 10.5162/EUROSENSORSXXXVI/OT6.79

Development and Characterization of Microfluidic Channels for Chromatography-on-a-Chip Applications

Rodolfo G. Rodrigues[1], Rafael Batista[1], Ana M. Azevedo[2,3], Virginia Chu[1], João Pedro Conde[1,3],

[1] Instituto de Engenharia de Sistemas e Computadores–Microsistemas e Nanotecnologias (INESC MN), Rua Alves Redol, 1000-029 Lisbon, Portugal,
[2] IBB—Institute for Bioengineering and Biosciences, Instituto Superior Técnico, Universidade de Lisboa, 1049-001 Lisboa, Portugal,
[3] Department of Bioengineering, Instituto Superior Técnico, Avenida Rovisco Pais, 1049-001 Lisbon, Portugal

Corresponding Author's e-mail address: joao.conde@tecnico.ulisboa.pt

Summary:

In this work, we designed and fabricated a microfluidic device to perform chromatographic separations. The device consists of a column filled with silica microbeads between smaller height channels working as a frit. To characterize the column efficiency, the breakthrough method was used with a solution of fluorescein isothiocyanate (FITC) in ethanol and by measuring the fluorescence signal. Several mobile phase velocities were tested to obtain retention times and plate heights.

Keywords: Microfluidics, Liquid Chromatography, Cyclic Olefin Copolymer, Breakthrough Curves, Silica Microbeads

Background

Liquid chromatography is a separation technique widely used for the detection of molecules present in complex solutions [1], but it requires trained users in a laboratory and consumes a large quantity of reagents. On the other hand, microfluidics is a technology that has the potential to significantly improve biological and chemical analysis by being inexpensive, portable, and fast [2]. The miniaturization of liquid chromatography using microfluidics combines both technologies but has not been studied in detail. This work aims to develop microfluidic channels for liquid chromatography that can have separation performances comparable to those obtained at macroscale.

Methodology

Computer numerical control (CNC) milling was used directly in cyclic olefin copolymer (COC) plates with a flat endmill with 0.4 mm diameter. The feed rate was maintained at 100 mm/min at 12000 rpm. The device sealing and connections are described elsewhere [2]. Briefly, the machined COC is drilled and sealed against the same type of COC by thermal bonding. After the sealing, PEEK connectors are glued to the device. Silica (SiO_2) microbeads with a diameter between 45 and 75 µm diluted in PEG 8000 30% (w/w) are loaded into the device with the help of a syringe pump. The design used (see Fig. 1) consists of three 1 cm long channels with 100 µm height, and between them are 20 µm height channels to trap the microbeads inside the middle channel.

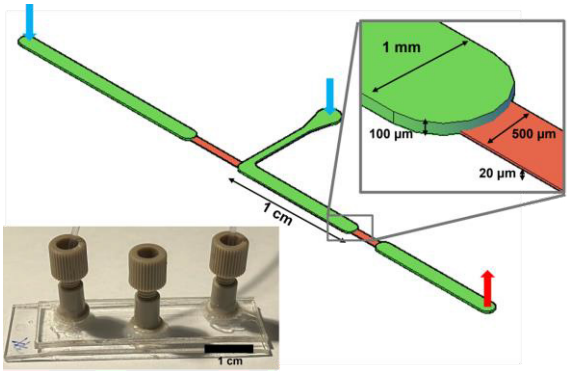

Fig. 1. Schematics of the chip design and a fabricated device in-use.

For breakthrough curve experiments, a solution of 12 µg/mL of fluorescein isothiocyanate (FITC) in ethanol was used, and the signal was acquired by fluorescence and quantified using ImageJ. The solution is flowed into the device at the desired flow, and time zero is taken when the fluorescence solution reaches the beginning of the microbeads. Several flow rates of the mobile phase were tested between 0.5 µL/min and 5 µL/min.

Results

In this device, we have a column of 1 cm in length packed with SiO_2 beads. A simple way to assess the column performance is by using the breakthrough curve method (or frontal chromatography). By performing breakthrough curves, we are observing the concentration of adsorbed analyte as a function of time, expecting the system to be fully saturated at the end of the experiment. In this case, our analyte was the fluorophore FITC, so the increasing adsorption was observed using a fluorescence microscope. In Fig. 2A are represented the breakthrough curves obtained for each flowrate tested (0.5 µL/min, 1 µL/min, 2.5 µL/min, and 5 µL/min).

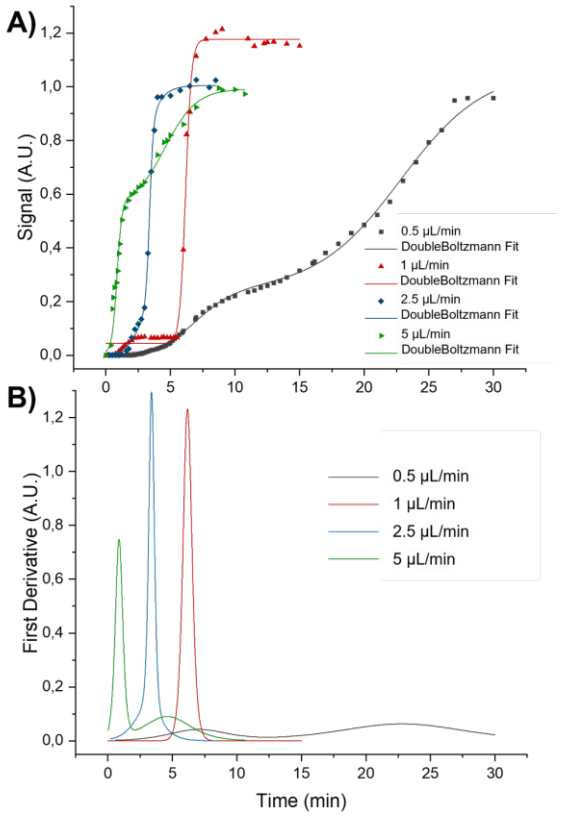

Fig. 2. A) Breakthrough curves and B) First Derivative plotted as a function of time for each flowrate.

To analyze the breakthrough data, the first derivative is calculated to obtain a pulse function, as seen in Fig. 1B. For all flowrates except for the 0.5 µL/min, a clear peak is observed, and as expected, the higher the flowrate, the closer to the origin is the peak. This system shows no retention of the FITC due to chemical interactions with SiO_2 beads, but the flow path is still interrupted by the beads, hence the retention times obtained. As for the 0.5 µL/min condition, the observed behavior may possibly be due to the B term of the van Deemter equation, the axial diffusion. Since the flow rate is lower, the residence time is longer, allowing the FITC to have more time to diffuse longitudinally and perhaps also within the pores. From the peak analysis it is possible to obtain the retention time (R_t) and the full width at half maximum (*FWHM*), and with these values to calculate the number of plates (N) and the plate height (H). At 1 µL/min we obtained 286 plates with a R_t of 6.17 min, resulting in a plate height of 34.99 µm. As expected, the retention time decreased for the other flow rates, being 3.37 min and 0.86 min for 2.5 µL/min and 5 µL/min, respectively, resulting in a decrease of the number of plates and increase of the plate height. For 2.5 µL/min we obtained 180 plates and H = 55.49 µm for 5 µL/min we obtained 9 plates and H = 1081.44 µm.

According to these results, using our microfluidic device we achieved the lowest plate height at 1 µL/min. By normalizing the number of plates, we obtained 28580 plates/m which is close to the range needed for HPLC [3].

Conclusions

Using our microfluidic device with a 1 cm long column and silica microbeads with a diameter between 45 and 75 µm we were able to achieve separation performances near the HPLC range. Increasing column length and decreasing microbead diameter to 5 µm is expected to drastically improve our separation efficiency, allowing us to obtain a device directly comparable to macroscale liquid chromatographic systems.

Acknowledgements

The authors thank the Fundação para a Ciência e a Tecnologia (FCT) for funding through the project VineSense (PTDC/BAA-DIG/4735/2020) [DOI: 10.54499/PTDC/BAA-DIG/4735/2020], the Research Unit INESC MN through the BASE (UIDB/0536/2020) [DOI: 10.54499/UIDB/05367/2020] and PROGRAMTICO (UIDP/0536/2020) [DOI: 10.54499/UIDP/05367/2020] programs, and doctoral grant for R. Rodrigues (2022.14483.BD).

References

[1] Y.I. Yashin, A.Y. Yashin, Chapter 10 – Liquid Chromatography, in *Chemical Analysis of Food: Techniques and Applications*, 285-310 (2012); doi: 10.1016/B978-0-12-384862-8.00010-8

[2] R.G. Rodrigues, P.G.M. Condelipes, R.R. Rosa, V. Chu, J.P. Conde, Scalable Processing of Cyclic Olefin Copolymer (COC) Microfluidic Biochips, *Micromachines* 14, 1837 (2023); doi: 10.3390/mi14101837

[3] S. Moldoveanu, V. David, Selection of the HPLC Method in Chemical Analysis (2017); ISBN: 978-0-12-803684-6

DOI 10.5162/EUROSENSORSXXXVI/OT6.80

Molecular weight measurement of cattle-emitted gases using whistle acoustic signals

Michitaka Yamamoto[1], *Rinka Yoshioka*[1], *Seiichi Takamatsu*[1], *Toshihiro Itoh*[1]
[1] *Department of Precision Engineering, Graduate School of Engineering, The University of Tokyo, 7-3-1 Hongo, Bunkyo-ku 113-8656, Tokyo, Japan*

Corresponding Author's e-mail address: yamamoto-michitaka@g.ecc.u-tokyo.ac.jp

Summary:
We experimentally revealed that the effect of temperature can theoretically be compensated in our proposed measurement method of the molecular weight of gas using whistles. The effect of temperature change on the molecular weight was around 0.03/°C, which is almost consistent with the theory. Furthermore, gas measurement with unknown molecular weight collected from cattle rumen fluid was demonstrated, with a molecular weight resolution of at least less than 1.5.

Keywords: sound and acoustic, gas sensor, molecular weight, Whistle, cattle

Introduction

There has been an increasing demand for simple measurement methods of gases; methane gas emitted by cattle has attracted much attention as a cause of global warming, and a simple method for measuring exhaled gas is required.

Recently, simple gas measurement methods based on acoustic signals have been proposed: the detection of hydrogen leakage by acoustic signals [1] and the detection of oxygen gas concentration [2]. The average molecular weight of gas changes when hydrogen leaks or oxygen concentration changes, which results in the change of sound velocity and resonant frequency of acoustic sound.

We're also developing a new sensing method to measure gas molecular weight using acoustic signals from two whistles [3][4]. Previous studies have demonstrated the basic principles and fundamental experimental results; however, they have not evaluated the impact of temperature [3],[4]. It remains uncertain whether temperature has only a negligible influence on these characteristics, or if other factors, such as changes in the whistle's characteristics with varying temperatures, might also play a role in the observed outcomes. In this paper, we experimentally evaluated the effect of temperature. Furthermore, gas measurement of unknown molecular weight was tested using gases from cattle rumen fluid.

DOI: 10.5162/EUROSENSORSXXXVI/OT6.80

Sensing mechanism [3][4]

The proposed sensing mechanism of gas molecular weight using whistles is shown in Fig. 1. The fundamental frequency *f* when gas flows into the whistle can be expressed by the following:

$$f = a\sqrt{\frac{kRT}{M}} + bQ + c \qquad (1)$$

where *M*, *Q*, and *T* are the molecular weight, flow rate, and temperature of the gas, respectively, and *k* and *R* are the specific heat ratio and gas constant. The *a* is a whistle-specific constant, and the *b* and *c* are constants determined by the type and combination of whistles. The gas's molecular weight and flow rate can be calculated from each whistle's multiple frequency measurement results.

From above equation, changes in temperature are expected to be theoretically calculated. However, temperature *T* may affect the specific heat ratio *K* and the properties of the whistles themselves and cause further errors. Therefore, we will attempt to evaluate the experimental effect of temperature *T* on this study.

Experiment methods

The shapes of the whistles used in this study are shown in Fig. 2. Two whistles with different sizes

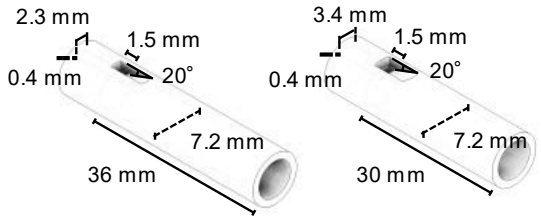

(a) *(b)*

Fig. 2. The images of the used two whistles. (a) Whistle 1, (b) Whistle 2.

were fabricated by a 3D printer (Keyence Corporation, Agilista) using acrylic UV curable resin (Keyence Corporation, AR-M2).

The frequency shift by temperature was evaluated by inserting two types of gases (N_2: molecular weight 28 and CO_2: molecular weight 44) with different temperatures from 22 to 28°C to each whistle. The sounds generated by the whistles were measured by a microphone (Ono Sokki Co., Ltd., MI-1271), and fundamental frequency was obtained.

As a demonstration, we also attempted to gas measurement of unknown molecular weight. With cattle breath analysis in mind, the molecular weight of the gas generated from cattle rumen fluid was collected and measured using the proposed method. For reference, the gas was also measured by using gas chromatograph (SHIMADZU CORPORATION, GC-2014) to know the actual molecular weight.

Experimental results

Figure 3 shows the effect of the temperature on each whistle in the case of measuring N_2 gas. It shows that the frequency is almost linear with the change in temperature, meaning that the effect of temperature is expected to be theoretically calculated. Because the experiment was conducted using plastic materials, which are considered susceptible to thermal effects, it seems that there is a theoretical possibility of compensating for temperature.

Noted that a change of 1 °C in temperature (which corresponds to an approximate 0.03 change in sqrt(T)) means that the frequency changes by 2-3 Hz/°C. It corresponds to the molecular weight change of around 0.03/°C, almost consistent with the theory. Though improvement of the accuracy to the molecular weight is the first requirement because it is still around 0.45 [4], theoretical temperature compensation is needed for accuracy measurement in the future

Figure 4 shows the measurement result of unknown gas generated from rumen liquid. The molecular weight error was at least less than 1.5. We intend to enhance the sensitivity further by refining the whistle in future experiments.

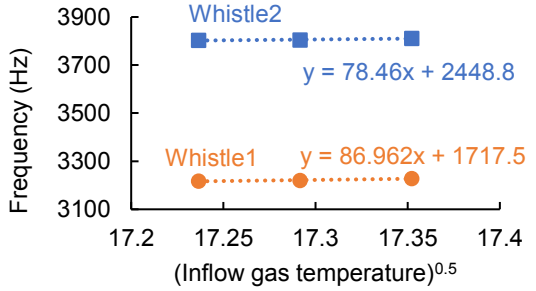

Fig. 3. Effect of temperature on the fundamental frequency of each whistle in case of N_2 gas.

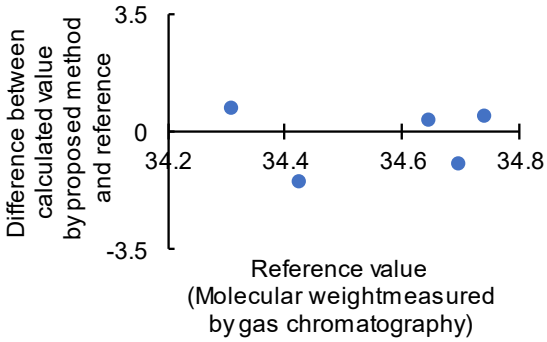

Fig. 4. The measurement result of unknown gas collected from rumen liquid.

Conclusions

We revealed that the effect of temperature can theoretically compensated in the proposed measurement method of the molecular weight of gas using whistles. The effect of temperature on the molecular weight was around 0.03/°C, which almost consistent with the theory. Furthermore, measurement of gas with unknown molecular weight was demonstrated, and the molecular weight resolution was at least less than 1.5. Noted that the sensitivity could be further improved by improving the measurement system and the whistle.

Acknowledgments

We appreciate Prof. S. Koike at Hokkaido University for his support. Part of this work was supported by JSPS KAKENHI Grant Number JP22K18778 and the Precise Measurement Technology Promotion Foundation.

References

[1] T. Okubo, S. Kijimoto, K. Matsuda and Y. Koba, *The Japan Society of Mechanical Enginerrs*, 75, no. 752, 912-918 (2009). (in Japanase)

[2] J. Wang, M. Chen, Q. Chen, H. Wang, *IEEE Sensors Journal*, 22, no. 21, 21281-21286 (2022).

[3] R. Yoshioka, M. Yamamoto, S. Takamatsu, T. Itoh, Proceedings in *2023 IEEE SENSORS*, Vienna, Austria, 1-4 (2023).

[4] R. Yoshioka, M. Yamamoto, S. Takamatsu, T. Itoh, *IEEJ Transactions on Sensors and Micromachines*, Accepted. (in Japanese)

DOI 10.5162/EUROSENSORSXXXVI/OT6.85

Plant on a Chip: Paper Fluidics for Spatio-Temporal Root Exudate Analysis

Daniel Patko[1,], Sepideh Izaddoust[1,2], Lionel X. Dupuy[3,4], Lourdes Basabe-Desmonts[2,4] and Fernando Benito-Lopez[1,*]*

[1]Microfluidics Cluster UPV/EHU, Analytical Microsystems & Materials for Lab-on-a-Chip Group, Analytical Chemistry Department, University of the Basque Country UPV/EHU, Leioa, Spain

[2]Microfluidics Cluster UPV/EHU, BIOMICs microfluidics Group, Lascaray Research Center, University of the Basque Country UPV/EHU, Vitoria-Gasteiz, Spain

[3]NEIKER, Derio, Spain

[4]IKERBASQUE, Basque Foundation for Science, Bilbao, Spain

*daniel.patko@gmail.com, fernando.benito@ehu.eus

Summary:

In order to develop a sustainable agriculture it is essential to use natural processes. Root exudates can attract beneficial microbes, increase the nutrient uptake from the soil and they can be a good indicator of the plant's stress responses. Unfortunately, the commonly used exudate collection methods cannot provide spatially and temporally detailed information. We developed a novel, wax patterned paper based microfluidic system to extract root exudates spatially and temporally. Using an integrated colorimetric glucose sensor we could reveal phenotypic differences between wheat varieties.

Keywords: Plant-on-a-chip, Paper-fluidics, Root exudates, Wax printing, Colorimetric detection

Background, Motivation and Objective

Our modern agriculture is far from being sustainable. A huge amount of the applied agrochemicals, such as fertilisers, leach into the environment [1,2] making an economic loss and an environmental damage. Using natural processes, like microbial interactions can address this challenge.

Soil microbiota has an undeniable role in the life of a plant. Microbes can increase its stress resilience or improve its nutrient uptake [3] . Using these interactions as plant fertilizers can decrease the ecological impact of agriculture, however we lack of essential knowledge regarding the nature of these processes. It is known that plants exude a wide range of molecules, such as sugars, to attract beneficial microorganisms [3,4], but the time dependency of this process is unknown, especially on single plant level.

The traditional way to detect root exudates is a labour active, time-consuming process, including purification steps and it requires trained personnel and a growth facility for the plants [5].

We developed an easy to use, cost-effective, modular, wax printed paper-based microfluidic system to overcome the above mentioned limitations (Figure 1). The developed chip is able to extract root exudates from a defined part of the root system, and able to follow the exudation changes over time. Moreover, it is possible to follow these changes on the single plant level.

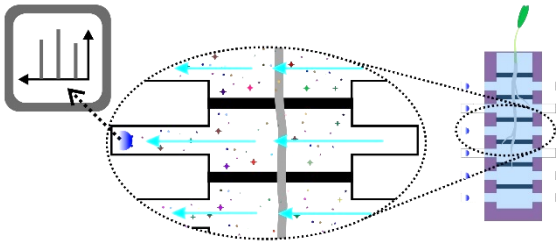

Figure 1: Scheme of the developed paper based microfluidic system for the investigation of root exudates. The exuded molecules can be delivered to the sensors using a flow generated by evaporation. The different root segments can be analyzed individually over time.

Description of the new System

The developed microfluidic system consists of a wax printed filter paper, a microscope slide and a polydimethylsiloxane (PDMS) slide. The wax is melted into the fiber structure of the filter paper creating hydrophobic barriers forming horizontal channels in parallel (Figure 2). The paper is also the growth substrate for the plant. For the experiments, as a relevant crop, we used wheat (*Triticum aestivum*).

An integrated a colorimetric TiO_2-alginate hydrogel based glucose sensor, developed by us [6],

was integrated at the outlet part of the paper channels to detect the exuded glucose by the plant root (Figure 2 right, picture).

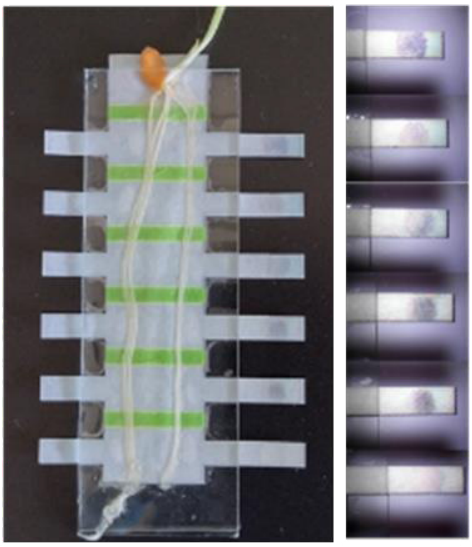

Figure 2. Picture of the microfluidic system with integrated glucose sensors (left) and magnified image of the sensors after exudate extraction (right). The colorimetric TiO_2-alginate hydrogel based glucose sensor clearly shows different colour intensities at different positions of the root.

Results

Using the developed patterned paper based microfluidic system the exuded glucose, by the root system, was detected and, along the root, we could capture the intensity differences in exudation. Moreover, glucose concentrations were determined colorimetrically and it was possible to differentiate between the exudation activity at different positions of root (Figure 3.).

Our method was capable to show, that the exudation starts at the top part of the root and with ageing, the younger parts are getting active too.

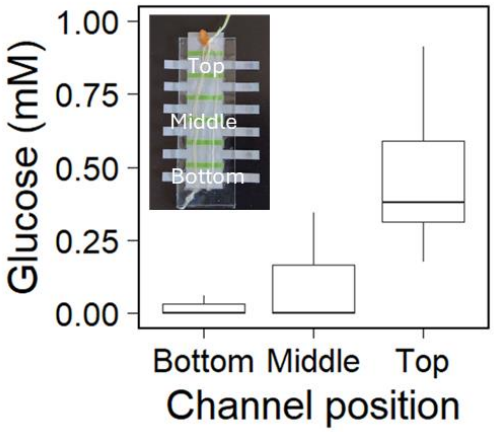

Figure 3. Graph presenting the produced amount of glucose during the 7 days of observation at different parts of the root system.

Acknowledgements

This work was supported by the European Commission's EXCELLENT SCIENCE - Marie Skłodowska-Curie Actions program, RhizoSheet MSCAIF, grant agreement number: 101028242. The "Ministerio de Ciencia y Educación de España" paña" under grant PID2020-120313GB-I00/AIE/10.13039/501100011033 y por FEDER una manerade hacer Europa, the Basque Government (Grant IT1633-22) and Proyecto de Investigación Fundamental Colaborativa – Investigación Fundamental ELKARTEK: KK-2023/0007.

References

[1] N. Beaudoin, J.K. Saad, C. Van Laethem, J.M. Machet, J. Maucorps, B. Mary, Nitrate leaching in intensive agriculture in Northern France: Effect of farming practices, soils and crop rotations, Agric Ecosyst Environ 111 (2005) 292–310. https://doi.org/10.1016/j.agee.2005.06.006.

[2] S. Delin, M. Stenberg, Effect of nitrogen fertilization on nitrate leaching in relation to grain yield response on loamy sand in Sweden, European Journal of Agronomy 52 (2014) 291–296. https://doi.org/10.1016/j.eja.2013.08.007.

[3] S.A. Rolfe, J. Griffiths, J. Ton, Crying out for help with root exudates: adaptive mechanisms by which stressed plants assemble health-promoting soil microbiomes, Curr Opin Microbiol 49 (2019) 73–82. https://doi.org/10.1016/j.mib.2019.10.003.

[4] J. Sasse, E. Martinoia, T. Northen, Feed Your Friends: Do Plant Exudates Shape the Root Microbiome?, Trends Plant Sci 23 (2018) 25–41. https://doi.org/10.1016/j.tplants.2017.09.003.

[5] A. Williams, H. Langridge, A.L. Straathof, G. Fox, H. Muhammadali, K.A. Hollywood, Y. Xu, R. Goodacre, F.T. de Vries, Comparing root exudate collection techniques: An improved hybrid method, Soil Biol Biochem 161 (2021) 108391. https://doi.org/10.1016/j.soilbio.2021.108391.

[6] U.B. Gunatilake, S. Garcia-Rey, E. Ojeda, L. Basabe-Desmonts, F. Benito-Lopez, TiO2Nanotubes Alginate Hydrogel Scaffold for Rapid Sensing of Sweat Biomarkers: Lactate and Glucose, ACS Appl Mater Interfaces 13 (2021) 37734–37745. https://doi.org/10.1021/acsami.1c11446.

DOI 10.5162/EUROSENSORSXXXVI/OT6.89

Fabrication of Nanochannels with Funnel-like Inlet Structures for the Analysis of Single DNA Molecules

Nicole Hintz[1,2], Christopher Johnson[3], Martina Hübner[1]
[1] Robert Bosch GmbH, Robert-Bosch-Campus 1, Renningen, Germany
[2] Institute for Microsensors, -actuators and -systems (IMSAS), Otto-Hahn-Allee 1, Bremen, Germany
[3] Robert Bosch LCC, 384 Santa Trinita Avenue, Sunnyvale, Ca, USA

E-mail address: nicole.hintz@de.bosch.com

Summary:
A new fabrication method for realizing fluidic nanochannels with funnel-like inlet structures in silicon technology is presented. Nanochannels are a useful tool for DNA analysis since the molecules must first be linearized to enter the nanochannels and the linearization is a prerequisite for DNA mapping or sequencing. Inlet structures, like funnels, help guiding the DNA and bringing it into the channels. The nanochannels demonstrated in this work are realized using standard MEMS processes and photolithography, enabling cheap and scalable production for a wide range of biotechnology applications.

Keywords: Nanochannel, Inlet structure, Funnel, MEMS Fabrication, DNA Analysis

Background and Motivation

Micro-biosensors bring many benefits through their miniaturization [1]. Micro- and nanoscale features allow manipulation of single cells or even molecules and the integration of their analysis on lab-on-chip systems. The sequencing and mapping of single DNA molecules is made possible by the linearization of single DNA molecules inside of a nanochannel [2]. When the dimensions of a structure are smaller than the persistence length of DNA, the DNA is forced to extend instead of the entropically-favorable coiled state, as sketched in figure 1. The negatively charged DNA can be pulled into a nanochannel by an electric field. Nevertheless, inserting the DNA into the channels is challenging. To change its conformation from coiled to linear the so-called entropic barrier has to be overcome [3].

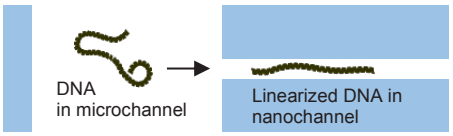

Fig. 1. Schematic of linearized DNA inserted into a nanochannel

Adding a funnel-like inlet to the nanochannel creates a gradient between the volume in front of the nanochannel and the channel itself, which makes the overcoming of the entropic barrier easier and lowers the needed electrical force [3]. A funneled inlet can also increase the capture rate of molecules in the channel and avoid hairpin formation and clogging of nanochannels [2,4].

Therefore, creating nanochannels with funnel-inlets with a cheap and scalable process is vital for the fabrication of DNA analysis systems. However, the fabrication of nanostructures poses challenges. Since the standard fabrication processes for microsystems are limited by the wavelength of the light used for photolithography structures smaller than 1 µm are difficult to achieve. There are methods to overcome this, like deep-UV lithography or electron beam lithography. A different method is focused ion beam milling (FIB) to directly create the nanostructures or a stamp to use in nanoimprint lithography (NIL). These mentioned methods are expensive and often not scalable [1]. To circumvent these expensive methods and the limit of photolithography, certain workarounds can be used to create nanostructures only with standard fabrication processes. For example, nanochannels can be fabricated by thin-film evaporation and etching of a sacrificial layer [5]. But the addition of funnel inlet structure to the channels is only reported in systems fabricated with NIL or FIB [2,3,4], and not for structures fabricated using only standard processes. Such a process was investigated for the first time and will be discussed here.

Description of the New Fabrication Method

The fabrication of long nanochannels with horizontal funnel-shaped inlet structures to facilitate the analysis of DNA molecules is shown schematically in Figure 2. The nanochannel is

created by selectively under-etching a sacrificial layer under a top layer. Therefore, the channel dimensions depend on the thickness of the sacrificial layer and the under etch time. The channel is then closed by a capping layer. Microchannels, that contact the nanochannels, are etched with an anisotropic process. To fabricate the funnel-shaped inlets of the channels, an additional etch step is added, which etches the material next to the nanochannel faster at the entrance than the inside of the channel. This step creates a horizontal funnel inlet.

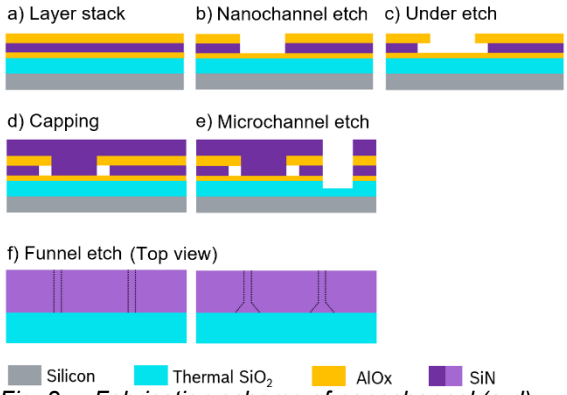

Fig. 2. Fabrication scheme of nanochannel (a-d), microchannel (e) and funnel-inlet (f).

Results

Nanochannels with a length of 50 µm have been fabricated, but channels with lengths up to several millimeters are possible with this fabrication method since the length is not the limiting factor in the fabrication. A cross section of a channel with a width of 250 nm and a height of 40 nm is displayed in figure 3.

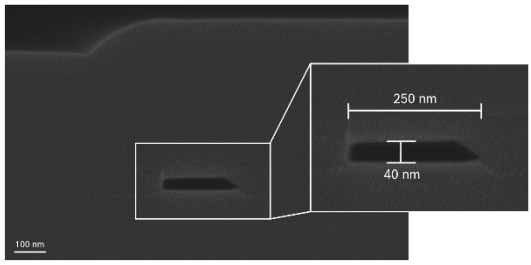

Fig. 3. Electron microscope picture of a nanochannel cross section with its dimensions.

The existence of a continuous nanochannel can be demonstrated with the help of a fluorescent solution. The solution is introduced in the upper microchannel, then fills the nanochannels by capillary forces and reaches the lower microchannel (see figure 4).

Different funnel inlet sizes can be created by varying the duration of etch step, with the funnel inlet getting larger and the angle shallower with increasing time, as seen in figure 5. The inlet size widens from roughly 200 nm nanochannel width to 1 µm. The influence of other parameters of the etch step on the funnel shape, like

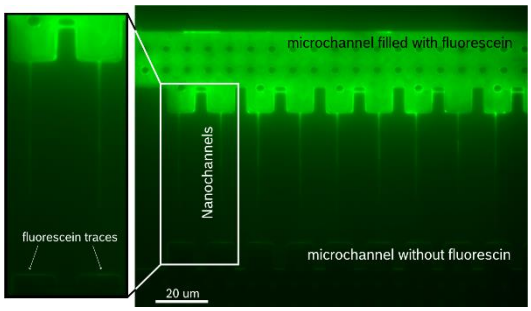

Fig. 4. Picture of a microchannel with several nanochannels. The fluorescein solution added in the upper microchannel got through the nanochannels into the lower microchannel.

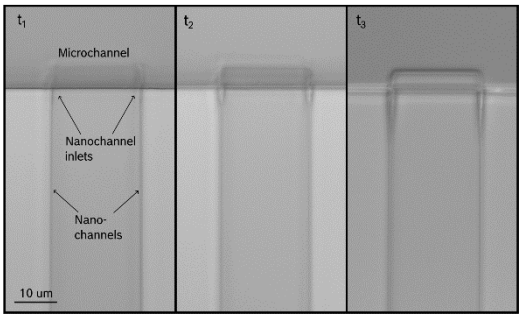

Fig. 5. Picture of funnel inlet shapes after different etching times ($t_1 < t_2 < t_3$).

pressure and flow rate of the etchant will be tested to create inlets with arbitrary shapes.

In conclusion, it can be said that nanochannels with inlet structures of different sizes have been successfully fabricated. The size of the inlets can be varied by the duration of the etch step. Inlet sizes of 1 µm have been created for a 200 nm wide channel.

This work was supported by BMBF FKZ 03ZU1208BH: nanodiag BW.

References

[1] J. O. Tegenfeldt *et al.*, Micro- and nanofluidics for DNA analysis, *Anal. Bioanal. Chem.* 378 (7), 1678–1692, (2004), doi: 10.1007/s00216-004-2526-0

[2] J. Wu *et al.*, Engineering inlet structures to enhance DNA capture into nanochannels in a polymer nanofluidic device produced via nanoimprint lithography, *Micro Nano Eng.* 21 (2023), doi: 10.1016/j.mne.2023.100230

[3] J. Zhou *et al.*, Enhanced nanochannel translocation and localization of genomic DNA molecules using three-dimensional nanofunnels, *Nat. Commun.* 8 (2017), doi: 10.1038/s41467-017-00951-4

[4] F. M. Esmek *et al.*, Sculpturing wafer-scale nanofluidic devices for DNA single molecule analysis, *Nanoscale* 11, 13620–13631 (2019), doi: 10.1039/C9NR02979F

[5] H. T. Hoang *et al.*, Wafer-scale thin encapsulated two-dimensional nanochannels and its application toward visualization of single molecules, *J. Colloid Interface Sci.* 367, 455–459, (2012), doi: 10.1016/j.jcis.2011.10.00

DOI 10.5162/EUROSENSORSXXXVI/OT6.97

Electroporation Monitoring by Machine Learning and Single Cell Morphodynamic on Lab-on-Chip

Gianni Antonelli[1], Francesca Camera[2], Arianna Mencattini[1], Arianna Casciati[2], Mirella Tanori[2], Alessandro Zambotti[2], Giorgia Curci[1], Joanna Filippi[1], Michele D'Orazio[1], Paola Casti[1], Caterina Merla[2], Eugenio Martinelli[1]

[1] Department of Electronic Engineering & Interdisciplinary Center for Advanced Studies on Lab-on-Chip and Organ on-Chip Applications, University of Rome Tor Vergata; Via del Politecnico,1; Rome (Italy)

[2] Division of Health Protection Technologies, Italian National Agency for Energy, New Technologies and Sustainable Economic Development (ENEA); Via Anguillarese, 301; Rome (Italy)

Corresponding Author's e-mail address: g.antonelli@ing.uniroma2.it

Summary:

Electroporation is a reliable, reproducible technique to induce biological cell membrane poration. Because of the biological and clinical interest in this technique, recently, many Lab-On-Chip platforms have been proposed to understand more about deep electroporation mechanisms. This led to the discovery of many electroporation side effects, such as cell contractivity and blebbing. In this work, we propose a new sensing system based on Lab-On-Chip and machine learning to correlate these side effects observed by brightfield time-lapse microscopy with electroporation efficiency.

Keywords: Electroporation, Lab-On-Chip, Machine Learning, Time-Lapse Microscopy,

Background, Motivation and Objective

Since its discovery in 1968, electroporation spread its applicability in biological and clinical research [1]. Delivering high electric fields on a biological tissue for short periods, usually nanoseconds or microseconds, permits the generations of nanopores on cells. Changing these parameters guarantees great flexibility of the technique in multiple applications, spanning electrochemotherapy, cell lysis, fusion, or bacteria inactivation.

Even though electroporation has been known for a long time, its inner mechanisms are still under study. For example, from the morphological point of view, it was discovered that cells react to the electric field application by contracting and blebbing [2].

These findings were significantly made possible by the slight transition in studying these phenomena from classical biological support (e.g., culture dishes) to Lab-On-Chip platforms, which allow the set-up of more complex experiments in a minimal environment.

Information extracted from these devices can sometimes be challenging to analyze without using more complex models, such as machine learning algorithms. Particularly in microscopy image analysis, these models permit extracting hidden features and intricate trends that are impossible to catch quantitatively by hand.

In this work, we present a sensing system based on a low-cost Lab-On-Chip platform able to correlate the electroporation efficiency with its side effects by applying a tailored machine learning algorithm on brightfield time-lapse microscopy images.

Method description

A Lab-On-Chip based on transferred Laser-Induced-Graphene (LIG) was designed and fabricated using a technique we recently proposed [3]. Briefly, LIG electrodes are first generated by laser scribing a polyimide sheet. Then, the printed geometries are transferred to a transparent, biocompatible PMMA substrate by surface solubilization.

The chip exhibited six pairs of interdigitated electrodes with different pitches, used to stimulate the U-87 glioblastoma cell line with several voltages and electric fields (Fig. 1). During the stimulation, fluorescence and brightfield time-lapse microscopy monitored calcium intake and cell contractility, respectively.

A custom machine-learning algorithm based on Particle Image Velocimetry (PIV) and cell segmentation computed single-cell contractivity and

internal calcium quantity tracking during the time-lapse [4].

Finally, the extrapolated peaks of cumulative velocity were thresholded and used to estimate the electroporation efficiency in the acquired frame. Similarly, we used the detected calcium intake spikes as the ground truth, calculating the real electroporation efficiency.

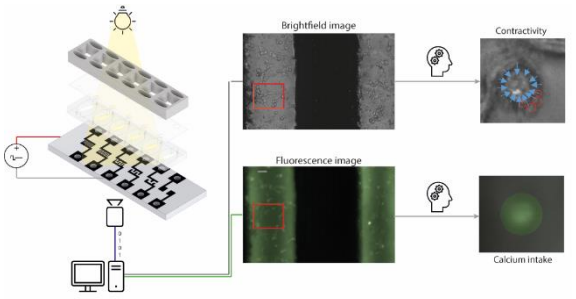

Fig.1. A Lab-On-Chip is designed to have six different interdigitated electrodes and separated chambers for cell culture. Each electrode pair is connected to a high-voltage pulse generator. Fluorescence and brightfield time-lapse microscopy are acquired at the same time. Each time-lapse frame is then analyzed using a tailored machine, computing cell contractivity and calcium intake.

Results

To better understand the behaviour of cell culture after electroporation, it was necessary to study cell movements and calcium presence before the stimulus. As expected, cells exhibited an independent movement, which was necessary to subtract from the one induced by the electric field application. Moreover, U-87 cells were demonstrated to contain a significant amount of calcium ions in their cytoplasm also before the poration stimulus.

Once the pulsed electric field was applied, cells started to contract and bleb, generating a peak in contraction detected by PIV. Calcium diffusion was observed to be almost instantaneous, while cell contractivity follows a second-scale dynamic. Moreover, as expected, the beginning of cell contractivity perfectly correlates with the fluorescence peak induced by calcium intake caused by cell poration (Fig. 2a).

Finally, velocity and fluorescence peaks from single cells were then separately thresholded and used to compute the electroporation efficiency of the experiment. As can be evinced from Fig. 2b, there is an almost complete correspondence between the efficiency computed by fluorescence and the one calculated from contraction ($R^2 = 0.931$ around the bisector). Moreover, these results were obtained by aggregating data from different electrodes and electric fields. This indicates that our sensing system can predict electroporation from brightfield time-lapse microscopy without additional fluorescent channels independent of the experimental conditions.

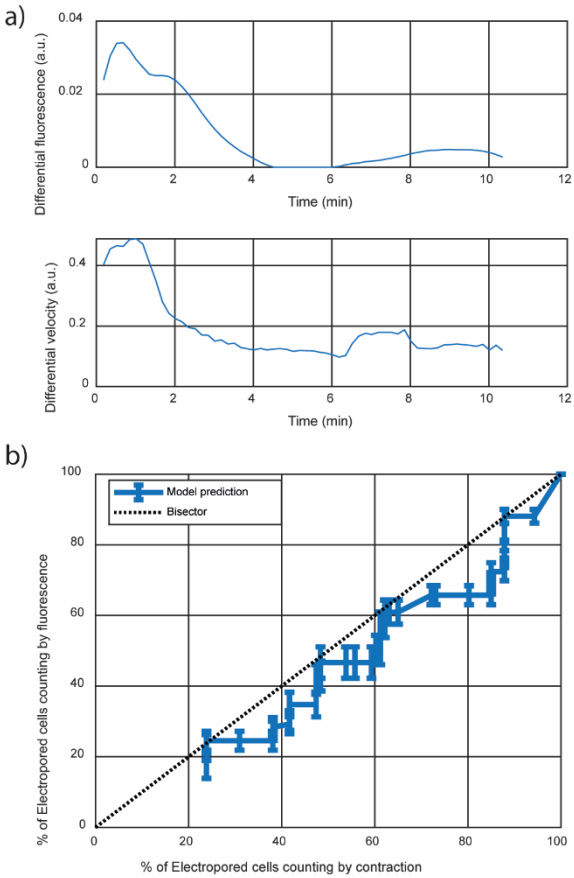

Fig 2. a) Fluorescence intensities from single cells during the time-lapse experiments are compared with the contractivity velocity calculated by PIV analysis. b) Average fluorescence intensity is correlated with the peak velocity. Cell population heterogeneity and different electrode geometries contribute to performance variability.

References

[1] T. F. Justesen, A. Orhan, H. Raskov, C. Nolsoe, and I. Gögenur, “Electroporation and Immunotherapy—Unleashing the Abscopal Effect,” *Cancers 2022, Vol. 14, Page 2876*, vol. 14, no. 12, p. 2876, Jun. 2022, doi: 10.3390/CANCERS14122876.

[2] P. M. Graybill, A. Jana, R. K. Kapania, A. S. Nain, and R. V. Davalos, “Single Cell Forces after Electroporation,” *ACS Nano*, vol. 15, no. 2, pp. 2554–2568, Feb. 2021, doi: 10.1021/ACSNANO.0C07020.

[3] G. Antonelli *et al.*, “Laser-Induced Graphene Wet Transfer Technique for Lab-On-Chip Applications,” Submitted

[4] G. Antonelli *et al.*, “A Lab-On-Chip sensing system for electroporation based on brightfield time-lapse,” Submitted

DOI 10.5162/EUROSENSORSXXXVI/OT6.111

DEVELOPMENT OF AN ISFET-BASED SYSTEM FOR GENETIC DETECTION OF LEUKEMIA ONCOGENE

Léony S. Oliveira[1], Norma Lucena-Silva[2], Marie Hangouët[3], Cesar A.S. Andrade[4], Maria D.L. Oliveira[4], Joan Bausells[5], Norman Pfeiffer[6], Nadia Zine[3], Abdelhamid Errachid[3]

[1] Programa de Pós-Graduação em Inovação Terapêutica, Universidade Federal de Pernambuco, 50670-901 Recife, PE, Brazil,

[2] Instituto Aggeu Magalhães, Fundação Oswaldo Cruz (Fiocruz), 50670-420 Recife, PE, Brazil. Laboratório de Biologia Molecular, Departamento de Oncologia Pediátrica, Instituto de Medicina Integral Professor Fernando Figueira (IMIP), 50070-550 Recife, PE, Brazil.

[3] Institute of Analytical Sciences (ISA) – UMR 5280, French National Center for Scientific Research (CNRS), 69100, Lyon, France.

[4] Laboratório de Biodispositivos Nanoestruturados, Departamento de Bioquímica, Universidade Federal de Pernambuco, 50670-901 Recife, PE, Brazil

[5] Fraunhofer IIS, Fraunhofer Institute for Integrated Circuits IIS, Am Wolfsmantel 33, Erlangen, 91058, Germany.

[6] Instituto de Microelectrónica de Barcelona (IMB-CNM,CSIC), Campus UAB, 08193 Bellaterra, Spain.

Corresponding Author's e-mail address: leony.oliveira@ufpe.br, abdelhamid.errachid-el-salhi@univ-lyon1.fr

Summary:

A Point-of-care device was developed using Ion-selective field-effect transistors (ISFETs) for real-time detection of molecular targets, eliminating the requirement for a highly controlled environment. This device successfully detected the translocation between chromosomes 12 and 21 (t(12;21)), which is one of the most common mutations associated with childhood acute lymphoblastic leukemia (ALL).

Keywords: ISFET, leukemia, point-of-care, potenciometry, genosensor.

Title

Development of an isfet-based system for genetic detection of leukemia oncogene.

Introduction

Acute lymphoblastic leukemia (ALL) is the most common childhood cancer, accounting for approximately 25% of cancer diagnoses. Accurate determination of the genetic mutations associated with leukemia is crucial for patient prognosis. One of the most recurrent mutations in ALL is the translocation between chromosomes 12 and 21 (t (12;21)) [1]. Current genetic diagnostic methods, such as fluorescence in situ hybridization (FISH) and reverse transcription quantitative polymerase chain reaction (RT-qPCR), are efficient in detecting these mutations. However, they often require lengthy experimental protocols and a highly controlled laboratory environment [2]. In contrast, point-of-care devices enable real-time detection of molecular targets without the need for a highly controlled environment. Ion-selective field-effect transistors (ISFETs) are miniaturized devices that can be utilized for genetic analysis through the hybridization of complementary DNA sequences [3].

Objective

In this study, we developed an ISFET-based system for the detection of t (12;21) in the pediatric population.

Methods

Therefore, the ISFET system was used for the detection of genetic markers in childhood ALL that had never been studied before in biosensors field (Fig.1a). For this The ISFET was initially characterized using different pH buffers to assess its ionic selectivity. Subsequently, the ISFET was coated with a layer of TESUD, and a specific DNA probe for t (12;21) was immobilized on its surface. The biorecognition process was evaluated through hybridization tests with plasmid samples at various concentrations. Potentiometry was employed to characterize all steps of the process.

Results and Discussion

The ISFET exhibited a decrease in drain-to-source current (I_{DS}) plateau with an increase in

pH (Fig.1b). In addition, the threshold potential (V_T) increased with higher pH levels, indicating the system's sensitivity to ion concentration (Fig.1c) [3].

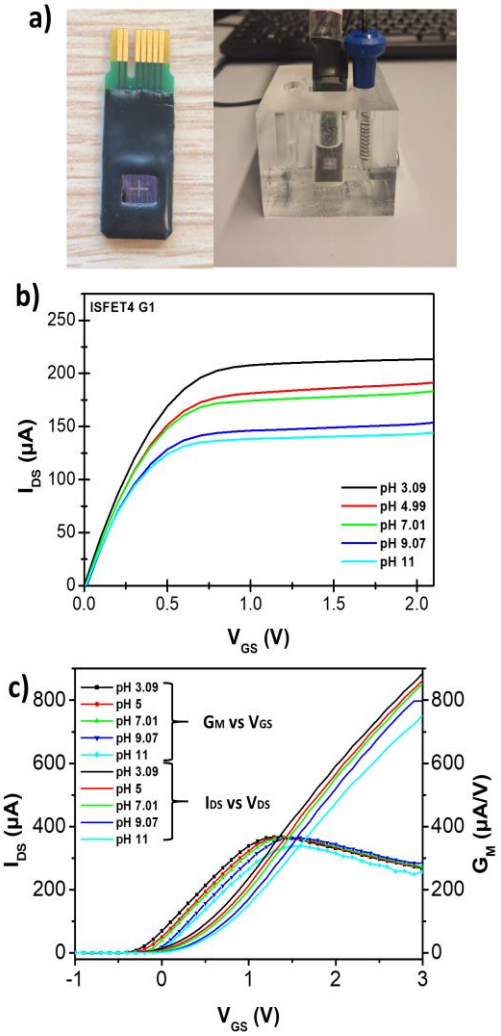

Fig. 1. ISFET system (a) and influence of pH on I_{DS} (b) and V_T (c) ISFETpH 3.09, 4.99, 7.01, 9.07 and 11.

In the hybridization tests, an increase in V_T and were observed with increasing sample concentrations in the same pH buffer, suggesting successful biorecognition through the hybridization process. This occurs because DNA is negatively charged due to phosphate groups in its structure. Thus, the hybridization process of the onto the ISFET increases the fixation of negative charge on the surface, leading to a change in the gate potential [4] In addition to surface charge alteration, the DNA hybridization process can also cause ionic redistribution in the medium [4]. Thus, a good linearity of response was achieved by correlating ΔV_T x Plasmid Concentration, indicating the system's detection sensitivity (Fig.2b).

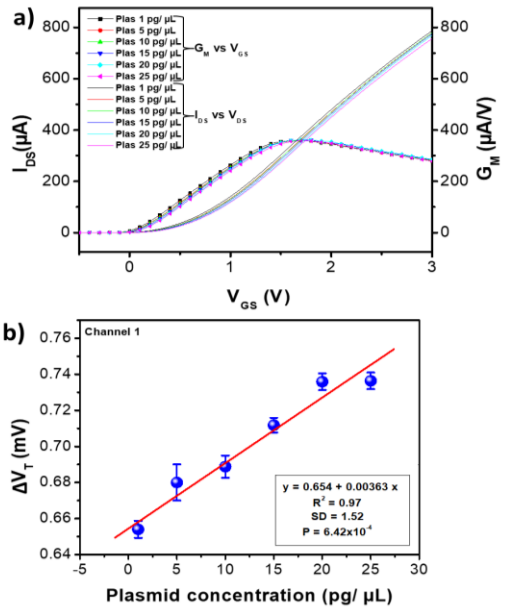

Fig. 2. Influence of hybridization on ISFET (a) and linear plot assays of V_T variation of ISFET (b).

Conclusion

The evaluated ISFET-based systems demonstrated promising performance for genetic detection of leukemic oncogenes, offering potential applications in clinical settings.

References

[1] S. K. Tasian, M. L. Loh and S. P. Hunger, Childhood acute lymphoblastic leukemia: Integrating genomics into therapy,*Cancer* 121, 3577-90 (2015); doi: 10.1002/cncr.29573.

[2] T. Pincez, R. Santiago, H. Bittencourt, I. Louis, M. Bilodeau, A. Rouette, L. Jouan, J. R. Landry, F. Couture, J. Richer, P. Teira, M. Duval and S. Cellot, Intensive monitoring of minimal residual disease and chimerism after allogeneic hematopoietic stem cell transplantation for acute leukemia in children,*Bone Marrow Transplant* 56, 2981-2989 (2021); doi: 10.1038/s41409-021-01408-5.

[3] H. Ben Halima, F. G. Bellagambi, F. Brunon, A. Alcacer, N. Pfeiffer, A. Heuberger, M. Hangouet, N. Zine, J. Bausells and A. Errachid, Immuno field-effect transistor (ImmunoFET) for detection of salivary cortisol using potentiometric and impedance spectroscopy for monitoring heart failure,*Talanta* 257, 123802 (2023); doi: 10.1016/j.talanta.2022.123802.

[4] H. Kawarada and A. R. Ruslinda, Diamond electrolyte solution gate FETs for DNA and protein sensors using DNA/RNA aptamers,*physica status solidi (a)* 208, 2005-2016 (2011); doi: 10.1002/pssa.201100503.

DOI 10.5162/EUROSENSORSXXXVI/OT6.116

Ion-Sensitive Field Effect Transistor (ISFET)-Based DNA Detection for Enterotoxigenic *E. coli* (ETEC)

Mongkol Techakasikornpanich[1], *Duangporn Polpanich*[2], *Marie Hangouet*[3], *Joan Bausells*[4], *Norman Pfeiffer*[5], *Nadia Zine*[3], *Kulachart Jangpataraponsa*[1]*,*Abdelhamid Errachid*[3]*, *and Abdelhamid Elaissari*[3]

[1] *Center for Research Innovation and Biomedical Informatics, Faculty of Medical Technology, Mahidol University, Bangkok 10700 Thailand,*

[2] *National Nanotechnology Center (NANOTEC), National Science and Technology Development Agency (NSTDA), Pathum Thani 12120, Thailand,*

[3] *Universite Claude Bernard Lyon 1, ISA, UMR 5280, CNRS, 5 rue de la Doua, 69100 Villeurbanne, France,*

[4] *Instituto de Microelectrónica de Barcelona (IMB-CNM,CSIC), Campus UAB, 08193 Bellaterra, Spain*

[5] *Fraunhofer IIS, Fraunhofer Institute for Integrated Circuits IIS, Am Wolfsmantel 33, Erlangen, 91058, Germany*

Corresponding Author's e-mail address:
kulachart.jan@mahidol.ac.th (Kulachart Jangpataraponsa),
abdelhamid.errachid-el-salhi@univ-lyon1.fr (Abdelhamid Errachid)

Summary:

In this study, we demonstrate novel bacterial detection using DNA hybridization-based electrochemical biosensors for enterotoxigenic *Escherichia coli* (ETEC). The ion-sensitive field-effect transducer (ISFET) was immobilized with LT-probe, which is specifically for the heat-labile gene of ETEC. Potentiometric measurement and Electrochemical impedance spectroscopy (EIS) are performed to improve the successful development of the detection of ETEC, which represents a promising technique for rapid and sensitive bacterial detection.

Keywords: ISFET biosensors, DNA-based biosensors, ETEC, Bacterial detection, DNA hybridization

Background

Enterotoxigenic Escherichia coli (ETEC) is foodborne pathogenic bacteria, that causes cholerae-like diarrhea in children younger than 5 years old. Due to the fecal-route infection, ETEC can be transmitted via contaminated food and beverage. The detection of ETEC is commonly identified by molecular-based detection, such as polymerase chain reaction (PCR) and real-time PCR (qPCR), which use a heat-labile toxin (LT) gene as a target. Although these methods are highly sensitive and specific to ETEC, they require expensive equipment and well-trained staff. Moreover, they may require an enrichment process, which is time-consuming [1], [2], [3]. Thus, the development of rapid, easy, and point-of-care (POC) detection is a challenge for bacterial detection. In recent years, ion-sensitive field effect transducer (ISFET)-based biosensors have gained interest in the fields of detection, due to miniaturization, cost-effectiveness, and high sensitivity [4], [5]. In this study, we developed a more rapid, highly sensitive, and highly specific DNA-based ISFET biosensor for the detection of ETEC contaminated in water.

Methods

The ISFET's surface was activated by UV/Ozone procleaner to modify hydroxyl groups on the surface and then were silanized with 11-(triethoxysilyl) undecanal (TESUD) by the vapor-phase method. After functionalization, the ISFET was placed in an oven at 100°C for 1h. The aminated-LT-probe was dropped and incubated overnight at 4°C. After that, the immobilized ISFET was rinsed with TE buffer pH 8 and dried with N_2. 1% Ethanolamine was dropped on the ISFET and incubated for 1 h at RT to block unspecific binding molecules. The DNA sample, extracted from ETEC, was heated for 5 min to denaturation of double-stranded DNA structure and incubated with the immobilized ISFET for 10 min. The ISFET was rinsed with PBS buffer pH 7.4 and dried with N_2. The potentiometry and electrochemical impedance spectroscopy (EIS) of the ISFET were determined using PBS buffer pH 7.4

Results

LT-probe immobilized ISFET was investigated by analyzing various concentrations of extracted DNA from ETEC ($1.9x10^{-5}$ to $1.9x10^{-1}$ µg/mL). Filtrate PBS was used as a negative control to provide the reference signal of the ISFET sensor. Potentiometry and EIS were measured in PBS solution pH 7.4. Fig. 1 demonstrates the responsible ISFET to various DNA samples, measured by drain current (I_{DS}) and transconductance (G_m) vs. gate-to-source voltage (V_{GS}) at drain-to-source voltage (V_{DS}) = 0.5 V. I_{DS} and G_m vs. V_{GS} have slightly shifted to the negative value when increasing the concentration of ETEC's DNA. The threshold voltage (V_T), extracted from I_{DS} and G_m vs. V_{GS}, demonstrated the decrease of V_T when increasing the bacterial concentration.

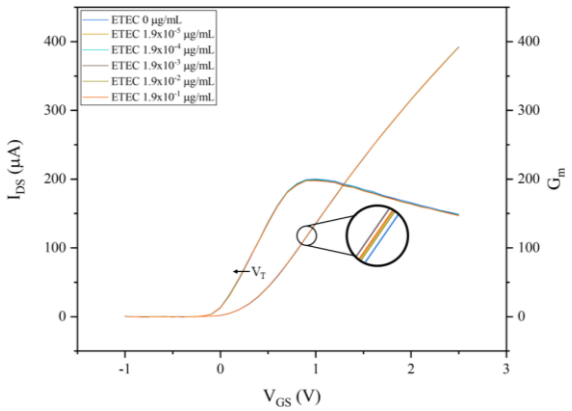

Fig. 1. I_{DS} and G_m vs V_{GS} obtained by analyzing ETEC's DNA samples in TE buffer ($1.9x10^{-5}$ to $1.9x10^{-1}$ µg/mL) at V_{DS} = 0.5 V.

Due to the narrow change of the potentiometric signal, EIS measurement was used to reach the sensitivity of the detection. The Nyquist plot of EIS at different concentrations of DNA samples ($1.9x10^{-5}$ to $1.9x10^{-1}$ µg/mL) decreased the charge transfer resistance on the modified ISFET surface, compared with the reference, ETEC 0 µg/mL, as shown in Fig 2.

These results improve the successful development of a label-free DNA-based ISFET sensor for the detection of ETEC's DNA using LT-probe.

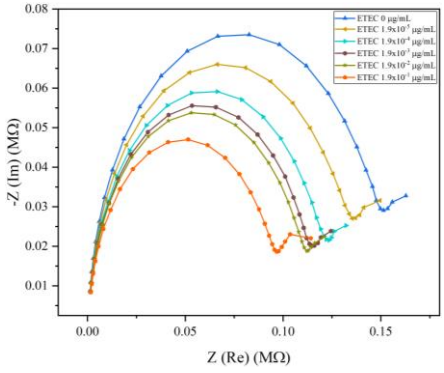

Fig. 2. Nyquist plots obtained by analyzing ETEC's DNA samples in TE buffer ($1.9x10^{-5}$ to $1.9x10^{-1}$ µg/mL). EIS frequency was ranged from 100 Hz to 200 KHz, with E_{ac} 100 mV and E_{dc} 0 V.

Conclusion

This work has proven the successful development of a DNA-based ISFET biosensor for the detection of heat-labile toxin gene which is specifically for ETEC. Potentiometry and EIS measurements were used to determine the efficiency of the ISFET sensor, which provided a decreasing trend when increasing the concentration of the DNA samples. It can represent the rapid detection of bacterial detection, which is a promising technique for point-of-care detection.

References

[1] K. Jangpatarapongsa, K. Saimuang, D. Polpanich, R. Thiramanas, M. Techakasikornpanich, P. Yudech, et al, Increased sensitivity of enterotoxigenic Escherichia coli detection in stool samples using oligonucleotide immobilized-magnetic nanoparticles, *Biotechnology Reports* 32, e00677 (2021); DOI: https://doi.org/10.1016/j.btre.2021.e00677

[2] Å. Lothigius, A. Janzon, Y. Begum, Å. Sjöling, F. Qadri, A. M. Svennerholm and I. Bölin, Enterotoxigenic Escherichia coli is detectable in water samples from an endemic area by real-time PCR, *Journal of Applied Microbiology* 104, 1128-1136 (2008); DOI: https://doi.org/10.1111/j.1365-2672.2007.03628.x

[3] S. Chakraborty, C. Harro, B. DeNearing, J. Brubaker, S. Connor, N. Maier, et al, Impact of lower challenge doses of enterotoxigenic Escherichia coli on clinical outcome, intestinal colonization and immune responses in adult volunteers, *PLOS Neglected Tropical Diseases* 12, e0006442 (2018); DOI: 10.1371/journal.pntd.0006442

[4] H. Ben Halima, F. G. Bellagambi, M. Hangouët, A. Alcacer, N. Pfeiffer, A. Heuberger, et al, A novel electrochemical strategy for NT-proBNP detection using IMFET for monitoring heart failure by saliva analysis, *Talanta* 251, 123759 (2023); DOI:https://doi.org/10.1016/j.talanta.2022.123759

[5] H. Ben Halima, F. G. Bellagambi, M. Hangouët, A. Alcacer, N. Pfeiffer, A. Heuberger, et al, A Novel IMFET Biosensor Strategy for Interleukin-10 Quantification for Early Screening Heart Failure Disease in Saliva, *Electroanalysis* 35, e202200141 (2023); DOI: https://doi.org/10.1002/elan.202200141

DOI 10.5162/EUROSENSORSXXXVI/OT6.132

Electropolymerization of porphyrinoids on LIG as EGFET-based sensor array for ascorbic acid detection

Kishore Pushparaj [1], Lorena Di Zazzo [2], Alexandro Catini [1], Rosamaria Capuano [1], Valerio Allegra [1], Gabriele Magna[2], Chiara Manganiello[1], Gianni Antonelli [1], Eugenio Martinelli [1], Roberto Paolesse [2], and Corrado di Natale [1]

[1] Department of Electronic Engineering, University of Rome Tor Vergata, 00133 Roma, Italy

[2] Department of Chemical Science and Technology, University of Rome Tor Vergata, 00133 Roma, Italy

Corresponding Author's e-mail address: dinatale@uniroma2.it

Summary:

Laser-induced graphene was obtained from polyimide films by lasing with a commercial CO_2 laser. Then porphyrinoids were electrosynthesized on the electrodes using cyclic voltammetry. These electrodes were employed as working electrodes in an extended gated field-effect transistor configuration. The array exhibits excellent sensitivity towards ascorbic acid and dopamine. Furthermore, artificial tears were tested with and without ascorbic acid as real samples.

Keywords: EGFET, laser-induced graphene, ascorbic acid, porphyrinoids, electrosynthesis.

1. Introduction:

L-ascorbic acid is a well-known water-soluble antioxidant present in many biological systems, and there are several ways to detect it [1]. ChemFET sensors are one of the recent interests in biological applications. Extended gate field effect transistor (EGFET) is quite modified from ion sensitive-FET sensors where the transducer is away from the electrolytic solution which gives the device long-term stability. Because MOSFETs are reusable in this technique, but the working electrode needs to be replaced, we need to pay attention to developing sensing materials. Preparation of electrodes is always a crucial part of the development of I sensors, where laser-induced graphene (LIG) is an easy method to obtain highly conductive graphene. Porphyrinoids are excellent ionophores materials that have been exploited in potentiometric sensors [2]. In this work, we electrosynthesized the porphyrinoids on laser-induced graphene (LIG) and used a sensor array using the EGFET technique to detect ascorbic acid in artificial tears.

2. Materials and methods:

A 125 µM polyimide sheet was lasered to produce LIG. The polyimide was cleaned with ethanol before laser illumination. Double lasing was performed with laser power of 10 W/cm2, at a rate of 20 cm/s and a resolution of 1000 PPI. The LIG obtained was used to electrosynthesis porphyrinoids in 0.1M TBAC. Electropolymerization was carried out as reported in our previous work [3]. This forms a sensor array consisting of 8 sensors: LIG, LIG/$Cu(NH_2)_3TPC$, LIG/ $Cu(NH_2)_3TPC\_LUT$, LIG/ $Co-PPh_3(NH_2)_3TPC$, LIG/ $Mn-Cl(NH_2)_3TPC$, LIG/ $Cu-5,10(NH_2)_2TPP$, LIG/ $5,15(NH_2)_2TPP$ and LIG/ $5,10(NH_2)_2TPP$ (left to right). Each electrode was connected to the gate terminal and a saturated calomel electrode was used to bias the gate as shown in Fig. 1. 100 µl of artificial tears (purchased from a pharmacy) were tested as a real sample in 1X PBS at.

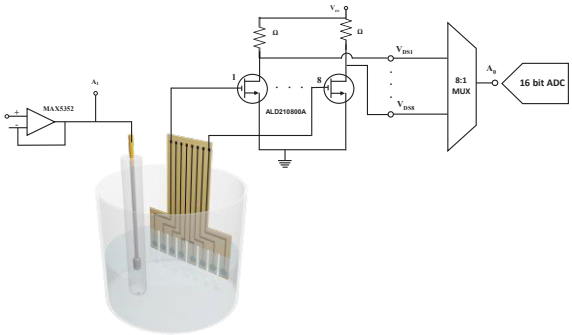

Figure 1. Schematic of the experimental setup.

3. Result and discussion:

Fig. 3 shows the principal component analysis (PCA) of the sensor array. The sensor was evaluated with ascorbic acid, dopamine, and artificial tears with and without ascorbic acid. The score plot shows the residual of the

repeated measurements. Fig 2 a) represents the scope plot of the sensor array based on ascorbic acid, dopamine, the mixture of dopamine and ascorbic, and synthetic tears with and without ascorbic acid Both PC1 and PC2 correspond to 97.77% of the total variance. The measurements were repeated twice with a two-sensor replica. Fig 3 b) Load plots indicate the execution of the sensor array where the sensor projects in different directions. It is noteworthy that Cu-5,10(NH_2)$_2$TPP is projected in the opposite direction with respect to the bare LIG electrode. On the other hand, LIG/ Cu(NH_2)$_3$TPC_LUT doesn't provide any information with respect to LIG. It is noticed that LIG contributes a lot more towards dopamine than electrosynthesized sensors.

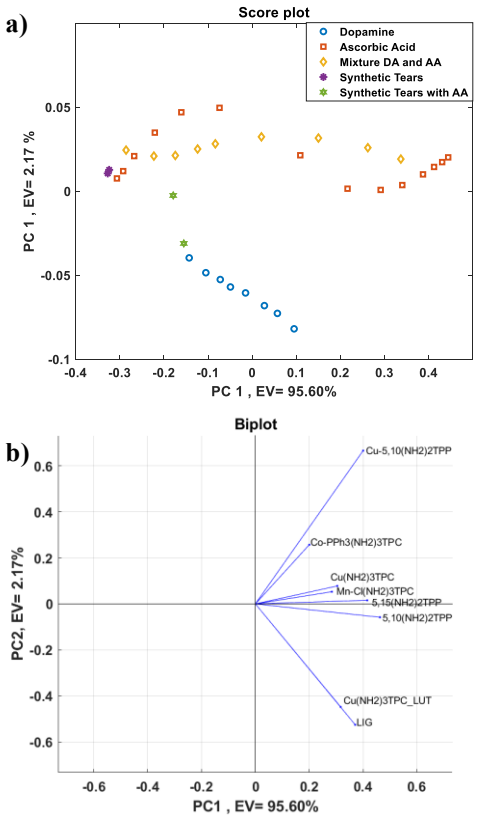

Fig 2. PCA of sensor array a) score plot based on ascorbic acid, dopamine, a mixture of dopamine and ascorbic, synthetic tears with and without ascorbic acid, b) biplot.

Reference:

[1]. Dhara, K.; Debiprosad, R.M. Review on Nanomaterials-Enabled Electrochemical Sensors for Ascorbic Acid Detection. *Anal Biochem* **2019**, *586*, 113415, doi:https://doi.org/10.1016/j.ab.2019.113415.

2. [2]. Pushparaj, K.; Catini, A.; Capuano, R.; Allegra, V.; Magna, G.; Antonelli, G.; Martinelli, E.; Agresti, A.; Pescetelli, S.; Sivalingam, Y.; et al. Nonenzymatic Potentiometric Detection of Ascorbic Acid with Porphyrin/ZnO-Functionalized Laser-Induced Graphene as an Electrode of EGFET Sensors. *ACS Omega* **2024**, *9*, 10650–10659, doi:10.1021/acsomega.3c09141.

3. [3]. Di Zazzo, L.; Kumar, A.; Meunier-Prest, R.; Di Natale, C.; Paolesse, R.; Bouvet, M. Electrosynthesized Copper Polycorroles as Versatile Materials in Double Lateral Heterojunctions. *Chemical Engineering Journal* **2023**, *458*, 141465, doi:https://doi.org/10.1016/j.cej.2023.141465.

DOI 10.5162/EUROSENSORSXXXVI/OT6.137

Insights into Graphene-Based Sensors for VOC biomarkers of lung cancer: A DFT Perspective

Ivan Shtepliuk[1], Jens Eriksson[2], Donatella Puglisi[2]
[1]Semiconductor Materials Division, Department of Physics, Chemistry and Biology-IFM, Linköping University, S-58183 Linköping, Sweden
[2]Sensor and Actuator Systems (SAS) Division, Department of Physics, Chemistry and Biology-IFM, Linköping University, S-58183 Linköping, Sweden

Corresponding Author's e-mail address: ivan.shtepliuk@liu.se

Summary:
In this work, we address key scientific questions regarding the use of graphene for lung cancer biomarker detection. The volatile organic compound (VOC) biomarkers of lung cancer were classified into nonpolar, polar with small dipole moments, and polar with large dipole moments. Using density functional theory (DFT) calculations, we examine the adsorption capacities of various VOC biomarkers on graphene surface. The analysis of binding energies provides valuable insights for designing sensitive and selective sensors for detecting lung cancer VOC biomarkers using graphene, potentially advancing early diagnosis and treatment of this disease.

Keywords: graphene, volatile organic compounds, lung cancer, density functional theory, adsorption.

Background and Motivation

Volatile organic compounds present in exhaled human breath and/or bioliquids e.g., blood can be considered as bioindicators of lung cancer [1]. There are at least 22 polar or non-polar VOCs [2, 3] that discriminate between healthy and lung cancer patients. Many studies have been dedicated to the detection and identification of VOCs of lung cancer by using conventional techniques, such as gas chromatography, mass spectrometry, radiography, tomography, cytology, and fluorescence bronchoscopy [4-6]. Yet, these methods encounter significant challenges: i) time-intensive breath analysis; ii) non-portable screening equipment; iii) high costs; iv) limited sensitivity to small lung cancer tumors and picomolar VOC concentrations. Recent efforts focus on finding gas-sensitive materials capable of detecting picomolar VOC concentrations linked to lung cancer. Conductive polymers, metal oxides, carbon nanotubes, gold nanoparticles, and graphene-based nanomaterials (GBM) have shown promise in developing sensing platforms [7-9]. GBM, in particular, holds great potential for commercializing affordable, rapid, and reproducible sensors for biomolecule identification. Such an enhanced potential of these materials in biosensing field is governed by the unique properties of GBM (huge carrier mobility, high electrical conductivity, high signal-to-noise ratio, large surface area of 2630 m^2/g, high electron-transfer rates, and low toxicity) [10]. These features create conditions for precise detection of foreign substances due to a large detection area, fast optical and electronic response of the system, change of the conductivity even at small concentrations of surface functional groups and bioanalytes. Indeed, different authors reported on fabrication of biosensors using oxidized graphene to detect such VOCs of lung cancer as p-xylene [11], decane [12], hexanal, heptanal, undecane [5].

Despite GBM's advantages in detecting VOCs as lung cancer indicators, previous studies lack systematic results, hindering scientists' understanding of practical graphene-family nanomaterial implementation. Challenges remain: (i) lack of a standardized database for graphene-biomarker interactions and specific interaction fingerprints, (ii) unclear physical mechanisms for sensing polar and nonpolar lung cancer biomarkers, and (iii) low sensitivity to nonpolar VOCs. The differences in adsorption abilities of graphene to polar and nonpolar lung cancer biomarkers depending on solvent effect are never discussed, and a comprehensive DFT analysis on adsorption capacity of GBM to VOC biomarkers of lung cancer has not been carried out, yet. Considering the key issues mentioned, we explore ways to address these unexplored scientific questions.

Method

Gaussian 16 package is utilized to perform all DFT calculations of VOC adsorption on gra-

phene using highly parametrized, empirical M05-2X exchange-correlation functional, with 6-31G(d) basis set. The binding energy of VOCs of lung cancer to a graphene is defined as: $E_b=E_{G+VOC}-(E_G+E_{VOC})$, where E_{G+VOC} is the total energy of the interacting graphene-VOC system, E_G is the total energy of isolated graphene, E_{VOC} is the total energy of VOC molecule.

Results

To classify and systemize the VOC biomarkers, we first calculated their dipole moments (see Fig. 1). Overall, these VOCs can be divided into three major classes: (i) nonpolar VOCs (decane, benzene, 1,4-dimethyl-benzene, cyclohexane), (ii) polar VOCs with small dipole moments (2,2,4,6,6-pentamethylheptane,2-methylheptane, undecane, methylcyclopentane, 1-methyl-2-pentylcyclopropane, 3-methyloctane, 3-methylnonane, 2,4-dimethylheptane) and (iii) polar VOCs with large dipole moments (hexanal, heptanal, 1,2,4-trimethylbenzene, 1-hexene, 1-heptene, 1-methylethenylbenzene, isoprene, styrene, trichlorofluoromethane). In addition, all these biomarkers can be classified as those that: (i) contain aromatic benzene rings (styrene, benzene, propylbenzene, 1,2,4-trimethylbenzene, 1,4-dimethyl-benzene,1-methylethenylbenzene) and (ii) do not contain hexagon carbon ring (others). These features strongly influence the interaction between VOCs and graphene-family nanomaterials. Molecules with hexagonal carbon rings align parallel to the graphene plane due to π-π stacking interaction.

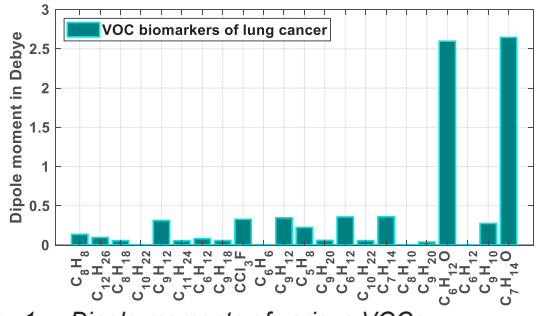

Fig. 1. Dipole moments of various VOCs.

Figure 2 shows the binding energies for each VOC on graphene. Some molecules such as 2,2,4,6,6-pentamethylheptane, undecane, and 1-methylethenylbenzene exhibit relatively high binding energies, indicating strong interactions with graphene. Aromatic compounds like styrene, propylbenzene, and benzene show moderate to high binding energies, likely due to π-π interactions with the graphene surface. VOCs with longer aliphatic chains (e.g., 2,2,4,6,6-pentamethylheptane, undecane) also show significant binding energies, possibly due to increased van der Waals interactions. The presence of functional groups (e.g., double bonds in 1-hexene, 1,4-dimethyl-benzene) may influence binding energies. The variability in binding energies suggests that a sensor based on graphene could selectively detect specific VOC biomarkers, improving the selectivity of lung cancer detection. By understanding the adsorption energies, sensor design can be optimized to target VOCs with the highest binding energies, improving sensor sensitivity.

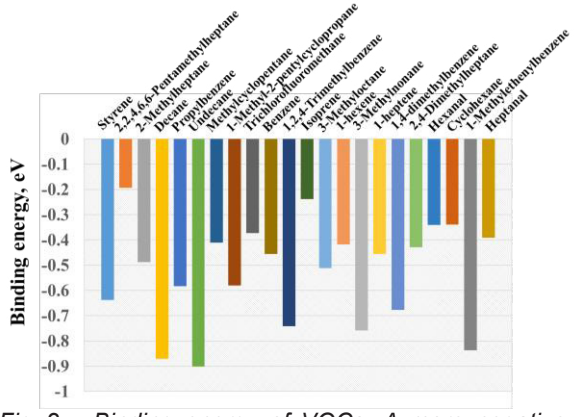

Fig. 2. Binding energy of VOCs. A more negative binding energy suggests a stronger bond to graphene.

This research was funded by the Swedish Research Council, Vetenskaprådet, grant No. 2023-07219, and Sweden's Innovation Agency, Vinnova, grant No. 2023-04186.

References

[1] S. N. Rai, et al. PLoS. ONE. 17, 11: e0277431(2022);doi:10.1371/journal.pone.0277431
[2] M. Philips, et al., *Lancet* 353, 1930 (1999); doi:10.1016/S0140-6736(98)07552-7
[3] M. Philips, R.N. Cataneo, A.J. Gagliardi, *Chest* 123, 211 (2003); doi: 10.1378/chest.123.6.2115
[4] A. Dent, et al., *Journal of Thoracic Disease*, 5, S540-S550 (2013); doi: 10.3978/j.issn.2072-1439.2013.08.44
[5] O. Barash, et al., *Lung Cancer Manage*. 2(6), 471–482 (2013); doi: 10.2217/LMT.13.58
[6] Y. Saalberg, et al., *Clinica Chimica Acta* 459, 5–9 (2016); doi: 10.1016/j.cca.2016.05.013
[7] P. J. Mazzone, *Journal of Thoracic Oncology*, 3, 774-780 (2008); doi: 10.1097/JTO.0b013e31817c7439
[8] M. P. Fernandes, et al., *Open Biomed Eng J*. 9, 228–233 (2015); doi: 10.2174/1874120701509010228
[9] Y. Li et al., *RSC Adv.* 7 (2017) 11959-11968; doi: 10.1039/c6ra25453e
[10] I. Shtepliuk, V. Khranoskyy, R. Yakimova. Semicond. *Sci. Technol.* 31, 113004 (2016); doi: 10.1088/0268-1242/31/11/113004
[11] S. Nag, et al., *J. Mater. Chem. B 2*, 6571 (2014); doi: 10.1039/C4TB01041H
[12] X. F. Zhang, et al. *Frontiers of Physics*, 11, 116801 (2016); doi: 10.1007/s11467-015-0519-4

DOI 10.5162/EUROSENSORSXXXVI/OT6.160

Microfluidic device with integrated microelectrodes for enhanced EIS sensitivity

Lilia Bató[1,2], János M. Bozorádi[1,2], Zoltán Vizvári[3], Péter Fürjes[1]

[1] Microsystems Lab., Inst. of Technical Physics and Materials Science, HUN-REN Centre for Energy Research, Budapest, Hungary
[2] Óbuda University Doctoral School on Materials Sciences and Technologies, Budapest, Hungary
[3] Symbolic Methods in Material Analysis and Tomography Research Group, Faculty of Engineering and Information Technology, University of Pecs, Pecs, Hungary

Corresponding Author: bato.lilia@ek.hun-ren.hu

Summary:
In this work a microfluidic device was created with nanostructured integrated platinum electrodes to enhance the sensitivity of Electrochemical Impedance Spectroscopy (EIS) in cell analytical applications. The sensing microelectrodes were structured using Focused Ion Beam milling creating two separate electrodes with gap sizes ranging from 200 nm to 1 µm. The decreased electrode distance allows improved sensitivity in EIS measurements, especially when a micrometer size particle or cell is trapped between the electrodes. The electrode design is supported by finite element modelling of the evolving electromagnetic field in the microfluidic channel.

Keywords: microfluidics, lab-on-a-chip, bioimpedance, electrochemical impedance spectroscopy

EIS measurements in cell analysis

In vitro study of individual cells or cell populations in a controlled chemical environment using specifically designed multifunctional microfluidic devices, such as Organ-on-Chips, offers sensitive and specific measurements that may facilitate drug discovery, screening, and the development of therapeutic strategies [1]. Combining these devices with integrated sensing systems, such as microelectrodes, can simultaneously maintain and monitor the behavior of cell populations real-time, meanwhile treating them with different chemical agents. This multidisciplinary approach can be essential in personalized medicine with further applications for antibiotic susceptibility testing [2].

Electrochemical Impedance Spectroscopy (EIS) is a non-invasive real-time technique that allows characterization of complex electrical properties of the cells while measuring the frequency dependent impedance of the system. Microelectrodes integrated inside a microfluidic system can be used for specific EIS measurements that enable cell analysis such as viability and growth monitoring. In biological applications of EIS an extensive range of frequencies is covered from 1 Hz to 10 GHz to get an insight into the inner electrochemical processes of the system regarding the electrode, the media, and the cellular properties as well. Accordingly, the spectra are divided into distinct dispersions regions α, β and γ [3]. Here, the α and β regions were measured to study both cellular and electrode properties.

Microfluidic system for EIS analysis

A compact multi-channel microfluidic system was created that can measure the EIS spectra of trapped cells using 2- or 4-electrodes architecture (Fig. 1). The central sensing microelectrodes were sectioned by Focused Ion Beam milling, creating two individual electrodes with a small gap ranging from 200 nm to 1 µm (Fig. 2). The system offers enhanced sensitivity owing to the nanometer scale electrode distances.

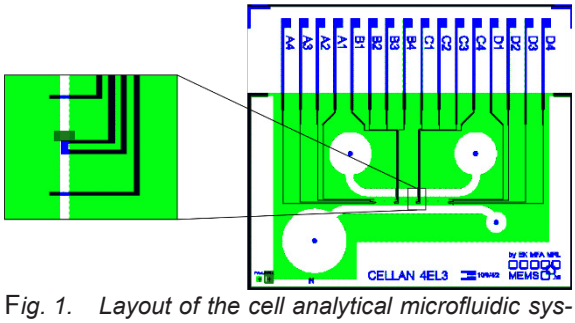

Fig. 1. Layout of the cell analytical microfluidic system and the position of the electrodes.

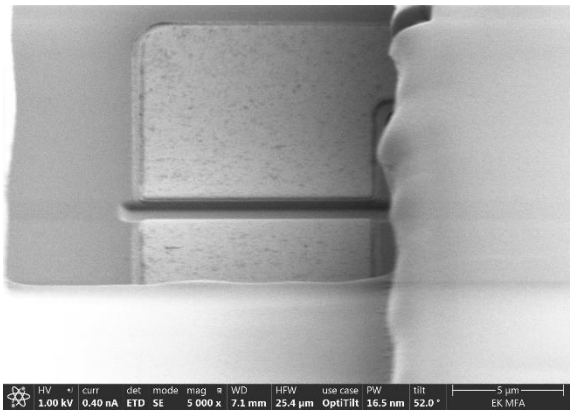

ig. 2. Sectioning the Pt electrodes with FIB milling. The gap size between the central electrodes is 1 µm.

Results

EIS measurements in 2-electrodes architecture were conducted using a PalmSens4 device, 4-electrode measurements were conducted by a bioimpedance analyzer developed by Vizvari et al. [4]. The Pt electrodes were fabricated on glass substrate, patterned by lift-off lithography. The microfluidic system contains two main inlet channels and 4 cross-channels for EIS measurements using the underlying electrodes. The cross-channels contain a trapping region, where cells or particles falling in the range of the channels' dimensions (e.g. yeast cells) can be localized over the sensing electrodes. The 10 µm deep microfluidic channels were fabricated in SU-8 by photolithography, then they were covered by a PDMS layer. The system is connected to the impedance spectroscopes via specifically designed PCBs (Fig. 3).

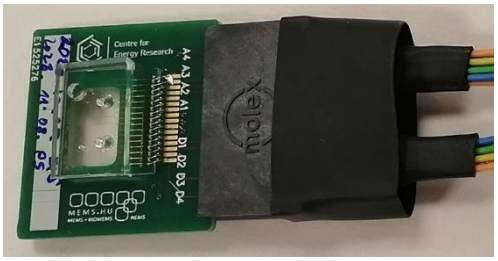

Fig. 3. The ready-to-use microfluidic device containing the cell trapping channels and the integrated electrodes.

During the measurements, the effects of the electrode distances, the stability and the reproducibility of the analytical system was characterized using different solutions, including cell culture media and cellular suspensions containing *Saccharomyces cerevisiae*. A finite element model was also developed to comprehend the electrical processes of the cellular system. The electric field developed in the channel was simulated by COMSOL Multiphysics with or without cells, the corresponding EIS spectra were compared to the corresponding measurements (Fig. 4). Initial tests with PBS, cell culture media (HEP G2) and cellular solutions yielded great reproducibility (Fig. 5). Comparison of 2- and 4-electrode measurements proved the benefit of using 4-electrodes in the low frequency range to eliminate parasitic effects.

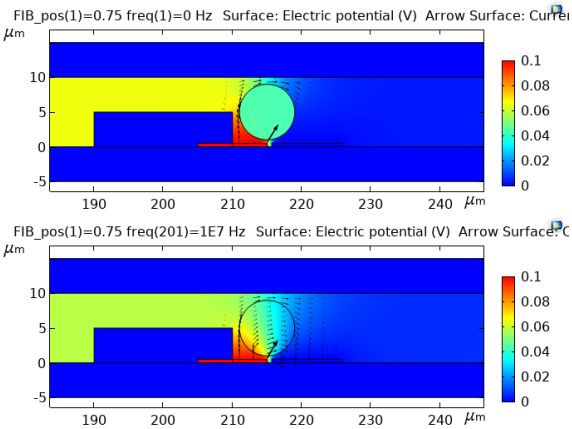

Fig. 4. FEM simulation of the electric filed over the electrodes when a cell is trapped at low (top) and high (bottom) frequencies.

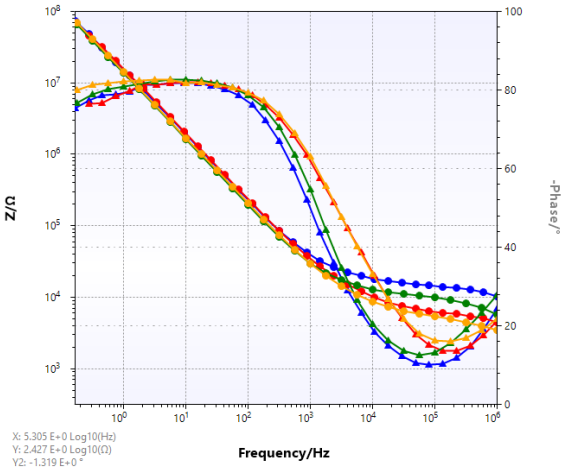

Fig. 5. Two electrode EIS spectra in PBS between two inner (red, yellow) and two outer electrodes (blue, green) in two different channels.

References

[1] L. A. Low et al., Organs-on-chips: into the next decade, *Nature Review Drug Discovery* 20, 345-361 (2020); doi: 10.1038/s41573-020-0079-3

[2] Z. Li et al., Microfluidic organ-on-a-chip system for disease modeling and drug development, *Biosensors,* 12, 370 (2022) doi: 10.3390/bios12060370

[3] K. Asami, Characterization of biological cells by dielectric spectroscopy, *Journal of Non-Crystalline Solids,* 305, 268-277 (2002) doi: 10.1016/s0022-3093(02)01110-9

[4] Z. Vizvari et al. Physical validation of a residual impedance rejection method during ultra-low frequency bio-impedance spectral measurements, *Sensors,* 20, 4686 (2020) doi: 10.3390/s201746

Nanosensor for GHB detection in urine samples

E. Garrido, A. Valero-Martínez, R. Martínez-Máñez, Universitat de València, València (Spain)

Unfortunately, this abstract is not available, as the contribution was not confirmed at the time the conference proceedings were finalized.

Nanosensor for GHB detection in urine samples

E. Garrido, A. Valero-Martínez, R. Martínez-Máñez, Universitat de València, València (Spain)

Unfortunately, this abstract is not available, as the contribution was not confirmed at the time the conference proceedings were finalized.

DOI 10.5162/EUROSENSORSXXXVI/OT6.195

Aptamer-based Electrochemical Sensor for the Monitoring of Carbamazepine in Freshwater Systems

Pierrick Clément, Alba Finelli, Xavier Lefèvre, Saleem Khan, Alexandra Beard, Raphaël Pugin
Centre Suisse d'Electronique et de Microtechnique, Jaquet-Droz 1, Neuchâtel, Switzerland

pierrick.clement@csem.ch

Summary:
Carbamazepine (CBZ) is an active compound in commonly used drug and is highly durable in the environment, particularly in wastewater, which raises concerns about potential risks to animals and humans. We present an aptamer-based electrochemical sensor labelled with a redox probe which conformational change upon binding event is recorded by square-waved voltammetry. The electrochemical sensor operated in concentrations range from 2.5 pM to 250 µM in buffer. This technology provides a potential method to enable the monitoring of CBZ in treated water.

Keywords: Aptamer, electrochemical sensor, carbamazepine, environment, wastewater

Introduction

Carbamazepine (CBZ) is an anticonvulsant and anti-epileptic drug that was classified in the contaminants of emerging concern (CECs) list due to its unintended persistence in the environment notably in treated wastewater (up to 10 nM for long term exposure) [1]. Commonly used techniques to detect CBZ are liquid chromatography-tandem mass spectroscopy (LC-MS/MS), high-performance liquid chromatography (HPLC), immunoassays and solid-phase extraction (SPE) coupled with chromatography. While these methods are accurate, they are time-consuming and require sophisticated instrumentation. Furthermore, they cannot be applied for on-site detection. Several efforts have been made to develop portable assay formats using electrochemical techniques for rapid detection of carbamazepine (CBZ) and its metabolites, aiming to address this challenge. Direct electrochemical methods utilize target reduction/oxidation (redox) processes for quantification without the need for affinity reagents. While these methods are straightforward, electroactive molecules present in the medium to analyze can lead to a false positive. Molecular imprinted polymers were also reported as artificial biomimetic receptors to improve the low specificity of direct detection however, they are less selective than anti-bodies. Alternatively, aptamers are a class of short single-stranded nucleic acids that can selectively interact with their target rivalling those of antibodies. Specific sequences are generated by an in vitro molecular evolution method known as systematic evolution of ligands by exponential enrichment (SELEX). They are particularly interesting for the detection of small molecules, such as CBZ, that do not have enough immunogenicity to generate a specific antibody. In this work, we developed an electrochemical aptasensor where a conformational change is induced by CBZ target binding within the aptamer structure, which subsequently alters electron transfer between a redox tag appended at a distance and the surface of an electrode. The aptamer was modified with a thiol group on the 5′-end for immobilization on the gold sensing electrode and a methylene blue (MB) tag on the 3′-end for readout [2].

Results

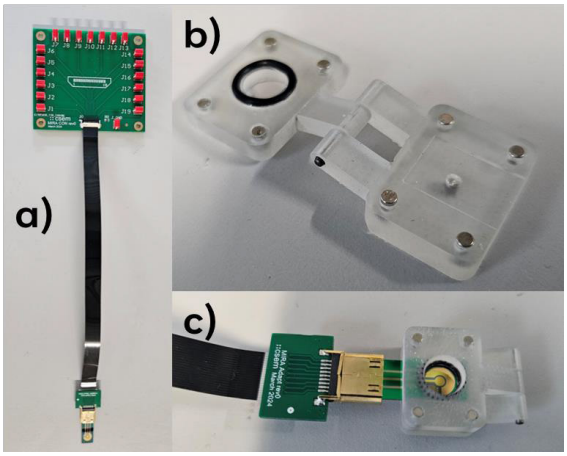

Fig 1. Picture of a) the sensing platform, b) the 3D printing cartridge and c) the sensor plugged in the HDMI mini connector with the cartridge integrated.

The gold electrodes were patterned on a silicon substrate with conventional clean room micro-

fabrication processes. Ag/AgCl electrode was deposited by aerosol jet printing technique. The chip is further integrated in an in-house developed sensing platform with a HDMI mini connector for an easy plug-and-play system. A 3D printed cartridge is integrated for drop-casting the sample on the sensor (see Fig.1). CBZ aptamer was covalently attached with the thiol function on the 3'-end by self-assembled-monolayer (SAM) on the gold working electrode overnight. For the sensor characterization, CBZ was diluted in PBS buffer (pH=7.4) at different concentrations and square-wave voltammetry (SWV) was recorded when the signal was stabilized. In Fig. 2, an increase of CBZ concentration is correlated with a decrease of the current.

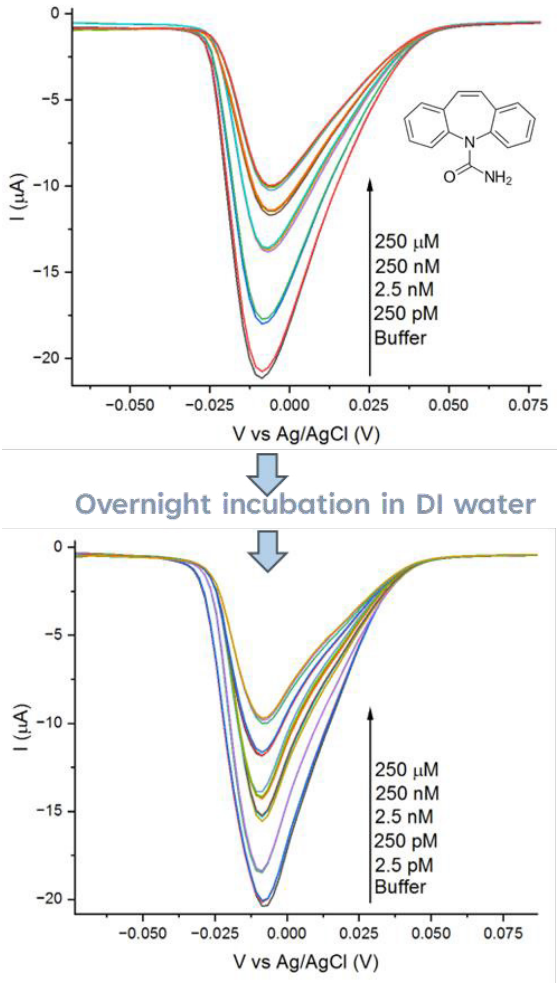

Fig. 2 SWV of the aptasensor showing its reversibility after overnight incubation in DI water.

It can be explained with the initial aptamer state being close to the gold electrode and allowing high-electron transfer rate with the MB. Upon binding with CBZ, the aptamer conformation switching moves the MB further away from the electrode which is transduced by a decrease of the current. A consequent advantage of aptamers is their reversible denaturation. By incubating the sensor in deionized (DI) water, the aptamer loses its conformation and CBZ is released in the solution. When it is reintroduced in PBS buffer, the aptamer goes back to its initial conformation and similar performances are observed as shown in Fig. 3.

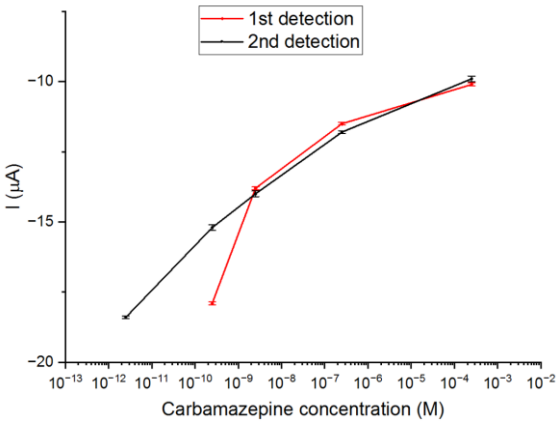

Fig. 3 Calibration curves of the aptasensor before (1st detection) and after (2nd detection) incubation in water

Conclusion

In this study, we have demonstrated the reversible detection of CBZ with a MB labelled aptamer electrochemical sensor. The developed sensor showed high sensitivity to CBZ down to 2.5 pM. Therefore, it holds great potential for the development of the next generation of portable on-site assays for the monitoring of CBZ in the environment.

References

[1] R. Fenz, A.P. Blaschke, M. Clara, H. Kroiss, D. Mascher, M. Zessner, *Water Science & Technology* 2005 52 (5), 205–213; doi: 10.2166/wst.2005.0135

[2] S. Chung, N. K. Singh, V. K. Gribkoff, D.A. Hall, *ACS Omega* 2022, 7, 39097−39106; doi: 10.1021/acsomega.2c04865

DOI 10.5162/EUROSENSORSXXXVI/OT6.196

MIP-based Sensors for Fast Nicotine Monitoring in Aerosol

Xavier Lefèvre, Pierrick Clement, Alba Finelli, Alexandra Beard, Raphaël Pugin
Centre Suisse d'Electronique et de Microtechnique, Jaquet-Droz 1, Neuchâtel, Switzerland

xavier.lefevre@csem.ch

Summary:
Nicotine is the main active component of tobacco. Its quantification in aerosols and particularly the amount delivered in lungs is of great interest to track its impact on health. Current detection methods rely on the use of mass spectroscopy coupled with liquid chromatography. However, this requires highly qualified personnel and expensive equipment. In this context, we demonstrated that Molecular Imprinted Polymers (MIP) as sensing layer deposited on electrodes are very efficient to allow fast and cheaper quantification of nicotine in aerosols.

Keywords: Molecularly imprinted polymers, nicotine detection, electrochemical sensors, fast response

Inhalation toxicological investigations and the development and pre-clinical testing of inhalable drugs require assessing the deposition kinetics of aerosol constituents on the epithelia of the respiratory tract or on in vitro models. A common in vitro approach is the deposition of the test aerosol on a trapping surface under controlled conditions, followed by quantification of deposited individual targeted aerosol constituents. This requires highly sensitive and selective analytical methodologies such as coupled chromatography - mass spectrometry, needing highly qualified personnel and expensive equipment and are not easily accessible. In this context, a promising technology for the quantification of aerosol deposition are chemically selective sensors and among them, molecularly imprinted polymers (MIP) showed very interesting abilities to selectively concentrate the target molecule for a better read-out. Matsui [1] reported one of the first nicotine MIPs in 1996. Nicotine MIPs were firstly used to preconcentrate nicotine before chromatography analysis [2] but quickly, attention turned on the analysis of cigarette smokes [3]. They also had interest for the delivery of nicotine through patches. Sensors were also developed for the analysis of residues in urines [4]. Finally, regarding detection methods, besides QCM [5], capacitive measurement [6] and optical detection [7] were used. No MIP for electrochemical detection of nicotine was mentioned. In this work, MIP were combined with electrochemical chips to build the nicotine sensors. Two approaches were evaluated: UV-curing of MIP on the electrode and electrodeposition.

MIP-based sensors are usually built by depositing preformed nanoparticles of MIP, but this leads to rather thick layers. We therefore focused on a polymer-based MIP formulation deposited as a thin film on the electrode and cured by UV exposure. The formulation is based on divinylbenzene and methacrylic acid, dicumyl peroxide being the activator of polymerization. Despite the polymer layer is insulating, we managed to deposit a very thin film (few 10ths of nanometers) to ensure sufficient recorded signal by using Pico-Pulse Jetting.

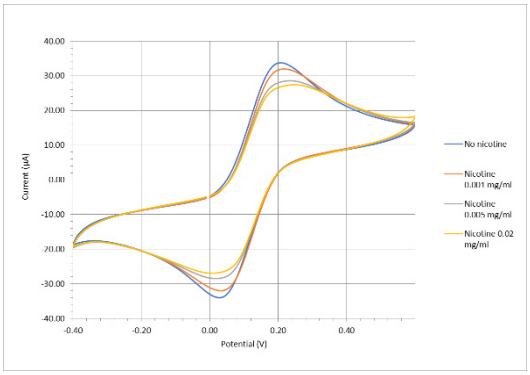

Fig. 1: detection of nicotine by MIP deposited by Pico-Pulse Jetting on working electrode of screen-printed carbon electrodes with Ag/AgCl reference.

MIP-based nicotine sensors were thus printed and further characterized. Direct monitoring of nicotine at its rather high redox potential was found to damage the sensing layer. Therefore, an indirect electrochemical measurement was developed using Fe(II)/Fe(III) as probe, avoiding high potential and deterioration of the MIP layer. This Fe(II)/Fe(III) potential value is directly linked to the presence of Nicotine and Fig. 1 shows an example of nicotine detection with this approach.

For such kind of sensors, calibration is then needed, and Fig. 2 shows a calibration curve obtained with our sensor over the nicotine concentration range of interest.

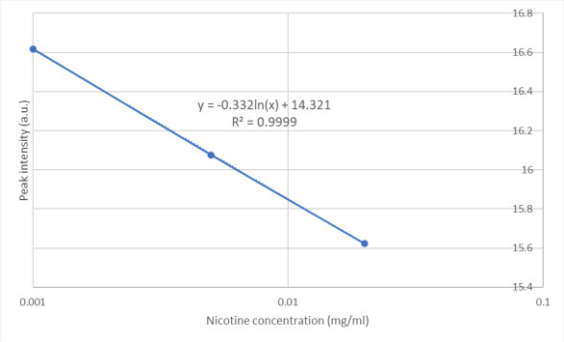

Fig. 2: calibration of MIP-based nicotine sensors fabricated by Pico-Pulse Jetting

Finally, we also investigated its sensitivity, its selectivity, and its stability. Very low amounts of nicotine (down to few ng/ml) were detectable in short times (10-15 min) allowing straightforward and fast measurements. The selectivity was very high even in presence of nicotine metabolites such as cotinine (Fig. 3). The sensor was exposed to various pH, solvents and biological media conditions and showed sufficient reliability for the foreseen application.

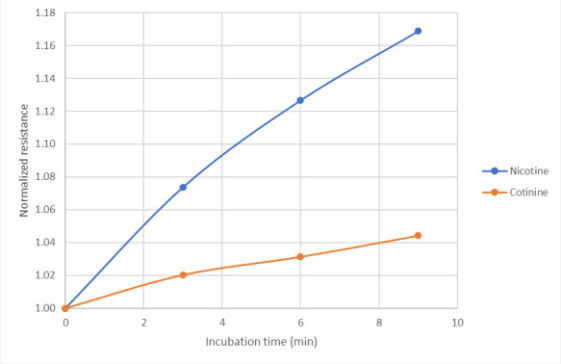

Fig. 3: selectivity of the MIP-based sensor fabricated by Pico-Pulse Jetting

Due to some limitations with in-situ UV-curing, we also studied MIP electrodeposition. For this purpose, we developed formulations and methods to reproducibly deposit MIP layers on electrodes by electrochemistry. Compared to standard MIP bulk-synthesis, this approach required the use of new electropolymerizable monomers such as aniline, pyrrole or thiophene. Several parameters allow a fine control on the created electrografted layer. The number of grafting cycles impacts the growth of the layer whereas the potential window used controls eventual cross-linking of the layer.
Formulations were then refined to increase the sensitivity and the selectivity by incorporating co-monomers such as acrylic acid or methyl acrylate. Those functional monomers promote more specific interactions with the target molecule nicotine which, in theory, enhances the selectivity. We were thus able to reach a very high sensitivity (in nanomolar/ppb range) together with keeping short analysis times (typically 3 to 5 minutes) and high selectivity.

We thus developed nicotine electrochemical sensors allowing fast and precise determination of nicotine in solution. Performances and robustness were optimized to achieve on-line measurement of nicotine levels in aerosols.

[1] J. Matsui, A. Kaneko, Y. Miyoshi, K. Yokoyama, E. Tamiya, and T. Takeuchi, “A Molecularly Imprinted Nicotine-Selective Polymer,” *Anal. Lett.*, vol. 29, no. 12, pp. 2071–2078, Sep. 1996, doi: 10.1080/00032719608002231.

[2] S. H. Hashemi and F. Keykha, “Application of the response surface methodology in the optimization of modified molecularly imprinted polymer based pipette-tip micro-solid phase extraction for spectrophotometric determination of nicotine in seawater and human plasma,” *Anal. Methods*, vol. 11, no. 42, pp. 5405–5412, 2019, doi: 10.1039/C9AY01496A.

[3] Y. Liu, S. Antwi-Boampong, J. J. BelBruno, M. A. Crane, and S. E. Tanski, “Detection of secondhand cigarette smoke via nicotine using conductive polymer films,” *Nicotine Tob. Res.*, vol. 15, no. 9, pp. 1511–1518, Sep. 2013, doi: 10.1093/ntr/ntt007.

[4] Y. Tan, J. Yin, C. Liang, H. Peng, L. Nie, and S. Yao, “A study of a new TSM bio-mimetic sensor using a molecularly imprinted polymer coating and its application for the determination of nicotine in human serum and urine,” *Bioelectrochemistry*, vol. 53, no. 2, pp. 141–148, 2001, doi: https://doi.org/10.1016/S0302-4598(00)00095-7.

[5] J. Alenus *et al.*, “Molecularly imprinted polymers as synthetic receptors for the QCM-D-based detection of l-nicotine in diluted saliva and urine samples,” *Anal. Bioanal. Chem.*, vol. 405, no. 20, pp. 6479–6487, 2013, doi: 10.1007/s00216-013-7080-1.

[6] K. Liu, W.-Z. Wei, J.-X. Zeng, X.-Y. Liu, and Y.-P. Gao, “Application of a novel electrosynthesized polydopamine-imprinted film to the capacitive sensing of nicotine,” *Anal. Bioanal. Chem.*, vol. 385, no. 4, pp. 724–729, 2006, doi: 10.1007/s00216-006-0489-z.

[7] N. Cennamo *et al.*, “A molecularly imprinted polymer on a plasmonic plastic optical fiber to detect perfluorinated compounds in water,” *Sensors*, vol. 18, no. 6, pp. 1–11, 2018, doi: 10.3390/s18061836.

DOI 10.5162/EUROSENSORSXXXVI/OT6.214

Micromachined SU-8/PMMA Sandwich Electrodes with Functional Graphene Coatings for Biopotential Monitoring

Seba Nur Alhasan[1], S. Sajjad Mirbakht[1], Saygun Guler[1], Osman Sahin[1], Muhammad Umar[1], Burcu Arman Kuzubasoglu[1], Murat Kaya Yapici[1,2,3]

[1] Faculty of Engineering and Natural Sciences, Sabanci University, Istanbul 34956, Turkey

[2] Department of Electrical Engineering, University of Washington, Seattle, WA 98195, USA

[3] Sabanci University Nanotechnology Research and Application Center, Istanbul 34956, Turkey

murat.yapici@sabanciuniv.edu

Summary:

Dry electrodes with high human biopotential signal recording quality is the promising future for wearable long-term health monitoring devices. Here, we present an ultrathin and flexible textile-like electrode composed of double-layered SU-8/PMMA microstructure fabricated using lithography-based microfabrication techniques featuring structures as fine as 100μm. Graphene oxide (GO) is introduced to the electrodes as an electrically conductive material using a single-step dip-coating method. To improve the electrical conductivity of the coated GO and hence, the performance of the electrodes, a reduction step using eco-friendly vitamin C (L-ascorbic acid) was carried out to transform GO to reduced graphene oxide (rGO). Our experimentation involved recording lead-I ECG signal acquisition using the fabricated electrodes, demonstrating their superior performance compared with Ag/AgCl wet electrodes with similarity up to 98.84% with distinguishable QRS peaks. The results pave the way towards a clinical-grade ECG signal performance.

Keywords: dry electrode, ECG, graphene oxide, microfabrication, vitamin C.

Introduction

Cardiovascular monitoring using electrocardiography (ECG) is an established technique to monitor the activity of the heart [1]. Typically Ag/AgCl wet electrodes are used to acquire biopotential signals such ECG [2]. Although these wet electrodes show highly accurate performance, they have various issues like the conductive gels drying out over time and problems with skin irritation [3]. In this study we propose a novel fabrication flow with the use of a hard mask (protection layer) avoiding the use of electron beam lithography (EBL). This work utilized industrial acrylic-based PMMA and SU-8; an epoxy-based material, to create textile-like mesh. The mesh arrangement of textile weaves makes these electrodes suitable for biopotential measurements on the skin, as this structure inherently guides signal energy in the "*z*" direction, perpendicular to the skin surface. To functionalize the electrode, graphene oxide was utilized, taking advantage of the superior capabilities of a simple, eco-friendly green reduction method using L-ascorbic acid.

Electrode fabrication

The fabrication (Fig. 1a) starts with depositing a 200 nm of SiO_2 as sacrificial layer. Then as supportive material 50 um negative photoresists SU-8-50 was spin coated at 3000 rpm then soft-baked at 65 °C for 7 min and 95 °C for 20 min then exposed to a dose of 140 mJ ultraviolet (UV) to produce a square-type microarray, post-exposure bake was then performed at 65 °C for 1 min and 95 °C for 6 min. The sample was then immersed in SU-8 developer. The next layer was PMMA, 495K MW PMMA-C4 was spin coated at 4000 rpm and was baked at 180° C for 10 min to produce 300nm. To selectively etch the PMMA, a layer of copper (Cu) was deposited on top of it. The copper layer was then patterned by spin-coating AZ5214 photoresist (PR) and exposed to UV light. Then O_2 plasma was performed for 3 minutes to etch the exposed regions of PMMA. After patterning the PMMA the Cu layer was removed by an etchant mixture of acetic acid and hydrogen solution. Finally, the electrode was released by immersion inside buffered oxide etch BOE 7:1 for 5 h. The released SU-8/PMMA sample was drop-casted by diluted GO graphene oxide suspension (4mg/mL) on a hydrophobic Teflon surface to confirm a uniform coating and dried at room temperature for one day. Next, the sample was immersed in 0.5 g/ml L-ascorbic acid and deionized water for three days at room temperature. After the reduction, the sample was washed by deionized water and left to dry (Fig. 1b). The electrode internal layers after wiring are demonstrated in Fig. 1c.

ECG signal recording

Data acquisition utilized an open-source unit (Cyton Board, OpenBCI) and recorded signals were processed using MATLAB. Electrocardiogram signals were recorded and compared with microfabricated electrodes against clinical-grade wet Ag/AgCl electrodes in a single-lead setup. The placement and an image of the microfabricated electrode during signal acquisition were illustrated in Fig. 1d.

Results and Conclusion

The resistance of the textile-like electrode was measured by a desktop multimeter and showed a relatively low resistance of 0.5 kΩ upon reduction. The flexibility of the electrodes was demonstrated in Fig. 1e, and their microscope images with and without rGO. The correlation function between the signals over a 10-second period was calculated to be 98.84%, indicating a strong correlation. This high correlation serves as validation for the high performance of the TPM electrode in capturing biopotential signals. Fig. 1f displays the two signals recorded over 10-second intervals.

Acknowledgments

Professor Murat Kaya Yapici appreciates the support of the Turkish Academy of Sciences (TUBA GEBIP'21) and the Science Academy (BAGEP'23).

References

[1] S. Savonitto et al., Prognostic value of the admission electrocardiogram in acute coronary syndromes, JAMA 281, (1999); doi: 10.1001/jama.281.8.707

[2] M. K. Yapici et al., Graphene-clad textile electrodes for electrocardiogram monitoring, Sens Actuators B 221, (2015); doi: 10.1016/j.snb.2015.07.111

[3] L. McNichol et al., Medical adhesives and patient safety: State of the science consensus statements for the assessment, prevention, and treatment of adhesive-related skin injuries, J. Wound, Ostomy Continence Nursing, 40, (2013); doi: 10.1097/WON.0b013e3182995516

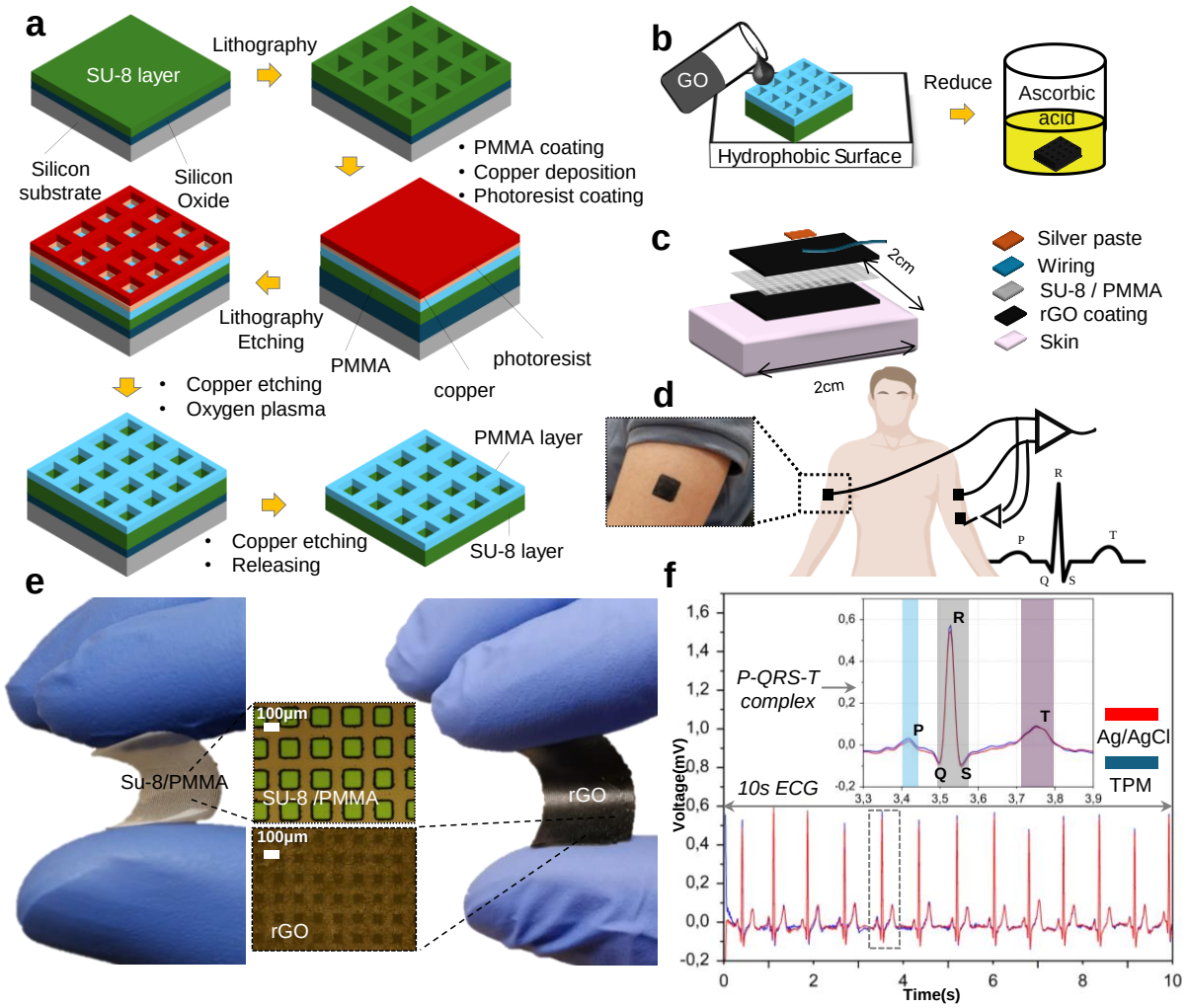

Fig. 1. (a) Fabrication steps of TPM electrode, (b) GO coating-reduction process, (c) exploded view of a TPM electrode showing its inner layers, (d) images of the electrode placed on the upper arm, (e) flexibility test applied by manually bending the electrode with under microscope images, and (f) Simultaneous ECG recording with textile-like electrodes and Ag/AgCl electrode

DOI 10.5162/EUROSENSORSXXXVI/OT6.217

3D Modelling of droplet formation in two-phase microfluidics for single-cell manipulation

Zsombor Szomor[1,2], *Eszter L. Tóth*[1], *Péter Fürjes*[1]

[1] *Microsystems Lab., Inst. of Technical Physics and Materials Science, HUN-REN Centre for Energy Research, Budapest, Hungary*
[2] *Óbuda University Doctoral School on Materials Sciences and Technologies, Budapest, Hungary*

Corresponding Author: szomor.zsombor@ek.hun-ren.hu

Summary:
In this study, the evolving hydrodynamic phenomena were modelled and characterized in complex two-phase micro-fluidic systems, aiming to enhance their applicability in advanced droplet-based single-cell sorting and analytical methodologies. An innovative Computational Fluid Dynamics (CFD) driven multi-dimensional optimization strategy was introduced and applied to explore the influence of geometric configurations and flow parameters. The droplet generation process has been studied by finite element modelling (FEM), utilizing the Laminar Flow and Level Set modules within COMSOL Multiphysics for numerical simulations. The proposed microfluidic system was manufactured and its behaviour was compared to the simulated characteristics. The experimental results supported the comprehension of the droplet formation in case variable volumetric flow rates and the interaction between flow dynamics and channel geometry. The effective control of the resultant droplet size distribution enables to determine the numbers of particles and cells confined.

Keywords: finite element modelling (FEM), two-phase microfluidics, single-cell, droplet formation, LoC

Motivation and Objectives

In the past twenty years, the adoption of micro-engineered systems has transformed the high-throughput analysis methods applied in the fields of chemical and biological sciences. Droplet-based microfluidic systems generate and manipulate distinct, physically separated fluid volumes or droplets. These multi-phase flow systems enable to utilise a wide range of easily accessible techniques for manipulating droplets, including splitting, merging, mixing, dilution and incubation. Droplets produced within two-phase microfluidic setups serve as optimal vessels for high-throughput cell screening applications. The response of individual cells to physical and chemical effects can be precisely examined in the micro-environment at the scale of cell size. This study employs high-performance finite element modelling (FEM) of these multi-phase systems for a thorough examination of hydrodynamic droplet generation process, primarily focusing on the effects of different flow rates and geometric parameters [1].

Fluid Dynamic Simulation Methods

COMSOL Multiphysics simulation code was employed to examine the droplet formation process in 3D two-phase models, aiming for a more precise understanding of the evolving flow characteristics. The analysis relies on numerically solving the governing Navier-Stokes and continuity equations. To characterize and compare microfluidic systems, the Capillary number (Ca) served as a commonly utilized parameter. Regarding droplet generation, including evolving droplet diameters and generation frequencies, the effects of volume flow ratios at the inlets, fluid viscosity, and interface tension were explored through successive parametric sweep simulations. Details of the main material properties of the fluids are provided in Table 1.

Tab. 1: Main material parameters of fluids

Material	Dynamic viscosity (μ)	Density (ρ)
Water	$1.95 \cdot 10^{-3}$ *Pa·s*	10^3 *kg/m³*
Silicon Oil	$20 \cdot 10^{-3}$ *Pa·s*	10^3 *kg/m³*

To manage reliable simulation of multiphase fluid flow, the Level Set technique, a robust computational approach was employed [2, 3]. This method was integrated with the Laminar Flow module to obtain precise results within the microfluidic approaches characterized by a predomi-

nance of low Reynolds numbers. The droplet diameters were calculated using a self-developed MATLAB script, which based on image analysis.

Numerical Results

According to the simulations, a significant change can be detected in the droplet diameters as the function of the flow rate and different geometric properties (Fig. 1). The average diameter was decreased from 98.27 µm to 62.16 µm when the flow rate of oil increased from 1.2 µl/s to 3.2 µl/s. The flow rate of water remained constant (0.2 µl/s). The size distribution of generated droplets was visualised by histograms created using the MATLAB software (Fig. 2).

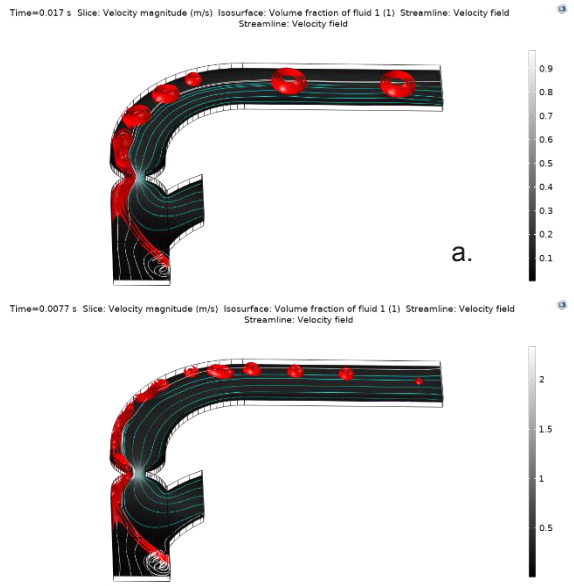

Fig. 1. Droplet generation in the 3D FEM model in the case of two different flow rates. The applied flow rates were: 0.2 µl/s (water), 1.2 µl/s (oil) in Figure 1.a and 0.2 µl/s (water), 3.2 µl/s (oil) in Figure 1.b.

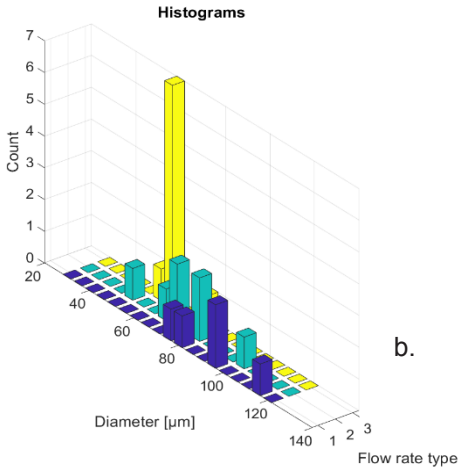

Fig. 2. Droplet size distributions based on the image analysis of the simulated droplet generation. While the flow rate of water was set to a constant value of 0.2 µl/s, three different oil flow rates were varied between 1.2 µl/s (1), 2 µl/s (2), and 3.2 µl/s (3).

Experimental Validation

To validate the numerical model, microfluidic devices were manufactured using soft lithography techniques in Polydimethylsiloxane (PDMS) polymer, featuring various geometrical configurations for droplet generation (Fig. 3). Experimental results indicate that factors such as the wetting characteristics of the aqueous phase significantly affect the frequency of droplet formation, whereas the velocity of the oil phase impacts the droplet size. Elevating either the flow rate of the oil phase or the Capillary number leads to a momentous reduction in droplet diameter.

The obtained results can support the establishment and optimisation of multi-phase microfluidic systems to achieve proposed size of microdroplets applicable as miniaturized reactors or cell containers in Lab-on-a-Chip and Organ-on-chip applications.

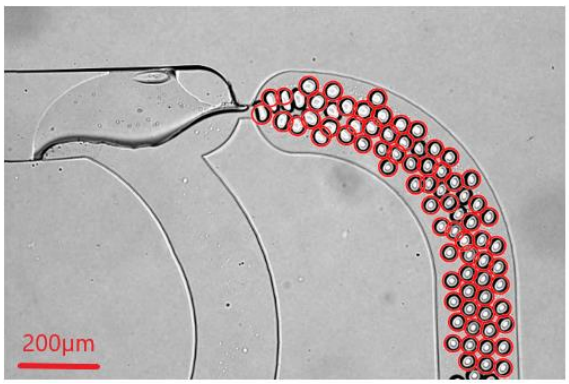

Fig. 3. Laboratory experiment to support the validation simulation results. The flow rate was set as 0.1 µl/s (water), 0.2 µl/s (oil). The droplet diameters were determined by MATLAB. The average diameter was 44.57 µm in this case.

References

[1] K. J. Donovan. „Computational fluid dynamics modeling of two - dimensional and three – dimesional segmented flow in microfluidic chips", San Jose State University, (2014). doi:10.31979/etd.3tzd-y6xm.

[2] H. A. Akhlaghi Amiri, A. A. Hamouda, „Evaluation of level set and phase field methods in modeling two phase flow with viscosity contrast through dual-permeability porous medium", Elsevier, International Journal of Multiphase Flow, (2013)

[3] „Two Methods for Modeling Free Surfaces in COMSOL Multiphysics", url: https://www.comsol.com/blogs/two-methods-for-modeling-free-surfaces-in-comsol-multiphysics/ (last access: 04-24-2024)

DOI 10.5162/EUROSENSORSXXXVI/OT6.228

A Simple Microfluidic System for Point-of-Care Therapeutic Drug Monitoring of Anticancer Drugs

András Füredi[1,2], Dóra Bereczki[1,3], Balázs Gombos[2,4], Pál Szabó[5], Péter Vajdovich[6], Péter Fürjes[1]

[1] Microsystems Lab., Inst. of Technical Physics and Materials Science, HUN-REN Centre for Energy Research, Budapest, Hungary,
[2] Drug Resistance Research Group, Institute of Molecular Life Sciences, HUN-REN Research Centre for Natural Sciences, Budapest, Hungary
[3] Óbuda University Doctoral School on Materials Sciences and Technologies, Budapest, Hungary
[4] Semmelweis University Doctoral School, Budapest, Hungary
[5] Centre for Structural Science, HUN-REN Research Centre for Natural Sciences, Budapest, Hungary
[6] Department of Clinical Pathology and Oncology, University of Veterinary Medicine Budapest, Budapest, Hungary

Corresponding Author: furedi.andras@ek.hun-ren.hu

Summary:

Therapeutic Drug Monitoring (TDM) would be a game changer for cancer therapy, however due to the current methods applied to follow the drug concentrations in the blood are expensive and require specialized expertise and instruments. Point-of-Care (PoC) TDM system has never realized. Here we present a fluorescence-based PoC microfluidic solution to monitor blood levels of anticancer agents. Using blood samples from mouse models of malignancies and veterinary cancer patients we prove our approach to be suitable for TDM in an experimental environment and have the potential to ultimately personalize chemotherapy.

Keywords: chemotherapy, therapeutic drug monitoring, drug resistance, microfluidics, fluorescence

Background, Motivation an Objective

Cancer claims almost 10 million lives annually, making it one of the major causes of death. Chemotherapy (CT) is a widely used option to treat malignancies, however CT protocols are established on a “one size fits all” basis and ignore inter-patient differences in drug pharmacokinetics which influence the blood levels of anticancer drugs, therefore leading to improper dosing in 50% of patients [1]. Missing target blood concentration will lead to drug resistance and/or unwanted side effects. Therapeutic Drug Monitoring (TDM) could be the key to improve and personalize CT, however the lack of an affordable Point-of-Care method is preventing its introduction to oncology. Mass spectrometry (MS) is the golden standard analytical approach to determine blood drug levels, but the instrument and specialized expertise to operate it are rarely available in the clinical environment. The high volume of blood required for MS analysis is also a challenge, because cancer patients are regularly weakened.

A Novel Microfluidic TDM Method

Exploiting the strong and specific fluorescence of anthracyclines [2], the most used CT agents, we propose a radically new microfluidic chip-based approach to rapidly determine plasma concentrations of several widely applied anticancer drugs (Figure 1.). Microvolume plasma separation and collection from a drop of blood (>50 μl) will be done with a specifically designed microfluidic chip, then plasma anthracycline concentration will be measured using a compatible spectrophotometer.

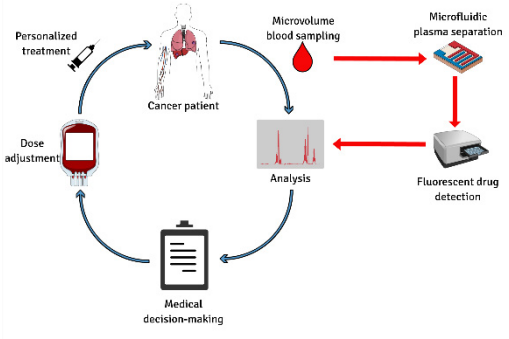

Fig 1. Our novel concept for microfluidic TDM.

Results

Anthracyclines (doxorubicin, daunorubicin, epirubicin, idarubicin, mitoxantrone, pixantrone) are not only the most effective anticancer chemotherapeutics, but they are also highly fluorescent. First, we showed that after sample preparation this autofluorescence is enough to detect doxorubicin (DOX, excitation: 490 nm, emission: 590 nm) in different solvents in a concentration dependent manner using 100 µl sample in a Tecan Spark fluorescent plate reader. To further reduce the required volume of sample, we designed a simple microfluidic chip with autonomous sample transport and proved the significant sample volume reduction (to ~ 7 µl) had no significant effect on the efficiency of fluorescence detection. The sensitivity and precision of the fluorescent measurements were validated by mass spectrometry based (Sciex 5600+ QTof) concentration determination. For the in vivo evaluation of our approach, we treated a mouse model of triple negative breast cancer with 6 mg/kg of pegylated liposomal doxorubicin (PLD) intravenously and took blood samples at 5 time points through retro-orbital bleeding. As Figure 2. shows, the individual pharmacokinetics of a mouse was determined, and the results were highly similar to the mass spectrometry measurements.

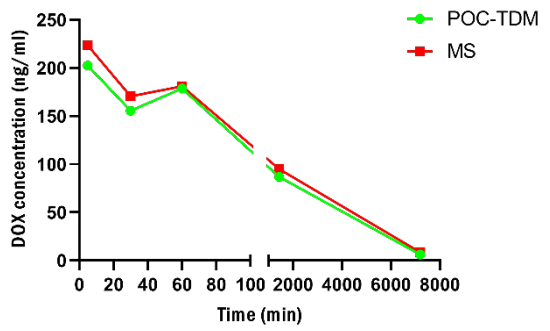

Fig 2. A representative pharmacokinetics curve of a single mouse treated with 6 mg/kg PLD. Blood concentrations measured by our point-of-care TDM chip (POC-TDM, green) was also determined by mass spectrometry (MS, red).

Furthermore, we tested our method in the veterinary clinical setting by analyzing blood samples from a cat cancer patient diagnosed with feline injection-site sarcoma (FISS). First, the patient was treated with epirubicin (25 mg/m^2, constant rate infusion for 60 minutes), but after there was no tumor response and the disease further progressed, the therapy was changed to PLD (1 mg/kg, constant rate infusion for 60 minutes) which stabilized the tumor and reduced its size. Comparing the pharmacokinetics of epirubicin and PLD revealed that, while epirubicin levels dropped significantly 60 minutes after administration, DOX concentrations was approximately 10 times higher, and it was not changed significantly in 270 minutes (Fig 3.).

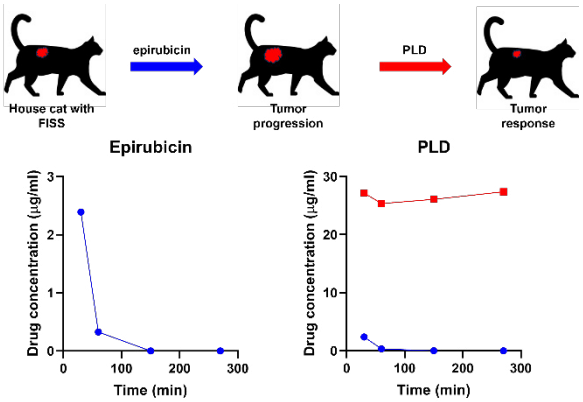

Fig 3. Our TDM method is capable of measuring epirubicin and DOX levels in veterinary patients. The progression of the FISS tumor was not influenced by epirubicin (blue) treatment, but PLD (red) therapy was partially successful due to the higher blood concentrations and longer circulation time.

PLD's increased concentration and retention time over epirubicin was a result of the liposomal formulation which shields DOX from enzymatic inactivation and metabolism [3].

Conclusion

As new anthracycline-based combinational therapies proved to be surprisingly efficient in various cancers [4], the need for more patient-tailored dosing is rising. We have established a novel POC-TDM microfluidic chip and a method to measure personal pharmacokinetics of individual patients treated with anthracycline chemotherapies ultimately opening a new avenue to personalized cancer care.

References

[1] J. Rebollo, B. Valenzuela, Use of therapeutic drug monitoring of cancer chemotherapy to modify initial per-protocol doses, Journal of Clinical Oncology, e13015 (2010), doi: 10.1200/jco.2010.28.15_suppl.e13015.

[2] N.S. Motlagh, P. Parvin, Fluorescence properties of several chemotherapy drugs: doxorubicin, paclitaxel and bleomycin, Biomedical Optics Express, (2016), doi: 10.1364/BOE.7.002400.

[3] A. Füredi, K. Szebényi, Pegylated liposomal formulation of doxorubicin overcomes drug resistance in a genetically engineered mouse model of breast cancer, Journal of Controlled Release, (2017), doi: 10.1016/j.jconrel.2017.07.010.

[4] K. Szebényi, A. Füredi, Effective targeting of breast cancer by the inhibition of P-glycoprotein mediated removal of toxic lipid peroxidation by-products from drug tolerant persister cells, Drug Resistance Updates, (2023), doi: 10.1016/j.drup.2023.101007

DOI 10.5162/EUROSENSORSXXXVI/OT6.229

Electrochemical assay for metal traces in marine environment by the Peaks Shift Analysis during catalysis

Ambre Brachfeld[1], Lylian Challier[1], Vincent Noel, Agathe Laes[2], Nicolas Le Poul[3]
[1]University Paris-Cité, ITODYS laboratory, 75014, Paris, France
[2]Laboratoire Détection Capteurs et Mesures, Unité Recherches et Développements Technologiques, Ifremer, Plouzané, France
[3]Laboratoire CEMCA UMR CNRS 6521, Université de Bretagne Occidentale, 6 Avenue Victor le Gorgeu, C.S. 93837, Brest 29238, France

ambrebrachfeld@gmail.com

lylian.challier@u-paris.fr

Summary:

An innovative electrochemical methodology is proposed for the quantitative *in situ* detection of trace metals in marine environment. This new method uses electrocatalysis to detect the catalyst instead of the substrate of the catalyst. As an example, we demonstrate that peak potential of proton reduction on copper during cyclic voltammetry is an effective method for the accurate detection of copper traces in aqueous media, with a detection limit (LOD) significantly lower than that of conventional electrochemical stripping methods (LOD = 1 nMol/L compared with 40 nMol/L, respectively).

Keywords: Copper sensor, Modified graphite electrode, Electrolyte engineering, Hydrogen evolution reaction, Peak shift analysis.

Tilte

Electrochemical assay for metal traces in marine environment by the Peaks Shift Analysis during catalysis

Background, Motivation an Objective

The detection of copper (Cu) at nanomolar concentrations represents a major challenge for marine water monitoring. Due to their relatively high sensitivity, selectivity and adaptability to *in-situ* measurements, electrochemical Cu(II) sensors appear to be ideally suited [1].

Description of the New Method

This innovative approach is based on a two-step procedure: (i) metal preconcentration at the surface of a specially modified electrode and (ii) the use of a reaction that can be electrocatalyzed by the metal, such as the HER (Hydrogen Evolution Reaction). Here, the originality lies in the use electrocatalysis to assay the catalyst (Cu) rather than the substrate. This approach uses the concentration-dependence of the peak potential in cyclic voltammetry to precisely determine metal surface concentration. Indeed, as stated by equation (1) for a case of Nernstian charge transfer (i.e. fast and reversible), the catalytic peak potential increases logarithmically with catalyst surface concentration :

$$E_{cat}^{0,ap} = E_{P/Q}^{0} + \frac{RT}{nF}\ln\left(\frac{k\Gamma_{P/Q}^{0}}{\sqrt{\frac{D_A nF\nu}{RT}}}\right) \quad (1)$$

With $E_{cat}^{0,ap}$ being the apparent standard catalytic potential, $E_{P/Q}^{0}$ the standard potential of the P/Q couple, $\Gamma_{P/Q}^{0}$ the surface concentration of the catalyst, D_s the diffusion coefficient of the substrate, k the rate constant of the catalytic reaction and υ the scan rate.

The so-called Peak Shift Analysis (PSA) method is based on collecting experimental data (peak potentials, metal stripping) to construct a calibration curve.

We illustrate this new procedure with copper detection. For this purpose, we fonctionalized pencil graphite electrodes (PGE) surfaces with different chelating molecules through a diazonium approach. The copper accumulated on the modified electrode was then used as catalyst for proton reduction in acidic media for further peak potential analysis.

Results

We first used *p*-aminobenzyl-*C*-functionalized Cyclam for electrode modification for its selectivity towards Cu(II) and its powerful chelating capability. However, this selectivity limits its application to other ions. To broaden the scope of our detection method, we sought a non-selective grafting molecule. Our choice fell on 4-Aminobenzoic acid (ABA), which promotes metal accumulation on the electrode through electrostatic interaction.

Electrodes modified with Cyclam (data not shown) and ABA shows an obvious concentration-dependence of the HER peak potential in cyclic voltammetry, as illustrated in Fig.1: increasing the concentration of copper in solution shifts the potential towards positive values. For the Cyclam and ABA-modified electrode, a copper concentration of less than 40 nmol/L can be detected with the PSA, while this is not possible with the conventional stripping analysis.

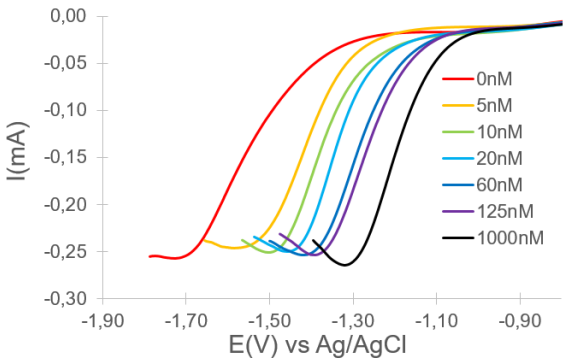

Fig. 1. Forward scan of the catalytic peaks measured after incubation of PGE/ABA in solution containing increasing Cu^{2+} concentrations (v=50mV/s, 0.1 mol/L Na_2So_4, pH=2.5)

Finally, 4-Bromobenzenediazonium tetrafluoroborate (BDT) was used as an ideal negative control due to its lack of electrostatic inte action with copper(II). No peak shift was recorded using this modified electrode.

The next step of this work is to demonstrate the versatility of this procedure in testing iron and manganese detection with PSA.

References

[1] L. Challier, et al, An ultrasensitive and highly selective nanomolar electrochemical sensor based on an electrocatalytic peak shift analysis approach for copper trace detection in water , Electrochimica Acta 434, 141298 (2022); doi:10.1016/j.electacta.2022.141298

DOI 10.5162/EUROSENSORSXXXVI/OT6.231

Towards Mass-Sensitive Assay Formats for Medical Drugs Using MIP Nanobodies

Peter A. Lieberzeit[1,2], Julia Völkle[1,2], Dalawan Limthin[3], Darinee Promthoyin[3]
[1] University of Vienna, Faculty for Chemistry, Department of Physical Chemistry, Waehringer Strasse 42, 1090 Vienna, Austria
[2] University of Vienna, Doctoral School of Chemistry, Waehringer Strasse 42, 1090 Vienna, Austria
[3] College of Materials Innovation and Technology, King Mongkut's Institute of Technology Ladkrabang, Bangkok, 10520, Thailand

Peter.Lieberzeit@univie.ac.at

Summary:
Solid-phase synthesis of molecularly imprinted polymers yields nanoparticles that inherently may replace antibodies in bioassays. Herein, we demonstrate the approach for mass-sensitive detection of two medical drugs, namely salbutamol and vancomycin. While both yield appreciable sensor responses on quartz crystal microbalances – for salbutamol including a competitive assay, the responses to vancomycin are limited due to template size (and, thus, fewer binding events). One way to overcome this is to link the MIP nanoparticles to heavier particles to increase the response per binding event.

Keywords: mass-sensitive sensing, molecularly imprinted polymers, nanoparticles, solid-phase synthesis, proteins, peptides

Background, Motivation an Objective

The last three decades have seen substantial progress in molecularly imprinted polymers (MIP), which – among others – have also firmly established themselves for designing chemical sensors [1]. Even though straightforward to synthesize and cost-effective, especially compared to natural antibodies, MIP come with certain limitations not least regarding batch-to-batch reproducibility [2]. This has so far prevented them from delivering on the promise of replacing natural systems in sensing formats and assays. The groups of S. Piletsky [3] and K. Haupt [4] have proposed a solid-phase approach to synthesize MIP nanoparticles (nanoMIPs) from immobilized template species, which display high binding site homogeneity and affinities comparable to those of natural antibodies.

Experimental Background

The research presented focuses on the development of nanoMIP-based gravimetric assay systems for the detection of medically relevant compounds. Combining nanoMIPs with highly sensitive quartz crystal microbalance (QCM) transducers allows for the design of reliable, robust, yet inexpensive sensing devices that can be used without the need for expensive laboratory equipment and trained personnel.

Via solid phase synthesis, nanoMIPs for the detection of salbutamol (SAL), a beta-agonist commonly used for asthma treatment and as leanness-enhancing agent in the meat industry as well as the antibiotic vancomycin were obtained and tested. The process involves immobilizing the respective template on silica gel by usual APTES modification followed by EDC/NHS-catayzed coupling. Consecutive washing steps with cold and hot water, respectively, allows for selectively enriching high-affinity particles for the respective analyte.

Furthermore, MIP nanobodies were conjugated to heavier inorganic nanoparticles to increase the QCM signal, owing to the higher mass increase per binding event.

Results

Binding affinity of the nanoMIPs was studied on dual channel QCM chips with one analyte-functionalized sensor surface, while the second measurement electrode was used for selectivity investigations.

As shown in Figure 1, injecting SAL-imprinted nanoMIPs results in strong, concentration-dependent frequency shifts for the template-

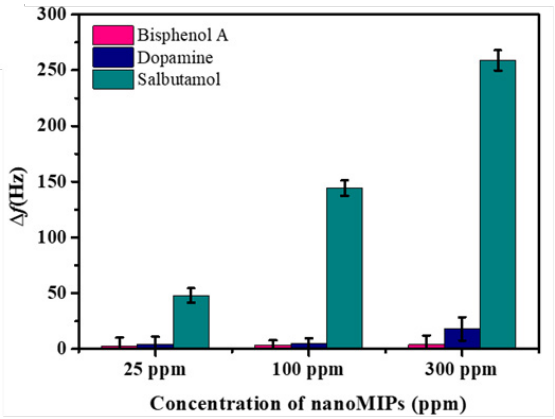

Fig. 1. Frequency response of QCMs modified with either SAL, bisphenol A or dopamine upon injection of varying concentrations of SAL-imprinted nanoMIPs.

functionalized electrode. Only negligible binding is visible on sensor surfaces modified with dopamine and bisphenol A, respectively.

Overall, this suggests appreciable affinity and selectivity of the SAL-MIPs. To establish a competitive assay, nanoMIPs at a fixed concentration of 300 ppm were mixed with varying concentrations of the analyte. As shown in Figure 2, one can observe an inverse relationship between SAL concentration and frequency shift, yielding a limit of detection of 2.85 ppm and a dynamic range of 2.5-50 ppm SAL in solution.

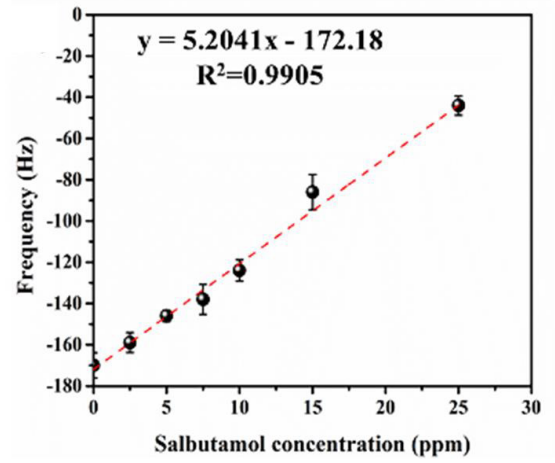

Fig. 2. Calibration curve for the competitive SAL-assay using mixtures of 300 ppm SAL-imprinted nanoMIPs and varying SAL-concentrations.

While for VM-imprinted MIPs, good selectivity compared to human serum albumin (HAS) is observed, the frequency response was significantly lower. This might be attributed to the size difference between the two analytes. With a sixfold molecular weight compared to SAL, the number of VM molecules that can be immobilized onto the sensor surface serving as nano-MIP binding site is significantly reduced. Thus, a concentration of 100 ppm of VM-imprinted nanoMIPs yields relatively low frequency shifts of -24 ± 4 Hz. To improve the limit of detection, the MIP particles were coupled to aminated TiO_2 nanoparticles via carbodiimide crosslinking. TiO_2 surface modification and coupling protocol were optimized towards minimal cluster formation. As shown in figure 3, first binding experiments on VM functionalized QCMs suggest a strong signal enhancing effect of the coupled MNPs with sensitivities in the sub-ppm region, proving that conjugation is a promising method for improving the obtainable limit of detection.

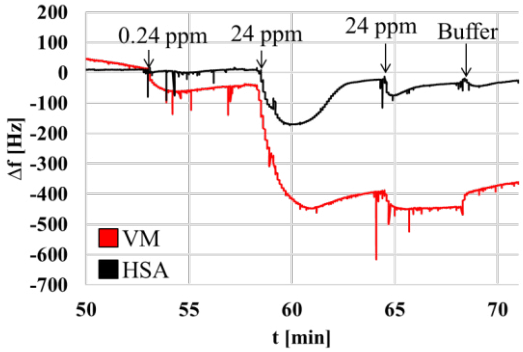

Fig. 3. QCM measurement with VM (red) and HSA (black) functionalized channel using increasing concentrations of VM-imprinted nanoMIPs conjugated to TiO_2 NPs.

References

[1] N. Leibl, K. Haupt, C. Gonzato, und L. Duma, Molecularly Imprinted Polymers for Chemical Sensing: A Tutorial Review, *Chemosensors* 9 (2021); doi: 10.3390/chemosensors9060123

[2] B. Bräuer, C. Unger, M. Werner, and P. A. Lieberzeit, Biomimetic Sensors to Detect Bioanalytes in Real-Life Samples Using Molecularly Imprinted Polymers: A Review, *Sensors* 21 (2021); doi: 10.3390/s21165550

[3] F. Canfarotta, A. Poma, A. Guerreiro, S. Piletsky, Solid-phase synthesis of molecularly imprinted nanoparticles, *Nature Protocols* 11:443–455 (2016); doi: 10.1038/nprot.2016.030

[4] S. Ambrosini, S. Beyazit, K. Haupt, B. Tse Sum Bui, Solid-phase synthesis of molecularly imprinted nanoparticles for protein recognition. *Chemical Communications* 49:6746 (2013); doi: 10.1039/c3cc41701h

DOI 10.5162/EUROSENSORSXXXVI/OT6.236

A Textile Electrochemical Sensor based on Ag Coated Fibers

Marc Martínez-Estrada[1], Ignacio Gil[1], Raúl Fernández-García[1]
[1] Department of Electronical Engineering, Universitat Politecnica de Catalunya; Terrassa, Spain.

Emails: marc.martinez.estrada@upc.edu, ignasi.gil@upc.edu and raul.fernandez-garcia@upc.edu

Summary:
A textile electrochemical sensor based on Ag coated embroidered fibers is presented to determine glucose concentration. The sensor design consists of 3-electrodes with different shapes and length. This design permits to perform a cyclic voltametric test with the sensor to observe the electrical properties changes produced by dropping of different glucose solutions. The increase of the current measured between the sensor electrodes provides enough information to identify the increase of the glucose concentration along the solutions.

Keywords: embroidered, textile, chemical, sensor, flexible

Background, Motivation an Objective

Electrochemical sensors have been one of the main challenges for the researchers who work integrating sensors over flexible substrates [1], [2], [3]. The electrochemical sensors integrated over substrates as textiles or clothes could provide the users a wide possibility of health care control applications.

Glucose is one of the main health parameters where the interest has been focused over the last years. The importance to control the concentration of glucose in blood/sweat is high to prevent hypoglycemia or hyperglycemia from diabetic people. Textile technologies have proved the possibility to integrate or built electrochemical sensor to measure the glucose concentration [4], [5]. To do it, some chemical treatments over the yarns need to be done to obtain the appropriate sensitivity. Chemical coatings or enzymatic treatments are performed over conventional yarns to obtain sensitive sensors to glucose or other chemical substances.

In this work, a textile embroidered electrochemical sensor has been designed to detect different concentrations of chemical substances. The sensor has been built using commercially available silver (Ag) conductive yarns without additional chemical or enzymatic treatments.

Description of the New Sensor and Experimental

The embroidered electrochemical sensor has been built following a 3-electrode sensor design where the longest electrode is the counter electrode (CE) the center electrode is the working electrode (WE) and the right electrode is the reference electrode (RE). Figure 1 shows the embroidered electrochemical sensor.

Fig 1. Embroidered electrochemical sensor with 3 electrodes. From Left to Right: CE, WE and RE electrodes.

To embroider the sensor a commercially silver conductive yarn, produced by Shieldex company[6], is used. The yarn has been made by coating with pure silver a polyamide multifilament yarn. Neither chemical treatment nor enzymatic treatment are applied to any of the electrodes to provide sensitivity to any chemical substance. The embroidered sensor is characterized with a Keithley Source Measurement unit SMU2636B (SMU). The process conducted to perform a cyclic voltammetry follows by: First the CE and WE electrodes are connected to the feed channel of the SMU and WE and RE to the measurement channel. Secondly, the cyclic voltammetry values are defined as the feed tension between -200 to 200 mV and scan rate 50mV/s.

To conclude a drop of the glucose solution sample is poured on the sensor and the test is conducted. The SMU obtain the current of both channels and the voltage generated on measurement channel.

To test the response of the sensor, four glucose solutions are prepared. The glucose concentrations present in the solutions are 90, 180, 1800 and 3600mg/dL, respectively.

Results

Sensor values are obtained performing a cyclic voltammetry with different glucose concentrations. To be more accurate with the results, four different embroidered sensors are prepared. Figure 2 shows the cyclic voltammetry graph of the sensors for each glucose concentration solution.

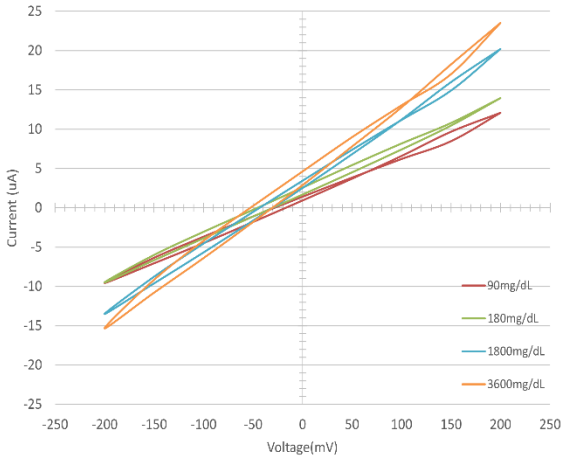

Fig 2. Cyclic voltammetry for the different glucose solutions.

It is observed how the increment in positive side voltage of the cyclic voltammetry values follows the increase of the glucose concentration over the solutions. The tendency observed demonstrates how the current values increases for the concentration increase on the sample solutions. The cyclic voltammetry shows a thin shape along the voltage swept due to the absence of chemical and enzymatic treatments to increase the sensitivity. Meaning that oxidation and reduction values during the cycle are very similar. Figure 3 shows one of the tension feeds points where the glucose effect on the sensor can be observed.

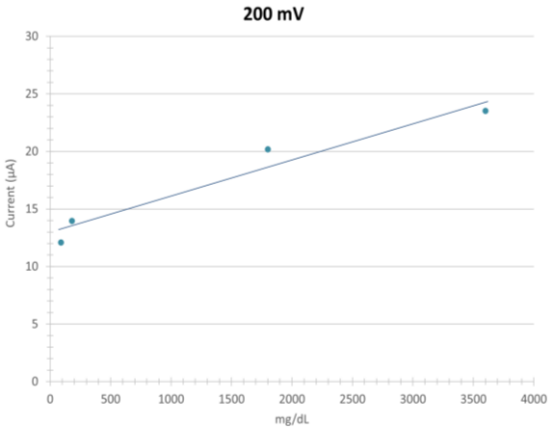

Fig 3. Linear regression for 200mV tension feed.

As it is shown in the graph, the tendency observed in 200mV of tension feed point shows a linear regression value of $y(\mu A)= 0.0031x(mg/dL) + 13$ with a $R^2=0.946$.

The embroidered sensor presented not only shows its ability to detect chemical substance concentration in solutions but also to be a good base to prepare selective sensor on wearable application by providing a stable sensor produced by Ag fibers.

References

[1] Y.-J. Kim, S. R. Chinnadayyala, H. T. N. Le, y S. Cho, «Sensitive Electrochemical Non-Enzymatic Detection of Glucose Based on Wireless Data Transmission», *Sensors*, vol. 22, n.º 7, Art. n.º 7, ene. 2022, doi: 10.3390/s22072787.

[2] J. Xu, Z. Yan, y Q. Liu, «Smartphone-Based Electrochemical Systems for Glucose Monitoring in Biofluids: A Review», *Sensors*, vol. 22, n.º 15, Art. n.º 15, ene. 2022, doi: 10.3390/s22155670.

[3] S. Kim *et al.*, «Soft, skin-interfaced microfluidic systems with integrated immunoassays, fluorometric sensors, and impedance measurement capabilities», *Proc. Natl. Acad. Sci.*, vol. 117, n.º 45, pp. 27906-27915, nov. 2020, doi: 10.1073/pnas.2012700117.

[4] A. Piper, I. Öberg Månsson, S. Khaliliazar, R. Landin, y M. M. Hamedi, «A disposable, wearable, flexible, stitched textile electrochemical biosensing platform», *Biosens. Bioelectron.*, vol. 194, p. 113604, dic. 2021, doi: 10.1016/j.bios.2021.113604.

[5] R. Wang, Q. Zhai, T. An, S. Gong, y W. Cheng, «Stretchable gold fiber-based wearable textile electrochemical biosensor for lactate monitoring in sweat», *Talanta*, vol. 222, p. 121484, ene. 2021, doi: 10.1016/j.talanta.2020.121484.

[6] Shieldex, «Shieldex® Conductive Twisted Yarn Silver Plated Nylon 66 Yarn 117/17 dtex 2-ply».

Acknowledgements

This work was supported by the Agencia Estatal de Investigación under the project PID2021-124288OB-I00.

DOI 10.5162/EUROSENSORSXXXVI/OT6.243

Potential use of meso-tetra (N-methyl-4-pyridyl) porphyrin to chlorogenic acid fluorescence detection

João Otávio Donizette Malafatti[1], Gabriele Magna[2], Francesco Pizzoli[2], Elaine Cristina Paris[1], Luiz Henrique Capparelli Mattoso[1], Corrado di Natale[2], Roberto Paolesse[2]

[1]National Nanotechnology Laboratory for Agriculture (LNNA), Embrapa Instrumentação, 13560-970, São Carlos - SP, Brazil.
[2] University of Rome Tor Vergata, 00133 Rome - RM, Italy.

Corresponding Author's e-mail address: jmalafatti@hotmail.com

Summary:

Chlorogenic acid (CGA) is widely used for biological and pharmacological activities. CGA can be harmful in high concentrations, so its control in wastewater became essential. Indicators or optical sensors are a practical and convenient way to detect CGA. In this context, porphyrins are widely used as optical receptors since they have a strong visible absorbance and may be fluorophores. Here, the UV-vis and fluorescence spectra revealed that meso-tetra (N-methyl-4-pyridyl) porphyrin (TMPyP) interacts with CGA at low molar ratios, suggesting its potential use for an optical sensor.

Keywords: fluorescence, porphyrin, polyphenol, sensor, wastewater.

Background, Motivation and Objective

Chlorogenic acid (CGA) is one of the most common polyphenols in plant, food, and biomedical products. Monitoring this antioxidant molecule is essential to evaluating the quality of manufacturing, such as coffee, and environmental aspects. The elevated abundance of CGA makes it an indicator of the total amount of polyphenols and an indicator of the quality of products [1]. As a consequence, the monitoring of CGA in water became of extreme importance to control the quality and contamination of waste.

In this context, optical and fluorescence sensors are appealing platforms in which the interaction between receptors and analytes can be detected by optical transducers. Fluorimetry is very attractive since it is a highly sensitive technique. On the other hand, the optical response occurring by analyte and sensing molecule interaction turns quick and easy visual monitor (change of color) [2,3]. Porphyrins are colored molecules with high extinction molar coefficients; they may be fluorescent with long emission wavelengths and have high chemical stability. This way, the target analyte interaction may be triggered by a change in absorbance or fluorescence spectra [4]. Sensors using porphyrins applied to CGA polyphenol have scarcely been reported [5] in the literature, with no examples of optical-based devices. Therefore, this study aimed to evaluate the possibility of developing an optical sensor based on meso-tetra (N-methyl-4-pyridyl) porphyrin (TMPyP) for detecting polyphenol CGA.

Description of the New Method or System

CGA (Sigma-Aldrich) monitoring was evaluated using the water-soluble porphyrin TMPyP. TMPyP is dissolved in DI water at 1.2 10^{-6} M concentration. Then CGA is added to the solution, considering TMPyP:CGA molar ratios ranging from 1:0.1 to 1:5 (1.2 10^{-7} – 6 10^{-6} mol L^{-1}). The spectroscopic methods were performed using ultraviolet-visible (UV-vis) range from 350 to 550 nm and fluorescence from 550 to 750 nm (with excitation at 422 nm).

Results

The initial results show that adding of CGA produces a decrease and a red shift of TMPyP absorbance spectra, proportional to the analyte concentration, as shown in Figure 1.

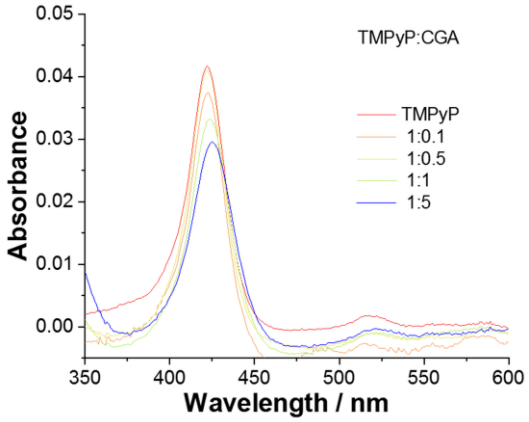

Fig. 1. TMPyP UV-vis spectrum vs CGA analyte ratio.

At the same time, the TMPyP fluorescence response in Figure 2 exhibits an intensity increase with the CGA addiction in this range evaluated (1.2 10^{-7} – 6 10^{-6} M). Remarkably, the concentration limit in wastewater by World Health Organization (WHO) is 2.8 10^{-7} M.

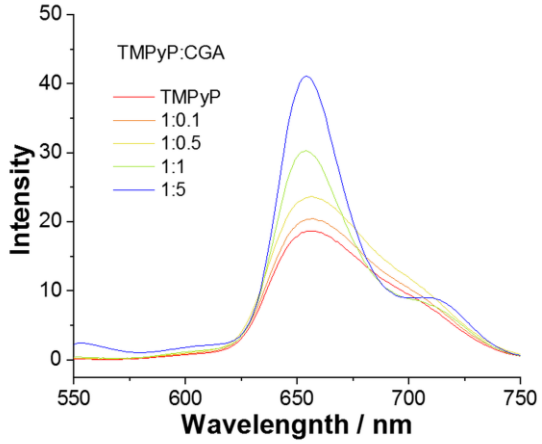

Fig. 2. TMPyP fluorescence spectrum vs CGA analyte ratio.

Conclusions

The results showed a potential use of TMPyP, a water-soluble porphyrin, as a chemical sensor to be applied in spectroscopic detection (UV-vis and fluorescence) of CGA polyphenol. The possibility to utilize this indicator in the solid state by its immobilization on substrates (such as filter papers, color catchers, nitrocellulose, etc.) or onto nanoporous structures (such as zeolite) may pave the way to the fabrication of susceptible sensors for this class of compounds.

Acknowledgments

This study was financed by FAPESP (Grant Number 2021/14992-1, 2023/03632-0). The authors acknowledge Embrapa (Grant Number 11.14.03.001.01.00), FINEP, SisNano, and AgroNano Network for financial support.

References

1. W. de J. R. Santos, M. Santhiago, I. V. P. Yoshida, and L. T. Kubota, *Analytica Chimica Acta* 695, 44–50 (2011).; doi:10.1016/j.aca.2011.03.018.

2. L. Lvova, F. Caroleo, A. Garau, V. Lippolis, L. Giorgi, V. Fusi, N. Zaccheroni, M. Lombardo, L. Prodi, C. Di Natale, and R. Paolesse, *Frontiers in Chemistry* 6, 1–10 (2018).; doi: 10.3389/fchem.2018.00258.

3. S. Patel, R. Jamunkar, D. Sinha, Monisha, T. K. Patle, T. Kant, K. Dewangan, and K. Shrivas, *Trends in Environmental Analytical Chemistry* 31, e00136 (2021).;doi: 10.1016/j.teac.2021.e00136.

4. P. Prosposito, L. Burratti, and I. Venditti, *Chemosensors* 8, 1–29 (2020).;doi:10.1016/j.aca.2011.03.018.

5. X. Zhao, J. Bai, X. Bo, and L. Guo, *Analytica Chimica Acta* 1075, 71–80 (2019).; doi:10.1016/j.aca.2019.05.030.

DOI 10.5162/EUROSENSORSXXXVI/OT6.246

Industrialized microfluidic cartridges with photonic chips

Siegfried Graf*, Mark Fretz, Roman Arnet
CSEM SA, Untere Gruendlistrasse 1, 6055 Alpnach, Switzerland
Mark.Fretz@csem.ch

Summary:

Integrating Photonic-Integrated Circuits (PICs) into microfluidic devices for diagnostics faces several challenges such as handling small PICs, ensuring interface access, managing temperature and UV sensitive coatings, and maintaining bubble-free sample transfer. CSEM offers unique services merging cleanroom packaging, microfluidic design, and prototyping, aiding PIC and diagnostics industry partners. Collaborations with different partners have led to tailored PIC integration solutions for sepsis detection, bioreactor contamination detection, food safety testing, and extracellular vesicle detection.

Keywords: hybrid PIC, microfluidic cartridge, chip integration, assembly, high volume production

Introduction

The integration of Photonic-Integrated Circuits (PICs) into microfluidic devices has wide ranging applications in the field of diagnostics. However, the requirements for the integration of PICs into microfluidics can vary significantly depending on the design and application of the PIC. For example, difficulties with handling due to the small size of PICs, the accessibility of optical and/or electrical interfaces, temperature and UV sensitive coatings, and bubble-free sample transfer are all challenges that are faced in microfluidic PIC integration. To aid our partners in the PIC and diagnostics industry, CSEM provides a unique combination of services by leveraging our in-house cleanroom packaging technologies and expertise with our microfluidic prototyping capabilities that are compatible with mass production.

CSEM has successfully collaborated with numerous partners on various integration solutions for PICs used for diagnostics, sepsis detection, contamination detection in bioreactors, food safety, as well as detection and counting of extracellular vesicles. Often, these solutions are specifically designed for passive or hybrid PICs, which may or may not have integrated light sources and photo detectors. Additionally, after several years of development, CSEM has developed a process for packaging small PICs (around 10 mm^2), allowing our partners to drastically reduce costs up to 10-fold, and significantly increase their market competitiveness.

Finally, CSEM has developed innovative solutions for in-line degassing, on-cartridge heating, and on-cartridge liquid storages.

Challenges

Chip geometry - Every customer uses a different PIC as outline in Figure 1. They have either been used for research purposes or towards a diagnostic disposable product.

Figure 1. (1) Bialoom PIC on stage – size 25mm x 25mm; (2) PHOTO-SENS PIC with VCSEL, photodiodes and NTC thermistor on chip – PIC size 3mm x 5 mm.

Reusable or low-cost fluidics - During the development phase, our customers often prefer to work with a reusable microfluidic solution while in the final application a disposable solution is inevitable. CSEM has therefore developed different PIC integration methods as outlined in Figure 2.

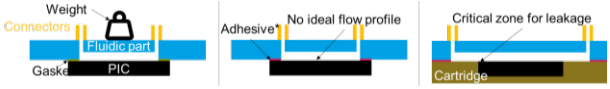

Figure 2. PIC integration methods. (left) sandwiching with a gasket, (middle) double adhesive bonding, (right) in-cartridge integration (not necessarily a PCB, also plastic substrate possible).

High sensitivity by preventing fouling - To prevent the loss of analytes from the sample reservoir to the detection site an antifouling surface is required. We have successfully applied

several different coatings from CSEM Optodex B, CSEM blocking agent but also Surfix's Coat & Close process. However, these coatings require solvent cleaning and plasma activation steps.

No air bubbles on sensor allowed - Depending on the PIC technology and measurement procedure, air bubbles passing the sensor might be detrimental to the measurement. For this reason, we have developed a miniaturized degassing solution. A degassing membrane is integrated inline with the fluidic channel which allows for efficient degassing.

UV-sensitive bio-functionalization - Depending on the application (such as sepsis detection, food safety and others), the sensing areas of the PICs have to be bio-functionalized with the appropriate receptor such as an antibody or aptamer. To ensure the highest sensitivity, these receptors need to be locally deposited on the sensing element. Examples will be shown.

Continuous and non-pulsating flow with preloaded liquids - CSEM has developed different ways to store and deliver liquids. In the project BIOCDx, liquids were stored in pre-filled syringe-like structures. In the project PHOTO-SENS, an alternative approach used pre-filled blisters. Emptying these blisters, however, results in a very high flow variability. To minimize this variability, we integrated an intermediate reservoir in the shape of a meander in which the volume of the blister can be emptied before being transferred to the PIC in a controlled way for priming, calibration, and washing.

Implementation example

In the project BIOCDx the goal was to detect protein signatures indicative of breast or prostate cancer for companion diagnostics. Lionix provided PICs (10mm x 10mm = 100mm^2) preassembled with a VCSEL and two arrays of 4 photodiodes which were encapsulated to protect the active components during the functionalization and spotting process. The PIC was bonded with a double adhesive tape onto a PCB from where wire bonds were made, and glop topped. This assembly was then bonded with a double adhesive onto the fluidic channel. The syringes are pre-filled and use a sacrificial valve to minimize the evaporation. Furthermore, the cartridge contains a blood separation membrane and on-cartridge valves to control the processes. In Figure 3 the cartridge is shown in the assembled state.

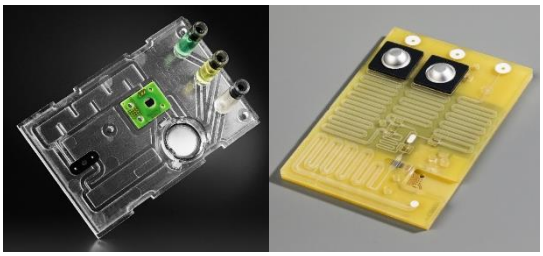

Figure 3. Photographs of the cartridges developed for (left) BIOCDx (right) PHOTO-SENS.

In the project PHOTO-SENS (www.photo-sens.eu) the goal was to detect pathogens in aquacultures to minimize the amount of antibiotics used. Surfix provided PICs (3mm x 5mm = 15 mm^2) which have been assembled with VCSEL, two arrays of 4 photodiodes and an NTC by PHIX (see figure 1 (images 2)). The cartridge designed by CSEM features a PCB bottom part and COC fluidic lid, which have both been anti-fouling coated by Surfix. Before encapsulation by CSEM, the hybrid PIC was placed flush to the PCB surface, and conductive glue was locally applied on the backside of the PIC for electrical contact with the on-chip heater. The fluidic lid was equipped with a double adhesive tape and blisters and sent to Surfix for bio-functionalization. In a final step, the lid was placed onto the PCB and a compression force was used to activate the adhesive.

The cartridge was then placed into the measurement instrument developed by LRE medical. where the cartridge is positioned, and the blisters are compressed to initiate fluid flow.

Summary and Conclusion

So far with every new PIC a different use case (e.g. sepsis detection, contamination detection in bio reactors, food safety, detection and counting of extra cellular vesicles, pathogen detection in aquacultures, cancer detection) was addressed, which resulted in a different microfluidic cartridge design and assembly strategy. Specific building blocks such as heaters, liquid reservoirs, sample injection, metering, flow front detection, degassing, and sample preparation have been developed alongside different PIC integration strategies. Currently, these different blocks can be combined to fulfill unique requirements for new use cases. A strong focus is always put on the compatibility with mass producible strategies (design for manufacturability) to ensure seamless technology transfer.

Acknowledgements

This work was supported by the European Funding Agency H2020 grant no 732309 (BIOCDx) and 965643 (PHOTO-SENS).

DOI 10.5162/EUROSENSORSXXXVI/OT6.248

3D-Printed Mouthguard with Integrated Microfluidic Drug Dispenser for Oral Cavity Applications

Tymon Janisz, Wojciech Kubicki, Rafał Walczak
Wroclaw University of Science and Technology, 63 Dluga St., 53-633 Wroclaw

Corresponding Author's e-mail address: tymon.janisz@pwr.edu.pl

Summary:

This study introduces an innovative 3D-printed mouthguard incorporating an integrated microfluidic drug dispenser. Fabricated from biocompatible resin utilizing Digital Light Processing (DLP) technology, the device allows for facile redesign and customization to accommodate individual dental anatomy. The integrated microfluidic system is equipped with two check valves, enabling simple and repeatable refilling, and dispensing of liquids from the internal reservoirs.

Keywords: 3D printing, microfluidics, drug dispensing, dental health

Introduction

Over the past decade, 3D printing has significantly impacted the dental industry, enabling the development of customized dental splints and mouthguards tailored for conditions such as bruxism and malocclusion [1, 2]. These advancements utilize 3D scans of the oral cavity to create models for designing personalized dental appliances. In this study, we propose a solution that integrates a microfluidic delivery system with a dental mouthguard, facilitating the dispensing of liquids for intraoral healing and therapy.

Materials and methods

The device was manufactured using Digital Light Processing (DLP) technology (Asiga), commonly employed for producing orthodontic appliances. An FDA-approved UV-curable resin (Pro3Dure) served as the construction material. The mouthguard's design is based on a standard dental splint model (Fig. 1a) and incorporates two integrated microfluidic dispensers, each with a liquid reservoir capacity of 105 µL.

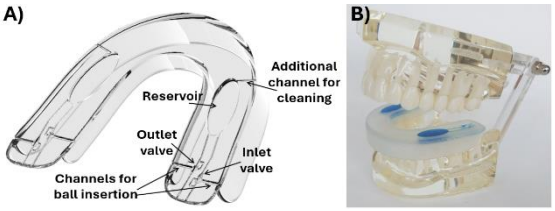

Fig. 1. 3D printed mouthguard: a) digital model containing two symmetrical drug dispensers, b) the mouthguard mounted in the human dental model (microfluidic system filled with a blue dye for contrast).

The upper and lower layers of the reservoir are designed as membranes that dispense the sample when compressed by teeth clenching. Each dispenser features two microfluidic channels with individual check valves operating in opposite directions, facilitating easy filling, and dispensing of the sample plug (Fig. 2). The dispenser's location can be customized according to a 3D scan of the dental structure (Fig. 1b).

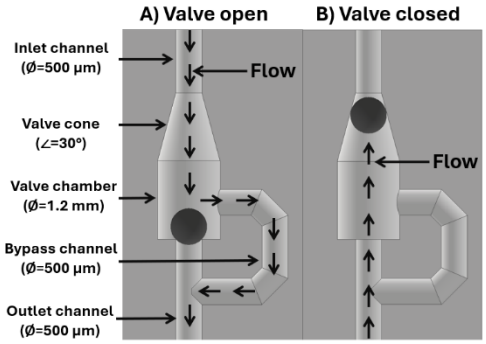

Fig. 2. schematic of the ball choke valve in open and closed mode.

Within the valve chamber, a steel microbead (Cospheric) was placed via an additional side channel, which was subsequently sealed after UV exposure to a resin droplet (Fig. 3). During compression, the microbead in the inlet valve moves toward its conical section, preventing flow, while the outlet valve remains open. In the refill stage, the valves operate oppositely, preventing the liquid from flowing back into the reservoir.

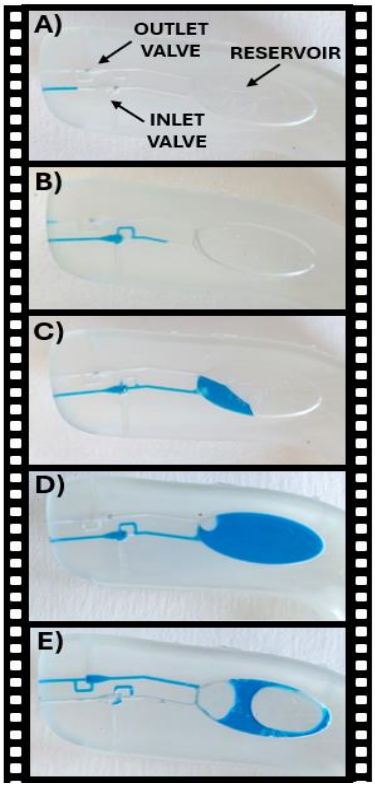

Fig. 3. Workflow sequence of the microfluidic drug dispenser: a) device empty, b) loading liquid through the input channel (inlet valve open, outlet valve closed), c) filling the reservoir with a liquid, d) device filled up, e) dispensing of the liquid from the reservoir forced by deflection of the membrane (inlet valve close, outlet valve opened.

Results

The design of the integrated microfluidic dispenser was optimized through a series of experiments using a pressure regulator, water tank, and measuring cylinder. Various microbeads with diameters ranging from 600 to 800 µm were tested, with the most extreme values of forward flow (open valve) and reverse flow (closed valve) observed for the 700 µm bead (Fig. 4a). The study identified that reverse flow (leakage) was caused by imperfections on the valve cone's surface, stemming from the printer's resolution limit of 35 µm. Nonetheless, the difference in flow between the open and closed modes was over 80 times greater. Additionally, it was confirmed that while forward flow increases linearly with pressure, reverse flow remains nearly constant (Fig. 4b).

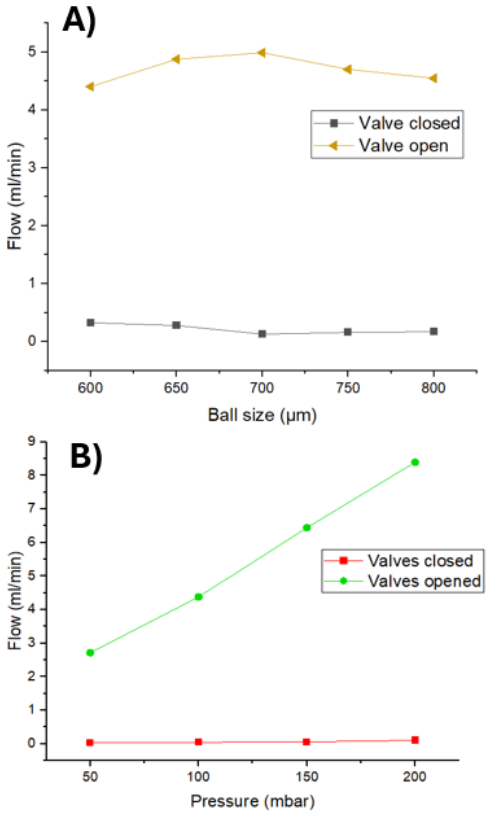

Fig. 4. Results of the forward (valve open) and reverse (valve closed) flow measurements of the microfluidic check valve: a) water flow in a function of ball size for constant pressure of 100 mbar, b) water flow in a function of applied pressure for ball size of 700 µm.

Summary

For the first time, a 3D-printed biocompatible mouthguard with an integrated microfluidic dispenser, equipped with a liquid refilling and distribution system, has been presented. The device can be easily replicated and customized to meet individual patient needs, paving the way for the development of 3D-printed intraoral microfluidic devices for personalized medicine.

Acknowledgement

This research was funded by the European Union's Horizon 2020 research and innovation programme under Marie Skłodowska-Curie grant agreement No. 872370, and Polish Ministry of Education and Science programme entitled the International Co-financed Projects (PWM, 5089/H2020/2020/2, 2019-2024).

References

[1] Shaikh, S. S., Nahar, P., Shaikh, S.Y., et al. Current perspectives of 3d printing in dental applications, Brazilian Dental Science, 2021, 24(3), doi.org/10.14295/bds.2021.v24i3.2481

[2] Balhaddad, A.A., Garcia, I.M., Mokeem, L. et al. Three-dimensional (3D) printing in dental practice: Applications, areas of interest, and level of evidence, Clinical Oral Investigations 27, 2023, 2465-2481 doi.org/10.1007/s00784-023-04983-7

DOI 10.5162/EUROSENSORSXXXVI/OT6.260

Characterization of an Integrated Pt Counter Electrode on GaN/AlGaN-ISFET Wheatstone Bridge pH-sensors

A. Hinz[1], *G. Steingelb*[1], *C. Habben*[1], *S. Figge*[1], *M. Eickhoff*[1]
[1]*Institute of Solid State Physics and MAPEX Center for Materials and Processes, University Bremen, Germany*

ahinz@uni-bremen.de

Summary:
GaN/AlGaN high electron mobility transistors (HEMT) were used as a pH-sensors, employing a Wheatstone bridge design in order to reduce parasitic effects on the sensor response. A Pt counter electrode was patterned directly on the sensor to achieve a more compact design and showed good operation characteristics. However, the signal stability was worse compared to an external counter electrode. In addition, we investigated the effect of different pH-sensitive gate layers, such as TiO_2 and Ta_2O_5, as well as the compensation of temperature effects and light-induced drift in the Wheatstone design.

Keywords: GaN/AlGaN, ISFET, Wheatstone Bridge, Heterostructure, pH-sensor

Introduction

Ion-sensitive field effect transistors (ISFETs) have attracted high research interest since their discovery by Bergveld in 1970 [1]. GaN/AlGaN HEMT structures have been demonstrated to exhibit excellent pH-sensor characteristics, such as a high, linear response, chemically inert surface and thus a small chemically induced drift [2]. However, these ISFETs also respond to other environmental parameters such as temperature or light and exhibit related signal drifts [3].

To reduce these effects, a Wheatstone bridge design was fabricated, consisting of one sensitive ISFET with the GaN gate exposed to the electrolyte FETs for which the gate was passivated by a 500 nm thick layer of sputter-deposited Al_2O_3. Thus, the latter ones do not show a pH response but are still affected by parasitic parameters. In addition, a Pt counter electrode was also processed on the chip to reduce the overall size of the sensor.

Methods

The Wheatstone bridges were fabricated on commercial wafers AlGaN/GaN HEMT structures (150 nm GaN/ 20 nm $Al_{0.25}Ga_{0.75}N$/ 3 nm GaN on HR-Si substrate, 2DEG charge density of > 8e12 cm^{-2} and mobility of > 1800 cm^2/Vs, supplied by soitec) with standard photolithographic methods. Heterostructures with and without 3 nm GaN cap were compared. A sketch of the sensor is depicted in Fig. 1.

The sensors were glued on a printed circuit board and the contacts were wire bonded to the board. For measurement in electrolyte the contacts were covered with silicone glue. The measurements were performed with a three-electrode setup in a temperature-controlled beaker. The used electrolyte was phosphate-buffered saline (PBS 0.05 mM). For the pH-measurements titrations with diluted HCl were performed.

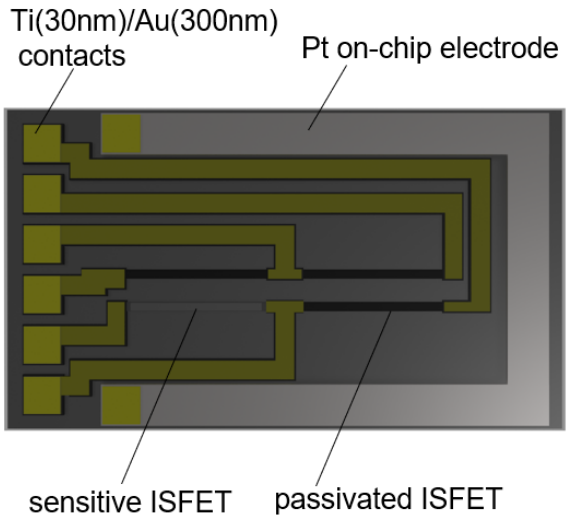

Fig. 1 Schematic of the device. The dimensions are 6 mm in length and 3.5 mm in width.

(1)

Results

To compare the on-chip electrode with an external counter electrode, pH-measurements with the sensitive ISFET only were performed. The drain-source current I_{DS} was regulated constant with the gate-source voltage V_{GS}. In Fig. 2. the measurement an external counter electrode is shown, Fig. 3 displays the results for the on-chip electrode. The sensors with an on-chip electrode exhibit a higher noise level, most likely due to the smaller distance to the gate, thus leading to a higher leakage current as it is also visible in the transfer characteristics.

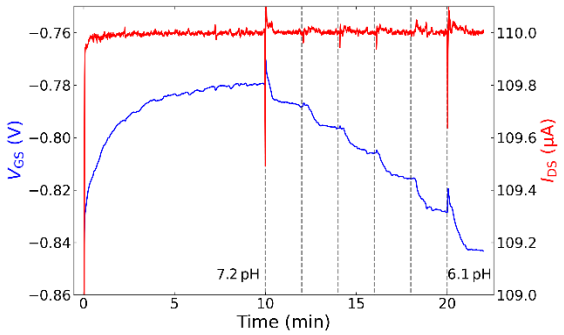

Fig. 2 pH-measurement with external counter electrode.

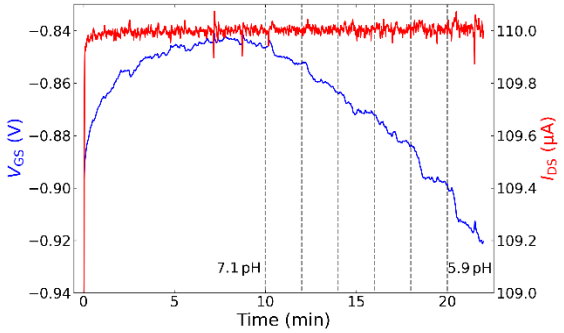

Fig. 3 pH-measurement with on-chip counter electrode.

A measurement with the on-chip electrode in the Wheatstone bridge configuration is depicted in Fig. 4. The bridge sensitivity of ≈ 2.5 mV/pH is similar to values reported in [4] (2.3 mV/pH).

Furthermore, temperature-dependent measurements were performed to analyse the compensation effects of the bridge and a significant reduction from 55 mV/°C to 7mV/°C. was found. Also, ultrathin coatings of the sensitive gate area with TiO_2 and Ta_2O_5 realized by Atomic Layer Deposition were carried out and their effect on the sensor performance was studied.

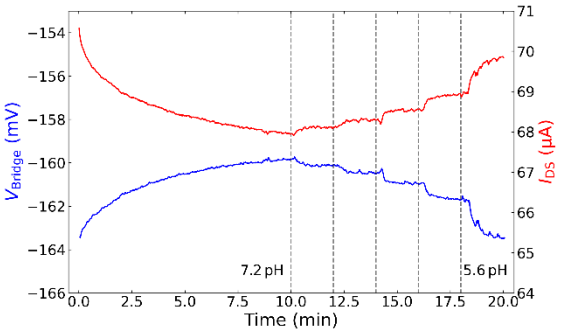

Fig. 4 pH-measurement in the Wheatstone Bridge configuration.

Perspective

The intention is to have a small and compact sensor. To add an on-chip reference electrode in addition would reduce the size of the sensor. Also, a combination of two different gate dielectrics on two sensitive ISFETs with differential read-out is a promising approach in that direction.

(1)

References

[1] P. Bergveld, Development of an Ion-Sensitive Solid-State Device for Neurophysiological Measurements, *IEEE Transactions on Biomedical Engineering* BME-17, 70-71 (1970); doi: 10.1109/TBME.1970.4502688

[2] G. Steinhoff, M. Hermann, W.J. Schaff, L.F. Eastman, M. Stutzmann, M. Eickhoff, pH response of GaN surfaces and its application for pH-sensitive field-effect transistors, *Applied Physics Letters* 83, 177-179 (2003); doi: 10.1063/1.1589188

[3] M.T. Hirsch, J.A. Wolk, W. Walukiewicz, E.E. Haller, Persistent photoconductivity in n-type GaN, *Applied Physics Letters* 25, 1098-1100 (1997); doi: 10.1063/1.119738

[4] D. Stock, G. M. Müntze, S. Figge, M. Eickhoff, Ion sensitive AlGaN/GaN field-effect transistors with monolithically integrated wheatstone bridge for temperature- and drift compensation in enzymatic biosensors, *Sensors and Actuators B: Chemical* 263, 20-26 (2018); doi: 10.1016/j.snb.2018.02.068

DOI 10.5162/EUROSENSORSXXXVI/OT6.263

Design and Verification of An Automated Non-contact Dielectric Sensor System

SHENG-HSUN HUANG[1], Xiang-XU Lin[1], YA-FU LIOU[2], KUDA WU[3], SHENG-YU PENG[4], CHII-WANN LIN[1,2,3]

1. Graduate Institute of Biomedical Electronics and Bioinformatics, National Taiwan University, Taipei 106319, Taiwan

2. Department of Biomedical Engineering, National Taiwan University, Taipei 106319, Taiwan

3. Biomedical Technology and Device Research Laboratories, Industrial Technology Research Institute, Hsinchu 310401, Taiwan

4. Department of Electrical Engineering, National Taiwan University of Science and Technology, Taipei 106335, Taiwan

Corresponding Author's e-mail address: cwlinx@ntu.edu.tw

Summary:

In biosensor research, it's important for the sensor to be non-invasive, label-free, and enable real-time sensing. Microwave dielectric sensors offer a promising solution. Our study proposed a dielectric sensor system integrating sensors and CMOS readout circuits. It measures substance permittivity by analyzing LC oscillator frequency and amplitude via an interdigit electrode antenna. Validation included measuring ethanol and methanol concentrations, showing strong correlation with VNA-measured permittivity. Real-time capabilities were verified by injecting air and DI water using a pump.

Keywords: dielectric constant, LC oscillator, interdigital electrode, permittivity, biosensor.

Introduction

When measuring biological samples, it's crucial for the sensor to be non-invasive, non-labeling, and capable of real-time sensing. Recently, antenna sensor architecture has emerged as a solution to meet these unmet needs. It utilizes electromagnetic waves to measure the permittivity of samples, which represents the relationship between electric displacement and applied electric fields. In a fundamental impedance experiment, we can calculate the complex permittivity as eq. (1) and (2). Admittance measurement reveals complex permittivity and distinguishes materials.

$$\varepsilon^* = \varepsilon' - j\varepsilon'' \quad (1)$$

$$\varepsilon' = \frac{Cd}{\varepsilon_0 A}, \varepsilon'' = \frac{d}{RA\omega\varepsilon_0} \quad (2)$$

Our study proposed a dielectric sensor system to measure the permittivity of materials under test. This sensor utilizes an interdigit antenna to generate an electric field. In addition, it employs an LC oscillator and incorporates digital readout circuits. Analysis of antenna resonance frequency and amplitude enables material permittivity inference and identification of biological substances.

Design of Dielectric Sensor System

Fig.1 shows the block diagram of the Dielectric Sensor System, which comprises a CMOS dielectric sensor [1], an amplitude readout circuit and a frequency readout circuit. The readout circuits help us digitalize the sensor's signal. The designed circuitry was fabricated by using the TSMC 0.18μm process. Besides, we have developed a digital microcontroller (STM32-L452REP) to interface with the readout circuits.

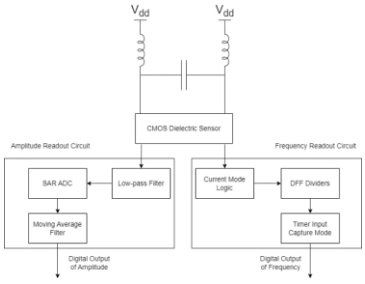

Fig.1 The block diagram of the Dielectric Sensor System.

The CMOS dielectric sensor uses interdigital electrodes as capacitors coupled with off-chip inductors to form an LC oscillator. Cross-coupled pair transistors cancel tank resistance (R_{eq})for stable resonance.

Fig.2 depicts the schematic of the cross-coupled LC oscillator. At resonance, parallel inductance-capacitance admittance reaches zero, allowing the resonant frequency and amplitude to be derived from eq. (3) and (4) respectively [1].

$$f = \frac{1}{2\pi\sqrt{LC}} \quad (3)$$

$$V = \frac{4}{\pi} I_{tail} R_{eq} \quad (4)$$

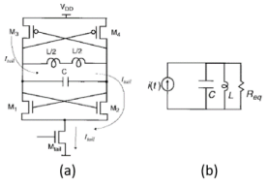

Fig. 2 The cross-coupled LC oscillator. (a) Schematic(b) Equivalent circuit [1]

By solving eq. (1), (2), (3), and (4), we can establish the relationship between the oscillating signal and permittivity. Eq. (5) and (6) show that f^{-2} is linear with ε', and $\frac{1}{Vf}$ is linear with ε''.

$$f^{-2} = 4\pi^2 L \frac{\varepsilon_0 A}{d} \varepsilon' \quad (5)$$

$$\frac{1}{Vf} = \frac{A\pi^2 L \varepsilon_0}{2 I_{tail} d} \varepsilon'' \quad (6)$$

The frequency readout circuit comprises a current mode logic circuit (CML), frequency dividers, and a timer input capture circuit. The CML converts the oscillating signal to digital logic levels, allowing division by D flip-flop (DFF) dividers. Through 9-stage DFF division, the frequency becomes low enough for detection via the microcontroller's timer input capture mode. Positive edges of the sensor's signal trigger storing the counter value in the compare and capture register (CCR). Sensor frequency is calculated using eq. (7).

$$f_{sensor} = \frac{f_{ref}}{\Delta CCR} \quad (7)$$

We measure the oscillating signal's amplitude by connecting one of the NMOS transistors from the cross-coupled pair to a low-pass filter. After filtering, it becomes a DC signal. The microcontroller reads this DC signal digitally through the embedded SAR SDC at 12-bit resolution, with VLSB at 0.439 mV. This digital output is further filtered using a moving average filter to minimize environmental interference.

Experiments and Results

Fig. 3 shows the device of our dielectric sensor system. We tested its performance by measuring 5 concentrations of ethanol and methanol samples. Parafilm was used to isolate the samples for non-invasive sensing. A 10 mL sample, with a diameter of 55 mm, was placed directly over the electrode, covering it entirely, at a height of about 4.2 mm. After a one-minute settling time, the system recorded one minute of sensor signals, from which average and standard deviation were calculated.

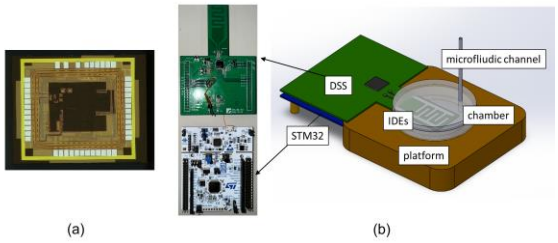

Fig. 3 The device of dielectric sensor system(a) The die photo of CMOS dielectric sensor. (b) The measurement setup.

Fig. 4 shows our sensor's signal correlation with substance permittivity from Vector Network Analyzer (VNA), following eq. (5) and (6). These results affirm high correlation, validating our dielectric sensor system's accuracy and reliability in permittivity measurement.

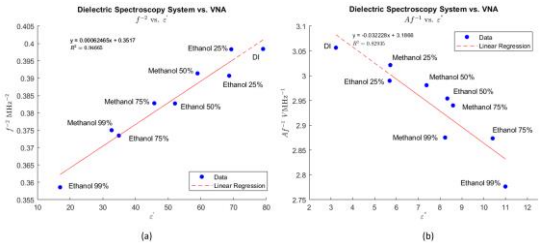

Fig. 4 Sensor output vs. substance's permittivity (a)f^{-2} $vs.\varepsilon'$ (b)$\frac{1}{Vf}$ $vs.\varepsilon''$.

To verify it's real-time sensing capability, we use a pump to inject DI water and observe the sensor's response over time. Our assumption is that both frequency and amplitude will decrease as DI water has a higher permittivity than air. Once the DI water is fully injected, the pump switches to injecting air. The signal will increase but won't return to its initial level due to the remaining water. Fig. 5 depicts these results, showing a signal decrease at 25 seconds and an increase at 270 seconds, matching our pump settings. These results confirm the real-time sensing capability of our dielectric sensor system.

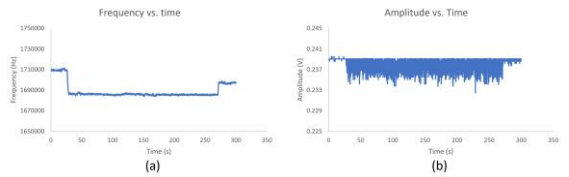

Fig. 4 Sensor output vs. time (a)Frequency vs. time (b)Amplitude vs. time.

References

[1] Wei-Liang Hsu（2022）◦ A CMOS Biosensor for Sensing Permittivity at Microwave Frequencies.

DOI 10.5162/EUROSENSORSXXXVI/OT6.265

Photoluminescence Lifetime Based pH and O_2 Sensors for the Analysis of Cell Metabolism

Dmitri B. Papkovsky, Liang Li, Alexander V. Zhdanov
School of Biochemistry and Cell Biology, University College Cork, Cork, Ireland

d.papkovsky@ucc.ie

Summary:

Sensor based systems for cell analysis are well established and actively used in biomedical research and drug development. However, sensor materials and detection principles embedded in the current systems are not optimal. We describe advanced solid-state sensing materials which provide photoluminescence lifetime based sensing of pH and O_2 and calibration-free operation on existing detection platforms. They are demonstrated with mammalian cells and tissue samples, measuring their Oxygen Consumption Rate (OCR) and Extracellular Acidification Rate (ECAR).

Keywords: Photoluminescent oxygen and pH sensors; Luminescence lifetime based sensing; OCR and ECA measurement; Cell metabolism and bioenergetics;

Introduction

Optochemical sensors, mainly the photoluminescent O_2 and pH sensors, have been successful in cell analysis. By allowing high throughput contact-less measurement of the oxidative phosphorylation (OCR) and glycolytic (ECAR) fluxes of cultured cells under different physiological conditions, they enable a detailed analysis of cell bioenergetics and metabolism. The two main sensing approaches are Luxcel Mitoxpress probes and Seahorse XF (eXtracellular Flux) analyzer.

Luxcel's open architecture platform uses soluble phosphorescent O_2 and pH probes and detection on a standard plate reader in standard microplates (with oil seal for the OCR) [1]. Having moderate sensitivity, this platform provides highly accurate, multiplexed, calibration-free detection, via lifetime based sensing of both O_2 and pH. While the integrated opto-mechanical XF analyzer operates with dedicated microchamber plates reversibly sealed with moving pistons which also contain solid-state O_2 and pH sensor coatings. Although the XF allows user-friendly hands-free operation with sensitive and sequential OCR and ECAR measurement and effector additions [2], it uses non-optimal and outdated sensor chemistries and intensity based sensing of O_2 and pH. So, there is a need in improved sensing materials and detection systems for such applications, particularly for pH and dual pH/O_2 sensing.

Description of the New Method or System

Recently, we have developed a panel of new solid-state fluorescent pH sensitive materials comprising fluorescent porphyrin dyes embedded in plasticized PVC matrix, together with a proton transfer agent (a lipophilic borate salt) [3]. Such materials show prominent reversible response to pH (pKa 6-7, tunable), changing their fluorescence intensity, intensity ratio and lifetime characteristics. The ns lifetime based detection, which has internal referencing capabilities, is particularly useful, as it enables the design of robust calibration-free pH sensing systems. Furthermore, the new pH sensors are multiplexable with Pt-porphyrin based O_2 sensors which phosphoresce in the μs time range. The resulting dual pH/O_2 lifetime based sensors have the same detection settings: 380-410 nm for the excitation and 600-670 nm for emission. This simplifies their detection and temporal multiplexing.

Results

We have carried out rigorous characterization and optimization of the new lifetime based pH sensors, for use in pH/ECAR measurements. Optimization parameters included the type of pH sensing dye (OEP, OEPK) and PTA (several borate salts), their concentrations and concentration ratio in the sensor, pH calibrations (Abs and FI spectra, fluorescence lifetimes), determination of the corresponding pKa values and measurement ranges. Such sensor coatings were applied on planar substrates (Mylar film) and on 96-well plates, and reproducibility

of disposable calibration-free pH sensors and batch-to-batch variability were studied, so as possible toxic action of the sensors on cells, operational and storage stability, response time, cross-sensitivity with the O_2 sensors.

Thus, images of the OEPK based sensor dots in Figure 1 reveal that their Intensity signals are strongly influenced by dye concentration and sensor thickness, while lifetime signals are determined mainly by sample pH, producing narrow and distinct distributions at different pH.

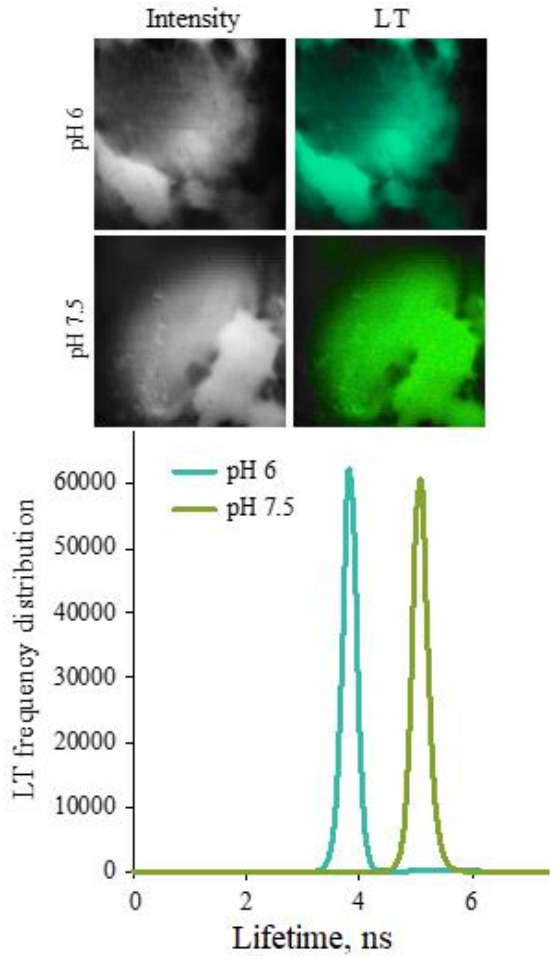

Figure 1. Fluorescence intensity and lifetime images of the OEPK based sensor coatings at pH 6.0 and 7.5 (top panel) and corresponding lifetime distributions (bottom panel), 21°C.

Since the sensors have stable and accurate LT calibration (Figure 2), they allow calibration-free operation on disposable or continuous basis for the measurement of pH and ECAR. Figure 2 also shows that the OEPK sensors are usable over the pH range 5.0 – 7.0 changing their lifetime from 3 ns to 6 ns, i.e. ~2-fold. And the OEP sensors work over the pH range 6.5 – 8.5 and have lifetime span from 7.5 ns to 12.5 ns.

Subsequently, the pH sensor coatings, deposited on suitable substrates (polyester film or polypropylene microplates), were demonstrated in the following biological experiments: i) ECAR measurements for HCT116 cells in 96WPs under different treatments [3]; ii) imaging extracellular pH in cultured multicellular spheroids formed by HCT116 cells [3], and iii) in ex-vivo tumor tissue and normal muscle tissue from mice [4]; iv) simultaneous ECAR/OCR measurement in HCT116 cells using OEPK/PtOEP dual pH/O_2 sensor coatings.

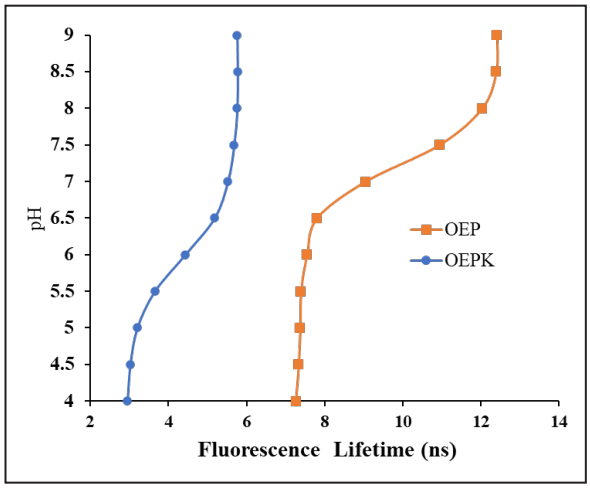

Fig. 2. Calibration curves for the pH sensors based on OEP and OEPK dyes in fluorescence lifetime scale, PBS, 21°C.

Overall, the new fluorescence lifetime based pH sensors and dual pH/O_2 sensors hold promise for use in cell analysis and tissue imaging.

Acknowledgement

Financial support of this work by the Science Foundation Ireland, grant SFI-12/RC/2276_P2, is gratefully acknowledged.

References

[1] B. Plitzko, S. Loesgen, Measurement of Oxygen Consumption Rate (OCR) and Extracellular Acidification Rate (ECAR) in Culture Cells for Assessment of the Energy Metabolism. Bio Protocols, 8(10): e2850 (2018).

[2] D.B. Papkovsky, A.V. Zhdanov, Cell Energy Budget platform for multi-parametric assessment of cell and tissue metabolism, Mitochondrial Medicine, 2nd Edn, Ch. 16, pp. 305-324 (2021).

[3] L. Li, A.V. Zhdanov, D.B. Papkovsky, Advanced multimodal solid-state optochemical pH and dual pH/O2 sensors for cell analysis, Sensors Actuators B: Chemical, 371: 132486 (2022).

[4] D. Angelone, L. Li, C. Devoy, A.B. Matheson, A.T. Erdogan, R.K. Henderson, M. Tangney, D. B. Papkovsky, S. Andersson-Engels, S.V.S. Konugolu, Metabolic imaging of tumor tissue samples using planar fluorescence lifetime-based pH sensors and a SPAD array imager, (2024, in preparation).

DOI 10.5162/EUROSENSORSXXXVI/OT7.31

A Nanophotonic Fiber-Tip Sensor for the Detection of Single Nanoparticles

Arthur L. Hendriks[1], Daan Rabelink[1], Mathias Dolci[1], Paco Dreverman[1], Mildred S. Cano-Velázquez[1], Luca Picelli[1], René P.J. van Veldhoven[1], Peter Zijlstra[1], Ewold Verhagen[2], Andrea Fiore[1]
[1] Department of Applied Physics and Science Education, and Eindhoven Hendrik Casimir Institute, Eindhoven University of Technology, 5600 MB, Eindhoven, The Netherlands,
[2] Center for Nanophotonics, AMOLF, Science Park 104, 1098 XG, Amsterdam, The Netherlands

a.l.hendriks@tue.nl

Summary:
We present a nanophotonic fiber-tip sensor with an unprecedented combination of quality factor, reflection modulation, and mode confinement by using advanced design methods. Due to this unique combination it allows for the detection of nanoscale objects, where we experimentally demonstrate the real-time detection of single 50 nm nanoparticles.

Keywords: Nanophotonics, Photonic Crystal Cavities, Fiber-Optic Sensors, Fiber-Tip Sensors, Nanoparticles

Introduction

Fiber-optic sensors allow for accurate and remote sensing of the properties of the surrounding medium while being minimally invasive and insensitive to electromagnetic interference. The most common fiber-optic sensor, the fiber Bragg grating (FBG), relies on the periodic modulation of the core of the fiber. FBGs are typically only sensitive to temperature and strain. To increase the functionalities of fiber-optic sensors, many types of "lab-on-fiber" technologies have been proposed and investigated, which combine a local resonant structure in or on the facet of an optical fiber [1,2]. Generally, fabrication methods for micro- or nanostructures on the tip of a fiber lack scalability and flexibility. However, recently, our group developed a wafer-to-fiber transfer technique where a suspended nanopatterned semiconductor membrane is defined and transferred to the fiber through a hole etched in the substrate [3]. Using this membrane-on-fiber technology, photonic crystals (PhCs) based on guided mode resonances were placed on top of a fiber. These designs have a relatively low quality factor and delocalized field distribution, which limit their sensing performance. In this work, we demonstrate that placing a photonic crystal cavity (PhCC) on a fiber-tip is possible. Using advanced design techniques we experimentally show fiber-tip sensors with quality factors in the order of multiple 1000s, tightly confined modes with $V_m=0.72$ $(\lambda/n)^3$, and efficient coupling with standard single mode fibers (SMF-28). This results in the highest Q/V ratio of any fiber-tip sensor with the added benefit of efficient coupling resulting in a large reflection modulation. An example of the fiber-sensor can be seen in Fig. 1. We demonstrate the practical use of the sensor in the real-time detection of single nanoparticle, which is made possible due to the highly localized mode. We specifically show the real-time detection of single 50 nm polystyrene particles.

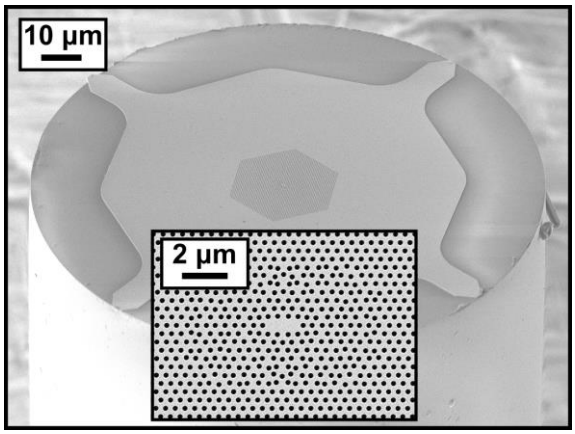

Fig. 1. Scanning electron microscope (SEM) image of the nanophotonic fiber-tip sensor. Inset: zoom-in of the optimized cavity.

Simulations

The main challenge for fiber-tip PhCCs is the spatial and angular mismatch with the fiber mode, leading to poor coupling efficiency. The PhCC radiation pattern can be controlled by repositioning a subset of holes and defining a subharmonic lattice [4], referred to as gentle

confinement and bandfolding respectively. In this work we make use of an open-source gradient-based optimization method based on guided mode expansion (GME), which alters the hole position surrounding the cavity to improve an objective function [5]. Here, we optimize the quality factor, the efficiency, and the mode volume. After optimization the result is simulated in the finite element method (FEM) software *COMSOL Multiphysics*. For our case the coupling efficiency increased from $\eta=0.008$ to $\eta=0.126$, while simultaneously increasing the quality factor from $Q=1850$ to $Q=4400$.

Characterization

The PhCCs were fabricated with standard semiconductor nanofabrication techniques and transferred to the facet of optical fibers using the approach described in Ref. [3]. For the PhCCs on fiber-tips we routinely obtain sensors with Q-factors in the multiple 1000s in combination with coupling efficiencies over 10%. This corresponds in a fiber-tip sensor with one of the highest Q/V ratios with considerably larger reflection modulations compared to other demonstrated fiber-tip sensors.

Sensing

Due to its narrow line width and high reflection modulation, the optimized PhCC on fiber-tip can be used as a precise sensor for multiple parameters. Here, we demonstrate two applications: refractive index (RI) sensing and single nanoparticle sensing.

Fiber-tip RI sensors have applications for in-line sensing and remote monitoring where the composition in (bio)chemical processes can be assessed, with the benefit of having an extremely small footprint. Furthermore, when adopting proper surface functionalization techniques RI sensors can be used for the specific detection of biomarkers. By dipping the fiber-tip sensor in solutions of deionized water (DI) and isopropanol (IPA) with a range of mixing ratios, we obtain a sensitivity of $S_n=79$ nm/RIU with a limit of detection of $LoD=3\sigma_\lambda/Sn=4.5\cdot10^{-6}$ RIU .

Additionally, using the unique features of our nanophotonic fiber-tip sensor we are able to sense single nanoscale objects such as nanoparticles. Here, we use an aqueous suspension of positively charged amine-coated polystyrene particles ($n=1.56$) with a diameter of 50 nm. Using plasma cleaning the surface of the sensor is activated which results in negatively charged hydroxyl groups that lead to random adsorption of the nanoparticles on the surface due to electrostatic interactions. In Fig. 2 the resonant wavelength shift as a function of time can be seen in the top graph and the differential shift can be seen in the bottom graph. Multiple discrete red-shifts are observed which are attributed to the binding of single 50 nm particles [6].

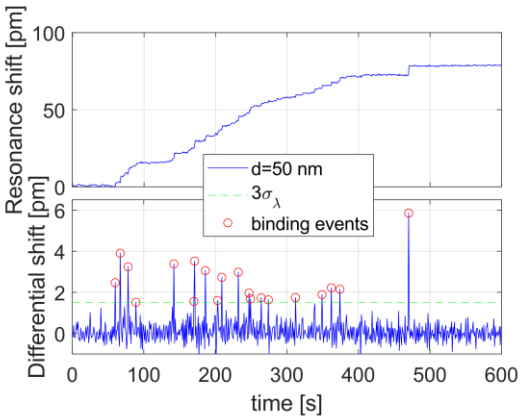

Fig. 2. Resonant wavelength shift (top) and differential shift (bottom) over time of binding of 50 nm particles on the PhCC fiber-tip sensor.

Conclusions and outlook

In this work, we showed a fiber-tip sensor with an unprecedented combination of quality factor, reflection modulation, and mode confinement. We demonstrated that this sensor can be used to detect single nanoparticles down to 50 nm in diameter. The proposed sensor has immediate applications in biosensing, industrial sensing, and air-quality monitoring. By using suspended structures and high-NA fibers, nanophotonic cavities with best-in-class characteristics can be realized with applications from single-photon emitters to nano-optomechanical sensors.

References

[1] A. Ricciardi et al., Lab-on-Fiber Technology: a new vision for chemical and biological sensing, Analyst 140, 8068 (2015) ; doi: 10.1039/C5AN01241D

[2] M. Pisco and A. Cusano, Lab-on-Fiber Technology: A Roadmap toward Multifunctional Plug and Play Platforms, Sensors 20, 4705 (2020); doi: 10.3390/s20174705

[3] L. Picelli et al. Scalable wafer-to-fiber transfer method for lab-on-fiber sensing, Appl. Phys. Lett. 117, 151101 (2020); doi: 10.1063/5.0021701

[4] N.V.Q. Tran et al., Vertical high emission in photonic crystal nanocavities by band-folding design, Phy. Rev. B. 82, 075120 (2010); doi: 10.1103/PhysRevB.82.075120

[5] M. Minkov et al., Inverse Design of Photonic Crystals through Automatic Differentiation. ACS Photonics (2020); doi: 10.1021/acsphotonics.0c00327

[6] A.L. Hendriks et al., Detecting Single Nanoparticles Using Fiber-Tip Nanophotonics. Optica (2024); doi: 10.1364/OPTICA.516575 (in press)

DOI 10.5162/EUROSENSORSXXXVI/OT7.37

Optical Sensing with Picometer-level Precision using an Integrated Multispectral Chip

M.S. Cano-Velázquez, A. van Klinken, S. Buntinx, A.L. Hendriks, C. Li, B.J. Heijnen, M. Dolci, L. Picelli, P.J. van Veldhoven, E. Verhagen, P. Zijlstra, A. Fiore
[1] Eindhoven University of Technology, Department of Applied Physics and Science Education, Eindhoven Hendrik Casimir Institute, P.O. Box 513, 5600 MB Eindhoven, The Netherlands
a.v.klinken@tue.nl

Summary (max 6 lines of text, no symbols):

Optical sensors enable remote measurement at high-precision, but the need for expensive readout equipment, such as a spectrometer, hampers their practical application. To overcome this limitation, we propose multispectral readout as an alternative approach for sensor readout, using a small number of photodetectors in an integrated chip. We demonstrate this concept using a multispectral chip with four photodetectors, reaching a wavelength imprecision of 5 pm for refractive index sensing and biosensing.

Keywords: optical sensors, readout, resonance wavelength, integrated chip, photodetectors, high-resolution, picometer, refractive index, bio sensor

Introduction

Optical sensors enable measurement of many different physical parameters with high precision, are immune to electromagnetic interference and allow remote sensing via optical fibers. Encoding the measurand in the optical spectrum, such as the wavelength of a resonance peak or dip, is widely used as it is most tolerant to external disturbances. Mostly, expensive readout equipment with high spectral resolution is used, such as a spectrometer or a laser-based interrogation system. However, in terms of cost and robustness, this readout equipment is not suited for most practical applications, e.g. in industry or healthcare.

From a fundamental point of view, high spectral resolution is not required to detect small spectral changes, e.g. a shift in the resonance wavelength. We suggest multispectral readout as an alternative approach using a limited number of photodetectors with low spectral resolution. Measuring the photocurrent of these photodetectors with high signal-to-noise ratio enables an accurate determination of the resonance wavelength. Based on information theory [1], it can be shown that the lowest imprecision can be reached if sensor and photodetectors have approximately the same linewidth.

Here, we present an integrated readout chip with an array of four photodetectors with a total area of 1.6 x 1.6 mm^2, which can be mass-produced at low cost. We show that the wavelength imprecision in the measurement of spectral features exceeds the performance of a spectrometer at equal integration time. We demonstrate this readout approach for two sensing applications: Refractive-index sensing on the fiber tip and biosensing.

Integrated multispectral chip

The multispectral chip consists of four resonant-cavity-enhanced photodetectors [2], fabricated using InP-membrane-on-silicone (IMOS) technology. [3] The absorbing layer is embedded in a planar microcavity, leading to enhanced absorption at specific wavelengths. [2] The four photodetectors achieve peak responsivities of 0.78-0.9 A/W at different wavelengths (see Fig. 1), as the optical path length between the mirrors is varied by a tuning layer. [3]

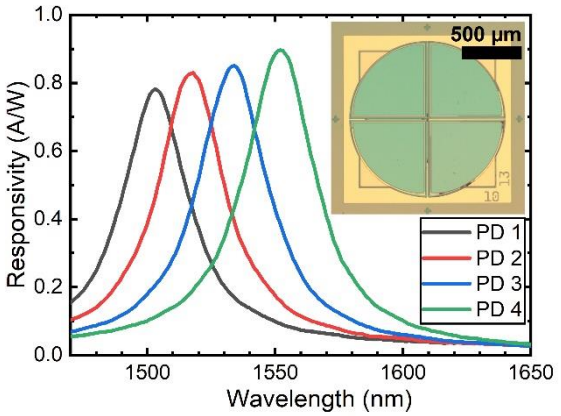

Fig. 1. Responsivity of the photodetectors (PD) in the multispectral chip (photo).

Refractive index sensing

The refractive index (RI) sensor consists of a 2D photonic crystal (PhC) (hexagonal lattice of holes in an InP slab) transferred to the cleaved facet of a multi-mode optical fiber with 105 µm core, using a mechanical transfer method developed within our group [4]. The PhC supports a resonance at 1519 nm, which leads to a peak with FWHM = 18.4 nm in the reflection spectrum. When the RI of the surrounding medium is varied by immersing the sensor in isopropanol-water mixtures with different concentrations, the resonance peak shifts (see Fig. 2) and the detected photocurrents change. Using a calibration set, for which the resonance wavelength is known, a prediction model is built to determine the wavelength directly from the measured photocurrents. Using this prediction model, we can experimentally demonstrate a wavelength imprecision of 5 pm, which exceeds the performance of the spectrometer (see Fig. 2). For this RI sensor, this wavelength imprecision corresponds to 3.7 x 10^{-5} RIU.

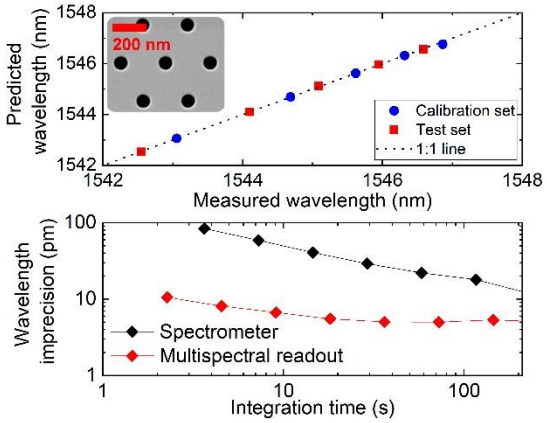

Fig. 2. RI sensing with multispectral readout. Top: accurate wavelength determination, Bottom: imprecision exceeds conventional spectrometer.

Biosensing

For biosensing, the surface of a 2D PhC (hexagonal lattice of holes in SiN layer on glass substrate) is functionalized with Immunoglobulin G (IgG, common biomarker) as receptor molecules by physisorption. This molecule specifically binds its natural antibody (anti-IgG), which leads to a local refractive index change and therefore a shift in the PhC resonant modes. From the corresponding photocurrent changes, the wavelength of the dominant resonance peak can directly be determined. To build a calibration data set, the biosensor is first exposed to isopropanol-water mixtures of various concentrations (see Fig. 3). The experimental data shows a clear correspondence of spectrometer data and the multispectral readout prediction. Additional experiments show that we can specifically detect anti-IgG molecules with in this way. When integrating over a few seconds, an imprecision of about 5 pm can also be reached for the readout of the biosensor. Assuming linearity between the biomarker concentration (anti-IgG, c=100 nM) and the total wavelength shift ($\Delta\lambda$=0.5 nm), this wavelength imprecision σ_λ corresponds to a limit of detection

$$LoD = 3\sigma_\lambda \, c / \Delta\lambda \; = 3 \text{ nM}$$

for this antibody-antigen pair.

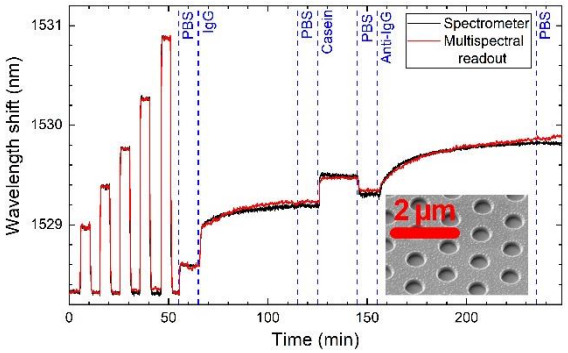

Fig. 3. Biosensing with multispectral readout: clear correspondence with spectrometer data.

Conclusion and Outlook

Resonance-based optical sensors enable the measurement of a large range of physical parameters with high sensitivity and under remote conditions. As an alternative to bulky, expensive and fragile readout equipment such as spectrometers, we propose multispectral readout, which is based on a limited number of photodetectors with low spectral resolution. We experimentally demonstrate this approach and show the detection of wavelength shifts down to 5 pm, exceeding the performance of a high-resolution spectrometer. As application cases, we present the readout of a fiber-tip refractive index sensor and a biosensor. This approach can pave the way for a broader application of optical sensors in industrial and health-care contexts without the need for expensive readout equipment.

References

[1] J. Chao et al., Fisher information theory for parameter estimation in single molecule microscopy: tutorial. *J. Opt. Soc. Am. A Opt. Image Sci. Vis.* 33, B36–57 (2016). doi: 10.1364/JOSAA.33.000B36

[2] S. Ünlü, S. Strite, Resonant cavity enhanced photonic devices, *J. Appl. Phys*. 78, 607–639 (1995); doi: 10.1063/1.360322

[3] A. van Klinken et al., High-performance photodetector arrays for near-infrared spectral sensing, *APL Photon.* 8, 041302 (2023); doi: 10.1063/5.0136921

[4] L. Picelli et al. Scalable wafer-to-fiber transfer method for lab-on-fiber sensing, *Appl. Phys. Lett.* 117, 151101 (2020); doi: 10.1063/5.0021701

DOI 10.5162/EUROSENSORSXXXVI/OT7.43

Tailoring Spectral Sensors for Specific Applications

D.M.J. van Elst[1], A. van Klinken[1], F. Ou[1,2], M.S. Cano-Velázquez[1], C. Li[1], M. Petruzzella[1,2], P.J. van Veldhoven[1] and A. Fiore[1]
[1] Department of Applied Physics and Science Education, Eindhoven Hendrik Casimir Institute, Eindhoven University of Technology, PO Box 513, NL 5600 MB Eindhoven, The Netherlands.
[2] MantiSpectra B.V., High Tech Campus 9, 5656 AE Eindhoven, The Netherlands.

Corresponding author: d.m.j.v.elst@tue.nl

Summary:
Spectral sensing in the near-infrared is a powerful method for non-destructive analysis of material composition in a wide variety of applications. A spectral sensor typically consists of an array of detectors, each responsive in a given spectral band. We have demonstrated an algorithm capable of tailoring spectral sensors to specific applications. By optimizing for all combinations of spectral bands a non-trivial solution can be found, outperforming hand-picked designs. High sensing performance can be achieved even with a few pixels, resulting in cost-effective spectral sensors with simple read-out.

Keywords: “Spectral sensors”, “application-specific”, “optimization”, “near-infrared”, “noise”

Motivation

Spectral sensing using near-infrared (NIR) light is becoming increasingly valuable for material analysis. The NIR region contains overtones of molecular bonds, enabling the analysis of chemical composition in a wide variety of fields. For this reason, miniaturized, portable sensing solutions are sought to replace expensive and bulky lab equipment in the chemical and agricultural sectors. We have earlier demonstrated a 16-pixel array of resonant-cavity detectors (900-1700nm) with a footprint of 2.25mm^2, without movable parts, providing robust performance for on-field sensing [1]. Fabrication can be done using optical lithography, making it suitable for mass production [2]. This method has proven effective for a wide variety of applications [3].

Due to the broad and overlapping spectral signatures of chemical bonds in solids and liquids, there is a lot of redundant information in NIR spectra. For example in filter-based sensing approaches this results in efforts to tailor the filter responses to suit the applications [4-7]. We propose and demonstrate an approach to the optimization of the number and structure of the pixels in a NIR spectral sensor to achieve improved performance and reduced fabrication and read-out complexity.

The effectiveness of such an approach is demonstrated for the measurement of ethanol concentration in water. We show that, even with a few pixels, high sensing performance can be achieved. Using a numerical optimization algorithm can result in a non-trivial solution that outperforms handpicked designs. Especially in noisy environments, fewer pixels on the same sensing area can outperform a higher number of channels due to increased signal-to-noise ratio (SNR), which is valuable in sensing systems with low optical throughput.

Method

The application-specific optimization is schematically represented in Fig.1. Our sensor pixels consist of InGaAs photodiodes integrated with a Fabry-Perot cavity, where the thickness

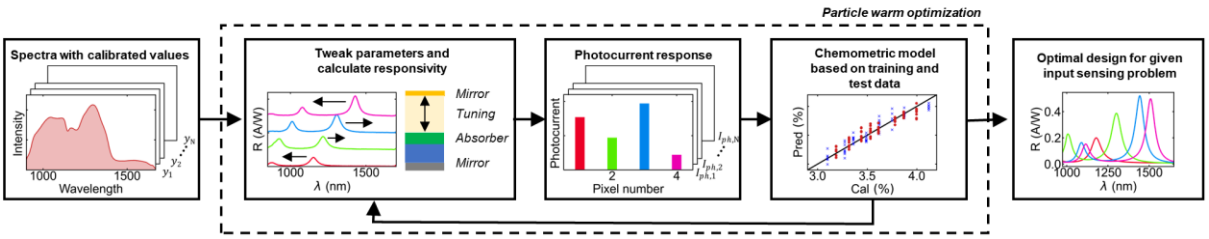

DOI: 10.5162/EUROSENSORSXXXVI/OT7.43

of a tuning layer controls the spectral position of the responsivity peaks. We note that each pixel presents multiple peaks, which makes intuition-based optimization challenging. In order to predict the performance of a sensor array with arbitrary configuration, the responsivity curves are simulated using the transfer-matrix method. The photocurrents are simulated by integrating the incident spectrum with the responsivity curves of each pixel. By applying white noise with standard deviation σ to the photocurrents, the result can be scaled to SNR. The photocurrents can be used for partial least squares (PLS) modelling to obtain the prediction accuracy of this configuration for the sensing problem. The accuracy is optimized using a particle-swarm optimization (PSO), where the input parameters are the thicknesses of the tuning layers which determines the resonant wavelengths. When varying the number of pixels the sensing area is kept the same, meaning that a 1-pixel device is expected to have 16 times the signal of a 16-pixel sensor. Additionally, the performance of an array is averaged over a range of noise values, corresponding to the experimental situation. In the optimization 60% of the dataset is used and 40% is kept as test data for the final design.

Results

Fig. 2 shows the results of the optimization applied to a dataset of transmission spectra for mixtures of ethanol in water, with varying concentrations from 0% to 53%. The optimization is performed for varying pixel configurations. It can be seen that the root-mean-square error of the PLS prediction increases with increasing noise σ for all amounts of pixels. Most notably, there are noise regions where a 4-pixel device outperforms 8- and 16-pixel devices.

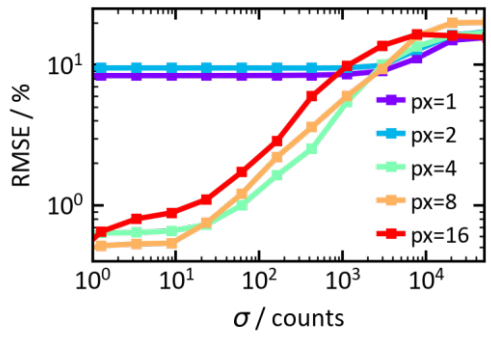

Fig. 1. Error of prediction vs noise on the readout for arrays with varying amounts of pixels.

Since this region corresponds to the expected SNR of our sensor, a 4-pixel device was further investigated before fabrication. Fig 3a shows the improving ratio of performance to deviation (RPD) on the training data throughout the iterations of the PSO. Because there are a lot of initial evaluations, the starting point is already reasonably good. An evaluation on test data kept outside of the optimization with σ=1, the optimal case in our region of interest, shows potential for up to RPD=22.1 (Fig. 3b). As an RPD of around 3-4 is generally considered a good model, this shows that even with few pixels, high sensing performance can be achieved. As a lower number of pixels reduces the complexity of fabrication and packaging, these results show the potential of application-specific spectral sensing. An experimental demonstration of this concept is under way and will be discussed at the conference.

This research was partially funded by the Nederlandse Organisatie voor Wetenschappelijk Onderzoek (NWO) Toegepaste en Technische Wetenschappen (TTW) project n. 17626 & 16670 and the NWO Nationale Wetenschapsagenda (NWA) Kleine Projecten NWA.1418.22.022.

References

[1] Hakkel, K. D., Petruzzella, M., Ou, F., Liu, T., Pagliano, F., Veldhoven, R. P. J. Van, & Fiore, A. Integrated near-infrared spectral sensing. *Nature Communications* 13, (2022); doi: 10.1038/s41467-021-27662-1

[2] Klinken, A. van, Elst, D. M. J. van, Li, C., Petruzzella, M., Hakkel, K. D., Ou, F., Pagliano, F., Veldhoven, R. van, & Fiore, A. High-performance photodetector arrays for near-infrared spectral sensing. *APL Photonics* 8, (2023); doi: 10.1063/5.0136921

[3] Ou, F., van Klinken, A., Ševo, P., Petruzzella, M., Li, C., van Elst, D. M. J., Hakkel, K. D., Pagliano, F., van Veldhoven, R. P. J., & Fiore, A, Handheld NIR Spectral Sensor Module Based on a Fully-Integrated Detector Array. *Sensors* 22 (2022); doi: 10.3390/S22187027

[4] Nelson, M. P., Aust, J. F., Dobrowolski, J. A., Verly, P. G., & Myrick, M. L. Multivariate Optical Computation for Predictive Spectroscopy. *Analytical Chemistry* 70 (1998); doi: 10.1021/AC970791W/ASSET/IMAGES/LARGE/AC970791WF00015.JPEG

[5] Tan, H., Cadusch, J. J., Meng, J., & Crozier, K. B., Genetic optimization of mid-infrared filters for a machine learning chemical classifier. 30(11), 18330–18347 (2022); doi: 10.1364/OE.459067

[6] J. Waterhouse, D., & Stoyanov, D., Optimized spectral filter design enables more accurate estimation of oxygen saturation in spectral imaging. *Biomedical Optics Express* 13, 2156. (2022); doi: 10.1364/boe.446975

[7] Ayala, L., Isensee, F., Wirkert, S. J., Vemuri, A. S., Maier-Hein, K. H., Fei, B., & Maier-Hein, L., Band selection for oxygenation estimation with multispectral/hyperspectral imaging. Biomedical *Optics Express* 13, 1224-1242, 13(3), 1224–1242 (2022); doi: 10.1364/BOE.441214

DOI 10.5162/EUROSENSORSXXXVI/OT9.253

Miniaturized Wireless Wearable Force Measurement System for Sports Science and Beyound

Chen-Hao Hung[1], Cheng-Yao Lo[1, 2]
[1] Department of Power Mechanical Engineering, National Tsing Hua University, 101, Section 2, Kuang Fu Road, Hsinchu 300044, Taiwan (R. O. C.).
[2] Institute of Power Mechanical Engineering, National Tsing Hua University, 101, Section 2, Kuang Fu Road, Hsinchu 300044, Taiwan (R. O. C.).

chengyao@mx.nthu.edu.tw

A wearable sensing module that was extensively miniaturized from the existing one was proposed, designed, fabricated, and verified in this work. The signal response was based on the capacitance change generated by the force acting on a corresponding capacitive pressure sensing element. Wireless communication was achieved through Bluetooth from practical viewpoint, along with the development of a user interface and database. Results indicate that the measurement tolerance was below 1% and the module was reduced by 85% in volume when compared with its previous counterpart.

Keywords: Database, force sensor, system miniaturization, wearable device,

Introduction

In the contemporary era of technological advancements, various types of sensors are being developed for monitoring various physical quantities, contributing to the widespread adoption of the Internet of Things

Among various system integration scenarios, one approach involves the miniaturization or scaling of sensor components compactly. An existing system composed of sensor components and wearable devices showed limited support on functionality and user experience (such as non-ergonomic feeling, bulky volume, heavy weight, and complex wiring) [1].

Our previous work [2] demonstrated that the capacitance measurement had to be done through a commercialized printed circuit board (PCB). When paired with another Bluetooth module, the transmission port was capable of data collection and processing.

Nevertheless, the size of the transmission port that includes the evaluation PCB, Bluetooth module, and battery was showed the aforementioned drawbacks. Consequently, we report an extensively miniaturized module that enhances the feasibility of practical applications by optimizing electronic components and their routings, particularly for wearable and sports science applications.

Design and Realization

To realize force sensing, a control unit was designed (Fig. 1). The signal processor captured the capacitive responses through the sensor in milliseconds, converted them into digital signals, and repassed them to the microprocessor. Subsequently, the microprocessor was able to transmit the digitized signals to the host computer by the Bluetooth low energy technique. After comparing with the database, the corresponding force values were calculated and exhibited to the user, completing the force sensing measurement.

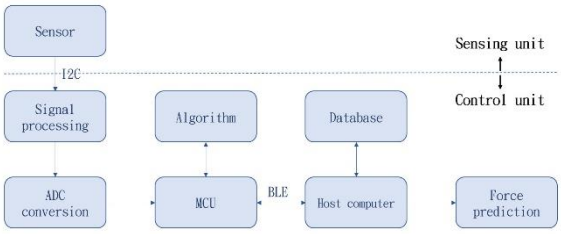

Fig. 1. System integration block diagram of the control and sensing unit

The control unit was integrated on a PCB. To connect the capacitive pressure sensing sensor, an edge connector with gold fingers was utilized, ensuring stable contact between the connector and interface. The overall circuit board size was measured 26.7 mm x 46.5 mm in the xy-plane (Fig. 2). Additionally, a lithium-ion polymer battery of similar same size (capacity of 1500 mAh) was stacked underneath in a watch fashion (Fig. 3(a)). The entire circuit board was further mounted in a 44 mm x 39 mm x 17 mm housing with an overall weight of 48 grams (Fig. 3(b)) and detachable wristband (Fig. 3(c)).

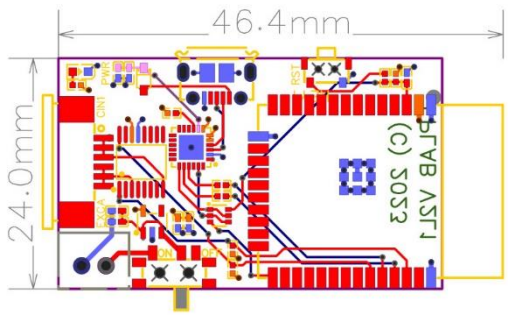

Fig. 2. Capacitance of Ceramic capacitors vs measured capacitance.

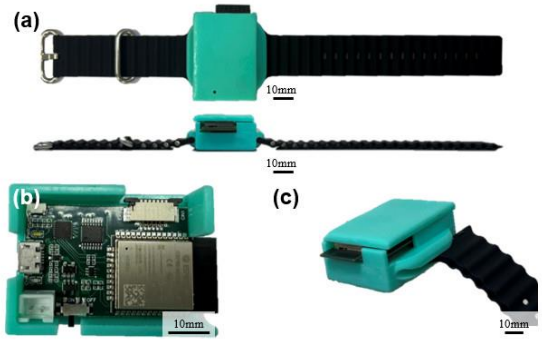

Fig. 3. The proof-of-concept of the (a) transmission port in whole, (b) enlarged housing and circuits, and (c) detachable wristband design. Scales are all 10 mm.

Figure 4 shows the accuracy verification of the proof-of-concept, in which capacitance measurement was conducted through commercialized standard ceramic capacitors (Fig. 4). The module exhibited a response delay of approximately 100 ms, and the measurement error was less than 0.3%.

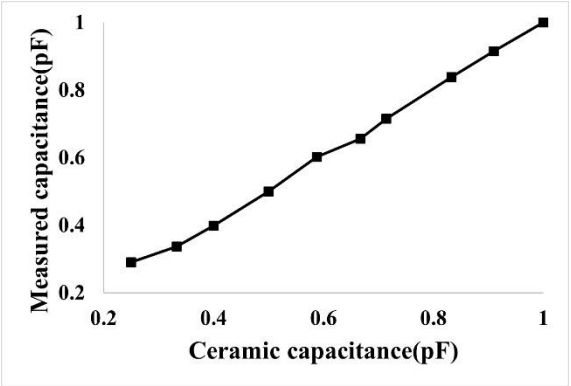

Fig. 4. Verification of capacitive responses between the commercialized capacitor and measured capacitance.

Results

Figure 5 shows the relationship between force and capacitance. The relative capacitance values of the pressure sensing element show a positive correlation, with followed the expectation and complied with the findings in literature [3]. The highest sensitivity occurred in the force range of 0 N to 1 N, which satisfied the required dynamic window of badminton posture monitoring [2]. The linear coefficient of determination reached 0.9975, indicating the accuracy of the existing sensor and the realized miniaturized transmission port.

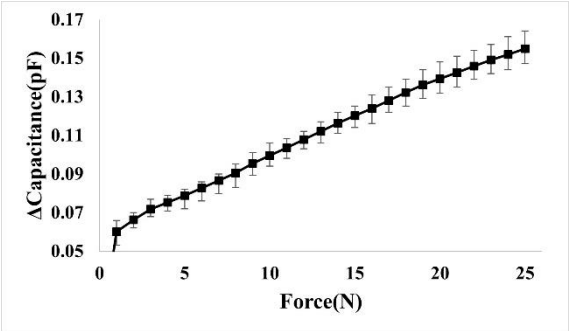

Fig. 5. Capacitance changes in actual application.

Figure 6 shows the results of a blind test of the control unit by installing the sensing unit on the industrial gripper (robot). the detection tolerance between the predicted and the actual force was less than 1%.

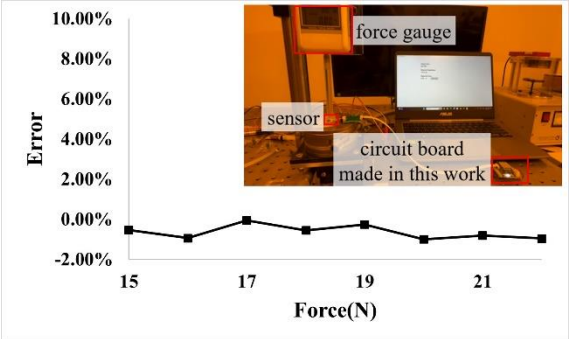

Fig. 6. The blind test results of the force measurement system with existing sensor and the proposed transmission port.

References

[1] *R. Kawasaki and S. Katsura. Shoe-type Wearable Device for Measuring Ground Reaction Force and Center of Pressure. 2023 IEEE 32nd International Symposium on Industrial Electronics (ISIE), Helsinki, Finland, 2023, pp. 1-6, doi: 10.1109/ISIE51358.2023.10228059.*

[2] *Zheng, YJ., Wang, WC., Chen, YY. et al. Wearable and wireless performance evaluation system for sports science with an example in badminton. Sci Rep 12, 16855 (2022); doi: 10.1038/s41598-022-21187-3.*

[3] *V. Palaniappan et al. Laser-Assisted Fabrication of a Highly Sensitive and Flexible Micro Pyramid-Structured Pressure Sensor for E-Skin Applications. IEEE Sensors Journal, vol. 20, no. 14, pp. 7605-7613, 15 July15, 2020, doi: 10.1109/JSEN.2020.2989146.*

DOI 10.5162/EUROSENSORSXXXVI/OT10.125

Harvesting body temperature to power wearable systems using sputtered flexible thermoelectrics

Joshua Curry, Marion Specht, Zhuo Feng, Abiodun Komolafe, Chris Craig, Daniel Hewak, Nick Harris, Ioannis Zeimpekis and Katrina A. Morgan
University of Southampton, Southampton, SO171BJ, United Kingdom

Corresponding Author's e-mail address: jsc3g14@soton.ac.uk

Summary:
Across the domain of Internet-of-Things sensors, a key factor which restricts the long-term operation of devices is energy. This restriction becomes especially prominent as the size of devices is decreased and flexibility is needed, for example in body-worn applications. This publication documents the design, optimisation, fabrication and verification of a novel flexible thermoelectric energy harvesting system for powering body-worn sensors. A solution is produced which is able to transmit temperature information at 25 minute intervals by harvesting 13.6 µW of energy from a 25K temperature difference.

Keywords: energy-harvesting, thermoelectrics, sputtering, optimisation, bluetooth

Background and Motivation

Energy harvesting systems for wearable technologies are often engineered to provide energy output during certain activities, for instance when the user is in a lit room or actively doing exercise. Few technologies can sustainably power a system at night or during periods of inactivity.

Thermoelectric energy harvesting devices are a technology which could potentially supplement this power deficit, by providing small amounts of power during inactive periods to allow for the continuous operation of devices, generated from the heat output of the user's body, thus removing the need for overnight charging [1]. Creating these in a flexible and wearable format, however, is challenging, owing to restricted power output caused by the thin film design.

In this work we have created an optimised flexible thermoelectric generator, using the deposition method of sputtering. Sputtering is a large-area and scalable technique that offers high degrees of material tuneability and control, ideal for producing flexible thermoelectric generators (f-TEGs) that offer energy outputs required by applications such as an Internet-of-things (IoT) sensing device [2].

Whilst several sputtered thermoelectric generators are proposed in existing literature [3], few are combined with real-world IoT devices in a system, due to the nanowatts of power produced. This work harnesses the power generated by the optimised flexible thermoelectric generators, and powers Bluetooth system, highlighting thermoelectrics potential for an energy harvesting system for wearable sensors.

Optimised f-TEGs

This work showcases the design, optimisation and manufacture of a novel flexible thermoelectric generator (f-TEG) for wearable applications. Traditional antimony telluride (Sb2Te3) and bismuth telluride (Bi2Te3) were selected as the p-type and n-type thermoelectric materials, owing to their high thermoelectric performance and allowing demonstration of improvements on current state-of-the-art. They are manufactured by sputtering onto a polyimide substrate, chosen to withstand the heat treatment needed to enhance material properties, whilst maintaining flexibility (see Fig 1b) [4]. Optimisation includes thermoelectric leg length (see Fig 1a), thermoelectric thickness, crystallinity and deposition speed. The aim of this was to achieve a manufacturable thermoelectric generator, with peak performance (see Fig 2).

f-TEGs powering a Bluetooth system

16 f-TEG units are connected in series to produce a maximum voltage which is capable of powering an energy-harvesting sensing device. The electrical energy output is then connected to an e-peas AEM2094 energy-harvesting SoC solution and NRF52 Bluetooth low-energy sensing device which could be utilised to relay data from a temperature sensor to a mobile device for collection and monitoring.

Results

The optimum design has a leg length of 6 mm, an overall area of 13 cm^2, and is 135 µm thick. The output power density for a single optimised generator at a 25K temperature difference is 0.33 µW/cm2.

Connecting 16 of the f-TEGs in series resulted in the voltage and current shown in Figure 3a, when swept through load resistances in a range of 0Ω to 1kΩ. For the test duration, the temperature differential was maintained at 24K (18ºC cold-side, 42ºC hot-side) and the load resistance was varied. A maximum power output of 38µW was achieved with a 20K temperature difference.

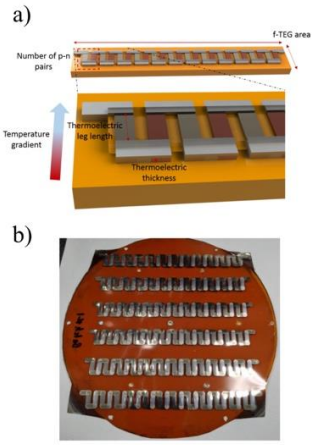

Fig. 1. a) 3D schematic of a f-TEG, with n-type and p-type thermoelectric legs connected electrically in series and thermally in parallel, on a polyimide substrate. b) Photograph of 6 fabricated f-TEGs sputtered in a scalable way.

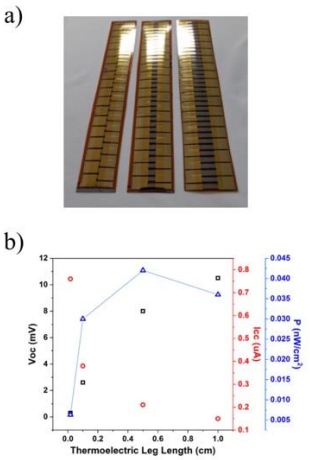

Fig. 2. a) Photo of thermoelectric generators with three different leg lengths (b) Output voltage, current and power density for thermoelectric generators with varying leg length, demonstrating optimised leg length.

When connected to the AEM2094 energy-harvester and Bluetooth device, the arrangement of f-TEGs was successfully utilised to charge a 6600 µF capacitor bank at 13.6 µW, allowing sensor data values to be transmitted once every 25 minutes with a 25 ºK difference.

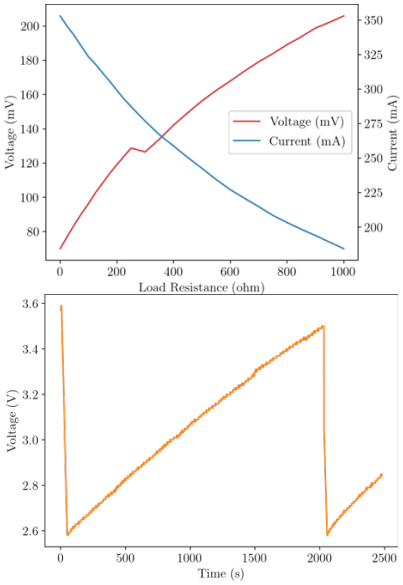

Fig. 3. a) Output of 16 f-TEGs in series at a variety of load resistances at 24K temperature differential b) Capacitor voltage over time demonstrating the harvester charging a capacitor.

Figure 3b shows the voltage held in the capacitor bank over time, with successful charge cycles switching power into the IoT sending device and allowing it to transmit the value of a temperature sensor to a nearby Bluetooth data collector.

This demonstrates this f-TEG systems capability as a chosen energy harvesting technology for body worn sensors, providing continuous power. Next steps are to sew this into a garment to perform body worn tests.

Funding

This work was funded by EU Horizon (825143) “Smart2Go”, EPSRC “Smart Cloth” (EP/X016730/1) and the UKRI Impact Accelerator Account fund.

References

[1] Wen, DL., Deng, HT., Liu, X. et al. Wearable multi-sensing double-chain thermoelectric generator. Microsyst Nanoeng 6, 68 (2020).

[2] Morgan, K.A., Tang, T., Zeimpekis, I. et al. High-throughput physical vapour deposition flexible thermoelectric generators. Sci Rep 9, 4393 (2019).

[3] Kong, D., Zhu, W., Guo, Z., & Deng, Y. High-performance flexible Bi2Te3 films based wearable thermoelectric generator for energy harvesting. Energy, 175, 292–299. (2019).

[4] Morgan, K.A., Zeimpekis, I., Hewak, D. Enhancing thermoelectric properties of bismuth telluride and germanium telluride thin films for wearable energy harvesting, Thin Solid Films Volume 741 (2022).

DOI 10.5162/EUROSENSORSXXXVI/OT10.184

Advanced Sensor Systems for Sustainable Building Modernization: A Technological Approach to Enhance CO2 Savings

Karl Giske[1], Madeleine Bankwitz[1], Christian Engel[2], Ricky Bendyk[1], Prof. Dr.-Ing. Sören Hirsch[1]
[1] Brandenburg University of Applied Science, Department of Engineering, Magdeburger Str. 50, 14770 Brandenburg/Havel, Germany
[2] TEPROSA GmbH, Paul-Ecke-Str. 6, 39114 Magdeburg, Germany

Corresponding author: karl.giske@th-brandenburg.de

Summary:
This work presents an advanced sensor-system design developed to improve diagnostic methods for sustainable building renovation, with focus on the optimization of energy efficiency and the achievement of significant CO2 reduction in the construction sector.

Keywords: Building Information Modeling, CO2 Reduction, Environmental Monitoring, Smart Sensor Networks, Non-Destructive Evaluation

Introduction

Considering the challenges posed by climate change, it is imperative to adopt innovative strategies in all sectors, with particular focus on construction and real estate, which are well-known contributors to energy consumption and CO2 emissions. Sustainable renovation represents a pivotal approach for enhancing energy efficiency, reducing energy demand and improving environmental footprints through precise resource management and energy-efficient construction practices [1].

In the field of building management, the focus on components such as facades, windows, insulating elements, etc. is of paramount importance, as regular inspections and condition assessments are vital for ensuring the structural integrity, functionality, reliability and lifespan of these complex structures [2]. However, conventional visual inspections are not capable of ensuring complete condition monitoring of these structures, resulting in incomplete evaluation and premature replacement [3]. Additionally, there is a lack of documentation, which is further compounded by the digitalization gap in this sector. The construction industry presents a challenge in the absence of reliable data to substantiate the accuracy of assumptions [4].

Consequently, integrated sensor systems may be regarded as a pivotal technology for overcoming these limitations, offering a non-destructive monitoring tool that may lead to an extension of the lifespan of the aforementioned elements [5].

Materials and Methods

The presented sensor system (Figure 1) is based on an ultra-low energy and miniaturized but nevertheless modular multi-channel data-capture platform with an advanced microcontroller platform at its core. Its intended purpose is to measure crucial environmental parameters such as temperature and humidity as well as mechanical loads, for example vibrations or shocks. The integration of this system into various components and spaces necessitates a novel approach, combining advanced circuit design and packaging technologies to create a super compact yet robust design.

For this purpose, a sensor system was designed, combining six channels of analog-to-digital conversion, complemented by a high bandwidth preprocessing stage used for filtering and signal conditioning. Additionally, a dual-stage voltage converter was added, providing a stable power supply from almost any source. Subsequently, the data undergoes processing, analysis and compression at the microcontroller level. This data is then transmitted via the standard UART interface to the communications module, which enables both wired and wireless communication. The integration of all components of the sensor system within very small dimensions was made possible using a multilayer circuit design, a minimum copper structure width of 50 µm,

innovative stacked micro-via technology and state-of-the-art sub-miniature XQFN and BGA packages.

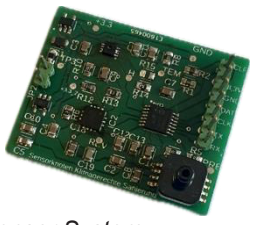

Fig. 1. Sensor System

By implementing highly efficient measurement and data processing routines, a single-digit mA average power consumption was achieved with standby currents in the lower µA range. This allows the use of energy harvesting as power source together with next generation solid-state batteries. Those features will be added to the sensor system in the near future.

A 3x5 (height x depth) array was constructed behind a balcony door using a sensor system. The sensors were positioned at a constant distance of 0.5m in both directions. The measurements were conducted in a 42m² room over a period of 35 minutes. The door was open for ten minutes.

Results

Figure 2 presents the results of the measurement, with the interval of airing marked in grey. The measurement matrix enables the analysis of dynamic changes over time and position. The temperature and CO2 concentration exhibit a rapid decline upon opening the door and a subsequent increase upon closure. In contrast, the humidity displays a precipitous decline following the opening of the door, followed by a gradual increase during airing. The outer humidity was above 50%. For graphical presentation, the sensor exhibiting the most characteristic behavior during the airing process was selected. The suitability of the sensor as a representative for the entire measurement array was evaluated through a correlation analysis of all values above the time.

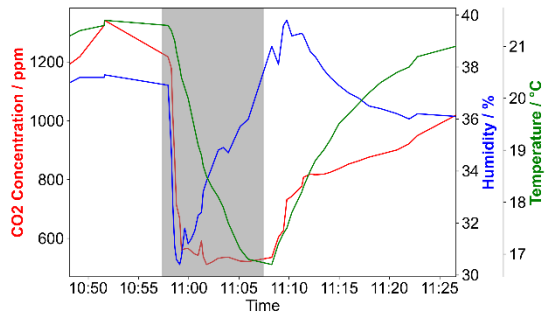

Fig. 2. Multimodal Status Measurement

Discussion and Conclusions

To summarize this process, it is possible to display a measurement with one point in this array. To analyze the dynamic sizes, it is necessary to include intelligent software. In the future, further miniaturization of the system is planned to facilitate the implementation of sensor networks in the field of building renovation. This development will be complemented by advanced wireless data management to ensure efficient and scalable monitoring of the renovation processes. Furthermore, preparations are being made for the integration of energy harvesting technologies to enable autonomous power supply for the sensors, thus contributing to the reduction of energy consumption and increasing CO2 savings. These technological advances lay the foundation for a new generation of sensor systems that pave the way for a more environmentally friendly and sustainable future in the renovation sector.

References

[1] Elhegazy, H.; Zhang, J.; Amoudi, O.; Zaki, J.N.; Yahia, M.; Eid, M.; Mahdi, I. (2023). An exploratory study on the impact of the construction industry on climate change. Journal of Industrial Integration and Management, 1-23. https://doi.org/10.1142/s2424862222500282

[2] Park, H.S.; Lee, H.; Adeli, H.; Lee, I. A new approach for health monitoring of structures: Terrestrial laser scanning. Comput.-Aided Civ. Infrastruct. Eng. 2007, 22, 19–30.

[3] Chew, M. Y. L., & Gan, V. J. L. (2022). Long-standing themes and future prospects for the inspection and maintenance of façade falling objects from tall buildings. Sensors (Basel, Switzerland), 22(16), 6070. https://doi.org/10.3390/s22166070

[4] Musarat, M. A.; Sadiq, A.; Alaloul, W. S.; Abdul Wahab, M. M. (2022). A systematic review on enhancement in quality of life through digitalization in the construction industry. Sustainability, 15(1), 202. https://doi.org/10.3390/su15010202

[5] Arabshahi, M., Wang, D., Sun, J., Rahnamayiezekavat, P., Tang, W., Wang, Y., & Wang, X. (2021). Review on sensing technology adoption in the construction industry. Sensors (Basel, Switzerland), 21(24), 8307.https://doi.org/10.3390/s21248307

DOI 10.5162/EUROSENSORSXXXVI/OT10.264

A Hybrid Piezoelectric - Electrostatic Energy Harvester for Wearable Biosensors

Sotiria D. Psoma [1], Ihor Sobianin[1], Antonios Tourlidakis[2]
[1] School of Engineering & Innovation, The Open University, Walton Hall, Milton Keynes MK7 6AA, UK
[2] Department of Mechanical Engineering, University of Western Macedonia, Kozani 50100, Greece

Corresponding Author's e-mail address: sotiria.psoma@open.ac.uk

Summary:
Biosensors play a crucial role in modern healthcare, providing continuous monitoring of various physiological parameters. However, the reliance on batteries that require replacement introduces interruptions in data acquisition process and for this reason energy harvesting methods that convert human body energy into electricity have attracted considerable research interest. In this study, a novel hybrid energy harvester that combines piezoelectric and reverse electrowetting on dielectric (REWOD) techniques is investigated. The key working principle revolved around the electrical double layer present in the REWOD component and coupling it with a piezoelectric generator via an electret. By harnessing biomechanical vibrations with a piezoelectric material and the REWOD unit, the overall power output of the biosensor was enhanced. The proposed design was evaluated through numerical simulations and a series of experimental tests. The findings contribute to the advancement of self-powered biosensors, enabling seamless and continuous data acquisition without relying on external batteries.

Keywords: energy harvesting, REWOD, piezoelectric, electrical double layer, wearable biosensors, continuous monitoring

Title

A Hybrid Piezoelectric - Electrostatic Energy Harvester for Wearable Biosensors

Headlines

This work discusses the development of a novel hybrid energy harvester that combines piezoelectric and reverse electrowetting on dielectric (REWOD) technologies.

Background, Motivation an Objective

Modern healthcare relies extensively on implantable and wearable biosensors to continuously monitor physiological data of patients. These devices can play a crucial role among others in disease prevention, treatment of injuries and facilitating recovery [1]. However, a significant drawback of biosensors lies in their reliance on batteries for power supply and batteries present in biosensors pose challenges such as miniaturization, potential electrolyte leakage, and costly replacement surgeries for implantable devices [2]. For instance, wearable glucose biosensors require the battery to be periodically changed, which introduces discontinuity in data acquisition and discomfort due to skin penetration.

These limitations can be addressed by development of energy harvesting devices. The human body has multiple energy sources that can be effectively harnessed by various transducers [3]. These sources include thermal energy, biochemical reactions, electrostatic charges, and biomechanical forces. However, relying solely on a single energy type may not yield optimal power output or guarantee that the energy is constantly available. Therefore, hybrid energy harvesters combine multiple energy generators to enhance overall performance.

This study investigates biomechanical energy produced by the human cardiovascular system. More specifically, pulsations from the radial artery serve as a reliable source of vibrations that can be scavenged. The proposed hybrid energy harvester combines piezoelectric and electrostatic generators to extract energy from a time-varying radial artery pressure.

Description of the energy harvester

Recent advancements in electrowetting have introduced a novel effect known as the reverse electrowetting on dielectric (REWOD). In a typical REWOD setup, a conductive liquid droplet is squeezed between two electrodes, one of which is coated with a dielectric material [4]. By modulating the distance between these electrodes, the electrical double layer (EDL), which formed at the fluid-electrode interface, can be

altered [5]. The formed variable capacitor can be used for charge accumulation.

The working principle of the designed energy harvester is described in Table 1 and Figure 1:

Tab. 1: Hybrid harvester states

State	Description
Initial State	The piezoelectric material and REWOD component are in equilibrium, with no electron flow.
External Pressure	When pressure is applied to the piezoelectric material, sustained deformation causes an electron flow between the electrodes. One of the electrodes becomes positively charged.
Electret Biasing	The shared electrode features an electret layer which biases the REWOD component. This prevents ions and counter ions in the EDL from changing positions. The EDL, which is formed on top of the electret, increases the overall capacitance of the system, maximizing charge generation.
Release of Pressure	As pressure is released and the harvester returns to its initial state, the process repeats, with electrons flowing in the opposite direction.

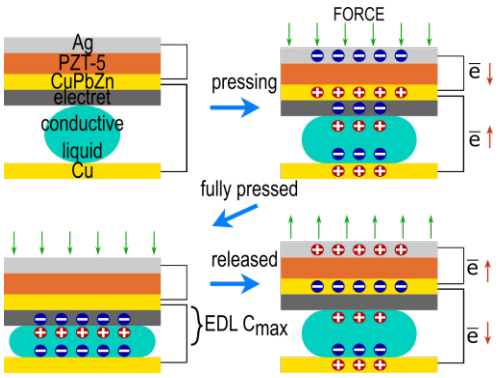

Fig. 1. Working principle of the energy harvester.

The hybrid energy harvester consists of a commercially available piezoelectric disc and a custom-designed printed circuit board (PCB) for the REWOD component. The piezoelectric disc incorporates PZT-5H ceramics, which is deposited onto a brass diaphragm (CuPbZn). In addition, the piezoelectric material is coated with silver (Ag). The REWOD component consists of a shared brass electrode coated with an electret and a counter electrode (Cu). Finally, the conductive liquid used in the system is NaCl.

Results

An experimental setup was designed to collect data on the performance of both the REWOD material and the piezoelectric material (Fig 2). The conceptual design of the harvester was tested in a frequency range from 1 to 2.5 Hz, as part of a series of parametric studies. From the results presented in Figure 3, it appears that the produced electrical power is proportional to the frequency.

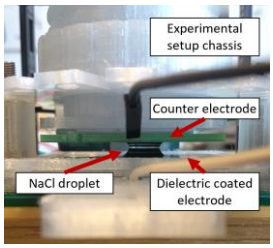

Fig. 2. Energy harvester configuration.

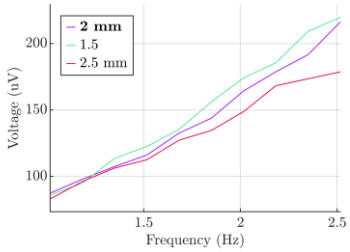

Fig. 3. Effect of initial distance between electrodes.

References

[1] Gambhir Sanjiv, S.; Ge, T.J.; Vermesh, O.; Spitler, R.; Gold Garry, E. Continuous health monitoring: An opportunity for precision health. *Sci. Transl. Med.* (2021), 13, eabe5383. DOI: 10.1126/scitranslmed.abe5383

[2] Ryu, H.; Park, H.-m.; Kim, M.-K.; Kim, B.; Myoung, H.S.; Kim, T.Y.; Yoon, H.-J.; Kwak, S.S.; Kim, J.; Hwang, T.H.; et al. Self-rechargeable cardiac pacemaker system with triboelectric nanogenerators. *Nat. Commun.* (2021), 12, 4374. DOI: https://doi.org/10.1038/s41467-021-24417-w

[3] Sobianin, I.; Psoma, S.D.; Tourlidakis, A. A 3D-Printed Piezoelectric Microdevice for Human Energy Harvesting for Wearable Biosensors. Micromachines (2024), 15, 118. DOI: https://doi.org/10.3390/mi15010118

[4] Adhikari, P.R.; Tasneem, N.T.; Reid, R.C.; Mahbub, I. Electrode and electrolyte configurations for low frequency motion energy harvesting based on reverse electrowetting. *Sci. Rep.* (2021), 11, 5030. DOI: https://doi.org/10.1038/s41598-021-84414-3

[5] Huynh, D.; Nguyen, T.; Nguyen, P; Abeyrathne, C.D.; Hossain, Md.S.; Skafidas, E. Environmentally friendly power generator based on moving liquid dielectric and double layer effect. *Sci Rep*. (2016), 6, 26708. DOI: https://doi.org/10.1038/srep26708

Poster

DOI 10.5162/EUROSENSORSXXXVI/PT1.1

A Support Vector Machine Learning Prediction Model of Evapotranspiration using Real-Time Sensor Node Data

Waqas A. K. Afridi[1], S. C. Mukhopadhyay[2], Bandita Mainali[3]
[123]School of Engineering, Macquarie University, Sydney, Australia

Waqas.afridi@mq.edu.au

Summary:
An IoT-enabled smart sensor node has been developed to acquire real-time field data and formulate an adaptable prediction model to predict crop Evapotranspiration (ETc) using a Support Vector Machine (SVM) learning algorithm. Integrating the SVM algorithm with real-time sensor nodes offers great potential to improve spatial and temporal resolution of water data uncertainty. In the model development, key input features are measured in real-time and computed using mathematical equations such as Penman-Monteith, which include soil-environmental parameters.

Keywords: Evapotranspiration, FAO56, KNIME, Machine learning, RStudio, SVM, Sensors, Water

Title

A Support Vector Machine Learning Prediction Model of Evapotranspiration using Real-Time Sensor Node Data.

Headlines

The paper outlines the existing Evapotranspiration estimation methods, machine learning modeling techniques, data collection and preprocessing, model development, and evaluation metrics, highlighting the significance of SVMs in advancing the field of ET prediction.

Background and Motivation

Water is the most critical resource for sustainable agriculture and hydrological ecosystems. According to WaterNSW and Natural-Resources-Access-Regulator 25–30% of NSW, Australia's groundwater data is unaccounted for due to the majority of monitoring sites being manually logged with minimal sensor integration, while ground bores are also expensive necessitating the need to develop a cost-effective automated system [1].

Description of the Developed Sensor Node

The current method is focused on developing an IoT-enabled low-cost embedded microcontroller system capable of delivering real-time sensor node data on a cloud server utilizing a LoRaWAN communication protocol [2]. The primary data is then analyzed to measure the statistical significance of the study parameters. The field data is then processed to model water loss in soil mainly by Evapotranspiration function using a machine learning algorithm. Furthermore, the research also focuses on the integration of a fabricated electromagnetic sensor with a microcontroller system to measure soil organic carbon which would significantly enhance the system's evaluation potential [3].

DOI: 10.5162/EUROSENSORSXXXVI/PT1.1

Preliminary Results

Initially, in-situ lab testing and sensor calibrations were performed as a baseline to validate sensor nodes' performance in the real field.

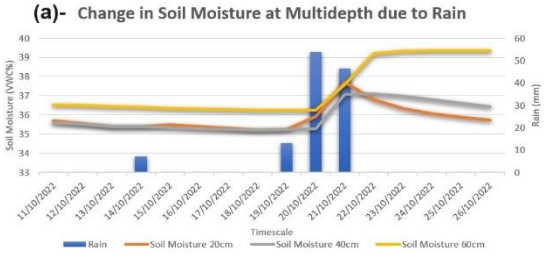

Fig. 2. Change in soil moisture content at subsequent depths after a rain event.

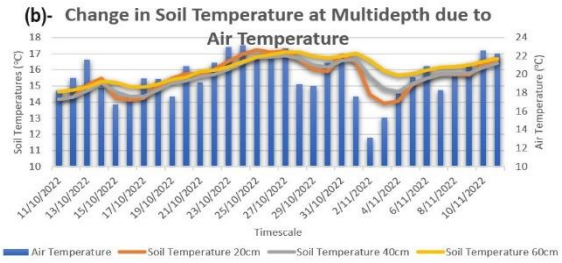

Fig. 3. Change in soil temperature at multi-depth due to varying air temperature.

Model Construction

The crop-evapotranspiration (ET_c-mm/d) prediction model was constructed based on the Support Vector Machine (SVM) Learning algorithm [4] in which various parameters are measured from the deployed sensor node and computed using mathematical equations in an R-programming tool, such as; Air Temperature (°C), Barometric Pressure (hPa), Wind Speed (Km/h), Relative Humidity (%), Rain (mm), Solar Exposure (MJ/m2), Soil Temperature (°C), and change in Soil Moisture (%VWC).

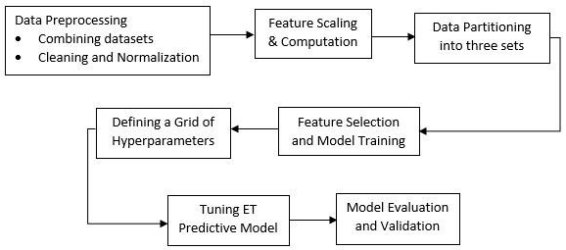

Fig. 4. Model Implementation Flowchart

The reference-evapotranspiration (ET_o-mm/d) was computed using the Penman-Monteith equation (1) [5].

$$ET_o = \frac{0.408\Delta(R_s - G) + \gamma\left(\frac{900}{T+273}\right)u_2(e_s - e_a)}{\Delta + \gamma(1 + 0.34u_2)} \quad (1)$$

Where,

Δ = Slope of Saturation Vapor Pressure Curve (kPa/°C)
Rs = Solar Radiation (MJ/m2 day-1)
G = Soil Heat Flux ≈ 0
Y = Psychrometric Constant
T = Air Temperature (℃)
u2 = Wind Speed (km/h)
es = Saturation Vapor Pressure (kPa)
ea = Actual Vapor Pressure (kPa)

Model Results

The results demonstrate the robustness and high predictability of the developed model based on the performance evaluation metrics: R^2, RMSE, and MAE [6]. The effectiveness of the proposed ET model in capturing complex relationships within soil and environmental parameters provides insights into its potential applications for water resource management and hydrological ecosystems.

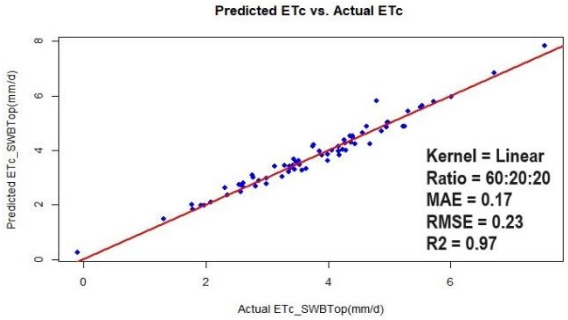

Fig. 5. Illustrating Evapotranspiration Prediction Model of the SVM Linear Kernel, (60:20:20)

Table 1. Evaluation Metrics for the ET Model with Best Hyperparamters Grid.

Kernel Function: Linear		Data Partition: 60:20:20
Evaluation Metrics		
MAE	RMSE	R^2
0.17	0.23	0.96

References

[1] WaterNSW | Chief Scientist & Engineer, “Review of water-related data collections , data infrastructure and capabilities,” New South Wales, 2020.

[2] W. A. K. Afridi, I. Vitoria, K. Jayasundera, S. C. Mukhopadhyay, and Z. Liu, “Development and Field Installation of Smart Sensor Nodes for Quantification of Missing Water in Soil,” *IEEE Sens. J.*, vol. 23, no. 21, pp. 26495–26502, 2023, doi: 10.1109/JSEN.2023.3317418.

[3] W. A. K. Afridi *et al.*, “Design an Electromagnetic Sensor to Measure the Organic Carbon in Soil and Its Validation With Standard Walkley–Black Method,” *IEEE Sensors Lett.*, vol. 7, no. 12, pp. 1–4, 2023, doi: 10.1109/lsens.2023.3328591.

[4] Y. Yao *et al.*, “Improving global terrestrial evapotranspiration estimation using support vector machine by integrating three process-based algorithms,” *Agric. For. Meteorol.*, vol. 242, no. October 2016, pp. 55–74, 2017, doi: 10.1016/j.agrformet.2017.04.011.

[5] B. Benli, A. Bruggeman, T. Oweis, and H. Üstün, “Performance of Penman-Monteith FAO56 in a Semiarid Highland Environment,” *J. Irrig. Drain. Eng.*, vol. 136, no. 11, pp. 757–765, 2010, doi: 10.1061/(asce)ir.1943-4774.0000249.

[6] V. Plevris, G. Solorzano, N. P. Bakas, and M. E. A. Ben Seghier, “Investigation of Performance Metrics in Regression Analysis and Machine Learning-Based Prediction Models,” *World Congr. Comput. Mech. ECCOMAS Congr.*, no. June, p. 2022, 2022, doi: 10.23967/eccomas.2022.155.

DOI 10.5162/EUROSENSORSXXXVI/PT1.4

Design and Test Evaluation of Cluster Dither for Inertial Measurement Unit with 3-Axis Ring Laser Gyroscopes

Cheonjoong Kim, Juneon An, Kyumin Shim
Agency for Defense Development, P.O. Box 35, Yuseong, Daejeon, South Korea

kcj3651@add.re.kr

Summary:
The purpose of this paper is to present a cluster dither design for applying continuous sinusoidal vibration to 3-axis RLGs simultaneously. Ring laser gyroscope (RLG) exhibits a specific range, known as the lock-in region, wherein the input angular velocity is too small to be measured. To mitigate the lock-in effect, a continuous mechanical sinusoidal vibration is applied to the body of the RLG, emanating from a dither mechanism. The proposed cluster dither design is verified through modeling and simulation (M&S). The validation of the proposed design is confirmed by test evaluation and manufacturing assessment.

Keywords: ring laser gyroscope, cluster dither, lock-in, natural frequency, sinusoidal vibration

Introduction

The RLG is a powerful tool to measure angular velocity. However, RLG has an inevitable deficiency caused by lock-in, where the input angular velocity is too small to be measured. To remove this lock-in region, the mechanical device called dither applies sinusoidal vibration to the RLG body. Generally, the dither is mounted at the center of the single-axis RLG body when the optical path length of an RLG is relatively large. However, if the RLG does not have enough optical path length, the mounting size for the dither in the quadrate RLG body is limited to inversely proportional to the square of the one-side length. This issue is a major concern in the dither design. To overcome this, this paper presents a new cluster dither design based on Ref [2], which can simultaneously apply mechanical sinusoidal vibration to 3-axis RLGs. The cluster dither is aimed to miniaturize an RLG-based inertial measurement unit (IMU). Results of the proposed design are verified through M&S. The performance of the proposed cluster dither is confirmed by manufacturing and test evaluation.

Cluster Dither Design

A conventional single-axis dither design is presented in Fig 1. As shown in Fig 1, the singe-axis dither is installed on the RLG housing using 3 fixing holes, and the RLG body is made to be fixed on the dither spoke. Thus, when any level voltage is applied to the PZT(pb-lead Zironcate Titanate) affixed to the dither spoke, the RLG body vibrates sinusoidally with a dither natural frequency and an amplitude corresponding to the voltage level applied to PZT. This physical structure of the dither highlights the natural frequency and the vibration amplitude as major design considerations. As depicted in Fig. 1, the dither spoke can be modeled as a cantilever beam [1]. Eq. (1) represents the natural frequency of the cantilever. Unfortunately, the cluster dither structure capable of simultaneously applying sinusoidal vibration to a 3-axis RLG deviates from the configuration depicted in Fig. 1. Furthermore, to install a 3-axis RLG on the cluster dither, some requirements should be fulfilled. First, 3 RLGs should be located at an interval of 120 degrees in the direction of dither rotation. Second, they are tilted at 54 degrees toward dither rotation. The cluster dither structure fulfilling such requirements is presented in Fig. 2. The dither spoke in Fig. 2 can be modeled as a cantilever, similar to the configuration depicted in Fig. 1. Which means that the cluster dither natural frequency can be obtained using Eq. (1). Following the selection of Invar as the material for the cluster dither and assuming an RLG with an optical path length of 10 cm, the required natural frequency to operate the RLG is determined to be 750 Hz. The final design of cluster dither is shown in Fig. 3. By using Eq. (1), the natural frequency of cluster dither is obtained as 783.57 Hz.

$$f_n = \frac{1}{2\pi}(\lambda L)_n^2 \sqrt{\frac{NEIL_f^2}{J_m L^3}} \qquad (1)$$

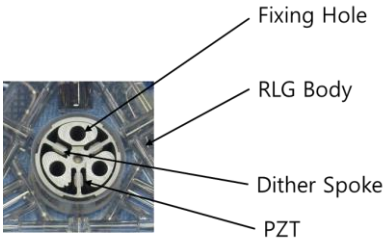

Fig. 1. The picture of typical single-axis dither.

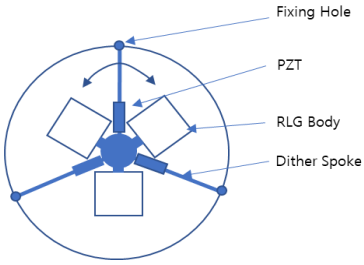

Fig. 2. The shape of cluster dither.

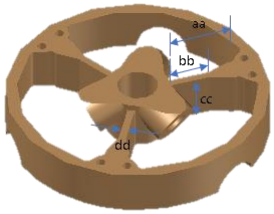

Fig. 3. The design result of cluster dither.

Cluster Dither Analysis and Test Results

To evaluate the proposed design validation, M&S is conducted using Solidworks. To verify the functionality of the cluster dither, the RLG body is modeled as a wheel-shaped structure with a moment of inertia equivalent to that of the RLG body. The M&S results are shown in Fig.4. The cluster dither natural frequency obtained in Fig.4 is 783.28Hz, which is almost the same as the theoretical frequency obtained from Eq. (1) implying theoretical natural frequency is reasonable. Further verifications using manufacturing and test evaluation have been carried out. The manufactured cluster dither is presented in Fig. 5. Fig. 5 shows the cluster dither installed in the center of the mounting fixture. The wheel-shaped structure as a replacement for the RLG is mounted on the cluster dither as depicted in Fig. 5. The manufactured cluster dither has an identical structure in Fig.4 except for the mounting part. The mounting part forms a square shape since the circular-shaped mounting part is hard to manufacture using existing machines. To confirm the performance of the dither structure, voltage range from 0 to 140V has been applied to the PZT. Then, the natural frequency of the manufactured cluster dither is measured. The measurement results in Fig. 6 shows that the cluster dither natural frequency is between 732 and 746Hz depending on the PZT voltage.

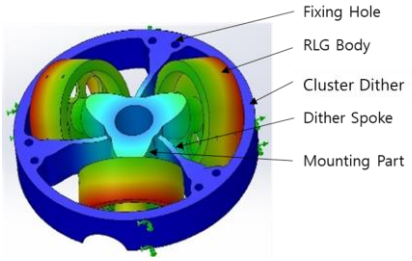

Fig. 4. The M&S result of cluster dither.

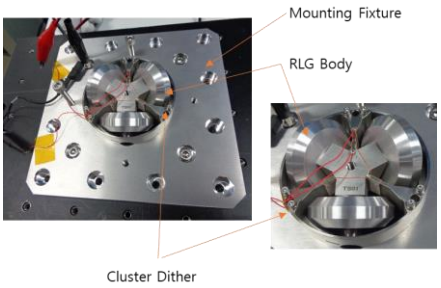

Fig. 5. The manufactured result of cluster dither.

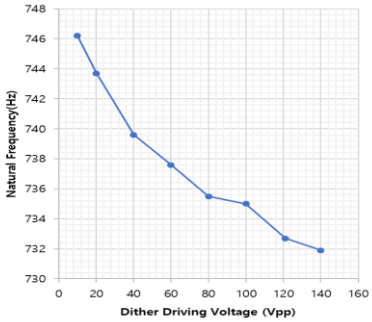

Fig. 6. The test result of cluster dither.

The natural frequency obtained from Eq. (1) and M&S is approximately 40Hz higher than the natural frequency in Fig.6. The difference in the natural frequency between the manufactured dither and the M&S modeled dither is caused by weight change and the mounting part shape difference during actual dither manufacturing.

Conclusion

This paper introduces a cluster dither design capable of simultaneously imparting continuous sinusoidal vibration to 3-axis RLG. The validation of the proposed cluster dither design has been conducted through M&S, test evaluations and manufacturing assessments. The results confirm the proposed design is valid.

References

[1] Lee, D. C., Moon, G., & Lee, J. C., Mechanical Dither Design for Ring Laser Gyroscope, KSME Int. J., 16, 481-491(2002); https://doi.org/10.1007/BF03185078

[2] J. G. Hanse, Cluster Dither Apparatus, U.S. Patent 5173745, 1992.

DOI 10.5162/EUROSENSORSXXXVI/PT1.9

Microbridge Resonators: Reducing Pull-in Voltage with Preserving Resonant Frequency

Haleh Nazemi[1], Youssef Elnemr[1], Arezoo Emadi[1]
[1] University of Windsor, 401 Sunset Avenue, Windsor, Ontario, Canada

Arezoo.emadi@uwindsor.ca

Summary:

This work introduces a unique microbridge resonator topology that is designed and developed to effectively reduce the device pull-in voltage by 16%. An analytical model incorporating the ratio between microbridge length and bottom electrode is presented, and finite element analysis is conducted using COMSOL Multiphysics. The proposed designs are fabricated utilizing a Multi-User MEMS sacrificial process and electrically characterized to demonstrate the approach.

Keywords: bridge sensor, electrode ratio, microelectromechanical systems, pull-in voltage, resonator

Introduction

Capacitive resonators comprise of a plate suspended over a bottom electrode. The performance of these resonators depends on their required operating DC voltage, which closely align with their pull-in voltage. The pull-in voltage is determined by the physical properties of the resonator, including the plate and bottom electrode overlapped area, plate thickness, gap height between the plate and bottom electrode, and its structural material properties. While there are a few studies presenting the impact of patterned top plate and bottom electrode on the required DC voltage and performance of circular resonators [1, 2], this exploration has yet to extend to other structures, such as microbridge resonators. This work develops an analytical model with experimentally demonstrated functionality that considers the ratio between the length of the microbridge and the bottom electrode as a key design parameter to influence the operating voltage. The developed model is employed to design microbridge resonators using a commercially available sacrificial technique with strategically designed ratios to enhance the device performance.

Microbridge Operating Mechanism and the Developed Analytical Model

Microbridge resonators consist of a deflectable plate anchored at both ends, which is suspended over a fixed bottom electrode, as shown in Fig. 1. When the DC voltage is applied, the plate deflects towards the electrode, altering the device capacitance. To maintain structural stability while operating at optimum condition, the applied voltage must remain close but below the resonator pull-in voltage [1, 2].

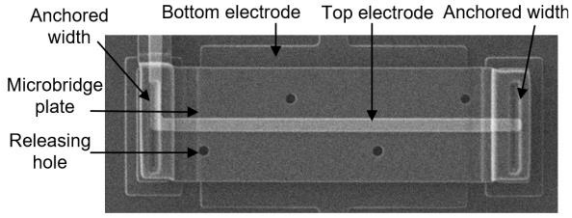

Fig. 1. Scanning electron microscopy (SEM) image of a designed and fabricated microbridge resonator.

The developed analytical model in this work considers the overlapping ratio between the bottom electrode's length and a strategically designed suspended microbridge's plate with the aim to reduce pull-in voltage. The model is employed to design the microbridge resonator, and finite element simulations are conducted to further analyze the effect of this ratio on the operating DC voltage of the microbridge. This model includes the structural properties of the microbridge, and the spring softening effect due to the applied DC bias voltage, shown in (1). In this model and similar to conventional resonators, a mass-spring-damper model is used to illustrate the behavior of the microbridge with small deflection under a uniform electrostatic force when parasitic capacitance is neglected. The stiffness can be calculated by (1)

$$k = 32Eb\left(\frac{t}{l}\right)^3 \frac{1}{8\left(\frac{l+w}{2l}\right)^3 - 20\left(\frac{l+w}{2l}\right)^2 + 14\left(\frac{l+w}{2l}\right) - 1} - \frac{\varepsilon_0 A V_{DC}^2}{g_0^3} \quad (1)$$

where microbridge's thickness, width and length are represented by t, b and l, respectively. w is

the length of the bottom electrode, A shows the area of the microbridge, V_{DC} is the applied DC voltage and g_0 is the gap height between the microbridge and the bottom electrode, and E is Young's modulus. The stiffness shown in (1) can be used to calculate the resonant frequency of the microbridge shown in (2) [3]

$$f_r = \frac{1}{2\pi}\sqrt{\frac{k}{m}} \qquad (2)$$

where f_r and m represent the resonant frequency and mass of the microbridge, respectively.

Microbridge Design and Fabrication

The proposed microbridge resonators are designed using MEMS L-Edit, as depicted in Fig. 1, and fabricated using a commercially available Multi-User MEMS process, PolyMUMPs [4]. The length and width of the polysilicon microbridges are 120 µm and 40 µm, respectively, with a thickness of 1.5 µm and a gap height of 750 nm. To solely investigate the effect of the ratio, all the design parameters are kept the same between the two designs. To demonstrate the proposed design concept, in one design the bottom electrode is extended underneath the bridge to 82 µm with the resonant frequency of 1.1 MHz, while in the other design, the bottom electrode length is 42 µm with the resonant frequency of 980 kHz. This represents ratios of 68% and 35% between the microbridge and the bottom electrode, respectively.

Results and Conclusion

Keysight E4990A impedance analyzer is used to measure the resonant frequency of the proposed microbridges up to their pull-in voltages when 500 mV AC is applied. The experimental results for both devices when DC voltage is swept are shown in Fig. 2. The measurements results indicate that the pull-in voltage for the microbridge with 68% and 35% ratios are 21V and 25V, respectively. Comparison between the presented analytical model, the conducted finite element analysis using COMSOL Multiphysics, the electrical characterization for the pull-in voltage and the resonant frequency of the proposed microbridges are shown in Fig. 3. The comparison is presented for the devices with the same dimensions and material properties while the bottom electrode topology varies.

It is demonstrated that the developed analytical model, conducted FEA analysis, and the electrical measurement results are in good agreement indicating that designing the bottom electrode topology with respect to the flexible microbridge reduces the pull-in voltage when other design parameters are the same. As illustrated in Fig. 3, the pull-in voltage reduces with the increase of the bottom electrode's length with respect to the microbridge's length.

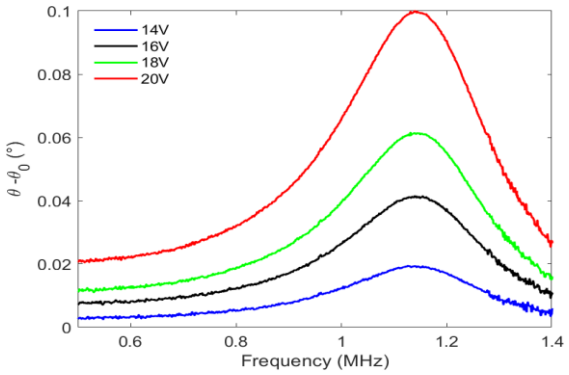

Fig. 2. Resonant frequency of microbridge with 68% ratio of the bottom electrode to the bridge length.

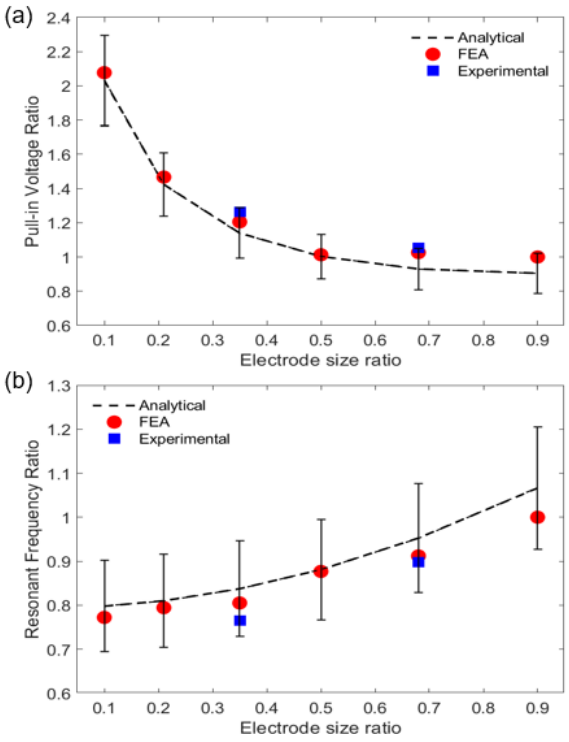

Fig. 3. Effect of electrode size ratio on (a) pull-in voltage and (b) resonant frequency, normalized by FEA at 90% ratio. The error bar denotes uncertainties in the fabrication process.

References

[1] A. İ. Yaşar, F. Yildiz and O. Eroğul, Evaluation of CMUT Performance Under Different Excitation Signals and Electrode Coverage, *11th International Conference on Electrical and Electronics Engineering (ELECO)*, 441-444, (2019); doi: 10.23919/ELECO47770.2019.8990518

[2] M. U. Nathani, H. Nazemi, C. Love, Y. Babu Lopez, S. Swaminathan, and A. Emadi, Capacitive based Micromachined Resonators for Low Level Mass Detection, *Micromachines*, 12(1), 13. (2020); doi: 10.3390/mi12010013

[3] Rebeiz, G. M., RF MEMS: Theory, design, and Technology, *Wiley* (2004)

[4] D. Koester, A. Cowen, R. Mahadevan, M. Stonefield and B. Hardy, *PolyMUMPs design handbook. MEMSCAP Inc*. (2003)

DOI 10.5162/EUROSENSORSXXXVI/PT1.41

On the Tunability of Resonant MEMS Sensor Subject to Blue Sideband Excitation

Erion Uka[1], Chengqi Lin[2], Jianlin Chen[2], Yuan Wang[3], Chun Zhao[1]
[1] School of Physics, Engineering & Technology, University of York, York, YO10 5DD, UK
[2] School of Microelectronics, Shanghai University, Shanghai, China
[3]Institute of Microelectronics, University of Macau, Zhuhai, China

erion.uka@york.ac.uk

Summary:

This work describes a new method and parameters by which the amplitude-frequency characteristics and sensitivity of a resonant MEMS sensor subject to the recently proposed blue sideband excitation (BSE) can be tuned. We show that the sensitivity of the BSE-based resonant MEMS sensor can be improved by 3 times via suppressing the intrinsic Duffing nonlinearity coefficient of the resonator. This paves the way for a new paradigm for highly sensitive and programmable multi-mode MEMS sensors.

Keywords: MEMS, resonant sensor, blue-sideband excitation (BSE), tunable sensitivity, multi-mode

Background

A new scheme of operating resonant MEMS sensors via blue-sideband excitation (BSE) has been proposed recently. As illustrated in Fig. 1, unlike the conventional direct driving method, the excitation frequency is at the sum of those of two modes of interest. The advantage of this new method is improving the sensitivity [1], circumventing the issue of feedthrough capacitance, as well as the capability of simultaneously detecting multiple parameters, e.g., acceleration and temperature [2]. These warrant further explorations of this newly emerging method, and this paper reports a new method to further improve the sensitivity towards realizing a new class of highly sensitive and programmable multi-mode MEMS sensors. In addition, as hypothesized in [1], the amplitude-frequency (A-f) effect in BSE (distinguish from the A-f effect in Duffing nonlinearity) can degrade the noise performance of resonant MEMS subject to BSE when operated in a closed-loop configuration. Here we report that the A-f effect in BSE can also be tuned with the same approach, thereby leading to a noise reduction in a closed-loop configuration.

Description of the New Method or System

The device-under-test for this work is a baseline double-ended tuning fork, as shown Fig. 2. The device is fabricated using the commercially available SOIMUMPS process, with a thickness of 25 µm. The device is placed in a vacuum chamber (pressure of 50mTorr) for characterizations. The bias voltage is generated using a DC power supply (Keysight EDU36311A). An additional DC voltage (V_{offset}) is applied to function as a proxy for stiffness perturbations experienced when operating the device as an accelerometer. The V_{offset} voltage, along with the BSE drive signal, $v_{actuate}$, is generated using an MFLI lock-in amplifier by Zurich Instruments. The motional current (i_{mot}) is converted to voltage using a custom-made transimpedance amplifier, the output of which is then fed to the MFLI. The tests were conducted in an open-loop configuration.

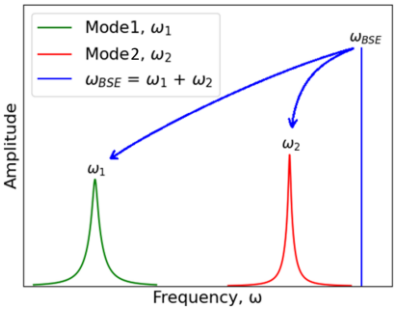

Fig. 1. Illustration of the blue-sideband excitation regime where the driving signal frequency is the sum of the resonant frequencies of modes 1 and 2.

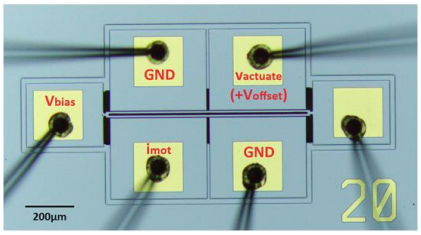

Fig. 2. Optical image of the MEMS resonator with length 830 µm, width 8 µm and thickness 25 µm.

Results

The measured resonant frequencies are 106.452kHz (Q-factor: 13k) for Mode 1 and 110.602kHz (Q-factor: 51k) for Mode 2. Simulated mode shapes are shown in Fig. 3.

Fig. 3. Mode shapes of Mode 1 and 2.

It is known that the Duffing nonlinearity coefficient of the resonator can be tuned by adjusting V_{bias}, i.e., nonlinearity softening. Based on this, we show that the nonlinear relationship between the BSE frequency and the output amplitude of Mode 2 (A-f effect in BSE) can also be tuned (see Fig. 4.). This is supported by our simulation by tuning the intrinsic Duffing nonlinearity coefficient only (See Fig. 5). We note that this can also be used to improve the sensitivity of such a resonant sensor.

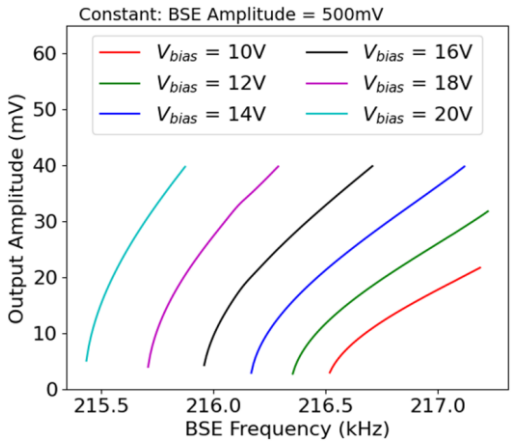

Fig. 4. The nonlinear relationship between output amplitude and BSE frequency of mode 2 for a range of bias voltages.

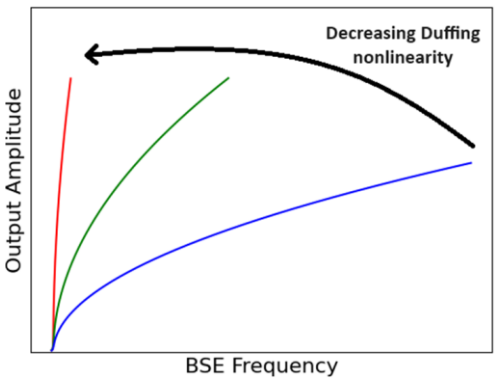

Fig. 5. Simulated results from the numerical model of the system. The results show that the nonlinear relationship between output amplitude and BSE frequency of mode 2 can be tuned by changing the intrinsic Duffing nonlinearity.

To obtain the sensitivity, the BSE drive signal is maintained at a constant, and the BSE frequency is tuned such that the output amplitude of Mode 2 is kept at 5mV, and the sensitivity figure is shown in Fig. 6. From the sensitivity results, it can be observed that by changing the V_{bias} from 10 V to 16 V, the sensitivity can be improved from 1.19 mV/V to 5.85 mV/V, a 4.9-fold increase. This demonstrates the feasibility of the new approach towards realizing a highly sensitive and programmable multi-mode sensor.

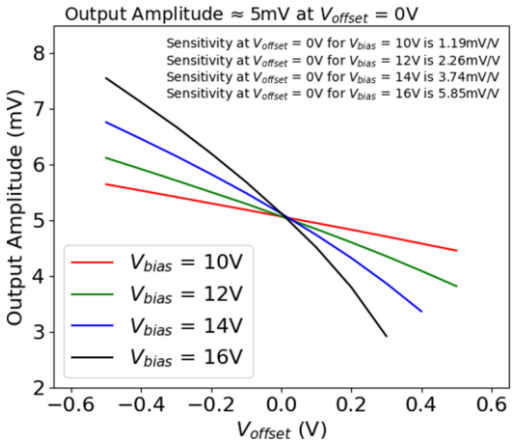

Fig. 6. The relationship between output amplitude and V_{offset} of mode 2 for a range of bias voltages for output amplitude = 5mV at V_{offset} = 0V setpoint, as well as the sensitivity values extracted at V_{offset} = 0V setpoint with different V_{bias} voltage, i.e., different Duffing nonlinearity coefficients

Conclusions

From the results obtained thus far, we confirmed the feasibility of our new approach by improving the sensitivity as well as the A-f effect in BSE (distinguish from the A-f effect in Duffing nonlinearity) via tuning the intrinsic Duffing nonlinearity coefficient of the resonator. We anticipate that the results can be extremely useful in realizing a new class of highly sensitive and programmable multi-mode resonant sensors subject to BSE. Ongoing experiments are focusing on obtaining more data at different operating points, e.g., the output amplitude of 10 mV, as well as the noise characterizations. We aim to show the efficacy of the method in not only improving the sensitivity but also the noise.

References

[1] L. Xu, J. Xi, L. Gao, F. Li, J. Pi, C. Li, K. Wang, X. Xiong, Y. Wang, H. Liu, X. Zou, C. Zhao, A closed-loop system for resonant MEMS sensors subject to blue-sideband excitation, *Journal of Microelectromechnical Systems,* 31.4, 690-699 (2022); doi: 10.1109/JMEMS.2022.3183021

[2] J. Xi, L. Xu, Y. Wang, H. Liu, X. Xiong, X. Zou, C. Li, F. Hu, C. Wang, M. Kraft, C. Zhao, Multiple Parameter Decoupling for Resonant MEMS Sensors Exploiting Blue Sideband Excitation, *Journal of Microelectromechnical Systems,* 32.5, 426-436 (2023); doi: 10.1109/JMEMS.2023.3293464

Toward Sensor Search Engine (SENSEE): A database for exploring trends in phosphate sensor research

E. McLamore, G. Moreira, C. Sanders, M. Torres, Clemson University, Clemson (USA),
S. P.A. Datta, Massachusetts Institute of Technology (MIT Auto-ID Labs), Cambridge (USA),
S. Bahramzadeh, Azad University (SRB), Tehran (Iran), J. H. Bhadha, University of Florida,
Belle Glade (USA)

Unfortunately, this abstract is not available, as the contribution was not confirmed at the time the conference proceedings were finalized.

Toward Sensor Search Engine (SENSEE): A database for exploring trends in phosphate sensor research

E. McLamore, G. Moreira, C. Sanders, M. Torres, Clemson University, Clemson (USA),
S. P.A. Datta, Massachusetts Institute of Technology (MIT Auto-ID Labs), Cambridge (USA),
S. Bahramzadeh, Azad University (SRB), Tehran (Iran), J. H. Bhadha, University of Florida,
Belle Glade (USA)

Unfortunately, this abstract is not available, as the contribution was not confirmed at the time the conference proceedings were finalized.

DOI 10.5162/EUROSENSORSXXXVI/PT1.55

Polymer-coated QCM Sensor Leveraging Energy Trapping Effect for Enhanced Detection of Volatile Organic Compounds

Youssef Elnemr[1], Haleh Nazemi[1], Arezoo Emadi[1]
[1] University of Windsor, 401 Sunset Avenue, Windsor, Ontario, Canada

Arezoo.emadi@uwindsor.ca

Summary:

This work presents a novel QCM sensor with a unique topology design, developed based on distribution of area for improving mass sensitivity (DAIS), for the VOC detection at parts per million (ppm) levels. A polymer sensing layer is applied to facilitate the adsorption of target analyte molecules during experimentational phase. The DAIS-QCM sensor exhibits superior mass sensitivity when exposed to various concentrations of VOC target analyte, showcasing an enhancement of over 10% in comparison to a conventional QCM sensor used as a reference.

Keywords: energy trapping effect, gas detection, mass sensitivity, polymer sensing layer, quartz crystal microbalance

Introduction

The detection of volatile organic compounds (VOCs) has gained interest due to its various applications domains, including environmental monitoring, industrial safety, and public health. The quartz crystal microbalance (QCM), a resonator sensor, is a widely used device for mass sensing application, owing to its capability to detect mass changes in nanogram range [1]. Through this paper we present a comparative analysis and experimental evaluation of a polymer-coated QCM sensor, leveraging a novel approach based on the utilization of energy trapping effect regions for mass loading area (MLA) for improved mass sensitivity [2]. The DAIS-QCM, as shown in Fig. 1, is derived from a finite elements analysis (FEA) on the impact of MLA on QCM sensor mass sensitivity. The findings reveal that the DAIS topology, featuring an array of circular electrodes with a radius of 0.62 mm and outer radius of 2.96 mm, outperforms the conventional QCM design, which features a conventional single electrode with radius of 4.25 mm. Despite the conventional QCM having a larger sensing electrode, which accommodates a greater mass loading area for more adsorption of target analyte molecules, the DAIS-QCM with an MLA of 21 mm², ~38% of the MLA of the conventional QCM, shows improved mass sensitivity by ~ 25% compared to the conventional QCM. This is attributed to the presence of the phenomena of energy trapping effect caused by the natural structure of quartz crystal substrate.

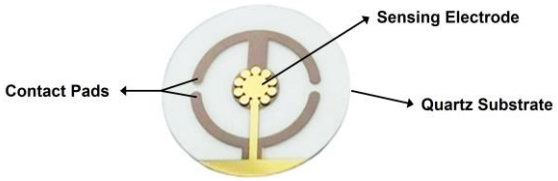

Fig. 1. A 5 MHz AT-cut QCM sensor, featuring a novel topology termed DAIS based on maximizing the energy trapping effect region by replacing the conventional single circular electrode with an array of smaller circular electrodes with 0.62 radii.

This paper further presents the maintained experimental setup and the materials used during the characterization process. both the DAIS-QCM and the conventional QCM are coated with polymer sensing layer and then subjected to identical concentrations of Ethanol to evaluate their sensing performance by observing the shift in their resonant frequencies. This paper introduces the DAIS-QCM as a promising avenue for enhanced VOC detection for various application domains.

Experimental Setup and Materials

To establish a basis for comparison, and validate the enhancement in sensing performance, DAIS-QCM is fabricated by Angstrom Engineering Inc., using eBeam evaporation technique. A 5 MHz QCM with a conventional topology serves as a reference device during the experimental process. The QCM sensors are then coated with Polyvinylpyrrolidone (PVP), a polymer reported for its efficacy in VOC detection through the adsorption of its molecules [3]. A

sensing material solution is prepared by dissolving 100 mg of PVP, from Polysciences, Inc. (catalog# 01052-250), in 10 mL of methanol, yielding a 0.1 weight percent (Wt.%) solution. The solution undergoes sonication for 20 minutes to ensure complete dissolution of the polymer. The deposition of the polymer is achieved through spin coating, depositing 100 µL of the solution, resulting in an approximate thickness of 0.1 µm. Both the DAIS and conventional polymer-based QCM sensors are tested under controlled conditions using a Plasmionique FLO07-TSV system to ensure consistency. Ethanol, a volatile organic compound, is introduced into the chamber through NI 5.0UH-T, a 5.0 ultra-high purity Nitrogen, selected as a carrier gas due to its non-reactive properties. The target analyte is exposed, commencing with a baseline of pure N_2 gas at a flow rate of 100 SCCM, followed by exposure to a mixture of N_2 and Ethanol-saturated vapors with concentrations listed in Tab. 1, while maintaining the total flow rate at 100 SCCM. This distinct pattern of exposure process is iterated thrice to ensure data reliability.

Tab. 1: Ethanol flow rates and corresponding concentrations

Flow rate (%)	Concentration (ppm)
2	1100
4	2300
6	3400
8	4600
10	5700

Results and Discussion

The QCM mass sensitivity (S) of the QCM is defined as the ratio of the change in resonant frequency (Δf) resulting from added mass (Δm) [2]. It serves as a key metric for the QCM's ability to detect mass changes, thereby reflecting its sensing performance. During the experiment, both sensors are exposed to same concentration of Ethanol. Therefore, the observed Δf indicates the sensing performance of the sensors, as the added mass (Δm) remains consistent for both sensors. The resonant frequency values over time, responding to identical concentrations of Ethanol, are plotted for both DAIS and conventional QCMs in Fig. 2(a). Despite the conventional QCM having a larger MLA, the unique design of DAIS-QCM enables it to achieve a higher resonant frequency shift, showcasing superior mass sensitivity. Additionally, the frequency shift slope of DAIS-QCM is more uniform compared to the conventional design, as presented in Fig. 2(b). The DAIS design, where the single circular electrode is replaced by an array of smaller electrodes to maximize the energy trapping effect region, yields enhancements in sensor mass sensitivity and its uniformity. Therefore, the unique design of DAIS is presented as a promising approach for enhanced detection of VOCs in various applications.

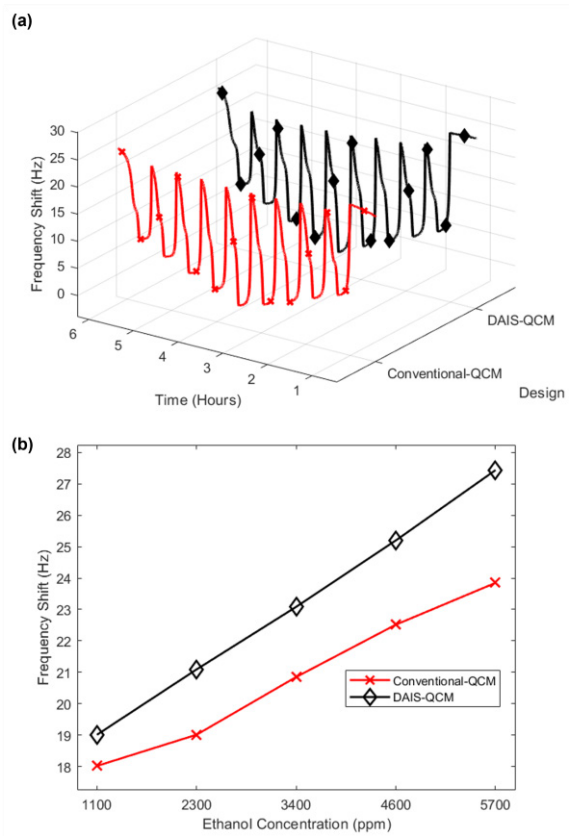

Fig. 2. (a) The graph from the experiment results illustrates the response of both DAIS-QCM and conventional QCM to variation in VOC target analyte Ethanol. (b) Comparative frequency shift characterization for Ethanol concentrations 1100, 2300, 3400, 4600, and 5700 ppm.

References

[1] X. Huang, Q. Chen, W. Pan, and Y. Yao, "Advances in the Mass Sensitivity Distribution of Quartz Crystal Microbalances: A Review," *Sensors 2022, Vol. 22, Page 5112*, vol. 22, no. 14, p. 5112, Jul. 2022, doi: 10.3390/S22145112.

[2] S. Swaminathan and A. Emadi, QCM With Electrode Configuration Based on Distribution of Area for Improving Mass Sensitivity (DAIS), US Patent, 63/321,848, 2023.

[3] X. Su, D. Chen, N. Li, A. C. Stevenson, G. Li, and R. Hu, "A wireless electrode-free QCM-D in a multi-resonance mode for volatile organic compounds discrimination," *Sens Actuators A Phys*, vol. 305, p. 111938, Apr. 2020, doi: 10.1016/J.SNA.2020.111938.

DOI 10.5162/EUROSENSORSXXXVI/PT1.56

Method for Increasing Amplitude of Cluster Dither in RLG-based Small-size Inertial Measurement Unit

Jun Eon An, Cheonjoong Kim, Kyoung Ho Chong
Agency for Defense Development, P.O. Box 35, Yuseong, Daejeon, South Korea

juneon@add.re.kr

Summary:
The lock-in problem affecting ring laser gyroscopes (RLGs) is typically alleviated by applying a mechanical vibration to the RLG body using a dither. A cluster dither, which can excite three RLGs simultaneously, can facilitate the miniaturization of RLG-based inertial measurement units (IMUs). This study examines the mechanical parameters of an IMU that affect the amplitude of the cluster dither. For this purpose, a model with two linearly damped coupled linear oscillators was used, and the theoretical analysis results were experimentally validated.

Keywords: lock-in, ring laser gyroscope, cluster dither, inertial measurement unit

Introduction

A dither is a device that alleviates the "lock-in" problem affecting ring laser gyroscopes (RLGs)—whereby the laser beams propagating in opposite directions become locked in phase—by applying mechanical vibration, such as rotational vibration, to the resonator. In a typical single-axis RLG, the rotation axis of a piezoelectrically driven dither is located on the RLG mount and coincides with the RLG's sensing axis. However, smaller RLGs have inadequate space in the mount to accommodate the motor required for such dithers. Instead, if the dither can be kept outside the RLG, three RLG bodies can be simultaneously provided with a single-axis dither. Such a dither is called a cluster dither [1], and it facilitates miniaturization of RLG-based inertial measurement units (IMUs). However, unlike typical single-axis dithers, cluster dithers lack the amplitude required to solve the lock-in problem; this is because the rotation axis of a cluster dither does not coincide with the RLG's sensing axis. The rotational vibration applied by the cluster dither to the RLG body decreases proportionally as the misalignment angle between the two axes increases. Moreover, the dither amplitude can be reduced by the vibration isolator, a component present in most IMUs, because the latter operates as a damper and thereby absorbs the rotational vibration produced by the cluster dither. An insufficient dither amplitude exacerbates the lock-in problem. To ensure sufficient dither amplitude, the preferred solution is to reduce the weight of the RLG. However, because the performance of an RLG is proportional to the resonator length, reducing the weight of the RLG reduces its performance. In this study, the structure of the IMU was approximated using a model with two linearly damped coupled linear oscillators. The optimal mechanical design variables for improving the amplitude of the cluster dither were derived for this model, and the derived variables were validated through theoretical and experimental analysis.

Two linearly damped coupled linear oscillators

Fig. 1 shows an RLG-based small IMU with a cluster dither. The dither is assembled in the lower housing connected to the vibration isolator, which is fixed to the body frame. Three RLGs are attached to the hub at 120° intervals. When the dither drive signal is applied, the dither produces rotational vibration, causing the RLGs to vibrate around its rotation axis. In this vibration system, the damping element of the vibration isolator attenuates the amplitude of the cluster dither.

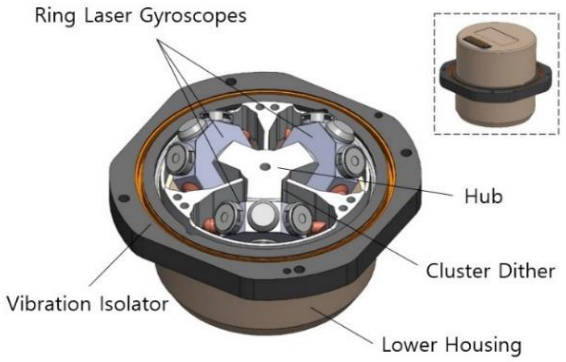

Fig. 1. RLG-based small-size inertial measurement unit with cluster dither

The IMU, including the vibration isolator, cluster dither, and RLGs, can be approximated by a model with two linearly damped coupled linear oscillators, as shown in Fig. 2 [2].

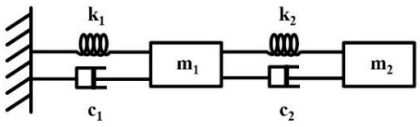

Fig. 2. Two linearly damped coupled linear oscillators

In the figure, k_1/k_2 and c_1/c_2 are the spring constant and damping constant of the vibration isolator/cluster dither, respectively; m_2 represents the hub and RLGs, which experience rotational vibration due to the dither drive signal ($F_d e^{i\omega t}$); and m_1 denotes the mass excluding m_2 in the IMU connected to the vibration isolator. In this approximate model, the rotation angle θ_2 of the cluster dither is expressed using Eq. (1):

$$\theta_2 = F_d \frac{I_1 I_2\left(\frac{\omega_1^2-\omega^2}{I_2}+\frac{\omega^2}{I_1}\right)+i\omega(\Gamma_1+\Gamma_2)}{\left[I_1 I_2\left(-\omega^2\left(\frac{\Gamma_1\Gamma_2}{I_1 I_2}+\frac{I_2\omega^2}{I_1}\right)\right)\right]-i\left[I_1 I_2\left(\omega^3\left(\frac{\Gamma_2}{I_1}+\frac{\Gamma_2}{I_2}\right)-\omega\left(\frac{\omega_1^2\Gamma_2}{I_2}\right)\right)\right]}, \quad (1)$$

where ω_1/ω and Γ_1 / Γ_2 are the angular frequencies and damping constant of the vibration isolator/cluster dither, respectively, and I_1 and I_2 are the moments of inertia of the masses corresponding to m_1 and m_2, respectively.

Eq. (1) shows that to increase the rotation angle of the cluster dither by modifying mechanical parameters, either the I_1/I_2 ratio must be increased, or the cluster dither must be manufactured to have a low resonant frequency. I_1 can be easily increased by increasing the diameter or housing weight of the IMU; however, this is not desirable for a small-size IMU. Conversely, reducing I_2 would require the RLG to be miniaturized by reducing the resonator length, which would reduce the performance of the RLG. Therefore, I_1 and I_2 must be optimally designed considering the size and performance of the IMU.

Analysis and test results

In this study, the I_1/I_2 ratio and dither drive signal frequency were set as the design variables, and the gain of the cluster dither amplitude was evaluated. The I_1/I_2 ratio was changed by adding a dummy mass to the housing, and two cluster dithers—one manufactured using stainless steel and the other using aluminum—were used to achieve different resonant frequencies (dither drive signal frequencies). To calculate the dither amplitude gain, modeling and simulation were conducted based on Eq. (1), and the output voltage of the piezoelectric material was experimentally measured. Figs. 3 and 4 present the simulation results and experimental measurements, respectively, which are observed to be in agreement. The dither amplitude gain increased with the I_1/I_2 ratio and was higher for the dither with the lower resonant frequency.

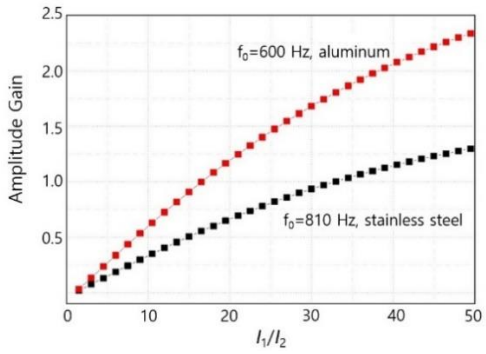

Fig. 3. Cluster dither amplitude gain determined via modeling and simulation

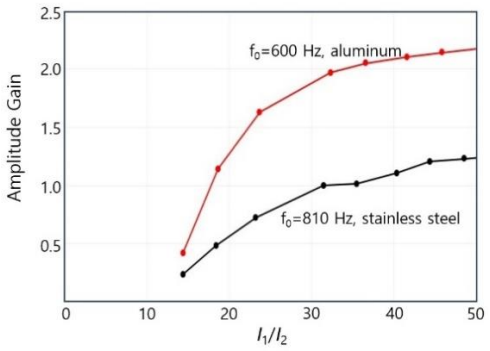

Fig. 4. Experimentally measured cluster dither amplitude gain

Conclusion

This study aimed to improve the amplitude of cluster dithers in an RLG-based IMU. To achieve this, the IMU was approximated by a model with two linearly damped coupled linear oscillators, and the optimal design variables were derived. Among the mechanical parameters, these variables were determined to be the moment of inertia ratio (I_1/I_2) and the dither drive frequency (resonant frequency). The correlation between the derived design variables and the cluster dither amplitude gain was verified through theoretical and experimental analysis. The findings confirmed that increasing the I_1/I_2 ratio and lowering the dither drive frequency can increase the dither amplitude. Thus, the dither amplitude and drive frequency are important design variables for solving the lock-in problem affecting RLGs, and their optimal values must be determined considering the performance of the RLG.

References

[1] J. G. Hanse, Cluster Dither Apparatus, U.S. Patent 5173745, 1992.

[2] Cline, Douglas. Variational principles in classical mechanics. University of Rochester River Campus Librarie, 2017.

DOI 10.5162/EUROSENSORSXXXVI/PT1.101

Magnetic Sensors of Oxygen Concentration

Alexey Vasiliev[1,2], Oleg Kul[2]
[1] Dubna state university, Universitetskaya str., Dubna, Moscow region, Russia
[2] LLC "C-Component", Tushinskaya 17, Moscow, 125362, Russia

Corresponding Author's e-mail address: A-A-Vasiliev@yandex.ru

Summary:
The analysis of the influence of the size of the oxygen sensor of thermomagnetic type to the performace of the sensor is carried out. It is shown that the necessary condition of the independence of the sensor response from the orientation of the sensor consists in the minimization of natural convection of air compared to the gas diffusion. The optimal size of the sensor is defined by fundamental constants of the gas medium.

Keywords: Oxygen, magnetic sensor, size effects.

Introduction

Detection of oxygen concentrations is vital in our everyday life, industrial and home safety, monitoring of technological processes and in many other fields of human activity. There three different ranges of this oxygen detection. The first one is the determination of oxygen in ambient air at concentrations close to 21 % (normal content of oxygen in air), the second is the determination of low concentrations of oxygen in inert gas, and the third is the detection of low concentrations of oxygen at low residual pressure in vacuum installations. Respectively, these three ranges require the application of different gas sensors. In addition, some of the applications, for example the measurement of oxygen in medicine, need very fast measurement of oxygen concentration with response time exceeding respiration rate (up to 100 respirations per minute).

The most known sensors used for the measurement of oxygen concentrations are the sensors of electrochemical type. These are the amperometric sensors with platinum working electrode and silver chloride reference electrode. The silver of the electrode is consumed in the process, and this limits the lifetime of the sensor. To improve this parameter, the sensors of Oxonium company (St. Petersburg) [1] restrict electrochemical current and use built-in amplifier; this permits to reach lifetime of the sensor up to 10 years.

Another type of the sensor used for ambient concentrations of oxygen is the sensor of magnetic type, which is the main topic of this work. Oxygen is the only paramagnetic gas (except NO), and this property lies in the basis of such type of gas sensors. Therefore, its concentration can be determined in two ways: using so-called "magnetic wind" resulting in the motion of oxygen-containing gas (air) in a gradient of magnetic field and gradient of temperature and using Senftleben effect, change in the diffusion cross-section of the triplet oxygen molecules in magnetic field. Magnetic field leads to precession of oxygen molecules and to decrease in heat conductivity of gas. This effect depends on the ratio of magnetic-field strength to gas pressure. Therefore, this type of gas sensor is applicable at low pressure of gas in a range 0.01 – 2 Torr. The threshold of O_2 detection is of about 10^{-5} Torr. This type of gas sensor can be used as used for the determination of oxygen concentration and, as well, as a leakage detection to a vacuum setup [2].

Model

Magnetic sensor of oxygen consists of a tube made of diamagnetic material placed in magnetic field of permanent magnet. This tube is equipped with heater and thermoanemometer measuring gas flow through the tube. Oxygen containing gas is attracted by magnetic field, on the other hand, magnetic susceptibility of this paramagnetic gas is reverse proportional to the square of magnetic-field strength. Therefore, if the gas is heated in the tube, the gradient of temperature leads to asymmetry of the system and to a permanent flow of gas in the direction from cold part to hot part of the system.

A very important advantage of this type gas sensor is a possibility to operate even in aggressive atmosphere. A disadvantage consists in the necessity to keep the orientation of the device because of competition between mag-

netic and natural convection due to a gradient of temperature.

To minimize this effect, it is necessary to consider the interference between the thermomagnetic and natural convection. The ideal condition for this is the situation, when the natural convection could be neglected and, therefore, when the thermomagnetic convection is independent of the orientation of the tube placed in magnetic field. In addition, to get response time sufficient for the measurement of oxygen concentration with characteristic time of < 10 ms, the dimension of the tube should be below a certain value defined by the diffusion processes.

Results about the influence of the microhotplate size to the convective heat exchange were obtained in [3]. Here we will use these data.

We considered the role of convection in the heat exchange of microhotplate. It was suggested that over microhotplate exists a virtual tube of upstreaming gas. In the case of recent work, this is real tube with diameter *d* and radius *r* heated up to temperature *T*. It is obvious, that the worst case, when the natural convection is most important compared to "magnetic wind" is a vertical orientation of this tube.

It was shown in [3] that the convection velocity of gas in this tube is equal to

$v = \frac{g \cdot \mu \cdot P \cdot r^2}{8 \cdot \eta \cdot R}(\frac{1}{T_r} - \frac{1}{T})$, where *g* is free fall acceleration, μ is mass of mole of gas, *P* – pressure, η – dynamic viscosity, *R* – gas constant, T_r – room temperature. Taking into account that $\eta = \nu \cdot \rho$, this could be rewritten as:

$v = \frac{g \cdot r^2 \cdot T_{ev}}{8 \cdot \nu}(\frac{1}{T_r} - \frac{1}{T})$, where T_{ev} is everage temperature of gas. Convection can be neglected, if the time of the gas motion due to convection through the tube with length *h* is larger than the time of back diffusion of gas.

$\frac{h}{v} >> \frac{h^2}{D}$, or $v << \frac{D}{h}$; substituting previous formula to the last one, we obtain

$\frac{g \cdot r^2 \cdot T_{ev}}{8 \cdot \nu}(\frac{1}{T_r} - \frac{1}{T}) < \frac{D}{h}$, and

$r^2 h << \frac{8D \cdot \nu}{g \cdot (\frac{T_{ev}}{T_r} - \frac{T_{ev}}{T})}$, in our case T_{ev}=*T*,

therefore

$r^2 h << \frac{8D \cdot \nu}{g \cdot (\frac{T}{T_r} - 1)}$; taking into account that both the values of diffusion coefficient and kinematic viscosity of air at working temperature of magnetic oxygen sensor are equal to about 2 cm^2/c, we can evaluate the dimension of the sensing element of gas sensor leading to the insensitivity of this element to the orientation of gas sensor in the gravitation field and, therefore, to its applicability in portable instruments.

Discussion

Let's consider usual macroscopic gas sensors, that is a glass tube equipped with flow meter and put to magnetic field. If the diameter of this tube is, for example 0.1 cm, $T=2 \cdot T_r$, the length of the tube should be by the order of magnitude $h << 3 \cdot 10^{-2}/r^2 \sim 3$ cm. It is clear that the fabrication of such small sensor by macroscopic tools is rather complicated.

Our colleagues [4] made an attempt to fabricate this kind of gas sensor, which can be used in portable devices including medical instrument using microfabrication. The sensor was fabricated as a small spiral made of 10 μm Pt glass-coated wire. The spiral diameter was of about 100 μm, length was of about 150 μm. The spiral was suspended on two platinum wires in housing of TO-46 type and placed in a gradient of magnetic field. The orientation of the spiral in magnetic field was more or less random.

The results of [4] show that the thermomagnetic sensor can be used for the determination of oxygen concentrations from approximately 0.1 vol. %, the response time of the sensor is below 0.1 s, therefore it can be applied for medical monitoring. Results of recent work will be used to design advanced microelectronic version of the sensor of both thermomagnetic type and sensor based on Senftleben effect.

References

[1] http://oxonsens.ru/

[2] A.P.Babichev, V.D.Brayko, N.M.Gorshunov *et al.*, Determination of oxygen admixture in fluorine, *russian journal "Applied physics"*, # 4, 67-69 (2012).

[3] Alexey Vasiliev, Alexey Shaposhnik, Oleg Kul, The Role of Convection and Size Effects in Sensor Microhotplate Heat Exchange, *Proceedings* 2024, 97(1), 150;

[4] M.V.Krupin. Early detection of fire on nuclear power station using thermomagnetic oxygen sensor. *PhD thesis,* Moscow 2015 (in Russian).

DOI 10.5162/EUROSENSORSXXXVI/PT1.186

Adaptive Accuracy Enhancement for Simultaneously-Firing Optical Position Sensor

Eduard Burian[1]
[1] *LOX Technologies s.r.o., Rusovská 7, 851 01 Bratislava, Slovakia*

eduard.burian@gmail.com

Summary:
An algorithm for adaptive accuracy enhancement of lateral position sensing based on quadrature spatio-temporal modulation is presented and its application in a prototype micropower optical position sensor with simultaneously-firing infrared emitters is reported. Substantial (4x) improvement in position accuracy over basic detection method has been observed using automated test stand where partial incapacity in one of the emitter channels has been simulated.

Keywords: position sensor, spatio-temporal, quadrature modulation, accuracy enhancement

Introduction

A micropower active optical position sensor measuring one-dimensional displacements lateral to optical axis over decimeter-wide gaps was recently presented [1]. Quadrature spatio-temporal modulation involving four simultaneously-firing infrared emitters and diffuse reference primer has been utilized in order to reduce ON-time for signal processing circuitry, allowing up-to two years of continual battery operation. However, variations in geometry of emitters due to manufacturing process as well as degradation of primer due industrial conditions and aging may result in worsening readout accuracy. To address both issues, an adaptive algorithm for determination of irregular gains in signal path involving emitters, primer and acquisition circuitry has been proposed and implemented in firmware of the prototype device.

Spatio-Temporal Modulation

Implemented position sensing based on spatio-temporal modulation involves four infrared emitters equipped with collimating lenses that illuminate primer pattern in four distinct spots with mutual spatial phase shift of 90°. At the same time, emitters are in regular intervals supplied with current bursts of constant frequency, but again of mutual temporal phase shifts of 90°. Incident infrared light is then modulated and reflected in dependence to the relative position of the recurring pattern printed on a diffuse strip. As a result of the spatial modulation, temporal phase shift to the overall reflected light is induced, revealing lateral displacement of the primer within one spatial period. Overall signal received in set of infrared detectors is amplified, converted and synchronously detected in digital domain, resulting in a complex value with phase angle directly proportional to the lateral displacement of the primer.

Algorithm for Irregular Gains

Because of irregularities in emitter circuitry and collimator geometries, as well as due aging and field conditions, detected in-phase and quadrature components can face irregular distortion observed as affine (shift and scale) transformation on complex plane. To account for it, a model for spatio-temporal modulation and subsequent synchronous demodulation process with distinct channel gains is introduced as

$$D = \frac{1}{T}\int_T \sum_n G_n I(\rho_n) I(\gamma_n) e^{-i\omega t}\,dt\ , \quad (1)$$

where D is detector output, $G_n > 0$ is arbitrary (presumably known) gain for *n*-th channel and $I(\varphi)$ is biased cosine function representing both spatial and temporal intensity modulation, governed by spatial and temporal modulation phases $\rho_n = 2\pi l / L + n\pi/2$ and $\gamma_n = \omega t - n\pi/2$. In case of uniform gains, spatial phase for given lateral displacement l can be found simply as argument of the complex detector output. However, for uneven and possibly time-variant gains, detected phase need to be corrected by inverted transformation in form

$$D_{COR} = \frac{\mathrm{Re}(8D) - G_0 + G_2}{G_0 + G_2} + i\frac{\mathrm{Im}(8D) + G_1 - G_3}{G_1 + G_3}\ . \quad (2)$$

Measured lateral position can be then evaluated by re-integrating changes in the phase of the corrected detector output using

$$\Delta l = \frac{L}{2\pi}\Delta \arg\left(D_{COR}\right) \qquad (3)$$

Adaptive Determination of Gains

For estimation of unknown channel gains, Fourier analysis of detector output at basic spatial frequencies is utilized. Components for integer spatial frequencies $k \in \langle -1,1 \rangle$ can be found as integrals

$$C_k = \frac{1}{L}\int_L D e^{-ik2\pi l/L}\, dl \qquad (4)$$

provided numerically for one or multiple spatial periods. This of course implies that primer is in relative movement in respect to sensor for at least one length L. By solving eq. (4) for unknown gains, we get

$$G_n = 4\,\mathrm{Re}\left(i^{2n}C_{-1} + i^{n}C_0 + C_1\right), \qquad (5)$$

applied in next cycle for gains in eq. (2). The process leads consecutively to enhancement of position accuracy and adaptation of gains for changing field conditions.

Testing and Results

To provide assessment of the algorithm, an automated test stand with configurable sensing gap distances, linear drive and precision position measurement has been readied (Fig. 1).

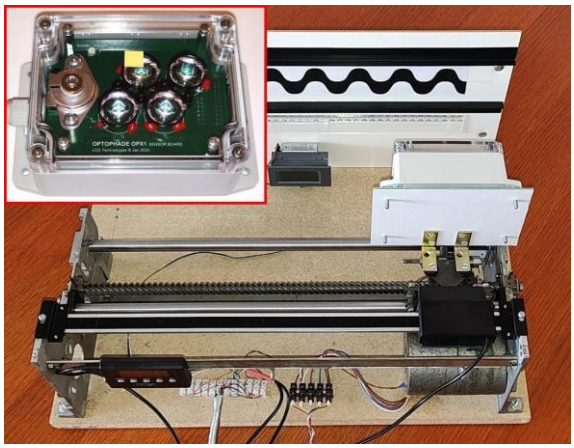

Fig 1. Automated test stand. Inset image: Front side of tested optical sensor with simulated incapacity.

Results for position error and performance of gain adaptation algorithm obtained for 125mm sensing gap can be seen in Fig. 2 and Fig. 3. Initially, as gains are set to equal value of 100, standard position error of 0.8-1mm is indicated. Later, with sufficient amount of detector data integrated, adaptation of gains started resulting in gradual enhancement in position accuracy to less than 0.2mm.

In next phase, we used a 1cm² paper strip for partially blocking of one of the infrared emitters. Subsequent surge in position error to approx. 10x of the settled value could be observed, however, as channel gains adapted, measurement error dropped again to almost previous level. Similar behavior could be observed after strip removal.

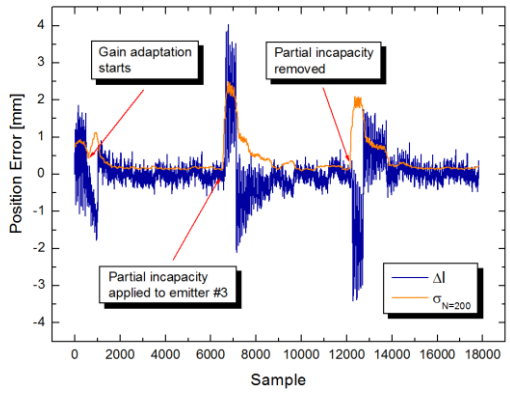

Fig. 2. Position error (blue) and standard deviation (orange) evaluated from preceding 200 samples.

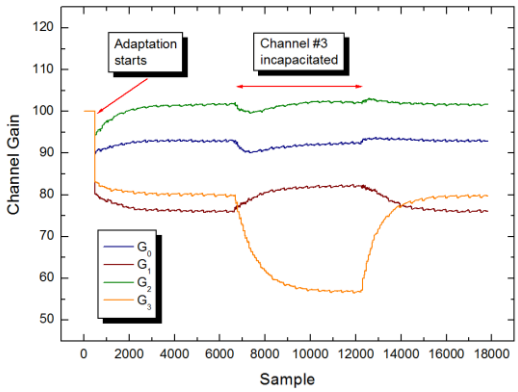

Fig. 3. Adaptation of channel gains with indication of initial and channel incapacity conditions.

Conclusion

Proposed modification to detection algorithm for active optical position sensor has been found effective in determination of both hardware-related as well as environmentally-induced irregularities in signal chain, enhancing accuracy of position sensing down to 0.2mm at >100mm sensing gap distances.

References

[1] E. Burian, "Micropower Active Optical Position Sensor for Decimeter-Range Sensing Gaps," *2023 IEEE SENSORS*, Vienna, Austria, 2023, pp. 1-3, doi: 10.1109/SENSORS56945.2023.10324868

DOI 10.5162/EUROSENSORSXXXVI/PT1.204

Design and Simulation of Quartz-on-Silicon Bulk Acoustic Waves Resonator for High Sensitivity Multiplex Biosensor

Muhammad Hamidullah[1], Aleksandr Oseev[1], Franck Chollet[1], and Thérèse Leblois[1]
[1]Université de Franche-Comté, CNRS, FEMTO-ST Institute, 25000 Besançon, France

muhammad.hamidullah@femto-st.fr

Summary:
We designed and simulated bulk acoustic waves (BAW) resonators based on a Quartz-on-Silicon substrate to achieve higher operating frequency than the standard commercially available Quartz Microbalance (QCM) biosensor. We used reflectors, based on Silicon multi-wall structures, to concentrate the acoustic energy within the individual transducer area, thus increasing the quality factor and preventing the crosstalk between adjacent sensors. The overall design will allow the application of BAW resonators for in-liquid biosensor arrays with higher sensitivity and multiplex sensing capability

Keywords: Biosensor, Bulk Acoustic Waves, Resonator, Multiplex sensing

Background, Motivation and Objective

Quartz Crystal Microbalance (QCM) is currently the most common type of Bulk Acoustic Wave (BAW) resonator used for biosensor applications [1]. The thickness shear-mode oscillation of the QCM makes it suitable to work in a liquid environment to capture and quantify bio-analytes. However, the current commercial QCM is limited in terms of the operating frequency, which maximum frequency of 10 MHz, with a plate thickness of 167 um.

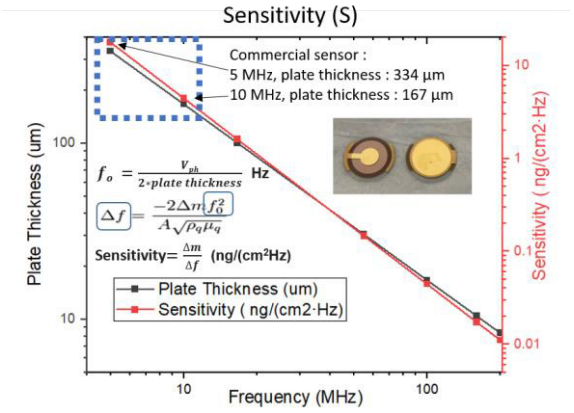

Fig. 1. The relationship of QCM plate thickness, frequency and theoretical sensitivity

Figure 1 shows the relationship between the QCM plate thickness, operating frequency and sensitivity, based on the Sauerbrey equation of QCM [2]. As shown in Figure 1, higher sensitivity can be achieved by increasing the operating frequency. However, to achieve higher frequency, a thinner plate is required, which will make the sensor device too fragile and too difficult to handle. Based on the Quartz-on-Silicon substrate and Silicon multiwall structure [3], we aim to design a high-frequency BAW biosensor with multiplex sensing capability.

Description of the Design

The illustration of our Quartz-on-Silicon BAW resonator with Silicon multiwall is shown in Figure 2. With the silicon substrate, we can reduce the thickness of the AT-cut Quartz plate to achieve higher frequency, while maintaining the total thickness of the device comparable with the standard QCM. Furthermore, the Silicon multiwall acts as reflectors that concentrate the acoustic energy within the individual transducer. At the same time, the reflectors prevent crosstalk between the transducers. The crosstalk prevention is required so that several transducers can be within a sensor device for multiplex sensing applications.

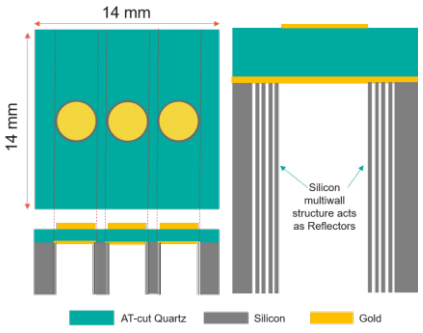

Fig. 2. The illustration of the Quartz-on-Silicon biosensors device with three transducers [3]

Simulation Results

COMSOL Multiphysics® simulation software is employed to simulate the proposed design, to calculate the quality factor (Q-factor), and to evaluate the crosstalk between the transducers. Firstly, we simulate the effect of the transducer size on the Quality factor of the resonators. Figure 3 shows the simulation result of the BAW resonator with a quartz plate thickness of

33 um and an operating frequency of around 48 MHz, with square transducer dimensions of 1x1 mm^2, 2x2 mm^2, and 3x3 mm^2. As shown in Figure 3, the Q-factor is highly affected by the size of the transducer, where a Q-factor of higher than 5000 is achieved with a larger transducer size of 3 mm

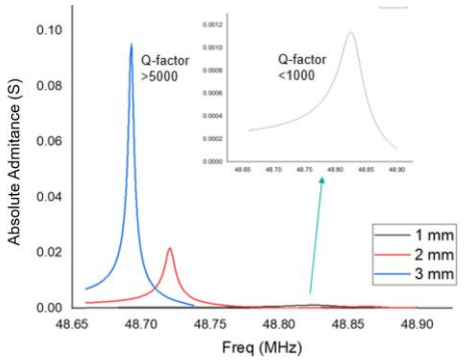

Fig. 3. The simulation results of the resonator frequency response and Q-factor with different transducer diameters.

Despite giving a higher Q-factor, a larger transducer reduces the distance between each transducer, which will increase the risk of crosstalk. To fit three 3-mm transducers within the area of 14*14 mm^2, the distance between transducers is only 1 mm or less. Thus, the simulation to evaluate the crosstalk between two adjacent transducers is performed and the results are shown in Figure 4.

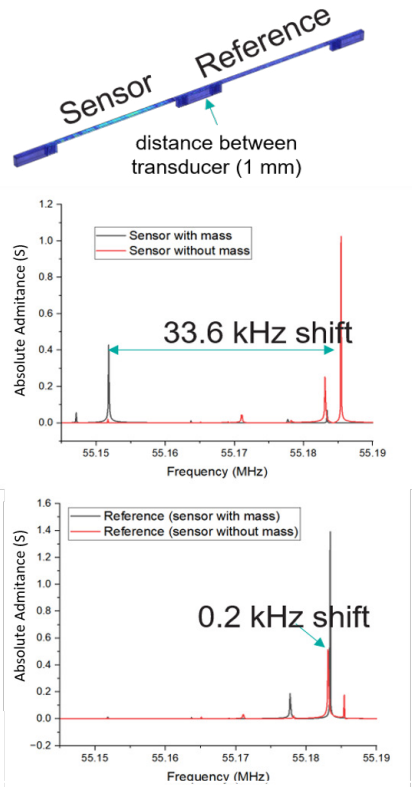

Fig. 4. The crosstalk simulation results of two adjacent transducers as a sensor and a reference

As shown in Figure 4, when a small mass is added to the transducer, it acts as a sensor and there is a significant shift in the resonator frequency. However, the shift in the reference resonator is merely 0.5% relative to the shift observed with the sensor. Thus the results show that the crosstalk is minimal even at a very close distance.

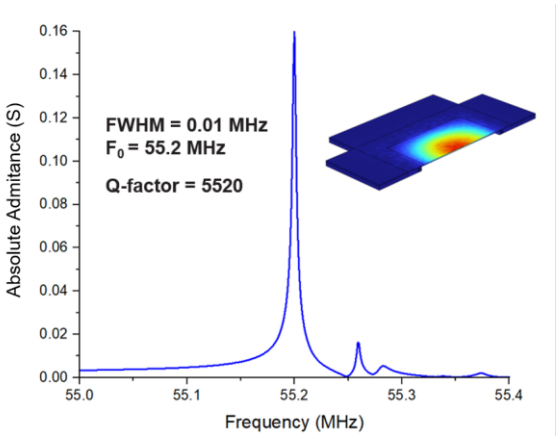

Fig. 5. The simulation results of a complete BAW resonator with Silicon multiwall reflectors

In addition to preventing the crosstalk between the transducer, the reflector is added to concentrate the energy and thus increase the Q-factor. Figure 5 shows simulation results of the full resonator structure with reflector, with a Quartz thickness of 30 um and with a square transducer dimension of 3x3 mm^2. Where the BAW resonator is expected to have a Q-factor of 5520 at the operating frequency of 55.2 MHz.

Conclusion

We have designed and simulated a BAW biosensor array device based on a Quartz-on-Silicon substrate and Silicon multiwall reflectors. Our simulation results show the feasibility of obtaining a high-frequency BAW resonator for in-liquid biosensors with higher theoretical sensitivity than standard QCM biosensors and with multiplex sensing capability.

References

[1] M. Pohanka, Quartz crystal microbalance (QCM) sensing materials in biosensors development, *International Journal of Electrochemical Science* 16(12), 211-220 (2021); doi:10.20964/2021.12.15

[2] J. Kankare, Sauerbrey equation of quartz crystal microbalance in liquid medium. *Langmuir*, *18*(18), 7092-7094 (2002); doi: 10.1021/la025911w

[3] A. Oseev, T. Leblois, Universite de Franche-Comte, 2024. Acoustic biosensor assay assembly. U.S. Patent Application 18/255,90

DOI 10.5162/EUROSENSORSXXXVI/PT1.207

Modeling and Quantifying Electrostatic Interactions for Kelvin-probe Measurements

E. David Deak[1], *Peter Gabor Szabo* [1], *Balazs Plesz* [1]
[1] *Budapest University of Technology and Economics*
Department of Electron Devices,
3. Műegyetem rkp., Budapest, Hungary

kaed.david@edu.bme.hu

Summary:
In this paper we propose a quantitative model for the interaction between a sampling electrode and a sample surface in a Kelvin-probe surface potential measurement. We briefly describe the Kelvin method, then we introduce a capacitance based electrostatic model to quantify the interaction. We use this model to derive the Point Spread Function (PSF) of the measurement which can be used to enhance physical measurements using a deconvolution-based approach.

Keywords: Kelvin-probe, electrostatic, capacitive, deconvolution, modeling

Background, Motivation an Objective

In semiconductor metrology the ability to measure electrostatic surface potential can give valuable insights into the surface state of the sample and the physical processes going on inside the bulk material. To measure this potential several methods have been formulated such as the use of ChemFETs [1] and the Kelvin-probe method [2]. During the Kelvin-probe measurement a vibrating electrode is put in proximity to the sample's surface and the two surfaces interact through the electric field to produce a changing current that transport charges onto the sampling electrode. The amount of current is proportional to the potential difference between the sample's surface and the vibrating electrode. By changing the sampling electrode static potential, the transport current can be minimized by which we can determine the sample surface's electrostatic potential in a non-contact manner.

The goal of our paper is to derive a mathematical model which describes the interaction and to generate the Point Spread Function of the measurement setup, which then can be used in a post processing step to increase the measurement resolution after the scanning of the sample.

Physical and Mathematical Model

The vibrating sampling electrode is coupled to the sample's surface through the electromagnetic interaction between them. However, since the characteristic length scale and frequencies used during the measurement, the interaction can be simplified to only the electrostatic field. This field can be modeled with lumped capacitances and in the limit as a distribution of surface capacitance density.

Due to the vibration of the sampling electrode the coupling capacitance varies in time. This variation, along with the constant electric potential, implies a change in the amount of charge on the surface of the sampling electrode. In addition, due to the continuity equation of electromagnetic, the change in charge must come from a current density that transports carriers. This current takes the form as described by eq. (1)

$$i(t) = \frac{\partial z(t)}{\partial t} \iint \frac{\partial c(t,\vec{r})}{\partial z} \left(U - \phi(\vec{r})\right) ds \qquad (1)$$

By changing the amount of charge on the sampling electrode, a charge redistribution process will undergo on the surface of the sample. This process can be characterized by the charge relaxation time, assuming space and time invariant material properties. The charge relaxation time is the product of the sample's specific resistivity and its electric permittivity. So long as the charge relaxation time is orders of magnitude smaller than the sampling electrode's period this charge redistribution can be neglected. This is the case for most of the semiconductor materials with charge relaxation time in the ballpark of ps. Assuming the magnitude of the change in charge is negligible compared to the thermally generated ones, which govern the chemical potential and the thermodynamical processes in the bulk of the sample material, the coupling between the surface potential and the surface charges can be neglected too.

With these simplifications one can create an equivalent circuit diagram for the measurement setup using lumped elements (Fig. 1).

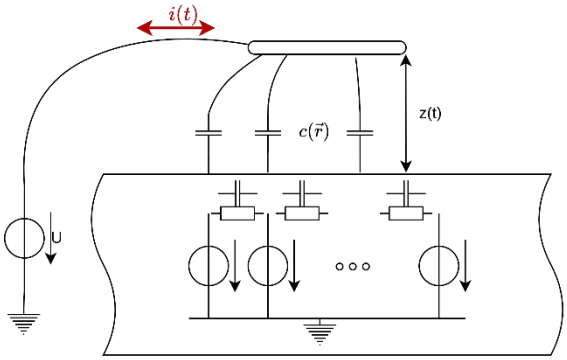

Fig. 1. Equivalent electrical model of the interaction between the sampling electrode and the sample's surface.

During the measurement the sampling electrode's potential is changed until the transport current is minimized. Assuming a homogenous surface potential distribution under the sampling electrode, the potential that minimizes the current is precisely the same as the sample's surface potential. In the case of a non-uniform potential distribution the optimal voltage on the sampling electrode will be the weighted average of the sample's potential distribution.

Since the relationship between the transport current and the surface potential distribution is linear it can be approximated with a matrix-vector equation. This equation can be used to predict the result of a measurement, given the underlying structures and potential distributions. In addition, the underlying potential distribution can also be estimated with it, given the measured sampling electrode's voltage and current waveform. Because many different potential distributions can result in a similar current waveform the estimated potential distribution won't be unique. Among these distributions, one can be chosen to minimize the residual error, by utilizing linear least squares method.

This method is analogous to the one utilized in optical systems where the image of a perfect point source is known well enough or at least estimated [3]. This image is called the Point Spread Function (or PSF for short), which is used to resolve smaller details that were captured by the optical system. In the image processing world this step is done by deconvolutions algorithms since the captured image is the convolution of the object and the PSF [3].

Results

By simulating the capacitive interaction between a square sampling electrode and the sample's surface one can acquire the necessary capacitance densities, which in turn enable the simulation of the measuring current in the case of different surface potential configurations, as seen in Fig. 2.

References

[1] Cui, Y., Wei, Q., Park, H., & Lieber, C. M. (2001). Nanowire Nanosensors for Highly Sensitive and Selective Detection of Biological and Chemical Species. In Science (Vol. 293, Issue 5533, pp. 1289–1292). American Association for the Advancement of Science (AAAS). https://doi.org/10.1126/science.1062711

[2] Baikie, I. D., & Estrup, P. J. (1998). Low-cost PC based scanning Kelvin probe. In Review of Scientific Instruments (Vol. 69, Issue 11, pp. 3902–3907). AIP Publishing. https://doi.org/10.1063/1.1149197

[3] Leist, M. et. al. (2024). Deconvolution of JWST/MIRI Images: Applications to an Active Galactic Nucleus Model and GATOS Observations of NGC 5728. In The Astronomical Journal (Vol. 167, Issue 3, p. 96). American Astronomical Society. https://doi.org/10.3847/1538-3881/ad1886

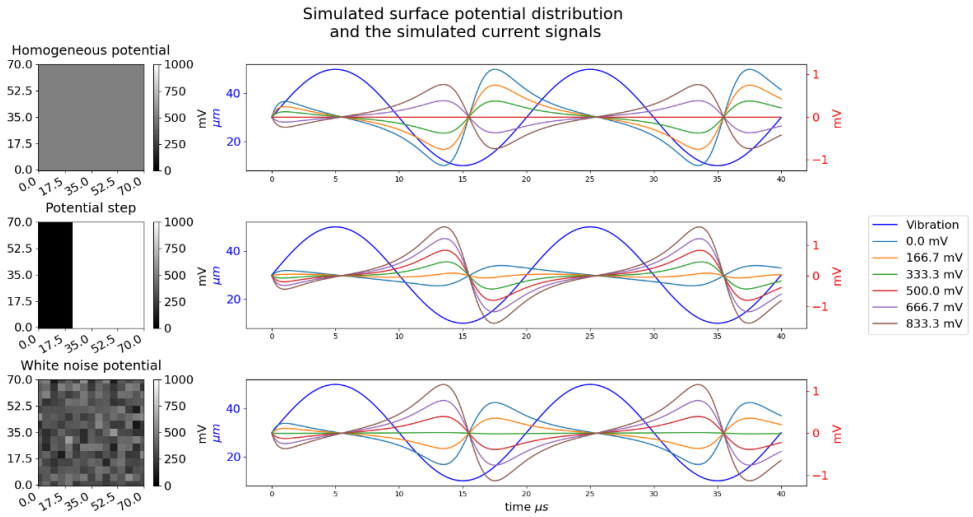

Fig. 2. Simulation of transport current due to different surface potential distributions and different sampling electrode potential.

DOI 10.5162/EUROSENSORSXXXVI/PT1.218

Remote and Self-Teaching Material for Sensorics: SensEdu

Gabor Harsanyi
Budapest University of Technology and Economics, Faculty of Electrical Engineering and Informatics, Department of Electronics Technology
H-1111, Műegyetem rkp. 3, Budapest, Hungary

Corresponding Author's e-mail address: harsanyi.gabor@vik.bme.hu

Summary:

Conventional teaching of sensors, based on lectures, static written materials, laboratories, etc., has become rather difficult at all levels of education, recently – especially during the period of pandemic. The main objective of the described material is multimedia-supported education material that teaches the theoretical physical-chemical-biological bases, operation principles and various application possibilities of classical and smart sensor devices for the next generation of intelligent systems. The new approach to teaching sensorics tries to exploit all the advantages of multimedia computer-aided teaching and remote internet availability. The course material is practically available for the technical community, for university professors for teaching and company courses on the internet and other informatics media, and has continuously been developed for many years. The lecture will highlight the structure of the course material and demonstrate the animated sensor examples.

Keywords: theory, teaching, education, internet-based learning, applications

Background, Motivation

Several e-based teaching materials were developed recently during the pandemic, that are following some formats available on the web [1,2]:

- The teacher is available in a small picture or given periods on the web
- Explanations are made with static text and figure
- A step-by-step view of the slides is needed (like with PowerPoint materials)
- Flexibility is available only with a table of content
- Tests for self-control can be added
- -> Absolute passive
- -> Nothing extra over reading a book with figures or listening to the teacher

The main specific reasons handle sensorics differently are as follows:

- Both sensor technologies and sensors' operation include dynamic processes that are difficult to illustrate and need many explanations.
- The number of sensing principles for various parameters became so large that they hardly can be included within one course

Description of the New Teaching Material

The planned new approach of teaching sensorics tries to exploit all the advantages of multimedia computer-aided teaching not only for keeping the competitiveness but also to overcome the above specific difficulties of the particular area:

- Dynamic processes and sensing effects will be illustrated by animation.
- A large amount of information could be available even though not all areas are used by everyone.
- Course users could teach themselves by selecting the particular route of their interest: the explanations from the basic sciences are connected to the material by hyperlinks.
- The course material is available for the technical community, and for university professors for teaching, and will continuously be developed on the internet and e-media.

Results

The Sensedu material has a menu with the following headlines [3,4]:

- Introduction: basic definitions and development trends.
- Technologies: manufacturing processes (like semiconductors, thin- and thick-film technologies, ceramics, etc.)

- Structures: devices for sensors (like resistors, transistors, diodes, etc.)
- Effects: physical-chemical and biological bases of sensors operation (like piezoelectricity, Hall-effect, etc.)
- Measuring parameters (like pressure, acceleration, pH, etc.)
- Applications (including industrial, household, automotive, etc.)

The Figures. below are some examples.

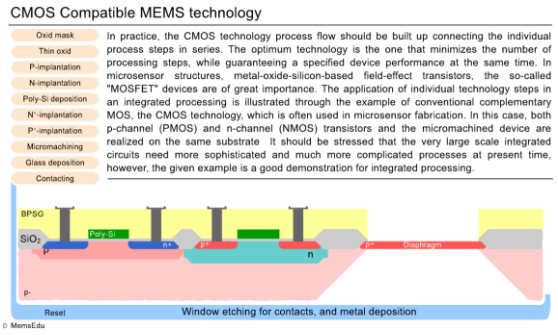

Fig. 1. Technology approach of a MEMS-compatible CMOS processing: the steps can be activated individually by pressing the buttons on the left side.

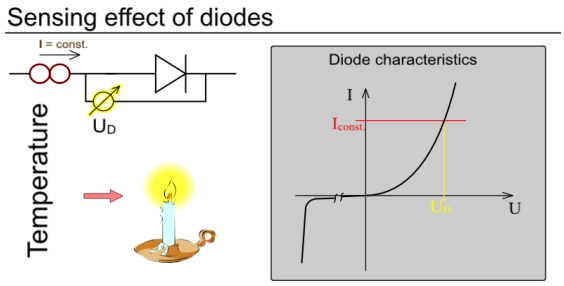

Fig. 2. General operation principle of a temperature-sensitive diode.

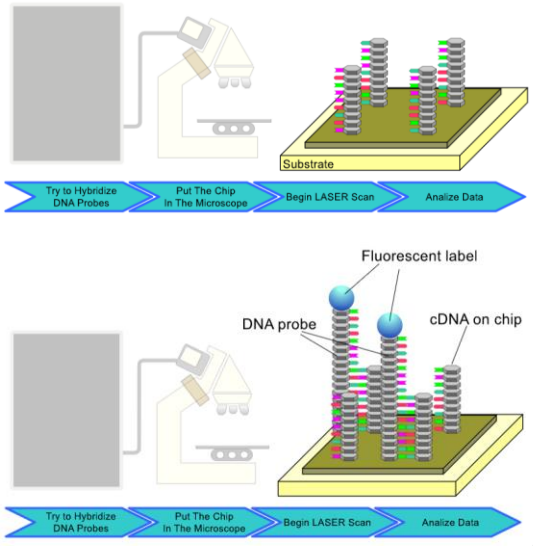

Fig. 4. Two stages of the animated illustration of the DNA chips: a) basic state, b) applying unknown DNA sample resulting in hybridization with the matching immobilized sequences.

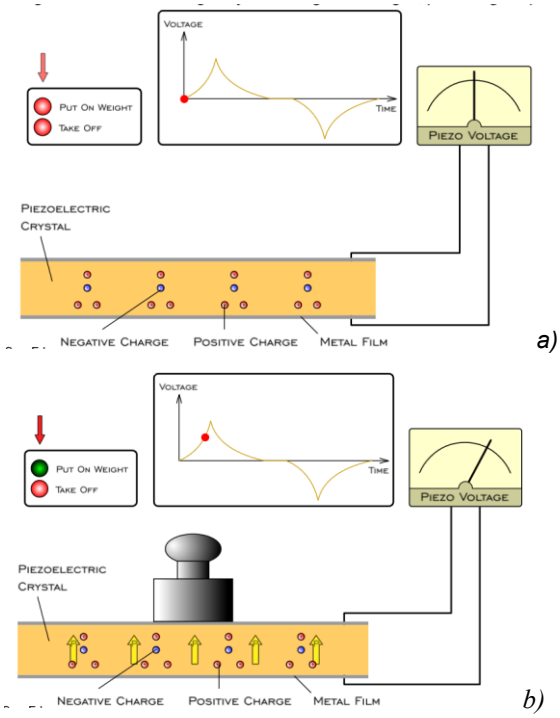

Fig. 3. Two stages of the animated illustration of the piezoelectric effect: a) basic state, b) applying force on the material, polarization and voltage impulse is generated.

References

[1] MicroElectronics Cloud Alliance, Cloud-based Teaching of Microelectronics Developed by 18 partners including Higher Education Institutes and SMEs, http://www.ett.bme.hu/meca/EP/index.html

[2] METIS, MicroElectronics Training, Industry and Skills, a project funded with support from the European Commission, https://www.metis4skills.eu/

[3] Harsanyi, G ; Lepsenyi, I ; Gordon, P ; Bojta, P ; Ballun, G ; Illyefalvi-Vitez, Z: SensEdu - An internet course for teaching sensorics, https://harsanyi.ett.bme.hu/sensedu/

[4] Harsanyi, G ; Lepsenyi, I ; Gordon, P ; Bojta, P ; Ballun, G ; Illyefalvi-Vitez, Z: SensEdu - An internet course for teaching sensorics, IEEE - IEEE 51st Electronic Components and Technology Conference, Orlando (FL), USA, (2001) pp. 1255-1260., doi: 10.1109/7361.987059

Annotation

A preliminary paper was originally published at the conference [4] but considerable progress has been achieved since 2001.

DOI 10.5162/EUROSENSORSXXXVI/PT1.225

Designing, Fabricating, and Analyzing the Whisker Sensor for Autonomous Surface Defect Detection

Mohammad Sadeghi[1], Alireza Abbasimoshaei[1], Calvin Schwartz[1], Thorsten A. Kern[1]
[1] Hamburg University of Technology, Eisendorfer Str. 38, Hamburg, Germany.

Corresponding Author's e-mail address: al.abbasimoshaei@tuhh.de

Abstract:
This paper presents a new bioinspired whisker sensor system tailored for surface defect detection. A rotational whisker sensor is designed and installed on a homemade wheeled robot, enabling active detection across a wide area. The sensor array is made of carbon fibers reinforced with polyepoxides and controlled by an ESP8266 microcontroller via Wi-Fi. The simulation investigation using Sim-Scape software indicates that adjusting dynamic parameters like frequency and response speed improves sensor performance. The study proposes that this approach proves effective in identifying surface anomaly, especially in noisy conditions.

Keywords: Whisker Sensor, Simulation, Autonomous Robot, Surface Defect, Frequency response.

Introduction

Drawing inspiration from nature's tactile systems has led to significant advancements in sensing technology and haptic feedback [1]. Whisker sensor technology, inspired by the tactile hairs of mammals, has emerged as a valuable addition to conventional optical and acoustic sensors [2]. These sensors are used in a variety of applications, ranging from obstacle avoidance to map reconstruction [2]. The Whisker sensor can be classified into different types based on their sensing principles, which include optical whisker sensors, magnetic whisker sensors, resistive whisker sensors, and piezoelectric whisker sensors [2-3]. Among these, magnetic whisker sensors, utilizing Hall sensors, stand out for their multidimensional capabilities, robust environmental adaptability, and high resolution [2]. In this context, a new whisker-based sensor system has been developed, integrated into an autonomous robot, enabling the detection of surface anomalies.

Material and Methods

In this section, the mechanical design and electronic configuration of the autonomous robot are initially described, followed by a discussion of sensor design and simulation procedure.

To accurately detect the shape of surface defects, a foundational robot capable of scanning in the XY plane is essential. In this context, a four-wheel robot was designed and fabricated inspired by the Geneva wheel concept. At the forefront, a rotor was intricately connected to a gear-like structure, enabling it to rotate smoothly via a DC stepper motor (Modelcraft RB350018). The integration of the L298N dual H-bridge motor driver ensured precise motor control, facilitating accurate positioning of the measurement unit. Speed regulation was achieved through an Arduino UNO controller in conjunction with a digital rotary encoder (KY04RE). The final design enables movement along both the X and Y axes, as well as angular movement around these axes, mimicking the behavior of active whiskers in animals. The whole system, including the sensor, was depicted in Fig. 1.

Various materials, including carbon fibers, spring steel, and polymers, were investigated in the literature for whisker sensor fabrication [2]. Carbon fibers reinforced with polyepoxides, with diameters of 0.28mm and 0.5mm, were selected for this study based on elasticity properties. As depicted in Fig. 1, a rotational sensor array was designed to provide convenient speed control compared to a linear array. This system included four whiskers attached to a holder 3D-printed adapter. Indirect whisker movement measurement was achieved using a digital three-axis IMU sensor (Melexis MLX90393 Triaxis), calibrated using Magneto software.

Simulation and modeling of the whisker array were conducted using Sim-Scape software. When the whisker makes contact with a surface, the resulting force is transmitted to a beam, which is excited until force equilibrium is achieved. The position of the whisker tip can then be calculated based on the position of the

beam's end. Taking into account the deflection of the whisker, which is assumed to be small, Euler-Bernoulli beam theory for a cantilever beam with an end load can be applied.

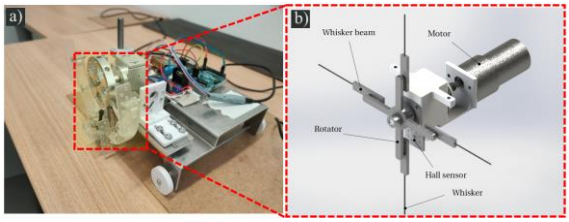

Fig. 1. a) Whisker-based surface monitoring robot, b) Schematic of sensor configuration.

Result and Discussion

Fig. 2 illustrates a spike in the whisker sensor signal occurring at 0.75S, when the surface is touched at low rotation speed. As the Whisker moves across the surface, it bends, storing energy in the spring as E = k * ϕ, with ϕ representing the angle. Upon leaving the surface, this stored energy is released, leading to oscillation and explaining the spikes observed in Fig. 2. Conversely, if the surface has a defect causing temporary loss of contact, this oscillation occurs earlier and can be detected via signal processing. Understanding dynamics behaviour is crucial for accurately detecting surface defect shape and dimensions, which can be facilitated by simulation studies.

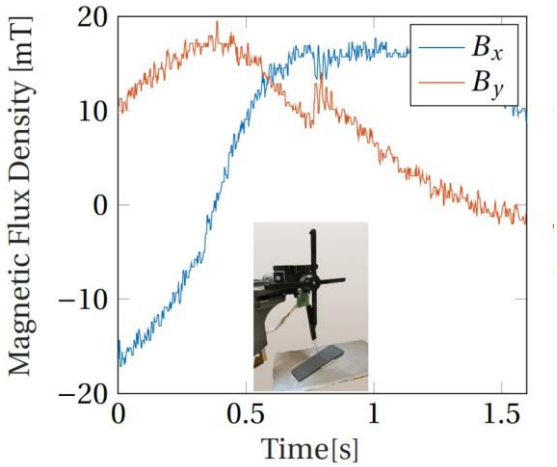

Fig. 2. a) Magnetic flux density of a moving whisker over the surface, with an inset showing the measurement apparatus.

The simulation has been conducted by moving the whisker across various surfaces. As illustrated in Fig. 3, surface irregularities cause vibrations in the whisker sensor, which can be reasonably approximated. However, as shown in the inset of Fig. 3, calibrating the frequency significantly impacts sensor performance. When the speed doesn't match properly, the whisker loses contact with the surface repeatedly, hindering the ability to gather information about the surface. One potential solution is to increase the natural frequency of the whisker system by optimizing sensor parameters such as elasticity, length, and diameter.

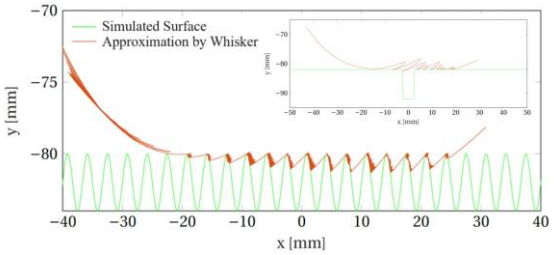

Fig. 3. Simulation results for detecting surface defects at low frequency (0.1 Hz), with an inset depicting sensor behavior at a higher frequency (1.6 Hz).

Conclusions

In this study, the capability of a whisker sensor for surface defect monitoring was investigated through simulation and experimental tests. A wheel explorer robot equipped with a custom hall-based whisker sensor was designed and fabricated for this purpose. The robot was operated through a Wi-Fi connection by an ESP8266 microcontroller. The rotational sensor array was constructed from carbon fibers reinforced with polyepoxides. Indirect measurement of whisker movement was accomplished using a digital three-axis IMU sensor (Melexis MLX90393), calibrated with Magneto software. Whisker array simulation was carried out using Sim-Scape software across various virtual surfaces. Results from both experimental tests and simulations suggest that the rotational whisker sensor shows promise for non-invasive surface monitoring applications, particularly in noisy open-air environments. Nevertheless, aspects such as whisker mechanical properties, resolution, and durability require further investigation, which can be pursued in future research.

References

[1] Kern, T. A., Hatzfeld, C., & Abbasimoshaei, A. (Eds.). (2022). Engineering haptic devices. Springer Nature.

[2] Wang, S.; Liu, J.; Liu, B.; Wang, H.; Si, J.; Xu, P.; Xu, M. Potential Applications of Whisker Sensors in Marine Science and Engineering: A Review. J. Mar. Sci. Eng. 2023, 11, 2108. DOI: https://doi.org/10.3390/jmse11112108.

[3] Kent, T.A.; Kim, S.; Kornilowicz, G.; Yuan, W.; Hartmann, M.J.; Bergbreiter, S. WhiskSight: A reconfigurable, vision-based, optical whisker sensing array for simultaneous contact, airflow, and inertia stimulus detection. IEEE Robot. Autom. Lett. 2021, 6, 3357–3364.

DOI 10.5162/EUROSENSORSXXXVI/PT1.270

The Optimal Axial Strain Distribution in a Piezoelectric Vibrating Energy Harvester (PVEH)

Eliya Salman[1], David Rosenstock[1], David Elata[1]
[1] Technion – Israel Institute of Technology, Faculty of Mechanical Engineering, Haifa, 32000, Israel

elata@technion.ac.il

Summary:
This study considers the optimal strain distribution in a piezoelectric vibrating energy harvester (PVEH), that maximizes the harvested energy. In many previous studies it was tacitly assumed that a uniform distribution of axial strain in the piezoelectric layer, ensures that the harvested energy is maximal. Though this assumption is intuitive, it was not supported by analysis. In this work we derive and present a formal analytic proof confirming that, for a given amount of energy in the vibrating structure, a uniform distribution of strain in the piezoelectric layer ensures that the harvested energy is maximal.

Keywords: Piezoelectric vibrating energy harvester (PVEH), piezoelectric unimorph, energy harvesting, strain distribution, variational analysis.

Background, Motivation and Objective

Piezoelectric vibrating energy harvester (PVEH) devices have been studied for over two decades [1], [2], [3]. The most prevalent PVEHs are constructed from a piezoelectric unimorph, in which an elastic cantilever is coated by a thin layer of piezoelectric material. This piezoelectric layer is sandwiched between a top and bottom electrode. When the piezoelectric unimorph is subjected to base excitations at its natural frequency, the amplitude of vibrations increases.

In previous studies it has been identified that an optimal planform of the unimorph cantilever may result in a uniform amplitude of axial strain in the piezoelectric layer. It was further assumed that such a uniform amplitude of strain maximizes the harvested energy. This seems to be intuitively sensible, but no formal proof of this has been provided.

The aim of the present study is to provide a formal proof, and show that for a given amount of vibration energy in a PVEH, a *uniform* distribution of axial strain ensures that the harvested energy is maximal.

Modelling – Analytic derivation

Figure 1 presents a schematic illustration of a piezoelectric cantilever unimorph, that is constructed from an elastic substrate of thickness h, coated with a thin piezoelectric layer of thickness h_{pe} (h_{pe}<<h). The beam length is L and the width $b(x)$ may be non-uniform.

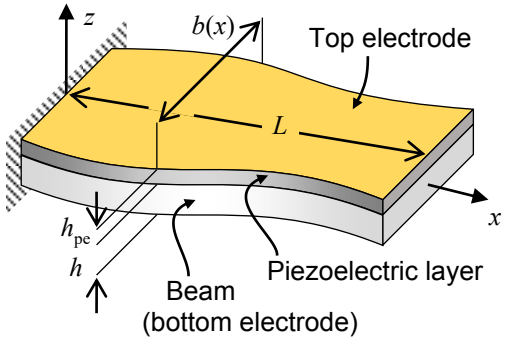

Fig. 1. Schematic description of a PVEH unimorph cantilever.

the electric energy U_E that may be harvested in one half of a motion cycle, is proportional to the product of the charge amplitude Q_{Short} that is transferred between the electrodes – if they are shorted (i.e. connected), and the amplitude of voltage difference V_{Open} between the electrodes – if they are open (i.e. disconnected) [4], [5]:

$$U_E = \frac{1}{2} Q_{\mathrm{Short}} V_{\mathrm{Open}} \tag{1}$$

In the piezoelectric layer, poling points in the z direction, such that material directions 1, 2 and 3, are parallel to the spatial axes x, y and z, respectively. According to the Euler-Bernoulli beam theory, and considering that the piezoelectric layer is thin, we may deduce that within the piezoelectric layer several terms vanish.

Within this layer, in terms of the Voight notation, the shear strains and stresses are zero (i.e. S_4=S_5=S_6=0 and T_4=T_5=T_6=0), and the transverse

stress T_3 is zero because the top surface of the unimorph is stress-free. Furthermore, due to geometrical considerations, the components of the electric field and electric displacement (i.e. flux) along the x and y axes vanish (i.e. E_1=E_2=0 and D_1=D_2=0). Finally, for cylindrical bending we may assume that S_2=0, and that S_1 is not a function of y. Because the piezoelectric layer is thin we may also consider S_1 within the piezoelectric layer to be independent of z (this is known as the small-piezoelectricity assumption [6], [7]), so that overall $S_1(x)$ is uniform in each cross-section, though it may vary along the beam.

Therefore, we get two coupled equations:

$$T_3(x) = 0 = C_{13}^E S_1(x) + C_{33}^E S_3(x) - e_{33} E_3 \tag{2}$$

$$D_3(x) = e_{31} S_1(x) + e_{33} S_3(x) + \varepsilon_{33}^S E_3 \tag{3}$$

By imposing electrostatic boundary conditions, we derive Q_{Short} and V_{Open}

$$Q_{\text{Short}} = \left(e_{31} - \frac{e_{33} C_{13}^E}{C_{33}^E} \right) \int_{x=0}^{L} S_1(x) b(x) dx \tag{4}$$

$$V_{\text{Open}} = -h_{pe} \left[\frac{C_{13}^E}{e_{33}} - \frac{C_{33}^E}{e_{33}} \frac{\left(e_{31} + \varepsilon_{33}^S \frac{C_{13}^E}{e_{33}} \right)}{\left(e_{33} + \varepsilon_{33}^S \frac{C_{33}^E}{e_{33}} \right)} \right] \frac{\int_{x=0}^{L} S_1(x) b(x) dx}{\int_{x=0}^{L} b(x) dx} \tag{5}$$

Substituting these expressions from (4) and (5) into (1), yields

$$U_E = \alpha \left(\int_{x=0}^{L} S_1(x) b(x) dx \right)^2 \Big/ \int_{x=0}^{L} b(x) dx \tag{6}$$

where α is a scalar that depends on material parameters and the thickness of the piezoelectric layer:

$$\alpha = -\frac{h_{pe}}{2} \left(e_{31} - \frac{e_{33} C_{13}^E}{C_{33}^E} \right) \left[\frac{C_{13}^E}{e_{33}} - \frac{C_{33}^E}{e_{33}} \frac{\left(e_{31} + \varepsilon_{33}^S \frac{C_{13}^E}{e_{33}} \right)}{\left(e_{33} + \varepsilon_{33}^S \frac{C_{33}^E}{e_{33}} \right)} \right] \tag{7}$$

The mechanical elastic energy stored in the beam due to bending is given by

$$U_M = \beta \int_{x=0}^{L} S_1^2(x) b(x) dx \tag{8}$$

where $\beta = E_Y h / 6$ and E_Y is Young modulus.

We wish to find the axial strain distribution function $S_1(x)$, which will maximize the electrostatic energy U_E for an arbitrary distribution of width $b(x)$. However, we aim to find the maximal electrostatic energy for all possible distributions on $S_1(x)$, which generate the same specific mechanical elastic energy U_M^*.

This can be done by considering a constrained Lagrangian, with a Lagrange multiplier λ and a functional J_λ

$$J_\lambda[S_1(x), \lambda] = U_E - \lambda \cdot \left(U_M - U_M^* \right) \tag{9}$$

Applying the first variation for the functional with respect to $S_1(x)$ and λ, yields

$$\delta J_\lambda = 2 \int_{x=0}^{L} \left\{ \alpha \frac{\int_{x'=0}^{L} S_1(x') b(x') dx'}{\int_{x'=0}^{L} b(x') dx'} - \lambda \beta \cdot S_1(x) \right\} b(x) \cdot \delta S_1(x) dx - \delta\lambda \cdot \left\{ \beta \int_{x=0}^{L} S_1^2(x) b(x) dx - U_M^* \right\} \tag{10}$$

Our goal is to identify the function form of $S_1(x)$ at which the electrostatic energy reaches its maximum. Therefore, according to (10), the variation must be equal to zero for any $\delta S_1(x)$ and any $\delta\lambda$. This requires that each one of the expressions that appear in curly brackets vanish, given that $b(x)$ cannot be zero. It follows that:

$$S_1(x) = \sqrt{U_M^* \Big/ \beta \int_{x=0}^{L} b(x) dx} \tag{11}$$

This confirms that the strain within the piezoelectric layer must be uniform.

Acknowledgement: This work was supported by the Israel Science Foundation, Grant 1820/22.

References

[1] A. Erturk and D. J. Inman, “Issues in mathematical modeling of piezoelectric energy harvesters,” *Smart Mater. Struct.*, vol. 17, no. 6, p. 65016, 2008.

[2] A. Erturk and D. J. Inman, “An experimentally validated bimorph cantilever model for piezoelectric energy harvesting from base excitations,” *Smart Mater. Struct.*, vol. 18, no. 2, p. 25009, 2009.

[3] A. Erturk and D. J. Inman, *Piezoelectric energy harvesting*. Chichester: Wiley, 2011.

[4] S. Du *et al.*, “A new electrode design method in piezoelectric vibration energy harvesters to maximize output power,” *Sensors Actuators A Phys.*, vol. 263, pp. 693–701, 2017.

[5] S. Lustig and D. Elata, “Ambiguous definitions of the piezoelectric coupling factor,” *J. Intell. Mater. Syst. Struct.*, 31(14), pp. 1689–1696, Jun. 2020.

[6] Michael Krommer, “On the correction of the Bernoulli-Euler beam theory for smart piezoelectric beams,” *Smart Mater. Struct.*, vol. 10, no. 4, p. 668, 2001.

[7] H. F. Tiersten, *Linear Piezoelectric Plate Vibrations: Elements of the Linear Theory of Piezoelectricity and the Vibrations Piezoelectric Plates*. Springer, 2013.

DOI 10.5162/EUROSENSORSXXXVI/PT2.60

Damage Localization in Mechanical Structures Based on a Virtual Sensor Approach

Leila Merzak [1], Elise Saoutieff [1], Celestin Ott [1], Sébastien Boisseau [1]
[1] CEA-Leti, Université Grenoble Alpes, F-38000 Grenoble, France

leila.merzak@cea.fr

Summary:

This paper introduces a new methodology for localizing damages in mechanical structures thanks to a Virtual Sensor approach. We combine physics-based models, finite element methods, real-time data and data-driven models using machine-learning algorithms to determine in real-time the “damage localization” on real-world mechanical structures with a reduced number of strain sensors. By leveraging finite elements, we have built synthetic database gathering the normal physical behavior of the mechanical structures under various force applications and abnormal behaviors induced by notches in the material. Machine-learning algorithms have been trained on synthetic data coming from simulations. The notches have been effectively localized in real-time on the real-world mechanical structure with a reduced number of strain sensors, validating the approach.

Keywords: Virtual sensor, Digital twin, Data driven models, Finite element method, Neural Networks.

Introduction

In mechanical engineering, maintaining the structural integrity of systems is crucial for their safe and efficient operation. Damages, manifesting as notches, cracks, or various forms of material degradation, can drastically affect a system's performance and reliability. Structural Health Monitoring (SHM) techniques, including both traditional and advanced sensor-based methods, are essential for detecting and evaluating such damages [1]. However, the application of SHM techniques often hindered by challenges like the requirement for extensive sensor networks and the complexities involved in optimizing sensor placement. Recent developments in digital twin technology present new opportunities for improving damage localization with a reduced number of well-chosen sensors [2]. A digital twin is a virtual model that mirrors a physical system, enabling real-time monitoring and predictions through a continuous flow of data between the physical and virtual entities [3]. In this paper, we propose a new refined Virtual Sensor framework that integrates comprehensive aspects of digital twin technology, from its conceptualization to practical deployment at a systemic level. Applied to a well-chosen case study, this framework demonstrates its effectiveness in localizing notches in mechanical structures in real-time, highlighting the potential of digital twins in predictive maintenance.

Methodology

The proposed Virtual Sensor framework detailed in the Fig. 1 provides a comprehensive method for creating a digital twin of a physical system.

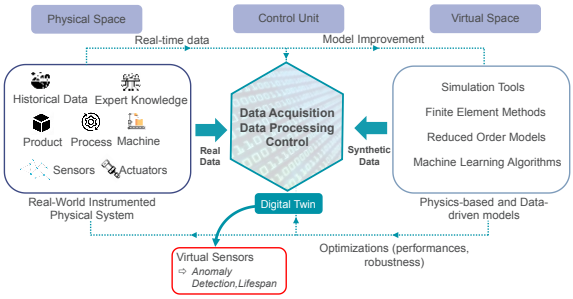

Fig. 1. Proposed Virtual Sensor Framework

It consists of three interconnected elements to achieve this. The physical space representing the real-world entity such as product, machine, or process [4]. Embedded in the physical space, sensor and actuators networks are actively involved in collecting data and executing actions based on instructions, respectively. The virtual space employs two types of models, Physics-based and Data-driven models. Physics-based models use Finite Element (FE) analysis and simulations to provide a deeper understanding of the system. Meanwhile, Data-driven models handle complex data efficiently using reduced order-modeling techniques, and analyze sensor data in order to predict potential issues or estimate system’s lifespan. The control unit serves as the core entity of the digital twin, with

communication protocols allowing for wired and wireless data transfer. This unit manages the information flow and potentially controls the system based on the model's prediction. It is also responsible for generating visual outputs and issuing alerts, alongside a data storage component for maintaining a historical record of information.

Case Study: Damage Localization

The proposed framework (Fig. 1) is applied to construct a digital twin of a mechanical structure in order to predict damage localization. Tests are performed on steel beams subjected to bending forces, including one undamaged specimen and four with notches. Each beam is equipped with four strain gauges positioned along its length. As detailed in the workflow (Fig. 2), two FE models were developed. The first model represents undamaged beam's normal behavior, while the second simulates the beams with localized notches. Data from these simulations were then used to build two separate data-driven models: (i) A Reduced-Order Model (ROM), trained on virtual strain sensor data from the undamaged beam simulations to predict strain based on the applied force. (ii) A Convolutional Neural Network (CNN) model, trained on virtual strain sensor data from the damaged beams simulations to predict the location of damage along the beam. The combined approach of these models consists of detecting first, deviations between ROM predictions and real strain data measured by the gauges. If significant deviations arise, the CNN is activated to localize the damage.

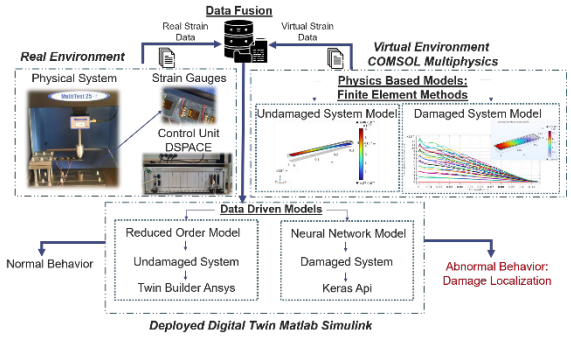

Fig. 2. Virtual Sensor Framework for Damage Localization

Reduced-Order Model for Strain Prediction

We employed ANSYS Static ROM Builder to create a ROM for real-time prediction of beam strain under various applied forces and Young's modulus values. This ROM efficiently approximates the strain response obtained from a high-fidelity FE model of the structure, previously built in COMSOL Multiphysics. The ROM creation method uses Singular Value Decomposition (SVD) for solution compression, coupled with an interpolation technique to predict strain within the defined force and Young's modulus ranges [5]. The performance of the ROM is evaluated based on two metrics: relative error and the maximum absolute error between the ROM-predicted strain field and the corresponding field obtained from the full-order FE model [5]. Our ROM achieved a maximum relative error of 0.008798%.

Convolutional Neural Network for Damage Localization

To predict the location of damage along the beam structure based on strain gauge data from four specific positions, a CNN was employed. The CNN architecture consisted of an input layer followed by three convolutional layers with 64 filters each. These convolutional layers employed ReLU (Rectified Linear Unit) activation functions and incorporated batch normalization to enhance learning stability. The Adam optimizer was chosen to efficiently train the model on a dataset of 380 strain value samples generated from simulations of various damage scenarios in COMSOL Multiphysics. The Mean Absolute Error (MAE) served as the loss function during training. The evaluation of the model's performance on a separate test set of 80 data points demonstrated a Mean Squared Error (MSE) of 5.2705e-07 and a MAE of 5.8641e-04.

The "damage localization" virtual sensor was finally validated on the real-world mechanical structure. The various notches localization have been found by using the real-time strain sensor data and the CNN with a precision quantified by a MAE of 3.92mm. This validates the good operation of the digital twin developed here and the opportunity of virtual sensors for damage localization on mechanical structures with a reduced number of sensors.

References

[1] M. Mitra et al., Guided wave based structural health monitoring: A review, *Smart Mater. Struct* 25, (2016); doi: 10.1088/0964-1726/25/5/053001

[2] D. J. Wagg et al., Digital Twins: State-of-the-Art and Future Directions for Modeling and Simulation in Engineering Dynamics Applications, *ASCE-ASME J Risk and Uncert in Engrg Sys Part B Mech Engrg* 6, (2020), doi: 10.1115/1.4046739

[3] M. Grieves, Digital Twin: Manufacturing Excellence Through Virtual Factory Replication, *White Paper*, (2015).

[4] E. P. Hinchy et al., Using finite element analysis to develop a digital twin of a manufacturing bending operation, *Procedia CIRP* 93, (2020), doi: 10.1016/j.procir.2020.03.031

[5] ANSYS, "Static ROM Builder." Twin Builder 2023 R1.1 Online Help.

Enhancing Autonomy in Agriculture: Integrating Advanced Sensory Systems for Robust Navigation of Autonomous Machine

P. Lepej, J. Rakun, VISTION d.o.o., Individual Machine Vision Solution (Slovenia),
K. Polovič, SMT d.o.o., Portoroz (Slovenia)

Unfortunately, this abstract is not available, as the contribution was not confirmed at the time the conference proceedings were finalized.

Enhancing Autonomy in Agriculture: Integrating Advanced Sensory Systems for Robust Navigation of Autonomous Machine

P. Lepej, J. Rakun, VISTION d.o.o., Individual Machine Vision Solution (Slovenia),
K. Polovič, SMT d.o.o., Portoroz (Slovenia)

Unfortunately, this abstract is not available, as the contribution was not confirmed at the time the conference proceedings were finalized.

DOI 10.5162/EUROSENSORSXXXVI/PT2.77

Comprehensive Odor Measurement with AI-Supported Chemical Analytics and a Transition to Sensor Systems

Gina Zeh[1], Helen Haug[1,2], Maximilian Koehne[1,3], Andreas T. Grasskamp[1], Tilman Sauerwald[1,3]
[1] Fraunhofer Institute for Process Engineering and Packaging IVV, Giggenhauser Str. 35, 85354 Freising, Germany,
[2] Friedrich-Alexander-Universität Erlangen–Nürnberg, Henkestraße 9, 91054 Erlangen, Germany
[3] Saarland University, Campus A5 1, 66123 Saarbrücken, Germany

Corresponding Author: gina.zeh@ivv.fraunhofer.de

Summary:
A reliable description of an odor includes both the overall impression of the odor-active volatile compounds and their chemical identity. Efficient methods for the chemical and sensory analysis of the aroma properties of a product or raw material enable a high sample throughput with maximum efficiency. For the evaluation and correlation of the extensive datasets, an AI-supported evaluation procedure was developed, which outputs the maximum information content from the available data in the shortest possible time. Based on the information obtained in this way, instrumental odor measurement systems can be developed to enable efficient odor measurement for specific applications.

Keywords: odor, aroma, odor analysis, sensor system, data analysis

Introduction

The evaluation and decoding of odor characteristics of products and raw materials contributes significantly to the development of new foods, packaging solutions and beverages. Ultimately, it is the sensory perception, especially the aroma, but also the appearance, that determines whether a product appeals or repels to consumers.

Unlike most other human senses, such as hearing and sight, smell is still difficult or impossible to translate into a universally applicable standard unit. On the one hand, this is due to the fact that the sense of smell exhibits strong inter-individual differences, which can be attributed to the genetic predisposition of certain receptors. On the other hand, the human correlation between an olfactory impression and the verbal expression of the impression can be understood as a linguistics of its own, which is learned depending on cultural background and habitat for the most part.

This dramatically complicates the validation of sensors that are intended to supplement or even completely replicate the human sense of smell. However, if this task is approached from the human sensory side, accompanied by instrumental analysis, a number of methods and techniques are already available that make it possible to validate technical odor sensors using established standard units and methods. This also requires the processing of comprehensive datasets from various corresponding measurement methods, for which we present an approach that is as holistic as it is efficient.

Odor Analysis by Comprehensive Measurement Technologies

The volatilome contains numerous volatile compounds, only a fraction of which can be detected by the human nose. Accordingly, the analysis of odor-active volatile organic compounds is based on two detection principles: The overall impression of a product or raw material, in particular direct differences to similar products and raw materials, is analyzed using the human nose as a detector in human sensory tests. The most potent odor-active compounds can then be worked out via sophisticated analytical methods. The previously determined odor-active substances are identified and, if necessary, quantified using gas chromatography (GC) in conjunction with suitable detectors (e.g., mass spectrometer; MS). Coupled systems, such as GC-MS fitted with an odorant detection port (GC-MS/O) enable a comprehensive analysis of odor mixtures and have established themselves as the gold standard in aroma analysis.

Smart Odor Analysis – KI-Assisted Data Analysis for Odor Assessment

The described gold standard enables a comprehensive, but also time-consuming and cost-

intensive analysis of the odor-active compounds in a sample. In many applications, however, the time factor is clearly in the foreground - a high sample throughput must lead to meaningful information in the shortest possible time.

In an attempt to solve this shortcoming, an assessment for AI-assisted odor analysis was developed. Based on efficient methods for human sensory investigations and complementary chemical analyses, a pipeline that supports efficient data analysis using statistical methods for data correlation and automated data processing is being continuously developed and expanded [1] [2]. The correlation of odor impressions and identities of single compounds opens the path to a variety of compiled information on odor characteristics in order to gain maximum information content with minimum effort. The concept is by- and inline-capable and allows the comparison of large sample sets. Following the successful proof of principle, as well as the testing and validation of different approaches and methods, e.g., using whiskey as an example, the transferability of the smart odor assessment approach to other product groups, such as new foods and plastic regrinds, is now under investigation [3].

Miniaturizing Gas Chromatography – a Toolbox for Instrumental Odor Measurement Systems

Instrumental gas analysis as laboratory analysis is ideal for obtaining comprehensive information on all volatile compounds present in a sample. For many applications, however, only specific information is required for a small selection of odor-active compounds, for example, to observe the formation of certain volatile markers for spoilage or fruit ripening [4].

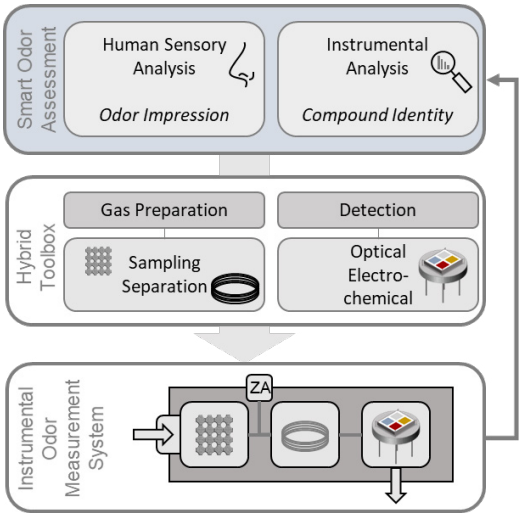

Figure 1: Workflow towards smart odor assessment supported by instrumental odor measurement systems.

Since these systems should be suitable for continuous monitoring in the production process or storage, a structural miniaturization of gas chromatography is an obvious choice. Many of the components required for this are already manufactured in series and are available in large quantities at low cost. This applies in particular to small, cost-effective broadband detectors, such as those found in the field of infrared sensors and metal oxide semiconductor gas sensors. For the latter it has been shown that they can have remarkably low detection limits of below 100 fg [5]. In order to increase selectivity, the volatile compounds are separated into their individual components on a short separation column prior to detection and detected individually on the sensor. Equipped with suitable software for calibration, such smart sensing systems can be used for continuous monitoring of odorants. Implemented in or in addition to the smart odor assessment approach, this has high potential for efficient low-cost odor evaluation.

References

[1] H. Haug, A.T. Grasskamp, S. Singh, A. Strube, T. Sauerwald, Quick insights into whisky—investigating rapid and efficient methods for sensory evaluation and chemical analysis. *Analytical and Bioanalytical Chemistry* 415(24), 6091-6106 (2023); doi: 10.1007/s00216-023-04883-5

[2] A.T. Grasskamp, S. Singh, H. Haug, T. Sauerwald, Assisting the automated analysis of chemical-analytical measurements in spirits using validated algorithms and an intuitive user interface, *Journal of Sensor and Sensor Systems* 12(1), 93-101 (2023); doi: 10.5194/jsss-12-93-2023

[3] H. Haug, G. Zeh, A. Grasskamp, A. Buettner, T. Sauerwald, Smart odor assessment to evaluate product performances efficiently, from plant proteins to plastics, *Talk ACS Spring 2024 Conference* (2024)

[4] M. Koehne, C. Schmidt, S. Singh, A.T. Grasskamp, T. Sauerwald, G. Zeh, Development of a gas chromatography system coupled to a metal-oxide semiconductor (MOS) sensor, with compensation of the temperature effects on the column for the measurement of ethene, *Journal of Sensors and Sensor Systems*, *12*(2), 215-223 (2023); doi: 10.5194/jsss-12-215-2023

[5] T. Baur, C. Schultealbert, A. Schuetze, T. Sauerwald, Novel method for the detection of short trace gas pulses with metal oxide semiconductor gas sensors, Journal of Sensors and Sensor Systems 7(1), 411-419 (2018); doi: 10.5194/jsss-7-411-2018

Acknowledgment

This research was funded by the Bavarian State Ministry of Economic Affairs, Regional Development and Energy (StMWi), within the project “Campus of the Senses” (grant no. 20-3410-2-14-3

DOI 10.5162/EUROSENSORSXXXVI/PT2.179

SMART ID-TAGS for LOCATING FREIGHT WAGONS and OPTIMIZING MAINTENANCE PROCESSES

Philipp Kersten[1], Johannes Buzin[1], Prof. Dr.-Ing. Sören Hirsch[1]
[1] University of Applied Sciences Brandenburg, Magdeburger Straße 50, 14770 Brandenburg an der Havel, Deutschland

philipp.kersten@th-brandenburg.de

Summary:
This work presents a prototype of a wireless ID tag that is to be used in the field of rail vehicle maintenance. The ID tag helps to localize vehicles, stores condition and environmental data and provides an interface to existing maintenance systems. Energy-saving, simple low-cost components are used in the circuit board design. The prototype can be further optimized in terms of size, energy efficiency and functions.

Keywords: ID Tag, wireless, efficiency, mobility, maintenance

Introduction

The railway system serves as a backbone of transportation infrastructure, facilitating global commerce and connectivity. However, ensuring the digitalization, reliability and safety of railway operations necessitates a proactive approach to maintenance [1]. Smart maintenance uses innovative sensor technologies tailored to the unique demands of railway, particularly in the context of environmental and biophysical data monitoring. To work with wireless components in dynamic systems is key here.

A smart ID tag serves as the foundation for digital wagon records in rail transport by integrating advanced sensor technologies into the railway-operating infrastructure. Special emphasis is placed on wireless communication protocols to facilitate effective monitoring of condition, environmental and positioning data. While sensors employed in various industries for condition monitoring and predictive maintenance, their adaptation to the railway environment presents unique challenges and opportunities. The dynamic nature of railway operations, coupled with the harsh environmental conditions, the need of energy saving solutions and stringent safety requirements, necessitates specialized sensors. The sensor system comprises a suite of advanced sensors capable of capturing environmental parameters such as temperature, humidity, vibration. Through the integration of wireless communication, a sensor network can enable real-time data collection, processing, and analysis, empowering railway operators with actionable insights for proactive maintenance decision-making.

Prototype Design Concept

The whole system works with a supply voltage of 3.3 V, which makes it perfect for battery applications, which can be additionally supported by energy harvesting technologies. An 8-bit Microcontroller collects data from two analog sensors IC's (integrated circuit). On the one hand, we detect vibrations that are transmitted to the sensor via structure-borne sound. The vibration data can be used to detect defects in machine parts or even flat spots on the wheelset of a freight wagon. The flat spots on a wheel produce a periodic impact that can be detected by measuring acceleration, as illustrated in Fig. 1, and applying a periodic peak detection algorithm to the signal.

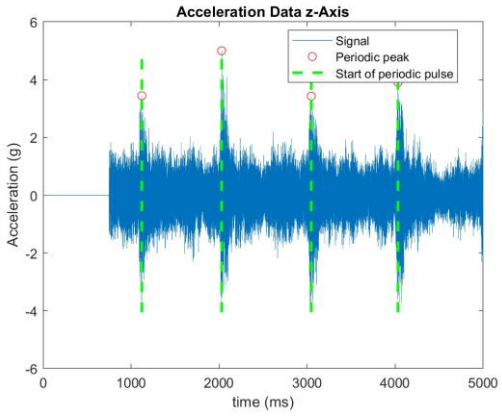

Fig.1 Detection of periodic signal

On the other hand, we measure temperature and humidity as examples of environmental data. These variables provide information about the condition of the environment surrounding

the sensor node. This data can later be used for correlations between defects and environmental influences in order to predict failures earlier. All data is transmitted to a radio module via UART. The module uses a Zigbee Network and operates in AT mode (Application Transparent), in which all data is simply forwarded to the target address. The localization of the vehicles operates by combining multiple technologies. The reason for this is to increase the robustness of the localization to counteract impairments such as the shielding of satellite signals in tunnels.[2] The ID tags communicate with each other via a mesh network and, in relation to a train, determine their position using Downlink TDoA (Time Difference of Arrival) [2]. Another way of calculation the position of the nodes is measuring and evaluating RSSI values of the received signals [3]. Fig. 2 illustrates a mesh network applied to the field of freight train localization. The green dots symbolize nodes for data collection. The blue ones are nodes for data forwarding or stationary nodes like balises in the infrastructure [4].

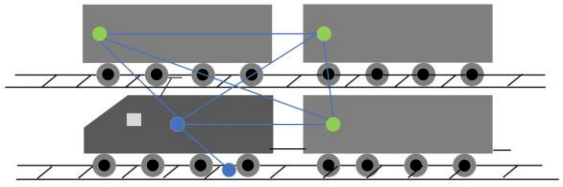

Fig. 2 Mesh Network for TDoA Localisation

Both the microcontroller and the radio module can be put into sleep mode to save energy. The module is in pin sleep mode, controlled by the microcontroller. However, this only happens in the event of successful network access. If a wagon does not move for a longer period, the entire system should be in sleep mode to avoid wasting energy. To detect the movement of the train and wake up the microcontroller, we use the 3-axis acceleration sensor on the circuit board, to be more precise the Analog Digital Converters interrupt enable function.

Fig. 3 shows a current prototype with external dimensions of 50 mm x 60 mm, which can easily be reduced to at least half the required space, if the small-factor packages of the components are used and the rear side of the PCB is fully utilized.

Fig. 3 PCB design of the Tag prototype.

Discussion and Conclusions

The presented smart ID tag demonstrates one way to integrate wireless technologies into railway systems. By including multiple sensors in the system, it can collect condition and environmental data with minimal invasive installation and legal authorization requirements. The greatest challenge lies in the interaction of different communication technologies in an energy saving way. Further research with Zigbee must test whether interference with other high-frequency signals, such as WLAN, occurs, as Olaby et al. 2022 measured in the context of RFID technology [5]. The programming of associated software and software interfaces to existing data processing programs. However, the data collected brings great benefit for training intelligent algorithms for predictive maintenance. The design tries to find the sweet spot between energy efficiency and functionality.

References

[1] Sarp Salih, Kuzlu Murat, Jovanovic Vukica, Guler Ozgur, Digitalization of Railway Transportation Through AI-Powered Services: Digital Twin Trains; DOI: 10.13140/RG.2.2.24165.47845

[2] Wen Long, Han Jinkun, Song Liangliang, Zhang Qi, Li Kai, *Wireless Communications and Mobile Computing*, Volume 2020; DOI: 10.1155/2020/8877654

[3] Uradzinski Marcin, Guo Hang, Liu Xiaokang, Yu Min, *Wireless Personal Communications,* Advanced Indoor Positioning Using Zigbee Wireless Technology, *DOI: 10.1007/s11277-017-4852-5*

[4] Muniandi Ganesan, *IET Blockchain*, Blockchain-enabled balise data security for train control system; DOI: 10.1049/blc2.12003

[5] Olaby, O.; Hamadache, M.; Soper, D.; Winship, P.; Dixon, R. Development of a Novel Railway Positioning System Using RFID Technology. Sensors 2022, 22, 2401. DOI: https://doi.org/10.3390/s22062401

DOI 10.5162/EUROSENSORSXXXVI/PT2.210

Towards fully hardware-based neuromorphic encoding for efficient vibration signal recognition

Tamás Zeffer[1,2], Tímea Nóra Török[3,1], László Pósa[1], Ferenc Braun[1], András Halbritter[3], János Volk[1]
[1] HUN-REN Centre for Energy Research, 1121 Budapest, Hungary
[2] Doctoral School on Material Sciences & Technologies, Óbuda University, 1034 Budapest, Hungary
[3] Budapest University of Technology and Economics, 1111 Budapest, Hungary

Corresponding Author's e-mail address: volk.janos@ek.hun-ren.hu

Summary:

Neuromorphic signal processing can enhance the efficiency of IoT sensors and support edge computing solutions. However, the preprocessing of the encoded signals, to be transferred to a spiking neural network, requires high computational power. In this work, we propose an energy-efficient hardware-based solution for the analysis of rapidly changing vibration or acoustic signals. This was inspired by the human cochlear implant, which exploits the plasticity of the human brain to enable clear speech recognition even on a very limited number of frequency channels (16-22). Our proposed hardware consists of a 16-channel frequency-selective MEMS cantilever array, and a VO_2 memristor nanogap based oscillator for amplitude sensitive spiking signal generation. To test our solution, we used Google Command Speech benchmark database.

Keywords: Spiking neural network, cantilever array, memristor oscillator, vibration analysis, edge computing

Motivation and Objective

For quite some time, it has been evident that biological systems surpass electronic counterparts in terms of energy efficiency, highlighting a significant gap. Therefore, the development of neuromorphic auditory hardware systems holds promise for achieving greater efficiency and performance in future hardware audio solution [1].

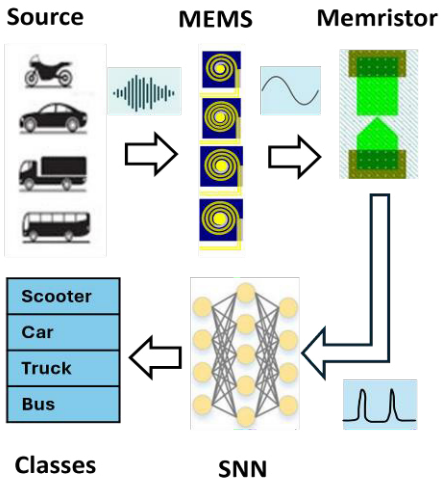

Fig. 1. Proposed SNN-based vibration source classification method using piezo-MEMS frequency sensitive cantilever array and memristor to encode amplified analogue signals into neural spikes.

In this paper, we propose a solution for FFT free neuromorphic encoding of acoustic and vibration spectrograms. It is based on our previous work, where similar cantilever arrays were used for a fully implantable cochlear implant [2]. Fig. 1 shows an application example of an Acoustic Vehicle Detection system. Specifically, MEMS cantilevers serve as sensors to detect the sound or seismic vibrations emitted by different vehicles. These cantilevers are tuned to specific resonant frequencies. Subsequently, the harmonic motion of each piezoelectric cantilever generates voltage outputs, which are processed by oscillatory circuitry to produce spikes. These circuits incorporate VO_2-based memristors, which play a crucial role in spike generation. The resulting spikes serve as inputs to a Spiking Neural Network (SNN), enabling the classification.

Description of the new method

For a concise SNN network, we have chosen the speech2spikes pipeline [3], which consists of blocks that initially utilize the Mel Spectrogram, followed by their Step-Forward and eventually by Cumulative Sums, to produce the input spikes to the SNN.

To achieve higher accuracy in hardware system design, we modeled our existing hardware ele-

ments in two distinct steps. Our models are based on the fabricated cantilever and memristor along with its experimental signals (Fig. 2) Initially, we aligned the data of our 4x4 spiral cantilevers to the parameters of the mel-spectrogram, changing the number of bins from 20 to 16, and reducing the frequency range to a minimum and a maximum frequency of 200 and 700 Hz [4].

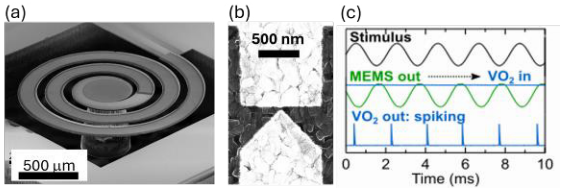

Fig. 2. Fabricated spiral shaped piezocantiver having tuned resonant frequency (a), the VO2 nanogap memristor (b), and the measured signal conversion (c).

Subsequently, we modeled the memristive oscillatory circuit, omitting the use of step-forward and cumulative sum pipeline algorithms. We summarized this two-step hardware design approach in the rows of the Table 1 below, marked as version 1 and 2 for clarity. Emulation of hardware is emphasized by the light blue background of the cells. The number of input neurons in the SNN network, determined by the bin numbers of the mel-spectrum or the count of spiral cantilevers designed for various natural frequencies. Each layer of the SNN network consists of 256 LIF neurons. Efficiency is measured in terms of accuracy.

Version	Bins	Frequencies	Methods
0	20	20…20.000 Hz	step-forward and cumulated sum algorithm
1	16	200…700 Hz	
2			emulated oscillatory circuit on measurements

Table 1. Co-deisgn of preprocessing MEMS and SNN with emulated hardware models. Cells in light blue denote the emulated components.

Results

We succeeded in achieving a 40% accuracy with the first version, which may signify a good result in our work. Although this represents promising progress, further optimization and refinement are needed to advance accuracy. Training and modeling of version 2 are still in progress. Unfortunately, the accuracy of the zeroth version during training fell short of expectations, showing only 70%. However, if we manage to find the appropriate training conditions, we believe that the accuracy will improve in version 2, following the published 88%.

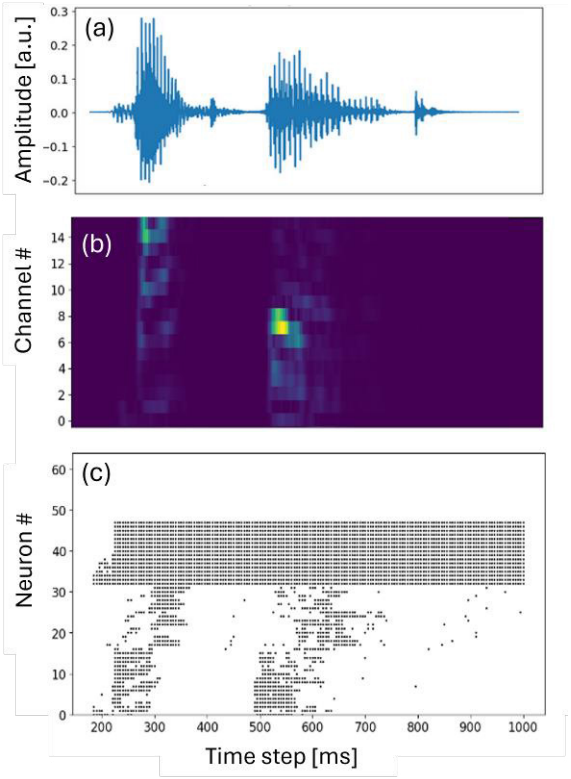

Fig. 3. (a) The preprocessing pipeline signals. Initially, the 'backward' GSC audio data (a) enters the pipeline and undergoes processing by the Mel Spectrogram algorithm with 16 bins (b). Eventually, the Step-forward and cumulative sums algorithm feeds 64 neurons of the SNN with its generated spikes (c).

References

[1] N. Kasabov *et al.*, “Evolving spatio-temporal data machines based on the NeuCube neuromorphic framework: Design methodology and selected applications,” *Neural Networks*, vol. 78, pp. 1–14, Jun. 2016, doi: 10.1016/j.neunet.2015.09.011.

[2] P. Udvardi *et al.*, “Spiral-Shaped Piezoelectric MEMS Cantilever Array for Fully Implantable Hearing Systems,” *Micromachines*, vol. 8, no. 10, p. 311, Oct. 2017, doi: 10.3390/mi8100311.

[3] K. M. Stewart, T. Shea, N. Pacik-Nelson, E. Gallo, and A. Danielescu, “Speech2Spikes: Efficient Audio Encoding Pipeline for Real-time Neuromorphic Systems,” in *Neuro-Inspired Computational Elements Conference*, San Antonio TX USA: ACM, Apr. 2023, pp. 71–78. doi: 10.1145/3584954.3584995.

[4] L. Pósa *et al.*, “Applying Neurodynamic Behavior of Mott Memristors for Auditory Sensing,” in *Proceedings of the Neuronics Conference*, València, Spain: FUNDACIO DE LA COMUNITAT VALENCIANA SCITO, Dec. 2023. doi: 10.29363/nanoge.neuronics.2024.017.

DOI 10.5162/EUROSENSORSXXXVI/PT2.300

Multi-sensor Platform for Indoor Air Quality Monitoring

Yuwei SHEN[1], Rouba ALRAMMOUZ[1], Marc FISCHER[1], Maxime MINOT[1], Riadh LAKHMI[1], Jean-Paul VIRICELLE[1], Mathilde RIEU[1]

[1] Mines Saint-Etienne, Univ Lyon, CNRS, UMR 5307 LGF, Centre SPIN, F-42023 Saint-Etienne, France

yuwei.shen@emse.fr

Summary:

Indoor air pollution has been a rising threat for public health. This study presents an indoor air quality monitoring platform integrating multiple sensors. It adopts calibration and compensation algorithms in order to improve gas measurement accuracy. A neural network-based gas recognition algorithm is also proposed. This approach promises more effective real-time IAQ monitoring for public health protection.

Keywords: indoor air quality, gas sensors, multi-sensor platform, neural networks

Background, Motivation and Objective

Indoor air quality (IAQ) is crucial for public health, as individuals typically spend around 80% of their time indoors. The World Health Organization reports that indoor air pollution causes over 3 million fatalities each year. Common indoor pollutants include carbon monoxide, volatile organic compounds, particulate matter, aerosols, and biological contaminants. These pollutants often originate from building materials, combustion from cooking appliances and fireplaces, and can be carried in from outdoors. The enclosed nature of indoor spaces condenses the concentration of these pollutants, resulting in a variety of health issues over both short and long exposure periods. Therefore, developing monitoring systems of indoor air quality is recognized as essential for health protection. Many multi-sensor platforms for IAQ monitoring were reported [1]. However, the literature either focuses on the advancement in sensing materials [2] or on gas identification using neural networks without any prior calibration or compensation algorithms [3]. The aim of this work is to develop a digital multi-sensor platform using commercial sensors for real-time IAQ monitoring.

Description of the System

Seven indoor air pollutants sensors were chosen for our application. They are capable of detecting a broad spectrum of indoor air pollutants within their exposure limits (Table 1). Since gas sensors are sensitive towards temperature and humidity changes, a temperature and humidity sensor for temperature and humidity compensation is included to complement the chosen set sensors. All eight sensors were then integrated onto a single printed circuit board, as shown in Figure 1.a. In order to facilitate real-time monitoring, data from the sensors are seamlessly transmitted and displayed via a dedicated Labview application. This integration enables continuous surveillance, empowering users with timely insights into indoor air quality dynamics.

The developed multi-sensor platform was characterized, calibrated and trained in the gas sensing test bench shown in figure 1.b. Our testing environment contains dual exposure chambers, offering precise control over airflow and humidity levels through a LabVIEW interface. It also enables sensor characterization under a mixture of up to 5 pollutants simultaneously.

Tab. 1: Target gases and their limits of exposure

Target gas	TVOC	HCHO	NO_2
Limit of exposure	750 ppb	16 ppb	1 ppm
Target gas	CO	CO_2	PM
Limit of exposure	35 ppm	3000 ppm	15 mg/m_3

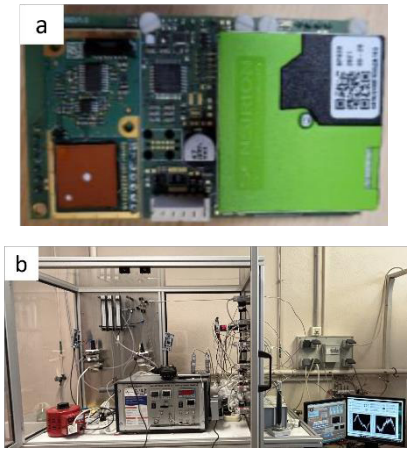

Fig 1.a. Multi-sensor board; b. Test bench at Mines Saint-Etienne.

Results

To ensure optimal performance, the sensors were first exposed to a variety of gases, including CO, NO_2, ethanol, acetone and various humidity levels. This step aimed to assess sensor sensitivity and selectivity across different pollutants. Figure 2 provides a representative illustration of the TVOC sensor's response, showcasing its pronounced sensitivity to VOCs while also highlighting potential interference from CO and humidity.

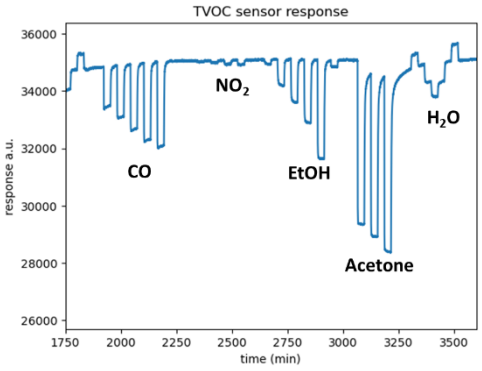

Fig 2. TVOC sensor's response under different exposure of CO, NO_2, ethanol, acetone, and humidity.

Following the initial calibration process, the sensor was exposed to various absolute humidity levels, in order to mitigate the impact of temperature and humidity variations. To effectively compensate for these environmental factors, we implemented a linear compensation algorithm, as illustrated in Figure 3. Furthermore, an algorithm for gas recognition and concentration detection employing neural networks is under development. This algorithm promises enhanced precision in identifying and quantifying pollutant concentrations, thereby enhancing the sensor's efficiency in indoor air quality monitoring.

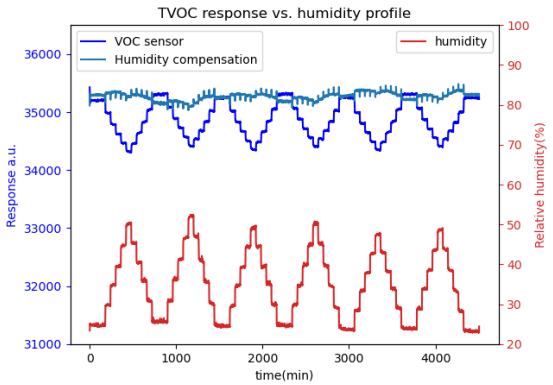

Fig 3. Temperature and humidity compensation for the TVOC sensor.

Conclusion

In this work, we have developed a multi-sensor platform tailored for indoor air pollutant detection. Through calibrations under diverse pollutants and the implementation of a humidity compensation algorithm, we have ensured the platform's reliability and gas measurement accuracy. A neural-network-based gas recognition algorithm is under development for gas identification. This approach promises to enhance the efficiency of multi-sensor platforms with embedded neural networks not only in terms of indoor air pollutants identification and quantification, but also in terms of data management, memory management and power consumption.

References

[1] A. Staerz, F. Roeck, U. Weimar, N. Barsan (2020). Electronic Nose. In Surface and Interface Science, K. Wandelt (Ed.). https://doi.org/10.1002/9783527822492.ch67

[2] G, Verma, A. Gokarna, H. Kadiri, K. Nomenyo, G. Lerondel, A. Gupta, Multiplexed Gas Sensor: Fabrication Strategies, Recent Progress, and Challenges, ACS Sensors, 2023, 8 (9), 3320-3337. DOI: 10.1021/acssensors.3c01244

[3] H. Chen, D. Huo, J. Zhang, Gas Recognition in E-Nose System: A Review, IEEE Transactions on Biomedical Circuits and Systems, 2022, 16, 2, 169-184, doi: 10.1109/TBCAS.2022.3166530.

DOI 10.5162/EUROSENSORSXXXVI/PT2.302

Advanced sensor system dedicated to real-time soil monitoring

Elise Saoutieff[1], Paul Fourcade[1], Célia Boko[1], Vincent Elhorga[1], Sébastien Boisseau[1], Iris Vogeler[2,8], Henk Smit[2], Nivedha Surendran[3], Axel Wille[3], Han Shao[4], Richard Murray[4], Alan O'Riordan[4], Lukasz Kulas[5], Patryk Kalkowski[5], Henrique Trindade[6], Lukas Kohl[7]

[1] Univ. Grenoble Alpes, CEA, Leti, Grenoble, France

[2] Christian-Albrechts-Universität, Kiel, Germany

[3] Fraunhofer Institute for Electronic Microsystems and Solid State Technologies, Munich, Germany

[4] Nanotechnology Group, Tyndall National Institute, Cork, Ireland

[5] Gdansk University of Technology, Gdansk, Poland

[6] University of Trás os Montes e Alto Douro, Quinta de Prados, Portugal

[7] University of Eastern Finland, Kuopio, Finland

[8] Aarhus University, Aarhus, Denmark

Corresponding Author's e-mail address elise.saoutieff@cea.fr

Summary:

The EU project FAMOSOS (Farm monitoring via real-time soil sensing) aims to develop a real-time monitoring system for soil data, including nitrogen (ammonium, nitrate, nitrite), moisture, pH, and dissolved oxygen with increased sensitivity, reduced response times and sample volumes. This IoT system will be composed of a wireless underground sensor network, composed of porous ceramic probe, combined with a micro pump, a sensor, and an antenna for wireless data transmission. The system will be tested in Germany, Portugal, and Finland, with data used in the biophysical Agricultural Production Systems Simulator (APSIM) model to identify sustainable, climate-resilient agricultural practices.

Keywords: soil monitoring, real-time, modelling, nano-electrodes, wireless underground IoT nodes

Famosos Objective

In 2015 alone, pollution led to an estimated 9 million premature deaths worldwide (16% of all deaths), 15 times more than from all wars and other forms of violence [1]. The zero-pollution vision for 2050 is *for air, water and soil pollution to be reduced to levels no longer considered harmful to health and natural ecosystems…. thereby creating a toxic-free environment*.

The EU is developing a more effective action plan [2] based on a 'zero pollution hierarchy' using the precautionary principle. Specifically, this plan calls out that where prevention at source is not (yet) possible, smart production and digital solutions for pollution tracking and reduction should be promoted. However, even if sensing platform for environmental monitoring already exist [3], a key challenge is the lack of effective digital monitoring tools [4] that provide real-time decision-making capacity and agency to end-users and stakeholders; including consumers, inspection services, industry operators, and environmental emergency responders.

FAMOSOS aims to enable more sustainable agricultural practices through real-time monitoring of N concentrations in the soil solution and the environmental conditions that drive them. This will be achieved through a novel sensor system [5], combined with laboratory and field experiments and modelling.

FAMOSOS will address these challenges:

1. Develop and test a tool for real-time in situ measurements of soil solution characteristics, including N concentrations (NH4, NO3) and oxidation status.
2. Estimate N losses (gaseous and leaching) from soil solution data and environmental drivers.
3. Improve our understanding of hot moments in N cycling after fertilization and rainfall/irrigation.
4. Develop smart fertilization practices depending on soil N concentrations.

In addition to detecting soil nutrient concentration, and predicting fertilisation requirements, soil and water detection can also allow for the early detection of contaminants.

Famosos System

FAMOSOS consists of three components that will be advanced in parallel: (i) sensor development, (ii) lab-field testing/measurements and (iii) Modelling & development for guiding N fertilisation.
The figure 1 described the concept.

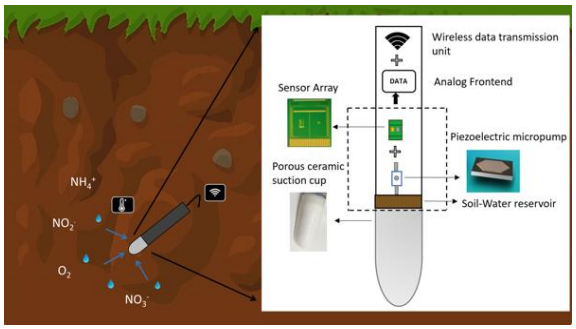

Fig. 1. FAMOSOS IoT system concept

The micro-pump and sensors already developed in Germany and Ireland will be evaluated, integrated with off-the-shelf suction cups, and need for adjustments or extensions of the sensors to operate under real conditions, as well as the sensor's requirements for proper operation (distance, reliability, ...) will be evaluated.
Concurrently, we will start with measurements and analysis of the data from the new probes, to i.e. relate soil N concentrations to fertiliser treatments. The experiments will start under controlled lab conditions, followed by in-situ measurements in the field.
The proposed cost-effective sensor system allows to measure continuous in-situ soil water N concentrations, using automated data acquisition and wireless data transmission through soil.

Results

By developing a tool which provides farmers with real-time information on the soil N status, FAMOSOS will make an important contribution to improving our understanding of soils for better management (optimized N fertilization strategies), which will further enable a more sustainable agricultural production (more efficient N use) and a healthier environment (decreased N leaching, N_2O emissions).

FAMOSOS illustrates the maturation of technologies towards broad adoption. The expected impact focuses on the benefits of the new sensor technologies to better understand N cycling in soils. This will increase the real-time decision-making capability of fertilizer management. Additionally, the project will create a new product, which can be marketed throughout Europe and worldwide.

References

[1] P. J. Landrigan *et al.,* "The Lancet Commission on pollution and health," *The Lancet*, vol. 391, no. 10119, pp. 462–512, 2018, doi: 10.1016/S0140-6736(17)32345-0.

[2] *EU Action Plan: 'Towards Zero Pollution for Air, Water and Soil'.* [Online]. Available: https://eur-lex.europa.eu/legal-content/EN/TXT/HTML/?uri=CELEX:52021DC0400&from=EN (accessed: Jun. 27 2024).

[3] E. Saoutieff et al., "Wearable Low-Power Sensing Platform for Environmental and Health Monitoring: The Convergence Project Sensors", **2021**, 21, 1802, doi: 10.3390/s21051802

[4] R. Murray et al., Room Temperature Sensing of Volatile Organic Compounds Using Hybrid Sno Nanoflower and Laser-Induced Graphitic Carbon Devices, 2023.

[5] R. Daly, T. Narayan, H. Shao, A. O'Riordan, and P. Lovera, "Platinum-Based Interdigitated Micro-Electrode Arrays for Reagent-Free Detection of Copper," *Sensors (Basel, Switzerland)*, vol. 21, no. 10, 2021, doi: 10.3390/s21103544

Acknowledgements

The project is funded as an EJP-SOIL external project by the Irish Department of Agriculture, Food and the Marine under grant agreement No. 2022EJPSOIL202, the Finnish Ministry of Agriculture (4400T-0569), the French National Research Agency (ANR) under grant ANR-23-SOIL-0002-04, and the German Federal Ministry of Education and Research BMBF under grant number 031B1377B.

DOI 10.5162/EUROSENSORSXXXVI/PT3.17

Functionalization of Black Phosphorus for Enhanced Hydrogen Detection

Arianna Rossi[1], Maria Caporali[2], Salvatore Impemba[2,3], Barbara Fabbri[1], Andrea Gaiardo[4], Matteo Valt[4], and Vincenzo Guidi[1]

[1] Department of Physics and Earth Science, University of Ferrara, Via Giuseppe Saragat 1/C, Ferrara 44122, Italy

[2] CNR-ICCOM, Via Madonna del Piano 10, Sesto Fiorentino 50019, Italy

[3] CSGI, Department of Chemistry, University of Florence, Via della Lastruccia 3, Sesto Fiorentino 50019, Italy

[4] Sensors and Devices Center, Bruno Kessler Foundation, Via Sommarive 18, Trento 38123, Italy

Corresponding Author's e-mail address: arianna.rossi@unife.it

Summary:

This study is dedicated to advancing phosphorene-based sensors for hydrogen detection. Through the strategic functionalization of phosphorene with urea, the sensor exhibits enhanced performance and exceptional stability in ambient air, making it well-suited for various applications. Extensive characterization techniques confirmed material stability and demonstrated the sensor's high sensitivity (up to 700 ppm) and selectivity for hydrogen at room temperature. The use of *operando* diffuse reflectance infrared Fourier transform provided real-time insights into the gas sensing mechanism, contributing to a deeper understanding of its operational principles.

Keywords: hydrogen detection, phosphorene, functionalization, 2D material, chemoresistive gas sensor

Introduction

Nowadays, hydrogen (H_2) stands as the definitive energy source of the twenty-first century, poised to replace conventional fossil fuels in the global power system. H_2, an odorless, flammable, and explosive gas, remains undetectable to the human senses even at concentrations of 4-75% in air [1]. This poses significant risks, necessitating sensors with high sensitivity and selectivity at low temperatures for detection during production, storage, and transportation. Commercially available H_2 gas sensors, including electrochemical and semiconductor devices, are promising, but face drawbacks such as lack of selectivity and high operating temperatures (200-600 °C) [2-3]. Two-dimensional materials (2D), such as graphene and transition metal dichalcogenides, have garnered significant interest for their distinctive properties, aimed at overcoming certain limitations. Their remarkable high-surface-to-volume ratio has been a focal point of attention. This characteristic results in a substantial active surface area, facilitating robust interactions with the target gas molecules. However, enhancing their performance remains a challenge. Recently, black Phosphorus (bP) has emerged as a potential solution due to its semiconductor properties, but its susceptibility to oxidation limits its practical use [4]. Surface functionalization strategies, such as incorporating nanoparticles or organic compounds, aim to improve stability and performance for gas sensing applications [5]. In this work, we proposed a new bP-functionalization with urea synthesis. This material can be used as a functional material for the fabrication of a chemoresistive gas sensor for H_2 detection, as suggested by catalytic properties featured in previous work [6-7]. Through a comprehensive morphological, chemical, and electrical characterization, we investigated environmental stability in dry air and sensing capabilities of amino-functionalized bP (bP-NH_2) films for H_2 detection at room temperature (RT). Finally, to evaluate the chemical interactions on the surface of the sensing film before and after the exposure of the target gas, we exploited a

dedicated test chamber for an *operando* diffuse reflectance infrared Fourier transform (DRIFT) spectroscopy.

Materials & Method

The bP-NH_2 nanosheets were characterized by powder X-ray diffraction (PXRD), scanning electron microscopy (SEM), Raman, UV-Visible (UV-vis), and X-ray photoelectron (XPS) spectroscopies. Then, the sensing film was electrically characterized by providing "3S" rules (sensitivity, selectivity, and stability).

Results

The functionalization was accomplished via wet chemical reaction between exfoliated bP and urea (see Fig. 1). The material stability in air and the integrated surface was confirmed by PXRD and Raman spectroscopy. XPS confirmed the presence of -NH_2 groups (about 3%) on the surface. Concerning UV-vis and impedance measurements, these highlighted a significant increase of the band gap value and downward shift of the conduction band level respect to pristine bP.

The sensing performance of bP-NH_2 device was evaluated in a wide range of concentration, starting from 50 to 700 ppm of H_2 at RT (Fig. 2). The sensor demonstrated long-term stability over a period of three months, exhibiting the ability to maintain its structural integrity and sensing capabilities even when continuously exposed to dry air conditions. The gas sensing mechanism was investigated thought an advanced technique, i.e. DRIFT spectroscopy, providing information about the chemical interaction between the oxygen preabsorbed species and the target gas.

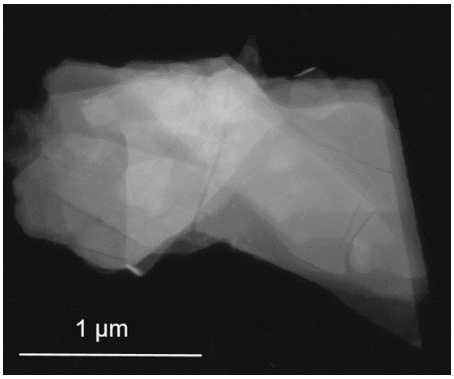

Fig. 1. STEM image of bP-NH_2 nanosheets.

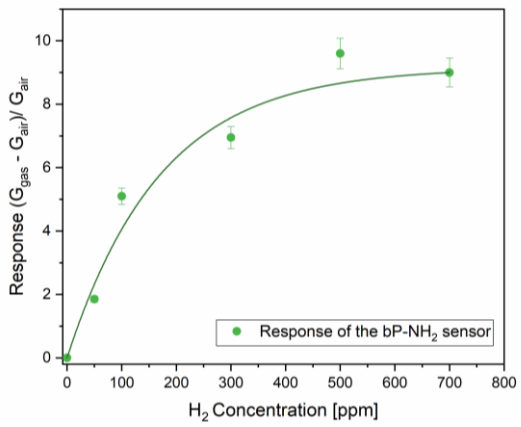

Fig. 2. Calibration curve of bP-NH_2 sensor at RT in dry conditions.

Acknowledgments

Funded POR FSE 2014/2020 by Regione Emilia-Romagna.

References

[1] S. Agarwal, S. Kumar et al., An efficient hydrogen gas sensors based on hierarchical Ag/ZnO hollow microstructures, *Sensors and Actuators B: Chemical,* 346, 130510 (2021); doi: 10.1016/j.snb.2021.130510

[2] G. Korotcenkov, S.Han et al., Review of electrochemical hydrogen sensors, *Chemistry Review*, 109, 1402-1433 (2009); doi: 10.1021/cr800339k

[3] H. Gu, Z. Wang et al., hydrogen gas sensors based on semiconductor oxide nanostructures, *Sensors*, 12 (5), 5517-5550 (2012); doi: 10.3390/s120505517

[4] N. Sultana, A. Degg et al., Synthesis, modification, and application pf black phosphorus, few-layer black phosphorous (FLBP), and phosphorene: a detailed review, *Materials Advanced*, 3 (14), 5557-5574 (2022); doi: 10.1039/D1MA01101D

[5] M. Valt, M. Caporali et al., Air stable nickel-decorated black phosphorous and its room-temperature chemiresistive gas sensors capabilities, *ACS Applied Materials & Interfaces*, 13 (37), 44711-44722 (2021); doi: 10.1021/acsami.1c10763

[6] G. Lee, S. Jung et al., Platinum- functionalized black phosphorus hydrogen sensors, *Applied Physics Letters*, 110 (24), 242103 (2017); doi: 10.1063/1.4985708

[7] L. Shao, H. Sun, et al., Facile preparation of NH_2-functionalized black phosphorene for the electrocatalytic hydrogen evolution reaction, *Journal of Materials Chemistry*, 6 (6), 2494-2499 (2018); doi: 10.1039/C7TA10884B

DOI 10.5162/EUROSENSORSXXXVI/PT3.49

Water Transfer Printing of Silver Ink-based Temperature Sensors

Rafika SELMI, Jean Charles FUSTEC, France LE BIHAN, Maxime HARNOIS.
Institut d'Electronique et des Technologies du numéRique, IETR, Rennes University, Rennes, France.

Corresponding Author's e-mail address: rafika.selmi@univ-rennes.fr

Summary:

This paper presents a reliable emerging technology to fabricate lightweight and conformal electronics on 3-D complex shapes and various materials, including everyday life objects. The novel technology consists in screen-printing of silver ink onto water soluble film. Next, a water transfer printing method is used to allow the substrate-free transfer of the screen-printed patterns. This process exhibits electrical functions similar to conventional screen-printing ones, enabling the fabrication of a highly sensitive and reproducible temperature sensors.

Keywords: Water Transfer Printing, Screen-printing, Silver Ink, Temperature Sensors.

Background, Motivation and Objective

The novel form of electronics is marked by the growth of innovative technologies aimed at making electronic more conformal, lightweight, connected and user-friendly, thereby opening up exciting new possibilities and applications in various aspects of everyday life [1], [2]. The main objective is to push back the limits of traditional 2-D electronic design by proposing to integrate electronic devices onto complex 3-D shapes, such as sensors, whose effectiveness is enhanced by bringing them closer to the object being monitored [3].

Description of the Method

Such an innovative technology is water transfer printing (WTP) [4]. It ensures the free-transfer of a highly sensitive temperature sensors to 3-D materials without any alteration of the device features, opening up many perspectives for the future of 3-D lightweight electronic.

Results

WTP process is a process commonly used in the industry to apply decorative patterns or designs onto three-dimensional surfaces. It is used since our pioneering work in 2017 [2] to transfer electronics from polyvinyl alcohol (PVA) substrate to arbitrary and daily live objects as shown in Fig.1. Firstly, sensor is screen-printed on PVA, which is then dried and cured to remove solvents and obtain optimum resistivity. Afterward, the PVA is gently deposited at the water surface to be dissolved, allowing electronic patterns to float. At last, a 3-D object is dipped through the floating patterns, resulting electronic active layer fixed conformally to the object surface.

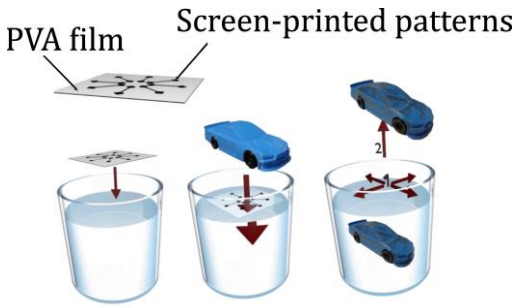

Fig. 1. WTP Process.

Our previous works already show the high degree of conformality as the technology is a substrate-free transfer [2], it's also important to note that this method does not affect the electrical performances of sensors as show in Fig.2. Indeed, sensors fabricated by WTP or directly screen printed on PET substrate highlight the same electrical behavior.

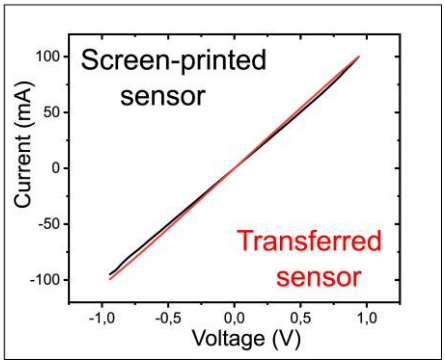

Fig. 2. I=f(V) characterization of a silver ink-based sensor after and before its transfer using WTP.

Basically, temperature sensor is an electronic device designed to measure and control the temperature of an object or a system. That's why the closer the sensor is to the object, the more accurate the measurement will be, which is guaranteed by our process. The resistance variation as function of temperature of a transferred silver ink-based temperature sensor is showed in Fig.3 shows. Indeed, the electrical response of the sensor is reproducible over more than four hours cycling.

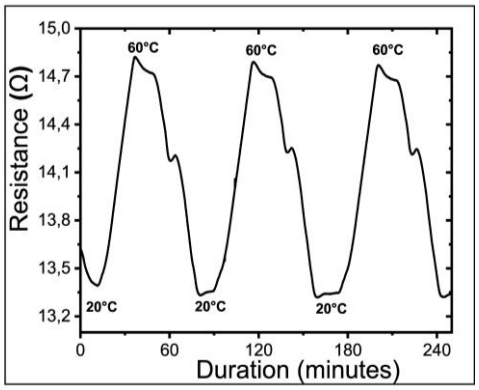

Fig. 3. Resistance variation as function of temperature of a silver ink-based temperature sensor.

Observing the graph, it's obvious that the resistance of the sensor decreases as the temperature decreases. This follows the classical behavior of metallic materials. Moreover, transferred silver ink-based sensor shows high sensitivity to temperature with 0.08 Ω/°C and 0.25%/°C. Note that, authors assume that the transferred silver sensors have been compared to screen-printed ones, demonstrating similar behavior, performance, and sensitivity. This is already confirmed by the I-V characterization shown in Fig.2

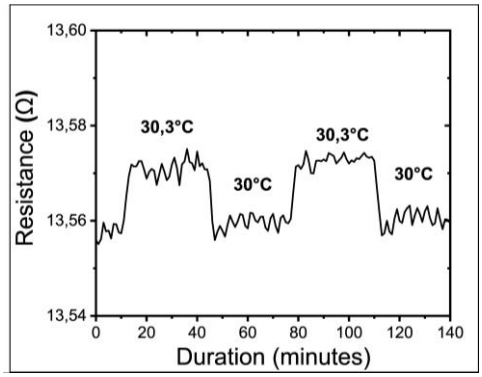

Fig. 4. Minimal variation of temperature detected by the silver ink-based temperature sensor.

The Fig.4 shows the smallest temperature variation that transferred sensor can reliably detect and measure without applying any mathematic complex treatment. This result proves the high efficiency and accuracy of the sensor, enabling it to distinguish a minimal temperature change of 0.3°C, despite background noise and fluctuations. Temperature sensors are placed in locations where temperature needs to be monitored, such as industrial environments, air conditioning systems, and medical laboratories.

In these application areas, various levels of humidity are defined, between [40% RH: 60% RH], an environment is considered as optimal, and between [60% RH: 100%RH], it's considered very humid. Fig.5 shows the impact of humidity on the transferred temperature sensor described previously. The result highlights that the sensor is not sensitive to humidity (either for optimal humidity or excessive one), regardless of the temperature value. This is ensuring the normal behaviour and stability of the transferred temperature sensor in all desired installation environments, disregarding humidity effect.

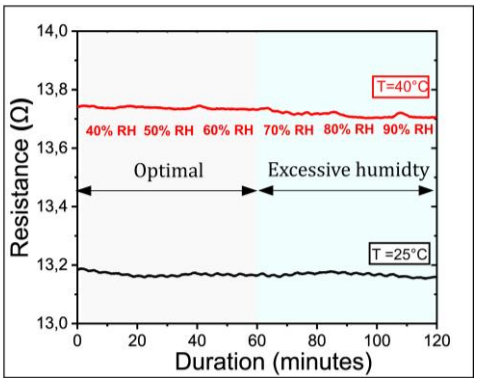

Fig. 5. Resistance variation of silver ink-based sensor as function of relative humidity ratio (%RH) at 25°C, and 40°C.

Conclusion

The WTP process surpasses the limits of traditional electronics manufacturing by enabling the integration of temperature sensors onto all complex objects, regardless of their shapes, while obviously maintaining the same performance as conventional screen-printed sensors.

References

[1] M. Harnois, F. Garcia-Castro, G. Herry, O. De Sagazan, et F. Le Bihan, « Eco-designed Conformable Inorganic Electronics to Improve the End of Life of Smart Objects: Sensor Processing and Applications », *ACS Appl. Electron. Mater.*, vol. 2, nº 2, p. 563-570, févr. 2020, doi: 10.1021/acsaelm.9b00807.

[2] B. Le Borgne, O. De Sagazan, S. Crand, E. Jacques, et M. Harnois, « Conformal Electronics Wrapped Around Daily Life Objects Using an Original Method: Water Transfer Printing », *ACS Appl. Mater. Interfaces*, vol. 9, nº 35, p. 29424-29429, sept. 2017, doi: 10.1021/acsami.7b07327.

[3] R. Selmi, J.-C. Fustec, M. Harnois, et F. L. Bihan, « Organic and Metallic Sensors on Complex 3-D Object Using an Original Method: Water Transfer Printing », *IEEE Sens. Lett.*, vol. 7, nº 9, p. 1-4, sept. 2023, doi: 10.1109/LSENS.2023.3301845.

[4] Harnois, Maxime, Jacques Emmanuel, and Brice Le Borgne., "Solvent transfer printing method." U.S. Patent No. 11,345,184. 31 May 2022.

DOI 10.5162/EUROSENSORSXXXVI/PT3.109

Self-Supported Flexible Magnetic Silica-Titania Based Sol-gel Glasses: a Forth-Coming Material for Sensing Applications

Daniel Alves Barcelos [1,2,4]*, *Laura C. J. Pereira* [3,4], *David Ortiz de Zárate* [5] , *Amadeu Griol* [5] , *M. Clara Gonçalves* [1,2]

[1] *Chemistry Engineering Department, Institute Superior Technical, University of Lisbon, Av. Rovisco Pais, 1049-001 Lisbon, Portugal*

[2] *Center of Structural Chemistry, Av. Rovisco Pais, 1049-001 Lisbon, Portugal*

[3] *Department of Engineering and Nuclear Science, Institute Superior Technical, University of Lisbon, Estrada Nacional 10, 2685-066 Bobadela LRS, Portugal*

[4] *Center of Science and Nuclear Technology, Institute Superior Technical, University of Lisbon, 2685-066 Bobadela LRS, Portugal*

[5] *Nanophotonics Technology Center, Universitat Politècnica de València, Camí de Vera s/n, 46022 Valencia, Spain*

danielbarcelos@tecnico.ulisboa.pt

Summary:

The objective of this study is to pioneer the fabrication of self-supported flexible silica-titania based glass with magnetic properties through low-temperature synthetic routes. In this regard, superparamagnetic iron oxide nanoparticles (SPIONs) were incorporated in the glass matrices (hybrid sol-gel silica precursors). Across the studied compositions, Young's modulus below 370 MPa demonstrate mechanical flexibility comparable to recognized flexible materials such as PET. Notably, the superparamagnetic behavior of SPIONs persisted at 300K even after their integration in the self-supported flexible glass matrices.

Keywords: flexible glasses, SPIONs, sol-gel process, inorganic glasses, low-temperature synthesis.

Background

Corning® Willow® Glass produced by (high temperature) roll-to-roll process represents a pioneering advancement in glass technology due to its exceptional mechanical performance and versatility. This innovative glass combines the inherent advantages of traditional inorganic glass with a remarkable degree of mechanical flexibility, rendering it applicable across a diverse array of domains, including semiconductor and solar cell technologies [1]. Metallic magnetic glasses, typically derived from the fusion of metallic components, find utility across a broad spectrum of industries encompassing catalysis, chemical processes, and biomedical sensor development. However, it is imperative to acknowledge that both Corning® Willow® Glass and metallic magnetic glasses demand high-temperature fabrication processes, thereby incurring substantial production costs and high ecological footprint. In respect of these drawbacks, there arises a compelling impetus to explore alternative materials that offer comparable functionalities while circumventing the challenges associated with high temperature synthesis. Among such alternatives, Superparamagnetic Iron Oxide Nanoparticles (SPIONs) emerge as a particularly noteworthy candidate. SPIONs exhibit superparamagnetic behavior at ambient temperatures, affording them the unique ability to magnetize and demagnetize rapidly in response to external magnetic fields [1]. Regarding the fabrication of self-supported flexible inorganic glass, a strategic approach is adopted, centered on the utilization of hybrid sol-gel silica precursors characterized by the presence of non-hydrolysable organic groups, which persist within the final glass molecular structure. Consequently, this 3D molecular architecture engenders a heightened degree of mechanical flexibility, akin to that of plastic materials, in the resultant products.

Motivation and objectives

This study is primarily focused on the fabrication of self-supported flexible magnetic silica-titania-based glasses with ambient temperature techniques, to achieve environmentally sustainable and economically feasible materials. The integration of SPIONs within the inorganic glass matrices enables the magnetic performance. The sol-gel synthesis of hybrid glass matrices and the co-precipitation method to produce SPIONs were the room temperature methodologies chosen.

Methods

A (80/20) SiO_2/TiO_2 molar ratio glass composition was settled. The sol-gel synthesis uses 3-Glycidyloxypropyl-trimethoxysilane (GPTMS), triethoxymethysilane (MTES) and triethoxyvinylsilane (VTES) (SiO_2 precursors);Titanium (IV) propoxide (TPOT) (TiO_2 precursor). For the SPIONs, a co-precipitation synthesis is based on the reduction of iron (III) chloride hexahydrate. SPIONs were covered with dextran T10 before incorporation in the glass matrix [2].

Results

This investigation marks a significant milestone by synthesizing self-supported flexible glassy materials with magnetic properties using low-temperature synthesis pathways, representing a novel contribution to the field. To the best of our knowledge, this represents the first instance of such materials being produced via these methodologies. Illustrative evidence of the attained outcomes is presented in Figure 1, wherein the bending capability of the self-supported flexible glass (Figure 1a) and the integration of Superparamagnetic Iron Oxide Nanoparticles (SPIONs) into a similar matrix (Figure 1b) are depicted.

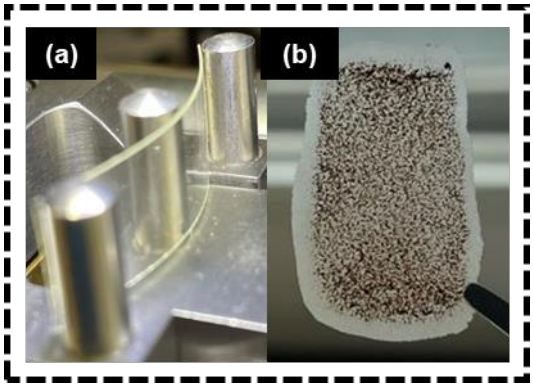

Fig. 1. (a) Self-supported flexible glass; (b) Self-supported magnetic flexible glass.

Additionally, Table 1 provides a comprehensive overview of the obtained results pertaining to the Young's Modulus of the synthesized samples denoted as A1 (GPTMS/TPOT), A2 (GPTMS-MTES/TPOT), and A3 (GPTMS-VTES/TPOT). These values, falling within a range comparable to that of Polyvinyl Chloride (PVC) (200-800 MPa), signify a level of flexibility surpassing that of high-density polyethylene (700 MPa) while exhibiting greater rigidity than low-density polyethylene (200 MPa) [3].

Tab. 1: Young's Modulus Self-Supported flexible glasses.

Sample	Young's Modulus (MPa)
A1	234 ± 12.4
A2	363 ± 20.7
A3	311 ± 17.3

The addition of Superparamagnetic Iron Oxide Nanoparticles (SPIONs) did not visibly affect the the magnetic characteristics of the synthesized materials. This claim is supported by the consistent observation of superparamagnetic behavior, as depicted in Figure 2. Moreover, the saturation magnetization closely aligns with the results obtained for unbound SPIONs. Furthermore, it is noteworthy that the remanent magnetization underwent an anticipated alteration after the successful integration of SPIONs. This phenomenon can be attributed to the cessation of relaxation via Brownian motion, a characteristic feature inherent to SPIONs post-incorporation.

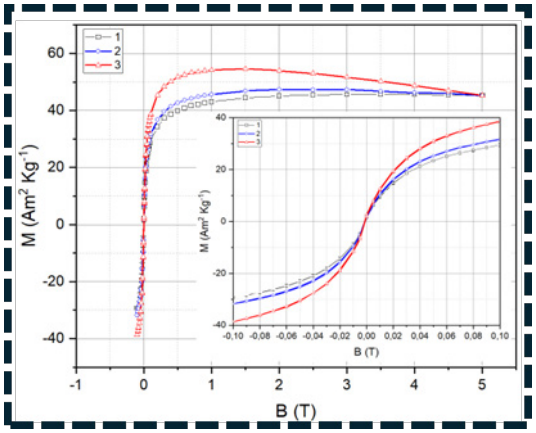

Fig. 2. Self-supported magnetic flexible glass M(H) at 300K (A1).

Furthermore, preliminary assessments concerning the sensing capabilities of the material were conducted, focusing on variations in ethanol concentrations (10%, 5%, and 2.5% v/v). Notably, these tests were conducted without the incorporation of SPIONs. The glasses demonstrated discernment among the distinct ethanol concentrations and exhibited a capacity to effectuate changes of 1,716 nm per unit of refractive index. These findings prefigure different utilization across diverse sensing applications, particularly within medical and environmental contexts.

References

[1] D.A. Barcelos, D.C. Leitao, L.C.J. Pereira, M.C. Gonçalves, *Materials* 14 (2021) 2926; doi: 10.3390/ma14112926.

[2] Matos, J.C.; Clara Gonçalves, M.; Pereira, L.C.J.; Vieira, B.J.C.; Waerenborgh, J.C. *Nanomaterials* 2019, 9, doi:10.3390/nano9070943

[3] D.R.H. Jones, M.F. Ashby, Elastic Moduli, in: *Engineering Materials 1*, Elsevier, 2019: pp. 31–47; doi: 10.1016/b978-0-08-102051-7.00003-8.

Acknowledgements

Financial support by FCT-PT through projects UIDB/00100/2020, UIDP/00100/2020, UID/Multi/04349/2019, LTHMFL-NECL LISBOA-01-0145-FEDER-875 022096 and PD/BD/150417/2019. EU-PROJECT: PROJECT: 101093042

DOI 10.5162/EUROSENSORSXXXVI/PT3.110

Printed Electronics on Flexible Substrates and In-Mold Electronics Process for Production Optimization

Duarte Dias[1], Isabel Pereira[1], Joana Gomes[1], Isaque Sá[1], Cíntia Martins[1], Luís Pereira[2]
[1] CeNTI – Centre for Nanotechnology and Smart Materials, Rua Fernando Mesquita 2785, 4760-034 V. N. Famalicão, Portugal,
[2] MICROplásticos, Cova da Serpe - Quiaios 3080-512 Figueira da Foz, Portugal

jogomes@centi.pt

Summary:
The InteliPart project, integrated within the Illiance High Performing Energy consortium, is oriented towards the creation of pioneering solutions involving the functionalization of plastic components. These solutions will focus on the reduction of process steps, addressing sustainability and improving cost-effectiveness. This work outlines the development of sensing and actuation technologies, namely capacitive sensors and light-emitting solutions, through printed electronics and their incorporation in plastic parts by injection molding processes, achieving In-Mold Electronics.

Keywords: printed electronics, screen printing, sensors, IME, production optimization.

IME Towards Production Optimization

Due to the current highly competitive manufacturing landscape, the reduction of production steps has emerged as a critical motivating factor for companies pursuing an efficiency enhancement and decrease of operational costs, while maintaining a competitive level. This production optimization provides an improvement of cost-effectiveness by eliminating unnecessary or redundant processes, which not only improves profitability, but also enables businesses to offer more competitive pricing in high-end components. Besides, process steps reduction is important to address sustainability and environmental concerns. In this scope, the InteliPart project – part of the Illiance High Performing Energy consortium – aims to create innovative solutions and advanced technologies through the functionalization of plastic parts. Combining the technologies of printed electronics and injection molding – In-Mold Electronics (IME), the main objective is to successfully integrate electronics in plastic parts for the development of functional components that could easily be incorporated in many interface applications towards new advanced electronic devices and appliances.

Printed Electronics and IME

Printed electronics is one of the highest growing markets in most recent years for its possibility to combine printing technologies and functional inks while assuring economical and functional advantages, as it can offer design flexibility and use of a large range of lightweight, thin and flexible materials, enabling the integration of electronics into unconventional shapes and surfaces, aligned with contemporary demands. This versatility opens new possibilities for product innovation and differentiation, further enhancing a company's competitive advantage.
The work herein presented aims at developing printed electronics sensing and actuation systems resorting to screen printing. Screen printing stands as a pivotal technology which offers an efficient deposition of functional materials onto flexible and rigid substrates, is cost-effective and allows for an easy scale up to roll-to-roll configuration, for large scale pre-production continuous printing. After printing, an additional step can be introduced to enhance the films' intelligence which consists of the assembly of surface mount devices (SMD) such as resistors, capacitors, and light-emitting diodes (LEDs) [1]. Moreover, IME offers a unique approach to the reduction of production steps. In the injection molding process, a polymer is injected against the surface of a film of printed electronics, promoting the adhesion of the layers. Hence, electronic functionalities are directly integrated during the injection molding process, resulting in a seamless product and efficient manufacturing workflow. Therefore, a significant simplification and streamlining of manufacturing processes can be achieved [2].
In these processes, materials are carefully selected to fulfil the end application requirements

and the different components designed for a customized solution.

Results

Preliminary tests regarding the integration of printed electronics through injection processes were performed, specifically of hybrid electronics films, *i.e.* containing a printed component with SMD. Firstly, conductive silver tracks for LEDs powering were screen printed onto a flexible substrate, followed by the assembly of LEDs on its surface. The printed films were then successfully integrated into plastic components through injection molding without degradation of the printed tracks nor any of the materials and devices involved in each production step. Besides, LEDs' displacement was not verified, maintaining their functionality once integrated on the plastic part. Therefore, a functional light-emitting part was achieved, as represented in Figure 1.

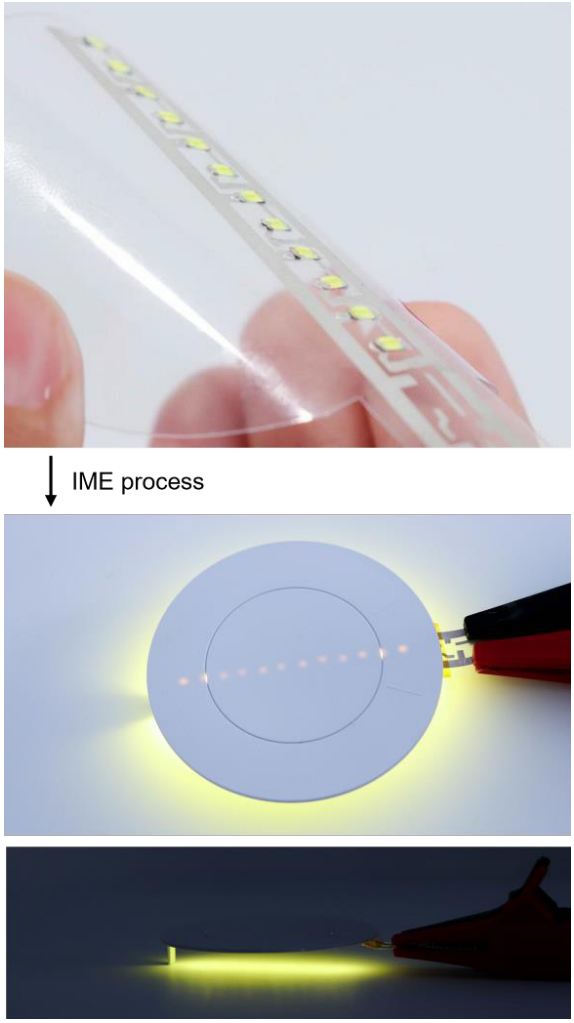

Fig. 1. Demonstration of preliminary test results on the integration of a screen printed film with assembled LEDs (top) on a plastic material through injection molding, achieving a light-emitting IME part (bottom).

Based on the favourable outcome attained in the preliminary tests, which proved the concept of eficiently incorporating a functional electronic film in a plastic component without affecting its initial properties, further electronics will be developed through screen printing and IME in order to achieve more advanced technologies. Under development and future work include a capacitive circuit, the pathways for LEDs powering and the respective control electronics. IME containing printed capacitive sensors will result on a part with touch response capabilities and the incorporation of LEDs will allow for a more appealing light solution. Additionally, through the course of the project, the functionalities inherent to the system will be specified, alongside the configuration of the plastic component's design. Moreover, in addition to injection tests, functional characterization tests and an evaluation of their properties will be conducted.

Acknowledgments

The present study was developed in the scope of the Project "Agenda ILLIANCE" [C644919832-00000035 | Project nº 46], financed by PRR – Plano de Recuperação e Resiliência under the Next Generation EU from the European Union.

References

[1] Y. Khan, A. Thielens, S. Muin, J. Ting, C. Baumbauer, A. C. Arias, A New Frontier of Printed Electronics: Flexible Hybrid Electronics, *Advanced Materials* 32, 1905279 (2020); doi: 10.1002/adma.201905279

[2] M. Beltrão, F. M. Duarte, J. C. Viana, V. Paulo, A review on in-mold electronics technology, *Polymer Engineering & Science* 62(4), 967–990 (2022); doi: 10.1002/pen.25918

DOI 10.5162/EUROSENSORSXXXVI/PT3.114

Precision Detection Unlocked: Electrochemical Sensing of PBTC with Molecularly Imprinted Polymers

Jirawan Jindakaew[1,2], Marie Hangouet[1], Chalita Ratanatawanate[3], Chariya Kaewsaneha[2], Pakorn Opaprakasit[2], Joan Bausells[4], Monique Sigaud[1], Nadia Zine[1], Abdelhamid Elaissari[1], Abdelhamid Errachid[1]*

[1] Universite Claude Bernard Lyon1, ISA, UMR5280, CNRS, 5 rue de la Doua, 69100 Villeurbanne, France
[2] School of Integrated Science and Innovation, Sirindhorn International Institute of Technology (SIIT), Thammasat University, Pathum Thani 12121, Thailand
[3] Environmental Nanotechnology Research Team, Nanohybrids and Coating Research Group, National Nanotechnology Center, National Science and Technology Development Agency, Pathum Thani 12120, Thailand
[4]Instituto de Microelectrónica de Barcelona (IMB-CNM, CSIC), Campus UAB, 08193 Bellaterra, Spain

*Corresponding author: abdelhamid.errachid-el-salhi@univ-lyon1.fr

Summary:

This study introduces a novel approach in creating sensitive and selective sensors for identifying PBTC in aqueous and real-water samples. It is based on the modified surface of Au microelectrodes with molecularly imprinted PDA polymer. The characterization of the resulting microsensor was carried out by using FTIR, CV and EIS techniques. EIS responses of the modified microelectrodes toward PBTC was well-proportional to the concentration in the range from 5−100 mg/mL indicating a good correlation. This developed device can be used for the detection of PBTC in water cooling system.

Keywords: MIPs, microsensor, PBTC, PDA, EIS

Introduction

Traditional methods for assessing orthophosphate concentrations face challenges in terms of cost, time, and complex analysis. Such limitations highlight that an on-site solution for rapid detection is needed to investigate within aquatic systems effectively [1]. In response to this analytical demand, applying molecularly imprinted polymers (MIPs) for electrochemical sensing has emerged as a significant development in environmental monitoring. MIPs are favored for their outstanding physical and chemical stability, high specificity, low-cost production, and quick responsiveness. When integrated with compact electrochemical sensors, the material enables the direct detection of specific substances in real-time with accurate results. Among various MIPs, polydopamine (PDA) stands out for its simple and mild polymerization process, versatility in adhering to a wide range of surfaces, and diverse binding mechanisms [2]. This research introduces a PDA-based MIPs electrochemical microsensor engineered for detecting PBTC—a critical orthophosphate compound used as an antiscalant in cooling water systems. Monitoring PBTC concentrations is crucial for balancing operational efficiency and environmental protection. It ensures the prevention of eutrophication and helps in complying with environmental regulations regarding phosphate discharge [3]. The sensor exhibits remarkable sensitivity and specificity for orthophosphate chemical detection under optimal conditions.

Methods

The surface of Au microelectrodes was cleaned and then immersed in an MHDA solution for an overnight incubation at 4°C. Subsequently, a mixture of EDC/NHS was applied to the prepared Au surface and allowed to react for 30 min at ambient temperature. The seed layer of PDA was then deposited onto the activated surface. Cyclic voltammetry (CV) was utilized to facilitate the electropolymerization of the NIPs and MIPs devices. To eliminate PBTC templates, the MIP chip was placed in 0.2 M H_2SO_4 for a duration of 30 min. Characterization of the resulting samples was conducted by using the CV and electrochemical impedance spectroscopy (EIS) techniques.

Results and Discussion

The surface characteristics of the modified microelectrodes were analyzed using FTIR spectroscopy (see Fig. 1). The analysis confirmed the successful binding of the PBTC template to PDA

by the electropolymerization process. The broad absorption band around 3400 cm^{-1} is attributed to the stretching vibrations of –OH bonds, indicative of the hydroxyl groups present in PDA. Additional peaks were observed, including the N–H band (3084, 1671, and 1559 cm^{-1}), C–H vibrations (2931, 2858, and 1467 cm^{-1}), and the C=O stretch at approximately 1670 cm^{-1}. Furthermore, the MIP spectra demonstrated the presence of a 1709 cm^{-1} peak for C–O stretching of carboxylic groups, and 1422 and 1205 cm^{-1} for the PO group, providing clearly evidence of PBTC incorporation.

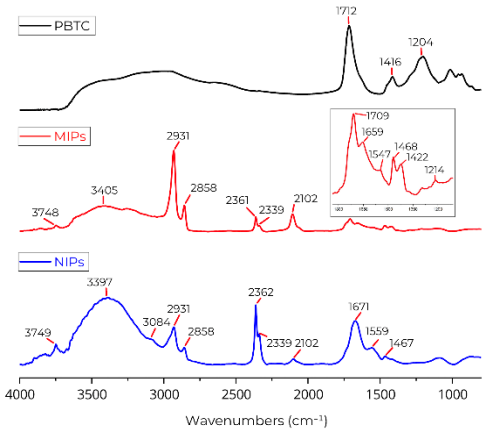

Fig. 1. FTIR analysis of the NIPs, MIPs and PBTC.

The electrochemical behaviors of the bare Au, NIPs, MIPs, extracted MIPs, and rebinding MIPs were evaluated in 5 mM $[Fe(CN)_6]^{3-/4-}$ and PBS solution using CV and EIS techniques (see Fig. 2a). CV results revealed a decrease in the current intensity of redox peaks for the modified electrodes compared to the bare Au. The redox peak of the MIPs was lower than the NIPs sensor, indicating that the reduction of the amplitude voltammogram was attributed to the presence of PBTC. After extraction of PBTC templates, a significant increase in redox peak was due to the PDA matrix providing the imprinted hole promoting the charge transfer.

EIS measurements featured a Nyquist plot where the semicircle at higher frequencies corresponds to electron transfer reactions. The bare Au electrode displayed a minimal electron transfer profile, indicative of a diffusion-driven process with swift electron transfer kinetics. The application of PBTC to the electrode's surface caused a noticeable increase in the semicircle's size on the Nyquist plot, which denotes an obstructive effect of the polymer that impedes electron transfer and increases the resistance to electron circulation. The impedance experienced a pronounced increase post-polymerization, due to the formation of the PDA film encapsulating the orthophosphate compound, which notably impedes electron transfer. The impedance was considerably reduced after the extraction of PBTC, presumably as a result of cavities left by the removed PBTC, thereby the electron transfer process. The semicircle expanded slightly after the PBTC was reintegrated, implying the effective reattachment of PBTC within the MIP at specific binding sites. Additionally, EIS graphs showed significant changes in response amplitudes as the concentration of PBTC increased. This suggests a correlation between the concentration of PBTC and the impedance of the PBTC sensor. Analyzing the data from EIS diagrams enabled the identification of a linear relationship (see Fig. 2b).

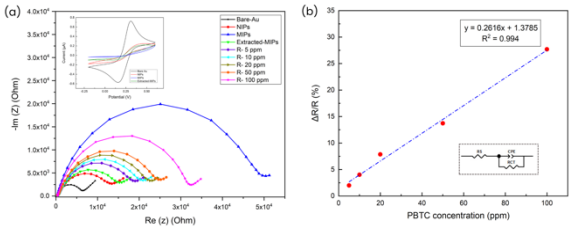

Fig. 2. (a) CV and EIS results and (b) sensitivity of molecularly imprinted microsensor based-on PDA.

Conclusions

This study highlighted the effectiveness of PDA-MIPs in achieving remarkable sensitivity and specificity in PBTC detection, crucial for ensuring operational efficiency and environmental protection against eutrophication. The electrochemical characterization through CV and EIS validated the sensor's ability to select PBTC with considerable precision. The findings, indicating a direct correlation between PBTC concentration and sensor impedance, pave the way for on-site, real-time monitoring of orthophosphate levels in aquatic systems. This breakthrough contributes substantially to the environmental monitoring field by offering a low-cost, efficient, and reliable solution to the challenges posed by traditional methods of phosphate concentration assessment.

References

[1] X. Zhu, J. Ma, Recent advances in the determination of phosphate in environmental water samples: Insights from practical perspectives, *TrAC Trends in Analytical Chemistry* 127, (2020); doi: 10.1016/j.trac.2020.115908

[2] M. Roushani, N. Zalpour, Selective detection of Asulam with in-situ dopamine electropolymerization based electrochemical MIP sensor, *Reactive and Functional Polymers* 169, (2021); doi: 10.1016/j.reactfunctpolym.2021.105069

[3] J. Kretzschmar, A. Wollenberg, S. Tsushima, K. Schmeide, M. Acker, 2-Phosphonobutane-1,2,4,-Tricarboxylic Acid (PBTC): pH-Dependent Behavior Studied by Means of Multinuclear NMR Spectroscopy, *Molecules* 27(13), (2022); doi: 10.3390/molecules27134067

DOI 10.5162/EUROSENSORSXXXVI/PT3.167

$A^{V}B^{VI}C^{VII}$ Semiconductor Materials for Sensing Applications

Daroczi L.[1], Kokenyesi S.[2], Csík A.[3], Csarnovich I.[4]

[1] Department of Solid State Physics, Institute of Physics, Faculty of Science and Technology, University of Debrecen, Debrecen, Bem sq 18/B, Hungary
[2] Department of Electrical Engineering, Institute of Physics, Faculty of Science and Technology, University of Debrecen, Debrecen, Bem sq 18/A, Hungary
[3] HUN-REN Institute for Nuclear Research, Debrecen, Bem sq 18/C, Hungary
[4] Department of Experimental Physics, Institute of Physics, Faculty of Science and Technology, University of Debrecen, Debrecen, Bem sq 18/A, Hungary

Corresponding Author's e-mail address: kiki@science.unideb.hu

Summary:
One-dimensional crystalline materials like SbSI from $A^{V}B^{VI}C^{VII}$ are attractive for application in different mechanical, electrical, optical sensing structures, while a number of two-three component glasses are excellent for patterning. In this paper we present the results obtained by investigations on interconnections between thin layer technology conditions, substrate materials and thin film structures in the direction of obtaining surface structures with different dimensions, applicable for spot- or two-three dimensional sensitive elements.

Keywords: Advanced materials, nanostructures, technology.

Introduction

There has been a growing interest in one-dimensional crystalline materials and structures, made on their basis due to the intensive developments in electronics, photonics towards nano-sized functional elements, enhanced parameters and applicability. Materials from the $A^{V}B^{VI}CV^{II}$ system, like SbSI, BiSI are crystalline while AsSI is usually amorphous glass, all of them are wide-band gap semiconductors photosensitive in 500- 700 nm spectral range. Materials from As-S-I system are amorphous, glassy, with most popular As_2S_3 composition used for very efficient amplitude-phase optical recording media [1,2]. The last may be combined with gold nanoparticles to increase efficiency and incorporate plasmonic effects when the structure is illuminated by resonant wavelength laser beam. An example of laser induced interference pattern on such a structure is presented on Fig.1.Iodine in ternary glass composition may decrease the stability of layers for optical recording, but some very stable, needle-like crystalline elements containing compositions are available. Especially, crystalline SbSI, BiSI are attractive due to the pronounced unidirectional, needle-like structure. SbSI is of main interest due to fact that it is ferroelectric , with the temperature of the ferroelectric phase transition close to 295 K. [3].

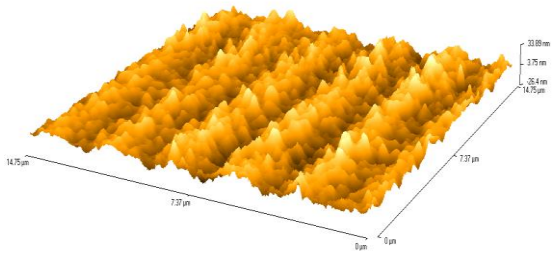

Fig.1. Surface relief recorded by laser beam on As_2S_3-AuNP layer

Such materials are attractive for fundamental research as well as prospective for applications in the fields of ferroelectricity, microelectronics and optoelectronics, as microcapacitors, sensors, solar cell and ultrasound devices [4,5, 6].Continuing our researches in thin film technology of multicomponent chalcogenide semiconductors we performed investigations on interconnections between thermal deposition technology, substrate structure including gold nanoparticles, thermal and e-beam, laser treatment with formation of one-two dimensional structural elements on the surface of separate layers or combined structures.

Technology and methods

Thermal evaporation in vacuum, mostly in special small-volume cells was performed from previously crashed As_2S_3 glass (if optical recording is required on the final structure) or single-crystalline, 5-10 mm long or crashed SbSI or BiSI (see Fig.2), what enables fast evaporation-condensation in thin layers on the surface of different substrates. Among the simplest were pure silica glass and silica glass covered by nanometers-thick gold layers, or gold nanoparticle-islands of 100-200 nm size (see Fig.3). More complex element may include As_2S_3 sub-layer as well. Optical microscope, dual beam scanning electron microscope type Thermo Fisher Scientific-Scios2 (FIB-SEM, Waltham, MA, USA), Horiba LabRam Raman spectrometer, AFM with green laser excitation were used for investigations of structure, it's transformations induced by annealing, laser and e-beam treatments.

Fig.2. Crashed SbSI crystals used for thin film thermal deposition.

Micrometer-thick SbSI layers were deposited on pure silica-glass substrates or on the glass, preliminary covered with a layer of gold nanoparticles with average dimensions in 30-100 nm range (see Fig.3).

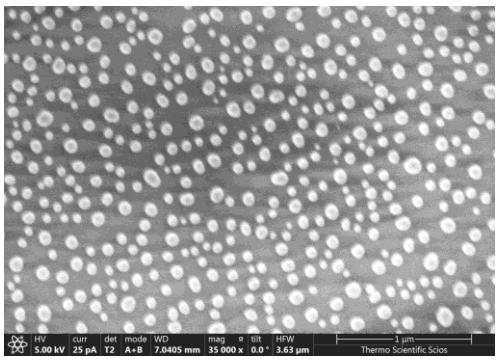

Fig.3. AuNP layer on the glass substrate.

The next step was the SbSI layer deposition.

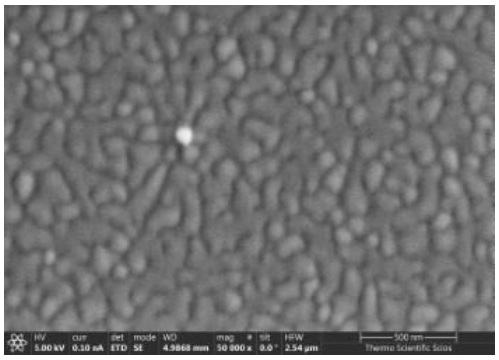

Fig.4. SbSI layer deposited on AuNP covered substrate.

Results

The main result of this experimental cycle consists in establishment of experimental conditions for rather simple fabrication of multicimponent, multifunctional thin layer structures from $A^{V}B^{VI}C^{VII}$ system, which may be used for optical, electrical, mechanical and thermal sensing elements creation, with special accent on possibilities of focused laser-beam recording point-, line-, or two-dimensional structures, photonic crystals. Presence of gold NPs with resonant plasmon excitation in the 510-600 nm spectral range enhances these processes, as it was shown by combined focused laser beam recording - Raman spectra measurements.

References

[1] M.L. Trunov, P.M. Lytvyn, P.M. Nagy, A. Csik, V.M. Rubish, S. Kökényesi. Physica Status Solidi B 251/7 (2014) 1354-1362.

[2] S. Charnovych , N. Dmitruk, N. Yurkovich, M. Shiplyak, S. Kokenyesi. Thin Solid Films 548 (2013) 419–424.

[3] V.M. Fridkin. Ferroelectrics 2 (1971) 119-125.

[4] Selami Palaz, Oral Oltulu, Amirullah M. Mamedov & Ekmel Ozbay, Ferroelectrics, 511/1 (2017) 12-21.

[5] A.Starczewska, M. Kępińska, P. Szperlich, P.Duka, M. Nowak. Optical Materials 100 (2020), 109606.

[6] . M. Voynarovych, A. V. Gomonnaia, A. M. Solomon, Yu. M. Azhniuk, A. A. Kikineshi, V. P. Pinzenik, M. Kis-Varga, L . Daroczy, V. V. Lopushansky. Journal of Optoelectronics and Advanced Materials, 5,(2003) 713 – 718.

DOI 10.5162/EUROSENSORSXXXVI/PT3.168

Photoluminescence Material Based on Arsenic Sulfide Cluster Impregnated in Porous Glasses for Sensing and Detection Applications

Burunkova Julia [1,2], Kokenyesi Sandor [2], Alkhalil George [1]
[1] Centre for Chemical Engineering, ITMO University, Saint Petersburg 197101, Russia,
[2] Department of Electrical Engineering, Debrecen University, Debrecen 4032, Hungary

Corresponding Author's : Dr. Kökényesi Sándor Jenő e-mail : kiki@science.unideb.hu

Summary:
We study the photoluminescence of new nanocomposite material consisting of arsenic sulfide doped in porous glasses and the effect of photoinduced structural transformations on it. Strong photoluminescence signal was observed in the samples when excited with lasers with excitation wavelengths of 405 and 532 nm. Also, the effect of laser irradiation on the photoluminescence of the samples was studied using confocal microscope with two different operating lasers 405 and 514 nm. It was observed that laser irradiation influences photoluminescence differently depending on the irradiation wavelength. Also, it was recording photonic structure on this material. Thus, the material combines the properties of photonic crystals and luminescent materials, allowing for both optical recording and luminescence emission, making it versatile for a range of sensing applications.

Keywords: Arsenic sulfide, photoinduced structural transformations, porous glasses, photoluminescence, photonic structure

Background, Motivation an Objective

Kolomiets' research group was the first to observe photoluminescence (PL) in arsenic sulfide glasses, which has since been widely studied by others [1, 2], taking into account factors such as composition, temperature, and excitation spectra. This paper focuses on the investigation of PL in arsenic sulfide doped in porous glasses (As2S3-PG nanocomposite) using various excitation wavelengths. The effects of gold nanoparticles on the intensity of PL are also presented, along with the influence of irradiating the samples using different lasers on their PL, as well as effects when recording photonic structure on a material. Synthesis and characterization of the optical properties of materials especially at a nanoscale and at a photonic structures is considered as important tasks for the engineering of photonic devices and systems.

Description of the New Method or System

The As2S3 doped porous glasses were prepared by dissolving As2S3 in propylamine and adding the porous glasses to the solution, followed by annealing. Here the photoinduced changes in the PL emission observed in the As2S3-PG composite were utilized for the recording of optical structure – a grating using TEM grating mask and a laser with 532 nm wavelength. Thus, a new As2S3-PG composite material was obtained that combines the properties of photonic crystals and luminescent materials, allowing for both optical recording and luminescence emission.

Results

The photoluminescence (PL) spectra of the As2S3-PG samples were measured under excitation with 405 nm and 532 nm lasers. To obtain more detailed information about the PL centers, deconvolution was performed due to the presence of multiple Gaussian peaks in the PL spectra. The peaks obtained from the deconvolution process and the PL spectra are shown in Fig. 1. The results indicate the presence of a broad and intense band at 511 nm when excited with a wavelength of 405 nm (Fig. 1a). The PL spectrum excited with 532 nm is dominated by a broad emission band centered around 596 nm with shoulder around 630 nm. The PL observed in the As2S3-PG samples investigated in this research does not conform to the established EPL ≈ Eg/2 rule that typically characterizes the intrinsic properties of chalcogenide glasses [2]. This could be attributed to the fact that the observed PL emission is originating from arsenic sulfide nanoparticles rather than its bulk form.

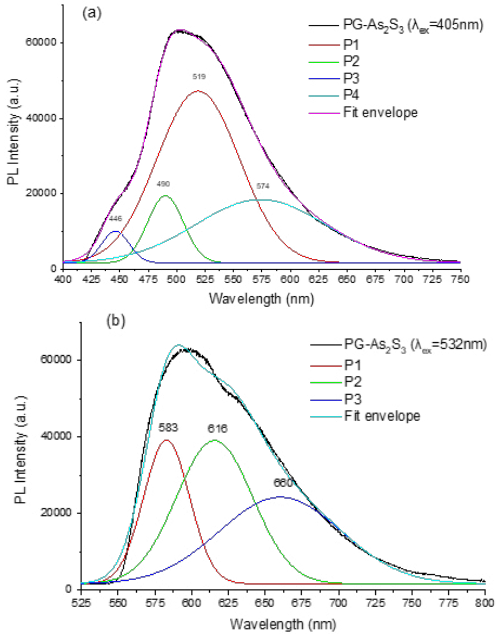

Fig. 1. Deconvoluted experimental PL spectra of As2S3-PG when excited with (a) 405 nm laser and (b) 532 nm laser. Deconvoluted spectra are represented by curves P1, P2, P3 and P4. The resulted sum of the deconvoluted spectra is represented by curve fit envelope.

The effect of AuNPs on the PL emission of As2S3-PG samples was investigated using confocal luminescent scanning microscopy (Fig. 2). Samples with and without AuNPs were analyzed, with both having the same concentration. The results showed that the presence of AuNPs led to a decrease in the PL emission intensity of As2S3-PG by 40% for excitation at 405 nm and by 30% for excitation at 514 nm. This effect was attributed to the strong semiconductor-metal coupling between As2S3 and Au, which resulted in the suppression of the plasmonic resonance of AuNPs and the quenching of excited states in As2S3.

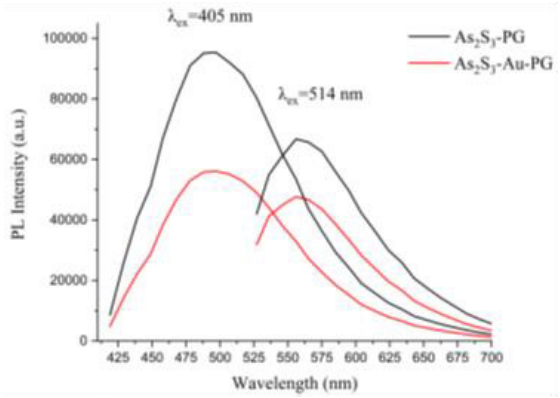

Fig. 2 - PL spectra of As2S3-PG (black curves) and As2S3-Au-PG (red curves) when excited at 405 nm and 514 nm.

The effect of irradiation with different photon energies on the PL emission of the samples was investigated. Under excitation with a 514 nm laser beam, the PL intensity of the samples decreased by 58% and 64% after irradiation with 405 nm and 514 nm lasers, respectively. Irradiation with a 405 nm laser beam resulted in a decrease in PL intensity in the irradiated region by 83% with the same laser but increase by 39% in regions irradiated with 514 nm. This effect is attributed to photoinduced structural transformations dependent on the laser wavelength. The decrease in PL intensity at 514 nm after irradiation can be explained by an increase in the bandgap energy of the samples caused by the irradiation. Increasing the bandgap energy brings the excitation wavelength at 405 nm closer to the resonant absorption-reemission wavelength, resulting in an increase in PL intensity. The formed nanocrystals have a relatively wide bandgap energy and exhibit PL emission in the 490 nm range. The photoinduced changes in the PL emission observed in the As2S3-PG composite were utilized for the recording of optical structure using the former technique and was studied by a confocal microscope (Fig. 3).

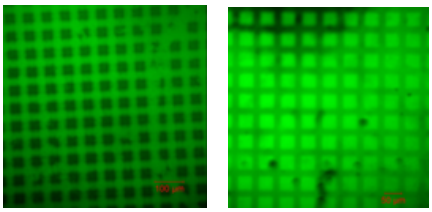

Fig. 3. Confocal microscope image of the recorded TEM grating in the reflected mode, when excited at (left) 514 nm and (right) 405 nm.

It is clear that when viewing the recorded grating with green laser it shows a converted image of what appears with blue laser. The composite material was shown to be effective in utilizing photoinduced changes for optical recording of photonic structures, which makes it suitable for sensing applications [3].

References

[1] B. Kolomiets, T.Mamontova, Radiative Recombination in Vitreous and Single Crystal As2S3,J.Non. Cryst.Solids, 4(C), 289–294(1970); doi:10.1515/9783112472743-044

[2] K. Murayama, Luminescence and Optically Detected ESR in A-As2S3, J. Non. Cryst. Solids, 35–36(2), 915–920(1980); doi:10.1016/0022-3093(80)90317-8

[3] L.Borodina, V.Borisov, Nanostructured Luminescent Gratings for Sensorics, Materials (Basel), 15(22) (2022); doi: 10.3390/ma15228195

DOI 10.5162/EUROSENSORSXXXVI/P3.171

Solvothermal synthesis of highly dispersed Pd-decorated ZnO with high sensitivity to acetone

Artem Mokrushin[1], Alexey Vasiliev[2,3], Nikolay Simonenko[1], Ilya Nagornov[1], Elizaveta Simonenko[1]

[1] Kurnakov Institute of General and Inorganic Chemistry of the Russian Academy of Sciences, Leninsky av. 31, 119991, Moscow, Russia
[2] Dubna state university, Universitetskaya strt., 19, 141980, Dubna, Moscow region, Russia
[3]LLC "C-Component", Tushinskaya 17, Moscow, 125362, Russia

Corresponding Author's e-mail address: A-A-Vasiliev@yandex.ru

Summary:
The present work describes a relatively simple and easily scalable synthesis procedure of highly dispersed zinc oxide decorated with nanoscale palladium. The nanopowder has been characterised using a number of physical and chemical analytical techniques (DSC/TGA, XRD, SEM, TEM, XPS, EDX). The glass-ceramic MEMS-type microhotplate fabricated by screen-printing process was used for the deposition of the sensing layer. It is shown that the nanomaterial based on palladium-decorated zinc oxide shows a high response to ultra-low acetone concentrations.

Keywords: MOS-gas sensor, zinc oxide (ZnO), palladium (Pd), ceramic MEMS, acetone.

Introduction

Many international organizations, in particular the World Health Organization (WHO), Pan American Health Organization (PAHO), European Environment Agency (EEA) and the United Nations (UN), in their updated roadmaps further emphasize the need for various activities and research on public health (including primary and community healthcare (P&CHC) and environmental protection [1]. Due to this agenda, the requirements to environmental and biosphere monitoring devices are increasing significantly. The development of new relatively simple and easily scalable methods for the synthesis of basic MOS materials as well as methods for their modification is one of the most important tasks for the development of modern gas sensors as well as multisensor electronic nose technologies. On the other hand ,the application of "nano-on-micro" approach with nano-particle sensing material deposited on microfabricated hotplate is important trend in sensor development. Earlier in our research group, nanomaterials based on individual zinc oxide [2], including those decorated with platinum [3, 4], were obtained by the solvothermal method using various solvents.

Materials and Methods

The present work describes a relatively simple and easily scalable synthesis of highly dispersed zinc oxide decorated with nanoscale palladium. ZnO obtained by thermal degradation of zinc acetylacetonate hydrate in *n*-butanol [2] was used for the synthesis of ZnO-xPd nanocomposites (x=0.5 mol.%). Palladium (II) chloride $PdCl_2$ was used as a precursor of palladium nanoparticles. A pre-calculated amount of palladium (II) chloride was added to the dispersion of zinc oxide in ethylene glycol, and the dispersion was subjected to thermal treatment. The obtained powder after separation, drying and additional heat treatment was used to prepare a paste. The nanopowder was characterized using different physical and chemical analysis methods (DSC/TGA, XRD, SEM, TEM, XPS, EDX).

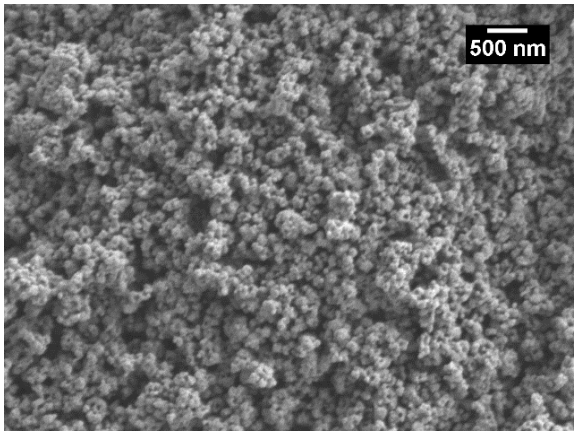

Fig. 1. SEM-micrograph of Pd-decorated ZnO powder

The sensing material was deposited onto the ceramic MEMS platforms using microextrusion printing system developed at the Institute of inorganic chemistry of RAS. The platforms were

cantilever-type structures made using screen-printing process with the application of sacrificial layer washable away after firing in a ultrasonic bath. The cantilever was equipped with microheater made of platinum composite material, the body of the microhotplate and isolation between microheater and sensing layer were made of composite containing alumina microparticles and SiO_2-B_2O_3-BaO-CaO-MgO-Al_2O_3 glass [5]. The electric leads to the sensing layer and to the microheater were made of platinum. The size of the chip was adjusted to the pin alignment of TO5 holder. The chip was fixed to the pins of TO5 with silver glue, which doesn't interact with other elements of the sensor at low temperature of the frame.

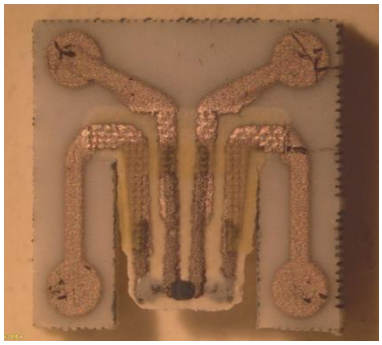

Fig. 2. Screen-printed cantilever type ceramic microhotplate with deposited sensing layer.

The cantilever type microhotplate with deposited sensing material is presented in Fig. 2. The microhotplate consumes approximately 120 mW of heating power at 450^{0}C.

Results

According to XRD data, ZnO powder has a crystalline structure of wurtzite phase (P63mc, PDF 01-070-8070). According to SEM data (Fig.1), ZnO consists mainly of nanoparticles with the size of 58±8 nm.

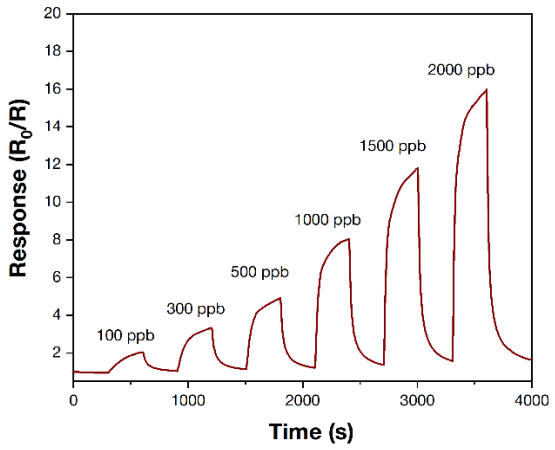

Fig. 3. Responses to 100-2000 ppb acetone at 300°C of Pd-decorated ZnO film

According to TEM data, Pd nanoparticles with an average size of 4±0.7 nm are located on the surface of ZnO. According to XPS data Pd is in oxidised state.

For the obtained ZnO-Pd film the gas-sensitive properties to a large number of analyte gases (CO, NH_3, NO_2, benzene (C_6H_6), acetone (C_3H_6O), ethanol (C_2H_5OH), H_2, methane (CH_4)) at 150-300°C were comprehensively studied.

It is shown that the highest response is observed when acetone is detected at 300°C. This temperature was tested and stabilized using pre-measured temperature coefficient of resistance (TCR) of the microheater. Fig.3 shows the responses (R/R_0) for 100-2000 ppb of acetone, which lie in a range from 2 to 16.

Thus, the obtained Pd-decorated ZnO nanomaterial shows high response to ultra-low acetone concentrations.

Acknowledgement

The research was supported by the Russian Science Foundation grant № 24-13-00254, (https://rscf.ru/project/24-13-00254/)

References

[1] C. Change, The essential environmental public health, Pan American Health Organization. (2021).

[2] I.A. Nagornov, A.S. Mokrushin, E.P. Simonenko, et al, Zinc oxide obtained by the solvothermal method with high sensitivity and selectivity to nitrogen dioxide, Ceramics International. 46 (2020) 7756–7766. https://doi.org/10.1016/j.ceramint.2019.11.279.

[3] A.S. Mokrushin, I.A. Nagornov, E.P. Simonenko, et al, Chemoresistive gas-sensitive ZnO/Pt nanocomposites films applied by microplotter printing with increased sensitivity to benzene and hydrogen, Materials Science & Engineering B. 271 (2021) 115233. https://doi.org/10.1016/j.mseb.2021.115233.

[4] A.S. Mokrushin, I.A. Nagornov, E.P. Simonenko, et al Effect of platinum nanoparticles on the chemoresistive gas sensitive properties of the ZnO/Pt composite, Ceramics International. 49 (2023) 17600–17610. https://doi.org/10.1016/j.ceramint.2023.02.126.

[5] Oleg Kul, Alexey Vasiliev, Andrey Nikitin, Anna Dmitrieva, Alexandr Bolshakov. Screen-printed ceramic MEMS for metal oxide gas sensor. MDPI Proceedings, 2024, 97(1), 128.

DOI 10.5162/EUROSENSORSXXXVI/PT3.299

Effective neutron absorption and conversion with thin $^{10}B_4C$ layers

Z. Zolnai[1], Z. Kis[2], N. Q. Khánh[1], Z. Kovács[1], G. Battistig[1], L. Szentmiklósi[2], and J. Volk[1]
[1] Institute of Technical Physics and Materials Science, HUN-REN Centre for Energy Research, Konkoly Thege Miklós út 29-33, H-1121 Budapest, Hungary
[2] Nuclear Analysis and Radiography Department, HUN-REN Centre for Energy Research, Konkoly-Thege Miklós út 29-33., H-1121 Budapest, Hungary

Corresponding Author's e-mail address: zolnai.zsolt@ek.hun-ren.hu

Summary:
Isotopically enriched boron carbide $^{10}B_4C$ thin layers were deposited on Si substrates using pulsed DC sputtering technique. The surface density of ^{10}B atoms vs. layer thickness was determined from SEM/EDS and proton backscattering spectrometry experiments. Good agreement was found between measured and calculated neutron absorption efficiencies when considering beam hardening of the poly-energetic cold neutron beam. The optimal layer thickness for maximum neutron absorption and ionoluminescence yield induced by the $^{10}B(n,\alpha)^7Li$ reaction products in a scintillator was ascertained.

Keywords: boron carbide, sputtering, thin layer, neutron absorption, charged particle detection

Background

Scintillation based neutron detector systems consist of a converter material, which interacts with neutrons and produces charged particles, and a scintillator material, which converts ionizing radiation into photons to be detected. Ongoing efforts for improved neutron detection capabilities aim to develop and deploy new converter/scintillator materials and optimized detector design.

Boron-based neutron absorbers offer a promising alternative to commercialized competitors, e.g. ^6Li-based ones. First, there is ca. four times higher capture cross-section of ^{10}B for thermal (cold) neutrons as compared to that of ^6Li. Secondly, lower kinetic energy (2.31 or 2.79 MeV) in the $^{10}B(n,\alpha)^7Li$ reaction is distributed on the daughter products as compared to the $^6Li(n,\alpha)^3H$ reaction with a higher energy release of 4.78 MeV (Therefore, there are shorter stopping ranges of the reaction products in the absorber and in a coupled scintillator layer for ^{10}B as compared to ^6Li), enabling significantly reduced neutron absorber thickness and also, more confined light production volume for scintillation-type ^{10}B-based neutron detector structures. In addition, similar size reduction on the lateral scale may result in enhanced lateral resolution for the neutron detection process.

A promising B-containing neutron absorber material is boron carbide, B_4C [1] with unique combination of properties beneficial for a wide range of applications in nuclear science and beyond. The high melting point (~2450 °C) and thermal stability enable its use in refractory applications. Due to its extreme abrasion resistance, it is applied as abrasive powders and coatings; it also excels in ballistic performance due to its low density and high hardness. Moreover, crystalline B_4C is a high-temperature semiconductor that can potentially be used for novel electronic applications.

A simple construction for neutron detection is a thin B_4C neutron absorber layer atop an efficient scintillator substrate. In this case, 1.47-MeV α and 0.84-MeV Li^+ particles, emitted in the $^{10}B(n,\alpha)^7Li$ reaction induce light emission, i.e., ionoluminescence (IL) in the scintillator. A promising scintillator material is e.g. Al_2O_3, with high radiation resistance and intense IL light emission [2]. Geometrical optimization based on well described energy conversion processes in the $^{10}B_4C/Al_2O_3$ system results in effective neutron capture and detection.

Methods

Isotopically enriched $^{10}B_4C$ layers were deposited on Si substrates by pulsed DC-sputtering. The thickness and atomic composition of the layers were measured by SEM/EDS and 1.6 MeV H^+-RBS. Neutron absorption experiments were performed with a poly-energetic cold neutron beam at the NORMA station of the Budapest Neutron Centre (BNC) [3, 4] equipped with

a ^{6}LiF:ZnS(Cu) scintillation screen and an Andor iKon-M 934 type CCD camera.

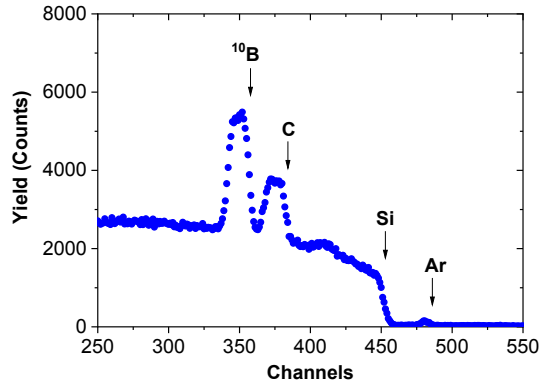

Fig. 1. 1.6 MeV proton-RBS spectrum of a $^{10}B_4C$ layer deposited on Si substrate. Arrows represent spectral edges for the different components in the sample.

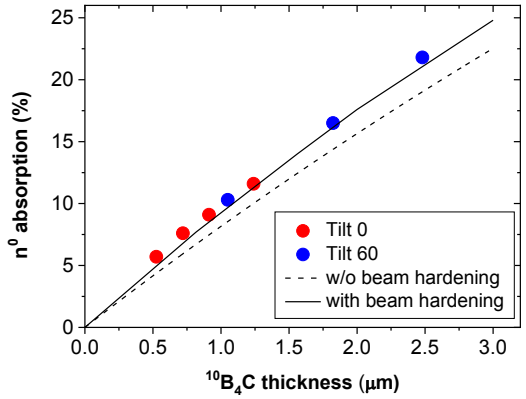

Fig. 2. Neutron absorption as a function of deposited $^{10}B_4C$ layer thickness. Dots represent experimental data recorded at 0° and 60° sample tilt angle, while the solid (dotted) line shows calculated values with (without) taking into account the $^{10}B_4C$ layer induced beam hardening for neutrons reaching the ^{6}LiF:ZnS(Cu) scintillation screen.

Results

Fig 1 shows a typical proton-RBS spectrum of a $^{10}B_4C$/Si sample. Enhanced elastic scattering cross section of protons for ^{10}B and C enables compositional and thickness analysis for the $^{10}B_4C$ layer with good accuracy and therefore the total number of ^{10}B isotopes/cm^2 can be evaluated. Some Ar content remaining in the layer after the sputter deposition process can be recognized. Fig. 2 shows neutron absorption as a function of deposited $^{10}B_4C$ layer thickness. NORMA measurements were performed on the absorber layers at two different sample tilt angles of 0° and 60° with respect to the neutron beam. As the solid line show, good agreement between measured and calculated absorption values can be obtained when the $^{10}B_4C$ layer induced beam hardening for the polyenergetic neutron beam, reaching the ^{6}LiF:ZnS(Cu) scintillation screen after crossing the sample, is taken into account.

When the Si substrate is replaced by a scintillator material, e.g. Al_2O_3, neutron induced energetic α and Li^+ particles, emitted by the $^{10}B_4C$ layer generate light during their electronic stopping in Al_2O_3. The optimal $^{10}B_4C$ layer thickness for maximum IL intensity can be determined considering well described ion-solid interactions, energy conversion processes, and system geometry. More details on such calculations and the related results will be presented.

References

[1] V. Domnich, S. Reynaud, R. A. Haber, and M. Chhowalla, Boron Carbide: Structure, Properties, and Stability under Stress, *Journal of the American Ceramic Society* 94, 3605–3628 (2011); doi: 10.1111/j.1551-2916.2011.04865.x

[2] G. M. Akselrod, M. S. Akselrod, E. R. Benton, and N. Yasuda, A novel Al_2O_3 fluorescent nuclear track detector for heavy charged particles and neutrons, *Nuclear Instruments and Methods in Physics Research* B 247, 295–306 (2006); doi: 10.1016/j.nimb.2006.01.056

[3] Z. Kis, The redesigned neutron imaging facility, NORMA at BNC, Budapest, *Rev. Sci. Instrum.*1, 95 (7): 073702 (2024); doi: 10.1063/5.0208844

[4] https://bnc.hu/norma/

DOI 10.5162/EUROSENSORSXXXVI/PT4.2

Assessing Multiple Myeloma Using Photoacoustic Spectrum Detection Method

Chi-Chang Chang
School of Medical Informatics, Chung Shan Medical University & IT office, Chung Shan Medical University Hospital, Taichung 40201, Taiwan

Corresponding Author's e-mail address changintw@gmail.com

Summary:
This study uses photoacoustic detection spectroscopy to develop a spectroscopic detection system and evaluate the feasibility of multiple myeloma. At the current stage, circuit board development has been completed and a synchronized photoacoustic detection platform for finger and test tubes has been established. This study found that a single-wavelength photoacoustic detection platform can be used to measure blood oxygen saturation. Furthermore, it was discovered that there is a corresponding relationship between the photoacoustic amplitude and the cysteine concentration. In the future, the cysteine solution concentration can be derived from the photoacoustic amplitude detected by the system.

Keywords: multiple myeloma, photoacoustic microscopy (PAM), photoacoustic (PA)

Introduction

Multiple myeloma (MM) is the second most common tumour of the hematologic system, affecting 488,000 people worldwide [1]. The treatment of MM cancer patients poses a significant challenge for physicians. However, continuous monitoring of progression and its effects on medications can be a helpful observational indicator for the treatment of multiple myeloma.

The principle of photoacoustic effect is that when an object absorbs laser energy, it generates ultrasonic waves. When the excited ultrasonic signals and the echo of the photoacoustic signal is detected using piezoelectric elements, the influence of light scattering is theoretically avoided. There are no concerns about radiation such as X-rays or CT scans, and the images are generated. Previous studies have shown that photoacoustic microscopy (PAM) can non-invasively measure and detect the reduced vascularization around hypoxic blood in patients with multiple myeloma using photoacoustic technology [2,3,4]. This project aims to implement a non-invasive photoacoustic detection system to evaluate patients with diabetes mellitus (DM) and multiple myeloma using urine, ex vivo blood, and finger vasculature. The goal is to observe whether simultaneous control of blood glucose can achieve therapeutic effects for multiple myeloma.

The photoacoustic detection system utilises an FPGA chip to control a laser with a wavelength of 638 nm for irradiation. When the samples in the test tube and the finger are irradiated with laser light, a photoacoustic effect occurs sequentially. The system uses piezoelectric ceramic elements to receive the photoacoustic signals from the samples, followed by three-stage amplification circuits for signal amplification, and uses a data acquisition system (DAQ) to capture the photoacoustic signals.

Method

In the laser-induced photoacoustic (PA) process, the acoustic signal, as described in reference [5], is generated due to the thermal expansion of the sample after absorbing optical energy. In this case, blood vessels act as the absorber, and we can obtain the PA signal:

$$P = A(\varepsilon_{HbO2}C_{HbO2} + \varepsilon_{HbR}C_{HbR}) \quad (1)$$

ε_{HbO2} and ε_{HbR} represent the absorption of oxyhemoglobin and hemoglobin, C_{HbO2} and C_{HbR} are for the blood oxygen concentration, as in Eq. (1), let red is $[\mathrm{HbO2}]$, $Green$ is$[Hb]$, eq. (1) can be simplified as follows:

$$P = (A_1C_{red} + A_2C_{green}) \quad (2)$$

whileλ is 658 nm:

$$A_1 = A \times \varepsilon_{HbO2} = 0.07A$$

$$A_2 = A \times \varepsilon_{HbR} = 0.81A$$

When the blood oxygen saturation is 99%, as in, e.g. (2)

$$P = (A_1C_{red} + A_2C_{green})$$

$$= (A_1 \times 0.99R + A_2 \times 0.01R)$$

$$= (0.0693 \times AR + 0.081 \times AR) = 0.0774AR$$

When the blood oxygen saturation is 97%, as in, e.g.

(2)

$$P = (A_1 \times 0.97R + A_2 \times 0.03R)$$

$$= (0.0679 \times AR + 0.0243 \times AR) = 0.0922AR$$

The constant AR is denoted as C, and the table below shows the signal size of P at various concentrations.

Tab. 1. 90~99% SO_2 V.S. SIGNAL SIGNAL SYSTEM P

Measure Signal	SO_2									
	90%	91%	92%	93%	94%	95%	96%	97%	98%	99%
P	0.144C	0.137C	0.129C	0.122C	0.114C	0.107C	0.099C	0.092C	0.084C	0.077C

The current system architecture measures the obtained signals, defining the maximum amplitude in the signal as peak-to-peak intensity. As shown in Fig. 1., $M_{pp(N)}$ represents the peak-to-peak value, which is the maximum value minus the minimum value in the signal [6].

$$M_{pp} = M_{max} - M_{min} \quad (5)$$

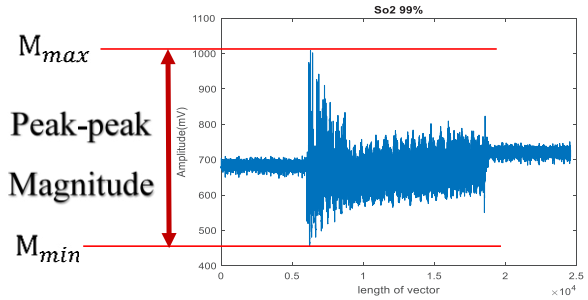

Fig. 1. Peak to peak voltage

Results

After experimental testing, the sensitivity of the photoacoustic signal at six different positions on the meshed piezoelectric ceramic plate was examined. Position B exhibited a more pronounced sensitivity, as shown in Fig. 2, where the values at Position B stand out. Following statistical analysis, Table 9 clearly indicates that the average value is around 3.09 mV, with a standard value range of approximately ±5.42 for position B. It can be observed that the response of Position B to the photoacoustic effect is more significant.

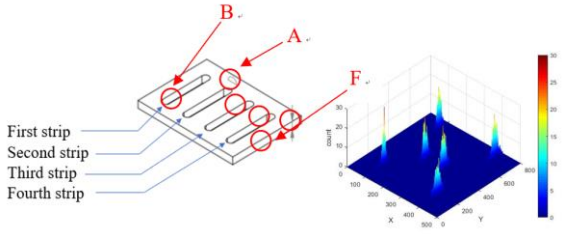

Fig. 2 Piezoelectric ceramic plate schematic and photoacoustic signal feedback distribution diagram

Tab. 2: Photoacoustic response of laser at six different positions on the meshed piezoelectric ceramic plate

650nm	A	B	C	D	E	F
mean	3.09	3.09	3.09	3.09	3.09	3.09
$\pm sd$(mV)	±4.57	±5.42	±5.09	±5.27	±4.72	±5.26
532nm	A	B	C	D	E	F
mean	3.09	3.09	3.09	3.09	3.09	3.09
$\pm sd$(mV)	±5.82	±6.48	±6.03	±6.00	±6.15	±6.00

The development of the optoacoustic platform has been completed in research, and the first version of the hardware prototype has been developed and released. Modifications were made to address issues from the previous version, and a second complete version was introduced. Using the hardware prototype of the first version, along with software development and multiple improvements in mechanical design, the entire optoacoustic platform system was integrated. The development included finger detection and test tube sample detection systems. The final product is shown in Fig. 3, with Fig. 4 depicting the finger measurement area, Fig. 5 showing the test tube measurement area, and Fig. 6 illustrating the system's operating interface.

Fig. 3. Completed design of the optoacoustic platform

Fig. 4. Area for finger measurements

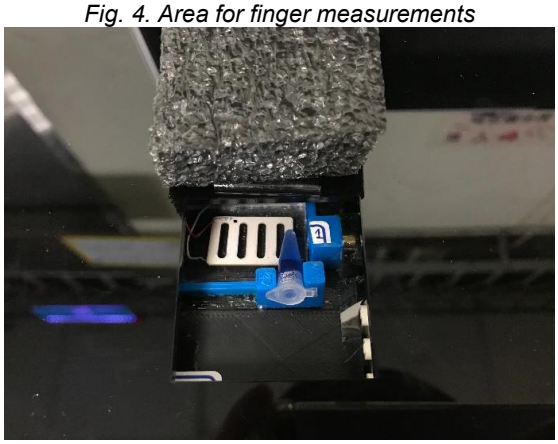

Fig. 5 Area for tube measurements

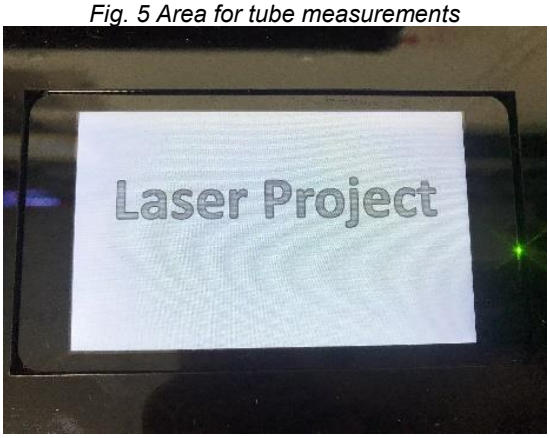

Fig. 6a. Operating interface of the system

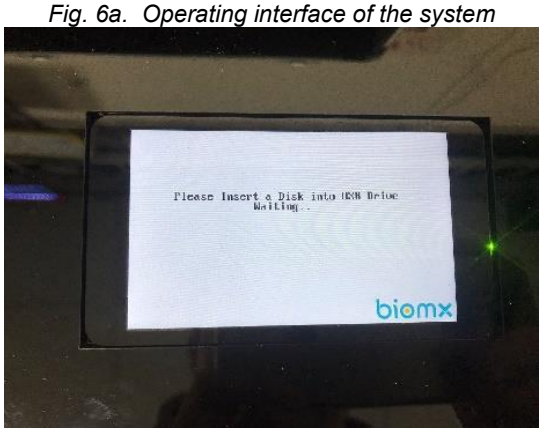

Fig. 6b. Operating interface of the system

Fig. 6c. Operating interface of the system

The optoacoustic tube detection platform allows for simple testing by inserting the sample tube into the designated mechanism. The input consists of a laser light source (usually at 640nm) and the echoed ultrasound signals can be quickly sampled by the system in real time for analysis, allowing for feature extraction based on the echoed signals.

References

[1] C. Tang, H. Hou, K. Huang, H. Qiu, Y. Liu, Treatment evolution and improved survival in multiple myeloma in Taiwan. *Ann Hematol.* 99(2), 321-330, (2020); doi: 10.1007/s00277-019-03858-w.

[2] [2] B. Cox, J. G. Laufer, S. R. Arridge, P. C. Beard, Quantitative spectroscopic photoacoustic imaging: A review," J. Biomed. Opt., 17, p. 061202, (2012); doi: 10.1117/1.JBO.17.6.061202.

[3] [3] L. V. Wang, Multiscale photoacoustic microscopy and computed tomography, Nature Photon., 3, 503-509, (2009); doi.org/10.1038/nphoton.2009.157

[4] [4] L. V. Wang, S. Hu, Photoacoustic tomography: In vivo imaging from organelles to organs, Science, 335, 1458-1462, (2012); doi: 10.1126/science.1216210.

[5] [5] A. Danielli, C.P. Favazza, K. Maslov, L. V. Wang, Single-wavelength functional photoacoustic microscopy in biological tissue, Opt. Lett., 36, 769-771, (2011)

[6] [6] W. B. Gratzer, Med. Res. Council Labs, Holly Hill, London.

DOI 10.5162/EUROSENSORSXXXVI/PT4.12

SNR Enhancement of a MEMS Thermal Acoustic Pressure Sensor

Akash Gupta[1], Achim Bittner[1], Alfons Dehé[1,2]
[1]Hahn-Schickard, Wilhelm Schickard Straße 10, 78052 Villingen-Schwenningen, Germany,
[2]Georg H.Endress Chair for Smart Systems Integration IMTEK, University of Freiburg, Germany

akash.gupta@hahn-schickard.de

Summary:
In this work, we investigate the different internal noise mechanism affecting the performance of our MEMS based dynamic pressure sensor based on thermal anemometric principle [1]. We present sensitivity and noise measurements for two different chip designs for a comparative analysis with theoretical values. Finally, we show that the design modification resulted in the enhancement of the Signal to Noise ratio (SNR) by 30 dB and the dynamic pressure detection lower limit by a factor by 20 dBSPL.

Keywords: thermal noise, acoustic, dynamic pressure, thermal sensor, lock-in amplifier

Motivation

To understand the performance limitations of our dynamic pressure sensor by measuring and calculating various internal noise affecting the sensor performance and develop a deeper understanding about the SNR enhancement via chip design modification.

Sensor Description and Noise Sources

The thermal flow sensor consisting of a heater and thermal sensors (thermopiles in this case) is modified by etching micro perforations with different dimensions as shown in Fig.1.

A periodic acoustic pressure difference across the membrane creates an oscillating flow through the perforations. This causes temperature oscillation (at double the acoustic frequency) at the right thermopile (TPR) which is measured as a voltage difference as shown in Fig 2.

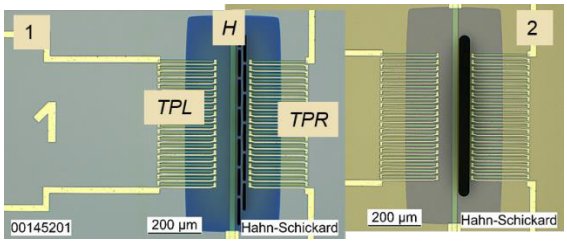

Fig 1: Top view of the fabricated chip design 1 (13 slits, 100 µm long, 10 µm wide) and design 2 (1 slit, 600 µm long, 40 µm wide) indicating the sensing thermopiles on right / left (TPR / TPL) and the heater in the center

The two internal noise affecting the system are discussed below.

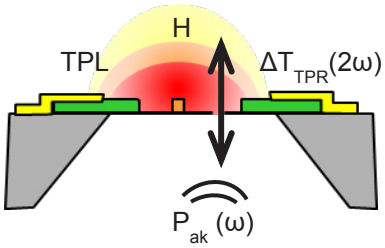

Fig 2: Side sketch of the sensor indicating input acoustic pressure generates an acoustic flow via the perforation that leads to a temperature (or Seebeck Voltage) oscillation at double frequency at the right thermopile TPR

1. Viscous Slit (Thermal-acoustic) Noise

This noise originates from the movement of particles in the slit due to thermal energy. It depends on the viscous resistance offered by the slit, the temperature of the gas molecules and is given as [2]

$$v_{n,ak}=\sqrt{4K_B T_{amb} R_{v,s}}\ [Pa/Hz^{0.5}] \quad (1).$$

The viscous resistance of chip 1 is almost 100 times higher than chip 2 due to the inverse cubic dependence on the width of the slit. This results in the acoustic slit noise of around 2.2 µPa for chip 1 and 0.2 µPa for chip 2 (in 1Hz BW) which is significantly lower than the SPL generated by the loudspeaker at a frequency of 20 Hz and hence not the limiting noise to our sensor.

The big advantage is that by decreasing the acoustic resistance, we reduce this noise on one hand but we increase the sensitivity on the other hand. The bigger slit offers lower viscous resistance. This allows for more volume flow that

eventually leads to higher temperature oscillations at the right thermopile.

2. Thermal Noise

This is the noise originating at the Thermopile (TP) due to its electrical resistance and it limits the lower temperature detection level. It is given by [2]

$$v_{n,th}=\sqrt{4K_B T_h R_{el,TP}}\ [V/Hz^{0.5}] \quad (2).$$

The thermal noise is calculated for both the chip designs as per Eq 2 and the results are summarized in Table 1.

Tab. 1: Thermal noise calculations for the right thermopile (TPR) for both the chip designs

Chip design	$R_{el,TPR}$ measured value	Calculated thermal noise using eq. 2
1	24.5 KΩ	20 nV/Hz$^{0.5}$ (-154 dBV/ Hz$^{0.5}$)
2	21.0 KΩ	18.6 nV/Hz$^{0.5}$ (-154.6 dBV/Hz$^{0.5}$)

Measurement Results and Discussion

The heater operates around 80°C above the room temperature. For a constant acoustic frequency of 20 Hz, the 40 Hz component of the TPR voltage is demodulated and plotted over an acoustic pressure sweep as shown in Fig. 3.

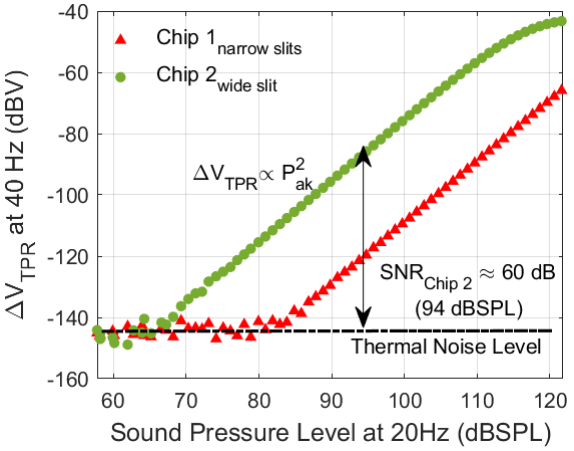

Fig 3: Pressure sensitivity measurements for both the chip designs at a frequency of 20 Hz. The SNR for chip 2 at 94 dBSPL is indicated

The sensitivity increases quadratically with the acoustic pressure in both the chip designs. However, the sensitivity of chip 2 is around 30 dB higher than chip 1 due to reduced acoustic slit resistance. However, the noise level remains the same for both the designs indicating that the thermal noise is the limiting factor in our sensor.

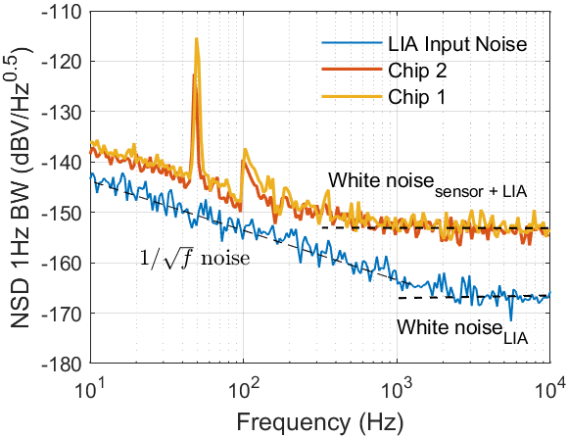

Fig 4: Noise measurements for the Lock-in amplifier (LIA) and the TPR of both the chip designs. The Flickr noise ($1/\sqrt{f}$) dominates at lower frequencies and the White noise dominates at higher frequencies

The noise measurements are performed inside an acoustic chamber to avoid any acoustic disturbances and to isolate from the external noise and are plotted in Fig 4. We can see that the noise spectrum contains Flickr noise that shows $1/\sqrt{f}$ response up to ~1 KHz (for Lock-in amplifier) and then the white noise starts to dominate and has flat response. For both the chips, the noise is almost similar and shows the similar response as the Lock-in amplifier (LIA) noise.

We can also see that the noise values calculated in Table 1 very accurately match the thermal noise level as shown in the measurements in Fig 4. The thermal noise level indicated in Fig 3 also closely corresponds to the noise values at 40 Hz as seen from the noise measurements in Fig 4.

Conclusion

The modification of the slit design increases the sensitivity without affecting the noise floor of the sensor. This eventually leads to an increased SNR (more than 50 times) and lower pressure detection limit (from 84 to 64 dBSPL) as proven by the measurements. Hence, this sensor offers an advantage in the ease of SNR enhancement by modifying the perforation design. Other SNR enhancement methods such as the operating heater temperature are currently under investigation.

References

[1] Gupta, A., Bittner, A., & Dehé, A., Novel Thermal MEMS Dynamic Pressure Sensor. Paper presented at the *2023 22nd International Conference on Solid-State Sensors, Actuators and Microsystems (Transducers), Kyoto, Japan*.

[2] T. B. Gabrielson, Mechanical-thermal noise in micromachined acoustic and vibration sensors, in *IEEE Transactions on Electron Devices*, vol. 40, no. 5, pp. 903-909, May 1993, doi: 10.1109/16.210197

DOI 10.5162/EUROSENSORSXXXVI/PT4.23

A New Area Efficient Folded Piezoelectric MEMS Speaker

Dennis Becker [1], *Achim Bittner* [1], *Robert Scharf* [2], *Christian Döring* [2], *Andreas Merz* [2], *Alfons Dehé* [1,3]
[1] *Hahn-Schickard, Wilhelm-Schickard-Str. 10, 78052 Villingen-Schwenningen, Germany*
[2] *Robert Bosch GmbH, Corporate Research, Robert-Bosch-Campus 1, 71272 Renningen, Germany*
[3] *Georg H. Endress Chair of Smart Systems Integration, Department of Microsystems Engineering – IMTEK, Albert-Ludwigs-Universität Freiburg, Georges-Köhler-Allee 103, 79110 Freiburg, Germany*

Dennis.Becker@hahn-schickard.de

Summary:
This paper demonstrates a novel concept for an area efficient piezoelectric MEMS speaker. A folded piezoelectric diaphragm can utilize the whole chip volume by adding up multiple laterally vibrating actuators. The actuation is accomplished by conformally deposited aluminum nitride (AlN) layers, which are fabricated using atomic layer deposition (ALD). This work describes the design, functionality and first performance of a MEMS speaker. Acoustic measurements show a sound pressure level (SPL) of 59 dB in a 0.13 cm^3 big coupled volume.

Keywords: MEMS, AlN, Speaker, Sidewall, Piezoelectric

Introduction

Miniaturization of loudspeakers generally results in smaller radiating areas and stiffer structures compromising the acoustic performance. Especially state-of-the-art micro-electro-mechanical-system (MEMS) developments make use of innovative membrane concepts, which avoid these difficulties and allow closing the gap to conventional speakers on the market. One example for this is the work by Stoppel et al., which presents a piezoelectric MEMS speaker with slit membranes for compliance reduction [1]. Hirano et al. reports another embodiment, where corrugations increase the membrane displacement of the speaker [2]. Apart from that, Kaiser et al. developed a different MEMS speaker concept, which uses electrostatically actuated beams [3]. Here, they vibrate laterally, which creates an increased active area out of a minimized chip volume. The present work aims to present an alternative concept for an area efficient piezoelectric MEMS speaker. It increased the active radiating area by manufacturing a three-dimensional folded membrane for lateral actuation. Previous work already proves the manufacturing concept of such a membrane [4].

The folded piezoelectric MEMS speaker

The folded structure of the presented piezoelectric MEMS speaker consists of multiple vertical actuators, which vibrate laterally. The starting material is a deep trenched wafer with an aspect ratio of 5:1, which defines the geometry of the speaker. The layers of the membrane stack are conformally deposited. A release etch from the backside utilizing SiO_2 as etch-stop reveals the folded membrane structure (Fig. 1). AlN as piezoelectric thin film is deposited using ALD to actuate the vertical structures [5]. N-doped polycrystalline silicon (Poly-Si) layers with aluminum (Al) pads electrically contact the piezoelectric layer along the folded structure.

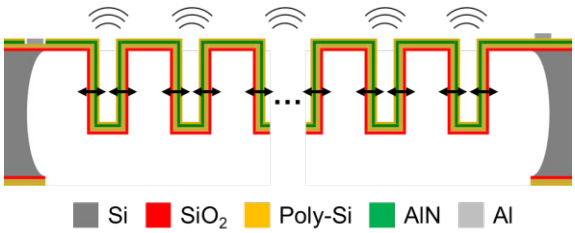

Fig. 1. Schematic cross-section of the folded piezoelectric MEMS speaker

This work utilizes lumped element modeling (LEM) to simulate the piezoelectric MEMS speaker on a multi-physical level. The equivalent circuit is separated into the electrical, mechanical and acoustical domains (Fig. 2). An electric capacitance $C_{e,AlN}$ represents the piezoelectric thin film. The electromechanical coupling T_{em} utilizes numerical simulations of the actuator deflection. Since the characterization of piezoelectric thin films on sidewalls of vertical structures is challenging, literature values are assumed for the modeling of the AlN [6]. A mass-spring-damper system is used to model the mechanical behavior $Z_{m,Mem}$ of the folded membrane. The resulting SPL is calculated in the acoustic domain with the measurement

setup impedance $Z_{a,S}$. This allows a comparison of the simulated data with the acoustic measurements of the speaker samples.

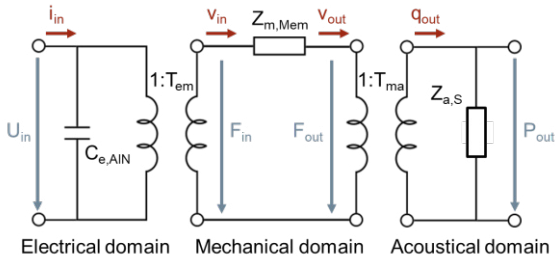

Fig. 2. Equivalent circuit of the piezoelectric MEMS speaker

Results

The MEMS speaker is characterized acoustically on wafer-level by placing the sample wafer on an Al-chuck and utilizing prober needles to apply the electrical input signal. Fig. 3 schematically illustrates the measurement setup.

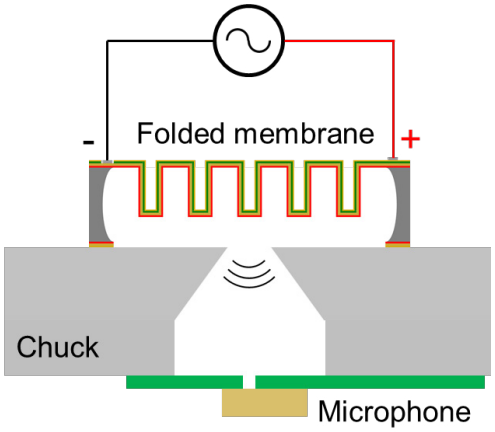

Fig. 3. Measurement setup for wafer-level speaker characterization

The audio analyzer APx525 from Audio Precision completes the measurement setup. An AC voltage is applied from 20 Hz to 20 kHz to drive the piezoelectric actuators against a coupled volume of 0.13 cm³. Fig. 4 compares the measured results with the LEM. A resonance is measured at 17.8 kHz. This is caused by the measurement setup and can also be seen in the modeled results at 17.3 kHz. Below this frequency, a flat response of 64 dB is simulated. The measurements show a SPL of 59 dB at 1 kHz, which is lower by nearly a factor of two compared to the simulation based on literature values. A leakage in the wafer-level measurement setup explains the high pass behavior for lower frequencies. Due to the miniaturized vertical actuators, the speaker resonance lies above the audible frequency range, which allows a desirable flat response up to 20 kHz.
In summary, this work proves the concept of a new piezoelectric MEMS speaker utilizing a folded area efficient structure. A piezoelectric ALD thin film laterally actuates multiple vertical structures to generate an acoustic signal of 59 dB. Compared with simulations based on literature values of sputtered AlN, these results only differ by 5 dB proving the functionality and potential of this MEMS transducer design.

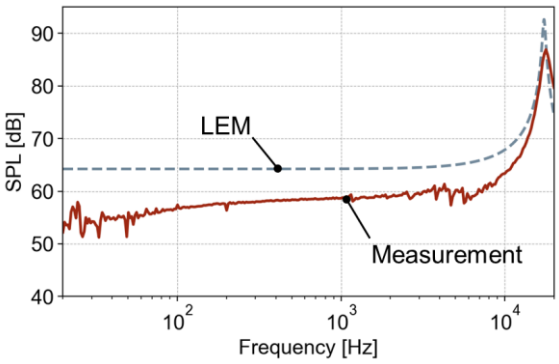

Fig. 4. Comparison of the measured and simulated SPL

This lays the foundation for the development of further design additions and novel characterization approaches, which could lead to an innovation boost in the field of acoustic MEMS transducers with its unique structure.

References

[1] F. Stoppel et al., New integrated full-range MEMS Speaker for in-ear applications, *IEEE Micro Electro Mechanical Systems*, 1068-1071 (2018); doi: 10.1109/MEMSYS.2018.8346744

[2] Y. Hirano et al., PZT MEMS speaker integrated with silicon-parylene composite corrugated diaphragm, *IEEE Micro Electro Mechanical Systems*, 255-258 (2022); doi: 10.1109/MEMS51670.2022.9699539

[3] B. Kaiser et al., The push-pull principle: an electrostatic actuator concept for low distortion acoustic transducers, *Microsyst Nanoeng 8*, 125 (2022); doi: 10.1038/s41378-022-00458-z

[4] D. Becker et al., Three-dimensional folded MEMS manufacturing for an efficient use of area, *MikroSystemTechnik Kongress 2023 - Proceedings*, 307-310 (2023)

[5] R. Scharf et al., Investigation of AlN thin film deposition into folded membrane MEMS structures, *10th International Piezoelectric MEMS Workshop* (2024)

[6] M. A. Fraga et al., Wide bandgap semiconductor thin films for piezoelectric and piezoresistive MEMS sensors applied at high temperatures: An overview, *Microsystem Tehnologies 20*, 9-21 (2023); doi: 10.1007/s00542-013-2029-z

A Low-Cost Flexible Capacitive Pressure Sensor for Motion Detection

R. Tchantchane, H. Zhou, S. Zhang, G. Alici, University of Wollon-gong,
New South Wales (Australia)

Unfortunately, this abstract is not available, as the contribution was not confirmed at the time the conference proceedings were finalized.

A Low-Cost Flexible Capacitive Pressure Sensor for Motion Detection

R. Tchantchane, H. Zhou, S. Zhang, G. Alici, University of Wollon-gong,
New South Wales (Australia)

Unfortunately, this abstract is not available, as the contribution was not confirmed at the time the conference proceedings were finalized.

DOI 10.5162/EUROSENSORSXXXVI/PT4.66

Improvement of temperature stability in MEMS differential resonant accelerometer by G-T correction

K. Masunishi[1], E. Ogawa[1], D. Ono[1], F. Miyazaki[1], K. Uchida[1], J. Ogawa[1], H. Murase[1], F. Ishibashi[1] and Y. Tomizawa[1]
[1] Corporate Research & Development Center, Toshiba Corporation, Kawasaki, Japan

kei1.masunishi@toshiba.co.jp

Summary:
This paper presents a method for reducing temperature drift in MEMS differential resonant accelerometer (DRA). Conventionally, the difference in resonant frequency between two beams is utilized to eliminate the effect of temperature. However, the temperature coefficients of frequency (*TCf*) of the two beams do not match perfectly, resulting in temperature drift. G-T correction was performed to account for the difference in *TCf*. The measured Allan deviation was BI > 1 μG for the differential correction, and a highly accurate bias instability of BI < 500 nG was achieved by applying G-T correction.

Keywords: MEMS, accelerometer, DRA, TCf, G-T correction

Introduction

Highly accurate and wide dynamic range (navigation grade) accelerometers are needed for autonomous operation of airplanes and automobiles. These accelerometers must also be robust against disturbances such as temperature changes. MEMS differential resonant accelerometer (DRA) are being investigated for such applications. Here, we report a method for reducing temperature drift in DRA.

Design

The structure and operating principle of a DRA is shown in Fig. 1 [1]. The prototype MCU-based module (5 × 5 × 1 cm) and DRA electrodes are shown in Fig. 2 [2]. When the inertial force due to acceleration acts on the proof mass, it rotates around the pivot, causing tension and compression stresses to be generated in opposite directions in the two resonant beams. Consequently, the resonant frequency also changes in the opposite direction. However, both resonant frequencies decrease as the temperature increases, due mainly to the temperature dependence of Young's modulus of Si. These relationships are expressed by the following equation.

$$\begin{pmatrix} f_1 \\ f_2 \end{pmatrix} = \begin{pmatrix} SF_1 & TCf_1 \\ SF_2 & TCf_2 \end{pmatrix} \begin{pmatrix} G \\ T \end{pmatrix} + \begin{pmatrix} c_1 \\ c_2 \end{pmatrix} \quad (1)$$

Here, f_i is the resonant frequency (Hz), SF_i is the scale factor (Hz/G), TCf_i is the temperature coefficient of frequency (Hz/degC), c_i is the initial bias (Hz), G is the acceleration (G), T is the temperature (degC), and the subscript i is the difference between beam 1 and beam 2.

Because our DRA has a structure that is supported by only one anchor, the two beams are less affected by thermal stress. In addition, asymmetric double T-shaped electrodes are added at the maximum displacement position of the two beams in order to improve the capacitive sensitivity dC/dy and dynamic range.

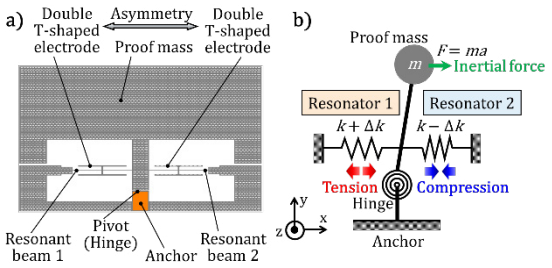

Fig. 1. (a) Structure of the MEMS DRA. (b) Concept of DRA acceleration measurement.

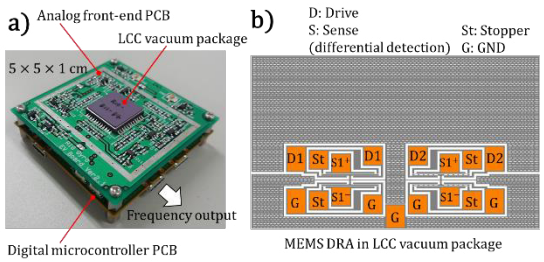

Fig. 2. (a) Photograph of the MCU-based DRA module. (b) Diagram of the MEMS DRA electrodes.

Correction methods

Differential correction

Conventionally, acceleration was measured by removing temperature dependence by taking the

difference between the resonant frequencies of two beams, as in the following equation [3].

$$\Delta G = \frac{\Delta f_1 - \Delta f_2}{SF_1 - SF_2} \quad (2)$$

Here, ΔG is the change in acceleration (G) and Δf_i is the change in resonant frequency (Hz).

G-T Correction

However, the *TCf* of the two resonant beams differed, and temperature drift occurred if only the differential was used. Therefore, we solved (1) assuming that *SF* and *TCf* are linearly independent and orthogonal, as in the following equation.

$$\Delta G = \frac{TCf_2 \cdot \Delta f_1 - TCf_1 \cdot \Delta f_2}{SF_1 \cdot TCf_2 - SF_2 \cdot TCf_1} \quad (3)$$

Experiment results

Measurements of SF and TCf

The results of *SF* and *TCf* measurements for the prototype DRA are shown in Figs.3 and 4, respectively. *SF* and *TCF* of two resonant beams were SF_1 = 14.2 Hz/G, SF_2 = −16.2 Hz/G, and TCf_1 = −0.63 Hz/degC, TCf_2 = −0.77 Hz/degC.

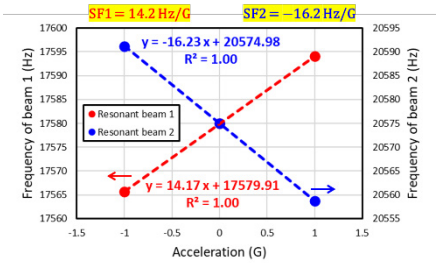

Fig. 3. SF measurement results for the DRA.

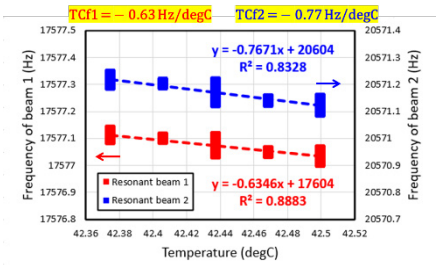

Fig. 4. TCf measurement results for the DRA.

Measurement of Allan deviation

DRA noise (velocity random walk (VRW)) is reduced in inverse proportion to the drive voltage Vac, as shown in the following equation.

$$\mathrm{VRW} \propto \frac{1}{V_{dc} \cdot V_{ac} \cdot \left(\frac{dC}{dy}_{drive}\right) \cdot SF} \quad (4)$$

Here, V_{dc} and V_{ac} are the DC and AC voltages of the drive, respectively, and dC/dy_{drive} is the capacitive sensitivity of the drive electrodes.

We varied Vac from 5 to 25 mV and measured the Allan deviation. The results obtained by differential correction are shown in Fig. 5. VRW was decreased by the drive voltage Vac. However, due to the effect of temperature drift, it bottomed out at about tBI = 20 s, and BI became 1.0 μG at Vac = 25 mV. The result obtained by G-T correction is shown in Fig. 6. Due to the effect of reduced temperature drift, the Allan deviation continued to decrease by −1/2 power, and finally BI became 430 nG at Vac = 25 mV.

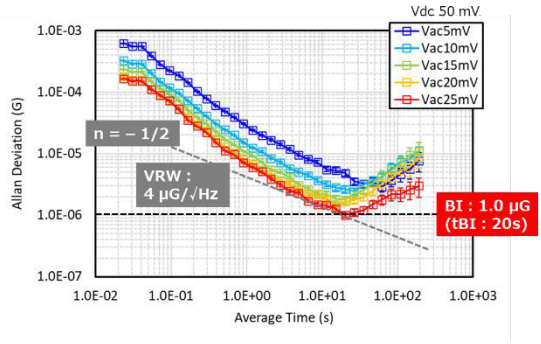

Fig. 5. Allan deviation of a DRA with differential correction.

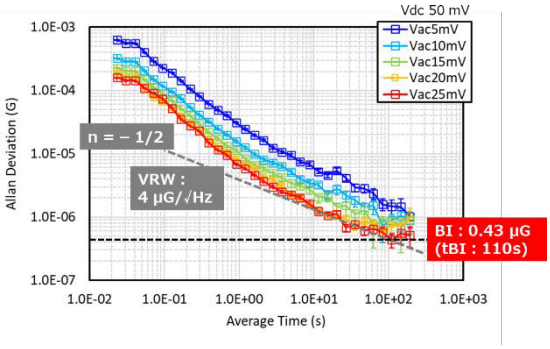

Fig. 6. Allan deviation of a DRA with G-T correction.

Conclusions

To improve the capacitive sensitivity dC/dy, double T-shaped electrodes were added. The effect of temperature drift in the DRA was reduced by applying G-T correction. As a result, a highly accurate bias instability of BI < 500 nG was achieved.

References

[1] B. Johnson, et al., IEEE INERTIAL2021, (2021)

[2] K. Masunishi, et al., IEEE MEMS2022, pp.150-153., (2022)

[3] D. Shin, et al., IEEE MEMS2017, pp.17-20., (2017)

Acknowledgements

The authors are grateful to Dr. R. Gando for his contributions during his tenure at Toshiba Corporation. This work was supported by the Innovative Science and Technology Initiative for Security Grant Number JPJ004596, ATLA, Japan.

DOI 10.5162/EUROSENSORSXXXVI/PT4.84

Capacitive Sensor based on Self-healing Ionic conductive hydrogels for Human Motion Detection

Gyeongyeong Lee[1], Jihoon Kim[1,]*

[1]Division of Advanced Materials Engineering, Kongju National University, Republic of Korea

Corresponding Author's e-mail address: jihoon.kim@kongju.ac.kr

Summary:

Poly (ethylene oxide) (PEO), known for its self-healing properties through hydrogen bond-forming hydroxyl groups, was used to synthesize hydrogels, and lithium bis (trifluoromethane sulfonyl) imide (LiTFSI) was added to impart ionic conductivity. The manufactured hydrogels were analyzed to evaluate their mechanical properties, self-healing abilities, and electrical characteristics. Based on these analyses, a self-healing capacitivie sensor was fabricated, which utilizes the unique properties of the hydrogel to monitor human movement.

Keywords: Hydrogel, self-healing, capacitive sensor, wearable sensor, human motion

Background, Motivation an Objective

Recently, flexible electronic devices have garnered significant attention due to their potential applications in diverse fields, including wearable sensors, energy storage devices, actuators, and soft robotics engineering [1]. However, these devices can undergo performance degradation from deformation or damage during use, leading to potential malfunctions. Consequently, the integration of self-healing capabilities, encompassing mechanical, electrical, and chemical properties, becomes vital to address scratches or mechanical damages. Ionic conductive hydrogels are regarded as ideal materials due to their distinctive 3D network structure, which arises from the physical or chemical crosslinking of polymers. This structure imparts elasticity and concurrently facilitates a favorable environment for ion movement. Furthermore, this material is recognized as a highly attractive substance due to its straightforward manufacturing process, cost-effectiveness, and high conductivity, along with its self-healing capabilities. In this study, we manufactured hydrogels using poly (ethylene oxide) (PEO) known for its effective self-healing properties through hydrogen bond-forming hydroxyl groups [2], and we introduced lithium bis (trifluoromethane sulfonimide) **(**LiTFSI**)** to impart ionic conductivity. The mechanical properties, self-healing ability, and electrical characteristics of the manufactured hydrogel were analyzed. Furthermore, finite element analysis will be utilized to establish the correlation between motion-induced mechanical modification and its corresponding changes in capacitance. Informed by these analysis results, we fabricated a self-healing capacitor sensor. This wearable sensor, leveraging ionic conductors, was subsequently tested in practical applications by recording capacitance variations to monitor human movement.

Description of the New Method or System

Hydrogels were synthesized using PEO, which possesses self-healing properties due to its hydroxyl groups forming hydrogen bonds. Ionic conductivity was imparted by adding LiTFSI. The self-healing properties between the produced poly (acrylic acid) (PAA)-PEO hydrogel and PAA-PEO-Li ion conductor were evaluated. Based on the analysis of these properties, a self-healing capacitive sensor was designed to monitor human movement by using the PAA-PEO-Li ion conductor as the upper and lower electrodes and the PAA-PEO hydrogel as the dielectric layer, with the interfaces connected through their self-healing capabilities.

Results

The self-healing elastomer was synthesized by combining high molecular weight PAA and PEO based on hydrogen bonding interactions. For the manufacturing of ion conductors, the electrolyte salt LiTFSI was chosen due to its high solubility in various solvents and polymers. The content of LiTFSI was varied to adjust the characteristics of the ion conductor. Additionally, to

manufacture a simple ion conductor through photoinitiated polymerization, the photoinitiator Diphenyl (2,4,6-trimethylbenzoyl) phosphine oxide (TPO) was added, and after UV exposure, the sample was placed in a constant temperature and humidity chamber to remove excess moisture and form a PAA-PEO hydrogel through hydrogen bonding.

The electrolyte salt LiTFSI doped in the ion conductor can move within the polymer network, granting high ionic conductivity to the ion conductor. The Nyquist plots of the ion conductor are displayed in Figure 1 and Table 1, as obtained through EIS tests. The ionic conductivity was calculated using equation (1), where L is the thickness of the sample, R is the bulk resistance obtained from the Nyquist plot of the impedance spectrum, and S is the cross-sectional area of the ion conductor. As seen in Figure 1 and Table 1, an increase in the LiTFSI content leads to enhanced ionic conductivity of the ion conductor.

$$\sigma = \frac{L}{RS} \quad (1)$$

To evaluate the self-healing behavior of the PAA-PEO hydrogel, rectangular bar-shaped samples of PAA-PEO and PAA-PEO-Li ion conductors measuring 10x40x2 [mm] were cut in half. The two pieces were compressed and cultured in a constant temperature and humidity chamber (25°C/90%). To utilize the self-healing properties in manufacturing a capacitive sensor, one side was compressed with the PAA-PEO hydrogel without the electrolyte salt, and the other side with the PAA-PEO-Li ion conductor containing the electrolyte salt. After healing for a certain period, the healing properties of the samples was assessed. It was confirmed that both the PAA-PEO hydrogel without electrolyte salt and the PAA-PEO-Li ion conductor pieces with electrolyte salt possessed self-healing properties. Additionally, it was confirmed that self-healing properties exist between the PAA-PEO hydrogel and the PAA-PEO-Li ion conductor pieces. This confirms the feasibility of manufacturing a capacitive sensor using self-healing properties.

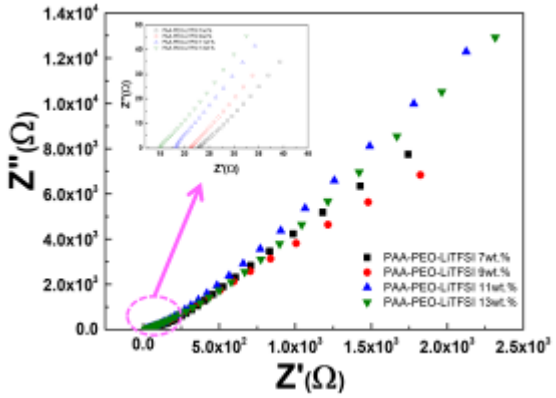

Fig. 1. Nyquist plot of impedance spectra of the PAA-PEO-Li ionic conductors with various LiTFSI content.

Tab. 1: Impedance and ionic conductivity of the PAA-PEO-Li ionic conductor with various LiTFSI contents

LiTFSI (wt.%)	Resistivity (Ω)	Ionic conductivity (S/cm)
7	22.87	1.93 X 10^{-3}
9	21.20	2.09 X 10^{-3}
11	18.07	2.45 X 10^{-3}
13	15.06	2.94 X 10^{-3}

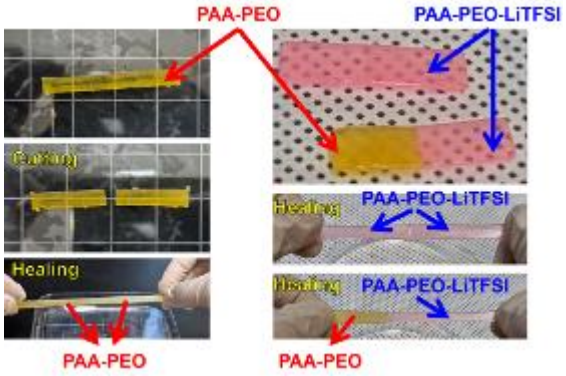

Fig. 2. A self-healing test: conducted by cutting the middle of a bar-shaped sample, reattaching it, and then pulling it apart.

References

[1] B. C. K. Tee, C. Wang, R. Allen, Z. Bao, An electrically and mechanically self-healing composite with pressure-and flexion-sensitive properties for electronic skin applications, *Nature nanotechnology* 7(12), 825-832 (2012); doi: https://doi.org/10.1038/nnano.2012.192

[2] J. Li, Z. Wang, L. Wen, J. Nie, S. Yang, J. Xu, S. Z. D. Cheng, Highly elastic fibers made from hydrogen-bonded polymer complex. *ACS Macro Letters 5*(7), 814-818 (2016); doi: https://doi.org/10.1021/acsmacrolett.6b00346

DOI 10.5162/EUROSENSORSXXXVI/PT4.96

Ultra-High Sensitivity LC Resonant Pressure Sensor Based on a Microstructured Ionogel Dielectric Layer

Chia-Yu Cho and Yao-Joe Yang*
National Taiwan University, Taipei, TAIWAN

*Corresponding Author: chiayucho@mems.me.ntu.edu.tw

Summary:

This study introduces a highly sensitive ionogel-based wireless pressure sensor, incorporating an inductor coil and a parallel-plate capacitor for pressure detection. A microstructured ionogel film was employed as the dielectric layer on the capacitor which significantly enhances the sensor performance. This effective improvement is largely due to the ultra-high capacitance generated by electron double layers at the interface between the ionogel film and the electrode. The sensitivity of the proposed device was recorded at 0.023 $mmHg^{-1}$, making it roughly 50 times more sensitive than similar capacitive devices without the ionogel film.

Keywords: pressure sensor, ionogel, electron double layer, LC resonator, phase-dip technique.

Background, Motivation an Objective

In recent years, the advancement of flexible pressure sensors for biomedical applications has garnered substantial interest [1]. The sensors of the capacitive type enjoy widespread popularity due to its simple design and straightforward manufacturing process. In [2], the use of a polyurethane ionogel as the dielectric in capacitive sensing systems was proposed to boost the device efficiency. Such improvement is chiefly due to the creation of electron double layers (EDLs) at the dielectric-electrode interface, which effectively elevates the capacitance, and in turn, the sensitivity of the sensors [3]. In this work, we propose a highly sensitive ionogel-based pressure sensor that incorporates an LC resonator for the passive power and signal transmission. Furthermore, this sensitivity enhancement substantially improves the device resolution.

Description of the New Method or System

Figure 1(a) shows the sensor layout with its components monolithically implemented on a flexible substrate, while Figure 1(b) illustrates the device configuration when folded to form a capacitor structure. The device consists of an electro-plated copper inductor, a pair of capacitor electrodes, and a microstructured ionogel film sandwiched between the capacitor electrodes. The surface of the ionogel film features numerous grooves, enabling it to accommodate buckled protrusions under external compression. Thus, the compressibility of the film is significantly improved due to its microstructured fillable surface. Figure 1(c) illustrates the sensing principle of the proposed device. The fabrication process of the device is detailed in Figure 2. The planar coil was realized by the conventional micromachining techniques, as depicted in Figures 2(a) to 2(f). A photodefinable PDMS prepolymer was spin-coated on the coil layer, and an ionogel film was placed in the PDMS cavities (Figures. 2(g)-2(j)). Note that the ionogel film was prepared using the similar technique using a sand paper [4]. Then, the LC tank layer was separated from the glass substrate (Figure 2(l)). Finally, the layer was folded to form a capacitor structure. Figure 3 shows the SEM image of the microstructured ionogel film. Figure 4 presents images of the assembled device, and a device folded and attached to curved surfaces.

Results

Figure 5 displays the setup used for characterizing the proposed device. Figure 6 illustrates the measured impedance phase at various pressures ranging from 0 to 225 mmHg. With no external pressure, the resonance frequency is approximately 406 MHz. As pressure increases, the total inductance rises, resulting in a decrease in the resonant frequency. Figure 7 shows the normalized resonant frequencies. The device with the ionogel film showed a sensitivity of 0.023 $mmHg^{-1}$ for pressures ranging from 0-30 mmHg, and 0.00042 $mmHg^{-1}$ for pressures ranging from 30-225 mmHg. These results show that the utilization of ionogel film significantly improved the device sensitivity.

Illustrations, Graphs, and Photographs

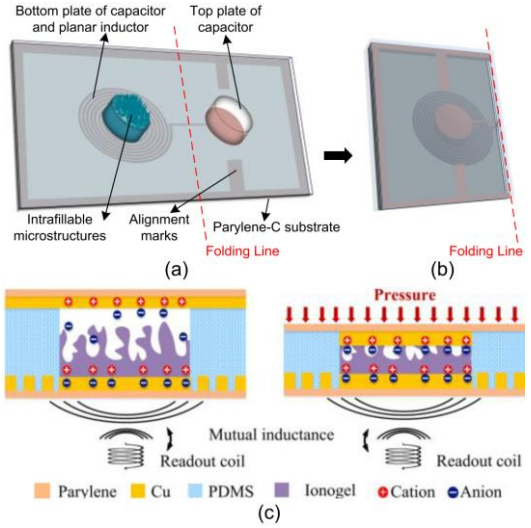

Fig. 1. The Schematic of the proposed device.

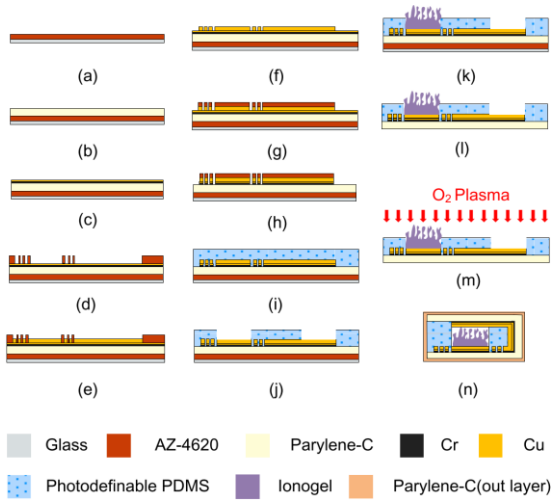

Figure 2: The fabrication process of the proposed device.

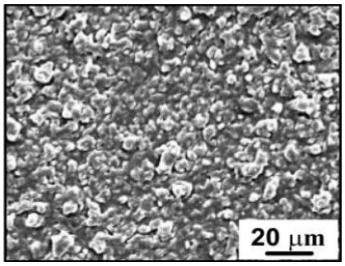

Figure 3: SEM pictures of microstructured ionogel films.

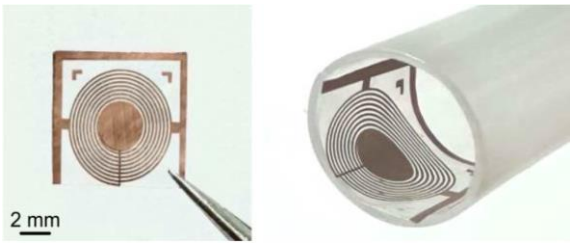

Figure 4: (a) The fabricated results. (b) The pressure sensor attached on curved surfaces.

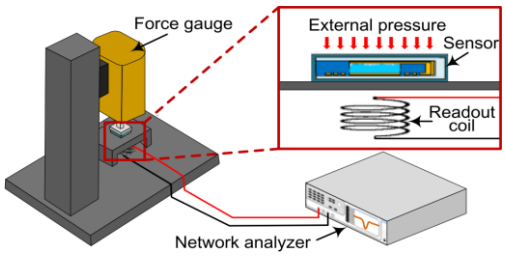

Figure 5: Schematic of pressure sensor test measurement setup.

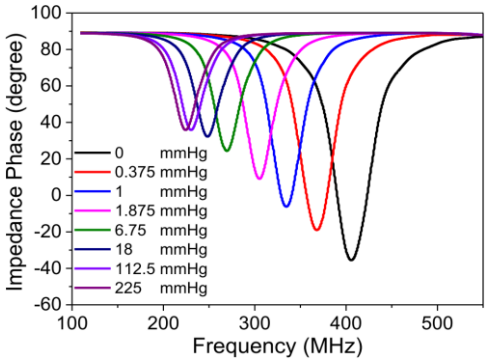

Figure 6: The measured impedance phase as a function of frequency for several applied pressures.

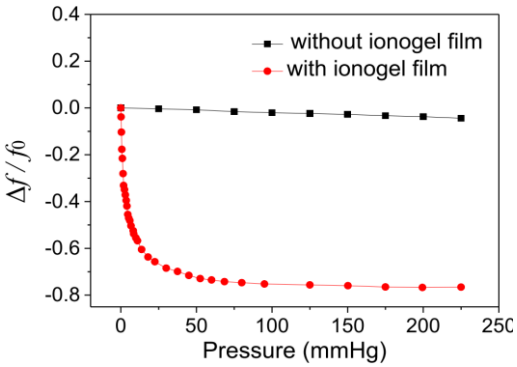

Figure 7: The normalized measured resonant frequencies vs. applied pressures.

References

[1] S. Pyo, J. Lee, K. Bae, S. Sim and J. Kim, Recent progress in flexible tactile sensors for human-interactive systems: from sensors to advanced applications, *Adv. Mater*,33(44), 2005902(2021); doi: 10.1002/adma.202005902

[2] Y. Liu, J. Wang, J. Chen, Q. Yuan and Y. Zhu, Ultrasensitive iontronic pressure sensor based on rose-structured ionogel dielectric layer and compressively porous electrodes, *Adv. Compos. Hybrid Mater*, 6(6), 210(2024); doi: 10.1007/s42114-023-00765-7

[3] B. Nie, R. Li, J. Cao, J. D. Brandt, and T. Pan, Flexible transparent iontronic film for interfacial capacitive pressure sensing, *Adv. Mater*, 27(39), 6055-6062(2015); doi: 10.1002/adma.201502556

[4] N. Bai, L. Wang, Q. Wang, J. Deng, Y. Wang, P. Lu and C. F. Guo, Graded intrafillable architecture-based iontronic pressure sensor with ultra-broad-range high sensitivity, *Nat. Commun*, 11(1), 209(2020); doi: 10.1038/s41467-019-14054-9

Low-Energy Passive Haptic Glove Based on Sensory Feed-back for Virtual Reality Training Applications

Kamat, I. Alvarado, S. Bhansali, Florida International University, Miami (USA)

Unfortunately, this abstract is not available, as the contribution was not confirmed at the time the conference proceedings were finalized.

Low-Energy Passive Haptic Glove Based on Sensory Feed-back for Virtual Reality Training Applications

Kamat, I. Alvarado, S. Bhansali, Florida International University, Miami (USA)

Unfortunately, this abstract is not available, as the contribution was not confirmed at the time the conference proceedings were finalized.

DOI 10.5162/EUROSENSORSXXXVI/PT4.170

Fully Screen-printed Highly Sensitive Strain Gauge with Low TCR

Mani Teja Vijjapu[1], *Manoj Jose*[1], *Jürgen Kosel*[1]
[1]*Sensor Systems Division, Silicon Austria Labs GmbH, Europastraße 12, Villach, 9524 Austria*

Correspondence: mani.vijjapu@silicon-austria.com

Abstract:

Strain gauges are essential in various industrial applications. Commercial strain gauges are developed using Constantan and Karma alloys due to their low temperature sensitivity. Creating alloy inks for printing poses challenges due to high sintering temperatures. Consequently, printed strain gauges (PSGs) are typically made using inks based on silver and carbon. However, the temperature coefficient of resistance (TCR) of these inks is high. In this work, a unique composite was developed using screen-printable ink with silver-coated glass (AgG) particles. The objective of this composite formulation was to increase strain sensitivity while reducing the temperature dependence of the printed strain gauges. The PSGs made with the composite showed a greater gauge factor of 60. Comprehensive characterization of the PSG, including environmental testing, cyclic strain performance, and dynamic strain responsivity, demonstrates the effectiveness and reliability of the developed composite.

Keywords: Printed Strain Gauges, Wearable Technologies, High gauge factor, Composite inks, Printed sensors

Introduction

Strain gauges (SGs) are sensors that convert compressive or tensile strains into electrical signals, usually in the form of variations in capacitance or resistance.[1] They are used where there is need of accurate assessment of force, strain, and torque in mechanically stressed components and in the diagnosis of structural damage.[2] Owing to structural simplicity and ease of electronic reading, resistive SGs are most commonly employed in industrial applications.

The sensitivity of resistive strain gauges is termed as the gauge factor (GF), which is defined as the relative change in the resistance of the strain gauge due to the applied mechanical strain. The gauge factor of commercial strain gauges made of alloys is typically around 2. However, such strain gauges are not suitable for wearable devices, where a high gauge factor and mechanical working range are needed. For instance, detecting human respiration rate requires extremely sensitive strain sensors,[3] and monitoring joint movements necessitates high stretchability.[4] Flexible and Printed technologies can be leveraged to meet the demands of such applications.

PSGs reported are dominantly employed Silver,[5] carbon[6], [7] or Silver/carbon composites,[8] which are susceptible to temperature variations that affect the accuracy of detecting mechanical deformations. Therefore, there is a critical need for PSGs that demonstrate reduced temperature dependence. In pursuit of this objective, a novel composite was developed, comprising a screen-printable non-conductive paste with a polyurethane (PU) matrix blended with AgG microparticles as conductive filler. As anticipated, PSGs made with this composite demonstrated minimal temperature dependence and high gauge factors.

Materials and methods

Tubicoat was utilized as the screen-printable paste. eConduct Glass 352000 – AgG served as the conductive filler. These two components were mixed at a ratio of 1:5 (Wt:Wt) in a speed mixer. The resulting paste, termed PU composite, was then used to print resistive PSGs, as depicted in Fig. 1a. Fig. 1b shows the PSG printed with the PU composite. Mechanical characterization of the PSG was conducted by adhering it to a dog-bone structure using a push-pull tester Zwick Roell, as shown in Fig. 1c. Fig. 1d demonstrates the flexibility of the PSG, and

the microscopic image in Fig. 1e illustrates the AgG particles embedded in the PU matrix.

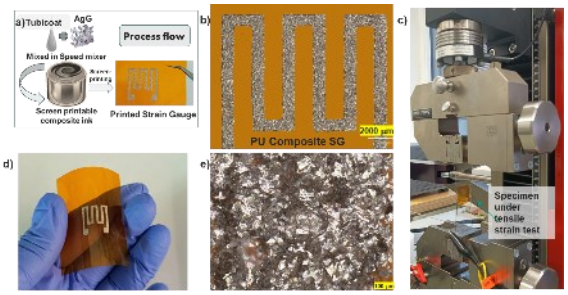

Fig. 1 (a) Printing of resistive PSGs using PU composite paste. (b) Printed PSG with PU composite. (c) Mechanical characterization setup with push-pull tester Zwick Roell. (d) Flexible PSG. (e) Microscopic image showing AgG particles embedded in PU matrix.

Results

The PSGs were tested to assess the thermal dependence in an environmental chamber. The sensor's thermal responsivity is < 0.5% per 10°C increase in temperature, as depicted in Fig. 2a. Compared to printed carbon-based temperature sensors,[9] the PSG exhibits significantly lower temperature dependence. This is attributed to the presence of glass as the core material for the conductive particle, which has a lower thermal expansion coefficient. As a result, there is no physical elongation in the PU composite-based printed trace, unlike nanoparticle inks with the binding matrix, where the interparticle distance increases due to thermal expansion, leading to higher variation.

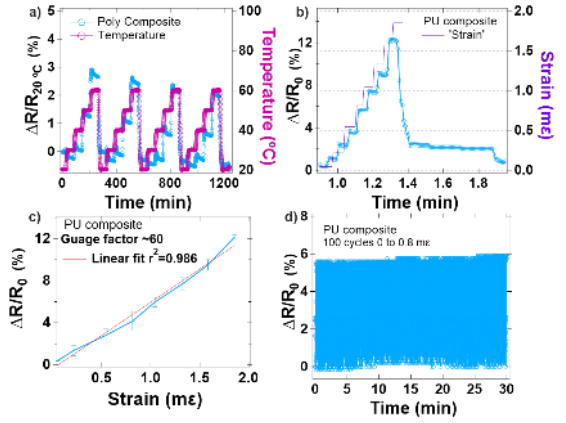

Fig. 2 Performance assessment of PSGs, showcasing temperature response, strain sensitivity, linearity, and repeatability.

Furthermore, the PSGs underwent testing by applying tensile strain up to 0.16%. The response of the PSG is depicted in Fig. 2b, and from the calibration plot (Fig. 2c), it is evident that the response is linear. The gauge factor is estimated to be around 60. The PSGs have demonstrated great repeatability when subjected to multiple stress cycles, as depicted in Fig. 2d. The conduction mechanism in these composite-based conductive traces is predominantly due to the tunneling, where electrons hop from particle to particle. When the interparticle distance increases due to the applied strain, the probability of hopping decreases, resulting in an increase in resistance. Such a high gauge factor is feasible due to this variation in interparticle distance between conductive particles.

In summary, the demonstrated PSGs exhibit significant potential for use across a range of applications, from structural monitoring to wearable technologies.

Acknowledgement

This work has been supported by Silicon Austria Labs (SAL), owned by the Republic of Austria, the Styrian Business Promotion Agency (SFG), the federal state of Carinthia, the Upper Austrian Research (UAR), and the Austrian Asso-ci-a-tion for the Elec-tric and Elec-tronics Industry (FEEI).

References

[1] H. Souri *et al.*, *Advanced Intelligent Systems*, vol. 2, no. 8, p. 2000039, Aug. 2020, doi: 10.1002/AISY.202000039.

[2] Y. Zhang, N. Anderson, S. Bland, S. Nutt, G. Jursich, and S. Joshi, *Sens Actuators A Phys*, vol. 253, pp. 165–172, Jan. 2017, doi: 10.1016/J.SNA.2016.10.007.

[3] C. S. Boland, *ACS Nano*, vol. 13, no. 12, pp. 13627–13636, Dec. 2019, doi: 10.1021/ACSNANO.9B06847/SUPPL_FILE/NN9B06847_SI_001.PDF.

[4] Y. Yang, L. Shi, Z. Cao, R. Wang, and J. Sun, *Adv Funct Mater*, vol. 29, no. 14, p. 1807882, Apr. 2019, doi: 10.1002/ADFM.201807882.

[5] N. Anderson, N. Szorc, V. Gunasekaran, S. Joshi, and G. Jursich, *Sens Actuators A Phys*, vol. 290, pp. 1–7, May 2019, doi: 10.1016/J.SNA.2019.02.028.

[6] S. Chun, A. Hong, Y. Choi, C. Ha, and W. Park, *Nanoscale*, vol. 8, no. 17, pp. 9185–9192, May 2016, doi: 10.1039/c6nr00774k.

[7] D. Maurya *et al.*, *Nature Communications 2020 11:1*, vol. 11, no. 1, pp. 1–10, Oct. 2020, doi: 10.1038/s41467-020-19088-y.

[8] A. K. Bose *et al.*, *FLEPS 2020 - IEEE International Conference on Flexible and Printable Sensors and Systems*, Aug. 2020, doi: 10.1109/FLEPS49123.2020.9239547.

[9] C. Bali, A. Brandlmaier, A. Ganster, O. Raab, J. Zapf, and A. Hübler, *Mater Today Proc*, vol. 3, no. 3, pp. 739–745, Jan. 2016, doi: 10.1016/J.MATPR.2016.02.005.

DOI 10.5162/EUROSENSORSXXXVI/PT4.193

Directivity and distance dependence of generated pressure field of bistable PMUTs

Michael Schneider[1,2], *Mahdi Mortada*[1,2], *Dominik Mayrhofer*[3], *Manfred Kaltenbacher*[3], *Ulrich Schmid*[1]
[1] *Institute of Sensor and Actuator Systems, TU Wien, 1040 Vienna, Austria*
[2] *Christian Doppler Laboratory for PiezoMEMS, TU Wien, 1040 Vienna, Austria*
[3] *Institute of Fundamentals and Theory in Electrical Engineering, TU Graz, 8010 Graz, Austria*

Corresponding Author's e-mail address: michael.schneider@tuwien.ac.at

Summary:
This work presents both the directivity pattern and distance dependence of the pressure field of a piezoelectric micromachined ultrasonic transducer (PMUT). The PMUT comprises a silicon membrane and an integrated piezoelectric transducer based on aluminum nitride (AlN). It exploits bistability to achieve large membrane displacements during switching between both ground states.

Keywords: PMUT, bistability, PiezoMEMS, aluminum nitride, acoustic MEMS

Introduction

Ultrasonic sound has been utilized for decades in medical diagnostics, gesture recognition, non-destructive testing and range finding, to mention a few. Given the ongoing trend towards miniaturization, micromachined ultrasonic transducers based on the piezoelectric effect (PMUTs) have been gaining a lot of attention recently due to operation at lower voltage levels and the lack of any counter-electrodes as required in capacitive MUTs.

One way of increasing the pressure output of a PMUT is to increase the stroke level of the membrane element. There have been many approaches to achieve this, including the use of flexural supports [1] or differential transducers [2]. Due to compressive stress induced buckling however, bistability has been shown most recently to be a highly effective approach to achieve high sound pressure levels from PMUTs [3]. In this work, we study the acoustic emission characteristics of such bistable PMUTs.

Experimental details

The PMUTs are fabricated starting from a 100 mm silicon on insulator (SOI) wafer coated with a stress-compensated silicon oxide and silicon nitride bi-layer for electrical insulation. The piezoelectric transducer comprises thermally evaporated bottom and top electrodes (chromium and gold) and a reactively sputter-deposited aluminum nitride thin film sandwiched between both electrodes. The membrane is defined by backside deep reactive ion etching and a subsequent hydrofluoric acid removal of the buried oxide layer to release the membrane. The stress in the AlN layer is tailored to ensure that the total compressive stress state in the membrane exceeds the critical stress limit required for buckling.

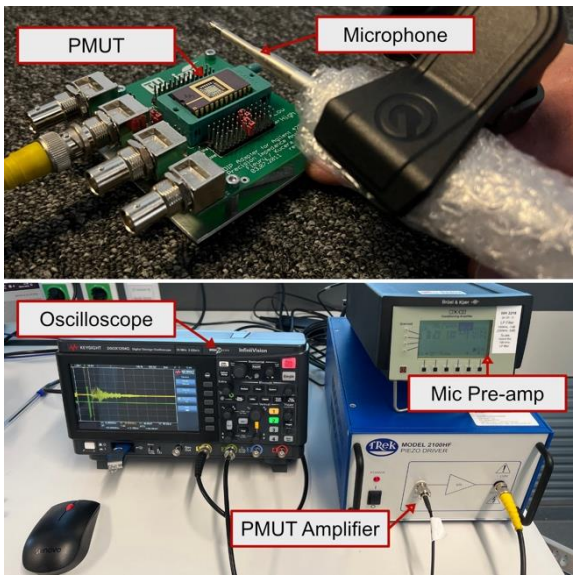

Figure 1. Measurement setup

The PMUT is electrically excited by applying a sinusoidal pulse train with *n* pulses to the AlN layer. The signal is generated using an Intermodulation products MLA-3 and is amplified by a factor of 50 using a Trek HF2100 broadband piezo amplifier. Membrane velocity is recorded using a Polytec single point laser Doppler vibrometer. Acoustic measurements are done using a Brüel and Kjær 4138 pressure field microphone with a frequency range of 6.5 Hz to 140 kHz. A pre-amplifier 2670 in combination

with a Nexus signal conditioner with a 140 kHz bandwidth extension is used, before the signal is recorded using a Keysight DSOX1204G oscilloscope. The measurement is performed inside a soundproof booth by Soundbricks. The setup is shown in Figure 1. More details can be found in [3].

Results and discussion

Figure 2 shows an exemplary measurement signal with the electrical excitation applied to the membrane (a), the membrane velocity (b) and the recorded pressure (c). In the red shaded region, the membrane is undergoing continuous snap-throughs between both ground states, whereas in the yellow shaded region the membrane rings down. The green shaded region marks the transition between these two regimes.

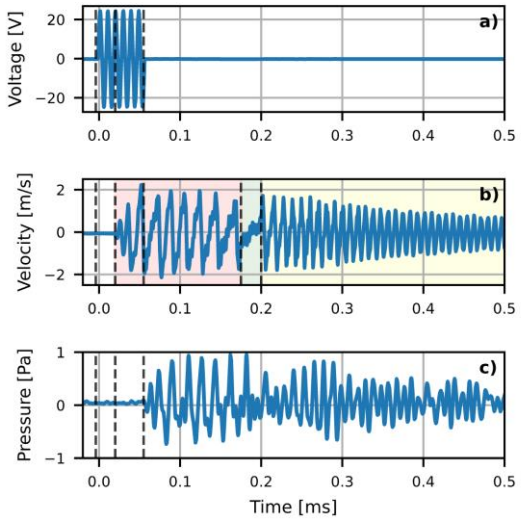

Figure 2: a) Excitation signal. b) LDV signal. c) Pressure measured with the microphone.

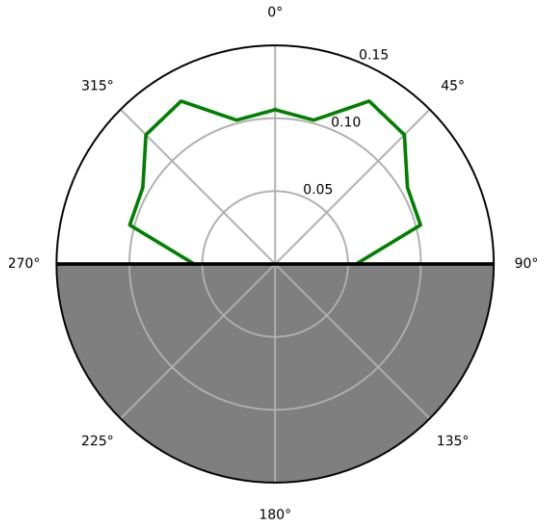

Figure 3: Emission pattern of the PMUT. The gray area is not measured, since the PMUT is mounted in such a way as to not allow downwards emission.

Figure 3 shows the directivity pattern of the PMUT measured at a distance of 92.5 mm. Distance is calibrated using the delay between electrical signal and sound (delay between electrical signal and LDV signal is compensated) and a speed of sound of 343 m/s. The PMUT featured an almost omnidirectional emission pattern with a significant drop only at 90° and 270° off-axis, which is due to the geometry of the measurement setup.

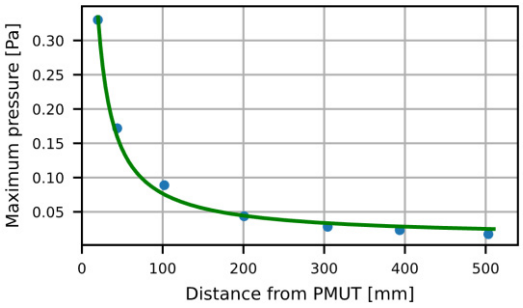

Figure 4: Distance dependence of pressure.

Figure 4 shows the impact of microphone distance *r* to maximum detected pressure measured at 0° on-axis and features the expected 1/*r* behavior. The straight line is a fit of a reciprocal function to the data. Distances were set by eye and subsequently calibrated using the same method as mentioned above.

Conclusion

The emission pattern of a bistable PMUT has been shown for the first time as well as the expected pressure decrease with distance. Future work will focus on a more in-depth study of these PMUTs, especially in continuous operation to provide proper sound pressure level values.

References

[1] A. Guedes, S. Shelton, R. Przybyla, I. Izyumin, B. Boser and D.A. Horsley, Aluminum nitride pMUT based on a flexurally-suspended membrane, Proc. 16th International Solid-State Sensors, Actuators and Microsystems Conference (2011); doi: 10.1109/TRANSDUCERS.2011.5969223.

[2] F. Sammoura, S. Shelton, S. Akhbari, D. Horsley and L. Lin, A two-port piezoelectric micromachined ultrasonic transducer, Proc. Joint IEEE ISAF/IWATMD/PFM (2014); doi: 10.1109/ISAF.2014.6923004.

[3] M. Schneider, M. Dorfmeister, P. Moll, M. Kaltenbacher and U. Schmid, Bi-Stable Aluminum Nitride-Based Piezoelectric Micromachined Ultrasonic Transducer (PMUT), *Journal of Microelectromechanical Systems* 29, 1-6 (2020); doi: 10.1109/JMEMS.2020.3004243.

DOI 10.5162/EUROSENSORSXXXVI/PT4.194

SiC micro hot wires for flow measurement in harsh environments

Sylvain KERN[1], Aurélien MAZZAMURRO[1], Cécile GHOUILA-HOURI[1], Djamila HOURLIER[1], Laure TANDT[1], Philippe PERNOD[1], Marc PORTAIL[2], Abdelkrim TALBI[1]
[1]Univ. Lille, CNRS, Centrale Lille, Université Polytechnique Hauts-de-France, UMR 8520-IEMN, 59000 Lille, France.
[2]Centre de Recherche sur l'Hétéro-Épitaxie et ses Applications, Rue Bernard Grégory, 06560 Valbonne, France.

sylvain.kern@univ-lille

Summary

The present study deals with an integrated effort in the process of fabricating a silicon carbide-based micromachined device for measuring turbulent airflow in harsh environments, involving SiC etching and silicon substrate under-etching to create the MEMS structure. These SiC-based MEMS structures have been electrically and thermally characterized, with resistance and TCR measurements *vs.* temperature.

Keywords: MEMS, silicon carbide, thermal flow sensors, harsh environments.

Background, Motivation an Objective

There is an increasing need to measure turbulent airflow in harsh environments: high temperature, high flow speeds and reactive gases [1]. Silicon carbide is a promising material, already used for power electronic applications [2] and in MEMS for its high bandgap, mechanical robustness, thermal and chemical stability [3], [4]. The semiconductor nature of the material enables to control the dopant concentration, making it suitable as an active element in MEMS devices, exploiting the piezoresistive and thermoresistive effects [5]. The usage of SiC enables these effects to be used in sensor designs for harsh environments applications [6]. In this work we will focus on the demonstration of proof of concept of SiC-based hot-wire sensors, for measurement of hot and high-Reynolds turbulent airflow.

Design and realisation

This work introduces a micromachined device aimed for thermal flow measurement in harsh environments, made with a double-clamped micro-wire structure.

Epitaxial 3C–SiC thin films have been deposited onto a silicon substrate using Chemical Vapor Deposition (CVD) process. N-type doping of the SiC film has been achieved by introducing nitrogen in the CVD reactor. A negative 2 × 10^{18} cm^{-3} level of doping has been measured on Van der Pauw structures using a Hall effect characterisation setup. Structure patterning was achieved using Reactive Ion Etching (RIE) with a / mixture, followed by an under-etch process.

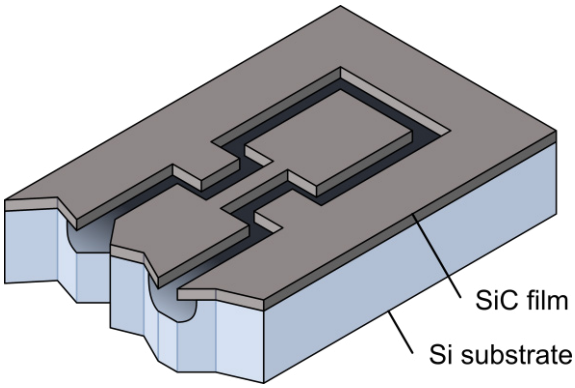

Fig. 1. Schematic view of the sensor micro-wire.

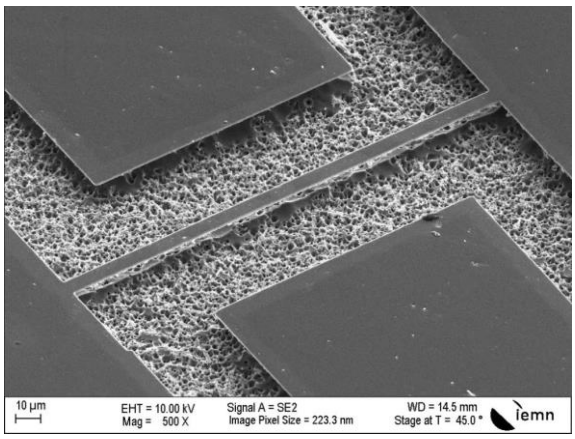

Fig. 2. SEM view of the sensor micro-wire.

Characterisation

First thermal and electrical characterisations of the device have been conducted, including current-voltage (I–V) curves to measure the electrical resistance of the micro-wire, as well as measurement of the Temperature Coefficient of Resistance (TCR) *vs.* the temperature. Emphasis is placed on the sensitivity evaluation for thermal sensors using SiC as an active layer. These measurements have been carried on temperatures ranging from 25 to 500 °C. A maximum TCR of 20000 ppm/K has been measured on a 180 °C overheat working point, which is much higher than what is typically obtained with metal-based hot wires (2000 – 4000 ppm/K).

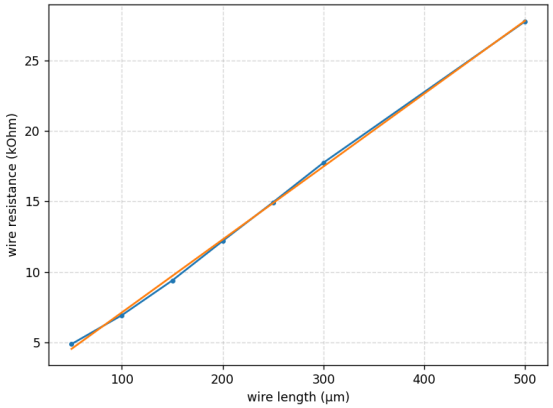

Fig. 3. Wire electrical resistance vs. *length.*

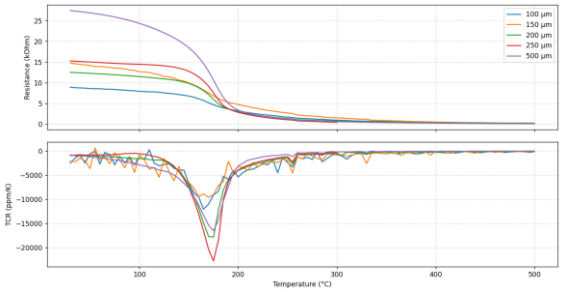

Fig. 4. Resistance and TCR measurements vs. *temperature.*

Conclusion

In conclusion, this study presents a proof of concept utilising SiC for the development of hot-wire sensors capable of measuring airflow in harsh environments. Through the fabrication and characterization of a SiC-based micro-wire structure, this study highlights the potential advantages of the material, making it a promising candidate for applications requiring thermal sensing in harsh environments.

Acknowledgement

This work was funded by the French National Research Agency (ANR) in the framework of the PEPR Électronique RESISTE project. It is also supported by the CPER RITMEA project. The authors also thank RENATECH, the French national nanofabrication network, and FEDER.

References

[1] V. Balakrishnan, H.-P. Phan, T. Dinh, D. V. Dao, and N.-T. Nguyen, “Thermal Flow Sensors for Harsh Environments,” Sensors, vol. 17, no. 9, 9, p. 2061, Sep. 2017, doi: gpbs62.

[2] X. She, A. Q. Huang, Ó. Lucía, and B. Ozpineci, “Review of Silicon Carbide Power Devices and Their Applications,” IEEE Transactions on Industrial Electronics, vol. 64, no. 10, pp. 8193–8205, Oct. 2017, doi: gf48v7.

[3] P. M. Sarro, “Silicon carbide as a new MEMS technology,” Sensors and Actuators A: Physical, vol. 82, no. 1, pp. 210–218, May 2000, doi: ck46fg.

[4] M. Mehregany, C. A. Zorman, N. Rajan, and C. H. Wu, “Silicon carbide MEMS for harsh environments,” Proceedings of the IEEE, vol. 86, no. 8, pp. 1594–1609, Aug. 1998, doi: dpv557.

[5] T. Dinh, N.-T. Nguyen, and D. V. Dao, “Applications of Thermoelectrical Effect in SiC,” in Thermoelectrical Effect in SiC for High-Temperature MEMS Sensors, T. Dinh, N.-T. Nguyen, and D. V. Dao, Eds., in SpringerBriefs in Applied Sciences and Technology., Singapore: Springer, 2018, pp. 85–106, doi: mspg.

[6] V. Balakrishnan, T. Dinh, H.-P. Phan, D. V. Dao, and N.-T. Nguyen, “Highly sensitive 3C-SiC on glass based thermal flow sensor realized using MEMS technology,” Sensors and Actuators A: Physical, vol. 279, pp. 293–305, Aug. 2018, doi: gfbgrf.

DOI 10.5162/EUROSENSORSXXXVI/PT4.200

Development of a novel silicon-based biocompatible EEG electrode

Ádám Salamon [1], *Gábor Rózsás* [1], *György Bognár* [1]
[1] *Department of Electron Devices, Budapest University of Technology and Economics Budapest, Hungary*

salamon.adamlaszlo@edu.bme.hu

Summary:
This paper presents a proof-of-concept silicon-based biocompatible dry/semi-dry platina EEG electrode prototype for future usage in BCI systems. Using silicon-based MEMS technology, varied topography can be created with dry and wet chemical milling. Other microtip-based electrodes achieve direct contact by penetrating the epidermis. Our approach is to increase the adheres and contact surface on hairy skin without penetrating into the skin surface.

Keywords: Electroencephalography, Electrodes, Brain-computer interfaces, Biomedical electrodes, Microelectromechanical

Introduction

There is increasing demand for applying the results of neuroscience and cognitive neuroscience in brain-machine interfaces in many interdisciplinary research areas. In recent decades, traditional conductive gels and silver/silver-chloride electrodes become less popular for electroencephalography (EEG) devices, and more convenient dry and semi-dry electrode systems have become commercially available. Their advantages are that they are more comfortable, gel dehydrates over time [1], and leave an unpleasant stain. However, dry and semi-dry electrode signal-noise ratio is usually lower than traditional wet EEG systems [1], [2]. As a result, these brain-machine interfaces often do not provide the expected performance.

This paper proposes a novel fabrication approach that integrates mechanical milling with a dicing saw and wet chemical etching, doping, and coating methods using semiconductor MEMS technology. The fabrication process begins with wet chemical etching of a 1000 µm thick silicon substrate. This way, the tips of the electrodes are formed. After that, mechanical milling is applied by a dicing saw to form square electrode geometries. Subsequently, the electrode material is further doped to achieve better electrical conductance. The platinum layer is deposited to the electrode surface in the last step to achieve sufficient electrode-skin contact.

The integration of Hybrid Mechanical Milling with Wet Chemical Etching processes in semiconductor MEMS technology enables the realization of intricate electrode designs with high precision and reproducibility.

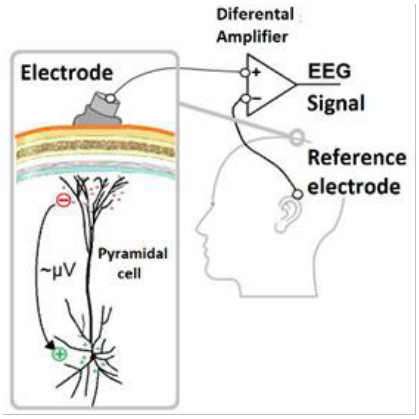

Fig. 1. The postsynaptic potential change of the pyramidal cells creates an electric dipole, the electric field measured by the EEG device.

Background, Motivation, and Objective

Our long-term vision is to develop a multisensory brain-computer interface (BCI) system for detecting students' stress, concentration, and arousal levels to evaluate different teaching methods. We intend to provide a tool for a more comprehensive understanding of students' cognitive and flow mental states by integrating multiple sensor systems, leading to the development of more effective teaching strategies and interventions that could ultimately improve educational outcomes. Currently, our focus is to improve the EEG recordings by experimenting with new electrodes and device structures to achieve a BCI system that can measure students' EEG during lessons quite comfortably.

Electrode manufacturing process

The electrode manufacturing process starts with a 1 mm thick, n-type phosphorous doped wafer with surface orientation of <100> and 1-2 Ωcm resistivity. The wafer is cleaned using the RCA1 and RCA2 standard processes. After that, a 200 nm thick oxide layer is grown on the surface by high-temperature dry oxidation to create a masking layer for the wet chemical etching. The pattern is created for the tips using a 400x400 µm rectangular mask in a 400x400 µm raster, as seen in Fig 2.

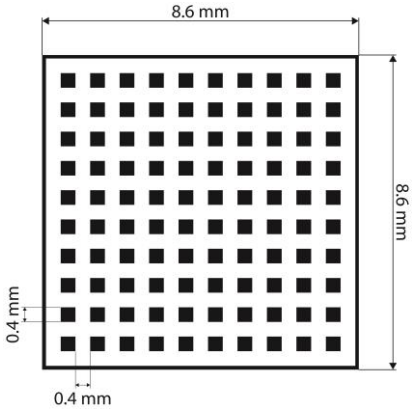

Fig. 2. Mask pattern for wet chemical etching.

The wet chemical etching is performed with 5wt% TMAH (Tetramethylammonium hydroxide) in purified H_2O for 80 minutes at 92°C to create an even D=100 µm deep anisotropic etching between the electrode tips. (Fig. 3.)

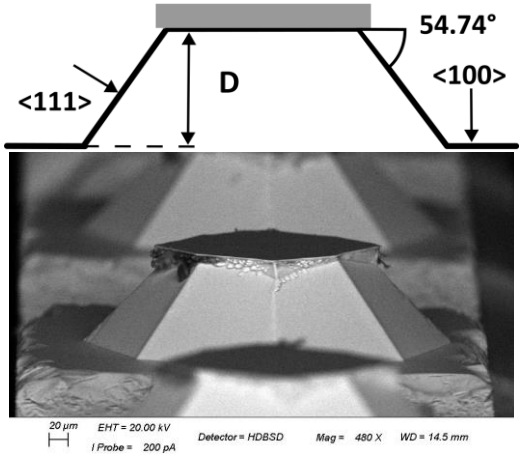

Fig.3. Electrode tips created by TMAH etching.

To create a homogenous etched surface and prevent the unwanted formation of micro pyramids 0.2 wt%/hour of APS (Ammonium Persulfate) was added to the solution.

The 400 µm deep ditches were created by a 300 µm thick dicing saw. (In the structure shown in Fig. 4., the staggered indentation is a by-product of the saw's geometry.) Hair can slip into the trenches, and in the future, we would like to experiment with filling them with skin conductance increasing materials.

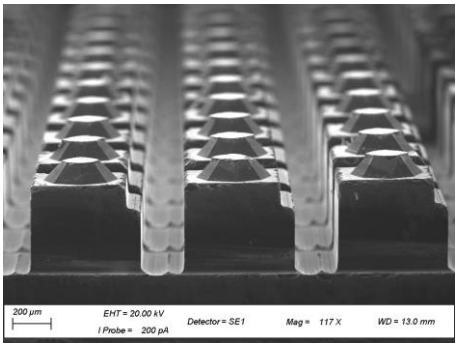

Fig. 4. Electrode structure.

To increase the conductivity of the silicon substrate, further doping with n-type phosphorus was performed to make the substrate highly doped near the surface. Finally, a ~100 nm platinum layer was sputtered on the electrode surface to increase the conductivity further and make it biocompatible and resistant to mecha-no-chemical effects. (Fig.5.)

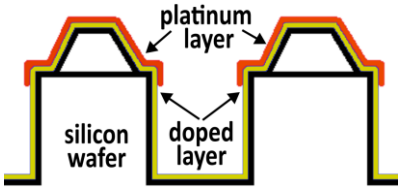

Fig. 5. Electrode final layer structure.

Results

This paper presented a platina-coated silicon-based dry EEG electrode prototype structure and its manufacturing process. The electrode's surface design adheres well to the skin's surface, even under slight pressure, without penetrating into its upper layers. The structure is sufficiently resistant and does not wear out during use. Further characterization and real-world EEG testing will proceed in the near future.

Acknowledgements

The research reported in this paper was fully funded by the K_20 grant through project No. 135224 of the National Research, Development and Innovation Office (NKFIH).

References

[1] S. Yao and Y. Zhu, “Nanomaterial-Enabled Dry Electrodes for Electrophysiological Sensing: A Review,” JOM, vol. 68, no. 4, pp. 1145–1155, Apr. 2016, doi: 10.1007/s11837-016-1818-0.

[2] P. Tallgren, S. Vanhatalo, K. Kaila, and J. Voipio, “Evaluation of commercially available electrodes and gels for recording of slow EEG potentials,” Clin. Neurophysiol., vol. 116, no. 4, pp. 799–806, Apr. 2005, doi: 10.1016/j.clinph.2004.10.001.

DOI 10.5162/EUROSENSORSXXXVI/PT4.212

Thermally Actuated Colloidal Tip SU-8 Scanning Probes

Ali Hosseinpour Shafaghi[1], Rayan Bajwa[1], Muhammad Umar[1], Murat Kaya Yapici [1,2,3]
[1] Faculty of Engineering and Natural Sciences, Sabanci University, Istanbul 34956, Turkey
[2] Department of Electrical Engineering, University of Washington, Seattle, WA 98195, USA
[3] Sabanci University Nanotechnology Research and Application Center, Istanbul 34956, Turkey

murat.yapici@sabanciuniv.edu

Summary:

This study presents significant advancements in microfabrication techniques for developing probes with diverse tip geometries and microspheres attached to probe tips for various applications. We introduce a novel method for transfer of spherical microparticles onto probe tips. First, the microparticles were assembled within cavities bulk-etched into (100) oriented single crystal silicon and subsequently the scanning probes were patterned using SU-8 as the structural material. Upon sacrificial layer etching, SU-8 scanning probes were released with spherical microparticle tips at the distal end of the cantilever. Additionally, we explored the integration of bimorph electrothermal actuators for precise probe actuation. Notably, our bimorph thermal actuator demonstrates superior displacement at lower voltages compared to the existing literature. The use of SU-8 as the probe material simplifies the fabrication process and enhances the device's biocompatibility. This property makes it particularly suitable for biomedical applications, extending the potential impact of this research beyond the scope of the current study.

Keywords: Actuator, Bimorph, Colloidal probe, Colloidal assembly, SU-8

Introduction

Cantilevers, especially those with colloidal tips are essential components in precision instruments, utilized across fields like biomedical diagnostics [1] and to quantify surface interfacial forces [2]. Particularly crucial in atomic force microscopy (AFM), they facilitate nanoscale imaging and manipulation [3]. Traditional AFM probes employ piezoelectric or electromagnetic actuation methods to control interactions with sample surfaces [4,5]. However, current cantilever technologies encounter challenges in sensitivity, integration, scalability, reproducibility, and long-term stability [6].

Recent advancements in the design and fabrication of cantilevers have aimed to address these issues. Thermally actuated cantilevers offering a potentially more controlled and adaptable approach compared to traditional piezoelectric actuation [7]. The use of thermally actuated mechanisms in colloidal probes can potentially enhance the sensitivity and adaptability of measurements, allowing for dynamic adjustments of probe properties in response to environmental changes or specific experimental needs. However, integrating these thermal mechanisms with colloidal probes presents a unique set of challenges and opportunities.

This study is motivated by the need to optimize thermally actuated systems, particularly when integrated with colloidal probes. It aims to develop a novel manufacturing protocol for fabricating customized tip geometries and configurations, including integration with complementary technologies like microfluidics, and addressing the associated design, fabrication, and optimization challenges.

Materials and Methods

The fabrication of cantilevers with various tip shapes or microspheres begins with cavity fabrication. First, $SiO_2/Si_3N_4/SiO_2$ layers are deposited on both sides of a Si wafer via PECVD. These layers are then patterned by lithography and etched using DRIE. For cantilevers with pyramidal tips or microspheres, the wafer is etched in KOH, and remaining SiO_2 is removed with BOE.

For cubic-tip cantilevers, we used DRIE instead of KOH etching. To fabricate cantilevers with both pyramidal and cubic tips, a 200 nm SiO_2 sacrificial layer was deposited, followed by spin-coating SU-8. After lithography patterning and

BOE immersion, the cantilevers were released. SEM images of the two tip shapes are shown in Fig. 1. Next, we attempted to attach microspheres to the cantilever tips using pyramidal cavities.

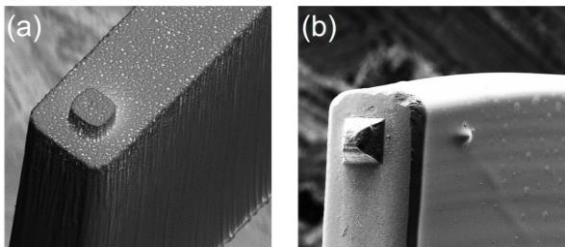

Fig. 1. SEM images showing (a) a cantilever with a cubic tip, and (b) a cantilever with a pyramidal tip

To transfer microspheres to the cantilever tips, we used an assembly process within the cavities, aided by capillary flow for precise positioning. However, coating with SU-8 initially displaced the particles, so we switched to the drop-casting technique for SU-8 coating, which serves as the cantilever material.

To drop-cast a 200 µm thick SU-8 film, we calculated the required SU-8 volume for each sample and applied it centrally using a micropipette. After soft-baking on a flat hot plate for even distribution, the SU-8 was UV-exposed through a mask, followed by post-exposure baking and development in PGMEA. The process finished with the release of the samples by etching away the sacrificial layer.

Fig. 2a, 2b illustrate the microsphere assembly on the cantilever tip. Fig. 2c shows an assembled microparticle inside the cavity. Side and top views of the cantilever confirm the microsphere attachment to the tip (Fig. 2d, 2e).

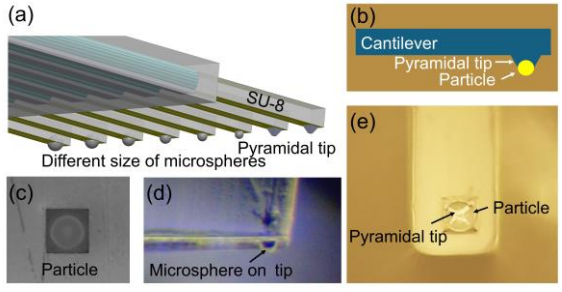

Fig. 2. (a),(b) Schematics of Microsphere Assembly on Cantilever Tip, (c) Assembled Microparticle within Cavity, (d) Cantilever with Microsphere Attached, (e) Top View of Microsphere on Cantilever Tip.

The final goal of this study was to fabricate cantilevers with various tip geometries or microspheres attached to the tip that could be actuated. Fig. 3a illustrates a schematic of an actuated cantilever. To achieve this, we employed a bimorph electrothermal actuator. Initially, a 250 nm thick layer of Cu was coated onto the sacrificial layer using a thermal evaporator, leaving the cavity area empty. To enhance adhesion, a 5 nm layer of Cr was deposited on both the top and bottom surfaces of the Cu. To apply the input voltage to the pads of the thermal actuator, a probe station was utilized (Fig. 3b). Fig. 3c depicts the Cu layer, which served as the active layer of the thermal actuator aligned with the cavities. Notably, there is no residual copper in the cavity area, and the cantilever can successfully actuate (Fig. 3d).

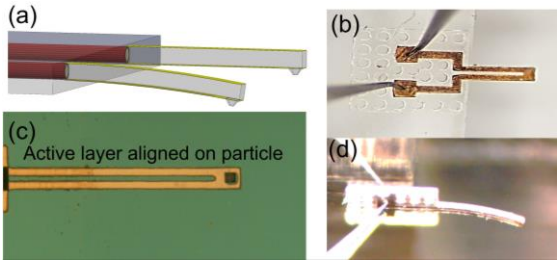

Fig. 3. (a) Schematic of an actuated cantilever, (b) Utilization of a probe station to drive the cantilever (c) image of the active Cu layer, (d) Actuated cantilever.

Acknowledgments

This work was supported by Sabanci University and The Scientific and Technological Research Council of Turkey (TUBITAK) grant number 120C135. Professor Murat Kaya Yapici appreciates the support of the Turkish Academy of Sciences (TUBA GEBIP'21 Award) and Science Academy (BAGEP'23 Award).

References

[1] A.K. Basu et al., Micro/Nano fabricated cantilever based biosensor platform: A review and recent progress, *Enzyme Microb. Technol.* 139, 109558 (2020); doi: 10.1016/j.enzmictec.2020.109558

[2] M.K. Yapici, J. Zou, Microfabrication of Colloidal Scanning Probes with Controllable Tip Radii of Curvature, *J. Micromech. Microeng.*19, 105021 (2009); doi: 10.1088/0960-1317/19/10/105021

[3] B.O. Alunda, Y.J. Lee, Review: Cantilever-based sensors for high speed atomic force microscopy, *Sensors* 20, 4784 (2020); doi: 10.3390/s20174784

[4] M.B. Coskun et al., Design, fabrication, and characterization of a piezoelectric AFM cantilever array, *IEEE Conf. Control Technol. Appl.* 227-232, (2019); doi: 10.1109/CCTA.2019.8920686

[5] Y. Tian et al., A novel method and system for calibrating the spring constant of atomic force microscope cantilever based on electromagnetic actuation, *Rev. Sci. Instrum.* 89, (2018); doi:10.1063/1.5051401

[6] Y. Zhu, T.-H. Chang, A review of microelectromechanical systems for nanoscale mechanical characterization, *J. Micromech. Microeng.* 25, 093001 (2015); doi: 10.1088/0960-1317/25/9/093001

[7] A. Potekhina, C. Wang, Review of electrothermal actuators and applications, *Actuators* 8, 69 (2019); doi: 10.3390/act8040069.

DOI 10.5162/EUROSENSORSXXXVI/PT4.234

Electrochemical Seismometers Using a SOI Chip with Four Micro-electrodes

Zhenyu Sun[1,2], Junbo, Wang[1,2], Deyong,chen[1,2], Jian,chen[1,2]
[1] Aerospace Information Research Institute, Chinese Academy of Sciences, Beijing 100190, CHINA
[2] University of Chinese Academy of Sciences, Beijing 100049, CHINA

jbwang@mail.ie.ac.cn

Summary:
This paper reports a new method to integrate four micro-electrodes on one SOI wafer with micro-vias of any size. 6 different SOI chips with nice insulation between each electrode was fabricated. After the test of electrochemical seismometers (ECSs), it shows that the ECSs using the chips with large diameter and small minimum inter-space of micro-vias feature small bandwidth but large peak sensitivity, which provides a valuable reference for the design of the ECSs meeting different performance.

Keywords: SOI, micro-electrodes, micro-vias, MEMS technologies, electrochemical seismometers.

Background, Motivation an Objective

Four micro-electrodes arraying on the sequence of anode-cathode-cathode-anode is the sensitive element of electrochemical seismometers (ECSs). They are typically formed on chips with numbers of micro-vias [1-3]. With the growingly development of the MEMS technologies, the tendency of them is to reduce the consumption of wafers and to increase the integration of electrode areas. In recent years, the number of electrodes fabricated on one wafer had already increase from one[1], two[2] to lately four[3]. However, the method presented by reference [3] was only applicable to chips with the micro-vias with large depth-to-diameter ratios. This paper supposed a new fabrication process of a SOI chip with four micro-electrodes, which could make vias of any size. 6 SOI chips were fabricated to compare the influence of different structural parameters on the performance.

Description of the New Method or System

This paper proposed a method to fabricate SOI chips with four micro-electrodes on one wafer. On the beginning, a SOI composed of two 200μm thick silicon and one 2um thick SiO_2 was prepared. After twice lithography and Deep Reactive Ion Etching (DRIE), the removal of the SiO_2 was achieved by using hydrogen fluoride to form insulating slot. Insulating layers of SiO_2 were firstly deposited on the both surfaces of the wafer by Chemical Vapor Deposition (CVD) before sputtering platinum on that. Finally, excess metal was removed by Ion Beam Etching (IBE), where the retained metal was protected by dry film.

Results

Six different SOI chips with four micro-electrodes having nice insulation between each electrode were fabricated. By assembled in a same ECS and using a same testing circuit, their response of sensitivity vs frequency was tested as the figure showed. The results supposed that the chips with large diameter and small minimum inter-space of micro-vias achieved small bandwidth but large peak sensitivity, of which the ECS using chip-1 had the smallest bandwidth of 2.90Hz-7.60Hz and the largest peak sensitivity of 12962.03V/(m/s) @5Hz. To the contrary, the ECS using chip-6 had the largest bandwidth of 0.84Hz-34.21Hz and the smallest peak sensitivity of 4098.83V/(m/s)@3Hz. This provided a valuable reference for the design of the ECS meeting different performance requirements.

References

[1] T. Deng, D. Chen, Microelectromechanical Systems-Based Electrochemical Seismic Sensors with Insulating Spacers Integrated Electrodes for Planetary Exploration, *IEEE Sensors Journal* 16, 650-653 (2016), doi: 10.1109/jsen.2015.2491783

[2] C. Xu, J. Wang, The Electrochemical Seismometer Based on Fine-Tune Sensing Electrodes for Undersea Exploration, *IEEE Sensors Journal* 20, 8194-8202 (2020), doi: 10.1109/JSEN.2020.2985702

[3] Z. Sun, T. Liang, Electrochemical Seismometer Based on One Single Silicon Chip with Four Electrodes, *22nd International Conference on Solid-State Sensors, Actuators and Microsystems*, 60-63 (2023)

DOI 10.5162/EUROSENSORSXXXVI/PT4.234

Figures

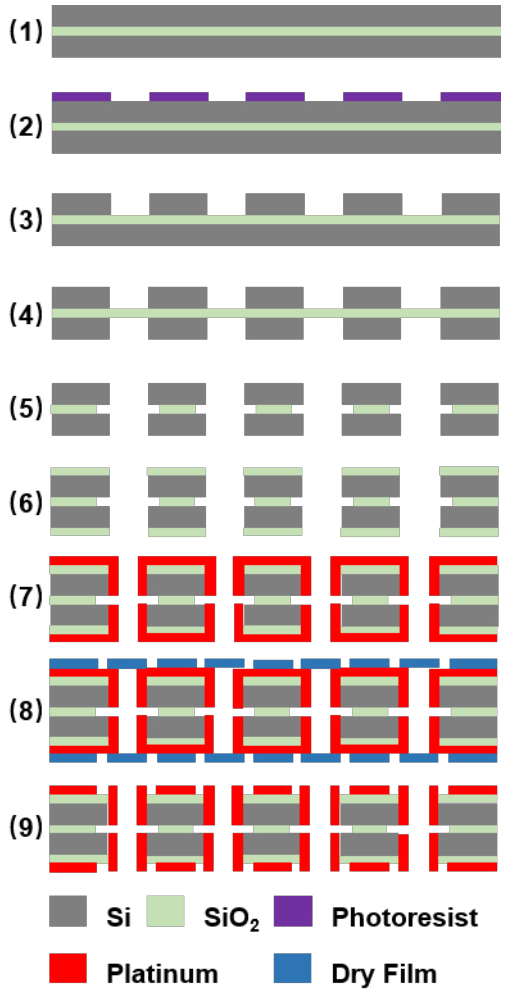

Fig. 1. Fabrication Process of a SOI chip with four micro-electrodes.

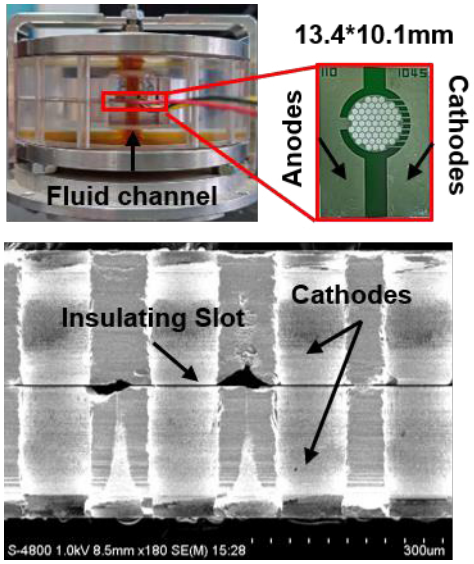

Fig. 2. Physical diagram of a MEMS electrochemical seismometer and a SOI chip with SEM diagram of its cross section.

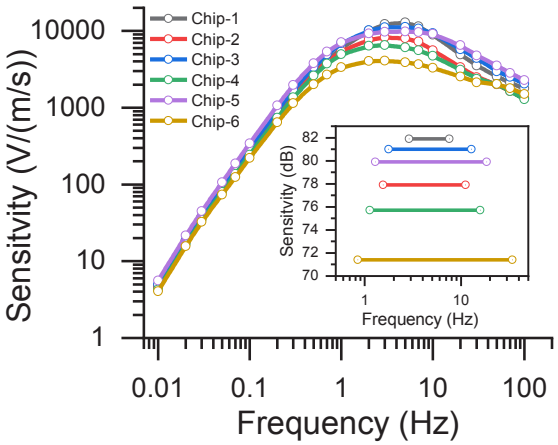

Fig. 3. Graph of sensitivity vs frequency for six different SOI chips, where the mini-graph is the bandwidth of them.

Tables

Tab. 1: Structural parameters of six different SOI chips

	Diameter of micro-vias	Minimum inter-space of micro-vias
Chip-1	110μm	10μm
Chip-2	100μm	15μm
Chip-3	90μm	10μm
Chip-4	80μm	15μm
Chip-5	70μm	10μm
Chip-6	60μm	15μm

Tab. 2: Bandwidth and peak sensitivity of six different SOI chips

	Bandwidth	Peak sensitivity
Chip-1	2.90Hz-7.60Hz	12962.03 V/(m/s)@5Hz
Chip-2	1.55Hz-11.15Hz	8262.24 V/(m/s)@3Hz
Chip-3	1.77Hz-12.87Hz	11318.51 V/(m/s)@5Hz
Chip-4	1.13Hz-15.80Hz	6524.09 V/(m/s)@3Hz
Chip-5	1.29Hz-18.55Hz	9851.62 V/(m/s)@5Hz
Chip-6	0.84Hz-34.21Hz	4098.83 V/(m/s)@3Hz

DOI 10.5162/EUROSENSORSXXXVI/PT4.238

Characterization of Gastric Tissue Samples with MEMS Force Sensor Based Indentation method

János Márk Bozorádi[1,2], Géza Papp[3], Zsófia Sz Bérces[2], Péter Fürjes[2]
[1] Microsystems Lab., Inst. of Technical Physics and Materials Science, HUN-REN Centre for Energy Research, Budapest, Hungary
[2] Óbuda University Doctoral School on Materials Sciences and Technologies, Budapest, Hungary
[3] Uzsoki Hospital, Budapest, Hungary

Corresponding Author's e-mail address: bozoradi.janos@ek.hun-ren.hu

Summary:

Considering the actual requirements in laparoscopic as well as robotic surgical practices and the advancements in utilisation of artificial intelligences in data analysis and decision making, the need for tissue mechanical analysis is greater than ever. However, the necessary data is still hard to acquire due to the existing gap between medical and engineering professionals in daily practice. Since the chosen methods of tissue characterization vary widely, we designed our measurement setup so that it resembles clinical practice as closely as possible. [1] In our cooperation with the Uzsoki Hospital, we present the results of our measurement system developed for gastrointestinal tissue characterization. We aim this as a pioneer project to form a basis for larger, more targeted data collection to improve medical professionals' decision-making during surgical procedures.

Keywords: mechanical tissue characterization, indentation, gastric, biomechanics

Background, Motivation an Objective

While laparoscopic surgeries are some of the most routine procedures today, postoperative complications can still arise and though advanced robotics are precise and beneficial, improvements of surgical tools are still in high demand. Probably the most critical aspect in need of developments is the quantitative assessment of the surgeon's tactile feedback. [2] To provide researchers and medical engineers accurate data regarding tissue properties systematic and controlled measurements with a large sample size are needed. A MEMS force sensor based [3] indentation type tissue mechanical analyser have been developed and deployed at the Surgery and Onco-surgery Ambulance of Uzsoki Hospital in Budapest. In our current pilot study, we demonstrate the capability of our system for ex-vivo tissue thickness measurement at a clinically relevant force range. Furthermore, post-processing the force-displacement data provided by the sensor and supported with the metadata acquired about the patient and tissue condition, forms a promising foundation for AI-supported decision-making algorithms. Our preliminary results demonstrates that the tissue analytical system would be integrated into a laparoscopic stapler, offering real-time data on tissue characteristics, and potentially providing decision-making support to surgeons during surgery.

Measurement System and Methodology

Our measurement setup integrates the MEMS piezoresistive 3D force sensor developed by HUN-REN CER's Microsystems Lab [3]. The setup applies the indentation method previously defined by Egorov et al. [4]. Since the medical objective of our long-term work is to adopt our tissue characterisation methodology in laparoscopic devices, indentation is the corresponding solution to mimic the compression type deformations emerging during laparoscopic gastric surgeries.

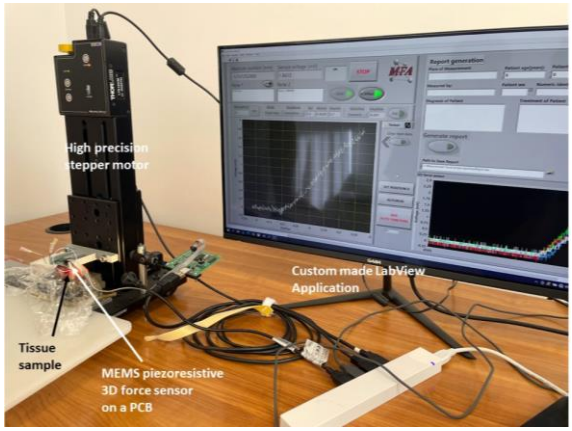

Fig. 1. Indentation type measurement system at the Uzsoki Hospital.

The measurement system is driven by a custom made LabView application and records the

force-displacement curve during controlled compression of the examined tissue. The force information is provided by the MEMS piezoresistive 3D force sensor while the accurate deformation is generated by a high precision stepper motor. The setup is quite robust for ex-vivo field experiments, although the sensor itself can be easily integrated into a laparoscopic jaw according to its form factor.

The tissue samples were mostly cancerous gastric leftovers which were removed during resection. The contact points of the sensor were chosen to be either on a tumorous (but measurable) region or near the sectioned and stapled line. Measurements on the anatomically important healthy regions were also executed for comparison the mechanical characteristics different tissue status. The majority of our measurements focused on different session of the colon, such as the transversum, the sigmoideum and the rectum, with additional samples obtained from the pancreas and the stomach. The experiments were accomplished under ethical authorization number IV/174- 2 /2022/EKU.

Results

A total of 42 ex vivo measurements have been implemented on 30 human tissue samples to date. Two representative experimental force – displacement functions are demonstrated in in *Figure 2.* They represent the diverse tissue biomechanical properties associated with different medical conditions.

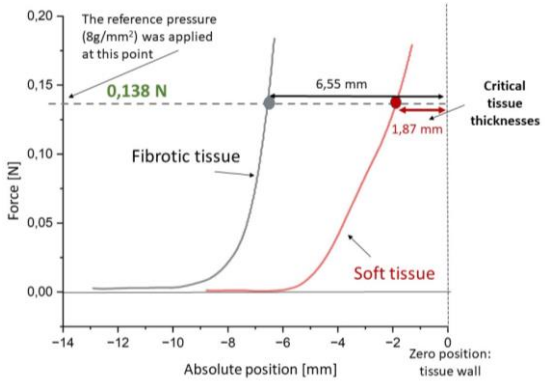

Fig. 2. Force-displacement curve of two pancreas samples

Considering the *F(d)* curve, the compressed tissue thickness can be determined from the displacement detected at the critical force value to be reached for optimal stapling during surgical procedure. The conventional pressure value between the stapler's jaws is considered to be 78,4 mN/mm^{2}in clinical practice. The detected critical force value corresponding to this pressure can be calculated as 138 mN considering the sensor's geometry.

Outlook

Accurate determination of the optimal thickness of the compressed tissue prior to stapling would represent a significant advancement in laparoscopic surgery. Moreover, the data obtained from the force – displacement measurements contain a wealth of relevant information regarding tissue biomechanics also. By extracting relevant parameters (such as uncompressed tissue thickness, Young-moduli, and others) from these datalines and analysing them with consideration medical metadata regarding patient vital signs, tissue condition and pathology, surgeons can establish a deeper understanding of how various pathological conditions affect tissue biomechanics and surgical results. With this background knowledge, these smart devices will be able to refine onsite surgical decision support during laparoscopic gastrointestinal surgeries.

Discussion

Testing different samples provided valuable insight on how these measurements can be carried out on a large scale by medical personnel. We are continuously refining both the software and user interface accordingly. This study demonstrates the ability to measure compressed tissue thickness and reveal clinically relevant differences in tissue characteristics, such as significant change in the biomechanical properties of a highly inflamed tissue compared to a healthy one. Based on our experiences, a handheld, laparoscope-like measurement system is to be developed for efficient large quantity data gathering. Critical feature is the precise laparoscope geometry compatible for usage in surgical environments.

[1] Ciara Durcan, Mokarram Hossain, Mechanical experimentation of the gastrointestinal tract: a systematic review, *Biomechanics and Modeling in Mechanobiology*, 2024 Feb;23(1):23-59. doi: 10.1007/s10237-023-01773-8.

[2] John C. Alverdy, Biologically inspired gastrointestinal stapler design: "Getting to Zero" complications, *The American Journal of Surgery* Volume 226, Issue 1, July 2023, Pages 48-52 https://doi.org/10.1016/j.amjsurg.2023.01.030

[3] J.M. Bozorádi., A. Nagy, Characterisation tissue elasticity by MEMS force sensors, *MNE-ES 2022 - Micro and Nano Engineering (MNE) & Eurosensors 2022 Conferences*, Leuven, Belgium, 2022

[4] V. Egorov, S. Tsyuryupa, Soft tissue elastometer, *Medical Engineering & Physics*, Volume 30, Issue 2, March 2008, Pages 206-212,

DOI 10.5162/EUROSENSORSXXXVI/PT4.262

Characterization of Magnetotorquer Magnetic Moment: magnetometric and fluxmetric methods

Elda Saunderson[1], Michal Janosek[2], Danie Gouws[1]
[1] South African National Space Agency, Hermanus, South Africa,
[2] Czech Technical University in Prague, Prague, Czech Republic

esaunderson@sansa.org.za

Summary:
Torquer rods for commercial spacecraft need to be characterized for qualification purposes. Very accurate characterization is possible using lengthy methods with accurate mechanical specifications, however, in the commercial environment this is not feasible. Three characterization methods, two magnetometric and one fluxmetric, are evaluated on robustness and uncertainty.

Keywords: Torquer rod, magnetic flux, coil, uncertainty, micro satellite

Introduction

Torque Rods are used on microsatellites, small satellites and cubesats as part of the attitude control systems [1] where the controllable magnetic moments of torque rods interact with the Earth's magnetic field. Torque rods consist of a solenoid winding with soft magnetic material as a core and their characteristic (magnetic moment) need to be verified during qualification.

Motivation and Objective

This paper investigates various methods to characterize torque rods accurately using methods that could be commercially viable in terms of time. We studied three methods: absolute and differential magnetometry using one or two magnetometric readings [1],[2], and an adaptation of a fluxmetric method used for permanent magnets [3]. Motivation for our work comes from the issue of accurately and repeatedly aligning the torque-rod relative to the magnetometer in the "single-point" magnetometric method, where the result uncertainty is dominated by distance uncertainty (tilt up to units of degrees produces negligible errors). Uncertainty due to mechanical placement was evaluated by repeated measurements with the rod removed and replaced, as well as at different axial displacements and orientation angles. The torque rod used in this study has a length of 375 mm and a nominal magnetic moment of 19 Am^2 at 296 mA; we used 200 mA for all measurements. All evaluations were executed in a magnetically quiet environment (<1nT p-p noise) and a fluxgate magnetometer (LEMI-011B) was used.

Magnetic field at specific distance

The classical method involves the measurement of magnetic flux density [1],[2]. The radial component of flux density $\mathbf{B_r}$ is measured when the torque rod of length **L** is energized at a set distance **R** (Fig. 1). This method is, however, extremely sensitive to the accurate distance between the rod and the magnetic sensor (its position in the magnetometer).

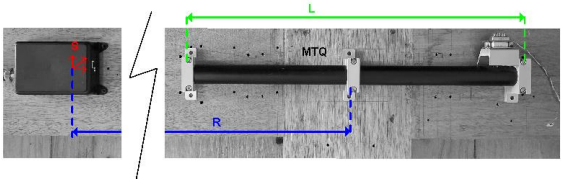

Fig. 1. Torque rod and magnetometer setup

Magnetic moment is calculated from eq. (1) [1].

$$m = \frac{4\pi}{\mu_0} \frac{1}{\frac{R}{L}\frac{1}{\sqrt{2}} \left(R^2 - RL + \frac{L^2}{4}\right)^{\frac{3}{2}} - \frac{R}{L}\frac{1}{\sqrt{2}} \left(R^2 + RL + \frac{L^2}{4}\right)^{\frac{3}{2}}} B_r \quad (1)$$

Two test points with accurate separation

Given the extreme sensitivity of the previous method regarding distance of placement, obvious from eq. (1), and the chance of human error involved, a variation of this method is proposed where two measurements are taken with the same sensor, at two set distances apart. Only the difference in distances i.e. by a spacer or precise magnetometer movement is required, which can be accurately established. In this case, we do not use the full equation (eq. (1)) but the classical un-corrected point-wise dipole field equation for $\mathbf{B_r}$ eq. (2) (valid only far away).

$$B_{r1} = \frac{\mu_0}{4\pi} \frac{2m\cos\alpha}{R^3} \quad (2)$$

We can then express the distance **R** and substitute to the same equation with **R+dR**:

$$B_{r2} = \frac{\frac{\mu_0}{4\pi}m}{\frac{\mu_0}{4\pi B_{r1}}m + 3\left(\sqrt[3]{\frac{\mu_0}{4\pi B_{r1}}m}\right)^2 dR + 3\left(\sqrt[3]{\frac{\mu_0}{4\pi B_{r1}}m}\right)dR^2 + dR^3} \quad (3)$$

Distances of 850 mm and 1000 mm were used, given a separation *dR* of 150 mm. The magnetic moment is calculated by minimizing eq. (3) where ***Br₁*** and ***Br₂*** is the magnetic flux density measured at the two positions respectively.

Fluxmetric method

The basis of the fluxmetric method is change in magnetic flux, as detected by a coil enclosing the flux lines of the magnetic dipole source (torque rod). We evaluated various Helmholtz coils as in [3], however, ended up using a solenoid which gave the best signal-noise ratio. The solenoid has a length of 600 mm, 300 turns, 350 mm diameter and a coil constant of 543.23 µT/A. The magnetic length of the torque rod is around 2/3 of the coil length, so we expected large errors as the coil homogeneity has been determined to be below 0.1 % within +-15 cm only. The torque rod was placed in the centre of the solenoid (see Fig. 2) and 200 mA applied. The change of magnetic flux in the coil was measured with a Hirst IFM03 Flux-meter. Magnetic moment is calculated from eq. (4)

$$m = \frac{\Delta\vartheta}{K} \quad (4)$$

where $\Delta\vartheta$ is the change in magnetic flux in Wb, and *K* is the coil constant in T/A (543.23 µT/A).

Fig. 2. Torque rod inserted in solenoid centre

Comparative summary of the three methods

Table 1 and Fig 3 shows results for the 3 methods when repeated 5 times (torque rod placed and removed) and also when misaligned. The most robust and most repeatable is the fluxmetric method, insensitive both to angular and axial misalignment; however, it is about +6% off both magnetometric methods. The single position calculation suffers, obviously, from a distance measurement error (+4% at 75 cm), which is suppressed with the differential two-point method. Surprisingly, the differential method works well even with classical dipole field equation eq. (2) uncorrected on rod length.

Tab. 1: Magnetic moments calculated

Criteria	Fluxmetric	Single point	Two points
Mean/5	12.114	11.430	11.432
10º	-1.2%	-1.0%	-0.1%
+1 cm	-0.08%	+4.4%	-

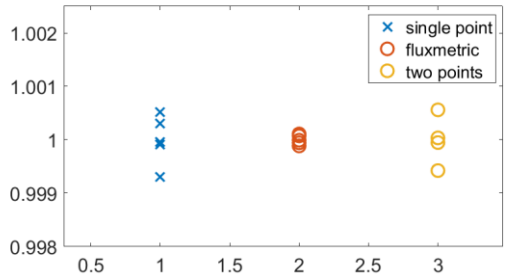

Fig. 3. Spread of 5 repeated measurements for all three methods (relative to the mean value)

Conclusions

The “revived” solenoid fluxmetric method shows the most consistent results, with a correction factor applied, however, a single magnetometric calibration would suffice. Its main advantage is that it does not need precise positioning (a 1 cm misplacement yielded only 0.08% error). The method with 2 magnetometers has potential when employing both equations for radial and tangential field to avoid effects of large angular misalignments, however, resulted in almost the same spread of values due to the small differential distance. Both methods have potential to lessen calibration uncertainty while reducing the alignment time. A promising modification of the two-point method would be a fixed set of two magnetometers where the exact magnetic distance would be precisely determined i.e. with the help of gradient coils.

References

[1] J. Lee, et al., On Determining Dipole Moments of a Magnetic Torquer Rod - Experiments and Discussions, *Canadian Aeronautics and Space Journal* 48 no 1, 61–67 (2002); doi:10.5589/q02-014

[2] K. Seleznyova, et al., Modelling the magnetic dipole. *European Journal of Physics*, 2016, 37.2: 025203.

[3] S. R. Trout, Use of Helmholtz coils for magnetic measurements. *IEEE Transactions on Magnetics*, 1988, 24.4: 2108-2111

DOI 10.5162/EUROSENSORSXXXVI/PT4.274

FOS4CMS: FBG monitoring in the CMS Experiment at CERN

Zoltan Szillasi[1 3], Francesco Fienga[2,3], Vincenzo Romano Marrazzo[2,3], Noemi Beni[1,3], Andrea Iracea[2], Salvatore Buontempo[4,3] and Giovanni Breglio[2,3]
[1] HUN-REN Institute for Nuclear Research (HUN-REN ATOMKI), H-4026 Debrecen, Hungary,
[2] Università degli Studi di Napoli Federico II, Department of Information Technology and Electrical Engineering (DIETI) IT-80125 Napoli, Italy,
[3] European Organization for Nuclear Research (CERN), CH-1211 Geneva, Switzerland,
[4] National Institute for Nuclear Physics (INFN), IT-80126 Napoli, Italy

Corresponding Author's e-mail address: Zoltan.Szillasi@cern.ch

Summary:
This paper provides an extensive overview of more than a decade of continuous data collected by the Fiber Optic Sensing for CMS (FOS4CMS) network, featuring over 1000 Fiber Bragg Grating (FBG) sensors. These FBG sensors have been instrumental in monitoring temperature and strain within the Compact Muon Solenoid (CMS) experiment at the Large Hadron Collider (LHC). Operational since 2009, the monitoring system underwent expansions during LHC Long Shutdowns (LS1 and LS2) and upgrades for LHC Run3.

Keywords: FBG sensor, CMS experiment, CERN, High energy physics

Introduction

In this document, we present data gathered by a network of approximately 1000 Fiber Bragg Grating (FBG) sensors, collectively known as FOS4CMS, pertains to temperature and strain measurements recorded during the operation of the Compact Muon Solenoid (CMS) experiment within the Large Hadron Collider (LHC) when colliding proton beams, as well as during maintenance periods over the course of the past fifteen years. This FBG data collection has been continuous, running 24/7 throughout this time frame. FBG sensors have been strategically positioned to monitor various aspects of the CMS experimental apparatus. paragraphs.

Materials and Methods

The CMS Experiment [1] features a highly intricate and extensive detector system, comprising a substantial superconductive magnetic solenoid capable of generating a magnetic field of up to 3.8T, accompanied by several sub- detectors designed to capture and quantify various elementary particles generated in the LHC collisions. This extensive detector spans dimensions of 21 meters in length, 15 meters in width, and 15 meters in height, residing in a cavern buried 100 meters below ground level. The CMS detector is segmented into distinct components: the primary body (referred to as the "barrel") consists of five disks, while the two extremities (known as the "endcaps") are constructed from four disks, each. Illustrated in Figure 1a, the detectors are composed of layered materials that leverage the distinct characteristics of particles to detect and measure their energy and momentum. The operation of the CMS Experiment is conducted under exceedingly complex environmental conditions, necessitating ongoing monitoring of temperature, structural integrity, relative humidity, and magnetic fields. At present, thorough monitoring covers the entire CMS area, aiming to gather real-time data on all subsystems, particularly crucial for temperature-sensitive equipment and precise thermal conditions.

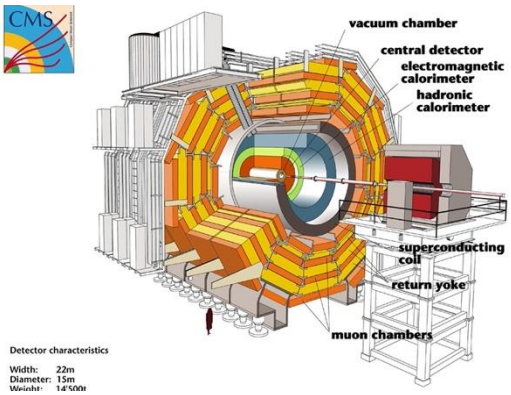

Fig. 1. Cutaway view showing the CMS detector © 2008-2023 CERN.

The existing multitude of detectors and electrical components within the CMS does not readily accommodate the installation of additional monitoring systems. Furthermore, the demanding operational conditions of the LHC, characterized by elevated levels of radiation and magnetic fields, often render conventional electronic sensors unsuitable for ensuring optimal functionality.

A noteworthy attribute of FBG sensors [2] is their spectral encoding, rendering them impervious to electromagnetic noise, optical carrier intensity modulation, and broadband-radiation-induced losses. Ionizing radiation primarily results in wavelength-dependent radiation-induced attenuation in optical fibers, as demonstrated in [3]. These unique characteristics empower the development of extended-distance sensing systems capable of operation in challenging environments, such as the underground experimental facilities at CERN.

Since 2009, our group has led the installation of FBG-based monitoring systems at CERN's underground CMS facility. Initially, the deployment included a gradual increase in the number of temperature and strain sensors, reaching a total of 200, which operated around the clock for a continuous three-year period during LHC collisions. Remarkably, these sensors functioned seamlessly without any interference with the CMS experiment's operational conditions [4].

From February 2013 to March 2015, the LHC underwent Long Shutdown 1 (LS1), during which our FBG monitoring system at the CERN CMS facility expanded. Throughout LHC Run2 (April 2015 to December 2018), the FOS4CMS system, comprising nearly one thousand FBG sensors, provided comprehensive coverage from the outer to inner components of the CMS experiment. Subsequently, during LHC LS2 (April 2018 to April 2022), we further expanded FOS4CMS. With the commencement of LHC Run3 in May 2023, the upgraded FOS4CMS system now monitors the CMS experimental apparatus.

The readout system for these FBGs relies on the Wavelength Division Multiplexing (WDM) technique, employing multiple interrogators whose outputs seamlessly integrate into the CMS Detector Control System [5].

Results

The results will be presented in the paper provides compelling experimental evidence affirming the robust viability of FBG sensors in the intricate and challenging environmental conditions of High Energy Physics (HEP).

The data cover a span exceeding fifteen years, showcasing the remarkable success of FBG measurements within the CMS experiment. Throughout this period, our FBG sensors actively monitored temperatures within the core of CMS, capturing strains in diverse locations during LHC collisions and under the influence of a high magnetic field.

References

[1] CMS collaboration, The CMS experiment at the CERN LHC, JINST 3 (2008) S08004; doi: 10.1234/s10000; doi: 10.1088/1748-0221/3/08/S08004

[2] K. O. Hill and G. Meltz, "Fiber Bragg grating technology fundamentals and overview," Journal of Lightwave Technology, vol. 15, no. 8, pp. 1263-1276, 1997; doi: 10.1109/50.618320

[3] Gusarov, A.; Hoeffgen, S.K. "Radiation Effects on Fiber Gratings". IEEE Trans. Nucl. Sci. 2013, 60, 2037-205; doi: 10.1109/TNS.2013.2252366

[4] M. A. Saccomanno, et al., Long-term temperature monitoring in CMS using fiber optic sensors, Sensors J., IEEE, Dec. 2012, pp. 3392-3398; doi: 10.1109/JSEN.2012.2205989

[5] Z. Szillasi, et al., One year of FOS measurements in CMS experiment at CERN, Phys. Procedia 37 (2012) 79-84; doi: 10.1016/j.phpro.2012.02.360

DOI 10.5162/EUROSENSORSXXXVI/PT4.292

An implantable ultrasonic sensor for continuous monitoring of wound rehabilitation

Ye Tian[1], Yueying Yang[1], Hanchuan Tang[1], Jianfeng Zang[1,2]
[1] School of Integrated Circuits and Wuhan National Laboratory for Optoelectronics, Huazhong University of Science and Technology, Wuhan, China. 430074
[2] The State Intelligent Laboratory of Digital Manufacturing Equipment and Technology, Huazhong University of Science and Technology, Wuhan, China. 430074

Corresponding Author's e-mail address: dr.ye.tian@gmail.com

Summary:

Implantable devices for continuous, wireless monitoring of tissue rehabilitation are crucial for personalized health. Traditional electronic sensors, though small and flexible, struggle with biomechanical matching, biodegradability, biocompatibility, and wireless monitoring. Here, we introduce an electronics-free implantable strain sensor using ultrasonic metagel for continuous monitoring of wound rehabilitation. Tested on porcine tendon and wounded tissue in live pigs, the metagel monitors tissue rehabilitation continuously and wirelessly.

Keywords: Implantable sensor, strain sensor, flexible sensor, acoustic metamaterials, ultrasound

Title

AN IMPLANTABLE ULTRASONIC SENSOR FOR CONTINUOUS MONITORING OF WOUND REHABILITATION

Background, Motivation an Objective

The development of the metagel strain sensor is rooted in the growing need for advanced monitoring solutions in personalized healthcare, particularly for wound rehabilitation[1]. Traditional implantable electronic sensors, despite being small and flexible, face significant challenges in terms of biomechanical compatibility, biodegradability, biocompatibility, and effective wireless monitoring[2,3]. These limitations can hinder their long-term use and integration with biological tissues. Motivated by these challenges, the metagel strain sensor in this work provide a more effective, biocompatible, and biodegradable alternative for continuous and wireless monitoring of tissue rehabilitation.

Description of the New Method or System

In this work, we present an ultrasonic implantable metagel strain sensor for continuous and wireless monitoring of internal tissue rehabilitation. By utilizing a hydrogel-based 2D phononic crystal structure, the metagel sensor can seamlessly integrate with soft tissues and wirelessly transmit strain data through ultrasonic bandgap shifts, offering a promising solution for real-time monitoring and rehabilitation of wounds.

Results

In this article, an ultrasonic strain sensor, composed of air cells in soft hydrogels, is designed for continuous monitoring of internal tissue rehabilitation. The ultrasonic metagel sensor stands out due to its all-hydrogel design, eliminating the need for rigid materials like semiconductor chips or metal components. As a result, the metagel sensor offers outstanding softness, biocompatibility, and biodegradability, along with the long communication distance, all of which are essential for implantable sensors in clinical applications.

The schematic of the metagel implant, which consists of periodic air columns embedded in soft hydrogels, is shown in **Fig. 1**. The wireless monitoring system uses an ultrasonic probe placed on the skin's surface. Deformation of the metagel causes a shift in the ultrasonic bandgap, detectable by the external ultrasonic probe. This probe emits ultrasounds towards the internal metagel implant and captures the returning echoes. By analyzing the spectral characteristics of these echoes, the sensor can detect internal tissue strains. The phononic crystal design, formed by the periodic structure, has an acoustic bandgap defined by its dimensional parameters. As the metagel stretches, the acoustic bandgap shifts to a higher frequency, causing a corresponding shift (Δf) in the peak frequency of the echoes.

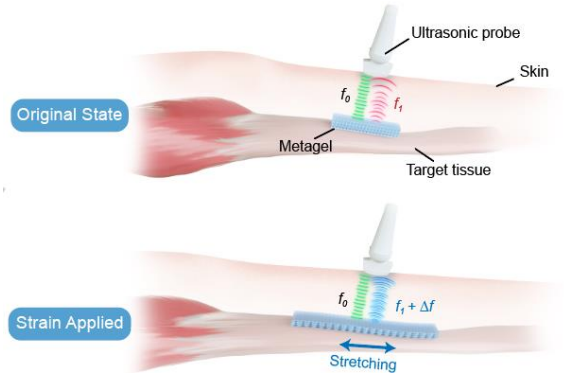

Fig. 1. Mechanism of the metagel strain sensor.

To characterize the frequency shift of the metagel sensor more clearly, the movement of the peak frequency was measured in a typical stretch-release cycle within 20% strain as shown in **Fig. 2**. The shift of the echo's peak frequency during the stretching process exhibited similar behavior to that during the release process, indicating dependable performance in 20% strain.

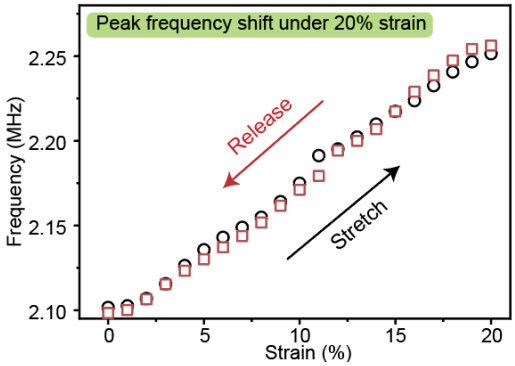

Fig. 2. Strain sensing ability of the metagel sensor.

To verify the strain sensing ability of the metagel sensor in vivo, the metagel was implanted on the broken tendon to monitor the tendon stretching in live pigs. The metagel sensor on the broken tendon shows a larger frequency shift than normal tendon under the same bending process (**Fig. 3**). Therefore, the metagel sensor can be used to monitor tendon dehiscence in clinical applications. After the ruptured tendon re-grows and connects, the frequency shift of the metagel sensor was reduced under the bending process of the pig's foot. Thus, the wound healing progress can be observed through long-term and continuous monitoring of tendon strains using the metagel sensor.

Similar to the monitoring of the broken tendon, the metagel sensor can also be used on the monitoring of the subcutaneous wound. Two subcutaneous wounds were created by tissue excision on the back of a pig, then a normal metagel and a metagel with growth factors were respectively attached on each wound to achieve two different wound healing rates, as shown in **Fig. 4**. According to amplitudes of the frequency shift generated by breathing, we can monitor the wound recovery process. The faster the wound tissue grows, the quicker the decrease in frequency shift generated by breathing.

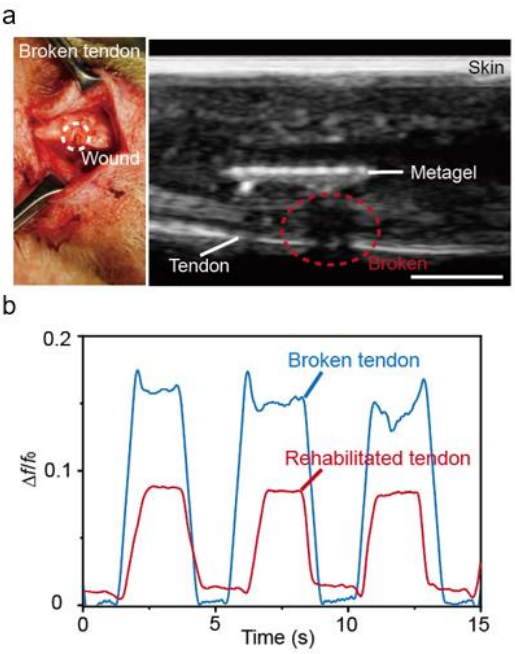

Fig. 3. Monitoring of the broken tendon's rehabilitation on day 1 (blue line) and day 7 (red line) post-implantation.

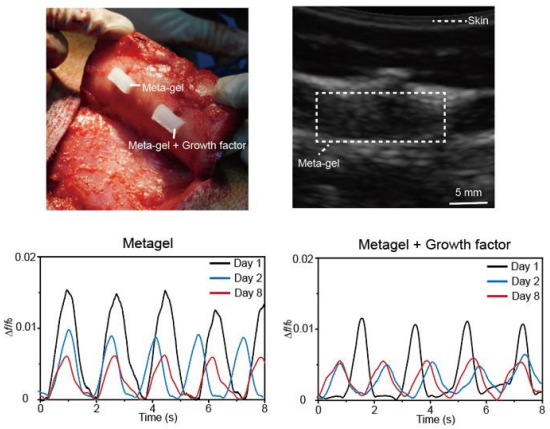

Fig. 4. Monitoring of the subcutaneous wound rehabilitation using the normal metagel (left) and metagel loaded with growth factors (right).

References

[1] D. Docheva, et al, Biologics for tendon repair. Adv. Drug Deliv. Rev. 84, 222-239 (2015); doi:10.1016/j.addr.2014.11.015

[2] S. Patel, H.Park, P. Bonato, L. Chan & M. Rodgers, A review of wearable sensors and systems with application in rehabilitation. J. Neuroeng. Rehabil. 9, 21 (2012). doi: 10.1186/1743-0003-9-21

[3] H. Tang, et al, Injectable ultrasonic sensor for wireless monitoring of intracranial signals. Nature 630, 84-90 (2024). doi: 10.1038/s41586-024-07334-y

DOI 10.5162/EUROSENSORSXXXVI/PT4.303

Development of Metallic inks for the Fabrication of a Flexible Metal Oxide Gas Sensors by Inkjet Printing Process

Le Porcher Bastien[1], *Rieu Mathilde*[1], *Viricelle Jean-Paul*[1]
[1] *Mines Saint-Etienne, Univ Lyon, CNRS, UMR 5307 LGF, Centre SPIN, F-42023 Saint-Etienne, France*

Corresponding Author: rieu@emse.fr

Summary:

This study focuses on developing a fully inkjet-printed gas sensor on a flexible substrate. The primary challenge lies in formulating metallic inks with long term stability, high concentration, and inkjet compatible properties. Two distinct methodologies were explored: one centered around nanoparticle-based synthesis, while the other one was particle-free. To achieve an operational sensor, numerous layers were deposited, ranging from gold electrodes to platinum resistance and a SnO_2 sensing layer. Every stage of the manufacturing process has been optimized , allowing to obtain a functional device.

Keywords: Nanoparticles synthesis, Metallic inks, Inkjet printing, Flexible electronic, SnO_2 sensing layer

Introduction

The context of this study is the preparation of a flexible gas sensor onto a plastic substrate, by inkjet printing. In order to get a full sensor, as shown in Fig. 1. semi-conductive metal oxide gas sensors are composed by a sensing material, here, tin dioxide. This layer allows the detection of different type of gas by measuring the resistance change of the semiconductor layer. This semiconductor layer is bridging two gold electrodes that are needed to acquire all the electrical measurement. Electrode are typically made of conductive material such as metals. Gold is frequently used in sensor fabrication field due to is low reactivity with gases. A heater is also printed on the back side of the heater. In this case, this heater is made of platinum layers connected to gold tracks and it is heating the sensor by using Joule effect.

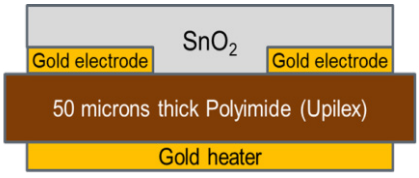

Fig. 1. Scheme of metal oxide gas sensor compositive layers [1]

SnO_2 inks and layers have been developed in previous works [1, 2]. Homemade metallic inks have now to be developed. The advantages of homemade inks comparing to commercial one's is that the compositions are controlled and no additives or pollutants are added.

All the intermediate steps of the metallic ink development involving particles synthesis, ink formulation, printing process, deposition, thermal treatment and coating characterization, will be discussed. At the end of the day, a fully inkjet printed sensor will be characterized.

Materials & methods

Gold nanoparticles (AuNPs) solutions have been made by an optimized Turkevich method [3] using Tanique Acid (TA) and Sodium Citrate (SC) in aqueous medium allowing to obtain 3.9mM solutions.

Platinum nanoparticles (PtNPs) solutions have been synthesized by reduction of a platinum salt by polyols reaction triggered by the presence of a 150°C ethylene glycol (EG) solution.

Both of these nanoparticles solutions have been formulated depending on their own properties (surface tension and viscosity) in order to obtain suitable ink for inkjet process. This was done by adding mixture of solvents to modify these initial values.

Particles free inks have also been developed based on metallic salt solvation in solvents mix, resulting in obtaining a concentrated gold ink and a concentrated platinum ink.

Finally, SnO_2 ink have been developed by a sol-gel process in presence of ethylene glycol that is allowing to obtain a ready to print tin dioxide ink [2].

All these steps were merged together to obtain a complete and functional gas sensor.

Results

The gold nanoparticles solution is composed by a 5 to 15nm gold particles as shown by the particle distribution. Addition of glycerol and isopropanol to the AuNPs solution led to decrease the surface tension from 73mN/m to 31.7 mN/m and to increase the viscosity from 1mPa.s to 14mPa.s. This ink was correctly printed after optimizing the waveform, the tension applied, the nozzle and platen temperature and the wettability of the substrate. A total number of layers of 100 was printed on PI foil and then dried at 110°C and then thermally treated at 350°C for 2 hours. Finally, coating was not continuous as shown by SEM image presented in Fig. 2.

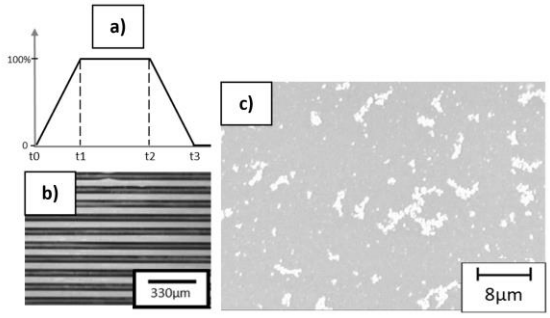

Fig. 2. a) waveform used for inkjet printing of AuNPs ink b) 1D lines obtained after deposition optimization and c) SEM image of 100 layers deposited AuNPs coating

Particle free ink is composed by $HAuCl_4$ directly dissolved in a mixture water, ethylene glycol and isopropanol. The viscosity and surface tension of this ink were measured and are 32 mN/m and 14 mPa.s. All the printing parameters were also optimized and then 60 layers were deposited. Coatings obtained after thermal treatment at 350°C, shown on the Fig. 3., are conductive. The measured resistivity is about 1.0×10^{-7} Ω.m.

Fig. 3. Deposit of 60 layers of particle free gold ink after thermal treatment at 350°C for 2 hours

Combination of AuNPs made ink and precursor made ink make possible to deposit homogeneous, high resolution, and conductive gold electrodes onto polyimide foils.

Polyvinylpyrrolidone (PVP) stabilized platinum nanoparticles has been synthesized by reduction of H_2PtCl_6 salt in near boiling point ethylene glycol solution [4]. Optimized synthesis led to obtaining concentrated EG-PtNPs solutions. This platinum nanoparticles solution was mixed isopropanol and different solvents in order to reach a suitable surface tension and viscosity for the inkjet printing process. This formulation led to deposition of homogeneous and conductive platinum coating by inkjet printing.

Tin dioxide ink is made of $SnCl_2$ which is made to react with NH_4OH and CH_3COOH in order to substitute Cl atom by OH ligand and then CH_3COOH. In presence of ethylene glycol, an oligomeric net named tin glycolate is formed allowing particles to be stable in solution [2].

All these layers were cured at a maximum temperature of 350°C in order to not degrade the PI substrate. This complete device was characterized under reducing and oxidizing gases. Discussion on the benefits of homemade inks will conclude this work

References

[1] Rieu M, Camara M, Tournier G, et al (2016) Fully inkjet printed SnO2 gas sensor on plastic substrate. Sensors and Actuators B: Chemical 236:1091–1097. https://doi.org/10.1016/j.snb.2016.06.042

[2] Kassem O, Saadaoui M, Rieu M, Viricelle J-P (2017) Synthesis and Inkjet Printing of SnO2 Ink on a Flexible Substrate for Gas Sensor Application. In: Proceedings of Eurosensors 2017, Paris, France, 3–6 September 2017. MDPI, p 622

[3] J. Turkevich, Discuss. Faraday Soc., 11 1951, 55, DOI.org/10.1039/DF9511100055

[4] Bonet F, Delmas V, Grugeon S, et al (1999) Synthesis of monodisperse Au, Pt, Pd, Ru and Ir nanoparticles in ethylene glycol. Nanostructured Materials 11:1277–1284. https://doi.org/10.1016/S0965-9773(99)00419-5

DOI 10.5162/EUROSENSORSXXXVI/PT4.307

Miniaturized Sensor Platform for the Determination of Impedance Spectroscopic Parameters in Environmental Monitoring

Martin Brandl, Thomas Posnicek
University for Continuing Education Krems, 3500 Krems, Austria

Martin.brandl@donau-uni.ac.at

Summary:
The soil moisture and the hydraulic properties of a soil matrix can only be characterized with considerable effort. Soil moisture is usually measured at specific points using moisture sensors, but a detailed spatial distribution of soil moisture cannot be derived from this. In order to achieve a comprehensive analysis of soil properties in 2D or 3D, a system for electrical impedance spectroscopy (EIS) or electrical impedance tomography (EIT) is presented, which is designed for field use.

Keywords: electrical impedance spectroscopy (EIS); electrical impedance tomography (EIT); blue-green infrastructure; sponge city; soil moisture

Introduction

Decentralized measures based on nature-based system solutions (including blue-green infrastructure) have proven to be essential for adapting to climate change and, in particular, to the intensification of heavy rainfall events, which overload existing sewer systems. These include green roofs, planted surface infiltration, raingardens, or retention area infiltration such as ponds. Increasing sealing in urban areas as well as low water retention capacity in the surrounding landscape elements and increasingly frequent heavy rainfall events lead to an overload of the rainwater and combined sewer system with consequences such as flooding, damage to infrastructure, buildings and people. During normal rainfall events, rainwater is quickly drained away via drainage systems such as canals or ditches and is not available to the local water balance to supply plants and trees, as well as contributing to groundwater recharge. In agricultural areas, heavy rainfall events lead to soil erosion and the entry of pollutants into surface waters and groundwater due to the lack of landscape barriers [1].

So-called decentralized solutions have become established as an adaptation measure, which throttle the inflow towards the sewer, retain water, store it, evaporate it and infiltrate it locally. Various forms of blue-green infrastructure such as green roofs, storage ponds and different types of infiltration systems are used here. This results in a reduction in runoff into the rainwater or combined sewer system, which prevents pluvial flooding due to overloading in the sewer. In addition, this contributes to the storage and use of rainwater for plants and their cooling effect, as well as increasing resilience to drought and heat and renewing groundwater through infiltration on site [2].

The principle of the sponge city is based on effectively absorbing rainwater, storing it, evaporating it and, if necessary, releasing it into the groundwater in a purified state. However, the functionality of the sponge city principle essentially depends on the retentive materials used and their properties in the subsoil. The characterization of the hydraulic properties of these materials can be determined by the soil moisture content. Soil moisture content is an essential index that is suitable for characterizing the water dynamics of the subsoil and its coupling nature with the overlying road conditions in terms of water infiltration, water storage and groundwater recharge, etc. However, due to the spatial heterogeneity of the subsurface and complex influencing factors, it remains a major challenge to map soil moisture content on a field scale in an urban environment.

Method and Results

Conventional methods for estimating soil water content such as direct sampling and the tensiometer cannot provide large-scale measurements or detailed spatial data on soil moisture. The principle of spatial impedance tomography presented here can provide a 2D or 3D measurement of local soil moisture.

Electrical impedance spectroscopy (EIS) or electrical impedance tomography (EIT) is a method for analyzing the electrical properties of materials and systems by exciting harmonic electrical signals at different frequencies. The recorded impedance vs. frequency is then related to the physical parameters or properties of materials and systems. Powerful and license-free tools are available for the evaluation of impedance spectroscopic data, such as "Electrical Impedance Tomography and Diffuse Optical Tomography Reconstruction Software" (EIDORS). EIDORS is a software package for image reconstruction in electrical impedance tomography (EIT) and diffuse optical tomography (DOT) [3]. Fig. 1 shows the general structure of the EIS system. Fig. 2 shows the pattern of the connected electrodes.

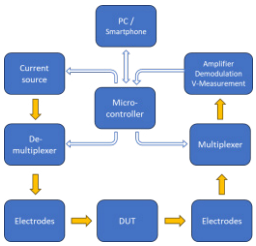

Fig. 1. Scheme of the EIS system.

In order to obtain a complete set of measurement data, a defined current (I_{typ}=1mA) was fed into the measuring arrangement at 2 electrodes and the voltage was measured between the other electrodes.

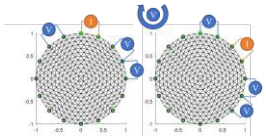

Fig. 2. Measuring principle.

This process was cyclically shifted clockwise by one electrode at a time to record a set of 208 measurement data. For the test setup, 16 electrodes with a diameter of D_E=4mm were placed in a measuring cylinder with a diameter of D_C=15cm. The measurement frequency for all tests was f_0=30kHz.

The results of the test setup are shown in Fig. 3. The measuring cylinder was filled with water and a plastic test tube with a diameter of D_T=3cm was placed in different positions. As the plastic has a much higher impedance than the liquid used (H_2O+NaCl), the position of the plastic tube is shown as an area with very low conductivity and confirms the proof of principle.

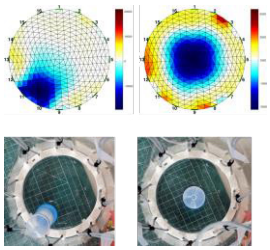

Fig. 3. Results from first experiments.

Acknowledgements

This project is funded by the Lower Austrian provincial government and the European Regional Development Fund (ERDF) with the project number WST3-F-5030664/036-2023.

References

[1] Almaaitah T, Appleby M, Rosenblat H, Drake J, Joksimovic D. The potential of Blue-Green infrastructure as a climate change adaptation strategy: A systematic literature review. Blue-Green Systems. 2021 Jan 1;3(1):223-48.

[2] Ghofrani Z, Sposito V, Faggian R. A comprehensive review of blue-green infrastructure concepts. International Journal of Environment and Sustainability. 2017 Mar 27;6(1).

[3] Zhu Y, Fan J, Xu Q, Xiang Y, Huang L, Wang Z, Yan X, Du T, Cheng Q. A new portable electrical impedance tomography system for measuring two-dimensional stem water content distribution. Agricultural and Forest Meteorology. 2022 Oct 15;325:109161.

Solution Processed Gold Nanoparticles-MoS2 Thin Film for NO2 Sensing

Ni, F. Z. Bouanis, A. Yassar, Ecole Polytechnique (LPICM, CNRS), Palaiseau (France)

Unfortunately, this abstract is not available, as the contribution was not confirmed at the time the conference proceedings were finalized.

Solution Processed Gold Nanoparticles-MoS2 Thin Film for NO2 Sensing

Ni, F. Z. Bouanis, A. Yassar, Ecole Polytechnique (LPICM, CNRS), Palaiseau (France)

Unfortunately, this abstract is not available, as the contribution was not confirmed at the time the conference proceedings were finalized.

Flexible gas sensor based on rGO-ZnO on PET substrate for NO2 detection at room temperature

A. A. Komorizono, R. R. Leite, V. R. Mastelaro, University of São Paulo, São Carlos, (Brazil),
S. De la Flor, E. Llobet, Universitat Rovira i Virgili, Tarragona (Spain)

Unfortunately, this abstract is not available, as the contribution was not confirmed at the time the conference proceedings were finalized.

Flexible gas sensor based on rGO-ZnO on PET substrate for NO2 detection at room temperature

A. A. Komorizono, R. R. Leite, V. R. Mastelaro, University of São Paulo, São Carlos, (Brazil),
S. De la Flor, E. Llobet, Universitat Rovira i Virgili, Tarragona (Spain)

Unfortunately, this abstract is not available, as the contribution was not confirmed at the time the conference proceedings were finalized.

DOI 10.5162/EUROSENSORSXXXVI/PT5.29

Electrochemical Deposition of Polyaniline on Laser-Induced Graphene for Room Temperature Ammonia Sensing

José Carlos Santos-Ceballos[1], Foad Salehnia[1], Frank Güell[2], Alfonso Romero[1], Xavier Vilanova[1]
[1] Universitat Rovira i Virgili, Microsystems Nanotechnologies for Chemical Analysis (MINOS), Tarragona, Catalunya, Spain
[2] Universitat de Barcelona, Energy Photonics Catalonia (ENFOCAT), Barcelona, Catalunya, Spain

josecarlos.santos@urv.cat, foad.salehnia@urv.cat

Summary:
This study explores the electrochemical modification of laser-induced graphene (LIG) with polyaniline (PANI)., resulting in the creation of a flexible chemoresistive PANI@LIG gas sensor for detecting ammonia (NH_3) levels at room temperature. The results obtained demonstrate that the deposition of PANI on LIG improves the response to NH_3. This work presents the first-time utilization of PANI@LIG for gas sensing and introduces a simple, yet effective, approach for fabricating wearable gas sensors that exhibit promising characteristics, including high sensitivity and flexibility. The findings open new avenues for developing low-cost, efficient, and portable gas detection systems.

Keywords: Laser-Induced Graphene, polyaniline, gas sensing, ammonia, flexible sensor

Introduction

Ammonia measurement is important in diverse applications from air quality monitoring to agricultural regulation and chemical industry safety. Due to the dangerous nature of NH_3, it is crucial to develop sensitive sensors for real-time monitoring [1]. In recent years, many NH_3 sensors have been developed, employing different technologies such as optical, electrochemical, and chemoresistive with both metal oxides and graphene-based sensors [2]. Among these, graphene-based sensors have increased their interest due to their ability to work at room temperature, making them an ideal candidate for wearable gas sensor applications [3]. However, traditional graphene synthesis methods pose challenges in terms of cost and integration into flexible electronics.

In 2014, a breakthrough approach was introduced for producing porous graphene films from commercial polymer films using a CO_2 infrared laser, termed laser-induced graphene (LIG) [4]. LIG exhibits high porosity, excellent electrical conductivity, and good mechanical flexibility making it suitable for various applications including electronic devices, catalysis, water purification, and biosensors [4]. Also, it has been used in gas sensing applications. Despite its potential, the utilization of LIG in NH_3 sensing has been limited due to its low response to this gas. Previous works have demonstrated that loading graphene with polyaniline (PANI) improves its sensitivity to NH_3 [5]. Building upon this concept, the current research works to develop an electrochemical method for fabricating gas sensors utilizing PANI@LIG.

Materials and Methods

For the fabrication of the LIG gas sensor (Fig.1 (a)), a commercially available polyimide film (50 µm) was used as a flexible substrate. LIG was synthesized using a CO_2 laser operating at a max power of 25 W. The laser beam scanned over the surface at a speed of 200 mm/s, a frequency of 12 kHz and 12% of laser power. The sensor has been designed with a sensing area of 3 x 6 mm^2. To improve the connection of the sensor with the measurement system, Ag ink was drop-casted on the region of the electrodes.

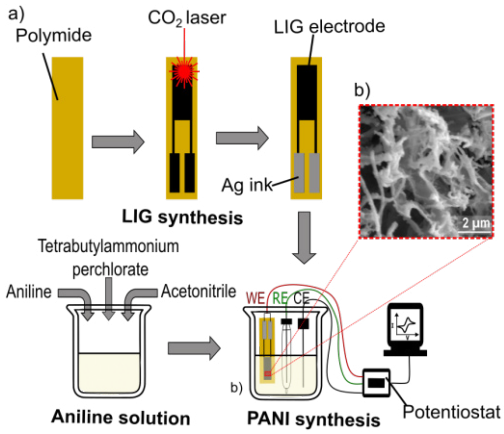

Fig. 1. Schematic illustration showing (a) the fabrication process and (b) SEM images of the PANI@LIG gas sensor.

Electrochemical growth was carried out using a potentiostat. A 3-electrode system comprised of bare LIG as working electrode, platinum wire auxiliary electrode, and Ag/AgCl reference electrode was used for experiments. The nanocomposite was prepared by cyclic voltammetry method electrode cycled at 50 mV/s between -0.2 and 1.3 V for 20 cycles in polymerization solution (0.1 M aniline/0.5 mM tetrabutylammonium perchlorate as the electrolyte /acetonitrile).

Results and Discussion

The SEM images show the morphology of PANI@LIG (Fig. 1(b)). The Raman spectra (Fig. 2) revealed prominent peaks corresponding to the characteristic vibrational modes of graphene and polyaniline.

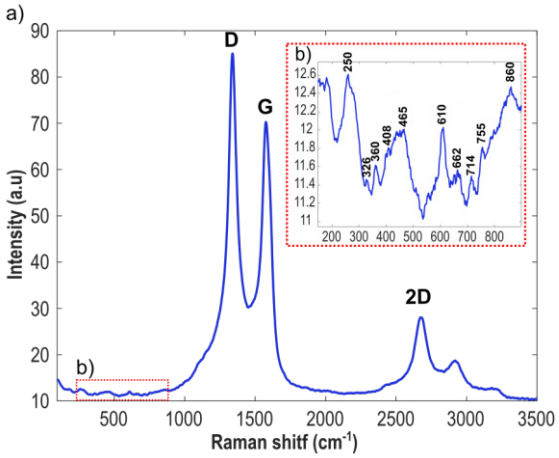

Fig. 2. Raman spectra of (a) the PANI@LIG gas sensor and (b) peaks corresponding to polyaniline.

The sensing performance of the LIG gas sensors developed for NH_3 detection was assessed through repeated cycles of response and recovery to concentrations of 5, 10, 25, 50, and 100 ppm. Fig. 3 illustrates the typical dynamic responses observed for the bare LIG (blue dots) and the PANI@LIG (red dots) gas sensors. The sensor responses (electrical resistance change) increased upon exposure to the target gas. The raised electrical resistance results from the decreased hole density and electrical conductivity of the p-type LIG upon exposure to the reducing NH_3 (electron donating). Fig. 3 demonstrates that the doped sensor shows an improved response and signal-to-noise ratio compared to the bare sensor. The PANI@LIG sensor exhibits responses that are up to 1.5 times higher in terms of the intensity of resistance changes induced by exposure to ammonia, compared to bare LIG.

Based on the experimental results, it can be inferred that although the response of the PANI@LIG sensor is not significant compared to that obtained in other investigations, the combination of these two nanomaterials exhibits a synergistic sensing effect, in which LIG and PANI interact with the NH_3, resulting in superior chemical gas sensing performance.

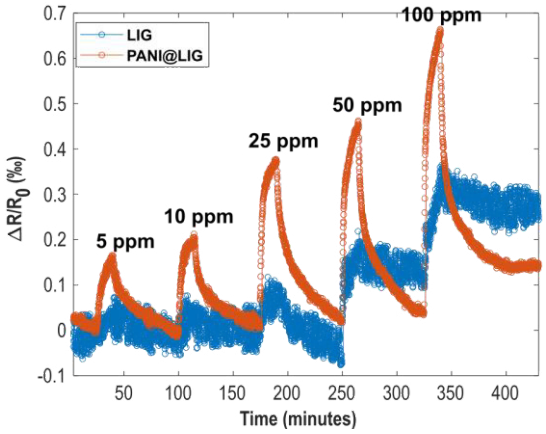

Fig. 3. Sensing performance of bare LIG (blue dots) and PANI@LIG (red dots) gas sensors to different concentrations of NH_3 at room temperature.

The development of a flexible room temperature chemical resistive sensor opens possibilities for NH_3 monitoring systems, offering advantages like a simple interface circuit, cost-effectiveness, low power consumption, and high portability, ideal for wearable gas sensors. Further optimization of electrochemical deposition methods is needed to enhance NH_3 sensor response, alongside comprehensive studies on humidity effect, repeatability, stability, and selectivity for future improvements.

References

[1] S. Aarya, Y. Kumar, and R. K. Chahota, “Recent Advances in Materials, Parameters, Performance and Technology in Ammonia Sensors: A Review,” *J Inorg Organomet Polym Mater*, vol. 30, no. 2, pp. 269–290, Feb. 2020, doi: 10.1007/s10904-019-01208-x.

[2] D. Kwak, Y. Lei, and R. Maric, “Ammonia gas sensors: A comprehensive review,” *Talanta*, vol. 204, pp. 713–730, Nov. 2019, doi: 10.1016/j.talanta.2019.06.034

[3] X. Tang, M. Debliquy, D. Lahem, Y. Yan, and J. P. Raskin, “A Review on Functionalized Graphene Sensors for Detection of Ammonia,” *Sensors 2021, Vol. 21, Page 1443*, vol. 21, no. 4, p. 1443, Feb. 2021, doi: 10.3390/S21041443

[4] T. D. Le *et al.*, “Recent Advances in Laser-Induced Graphene: Mechanism, Fabrication, Properties, and Applications in Flexible Electronics,” *Adv Funct Mater*, vol. 32, no. 48, p. 2205158, Nov. 2022, doi: 10.1002/adfm.202205158

[5] Y. Guo *et al.*, “Hierarchical graphene–polyaniline nanocomposite films for high-performance flexible electronic gas sensors,” *Nanoscale*, vol. 8, no. 23, pp. 12073–12080, Jun. 2016, doi: 10.1039/C6NR02540D.

DOI 10.5162/EUROSENSORSXXXVI/PT5.34

Voltammetric Sensing of Benzotriazole at Single-Walled Carbon Nanotube Modified Screen-Printed Electrodes

Neža Sodnik[1], Melanija Hadolin[1,2], Zoran Samardžija[1], Kristina Žagar Soderžnik[1,3]
[1]Department for Nanostructured Materials, Jožef Stefan Institute, Jamova cesta 39, SI-1000 Ljubljana, Slovenia,
[2]Faculty of Chemistry and Chemical Technology, Večna pot 113, SI-1000 Ljubljana, Slovenia
[3]Jožef Stefan International Postgraduate School, Jamova cesta 39, SI-1000 Ljubljana, Slovenia

Corresponding Author's e-mail address: neza.sodnik@ijs.si

Summary:
Benzotriazole and its derivatives are ubiquitous in industries due to their diverse applications, yet their persistence in the environment poses ecological concerns. This study proposes a carbon nanotube-Nafion-modified screen-printed electrode for electrochemical detection of benzotriazole, addressing the need for cost-effective and rapid monitoring methods. Electrochemical analysis revealed a single reduction peak, leading to an LOD of 2 µM with square wave voltammetry. This approach offers a comparable alternative to commercial electrodes, underscoring its potential for environmental monitoring.

Keywords: Benzotriazole, persistent organic pollutant, voltammetric sensor, screen-printed electrode, single-walled carbon nanotubes.

Introduction

Benzotriazole (BTA) and its derivatives are extensively utilised in various industries for their properties as corrosion inhibitors, UV radiation filters and plastic stabilisers. BTA is therefore found in food packaging, dishwashing detergents, textiles, lubricants, antifreeze, aircraft de-icing fluids and other commercial and industrial products. [1,2]

Due to its solubility in water and resistance to biodegradation, BTA can persist in the environment. The inclusion of BTA as an additive in dishwashing detergents and tablets leads to its direct discharge into wastewater treatment plants, where it is only partially removed during the treatment process. As a result, BTA is prevalent in natural waters at nanomolar concentrations. While these concentrations may not pose an immediate threat to human health, the persistent nature and potential bioavailability of BTA can lead to long-term environmental consequences, which have yet to be sufficiently investigated. [1,2]

Currently, the primary methods for analyzing BTA in environmental samples involve solid-phase extraction followed by gas chromatography-mass spectrometry or liquid chromatography-mass spectrometry. However, there is a need for cost-effective, fast, reliable, in-situ detection of BTA for real-time monitoring of environmental samples. Given that BTA and some of its derivatives can be electrochemically reduced at low potentials, electrochemical detection on screen-printed electrodes (SPE) emerges as a promising approach. SPEs offer a more cost-effective, portable alternative to traditional electrochemical setups, which use conventional electrodes such as glassy carbon and mercury drop electrodes. In this work, a sensor based on carbon nanotube-Nafion-modified SPE (SPE-C/SWCNT) is proposed.

Materials and Methods

1 mg/mL dispersions of carboxyl-functionalised single-walled carbon nanotubes (SWCNT) were prepared in a 1:1 (v/v) mixture of DMF and water containing 1 wt.% Nafion. The dispersions were sonicated until fully dispersed. The sensor was fabricated by drop-casting 4 µL of the CNT suspension on the working electrode of the SPE (DRP-150, Dropsens, Metrohm) and allowing it to dry at room temperature overnight.

BTA solutions were prepared in Britton-Robinson buffer (pH 2.4) and analysed using cyclic voltammetry (CV) and square wave voltammetry (SWV). The electrochemical measurements were carried out by the PalmSens4 potentiostat. words.

Results and discussion

The coverage of the working electrode by the drop-casted material was assessed using scanning electron microscopy (SEM). As seen in Fig.

1, the SWCNTs are anchored to the working electrode by a Nafion membrane, resulting in satisfactory surface coverage.

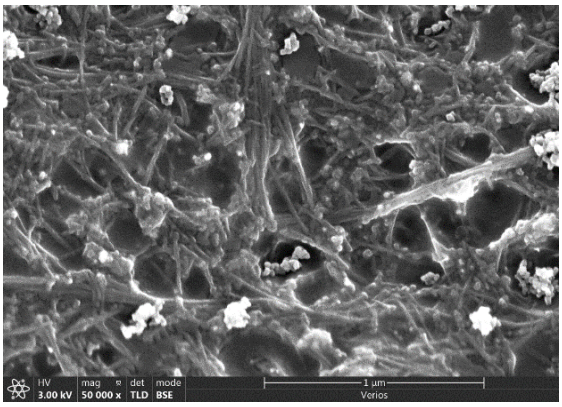

Fig. 1. SEM image of the working electrode surface modified with SWCNT and Nafion.

The electrochemical behaviour of BTA on the SPE-C/SWCNT was evaluated via CV. BTA exhibited a single reduction peak around –1,4 V with no observable oxidation peak during the reverse scan.

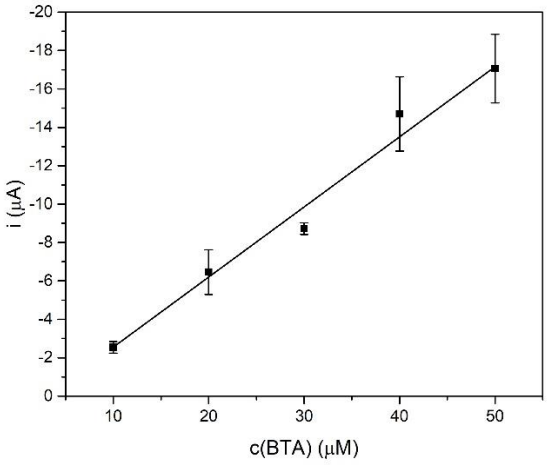

Fig. 2. Plot of the reduction peak current recorded on SPE-C/SWCNT for different concentrations of BTA in Britton-Robinson buffer at pH 2.4.

The SPE-C/SWCNT exhibited significant adsorption capacity for BTA. As a result, SWV analysis was performed after a 60 s preconcentration period at –1 V. With this approach, an LOD of 2 µM was achieved. This LOD is comparable to that obtained for BTA detection using commercially available SPE with a SWCNT working electrode [2], indicating that homemade modified SPEs offer a versatile alternative to commercial counterparts. Furthermore, by adjusting the composition, it may be possible to achieve an even lower LOD, comparable to those achieved using modified glassy carbon electrodes [3], making the proposed sensor suitable for real sample monitoring.

References

[1] A.N. Ababneh, M.A. Abu-Dalo, C. Horn, M.T. Hernandez, Polarographic determination of benzotriazoles and their sorption behavior on granular activated carbon, International Journal of Environmental Science and Technology 16 (2019) 833–842. https://doi.org/10.1007/s13762-018-1706-y.

[2] A. Muschietti, N. Serrano, C. Ariño, M.S. Díaz-Cruz, J.M. Díaz-Cruz, Screen-printed electrodes for the voltammetric sensing of benzotriazoles in water, Sensors (Switzerland) 20 (2020). https://doi.org/10.3390/s20071839.

[3] Y. Zheng, F. Yang, J. Zhang, W. Pu, C. Yang, Voltammetric behaviors of an emerging pollutant benzotriazole on multiwall carbon nanotubes (MWNTs)—Nafion modified electrode in various pH mediums, Ionics (Kiel) 22 (2016) 2059–2066. https://doi.org/10.1007/s11581-016-1738-6.

Acknowledgement

The authors acknowledge the funding of our research activities by the ARRS through projects J2-3051.

.

New Tool to Unravel Interactions Between Gas and Sensitive Surface Through the Simultaneous Characterization of Gas Uptake and Electrical Properties of the Material

M. Pascaud, C. Duc, N. Redon, M. N. Romanias, F. Thevenet, C. Samuel, University of Lille, Lille (France), A. Fresneau, TERA Sensor, Rousset (France)

Unfortunately, this abstract is not available, as the contribution was not confirmed at the time the conference proceedings were finalized.

New Tool to Unravel Interactions Between Gas and Sensitive Surface Through the Simultaneous Characterization of Gas Uptake and Electrical Properties of the Material

M. Pascaud, C. Duc, N. Redon, M. N. Romanias, F. Thevenet, C. Samuel, University of Lille, Lille (France), A. Fresneau, TERA Sensor, Rousset (France)

Unfortunately, this abstract is not available, as the contribution was not confirmed at the time the conference proceedings were finalized.

DOI 10.5162/EUROSENSORSXXXVI/PT5.45

Transient IR Spectroscopy as a Novel Approach to Unravel the Active Surface Species of Chemoresistive Gas Sensors

Maximilian Pfeiffer[1], *Christian Hess*[1]
[1] *Eduard-Zintl-Institute of Inorganic and Physical Chemistry, Technical University of Darmstadt, Peter-Grünberg-Str. 8, 64287 Darmstadt, Germany*.

maximilian.pfeiffer@tu-darmstadt.de

Summary:
Transient IR spectroscopy was used as a novel method for the mechanistic investigation of sensor materials for chemoresistive metal oxide gas sensors. Taking unloaded and gold-loaded tin oxide as an example, it was shown that *in situ* modulation-excitation spectroscopy (MES) combined with phase sensitive detection (PSD) allows the identification of the active species of the sensor reactions towards ethanol and CO, as well as the observation of new surface adsorbates such as CO adsorbed on partially negatively charged gold nanoparticles (CO-Au$^{\delta-}$) not accessible under steady state conditions.

Keywords: Chemiresistors, tin oxide, IR spectroscopy, transient methods, mechanistic investigation

1 Introduction

To enable a rational design based on new and established chemoresistive sensor materials, a deep understanding of the underlying sensor mechanism is of great importance. Various approaches based on *in situ* and *operando* spectroscopy are available for the investigation of chemoresistive gas sensors based on metal oxides as a sensor material [1-3]. Using these methods, new and important insights into the sensing mechanism of unloaded and loaded sensor materials such as SnO_2 [1-3] could be obtained, as previous studies based on IR, Raman and UV-VIS spectroscopy have shown [1-3].

Despite the great potential of established *operando* spectroscopic methods, it is often difficult to clearly identify the active surface species that are involved in the primary sensor response based on their vibrational bands in the IR and Raman spectra. These vibrational bands of active species are often masked by spectator species that accumulate at the surface but do not participate in the sensor response. However, already established *in situ* spectroscopic approaches for the investigation of chemoresistive gas sensors can be complemented by transient spectroscopic methods, such as MES based on diffuse reflectance infrared Fourier transform spectroscopy (ME-DRIFTS), to isolate these hidden active surface species and obtain further information about the underlying sensor mechanism [4]. Unraveling these interactions of the gas phase with the sensor surface (reception) is integral for improving sensor properties such as sensitivity, reversibility and selectivity towards the specific analyte gas to be detected.

2 Experimental

Commercial tin(IV) oxide SnO_2 (Sigma Aldrich) was used for the IR measurements in this work. Gold was loaded by wet impregnation using a 1 mM aqueous $HAuCl_4$ solution and a 30 mM aqueous ammonia solution [4]. IR spectra were recorded on a Vertex 70 IR spectrometer (Bruker) and an Invenio R IR spectrometer (Bruker), each equipped with a built-in liquid nitrogen cooled MCT and a heatable Praying Mantis gas cell (Praying Mantis High Temperature, Harrick Scientific Products). During the ME-DRIFTS periodic measurements (period length: $T_{t,EtOH}$ = 133.33 s; $T_{t,CO}$ = 366.35 s), the sensor material is first exposed to 500 ppm of the corresponding analyte ethanol or CO, each in synthetic air as carrier gas, and then to synthetic air without the analyte, by switching the gas feed with a 4-way-valve controlled by the IR-spectrometer. The raw spectra recorded are subjected to a background subtraction and afterwards demodulated using PSD and thus transferred from the time to the phase domain by using a Fourier transformation.

3 Results and Discussions

Fig. 1a) shows PSD spectra obtained during ethanol gas sensing over Au/SnO_2 at 150 °C. In the first half period during ethanol exposure, vibrational bands for ethanol (~22 s), as well as formate and acetate species (~24 s) can be observed, as well as some terminal hydroxyl-groups (~19 s). Other terminal, as well as

bridged hydroxyl-groups are also observed in the second half period (~95-107 s), where no ethanol is present, showing their consumption on the time scale of ethanol exposure and formate/acetate formation. At around 2030 cm^{-1}, two overlapping vibrational bands can be observed (~100 s), which cannot be observed under stationary conditions, but under the periodically changing conditions used here. They can be assigned to CO adsorbed on partially negatively charged gold nanoparticles ($CO\text{-}Au^{\delta-}$) [4] and represent a surface adsorbate that was not previously observed during ethanol gas sensing. Carbonates and carboxylates can also be observed in the second half period (~91 s). Due to their time values in the second half period, they are not formed directly during the sensor reaction with ethanol, but by decomposition of formate and acetate-species as well as readsorption of CO_2 from the gas phase.

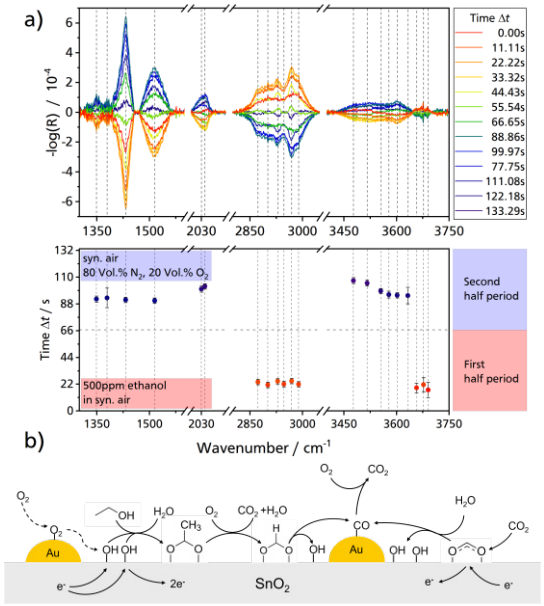

Fig. 1: a): PSD spectra for 0.58 wt.% Au/SnO_2 during pulsing of 500 ppm ethanol in synthetic air at 150 °C (Top) with assigned time values Δt (Bottom); b): Proposed mechanism for ethanol gas sensing over gold-loaded tin oxide.

Based on these spectroscopic results, we propose the mechanism for ethanol gas sensing over gold-loaded shown in Fig. 1b), involving an oxygen-spillover from gold on the surface of tin oxide [3]. In the course of the sensor reaction, hydroxyl-species are consumed during the adsorption of ethanol and stepwise oxidation to formate and acetate species, releasing electrons into the conduction band. These surface species formed can decompose in vicinity to gold, forming hydroxyl-species as well as CO, which adsorbs on gold and is oxidized to CO_2 before desorbing into the gas phase. CO_2 can then readsorb, binding electrons from the conduction band [4].

Tin oxide and gold-loaded tin oxide were also recently investigated during CO gas sensing using *in situ* modulation excitation DRIFT spectroscopy. New insights into the proposed sensor mechanism [2,3] including the temporal evolution of reaction intermediates were obtained, which are not available under stationary conditions. Our results show that carbonates are not directly involved in the primary sensor response to CO exposure and the formation of CO_2 from CO with the participation of lattice oxygen. Carbonates are mainly formed after the surface reaction by readsorption of CO_2 from the gas phase, where they can impair the regeneration of the sensor material after the end of the CO exposure by remaining on the sensor surface, similar to the behavior observed during ethanol gas sensing.

Based on the presented results we can conclude that the sensing mechanism of ethanol gas sensing is characterized by the formation and consumption of hydroxyl groups, as well as the formation of formate and acetate as surface adsorbates [4], while the mechanism of CO gas sensing is primarily based on a redox mechanism involving the consumption of surface lattice oxygen atoms and the formation of CO_2.

Our results show the great potential of transient *in situ* spectroscopic methods for investigating the surface reaction of chemoresistive gas sensors in presence of different analytes to gain new insights in presence of intermediary surface species and their temporal evolution. Therefore, this transient approach can strongly facilitate the rational design of chemoresistive gas sensors with improved sensing properties.

References

[1] A.-K. Elger, C. Hess, Elucidating the Mechanism of Working SnO_2 Gas Sensors Using Combined Operando UV/Vis, Raman, and IR Spectroscopy, *Angewandte Chemie International Edition*, 58, 15057 (2019); doi: 10.1002/anie.201908871

[2] D. Degler, S. Wicker, U. Weimar, N. Barsan, Identifying the Active Oxygen Species in SnO_2 Based Gas Sensing Materials: An Operando IR Spectroscopy Study, *Journal of Physical Chemistry C*, 119, 21 (2015); doi: 10.1021/acs.jpcc.5b04082

[3] D. Degler, S. Rank, S. Müller, H. W. Pereira de Carvalho, J.-D. Grunwaldt, U. Weimar, N. Barsan, Gold-Loaded Tin Dioxide Gas Sensing Materials: Mechanistic Insights and the Role of Gold Dispersion, *ACS Sensors*, 1, 1322-1329 (2016); doi: 10.1021/acssensors.6b00477

[4] M. Pfeiffer, C. Hess, Application of Transient Infrared Spectroscopy To Investigate the Role of Gold in Ethanol Gas Sensing over Au/SnO_2, *Journal of Physical Chemistry C*,126, 8, 3980–3992 (2022); doi: 10.1021/acs.jpcc.1c10384

Exploring recognition-transduction materials for orthophosphate sensing in surface waters

E. McLamore, G. Moreira, M. Torres, Clemson University, Clemson (USA), A. Shaw, Arizona State University, Phoenix (USA), N. Amin, W. Gao, North Carolina State University, Raleigh (USA), J. H. Bhadha, A. M.D. Mahmud, University of Florida, Belle Glade (USA)

Unfortunately, this abstract is not available, as the contribution was not confirmed at the time the conference proceedings were finalized.

Exploring recognition-transduction materials for orthophosphate sensing in surface waters

E. McLamore, G. Moreira, M. Torres, Clemson University, Clemson (USA), A. Shaw, Arizona State University, Phoenix (USA), N. Amin, W. Gao, North Carolina State University, Raleigh (USA), J. H. Bhadha, A. M.D. Mahmud, University of Florida, Belle Glade (USA)

Unfortunately, this abstract is not available, as the contribution was not confirmed at the time the conference proceedings were finalized.

DOI 10.5162/EUROSENSORSXXXVI/PT5.57

Synthesis of 2-Dimensional WS_2 Nanoflakes with NO_2 Selectivity at Room Temperature

Hong Dang Nguyen, Sun-Woo Choi
Department of Materials Science and Engineering, Kangwon National University, Samcheok-si, Gangwon-do 25913, Republic of Korea,

Corresponding Author's e-mail address: csw0427@kangwon.ac.kr

Summary:
We have synthesized 2-dimenstional (2D) WS_2 nanoflakes utilizing chemical vapor deposition to detect hazardous and harmful gas species at room temperature. The synthesized WS_2 nanoflakes were characterized via scanning electron microscopy, transmission electron microscopy, X-ray diffraction, X-ray photoelectron spectroscopy, and Raman spectroscopy. In addition, to verify the detection of hazardous and harmful gases at room temperature, we systematically investigated the gas sensing performances of 2D WS_2 nanoflake-based gas sensors using NO_2, NH_3, C_2H_5OH, C_3H_6O, and H_2 gases. Although the 2D WS_2 nanoflakes showed lower NO_2 response than that of a similar exfoliated WS_2 nanoflakes, unlike the exfoliated WS_2 nanoflakes, the 2D WS_2 nanoflakes exhibited good NO_2 selectivity. These results indicate that the CVD-grown 2D WS_2 nanoflakes can be applicable to sensing material for detecting NO_2 at room temperature.

Keywords: 2-dimensional WS_2, chemical vapor deposition, gas sensing, room temperature, NO_2 selectivity

Background, Motivation an Objective

In modern society, highly sensitive and selective gas sensors that can quickly detect hazardous and harmful gases are necessary to a variety of applications, including air quality monitoring [1], tracking exhaust emissions for vehicles [2], preventing crops from the pests [3] and disease diagnoses [4].

Among the different gas species, in particular, nitrogen dioxide (NO_2) is well known as a poisonous and fatal to human beings even exposure to as low as ppm-level. Additionally, NO_2 gas molecules easily react with other chemicals in the atmosphere, resulting in the acid rain, ozone layer depletion, and global warming. Hence, development of highly sensitive and selective NO_2 gas sensors is urgent.

In recent decades, the semiconducting material-based gas sensors have attracted considerable interest because of their excellent properties, such as high response, thermal stability, miniaturization, compatibility with electronics, and applicability for mass production [5,6]. However, to detect the gas molecules utilizing semiconducting material-based gas sensors, the high temperature (> 200℃) should be needed, causing the huge power consumption. Furthermore, selectivity for certain gas molecules is also important parameter in practice gas sensor applications. Therefore, we attempted to implement the gas sensors operating at room temperature with NO_2 selectivity.

In this present, we successfully fabricated NO_2 gas sensors based on 2-dimenstional (2D) WS_2 nanoflakes utilizing the chemical vapor deposition (CVD). The fabricated sensors showed the best NO_2 response at room temperature compared to NO_2, NH_3, C_2H_5OH, C_3H_6O, and H_2 gases.

Description of the New Method or System

To synthesize the 2D WS_2 nanoflakes, WO_3 and sulfur powder were used as precursors and hydrogen (99.999%) gas was used as a carrier gas. We systematically investigated the sensing performances of CVD-grown 2D WS_2 nanoflakes at room temperature, compared to those of exfoliated WS_2 nanoflakes. Interestingly, CVD-grown 2D WS_2 nanoflakes exhibited good NO_2 selectivity while exfoliated 2D WS_2 nanoflakes relatively showed poor gas selectivity.

Results

Fig. 1 shows the results of transmission electron microscopy (TEM) of CVD-grown 2D WS_2 nanoflakes. As shown in Fig. 1(a), the 2D

WS_2 nanoflakes consist of a few layers of WS_2 nanosheets. Fig. 2(b) exhibits the high-resolution TEM image of 2D WS_2 nanoflake, indicating high quality of crystallinity.

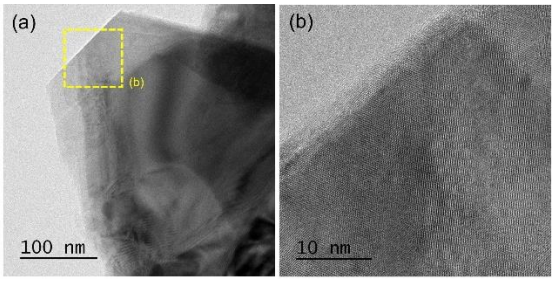

Fig. 1. TEM images of 2D WS_2 nanoflakes

In addition, the component analysis were also conducted utilizing the energy-dispersive spectroscopy (EDS) equipped with TEM. The EDS results clearly show that the 2D WS_2 nanoflakes were successfully synthesized (Fig. 2). The EDS results are in agreement with X-ray diffraction result (not shown in this abstract).

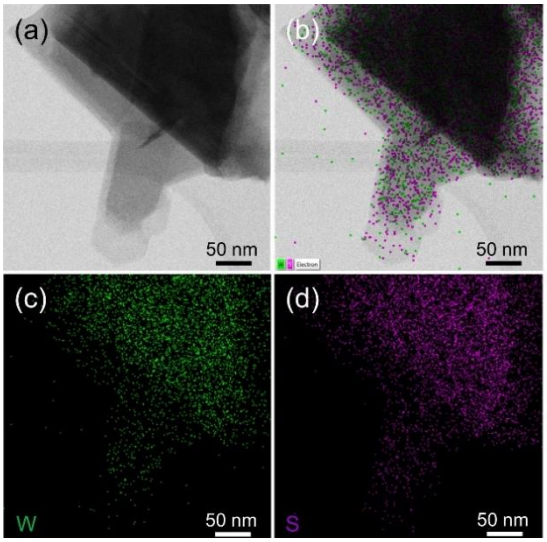

Fig. 2. The EDS results of 2D WS_2 nanoflakes

The sensing performances of 2D WS_2 nanoflakes were systematically investigated at room temperature, compared to exfoliated 2D WS_2 nanoflakes. The all gas responses in this study were calculated using following equation:

$$S(\%) = \frac{R_{air} - R_{gas}}{R_{air}} \times 100$$

, where R_{air} and R_{gas} are the resistance when exposing to air and target gas, respectively. The transient NO_2 response curves of 2D WS_2 nanoflakes measured at room temperature are shown in Fig. 3(a). To confirm the NO_2 selectivity of 2D WS_2 nanoflakes, we also measured the gas response toward other gases including NH_3, C_2H_5OH, C_3H_6O, and H_2. As shown in Fig. 3(b), the NO_2 response of 2D WS_2 nanoflakes is at least 2 times higher than those of other gases. Therefore, it is reasonable to claim that the 2D WS_2 nanoflakes are promising candidate to apply to actual NO_2 sensors.

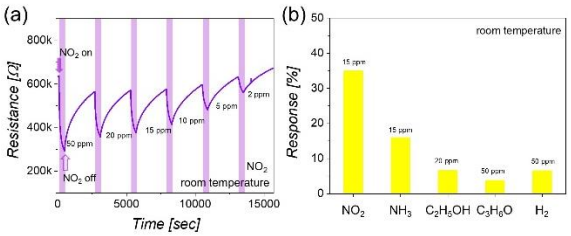

Fig. 3. NO_2 sensing results of 2D WS_2 nanoflakes

Interestingly, even though the exfoliated 2D WS_2 nanoflakes showed better gas response than CVD-grown 2D WS_2 nanoflakes, the difference in gas responses was not obtained. In other words, the exfoliated 2D WS_2 nanoflakes did not show the gas selectivity.

References

[1] M. C. Carotta, G. Martinelli, L. Crema, M. Gallana, M. Merli, G. Ghiotti, E. Traversa, Array of Thick Film Sensors for Atmospheric Pollutant Monitoring, *Sens. Actuators B Chem*. 68, 1-8 (2000); doi: http://dx.doi.org/10.1016/S0925-4005(00)00439-1.

[2] Q. Shen, X. Xie, M. Peng, N. Sun, H. Shao, H. Zheng, Z. Wen, X. Sun, Self-Powered Vehicle Emission Testing System Based on Coupling of Triboelectric and Chemoresistive Effects. *Adv. Funct.Mater*. 28, 1703420 (2018); doi: 10.1002/adfm.201703420.

[3] T. Seesaard, N. Goel, M. Kumar, C. Wongchoosuk, Advances in Gas Sensors and Electronic Nose Technologies for Agricultural Cycle Applications. *Comput. Electron. Agric*. 193, 106673 (2022); doi: 10.1016/j.compag.2021.106673.

[4] A. Staerz, U. Weimar, N. Barsan, Understanding the Potential of WO_3 Based Sensors for Breath Analysis. *Sensors* 16, 1815 (2016); doi: https://doi.org/10.3390/s16111815.

[5] S. Behi, J. Casanova-Chafer, E. González, N. Bohli, E. Llobet, A. Abdelghani, Metal Loaded Nano-Carbon Gas Sensor Array for Pollutant Detection. *Nanotechnology* 33, 195501 (2022); doi :10.1088/1361-6528/ac4e43.

[6] T. Pham, G. Li, E. Bekyarova, E. Itkis, A. Mulchandani, MoS_2-Based Optoelectronic Gas Sensor with Sub-Parts-per-Billion Limit of NO_2 Gas Detection. *ACS Nano* 13, 3196-3205 (2019); doi: 10.1021/acsnano.8b08778.

DOI 10.5162/EUROSENSORSXXXVI/PT5.59

Pt-nanoparticles decorated Amorphous/Crystalline *a*-V_2O_5/VO_2 Thin Films for NO_2 and H_2 sensing

Maria Basso[1], Valentina Paolucci[2], Vittorio Ricci[2], Natarajan Thirugnanam[1], Alessandro Martucci[1], Carlo Cantalini[2]

[1]Department of Industrial Engineering (DIIIE), University of L'Aquila, Roio 67100 L'Aquila, Italy.

[2]Department of Industrial Engineering (DII), University of Padova, Via Marzolo 9, Padova 35131, Italy.

Corresponding email: vittorio.ricci@graduate.univaq.it

Summary:

We report that nanosecond pulsed laser annealing (PLA) of solution based VO_2 thin films yields high surface area amorphous/crystalline *a*-V_2O_5/VO_2 nanostructures with promising chemoresistive gas sensing response to NO_2 (400 ppb –1 ppm) at 100 °C temperature. In addition, Pt-nanoparticles (Pt-NPs) decorated *a*-V_2O_5/VO_2 show excellent response to H_2 (5 – 100 ppm) with limit of detection (LOD) as low as 5 ppm. Remarkably Pt-NPs loading resulted to neutralize the humidity cross response (10 - 80% RH) to H_2 sensing, opening new perspectives for selective H_2 detection in humid environments.

Keywords: VO_2, V_2O_5, Pt-Decorated, chemoresistive, NO_2, H_2, gas sensor

Background, Motivation an Objective

Vanadium V_xO_y metal-oxides (V-MO), enclosing a large variety of the vanadium element in several oxidation states, (i.e. V^{3+}, V^{4+}, and V^{5+}), have been acknowledged as promising *n*-type material interfaces in gas sensing applications [1]. V-MO films have been deposited over dedicated substrates, using various physical and chemical techniques, such as thermal evaporation, electron beam evaporation, magnetron sputtering, sol−gel, electrochemical deposition, and hydrothermal methods. Moreover, recent investigations highlighted that V-MO nanostructures can be conveniently decorated with catalytic nanoparticles [2], or eventually engineered in complex heterostructures [3], to exploit superior room temperature gas sensing properties. All the above-mentioned synthesis techniques require however, high annealing temperatures (~ 550 °C) to properly fix crystallinity and stoichiometry, which severely endanger the mechanical adhesion of the metal electrodes (Ta/Pt) with the SiO_2 and Si_3N_4 substrates. To solve this problem, we applied nanosecond pulsed laser annealing (ns-PLA), which allows for local temperature increases within the film without involving the substrate, to synthesize amorphous/crystalline *a*-V_2O_5/VO_2 heterostructures chemoresistive gas sensors for NO_2 detection (400 ppb –1 ppm) at 100 °C operating temperature. We also demonstrated that Pt-nanoparticles (Pt-NPs) decoration greatly improves both the H_2 gas response (5 – 100 ppm) and the humidity cross sensitivity.

Description of the New Method or System

The versatility of sol-gel reactions was combined with ultrafast ns-PLA for the simultaneous crystallization and nanostructuring of V-MO thin films. Specifically, V-MO thin films were synthetized from a non-carcinogenic precursor and irradiated with a KrF excimer laser at room temperature in air. As shown in Fig. 1, the irradiation with 10 laser pulses induces the crystallization of a VO_2 phase inside an amorphous matrix. XPS analysis revealed that the composition of the amorphous phase is V_2O_5, which resulted to be dominant (~ 80%) as respect to crystalline VO_2 (~ 20%). In conclusion we synthesized an amorphous/crystalline *a*-V_2O_5/VO_2 heterostructure as a novel interface for gas sensing applications.

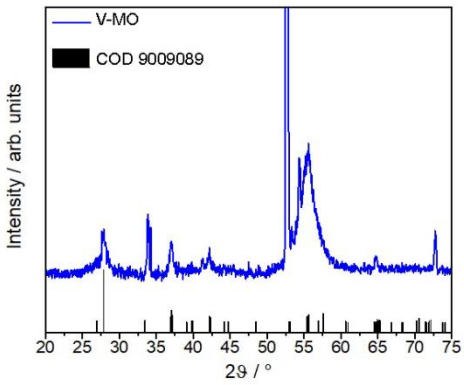

Fig. 1. Grazing Incidence GI-XRD of 10 ns-PLA annealed sol-gel deposited V-MO thin film. Peaks attributed to crystalline VO_2.

Results and Discussion

We firstly investigated the electrical response to NO_2 (10 – 80% @25 °C) of the *a*-V_2O_5/VO_2 heterostructure, in dry air at 100 °C operating temperature (OT), as shown in Fig. 2.

Upon exposure to NO_2 resistance increases, yielding a sensor's signal response (RR = R_g/R_a) of 1.6 ± 0.2 corresponding to 1 ppm NO_2 and a limit of detection (LOD) of 400 ppb.

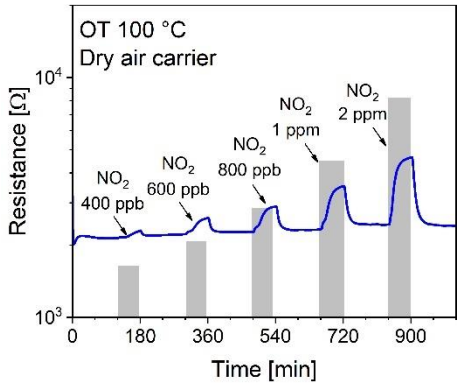

Fig. 2. Gas sensing response of the a-V_2O_5/VO_2 to NO_2 (400 ppb - 2 ppm) in dry air at 100 °C operating temperature (OT).

Considering that *a*-V_2O_5/VO_2 heterostructure scarcely responds to H_2 gas (here not shown), *a*-V_2O_5/VO_2 heterostructure was decorated with Pt-NPs and the H_2 response recorded as shown in Fig. 3.

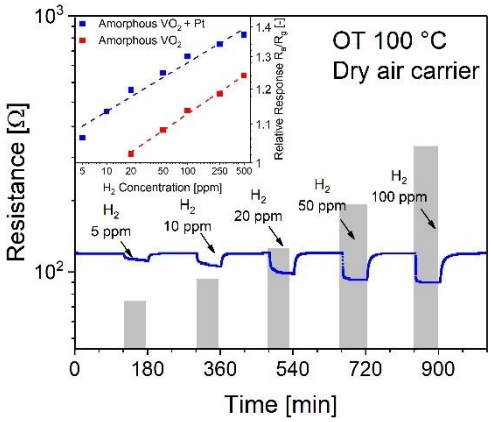

Fig. 3. Gas sensing response of the Pt-NPs decorated a-V_2O_5/VO_2 to H_2 (5 ppm - 100 ppm) in dry air at 100 °C. Inset: comparison of the calibration lines of the a-V_2O_5/VO_2 (red line) and Pt-NPs decorated a-V_2O_5/VO_2 (blue line).

Pt-NPs decoration highly improves the H_2 gas response. LOD as low as 5 ppm H_2 and a linear response of the calibration line (inset of Fig. 3) at 100 °C OT, confirm the positive effect of Pt-NPs decoration over *a*-V_2O_5/VO_2. As an interesting remark, we noticed (here not shown) that Pt-NPs decoration of *a*-V_2O_5/VO_2 almost annihilates NO_2 gas response.

Humidity cross sensitivity test in the 10 - 80% RH range (RH @25 °C) revealed a substantial lack of selectivity of the *a*-V_2O_5/VO_2 interface to detect NO_2 gas in humid environment. Opposedly, Pt-NPs *a*-V_2O_5/VO_2 interface exhibits an excellent selectivity to detect H_2 gas in the presence of humidity.

As a concluding remark, we envisaged two gas sensing mechanisms. The first considers the "not decorated", the second the "decorated" *a*-V_2O_5/VO_2 heterostructures, when exposed to NO_2 and H_2 gases.

Not decorated *a*-V_2O_5/VO_2 heterostructure responds according to reactions (1) and (2) to NO_2 and H_2 gases. The stronger electronegativity of NO_2 molecules, as respect to H_2, accounts for the prevalence of reaction (1) as respect to reaction (2). This situation is experimentally demonstrated by the higher response to NO_2 as respect to H_2 of the *a*-V_2O_5/VO_2 interface.

$$2H_2 + (O_2' - V_O^{\bullet\bullet})_{ADS} \rightleftharpoons 2H_2O_{(g)} + V_O^{\bullet\bullet} + e' \quad (1)$$

$$NO_{2(g)} + (O_2' - V_O^{\bullet\bullet})_{ADS} \rightleftharpoons (NO_2' - V_O^{\bullet\bullet})_{ADS} + O_{2(g)} \quad (2)$$

Platinum in Pt-NPs decorated *a*-V_2O_5/VO_2 heterostructure acts as a catalyst which activates the dissociation of hydrogen molecule to atomic H, which diffuses into the *a*-V_2O_5/VO_2 layer resulting in the hydrogenation (reaction (3)) of V_2O_5 into $H_xV_2O_5$ [4].

$$V_2O_5 + \mathrm{H} \rightleftharpoons H_xV_2O_5 \quad (3)$$

$$4H_xV_2O_5 + O_2' \rightleftharpoons 4V_2O_5 + 2H_2\mathrm{O} + \mathrm{e}' \quad (4)$$

Beside reaction (2), which always contributes to the decrease of the resistance, regardless the Pt-NPs decorating effect, in Pt-NPs decorated *a*-V_2O_5/VO_2, reaction (4) further contributes to the production of electrons. In conclusion, for Pt-NPs decorated film reaction (4) accounts for the enhanced response of the decorated platforms as respect to the not decorated ones to H_2 gas, as attested by the calibration lines in the inset of Fig. 3.

References

[1]. J. Jaiswal *et al.*, Vertically Alligned Porous V_xO_y Nanofilms with Pt Decoration for Sub-ppm H_2 Gas sensors, *ACS Appl. Nano Mater*. 6, 2646-2657 (2023); doi: 10.1021/acsanm.2c05058

[2]. J.M. Baik *et al.*, Pd-Sensitized Single Vanadium Oxide Nanowires: Highly Responsive Hydrogen Sensing Based on the Metal-Insulator Transition, *Nano Lett*. 9 (12), 3980-3984 (2009); doi: 10.1021/nl902020t

[3]. B. Li *et al.*, Enhanced Pd/a-WO_3/VO_2 Hydrogen Gas Sensor Based on VO_2 Phase Transition Layer, *Small Methods*, 6 (12), 2200931 (2022); doi: 10.1002/smtd.202200931

[4]. Y. Lu *et al.*, Hydrogenated V_2O_5 with Improved Optical and Electrochemical Activities for Photo-Accelerated Litium-Ion Batteries, *Small* 20 (14), 2308869 (2024); doi: 10.1002/smll.202308869

DOI 10.5162/EUROSENSORSXXXVI/PT5.61

First-Order Time Derivative Response of MoS_2 Nanofilm on TiO_2 Nanotubes to NO_2

Smisitel Petr[1], Jan M. Macak[3], Jaromir Hubalek[1,2]
[1] Central European Institute of Technology (CEITEC), Brno University of Technology, Purkynova 656/123, 612 00 Brno, Czech Republic,
[2] Department of Microelectronics, Faculty of Electrical Engineering and Communication (FEEC), Brno University of Technology, Technicka 3058/10, 616 00 Brno, Czech Republic,
[3] Center of Materials and Nanotechnologies, Faculty of Chemical Technology, University of Pardubice, Nam. Cs. Legii 565, 53002 Pardubice, Czech Republic

Petr.Smisitel@ceitec.vutbr.cz

Summary:
ALD grown MoS_2 nanofilm on TiO_2 nanotubes support were studied as NO_2 gas sensor. In addition to traditional relative resistance response, we show that a rarely studied first-order derivative response is an excellent alternative with monotone dependency on concentration and fast response time, avoiding the need for long gas exposure periods to achieve high and stable sensor response.

Keywords: molybdenum dichalcogenides, molybdenum sulphide, nanostructures, gas sensors, derivative response

Background, Motivation and Objective

2D structured molybdenum dichalcogenides are promising materials for chemical sensors devoted to environmental pollutants, such as NO_2, NH_3, CO and volatile organic compounds [1].

We studied ALD grown MoS_2 nanofilm on TiO_2 nanotube supports [2] regarding its gas sensing properties. In order to minimize the sensors response and recovery times we utilized a first-order time-derivative response which was rarely used in gas sensing experiments [3], [4], and can provide better results than routinely used normalized resistance response.

MoS_2 samples fabrication

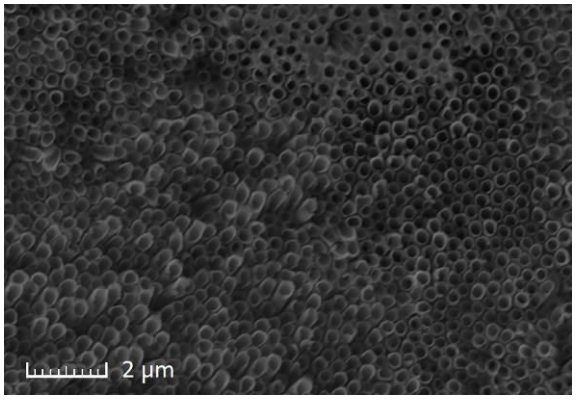

Fig. 1. SEM image of TiO_2 nanotubes decorated with 3 ALD cycles of MoS_2.

TiO_2 nanotubes with 20 µm average thickness and 110 nm in diameter were used as a base, with two dimensional MoS_2 nanostructures grown via Atomic Layer Deposition (ALD) technique (see Fig. 1), resulting in homogenously distributed nanofilm over the entire nanotube layer. The thickness of MoS is determined by the number of ALD cycles, 3 cycles were performed. In detailed fabrication process was described in [2]. Golden electrodes were deposited over the layer to form the electrical connection.

Methodology

Before any characterization, the sample was stabilized under constant 200 sccm synthetic air (SA) flow and 150 °C for a week, until the resistance baseline was stabilized. All gas sensing experiments were performed with sample connected to constant voltage of 0.5 V and constant gas flow of 200 sccm. Desired NO_2 concentration was achieved by mixing 10 ppm NO_2 in SA with pure SA, limiting the obtainable concentrations. Two different sensor responses were evaluated. The relative resistance response was calculated as $R_{rez} = R_{NO2}/R_{SA}$, where R_{SA} is the resistance baseline in SA and R_{NO2} is the maximum resistance reached during the NO_2 exposition. The first-order time derivation was calculated as a slope of linear fit over 20 seconds time period and the maximum was taken as derivative response.

Gas Sensing Characterization

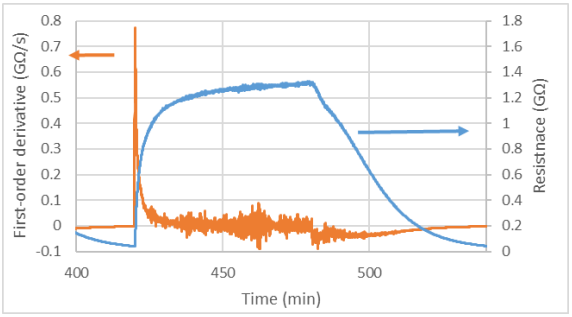

Fig. 2. Time dependence of resistance and its time derivation for 60 min exposure to 2 ppm of NO_2.

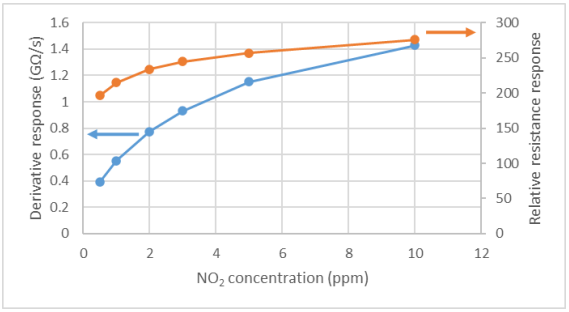

Fig. 3. Dependence of resistive and derivative sensor response on NO_2 concentration, 60 min exposures.

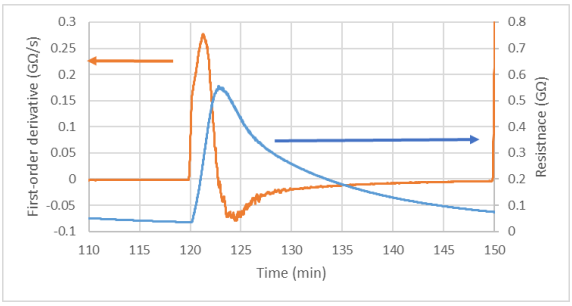

Fig. 4. Time dependence of resistance and its time derivation for 1 min exposure to 2 ppm of NO_2.

Typical experiment comprised of 60 min NO_2, 60 min SA purge cycles, repeated with increasing concentration. The first cycle was discarded as it was significantly distorted by adsorption in the apparatus gas lines and the measurement chamber. Fig. 2 shows the detail of one cycle. While the resistance was rapidly rising for cca 15 minutes followed by slower increase for the rest of the exposure period, the first-order time derivative peaks within the first minute, returning to smaller values for the rest of the gas exposure period. This makes the derivative response a much better choice for fast detections, as the magnitude of the response is not dependent on prolonged gas exposures. Fig. 4 shows the one cycle of 1 min exposure and 19 min SA purge, which is sufficient for the derivative response operation. However, the limitations of our apparatus (mainly the 140 cm^3 volume of the test chamber compared to 200 sccm gas flow) are limiting the precision of these measurements, resulting in smaller derivative response than obtained with longer exposures, as well as being the limiting factor for the recovery.

Adsorption States – Deep and Shallow – Influencing Response and Recovery Times

Sensor response is determined by the NO_2 adsorption on MoS_2 surface. Deep adsorption levels with high adsorption energy traps the molecule on the surface slowing down sensor recovery. However, the ab-initio calculations show that on the pristine surface of MoS_2, there are multiple shallow adsorption states with nearly identical binding energy around 0.20 eV [5]. Although they also discuss the existence of deep adsorption levels on defects and edges, the initial adsorption speed, and consequently the derivative response, would be determined mainly by the shallow adsorption states, which are the most numerous and easily depopulated, reducing the necessity of long recovery periods connected to slow depopulation of deep adsorption levels.

Conclusions

MoS_2 nanosheets responds well to nitrogen dioxide. While the resistive response takes tens of minutes to reach stabilized value, the first-order time derivative response peaks within the first minute, thus being much more suitable response function.

References

[1] D. Zappa, Molybdenum Dichalcogenides for Environmental Chemical Sensing, *Materials* 10, 1418 (2017); doi: 10.3390/ma10121418

[2] H. Sopha, A.T. Tesfaye, R. Zazpe, J. Michalicka, F. Dvorak, L. Hromadko, M. Krbal, J. Prikryl, T. Djenizian, J.M. Macak, ALD growth of MoS2 nanosheets on TiO2 nanotube supports, *FlatChem* 17 (2019); doi: 10.1016/j.flatc.2019.100130

[3] M. Rodner, J. Eriksson, First-order time-derivative readout of epitaxial graphene-based gas sensors for fast analyte determination, *Sensors and Actuators Reports* 2, 1, 100012 (2020); doi: 10.1016/j.snr.2020.100012

[4] N.K. Plugotarenko; T.N. Myasoedova; S.P. Novikov; T.S. Mikhailova, Comparative Analysis of Derivative Parameters of Chemoresistive Sensor Signals for Gas Concentration Estimation, *Chemosensors* 10, 126 (2022); doi: 10.3390/chemosensors10040126

[5] V. M. Bermudez, Computational Study of the Adsorption of NO2 on Monolayer MoS2, *The Journal of Physical Chemistry C* 124(28), 15275-15284 (2020); doi: 10.1021/acs.jpcc.0c03786

DOI 10.5162/EUROSENSORSXXXVI/PT5.63

Rumen Bolus Extraction Method Using Absorbent Polymer for Timed Density Control

Jarred Fastier-Wooller[1], Yusuke Yashiro[2], Michitaka Yamamoto[2], Yoshihiro Muneta[2], Hiroshi Sawada[2], Reina Nishiura[2], Shozo Arai[2], Seiichi Takamatsu[1], Toshihiro Itoh[1]
[1] The University of Tokyo, 7-3-1 Hongo, Bunkyo-ku 113-8656, Tokyo, Japan,
[2] National Agriculture and Food Research Organisation, 3-1-5 Kannodai, Tsukuba-shi 305-0856, Ibaraki, Japan

jarredfw@g.ecc.u-tokyo.ac.jp

Summary:
The rumen of cattle can be monitored using an electronic rumen bolus, which is designed to remain permanently in the rumen. However, rumen boluses with pH sensing capabilities often only function for approximately 3 to 6 months. After this period, the rumen boluses are generally retrieved through surgery or autopsy. We propose an alternative method of retrieval by manipulating the devices density to allow for time-gated natural excretion of a rumen bolus. The excreted device can then be recycled or recharged and used again to reduce waste and improve uptime of p monitoring in the rumen of cattle.

Keywords: rumen bolus, density control, absorbent polymer.

Introduction

Significant improvements in agricultural livestock techniques and technologies have been developed to reduce greenhouse gas emissions, improve productivity, and improve the overall quality of life for cattle. The enhancement of data quality and collection methods is crucial for advancing research in areas such as drug delivery, feed composition, and environmental changes [1]. Devices often referred to as electric rumen boluses provide a direct and autonomous method, as opposed to intermittent and invasive testing. An electric rumen bolus is a swallowable device designed to remain indefinitely in the rumen and perform measurements over 1-5 years or 3-6 months for pH-capable devices. These limitations typically stem from battery life and sensor drift. For pH sensing, this is due to the sensor surface becoming dirty and a lack of maintenance or recalibration [2]. Rumen boluses can remain within the rumen long term by adhering to specific density parameters. Densities of 1.3-1.6 g/cm^3 result in delayed expulsion, densities greater than 1.6 g/cm^3 prevent rumination, and densities greater than 3.0 g/cm^3 are considered permanent [3]. Therefore, it is possible to artificially control the time before an object can be naturally defecated by manipulating its density. We propose a variable density module capable of utilizing the surrounding rumen fluid to inflate over time, thus varying the density enough to pass through the digestive system naturally after a desired duration. Herein, we implement and verify that our variable density module can function normally in a cow's digestive system.

Design and Fabrication

The proposed design comprises a polymer casing that contains an absorbent polymer and a stretchable membrane. Rumen liquid enters through the liquid inlets and is absorbed by the absorbent polymer, causing it to expand and alter the overall density of the device. The analysis of the mechanism and module functionality is reported in our previous work [4]. However, considering the safety and psychological burden on the fistula cows used in the experiment, we redesigned our original device and pre-inflated it for ejection in approximately 36 hours (Fig. 1).

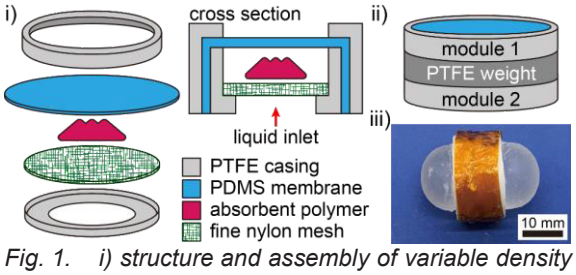

Fig. 1. i) structure and assembly of variable density module. ii) assembled device with PTFE weight. iii) fabricated device after inflation with Kapton tape layer.

The outer frame of the density variable module was made of Teflon (PTFE) using a bench-top CNC milling machine (KitMill CL100, ORIGINALMIND). The device is assembled by sandwiching a 1.00 mm thick PDMS membrane, 0.3 g of water-absorbent polymer, and nylon mesh

(PA-263μ, Azwan) together with cyanoacrylate (04612, Konishi) and silicone (HJ-148, Cemedine) as adhesives. A variable density module was adhered to each side of a solid 3.5 x 20 mm PTFE disc to form a single device. A diameter of 20 mm is appropriate to prevent duodenal obstruction. The overall weight of the assembled device was 1.4 g with a density of 1.7 g/cm^3. The estimated excretion time was reduced to 36 hours by pre-inflating the device in distilled water to an appropriate density of 1.3 g/cm^3 [5]. The outer frame of the modules and the sides of the weight were wrapped with Kapton tape and coated with a silicone adhesive for intestinal protection and improved visibility in feces.

Method

One fistula cow is herded into a paddock in the early morning without food, and two variable density devices are inserted through the fistula. Device 1 (D1) in the rumen and device 2 (D2) in the reticulum (Fig. 2i). The diet of the fistula cow was not restricted. However, the cow was kept in the paddock to aid in the monitoring of the manure and habitat for discharged devices during a one-week observation period.

Results and Discussion

D1 was confirmed to be discharged between 30 and 40 hours after being inserted into the rumen. The discharged device was found at some distance from the feces, with the weight and variable density modules separated. One of D1's PDMS membranes ruptured, with water-absorbent polymer found near the damaged device. The location of each part of D1 indicates the device remained in one piece until it was stepped on by the cow. This is further supported by the visibility and location of scattered polymer (Fig. 2ii-iii).

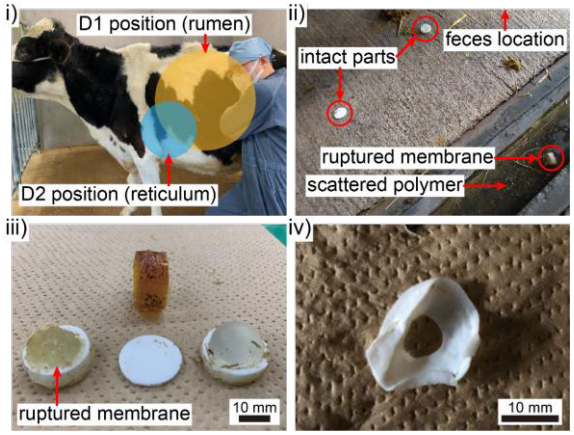

Fig. 2. i) placement of devices D1 and D2 in fistula cow. ii) site where D1 discharge was confirmed at 40 hours. iii) discharged components of D1. iv) warped component of D2 confirmed at 140 hours.

The ejection time of D1 was around 36 hours. However, parts of D2 were discharged between 130 and 140 hours. The parts were significantly deformed by intestinal pressure (Fig. 2iv). If the device broke in the rumen or reticulum, it would remain there, as the density of PTFE is 2.2 g/cm^3. Therefore, the device and weights are considered to have failed after migrating past the reticulum. Ongoing monitoring of the cow's health and wellbeing has shown no negative short-term or long-term effects. Our density-controlled device has demonstrated the capability to be excreted naturally with feces, but the strength of the device and the adhesive method need further improvement.

Conclusion

Our proposed variable density module was integrated with PTFE weights and implemented directly into the rumen and reticulum. The device placed in the rumen was successfully passed through the digestive system and defecated within 40 hours. The device placed in the reticulum was damaged and partially passed within 140 hours. This experiment has demonstrated our device's potential for controlled natural passage through the digestive system of cattle. Further investigations and improvements are planned.

Acknowledgment

This work was supported by Cabinet Office, Government of Japan, Cross-ministerial Moonshot Agriculture, Forestry and Fisheries Research and Development Program, "Technologies for Smart Bio-industry and Agriculture" (funding agency: Bio-oriented Technology Research Advancement Institution).

This work was supported by the National Institute of Animal Health, NARO.

References

[1] É. Hajnal, et al., Dairy Cattle Rumen Bolus Developments with Special Regard to the Applicable Artificiall (AI) Methods. *Sensors* 22(18), 6812 (2022); doi: 10.3390/s22186812

[2] C. Shimodan, et al, Stability Evaluation of Reference and Indicating Electrodes of pH Sensor During Monitoring of Cow's Rumen, Sensors and Materials 35, 15-24 (2023); doi: 10.18494/SAM4201

[3] J. Ghirardi, et al., Evaluation of the Retention of Electronic Identification Boluses in the Forestomachs of Cattle, *Journal of animal science* 84(8), 2260-2268 (2006). doi: 10.2527/jas.2005-758

[4] Y. Yashiro, et al., Design of Density-Variable Devices for Excretable Rumen Sensors for Cattle, *2022 IEEE Sensors*, 01-04 (2022); doi: 10.1109/SENSORS52175.2022.9967253

[5] F. Dufreneix, et al., Influence of Particle Size and Density on Mean Retention Time in the Rumen of Dairy Cows, *Journal of dairy science* 102(4), 3010-3022 (2019); doi: 10.3168/jds.2018-15926

DOI 10.5162/EUROSENSORSXXXVI/PT5.68

Fe-doped SnO_2 based gas sensor produced by SILAR for acetone gas sensing

Yernar Shynybekov[*1], *Baktiyar Soltabayev*[1], *Nazerke Sagidolda*[1], *Almagul Mentbayeva*[2], *Amanzhol Turlybekuly*[1]
[1]*National Laboratory Astana, Nazarbayev University, Astana, Kazakhstan*
[2]*Department of Chemical and Materials Engineering, School of Engineering and Digital Sciences, Nazarbayev University, Astana, Kazakhstan*

yernar.shynybekov@nu.edu.kz

Summary:
The findings suggest that Fe-doped SnO_2 sensors, synthesized through the SILAR method, exhibit promising capabilities for detecting acetone efficiently, offering an effective solution for developing high-performance gas sensors with specific selectivity to acetone vapor.

Keywords: acetone gas sensors, MOS, SILAR, nanoparticles

Volatile organic compound (VOC) vapors hold considerable importance due to their substantial presence among indoor environmental pollutants, posing a detrimental impact on human health. It has been confirmed a strong correlation between the emission of VOCs and the incidence of certain types of cancers [1]. The VOCs as acetone, which is also referred to as propanone, dimethyl ketone, 2-propanone, propan-2-one, and β-ketopropane, finds widespread usage in both laboratory and industrial settings [2]. The acetone is detectable in the breath of individuals with diabetes, serving as a potential biomarker for diagnosing the condition [3]. Research findings suggest that employing a non-invasive, painless, rapid, and cost-effective method for diagnosing diabetes, which involves measuring the concentration of acetone in breath, could serve as a viable alternative to traditional blood analysis techniques [4]. Hence, there is considerable interest in efficiently detecting acetone levels.

Metal-oxide-semiconductors (MOSs) as a class of chemoresistive sensors have attracted great attention in environmental monitoring due to their sensitivity to various gases and VOCs. Their ability to detect changes in electrical resistance in response to interactions with target molecules makes them valuable for applications such as air quality monitoring, industrial safety, and medical diagnostics [5–7].

In recent times, significant endeavors have been directed towards the creation of gas sensors utilizing a range of oxide semiconductors such as SnO_2, WO_3, In_2O_3, ZnO, NiO, MnO_2, and V_2O_5. Among the oxide semiconductors, SnO_2, characterized as an n-type semiconductor with a wide band gap of 3.6 eV, has garnered significant attention owing to its superior performance and remarkable chemical stability. Certainly, doping is indeed a promising strategy for enhancing the gas sensitivity and selectivity of oxide semiconductor gas sensors. Doping involves introducing specific impurities or foreign elements into the semiconductor material to alter its electrical and chemical properties. The desired sensors can be obtained by successive ionic layer adsorption and reaction (SILAR) method. The TiO_2/CuO heterostructure gas sensors were synthesized by SILAR method using $SnCl_2$ as source of Sn and $FeCl_2$ as source of Fe. Doping has the capacity to modify the grain size, crystal structure, oxygen distribution, and carrier concentration of gas sensing materials, thereby amplifying the

sensing properties of SnO_2 sensor. The uniform conditions 100 ppm gases and 175^oC were employed for every gas selectivity assessment, showcasing the viability of employing Fe-doped SnO_2 as sensor for detecting volatile organic compound especially acetone. 0.5 mol.% Fe-doped SnO_2 showed high response and high selectivity to acetone among we used gases and fast recovery time approximately 20 sec. Thus, the research findings indicate that the Fe-doped SnO_2 sensors synthesized by SILAR method showed high selectivity to acetone vapour in air atmosphere and fast recovery time. Therefore, doping Fe ions into SnO_2 promise as an effective approach for developing and producing high-performance gas sensors selective to acetone.

Acknowledgements

This research has been funded by the Science Committee of the Ministry of Education and Science of the Republic of Kazakhstan (Grant No. AP14872138, Innovative strategy to recognize the diabetic state of people: metal oxide nanorods as ultrasensitive exhaled gas sensor).

References:

(1) Al-Hardan, N. H.; Abdullah, M. J.; Abdul Aziz, A.; Ahmad, H.; Low, L. Y. ZnO Thin Films for VOC Sensing Applications. *Vacuum* 2010, *85* (1), 101–106. https://doi.org/10.1016/j.vacuum.2010.04.009.

(2) Allen, P. W.; Bowen, H. J. M.; Sutton, L. E.; Bastiansen, O. The Molecular Structure of Acetone. *Trans. Faraday Soc.* 1952, *48*, 991. https://doi.org/10.1039/tf9524800991.

(3) Gardner, J. W.; Shin, H. W.; Hines, E. L. An Electronic Nose System to Diagnose Illness. *Sensors and Actuators B: Chemical* 2000, *70* (1–3), 19–24. https://doi.org/10.1016/S0925-4005(00)00548-7.

(4) Righettoni, M.; Tricoli, A.; Pratsinis, S. E. Si:WO_3 Sensors for Highly Selective Detection of Acetone for Easy Diagnosis of Diabetes by Breath Analysis. *Anal. Chem.* 2010, *82* (9), 3581–3587. https://doi.org/10.1021/ac902695n.

(5) Lee, D.-S.; Lim, J.-W.; Lee, S.-M.; Huh, J.-S.; Lee, D.-D. Fabrication and Characterization of Micro-Gas Sensor for Nitrogen Oxides Gas Detection. *Sensors and Actuators B: Chemical* 2000, *64* (1–3), 31–36. https://doi.org/10.1016/S0925-4005(99)00479-7.

(6) Alizadeh, N.; Jamalabadi, H.; Tavoli, F. Breath Acetone Sensors as Non-Invasive Health Monitoring Systems: A Review. *IEEE Sensors Journal* 2020, *20* (1), 5–31. https://doi.org/10.1109/JSEN.2019.2942693.

(7) Li, J.; Xian, J.; Wang, W.; Cheng, K.; Zeng, M.; Zhang, A.; Wu, S.; Gao, X.; Lu, X.; Liu, J.-M. Ultrafast Response and High-Sensitivity Acetone Gas Sensor Based on Porous Hollow Ru-Doped SnO2 Nanotubes. *Sensors and Actuators B: Chemical* 2022, *352*, 131061. https://doi.org/10.1016/j.snb.2021.131061.

DOI 10.5162/EUROSENSORSXXXVI/PT5.82

Multi-analyte Electrochemical Sensor Based on Graphene Oxide and Gold Nanoparticles Electrode

Nadia Moukri[1], Bernardo Patella[1], Federico Massaro[1], Chiara Cipollina[2,3], Elisabetta Pace[3] Rosalinda Inguanta[1]

[1] Università degli Studi di Palermo, Viale delle scienze 6, 90128, Palermo, Italy

[2] Fondazione Ri.MED, Via Ugo La Malfa 153, 90146, Palermo, Italy

[3] Istituto di Farmacologia Traslazionale (IFT), Via Ugo La Malfa 153, 90146, Palermo, Italy

nadia.moukri@unipa.it

Summary:

This paper presents the preliminary results concerning a novel multianalyte sensor platform, developed through laser scribing. Featuring two different working electrodes and one counter and reference electrode, the platform was preliminary used for uric acid detection. Modification of one working electrode with co-electrodeposited reduced graphene oxide and gold nanoparticles enables highly sensitive detection using square-wave voltammetry. This platform holds promising applications for multi-analyte rapid and accurate detection in diverse biomedical backgrounds.

Keywords: Electrochemical sensor, nanomaterials, electrochemistry, multiplex sensor, multi-analyte.

Introduction

In healthcare, there is a rising demand for a device that quickly and accurately identifies and measures metabolites in body fluids for rapid disease diagnosis and monitoring. Uric acid (UA), is found in serum and urine as it is excreted by the kidneys and plays a crucial role in various human physiological processes [1]. Elevated levels of UA can be related to various disease conditions, such as gout [2] or cardiovascular diseases [3]. Therefore, monitoring of UA levels is necessary due to its potential impact on health. Hence, numerous detection technologies have been developed. Among them, electrochemical methods enable rapid, simple, and accurate analysis with reduced sample volumes. The UA electrochemical detection depends on the electrocatalytic ability of the electrode to directly oxidize UA [4]. Nanomaterials, with their exceptional properties such as high surface area and catalytic activity [5], are well-suited for improving the performance of UA sensors in terms of sensitivity, selectivity, and low limit of detection. Indeed, reduced graphene oxide (rGO) was widely used as electrode substrates for sensitive detection of UA [6]. The performance can be further improved, by introducing nanoparticles (NPs) of noble metals, such as gold [7] or platinum [8]. In this study, an Indium Tin Oxide Polyethylene terephthalate (ITO-PET) substrate was used to create a multi-analyte sensor platform. A CO_2 laser was employed to create two working electrodes, the reference electrode, and the counter electrode on the same ITO-PET sheet. One working electrode was modified with co-electrodeposited rGO and AuNPs.

Experimental

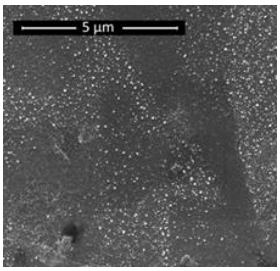

Fig. 1 rGO/AuNPs/ITO-PET electrode SEM image.

An ITO-PET sheet served as the substrate for the sensor platform. The design comprises two working electrodes (E1 and E2), a reference electrode (R), and a counter electrode (C). To achieve the formation of these four electrically insulated electrodes, the thin layer of ITO covering the PET was removed using a CO_2 laser (with a nominal power of 50 W) imposing a laser power of 1.75 W and speed of 50 mm s^{-1}.

GO and AuNPs were co-deposited on E1 electrode according to the method described in our previous work [9]. Briefly, the deposition was conducted at -0.8 V vs SCE for 200 s in acetate buffer solution (ABS) containing 0.25 mM of

$HAuCl_4$ and 0.5 mg mL^{-1} of GO. A platinum mesh was used as a counter electrode. Afterwards, the R electrode was covered with an Ag/AgCl conductive paste.

UA detection measurements were conducted in a 3D-printed cell with a volume of 3 mL. Square wave voltammetry (SWV) was performed in the range potential from -0.5 to 0.4 V vs Ag/AgCl, with a pulse of 0.025 V for 0.02 s and a step height of 1 mV.

Results

As described in our previous work [9], the potentiostatically co-deposition method ensured a uniform coating of rGO decorated with AuNPs of about 25 nm, clearly visible in the SEM image of Fig. 1.

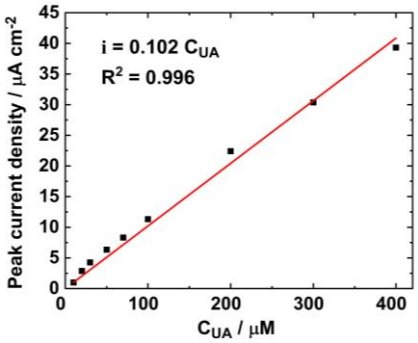

Fig. 2 Calibration line obtained with rGO/AuNPs ITOPET sensor.

The sensor calibration was performed in a Phosphate Buffer (PB, pH 7.4) varying the concentration of UA from 10 to 500 µM. The SWV voltammogram exhibited an oxidation peak at 0.15 V within the potential range of -0.5 to 0.4 V vs Ag/AgCl. This peak intensity increased with higher UA concentration. A linear range between 10 to 400 µM was observed, the calibration line is reported in Fig. 2. A satisfactory sensitivity of 0.102 µA μM^{-1} cm^{-2} was achieved. The proposed sensor performances were comparable to other studies utilizing rGO/NPs-based electrodes [10].

These preliminary satisfactory results demonstrate the feasibility of utilizing the proposed laser-scribed ITO-PET device as a sensor platform integrating internal reference and counter electrodes. This simple method allows for various designs, including those with single or multiple electrodes. According to the proposed design, the other electrode E2 could be properly modified for the detection of another analyte. Thus, further investigation would be necessary to assess the multiplex-sensor performance and its behavior in real samples.

Acknowledgments

This work was partially financed by the project PRIN 2022 PNRR, P2022CHAHX, “Development and validation of an innovative multianalyte sensor for the simultaneous evaluation of biomarkers of oxidative stress and inflammation in advanced experimental models of chronic airways diseases”.

References

[1] Y.M. Roman, The Role of Uric Acid in Human Health: Insights from the Uricase Gene, JPM 13 (2023) 1409. https://doi.org/10.3390/jpm13091409.

[2] G. Ragab, M. Elshahaly, T. Bardin, Gout: An old disease in new perspective – A review, Journal of Advanced Research 8 (2017) 495–511. https://doi.org/10.1016/j.jare.2017.04.008.

[3] D.I. Feig, D.-H. Kang, R.J. Johnson, Uric Acid and Cardiovascular Risk, N Engl J Med 359 (2008) 1811–1821. https://doi.org/10.1056/NEJMra0800885.

[4] M. Sun, C. Cui, H. Chen, D. Wang, W. Zhang, W. Guo, Enzymatic and Non-Enzymatic Uric Acid Electrochemical Biosensors: A Review, ChemPlusChem 88 (2023) e202300262. https://doi.org/10.1002/cplu.202300262.

[5] A. Curulli, Electrochemical Biosensors in Food Safety: Challenges and Perspectives, Molecules 26 (2021) 2940. https://doi.org/10.3390/molecules26102940.

[6] H. Zhang, S. Liu, Electrochemical sensors based on nitrogen-doped reduced graphene oxide for the simultaneous detection of ascorbic acid, dopamine and uric acid, Journal of Alloys and Compounds 842 (2020) 155873. https://doi.org/10.1016/j.jallcom.2020.155873.

[7] C.-S. Lee, S. Yu, T. Kim, One-Step Electrochemical Fabrication of Reduced Graphene Oxide/Gold Nanoparticles Nanocomposite-Modified Electrode for Simultaneous Detection of Dopamine, Ascorbic Acid, and Uric Acid, Nanomaterials 8 (2017) 17. https://doi.org/10.3390/nano8010017.

[8] T.-Q. Xu, Q.-L. Zhang, J.-N. Zhen, Simultaneous determination of dopamine and uric acid in the presence of ascorbic acid using Pt nanoparticles supported on reduced graphene oxide, Electrochimica Acta 115 (2014) 109–115. https://doi.org/10.1016/j.electacta.2013.10.147

[9] B. Patella, A. Sortino, F. Mazzara, R. Inguanta, Electrochemical detection of dopamine with negligible interference from ascorbic and uric acid by means of reduced graphene oxide and metals-NPs based electrodes, Analytica Chimica Acta 1187 (2021) 339124. https://doi.org/10.1016/j.aca.2021.339124.

[10] T.K. Aparna, R. Sivasubramanian, M.A. Dar, One-pot synthesis of Au-Cu2O/rGO nanocomposite based electrochemical sensor for selective and simultaneous detection of dopamine and uric acid, Journal of Alloys and Copounds 741(2018)1130–1141. https://doi.org/10.1016/j.jallcom.2018.01.205.

DOI 10.5162/EUROSENSORSXXXVI/PT5.91

Low-bandgap Polymers, a New Sensitive Surface for Ammonia Detection

Marcelo S. Borro[1,2], Maria L. Braunger[3], Edilene A. da Silva[2,4], Christine Lartigau-Dagron[3], Roger C. Hiorns[3], Nathalie Redon[1], Caroline Duc[1], Clarissa A. Olivati[2]

[1] IMT Nord Europe, Institut Mines-Télecom, Univ. Lille, Centre for Energy and Environment, F-59000 Lille, France

[2] São Paulo State University (Unesp), School of Science and Technology, 19060-900 Presidente Prudente, Brazil

[3]Instituto de Física "Gleb Wataghin" (IFGW), Universidade Estadual de Campinas (UNICAMP), 13083-859, Campinas, SP, Brazil

[4]Institut des Sciences Analytiques et de Physico-chimie pour L'Environnement et Les Materiaux, Université de Pau et des Pays de L'Adour, E2S UPPA, CNRS, IPREM, 64000 Pau, France

marcelo.borro@unesp.br

Summary:

Ammonia (NH_3) gas presents risks to human health and environment, requiring continuous monitoring using reliable sensors. The versatility and the sensitivity to ammonia of conductive polymers make them excellent candidates for use as active layers in sensors. In this study, our goal is to analyze and compare the response of two chemiresistive sensors fabricated using two low-bandgap polymers with distinct functional groups in their side chains to detect NH_3. The manufactured sensors exhibit high sensitivity to NH_3 (0,37%/ppb and 0,27%/ppb, respectively) and a good repeatability.

Keywords: Gas sensors, drop-casting, semiconducting polymers, thin film, chemiresistive sensor

Introduction

NH_3 is a hazardous compound commonly found in products and industrial environments. Even at low concentrations, in parts per million (ppm) levels, this compound can present significant risks to human health and to the environment due to a high level of toxicity and its capacity to react with acids forming harmful aerosols. Therefore, the detection of this gas becomes necessary to mitigate potential environmental and health risks [1].

Conductive polymers (CPs) have appeared as a promising active layer of sensors to detect compounds like NH_3. Compared to metal-oxide semiconductors, CPs present a lower cost, an ease of processing, a high sensitivity, and an ability to work at room temperature [2]. Moreover, the capacity to add/modify functional groups during the synthesis enhances their adaptability and versatility, providing the possibility to target more specific applications.

CPs with narrow bandgaps were widely studied because of their capacity to exhibit intrinsic electrical conductivity without doping and their broad absorption spectrum which can be beneficial for applications in organic devices. For instance, Low-bandgap polymers have exhibited good selectivity and sensitivity in detecting NH_3 when applied in Field Effect Transistor Sensors [3]. This study aims to evaluate the application of those materials in simplest devices such as chemiresistive sensors, known for their low cost and easy implementation.

Materials and Methods

The active layer of the sensors were the low-bandgap polymers poly[4,4'-diethylhexyl-4H - cyclopenta [2,1-b;3,4-b'] dithiophene - alt - 2,5 - didodecyl-3,6 - bis (thiophen-2-yl)pyrrolo[3,4-c]-pyrrole-1,4-dione] (PCPDPDPP_C12) and poly[4,4' -diethylhexyl-4H-cyclopenta [2,1-b;3,4-b'] dithiophene – alt -2,5- di(2-(2-(2-methoxyethoxy)ethoxy) ethyl-3,6-bis (thiophen-2-yl) pyrrolo[3,4-c] -pyrrole-1,4-dione] (PCPDPDPP_TEG), both synthesized according the process described previously [4]. From this point forward, the materials will be referred as C12 and TEG, respectively.

Both polymers were dispersed in Chloroform (1 mg/mL) and agitated using an ultrasonic bath for 2 hours. To make the sensors, 6 µL of the solution was drop-casted onto gold interdigitated electrodes, 50 µm of space between the digits, and allowed to dry for 3 hours at ambient temperature.

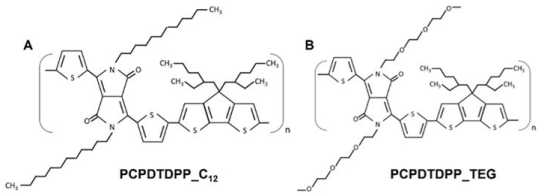

Fig 1 – Molecular structure of the low-bandgap polymers A) PCPDTDPP_C12 and B) PCPDTDPP_TEG.

To characterize the sensors, two cards with 10 devices each were placed inside a treated stainless-steel chamber at room temperature (~23 °C) and monitored by a Sensirion SHT21 temperature and relative humidity (RH) sensor. The NH_3 gas in nitrogen was obtained from Messer (9,70 ppm concentration). The flow rate was set for 4 L/min, with the NH_3 concentration ranging from 50 to 2000 ppb. RH was maintained at 50% using an Omicron gas generation and dilution system, model OMI-SR042A-A. Sensors resistances was measured by the Agilent Data Acquisition/Switch Unit, model 34970A, and NH_3 concentration inside the chamber was monitored by LGR gas analyzer, model 907-0016-0000.

Results

In general, independently of the functional group, all sensors show an increase in the resistance values when exposed to NH_3.

Fig 2 shows the continuous response-recovery curves for NH_3. A direct correlation between the intensity of the response and the concentration of ammonia used in the cycles was noticeable. This increase shows that both materials are sensitive for NH3 and can be used as detectors.

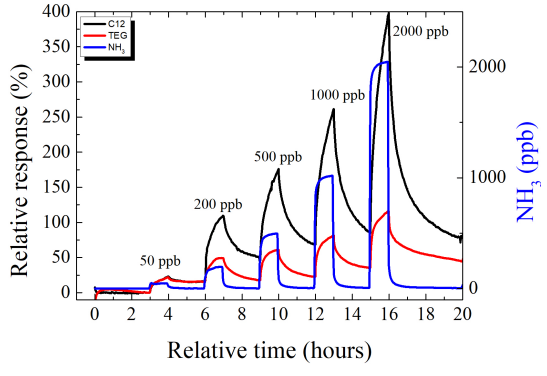

Fig 2 - Response of the PCPDTDPP_C12 and TEG NH_3 sensors at 50% RH in continuous response-recovery curves.

Furthermore, sensors based on C12 polymer proved to be more stable in terms of reproducibility and had lower resistance values (ranging between 0,2 MΩ to 9 MΩ). More TEG sensors were going out of scale due to high resistance values (from 30 MΩ to more than 100 MΩ) causing difficulties in analyzing their reproducibility. The observed difference for resistance values can be attributed to functional groups in the side chains: twelve carbons to C12 and a trietyleneglycol to TEG.

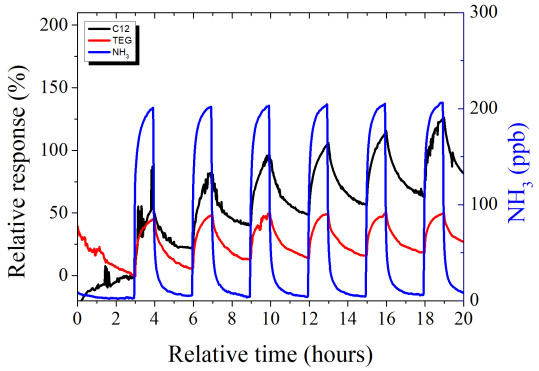

Fig 3 – Repeatability study of the PCPDTDPP_C12 and TEG sensors at 50% RH and 200 ppb of NH_3.

Fig 3 exhibits the repeatability curves response. In terms of repeatability, both sensors demonstrated a low coefficient of variation over the 6 cycles of NH_3, with C12 sensors showing approximately 18% variance and TEG sensors demonstrating around 13%. Moreover, C12 and TEG present a high sensitivity at 0,37%/ppb and 0,27%/ppb for 200 ppb of NH_3, respectively.

To summarize, both sensors exhibited sensitivity to NH_3, displaying good repeatability and sensitivity at 50% RH, with C12 demonstrating superior stability and lower resistance values.

References

[1] B. Timmer, W. Olthuis, A. Van den Berg, Ammonia sensors and their applications—a review, Sensors and Actuators B: Chemical 107, Issue 2, 666-677, (2005) doi: 10.1016/j.snb.2004.11.054.

[2] S. Aarya, Y. Kumar, R. K. Chahota, Recent Advances in Materials, Parameters, Performance and Technology in Ammonia Sensors: A Review. Journal of Inorganic and Organometallic Polymers and Materials, (2019); doi:10.1007/s10904-019-01208-x.

[3] Z. Wang, Z. Liu, L. Chen, Y. Yang, J. Ma, X. Zhang, Y. Guo, G. Zhang, D. Zhang. Highly Sensitive Field-Effect Ammonia/Amine Sensors with Low Driving Voltage Based on Low Bandgap Polymers, Advanced Electronic Materials 4, Issue 5 (2018); Doi: 10.1002/aelm.201800025.

[4] E. A. da Silva, A. Gregor, J. D. Fernandes, C. Njel, R. Dedryvère, C. J. L. Constantino, R. C. Hiorns, C. Lartigau-Dagron, C. A. Olivati, Understanding the langmuir and Langmuir-Schaefer film conformation of low-bandgap polymers and their bulk heterojunctions with PCBM, Nanotechnology 31, 315712 (2020) doi: 10.1088/1361-6528/ab8b0b.

DOI 10.5162/EUROSENSORSXXXVI/PT5.92

Enhancement of Receptor Function on Metal Oxide Semiconductor Gas Sensors for Ultra Selectivity

Kengo Shimanoe[1], *Haoyue Yang*[2], *Koichi Suematsu*[1], *Ken Watanabe*[1]
[1] *Faculty of Engineering Sciences, Kyushu University, Kasuga, Fukuoka 816-8580, Japan,*
[2] *Interdisciplinary Graduate School of Engineering Sciences, Kyushu University, Kasuga, Fukuoka 816-8580, Japan*

shimanoe.kengo.695@m.kyushu-u.ac.jp

Summary:
In this study, we investigated the combination of receptor function, one of the material design guidelines for semiconductor gas sensors, and the gas adsorption characteristics during MEMS driving, along with the reaction with adsorbed oxygen during heating, to achieve ultra-high selectivity. Specifically, by using MoO3-loaded SnO2 particles as the sensing film of MEMS gas sensors and applying double-pulse driving, we found a significant improvement in ethanol sensitivity compared to methanol.

Keywords: semiconductor gas sensor, receptor function, selectivity, acidic oxides, tin dioxide

Introduction

As guidelines for material design in semiconductor gas sensors, we propose three important factors (Yamazoe-Shimanoe Design) [1]: receptor function, transducer function, and utility factor. Among these factors, those related to gas selectivity are receptor function and utility factor. Receptor function directly relates to factors such as chemical reactivity and functional group characteristics. We aim to maximize this receptor function to propose gas sensors with ultra-high selectivity. Specifically, tin oxide, which has the ability to adsorb negatively charged oxygen, is used as the base material, while acidic oxides that do not possess the ability to adsorb negatively charged oxygen are loaded as receptors on the base material. In this sensor material, adsorption of the target gas to the receptor and the partial oxidation reaction of the adsorbed gas with negatively charged oxygen proceed, resulting in ultra-high selectivity. In this study, we report the fundamental characteristics using MEMS sensors.

Experimental

SnO_2 nanoparticles were synthesized using hydrothermal treatment using 1 M of $SnCl_4 \cdot 5H_2O$ solution and NH_4HCO_3 solutions. After removing Cl^- ion by centrifugation, the gel was dispersed into deionized water with stirring. Then the pH of mixture was adjusted to 10.5 by tetramethylammonium hydroxide (15 %) solution. Subsequently the mixture was transferred to a Teflon-lined autoclave and held at 200°C for 10 h in an oven. The transparent sol was dried in vacuum, and then annealed at 600°C for 3 h under O_2 flow to prepare the SnO_2 nanoparticles. As receptors, we selected MoO_3 which is one of acidic oxides. MoO_3-loaded SnO_2 was prepared through impregnation method. The MEMS sensor was fabricated by the micromanipulation method using MoO_3-loaded SnO_2. For MEMS

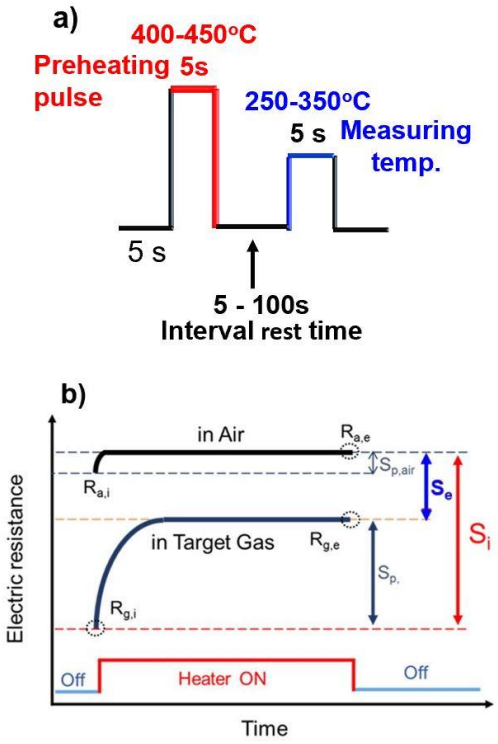

Fig. 1. (a) Operating processes during double-pulse-driven mode; (b) Explanation of the sensor responses.

sensors, the electrical resistance of obtained gas sensors was evaluated using double-pulse-driven mode [2-3], as described in Figure 1. The preheating and measurement temperature was respectively set to 450°C and 350°C. During the detection process, the electrical resistance of sensor could be divided to R_a (the resistance in air), $R_{g,i}$ (the resistance in gas at the initial of measurement phase), and $R_{g,e}$ (the resistance in gas at the end of measurement phase). On the basis, we proposed three different sensor responses, S_e (R_a /$R_{g,e}$), S_p ($R_{g,e}$ /$R_{g,i}$), and S_i (R_a /$R_{g,i}$).

Results

Fig. 2a)-b) shows sensor responses S_p, S_i and S_e of neat-SnO_2 and MoO_3-loaded SnO_2 microsensors to 10 ppm ethanol and methanol measured at 350°C under double-pulse-driven (DP) mode. Herein, S_p ($R_{g,e}$ /$R_{g,i}$) primarily represented the combustion of adsorbed and condensed gas molecules during measuring period. And S_i (R_a /$R_{g,i}$) referred to the total resistance change between air and target gas atmosphere, including gas adsorption and combustion in the sensing layer. It was clear that neat-SnO_2 exhibited an extremely minimal S_p of about 3, demonstrating the weak combustion of adsorbed ethanol molecules in the sensing layer of SnO_2. Meanwhile, S_p of MoO_3-loaded SnO_2 to 10 ppm ethanol was approximately 496. Generally, the sensing performance of resistive-type gas sensor was evaluated by the change in electrical resistance between air and gas atmosphere. The improved S_p value indicated it is possible to accomplish gas detection only by monitoring the behavior of microsensor in gas atmosphere. Moreover, S_i values showed similar results with S_p, MoO_3-loaded SnO_2 exhibited distinctly higher response to ethanol than neat-SnO_2 microsensor. The sensor responses (S_e) of neat-SnO_2 and MoO_3-loaded SnO_2 microsensors to 10 ppm ethanol and methanol at 350°C are shown in Fig. 2c). Conversely, the MoO_3-loaded SnO_2 microsensor exhibited much lower S_e values for both ethanol and methanol compared to the neat-SnO_2 microsensor.

The results prove the significant effect of receptor material design on improving the gas sensing performance by controlling the reaction pathway and gas adsorption.

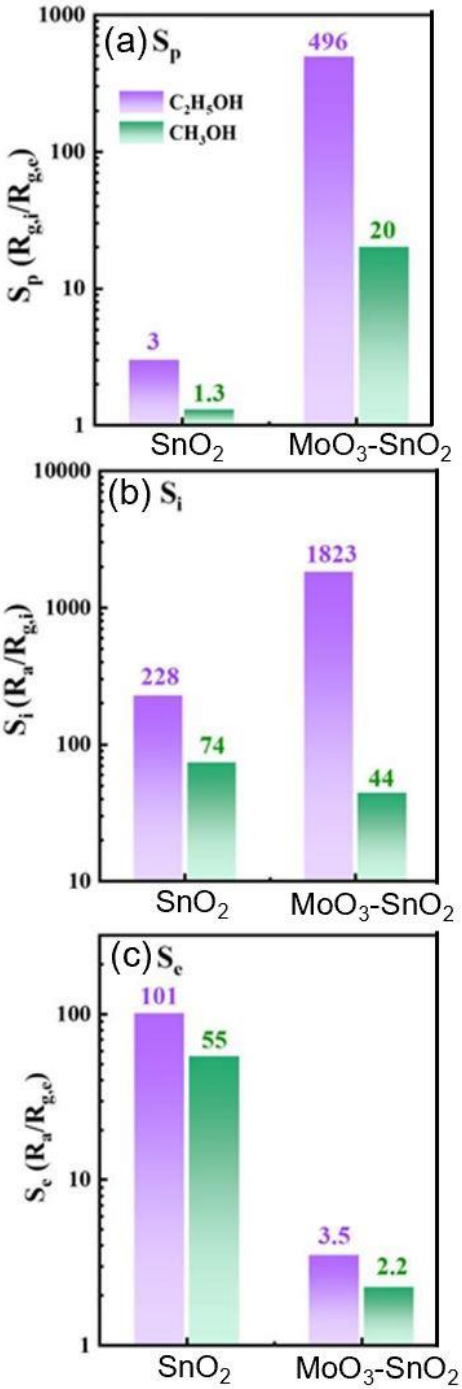

Fig. 2. (a) S_p, (b) S_i and (c) S_e values of neat-SnO_2 and MoO_3-loaded SnO_2 microsensors to 10 ppm ethanol and methanol under DP-mode.

References

[1] N. Yamazoe and K. Shimanoe, Science and Technology of chemiresister gas sensors, Nova Science Publishers, Inc., 2007, pp.1-32.

[2] K. Suematsu, W. Harano, T. Oyama, Y. Shin, K. Watanabe and K. Shimanoe, "Pulse-Driven Semiconductor Gas Sensors Toward ppt Level Toluene Detection", Anal. Chem., vol. 90 (19), pp. 11219-11223, 2018.

[3] K. Suematsu, W. Harano, S. Yamasaki, K. Watanabe, K. Shimanoe, "One-Trillionth Level Toluene Detection Using a Dual-Designed Semiconductor Gas Sensor: Material and Sensor-Driven Designs", ACS Appl. Electron. Mater., vol. 2 (9), pp. 4122-4126, 2020.

DOI 10.5162/EUROSENSORSXXXVI/PT5.95

Humidity Amplified Sensitivity in a highly selective H_2S Gas Sensor Using MXene-conjugated Polymer Composite

Seyed Hossein Hosseini Shokouh[1,], Jin Zhou[1], Zhong-Peng Lyu(Lv)[2,*], Krisztian Kordas[1]*
[1] Microelectronics Research Unit, Faculty of Information Technology and Electrical Engineering, University of Oulu, FIN-90014 Oulu, Finland,
[2] Department of Applied Physics, Aalto University, FIN-00076 Aalto, Finland

Corresponding Author's e-mail address: seyed.hosseinishokouh@aalto.fi; zhongpeng.lyu@aalto.fi

Summary:
Highly sensitive and selective H_2S sensors are required for human health and environmental monitoring. However, the humidity in the real working environment always harms either the sensitivity or selectivity of the H_2S sensors. Here we reported a significant amplified sensitivity towards H_2S gas induced by the variation of humidity for a chemiresistive sensor, which is based on $Ti_3C_2T_x$ MXene-conjugated polymer composite. The sensor also provides a unique selectivity to H_2S with a negative response, while positive to water vapor and most of the other analytes.

Keywords: H_2S sensing, $Ti_3C_2T_x$ MXene, humidity effect, intercalation, conjugated polymers

Introduction

Humidity is often regarded as a prevalent factor that diminishes the sensitivity and selectivity of various types of gas sensors based on nanomaterials [1-3]. In the practical applications, water vapor was inevitably mixed with the analytes, which requires humidity filter to reduce the moisture content prior to analysis. For the chemiresistive gas sensors based on absorption, the water vapor can interfere with the active sensing materials in different manners, e.g., competitive adsorption, surface blocking, chemical reaction, and conductivity modulation, etc. To tackle these issues, researchers have developed anti-humidity gas sensors, where the active surfaces were inert to water vapor. However, the reinforcement of the water humidity resistance always accompanies with reduced sensitivity or selectivity, longer response time, higher cost or complexity, limited measurement range. It is ideal to have a highly sensitive and selective chemiresistive gas sensor which does not affected by moisture, even the performance can be enhanced under high humidity environment.

New Method

Utilizing the highly negative surface potential of $Ti_3C_2T_x$ flakes and polar charged nitrogen of conjugated polymers (poly[3,6-diamino-10-methylacridinium chloride-co-3,6-diaminoacridine-squaraine], PDS-Cl), we simply used physical blending to fabricate the sensing material. The PDS-Cl has intercalated in the MXene layers, preserving the high selectivity of MXene while enhances the sensing response of composite sensor [4].

The humidity amplification effect was seldom reported in gas sensor systems [5,6]. To the best of our knowledge, this is the first demonstration that MXene based gas sensor can have an enhanced sensitivity in higher humidity environment. Our work has demonstrated the versatility of MXene-based gas sensors in real-life scenarios.

Results

Figure 1 demonstrates the H_2S sensing response of the MXene-polymer sensor for different concentration of analytes at relative humidity (RH) of less than 10%. The lowest limit of detection for sensor is 0.5 ppm.

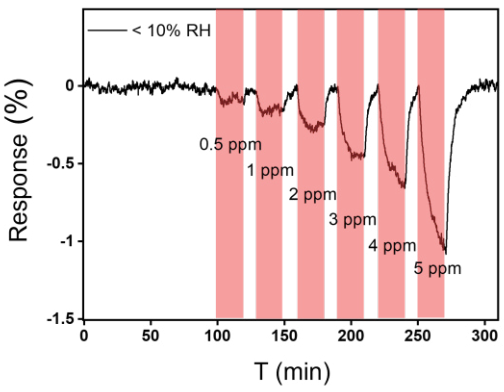

Fig. 1. Dynamic sensing response of MXene-polymer for different concentrations of H_2S. The

baseline is subtracted for clarity and readability of the signal.

Gas sensing response

The gas response is calculated using Equation 1:

$$S(\%) = \frac{Rg - R0}{R0} \times 100\% \qquad (1)$$

where R_0 and R_g are the resistances of the sensor upon exposure to N_2 and the target gas, respectively.

Strikingly the sensing response of sensor under higher level of RH will improve, as indicated in Figure 2. The sensing response, summarized in Table 1, shows a linear sensing response at different RH level.

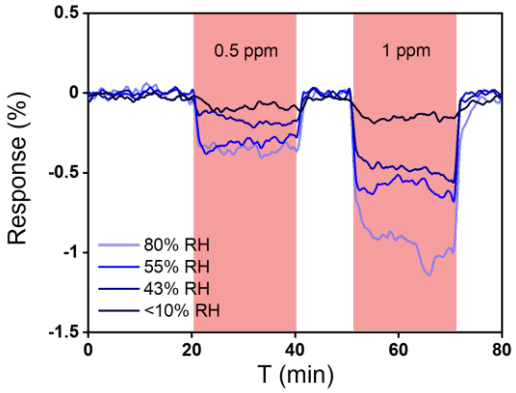

Fig. 2. The gas sensing response of sensor under different RH for 0.5 and 1 ppm H_2S.

Sensing mechanism

In the case of MXene/PDS-Cl composite, the polymer opens the interlayer spaces and by increasing the RH level, the H_2O molecules will intercalate between layers and provide even higher number of accessible active sites as shown in Figures 3. This can lead to enhancement of the charge transfer effect and result in higher sensing response.

Tab. 1: Response of MXene composite sensor under different RH

H_2S Concentration / RH (%)	**0.5** ppm	**1** ppm
<10% RH	**-0.1%**	**-0.2%**
43% RH	**-0.2%**	**-0.5%**
55% RH	**-0.3%**	**-0.6%**
78% RH	**-0.4%**	**-1%**

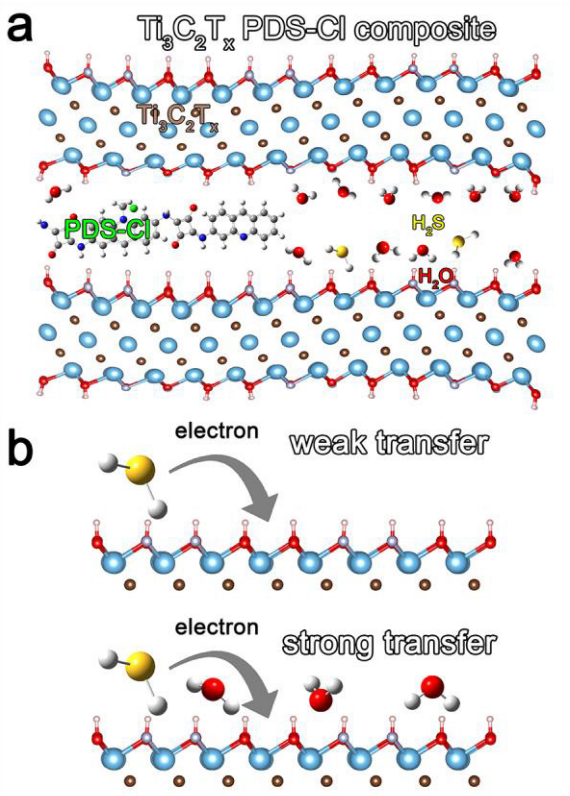

Fig. 3. (a) Schematic illustration of the structure of our MXene-polymer composite. (b) Proposed mechanism of the amplification sensitivity for H_2S sensing.

References

[1] Chen, Dazhi, and Yong J. Yuan. IEEE Sensors Journal 15, 6749–60 (2015); doi: 10.1109/JSEN.2015.2457931.

[2] Lao, Chang Shi, Qin Kuang, Zhong L. Wang, Myung-Chul Park, and Yulin Deng. Applied Physics Letters 90, 262107 (2007); doi: 10.1063/1.2748097.

[3] Steinhauer, S., A. Köck, C. Gspan, W. Grogger, L. K. J. Vandamme, and D. Pogany. Applied Physics Letters 107, 123112 (2015); doi: 10.1063/1.4931706.

[4] Hosseini-Shokouh, Seyed Hossein, Jin Zhou, Ethan Berger, Zhong-Peng Lv, Xiaodan Hong, Vesa Virtanen, Krisztian Kordas, and Hannu-Pekka Komsa. ACS Applied Materials & Interfaces 15, 7063–73 (2023); doi: 10.1021/acsami.2c19883.

[5] Wang, Bo, Xusheng Dong, Zi Wang, Yanfang Wang, and Zhongyu Hou. IEEE Electron Device Letters 41, 908–11 (2020); doi: 10.1109/LED.2020.2987948.

[6] Ghahrizjani, Reza Taheri, Reza Mostafavian Maleki, Mashhood Ghafarkani, Asghar Esmaeili, Mohsen Ameri, Ezeddin Mohajerani, Naser Safari, Yuhai Dou, and Shi-Xue Dou. Sensors and Actuators B: Chemical 391, 134045 (2023); doi: 10.1016/j.snb.2023.134045.

DOI 10.5162/EUROSENSORSXXXVI/PT5.98

Synergy between Metal Oxides, Metal-organic Frameworks, and Multivariate Statistics for Selective Room Temperature Gas Sensing

Guillem Domènech-Gil[1,2], Anna Estany-Macià[1,2], Ignasi Fort-Grandas[1,2,3], Manel López[1,2], Paolo Pellegrino[1,2], Mauricio Moreno-Sereno[1,2], Albert Romano-Rodríguez[1,2]

[1] Department of Electronic and Biomedical Engineering, University of Barcelona (UB), 08028 Barcelona, Spain

[2] Institute of Nanoscience and Nanotechnology (IN2UB), University of Barcelona (UB), 08028 Barcelona, Spain

[3] Department of Inorganic and Organic Chemistry, University of Barcelona (UB), 08028 Barcelona, Spain

Corresponding Author's e-mail address: guillemdomenech@ub.edu, albert.romano@ub.edu

Summary:

The use of metal oxides for gas sensing applications is a common and commercialized strategy but, in most cases, these materials present two important drawbacks: a cross-sensitivity to common gas species and a high operation temperature (100-400 °C). It has been recently reported that, on its turn, metal-organic frameworks can sense gases at room temperature, offering the so-called "sieving effect" that allow them to work as filters for improved selectivity. This research explores metal-organic frameworks and their potential synergy with metal oxides and multivariate statistics to create next-generation gas sensors.

Keywords: Gas sensor, metal oxide nanowires, metal-organic frameworks, machine learning, greenhouse gas

Headlines

Recently reported metal-organic frameworks offer the possibility of operating gas sensors at room temperature and, therefore, their integration in common use electronic devices.

The synergy of new sensing materials that exhibit the sieving effect, combined with multivariate statistic techniques, can enhance the selectivity of gas sensors.

Background, Motivation an Objective

Metal oxides (MOx) have been investigated and commercialized as gas sensing materials for several decades because they offer high sensitivity, easiness of integration, robustness of the final device, and they are cost-efficient. However, they show cross-sensitivity to many gas species, especially to moisture, many times providing false readings. Furthermore, it is well-known that these materials need high temperatures (100-400 °C) to operate in optimal conditions [1], what makes it challenging to integrate MOx-based gas sensors in common electronic devices, such as smartphones, and, at the same time, this induces power consumptions that hinder deploying these sensors in remote locations with reduced access to power grid.

Recently, metal-organic frameworks (MOFs) have been demonstrated to work as gas sensing materials as well, being sensitive to a large variety of gases while operating at room temperature, thus increasing their potential for practical applications, and presenting easiness of integration, robustness of the final device and cost-efficiency as good as MOx [2]. Moreover, they show the so-called sieving effect [3] through which MOFs, depending on the size of their pores, electron affinity and/or specific functional groups, can act as a filter for certain gases.

Our goal is to explore MOx, MOFs, and possible synergies between them to obtain novel gas sensors with enhanced features for practical applications such as room temperature operation with fast response times and/or increased selectivity.

Methodology

By means of chemical vapor deposition, we synthesize assemblies of single-crystal MOx nanowires and, by using chemical routes, we synthesize MOFs, both directly and site-selectively integrated on interdigitate electrodes. In this

way, we obtain gas sensors that offer new sensing characteristics with few fabrication steps. These sensors operate at room temperature, opening the path to integration of gas sensors in common electronic devices. The obtained data are treated via multivariate statistic techniques to assess the discrimination power of the fabricated sensors.

Results

We will present the gas sensing behavior observed for the fabricated MOx- and MOF-based sensors when exposed to CO_2 and CH_4 ranging from 300 to 1200 ppm and from 1 to 10 ppm, respectively, diluted in dry and humid synthetic air. As an example, Figure 1a shows one of the MOx single-crystal nanowire forests directly grown onto interdigitate electrodes, while Figure 1b demonstrates the discrimination power by means of principal component analysis of the response of one of the synthesized MOFs.

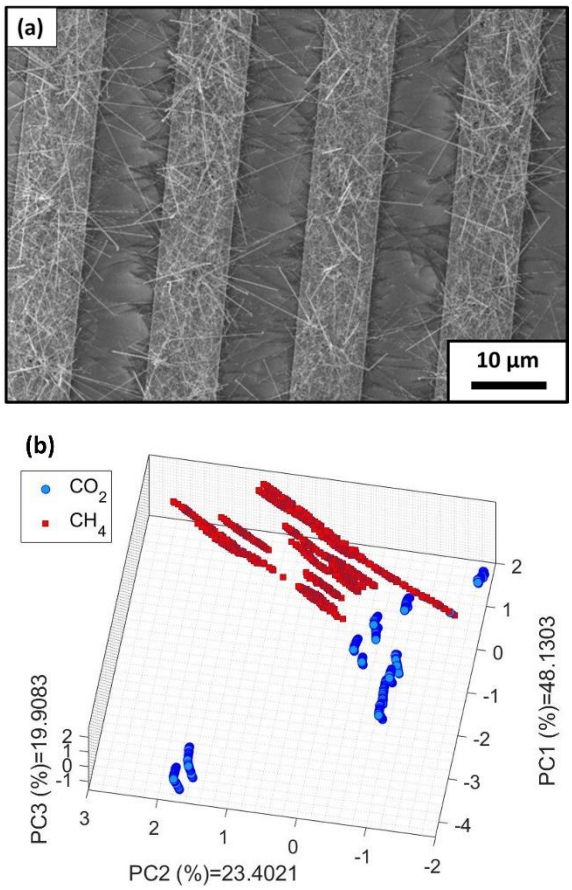

Fig. 1. (a) Metal oxide nanowires site-selectively grown on interdigitate electrodes by means of chemical vapor deposition and (b) results of principal component analysis from gas measurements of a metal-organic framework layer when exposed to carbon dioxide and methane ranging from 300 to 1200 ppm and from 1 to 10 ppm, respectively.

References

[1] P. Shankar, J.B.B. Rayappan, Gas sensing mechanism of metal oxides: The role of ambient atmosphere, type of semiconductor and gases - A review, *Science Letters Journal* 4, 126 (2015); doi: NA.

[2] H. Yuan, N. Li, W. Fan, H. Cai, D. Zhao, Metal-Organic Framework Based Gas Sensors, *Advanced Science* 9, 2104374 (2022); doi: 10.1002/advs.202104374.

[3] C. Zhang, R.P. Lively, K. Zhang, J.R. Johnson, O. Karvan, W.J. Koros, Unexpected Molecular Sieving Properties of Zeolitic Imidazolate framework-8, *The Journal of Physical Chemistry Letters* 3, 2130–2134 (2012); doi: 10.1021/jz300855a

DOI 10.5162/EUROSENSORSXXXVI/PT5.106

The Development of Optical Sensors for Heavy Metal Ions detection on Nanocellulose substrate

Mahsa Mousavi Langari[1], Larisa Lvova[2], Roberto Paolesse[2], Jalel Labidi[1]*
[1]Department of Chemical and Environmental Engineering, University of the Basque Country UPV/EHU, San Sebastian, Spain,
[2]Department of Chemical Science and Technologies, University of Tor Vergata, Rome, Italy

Larisa.lvova@uniroma2.it

Summary:
This study presents two novel all-solid-state optodes, emloyed for detecting different heavy metal ions (HMIs) in waters. For this reason, PVC-based polymeric membranes, containing tetraphenylporphyrin (TPP) and Zn(II)TPP-1,3-bis(2-pyridylimino)isoindoline-Crown (ZnPC) as cation-sensitive ionophores, were embedded in nanocellulose substrate. In addition, a water-soluble porphyrin and silver nanoparticles (AgNPs) were doped with nanocellulose to devise an aqueous sensing suspension. The optical response of these chemical sensors displayed a successful detection of multiple HMIs.

Keywords: Chemical sensors, Nanocellulose, Porphyrin ligands, HMIs, Optical detection

Background, Motivation and Objective

A rise in the level of HMIs in water resources, mainly due to industrial activities, has caused mounting concern about human health. Accordingly, the fabrication of sensing platforms aimed at monitoring HMIs has attracted researchers´ attention [1]. Among all, optical sensors are of substantial interest owing to their privileges, including fast response, excellent sensitivity, and easy usage. Porphyrins and their analogues have been actively used as a sensing materials for the development of chemical sensors over the last decades [2]. It is noteworthy to mention that the utilization of porphyrin ligands in optical sensors opens up new possibilities in detecting HMIs thanks to their ability in hosting and chelating several ions [3]. On the other hand, Nanocellulose, offering unique properties, like biodegradablity, non-toxicity, and sustainablity, can be a promising candidate in sensing platforms [4]. As a result, the integration of porphyrin ligands in nanocellulose substrate leads to a selectivite, sensitivite and biocompatible optical sensor.
The objective of this work is the development of optical sensing platforms in which porphyrin ligands are incorporated in PVC-based polymeric matrix; and nanocellulose applied as a solid support is investigated as well. It should be noted that these are the first steps of series of experiments for development of optical sensors for HMIs with nanocellulose as a solid support, the further studies are in progress.

Two sensing materials based on plasticized PVC membranes were prepared by incorporating 1 wt% of one of the porphyrin ligands and 5 wt% of TpClPBK cation exchanger as it was reported previously [3]. The membrane cocktails in THF (2 µl) were deposited on the small round pieces of freeze-dried nanocellulose (~d= 0.5 cm), isolated from bleached eucalyptus pulp by using high-pressure homogenizer (100-700 bar, 20 cycles, 10 $L.h^{-1}$). The performance of the obtained sensing platform in recognizing different concentrations (10^{-7}-10^{-1} M) of variant HMIs (Ni^{2+}, Cu^{2+}, Co^{2+}, Hg^{2+}, Pb^{2+}, Cd^{2+}, Zn^{2+}) were examined. For this reason, 5 µl of all the concentrations of each HMIs were deposited on the prepared sensing optodes.
Additionally, NC was used to facilitate the upload of free base 5, 10, 15, 20 tetrasulpho-penyl porphyrin (TPP-$(SO_3)_4$) on AgNPs. The TPP-$(SO_3)_4$/NC@AgNPs suspension was then used for HMIs optical sensing. The suspension was synthesized according to the literature [5,6] in one-pot procedure through drop-by-drop addition of sodium citrate (2.4×10^{-3} M) into aqueous suspension of NC (0.1 wt%, at boiling point) to which $AgNO_3$ and TPP-$(SO_3)_4$ in 10:1 mass ratio were dissolved. The mixture was refluxed for 40 min. To investigate the performance of the sensing suspension, the HMIs mentioned before were added to it so that obtaining different concentrations of them (10^{-5}-10^{-3} M) in the suspension.

Description of the New Method or System

To the best knowledge of the authors, this is the first time that nanocellulose is exploited as a substrate for porphyrin ligands. Besides, a naked-eye observation in the attained sensing suspension opens a perspective for newly developed NC-based composite materials doped with porphyrins for development of optical sensors for HMIs detection.

Results

Fig. 1(a, b) depicts the images of TPP- and ZnPC-based optodes in response to all the concentrations of the aforementioned HMIS. As can be seen in Fig. 1a, the optical response of the TPP-based optode to all the ions except Zn^{2+} is visible by naked-eye and appears in color change from red to green by increase in their concentrations, attributed to the formation of the sitting-a-top complex of porphyrin with HMIs [2]. In contrary, Fig. 1b depicts that ZnPC-based optode does not have an observable response to the HMIs. However, grayscale color model showed the considerable change in the intensity of its color in the presence of Cu^{2+}, Hg^{2+} and Zn^{2+}. In this case, the response of the ZnPC ligand corresponds to the binding of HMIs by the crown ether cavity [3]. The data extracted by means of ImageJ software [8].

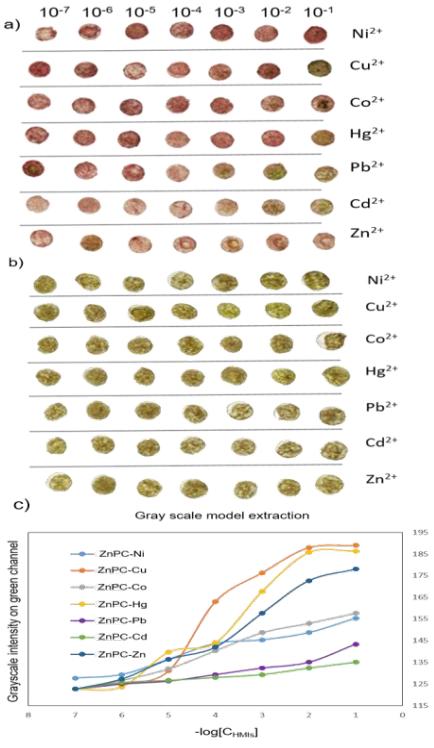

Fig. 1. The images of a) TPP-, b) ZnPC-based optodes in the presence of HMIs in a 10^{-7}-10^{-1} M range of concentrations, c) Plotted data extracted from ZnPC-based optodes by Grayscale model.

Fig. 2a indicates the UV-Vis spectra of TPP-$(SO_3)_4$/NC@AgNPs in the presence of growing concentrations of Hg^{2+}, and the variation of peak intensity as well as red shift of Soret band (typical for porphyrin complexes). Moreover, as can be seen in Fig. 2b, the evident color change of the sensing suspension upon the addition of 10^{-3} M Co^{2+}, Hg^{2+} and Cd^{2+} can be observed. More details on optical signal extraction and HMIs quantitative analysis will be discussed in our presentation.

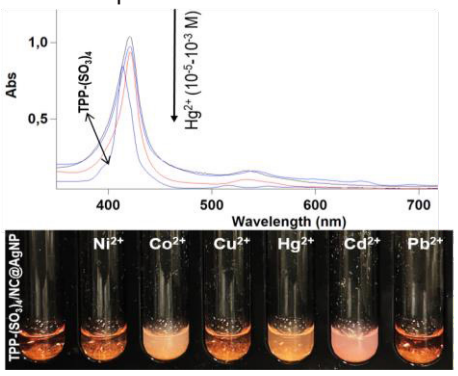

Fig. 2. a) UV-vis spectra of TPP-$(SO_3)_4$/NC@AgNPs aqueous solution in the presence of growing concentrations of Hg^{2+}, b) the image of as synthesized TPP-$(SO_3)_4$/NC@AgNPs, upon the addition of 10^{-3} M solutions of different HMIs.

References

[1] B. Balusamy, *et al*. Functionalized Electrospun Nanofibers as a Versatile Platform for Colorimetric Detection of Heavy Metal Ions in Water: A Review, *Materials* 13, 10 (2020); doi: 10.3390/ma13102421

[2] R. Paolesse, *et al*. Porphyrinoids for Chemical Sensor Applications, *Chemical Reviews* 117, 2517–2583 (2017); doi: 10.1021/acs.chemrev.6b00361

[3] L. Lvova, *et al*. Fast Optical Sensing of Metals : A Case Study of Cu^{2+} Assessment in Soils, *ECS Journal of Solid State Science and Technology* 9 2162-8777 (2020); doi: 10.1149/2162-8777/aba0d

[4] T. Ma, *et al*. Nanocellulose: a Promising Green Treasure from Food Wastes to Available Food Materials, *Critical Review Food Science and Nutrition* 62, 989–1002 (2022); doi: 10.1080/10408398.2020.1832440

[5] M.X. Quan, *et al*. Microwave-Assisted Synthesis of Silver Nanoparticles for Multimode Colorimetric Sensing of Multiplex Metal Ions and Molecular Informatization Applications, *ACS Applied Materials & Interfaces* 14, 9480–9491 (2022); doi: 10.1021/acsami. 1c23559

[6] D. Musino, C. Rivard, G. Landrot, B. Novales, T. Rabilloud, I. Capron, Hydroxyl Groups on Cellulose Nanocrystal Surfaces form Nucleation Points for Silver Nanoparticles of Varying Shapes and Sizes, *Journal Colloid and Interface Science* 584, 360–371 (2021); doi: 10.1016/j.jcis.2020.09.082

[7] https://ij.imjoy.io/

DOI 10.5162/EUROSENSORSXXXVI/PT5.122

Development of the Method for the Detection of Benziso-thiazolinone

Jelena Vujančević[1], Neža Sodnik[1], Abhilash Krishnamurthy[1], Zoran Samardžija[1], Kristina Žagar Soderžnik[1]

[1]Jožef Stefan Institute, Jamova cesta 39, 1000 Ljubljana, Slovenia

Corresponding Author's e-mail address: jelena.vujancevic@ijs.si

Summary:

Benzisothiazolinone (BIT) serves as an antimicrobial agent in water-based products, acting as a preservative. Exposure to BIT in such products can lead to sensitization and allergic contact dermatitis upon dermal contact. This study aims to detect BIT using portable electrochemical sensors, specifically investigating screen-printed electrodes with carbon and gold-based working electrodes. Cycle voltammetry and square wave voltammetry were employed and compared to establish an effective detection method for BIT.

Keywords: isothiazolinone-based biocide, electrochemical sensors, cyclic voltammetry, square wave voltammetry, screen-printed electrodes.

Title

Development of the Method for the Detection of Benzisothiazolinone.

Headlines

Fast Detection and Monitoring of Benzisothiazolinone biocide by portable electrochemical sensors.

Background, Motivation an Objective

Benzisothiazolinone (BIT) functions as an antimicrobial agent present in a range of products, including laundry detergents, water-based paints, and food packaging materials, among others, contributing significantly to municipal wastewater contamination. Exposure to BIT can lead to skin sensitization and allergic reactions, particularly in individuals with pre-existing skin conditions. Its introduction into water through direct discharge or runoff poses risks to aquatic ecosystems, affecting fish and algae. The persistent nature of BIT underscores the necessity for novel detection and monitoring methods. Electrochemical techniques offer promising solutions due to their simplicity, rapid response times, affordability, and widespread acceptance. Among these, cyclic voltammetry (CV) is commonly used despite its limitations, notably capacitive contributions affecting sensitivity. To mitigate this, pulse techniques like square wave voltammetry (SWV) have been developed, offering faster and more sensitive detection. In this study, we employ two electrochemical voltammetric techniques using screen-printed electrodes to detect BIT.

Description of the New Method or System

Two types of screen-printed electrodes (SPE) were utilized: one with a carbon-based working electrode and the other with a gold-based working electrode. The counter and reference electrodes remained consistent, consisting of platinum and silver, respectively. Electrochemical measurements were conducted using the portable potentiostat PalmSens. The initial study involved the use of the redox probe $Fe(CN)_6^{3-/4-}$ to evaluate screen-printed electrodes. Cyclic voltammetry (CV) covered a potential window from 0 V to 1 V with a step size of 10 mV, while square wave voltammetry (SWV) ranged between 0.2 V and 0.9 V with a step size of 10 mV.

Results

A concise evaluation of the electrochemical behavior of $Fe(CN)_6^{3-/4-}$ at carbon-based and gold-based SPE was depicted in Fig. 1, demonstrating the better performance of the gold-based electrode in terms of peak-to-peak separation and peak maximum. Further analyses of SPEs were done using CV and SWV in the BIT solution at different concentrations. The electrochemical detection of benzisothiazolinone biocide relies on irre-

versible oxidation, manifested by a peak at 0.7 V vs. Ag/AgCl in the voltammogram. We utilized cyclic voltammetry and square wave voltammetry to construct calibration curves, determining sensitivity and limit of detection (LOD) under specific conditions (Fig. 2). SWV notably enhanced sensitivity for carbon-based SPE electrodes compared to CV, while gold-based SPE exhibited similar sensitivities with both methods. For gold-based SPE, CV and SWV showed comparable LOD and LOQ for BIT detection, whereas SWV proved superior for BIT detection and monitoring with carbon-based SPE electrodes. While the redox behavior suggested superior performance for the gold-based electrode, both cyclic voltammetry and square wave voltammetry revealed that the carbon-based electrode exhibited better performance.

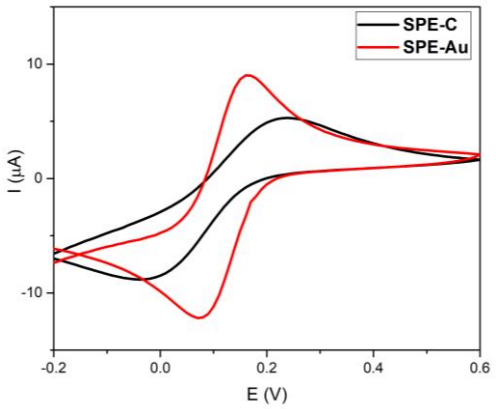

Fig. 1. Redox behavior of $Fe(CN)_6^{3-/4-}$ using carbon-based and gold-based SPE.

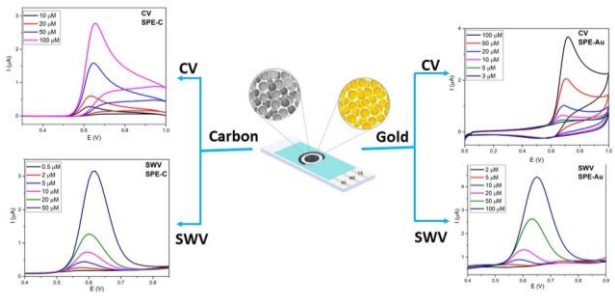

Fig. 2. Carbon and gold-based SPE for comparison of CV and SWV voltammograms [3].

(1)

References

[1] V. Silva, C. Silva, P. Soares, E. M. Garrido, F. Borges, J. Garrido, *Molecules.* 25, 191 (2020), doi: 10.3390/molecules25040991

[2] I. Paun, F. Pirvu, V. I. Iancu, F. L. Chiriac, *J. Environ. Res. Public Health*. 19, 7777 (2022), doi: 10.3390/ijerph19137777

[3] Created with BioRender.com

DOI 10.5162/EUROSENSORSXXXVI/PT5.127

Conductive MOFs for Chemoresistive Sensing of Greenhouse Gases Suitable for Internet of Things

Ignasi Fort-Grandas[1,2,3], *Yuzelfy Mendoza-Gamero*[1,2,3], *Guillem Domènech-Gil*[1,2], *Paolo Pellegrino*[1,2], *Mauricio Moreno-Sereno*[1,2], *Daniel Sainz* [2,3], *Anton Vidal-Ferran*[2,3,4], *Albert Romano-Rodríguez*[1,2]

1 Department of Electronic and Biomedical Engineering, University of Barcelona (UB), 08028 Barcelona, Spain
2 Institute of Nanoscience and Nanotechnology (IN2UB), University of Barcelona (UB), 08028 Barcelona, Spain
3 Department of Inorganic and Organic Chemistry, University of Barcelona (UB), 08028 Barcelona, Spain
4 Catalan Institute for Research and Advanced Studies (ICREA)

Corresponding Author's e-mail address: ignfrotga_9@ub.edu

Summary:

The importance of monitoring greenhouse gas (GHGs) levels with miniaturized and efficient devices has become an important challenge which remains unresolved. In this work, we make use of the recently growing field of metal-organic frameworks (MOFs) to develop conductive materials and test them as room-temperature chemiresistive sensors for CO_2, CH_4 and N_2O.

Keywords: Gas sensors, Greenhouse Gases, metal-organic frameworks, conductive MOFs, chemoresistive.

Background, Motivation an Objective

The direction of sustainability and overall health concerns in which society is moving towards has brought an increasing demand of reliable and affordable new materials-based sensing systems capable of monitoring key Greenhouse Gases (GHGs). However, significant challenges remain for the precise and efficient monitoring GHGs since current monitoring systems are complex, bulky and expensive, having them bound to few fixed locations.

Most solid-state gas sensing technologies come from devices that are made from semiconducting metal oxides (MOX), whose improved properties have been achieved through intensive research on advanced material micro/nanofabrication. Despite these large efforts, two major drawbacks remain: their relatively high operating temperature (above 150 ºC) and their poor selectivity, i.e., their inability to correctly discriminate and quantify the concentration of a specific gas within a mixture [1]. Improvement in the operation temperature has been achieved by replacing MOX by metal-organic frameworks (MOFs) as sensing material in chemoresistors [2].

MOFs are organic-inorganic hybrid crystalline materials consisting in a regular array of metal "nodes" surrounded by organic "linker" molecules that form a cage-like structure with extremely high surface area and porosity. The huge structural and chemical diversity provided by the available metals and linkers allows almost infinite possibilities of tuning the properties of MOFs. This porosity, together with the strong interaction between the material and the surrounding ambient, has made MOFs ideal material for gas capture and conversion [3], as well as very interesting candidates for sensing. Among the different properties that MOFs can present, a reduced subfamily, known as conductive MOFs, present an electrical conductivity which is comparable to that of solid-state semiconducting materials. In addition, some of them present the ability to change their conductance by the chemical atmosphere surrounding them [4].

In this work we will present the results of our study of triphenylene derivative MOFs for chemiresistive gas sensing of CO_2 and CH_4.

Description of the New Method or System

Triphenylene derivative MOFs with 2,3,6,7,10,11-hexahydroxytriphenylene (HHTP) and 2,3,6,7,10,11-hexaaminotriphenylene (HITP) were synthesized by a modified solvothermal approach in relation to that published in literature [5], obtaining $M_3(HOTP)_2$ and $M_3(HITP)_2$ respectively (where M=Co(II), Ni(II),

Cu(II), Zn(II)). We have optimized the synthesis parameters and we have studied, as well, the use of different coordinating solvent to modulate the growth and to yield high-quality crystalline MOF nanoparticles, as shown in Figure 1a.

For the sensor fabrication, a suspension of the corresponding MOF in water was drop-casted onto interdigitated electrodes (IDE) to obtain a thin layer of deposited MOF.

Results

The synthesized material typically present rod-like shape, as shown in Figure 1a, for the $Cu_3(HHTP)_2$ MOF. Similar structures have been observed for most of the synthesized MOFs, with a slight variation as a function of both the organic ligand and the metal and its salt. Most of these materials present chemoresistive response to the two most important GHGs, namely to CO_2 at concentrations between 100 to 700 ppm and to CH_4, from 0.5 to 15 ppm. For both cases these gas concentration values are comparable to the background ambient concentration. Figure 1b shows the response of one of these sensors to CH_4, between 0.5 and 2 ppm.

In the presentation we will discuss the gas sensing results as a function of the MOF constituents (ligand and metal) and of the gases to be detected.

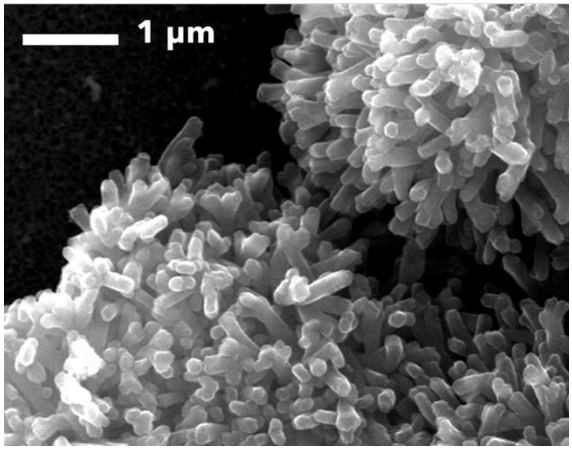

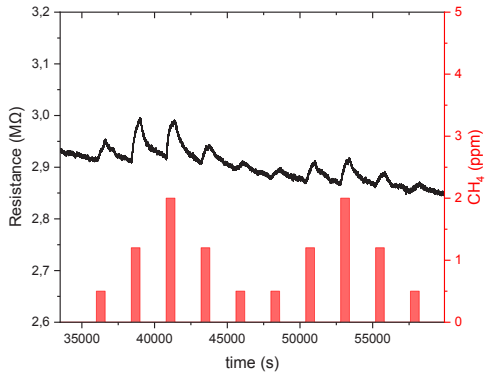

Fig. 1. (a) SEM image of $Cu_3(HHTP)_2$ nanoparticles. (b) Resistance variation of $Cu_3(HHTP)_2$ when exposed to CH_4 pulses of different concentrations.

References

[1] T. Lin, X. Lv, Z. Hu, A. Xu, C. Feng, Semiconductor Metal Oxides as Chemoresistive Sensors for Detecting Volatile Organic Compounds, *Sensors* 19, 233 (2019); doi: 10.3390/s19020233.

[2] Y. Li, A. Xiao, B. Zou, H. Zhang, K. Yan, Y. Lin, Advances of metal–organic frameworks for gas sensing, *Polyhedron* 154, 83-97 (2018); doi: 10.1016/j.poly.2018.07.028.

[3] M. Ding, R. Flaig, H. Jiang, O. Yaghi, Carbon capture and conversion using metal–organic frameworks and MOF-based materials, *Chem Soc Rev* 48, 2783-2828 (2019); doi: 10.1039/C8CS00829A.

[4] E. Miner, L. Wang, M. Dincă, Modular O_2 electroreduction activity in triphenylene-based metal-organic frameworks Chem. Sci. 9, 6286-6291, (2018); doi: 10.1039/c8sc02049c.

[5] M. Campbell, S. Liu, T. Swager, M. Dincă, Chemiresistive Sensor Arrays from Conductive 2D Metal–Organic Frameworks *J. Am. Chem. Soc*. 43, 13780-13783 (2015); doi: 10.1021/jacs.5b09600.

Characterization of YSZ layer deposited by reactive sputtering for oxygen microsensor development

A. Benayache, V. Martini, K. Aguir, Aix Marseille University, Marseille (France), C. Marlot, SETNAG, Marseille (France)

Unfortunately, this abstract is not available, as the contribution was not confirmed at the time the conference proceedings were finalized.

Characterization of YSZ layer deposited by reactive sputtering for oxygen microsensor development

A. Benayache, V. Martini, K. Aguir, Aix Marseille University, Marseille (France), C. Marlot, SETNAG, Marseille (France)

Unfortunately, this abstract is not available, as the contribution was not confirmed at the time the conference proceedings were finalized.

DOI 10.5162/EUROSENSORSXXXVI/PT5.131

Enhancement of the gasistor device by separation of the gas sensing and the memristive cells

Michal Patrnčiak [a], *Ľubomír Staňo, Ihor Shpetnyy, Marek Vidiš, Martin Moško, Tomáš Roch, Maroš Gregor, Tomáš Plecenik*
Centre for Nanotechnology and Advanced Materials, Faculty of Mathematics, Physics and Informatics, Comenius University Bratislava, Mlynská Dolina, 842 48 Bratislava, Slovakia

[a] patrnciak4@uniba.sk

Summary:
The gasistor is a device, which combines gas sensing and resistive switching in a single capacitor-like metal/metal oxide/metal cell. It works as a gas sensor with memristive memory or as a thyristor-like switch triggered by a change in the target gas concentration. The same metal oxide layer and the same cell used for gas-sensing is also used for resistive switching. The mutual entanglement of their fabrication parameters impedes the ability to separately adjust the two functionalities. In this work the two parts (sensor and memristor) are developed separately, allowing for their individual tuning, targeting specific gas concentration and improving the sensitivity of the gasistor device.

Keywords: Gasistor, hydrogen gas sensor, memristor, titanium dioxide, nanoporous electrode

The gasistor

The gasistor[1] is a device, which combines gas sensing and resistive switching in a single capacitor-like metal/metal oxide/metal cell. It has the ability to switch from high-resistance to low-resistance state when the concentration of a reducing gas in its vicinity reaches a pre-set value. The structure of the device is equivalent to chemiresistive gas sensor in a capacitor-like Pt/TiO_2/Pt arrangement[2]. The sensor reacts to the presence of hydrogen gas in an oxidizing atmosphere (air). The memristive (resistive switching) functionality is allowed by a conductive filament formed by soft dielectric breakdown in the TiO_2. The region of conductive filament is rich in oxygen vacancies and can be considered gas-insensitive. The device can thus be modelled as being composed of 2 separate devices – non-memristive gas sensor and gas-insensitive memristor - connected in parallel. The key feature of the memristor is its hysteretic I(V) curve, which indicates the existence of at least two resistance states. The transition between those states can be continuous or abrupt. The memristors used in the gasistor tend to switch abruptly. The switch is induced by high enough electric field in the memristor, i.e. the voltage applied to its terminals. In the case of switching just between two resistance states, those states are LRS (low resistance state) and HRS (high resistance state). The threshold voltages are V_{set} - voltage required to switch the device from HRS to LRS and V_{reset} required to switch from LRS to HRS. In the case of bipolar resistive switching, these two voltages are in opposite polarities (this is also the case of a gasistor). The model [1] assumes that in the HRS and LRS the conductive filament is shortened or prolonged, respectively.

The working principle of gasistor assumes comparable resistances of the hydrogen gas sensor at studied conditions[1] (hydrogen gas concentration, temperature and humidity) and the memristor in the HRS. The process of the gas-induced resistive switching requires the gasistor to be biased by a suitable constant current, the hydrogen gas concentration to be above desired switching concentration and the memristor part to be in the HRS. After that, when the hydrogen concentration drops, the resistance of the gas sensing part increases, along with voltage applied to the gasistor. When the voltage reaches V_{set}, the memristive part switches from HRS to LRS. The LRS is stable until it is re-set on purpose in the opposite polarity, thus effectively providing the gasistor with a long-term memory function.

The separation of the gas sensing and the memristive cells

However, the above-mentioned condition of resistances of the gas-sensing and memristive part being similar is difficult to achieve, especially for lower hydrogen concentrations. The base resistance of gas sensor

(subjected to air at room temperature) is typically higher than 10^{12} Ω, while the memristor after electroforming in the HRS reaches resistances of up to 10^{7} Ω[1]. The adjustment of such devices simultaneously is a challenging task. Therefore, this work focuses on the isolation of the two parts (Fig.1) and their separate characterization. We show that we can improve the gas sensor by implementing large-scale (> 100x100 μm^2) nanoporous top electrode, as the sensing process occurs at the edges of the top electrode, since the Pt layer is almost impermeable to hydrogen and water vapor. Implementation of the large-scale nanoporous top electrode effectively decreases the base resistance, while maintaining the sensitivity. Increasing the area of the memristor would be undesirable, as the increased capacity leads to several problems and the electroforming on such structures often leads to lower resistances. The opposite can be done to increase the resistance of the HRS. Separating the cells also allows us to isolate the memristive part from the surrounding atmosphere by a passivation SiO_2 layer (Fig.2), which will allow easier analysis of the device functionality. Fine-tuning of both devices separately will lead to a gasistor device targeting specific gas concentrations, with higher sensitivity.

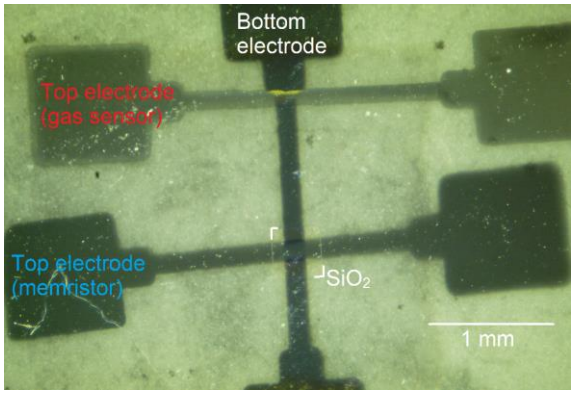

Fig.1: Hydrogen gas sensor and memristor with an equal area (~150 × 150 μm)

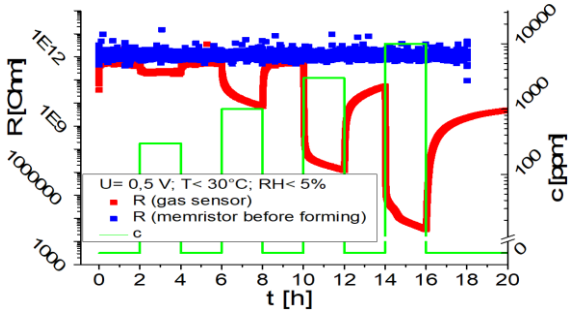

Fig.2: Resistance response to hydrogen concentration (green) of: separate memristor passivated by SiO_2 layer (blue) and gas sensor with nanoporous top electrode (red) in an arrangement as shown in Fig.1.

Acknowledgements

This work was supported by the Slovak Research and Development Agency under the contract No. APVV-21-0053 and by the Scientific Grant Agency of the Slovak Ministry of Education, Sciences, Research and Sport (Grant No. VEGA 1/0062/22). It is also the result of support under the Operational Program Integrated Infrastructure for the projects: Advancing University Capacity and Competence in Research, Development and Innovation (ACCORD, ITMS2014+:313021X329) and UpScale of Comenius University Capacities and Competence in Research, Development and Innovation (USCCCORD, ITMS 2014+: 313021BUZ3), co-financed by the European Regional Development Fund.

References

[1] M. Vidiš, T. Plecenik, M. Moško, et al., Gasistor: A memristor based gas-triggered switch and gas sensor with memory, Appl. Phys. Lett. 115 (2019) 093504.

[2] Z. Li, A. A. Haidry, T. Plecenik et al., Influence of nanoscale TiO2 film thickness on gas sensing properties of capacitor-like Pt/TiO2/Pt sensing structure, Applied Surface Science, vol. 499 (2020) 143909.

SAW sensor structures with rr-P3HT polymer films for humidity low level detection

W. Jakubik, J. Wrotniak, P. Powroźnik, Silesian University of Technology, Gliwice (Poland)

Unfortunately, this abstract is not available, as the contribution was not confirmed at the time the conference proceedings were finalized.

SAW sensor structures with rr-P3HT polymer films for humidity low level detection

W. Jakubik, J. Wrotniak, P. Powroźnik, Silesian University of Technology, Gliwice (Poland)

Unfortunately, this abstract is not available, as the contribution was not confirmed at the time the conference proceedings were finalized.

DOI 10.5162/EUROSENSORSXXXVI/PT5.142

ZIF-8-based surface plasmon resonance sensors for chemical vapor optical detection with LEDs

Anna Estany-Macià[1,2], Guillem Domènech-Gil[1,2], Ignasi Fort-Grandas[1,2], Winnie E. Svendsen[3], Maria Dimaki[3] , Albert Romano-Rodríguez[1,2], Mauricio Moreno-Sereno[1,2]

[1] Department of Electronics and Biomedical Engineering, University of Barcelona (UB), 08028 Barcelona, Spain

[2] Institute of Nanoscience and Nanotechnology (IN2UB), University of Barcelona (UB), 08028 Barcelona, Spain

[3] Group NABIS, Nanotech Department, Technical University of Denmark (DTU), 2800 Kongens Lyngby, Denmark

Corresponding Author's e-mail address: anna_estany@ub.edu, mauricio.moreno@ub.edu

Summary:

The use of sorption coatings to functionalize samples is a frequent strategy to enhance the sensitivity and selectivity of some gas sensors. In this regard, metal-organic frameworks have recently attracted attention because their nanometre-sized pores allow the molecular adsorption of gases into their structure, which modulates the refractive index of this material depending on the amount of adsorbed gas molecules. This research explores their use in surface plasmon resonance sensors for volatile organic compound optical detection and the further miniaturization of the sensing device to achieve smaller and portable gas sensors.

Keywords: Gas sensor, surface plasmon resonance, optical detection, metal-organic frameworks, volatile organic compounds

Headlines

Surface plasmons generated between a metal film and its surroundings are extremely sensitive to the composition of the neighboring and can be used in gas sensing applications.

Metal organic frameworks can increase the sensitivity of gas sensors by several orders of magnitude.

Background, Motivation an Objective

Volatile organic compounds (VOCs) have been linked to several health issues and other environmental problems such as global warming by infrared absorption or formation of ground-level ozone [1]. Therefore, the analysis of VOCs is key to monitor air quality and prevent severe health problems that occur due to their long-term inhalation and exposure.

Gas chromatography coupled with mass spectroscopy (GC-MS) is currently the established method for VOCs analysis. However, GC-MS is expensive, bulky, and must be done off-site. Even though there are more practical methods, also sensitive to VOCs, they present cross-sensitivity to many gases, making it difficult to distinguish between gas species and affecting its response.

In this sense, a pathway to increase the response of gas sensors relies on the functionalization of their surface with porous solids in order to increment the concentration of gas molecules at the surface and even tailor selectivity by chemical affinity or pore size [2]. On this matter, metal-organic frameworks (MOFs) are porous materials with a refractive index (RI) that is modified depending on the amount of adsorbed gas molecules in its structure. Therefore, tracking the variation of the MOF when exposed to different gaseous atmospheres via RI sensing mechanisms such as Fabry-Pérot interferometry or surface plasmon resonance (SPR) [3] can lead to a new generation of gas sensors.

Our goal is to monitor different VOC concentrations with MOF-coated SPR sensors by tracking the red-shift of the surface plasmon resonance wavelength under the different atmospheres. In parallel, we are also working on the miniaturization of our monitoring system to obtain portable, cost-efficient and smaller gas sensors.

Methodology

The ZIF-8 film (Fig. 1a), which is the MOF that has been used, is grown via the layer-by-layer deposition method reported by Hupp *et. al.* [4]

on top of SPR substrates containing gratings with periods of Λ=400 nm and Λ=500 nm. Gas sensing measurements are then conducted via spectral interrogation on the fabricated samples at room temperature, which are placed in a holder inside a home-built aluminum chamber with a quartz window and connected to two mass flow controllers (MFC) that command the gas flux entering the gas chamber.

In addition to the previously presented results in Eurosensors 2023 [5] and considering the miniaturization of the current optical set-up, measurements are now being conducted by illuminating the sample with LEDs instead of white light. With this aim, the LED needs to be adjusted to the period of the diffraction gratings and the thickness of the deposited ZIF-8 film, both responsible for the resulting SPR wavelength, to obtain the maximum sensitivity of our sensors (Fig. 1b).

To further miniaturize our device, we have also substituted the spectrometer for a photodiode (PD) and gas measurements are currently being tested.

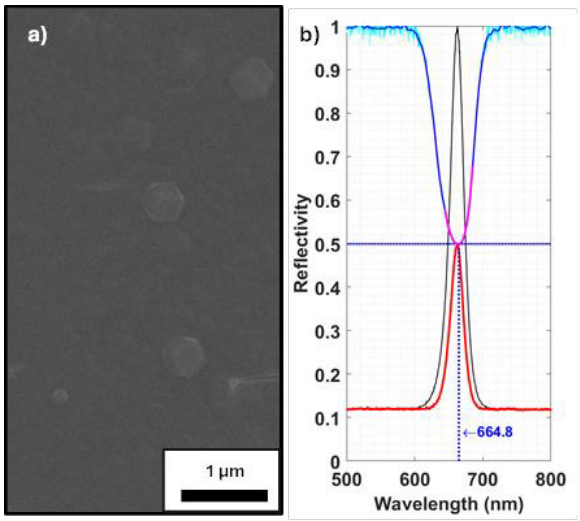

Fig. 1. (a) SEM image of a ZIF-8 layer (b) spectrum of a 660nm-LED (black curve) adjusted to the Λ=400 nm SPR dip (blue curve). The red curve represents the simulated response that would be acquired with a PD.

Results

We will present the gas sensing results of the fabricated samples when exposed to different concentrations of VOCs using LEDs as illumination source, as well as the simulated response with a PD. As an example, Fig. 2a shows the simulated reflectivity that would be acquired with a PD, while Fig. 2b shows a preliminary result of the response of the sensor to synthetic air (SA) and saturated ethanol (EtOH) pulses.

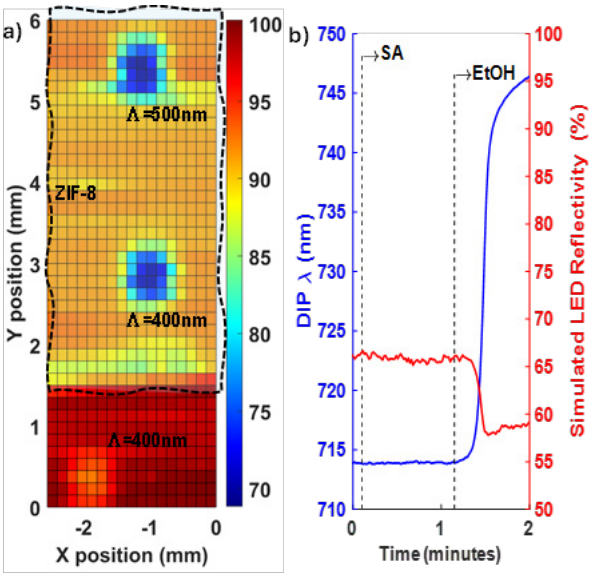

Fig. 2. (a) Simulated reflectivity acquired by a PD using a 660nm-LED to scan the chip (b) red-shift of the Λ=400 nm SPR dip under SA and saturated EtOH atmospheres (blue curve) when illuminating with a 680nm-LED and simulated PD response (red curve).

References

[1] Montero-Montoya, R., López-Vargas, R., & Arellano-Aguilar, O. (2018). Volatile organic compounds in air: sources, distribution, exposure and associated illnesses in children. Annals of Global Health, 84(2), 225–238. DOI: https://doi.org/10.29024/aogh.910

[2] Qin, P., Day, B. A., Okur, S., Li, C., Chandresh, A., Wilmer, C. E., & Heinke, L. (2022). VOC Mixture Sensing with a MOF Film Sensor Array: Detection and Discrimination of Xylene Isomers and Their Ternary Blends. ACS Sensors, 7(6), 1666–1675. DOI: https://doi.org/10.1021/acssensors.2c00301

[3] Shen, Y., Tissot, A., & Serre, C. (2022). Recent progress on MOF-based optical sensors for VOC sensing. Chemical Science, 13(47), 13978–14007. DOI: https://doi.org/10.1039/d2sc04314a

[4] Lü, G., & Hupp, J. T. (2010). Metal−Organic frameworks as sensors: A ZIF-8 based Fabry−Pérot device as a selective sensor for chemical vapors and gases. Journal of the American Chemical Society, 132(23), 7832–7833. DOI: https://doi.org/10.1021/ja101415b

[5] Estany-Macià, A., Fort-Grandas, I., Joshi, N., Svendsen, W. E., Dimaki, M., Romano-Rodríguez, A., & Moreno-Sereno, M. (2024). ZIF-8 Films and Surface Plasmon Resonance for Chemical Vapor Detection. Proceedings. DOI: https://doi.org/10.3390/proceedings2024097126

DOI 10.5162/EUROSENSORSXXXVI/PT5.144

Reactive Oxygen Species-Responsive Thin Films that Display Distinct Color and Pattern Changes

Yasumasa Kanekiyo
Kitami Institute of Technology, 165 Koen-cho, Kitami, Hokkaido 090-8507, Japan

kanekiyo@mail.kitami-it.ac.jp

Summary:
Novel methodologies for the preparation of reactive oxygen species (ROS)-responsive thin-film sensors that display distinct color and pattern changes were developed. The ROS-responsive thin films presented herein are advantageous for the development of ROS sensors because of their relatively simple preparation and non-complex organic synthesis. In addition, there is virtually no limitation to choosing dyes, and any kind of visual color and pattern changes can be realized.

Keywords: reactive oxygen species, hydrogen peroxide, hypochlorous acid, boronic acid, thin film

Introduction

Boronic acids are known to form boronate esters with polyhydroxy compounds such as saccharides through reversible boronate-diol interactions. Moreover, boronic acids give rise to their phenol derivatives after reaction with reactive oxygen species (ROS) such as hydrogen peroxide (H_2O_2) and hypochlorous acid. The latter reaction has been utilized to develop colorimetric and fluorescent ROS sensing probes through a strategy in which a boronic acid moiety is directly connected to a chromophoric or fluorophoric group. Boronic acid-based ROS probes are advantageous over conventional enzyme-based sensors in terms of durability and reproducibility because of absence of unstable bioorganic substances such as enzymes. However, one of the drawbacks of the boronic acid-based probes is the necessity of complicated organic synthesis. Moreover, limited color change could be an obstacle for developing user-friendly sensors. Thus, to realize a widely used ROS sensor at a low cost, it is necessary to introduce a novel methodology.

Our research group has developed thin-film-based colorimetric sensing systems that exhibit unprecedentedly large color changes [1,2]. The preparation of these sensors is relatively simple and does not require complex organic syntheses. Moreover, this methodology is the most advantageous as compared to other methodologies as no limitation in selecting dyes for the coloring of the thin films exists. We hypothesized that this mechanism would be applicable for ROS sensing by utilizing the interaction of boronic acids with ROS. Accordingly, thin films containing ROS-responsive boronic acid units in addition to positively charged tertiary amine units with different compositions were prepared. The thin films were immersed in aqueous dye solutions before or after reaction with ROS in an aqueous solution. As a result, the color and/or pattern of the thin films changed distinctly in response to ROS concentration [3].

Experimental

The ROS-responsive thin films were prepared on a glass slide by the radical copolymerization of boronic acid monomer **1**, tertiary amine monomer **2**, acrylamide **3**, and crosslinker **4** in the presence of an initiator **5** (Fig. 1). The monomer solutions were poured onto the glass surface of the slides using a micropipette and covered with an acrylic plate. Polymerization was conducted by irradiating the sandwiched monomer solution with UV light (365 nm) using a UV lamp under nitrogen atmosphere at 20–25 °C for 3 h. After removing the acrylic plate from the glass slide, the resulting thin films were washed with water and air-dried. Then, the sensor was immersed in aqueous solutions containing ROS at 25 °C for 1–60 min. Subsequently, the sensor was immersed in an aqueous dye solution at 25 °C for 1–60 min. Polyols such as fructose or sorbitol were sometimes added to the ROS or dye solutions to enhance the change in charge state of the boronic acid moiety. In the case where colored samples were used for ROS response, the experimental order was reversed: the thin film was immersed in a dye solution, then reacted with ROS.

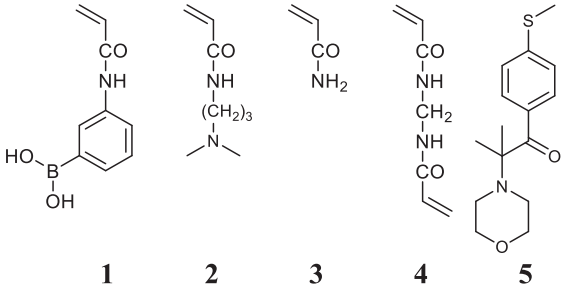

Fig. 1. Chemical structures of monomers.

Results and Discussion

The dependency of H_2O_2 concentration on the color of thin films at different reaction times at pH 7.4 was measured (Fig. 2). The sensor displayed a visible color change from colorless to blue at 4 μM. The color deepened with increasing reaction time and H_2O_2 concentration. This behavior can be attributed to the change in the charge state of the thin film. Before reacting with H_2O_2, the cationic charges on the thin film should be electrostatically neutralized by boronate groups, resulting in lack of adsorption ability for anionic dyes. After reacting with H_2O_2, the thin film was colored with an anionic dye because the boronate groups were converted into neutral phenol groups and thus the thin film became positively-charged. A plausible response mechanism is illustrated in Fig. 3.

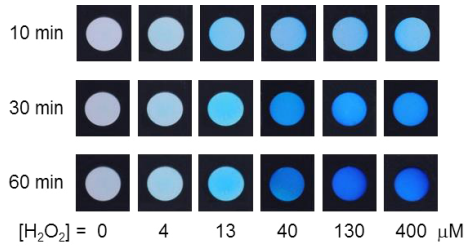

Fig. 2. H_2O_2 concentration-dependent color changes in the thin film colored by Fast Green FCF in the presence of fructose at pH 7.4.

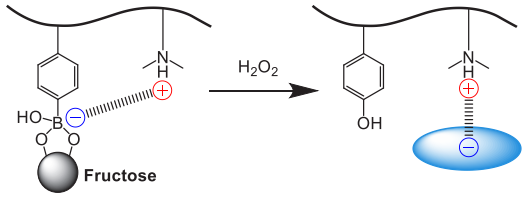

Fig. 3. Mechanism of hydrogen peroxide-responsive color change in the thin film in the presence of fructose at pH 7.4.H_2O_2 concentration-dependent color changes in the thin film.

Instead of an anionic dye, a monovalent cationic red dye (Safranin T) was used to color the thin film after reacting with H_2O_2 (Fig. 4). The thin film was colored red when the H_2O_2 concentration was lower than 13 μM. A further increase in H_2O_2 concentration resulted in a decrease in the adsorption of the dye, which became almost colorless when the H_2O_2 concentration was above 130 μM. In addition, experiments were conducted by simultaneously using anionic and cationic dyes for coloring (Fig. 5). When the H_2O_2 concentration was lower than 40 μM, the thin film became red due to the adsorption of the cationic red dye. By increasing the H_2O_2 concentration from 40 μM to 100 μM, the color of the thin film gradually changed from red to blue. The thin film finally became blue when the H_2O_2 concentration was higher than 100 μM.

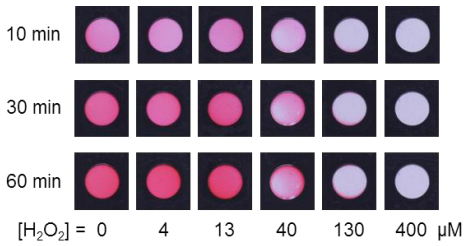

Fig. 4. H_2O_2 concentration-dependent color changes in the thin film colored by Safranin T in the presence of fructose at pH 7.4.

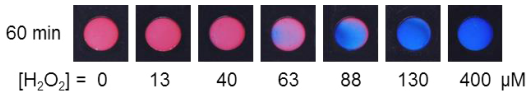

Fig. 5. H_2O_2 concentration-dependent color changes in the thin film colored by Fast Green FCF and Safranin T in the presence of fructose at pH 7.4.

Because the response mechanism of the present method is based on changes in the charge state of the thin films, principally, any kind of anionic or cationic dyes can be used. To confirm this experimentally, various dyes were used to color the thin films. Accordingly, I successfully established a novel methodology for creating H_2O_2 sensors that exhibit diverse color changes. In the conference, I will also talk about sensors with changing patterns and hypochlorous acid sensors.

References

[1] Y. Iwami, T. Yokozawa, W. Takayoshi, Y. Kanekiyo, Multicolor Saccharide-Sensing Chips based on Boronic Acid-Containing Thin Films Showing Stepwise Release and Binding of Dyes, *Talanta* 85, 829–33 (2011); doi: 10.1016/j.talanta.2011.04.068

[2] T. Denda, R. Mizutani, M. Iijima, H. Nakahashi, H. Yamamoto, Y. Kanekiyo, Thin Films Exhibiting Multicolor Changes Induced by Formaldehyde-Responsive Release of Anionic Dyes, Talanta 144, 816–22 (2015); doi.org/10.1016/j.talanta.2015.06.012

[3] H. Nakahashi, K. Takeshima, S. Matsubara, Y. Kanekiyo, Distinct Color Changes in Hydrogen Peroxide-Responsive Thin Films Consisting of Boronic Acid-Containing Polymers, Dyes and Pigments 218, 111450 (2023); doi.org/10.1016/j.dyepig.2023.111450

DOI 10.5162/EUROSENSORSXXXVI/PT5.149

AI-enabled rapid method for complex quality assessment of edible oils

Asia Kalinichenko, Nicolae Bârsan, Benjamin Junker, André Sackmann, Udo Weimar
Institute of Physical and Theoretical Chemistry, Eberhard Karls University of Tuebingen, 72076 Tuebingen, Germany

Corresponding Author's e-mail address: asya.kalinichenko@ipc.uni-tuebingen.de

Summary: The research aimed to replace a set of standard methods for edible oil quality control by developing an AI-enabled rapid headspace analysis procedure. The use of a ceramic sensor array confirmed the feasibility of assessment of oil oxidation under static conditions, however, it was unable accurately predicting individual quality parameters. Due to the impracticality of applying selective enhancement approaches to ceramic sensors, an array of commercially available microsensors were used in combination with different temperature modulation modes.

Keywords: SMOX-based sensors, temperature modulations; quality assessment; edible oils; AI.

Introduction. The applications of chemical sensors for monitoring the quality/safety of food products, including edible oils, have not found sufficient implementation to date in the industry. If the control of technological processes is mainly monitored by physical sensors, monitoring a complex food matrix has been limited due to constraints in sensor characteristics and the lack of progress in data science. However, advancements in today's chemical sensor development, such as the miniaturized Sensirion Gas Platform (SGP) multi-pixel gas sensor [1], as well as deep machine learning algorithms incorporating elements of artificial intelligence (AI), offer the potential to enhance the sensitivity and selectivity of novel alternative methods and to provide necessary multidimensional information about the sample's state and the physicochemical reactions occurring within it.

Needs of industry. Quality control of vegetable oils ready for distribution is mandatory requirements regulated by both international and local authorities [2, 3] through a set of physico-chemical methods [4, 5]. Such methods are characterized by significant disadvantages, such as the necessity to use a large amount of suitable solvent mixtures for sample dissolution before titration (peroxide and acid values (PV and AV, respectively)), long measurement times, poor repeatability (moisture and volatile matter content, MVC), lengthy and multi-stage sample preparation for the analysis of the anisidine value (p-AV), and the need to measure a set of parameters together to account for possible various types of spoilage determined by the different compositions of oils. The current speeds and production volumes ask for a critical examination of traditional analytical chemistry approaches for food analysis to ensure effective monitoring of their quality and safety.

Experiment and results. Samples of various cold-pressed and refined vegetable oils were taken from production for quality analysis during the oxidation process: sunflower, rapeseed, and olive oils of different geographical origins. The oils were exposed to autoxidation to facilitate the transfer of the obtained models to real-life conditions, because the mixtures of formed oxidized compounds and their concentrations vary in the nature and composition of oils, as well as in the conditions and extent of oxidation.

The reference parameters, required to enable a comprehensive monitoring of oil quality, were used, regardless of the possible product spoilage mechanism. We monitored: MVC and AV as indicators of lipolysis; PV and p-AV values, which together can provide information about primary and secondary products of oxidation.

At the initial stage, sensors TGS 2600, TGS 2620, and FIS SB-AQ1-06 were investigated (Figaro, USA; Nissha FIS, Japan). Extracted parameters at the beginning and end of the transient response to oil vapors under constant sensor heating were used as input data for principal component analysis (PCA).

PCA was used for exploratory analysis and discovering informativeness and hidden dependencies in the data. Its essence lies in assuming linearity of data relationships and their projection onto a subspace of orthogonal vectors where the variance is maximized. These vectors, called principal components (PC), determine the directions of greatest variability (informativeness) of the data. In other words, it's a linear projection

that minimizes the mean squared distance between the original points and their projections. The data matrix was autoscaled. PCA was performed based on the singular value decomposition algorithm and cross validated. PC1 corresponds to the direction of maximum variation in the data. In the Fig.1, we observe the clear trend of changes in the quality of oil samples along PC1 (86% of explained variance), as well as the separation of two types of oils along PC2 (13%).

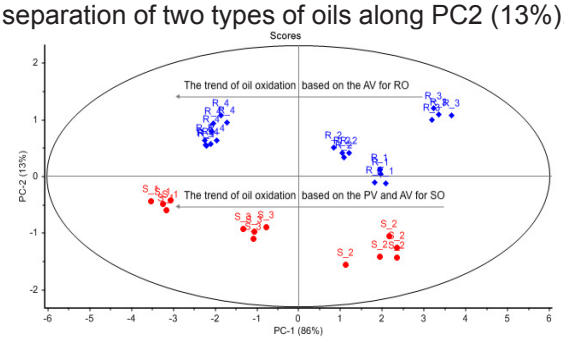

Fig. 1. PCA scores plot based on the responses of three sensors to various qualities of sunflower (SO) and rapeseed (RO) refined oils from six different manufactures.

For the differentiation among individual quality parameters and for a more precise prediction of the PV, AV, p-AV, MVC, it is necessary to increase the dimensionality and orthogonality of the sensor arrays. The sensors used in the first set of experiments also show strong multicollinearity (correlation of more than 0,96 between the TGS 2600 and TGS 2620) in prediction the PV and AV parameters.

A possible approach to selectivity enhancement is the operation of the sensors in different heating profiles; besides that, such practice is not recommended by manufacturers, their relatively large mass makes fast modulation impossible, besides this they have a considerable power consumption and even influence on the composition of the gaseous samples they are exposed to. The alternative increase of the sensor array by increasing the sensor number is not considered feasible for this application. The SGP 40 sensor (Sensirion AG, Switzerland), in this context, presents itself as an optimal solution for a miniaturized device with the capability to enhance selectivity through individual temperature modulation of each of its four pixels (Fig. 2). Figure 2 shows one modulation of 19 temperature steps (1 ramp), which resulted in 76 responses (19 steps x 4 pixels) from the device for a 3-minute measurement.

The used sensor array consisted of three SGP40 sensors (3 x 4 pixels) with different temperature modulation modes for each, mounted in a sensor chamber that allows for direct measurement of the oil headspace.

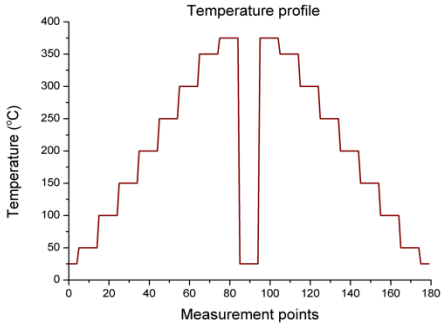

Fig. 2. One of the three temperature modulation modes, applied for the SGP40 sensors.

As the sensors measure the total VOC content simultaneously present in the oil headspace, our approach ensures the high sensitivity and broadband-sensing capabilities towards various classes of VOCs and individual target gases. The same procedure was performed for ambient air to take into consideration the baseline change, humidity compensation and the sensor signal normalisation.

In parallel the composition of oil VOCs during oxidation was investigated using GC-MS. Groups of markers that most correlate with quality parameters (PV, AV, MVC, p-AV) were selected. Based on this data, specific gas mixtures were prepeared for investigating the sensor characteristics of the array using gas mixing system, as well as proposing conversion factors from signals to the correlating physicochemical parameters.

Recurrent neural network (LSTM) with long-term memory was used to analyze time-series data sets of the oil oxidation process and operating states of sensors. For classification different gas markers to 4 groups related to different quality parameters was used convolutional network.

The research is at control-defining stage, as well as the drawing of final conclusions.

References

[1] Rüffer, D., Hoehne, F., & Bühler, J. New Digital Metal-Oxide (MOx) Sensor Platform. Sensors, 18(4), 1052 (2018). doi: 10.3390/s18041052

[2] Leitsätze für Speisefette und Speiseöle vom 02.07.2020 (BAnz AT 18.08.2020 B3, GMBl 2020 S. 530). Available online: https://rb.gy/ae1s4f.

[3] EU (2022). Commission Delegated Regulation (EU) 2022/2104 supplementing Regulation (EU) No 1308/2013 as regards marketing standards for olive oil, and repealing Commission Regulation (EEC) No 2568/91. Available online: https://rb.gy/6d7efz.

[4] ISO 3960:2017. *Animal and vegetable fats and oils – Determination of peroxide value. Iodometric (visual) endpoint determination*. 5th ed., 10 pages.

[5] ISO 660:2020. *Animal and vegetable fats and oils – Determination of acid value and acidity*. 4th ed., 12 pages.

DOI 10.5162/EUROSENSORSXXXVI/PT5.152

Cation-Anion Influence in Lead Halide Perovskites Supported on Graphene for NH_3 Detection

Juan Casanova-Chafer[1,2], Rocio Garcia-Aboal[3], Pedro Atienzar[3], Eduard Llobet[2]

[1] Université de Mons, 7000 Mons, Belgium
[2] Universitat Rovira i Virgili, 43007 Tarragona, Spain
[2] Instituto de Tecnología Química (ITQ-UPV), 46022 Valencia, Spain

juan.casanovachafer@umons.ac.be

Summary:
Chemiresistive sensors offer a promising option for establishing extensive sensing networks, providing a cost-effective and energy-efficient solution. This study introduces novel hybrids consisting of lead halide perovskite nanocrystals decorating graphene, operable under ambient temperature conditions. Evaluating the impact of two cations (methylammonium and cesium) and two anions (chlorine and bromine), $MAPbBr_3$ emerges as the most promising composition for NH_3 detection at room temperature.

Keywords: gas sensor, NH_3 detection, chemical resistive sensor, graphene, lead halide perovskites

Background, Motivation an Objective

In recent decades, the escalating threat of air pollution has underscored the urgent need for continuous monitoring to safeguard both the environment and public health. However, establishing a large air quality sensor network requires reliable, cost-effective, and energy-efficient sensing devices. Chemiresistive sensors, owing to their simple fabrication and operation, emerge as a promising option. Graphene has garnered considerable attention, albeit with limited gas sensitivity and selectivity owing to its inherent chemical inertness [1].

In response to this challenge, significant research efforts have shifted towards leveraging perovskites for gas sensing applications. Perovskites offer advantages such as room-temperature operation and tunable bandgap. Despite their promise, perovskites suffer from instability in humid conditions, limiting their commercial viability. Recent studies have demonstrated that dispersing perovskite nanocrystals on graphene effectively shields them from ambient moisture, thus mitigating long-term degradation [2].

This advancement suggests that decorating graphene with perovskite nanocrystals (NCs) holds immense potential for developing gas sensors that are both sensitive and selective, while also being cost-effective and energy-efficient.

Method

The influence of both anions and cations in lead halide perovskites for NH_3 detection has been investigated for the first time. The perovskite composition significantly affects sensing performance. Lead halide perovskites are typically structured as ABX_3, with B representing Pb^{+2} and A representing a cation. In this study, an organic methylammonium (MA+) and an inorganic cesium (Cs+) were utilized as cations. The X_3 denotes the anion, with Cl^- and Br^- being employed. Various synthesis methods, as outlined in our previous publication [3], were employed to obtain different compositions ($MAPbBr_3$, $MAPbCl_3$, and $CsPbBr_3$).

Briefly, for $MAPbX_3$ (where X = Br^-, Cl^-), the synthesis included preparing solutions of oleic acid (OA), 1-octadene (ODE), and octylammonium bromide (OABr). Specific solutions for each perovskite anion were then prepared using different precursors for Br^- (MABr and $PbBr_2$) and Cl^- (MACl and $PbCl_2$) anions. These solutions were combined, cooled, and acetone was added to induce nanocrystal precipitation.

After centrifugation, the precipitates were dispersed in toluene. For $CsPbBr_3$, Cs-oleate was prepared by mixing Cs_2CO_3, ODE, and OA in a heated flask. Another solution, consisting of $PbBr_2$ and ODE, was prepared, dried, and injected with oleylamine (OLA) and Cs-oleate. After solubilization, the solution was cooled, and tert-butyl alcohol (tBuOH) was added for precipitation. The resulting $CsPbBr_3$ nanocrystals were redispersed in hexane after centrifugation.

Subsequently, a graphene solution underwent pulsed sonication (1s on/2s off) at 280 W for 90 minutes to ensure proper exfoliation. The perovskite NCs were then added (5% wt.) to the solution, and the mixture was vigorously stirred for 1 hour. The resulting hybrids were deposited onto alumina substrates containing screen-printed platinum interdigitated electrodes. The developed sensors were enclosed in an airtight Teflon chamber connected to calibrated gas cylinders.

Results

Various dilutions of NH_3 with dry air were prepared to achieve different concentrations (25, 50, 75, and 100 ppm). Before exposure to the target gas concentration for 5 minutes, the sensors were stabilized under synthetic dry air for 15 minutes. The sensors were tested at room temperature to minimize power consumption, extend the active nanomaterials' lifetime, and prevent perovskite degradation.

Fig. 1 depicts electrical responses recorded upon NH_3 exposure during cycles, illustrating a high level of reversibility in the interaction, almost fully recovering the initial baseline resistance. Additionally, despite operating in dynamic mode, the sensors exhibited high repeatability.

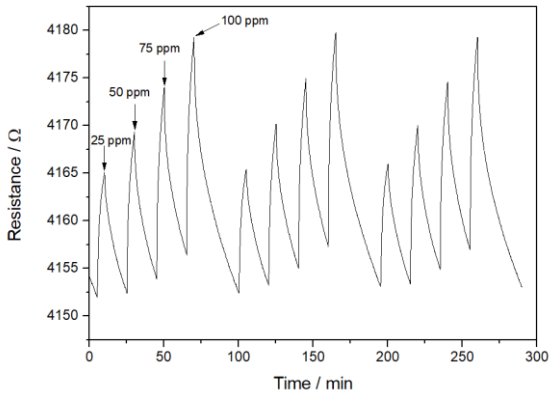

Fig. 1. Example of the electrical responses using $MAPbBr_3$ NCs decorating graphene to detect four concentrations (25, 50, 75 and 100 ppm) of NH_3 during 3 consecutive cycles.

Fig. 2 compares the sensing performance of the different hybrids in detecting NH_3. Several conclusions can be drawn. Firstly, bare graphene exhibited lower responses to NH_3 compared to decorated graphene, indicating that the presence of perovskite nanocrystals (NCs) on graphene enhances sensitivity to the target gas, regardless of perovskite composition.

Secondly, among the various perovskites employed, $MAPbBr_3$ demonstrated notably better sensing responses than $MAPbCl_3$ and $CsPbBr_3$. Specifically, for 100 ppm of NH_3, $MAPbBr_3$ NCs exhibited approximately three times higher responses than the other perovskite compositions. This suggests that $MAPbBr_3$ likely possesses an optimal energy-level alignment with graphene for hole extraction, as the hybrids function as p-type semiconductors for electron donor gases like NH_3.

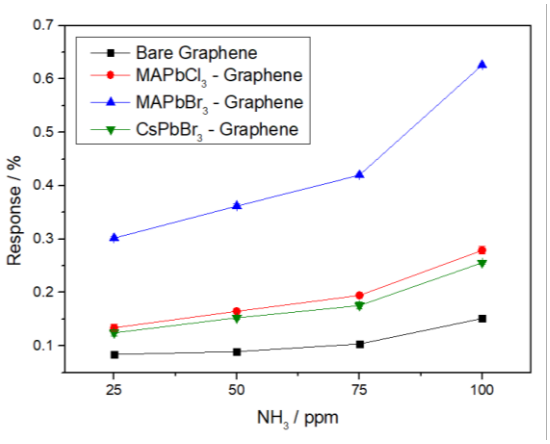

Fig. 2. Calibration curves comparing 4 sensor compositions for detecting NH_3.

Moreover, $MAPbBr_3$ tends to feature a higher density of trap states compared to $MAPbCl_3$ and $CsPbBr_3$, which could potentially interact with gas compounds. Furthermore, experimental findings reveal that $MAPbBr_3$ exhibits a lower photoluminescence quantum yield, indicating a higher concentration of defects that may also facilitate interaction with NH_3.

References

[1] P. Recum, T. Hirsch, Graphene-based chemiresistive gas sensors, *Nanoscale Adv.* 6, 11-31 (2024); DOI: 10.1039/D3NA00423F.

[2] J. Casanova-Chafer, R. Garcia-Aboal, P. Atienzar and E. Llobet, Unraveling the Gas-Sensing Mechanisms of Lead-Free Perovskites Supported on Graphene, *ACS Sensors* 7, 12, 3753–3763 (2022); DOI: 10.1021/acssensors.2c01581.

[3] J. Casanova-Chafer, R. Garcia-Aboal, P. Atienzar and E. Llobet, The role of anions and cations in the gas sensing mechanisms of graphene decorated with lead halide perovskite nanocrystals, *Chem Comm* 56, 8956-8959 (2020); DOI: 10.1039/D0CC02984J.

DOI 10.5162/EUROSENSORSXXXVI/PT5.155

Development and Application of an Electrochemical Sensor for Hydrogen Peroxide in Alkaline Media Based on Flash Graphene

Ema Gričar[1], Boštjan Genorio[1], Mitja Kolar[1]
[1] University of Ljubljana, Faculty of Chemistry and Chemical Technology, Večna pot 113, 1000 Ljubljana, Slovenia
ema.gricar@fkkt.uni-lj.si

Summary:
With the development of a novel microfluidic system for environmentally friendly electrochemical production of hydrogen peroxide, a need for a specifically designed electrochemical sensor for hydrogen peroxide in alkaline media (pH 13) arises. Flash graphene was used to modify the carbon screen-printed electrode together with manganese dioxide. The proposed sensor exhibited two linear ranges (1 to 100 $\mu molL^{-1}$, and 100 to 1000 $\mu molL^{-1}$), the sensitivity of 0.244 $\mu A \mu M^{-1} cm^{-2}$ and the limit of detection was 0.238 $\mu molL^{-1}$.

Keywords: flash graphene, electrochemical sensor, screen-printed electrode, carbon electrode, hydrogen peroxide.

Introduction

Electrochemical sensors stand at the frontier of the ever-expanding electrochemical research with their favorable properties. These include high selectivity and sensitivity, low cost, robustness, portability, generally wide linear range, and what is most important for the presented research – rapid response time, possible miniaturization and integration, and minimal (or none) sample preparation steps.

Hydrogen peroxide (H_2O_2) is a small inorganic molecule that is important in various fields. It is a transparent, slightly viscous liquid with a pungent odor. In biological systems, it is a byproduct of numerous enzymatic processes, as well as a signaling agent (in strictly regulated, low concentrations) [1]. Additional to its biological role, H_2O_2 is present in numerous energy conversion devices, such as fuel cells and Li-air batteries, both of which utilize the oxygen reduction reaction. Its use as an antimicrobial, bleaching, and oxidizing agent is successful partly due to the fact it yields only water and oxygen as byproducts and is as such considered environmentally friendly [2]. The anthraquinone oxidation process remains the predominant method for industrial-scale H_2O_2 production. However, the necessity for complex safety measures, additional purification due to the use of stabilizers, and lower cost-effectiveness due to the use of palladium-based catalyst and the anthraquinone carrier, prompt interest in developing decentralized, on-site H_2O_2 production. Utilizing a selective $2e^-$ oxygen reduction reaction, this process can be carried out electrochemically. Some such systems with selective catalysts have been reported [3], whereas the aim of this work is to develop an electrochemical sensor for H_2O_2 that can be integrated into a microfluidic device for electrochemical H_2O_2, and therefore monitor its concentration in the system.

Many electrochemical sensors for H_2O_2 have been described, using various electrode materials and modifications. Often a combination of carbon nanomaterials and metal oxides are deposited onto an electrode surface to increase the surface area of the electrode and to catalyze the degradation of H_2O_2, respectively [4]. Recently, flash graphene (FG) has attracted a lot of attention [5] also as a potential new material for the use in electrochemical sensors. Its novelty and attractiveness lie in the production method, flash Joule heating, where the source material is rapidly heated using high electronic currents, as well as the fact that theoretically any carbon containing source can be turned into a high value material, namely FG. In the presented work, FG was used for the first time in combination with MnO_2 to modify carbon screen-printed electrodes and amperometrically detect H_2O_2 in alkaline (pH 13) media.

Results

Cyclic voltammetry was used to study the general electrochemical properties of modified electrodes utilizing a commonly used electrochemical probe $[K_4[Fe(CN)_6]/K_3[Fe(CN)_6]$. Peak heights and peak-to-peak separations indicated the optimal modification of the electrodes – 2 drop-casted layers of FG and MnO_2 dispersed in 50 % ethanol with 5 % Nafion. The expected increase in the surface area when FG is present on the electrode was indicated with an increased capacitive current and confirmed with the calculation of electrode surface areas using Randles-Ševčik equation. The surface areas for non-modified and modified electrodes were 0.1789 cm^2 and 0.2522 cm^2, respectively.

Since the target application of this sensor is continuous monitoring of H_2O_2 concentrations in a microfluidic device, where the electrochemical production of H_2O_2 takes place, the optimization of experimental parameters must be considered. Efficient, carbon-based, electrocatalysts have been shown to be active and selective towards $2e^-$ oxygen reduction reaction at high pH [3]. Therefore, to successfully integrate the produced sensor into such a device it must be efficient and stable at high pH values. The use of 0.1 M KNO_3 in 0.1 M KOH as a medium has shown satisfactory results. The detection of the analyte was carried out with hydrodynamic amperometry. The operating potential was optimized and was 0.15 V (vs Ag).

Proposed sensor has two linear ranges, first spans from 1 to 100 $\mu molL^{-1}$, the second from 100 to 1000 $\mu molL^{-1}$. Considering the expected concentration of electrochemically produced H_2O_2, the lower linear range will be in use for the present batch sensor setup. The sensitivity of the electrode in this range is 0.244 $\mu A\mu M^{-1}cm^{-2}$. Limit of detection was calculated as 0.238 $\mu molL^{-1}$.

The results of the work so far are highly satisfactory considering the harsh alkaline working conditions. First tests on the real samples have already been carried out and the results are in agreement with other detection techniques that were used for the monitoring of H_2O_2 concentration produced in the microreactor, namely optical H_2O_2 sensor, designed by Tjell *et al.* [6]. The results differ by less than ±5 %. Furthermore, the results so far indicate the possibility of multiple uses of a single screen-printed electrode.

References

[1] Veal, E., Day, A., Hydrogen peroxide as a signaling molecule, *Antioxidants & redox signaling* 15(1), 147-151 (2011); doi: 10.1089/ars.2011.3968

[2] Xu, J., Zheng, X., Feng, Z. et al., Organic wastewater treatment by a single-atom catalyst and electrolytically produced H_2O_2, *Nature Sustainability* 4, 223-241 (2021); doi: 10.1038/s41893-020-00635-w

[3] Martins, P. F. B. D., Plazl, I., Strmcnik, D., Genorio, B., Prospect of microfluidic devices for on-site electrochemical production of hydrogen peroxide, *Current Opinion in Electrochemistry* 38, 101223 (2023); doi: 10.1016/j.coelec.2023.101223

[4] Gričar, E., Kalcher, K., Genorio, B., Kolar, M., Highly sensitive amperometric detection of hydrogen peroxide in saliva based on N-doped graphene nanoribbons and MnO_2 modified carbon paste electrodes, *Sensors* 21(24), 8301 (2021); doi: 10.3390/s21248301

[5] Luong, D. X., bets, K. V., Algozeeb, W. A. et al., Gram-scale bottom-up flash graphene synthesis, *Nature* 577, 647-651 (2020); doi: 10.1038/s41586-020-1938-0

[6] Tjell, A. Ø., Jud, B., Schaller-Ammann, R., Mayr, T., Optical hydrogen peroxide sensor for measurements in flow, *Sensors and Actuators B: Chemical* 400, 134904 (2024); doi: 10.1016/j.snb.2023.134904

DOI 10.5162/EUROSENSORSXXXVI/PT5.174

Chip-set for Chemoresistive Gas Sensors

Kitti Pankász[1], Csaba Dücső[2]
[1] Budapest University of Technology and Economics, Műegyetem rkp. 3, Budapest, 1111 Hungary
[2] HUN-REN, Centre for Energy Research, Konkoly-Thege street 29-33, Budapest, 1121 Hungary

Corresponding Author's e-mail address: ducso.csaba@ek.hun-ren.hu

Summary:
A chip set for development of chemoresistive gas sensors is presented. The basic chip carries three microheaters with resistance measuring electrodes on their top. Manually aligned masking chips enable local deposition of the sensing layer on the heaters' surface. The use of the chip set facilitates the functional characterization of the sensing layer without the need of chip processing capabilities.

Keywords: gas sensors, chemoresistive layers, microheater chip

Introduction

In spite of the half-century long continuous research and the relatively limited practical use of the chemoresistive solid state gas sensors, still large effort is dedicated for development of new sensing materials. New composition of thin layers [1], 3D nanostructures [2] and large variety of sensitizing methods aim at the improvement of sensitivity and selectivity. Although the vast majority of the reported sensors suffer from poor selectivity and dynamics, the promise of extremely low costs and the ppm level sensitivities keep many research groups continuing the development better sensing materials.

As the transduction principle relays on physi-, and chemisorption phenomena the sensors are operated at elevated temperatures. Consequently, to ensure battery backed operation, its power dissipation must be kept as low as possible. Although several laboratories and manufacturers have developed low power consumption microheater structures, their fabrication requires wafer processing lines. Thereby the access to the basic device is limited for many laboratories. In this work we present the first version of a set of microheater chip and aligned local masking chips to facilitate laterally selective deposition of the sensing layers and easy testing the sensor characteristics without the need for the complex technical background.

Results and discussion

1) The sensor chip

The 3.5x3.5 mm^2 chip contains three microheaters of 150μm diameter as suspended on a 500 μm circular membrane. The heater is an embedded Pt filament what encapsulated in a $SiO_2/Si_3N_4/SiO_2$ multilayer structure. The cross section (Fig.1), and the design considerations were reported earlier [3].

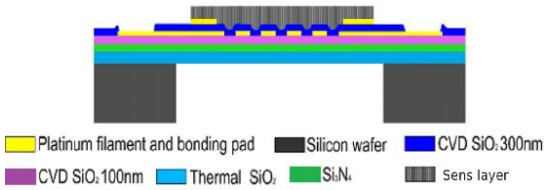

Fig. 1. The cross section of the microheater with the sensing layer on top.

DRIE backside Si etching process provides the membrane release to get the reduced power dissipation as represented in Fig.2.

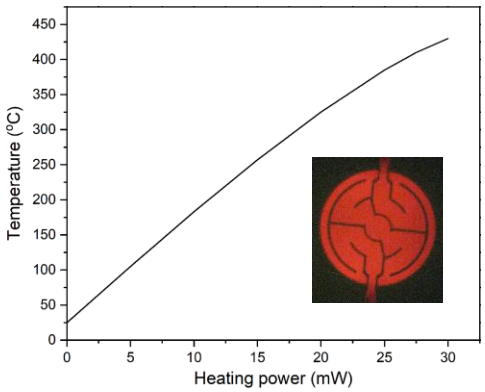

Fig. 2. Temperature-power characteristics of the microhotplate. The colour of the inset demonstrates the temperature uniformity of the heater @ 650°C.

The filament geometry provides uniform (<±3%) temperature distribution over the heated surface. It is visibly demonstrated by the inset of

Fig. 2, showing uniform colour at 650°C. However, according to the long-term tests, de device stability is guaranteed below 500°C.

Pt electrodes are formed on the top of the heater to measure the resistance of the gas sensitive layer. We offer two versions having 10 and 100 µm electrode distances to better match with the characteristic resistivity of the sensor layer. The three independently heated micro hotplates can be operated at different temperatures, thereby accelerates the screening the temperature vs. response characteristics; or setting the same heating power an average response can be calculated to more accurately characterize the sensor properties (Fig. 3).

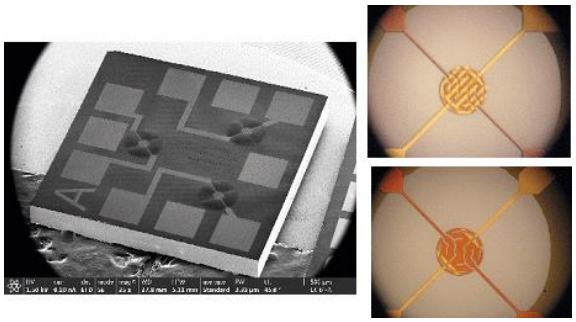

Fig. 3. The chip contains 3 identical microhotplates with 10 µm (top right) or 100 µm (bottom right) electrode distances.

2) Masking for locally selective deposition

Various processes have been reported for formation and deposition of the sensing layers; e.g. PVD and CVD methods as well as droplet or screen-printing techniques from separately synthetized suspensions. In our approach we fabricate masking chips for PVD and CVD layer depositions. Although the wet chemical synthesis of 3D nanostructured sensing materials dominate the current research activity, the proposed setup is partially meets the suspension-associated requirements. The droplet technique inherently provides local deposition, whereas the screen-printing is not compatible with the fragile thin membranes.

Considering the typical substrate temperatures of the conventional thin film PVD and CVD processes, we formed alternative masks for the deposition-through process: a 3D printed plastic version up to 60°C and perforated Si membrane for higher temperatures. Auxiliary chip holder enables the proper alignment of the chip and the mask. The setup is adaptable for both substrate positions (top down or bottom up) in the deposition system (Fig.4).

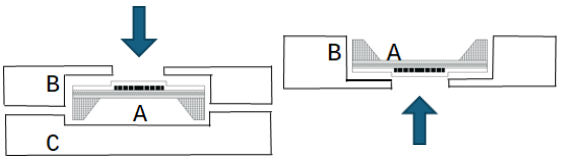

Fig. 4. Substrate positions in the deposition chamber: test chip (A), mask (B), auxiliary holder (C). The arrows indicate the direction of the precursor flow.

Beside the single-chip masks, we also fabricated masking caps for mounted and wire bounded chip. The recessed centre part with three openings is in a close vicinity of the chip surface but the bonding wires remain intact. This ultimate solution may perfectly assist in the R&D work by providing completely ready-to-test devices right after the sensing layer deposition.

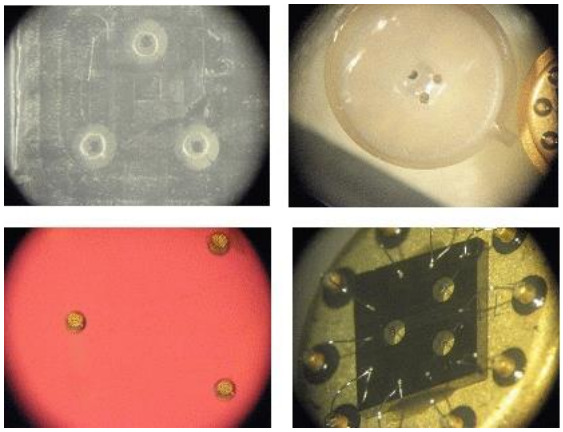

Fig. 5. The three heaters as seen in the vias of the transparent plastic (top left) and c-Si membrane (bottom left) masking elements. The 3D printed masking cap (top right) on a TO mounted chip (bottom right).

References

[1] Mirzaei, A. et al., Room Temperature Chemiresistive Gas Sensors Based on 2D MXenes, *Sensors* Volume 23, Issue 21 November 2023, DOI: 10.3390/s2321882

[2] Galstyan, V. et al. Progress towards chemical gas sensors: Nanowires and 2D semiconductors, *Sensors and Actuators B: Chemical* Volume 35715 April 2022, DOI: 10.1016/j.snb.2022.131466

[3] Biró, F. et al., An analytical method to design annular microfilaments with uniform temperature, Microsystem Technologies, 28(11), pp. 2511–2528, 10.1007/s00542-022-05376-8

Acknowledgement

This work was supported by the Hungarian Ministry of Culture and Innovation via Grant TKP2021-NVA-03.

DOI 10.5162/EUROSENSORSXXXVI/PT5.178

Boron-doped Diamond Electrodes for sensing narcotics using Electrochemiluminescence

A. Blot[1], E. Scorsone[1]

[1] Université Paris-Saclay, CEA, List, F-91120 Palaiseau, France

adeline.blot@cea.fr

emmanuel.scorsone@cea.fr

Summary:

In this study, we increase the range of applications of boron-doped diamond electrodes as electrochemical sensor for narcotics detection, using electrochemiluminescence (ECL) principles. The method involves the enhancement of the chemiluminescence from permanganate ions upon oxidation of narcotic molecules in electrolytic solution, and has been demonstrated e.g. for Δ-9-tetrahydrocannabinol (THC) with typical limits of detection below 15 ng/mL (47.7 nM).

Keywords: boron-doped diamond electrodes, electrochemical sensor, electrochemiluminescence, narcotics detection, reusable electrodes.

Boron-doped diamond (BDD) is a very interesting electrode material due to the variety of assets it features when compared to more conventional electrode materials. The polycrystalline structure of boron doped diamond ensures high stability including resilience to corrosion, alongside with a low double layer capacitance and wide potential window in aqueous media.[1] In addition, such electrodes may be electrochemically pretreated before measurements to overcome the issue of fouling. For instance using sequences of current pulses with high densities has proven effectiveness to achieve this goal [2]. All these properties made BDD electrodes suitable for electrochemiluminescence (ECL) in sensor applications, potentially offering better sensitivity than standard amperometric methods. Besides, the increase of recreational drugs consumption has become a major societal issue nowadays. In the context of road safety, conventional sensors for control generally use antibodies, functionalised with a tracer. As saliva samples are being analysed, the low solubility of the drugs in aqueous media make it challenging to detect molecules in trace amount. Thus second post toxicology analyses, using traditional methods in laboratory, are required for legal validation, which also present limitations [3]. These constrains have conducted to develop new reliable sensors for drug detection. In this context, ECL has shown promising results for drugs detection with a fast, sensitive and scalable method [4].

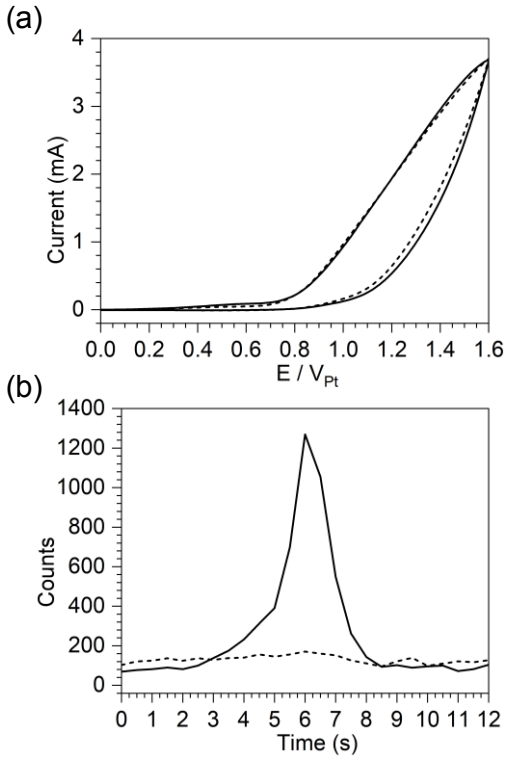

Figure 1: Electrochemiluminescence measurement with (a) cyclic voltammetry of $KMnO_4$ 152 µM pH 3 buffer in Na_2SO_4 0.1 M (dash) and 2 µL of THC 24.5 nM deposited on the electrode surface in $KMnO_4$ buffer (line) and the corresponding ECL measurement (b) with $KMnO_4$ (dash) and in presence of THC (line)

In this work, we were able to detect a variety of illicit substances (THC, Amphetamine, Cocaine, Methamphetamine, Benzoylecgonine, rac-MDMA, morphine, etc) using BDD electrodes while carefully selecting the ECL luminescent probes, leading to quenching / enhancing properties upon exposure to narcotics, depending on the choice of co-reactants. For instance, we identified permanganate ions as efficient ECL probes in aqueous media. To our knowledge permanganates have been reported as chemiluminescent probes when associated with long chains of polyphosphates [5], but not as electrochemiluminescent probe before. Figure 1 shows the ECL detection of THC in the presence of permanganate at a concentration of 24.5 nM. At this concentration levels cyclic-voltammetry curves do not show any significant oxidation signal due to the presence of THC (Figure 1.a). By contrast, Figure 1.b shows the resulting ECL response. Here the blank solution of $KMnO_4$ does not exhibit any light emission within the voltage range of 0 V to 1.6 V. However, after drop casting 2 µL of THC at a concentration of 24.5 nM on the electrode surface, a peak of luminescence is detected leading to the detection of THC. These results will be discussed further during the conference and more results presented with other narcotic compounds.

References

[1] Y. Einaga, J. Foord, et G. Swain, Diamond electrodes: Diversity and maturity, *Mrs Bulletin*, vol. 39, nº 6, p. 525-532, juin 2014, doi: 10.1557/mrs.2014.94.

[2] R. Kiran, E. Scorsone, J. de Sanoit, J.-C. Arnault, P. Mailley, et P. Bergonzo, Boron Doped Diamond Electrodes for Direct Measurement in Biological Fluids: An In Situ Regeneration Approach, *Journal of the Electrochemical Society*, vol. 160, nº 1, p. H67-H73, 2013, doi: 10.1149/2.014302jes.

[3] O. Beck, L. Rausberg, Y. Al-Saffar, T. Villen, L. Karlsson, T. Hansson, et A. Helander, Detectability of new psychoactive substances, 'legal highs', in CEDIA, EMIT, and KIMS immunochemical screening assays for drugs of abuse, *Drug Testing and Analysis*, vol. 6, nº 5, p. 492-499, mai 2014, doi: 10.1002/dta.1641.

[4] K. Brown, P. Allan, P. S. Francis, et L. Dennany, Psychoactive Substances and How to Find Them: Electrochemiluminescence as a Strategy for Identification and Differentiation of Drug Species, *Journal of the Electrochemical Society*, vol. 167, nº 16, p. 166502, déc. 2020, doi: 10.1149/1945-7111/abc9db.

[5] B. J. Holland, J. L. Adcock, P. N. Nesterenko, A. Peristyy, P. G. Stevenson, N. W. Barnett, X. A. Conlan, P. S. Francis, The importance of chain length for the polyphosphate enhancement of acidic potassium permanganate chemiluminescence, *Analytica Chimica Acta*, vol. 842, p. 35-41, sept. 2014, doi: 10.1016/j.aca.2014.07.012.

DOI 10.5162/EUROSENSORSXXXVI/PT5.185

Towards Metal-Organic Framework based Optical Sensors for Pesticides Detection

Alba Finelli[1], *Pierrick Clément*[1], *Xavier Lefèvre*[1], *Alexandra Beard*[1], *Raphaël Pugin*[1]
[1] *CSEM, Rue Jaquet-Droz 1, 2002 Neuchâtel, Switzerland*

Alba.finelli@csem.ch

Summary:
Organophosphates are extensively employed as pesticides in intensive agriculture. Being strong nerve agents, they represent one of the most common causes of poisoning in the world. Given their detrimental impact on both human health and the ecosystem, it is critical to develop a compact, reliable, fast, selective, and low-cost sensor able to detect pesticides residues in aqueous medium such as drinking water, foods, and soil samples.

Keywords: Metal organic frameworks, Optical sensor, Nitro compounds, Pesticides, Sensing layer

Introduction

Exhibiting a high surface area, metal-organic frameworks (MOFs) can be customized to effectively adsorb the targeted analytes. Interest in integrating such porous materials as selective adsorbent layers in chemical sensors has increased lately [1]. Though, refinement of sensing materials and transducer mechanisms is still essential to increase the reliability, selectivity, and response kinetics to a level suitable for commercial purposes. While MOFs seem excellent candidates for selective sensing, several studies demonstrate a higher response for the selected analyte compared to interferents because the compounds are tested each independently. In real-world applications, the sensor will be exposed to all components concurrently, including some interferents present at much higher concentrations than the analyte. One way to address the selectivity challenge is to combine cross-sensitive sensors to form an array or "electronic nose" (e-nose) [2].

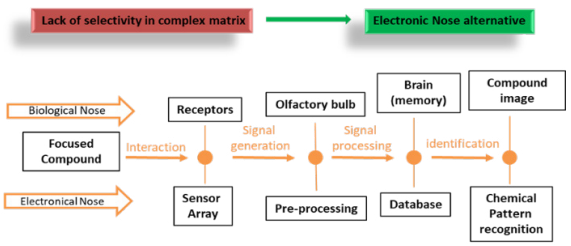

Fig. 1. E-nose concept schema.

When the combined response of the array contains enough non-correlated information, the focused analyte can be monitored in a complex environment via chemometric data analysis (Figure 1).

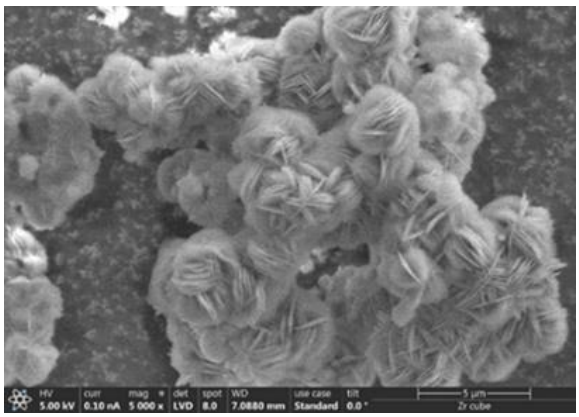

Fig. 2. Scanning electron micrograph of ursin-like Zr-MOF.

Results

Due to the variety of organophosphate pesticides, nitro-based compounds have been focused on this study. Luminescent Zr-MOFs have been synthesized for the specific uptake of the toxic analytes from 1,2,4,5-tetrakis(4-carboxyphenyl) benzene and Zr(IV)[3]. Characterization by X-ray diffraction (PXRD) and SEM (Figure 2) shows an ursin-like morphology. Due to the luminescence properties of the MOF, the first sensing tests have been done by fluorimetry. Together with a surface area corresponding

to 1453.2 m^2/g and micropores size of about 0.60 nm, this MOF has shown a specific affinity with nitro-based family by the quenching of the luminescence of the fluorophore via adsorption. Zr-MOF has been tested in the presence of other compounds containing a nitro group as well as nitrates and nitrites salts (Figure 3). It can be observed that all compounds containing a nitro group extinguish the fluorescence to varying degrees. The most probable explanation is that the presence of the $-NO_2$ group has caused the transfer of photoexcited electrons from the Zr-MOF to the nitro compounds. Therefore, the quenching of the MOF will strongly depend on the electro-attractive properties of the nitro compound. We could then observe a lack of selectivity of this MOF when targeting a specific compound, but it appears to be reactive to most nitro compounds.

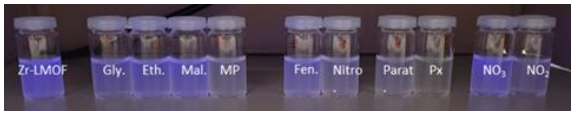

Fig. 3. Photoluminescence responses of Zr-MOF against 10 organophosphates compounds containing nitro group. The final concentration of all the compounds is 0.012 mM.

The interesting luminescent properties of Zr-MOF have been utilized to create an active layer for detecting pollutant compounds containing a nitro group. For this purpose, the MOF was incorporated into a silica-based sol-gel. This compound can then be deposited onto a transparent surface such as PET via spin, bar, or spray coating (Figure 4). The coated layer has shown to be sufficiently hydrophilic to enable a rapid response to the presence of this family of pollutants. Further characterizations are now ongoing to evaluate and confirm the reliability, selectivity, and sensitivity of the final sensor.

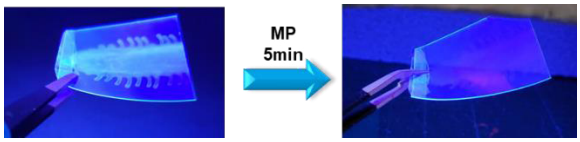

Fig. 4. MOF-based coating quenched off by the presence of methyl parathion (MP) after 5 minutes.

Conclusion

To conclude, we acknowledge that the selectivity of MOFs can be a significant limitation for the development of an optimal sensor especially for real-world applications. To tackle this primary challenge, the design of an electronic e-nose concept could be developed using the remarkable proprieties of MOFs for the detection of pollutant families. By integrating multiple MOF-based sensors with cross-sensitivity, we could effectively identify compounds within the same family.

References

[1] Furukawa H, Cordova KE, O'Keeffe M, Yaghi OM. The chemistry and applications of metal-organic frameworks. *Science* 30 (2013) 341

[2] Freund R., et al. "The Current Status of MOF and COF Applications." *Angewandte Chemie International Edition* (2021)

[3] He, K., Li, Z., Wang, L., Fu, Y., Quan, H., Li, Y., ... & Xu, X. A water-stable luminescent metal–organic framework for rapid and visible sensing of organophosphorus pesticides. *ACS applied materials & interfaces* 11 (2019) 26250

DOI 10.5162/EUROSENSORSXXXVI/PT5.203

Solid support counts: towards development of all-solid state sensor for ketoprofen

Larisa Lvova1, Pierangela Di Menna[1], Giammarco Maria Romano[2], Andrea Bencini[2], Roberto Paolesse[1]

[1]Department of Chemical Science and Technologies, University of Tor Vergata, Rome, Italy
[2]Department of Chemistry "Ugo Schiff", University of Florence, Sesto Fiorentino, Italy
larisa.lvova@uniroma2.it

Summary:

The properties of all-solid-state optical sensors based on the polyamine receptors PP-1 and PP-2 bearing pyrene fluorogenic groups able to signal selective ketoprofen, KP, binding through the enhancement of the fluorescence emission have been investigated. The series of PVC polymeric membranes, plasticized with different plasticizers and doped with fully protonated PP-2 ligand, together with TDACl or TDMACl anion exchanger in 1:1, 1:2 and 1:3eq. ratio was studied in order to tune the highest selectivity toward KP. The appropriate choice of a solid support, selecting from cellulose-based or glass materials, influences significantly the performance of sensor. The fluorescent intensity of developed optical sensors increased with KP concentration growth. The images of sensors were acquired with smartphone and digitalized with a free on-line software of image processing in order to construct calibration model. Developed chemical sensors have shown the possibility to detect KP in the concentration range 2 μM – 0.1mM, with low influence of several interfering ions of the similar structure, such as naproxen, ibuprofen and benzoate. All-solid state sensor on paper support was successfully applied for KP assessment in pharmaceutical composition OkiTask with RSD of 2.1% and recoveries in range 98-102%.

Keywords: all-solid-state fluorimetric sensors, ketoprofen, polyamine bis-pyrene receptors, pharmaceutical analysis.

Background, Motivation and Objective

The ketoprofen (KF) main action is an inhibition of prostaglandin synthesis with cyclooxygenase enzyme, that make it an effective against acute and chronic pain courses [1]. KF has been recently recognized as an emerging contaminant with high environmental impact due to its chemical stability, lack of efficient methodologies for removal from waste, and widespread consumption [2]. Hence, rapid and effective detection of KF is an actual analytical task. The chemical sensors are an effective alternative to the tedious and time-consuming standard instrumental analysis, like HPLC-MS, recommended for KF detection. Previously several types of chemical sensors and multisensor systems for KF were reported [3-7]; among them optical sensors are the most attractive since they do not require sophisticated hardware, can be wireless and their output may be estimated with common optoelectronic devices or simply through 'naked-eye' observation. Also, a fast response time, acceptable sensitivity, and selectivity, together with low cost and easiness in handling make optical sensors very requested.

In this work, 6 sensing materials were prepared by incorporating 1 wt% of PP-1 ligand and 1- 5 wt% of TDACl or TDMACl anion-exchangers inside plasticized PVC membranes, Table 1. The membrane cocktails in THF were then treated with TFA in order fully protonate fluorophore in membrane phase and to tune optical response towards KP. The 2 μl of each sensing membrane were deposited on different solid supports (glass, filter paper or cellulose fiber used as color catcher material in laundry). The performance of the obtained sensing platform in recognizing KP and interfering anions as NS^-, IB^-, $Benz^-$, ClO_4^-, SCN^-, as well as Cu^{2+} and Zn^{2+} cations was examined. For this, 5 μl of tested solution were dropped over the prepared sensing sports, the image of overall sensing platform, containing from 6 to 11 sensing spots with deposited on them solutions of KP in concentration range 2 μM – 0.1mM, and/or interfering ions was registered with a smartphone and

digitalized with a free on-line software ImageJ [8] in order to construct calibration curve in co-ordinates luminescence intensity vs log[KP].

Results

The chemical structures of novel polyamine receptors PP-1 and PP-2 bearing pyrene fluorogenic groups are shown in Figure 1A. As it was previously reported, the protonated PP-1 receptor in 0.005 M TRIS-HCl/EtOH solutions (1:1 vol/vol, pH = 7), shows a significant increase of fluorescence intensity at λ_{ex} =360nm and upon titration with KP^- ions due to the inhibition of the photoinduced electron transfer (PET) process between the non protonated amines and the pyrene units in receptor structure [9].

Table 1. Composition of tested polymeric membranes, doped with 1 wt% of PP-2.

N	Plasticizer	PP-1:TDACl, mol : mol	TFA, eq.
Mb1*	TOP	1 : 0.7	-
Mb1	TOP	1 : 0.7	3 eq
Mb2	DOS	1 : 0.7	3 eq
Mb3	DOS	1 : 0.7	-
Mb4	DOS	1 : 1.5	3 eq
Mb5	DOS	1 : 2.8	3 eq

Fig. 1. (a) Chemical structures of KP-H, PP-1 and PP-2; (b) the photogram of PP-2-based all-solid-state optodes deposited on glass support; (c) the photogram and (d) relative luminescence intensity of membrane Mb5 deposited on filter paper support for 40 μM KP and different interfering ions the extracted from (c). λ_{ex} =360nm

Through addition of trifluoroacetic acid, TFA, in polymeric membranes Mb1, Mb2, Mb4 and Mb5, in 1:1 ratio in respect to PP-1 amount, the protonated (on -NH groups) form of fluorophore was obtained. These membranes were deposited on solid support (glass or paper) and their response towards KP and selectivity properties were studied, Figure 1c,d. The optimized all-solid-state optodes have shown the linear increase of fluorescence intensity upon illumination at 365 nm in presence of KP in the concentration range 2 μM – 0.1mM, and few influence of all tested interfering ions, Figure 1d. The membrane Mb5 based on fully protonated PP-2 ligand, with TDMACl anion exchanger in ratio 1:3 eq. in respect to fluorophore, and plasticized with DOS plasticizer, had the best optical response, and was applied for KP assessment in pharmaceutical composition OkiTask with RSD of 2.1% and recoveries in range 98-102%.

The detailed discussion on all-solid-state optodes selectivity evaluations, influence of solid support material and the applications for ketoprofen assessment in real samples as waste waters and biological samples (urine of patients in treatment several hours after KP assuming) will be illustrated in our presentation.

References

[1] Wilkinson J, Hooda PS, Barker J, Barton S, Swinden J, Environ. Pollut., 2017, 231, 954.
[2] Non-Steroidal Anti-Inflammatory Drugs in Water, ed. L. M. Gomez-Olivan, Springer International Publishing, 2020.
[3] Lenik J, J. Anal. Chem. 2012, 67, 543.
[4] Mostafa IM, Meng C, Dong Z, Lou B, Xu G, Anal. Sci. 2022, 38, 23.
[5] Shishkanova TV, Broncov G, Skalova A, Prokopec V, Člupek M, Kral V, Electroanalysis 2019, 31, 1.
[6] Farotto S, Picci G, Milia J, Caltagirone C, Lippolis V, Aragoni MC, DiNatale C, Paolesse R, Lvova L, ACS Sens. 2023, 8, 3225.
[7] Romano GM, Mummolo L, Savastano M, Paoli P, Rossi P, Prodi L, Bencini A, Chem. Commun. 2022, 58, 7022.
[8] https://imagej.net/ij/
[9] P. Di Menna, G.M. Romano, A. Bencini, R. Paolesse, L. Lvova, A fluorescent sensor array for ketoprofen assessment, in Proceedings of ISOEN 2024, Grapevine, USA, 12-15 May, 2024.

DOI 10.5162/EUROSENSORSXXXVI/PT5.211

NO_2 Gas Sensor with Inkjet-Printed Zinc Oxide and Boron-Doped Diamond Layer

Alexandr Laposa[1], *Jiri Kroutil*[1], *Vojtech Povolny*[1], *Ondrej Kaman*[2], *Pavel Hazdra*[1]
[1] *Faculty of Electrical Engineering, Czech Technical University in Prague, 166 27 Prague, Czech Republic,*
[2] *Institute of Physics of the Czech Academy of Sciences, 182 00 Prague, Czech Republic*

laposale@fel.cvut.cz

Summary:

In this paper, we present a gas sensor with a sensing layer composed of Zinc Oxide (ZnO) and Boron-Doped Diamond (BDD) nanoparticles, deposited via inkjet printing technology. The sensor operates at room temperature and uses UV illumination to enhance its sensitivity and stabilize its responses. We investigated the gas-sensing capabilities of the ZnO-BDD layer for detecting low concentrations (ppm level) of NO2 in synthetic air.

Keywords: boron doped diamond, zinc oxide, ink, inkjet printing, UV light, gas sensor.

Introduction

The detection of gaseous substances, especially toxic ones, is crucial across various sectors such as automotive, aviation, agriculture, security, healthcare, defense, industry, and environmental monitoring. This includes applications in food freshness and quality prediction [1].

Inkjet printing is an attractive method for fabricating micro and nano functional structures due to its low cost and good material compatibility. This technology allows for the deposition of layers with small thicknesses and larger surface areas, potentially enhancing the sensitivity of gas sensors. Inkjet printing accommodates a wide range of liquids, optimized for various substrates, including non-flat, rigid, or flexible ones. Furthermore, it enables short production times, low costs, and highly efficient material usage [2].

Metal oxide nanomaterials are widely used in advanced technologies due to their unique structure, morphology, and chemical, optical, and electrical properties [2]. These materials are particularly valued in the fabrication of gas sensors because of their high sensitivity, fast response and recovery times, low cost, and flexibility [3]. Additionally, UV light irradiation has been employed to enhance the sensing characteristics and sensitivity of these sensors [4]-[5].

Experimental

Solvothermal synthesis was used for preparation of ZnO nanoparticles. Zinc acetate dihydrate (0.66 g) was dissolved in methanol (30 mL), and the solution was transferred into a 50 mL Teflon insert of Berghof DAB-2 pressure vessel. The vessel was heated to 150 °C for 12 h, and then cooled to room temperature spontaneously. The particles were collected by exhaustive centrifugation and washed in three cycles of redispersion in ethanol followed by centrifugation. For preparation of the ZnO ink, a fine fraction of particles was isolated by two consecutive mass fractionation steps. These steps involved centrifugation in water and ethylene glycol-water mixture at 262 and 116 rcf (relative centrifugal force), respectively, after which the corresponding supernatants were separated. The final ink was prepared in the ethylene glycol – water mixture (1:1), and its concentration was adjusted to ~4 mg(ZnO)g^{-1}.

The BDD ink was prepared by mixing a commercially available aqueous suspension of B-doped nanodiamonds with the mean size of 50 nm with ethylene glycol in volumetric ratio of 1 : 1 under application of ultrasound agitation. The so-obtained suspension with the concentration of 2.5 mg/mL was directly used for the inkjet printing (see Figs.1 and 2).

Both inks exhibit stable printing properties, and no degradation was observed when stored at room temperature for several months. Printing was conducted using a drop-on-demand Fujifilm DMP-2831 inkjet printer equipped with a

piezoelectric Dimatix Cartridge-Samba G3L printhead under the following conditions: a nozzle diameter of 17 µm, a native drop volume of 2.4 pl, a cartridge height of 750 µm, and an ink printing resolution of 2540 dpi. The print mode was set to 4 times 1 pass, involving two layers of ZnO ink and two layers of BDD ink (four layers in total), with each layer being printed onto a completely dry previous layer. The jetting frequency was 2 kHz, the drop velocity was 9.5 m/s, the cartridge temperature was 32 °C, and the substrate temperature was 40 °C.

Optimal printing conditions were achieved using Ohnesorge theory and piezoelectric waveform optimization. Optical images (Fig.4) show the patterning capability over an active area of 1.2 x 1.2 mm^2 on a Micrux ED-dIDE1-Au substrate with interdigital electrodes (30 pairs of Ti/Au interdigital electrodes, 10 µm electrode width and 10 µm gap). The thickness of the BDD-ZnO active layer was approximately 100 nm.

Gas sensing measurements were performed using an in-house developed setup [6]. The baseline resistance of the sensor is approximately 500 kΩ under UVLED at 365 nm with an intensity of 50 $\mu W.cm^{-2}$. The graphs indicate relatively stable responses (Fig.5).

Results

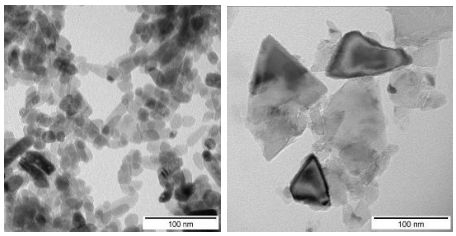

Fig. 1. Transmission electron micrograph of ZnO (left) and BDD (right) nanoparticles (Philips CM 120).

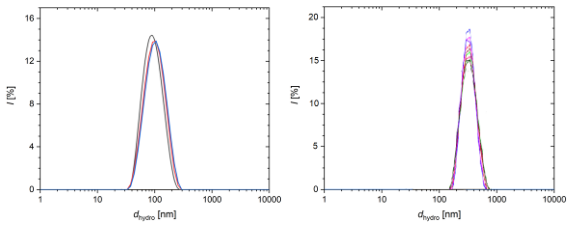

Fig. 2. Intensity distribution of hydrodynamic size of ZnO (left) and BDD (right) nanoparticles in ethylene glycol – water mixture (1:1) based on dynamic light scattering measurements at 25 °C (DLS, Malvern Zetasizer Nano ZS).

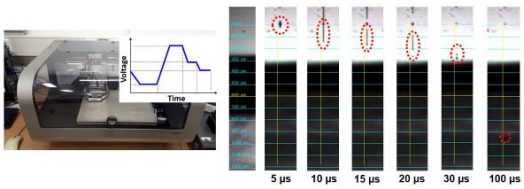

Fig. 3. Waveform for the printing process of both the ZnO and BDD inks, and view of firing droplets.

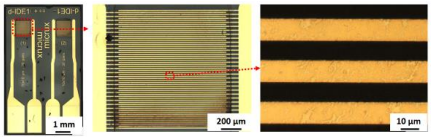

Fig. 4. Optical images of the realized sensor with inkjet printed ZnO-BDD active layer(Olympus BX-60).

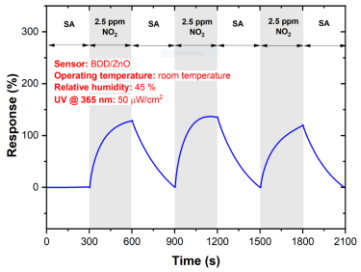

Fig. 5. Dynamic sensing response curves of the sensor with inkjet printed ZnO-BDD active layer for constant concentration of NO_2 at room temperature.

Conclusions

We demonstrated the fabrication and characterization of gas sensors featuring a printed nanoparticle ZnO-BDD active layer that operates at room temperature. Perspective inkjet printing technology was used for the selective deposition of Diamond-ZnO nanoparticles.

Acknowledgment

This work was supported by the Czech Science Foundation grant No. 22-04533S.

References

[1] T. Zhang et al., “Inkjet-printed ZnO-based MEMS sensor array combined with feature selection algorithm for VOCs gas analysis,” Sensors Actuators B Chem., vol. 382, p. 133555, May 2023, doi: 10.1016/j.snb.2023.133555.

[2] N. Omerovic, M. Radovic, S. Savic, and J. Katona, “Preparation of TiO2 and ZnO dispersions for inkjet printing of flexible sensing devices,” Process. Appl. Ceram., vol. 12, no. 4, pp. 326–334, 2018, doi: 10.2298/PAC1804326O.

[3] P. Yoboué et al., “CONTROLLED ZnO DEPOSITS FOR GAS SENSORS,” Int. J. Mater. Eng. Technol., vol. 18, no. 2, pp. 55–66, Dec. 2019, doi: 10.17654/MT018020055.

[4] N. D. Chinh et al., “NO gas sensing kinetics at room temperature under UV light irradiation of In2O3 nanostructures,” Sci. Rep., vol. 6, no. April, pp. 1–11, 2016, doi: 10.1038/srep35066.

[5] L. F. da Silva et al., “UV-enhanced ozone gas sensing response of ZnO-SnO2 heterojunctions at room temperature,” Sensors Actuators, B Chem., vol. 240, pp. 573–579, 2017, doi: 10.1016/j.snb.2016.08.158.

[6] A. Laposa et al., “Inkjet Seeded CVD-Grown Hydrogenated Diamond Gas Sensor Under UV-LED Illumination,” IEEE Sens J., vol. 20, no. 3, Feb. 2020, doi: 10.1109/JSEN.2019.294694

Two-dimensional (2D TMDs) Hybrid Materials for Detection of Hazardous Gases

V. B. Patil, Punyashlok Ahilyadevi Holkar Solapur University, Solapur (India)

Unfortunately, this abstract is not available, as the contribution was not confirmed at the time the conference proceedings were finalized.

Two-dimensional (2D TMDs) Hybrid Materials for Detection of Hazardous Gases

V. B. Patil, Punyashlok Ahilyadevi Holkar Solapur University, Solapur (India)

Unfortunately, this abstract is not available, as the contribution was not confirmed at the time the conference proceedings were finalized.

Enhanced NO2 sensing properties obtained by CeO2-ZnO mixed metal oxide

M. Chougule, Commerce & Science College, Sindhudurg (India), V. Patil,
PAH Solapur University, Solapur (India)

Unfortunately, this abstract is not available, as the contribution was not confirmed at the time the conference proceedings were finalized.

Enhanced NO2 sensing properties obtained by CeO2-ZnO mixed metal oxide

M. Chougule, Commerce & Science College, Sindhudurg (India), V. Patil,
PAH Solapur University, Solapur (India)

Unfortunately, this abstract is not available, as the contribution was not confirmed at the time the conference proceedings were finalized.

DOI 10.5162/EUROSENSORSXXXVI/PT5.230

3D Printed Micro-Gas Chromatography (µ-GC) System for Improved Low-Cost VOC sensing

Usman Yaqoob, Siavash Esfahani, Marina Cole, Julian W. Gardner
School of Engineering, University of Warwick, Coventry CV4 7AL, UK

J.W.Gardner@warwick.ac.uk

Summary:

This paper describes the custom design of a 3D printed µ-GC column that is combined with commercial MOX gas sensors. A spiral-shaped column is designed in SolidWorks, the 3D printed structure is coated with OV-1, and integrated into an e-nose sensor system. 2-methyl butanol mixed with ethanol was used to test the µ-GC's ability to separate compounds based on their molecular affinity to the PDMS coating. Our preliminary results demonstrate the potential of a basic, low-cost 3D printed µ-GC based system to offer better selectivity than MOX sensors alone.

Keywords: Gas Micro chromatography, 3D printing, Metal oxide sensors, Volatile organic compounds (VOCs).

Background, Motivation an Objective

Conventional gas chromatography (GC) is known for its high accuracy and versatility in analyzing complex mixtures of chemical compounds having similar physicochemical properties. However, they are expensive, bulky and require high power, making them unsuitable for field-portable applications. Therefore, there is a clear need for economical, compact, and energy efficient alternatives that can provide comparable performance [1]. Recently, there has been an increase in effort to fabricate µ-GCs on a Si substrate using a simple Lift-off process. This approach enables the fabrication of miniature columns with precise control over dimensions and geometries, which may facilitate an efficient separation of target compounds. However, this method involves microsystems processing, which is costly and time-consuming for low volume applications. Here we are using a low-cost 3D printer (Elegoo Mars 4 Ultra) that can write micro-channels into a plastic resin in less than an hour.

One of the proposed applications of a portable µ-GC system is in plant pest control, which in turn could lead to the reduction of pesticide use. Plants emit specific volatiles when diseased or attracted by pests and one of identified compounds, 2-methyl butanol, is used for preliminary characterization of the proposed 3D printed µ-GC.

Design, Fabrication and Methodology

In this preliminary study, we have made a relatively short column length of 1.2 m (see Figure 1). The overall dimensions of the printed µ-GC substrate are 40mm × 40mm × 5mm (length, width, and height) with a channel length of approximately 1.2 m, width of 0.5 mm, and depth of 0.4 mm. The channel walls were injection coated with an OV-1 stationary phase and the substrate sealed with 1.0 mm thick polyethylene terephthalate (PET) sheet. The µ-GC performance was investigated by employing ScioSense ENS161 metal oxide gas sensors before (S1) and after (S2) the µ-column (see Figure 2). 2-methyl butanol was chosen to assess the performance of the fabricated µ-GC column. Upon exposure to 2-methyl butanol, S2 showed delayed and reduced magnitude response curves as compared to S1 indicating that the compounds are affected by the OV-1 film. The variation in S2 response can be utilized to calibrate the µ-GC for different compound molecules.

A photograph of the entire designed column is shown in Figure 1(a) together with an insert revealing the channel dimensions and shape. Figure 1(b) shows the final OV-1 coated and fully sealed 3D printed µ-GC.

The µ-GC coating was prepared by first dissolving 0.025g of OV-1 in 5 ml of dichloromethane. The solution was then injected into the channel while the µ-GC substrate was placed on top of a hotplate set to 45^{o}C. Afterwards, UV resin was spun coated on PET substrate and placed on the channel surface for sealing. The device was then tested for leaks before final assembly into the prototype system. Figure 2 depicts the µ-GC setup, comprising the two sensor chambers housing metal oxide sensors, the fully sealed µ-GC column, and a microcontroller (Feather TFT: ESP32-S3). In this arrangement,

the target VOCs pass first through the S1 chamber, then the µ-GC column, and finally the S2 chamber, while the microcontroller continuously monitors the resistance change of both sensors over time.

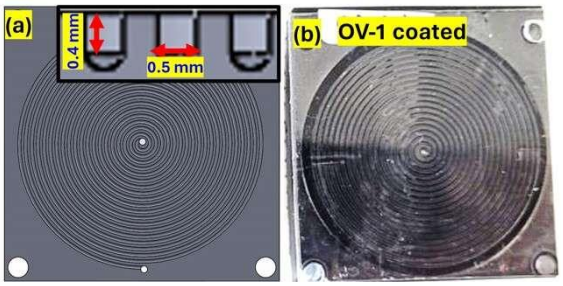

Fig. 1. (a) CAD design (b) sealed µ-GC.

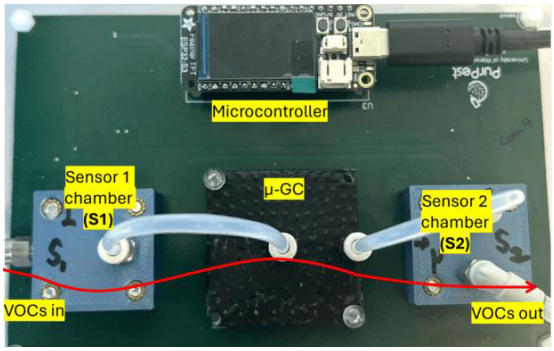

Fig. 2. µ-GC based e-nose.

Results and Discussions

Fig. 3 shows the response of sensors S1 and S2 to the mixture of 0.7 ppm pulses of 2-methyl butanol and 0.2 ppm of ethanol as a known interferant. Results indicate that OV-1 coated µ-GC column absorbs the compounds and releases them when dry air flows through the channel. This causes a delay and reduction in S2 response magnitude. As it can be seen from the enlarged image of the first cycle that the response and recovery time for S2 were delayed around 80 s and 50 s, respectively (see Figure 3(b)). On the other hand, the response magnitude for S2 was reduced by about 66% as compared to S1.

Our preliminary results suggest that this highly economical 3D printed µ-GC column holds potential for identifying different VOCs at PPM level. This cost-effective 3D printed µ-GC offers a promising method for quick onsite analysis of compound mixtures. The integration the µ-GC in front of a multi-sensor e-nose could enhance compound classification performance [2]. Further work includes detailed parametric investigations of coating thickness, optimum temperature, flow-rate, injection pulse width, and µ-column dimensions, as well as advanced processing of the time-dependent responses.

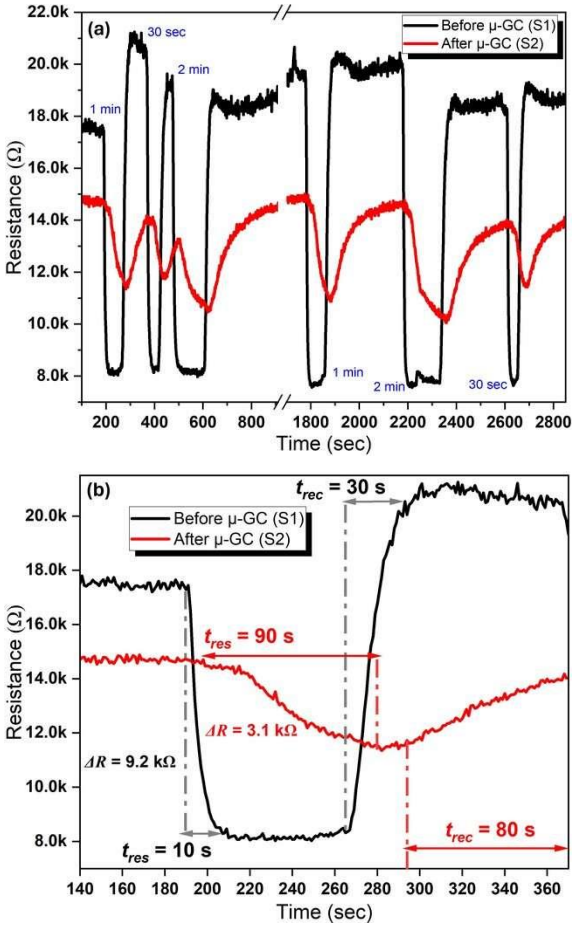

Fig. 3. Two repeats of sensors' response before and after OV-1 coated µ-GC column to 2-methyl butanol mixed with ethanol (a) at different exposure time, and (b) first cycle enlarged response curve.

References

[1] B. P. Regmi, M. Agah, Micro Gas Chromatography: An Overview of Critical Components and Their Integration, Anal. Chem. 90, 13133-13150 (2018); doi.org/10.1021/acs.analchem.8b01461

[2] F. K. Che Harun, J. E. Taylor, J. A. Covington, J. W. Gardner, An electronic nose employing dual channel odour separation columns with large chemosensor arrays for advanced odour discrimination, Sens. and Actuat. B: Chemical. 141, 134-140 (2009); doi.org/10.1016/j.snb.2009.05.036.

Acknowledgement

This work is supported by the project "PurPest under Horizon Europe Program (grant #101060634), the Horizon Research and Innovation Action (RIA) from European Research Executive Agency (REA).

DOI 10.5162/EUROSENSORSXXXVI/PT5.241

In-situ Synthesis of MIP Thin Films on QCM Electrodes to Sense Engineered Nanoparticles

Mahdieh Bagheri[1,2], Illia Selvistrovich[1], Shahin Haghdoust[1], Peter Lieberzeit[1,2]
[1 1] University of Vienna, Faculty for Chemistry, Department of Physical Chemistry, Waehringer Strasse 42, 1090 Vienna, Austria
[2] University of Vienna, Doctoral School of Chemistry, Waehringer Strasse 42, 1090 Vienna, Austria
Peter.Lieberzeit@univie.ac.at

Summary:

Herein, we report molecularly imprinted polymer (MIP) and non-imprinted polymer (NIP) thin films on quartz crystal microbalances (QCM) via in-situ polymerization to detect Engineered nanoparticles. This study focuses on controlling polymerization for controlling thickness in terms of optimal particle removal from the polymer. The sensing behavior of polymeric sensors using QCM is investigated by comparing MIP sensitivity against NIP and analyzing MIP selectivity based on particle properties.

Keywords: in-situ MIP, QCM measurement, Raft polymerization, Gold NPs, Magnetite NPs

Introduction

Detecting Engineered NPs (ENPs) is particularly important due to their extensive application in biomedicine [1], environmental monitoring, and industrial processes. Established instrumental techniques, such as single particle inductively coupled plasma mass spectrometry (SP-ICP-MS), are used to detect and characterize engineered nanoparticles (ENPs) in complex environmental matrices by measuring their concentration and size distribution[2, 3]. To address this, recent research has focused on approaches such as molecularly imprinted polymers (MIPs). However, detecting nanoparticles requires depositing very thin films on device surfaces in a reproducible manner: they need to be thinner than the particle radius.

Synthesizing

To achieve this, we report on synthesizing MIP and NIP thin films in situ on Quartz Crystal Microbalances (QCMs) using controlled radical polymerization, namely Reversible Addition-Fragmentation chain Transfer (RAFT). Methyl methacrylate (MMA) and EDGMA were used as the monomer and cross-linker in a molar ratio of 1:1. Herein, 4-Cyano-4-(phenylcarbonothioylthio) pentanoic acid (CPA) was chosen as the RAFT agent because of its high reactivity with acrylic monomers.

Here we mainly focused on imprinting gold NPs (GNPs) and magnetite NPs (MNPs) in the size range of 20–70 nm. For that purpose, it is essential to characterize polymer *growth in situ* as a function of polymerization time (PT) to control the thickness of polymer layers. During sensor measurements, QCMs served to assess the binding affinity of in-situ MIP films by comparing it against the corresponding non-imprinted polymers (NIPs) when detecting ENPs. To completely characterize the systems, the selectivity behavior of MIPs was studied based on different particle cores, shells, and particle sizes, respectively.

Results

The polymer height is investigated using a network analyzer based on the change in resonance frequencies of QCM electrodes before and after polymerization for NIP. As illustrated in Fig. 1, polymer growth was measured for two series of NIP samples over 7 hours. The results indicate that maximum growth of NIP occurred between 2 to 6 PT. The polymer thickness reached the optimal height of 10 nm after 4 hours of polymerization.

Fig. 2 shows the AFM images of gold MIP surfaces after removing NPs, confirming successful imprinting of 75 nm GNPs onto the MIP surface without polymer overgrowth. The AFM height profiles of two different particle spots (1,3) display cavities in the polymer surface aligning well with the size and shape of GNPs.

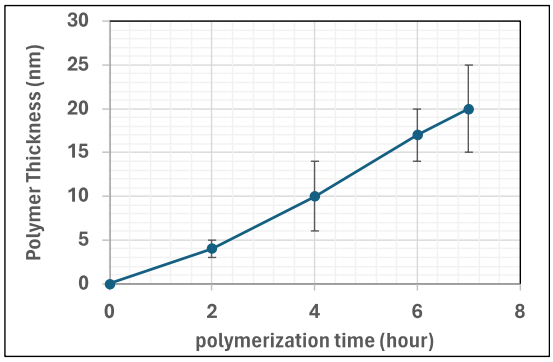

Fig. 1. Growth of polymer thickness as a function of a polymerization time (PT=1-7 hours) for NIP

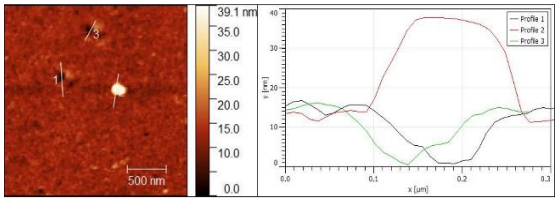

Fig. 2. Left-hand side AFM images of GNPs MIP surface after polymerization and particle removal. On the right-hand side profile of the particle and cavity size.

After successful imprinting, the NPs are removed from the polymer and leave behind cavities that selectively bind to the target NPs. MNPs removal was facilitated by a magnet, while for GNPs, the outer layer of NPs covered with 16-MHDA instead of PVP shell as a hydrophilic layer, ensuring effective washing off from cavities. Table 1 summarizes the responses average of MNPs MIP and the respective measured signals of NIP channels in 2mM citrate buffer as the background at c= 6e^{15}, 3e^{15}, 1.5e^{15}, and 7.5e^{14} n/L, respectively. The corresponding limit of detection is around 8.25e^{13} n/L NPs based on the noise of the bassline and slop of MIP sensor characteristics.

Table 1. Sensor responses of both MNPs MIP and NIP sensors, at listed concentrations on QCM.

MNP concentration (n/L)	Average signal of two-MIP channels (Hz)	Average signal of two-NIP channels (Hz)
6e ^{15}	-550	-180
3e^{15}	-271	-78
1.5 e^{15}	-137	-35
7.5e^{14}	-68	-12

Alternatively, the surface of MIP was characterized using AFM to verify the binding of the MNPs directly into the cavities.

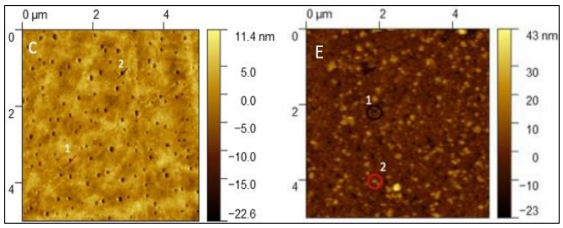

Fig. 3. The right-hand side AFM image is the MIP surface after MNPs removal and washing the polymer surface, Left-hand side AFM image of the MIP surface after rebinding MNPs to the MIP surface.

Selectivity studies revealed that the binding process of NPs is controlled by their shell properties, such as zeta potential, pH, and functional groups, while sensitivity strongly relies on the respective core materials. The selectivity factor of the MNPs-PVP sensor against its PVP stabilizer is approximately 9.3. Moreover, the imprinted MNPs-PVP film demonstrates high selectivity against MNPs with the same diameter but with an oleic acid shell, with a relative selectivity of only 14% compared to the MNPs-PVP sensor response. The MNP MIP sensor exhibits selectivity factors of approximately 67% and 6% against 20 nm and 60 nm SiO2 NPs with silanol surfaces, respectively. Similarly, against 20 nm and 40 nm TiO2 NPs containing surface hydroxyl groups, the corresponding selectivity factors are 48.1% and 15%, respectively. These results underscore the significant size and shell selectivity of the in-situ synthesized MIP. However, when competitor NPs and target NPs share the same size, these factors are inherently lower.

References

1. M. Bundschuh, et al., Nanoparticles in the environment: where do we come from, where do we go to? *Environmental Sciences Europe* 30,6 (2018); doi:10.1186/s12302-018-0132-6

2. A. Grasso, M. Ferrante, et al., Chemical Characterization and Quantification of Silver Nanoparticles (Ag-NPs) and Dissolved Ag in Seafood by Single Particle ICP-MS: Assessment of Dietary Exposure, *international Journal of Environmental Research and Public Health 18, 4076 (2021);* doi:10.3390/ijerph18084076

3. Proulx, Kim et al. "Separation, detection and characterization of nanomaterials in municipal wastewaters using hydrodynamic chromatography coupled to ICPMS and single particle ICPMS." Analytical and bioanalytical chemistry 408, 5147-55 (2016); doi:10.1007/s00216-016-9451-x

DOI 10.5162/EUROSENSORSXXXVI/PT5.242

Combustion-Aerosol made Chemoresistive Gas Sensors and Devices

Andreas Güntner
Human-centered Sensing Laboratory, ETH Zürich, Sonneggstr 3, 8092 Zürich, Switzerland.

Corresponding Author's e-mail address: andregue@ethz.ch

Summary:
Advances in combustion-aerosol gas sensors enable today mobile health monitoring, on-site food safety assessment and air quality tracking to immediately alert people of potential hazards. This presentation will discuss examples of sensors made by combustion aerosol technology highlighting their distinct advantages over traditional wet chemistry processing. These advantages are traced to combustion's steep temperature gradients and high particle concentrations during sensing particle formation and film deposition. Finally, sensor systems (arrays and filters) and their integration into devices with validation under realistic conditions is presented.

Keywords: Chemoresistive sensor, Gas sensor, Nanotechnology, Porous films, Inorganic materials

Flame-made gas sensors enable today hand-held devices [1] for mobile health monitoring, on-site food safety assessment and air quality tracking to immediately alert people of potential hazards. Therein, combustion aerosol technology has distinct advantages for the assembly of chemoresistive gas sensors compared to their traditional wet chemistry synthesis. These advantages are traced to combustion's steep temperature gradients and high particle concentrations during sensing particle formation. This gives direct access to a plethora of material compositions (e.g. metastable phases, solid solutions, mixed oxides) and fractal-like porous but rigid structures that can lead to unique sensor selectivity, sensitivity and stability along with short response and recovery times [2].

The characteristics of sensing films and their operation determine the performance of gas sensors. Figure 1 summarizes the assembly of flame-made gas sensors. Conventionally they are put together using flame-made metal-oxide particles collected on filters. Then, such particles are suspended in fluids to form slurries or pastes that are screen-printed, doctor-bladed, drop- or spin-coated onto sensor substrates followed by drying and stabilization annealing to form the sensing films. Alternatively, such films are assembled by flame-aerosol deposition onto sensor substrates bypassing all wet-chemistry steps. These films are grown by combustion of appropriate precursors and deposition of either molecular clusters (i.e., Combustion Chemical Vapor Deposition) or particles. During such deposition, the electric resistance of the sensing film can be measured online to optimally determine its thickness and interconnectivity [3].

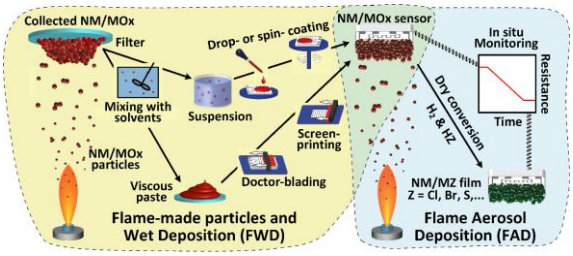

Fig. 1. Gas sensing films by flame-made noble metal / metal oxide particles and their wet chemistry deposition or flame aerosol deposition to sensing substrates with optional resistance monitoring and even in situ reduction (e.g. with H_2) - conversion to non-oxide films. Adapted from [1].

An inherent limitation of flame-made gas sensors is their limitation to metal-oxides due to the oxidizing flame environment. Here, I will discuss how such metal-oxide films can be converted to metal bromides, sulfides or nitrides by post-deposition exposure to reactive gas atmospheres, while preserving the porous architecture of flame-aerosol deposited films (Figure 2). This opens new avenues for unique sensing performance, even at room temperature [4].

In this presentation, recent advances on the design of gas sensors based on metal-bromide (e.g., CuBr) and -nitrides will be presented that enable the quantification of air pollutants like NO_2 and NH_3 down to few part-per-billion concentrations at high relative humidity. We will elaborate on film morphology and material

composition effects and discuss structure-function relationships.

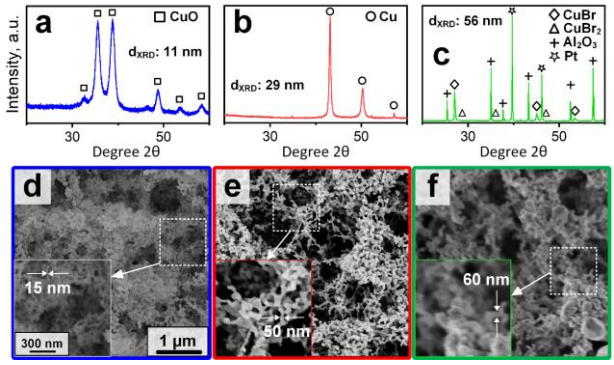

Fig. 2. *XRD patterns of powders (a-b) and when deposited as film (c) by flame spray pyrolysis as-prepared (a), after the dry reduction (b) and bromination (c) together with top-view SEM images of the corresponding films (d-f). Note that a and b were obtained from the powders as the XRD signals of the actual films were too weak. Reference peak positions for monoclinic CuO (squares), cubic Cu (circles), cubic CuBr (diamonds), monoclinic $CuBr_2$ (triangles), cubic Pt (stars) and rhombohedral Al_2O_3 (crosses) are indicated together with crystal sizes of CuO (a), Cu (b) and CuBr (c), as calculated by Rietveld refinement from the XRD patterns. Note that the Pt and Al_2O_3 in c are associated to the substrate. Adapted from [2].*

References

[1] Güntner, A.T., D'Andria M., van den Broek, J. (2023) *Nature Rev. Bioeng.* 1, 385-387; doi: 10.1038/s44222-023-00068-y

[2] Güntner, A.T., Pineau, N.J., Pratsinis, S.E. (2022) *Prog. Energy Combust. Sci.* 90, 100992; doi: 10.1016/j.pecs.2022.100992

[3] Blattmann, C.O., Güntner, A.T., Pratsinis, S.E. (2017) *ACS Appl. Mater. Interfaces* 9, 23926−23933; doi: 10.1021/acsami.7b04530

[4] Güntner, A.T., Pineau, N., Pratsinis, S.E. (2020) *Adv. Sci.* **7**, 1903390; doi: 10.1002/advs.201903390

DOI 10.5162/EUROSENSORSXXXVI/PT5.250

Co_3O_4-NiO Nanocomposites for the Electrochemical Determination of L-Tyrosine

*Madiha Khan[1,*2], Khouloud Abid [1,2], Viviana Bressi [1], Giovanni Neri [1]*

[1] *Department of Engineering, University of Messina, C.da Di Dio,1-98166 Messina, Italy; madihakhan7121992@gmail.com, khouloud.abid@unime.it , vibressi@unime.it, , giovanni.neri@unime.it*
[2]*Department of Physics, Air University, PAF complex, E-9, Islamabad, 4400, Pakistan; madihakhan7121992@gmail.com*
[3] *CNR IPCF Istituto per i Processi Chimico-Fisici, viale F. Stagno D'Alcontres 37, Messina, Italy.*

Corresponding Author's e-mail address madihakhan7121992@gmail.com

Summary:

Co_3O_4-NiO nanocomposites at different molar ratios have been prepared using a simple sol–gel method. The composite were used as electrode materials for detecting L-tyrosine, modifying a screen printed electrode (SPCE). The electrochemical sensor response to L-Tyrosine (concentration-Tyr) in PBS pH=7.4 and at [0μM–100μM] has been investigated by using cyclic voltammetry (CV).Results obtained demonstrated that the composite Co_3O_4-NiO/SPCE sensors exhibit good electroanalytical performances, with a maximum of sensitivity exibited at a Co_3O_4:NiO ratio = 1.

Keywords: Cobalt Oxide-Nickel Oxide nanocomposite, Tyrosine, Electrochemical sensor.

Introduction

Tyrosine (Tyr) is an aromatic amino acid critical to the synthesis of compounds such as neurotransmitters and melanin [1,2]. Abnormal Tyr concentrations in plasma/urine can also be used as a biomarker in the detection of various diseases like alkaptonuria, tyrosinemia, and liver disease [3]. Therefore, an easy quantification assay of Tyr is critical. To attend this purpose, researchers have developed numerous analytical methods. However, implementing such methods is expensive and complex, thus, the necessity of the development of a sensitive and low-cost platform for the determination of Tyr is mandatory.

In this study, Co_3O_4-NiO nanocomposites (NCs) are synthesized through the sol-gel method and employed to improve the detection of Tyr by means of electrochemical sensors, modified by NCs of different Co_3O_4-NiO ratios.

Materials and Methods

a. Co3O4-NiO preparation

The synthesis of Co_3O_4-NiO NC was carried out as follows: first, 1.19g of Co_3O_4 was dissolved in 10mL of hydrochloric acid (HCl) and continuously stirred at room temperature until the solution became transparent and uniform. Then, various quantities of pure nickel oxide at 0.186 and 0.37g were dissolved in 2M citric acid (HOC (CO2H) ($CH_2CO_2H)_2$) solution and stirred at room temperature till the solution became transparent and uniform.
Subsequently, the Co_3O_4 and NiO solutions were mixed and placed on a heating plate at a temperature of ~350°C. The materials were fully burned, and, in this way, two samples were obtained with different Co_3O_4-NiO molar ratios. At last, the powdered samples were annealed in a glass furnace for 2 hours at 400°C.

b. Electrode preparation.

The modified SPCE electrodes are prepared by a simple drop-casting method with Co_3O_4-NiO NC. Herein, 1mg of Co_3O_4-NiO NC is dissolved in 1mL aqueous solution was assembled through the dispersion of 1 mg Co_3O_4-NiO NC and ultrasonication for 1 hour.

a. Electrochemical tests.

The modified screen-printed carbon electrode (SPCE) were prepared by dispersing the NC electrode materials on the working carbon electrode of SPCE platform (Metrohm-DropSens). All electrochemical analyses were performed using a Metrohom Autolab galvanostatic potentiostat equipped with NOVA 2.1 data acquisition software.

Results and Discussion

XRD patterns are depicted in Figure 1. Reflection peaks of NiO and Co_3O_4 are observed in the diffraction patterns oft he composite samples, indicating they are through composites.

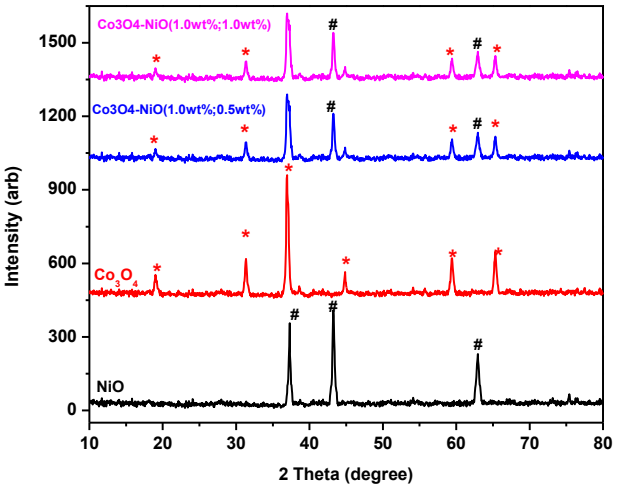

Fig.1. XRD spectra of pure NiO (black line), pure Co_3O_4 (red line), Co_3O_4-NiO(1.0wt%;0.5wt%) (blue line), and Co_3O_4-NiO(1.0wt%;1.0wt%) (pink line)

a. Electrochemical Tests

The L-Tyr determination is performed by voltammetric technique at different concentrations (see Figure. 2a) to compare the sensitivity of the modified electrodes Calibration curves are plotted and presented in Figure.2b, showing that the composite Co_3O_4-NiO/SPCE sensors exhibit good electroanalytical performances, with a maximum of sensitivity exibited at a Co_3O_4:NiO ratio = 1.

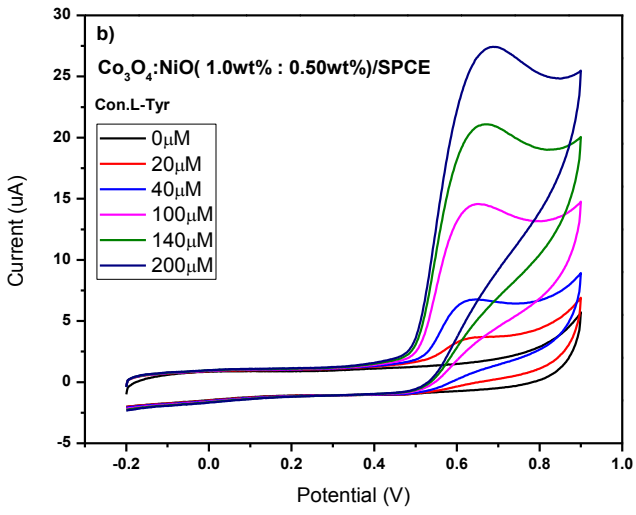

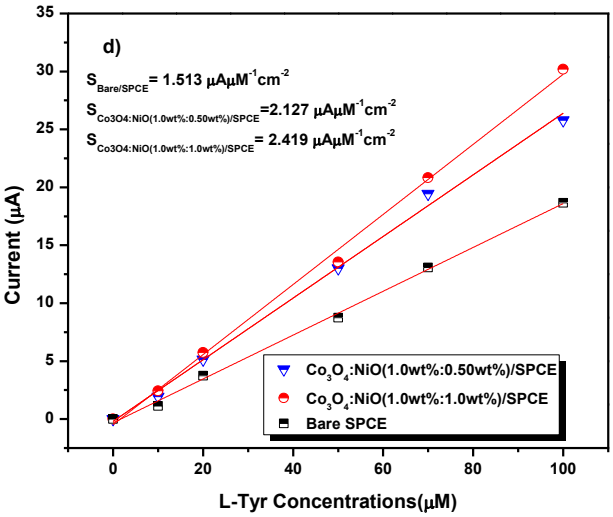

Figure.2. a) CV test in PBS solution containing L-Tyr (0μM-200μM) at 50mV/s scan rate on (a) Co_3O_4LNiO (1.0wt%:0.5wt%) and d) the calibration curve.

Conclusion

Co_3O_4-NiO NCs have been synthesized successfully via the sol–gel method .XRD, SEM and EDX measurements indicate a NC structure and the presence of crystalline metal oxide nanoparticles. More studies are to be done in order to optimize the synthetic approach to improve the quality of Co_3O_4-NiO doped films, which to the best of our knowledge may represent a new electrode material for electrochemical sensing applications.

References

[1] Alkawsi, G., et al., Review of Renewable Energy-Based Charging Infrastructure for Electric Vehicles. Applied Sciences, 2021. **11**(9): p. 3847.

[2] Hosny, N.M., Synthesis, characterization and optical band gap of NiO nanoparticles derived from anthranilic acid precursors via a thermal decomposition route. Polyhedron, 2011. **30**(3): p. 470-476.

[3] Danjumma, S.G., Y. Abubakar, and S. Suleiman, *Nickel oxide (NiO) devices and applications: a review.* Int. J. Eng. Res. Technol, 2019. **8**: p. 12-21.

DOI 10.5162/EUROSENSORSXXXVI/PT5.255

Colorimetric sensor based on silver faujasite for chlorogenic acid polyphenol detection

João Otávio Donizette Malafatti[1], Elaine Cristina Paris[1], Luiz Henrique Capparelli Mattoso[1]

[1] Nanotechnology Laboratory for Agriculture (LNNA), Embrapa Instrumentação, XV de Novembro St., 1452, zip code 13560-970, São Carlos - SP, Brazil.

Corresponding Author's e-mail address jmalafatti@hotmail.com

Summary:

Silver-based materials show a great potential to be applied in sensors due to their optical, electronic, and chemical properties. In this work, we report the use of a zeolite framework modified with silver ions as a colorimetric sensing array for the detection of chlorogenic acid (CGA). The detection was done by digital image colorimetry (DIC) based technique integrated with a smartphone. Red, green, and blue (RGB) was able to monitor CGA in the range of 1 – 20 mg L^{-1}. with the limit of detection (LOD) of 0.39 mg L^{-1}.

Keywords: polyphenol, coffee, smartphone, zeolite, silver.

Background, Motivation an Objective

Coffee is one of the most widely consumed drinks in the world and is a commodity with high production and significance. The coffee beans are obtained after washing stages to remove impurities, drying, and peeling the skin. Wetting rote eliminates coffee compounds, increasing the quality of the final bean [1]. The elevated abundance of CGA makes this polyphenol an indicator of the polyphenols and quality products [2]. *Colorimetric sensors* are a promising alternative, in which the color change occurs by analyte and sensor array interaction turns easy visual monitoring [3]. Silver-based materials are highly suitable for sensor platforms to electrons on the surface interacting with electromagnetic radiation in the visible spectrum region (400 nm). Thus, the target molecule promotes a surface modification accompanied by a change in color [4]. A colorimetric sensor applied to CGA polyphenol has yet to be fully elucidated [5], making further studies necessary. Therefore, this study aimed to evaluate a sensor based on faujasite zeolite with a surface modified with Ag^{+} ions (AgFAU) as a colorimetric sensor for detecting the polyphenol CGA.

Description of the New Method or System

The colorimetric detection was performed by using a FAU-Ag dispersion (1 mg mL^{-1}) in sodium carbonate/bicarbonate buffer (pH 10.7). Different concentrations of CGA (1, 2.5, 5, 7.5, 10, 15 and 20 mg L^{-1}) were added to the FAU-Ag dispersion. RGB color detector smartphone APP was employed to obtain the color space parameters R (red), G (green), and B (blue) for statistical analyses. The photos were taken using a portable mini studio box (InstaFold) with cold white LED6000L lighting and defined dimensions (38 cm height, 36 cm length, and 39 cm depth). The box has an upper opening accommodating the cell phone and a fixed working distance. Hence, the object images were protected from the external environment's illumination.

Results

The optical behavior of the AgFAU in the presence of GCA at different concentrations 1 – 20 mg L^{-1} (0 to 56 µmol L^{-1}) is exhibited in Figure 4. As can be noted, the color changed from yellow to brown as the concentration of GCA increased.

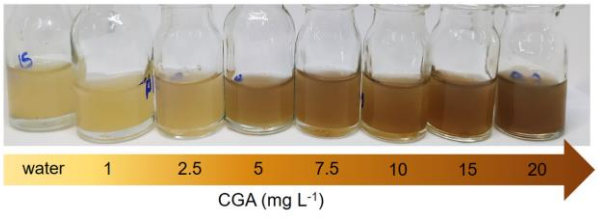

Fig. 1. FAU-Ag solution color by CGA concentration

Figure 2 shows that the R and G parameters best fit found was the cubic model with R^2 of

0.99282 and 0.98827, respectively. The best fit for the B parameter was the quadratic model with an R^2 of 0.90377. LOQ media was 1.3 ± 0.5 mg L^{-1}, being closest to the experimental result of 1 mg L^{-1} CGA, showing an adequate approach.

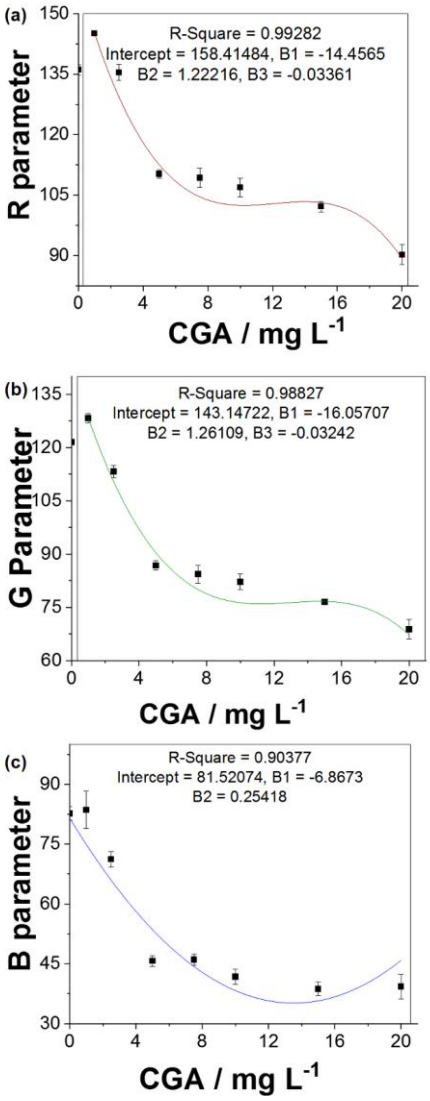

Fig. 2. Quantitative measurements of the CGA analyte from partial least square regression (PLSR)

PCA analysis shows a high dispersion at 50x dilution in the reproducibility of the analyzed samples.

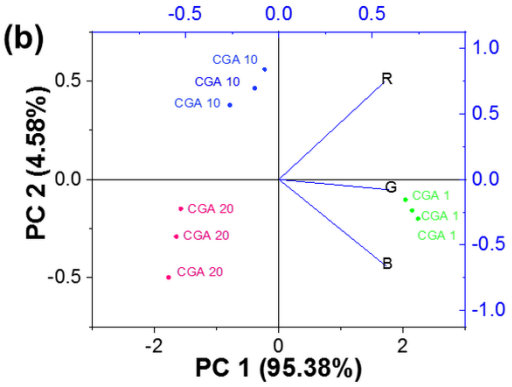

Fig. 3. PCA statistical analysis

This possible oxidative mechanism is also correlated to reactive groups in CGA molecule from hydroxyl radicals generated, causing the electron transfer. In general, phenols are associated to Fenton reactions showing as scaggering radicals (hydroxyls), maintained in a ressonance structure. As consequence, the electronic density is increased and free-radicals are avaliable to ion metal redox [6].

Acknowledgments

This study was financed by FAPESP (Grant Number 2021/14992-1, 2023/03632-0). The authors acknowledge Embrapa (Grant Number 11.14.03.001.01.00), FINEP, SisNano, and AgroNano Network for financial support.

References

[1] S. Das, *Coffee Science* 16, e161976-e161982, (2021); doi.org/10.25186/.v16i.1976

[2] W. de J. R. Santos, M. Santhiago, I. V. P. Yoshida, and L. T. Kubota, *Analytica Chimica Acta* 695, 44–50 (2011); doi.org/10.1016/j.aca.2011.03.018

[3] A. Piriya V.S, P. Joseph, K. Daniel S.C.G., S. Lakshmanan, T. Kinoshita, and S. Muthusamy, *Materials Science and Engineering C* 78, 1231–1245 (2017); doi.org/10.1016/j.msec.2017.05.018

[4] P. Prosposito, L. Burratti, and I. Venditti, *Chemosensors* 8, 1–29 (2020); doi.org/10.3390/CHEMOSENSORS8020026

[5] D. Yao, Y. Wang, and H. Li, *Sensors and Actuators, B: Chemical* 305, 127451 (2020); doi.org/10.1016/j.snb.2019.127451

[6] J. Tošović, S. Marković, J. M. Dimitrić Marković, M. Mojović, and D. Milenković, *Food Chemistry* 237, 390–398 (2017); /doi.org/10.1016/j.foodchem.2017.05.080

DOI 10.5162/EUROSENSORSXXXVI/PT5.285

The Right Nose for Electronic Noses

Max Köhne[1,2], Omar Tarek Penagos Carrascal[1], Gina Zeh[1], Tilman Sauerwald[1,2]
[1] Fraunhofer IVV, Giggenhauser Straße 35, 85354 Freising, Germany
[2] Saarland University, Department for Systems Engineering, 66123 Saarbrücken, Germany

Corresponding tilman.sauerwald@ivv.fraunhofer.de

Summary:
The article describes an instrument and a method for the characterization and validation of devices for instrumental odor measurement, especially miniaturized devices based inexpensive sensors. For this purpose, a test environment has been developed based on a combination of gas chromatography - mass spectrometry, odor measurement using olfactometry and sensor characterization. The system enables the connection of various gas sensors in a heated test chamber, which can be operated with an additional make-up gas flow. This allows testing conditions close to typical operating conditions, which is important for many sensor types e.g. metal oxide gas sensors. Our systems can measure rate constants for the kinetic processes on the sensor surface very efficiently allowing the modelling of virtual multi-sensors array using temperature-cycled operated (TCO). In this way, an optimized system approach can be quickly determined, set up and tested.

Keywords: instrumental odor measurement, electronic nose, gas chromatography, gas sensors

Introduction

Devices for instrumental odor measurement, so-called electronic noses, have been known for over 50 years [1] and they perform a variety of tasks in quality monitoring of raw materials and finished goods as well as in the measurement of odor emissions and environmental odors. Despite this success, the euphoria about these systems, especially in the 1990s, has not been fulfilled; small, inexpensive and fast systems still fall short in comparison to the human nose in terms of performance, especially when a large number of different odors are to be distinguished simultaneously. In addition, the training and calibration effort is very high. An efficient method of calibration could be a coupling of GC-MS/O and sensor array, which can integrate odor characterization and sensor characterization. Even though Hofmann et al. [2] described such a system as GC-SOMSA almost 25 years ago, it has not been used frequently. One reason is, that for many sensors the response to short gas pulses differs significantly from the response to static test gases. Another reason is that sensors are frequently operated in dynamic conditions, such as TCO to improve sensitivity and selectivity [3]. Therefore a sole measurement with a GC-SOMSA is not sufficient for a device characterization.

Recently we have demonstrated that a rate constant model is capable to predict the performance of sensors with TCO [4] and that short gas pulses can be used to determine the rate constants [5]. With this model it is possible to get a full characterization using a GC-SOMSA device and a small set of characterization measurements.

System concept

The test instrument (Figure 1) is based on a commercial GC (Thermo Scientific Trace 1610, Thermofisher) with mass spectrometer (Thermo Scientific ISQ 7610 Single Quadrupol Mass Spectrometer) equipped with an odor detector port (ODP). In parallel to the ODP a sensor port (SP) is connected in a split ratio of 1:1 between these ports.

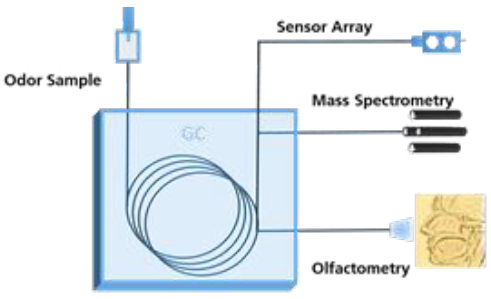

Figure 1: Schematic of the GC-SOMSA system modified after [1]

The transfer line to ODP and SP can be heated up to 200 °C to avoid condensation of semivolatiles. The sensor port is equipped with a heating cartridge, which allows a respective heating of

the sensor port. However, the temperature will be restricted by the thermal stability of the sensor electronic, which is separated only by a thin insulating layer of Teflon. The maximum temperature needs, therefore, to be tested for each type of sensor device. For integrated devices it is typically restricted to 100 °C. The chamber can be flushed with a make-up gas flow e.g. of synthetic air in the range between 0-20 sccm.

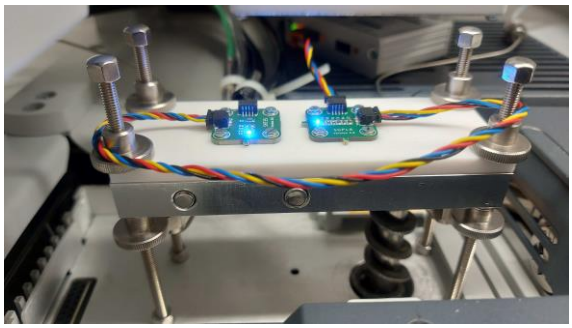

Figure 2: picture of the sensor port equipped with two sensor electronics

Sensor model

Metal oxide gas sensors can be described by a set of rate equations for the desorption and adsorption of gases at the surface. In typical operating conditions (low concentrations reducing gases in air) adsorbed oxygen is the most important species and the rate equation for the adsorption and desorption of oxygen can be used to model the sensor system. However, the rate for the desorption of oxygen is modulated by all reducing compounds, which is the case for most odorants. The desorption of oxygen is then modulated by the reaction with the reducing gas, which can typically exceed the spontaneous desorption by orders of magnitude as demonstrated in [4]. On the other hand the re-adsorption of oxygen is a relatively slow process which can be decoupled form the gas reaction. We have be demonstrated that at low operating temperature e.g. 50 °C no significant re-oxidation of the surface occurs over a period of several minutes. At higher temperature the processes still can be separated e.g. by forming the derivative of the sensor signal as long as the oxygen adsorption/desorption has a higher time constant as the reaction of oxygen with reducing gas.

Discussion

The development of electronic nose could profit from the recent advances in sensor integration as highly integrated gas sensor devices [6] enabling temperature-cycled operation at very low costs per item are available. However, system characterization and validation is often very costly and inhibit the use of those devices. To address this shortcoming, we have described of system and process for the characterization and validation of instrumental odor measurement devices and combined it with a recent model for gas sensors in temperature-cycled operation. This regenerates a very powerful tool for the development of new application specific solutions for odor measurement. The system is not only limited to this application, but can also be utilized for the development of small sensor-GC systems.

Literature

[1] J. W. Gardner, P. N. Bartlett, “A brief history of electronic noses“, Sensors and Actuators B, vol. 18-19, pp. 211-220, 1994.

[2] T. Hofmann, P. Schieberle, C. Krummel, A. Freiling, J. Bock, L. Heinert, D. Kohl, High resolution gas chromatography/selective odorant measurement by multisensory array (HRGC/SOMSA): a useful approach to standardize multisensory arrays for use in the detection of key food odorants, Sensors and Actuators B 41 (1997) 81-87

[3] A. Schütze and T. Sauerwald, “Dynamic Operation of Semiconductor Sensors,” in Semiconductor Gas Sensors, 2nd ed., R. Jaaniso and O. K. Tan, Eds. .

[4] C. Schultealbert, T. Baur, A. Schütze, S. Böttcher, and T. Sauerwald, “A novel approach towards calibrated measurement of trace gases using metal oxide semiconductor sensors,” Sensors Actuators B. Chem., vol. 239, pp. 390–396, 2017,

[5] T. Baur, A. Schütze, and T. Sauerwald, “Detection of short gas pulses for trace gas analysis,” Tech. Mess., vol. 84, no. s1, 2017, doi: 10.1515/teme-2017-0035.

[6] D. Rüffer, F. Hoehne, and J. Bühler, “New digital metal-oxide (MOx) sensor platform,” Sensors (Switzerland), vol. 18, no. 4, 2018

DOI 10.5162/EUROSENSORSXXXVI/PT5.289

High Performance Potentiometric Sensor for Monitoring High Concentration Hydrogen Based on Pd-Pt Composite Electrode

Kyeong Joon Jo, Seong-Cheol Kim, Seung-Yun Lee

Department of Materials Science and Engineering, Hanbat National University, Daejeon 34158, Republic of Korea

Corresponding Author's e-mail address: sy_lee@hanbat.ac.kr

Summary:

A potentiometric high concentration hydrogen sensor including a Pd-Pt composite electrode was fabricated by combining a Pt electrode and a Pd nanoparticle layer. The hot-pressing method was used to manufacture a multilayer structure of Pt electrode/Nafion electrolyte/Pt electrode. Pd nanocolloids were synthesized using Pd powder and a solvent, and then coated on the upper Pt electrode to form a Pd nanoparticle layer. The fabricated sensor showed a fast and stable response in the hydrogen concentration range of 70 to 100%, enabling monitoring of hydrogen fuel used in fuel cell vehicles.

Keywords: hydrogen sensor, palladium, nanoparticle, composite electrode, fuel cell

Introduction

Net-zero carbon emissions policies enhance the development of hydrogen-related technologies. Detecting hydrogen leaks and measuring hydrogen concentrations are essential for hydrogen production, storage, and transportation [1]. Current hydrogen sensor technology focuses on detecting hydrogen leaks at the ppm level. However, it is not suitable for accurately monitoring high concentrations of hydrogen gas. In particular, hydrogen sensors to accurately measure the hydrogen concentration in hydrogen fuel cell vehicles, which ranges from 70 to 100%, have not been commercialized [2].

There are various types of hydrogen sensors, including metal oxide sensors, piezoelectric-based sensors, gas chromatography, and electrochemical sensors. Among them, electrochemical sensors are highly promising for practical applications due to their relatively simple structure and low power consumption. Electrochemical sensors consist of an electrode-electrolyte-electrode multilayer structure, and the catalyst within the electrode accelerates the electrochemical process. Palladium (Pd) can be used as another catalyst material together with platinum (Pt), the leading catalyst material, because hydrogen dissociation occurs on the Pd surface with a minimal activation energy barrier. Thus, in this study, we fabricated a composite catalyst electrode structure by adding a Pd nanoparticle layer to the conventional Pt catalyst electrode. Its impact on the performance of potentiometric electrochemical sensors was examined by manufacturing high concentration hydrogen sensors. The resulting sensor exhibited a more stable response to high concentrations of hydrogen, compared to the sensor containing only the Pt catalyst.

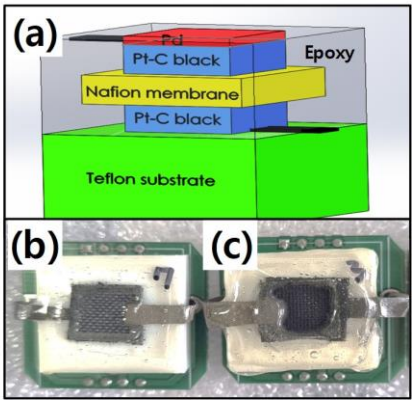

Fig. 1. (a) Schematic diagram of a high concentration hydrogen sensor with a Pd-Pt composite electrode. (b) Plan-view image of a fabricated hydrogen sensor with conventional Pt electrodes (no Pd nanoparticle layer). (c) Plan-view image of a fabricated hydrogen sensor with a Pd-Pt composite electrode.

Experimental

The Pd nanocolloid solution was prepared by mixing Pd powder and methyl isobutyl ketone solvent. Pd and methyl isobutyl ketone were

transferred to a cleaned small vial and stirred at 20 rpm for 20 min to produce a 2 wt% Pd solution. The hot-pressing method was adopted to fabricate the hydrogen sensor. A multilayer structure of Pt electrode/Nafion electrolyte/Pt electrode was manufactured under the hot-pressing conditions (temperature, time, pressure) of 60 °C, 60 sec, and 2 Mpa. The Pt electrode containing carbon paper coated with Pt-carbon black were purchased from a commercial material supplier (NARA Cell Tech). In order to form external terminals, metal tape was attached to the upper Pt and lower Pt electrodes, and the multilayer structure was sealed with epoxy, excluding the surface of the upper Pt electrode. The hydrogen sensor was completed by applying Pd solution on the Pt electrode and drying it.

Results

Fig. 1(a) shows a schematic diagram of a high concentration hydrogen sensor with a Pd-Pt composite electrode. The epoxy separates the lower counter electrode from the outside, allowing only the upper working electrode to respond to hydrogen. Fig. 1(b) and 1(c) show the hydrogen sensors manufactured using conventional Pt electrodes and a Pd-Pt composite electrode, respectively. As shown in Fig. 1(c), the color of the upper electrode appears dark black due to the coating of a Pd nanoparticle layer on a Pt electrode.

The hydrogen sensor operates based on the principle of a concentration cell. The hydrogen sensor is divided into a working electrode exposed to high concentration hydrogen gas and a counter electrode separated from the outside with epoxy. Since hydrogen dissociation occurs actively in the working electrode, hydrogen concentration can be measured by the electromotive force generated by the difference in hydrogen activity between the two electrodes.

Fig. 2(a) shows the voltage response of a hydrogen sensor employing only Pt electrodes, periodically exposed to pure hydrogen and nitrogen gases. When the sensor is exposed to pure hydrogen gas (100% H_2), significant fluctuations, in which the voltage drops to approximately −20 mV and then increases rapidly, occur. Fig. 2(b) shows the voltage response of a hydrogen sensor employing a Pd-Pt composite electrode. Unlike the previous result in Fig. 2(a), no fluctuations are observed and the sensor shows a stable voltage response. Pd activates the adsorption of oxygen ions, resulting in the reaction of hydrogen and oxygen ions to form H_2O [3]. Oxygen ions are formed from residual oxygen gas in the sensor measurement system. Thus, the use of Pd is thought to prevent voltage fluctuations by reducing a transient overshoot in hydrogen ion concentration during hydrogen injection. The T90 response time of the sensor is very fast, less than 10 seconds.

Fig. 3(b) shows the voltage response of a hydrogen sensor for a gas mixture of 70% hydrogen and 30% nitrogen (70% H_2). The electromotive force at a hydrogen concentration of 70% is smaller than that at a hydrogen concentration of 100% (Fig. 3(a)), and the electromotive force difference for the two concentrations is 11.6 mV. This indicates that hydrogen gas in fuel cell vehicles with a concentration ranging from 70 to 100% can be effectively monitored using the hydrogen sensor based on Pd-Pt composite electrode.

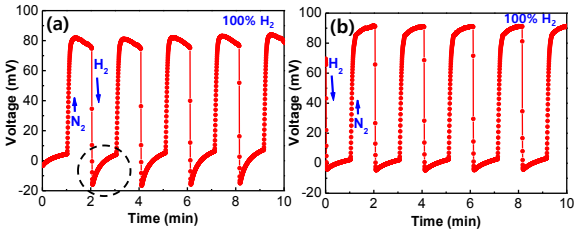

Fig. 2. Response curves of hydrogen sensors with different electrodes: (a) conventional Pt electrodes, (b) Pd-Pt composite electrode.

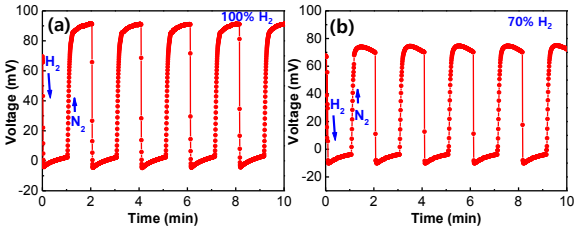

Fig. 3. Response curves of a hydrogen sensor with a Pd-Pt composite electrode, exposed to different hydrogen concentrations: (a) 100%, (b) 70%.

References

[1] T. Hübert, L. Boon-Brett, G. Black, U. Banacha, Hydrogen sensors – A review, *Sensors and Actuators B* 157, 329-352 (2011); doi: 10.1016/j.snb.2011.04.070

[2] Y. Liu, Y. Lei, X. Mao, H. Qian, H. Wen, S. Xia, Y. Xiang, Q. Chen, B. Xie, J. Hu, Wide-concentration-range hydrogen sensing using palladium-loaded SnO_2 nanoparticle films and understanding of hydrogen concentration-dependent sensing mechanism, *International Journal of Hydrogen Energy* 62, 783-793 (2024); doi: 10.1016/j.ijhydene.2024.03.037

[3] J. Park, J. Yoon, Humidity dependence removal technology in oxide semiconductor gas sensors, *Journal of the Korean Institute of Electrical and Electronic Material Engineers* 37, 347-357 (2024); doi: 10.4313/JKEM.2024.37.4.1

DOI 10.5162/EUROSENSORSXXXVI/PT5.291

Development of fluorimetric chemosensor for GBL detection in saliva and beverages

Jordi Roig [1,2] Carlos Herrera,[1,2] Salvador Gil, [1,2,3] Jose A. Sáez[1,2], Pablo Gaviña [1,2,3]
[1]Instituto Interuniversitario de Investigación de Reconocimiento Molecular y Desarrollo Tecnológico (IDM), Universitat Politècnica de València, Universitat de València, Spain
[2]Departamento de Química Orgánica, Universidad de Valencia,Doctor Moliner 50, 46100,Burjassot, Valencia, Spain
[3]CIBER de Bioingeniería, Biomateriales y Nanomedicina (CIBER-BBN), Spain

jordi.roig@uv.es

Summary:
γ-butyrolactone (GBL), a substance commonly used in various industries, has gained notoriety as a drug-facilitated sexual assault (DFSA) agent due to its rapid conversion to γ-hydroxybutyric acid (GHB) in human metabolism. The increasing illicit use of GBL has led to the development of assays for its rapid detection, thereby stimulating interest in optical sensors able to detect it. Herein we present a new fluorescent chemosensor that has been developed for the fast and reliable detection of GBL in saliva and soft drinks as well as alcoholic beverages.

Keywords: GBL, optical chemosensor, GHB, naphthoxazole, fluorescein

Background, Motivation and Objective

γ-butyrolactone (GBL) is a chemical substance that is commonly used as a solvent or additive in the manufacture of fertilizers, herbicides and pharmaceuticals. In recent years, it has been employed as a drug-facilitated sexual assault (DFSA) agent [1]. Following its oral intake, GBL is rapidly metabolized into γ-hydroxybutyric acid (GHB), one of the most used drugs in chemical submission assaults due to its sedative effect on the body [2]. The increasing illicit use of GBL has prompted us to develop simple yet sensitive assays for its in situ detection in alcoholic and soft drinks, as well as in biological matrices such as saliva.
Previously, we reported two new optical probes based on the naphthoxazole core to detect GHB in real-time in real samples of soft drinks and alcoholic beverages and saliva [3]. This discovery prompted us to design a fluorescent chemosensor to further increase the sensitivity and selectivity in the detection of GBL in saliva and in alcoholic beverages. The chemosensor is based on a fluorescein derivative in which a naphthoxazole ring is present.

Description of the New Method or System

To synthesize this new fluorescent chemosensor, 3-Amino-2-naphthoxazole was reacted with fluorescein-5-isothiocyanate and triethylamine to form the corresponding thiourea. Next, tetrabutylammonium iodide and hydrogen peroxide were added to form the corresponding 2-aminonaphthoxazole (see **Figure 1**).

The application of basic medium results in the activation of the lactone present in the fluorescein moiety of the new chemosensor, thereby initiating the generation of a fluorescent signal. From there, the acid-base properties of GBL are harnessed to induce a quenching of the fluorescence of the chemosensor (see **Figure 2**).

Results

The detection of GBL was conducted in aqueous media, saliva, and soft drinks/alcoholic beverages. A qualitative detection limit could be established visually in both aqueous media and saliva. Furthermore, optimal conditions for the detection of GBL in alcoholic beverages have been identified.

Illustrations, Graphs, and Photographs

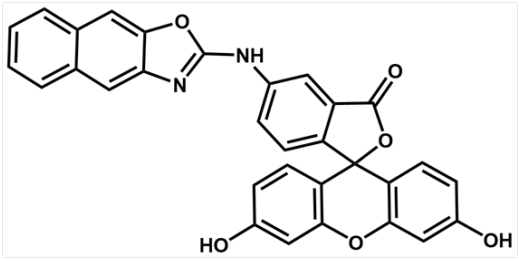

Fig. 1. Structure of the fluorescent chemosensor used in the detection of GBL.

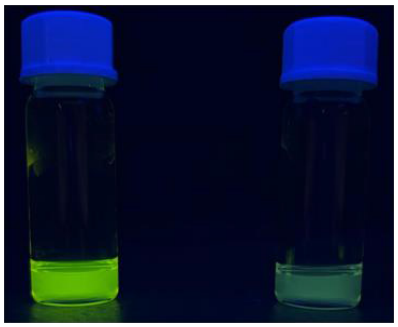

Fig. 2. ON-OFF fluorescence change observed under UV light of the chemosensor in the presence of GBL.

References

[1] A. Alías, M. I. Folgar, C. S. Taboada, A. R. Boubeta, K. Mccartan, Drug-facilitated sexual assault and chemical submission. *Pychology, Society, & Education* 9, 263-282 (2017); doi: 10.25115/psye.v9i2.701

[2] L. Dufayet, S. Bargel, *et al.,* Gamma-hydroxybutyrate (GHB), 1,4-butanediol (1,4-BD), and gamma-butyrolactone (GBL) intoxication: A state-of-the-art review, *Regulatory Toxicology and Pharmacology* 142, (2023); doi: 10.1016/j.yrtph.2023.105435

[3] S. Rodríguez-Nuévalos, A. M. Costero, *et al.,* Protection against chemical submission: Naked-eye detection of gamma-hydroxybutyric acid (GHB) in soft drinks and alcoholic beverages. *Chemical Communications* 56, 12600-12603 (2020); doi: 10.1039/D0CC05387B

Acknowledgments

The authors gratefully acknowledge grant PID2021-126304OB-C42 funded by the Spanish MCIN/AEI/10.13039/501100011033 and by “ERDF A way of making Europe, EU” and grant PDC2022-133576-C22 funded by the Spanish MCIN/AEI/10.13039/501100011033 and by the European Union “NextGenerationEU”/PRTR”. SCSIE (Universidad de Valencia) is gratefully acknowledged for all the equipment employed. NMR of compounds was registered at the U26 facility of ICTS “NAMBIOSIS” at the Universitat of València.

DOI 10.5162/EUROSENSORSXXXVI/PT5.296

Metal-Organic Frameworks (MOFs)-Based Chemoresistive gas Sensors for Early Thermal Runaway Detection in Lithium-ion Batteries

Ignasi Fort-Grandas[1,2,3], Safa Aljemazi[2], Anna Estany-Macià[1,2], Yuzelfy Mendoza-Gamero[1,2,3], Paolo Pellegrino[1,2], Manel López[1,2], Christophe Serre[1,2], Arnald Grabulosa-Rodriguez[2,3], Mauricio Moreno-Sereno[1,2], Daniel Sainz[2,3], Anton Vidal-Ferran[2,3,4], Guillem Domènech-Gil[1,2], Albert Romano-Rodriguez[1,2,]*

[1] Department of Electronic and Biomedical Engineering, Universitat de Barcelona (UB), 08028 Barcelona, Spain

[2] Institute of Nanoscience and Nanotechnology (IN2UB), Universitat de Barcelona (UB), 08028 Barcelona, Spain

[3] Department of Inorganic and Organic Chemistry, Universitat de Barcelona (UB), 08028 Barcelona, Spain

[4]Catalan Institution of Research and Advanced Studies (ICREA), 08010 Barcelona, Spain

Corresponding Author's e-mail address: albert.romano@ub.edu

Summary:

Lithium-ion batteries (LiB) are used nowadays in a large number of applications, from electric vehicles to mobile phones and laptops, among others. The hazard of the operation of the LiBs is their thermal runaway, which can give rise to fire and explosion. Prior to these processes and while the battery is degrading, toxic and flammable gases are generated, whose detection could help in reducing the hazards. In this work, we synthesize conductive metal-organic frameworks (MOFs) and we prepare and we test them as room-temperature chemoresistive sensors for CO_2, CH_4 and H_2.

Keywords: chemoresistive gas sensors, metal-organic frameworks (MOFs), tryphenylene, lithium-ion batteries, thermal runaway

Background, Motivation and Objective

Lithium-ion batteries (LIBs) are used nowadays in a large number of applications, like electrical vehicles, laptops, mobile phones, … From the safety point of view, the major risk of LiB is their potential thermal runaway due to overcharging, internal/external short circuiting, and thermal failure, which can give rise to fire and explosion. During the initial stages of these runaway processes and before any reduction in the output voltage can be detected, the battery emits toxic and flammable gases, mainly CO_2 and H_2, but also CO, C_xH_y and VOCs [1]. Detecting these gases at an early stage could help in preventing the mentioned hazards.

Chemoresistive gas sensors based on metal oxides are known for more than 50 years and present high sensitivity to several gases, low cost, small size, easy operation and integration capabilities, but usually require high operating temperatures, making them not suitable for their integration into batteries. Promising results of chemoresistance at room temperature (RT) operation has been obtained with a specific family of metal-organic framework materials (MOFs), those based on triphenylene ligands [2,3]. In this work we will present the results of chemoresistive gas sensor fabrication and their response to several of the gases relevant in LiB degradation.

Methodology

For the formation of the MOF, hexahydroxytriphenylene (HHTP) has been used as the ligand and has been mixed with different metallic salts of cupper or nickel, following a modified route to the one described in [3]. The resulting black powder was collected by centrifugation, washed several times with distilled water and ethanol, and dried under nitrogen flow. These powders were structurally and chemically characterised to confirm the MOF formation and the crystalline nature.

For the fabrication of the resistive devices, the MOF powder was dispersed in water and drop casted onto either fused silica or oxidised silicon substrates containing interdigitated Cr/Au electrodes, which were fabricated using photolithography, metal deposition and lift-off processes. These devices were first electrically

characterised at room temperature to determine their I-V characteristics. The devices were next introduced in a self-designed gas tight chamber and were exposed to different pulses of the gases of interest, diluted in dry air, while their electrical resistance was monitored.

Results and discussion

The structural characterisation confirmed the crystalline nature of the MOFs, with typical pore size in the range of 1.9 to 2.1 nm, while the overall crystallite size is in the range of few to several hundreds of nanometres.

The chemoresistive sensing behaviour of these devices is demonstrated by exposing, e.g., to a pulse of 150 ppm of CO_2 diluted in dry air, as presented in Figure 1, showing a resistance increase of about 2%, while the baseline resistance is almost recovered after removal of the gas. This suggests some poisoning of the sensors during operation, which is consistent with the high absorption properties of this material, which is largely investigated for CO_2 capture [4].

The complete gas sensing response of the devices will be presented and discussed during the presentation. A critical discussion of the feasibility of these devices for early thermal runaway detection in LiB will be carried out.

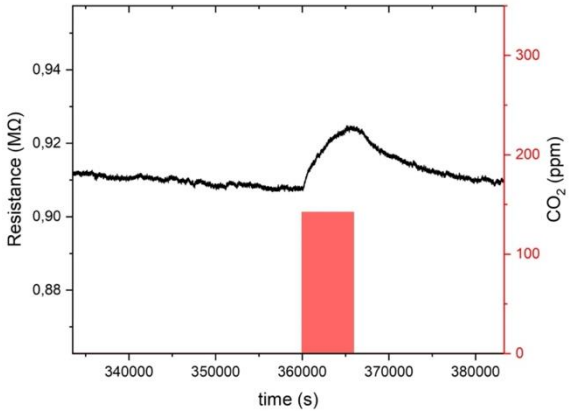

Fig. 1. Resistance variation of a $Cu_3(HHTP)_2$ MOF in the presence of 150 ppm of CO_2 diluted in dry synthetic air.

References

[1] C. Essl, L. Seifert, M. Rabe, A. Fuchs: Early detection of failing automotive batteries using gas sensors, *Batteries* 7, 25 (2021); doi: 10.3390/batteries

[2] W.T. Koo, J.S. Jang, I.D. Kim: Metal-Organic Frameworks for Chemiresistive Sensors, *Chem* 5, 1938-1963 (2019); doi: 10.1021/cr300014x

[3] M.G. Campbell, D. Sheberla, S.F. Liu, T.M. Swager, M. Dinca: Cu_3(hexaiminotriphenylene)$_2$: An electrically conductive 2D metal-organic framework for chemiresistive sensing, *Angewandte Chemie - International Edition* 54, 4349–4352 (2015); doi: 10.1002/anie.201411854.

DOI 10.5162/EUROSENSORSXXXVI/PT5.297

Multi-Gas sensor array based on SnO_2 and CuO thin films functionalized with Ag and Cu nanoparticles

Larissa Egger[1], Anton Köck[1], Alessandro Togni[2], Christian Mitterer[3]
[1] Materials Center Leoben Forschung GmbH, Roseggerstraße 12, 8700 Leoben, Austria
[2] Department of Engineering "Enzo Ferrari", University of Modena and Reggio Emilia, Modena, 41125, Italy
[3] Department of Materials Science, Montanuniversität Leoben, Leoben, 8700, Austria

Correspondence: larissa.egger@mcl.at

Summary:
We have realized a multi-gas sensor array, which employs 4 different sensor materials: bare SnO_2, and CuO films, and SnO_2, and CuO films, functionalized with Ag- and Cu-nanoparticles. The sensors have been screened towards 6 specifics get gases (CO_2, CO, NO, acetone, NH_3, specific hydrogen carbide mixture) which are relevant for air quality monitoring in the harsh environment of mines. The sensing materials show specific response to the test gases, which enables an identification of the test gases by adjusting the operation temperature and applying a proper calibration method.

Keywords: metal oxide, nanomaterials, nanoparticles, gas sensors, sensor array

Introduction

Indoor air quality (IAQ) monitoring plays an important role in public health and well-being, Poor IAQ has been linked to a variety of health issues ranging from transient discomfort and headache, to respiratory diseases and cardiovascular problems. In particular in harsh environment, such as industrial settings or mines, AQ monitoring is key to maintain a safe working environment.

Conductometric gas sensors, which rely on changes of the electrical conductance of a gas sensitive material due to the surrounding gas, are very good candidates for IAQ. Mostly, metal oxides (MOx) like SnO_2, ZnO or CuO are used because of their high sensitivity to a large variety of gases [1]. For AQ, however, selectivity – the property to distinguish a single target gas out of a gas mixture – is a most important issue. A very promising approach to achieve a high degree of selectivity is to functionalize the surface of MOx sensors by metallic nanoparticles such as Au, Pd, or Pt [2, 3].

We have realized a 4 x multi-gas sensor array, which employs 4 different sensor materials: bare SnO_2, and CuO films, and SnO_2, and CuO films, functionalized with Ag- and Cu-nanoparticles. The goal of this sensor array is to monitor the AQ in the harsh environment of mines. Hence, the sensors have been screened towards 6 specifics get gases: CO_2, CO, NO, acetone, NH_3, and a hydrogen carbide mixture (HC_{mix}, equal mixture of 500 ppm of acetylene, ethane, ethene and propene). Table 1 lists the target gases relevant for AQ in mines and includes the required measurement range as well as the maximum workplace concentrations.

Target Gas	Concentration Range	MAK* concentration
CO_2	400 - 5000 ppm	5000 ppm
CO	1 - 50 ppm	30 ppm
NO	1 - 50 ppm	25 ppm
Acetone	1 - 5 ppm	500 ppm
HCmix**	1 - 30 ppm	not defined
NH_3	1 - 50 ppm	20 ppm
* Maximum workplace concentration		
** HCmix = mixture of acetylene, ethan, ethen and propen		

Sensor Fabrication

SiN-based micro-hotplate chips incorporating a heating structure (up to 500°C) and electrodes, have been used as carriers for the sensing films. The sensors are fabricated as follows: First, a negative lift-off resist mask is structured by photolithography. Then the chips are coated with 50 nm SnO_2 and CuO, respectively, using reactive magnetron sputtering. This is followed by a lift-off process to structure the sensing films into a circular shape (diameter 450 µm) and an annealing process at 400°C in dry synthetic air. Finally, two out of four sensors are functionalized with Ag, and Cu nanoparticles via

magnetron sputter inert gas condensation. The 4 chips are mounted on a Kyocera socket, wire bonded, and form the multi-gas sensor array.

Sensor characterization and results

All sensors have been characterized simultaneously in an automated gas measurement setup. Synthetic air, with controlled humidity (25% and 75% rh), serves as the background gas. The target gases are subsequently introduced into the setup for 5 min at low concentration (500 ppm CO_2, 5 ppm CO, 1 ppm NO, 1 ppm acetone, 1 ppm NH_3, and 5 ppm HC_{mix}). After 10 min in synthetic air, the target gases are introduced for 5 min at high concentration around the MAK limits (2500 ppm CO_2, 25 ppm CO, 5 ppm NO, 5 ppm acetone, 5 ppm NH_3, and 25 ppm HC_{mix}).

The relative resistance changes due to the interaction with the test gas, i.e. the sensor response S, has been calculated according to:

$$S = \frac{R_{air} - R_{gas}}{R_{air}} \quad (1)$$

where R_{gas} is the sensor resistance in the presence of the test gas and R_{air} is the sensor resistance in pure synthetic air.

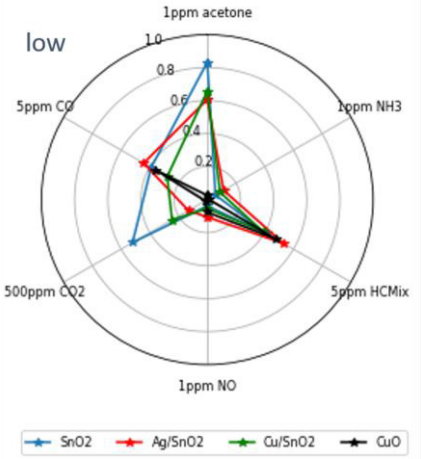

Fig.1 Response of four sensors towards 6 test gases for low concentrations (300°C operation temperature, 75% rh in background gas).

In order to accurately identify the target gases, we analyzed sensor drift and developed a calibration method to evaluate the sensitivity and selectivity of all devices. Fig. 1 presents the results for 4 sensor devices towards the 6 target gases at low concentration values at 300°C operating temperatures and 75% relative humidity. The high humidity was chosen to simulate the humidity levels in mines.

Discussion and Conclusion

As obvious from Fig. 1 and Fig. 2, the different sensing materials show specific responses to the test gases, which enables an identification of the test gases. This demonstrates the potential of our sensor system in real-world environments where variations in temperature and humidity are common. Future work will focus on refining the calibration process to enhance accuracy and reliability under varying environmental conditions, thereby improving the system's applicability for industrial and safety-critical applications.

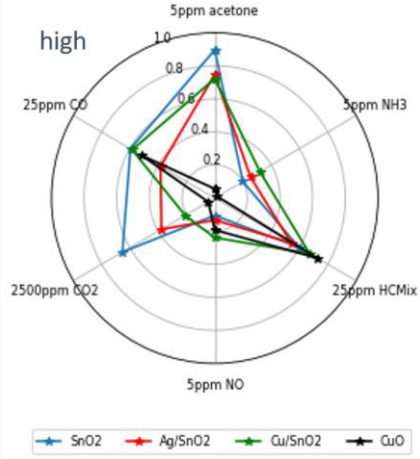

Fig.2 Response of four sensors towards 6 test gases for high concentrations (300°C operation temperature, 75% rh in background gas).

References

[1] N. Barsan, D. Koziej, U. Weimar, Metal oxide-based gas sensor research: How to? *Sensors Actuators, B* Chem., vol. 121, no. 1, pp. 18–35, 2007, https://doi.org/10.1016/j.snb.2006.09.047

[2] C. Wang, L. Yin, L. Zhang, D. Xiang, R. Gao, Metal Oxide Gas Sensors: Sensitivity and Influencing Factors, *Sensors*, 10, 2010, 10, 2088-2106, https://doi.org/10.3390/s100302088

[3] F. Sosada-Ludwikowska, L. Reiner, L. Egger, E. Lackner, J. Krainer, R. Wimmer-Teubenbacher, V. Singh, S. Steinhauer, P. Grammatikopoulos, Anton Koeck, Adjusting surface coverage of Pt nanocatalyst decoration for selectivity control in CMOS-integrated SnO_2 thin film gas sensors", *Nanoscale Adv*., 2024, https://doi.org/10.1039/D3NA00552F

Funding

Most of the work has been performed within the ECSEL project "CHARM – Challenging environments tolerant Smart systems for IoT & AI", which has received funding from the ECSEL Joint Undertaking (JU) under grant agreement No 876362. The JU receives support from the European Union's Horizon 2020 research and innovation programme and Austria, Belgium, Czech Republic, Finland, Germany, Italy, Latvia, Netherlands, Poland, Switzerland.

Part of the work has been performed within the project "Nano4E - Nano4E - Integrated thermo-optically activated Nanosensors for environmental monitoring", which receives funding from the Austrian Funding Agency FFG (project No: FO999899024).

DOI 10.5162/EUROSENSORSXXXVI/PT5.305

New Tool to Unravel Interactions Between Gas and Sensitive Surface Through the Simultaneous Characterization of Gas Uptake and Electrical Properties of the Material

Marius Pascaud[1,2], Caroline Duc[1], Nathalie Redon[1], Cedric Samuel[3], Alexandra Fresneau[2], Manolis N Romanias[1], Frederic Thevenet[1]

[1] IMT Nord Europe, Institut Mines-Telecom, Univ. Lille, Centre for Energy and Environment, F-59000 Lille, France,

[2] TERA Sensor, ZI Rousset, 1200 avenue Olivier Perroy, F-13790 Rousset, France

[3] IMT Nord Europe, Institut Mines-Telecom, Univ. Lille, Centre for Materials and Processes, F-59000 Lille, France

marius.pascaud@imt-nord-europe.fr

Summary:

This work presents an innovative setup for simultaneous determination of (i) electrical gas sensor response and (ii) uptake of target gas on sensitive material. Operating under atmospheric pressure and at 298K, it is designed to work under a wide range of gas flow, relative humidity and target gas concentration. Results validate the system effectiveness in monitoring gas uptake and sensor responses simultaneously, offering insights into physicochemical processes related to gas detection.

Keywords: Gas sensors, Conductive polymers, Ammonia detection, Polyaniline, Uptake quantification

Introduction and Objectives

The last decade has seen a growing interest for air quality, leading to different approaches developed to monitor air pollution such as sensors. Among them, resistive sensors based on metal oxides or conductive polymers are promising for gas detection because of: (i) low limit of detection, (ii) high tunability and (iii) low manufacturing cost [1]. While these gas sensors can achieve high sensitivity (ppt range), selectivity and high processability with low energy consumption [2], drivers of their performances are still not fully understood [3]. Addressing accurately gas-sensor interactions could enhance the understanding of the physicochemical parameters responsible for the limitations of the sensors and facilitate their optimization. Indeed, this work proposes the development of a new experimental setup for monitoring simultaneously sensors electrical response and gas uptake on the sensitive material: the Cell for Atmospheric Pressure Uptake and SensINg Experiment (CAPUSINE). For the first time, quantification of the amount of gas (ammonia, NH_3) taken up by a sensitive surface based on conductive polymer (doped polyaniline, dPAni), is monitored under atmospheric pressure conditions, at 298 K, simultaneously with the sensor response. The developed setup is easily applicable to others sensing materials and gaseous species thanks to the ability of the analyser to monitor different types of gas, making CAPUSINE a powerful tool to unravel interactions between gases and sensors.

Material and Method

CAPUSINE, consists in four main parts: (i) gas generation system, (ii) sample cell, (iii) online reference analyser and (iv) gas sensors under study.

Gas generation system: Three drivers of the gas intake are controlled: (i) relative humidity (%) known to significantly affect sensor response, (ii) target gas concentration (ppm) and the (iii) gas flow ($mL.min^{-1}$) which impacts the residence time of the gas in the sample cell.

Sample cell for uptake: The sample cell consists of a ¼ inch steel tube, featuring sieve with a mesh size of 250 µm to prevent drift of powder samples. Interestingly, specific surface area (SSA, $m^2.g^{-1}$) of the sensor material serves as a normalization factor for comparing results across different experiments. To limit gas interactions with walls, treated steel (Sulfinert®, Silcotek) is used. The geometry of the cell ensures thorough exposure of the material to the gas flow.

Analyser: SIFT-MS is used to monitor concentration profiles of the target gas. SIFT-MS has low intake flow (30 $mL.min^{-1}$), a high temporal resolution (1 measurement every 3 seconds)

and an ability to monitor a wide variety of gaseous species without water interference.

Gas sensors: To corelate the uptake of target gas on sensor electrical response, CAPUSINE is also equipped with two gas sensors based on the same material (Fig. 1): one upstream, located in the sample chamber, and a second downstream, located just before the analyser (Fig. 1). The two sensors could allow for the corelation of uptake and sensor response and their measurements are also compared to the analyser.

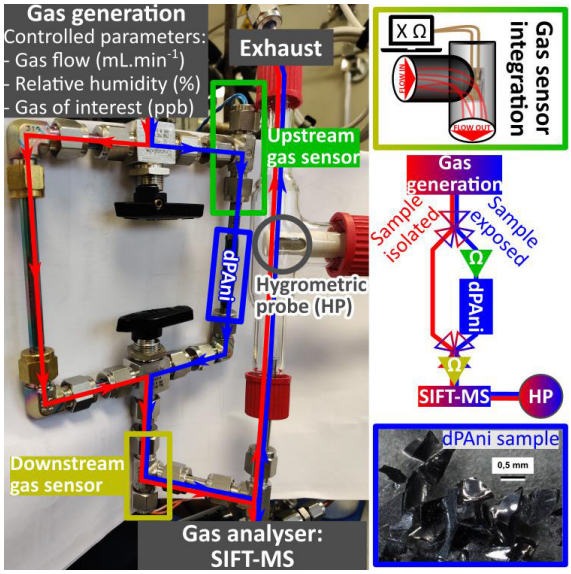

Fig. 1. CAPUSINE general description

Results and Discussions

A typical experiment conducted in CAPUSINE follows 4 steps (Fig. 2). (i) A fresh dPAni sample (50 mg corresponding to 1.5 × 10^{-3} m^2) is placed in the sample cell and equilibrated with controlled relative humidity. (ii) The gas flow is redirected to the bypass, isolating the sample, and the gas of interest (NH_3) is set to targeted concentration (2 ppm). (iii) Upon stabilization of pollutant concentration, the flow is switched to expose dPAni, initiating NH_3 uptake. (iv) After reaching equilibrium ([NH_3] is equal to the beginning of step (iii)), the flow returns to the bypass for NH_3 concentration control. The amount of NH_3 taken up can be retrieved from integration of the area under NH_3 profile from SIFT-MS (light blue area in Fig. 2).

To validate that the observed uptake is solely attributed to dPAni, two experiments were conducted. First, without any sensor neither dPAni, no change in NH_3 signal occurred upon switching from bypass to the empty sample cell. Second, with sensors but no dPAni, sensors took up, up to 8 × 10^{14} NH_3 molecules in the first 10 minutes, i.e. 1 % of NH_3 molecules in the flow over this period of time and less than 3 % of the NH_3 taken up by dPAni (Fig. 2). Hence, sensors used interacts negligibly with NH_3, confirming that the observed uptake in Fig. 2 is mainly due to NH_3 uptake on dPAni.

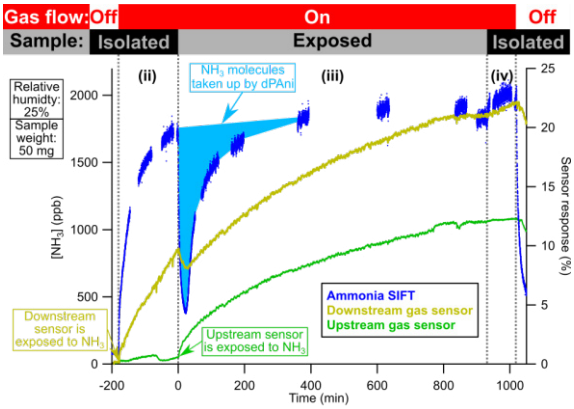

Fig. 2. CAPUSINE experiment with dPAni and NH_3, at 25% RH.

As, dPAni is exposed to 2 ppm of NH_3, it uptakes 2.7 × 10^{16} molecules.cm^{-2} (Fig. 2). Notably, the downstream sensor response mirrors the uptake monitored by SIFT-MS. The same experiment can be repeated at different levels of humidity to observe the impact of water on uptake and sensor response. The impact of interfering gas species can also be explored by replacing or mixing NH_3 with another gas.

To conclude, CAPUSINE experimental setup enables simultaneous monitoring of gas uptake and sensor response within a realistic environment, with control over the relative humidity and gas phase composition. This innovative setup is expected to be able to provides deep insights into the physicochemical processes contributing to the response of resistive gas sensor. Thanks to its versatility, CAPUSINE is anticipated to be applicable to a wide range of solid gas sensors and capable of accommodating various gaseous mixtures.

References

[1] D. Kwak, Y. Lei, and R. Maric, 'Ammonia gas sensors: A comprehensive review', *Talanta*, vol. 204, pp. 713–730, Nov. 2019, doi: 10.1016/j.talanta.2019.06.034.

[2] S. Pandey, 'Highly sensitive and selective chemiresistor gas/vapor sensors based on polyaniline nanocomposite: A comprehensive review', *J Sci-Adv Mater Dev*, vol. 1, no. 4, pp. 431–453, Dec. 2016, doi: 10.1016/j.jsamd.2016.10.005.

[3] N. R. Tanguy, M. Thompson, and N. Yan, 'A review on advances in application of polyaniline for ammonia detection', *Sens. Actuators B Chem.*, vol. 257, pp. 1044–1064, Mar. 2018, doi: 10.1016/j.snb.2017.11.008.

DOI 10.5162/EUROSENSORSXXXVI/PT5.308

Preliminary Study on the Poisoning Effect of Different Materials on MOX Sensors

Beatrice Julia Lotesoriere[1], Stefano Robbiani[2], Ana Maria Tischer[1], Lucia Corrà[1], Emanuele Zanni[2], Anna Gianfranceschi[2], Lucia Giuffrida[2], Laura Capelli[1], Raffaele Dellacà[2]

[1] Politecnico di Milano, Department of Chemistry, Materials and Chemical Engineering "Giulio Natta", Piazza Leonardo da Vinci 32, Milan, Italy
[2] Politecnico di Milano, Department of Electronics, Information, and Bioengineering, Via Giuseppe Colombo 40, 20133 Milan, Italy

Corresponding author: lucia.corra@polimi.it

Summary:

Additive fabrication techniques have opened new possibilities for the realization of sensors chambers of different shapes, to optimize performances. The objective of this work is to carry out a first experimental study to evaluate the poisoning effect of some new materials on commonly use MOX sensors. Effects of PEEK, 3D Print Resin and Silicone on TGS2610 and TGS2611 is investigated. Gas sensors response to different calibrants is recorded before and after sensors' exposition to the materials, resulting in reduction of the response for Silicone and Resin, while PEEK do not affect sensors' response.

Keywords: chemical sensors, contamination, 3D Print, Resin, Silicone, Siloxanes, PEEK

Background, Motivation and Objective

Several studies show how the geometry and the fluid dynamics of gas sensor chamber affect the sensor responses, especially in terms of response time, amplitude, and stability [1]. Nowadays, additive fabrication techniques like 3D printing have become more precise and affordable, and have opened up new possibilities for the realization of sensor chambers of different shapes, with the purpose of obtaining optimized performances according to the application. However, whenever introducing a new material, besides considering safety issues, ease of processability and cost, it is important to verify its compatibility with odour analysis. Some evaluations regarding the inert behaviour and recovery of VOCs for different sampling materials have been included in the recent revision of the European Standard about dynamic olfactometry (EN 13725:2022) [2]. In the specific case of e-nose applications, it is of fundamental importance to verify that the VOCs that are released by all the materials [3] used for the manufacturing of the sampling line and analysis system do not have a poisoning effect on the gas sensors.

In this context, the objective of this work is to carry out a first experimental study to evaluate the poisoning effect of some materials that are commonly used in biomedical devices, and that could potentially be used to design fit-for-purpose sampling systems and sensors' chambers for e-nose applications.

Description of the New Method or System

A dedicated setup was developed to specifically investigate the poisoning of some commercial MOX sensors (i.e., 5 TGS2610 and 5 TGS2611, Figaro Inc., Osaka, Japan) towards some materials that could be used for the realization of e-nose systems for biomedical applications, including polyetheretherketone (PEEK), Resin (Biomed Clear, Formlabs, Massachusetts, USA), "Boiled" Resin (pre-treated by boiling in distilled water for 2 h at 100 °C), and Silicon. Even though the poisoning effect of siloxanes on MOX sensors has already been reported in literature [4], it was decided to include it in the study as a reference, because it is often used for the realization of biomedical components such as face masks [3]. The experimental part consisted of three different phases. First, gas sensors were tested before poisoning to evaluate the sensors' responses towards different calibrants (i.e., butanol 20 ppm, isobutylene 20 ppm, 4-heptanone 20 ppm, methane 750 ppm) without any potential interferent. To do this, all the gas sensors were installed in a glass sensors' chamber equipped with a temperature and humidity sensor (SHT40, Sensirion, Switzerland) to monitor stability of environmental conditions. The gaseous calibrants were stored in 18 L Nalophan™ bags and conditioned for 3 h before analysis in room conditions at 22 °C and 40%RH. The tests were carried out alternating air and gaseous samples to stabilize

and restore the sensors' baseline before and after each analysis controlled by 2 shut-off valves: 15 min of air sample analysis, 15 min of calibrant sample analysis, and 15 min of air sample analysis. The samples were injected at a constant flowrate of 1 l/min into the chamber by a lung-pump system of two flux drums (Fig. 1a). After that, gas sensors were placed in pairs (i.e., one TGS2610 and one TGS2611) in 5 flasks of 50 mL StonyLab®: 4 flasks with a piece of one of the 4 poisoning materials considered with an equivalent surface area of 11 cm^2 and a flask with no poisoning material to be used as a blank. To accelerate the VOCs release, the flasks containing a pair of sensors each were places in a ventilated oven (AEG BSK798280B) at 80 °C for 15 days (Fig.1b). Finally, the effect of the contaminants on sensor responses was evaluated by repeating the same analyses carried out before poisoning at the same controlled conditions (i.e., 40% RH, 22°C).

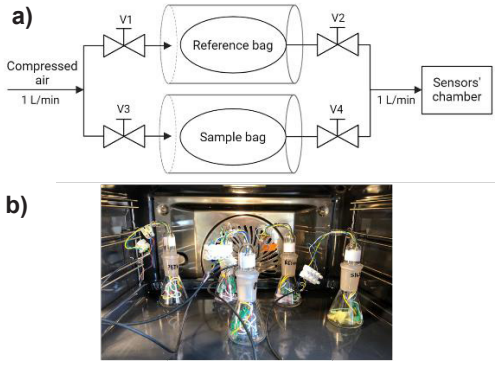

Fig. 1. a) Sample delivery system to the sensors' chamber; b) Sensors poisoning in the oven

Results

Sensors' outputs were compared with respect to the sensors' responses obtained before poisoning and with respect to the readings of the blank analysis in terms of baseline shift and signal amplitude. Fig. 2a and Fig. 2b show a comparison of the sensors' responses (in terms of raw resistance values and normalized resistances ($R-R_0$), respectively) after 2 weeks of permanence in the oven. The results obtained, besides proving that after 2 weeks the response of the sensors in contact with the silicon are substantially zeroed, also show that the only materials, among the ones tested, resulting in almost no alteration compared to the blank sample, is PEEK. Boiling the resin results in an improvement compared to the resin without pre-treatment, but it still doesn't seem suitable for long-term applications. Further studies should investigate other materials and other possible pre-treatments.

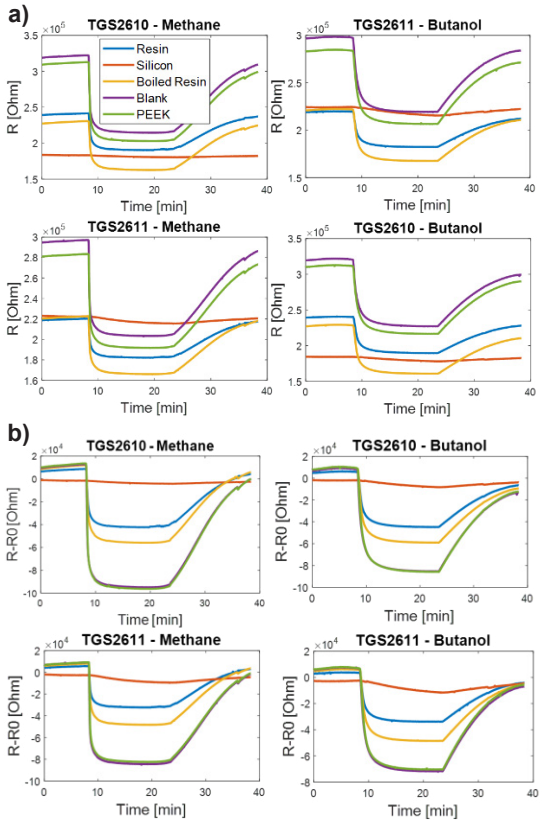

Fig. 2. Sensor responses: a) resistance values; b) normalized resistances

Funding

This study was co-funded by the National Plan for NRRP Complementary Investments (PNC) - project n. PNC0000003 - AdvaNced Technologies for Human-centrEd Medicine (ANTHEM). This work reflects only the authors' views and opinions, neither the Ministry for University and Research nor the European Commission can be considered responsible for them.

References

[1] S. Robbiani et al., Physical Confounding Factors Affecting Gas Sensors Response: A Review on Effects and Compensation Strategies for Electronic Nose Applications. *Chemosensors*, 11(10), 514 (2023); doi: 10.3390/chemosensors11100514

[2] P. Kasper et al., A. Effects of dilution systems in olfactometry on the recovery of typical livestock odorants determined by PTR-MS. *Sensors*, 17(8), 1859 (2017); doi: 10.3390/s17081859

[3] Y.L. Pham et al., Emissions and uptake of volatiles by sampling components in breath analysis. *Journal of Breath Research*, 17(3), 037102 (2023); doi: 10.1088/1752-7163/acce34

[4] A. Khorramifar et al. (2023). Environmental engineering applications of electronic nose systems based on MOX gas sensors. *Sensors*, 23(12), 5716 (2023); doi: 10.3390/s23125716.

DOI 10.5162/EUROSENSORSXXXVI/PT6.14

Onsite Single-Step Device for Early Detection of Infections and Drought Stress in Vineyards

Cristiana Domingues[1], Ana Margarida Fortes[2], Virginia Chu[1], João Pedro Conde[1,3]
[1]Instituto de Engenharia de Sistemas e Computadores – Microsistemas e Nanotecnologias (INESC-MN), Rua Alves Redol, 1000-029, Lisbon, Portugal
[2]BioISI, Faculdade de Ciências de Lisboa, Universidade de Lisboa, Lisbon, Portugal
[3]Department of Bioengineering, Instituto Superior Técnico, Avenida Rovisco Pais 1049-001, Lisbon, Portugal,

joao.conde@tecnico.ulisboa.pt

Summary:

Agriculture is an important part of the economy of most countries. In general, it is important to monitor and prevent biotic (infections) and abiotic stresses (droughts or excessive watering) that can significantly affect crop yield. For this reason, there is a need to develop a fast and low-cost platform that can be used in the field to monitor plant response to various types of stresses. For portability, microfluidics was the platform of choice for targeting two biomarkers: abscisic acid, related to plant ripening and to plant response to drought stress; and salicylic acid, related to the plant response to infection.

Keywords: microfluidics, biosensor, antibody, aptamer, capillarity

Introduction

Biotic (infections) and abiotic stresses (droughts and floods) greatly affect the yield in food and feed production. The incidence of these stress factors has become increasingly more frequent and damaging because of climate change. To prevent the loss of crops, it would be beneficial to develop a portable, low cost, user-friendly platform, that can be used in the field to perform tests for the early detection of changes in the vine, thus allowing for prompt and appropriate response. Currently, routine sampling of crops must be sent to central analytical laboratories which is time-consuming and costly.

A device based on microfluidics technology that can provide the needed portability and potential low cost due to the small volume of reagents. Also, because of the smaller distances for diffusion, the reaction times can be faster making it appropriate for regular on-site testing. Under stress conditions, the concentration of several phytohormone in the plant changes. In this paper, we demonstrate a microfluidic device that can monitor two such phytohormones: abscisic acid (ABA) for tolerance mechanisms against drought stress, and salicylic acid (SA) for infections. [1]

Methods and Results

ABA is detected using a competitive immunoassay (Fig.1(A)). The sample under analysis is mixed with a conjugated molecule composed of ABA and bovine serum albumin (BSA), labelled with Alexa430 (ABA-BSA-Alexa430).

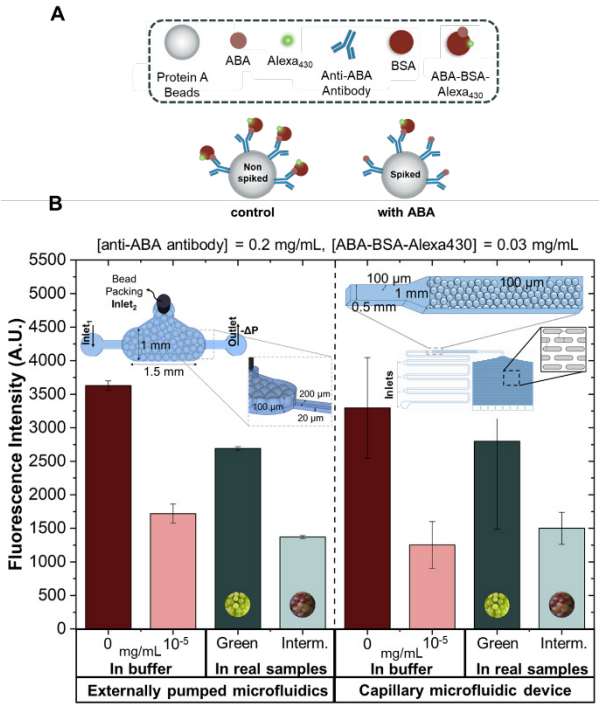

Fig. 1. Competitive Immunoassay for ABA detection: (A) Schematic representation of the assay for a spiked and non-spiked sample (B) Fluorescence response curve for different target ABA concentrations and for different stages of ripening, for the two different systems. The left side uses externally pumped microfluidics, and the right side uses a capillary microfluidic device. The error bars represent the ± standard deviation.

In the presence of ABA, the free analyte in solution will compete with the ABA-BSA-Alexa430 for the binding sites of the anti-ABA antibody, bound by the constant zone of the antibody to protein A microbeads, and therefore, the higher the concentration of free analyte, the lower the fluorescence signal. This method was developed using a microfluidic device, fabricated with polydimethylsiloxane (PDMS) using soft lithography techniques, using external syringe pumps. [1] Self-pumping microfluidic devices that rely on capillary forces to drive the fluids were also developed to increase ease of use and the portability. [2] Fig.1(B) shows the ABA detection both in buffer and in real grape samples picked during the *veraison*. In this stage of ripening, there is a surge in ABA which can be detected as a decrease in the fluorescence signal. As can be seen in Fig 1(B), the two different devices, one that uses an external pumping system, on the left, and the capillary device, on the right, are both capable of detecting ABA, and the results for both devices are identical.

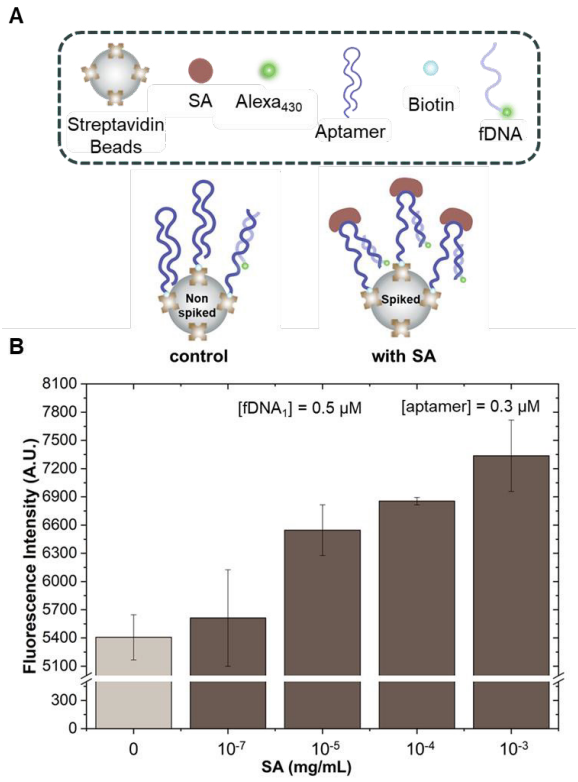

Fig. 2. Assay for SA detection in binding buffer: (A) Schematic representation of the aptamer assay for a spiked and non-spiked sample (B) Fluorescence response curve for different target SA concentrations. The error bars represent the ± standard deviation.

Additionally, an assay for SA detection using biotinylated SA aptamers immobilized on streptavidin beads as a capture agent was also developed (Fig.2(A)). A fluorescently labeled DNA strand complementary to the SA aptamer, binds to the aptamer leading to an increase in signal. In the presence of SA, the binding affinity increases leading to an increase in the fluorescence signal. Preliminary results also show the detection of SA in a microfluidic chip (Fig.2(B)). Using the SA detection method, it is possible to detect concentrations within the range of interest for infections, which is in the 10^{-6}-10^{-4} mg/mL range.

Due to the complexity of the cell matrix of the grapevines and grapes, sample pre-treatment is required before analysis. [1] Since the sample treatment should be performed in the field, the currently required centrifugation step must be replaced prior to in-field usage.

In our presentation, we will describe the microfabrication of the standard and capillary microfluidic chips, the protocols for the assays for detection of the phytohormones ABA and SA, the sample preparation protocols, and the validation of the assays with real grape samples.

Acknowledgements

The authors thank P. Monteiro and I. Petrou for helping with the capillary chip assays. C. Domingues acknowledges FCT for a PhD grant (2020.09377.BD). This work was partially funded by FCT through the project VineSense (PTDC/BAA-DIG/4735/2020) [http://doi.org/10.54499/PTDC/BAA-DIG/4735]. INESC-MN acknowledges FCT for funding through the Research Unit UIDB/0536/2020 and UIDP/0536/2020.

References

[1] C. Domingues, R. Meirinho, R.G. Rodrigues, A.M. Fortes, V. Chu, J.P. Conde, Competitive Immunoassay in a Microfluidic Biochip for In-Field Detection of Abscisic Acid in Grapes, Biosensors. 14 (2024) 123. https://doi.org/10.3390/bios14030123.

[2] T.Q. Vo, M. Barisik, B. Kim, Near-surface viscosity effects on capillary rise of water in nanotubes, Phys. Rev. E - Stat. Nonlinear, Soft Matter Phys. (2015). https://doi.org/10.1103/PhysRevE.92.053009.

DOI 10.5162/EUROSENSORSXXXVI/PT6.32

Nanozyme activity of platinum nanoparticles prepared by pulsed laser ablation

Steffen Kurzhals[1], Mariangela Fedel[2], Laszlo Sajti[2], Eva Melnik[1], Rainer Hainberger[1]
[1]AIT Austrian Institute of Technology GmbH, Giefinggasse 4, 1210, Vienna, Austria
[2] RHP-Technology GmbH, Viktor Kaplan Straße 2, 2700 Wiener Neustadt, Austria

steffen.kurzhals@ait.ac.at

Abstract: Platinum nanoparticles (Pt-NPs) were generated by pulsed laser ablation in liquid and proved to be stable in aqueous dispersion for at least six months when stabilized by small amount of sodium citrate. Their nanozyme activity was tested photometrically with tetramethylbenzidine (TMB) in the absence and presence of hydrogen peroxide (H_2O_2) at 22°C, which lead to specific activities (SA) of 1.9U/mg Pt-NPs and 375U/mg Pt-NPs and limits of detection (LOD) of 1.86pmol/L and 0.026pmol/L, respectively. In comparison, a SA of 289U/mg and a LOD of 36pmol/L were determined for a recombinant horseradish peroxidase in presence of H_2O_2 at 22°C. In particular, the lower detection limit of Pt-NPs by a factor of 1384 compared to the recombinant horseradish peroxidase indicates their great potential for future bioassays.

Keywords: platinum, nanoparticles, nanozyme, horseradish peroxidase, specific activity

Introduction

Nanoparticles (NP) with enzyme-like catalytic activities, also referred to as nanozymes, are promising for the use in bioassays, as they have several advantages over natural enzymes such as higher stability, resistance to external conditions, and strong catalytic performance [1]. Furthermore, they can be tailored for specific applications (e.g., sample preparation, purification, labelling) [2] by bioconjugation of the metal surface to biomolecules. In this study, ultrapure Pt-NPs, prepared by pulsed laser ablation in liquid (PLAL) are investigated on their nanozyme activity (peroxidase and oxidase capability) and compared in their activity to recombinant horseradish peroxidase (HRP).

Materials and Methods

HRP was purchased from Assay Genie. Hydrogen peroxide (H_2O_2) (31wt%), tetramethylbenzidine (TMB), sodium acetate trihydrate and acetic acid were purchased from Sigma Aldrich. Ultrapure, spherical Pt-NPs were synthesized in 0.5mM sodium citrate aqueous solution by PLAL to a final NP concentration of 0.97 mg/mL [3]. Storage stability of at least six months was observed by visual inspection. The mean diameter of the Pt-NPs was measured with a Zeiss Gemini Scattering electron microscope (SEM) using the secondary electron detector and 5kV accelerating voltage. A dilution of Pt-NPs in 0.5mM citrate solution containing 25µg/mL bovine serum albumin were drop casted on a cleaned silica wafer piece and allowed to dry at room temperature. SEM image analysis for mean diameter (D) determination was performed with ImageJ open-source software. A measurement protocol was adapted from Jiang et al. [4] to measure specific peroxidase activities for the enzyme and nanozyme. 0-12.88ng/171.8µl Pt-NPs or HRP in acetate buffer (200mM, pH: 3.6) were mixed in a well of a 96 well-plate with 8.6µL TMB in dimethyl sulfoxide (10mg/mL) and 19.7µL H_2O_2. For measuring oxidase activity, H_2O_2 was replaced with acetate buffer. Absorbance was measured at a wavelength of λ=652nm and at 22°C in triplicates on a Perkin Elmer Enspire Plate Reader (60 repeats, interval 10s). The specific activity *SA* (U/mg) was calculated via the equation:

$$SA = (V/(\varepsilon \times l) \times (\Delta A/\Delta t))/W, \quad (1)$$

where V is the total reaction volume (200µL), ε the extinction coefficient of TMB at a wavelength of 652nm (39000M^{-1} cm^{-1}), l the optical path length (0.56cm), $\Delta A/\Delta t$ the initial change in absorbance per minute (derived from a linear fit over the first 100s), and W the weight per well of enzyme or Pt-NP in mg. The limit of detection (LOD) was determined by the intersection of the linear fit of the absorbance values (after 100s) with the blank value plus three times the standard deviation (SD). The molar concentration of Pt-NPs was calculated from W, the Pt density (21.45g/cm^3) and the volume of the Pt-NPs, calculated from the mean diameter derived by SEM [5].

Results and Discussion

The mean diameter of the Pt-NPs amounted to 10.9±4.5nm. Crucial for the activity measurement was the stability in the acetate buffer at

low pH of 3.6. Under these conditions, 63µg/ml Pt-NPs kept their slightly yellowish color for at least 30min, and thus, activity measurements with and without H_2O_2 were performed in this time frame. Recombinant HRP was characterized as reference with the TMB/H_2O_2 assay. For the TMB/H_2O_2 assay a SA for HRP of 289U/mg and a SA for Pt-NPs of 375U/mg could be calculated. In absence of H_2O_2, a SA for Pt-NPs of 1.9U/mg Pt-NPs could be observed. In literature, SAs of NPs with other core materials such as gold, carbon, magnetite, are reported for 37°C with H_2O_2 ranging from 1.6-5.1U/mg [4]. Citrate-capped Pt-NPs (diameter of 2.5nm), which are chemically synthesized are reported with similar SAs of 323.7U/mg at 55°C with H_2O_2 [6].

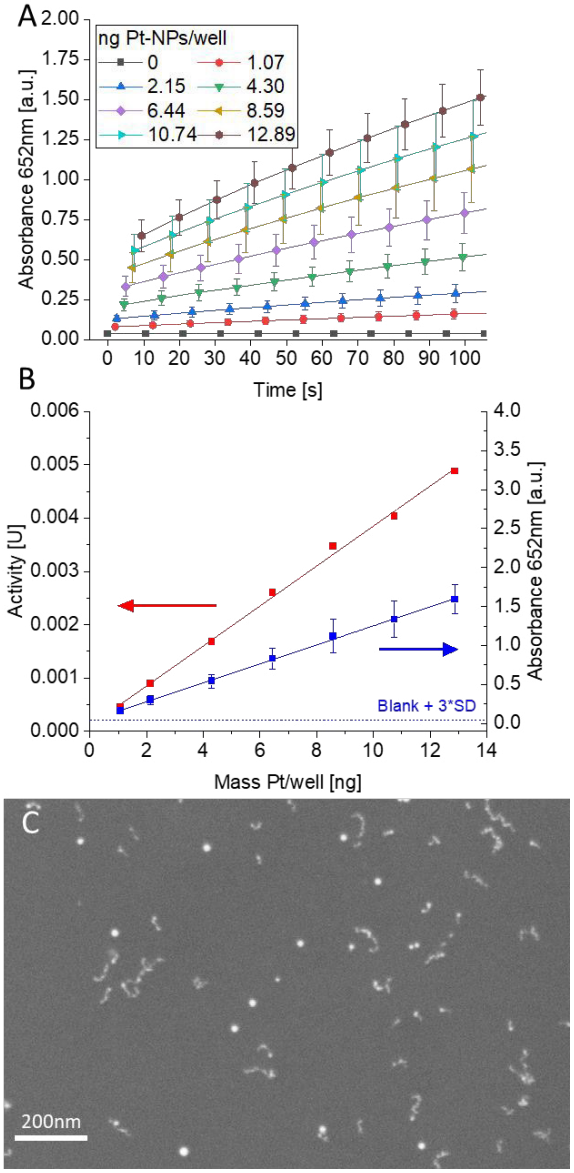

Fig. 1. A) 100s absorbance measurement of Pt-NPs with TMB/H_2O_2, B) activity (left y-axis) and absorbance at λ=652nm after 100s (right y-axis) vs mass Pt-NPs/well, C) SEM image of Pt-NPs, 200k× magnification.

Tab. 1: Overview of SAs and LODs

Enzyme/ nanozyme	Specific activity in U/mg (correlation R^2)	LOD in ng/ml (pmol/L)
Peroxidase activity (H_2O_2 present)		
HRP	289.0 ± 6.5 (0.9975)	1.6 (36)
Pt-NPs	374.8 ± 8.9 (0.9972)	0.231 (0.026)
Oxidase activity (no H_2O_2 present)		
Pt-NPs	1.86 ± 0.06 (0.9940)	16.7 (1.91)

Analyzing the Pt-NPs of this study, a value of 1.86pmol/L without H_2O_2 and 0.026pmol/L with H_2O_2 is found for the LOD, which is significantly below the value of 36pmol/L measured for HRP using the TMB/H_2O_2 assay (see Tab.1).
In summary, the Pt-NPs exhibit excellent peroxidase-specific activity and a low LOD at 22°C, even in the absence of H_2O_2. This makes the PLAL-produced Pt-NPs promising nanozymes for use in bioassays.
Future studies need to investigate the influence of dissolved oxygen in the measurement buffer to understand the oxidase activity of Pt-NPs.

References

[1] S. Singh, Nanomaterials Exhibiting Enzyme-Like Properties (Nanozymes): Current Advances and Future Perspectives, Frontiers in chemistry 7:46, doi: 10.3389/fchem.2019.00046

[2] A. de la Escosura-Muñiz, L. Baptista-Pires, L. Serrano, et al., Magnetic Bead/Gold Nanoparticle Double-Labeled Primers for Electrochemical Detection of Isothermal Amplified Leishmania DNA. Small 12 (2), 205–213.

[3] M. Urban, G. Rosati, G. Maroli, et al., Nanostructure Tuning of Gold Nanoparticles Films via Click Sintering, Small, (2023); doi: 10.1002/smll.202306167

[4] B. Jiang, D. Duan, L. Gao, et al., Standardized assays for determining the catalytic activity and kinetics of peroxidase-like nanozymes, Nature Protocols 13 (7), 1506-1520

[5] J. Shang, X. Gao, Nanoparticle counting: towards accurate determination of the molar concentration, Chemical Society Reviews, (2014), 43, 7267-7278

[6] S. He, L. Yang, P. Balasubramanian, et al., Osmium nanozyme as peroxidase mimic with high performance and negligible interference of O_2, Journal of Materials Chemistry A, (2020), 8, 25226-25234

Funding: This work has received funding from the Austrian Research Promotion Agency (FFG) under the NanoPredict (grant no. FO999899038).

DOI 10.5162/EUROSENSORSXXXVI/PT6.58

Peptide-based biosensor for real-time monitoring of protease biomarkers

Pratika Rai[1], *Prof. Dr. Alexey Tarasov*[1]
[1] *Faculty of Computer Sciences and Microsystems Technology, Kaiserslautern University of Applied Sciences, Amerikastr. 1, 66482, Zweibrücken, Germany*
pratika.rai@hs-kl.de

Summary:

Here we propose a peptide-based assay using a specific combination of linker and peptides to design a robust biosensor for proteases. The implementation of a cleavage-based mechanism results in the sensitive and specific detection of a clinically relevant biomarker (MMP-9). The developed assay is characterized using real-time electrical and optical techniques and demonstrates its potential as a tool for the detection of MMP-9.

Keywords: peptide interface, protease biosensor, matrix metalloproteinase (MMP-9), optical technique, electrochemical technique

Background, Motivation and Objectives

Biosensors provide a sensitive and highly selective means of detecting biomarkers. The biosensor is typically based on the measurement of signal changes resulting from the biomolecular interactions that occur at the interface between the electrode and biomolecular layers. Among the various disease biomarkers, enzyme-based biomarkers such as proteases show significant potential in the design of a sensitive biosensor due to their robust cleavage mechanism. Peptides are cleaved by protease at specific sites (Fig. 1), and can therefore be used as one of the most promising candidates for monitoring protease activity [2, 3]. Among the different classes of proteases, overexpression of MMP-9 (matrix metalloproteinase - 9) is associated with diseases such as cancer [2], and neurodegenerative or inflammatory diseases [1]. Therefore, the early clinical detection of MMP-9 is essential to intervene in disease progression and would lead to new treatment options for patients. In recent years, there has been significant development in the field of protease biosensors using peptides as substrates [2, 3]. However, the problem of false signal contributions due to non-specific binding of cleaved peptide fragments or proteases themselves on the sensing electrode reduces the detection sensitivity [3]. A further challenge is the cross-reactivity of peptides with other proteases or proteins present in the biological samples [3]. In this paper, we report the development of a specific peptide interface on a gold surface, modified with a PEG-based linker molecule, for the detection of MMP-9. The assay was optically monitored in situ by non-invasive multi-parametric surface plasmon resonance (MP-SPR) spectroscopy. The results obtained were further validated by electrochemical measurements. The concentration-dependent activity of MMP-9 on the sensing platform is analyzed and compared.

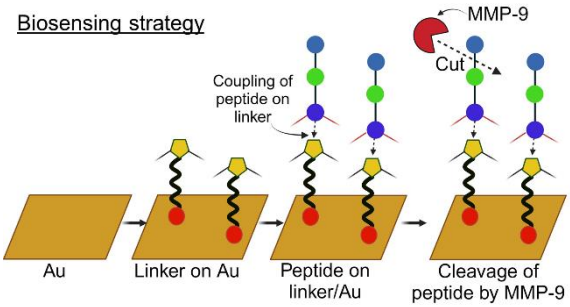

Fig. 1. Biosensing strategy of the proposed peptide-based MMP-9 assay.

Research novelty

The combined optical and electrical monitoring of MMP-9 using the peptide cleavage mechanism has not been extensively explored. Our work contributes a simple, rapid, and sensitive MMP-9 assay that has been validated in real time by optical (MP-SPR) and electrical (potentiometric) detection methods. The label-free assay using PEG-based linker molecules reduces the false signal contribution due to non-

specific binding of MMP-9 or the cleaved peptide fragments on the sensor surface. The electrical characterization of the surface by comparing the change in the potential difference is performed at a very low current (1 nA). To the best of our knowledge, this is the first report on the potentiometric study of peptides for MMP-9 detection and shows potential application in the design of point-of-care devices.

Results

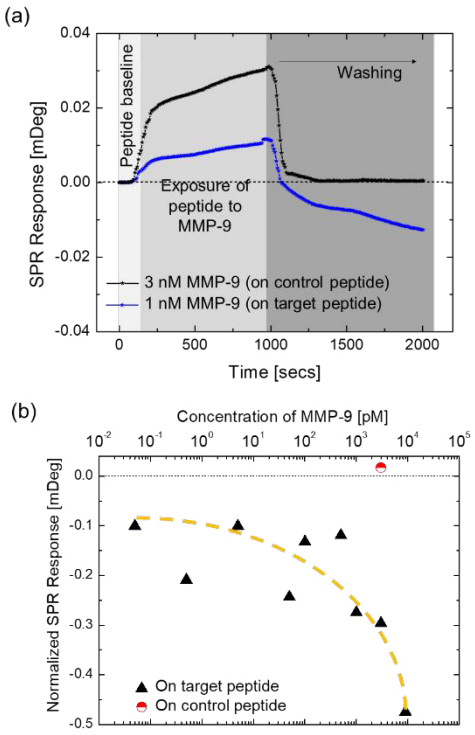

Fig. 2. a) SPR sensogram showing the peptide baseline, its subsequent exposure to MMP-9, followed by the buffer washing step. The SPR response of the target peptide to 3 nM MMP-9 goes below the baseline during the washing step. By contrast, the signal response of the control peptide to 3 nM MMP-9 goes back to the baseline. b) Normalized SPR response at different concentrations of MMP-9 in buffer (PBS, pH 7.4). The dashed line is a guide to the eye.

By modifying the surface of Au with SAMs of PEG-based linker molecule (450 µM), we first validated the significant reduction in the non-specific binding of control peptides (195 µM) and MMP-9 using MP-SPR. This proved that the assay is suitable to develop a specific and sensitive peptide biosensor. Figure 2a, b shows the proteolytic hydrolysis of the target peptide (195 µM) upon exposure to various concentrations of MMP-9. As expected, the control peptide, which does not contain any MMP-9 cleavage sites, was not digested. Using this assay, we were able to qualitatively detect MMP-9 at concentrations as low as 0.05 pM. In the next step, the proposed assay was tested in the electrical measurement setup where we observed a linear dependence of the signal response on the MMP-9 concentration up to 1 nM (Fig. 3b). Future experiments are planned to test the MMP-9 activity in the electrical setup in buffer as well as in complex samples at different MMP-9 concentrations.

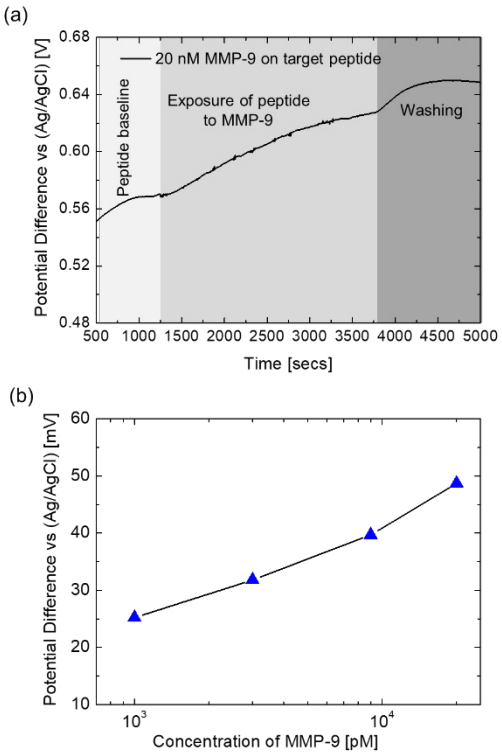

Fig. 3. a) Time profile of the change in the potential difference of the peptide/linker modified Au surface versus the Ag/AgCl reference electrode upon exposure to 20 nM MMP-9 in culture medium (RPMI-1640). b) Dependence of the signal response upon exposure to different concentrations of MMP-9 ranging between 1 – 20 nM.

References

[1] A. Hugo, T. Rodrigues, J. K. Mader, W. Knoll, V. Bouchiat, S. Szunerits, Matrix metalloproteinase sensing in wound fluids: Are graphene-based field effect transistors a viable alternative? Biosensors and bioelectronics, X 13, 100305 (2023); doi.org/10.1016/j.biosx.2023.100305

[2] D.S. Shin, Y. Liu, Y. Gao, T. Kwa, Z. Matharu, A. Revzin, Micropatterned surfaces functionalized with electroactive peptides for detecting protease release from cells, Analytical, 85 (1), 220-227 (2013); doi:10.1021/ac302547p

[3] P. Rai, S. N., Hoba, C. Kersten, C. Buchmann, T. Schirmeister, R. J. Subirana-Slotos, K. Endres, B. Bufe, A. Tarasov, Protease detection in the biosensor era: A review, Biosensors and bioelectronics, 244, 115788 (2024); doi.org/10.1016/j.bios.2023.115788

Fluidic Electrochemical Sensor Platform for Pollution Monitoring

D. Kuscer, B. Repič, D. Belavič, Jožef Stefan Institute, Ljubljana (Slovenia), M. Dekleva, G. Marolt, H. Prosen, University of Ljubljana, Ljubljana (Slovenia)

Unfortunately, this abstract is not available, as the contribution was not confirmed at the time the conference proceedings were finalized.

Fluidic Electrochemical Sensor Platform for Pollution Monitoring

D. Kuscer, B. Repič, D. Belavič, Jožef Stefan Institute, Ljubljana (Slovenia), M. Dekleva, G. Marolt, H. Prosen, University of Ljubljana, Ljubljana (Slovenia)

Unfortunately, this abstract is not available, as the contribution was not confirmed at the time the conference proceedings were finalized.

Printed capillary microfluidic biosensors

Z. Zhang, S. Lang, Y. Farhan, Y. Tao, G. Xiao, (NRC) Advanced Electronics and Photonics Research Center, Ottawa (Canada), Z. Wang, C. Xu2, McMaster University, Hamilton (Canada)

Unfortunately, this abstract is not available, as the contribution was not confirmed at the time the conference proceedings were finalized.

Printed capillary microfluidic biosensors

Z. Zhang, S. Lang, Y. Farhan, Y. Tao, G. Xiao, (NRC) Advanced Electronics and Photonics Research Center, Ottawa (Canada), Z. Wang, C. Xu2, McMaster University, Hamilton (Canada)

Unfortunately, this abstract is not available, as the contribution was not confirmed at the time the conference proceedings were finalized.

DOI 10.5162/EUROSENSORSXXXVI/PT6.94

Fluorescence-based point of care device for real-time rapid detection of SARS-CoV-2

Than Linh Quyen, Huynh Van Ngoc, Aaydha Chidambara Vinayaka, Dang Duong Bang, Anders Wolff, Maria Dimaki, Winnie Edith Svendsen

Department of Biotechnology and Biomedicine, Technical University of Denmark (DTU-Bioengineering), DK-2800 Kgs. Lyngby, Denmark.

Corresponding Author's e-mail address: quylin@dtu.dk

Summary

We report the development of fluorescence-based point-of-care device (fPOC) for rapid, on-site and at-site detection of SARS-CoV-2 using real-time reverse transcription loop-mediated isothermal amplification (RT-rLAMP). The system includes three main parts: optical setup, heating elements, and injection molded cartridge with 12 reaction chambers. By integrating the RT-LAMP on the fPOC system, the fPOC device can detect the presence of SARS-CoV-2 in clinical samples within 50 min with 99% relative accuracy, 97.5% relative specificity, and 100% relative sensitivity compared to RT-qPCR.

Keywords: point-of-care (POC), fluorescence detection, SARS-CoV-2, COVID-19, Loop-Mediated isothermal amplification (LAMP)

Background

COVID-19 caused by SARS-CoV-2 killed more than 6.9 million people and led to remarkable social turmoil and economic disruption [1]. Antigen-based quick tests have been developed and are used to detect SARS-CoV-2 in clinical samples. However, they do not reach the sensitivity required to detect the early phases of a SARS-CoV-2 infection [2-3]. Several POC devices for the detection of SARS-CoV-2 have been reported [4-6]. These POC systems had a simple design and fast detection. However, the number of samples tested per run was limited. In addition, the test cartridge was complicated and remained high cost for fabrication [7-8]. In this work, we report a fluorescence point-of-care system based on RT-LAMP technology that can overcome these drawbacks of current point-of-care systems.

Fluoresence-based Point-of-Care Device (fPOC)

The fPOC device comprises of three main parts: (1) optical setup including a light source (LED), a phototransistor and EX/EM filters; two heating elements (top and bottom heaters) to maintain the temperature (60-65^{o}C) for the rRT-LAMP reaction (Fig. 1); and (3) an injection molded cartridge with 12 reaction chambers (Fig. 2a). The cartridge was designed with special pyramid shaped optical structures located next to the reaction chambers for reflecting the LED light to the reaction chambers at 90^{0} right angle (Fig. 1). The reaction chamber is heated rapidly and maintained at the reaction temperature (60-65^{o}C) by a bottom heater and a transparent top heater. The targeted nucleic acids in the samples were amplified by RT-LAMP within the chambers and detected by SYTO-9 DNA intercalating dye. The fluorescence signals are recorded and plotted in real-time using the Parallax Data Acquisition tool (PLX-DAQ) software on an external computer. Threshold values that were used to define whether the sample was negative or positive were determined by analysing 92 nagative and 184 positive samples on fPOC. The sample was considered as positive when the fluorescence intensity was larger than the threshold value.

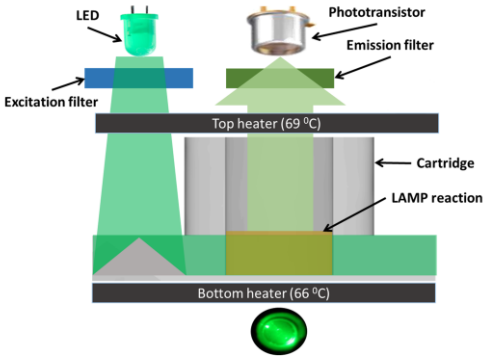

Fig. 1. fPOC working principle.

Results

The performance of fPOC was evaluated using 98 clinical samples including 58 positive and 40 negative samples confirmed by Luna® Universal One-Step RT-qPCR. Of 98 samples tested, 59 and 39 samples showed positive and negative results in the fPOC system, respectively; while 58 and 40 samples were observed positive and negative by RT-qPCR (Table 1). In comparison, fPOC showed 99% relative accuracy, 97.5% relative specificity, and 100% relative sensitivity to RT-qPCR. Moreover, the Cohens Kappa index (0.98) showed excellent agreement between these 2 methods. This result showed great potential for the use of fPOC for rapid on-site screening of SARS-CoV-2 virus in the pandemic management.

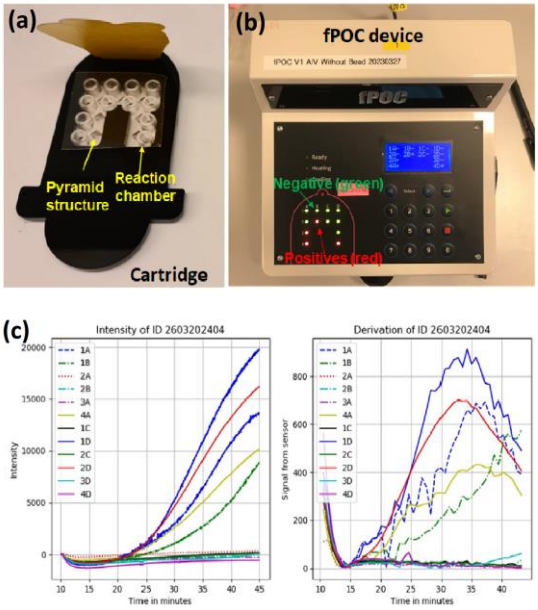

Fig. 2. (a) cartridge used in fPOC device; (b) fPOC device; (c) real-time amplification curve and derivation of amplification curve.

Table 1: Results of clinical samples tested on the fPOC and RT-qPCR

	RT-PCR			
	LOB 35	Positive	Negative	Total
fPOC	Positive	58	1	59
	Negative	0	39	39
	Total	58	40	***98***

References

[1] https://www.who.int/emergencies/diseases/novel-coronavirus-2019

[2] https://ec.europa.eu/health/sites/health/files/preparedness_response/docs/common_testingapproach_covid-19_en.pdf)

[3] https://www.sundhed.dk/sundhedsfaglig/laegehaandbogen/undersoegelser-og-proever/klinisk-biokemi/blodproever/antigentest-sars-cov-2-covid-19/

[4] Soares, R. R. G., Akhtar, A. S., Pinto, I. F., Lapins, N., Barrett, D., Sandh, G., et al. Sample-to-answer COVID-19 nucleic acid testing using a low-cost centrifugal microfluidic platform with bead-based signal enhancement and smartphone read-out. *Lab Chip* 21, 2932–2944 (2021); doi:10.1039/d1lc00266j

[5] Torezin Mendonça, G., Cassaboni Stracke, M., de Oliveira Coelho, B., Bruna Soligo Sanchuki, H., Klassen de Oliveira, V., Klerynton Marchini, F., et al. A new RT-LAMP-on-a-chip instrument for SARS-CoV-2 diagnostics. *Microchem. J.* 180, 107600 (2022); doi:10.1016/j.microc.2022.107600.

[6] Trick, A. Y., Chen, F. E., Chen, L., Lee, P. W., Hasnain, A. C., Mostafa, H. H., et al. (2022). Point-of-care platform for rapid multiplexed detection of SARS-CoV-2 variants and respiratory pathogens. *Adv. Mater. Technol.* 7, 1–11 (2022); doi:10.1002/admt.202101013.

[7] Beduk, D., Ilton de Oliveira Filho, J., Beduk, T., Harmanci, D., Zihnioglu, F., Cicek, C., et al. “All In One” SARS-CoV-2 variant recognition platform: Machine learning-enabled point of care diagnostics. *Biosens. Bioelectron. X* 10, 1–7 (2022); doi:10.1016/j.biosx.2022.100105.

[8] Kaci, K., del Caño, R., Luna, M., Milán-Rois, P., Castellanos, M., Abreu, M., et al. Paving the way to point of care (POC) devices for SARS-CoV-2 detection. *Talanta* 247, 123542 (2022); doi:10.1016/j.talanta.2022.123542.

Development of silicon hollow microneedles with beveled tip for medical applications

A. Bagolini, S. Pedrotti, C. Collini, N. Yadav, L. Lorenelli, M. Valt, N. Di Novo, Bruno Kessler Foundation, Trento (Italy

Unfortunately, this abstract is not available, as the contribution was not confirmed at the time the conference proceedings were finalized.

Development of silicon hollow microneedles with beveled tip for medical applications

A. Bagolini, S. Pedrotti, C. Collini, N. Yadav, L. Lorenelli, M. Valt, N. Di Novo, Bruno Kessler Foundation, Trento (Italy

Unfortunately, this abstract is not available, as the contribution was not confirmed at the time the conference proceedings were finalized.

DOI 10.5162/EUROSENSORSXXXVI/PT6.115

Electrochemical Biosensor Platform for Leptospirosis Diagnosis in Urine Samples

Patcharapan Suwannin[1,2], Kulachart Jangpatarapongsa[2], Monique Sigaud[1], Nadia Zine[1], Abdelhamid Elaissari[1], Abdelhamid Errachid[1*]

[1] *Universite Claude Bernard Lyon1, ISA, UMR5280, CNRS, 5 rue de la Doua, 69100 Villeurbanne, FRANCE*

[2]*Center for Research Innovation and Biomedical Informatics, Faculty of Medical Technology, Mahidol University, Bangkok 10700 Thailand.*

Corresponding Author's e-mail address:

abdelhamid.errachid@univ-lyon1.fr (Abdelhamid Errachid)

Summary:

We developed a sensitive genosensor to detect DNA *Leptospira interrogan* bacteria in urine sample that is non-invasive patient sample collection. Diazonium salt was electrodeposited onto the gold working electrode, showing external carboxylic acid from the surface, and the specific Loa22-probe to leptospires was immobilized. After that, targeted DNA testing showed the EIS change in the range of 0.5×10^{-5} - 0.016 pg/ml with a correlation R^2 of 0.9726. The high sensitivity was indicated 0.5×10^{-5} pg/ml. In addition, the developed sensor was highly specific with other urine-contaminated bacteria.

Keywords: Genosensor, CMA, Screen-printed electrode, Leptospirosis

Background

Leptospirosis is the pathogenic *Leptospira* bacteria of infection. This can cause the disease in both humans and animals. The clinical manifestations are mild to moderate and not specific leading to 90% of fever-developed patients are undifferentiated febrile illnesses [1]. Hence, laboratory testing with high accuracy is required. Recently, the electrochemical sensor has been remarkable in medical device development for easy-to-use portable and point-of-care testing [2, 3]. Therefore, DNA sensors are alternative way for early stage of the disease detection with high sensitivity, accuracy, and stability[4, 5].

In this study, we developed the genosensor to detect DNA of leptospires bacteria in the urine sample. The gold (Au) working electrode was deposited by a 4-carboxymethyl aryl diazonium (CMA) molecule before immobilizing a Loa22-specific single-stranded DNA (ssDNA) probe. The specificity with other contaminated bacteria in the urine was tested.

Methods

The Au electrode was electrodeposited by CMA solution 15 times on ice, showing a carboxyl group (-COOH). Carbodiimide crosslinking stimulated -COOH group by using 0.4 M of 1-ethyl- 3-(3-dimethyl aminopropyl) carbodiimide (EDC) and 0.2 M N-hydroxysuccinimide (NHS) in a ratio of 1:1 v/v with the amine at 5' end of *Loa22* oligonucleotide probe. Then, the surface was blocked with 5% bovine serum albumin for 30 min. The DNA sample was denatured at 95 °C for 5 min to hybridize leptospires DNA with modified working electrode for 25 min at RT. The surface was characterized by cyclic voltammetry (CV), and electrochemical impedance spectroscopy (EIS).

Results

The Nyquist plots of electrode modified were fitted by Randles equivalent circuit model (see Fig. 1c). The impedance result of DNA in different concentrations from 0 to 0.0016 pg/ml (see Fig. 1a). The impedance was decreased when increased DNA target concentration. This pattern causes the polyanionic nature of the DNA, the negative charges of a phosphate group are accumulated leading to another charge transfer partway [6].

To analyze the R_{ct} between each concentration, the DNA at 0 pg/ml was normalized with other DNA concentrations. This can be demonstrated by the sensitivity of the work. A calibration curve is demonstrated in the percentage of $\Delta\%R_{ct} = [R_{ct}(\text{initial}) - R_{ct}(\text{sample})] / R_{ct}(\text{initial}) \times$

100 to each concentration of DNA leptospires from 0 to 0.016 pg/ml with an R^2 value of 0.9726 with showing linear fitting regression equation as %ΔRct = 5.4941(ln DNA concentration) + 99.477 (see Fig. 1b). The result demonstrated a low detection limit of 5 fg/µl or 5 ag/ml.

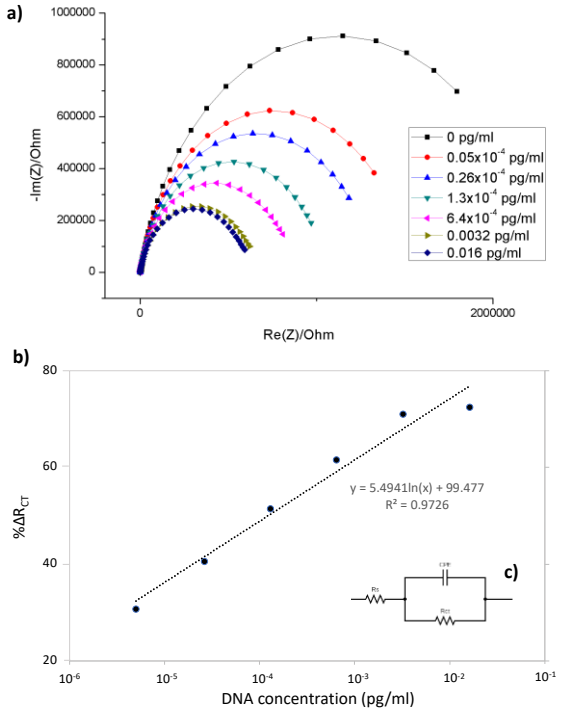

Fig. 1. a) EIS impedance after leptospires DNA various concentrations from 0 to 0.016 pg/ml in the solution of $[Fe(CN)_6]^{3-/4-}$ 5 mM in PBS. b) linear relationship between 0 to 0.016 pg/ml.

The specificity was examined with other bacteria that can be contaminated in urine sample e.g., *Escherichia coli*, *Staphylococcus aureus*, and *Salmonella typhi* and non-pathogenic leptospires *L. biflexa* serovar Patoc. The impedance result was calculated to $\Delta\%R_{ct}$ for specificity testing. These results of the pathogenic *Leptospira* serovar *Sherman*i demonstrated highest impedance response when compare with other bacteria. This result showed high specific of the genosensor to detect leptospires bacteria (see Fig 2).

The developed assay genosensor was advantageous in leptospirosis detection with the highest sensitivity and specificity. This could be examined the leptospira in urine and environment samples. This platform showed various advantages e.g., rapid analysis and low sample volume, which could screen leptospirosis disease in the early-stage infection.

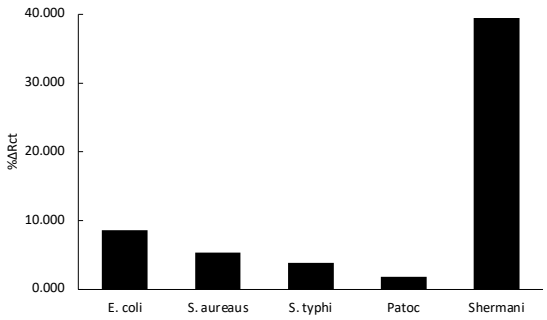

Fig. 2. Specificity testing of other bacteria e.g., E. coli, S. aureus, S. typhi, non-pathogenic leptospires, leptospires serovar Patoc and leptospires serovar Shermani.

Conclusion

The Fabrication genosensor for leptospires DNA detection in urine sample was successfully designed, demonstrating a sensitive and selective genosensor. Diazonium salt was electrodeposited onto the gold working electrode, showing external carboxylic acid from the surface, and the specific Loa22-probe to leptospires was immobilized. To verify the specificity of genosensors against other bacteria that may contaminate urine, e.g., *E. coli, S. aureus*, and *S. typhi* and non-pathogenic leptospires *L. biflexa* serovar Patoc the genosensor demonstrated excellent specific against pathogenic leptospires.

References

[1] S. V. Budihal and K. Perwez, "Leptospirosis diagnosis: competancy of various laboratory tests,", *J Clin Diagn Res*, vol. 8, no. 1, 199-202, (2014), doi: 10.7860/jcdr/2014/6593.3950.

[2] J. L. Hammond, N. Formisano, P. Estrela, S. Carrara, and J. Tkac, "Electrochemical biosensors and nanobiosensors,", *Essays Biochem*, vol. 60, no. 1, 69-80, (2016), doi: 10.1042/ebc20150008.

[3] D. Zhang and Q. Liu, "Biosensors and bioelectronics on smartphone for portable biochemical detection," *Biosensors and Bioelectronics*, vol. 75, 273-284, (2016), doi: https://doi.org/10.1016/j.bios.2015.08.037.

[4] D. Kala et al., "AuNPs/CNF-modified DNA biosensor for early and quick detection of O. tsutsugamushi in patients suffering from scrub typhus," *3 Biotech*, vol. 10, no. 10, 446, (2020), doi: 10.1007/s13205-020-02432-w.

[5] A. Kaushal, S. Singh, A. Kumar, and D. Kumar, "Nano-Au/cMWCNT Modified speB Gene Specific Amperometric Sensor for Rapidly Detecting Streptococcus pyogenes causing Rheumatic Heart Disease,", *Indian J Microbiol*, vol. 57, no. 1, 121-124, (2017), doi: 10.1007/s12088-016-0636-y.

[6] I. A. M. Frias, C. A. S. Andrade, V. Q. Balbino, and C. P. de Melo, "Use of magnetically disentangled thiolated carbon nanotubes as a label-free impedimetric genosensor for detecting canine Leishmania spp. infection," *Carbon*, vol. 117, 33-40, (2017), doi: https://doi.org/10.1016/j.carbon.2017.02.0

DOI 10.5162/EUROSENSORSXXXVI/PT6.120

PCR-free detection of miRNA biomarkers for neurodegenerative disorders

Paolo Calorenni[1], Laura Maria De Plano[1], Antonella Caccamo[1], Emanuele Luigi Sciuto[1], Salvatore Oddo[1], and Sabrina Conoci[1,2,3]
[1] University of Messina, V.le Ferdinando Stagno d'Alcontres, 31, Messina, Italy
[2] University of Bologna, Via Selmi 2, Bologna, Italy
[3]URT Lab Sens - CNR-DSFTM, Viale F. Stagno D'Alcontres 37, Messina, Italy

Corresponding Author's e-mail address: emanueleluigi.sciuto@unime.it

Summary:
A PCR-free strategy for microRNAs (miRNAs or miR-) fast and accurate detection is presented. The approach relies on the functionalization of a gold working electrode (WE) with an array of oligonucleotide probes selective for two miRNAs biomarkers that affect some intracellular processes related to human neurodegenerative disorders. The electrochemical impedance spectroscopy (EIS) analysis performed on the modified electrode allowed to directly sense the probes/miRNA duplex formation in a fast and accurate mode that is suitable for Point-of-Care (PoC) diagnostic applications.

Keywords: PCR-free detection; miRNAs; neurodegenerative disorders; solid state hybridization; EIS analysis; PoC.

Introduction

MiRNAs are small non-coding RNA molecules that introduced a new frontier of diagnostics to screen and predict human diseases at an early stage, when therapies could be more effective against the pathological onset. Some miRNAs are involved in various aspects of human neurodegenerative disorders, including the Alzheimer's disease pathogenesis. This is the case of miR-34a, whose dysregulation can affect regulating processes such as neuronal apoptosis, inflammation and Aβ metabolism, and miR-29a, that can conditionate the synaptic plasticity and neuronal survival. Both miRNAs are free to circulate in the bloodstream and easy to be extracted and purified, which makes them potential biomarkers for molecular diagnostics applications and integration into PoC technologies [1,2].
Within this perspective, a PCR-free strategy can be a suitable approach for the development of new point-of-care devices for massive screening [3-5].
In this contribution a PCR-free strategy for the selective and fast detection of miR-34a and miR-29a is proposed. The detection approach is based on the EIS analysis of a gold working electrode that is functionalized with an array of miRNA-specific oligonucleotide capture probes. Thanks to their specific design, probes can hybridize at solid state with the miRNA targets and these are revealed by measuring the resistance and capacitance variations due to the duplex formation, without any PCR amplification and long thermal cycling, thus, simplifying the complexity of analysis and the architecture of the entire detection system towards a PoC format.

Materials and method

The oligonucleotide capture probes for miRNA PCR-free detection have been designed as follows: miR-34a probe → HS-C6-ACAACCAGCTAAGACACTGCCA; miR-29a probe → HS-C6-TAACCGATTTCAGATGGTGCTA. More precisely, a chain of 6 carbon atoms (C6) has been added at 5' end of each sequence, working as spacer for the right orientation of probes once immobilized on the surface. Upstream the spacer a thiol (SH-) group has been added for the probes grafting on the metallic surface of the EC chip. Synthetic ribonucleotide sequence of mature miR-34a and miR-29a have been purchased by MetaBion and used as targets.
As schemed in Fig. 1, the WE surface has been modified by a first a cleaning step performed with alumina slurry and a sonication in a 1:1 solution of ethanol and ultrapure water. Subsequently, a CV voltammetry in H_2SO_4 has been applied to the electrode to complete its surface cleaning. For the functionalization with capture probes, the electrode surface has been incubated in a 1:10 solution of 6-mercapto-1-hexanol and probes in PBS 10 mM (pH=7.4) at 25°C for 4h with 70rpm/min agitation, to graft a

self-assembled monolayer of thiolate probes. Lastly, the functionalized electrode has been dipped into a 1µM solution of miRNA targets in PBS 10 mM (pH=5.5) and this has been incubated at 50 °C for 3h30 for the final hybridization.

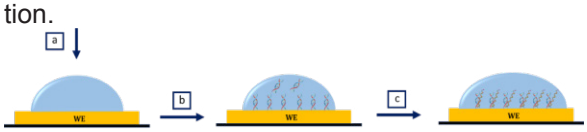

Fig 1. Electrode gold surface preparation: (a) surface cleaning; (b) probes grafting; (c) miRNA hybridization.

The electrochemical Impedance Spectroscopy (EIS) analysis of the solid-state hybridization with the miRNAs has been performed by preparing an electrochemical cell that has been properly assembled including the functionalized WE, a Pt wire as counter electrode (CE), and an Ag/AgCl reference electrode (RE). All electrodes have been dipped into a 5 mM solution of $[Fe(CN)6]^{-3/-4}$ in PB buffer (pH=6.8), used as redox-active analyte. The EIS has been done in the frequency range of 200 MHz to 100 MHz and by fixing current and potential at 1 mA and 0.240V, respectively.

Results

Nyquist plots shown in Fig. 2 have been obtained by the EIS analysis performed after probes grafting and miR-34a and 29a hybridization (Fig. 2a and 2b, respectively) on the WE surface. The resistance values confirmed the effectiveness of the functionalization process, comparing the bare gold WE to the probes-modified WE, and the miRNA PCR-free detection. Indeed, the resistance of 210 Ω measured on the bare surface (black curve) increased to 1338 Ω after the 34a probes grafting and 1377 Ω after the 29a probes addition (green and blue curves in figures), probably due to the steric hindrance and electrostatic repulsion produced between the probes and the formed passivating layer. The resistance furtherly increased up to 1730 Ω and 2061 Ω after the miR-34a and miR-29a hybridization (orange and red curves) as consequence of the perfect match formation and the doubled number of strands added to the surface dielectric, proving the ability of this strategy to directly sense the miRNAs without further amplifications.

Fundings

This work has been funded by co-financing of the European Union - FSE-REACT-EU, PON Research and Innovation 2014-2020 DM1062 / 2021 (CUP J45F21001750007) and the European Union (NextGeneration EU) through the MUR-PNRR project SAMOTHRACE (ECS00000022).

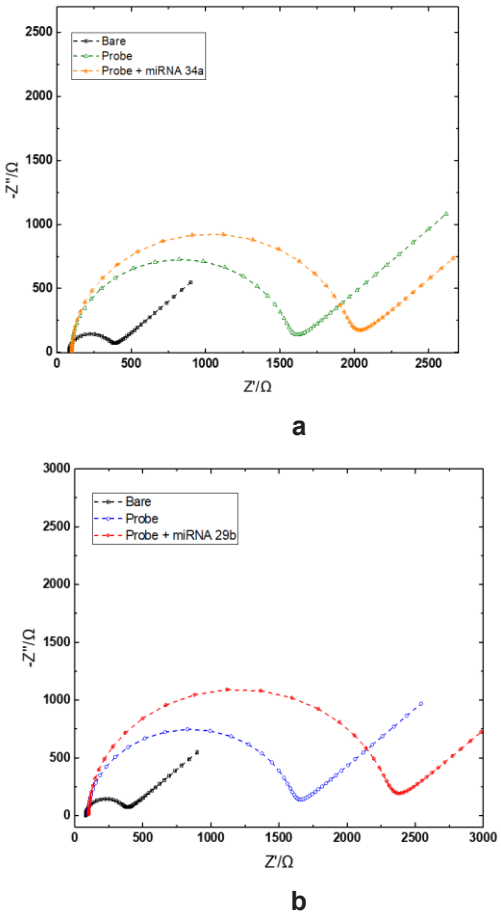

Fig 2. EIS analysis of miR-34a (a) and miR-29a (b) by probe-modified gold WE surface.

References

[1] E. Cardona, C. Guyomar, T. Desvignes, J. Montfort, S. Guendouz, J. H. Postlethwait, S. Skiba-Cassy, J. Bobe, *BMC Biology* 19, 235 (2021)

[2] *M. H. Sohel, Achievements in the Life Sciences* 10, 17 (2016); doi: 10.1016/j.als.2016.11.007

[3] P.Calorenni, AA Leonardi, EL Sciuto, MG Rizzo, MJ Lo Faro, B Fazio, A Irrera, S Conoci, Advanced Healthcare Materials 12, 2023, Article number 2300512 – DOI 10.1002/adhm.202300512

[4] P. Nikolaou, EL Sciuto, A Zanut, S Petralia, G Valenti, L Prodi, S Conoci, Biosensors and Bioelectronics, 2022, Article number 114165- DOI 10.1016/j.bios.2022.11416

[5] Petralia S., Sciuto E.L., Di Pietro M.L., Zimbone M., Grimaldi M.G., Conoci S. Analyst, 2017, 142, 2090 2093

DOI 10.5162/EUROSENSORSXXXVI/PT6.121

Direct Electrode Modification of Paper-based Microfluidic Electrochemical Sensors Through Electrodeposition and Electropolymerization for Clozapine Sensing

Mohammad Hossein Ghanbari [1, 2], *Bastian J.M. Etzold* [1, 2, *]

[1]*Friedrich-Alexander-Universität Erlangen-Nürnberg, Power-To-X Technologies; 90762 Fürth, Germany*
[2]*Technische Universität Darmstadt, Ernst-Berl-Institute for Technical Chemistry and Macromolecular Science, Peter-Grünberg-Straße 8, 64287, Darmstadt, Germany*

bastian.etzold@fau.de

Summary:

Here we demonstrate the superior performance of microfluidic electrochemical sensors (µCS) over screen-printed carbon-based electrodes (SPCE). Additionally, electrodeposition of gold nanoparticles (ED (AuNPs)) and electropolymerization of L-cysteine (EP (L-cys)) are introduced for the first time for modifying the working electrode through a paper-based microfluidic sensor. Also, the sensor was employed for clozapine (CLZ) sensing in human blood plasma, which depicted the excellent applicability of the device which making it a promising platform for point-of-care diagnostics.

Keywords: Microfluidic electrochemical sensor, Paper-based sensor, Electrodeposition, Electropolymerization.

Introduction

Schizophrenia is a debilitating mental disorder characterized by disruptions in perceiving reality which clozapine (CLZ) stands out as the most promising drug for treating that.

Using catalytic active modifiers and additives e.g. to improve electron or ion transport in electrochemical sensors usually offers significant benefits by improving sensitivity and selectivity. An elegant way to introduce both is electrodeposition (ED) and electropolymerization (EP). Despite classical static devices with glassy carbon electrodes or SPCE electrodes paper-based microfluidic electrochemical sensors have gained significant attention [1]. Advantages are simplicity, portability, cost-effectiveness, and potential for point-of-care applications. Although ED of AuNPs and EP of (L-cys) improved the sensing in classical static devices, electrodes for microfluidic systems have up to now not been functionalized by these approaches. Furthermore, despite an external functionalization a direct ED and EP onto the electrode within the final paper-based microfluidic device could be possible, but was not reported up to now.

Scope of this study is to find proper conditions for the ED of AuNPs and EP of (L-cys) onto the electrodes of paper-based microfluidic electrochemical sensor, while using the microfluidic channel also for transport of the electrodeposition solution [2]. Furthermore, the study compares the performance of widely employed SPCE electrodes to µCS based systems. Ultimately, the µCS/S (ED & EP) employed for CLZ sensing in real blood serum successfully.

Experimental

The alignment of the component for the µCS device is sketched in Scheme 1. After providing the $HAuCl_4$ and L-cysteine solution through the sponge the electrochemical fabrication and detection are carried out through cyclic voltammetry (CV). AuNPs were electrodeposited and L-cys were electropolymerized simultaneously through the µCS by handling a potential window of −1.5 to +2.2 V at a scan rate of 100 mV s^{-1} via CV run for 10 cycles in a solution of 0.1 M PBS at pH = 6.0 consists of 1.0 mM $HAuCl_4$ and 1.0 mM L-cys. As a result, the prepared simultaneous ED of AuNPs and EP of L-cys through a paper-based microfluidic sensor (µCS/S (ED & EP)) was used after 3 CV runs in 0.1 M PBS at pH = 6.0 and employed as the sensor. Electrochemical measurements were performed using an Ivium Potentiostat (Vertex) controlled with IviumSoft software. Scanning electron microscope (SEM), CV, and electrochemical impedance spectroscopy (EIS) were employed to certify that the AuNPs and poly (L-cys) were attached successfully to the working electrode surface.

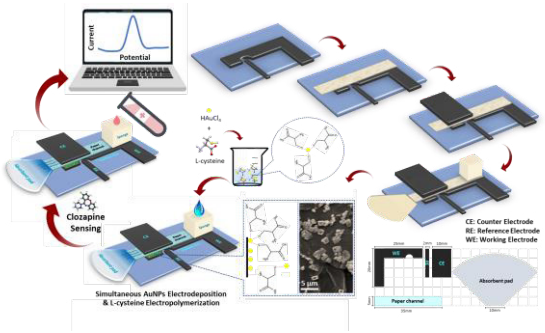

Scheme. 1. μCS/S (ED & EP) sensor assembling process.

Results and discussion

To confirm the immobilization of each substrate onto the working electrode, CVs and EIS of the platforms were recorded in a solution consisting of 5.0 mM of $[Fe(CN)6]^{3-/4-}$. By modifying the platforms by simultaneous ED of AuNPs and EP of (L-cys) not only did peak currents increase dramatically but also ΔE_p were decreased to 17 mV and 13 mV for SPCE/S (ED & EP) and μCS/S (ED & EP), respectively. By comparing the EIS curves related to the bare SPCE and μCS it is clear that the R_{ct} value for μCS (46 Ω) is much lower than SPCE (690 Ω). It may be attributed to the 3D and sandwich-like structure of μCS devices. SPCE/S (ED & EP) and μCS/S (ED & EP) present very smaller semicircles with R_{ct} values of 225 Ω and 13 Ω, respectively. The herein-reported EIS data corroborate the preceding results related to the CV data and both confirm that the electrode for sensing is successfully obtained.

Square wave voltammetry (SWV) was applied for CLZ analysis under the optimized protocols (Fig. 1A) and calibration plot for that were constructed under optimal conditions in which the peak currents of CLZ increase linearly with concentration from 0.5 to 10.0 μM in 0.1 M ABS in pH = 8.0 (Fig. 1B). The limit of detection (LOD) and quantitation (LOQ) were calculated to be 70 nM and 0.23 μM, respectively.

For the stability study, the SWV signal employed in the presence of 3.0 μM of CLZ in 0.1 M PBS with pH = 8.0 for 6 consecutive SWVs and the peak current response is depicted against the replicate (Fig. 1C). The anodic stripping current exhibits only a marginal decrease (11%) after 6 repetitions. This slight reduction is likely attributed to the depletion of the analyte within the sampling sponge or/and the filling or removal of the modifier layer from the WE surface. This investigation also shows the great robustness of μCS/S (ED & EP) for drug sensing applications.

To determine the sensor's ability to CLZ sensing in the presence of possible potentially interfering substances, selectivity studies were carried out (Fig. 1D). Results show that with 30.0 μM ascorbic acid, 30.0 μM uric acid did not significant interfere with 10.0 μM CLZ and the sensor was able to detect CLZ even in the presence of these common interfering substances. However, in the presence of 30.0 μM glucose, the CLZ signal drops by 20%, in the presence of 30.0 μM ascorbic acid, 30.0 μM uric acid and 30.0 μM glucose as a same time did not significant interfere with 10.0 μM CLZ. The sensor exhibited a negligible altering current and gave notable selectivity in CLZ sensing in the presence of ascorbic acid, glucose and uric acid as common interfering biomolecules.

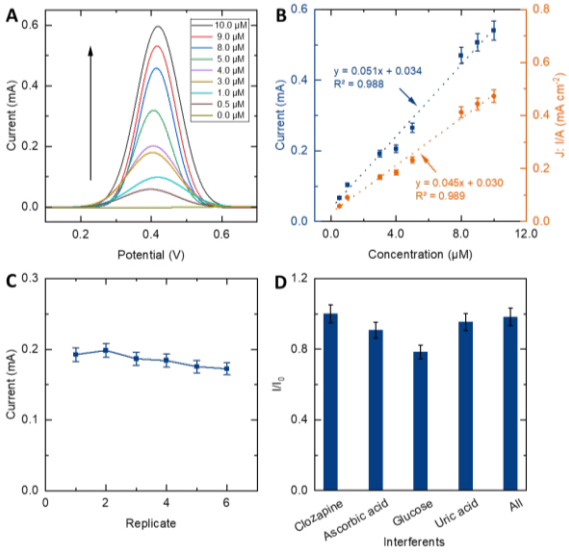

Fig. 1. (A) SWVs of the μCS/S (ED & EP) for different concentrations of CLZ, (B) the calibration plot of Ipa vs. CLZ concentration, (C) Stability study, and (D) selectivity study.

Conclusion

The μCS offers several advantages over SPCE in terms of cost, simplicity, and sensitivity. These advantages are due to the combined microfluidic configuration, 3D electrode layout, and a unique electrochemical modifier. The μCS/S (ED & EP) is capable of detecting CLZ with a wide linear range, low LOD, and high sensitivity. We believe our findings have significant implications in developing other portable, fast, and cost-effective electrochemical sensors, such as clinical diagnosis and security inspection.

References

[1] L.-L Shen, et al., Paper-based microfluidics for electrochemical applications, *ChemElectroChem* 7.1, 10-30 (2020); doi: 10.1002/celc.201901495

[2] MH Ghanbari, et al., Superior performance of N-doped carbon Nanoonions/Nafion based microfluidic electrochemical Cd2+ sensor when compared to Screen-Printed Carbon-Based electrode devices, *Microchemical Journal* 110506 (2024); doi: 10.1016/j.microc.2024.110506

DOI 10.5162/EUROSENSORSXXXVI/PT6.124

Electrochemical detection of pathogen nucleic acid for bio-sensing application

Emanuele Luigi Sciuto[1], Paolo Calorenni[1], Tommaso Gritti[2], Stefania Varani[2], Giovanni Valenti[2],Maria Vittoria Balli[2], Luca Prodi[2] and Sabrina Conoci[1,2,3]
[1] University of Messina, V.le Ferdinando Stagno d'Alcontres, 31, Messina, Italy
[2] University of Bologna, Via Selmi 2, Bologna, Italy
[3]URT Lab Sens - CNR-DSFTM, Viale F. Stagno D'Alcontres 37, Messina, Italy

Corresponding Author's e-mail address: emanueleluigi.sciuto@unime.it

Summary:
Electrochemical impedance spectroscopy (EIS)-based detection of protozoan *Leishmania infantum* (LI) kinetoplastic (k)DNA is presented. Thanks to self-assembled monolayer of oligonucleotide probes on the top of a gold electrode surface, the method allowed to perform a molecular quantification of kDNA copies excluding the time-consuming amplification of genetic target and avoiding the complex procedures of conventional diagnostic methods.

Keywords: Electrochemical Impedance Spectroscopy; *Leishmania infantum* kDNA; cooperative hybridization; molecular sensing.

Introduction

Infectious diseases area major threat for mankind. This health burden challenged all populations, especially those of developing countries, where undernutrition, poor hygiene practice, and underdeveloped health systems do not guarantee access to appropriate treatments. Moreover, the lack of effective monitoring facilities fails to keep infectious diseases epidemic under control. The COVID-19 pandemic has increased this threat even more causing, only in its first year, millions of deaths and impacting dramatically the quality of life worldwide. The COVID-19 outbreak highlights as the availability of diagnostic methods that are, in the meantime, fast, cheap, reliable and able to provide genetic response, is crucial for the management of these diseases. This is not only the case of SARS-CoV-2, as the problem of fast genetic detection is common to all infectious agents, such as viruses, bacteria, and parasites, including those that could potentially be the cause of the next pandemics [1-3].

In this contribution, we present the genetic detection of protozoan *Leishmania infantum* trough an capacitive quantification based on EIS (electrochemical impedance spectroscopy). This paves the way to develop nanobiotechnological platform to address, at the same time, the problem of cost, simplicity, reliability, and sensitivity of the pathogen detection, making a breakthrough advancement in the fight against communicable diseases.

Materials and method

Two oligonucleotide capture probes have been selected and customized for the detection of kDNA target: LI-1 probe → HS-C6-5'-CTTTTCTGGTCCTCCGGGTAGG-3'; LI-2 probe → HS-C6-5'-CCACCCGGCCCTATTTTACACCAA-3'.
Both probes are modified at 5' end with a thiol group that favors the chain grafting on the sensing surface. Moreover, they are complementary to two regions of the same kDNA gene to perform a cooperative hybridization mechanism that increases the yield and stability of the probe/target duplex.
The kDNA target has been extracted and purified from LI cultures and used at the final concentration of 10^6-10^3-10 copies/µL.
Fig. 1 reports the functionalization of the sensing surface that is a gold surface of a 2 mm diameter gold working electrode (from CHInstruments). This surface has been modified by a first a cleaning step performed with alumina slurry and CV cycles with H_2SO_4. Then, thiolate capture probes have been grafted at 25°C for 4 h on the gold surface that, subsequently, has been passivated with 6-mercapto-1-hexanol at 25°C overnight. For the quantification by EIS analysis, the sensing surface has been dipped into three solutions of kDNA at 10^6-10^3-10 copies/µL in PBS and incubated at 50°C for 3h30 to trig the cooperative hybridization.

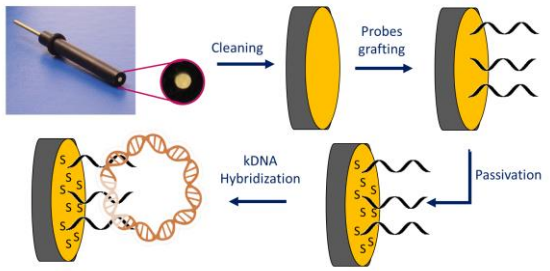

Fig 1. Chemical protocol of electrode sensing surface functionalization.

kDNA detection and quantification has been performed by EIS analysis. For the test, the functionalized gold electrode has been included as working electrode (WE) in an electrochemical cell that has been properly assembled with a Pt wire as counter electrode (CE) and an Ag/AgCl reference electrode (RE). Then, the cell has been exposed to a solution of 5 mM of $[Fe(CN)_6]^{-3/-4}$ that was used as redox mediator. Measurements have been done at 200 MHz to 100 MHz frequency range, 1mA current and 0.234V potential.

Results

Results of EIS analysis are reported in the Nyquist plot of Fig. 2 and Table 1. The analysis has been performed using the sensing WE before and after the functionalization, in order to assay the effectiveness of the chemical protocol, and after the hybridization with the three concentrations of kDNA. As shown, the trend of resistance and capacitance confirm the probes grafting and thiol passivation of the WE gold surface, with an increase of values from the 210 Ω of bare gold to the 663.75 Ω and 1901.6 Ω of probe and probe+thiol modified surfaces (black, green and purple curves in Fig. 2, respectively). This could be due to the electrostatic forces and steric hindrance brought by the grafted oligos and the increase of stationary charges caused by the thiol passivator addition [4]. Once hybridized to the kDNA, the system resistance furtherly increased to 2712.7 Ω, 3895.1 Ω and Ω 13240 Ω consistently with the concentration of the 10-10^3-10^6copies/µL solutions (orange, red and blue curves, respectively) as consequence of the increased number of nucleic acid strands added to the surface. These results proved the sensing performances of the method and its suitability for fast molecular sensing applications.

Tab. 1: Resistance and capacitance values of EIS analysis.

WE surface	R2 (Ω)	C_{DL}(nF/mm²)
Au Bare	210	3,18
Probe	663,75	41,56
Probe+thiol	1901,6	50,1
kDNA (10 cps/µL)	2712,7	51,1
kDNA (10^3/cps/µL)	3895,1	55,5
kDNA (10^6/cps/µL)	13240	79,02

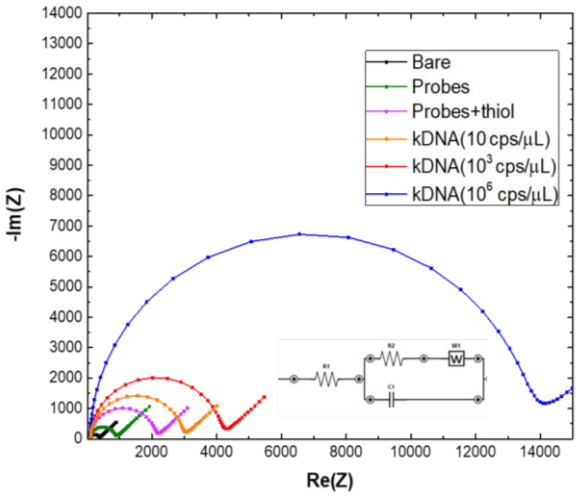

Fig 2. EIS quantification test of kDNA by probe-modified WE.

Acknowledgement

The research was supported by the European Union's Horizon Europe EIC Pathfinder Open programme "ECLIPSE project" (Grant Agreement Nr. 101046787).

References

[1] [1] P. Nikolaou, EL Sciuto, A Zanut, S Petralia, G Valenti, L Prodi, S Conoci, Biosensors and Bioelectronics, 2022, Article number 114165- DOI 10.1016/j.bios.2022.11416

[2] Petralia S., Sciuto E.L., Di Pietro M.L., Zimbone M., Grimaldi M.G., Conoci S. Analyst, 2017, 142, 2090 2093

[3] A. T. Celebi, M. Olgiati, F. Altmann, M. Kogler, L. Kalchgruber, J. Appenroth, U. Ramach, M. Valtiner, L. L. E. Mears, in *Encyclopedia of Solid-Liquid Interfaces* (First Edition) (Eds: K. Wandelt, G. Bussetti), Elsevier, Oxford,8–28 (2024).

[4] AA Leonardi, MJ Lo Faro, S. Petralia, B. Fazio, Barbara, P. Musumeci, Paolo, S Conoci, A. Irrera, F. Priolo, ACS Sensors, 2018 1690 - 169728 – DOI 10.1021/acssensors.8b00422

DOI 10.5162/EUROSENSORSXXXVI/PT6.126

3D Printed Microfluidic Lab-on-a-Disk for Centrifugal Droplet Generation

Wojciech Kubicki[1], Aung Thiha[2], Tymon Janisz[1], Karunan Joseph[2], Nurul Fauzani Jamaluddin[2], Marc Madou[3], Rafał Walczak[1], Goran Stojanović[4], Fatimah Ibrahim[2]
[1] Wrocław University of Science and Technology, Wrocław, Poland
[2] University of Malaya, Kuala Lumpur, Malaysia
[3] University of California, Irvine, USA
[4] University of Novi Sad, Novi Sad, Serbia

wojciech.kubicki@pwr.edu.pl

Summary:
A 3D printed microfluidic lab-on-a-disk (LOAD) for generation of oil-in-water droplets is presented. The device is the first solution combining droplet microfluidics, centrifugal technique, and additive manufacturing technology. Compared to standard LOADs, which are fabricated using subtractive methods, additive manufacturing technology has enabled development of a new research tool that can be easily and quickly replicated or redesigned for versatile microfluidic lab processes, e.g. sample preparation, biochemical reactions, or biomarker detection, with high potential for point-of-care applications.

Keywords: lab-on-a-disk, 3D printing, droplet generation, centrifugal technique, microfluidics

Introduction

Droplet microfluidics enable repeatable generation and precise control of discrete volumes of fluids in the nano- and picolitre range. Droplets of water-in-oil or oil-in-water can be used as individual microreactors, cell incubators, or drug delivery systems [1]. Unlike pressure-driven or electrokinetic fluid propulsion methods, the implementation of the centrifugal technique, also called as laboratory-on-a-disk, is one of the prospective improvements towards a real point-of-care application of droplet-based devices [2]. However, until now most lab-disks have been made of poly(methyl methacrylate) (PMMA) using only subtractive manufacturing methods, that require multistep patterning and lamination of polymer layers, which has challenged the spread of LOAD devices [3]. In this work, a monolithic lab-on-a-disk for centrifugal droplet generation, which was fabricated in a single additive manufacturing process, is presented.

Methods

The dimensions of the device are 120 mm in diameter, 15 mm central mounting hole, and a thickness of 1.4 mm, similar to a standard CD. The structure contains 4 radial microfluidic units for the generation of various droplet volumes according to the centrifugal profile (Fig. 1a). Each unit consists of an input chamber for a dispersed phase, a microchannel with a nozzle, and an output chamber for a continuous phase.

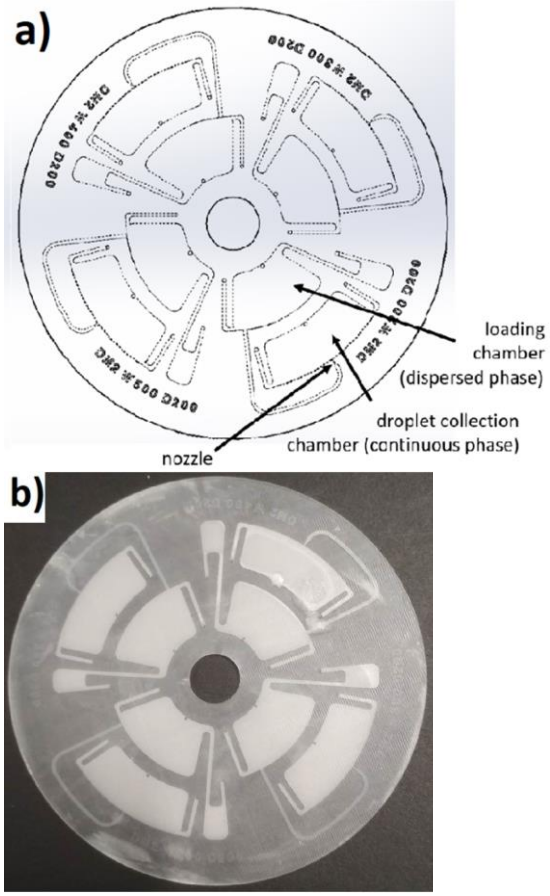

Fig. 1. A developed microfluidic lab-on-a-disk for droplet generation: a) model of the device, b) ready-to-use device (diameter of a standard compact disk).

The lab-disk was fabricated using multi-jet 3D printing technology from a semitransparent and biodegradable polymer (VisiJet M3 Crystal) and wax-like support material (Fig. 1b). Compared to subtractive technology used to manufacture PMMA LOADs, the additive manufacturing process allows for faster and simpler fabrication of the device with a minimum staff engagement and required high-tech equipment. Moreover, the monolithic structure provides homogeneous surface properties of the microfluidic units.

The spinning experiments were performed using laboratory setup for centrifugal analysis, comprising: BLDC motor, tachometer, illuminator, high speed camera, data acquisition card, and computer with dedicated control software. The microscopic images of the droplets were processed using a developed graphical application (LabVIEW), which enabled detection of spherical objects, calculation of their dimensions based on the scale pattern, and visualization of the statistical data.

Results

The monolithic lab-disk was characterized, including mechanical properties (e.g. deflection during spinning), impact of the chemical pretreatment (contact angle measurement for various organic solvents applied), and determination of the burst speed of oil and water. The device allowed the production of repeatable volumes of oil-in-water microdroplets without any additives, and with the use of the centrifugal force only (Fig. 2). Various spin profiles and nozzle widths were investigated to produce microdroplets in an approx. volume range from 5 to 270 nL. It was also noted that the influence of droplet generation speed on the average droplet volume is negligible below the value of the burst speed of water or oil, providing the emulsion with almost constant dispersion.

Conclusions

The first 3D printed lab-disk microfluidic device enabled the generation of oil-water emulsions with precisely controlled volumes. The software developed allowed for automatic image analysis and visualization of the results. Obtained diluted emulsions of essential oils in water can be used e.g. in intraoral microfluidic dispensers for therapeutic applications (as it is being investigated in other works). Applied here centrifugal technique combined with additive manufacturing technology can be implemented to develop novel portable instruments (similar to CD players) equipped with monolithic lab-disks, which could be easily adapted to other applications.

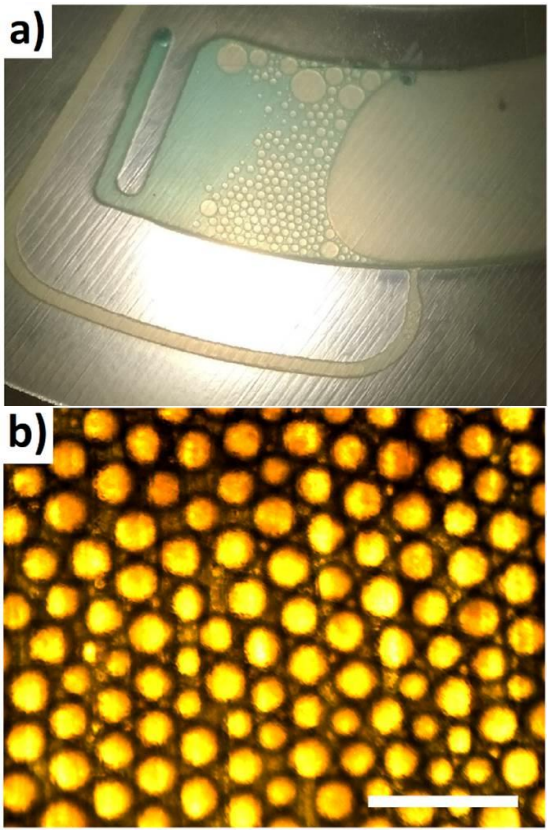

Fig. 2. The results of centrifugal droplet generation in the lab-on-a-disk: a) close-up of the output chamber after the emulsification process (some droplets merged after the device had been dismounted), b) magnified view of oil-in-water droplets generated in the output chamber (the bar indicates 1 mm).

References

[1] S.Y. Teh, R. Lin *et al.*, Droplet microfluidics, *Lab Chip* 8, 198-220 (2008); doi: 10.1039/B715524G

[2] M. Tang, G. Wang *et al.*, A Review of Biomedical Centrifugal Microfluidic Platforms, *Micromachines* 7, 26 (2016); doi: 10.3390/mi7020026

[3] R. Gorkin, J. Park *et al.*, Centrifugal microfluidics for biomedical applications, *Lab Chip* 10, 1758-1773 (2010); doi: 10.1039/B924109D

Acknowledgement

This research was funded by EU Horizon 2020 Marie Skłodowska-Curie Actions Research and Innovation Staff Exchange program (H2020-MSCA-RISE) in the project “SALSETH” (grant number 872370), and by the Polish Ministry of Education and Science program entitled “PMW – Co-financed International Projects” (grant number 5089/H2020/2020/2) in a period 2019-2024.

Enhanced MIP-based Electrochemical Sensing of Estrogen and Progesterone for Improved Management of Women's Health

V. Kamat, J. Lagier, S. Bhansali, Florida International University, Miami (USA)

Unfortunately, this abstract is not available, as the contribution was not confirmed at the time the conference proceedings were finalized.

Enhanced MIP-based Electrochemical Sensing of Estrogen and Progesterone for Improved Management of Women's Health

V. Kamat, J. Lagier, S. Bhansali, Florida International University, Miami (USA)

Unfortunately, this abstract is not available, as the contribution was not confirmed at the time the conference proceedings were finalized.

Compact System for Stimulation and Recording of Field Potentials from Cardiac Tissue Preparations

A. Velarte, A. Otín, E. Pueyo, Instituto de Investigación en Ingeniería de Aragón, Zaragoza (Spain)

Unfortunately, this abstract is not available, as the contribution was not confirmed at the time the conference proceedings were finalized.

Compact System for Stimulation and Recording of Field Potentials from Cardiac Tissue Preparations

A. Velarte, A. Otín, E. Pueyo, Instituto de Investigación en Ingeniería de Aragón, Zaragoza (Spain)

Unfortunately, this abstract is not available, as the contribution was not confirmed at the time the conference proceedings were finalized.

DOI 10.5162/EUROSENSORSXXXVI/PT6.182

An Application to Count Yeast Cells Using Novel Lab-On-a-Chip Solution for the Wine Value Chain

Ismael Benito-Altamirano[1,3], Sergio Moreno[1], David M. Vaz-Romero[1], Anna Puig-Pujol[2], Gemma Roca-Domènech[2], Joan Canals[1], Anna Vilà[1], J. Daniel Prades[1], Ángel Diéguez[1]
[1] Department of Electronic and Biomedical Engineering, Universitat de Barcelona, Martí i Franquès 1, 08028 Barcelona, Spain
[2] INCAVI-IRTA. Catalan Institute of Vine and Wine - Institute of Agrifood Research and Technology. Plaça Àgora, 2. 08720 Vilafranca del Penedès, Barcelona, Spain
[3] eHealth Center, Faculty of Computer Science, Multimedia and Telecommunications, Universitat Oberta de Catalunya, Rambla del Poblenou, 156, Sant Martí, 08018 Barcelona, Spain

ismael.benito@ub.edu

Summary:
Lab-on-a-chip solutions have emerged as a viable cost-effective portable solution to bring laboratory capabilities elsewhere. This kind of technologies enable to speed up decision-making process in several industry value chains. In this work, we present an application to count yeast cells along the wine production value chain. Our solution is based upon a microscope-on-a-chip device designed with out-of-the-shelf components. The solution also relies on top of state-of-the-art computer vision solutions and we demonstrate it operates to the same standards as optical microscopy.

Keywords: Lab-on-a-chip, holography, microfluidics, computer vision, wine quality.

Introduction

In recent years, lab-on-a-chip solutions have emerged as *in situ* solutions to traditional sample analysis for several biomedical essays. Despite this, several proposals need the fabrication of expensive custom components. In this work, we present a cost-effective solution aimed to automate a problem presented in the wine industry: certain types of wines as sparkling wines require a strict yeast count at specific stages of their production. The wine industry is one of the industries with more impact in Western Europe. According to the annual report State of the Work vine and wine sector (2022), four Western-European countries (Spain, France, Italy and Portugal) are present in the top ten countries for vineyard surface area of the globe, netting a total 36,9% of the vineyard surface area of the Earth [1].

Proposal

Here, we present an approach to use out-of-the-shelf components to create a laboratory setup to solve this problem, which consists of a lensless holographic microscope built on top of commercial components, like a lensless camera (37U Series, The Imaging Source) and an LED micro-display (JBD013 Series, Jade Bird Display), alongside with custom 3D-printed parts and common laboratory disposables. We have previously introduced similar experiences using these kind of microscope-on-a-chip technologies applied to other fields [2].

This set-up is connected to a novel application, developed using Python programming language and the QT desktop application framework. Such application can capture real-time images from the wine samples. Later, the user can execute several steps of a computer vision pipeline to post-process the images and count the cells. A typical pipeline consists of: normalization, feature extraction, image composition (to increase both resolution and scanning area), holographic reconstruction and particle count. Our application implements state-of-the-art computer vision and machine learning algorithms to extract the features of the images in the first place to create composite images to increase the sensing range of the microscope, for example the well-known SIFT method [5]; also regarding the particle count, for example, the Hough transform [3] or the YOLO neural network [4].

Results

A series of experiments were designed to test the viability of our setup as an alternative to confocal imaging in order to measure cells of *Saccharomyces cerevisiae* in white wine samples.

Here, we present a few of these results. For example, as a qualitative result, Fig. 1 shows, in a visual inspection, how the microscopy technique is able to recover cells images from the holographic reconstructions of the captured images. Moreover, this figure –extracted from our graphical framework interface– shows the automatic count of cells using the Hough transform method. For this sample, a total 80 cells were retrieved, which implies a $9.70 \cdot 10^6$ cells/mL count in the wine sample. As it can be seen in the image, the resolution of the reconstructed image is around 2-3 µm, half the size of a typical *Saccharomyces cerevisiae* cell.

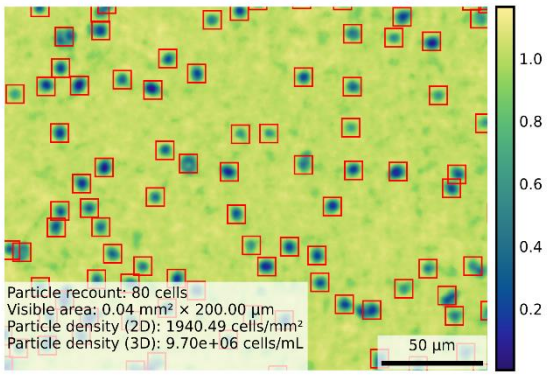

Fig. 1. A capture from our microscope-on-a-chip setup. The capture is the result of applying a reconstruction algorithm that consists on: normalization, feature extraction, image composition (from a 5x5 mosaic to a single image), holographic reconstruction and particle count.

Finally, we compared our lab-on-a-chip measurements with ones from the optical microscopy. We created a culture of *Saccharomyces cerevisiae* and diluted it to lower concentrations exposing the samples the both devices. Fig. 2 shows the calibration comparison between both sets of measurements.

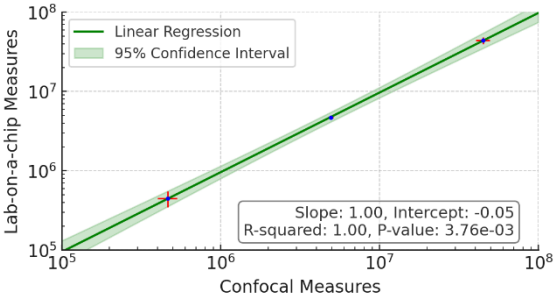

Fig. 2. The calibration measurements of our lab-on-a-chip setup for cell counting.

Acknowledgements

This work has received funding from FEADER and DACC of the GenCat. with grant 56-30123 2021-2A. This work has also received funding from Grants PID2019-105714RB-I00 and PID2022-136833OB-C21 funded by MICIU/AEI/10.13039/501100011033 and the European Regional Development Fund.

References

[1]International Organisation of Vine and Wine, “State of the World Vine and Wine Sector in 2022,” International Organisation of Vine and Wine, Paris, France, Apr. 2023. Accessed: Apr. 12, 2024. [Online]. Available: https://www.oiv.int/sites/default/files/documents/OIV_State_of_the_world_Vine_and_Wine_sector_in_2022_2.pdf

[2]A. Vilà, S. Moreno, J. Canals, and A. Diéguez, “A Compact Raster Lensless Microscope Based on a Microdisplay,” Sensors, vol. 21, no. 17, p. 5941, Sep. 2021, doi: 10.3390/s21175941.

[3]G. K. Chadha, A. Srivastava, A. Singh, R. Gupta, and D. Singla, “An Automated Method for Counting Red Blood Cells using Image Processing,” Procedia Computer Science, vol. 167, pp. 769–778, 2020, doi: 10.1016/j.procs.2020.03.408.

[4]D. Zhang, P. Zhang, and L. Wang, “Cell Counting Algorithm Based on YOLOv3 and Image Density Estimation,” in 2019 IEEE 4th International Conference on Signal and Image Processing (ICSIP), Wuxi, China: IEEE, 2019, pp. 920–924. doi: 10.1109/SIPROCESS.2019.8868603.

[5]F. Guo, J. Yang, Y. Chen, and B. Yao, “Research on image detection and matching based on SIFT features,” in 2018 3rd International Conference on Control and Robotics Engineering (ICCRE), Apr. 2018, pp. 130–134. doi: 10.1109/ICCRE.2018.8376448.

DOI 10.5162/EUROSENSORSXXXVI/PT6.188

CogniFlow: Integrated Modular System For Automated Droplet Microfluidic Bioanalysis

Rauno Jõemaa[1], Fariha Afrin[1], Nafisat Gyimah[1], Kanwal Ashraf[1], Kaiser Pärnamets[1], Lucas Giese[2], Mathieu Rocancourt[2], Tamás Pardy[1]
[1] Tallinn University of Technology, 5 Ehitajate tee, 19086 Tallinn, Estonia,
[2] ENSEA, 6 Av. Du Ponceau, 95000 Cergy, France

tamas.pardy@taltech.ee

Summary: Droplet microfluidics uses discrete, chemically isolated droplets to multiplex reactions in bioanalysis. Droplets also allow process control exceeding traditional means, as well as continuous flow microfluidics. Here we present the concept of CogniFlow, an integrated, modular droplet microfluidic instrumentation platform, which automates complete droplet generation, imaging and detection workflows. The platform is demonstrated in cell encapsulation and detection. It is our hope that CogniFlow can significantly lower the entry barrier to instrumenting existing droplet bioanalytical workflows.

Keywords: droplets, microfluidics, instrumentation, control, cognitronics

Introduction

Droplets allow excellent process control by chemically isolating pico- to nanoliter range reaction volumes (like tiny test tubes), allowing selection of samples from a pool of millions of non-specific targets, which would be nearly impossible with conventional tools (e.g. well-plate stations) [1], [2]. This has opened the way to novel applications in microfluidic bioanalysis and biotechnology [3]. However, biology teams desiring to automate their droplet-based workflows today primarily load functions onto highly complex microfluidic chips, and/or use combinations of general-purpose off-the-shelf instruments, resulting in highly complex, expensive systems, which are difficult to scale and replicate, take significant time to build and are not energy-efficient [4], [5]. In this poster, we propose a technology platform that can address these challenges and reduce development time and cost associated with instrumenting droplet bioanalytical and biotechnology applications. In our previous paper we presented the droplet generation module of the platform [6]. In this poster, we present the integrated system, including droplet imaging and detection.

Novelty

CogniFlow offers the following novelties:

Transferability: modules are compact and portable, can be swapped, but the system has its standards. System can be reconfigured (e.g. different filters, lenses and light sources, camera vs. photodiode etc.), but workflows are easily replicated between labs.

Scalability: Low cost (<1k€-2k€/module, using 3D printed parts, low-cost electronics and optics) and standardization ensure easy replication of results in different labs, as well as scaling up throughput. Despite the low cost, performance of thus-far demonstrated components has been on par with comparable systems [6].

Efficiency: modules have power consumption ~10-20W, enabling battery operation. Wireless communication via ECAL [7] further reduces device footprint and increases portability. Optimizations to flow control reduce reagent waste.

Total automation: CogniFlow has 3 main modules: 1. Droplet generation/encapsulation [6], 2. Droplet imaging and 3. Embedded object classification algorithm. These cover a complete droplet-based imaging or light intensity analysis workflow.

Demonstrations in literature meeting the majority of the aforementioned criteria are rare [1], [2].

System modules and results

Droplet generation [6]: the first demonstrated module of the platform generated droplets in 50-200 um range with 5-10% coefficient of variability at up to 1kdps (1000 droplets per second). We controlled pressure drop and droplet size in a piezoelectric pumping setup with rapid and precise controller response, but a simple and inexpensive setup. On the poster, we mention this module for the sake of completeness.

Droplet imaging: the second module of the system presented here for the first time is based on an affordable optical setup using a Basler

acA640-750uc and a cheap 20x magnification lens to achieve ~750 dps imaging rate [8]. The integrated system (Fig. 1) is built on the same framework as the first module, by swapping internal components. The footprint is 22 x 33 x 40 cm. Imaging system output with encapsulated cells is shown in Fig. 2.

Object detection *(Fig. 3):* a droplet segmentation and object classification algorithm based on YOLOv4 and TinyYOLOv4 is presented, which is capable of detecting single cells in droplets with 85% accuracy on an image stream of droplets in flow provided by our academic partners. The algorithm can run on an NVIDIA® Jetson Nano™ AI accelerator. The AI accelerator board fits on top of the electronics stack of the second module (Fig 1. left), and while it will double system power consumption, the total will still be well below what PD3.0+ compliant power bank can provide.

Between the two hardware and the one software module presented here, the following solutions are in common: both hardware modules rely on a Raspberry Pi 4 for control and communication. Wireless communication is implemented via ECAL, as presented in [6], however, for experiments, a wired Ethernet connection is also possible. Power electronics is the same between module 1 and 2, as is the mechanical frame, which consists of 3D printed parts and commonly used metal fasteners.

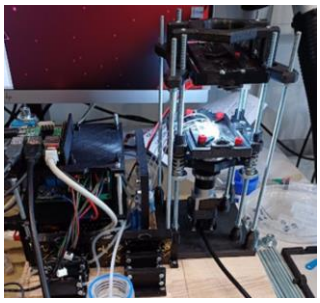

Figure 1: Integrated droplet imaging module of the CogniFlow platform. The mechanical frame and enclosure (not shown here) are shared between all platform modules, optics and electronics stages are changed according to the purpose.

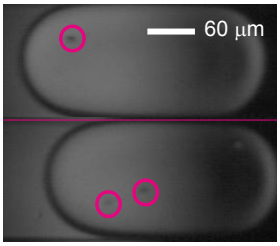

Figure 2: Droplets imaged with the droplet imaging module of CogniFlow using an affordable optical setup. Highlighted objects are algae cells encapsulated. Reagents used for droplet generation are described in [6].

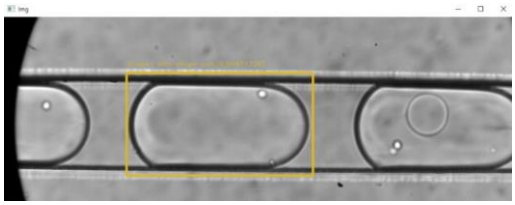

Figure 3: Object detection algorithm demonstration. Reference video of droplets with microbeads and cells encapsulated was kindly provided by University of Warsaw to test the algorithm on an independent dataset.

References

[1] C. Huang, Y. Jiang, Y. Li, and H. Zhang, 'Droplet Detection and Sorting System in Microfluidics: A Review', *Micromachines (Basel)*, vol. 14, no. 1, p. 103, Dec. 2022, doi: 10.3390/mi14010103.

[2] M. Gantz, S. Neun, E. J. Medcalf, L. D. van Vliet, and F. Hollfelder, 'Ultrahigh-Throughput Enzyme Engineering and Discovery in In Vitro Compartments', *Chem Rev*, vol. 123, no. 9, pp. 5571–5611, 2023, doi: 10.1021/acs.chemrev.2c00910.

[3] T. S. Kaminski, O. Scheler, and P. Garstecki, 'Droplet microfluidics for microbiology: techniques, applications and challenges', *Lab Chip*, vol. 16, no. 12, pp. 2168–2187, 2016, doi: 10.1039/C6LC00367B.

[4] Y. Zhou, Z. Yu, M. Wu, Y. Lan, C. Jia, and J. Zhao, 'Single-cell sorting using integrated pneumatic valve droplet microfluidic chip', *Talanta*, vol. 253, p. 124044, Feb. 2023, doi: 10.1016/J.TALANTA.2022.124044.

[5] Atrandi Biosciences, 'Styx | Atrandi Biosciences'. Accessed: Feb. 03, 2024. [Online]. Available: https://atrandi.com/styx

[6] R. Jõemaa *et al.*, 'CogniFlow-Drop: Integrated Modular System for Automated Generation of Droplets in Microfluidic Applications', *IEEE Access*, vol. 11, pp. 104905–104929, 2023, doi: 10.1109/ACCESS.2023.3316726.

[7] K. Ashraf, Y. Le Moullec, T. Pardy, and T. Rang, 'Design of Cyber Bio-analytical Physical Systems: Formal methods, architectures, and multi-system interaction strategies', *Microprocess Microsyst*, vol. 97, Mar. 2023, doi: 10.1016/J.MICPRO.2023.104780.

[8] K. Parnamets, A. Koel, T. Pardy, and T. Rang, 'Open Source Hardware Cost-Effective Imaging Sensors for High-Throughput Droplet Microfluidic Systems', *Proceedings of the 2022 26th International Conference Electronics, ELECTRONICS 2022*, 2022, doi: 10.1109/IEEECONF55059.2022.9810383.

DOI 10.5162/EUROSENSORSXXXVI/PT6.192

Portable Fluorescence Microscope applied to Organ-on-a-Chip Models

Sergio Moreno[1], *Anna Vilà*[1], *Javier Ramón-Azcón*[2], *J. Daniel-Prades*[1], *Angel Diéguez*[1]
[1] *Department of Electronic and Biomedical Engineering, University of Barcelona, Martí I Franquès, 1 08028, Barcelona, Spain*
[2] *Institute for Bioengineering of Catalonia (IBEC), The Barcelona Institute of Science and Technology (BIST), Baldiri Reixac 10-12, 08028 Barcelona, Spain*

sergiomoreno@ub.edu

Summary:
Compact microscopy represents a revolutionary concept that allows for qualitative and quantitative improvements in the analysis of samples. Recently, a compact bright-field microscope based on raster scanning has been developed. This work presents an update to this compact microscope with fluorescence capabilities. This novel capability has been validated using a sample of an Organ-on-a-Chip (OOC) of a muscle stained with Alexa Fluor 488. The objective of this process is to detect and evaluate immunofluorescence, which is used to assess the maturity status of the biological model.

Keywords: Ultra-compact microscope, fluorescence, microdisplay, single photon avalanche diode, organ-on-a-chip

Introduction

Biotechnology has profoundly impacted our ability to observe and analyze biological samples. This transformation is attributed to the advancement of conventional microscopy techniques such as brightfield [1] or fluorescence [2]. However, the devices used with these techniques have a very bulky setup and a fixed location that limit their usefulness in certain applications. The integration of compact microscopy into smaller, more portable systems would facilitate its use in in-situ settings, such as laboratories or even at the point of care (POC). The first highly compact microscope based on nano-illumination was presented by Franch *et al.* in [3]. The microscope sensor was based on a 16 x 16 pixel SPADs camera fabricated in a 0.35 µm HV-CMOS process. The emitting part consisted of an 8 x 8 Gallium Nitride (GaN) LED array with a size of 5 µm and a pitch of 10 µm. Vilà *et al.* describes in [4] a prototype of a electronically activated scanning transmission microscope based on a microdisplay and a CMOS imaging camera. This device has the significant advantage that, as it is based on only two chips, it has a high level of compactness and portability. In addition, it has a field of view of several millimeters and a resolution of up to 2 µm.

This work presents a new version of the compact microscope with fluorescence capabilities. This improvement over the bright field prototype enables the microscope to be used for a wide variety of biological applications. In particular, the microscope employs a microdisplay for lens-free fluorescence imaging in organ-on-a-chip (OOC) applications.

Materials and Methods

The compact fluorescence microscope integrates a single-pixel detector and microdisplay. The image sensor is a single-photon avalanche detector (SPAD), which replaces the conventional CMOS camera. The SPAD has a diameter of 10 µm, a dark count rate (DCR) of less than 1 kcps, and a photodetection probability (PDP) of approximately 10 %. The remaining electronic components are responsible for classifying the arrival times of the photons in the form of a histogram. This configuration allows for measurements to be made over a range of approximately 70 ns to 470 ns with a resolution of up to 150 ps. On the other hand, the display chip is a 0.13-inch AmµLED™ microLED display with a resolution of 640 x 480. The diameter of the light-emitting diodes (LEDs) is 2 µm, and they are arranged with a pitch of 4 µm, resulting in a range of gray intensity levels that can be represented by four bits. The display is equipped with a digital interface that employs serial peripheral interface (SPI) connectivity. The monochrome panel offers a luminance of 0.5 million nits for blue (455 nm ± 15 nm).

Figure 1 illustrates a representation of the setup used for the fluorescence microscope. The setup comprises no optical elements beyond a band-pass filter between the sample and the sensor. The purpose of the filter is to eliminate the light from the display from being detected. However, the lack of a lens to concentrate the light implies that we require the activation of more than a single LED to cause the excitation of the fluorophores. Therefore, N x N LED patterns are employed to enhance the excitation signal level.

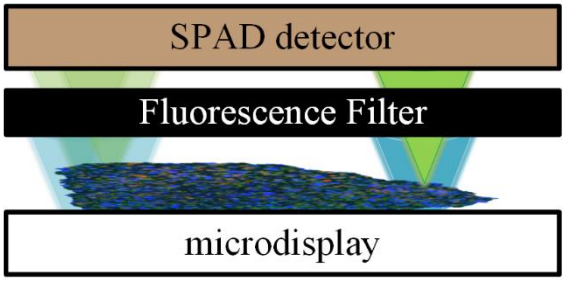

Figure 1. Representation of compact fluorescence microscope.

Results

A proof-of-concept experiment was conducted to validate the potential of the microscope for fluorescence visualization in OOC. The experiment was based on a 3D skeletal muscle on a chip. The OOC used by Fernandez-Costa et al. in [5] is employed in this study. This method involves the use of an alpha-actinin sarcomeric immunofluorescence stain to visualize sarcomeric structures within skeletal muscle tissues. This approach allows for the real-time study of the interaction between the muscle and the pancreatic islets. Figure 2 illustrates the image reconstructed with the microscope. The resulting fluorescence is represented in green and results from staining the sample with Alexa Fluor 488. The sample has been scanned in 2D using a 2 x 2 µLED illumination pattern. Additionally, a fluorescein isothiocyanate (FITC) emission filter with a central wavelength of 530 nm and a full width at half maximum (FWHM) of 43 nm is employed, thus eliminating the excitation light from the microdisplay.

The results demonstrate that the microscope can detect sarcomeric immunofluorescence emission in muscle tissue. Visualizing the presence of these sarcomeric structures allows for the evaluation of the functionality of muscle tissues on a chip and the confirmation of muscle tissue maturation.

Our results validate the microscope to be used for observing fluorescence in biological samples such as OOCs, which will benefit from improvements in microdisplay technology, including enhanced light power, reduced pitch, and switching capabilities. These advancements will enable higher image resolution and the possibility of implementing lifetime measurements.

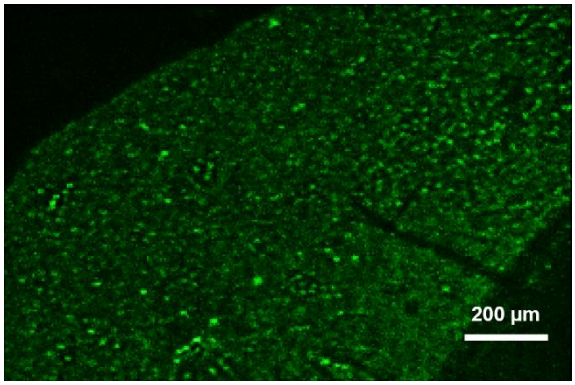

Figure 2. Captured fluorescence image of muscle tissue.

Acknowledgement

This work has received funding from Grants PID2019-105714RB-I00 and PID2022-136833OB-C21 funded by MICIU/AEI/10.13039/501100011033 and the European Regional Development Fund.

References

[1] F. Cai, T. Wang, W. Lu, and X. Zhang, “High-resolution mobile bio-microscope with smartphone telephoto camera lens,” *Optik*, vol. 207, p. 164449, Apr. 2020, doi: 10.1016/j.ijleo.2020.164449.

[2] S. Daetwyler and R. P. Fiolka, “Light-sheets and smart microscopy, an exciting future is dawning,” *Commun. Biol.*, vol. 6, no. 1, pp. 1–11, May 2023, doi: 10.1038/s42003-023-04857-4.

[3] “Nano illumination microscopy: a technique based on scanning with an array of individually addressable nanoLEDs.” Accessed: Apr. 26, 2024. [Online]. Available: https://opg.optica.org/oe/fulltext.cfm?uri=oe-28-13-19044&id=432580

[4] A. Vilà, S. Moreno, J. Canals, and A. Diéguez, “A Compact Raster Lensless Microscope Based on a Microdisplay,” *Sensors*, vol. 21, no. 17, Art. no. 17, Jan. 2021, doi: 10.3390/s21175941.

[5] J. M. Fernández-Costa, X. Fernández-Garibay, F. Velasco-Mallorquí, and J. Ramón-Azcón, “Bioengineered in vitro skeletal muscles as new tools for muscular dystrophies preclinical studies,” *J. Tissue Eng.*, vol. 12, p. 2041731420981339, Jan. 2021, doi: 10.1177/2041731420981339.

DOI 10.5162/EUROSENSORSXXXVI/PT6.198

Development of a Novel Self-Immolative System Activated by DT-diaphorase for Hypoxic Environments

Paula Rodrigo[1], Jose A. Sáez[1,2], Mariana Barros[1], Pau Arroyo[1,2], Pablo Gaviña[1,2,3]
[1] Instituto Interuniversitario de Investigación de Reconocimiento Molecular y Desarrollo Tecnológico (IDM), Universitat Politècnica de València, Universitat de València, Spain
[2] Departamento de Química Orgánica, Universitat de València, Doctor Moliner 50, Valencia, Spain
[3] CIBER de Bioingeniería, Biomateriales y Nanomedicina (CIBER-BBN), Spain

paula.rodrigo@uv.es

Summary:
In this work, a total synthesis of a self-immolative material has been done. Firstly, MCM-41 nanoparticles were synthesized, after that, they were loaded with a fluorophore, and finally the pores were capped with an azo-based molecule. The aim of this work is to detect hypoxic environments based on the overexpression of DT-diaphorase, leading to the breakdown of the azo bond and the releasing of the fluorophore.

Keywords: hypoxia, nanotechnology, DT-diaphorase, MCM-41

Background, Motivation an Objective

Cancer remains a persistent challenge in contemporary healthcare, despite advancements in chemotherapy. By identifying cancer before it spreads, patients often undergo less aggressive therapies with fewer side effects, preserving their quality of life. Moreover, early detection increases the likelihood of successful treatment outcomes and long-term survival. Therefore, investing in methods and technologies for early cancer detection is crucial in improving patient outcomes and reducing the burden of cancer-related treatments [1].

Solid tumors frequently thrive in hypoxic environments, decreasing the amount of oxygen available, and increasing the resistance of the tumor to radiotherapy treatments due to the lack of oxygen-free radicals, required to induce DNA damage; they are also resistant to chemotherapy, due to the ineffectiveness of the drugs to reach these environments via the circulation [2]. Notably, these environments exhibit heightened levels of reductase enzymes like DT-diaphorase, azoreductase and nitroreductase [3].

The aim of this study is to synthesize a novel self-immolative gate responsive to the presence of DT-diaphorase, facilitating a controlled release of the fluorophore encapsulated within the MCM-41 nanoparticle pores. This approach aims to trigger fluorophore liberation upon enzymatic activation, offering a potential avenue for diagnostic applications.

Description of the New Method or System

Within the context of this study, a novel molecule featuring an azo bond has been synthesized. This molecule has the particularity of breaking in the presence of DT-diaphorase, an enzyme commonly overexpressed in hypoxic environments characteristic of solid tumors. Serving as a cap for the MCM-41, retaining the fluorophore from spreading. When DT-diaphorase is in the media, the azo bond undergoes cleavage, facilitating the release of fluorophore.

Results

Throughout this investigation, MCM-41 nanoparticles have been synthesized and characterized by X-ray powder diffraction (XRD) and transmission electron microscopy (TEM).

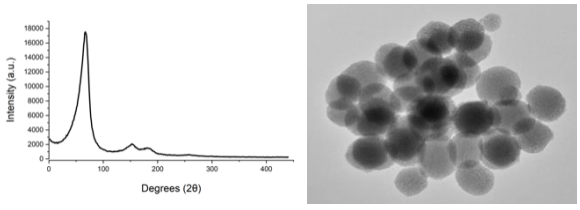

(A) DOI:

Fig. 1. (A) XRD pattern for MCM-41 and, (B) TEM image of empty MCM-41.

Upon successful synthesis of MCM-41, the nanoparticle pores were loaded with rhodamine B, and subsequently capped with the synthesized gate as depicted in Figure 2. This gate is the product of a three-step synthesis process.

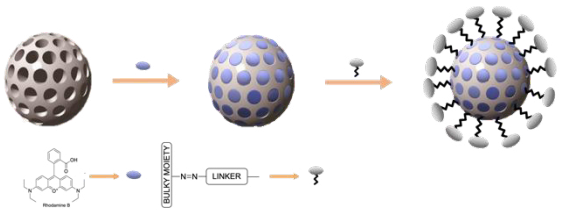

Fig. 2. Representation of the MCM-41 gated nanomaterial loaded with Rhodamine B.

Thereafter, the nanomaterial is exposed to DT-diaphorase, allowing for the measurement of fluorophore release upon enzymatic cleavage of the azo bond. This release was quantified by monitoring the increase in fluorescence intensity exhibited by rhodamine B.

References

[1] H. Chen, Z. Zhen, T. Todd, P. Chu, J. Xie, *Materials Science and Engineering* 74, 35-69 (2013); doi: 10.1016/j.mser.2013.03.001

[2] M. Christiane, J. Chiche, J. Pouysségur, *Journal of Molecular Medicine* 85, 1301-1207 (2007); doi: 10.1007/s00109-007-0281-3

[3] S. Sormendi, B. Wielockx, *Frontiers in Immunology* 9 (2018); doi: 10.3389/fimmu.2018.00040

Acknowledgements

Grant PID2021-1263040-B-C42 funded by MICINN/AEI/10.13039/501100011033 and, by “ERDF, A way of making Europe”. Project UV-INV-PROVAL21-1871796 by the "Valoritza i Transfereix” program 2021 of the Universitat de València. Project CIAICO/2022/146 funded by Conselleria de Educación, Universidades y Empleo de la Generalitat Valenciana. SCSIE (Universitat de València) is gratefully acknowledged for all the equipment employed. NMR was registered at the U26 facility of ICTS “NANBIOSIS” at the Universitat de València.

DOI 10.5162/EUROSENSORSXXXVI/PT6.205

Label-free Impedimetric Immunosensor for the Detection of Fibulin 2 as a Novel Biomarker for the Diagnosis of Hypertrophic Cardiomyopathy in Human Saliva

Ayman Ali Saeed[1], Ayman Maher Ibrahim[2,3], Naglaa Mohammed Nooredeen[4], Mohamed Mahmoud Eissa[4], Mohammed Nooredeen Abbas[1], Marie Hangouët[5], Joan Bausells[6], Abdelhamid Errachid[5]* and Nadia Zine[5]*

[1] *Applied Organic Chemistry Department, Chemical Industries Research Institute, National Research Centre (NRC), Dokki, Giza 12622, Egypt,*
[2] *Life Sciences Research Department, Aswan Heart Centre, Aswan, Egypt,*
[3] *Zoology Department, Faculty of Science, Cairo University, Giza 12613, Egypt,*
[4] *Polymers and Pigments Department, Chemical Industries Research Institute, National Research Centre (NRC), Dokki, Giza 12622, Egypt,*
[5] *Institut des Sciences Analytiques (ISA), Université Claude Bernard Lyon 1, 5 rue de la Doua, 69100 Villeurbanne, Lyon, France,*
[6] *Instituto de Microelectrónica de Barcelona (IMB-CNM-CSIC), Campus Universitat Autònoma de Barcelona (UAB), Barcelona 08193, Spain*

Corresponding Author's e-mail address: aa.saeed@nrc.sci.eg and abdelhamid.errachid@univ-lyon1.fr

Summary:

a novel label-free impedimetric immunosensor was developed for the detection of a recently recognized as a new promising cardiac biomarker, fibulin 2 (FBLN2), for the diagnosis of hypertrophic cardiomyopathy. The approach is based on immobilization of the corresponding antibody, anti-Fibulin 2 (anti-FBLN2), onto array of gold microelectrodes functionalized with 16-mercaptohexadecanoic acid (MHDA). The assembly of 16-MHDA onto the gold working microelectrodes was confirmed by cyclic voltammetry (CV), while the interaction between FBLN2 and anti-FBLN2 was monitored using electrochemical impedance spectroscopy (EIS). Additionally, the different stages of surface modification were characterized using contact angle measurement (CAM), FTIR and Atomic Force Microscopy (AFM) in order to confirm the success of immobilization process. The analytical performance of the proposed immunosensor was evaluated and the immunosensor exhibited a high sensitivity with a good linearity in the range from 5 to 25 pg/mL with R^2 of 0.976. The developed immunosensor will be used for the detection of FBLN2 in human saliva using standard addition method.

Keywords: Electrochemical impedance spectroscopy, Impedimetric immunosensor, Fibulin 2, Hypertrophic Cardiomyopathy, Human saliva.

Introduction

A distinctive hallmark of Hypertrophic Cardiomyopathy (HCM) is the thickening of the left ventricle accompanied by Extracellular Matrix (ECM) remodeling, typically characterized by increased interstitial fibrosis [1]. The disease exhibits heterogeneity in clinical and pathological presentations, as well as in genetic backgrounds [2].

The ECM constitutes an intricate network of proteins essential for preserving the structural integrity and functional homeostasis of cardiac tissue. Maintaining a balance in collagen synthesis and degradation, protease activity, and the presence of fibulins, cytokines, and chemokines is critical for preserving cardiac function [3]. These myocardial changes in ECM composition can partially be monitored in the circulation due to the shedding and solubility of a group of relevant ECM proteins. These shed proteins can then be utilized as biomarkers for HCM. To date, limited numbers of gold standard biomarkers have been assigned for cardiovascular conditions prognosis and diagnosis, such as B-type natriuretic peptide (BNP), Cardiac troponin (cTNT) and N-terminal pro-BNP (NT-pro-BNP).

Fibulin-2 (FBLN2), an ECM glycoprotein, has recently reported to be upregulated in the myocardium of HCM patients and further been suggested as a potential biomarker for HCM patients [4]. FBLN2 is present in the ECM and is involved in elastic fiber assembly and stabilization [5]. Previous reports also indicated that FBLN2 plays an essential role in Ang II-induced TGF-β signaling and subsequent myocardial fibrosis. Therefore, accurate measurement of FBLN2 in the circulation of HCM patients will support these findings and further help intro-

duce a non-invasive and effective platform for patients follow up.

An fast and sensitive detection of FBLN2 is needed to replace the ELISA which is a lab-based technique and requires a qualified personnel. In this study, we developed a novel label-free impedimetric immunosensor for the detection of a recently recognized cardiac biomarker, FBLN2, in saliva. To the best of our knowledge, the obtained sensor is the first to electrochemically measure the newly announced HCM biomarker FBLN2.

Materials

Anti-Fibulin 2 antibody was purchased from abcam. Recombinant human fibulin 2 protein was purchased from R&D SYSTEMS. 16-Mercaptohexadecanoic acid, ethanolamine, N-hydroxysuccinimide (NHS), and PBS tablets were purchased from Sigma-Aldrich. 1-Ethyl-3-(3-dimethylaminopropyl) carbodiimide (EDC) was purchased from CARL ROTH.

Apparatus

Electrochemical measurements were carried out using an electrochemical workstation, Bio-Logic SP-200 potentiostat. The developed chip produced by silicon technology integrtes four gold microelectrodes with four gold working electrodes, two Ag/AgCl reference μelectrodes and one Pt counter μelectrode.

Method

The gold microelectrodes were firsly cleaned using KOH and H_2O_2, followed by washing with acetone and dried under nitrogen. They were then incubated in MHDA. The carboxylic groups were activated using EDC/NHS then allowed to react with the amino groups of the anti-FBLN2 for 1 hr. The anti-FBLN2-modified electrodes were then immersed in different concentrations of FBLN2 and the EIS was recorded for each.

Results

The performed characterization proved the success of the immobilization process as the peaks of redox couple disappeared after assembly of MHDA onto the surface due to the blocking of the charge transfer (Fig.1).

The analytical performance of the proposed sensor was evaluated by EIS and the sensor exhibited a high sensitivity with a good linearity from 5 to 25 pg/mL with R^2 of 0.976 (Fig. 2).

Ongoing work

We are working on the interference study and the detection of FBLN2 in human saliva.

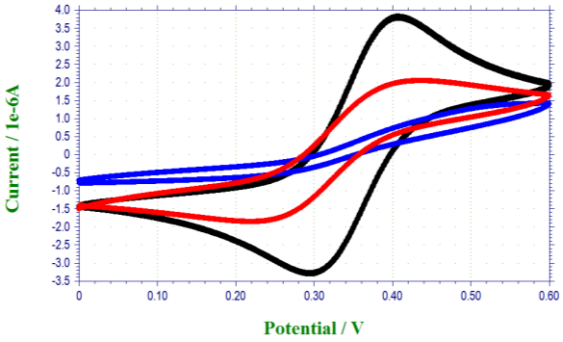

Fig. 1. Electrochemical characterization by CV recorded at each stage of electrode modification in 5 mM of K3[Fe(CN)6]/K4[Fe(CN)6] in PBS pH 7.4.

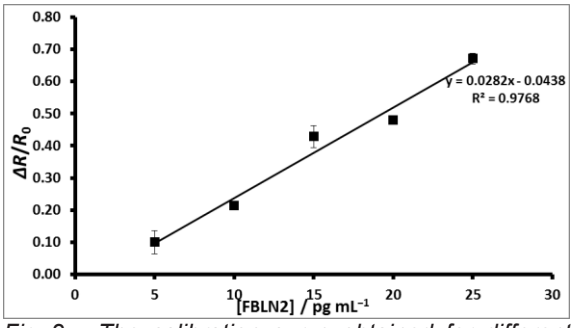

Fig. 2. The calibration curve obtained for different concentrations of FBLN2 using EIS .

References

[1] N. Frey, M. Luedde, H. A. Katus, Mechanisms of disease: hypertrophic cardiomyopathy, *Nature Reviews. Cardiology* 9(2), 91–100 (2011); doi: 10.1038/NRCARDIO.2011.159

[2] R. Walsh, J. A. Offerhaus, R. Tadros, C. R. Bezzina, Minor hypertrophic cardiomyopathy genes, major insights into the genetics of cardiomyopathies, *Nature Reviews Cardiology* 19(3), 151–167 (2021); doi: 10.1038/s41569-021-00608-2

[3] N. G. Frangogiannis, The extracellular matrix in myocardial injury, repair, and remodeling, *The Journal of Clinical Investigation* 127(5), 1600–1612 (2017); doi: 10.1172/JCI87491

[4] A. M. Ibrahim, M. Roshdy, S. Elshorbagy, M. Hosny, S. Halawa, D. Yehia, H. A. Elfawy, A. Eldessouki, F. Mohamed, A. Ellithy, M. Abdelfattah, A. Elsawy, M. Elkhatib, M. Allouba, A. Elguindy, Y. Aguib, M. Yacoub, An Investigation of Fibulin-2 in Hypertrophic Cardiomyopathy, *International Journal of Molecular Sciences* 21, 7176 (2020); doi: 10.3390/ijms21197176.

[5] D. Olijnyk, A. M. Ibrahim, R. K. Ferrier, T. Tsuda, M. L. Chu, B. A. Gusterson, T. Stein, J. S. Morris, Fibulin-2 is involved in early extracellular matrix development of the outgrowing mouse mammary epithelium, *Cellular and Molecular Life Sciences* 71(19), 3811–3828 (2014); doi: 10.1007/S00018-014-1577-4/FIGURES/8

Development of a Lateral Flow Assay Biosensor for miRNA-34a and miRNA-155 Detection Utilizing the Rolling Circle Amplification

F. Rahbar Kouibaran, G. Zuccheri, I. Diemberger, University of Bologna, Bologna (Italy)

Unfortunately, this abstract is not available, as the contribution was not confirmed at the time the conference proceedings were finalized.

Development of a Lateral Flow Assay Biosensor for miRNA-34a and miRNA-155 Detection Utilizing the Rolling Circle Amplification

F. Rahbar Kouibaran, G. Zuccheri, I. Diemberger, University of Bologna, Bologna (Italy)

Unfortunately, this abstract is not available, as the contribution was not confirmed at the time the conference proceedings were finalized.

DOI 10.5162/EUROSENSORSXXXVI/PT6.226

Electrospun Silk Fibroin for Green Smart Sensors

Marc Navarro[1], Carla Blanes[1], Sara Santiago[2], Pablo Rodríguez[1], Silvia Mena[1], S.D. Aznar-Cervantes[3], Xavier Muñoz[1], Gonzalo Murillo[1]
[1] Institute of Microelectronics of Barcelona (IMB-CNM, CSIC), Barcelona, 08193, SPAIN
[2] Departamento Química Analítica. Universidad Complutense de Madrid, Madrid, 28040, SPAIN
[3] Instituto Murciano de Investigación y Desarrollo Agrario y Alimentario (IMIDA), Department of Biotechnology, Murcia, 30150, SPAIN

marc.navarro@imb-cnm.csic.es

Summary:
The rapid expansion of the silicon chip industry has led to an increase in interest in green electronics, especially those utilizing bio-composites like silk fibroin (SF). This study presents an electrospun SF membrane adaptable for sensing Escherichia coli. Using a solvent-free process, SF was doped with metabolic indicators, electrospun, and annealed.

Keywords: silk fibroin, electrospinning, biosensor, green electronics, bacteria detection

Background, Motivation an Objective

The significance of green electronics has risen in recent years due to the rapid expansion of the silicon chip industry and the resultant e-waste. Projections indicate that by 2030, the silicon chip industry will double its manufacturing capacity, leading to nearly 75 million tons of e-waste [1]. Sustainability in products is evaluated based on their reusability, lifespan, and recyclability, with biodegradability offering notable benefits for healthcare and environmental applications. In this context, green electronic components made from bio-composites are becoming an appealing alternative to traditional silicon-based technologies.

Silk fibroin (SF) possesses excellent mechanical properties, biocompatibility, and adjustable biodegradability. It also exhibits crystalline polymorphism, enabling it to transform structurally from α-helix domains to antiparallel β-sheets [2]. These attributes make SF a highly promising material for green electronics, offering extensive opportunities for processing, functionalization, and various applications.

In this work, we present an electrospun SF membrane that can be adapted during the fabrication process to function as a sensing device. By doping the silk fibroin films with selective metabolic indicators, such as MacConkey or Chromogenic Coliforms Agar (CCA), the membrane can specifically detect Escherichia coli.

Description of the New Method or System

A 21% (w/w) SF + 20% MacConkey solution was used to electrospin the membrane in the Fluidnatek LE-10 electrospinner, employing a completely green and sustainable process based on a solvent-free solution. The collector was covered with aluminum foil. A total of 1 mL of aqueous solution was electrospun under conditions that ensured a stable Taylor cone. A voltage of +12 kV was applied to the capillary tube, the collector was placed 15 cm from the tip, and the injection rate was set to 0.2 $mL \cdot h^{-1}$. After fabrication, the electrospun meshes were annealed by immersion in absolute methanol for 45 minutes to induce crystallinity [3]. Figure 1 shows the electrospinning and post-treatment annealing set-up.

Results

Figure 2 shows SEM images of the electrospun membranes, both untreated and after annealing, for both the control (SF solution) and the SF + MacConkey solution. Methanol annealing significantly reduces the membrane's porosity and increases fiber thickness. Figure 3 displays the FTIR spectra of the SF membrane (blue), with β-sheets amide I and II peaks at 1620 cm^{-1} and 1515 cm^{-1}, respectively, indicating a higher number of β-sheets transitioning from α-structures after methanol annealing (orange) [4]. We are currently characterizing the porosity using Brunauer–Emmett–Teller analysis and further optimizing the doping of SF with MacConkey and CCA to assess bacterial activity.

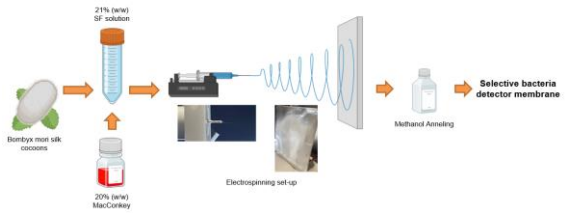

Fig. 1. Schematic representing the solution preparation, electrospinning and post-treatment set-up.

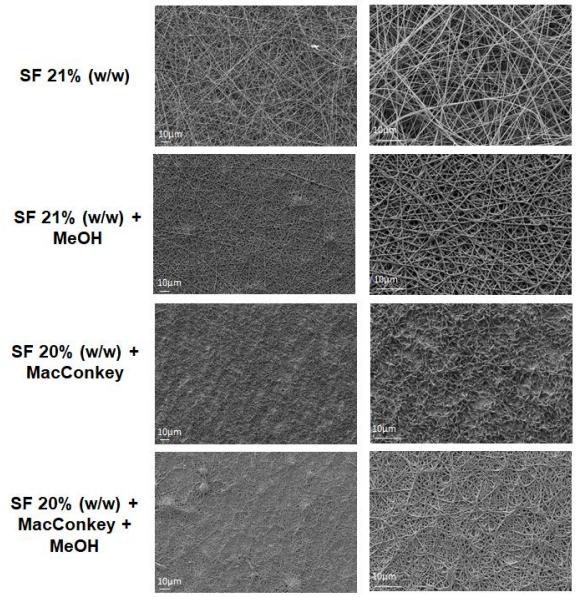

Fig. 2. SEM images of electrospun SF membrane without post-treatment (first row), with methanol treatment (second row), electrospun SF + MacConkey membrane (third row) and electrospun SF + MacConkey membrane with methanol (four row).

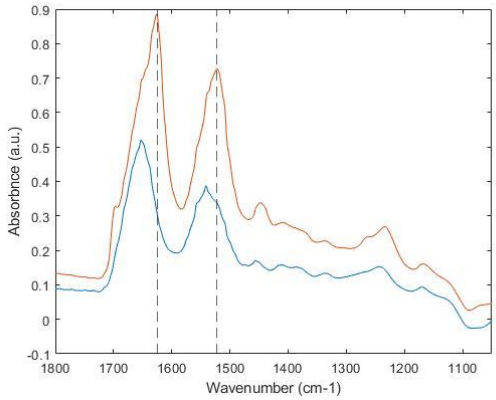

Fig. 3. FTIR spectra of electrospun membranes and β-sheets amide I (1620 cm-1) and II (1515 cm) peaks

References

[1] B. Tansel et al., From electronic consumer products to e-wastes: Global outlook, waste quantities, recycling challenges, *Environ. Int. 2017*, 98, 35–45. doi: 10.1016/j.envint.2016.10.002

[2] A. Veronica et al., An Insight into Tunable Innate Piezoelectricity of Silk for Green Bioelectronics, *ChemPhysChem. 22 (2021)*, 2266-2280. doi: 10.1002/cphc.202100279

[3] S. Aznar-Cervantes et al. Electrospun silk fibroin scaffolds coated with reduced graphene promote neurite outgrowth of PC-12 cells under electrical stimulation, *Materials Science and Engineering C. 79 (2017),* 315-325. doi: 10.1016/j.msec.2017.05.055

[4] M, Wang et al., Mechanical properties of electrospun silk fibers, *Macromolecules. 37 (2004),* 6856-6864. doi: 10.1021/MA048988V.

DOI 10.5162/EUROSENSORSXXXVI/PT6.247

Cells and Model Particles in Lateral Focusing Microfluidics

Anita Bányai [1,2,3,], Enikő Farkas [1], Hajnalka Jankovics [4], Inna Székács [1] , Eszter Leelőssyné Tóth [1] , Ferenc Vonderviszt [4] , Róbert Horváth [1] , Máté Varga [2] and Péter Fürjes [1]*

[1] Institute of Technical Physics and Materials Science, HUN-REN Centre for Energy Research, Budapest, Hungary
[2] 77 Elektronika Ltd., Budapest, Hungary
[3] Doctoral School on Materials Sciences and Technologies, Óbuda University, Budapest, Hungary
[4] Research Institute of Biomolecular and Chemical Engineering, University of Pannonia, Veszprém, Hungary

Corresponding Author: banyai.anita@ek.hun-ren.hu

Summary:

In the field of medical diagnostics, the microfluidic devices are widely applied for implementation accelerated sample handling steps although reliable and reproducible results are to be achieved. In many cases, the medium must be pre-filtered to extract the target before analysis. In this work the aim was to gain better understanding of particle and cell behaviour in special lateral focusing systems, dedicated for size dependent separation and lateral positioning the target above the sensor zone. Fluorescent polystyrene beads in the size range of Ø = 0.5 -16.5 µm were injected into the asymmetrically curved microfluidic system, and their size dependent trajectories and lateral positions were recorded. A particle map was defined according to their lateral positions and compared to the behaviour of real cell-types (Escherichia coli, Red Blood Cell, Saccharomyces cerevisiae, HeLa), considering their morphology and size. The results highlight the importance of living cell's morphology significantly affecting the cell movement in microfluidic channels compared to the rigid, spherical beads.

Keywords: microfluidics, dean flow, hydrodynamic lift, lateral focusing, cell manipulation

Background, Motivation an Objective

Among the suitable particle separation methods, a passive, label-free solution, the lateral focusing technique was analysed for comprehension the micro-scale hydrodynamic processes governing the cell movements in such microfluidic systems. In continuous Poiseuille flow, inertial lifting forces (shear-gradient lift force, wall-effect induced lift force) are acting on the extended shells and influencing their lateral migration. In terms of particle size, larger beads settle sooner, approaching their equilibrium position, although the sorting of small particles is quite challenging, while their lateral migration occurs more slowly. By varying the geometry of the microfluidic system as channel cross-section, the number and pattern of the particle size specific equilibrium positions in the channel cross-section can be tuned.

In an asymmetric curvilinear channel, the focusing nodes can be reduced to a single sheet or point. Due to the curvature of the geometry, a secondary flow is formed to generate counter rotating Dean-vortices in the channel cross-section. In this flow the particles experience an evolving Dean-drag-force, which further helps focusing them to a certain extent. Dino Di Carlo et. al. [1] was a pioneer in the topic and defined a focusing criteria (*Eq. 1*) based on the ratio of bead diameters (a) and hydraulic diameter of the channel (D_h):

$$\frac{a}{D_h} > 0.07, \qquad \textit{(Eq. 1)},$$

where $D_h = \frac{2wh}{w+h}$, w and h are channel width and height, respectively.

Microfluidic System applied

The particle-size-dependent lateral focusing phenomenon was examined in our study by intensive variation of geometrical parameters (height and critical width) of the asymmetrically curved serpentine channel. The measurements were implemented in a ~35 mm long channel consisting a periodic sequence of 23 curvatures. The lateral positions of the fluorescent beads and the biological cells were recorded at the end of the channel in the major curvature having 300 µm width. The applied flow rates were varied between 0.5 and 2 µL and the minimal flow rates required for efficient lateral focusing at a given channel size were also determined. [2]

Results and discussion

We proved that in the channel characterised with 25 µm height and 50 µm critical width (H25_W_{cr}50), the focusing of rigid particles having diameters of Ø 15.8 and 4.8 µm is successful

at 0.5 µL/s flow rate, although the focusing positions were determined at 1 µL/s flow rates for several particle sizes as presented in Fig. 1. In the designed curvilinear channel the size dependent focusing positions of the rigid, spherical polystyrene beads were represented by a precise bead map and compared to the behaviour of multi-dimensional, deformable cells (see Fig. 2 and Table 1). [3] In this microfluidic system the later focusing was possible theoretically above the diameter of 2.4 µm.

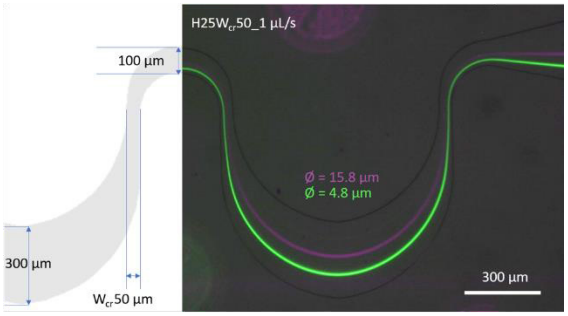

Fig. 1. Lateral focusing fluorescent beads (Ø 5.8 and 4.8 µm) at 1 µL/s flow rate in H25_W$_{cr}$50 type curvilinear microchannel.

The lateral focusing phenomena of Escherichia coli bacteria, Red Blood Cells, Saccharomyces cerevisiae yeast and HeLa cancer cells were characterised and compared to the behaviour of rigid polystyrene beads falling in the diameter range of 0.5 - 16.5 µm as presented in Table 1.

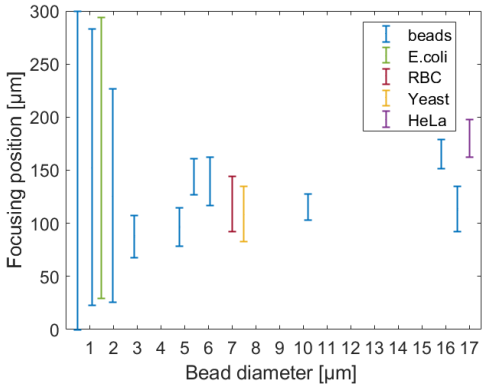

Fig. 2. The focusing positions or concentration ranges of rigid beads and target cells in H25_W$_{cr}$50 type channel at 1 µl/s flow rate.

Conclusion

Our experiences (see Fig. 2 and Table 1) project that the stick-shaped cells presumably take up oscillatory motion in the flow, they are not focused in a single point and their degree of concentration best matches with the 1.1 µm beads. RBC cells may adopt a tumbling motion, they were focused according to their larger dimension and their lateral position can be mostly represented by the 6.08 µm diameter beads. The spherical yeast cells characterised by an average diameter of 9.75 µm could be modelled by 10.2 µm diameter beads. The inhomogeneous, deformable cancer cells can be typified by variable sizes with the mean of 24 µm. In our microfluidic system the 15.8 µm beads were the most capable model regarding their lateral position.

Table 1: Size-dependent lateral focusing of beads and cells (see Fig. 2)

	Particle diameter (a) [µm]	$\frac{a}{D_h}$	*Focused position / range [µm]*
Polysterene beads	0.5	0.015	[0–300]
	1.1	0.033	[22.6–283]
	1.97	0.059	[25.5–226.4]
	2.9	0.087	[67.9–107.5]
	4.8	0.144	[78.6–114.3]
	5.4	0.162	[126.8–160.8]
	6.08	0.182	[117–162]
	10.2	0.306	[103.03–127.3]
	15.8	0.474	[151.5–178.6]
	16.5	0.495	[91.8–134.7]
E. coli	0.5	0.015	[28.37–294.3]
	2.0	0.060	
RBC	2.5	0.075	[91.8–143.9]
	8.0	0.240	
Yeast	5.0	0.150	[82.7–134.7]
	10.0	0.300	
HELA	16.0	0.480	[162.4–197.9]
	29.0	0.870	

References

[1] D. D. Carlo, D. Irimia, R. G. Tompkins, and M. Toner, ‘Continuous inertial focusing, ordering, and separation of particles in microchannels’, *Proc. Natl. Acad. Sci.*, vol. 104, no. 48, pp. 18892–18897, Nov. 2007, doi: 10.1073/pnas.0704958104.

[2] A. Bányai, E. L. Tóth, M. Varga, and P. Fürjes, ‘Geometry-Dependent Efficiency of Dean-Flow Affected Lateral Particle Focusing and Separation in Periodically Inhomogeneous Microfluidic Channels’, *Sensors*, vol. 22, no. 9, Art. no. 9, Jan. 2022, doi: 10.3390/s22093474.

[3] A. Bányai *et al.*, ‘Dean-Flow Affected Lateral Focusing and Separation of Particles and Cells in Periodically Inhomogeneous Microfluidic Channels’, *Sensors*, vol. 23, no. 2, Art. no. 2, Jan. 2023, doi: 10.3390/s23020800.

DOI 10.5162/EUROSENSORSXXXVI/PT6.257

Investigating the optical response of an LSPR sensor based on hexagonally arranged nanoparticles

Rebeka Kovács[1,2], Attila Bonyár[1,2],
[1] Department of Electronics Technology, Faculty of Electrical Engineering and Informatics, Budapest University of Technology and Economics, Budapest, Hungary
[2] Institute for Solid State Physics and Optics Wigner Research Centre for Physics of the Hungarian Academy of Sciences, Budapest, Hungary

kovacsrebeka@edu.bme.hu

Summary:
This paper focuses on the optimazation of a localized surface plasmon resonance (LSPR) based sensor element intended for biosensing applications. Finite element method (FEM) was used for the design of a digital twin of a physically realized plasmonic sensor consisting of hexagonally arranged ellipsoidal nanoparticle arrangements. The effect of light illumination conditions, namely polarization type and angle of incidence on the refractive index sensitivity of the particle arrangements is studied.

Keywords: finite element method (FEM), localized surface plasmon resonance (LSPR), plasmonic nanostructure, refractive index sensing, polarization

Background, Motivation and Objective

In the past decades, the investigation of refractive index sensing-based label-free optical applications have been in the spotlight due to their fast analysis time and many potential applications [1]. Localized surface plasmon polaritons are formed by the electric and magnetic fields of the incident electromagnetic wave, which causes free electron oscillations at the surface of the metallic nanoparticles [2]. The amplifying of scattering and absorption of the incident light can be utilized in many sensing applications [3]. The performance of these biosensors is highly affected by the geometrical properties of the nanoparticles, the refractive index of the surrounding media and the incident electromagnetic field. In a previous research linearly and circularly polarized electromagnetic waves were investigated, with the incident light's propagation direction perpendicular to the plane of the nanoparticles [4]. This work focuses on the effect of various angles of the incident electromagnetic wave to enhance the refractive index sensitivity (*RIS*) of the sensor. The calculations were carried out with the finite element method (FEM), which is a numerical simulation method that can be used for analyzing different electromagnetic problems. It uses Maxwell's equations by discretizing the geometry of the model, and it allows us to apply it for periodic nanoparticle arrangements [5].

Description of the New Method or System

The design of the periodic structure of the digital twin of the ellipsoid nanoparticles, and the calculations were carried out using COMSOL Multiphysics 3.5 software's Wave Optics module. A hexagonal unit cell was created for the ellipsoidal nanoparticles. The geometrical properties for the digital twin of the arrangement was calculated from experimental results and Scanning Electron Microscope (SEM) images (Figure 1.). Additionally, an SiO_2 pillar was added to the model, to simulate the experiments more precisely.

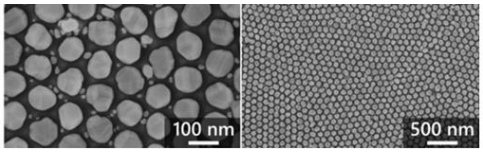

Fig. 1. SEM images of the nanoparticle arrangement over the aluminum template. Reproduced from ***Hiba! A hivatkozási forrás nem található.****.*

The meshing of the unit cell is presented in Figure 2.

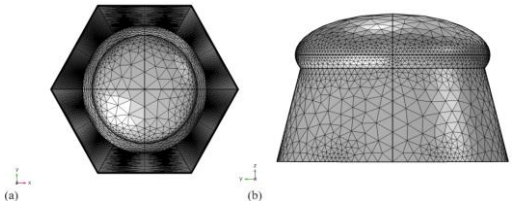

Fig. 2. The meshing of the (a) hexagonal unit cell with the substrate, and (b) the pillar.

Magnetic and electric modes were both investigated with the help of a periodic port. With linearly polarized incident wave the lowest and strongest levels of coupling between the nanoparticles were investigated with various angles of the incoming electromagnetic wave. Furthermore, the effect of changing the angle of the incident light was simulated with circularly polarized light. The sensors have been in their response of refractive index changes of the surrounding medium, thus the *RIS* can be described as:

$$RIS = \frac{\Delta\lambda}{\Delta n}$$

Results

The elevation angle of incidence (*Θ*) describes the deviation from the normal perpendicular angle of the incoming wave. Two cases of linearly polarized light were investigated (Figure 3.)

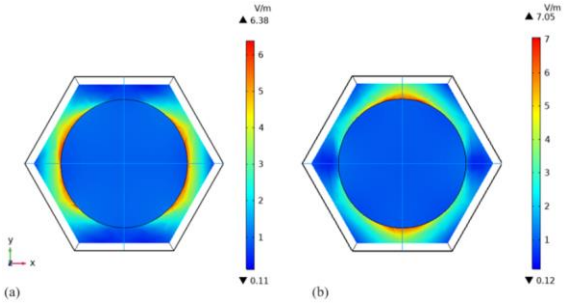

Fig. 3. Normalized electric field distribution with p-polarized light (a) ϕ =0°, (b) ϕ= 90° in air (n=1).

The effect of various angles of the incident wave were further studied in S and P polarization, the results on the *RIS* is presented in Figure 4.

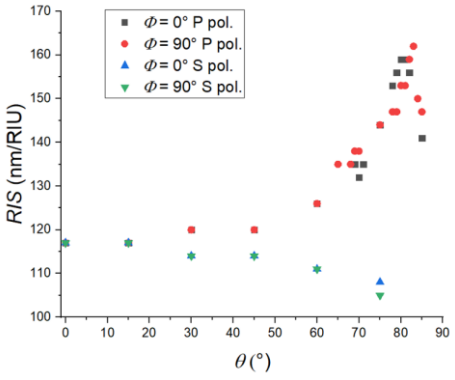

Fig. 4. The effect of changing the angle of the incident light (Θ) in S- and P-polarizaton

Figure 5. presents the changes in the electric field in case of circular polarization with two different angles of the incident light.

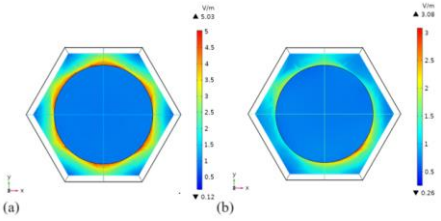

Fig. 5. Normalized electric field distribution with circularly polarized light at (a) Θ = 15°, (b) Θ = 60° in air (n=1).

Acknowledgement

This work was partially supported by Nanoplasmonic Laser Fusion Research Laboratory (NAPLIFE) project financed by the National Research and Innovation Office (2022-2.1.1-NL-2022-00002), Hungary. The research was also supported by the National Research and Innovation Office under project number: 2020-1.2.3-EUREKA-2022-00030. The project is also supported by the Doctoral Excellence Fellowship Programme (DCEP) is funded by the National Research Development and Innovation Fund of the Ministry of Culture and Innovation and the Budapest University of Technology and Economics, under a grant agreement with the National Research, Development and Innovation Office. This work is also supported by the ÚNKP-23-3-I-BME-269 New National Excellence Program of the Ministry for Culture and Innovation from the source of National Research, Development and Innovation Fund.

References

[1] S. Unser, I. Bruzas, J. He, L. Sa-gle. Localized Surface Plasmon Resonance Biosensing: Current Challenges and Approaches. Sensors.15(7), 15684-15716. (2015); https://doi.org/10.3390/s150715684

[2] Lee. K.S, El-Sayed. M.A. Dependence of the enhanced optical scattering efficiency relative to that of absorption for gold metal nanorods on aspect ratio, size, end-cap shape, and medium refractive index. J Phys Chem B. Nov. 3;109(43):20331-8. (2005); doi: 10.1021/jp054385p.

[3] P. P. Austin Suthanthiraraj and A. K. Sen, Localized surface plasmon resonance (LSPR) biosensor based on thermally annealed silver nanostructures with on-chip blood-plasma separation for the detection of dengue non-structural protein NS1 antigen, Biosensors and Bioelectronics, vol. 132, pp. 38–46, May (2019); doi: 10.1016/j.bios.2019.02.036

[4] R. Kovács, A. Bonyár. Investigation of the Refracitve Index Sensitivity of Hexagonally Arranged Gold Nanoparticles With Finite Element Method (FEM)" 18th IEEE Nanotechnology Materials and Devices conference, NMDC, pp. 309-312. 4p. (2023)

[5] Yee, K. Numerical solution of initial boundary value problems involving maxwell's equations in isotropic media. IEEE Trans. Antennas Propag.pp. 14, 302–307. (1966)

[6] S. Zangana, T. Lednicky A. Bonyar. "Three Generations of Surface Nanocomposites Based on hexagonally Ordered Gold Nanoparticle Layers and Their Application for Surface-Enhanced Raman Spectroscopy" Chemosensors 11(4), 235 (2023)

DOI 10.5162/EUROSENSORSXXXVI/PT6.259

Detection of Nucleic Acids Based on Localized Surface Plasmon Resonance

Nóra Tarpataki[1,2], Dorottya Enikő Tóth[1], Attila Bonyár[1,2]
[1] Department of Electronics Technology, Faculty of Electrical Engineering and Informatics, Budapest University of Technology and Economics, Egry József street 18 Budapest, Hungary,
[2] Institute for Solid State Physics and Optics, Wigner Research Centre for Physics of the Hungarian Academy of Sciences, Konkoly-Thege Miklós út 29-33 Budapest, Hungary

tarpatakin@edu.bme.hu

Summary:
The main aim of this work is to test and optimize protocols for immobilizing probe-DNA and detect its complementary target-DNA strand in a microfluidic cell, as well as to provide data on the sensitivity of the sensor. For this purpose, we tested different nanostructures, namely gold nanoislands on glass substrates, created by the solid-state dewetting method and gold nanotriangles created by chemical synthesis and bonded to the substrate by subsequent surface chemistry. The sensor element, prepared on a glass slide was bonded to a PDMS-based microfluidic system. The peak shift of localized surface plasmon resonance absorption was monitored with an optical spectrometer.

Keywords: localized surface plasmon resonance (LSPR), gold nanostructures, microfluidics, nucleic acid, biosensor sensitivity

Background, Motivation and Objective

Biosensors are analytical devices designed to detect the presence of a target molecule in a sample [1]. They can be divided into two main groups based on whether they use labels or not. The former relies on a label to generate and amplify the signal, while the latter is label-free: the signal is caused solely by the presence of the analyte [2].

One phenomenon used in label-free methods is localized surface plasmon resonance (LSPR). This occurs when an electromagnetic wave (i.e. light) interacts with a noble metal nanoparticle. At a specific wavelength, resonance takes place and causes the electrons to oscillate. This can be observed as an absorbance peak in the spectrum. [2, 3]

The resonance wavelength is affected by a number of different parameters, including the nanoparticles' size, shape, material and the refractive index of the medium. This enables nanoparticles to function as sensors: the presence of the analyte increases the refractive index in their environment, resulting in a shift of the absorbance peak in the spectrum. [2]

Description of the New Method or System

The refractive index sensitivity of a LSPR sensor can be influenced through the proprieties of the nanoparticles. Particles with anisotropic form and sharp edges provide greater sensitivity [4], [5]. Therefore, in this work, gold nanotriangles were synthesized according to E. Podlesnaia's work [6]. They were then immobilized to glass slides through silane-chemistry, which were integrated into PDMS-based (poly-dimethyl-siloxane) microfluidic cells to enable measurements. Gold nanoislands on glass substrates prepared by solid state dewetting (thermal annealing) were also used for the experiments to compare the performance of the nanotriangles.

Fig. 1 Two of the microfluidic cells used during the measurements.

Different cell geometries, DNA immobilizing methods and buffers were tested in order to optimize the procedure. Data were collected by monitoring the process with a spectrophotometer. Two of these tested microfluidic cells are shown in Fig. .

Results

In the final article, results will be provided concerning the efficiency of the tested protocols, including time frames, buffer types (e.g. trisodium citrate) and concentrations, flow rates as well as cell geometries.

The spectra will be evaluated, and the position of the peaks will be investigated as a function of time. Fig. provides an example of this type of measurement (blue: peak position in the function of time, evaluated by a custom Matlab code, red: trendline of the peak shift). Finally, the sensitivity of the sensor will be investigated and presented.

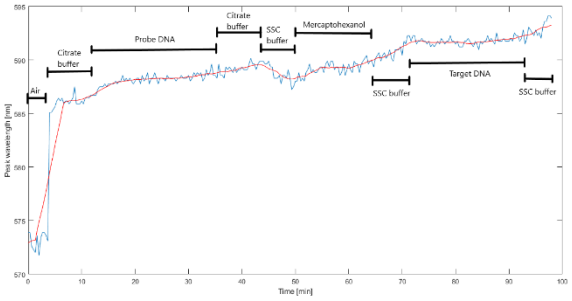

Fig. 2 Example of shift of the LSPR peak during the measurements.

As shown in Fig. , the first jump corresponds with the shift between air and citrate buffer, as the latter enters the channel. DNA immobilization causes a redshift of around 2-3 nm. Hybridization with target DNA causes a similar shift in this experiment.

Acknowledgements

Prepared with the professional support of the Doctoral Student Scholarship Program of the Cooperative Doctoral Program of the Ministry for Innovation and Technology from the source of the National Research, Development and Innovation Fund.

This work was partially supported by Nanoplasmonic Laser Fusion Research Laboratory project financed by the National Research and Innovation Office (2022-2.1.1-NL-2022-00002), Hungary. This research conducted at Budapest University of Technology and Economics was funded by the National Research, Development, and Innovation Fund of Hungary under Grant TKP2021-EGA-02. The research was also supported by the National Research and Innovation Office under project number: 2020-1.2.3-EUREKA-2022-00030. Attila Bonyár is also grateful for the support of the Hungarian Academy of Engineering and the “MICHELBERGER MESTERDÍJ” Scholarship.

References

[1] Tetyana Phumlani, Shumbula Poslet Morgan, and Njengele-Tetyana Zikhona, “Biosensors: Design, Development and Applications,” in *Nanopores*, Ameen Sadia, Akhtar M. Shaheer, and Shin Hyung-Shik, Eds., IntechOpen, 2021.

[2] K. M. Mayer and J. H. Hafner, “Localized surface plasmon resonance sensors,” *Chemical Reviews*, vol. 111, no. 6. pp. 3828–3857, Jun. 08, 2011. doi: 10.1021/cr100313v.

[3] J. L. Hammond, N. Bhalla, S. D. Rafiee, and P. Estrela, “Localized surface plasmon resonance as a biosensing platform for developing countries,” *Biosensors*, vol. 4, no. 2. MDPI, pp. 172–188, 2014. doi: 10.3390/bios4020172.

[4] J. J. Mock, D. R. Smith, and S. Schultz, “Local refractive index dependence of plasmon resonance spectra from individual nanoparticles,” *Nano Lett*, vol. 3, no. 4, pp. 485–491, Apr. 2003, doi: 10.1021/nl0340475.

[5] K. S. Lee and M. A. El-Sayed, “Gold and silver nanoparticles in sensing and imaging: Sensitivity of plasmon response to size, shape, and metal composition,” *Journal of Physical Chemistry B*, vol. 110, no. 39, pp. 19220–19225, Oct. 2006, doi: 10.1021/jp062536y.

[6] E. Podlesnaia, A. Csáki, and W. Fritzsche, “Time optimization of seed-mediated gold nanotriangle synthesis based on kinetic studies,” *Nanomaterials*, vol. 11, no. 4, 2021, doi: 10.3390/nano11041049.

DOI 10.5162/EUROSENSORSXXXVI/PT6.261

Sustainable and battery-less self-powered glucose sensor for diabetes screening applications

A.Visús, J.González-Sanz, S.Liébana, S.Pérez-Jiménez and N.Sabate
Institute of Microelectronics of Barcelona (IMB-CNM-CSIC), carrer Til.lers sn, Campus UAB, 08193 Bellaterra-Barcelona, Spain
Julia.gonzalez@imb-cnm.csic.es

Summary:
Our proposal introduces a glucose sensor designed to make a first screen diabetes stages by measuring the current, which varies according to the glucose level. The developed sensor based on simple electronic system and affordable materials, reduce both cost and environmental impact. The circuit can store various voltage values, each proportional to the glucose concentration in the human plasma sample.

Keywords: Diabetes screening, glucose sensor, self-powered strip, screen-printing, sustainable devices.

Background, Motivation and Objective

In the last decade, diabetes has become a worldwide silent pandemic with millions of undiagnosed patients. Awareness of diabetic conditions is considered to be a crucial first step in changing eating habits and seeking treatment, as the side effects of this condition are generally unnoticed until irreversible damage arises in the kidneys, eyes, or feet [1]. However, campaigns take place in very localized spots, with a very modest impact on the population. Two main reasons are campaign costs, which in low- and medium-income countries are covered by non-governmental organizations, and their modus operandi, which involves glucose level measurement performed by volunteers with glucometer devices at a specific stand during a particular day, where individuals with abnormal glucose levels are informed about their health status. This work aims to address this problem of late detection, especially in lower- and middle-income countries (LMICs), and make the monitoring and treatment of the disease more accessible [2]. Here, we propose a novel and battery-less glucometer that functions upon the addition of a drop of blood, and voltage leads to a result that can be read with a simple voltameter. The solution not only reduces the cost of the device but also the carbon footprint and simplifies end-of-life disposal, adopting eco-friendly features.

Description of the New Method or System

The device core is based on an enzymatic fuel cell activated by the glucose concentration present in a blood sample. The fuel cell encompasses an anode that oxidizes the glucose and a cathode that performs a non-limiting reduction reaction. In comparison to intricate systems with sophisticated electronics, our circuit operates the fuel cell signal with just two resistors, a capacitor, and a diode. One of the resistors subjects the fuel cell to a high current demand that causes a voltage drop, which depends on the glucose content of the sample. The dropping time is then computed with a parallel RC circuit, in which the built-up voltage in the capacitor is proportional to the initial glucose concentration. The capacitor acts as a physical memory element, readable at any moment [3]. Figure 1 shows the schematic of the circuit.

Experimental section

The fuel cell electrodes are fabricated by screen-printing method over a PET flexible substrate. The anode consists of a carbon-based electrode in which a mixture of Hexaammineruthenium(III) chloride mediator and glucose oxidase (GOX) enzyme is deposited and dried. The cathode contains a home-made ink based on carbon and AgxO powder. The electrode region has been defined by means of PSA laser-cut adhesives. A 4.6 x 2 mm glass-fiber paper is used to hold the 3.75µl plasma samples. Figure 2 shows our self-powered sensor compared to the commercial glucose strip.

We aimed to demonstrate that the self-powered glucose strip developed in our laboratory can discriminate between normal glucose status (below 100 mg/dL), pre-diabetic (between 100 and 125 mg/dL), diabetic (over 125 mg/dL), and highly alarming status (over 270 mg/dL). Our experiment consisted of measuring different glucose concentrations at values limiting the different classification regions in human plasma. The

distinction of these glucose levels, translated into current levels by the battery, is made by resistor R1. Figure 3 shows the evolution of the fuel cell voltage when connected to R1 at different glucose concentrations and the measured built-up voltages across the capacitor for the different tested glucose concentrations. Furthermore, the parallel branch formed by resistor R2 with a higher resistivity value than R1, diode D, and Capacitor C is used to store the charge. The charging time of the capacitor is limited by the diode. Once the voltage of the fuel cell becomes lower than the threshold of the diode, the capacitor stops increasing its voltage. In Figure 4, we can see the final voltage of the capacitor for the different concentrations measured, corresponding to the diabetes limits.

Illustrations, Graphs, and Photographs

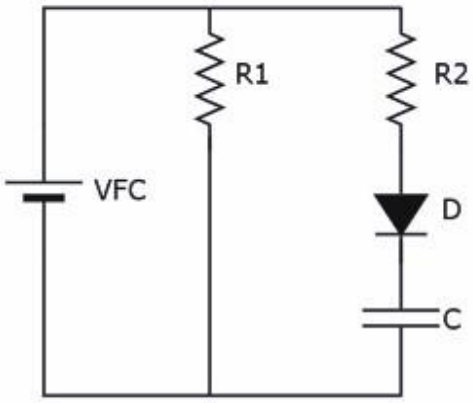

Fig. 1: Schematic of the circuit.

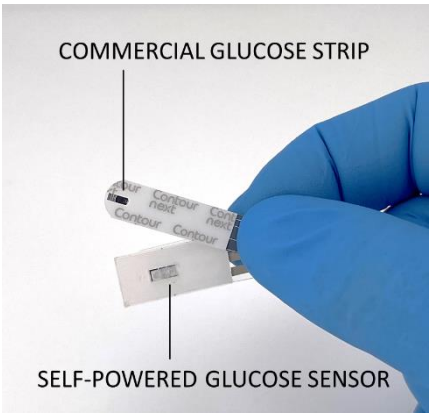

Fig. 2: Picture of the fabricated self-powered glucose sensor and a commercial glucose strip.

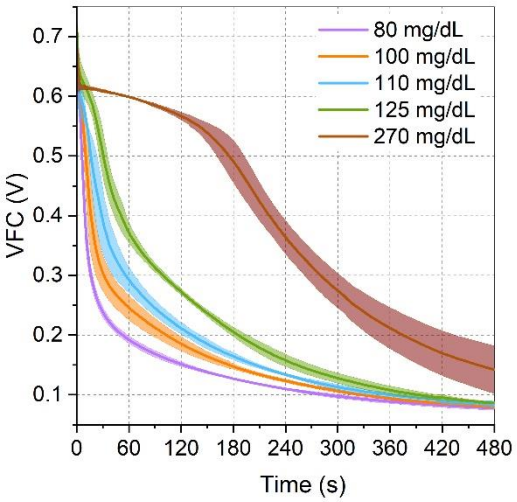

Fig. 3: Voltage evolution of the fuel cell over time for different concentrations of glucose in plasma sample.

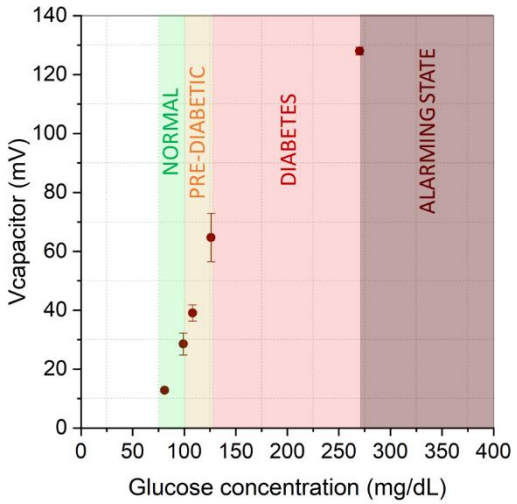

Fig. 4: Capacitor charged voltage represented within the range of glucose concentration.

References

[1] “Diabetes,” World Health Organization, https://www.who.int/es/news-room/fact-sheets/detail/diabetes (accessed May 15, 2024).

[2] Sun, H. et al. (2022). IDF Diabetes Atlas: Global, regional and country-level diabetes prevalence estimates for 2021 and projections for 2045. Diabetes Research and Clinical Practice, 183, 109119. https://doi.org/10.1016/j.diabres.2021.109119.

[3] S. K. Sailapu, S. Liébana, I. Merino-Jimenez, J. P. Esquivel, and N. Sabaté, "Towards a RE-ASSURED reality: A less-is-more electronic design strategy for self-powered glucose test," Biosensors and Bioelectronics, vol. 243, pp. 115708, 2024, doi: 10.1016/j.bios.2023.115708.

DOI 10.5162/EUROSENSORSXXXVI/PT6.284

Evaluation of Cell Plating Efficiency on Polymer Surfaces for Organ-on-a-Chip Applications

Gulsen Zal[1], Atike Nur Seyitoglu[1], Rayan Bajwa[1], Ozlem Kutlu[3], Murat Kaya Yapici[1,2,3]
[1] Faculty of Engineering and Natural Sciences, Sabanci University, Istanbul 34956, Turkey
[2] Department of Electrical Engineering, University of Washington, Seattle, WA 98195, USA
[3] Sabanci University Nanotechnology Research and Application Center, Istanbul 34956, Turkey

murat.yapici@sabanciuniv.edu

Summary:

Due to their many benefits, polymers have gained popularity recently, particularly in the biomedical industry. SU-8 and polydimethylsiloxane (PDMS) in particular have drawn attention for their advantageous qualities, such as chemical stability and biocompatibility. Proper cellular function in biological environments depends on effective cell-surface interactions. As such, in this work, a method of surface modification that involves coating Poly-L-lysine (PLL) and applying oxygen plasma treatment is reported which appears to be promising in improving the adhesion of HEK 293 cells to PDMS and SU-8 surfaces.

Keywords: Cell attachment, HEK 293 cells, Hydrophilic surfaces, PDMS, Poly-L lysine

Introduction

In recent years the usage of polymers has gained importance especially for biomedical applications. The studies suggest that the interest towards polymers such as Polydimethylsiloxane (PDMS), and SU-8 is caused by their biomechanical features such as chemical stability, transparency, biocompatibility.

PDMS, and SU-8 are widely used polymers in biotechnology. However, in biological applications cell-surface interactions are crucial for cells to function properly. Therefore, we propose a new surface modification method that enables attachment of HEK 293 cells to PDMS and SU-8 surfaces. In this study, PDMS and SU-8 surfaces were treated with oxygen plasma to make the surfaces hydrophilic then after sterilization the surfaces were coated with Poly-L-lysine (PLL). PLL is a synthetically produced compound composed of amino acid lysine. PLL is mainly utilized particularly for the cells that are hard to attach to surfaces for enhancing cell attachment. After the surface modifications, we observed that HEK 293 cells successfully adhere to treated PDMS and SU-8 surfaces.

Materials and Methods

To test the cell plating, PDMS and SU-8 were coated onto 4 inch glass wafers. In order to form a 50 µm-thick layer of SU-8, SU-8 3050 (Microchem. Corp., Westborough, MA, USA) was carefully applied onto the wafer surface and the substrate was spinned first at 500 then at 3000 rpm with a spin coater. Then, using a KLA Tencor profiler, the thickness of the SU-8 3050 resin, was verified as ~ 50 µm. To prepare the PDMS coating, the prepolymer base and curing base were carefully mixed at a 10:1 ratio for 10 minutes. The mixture was both spin-coated onto the wafer, and also the excess was poured into a plastic petri dish to create additional PDMS elastomers to act as reservoirs to contain the cells and culturing media. The prepared PDMS mixture was placed under a vacuum desiccator. The degassed PDMS mixture was then cured for 3 h at 70°C inside a vacuum oven. The SU-8 coated glass slide and PDMS samples were activated by subjecting them to oxygen plasma for one minute. PDMS and SU-8 coated wafer surfaces were sticked to pre-cut and cured PDMS pieces by gluing with drops of uncured PDMS and heating on a hot-plate.

For the culturing of HEK 293 cells, the cells were grown in DMEM (%10fbs+%1 pen-strep+%1l-glutamine) media at incubator. Before the culturing the media was removed then 1mL trypsin was added and waited for a minute at 37°C to detach the cells from the petri dish. Next, 4mL DMEM was added onto the cells. The cells were counted by using a cell counter device. After the determination of cell numbers, the cells were centrifuged at 300g for 5 minutes. Then the volume was determined according to the substrate. The new media was

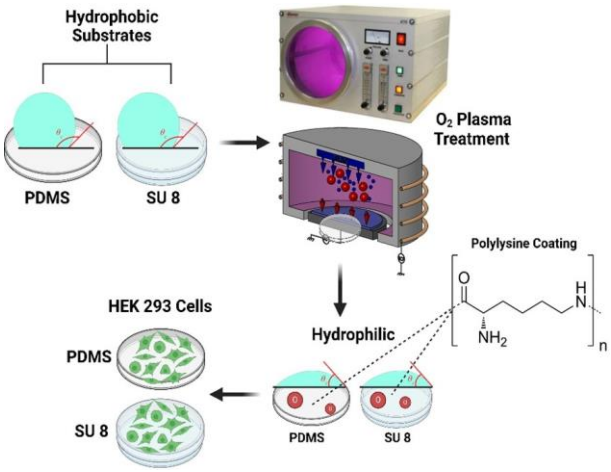

Fig. 1. Methodology diagrams of producing PDMS and SU-8 substrate and plating of HEK 293 cells on the substrates.

added accordingly as 30000 cell/cm^2. Next, the petridish was stirred smoothly and left inside the incubator at 37°C. The experimental procedure concerning cell plating on PDMS/SU-8 coated surfaces is summarized in Fig. 1.

Results

Table 1: Experimental design and results of two different substrates (X: failed attachment, ✓: succussed attachment).

Polymers/Surface Modification	PDMS	SU-8
Bare Polymer	X	X
Poly-L-lysine Coating	X	X
O_2 Plasma Treatment + Poly-L-lysine	✓	✓

As seen in Table 1, in this study, PDMS and SU-8 materials were coated with poly-L-lysine without any O_2-plasma treatment, and with poly-L-lysine and with O_2-plasma treatment, and cell culturing was performed on these surfaces. As seen in Figure 2, cell attachment was successful only on the PDMS and SU8 materials that were O_2-plasma treated and coated with poly-L-lysine.

Fig 2. a, demonstrates the HEK 293 cell viability on standard cell culture plates as a control experiment. When the same cells were cultured on a PDMS substrate with poly-L-lysine which was non-treated via oxygen plasma in *Fig 2. b*, it was seen that HEK 293 cells were not alive and did not attach to the PDMS- poly-L-lysine substrate.

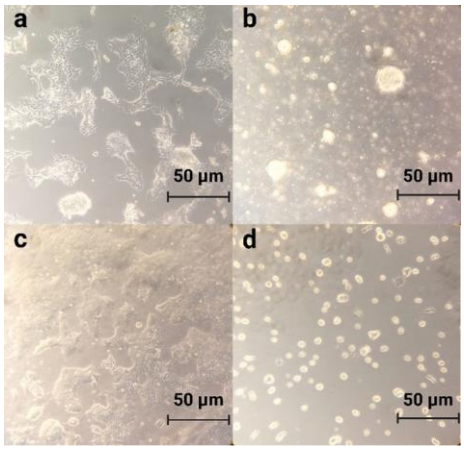

*Fig. 2. **a** control HEK 293 cells, **b** HEK 293 cells on PDMS with poly-L-lysine, **c** HEK 293 cells on oxygen plasma PDMS with poly-L-lysine, and **d** HEK 293 cells on SU8 coated plate with poly-L-lysine.*

In *Fig 2. c*, HEK 293 cells successfully clustered and remained viable on the PDMS substrate that was treated with O_2-plasma and afterwards coated with poly-L-lysine. Similar to *Fig 2. b, Fig 2. d* shows optical microscope images of SU-8 substrates without oxygen plasma treatment but with poly-L-lysine coating, where the HEK 293 cells do not attach to the substrates.

These results show that both oxygen plasma treatment and poly-L-lysine coating are needed to adjust the surface conditions for proper cell plating.

Acknowledgments

Professor Murat Kaya Yapici appreciates the support of the Turkish Academy of Sciences (TUBA) within the framework of the Outstanding Young Scientist Award Program (GEBIP'21) and Science Academy Young Scientist Award Program (BAGEP'23).

References

[1] A. Victor, J. Ribeiro, F. Araújo, Study of PDMS characterization and its applications in biomedicine: A Review, *Journal of Mechanical Engineering and Biomechanics* 4, 1–9 (2019); doi:10.24243/jmeb/4.1.163

[2] Y. Iwasaki et al., Selective cell attachment to a biomimetic polymer surface through the recognition of cell-surface tags, *Bioconjugate Chemistry*, 16, 567–575 (2005); doi:10.1021/bc049707r

[3] R.M. Johann, Ch. Baiotto, Ph. Renaud, Micropatterned surfaces of PDMS as growth templates for HEK 293 cells, *Biomedical Microdevices* 9, 475–485 (2007); doi:10.1007/s10544-007-9054-6

[4] T. Yoshida, T. Nagasawa, epsilon-poly-L-lysine: Microbial production, biodegradation and application potential, *Applied Microbiology and Biotechnology* 62, 21–26 (2003); doi:10.1007/s00253-003-1312-9

DOI 10.5162/EUROSENSORSXXXVI/PT6.304

Real-time water monitoring with advanced biosensor systems

Elise Saoutieff[1], Paul Fourcade[1], Célia Boko[1], Guillaume Nonglaton[1], Luana Cuvillier[1], Vincent Elhorga[1], Sébastien Boisseau[1], Han Shao[2], Richard Murray[2], Alan O'Riordan[2], Gerry Mouzakitis[2], Sonia Mecacci[3], Vitor A.P. Martins dos Santos[3], Enrique Asin Garcia[3], Arjan GJ Tibbe[4], Thijs Besseling[4], Adriana Karcz [4], Joris van Nieuwstadt [4], Gabriela Dudnik[5], Abdessamad Falhi[5], André Fivaz[5], Cecilia Jimenez-Jorquera[6], Josep Maria Margarit-Taulé[6], Serge Goussaert[7], Darragh O'Suilleabhain[8], Julie Ng-A-Tham[9], Cécile van der Vlugt[9], Petra Hogervorst[9]

[1] Univ. Grenoble Alpes, CEA, Leti, Grenoble, France
[2] Nanotechnology Group, Tyndall National Institute, Cork, Ireland
[3] Wageningen University, Wageningen, Netherlands
[4] OnePlanet Research Center, IMEC, Eindhoven, Netherlands
[5] CSEM, Neuchâtel, Switzerland
[6] IMB-CNM, CSIC, Madrid, Spain
[7] Portfolio Concentrate Company, Dublin, Ireland
[8] Cork County Council, Cork, Ireland
[9] RIVM, Bilthoven, Netherlands

Corresponding Author's e-mail address elise.saoutieff@cea.fr

Summary:

BIOSENSEI (Biosensor-based diagnostic platform enabling real-time monitoring of existing and emerging pollutants) aims to develop a biosensor-based real-time monitoring system for typical nutrients (nitrates and phosphates), and Estrogentic endocrine-disrupters, PFAS (Perfluoroalkyl, and polyfluoroalkyl substances) and Mircocystines. This will allow for the first, continuous reliable, real-time, robust monitoring and detection of these pollutants in soil moisture and watercourses by cellular-based biosensors. This system will utilize a biosensor to detect the target analytes and express signals for combinatory detection by both electrochemical and fluorescence transducers with machine learning enhanced interpretation and decision-making. The system will be tested in Ireland, the Netherlands and Industrial use-cases

Keywords: water monitoring, real-time, modelling, Biosensor, machine learning

BioSensei Objective

In January 2023, the EU Drinking Water Directive [1] was revised to provide higher human health protection by implementing more stringent water quality standards, tackling pollutants of concern, such as PFAS, endocrine disruptors (EDs) and microcystins. These are of special concern due to the combination of their difficulty in real-time detection using current methods and their significant negative effects, e.g. EDs interfere with the action of the female hormone estrogen [2] and are bioactive at very low concentrations (below ng/L). Further, the application of animal manure or sludge bio-solids to agriculture lands has been identified as a main source of livestock-secreted estrogens [3], indicating that reducing over-fertilisation could also reduce associated pollution affects.

BIOSENSEI aims to facilitate novel real-time monitoring for these critical pollutants including Nutrients (nitrates [4], phosphates [5]), EDs, PFAS and microcystins in soil and water. This will be demonstrated through the combination of state-of-the-art electrochemical and fluorescent sensors [6] as transducers for highly specific biosensors. BIOSENSEI aims to:

1. Follow a sustainable-and-safe-by-design approach for sensor development
2. Develop and test whole-cell biosensors to detect a diverse range of analytes to produce detectable signals with high specificity
3. Utilize a bimodal sensing approach (electrochemical and fluorescence-based sensors) as transducers for biosensor-generated signals

4. Develop advanced neural edge tools for multi-sensor data fusion, maximizing sensitivity, selectivity, LOD, and lifetime enhancement of target analytes

BioSensei System

BioSensei aims to push the bounds on what is detectable in-situ, in real-time. The innovative approach will broaden the possibilities of monitorable pollutants and allow for future broad-scale monitoring.

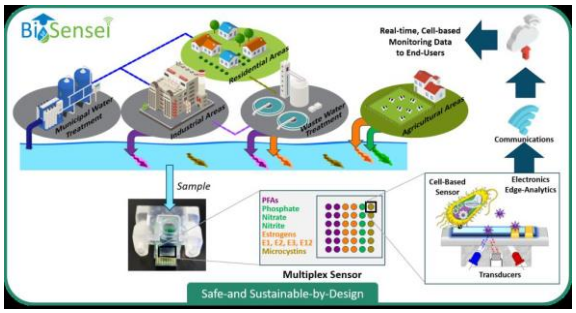

Figure 2. BIOSENSEI system Concept

Established electrochemical and fluorescence sensors will be integrated with encapsulated wildtype microbes, or or genetically modified organisms capable of responding to pollutant analyte presence. These microbes will be immobilised within the sensor enclosure to prevent accidental release and allow for their controlled maintenance and disposal.
Based on previous work [7], novel analog front ends will be developed to the combinatorial sensing approach and sampling conditions. These systems will transfer sensor data to the cloud to facilitate long-term autonomous sensing.

Multi-sensor data fusion methods will be used to determine underlying relationships between the measured (bio)chemical properties, cross-sensitivity in sensor measurements can be exploited to calibrate for environmental effects such as temperature, pH aging or contamination by other chemical species.

Finally, the biosensor will be demonstrated in an industrial setting, a protected ecological site, in agricultural regulatory use case.

Results

BIOSENSEI's vision is to enhance water quality and achieve the highest standards for groundwater in Europe by advancing real-time, cell-based water quality monitoring technologies and minimizing the harmful impacts of water pollution on ecosystems and human health. In both instances, the inclusion of user-case studies will provide region- and application-specific data fostering both climate mitigation in different climatic zones and raising awareness of pollution prevalence.

BIOSENSEI instead focuses on the initial development and assessment of a new technology. The potential for its future implementation, in a similar manner to FAMOSOS, is however evident, despite the early state of the technology. In addition, the facile sensing enabled in real-time has the potential for significant humanitarian benefits, given the extensive health risks of pollution, and the present difficulty in their detection.

References

[1] Drinking water directive. [Online]. Available: https://eur-lex.europa.eu/eli/dir/2020/2184/oj (accessed: Jun. 27 2024).

[2] M. Adeel, X. Song, Y. Wang, D. Francis, and Y. Yang, "Environmental impact of estrogens on human, animal and plant life: A critical review," Environment international, vol. 99, pp. 107–119, 2017, doi: 10.1016/j.envint.2016.12.010.

[3] Environmental quality standards in the field of water policy. [Online]. Available: https://eur-lex.europa.eu/eli/dir/2008/105/oj (accessed: Jun. 27 2024).

[4] Alan. O'Riordan, Han. Shao, Tarun. Narayan, "A working electrode, a reference electrode, a sensor, and a method of manufacture thereof"," UK UK2309536.7.

[5] T. Narayan, M.-K. Reidy, S. Heelan, A. O'Riordan, and H. Shao, "Real-Time Electrochemical Sensor for Phosphate Sensing in Water," in 2023 IEEE SENSORS Vienna, Austria, pp. 1–4.

[6] L. A. Wasiewska, F. G. Diaz, H. Shao, C. M. Burgess, G. Duffy, and A. O'Riordan, "Highly sensitive electrochemical sensor for the detection of Shiga toxin-producing E. coli (STEC) using interdigitated micro-electrodes selectively modified with a chitosan-gold nanocomposite," 0013-4686, vol. 426, p. 140748, 2022, doi: 10.1016/j.electacta.2022.140748.

[7] E. Saoutieff et al., "Wearable Low-Power Sensing Platform for Environmental and Health Monitoring: The Convergence Project Sensors", **2021**, 21, 1802, doi: 10.3390/s21051802

Acknowledgements

The project is funded by the European Union's Horizon Europe Framework Programme (Horizon) under grant agreement 101135241 – BioSensei.

DOI 10.5162/EUROSENSORSXXXVI/PT7.123

The power of using combinatorial materials science and finite element methods in the optimization of sensing by gold nanostructures

Peter Petrik[1,2], Deshabrato Mukherjee[1,3], Krisztián Kertész[1], Zsolt Zolnai[1], Zoltán Kovács[1], András Deák[1], András Pálinkás[1], Zoltán Osváth[1], Dániel Olasz[1,4], Alekszej Romanenko[1,5], Thomas Siefke[6], Sven Burger[7], Miklós Fried[1,8], György Sáfrán[1]

[1] Institute of Technical Physics and Materials Science, Centre for Energy Research, Hungarian Research Network, Konkoly Thege Miklós Str. 29-33, Budapest, 1121, Hungary,

[2] Department of Electrical Engineering, Institute of Physics, Faculty of Science and Technology, University of Debrecen, Bem tér 18, Debrecen, 4026, Hungary

[3] Doctoral School of Materials Sciences and Technologies, Óbuda University, Népszínház u. 8, Budapest, 1081, Hungary

[4] Department of Materials Physics, Eötvös Loránd University, Pázmány Péter Sétány 1/A, Budapest, 1117, Hungary

[5] Doctoral School of Chemistry, Eötvös Loránd University, Pázmány Péter Sétány 1/A, Budapest, H-1117, Hungary

[6] Friedrich-Schiller-Universität Jena, Albert-Einstein-Str. 15, D-07745 Jena, Germany

[7] Zuse Institute Berlin (ZIB) & JCMwave GmbH, Takustraße 7, Berlin, 14195, Germany

[8] Institute of Microelectronics and Technology, Kandó Kálmán Faculty of Electrical Engineering, Óbuda University, H-1084 Budapest, Hungary

petrik.peter@ek.hun-ren.hu

Summary:

Gold nanostructures were created using combinatorial magnetron sputtering and annealing, as well as by electron beam lithography to create nanostructures for plasmonic and Raman sensing. The optical response of the structures was measured by reflectometry, Raman spectroscopy and spectroscopic ellipsometry to study the accuracy of dimensional metrology and the performance of the structures for sensing. The structure was analyzed based on finite element calculations supported by electron microscopy measurements. The sensing performance of the deposited nanoparticles was explained by the density and size distribution on the surface as a function of the amount of deposited material. The measurements and finite element models on the grating structures revealed the most sensitive parameter ranges for dimensional metrology and sensing performance of the structures.

Keywords: Optical characterization, sensors, gold nanoparticles, plasmonics, combinatorial materials science, ellipsometry

Background, Motivation an Objective

The importance of plasmonic nanostructures in sensing doesn't need to be emphasized due to numerous studies and applications in recent years. The large number of possible configurations and combinations of materials necessitates powerful methods for the optimization and generation of databases of optical and structural properties. Combinatorial materials science is an established method with new optimized approaches [1,2] to improve the quality and controllability of the created materials and structures. The current work is a utilization of these opportunities for a range of materials properties for metrology and sensing.

Results

Two types of gold nanostructures have been investigated. The first one is created by annealing of gold layers with a gradually changing thickness on glass slides to generate gold nanoparticles for plasmonic and Raman investigations. The second type is a gold grating structure (Fig. 1) created by electron beam lithography. Both structures have been investigated by optical methods to determine the structures and to utilize them for (optical reflection and Raman) sensing. Finite element modeling and electron microscopy measurements supported the study by providing explanations of the sensing behavior of the structures. Both the gold nanoparticles created by sputtering and annealing and the grating structures created by electron beam lithography could be modeled using suitable finite element approaches. The simulations agreed with measurements in both cases, explaining the major phenomena.

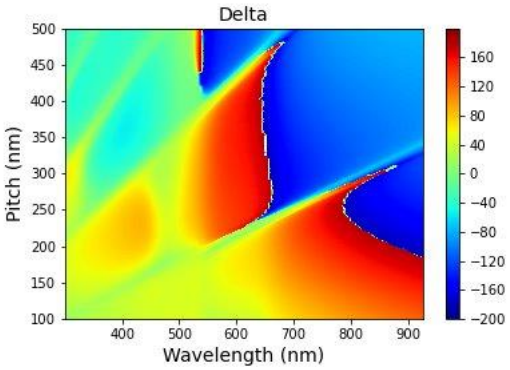

Fig. 1. Phase shift of the reflection coefficients of light polarized parallel and perpendicular to the plane of incidence as a function of the period (Pitch) and the wavelength on a gold grating in Kretschmann configuration ([glass ambient]/[gold grating (thickness of 60nm, grating line width of 50 nm)]/[water substrate]) at an angle of incidence of 70°.

References

[1] G. Sáfrán, "One-sample concept" micro-combinatory for high throughput TEM of binary films, Ultramicroscopy 187 (2018) 50–55.

[2] G. Sáfrán, P. Petrik, N. Szász, D. Olasz, N.Q. Chinh, M. Serényi, Review on High-Throughput Micro-Combinatorial Characterization of Binary and Ternary Layers towards Databases, Materials 16 (2023) 3005. https://doi.org/10.3390/ma16083005.

[3] D. Mukherjee, K. Kertész, Z. Zolnai, Z. Kovács, A. Deák, A. Pálinkás, Z. Osváth, D. Olasz, A. Romanenko, M. Fried, S. Burger, G. Sáfrán, P. Petrik, Optimized sensing on gold nanoparticles created by graded-layer magnetron sputtering and annealing, submitted for publication.

DOI 10.5162/EUROSENSORSXXXVI/PT7.143

Effect of Particle Size Distribution on the Refractive Index Sensitivity of Plasmonic Nanoparticles

Géza Szántó[1,2]
[1] Department of Experimental Physics, Institute of Physics, Faculty of Science and Technology, University of Debrecen, Bem tér 18/a, Debrecen, 4026 Hungary,
[2] Institute for Technical Physics and Materials Science, Center for Energy Research, Konkoly-Thege Miklós út 29-33, 1121 Budapest, Hungary

szanto.geza@science.unideb.hu

Summary:
Numerical simulation was used to investigate the extinction cross-section and bulk refractive index sensitivity of size-distributed gold and silver nanoparticles. Spherical and cube-shaped particles have also been studied. The results confirmed that the optical properties and bulk refractive index sensitivity of these nanoparticles are significantly influenced by their size distribution. If the particles are more uniform, this results in higher sensitivity.

Keywords: bulk refractive index sensitivity, size distribution, localized surface plasmon resonance, simulation

Background, Motivation an Objective

One of the most important applications of localized surface plasmon resonance is the use of the phenomenon to make sensors [1]. In general, one tries to describe a given nanoparticle system by simulating a single typical particle. Therefore, there is a large literature on how the shape or material of a particle affects its optical properties. In reality, however, it is not possible to make an accurate model with a single particle. The size distributions of nanoparticles generally follow a log-normal distribution [2] and the size distribution of particles in a solution has a significant effect on its optical properties [3]. The aim of this article is to show how important the often neglected size distribution really is.

Description of the New Method

The synthesis method used significantly influences both the mean value and standard deviation of nanoparticle size. However, within a given method, these variables are not independent of each other. The simulations were evaluated based on the simple but useful assumption that the mean value and standard deviation are proportional to each other. This assumption is supported by experimental data [4].

Results

In this study, the extinction cross-section and bulk refractive index sensitivity of size-distributed gold and silver nanoparticles, both spherical and cubic, were investigated using the finite element method. The research showed that these properties are significantly influenced by the size distribution of the nanoparticles. A lower standard deviation in the distribution results in higher sensitivity. (see Fig. 1).

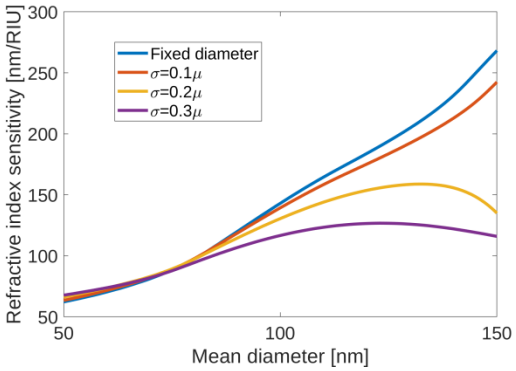

Fig. 1. Bulk refractive index sensitivity of gold spheres with normal distribution. (Assuming several different proportionality factors between the mean and the standard deviation of the particle size.)

The effects of both normal and log-normal size distributions were investigated.

References

[1] K.M. Mayer, J.H. Hafner, Localized Surface Plasmon Resonance Sensors, *Chem. Rev.* 111, 3828–3857 (2011); doi: 10.1021/cr100313v

[2] R. Borah, S.W. Verbruggen, Effect of Size Distribution, Skewness and Roughness on the Optical Properties of Colloidal Plasmonic Nanoparticles, *Colloids and Surfaces A: Physicochemical and*

Engineering Aspects 640, 128521 (2022); doi: 10.1016/j.colsurfa.2022.128521

[3] L.B. Kiss, J. Söderlund, G.A. Niklasson, C.G. Granqvist, New Approach to the Origin of Lognormal Size Distributions of Nanoparticles, *Nanotechnology* 10, 25 (1999); doi: 10.1088/0957-4484/10/1/006

[4] P. Van Thai, S. Abe, K. Kosugi, N. Saito, K. Takahashi, T. Sasaki, T. Kikuchi, Size/shape control of gold nanoparticles synthesized by alternating current glow discharge over liquid: the role of pH, *Mater. Res. Express* 6, 095074 (2019); doi: 10.1088/2053-1591/ab3038.

Simulation of Heat Propagation Processes and Estima-tion of the Signal-to-Noise Ratio of a Thermoelectric Sin-gle Photon Detector

A. Kuzanyan, V. Nikoghosyan, A. Kuzanyan, Armenian National Academy of Sciences, Ashtarak (Armenia)

Unfortunately, this abstract is not available, as the contribution was not confirmed at the time the conference proceedings were finalized.

Simulation of Heat Propagation Processes and Estima-tion of the Signal-to-Noise Ratio of a Thermoelectric Sin-gle Photon Detector

A. Kuzanyan, V. Nikoghosyan, A. Kuzanyan, Armenian National Academy of Sciences, Ashtarak (Armenia)

Unfortunately, this abstract is not available, as the contribution was not confirmed at the time the conference proceedings were finalized.

DOI 10.5162/EUROSENSORSXXXVI/PT7.254

Design, Fabrication and Validation of N-doped Si/Au/Al Schottky Barrier Device for detecting Surface Plasmon Resonance-Induced Hot-Electrons

Chun-Yen Chien[1], Chao Wang[1], Zu-Han Yang[2], Chang-Ru Guo[3], Chien-Hung Yang[3], Tzu-Hang Wu[1], Chii-Wann Lin[1,2,]*

[1] Department of Biomedical Engineering College of Medicine and College of Engineering, National Taiwan University, Taipei Taiwan

[2] Institute of Bio-electronics and Biomedical Informatics, National Taiwan University, Taipei Taiwan

[3] Graduate School of Advanced Technology, National Taiwan University, Taipei Taiwan

corresponding author e-mail address: cwlinx@ntu.edu.tw

Summary:

Traditional Surface Plasmon Resonance (SPR) biosensors, which measure scattering light to characterize biomolecular interactions. This study introduces a novel SPR sensor design based on SPR-induced hot electrons using a Schottky barrier structure (Au/n-Si/Al). This innovative design filters higher energy surface plasmons and enables current sensing. We established the device fabrication processes, including design, debugging, and fabrication, developed the measurement system, conducted device testing, and thoroughly analyzed the chip's electrical and optical characteristics.

Keywords: Surface Plasmon Resonance (SPR), Schottky Barrier, hot electron, Biosensor, MEMS.

INTRODUCTION

Surface Plasmon Resonance (SPR) is a precise optical phenomenon with biochemistry, chemical sensing, surface science, and nanotechnology applications. Traditionally, it involves using a high refractive index prism (BK-7, n=1.571) as a coupler to match the momentum of a thin metallic film (Au, n=0.4941 + 10.353i @1550nm, d=50 nm) at a specific incident angle, SPR angle, to observe the diminished total reflection, as shown in Fig.1. This provides insights into optical properties of materials and aids in analyzing biomolecule interactions, monitoring chemical kinetics, and studying nanostructures. By immobilizing recognition molecules on a metal surface allows real-time monitoring of target-binding events, aiding in drug screening and analyzing disease mechanisms.[1]

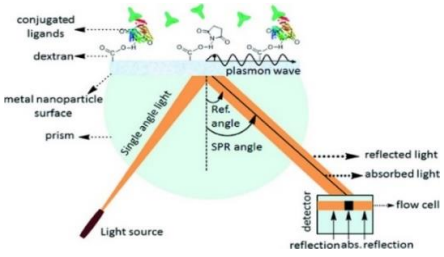

Fig.1. Basic SPR optical setup for biosensing. [2]

Photovoltaic Effect

The photovoltaic effect occurs when a semiconductor or semiconductor-metal combination generates voltage and current upon light or electromagnetic radiation exposure. It's akin to the photoelectric effect but internally related (1) [3]. In this effect, due to heterogeneous material interface, like PN junction formation, excited electrons and holes move oppositely under the established electric field, leading to charge separation.

$$Vo = \frac{kT}{q}\ln\left(\frac{N_A N_D}{{n_i}^2}\right) \quad (1)$$

Schottky Contacts and Ohmic Contacts

In 2017, predecessors organized the conditions for forming Schottky and Ohmic contacts. Different types of contacts can be formed depending on the difference in material work functions. We can utilize Schottky contacts to establish barriers to filter out electrons generated on the metal surface. Through these methods, we can screen out the current generated by SPR.(2) [4]

$$q\phi_{Bn0} = q(\phi_m - \chi) \quad (2)$$

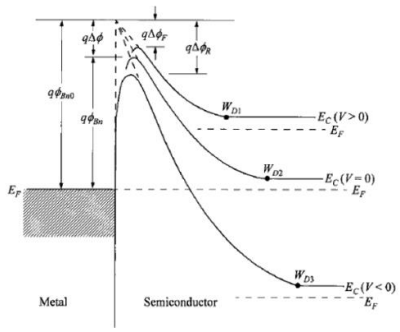

Fig. 2. Schottky contact between metal and semiconductor. [4]

Simulation

Firstly, we used Matlab code (R2015) to simulate the SPR phenomena containing Au (48nm)/Cr (2nm)/Prism (n = 1.5098) under various incident angles and wavelengths. These results provide the fundamental behaviors of surface plasmon waves on the planar interface, especially for the lateral propagation distance for the placement of the Schottky barrier. We also used COMSOL (5.3a) to simulate the penetration depth of NIR wavelength and the generation of hot electrons under Au (48nm)/N-doped Si (10um) and Au (48nm)/N-doped Si (1um). The parameters of used materials are listed sequentially in the following table for reference.

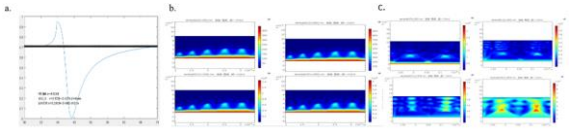

Fig. 3. The SPR simulation results, a. with Matlab and b. 10um N-doped Si with COMSOL c. 1um N-doped Si with COMSOL

Tab 1:The material, thickness and refractive index of our chip

Material	*Thickness*	*N (n + ik)@ 1550nm*
Au	48nm	0.4941 + 10.353i
N-doped Si	500um	3.6730 + 0.005i
Aluminum plate	0.8mm	1.5237 + 15.115i

Chip Design

We redesigned Au/N-doped Si/Al to support SPR wave generation on the Au surface and used Au/N-doped Si to establish Schottky barriers for detecting higher-energy hot electrons. Fig 4 shows the plasmonic chip and PCB assembly. In the aluminum substrate, two holes connect to the pins of USB connector. The N-doped Si coated with gold is bonded to aluminum substrate using Ag glue. Aluminum wires pass through holes from the gold layer, connecting to the USB socket pins to form a complete circuit.

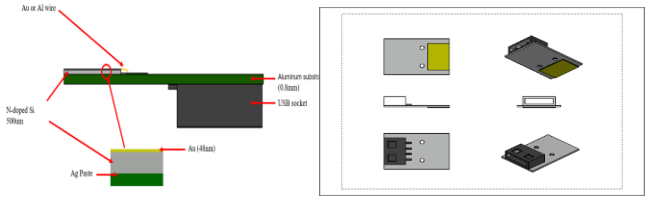

Fig. 4. The design of the plasmonic chip and PCB assembly.

Fabricated Chip & Measurement Setup

In the measurement phase, this study will utilize 1.a probe measurement system architecture, 2.USB measurement and 3.Lock-In Amplifier (LIA) System. We will attempt various measurement methods to determine the basic properties of the SPR chip.

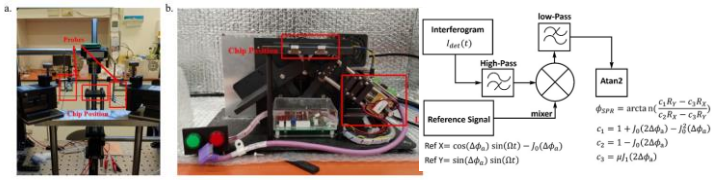

Fig. 5. a. Plasmonic Chip Measurement System and b. SPR Measurement System and modified LIA algorithm System

Current Results

Based on the current chip results, it's evident that the resistance between N-doped Si/Au remains high. This could potentially be attributed to surface roughness, suggesting the need for a more comprehensive cleaning procedure.

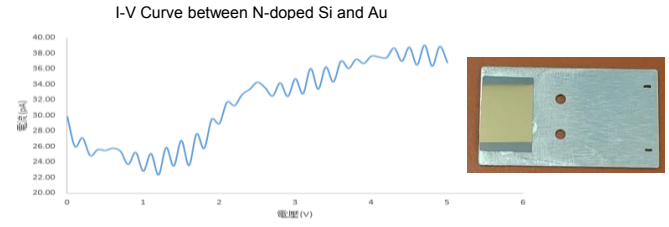

Fig. 6. Chip and I-V Curve between N-doped Si/Au.

Acknowledgements

This project is supported by National Science and Technology Council (MOST 111-2221-E-002 -079 -MY3) in Taiwan.

References

[1] Homola, J. and M. Piliarik, Surface plasmon resonance (SPR) sensors, in Surface plasmon resonance based sensors. 2006, Springer.
[2] Muhammad Aamir Iqbal, et al.Basic concepts, advances and emerging applications of nanophotonics, Arabian Journal of Chemistry, 2023.
[3] Clavero, C., Plasmon-induced hot-electron generation at nanoparticle/metal oxide interfaces for photovoltaic and photocatalytic devices. Nature Photonics, 2014
[4] Haibin Tang, Plasmonic hot electrons for sensing, photodetection, and solar energy applications: A perspective, 2020.

DOI 10.5162/EUROSENSORSXXXVI/PT7.272

Accurate silicon epitaxial multilayer characterization for CMOS imager applications

Peter Basa[1], *Eszter Najbauer, Szilvia Biro, Lucza Sinkó, Zsolt Durkó, Zoltan Kiss, Gyorgy Nadudvari*
[1] *Semilab Co. Ltd., 1117 Budapest, Prielle K. u. 2., HUNGARY*

peter.basa@semilab.hu

Summary:

Silicon epitaxial layer technology provides a key building block for charged particle tracking devices, eg. complementary metal-oxide semiconductor (CMOS) active pixel sensors. Such detector elements are realized on a thick (~775um) heavily doped top quality 12" silicon substrate with a subsequent thin (~1-20um) lightly doped silicon epitaxial layer or multilayer deposition. This epitaxial layer structure also provides virtual substrate for further CMOS manufacturing steps, relatively free of metal contamination and/or crystallographic defects [1,2].

Accurate characterization of such structures, in terms of multilayer thickness, dopant concentrations, and buried defect density is possible with advanced optical instrumentation [3-6]. A round-robin test series were conducted on typical samples with silicon epilayer structures, including Fourier-transform infrared (FTIR) reflectometry, with results confirmed by spreading resistance profiling (SRP) and imaging photoluminescence (PL) techniques.

Keywords: silicon, epitaxial layers, epi, FTIR, spreading resistance profiling, CMOS, imaging sensors

Results:

Advanced optical modeling was applied to the acquired infrared reflection spectra on Si wafers with epitaxial multilayers. A typical result is shown in Fig. 1, where the so-called transition zone (TZ) in between the epilayer and the substrate was modeled by a series of sub-layers with varying charge carrier density.

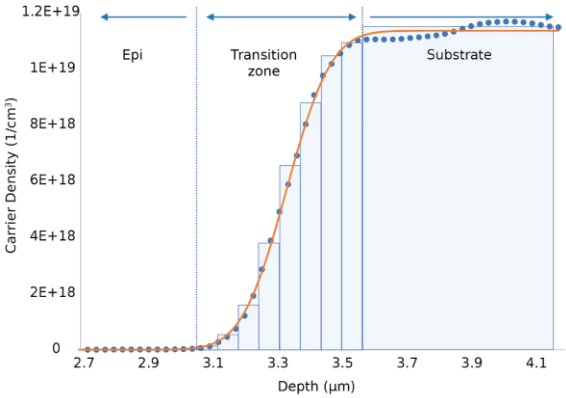

Fig. 1. Characteristic result of the applied advanced infrared optical modeling on Si epilayer structures.

The obtained optical carrier density profile was confirmed by a direct electrical technique, spreading resistance profiling (SRP). Fig. 2 shows the edge of the samples that were beveled at a shallow angle to prepare them for SRP measurements.

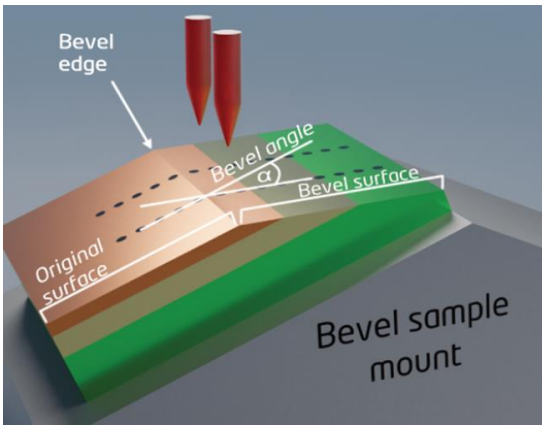

Fig. 2. Schematic diagram of the SRP measurement sequence

Common methods for detecting defects related to epitaxial layer gworth in silicon are usually time-consuming and often destructive. By contrast, Semilab's PL imaging technique (so-called EnVision) provides a quick, non-destructive way of finding these defects [4-6]. Additionally, the online neural network-based analysis offers classification of the found defects. The obtained results are consistent with traditional etch-based methods [4]. Validation of

the PL results were performed by semiconductor reference fabs on processed electronic devices, as shown in Fig. 3.

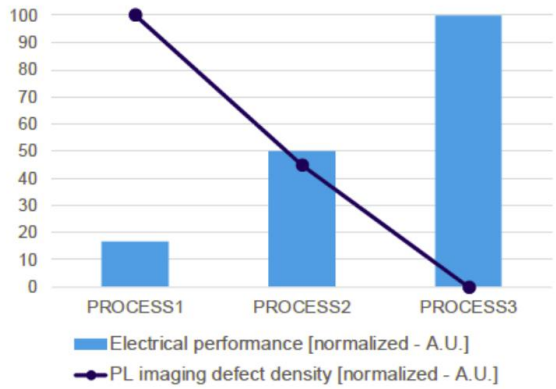

Fig. 3. Reduction of defect cound achieved during optimization of process used for P-N junctions in CMOS imager devices [5]

References:

[1] A. Lahav, A. Fenigstein, A. Strum, S. Rizzolo, “Backside illuminated (BSI) complementary metal-oxide-semiconductor (CMOS) image sensors”, in: Woodhead Publishing Series in Electronic and Optical Materials, High Performance Silicon Imaging (Second Edition), Woodhead Publishing, pp. 95-117, doi: 10.1016/B978-0-08-102434-8.00004-0

[2] A. Onaka-Masada, T. Kadono, R. Okuyama, R. Hirose, K. Kobayashi, A. Suzuki, Y. Koga, K. Kurita, “Reduction of Dark Current in CMOS Image Sensor Pixels Using Hydrocarbon-Molecular-Ion-Implanted Double Epitaxial Si Wafers”, *Sensors 20*, 6620 (2020) doi:10.3390/s20226620

[3] E. E. Najbauer, L. Sinkó, Sz. Biró, Zs. Durkó, P. Basa, “Epitaxial silicon transition zone measurements by spreading resistance profiling and Fourier transform infrared reflectometry”, *Applied Research*, *e202300146* (2024); doi: 10.1002/appl.202300146

[4] M. L. Polignano, A. Galbiati, I. Mica, D. Magni, D. Cseh, F. Jay, P. Basa, N. Laurent, I. Lajtos, G. Molnar, L. Dudas, L. Roszol, and L. Jastrzebski, “Analysis of Near-Surface Metal Contamination by Photoluminescence Measurements”, *ECS Journal of Solid State Science and Technology 7*, R12 (2018)

[5] R. Duru, D. Le-Cunff, M. Cannac, N. Laurent, L. Dudas, Z. Kiss, D. Cseh, I. Lajtos, F. Jay, Gy. Nadudvari, “Photoluminescence for In-line Buried Defects Detection in Silicon Devices”, *28th Annual SEMI Advanced Semiconductor Manufacturing Conference (ASMC)*, Saratoga Springs, NY, USA, 2017, pp. 262-266, doi: 10.1109/ASMC.2017.7969241.

[6] J. Frascaroli, M. Tonini, S. Colombo, L. Livellara, L. Mariani, P. Targa, R. Fumagalli, V. Samu, M. Nagy, G. Molnár, Á. Horváth, Z. Bartal, Z. Kiss, T. Sipőcz, I. Mica, “Automatic Defect Detection in Epitaxial Layers by Micro Photoluminescence Imaging”, *IEEE Transactions on Semiconductor Manufacturing 35*, 540 (2022) doi: 10.1109/TSM.2022.3189847

DOI 10.5162/EUROSENSORSXXXVI/PT7.301

Last developments in the angular response and deformation characterization of resonant micromirrors

Clement Fleury[1], *Muhammad-Hassan Khan*[1], *Diana Mori*[1], *Sara Guerreiro*[1], *Rodrigo Tumolin Rocha*[1], *Dominik Holzmann*[1], *Takashi Sasaki*[1], *Adrien Piot*[1]
[1] *Silicon Austria Labs GmbH, Sandgasse 34, 8010 Graz, Austria*

Clement.fleury@silicon-austria.com

Summary:

Characterization of micromirror in terms of optical performance during actuation has always been challenging. Two years ago, we introduced a method that makes use of digital holography and variable mirror positioning to sample the shape of the mirror at an arbitrary position in its movement. Here we present further development of the technique, including a methodology to perform fast frequency sweeps. We demonstrate the capabilities by comparing the deformation to analytical derivation from amplitude and frequency.

Keywords: MEMS mirrors, characterization, dynamic deformation

Background, Motivation an Objective

Resonant MEMS mirrors are a component of choice for numerous applications such as Pico projection, LIDAR, and endoscopy. Depending on the use, the critical parameters are the resonant frequency, scanning angle and optical quality. Deformations produce aberrations, and increase drastically with mirror diameter, which is required to lower diffraction. Increasing thickness lowers deformation, but also affects resonance frequency. Localized backside reinforcement (BSR) has been used to reduce deformation while keeping the mass low. This complex tradeoff must ultimately be assessed through characterization. We propose here a fast method to collect all relevant parameters of a resonating mirror to give fast feedback to MEMS engineers.

Description of the New Method

The method is an improvement on the method presented in [2]. It makes use of a commercial Digital Holographic Microscope (DHM R2200 by Lyncee Tec) and a 6 axes goniometer stage (Standa 8-0021), enabling virtually unlimited mirror amplitude. An automated turret for the microscope objective enables a fully automatized sequence.

The new method works in two main steps: Angular response, and shape measurement.

If the resonance frequency is unknown, or if a mode search is needed, a frequency sweep is performed using the DHM in 100% laser duty-cycle mode over a large frequency range. A high magnification objective is used, targeting the center of the mirror to enable capturing high slope topography. Once the mode is localized, a second sweep with a lower step and range is performed, this time with 4 samples per period at a laser duty cycle of 1%. From the analysis of the data, rotation axis, amplitude and phase of the mirror movement is extracted for every frequency.

The shape measurement is then performed at the desired frequencies – often resonance. The objective is changed to lowest magnification to cover the whole mirror. Using the motorized goniometer, the previously gathered information of the rotation axis, amplitude and phase of the mirror is used to keep the MEMS in such a way that the mirror part lies in the object plane for the measurement at each phase. The data is then analyzed to determine the amplitude map of the mirror for different harmonics (including 0^{th}, corresponding to static deformation). As a demonstration, an experimental validation of the analytical formula (eq. 1) for deformation is performed on a mirror like the one presented in [2], where the RMS of the deformation amplitude map in and between two modes is compared to the following model [3].

Eq. 1
$$\delta = c\frac{Af^2D^5}{Et^2}$$

With δ the deflection, A the amplitude, f the frequency, D the diameter of the mirror, t its thickness, and E its Young modulus. c is a constant. We substitute deflection for RMS as it is less sensitive to noise than min/max values.

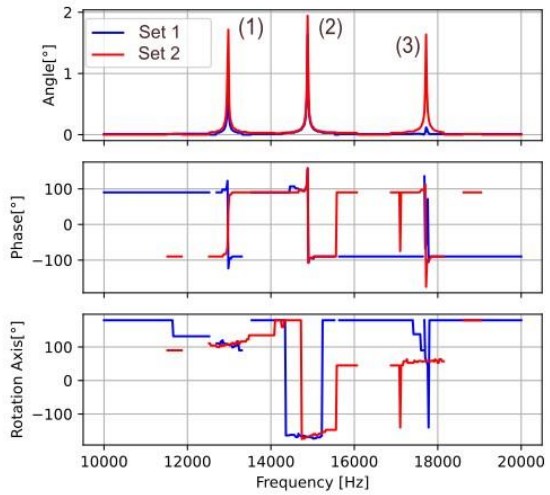

Fig. 1. Amplitude, phase and rotation axis vs. frequency of the mirror without BSR.

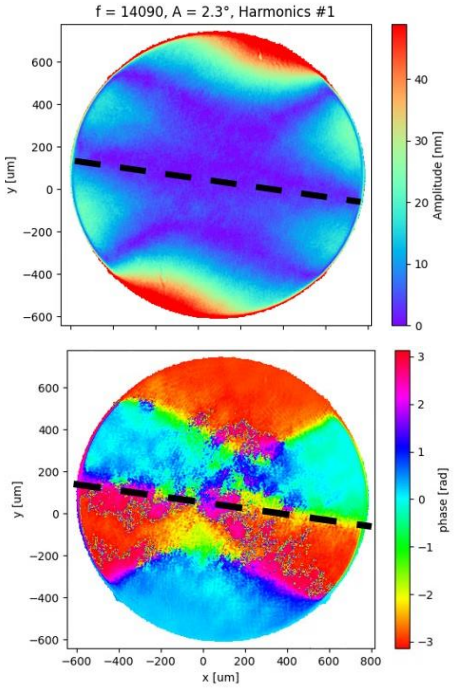

Fig. 2. Mirror (with BSR) amplitude and phase map at resonance (2). Axis shown with dashed line.

Results

Figure 1 shows the result of two frequency sweeps using the presented measurement technique using 4 x 1% duty cycle on a 2D mirror. Two sets of electrodes are used, one optimized for the actuation of different modes. The actuation of set 1 is shown in red and set 2 in blue. Three peaks are visible in amplitude, corresponding to three different modes. Each amplitude peak corresponds to a typical phase response for a resonance mode. The rotation axis can be seen in the last figure. For mode (1) and (2), a frequency dependence in the rotation axis is visible.

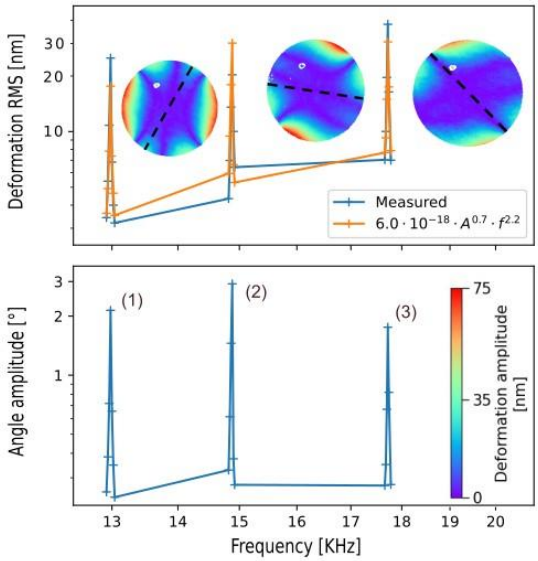

Fig. 3. RMS of the dynamic deformation (with deformation shape and axis) and amplitude of the mirror (without BSR) vs. frequency (log-log).

Figure 2 shows the amplitude and phase map of the deformation at the resonance corresponding to the middle peak. Such a measurement was made for frequencies that display an amplitude higher than .2°.

Figure 3 shows the RMS values versus frequency for the three peaks, with the corresponding amplitude shown below. Fitting the exponents gives dependencies in 0.7 for A, and 2.2 for f. The small difference between the model parameters and extracted parameters may be due to the asymmetry created by the anchor geometry, also visible in the difference between deformation shapes.

Acknowledgement

This work has been jointly supported by the Republic of Austria, the Styrian Business Promotion Agency (SFG), the federal state of Carinthia, the Upper Austrian Research (UAR), and the Austrian Association for the Electric and Electronics Industry (FEEI).

References

[1] P. Thakkar et al., “Measuring angle-resolved dynamic deformation of micromirrors with digital stroboscopic holography,” p. 29, May 2022, doi: 10.1117/12.2621325.

[2] A. Piot et al., “Resonant PZT MEMS Mirror with Segmented Electrodes,” Proceedings of the IEEE International Conference on Micro Electromechanical Systems (MEMS), vol. 2020-January, pp. 517–520, Jan. 2020, doi: 10.1109/MEMS46641.2020.9056124.

[3] P. J. Brosens, “Dynamic Mirror Distortions in Optical Scanning,” Appl. Opt., vol. 11, no. 12, pp. 2987–2989, Dec. 1972, doi: 10.1364/AO.11.002987.

DOI 10.5162/EUROSENSORSXXXVI/PT7.306

Stationary Gas Sensor Networks for Continuous Leakage Detection

Gabriel Rodriguez Gutierrez[1], Daniel Marín López[2], Xinjie Zhou[1], Alvaro Ortiz Perez[1], Jordi Fonollosa[2], and Stefan Palzer[1]

[1]Professorship for Sensors, Department of Electrical Engineering and Information Technology, TU Dortmund, Dortmund, 44227, Germany

[2]Bioinformatics and Biomedical Signals Laboratory, Research Center for Biomedical Engineering (CREB), Universitat Politècnica de Catalunya (UPC), Barcelona, 08028, Spain

stefan.palzer@tu-dortmund.de

stefan.palzer@tu-dortmund.de

Summary:

Continuous monitoring of Biogas installations is a means to improve safety and detect failures occurring only under specific operational conditions. Stationary methane sensor networks are able to perform this task by providing temporarily and spatially resolved data on methane concentrations. Therefore, the reliability and precision of the concentration data of individual nodes is paramount. This contribution presents the setting up of such a wireless gas sensor network based on a miniaturized, photoacoustic methane detection approach via multi-unit calibration. The results highlight the importance and potential of reliable calibration methods as basis for gas flux measurements using stationary sensor nodes.

Keywords: leakage detection; gas sensor network; photoacoustic-based NDIR

Introduction

Several conceptually different approaches for scalable monitoring of methane leakages are currently subject to intensive research and development efforts [1]. This high relevance is due to the ubiquitous use of methane in many industries and the associated high environmental and economic impact as well as the safety-related issues. While satellite-based methods are able to provide a global overview, the continuous detection of leaks on small and medium spatial scales is currently not solved in a techno-economic satisfactory way. The use of distributed gas sensor networks to determine gas flows from a 3D data point cloud of concentration measurements with adequate temporal and spatial resolution is a possible route, if combined with measurements of wind speed, wind direction, temperature, and pressure. Based on the gas flow determination one can then determine the location and strength of leaks. The use of stationary gas sensing networks in this scenario allows for a continuous monitoring at arbitrary sites.

Modeling gas dispersion has shown promise [2], offering the potential for using low-cost, miniaturized sensors to measure environmental factors. Indirect photoacoustic gas sensors offer promising features in terms selectivity and sensitivity in a smaller size as compared to standard non-dispersive infrared spectroscopy (NDIR) devices [3]. Yet, ensuring reliability and repeatability across a large-scale network is critical. This study delves into a calibration method for consistent data quality across sensor nodes based on custom-build, miniaturized indirect photoacoustic sensors using mid-infrared light emitting diodes (mid-ir LED) at 3.5 µm to excite photoacoutic waves.

Gas Sensor Network

The gas sensor network is based on individual nodes, each of which feature a GPS module NEO-6M for geolocalization and data synchronization, an integrated temperature, humidity, and pressure sensor BME280 from Bosch, a LoRaWAN module for wireless, long range data transfer. The determination of a leak's source and strength is possible by using stationary gas sensor networks and to this end a total of 10 sensor nodes with the same setup and particularly with the same optical path length for NDIR-type photoacoustic detection of methane have been built. As light source a mid-infrared light emitting diode (MID-IR LED) L15893-0330M from Hamamatsu Photonics K.K. with a central emission wavelength of 3.5 µm is employed. Its output is modulated with a sinusoidal current modulation at a frequency of ω_{mod} = 300 Hz. The photoacoustic detector consists of a hermetically sealed cell filled with

pure methane at 1 bar pressure, and includes a microphone ICS-40720 from TDK-Invensense Inc. mounted onto a TO 5 socket and bonded to it, as well as 0.5 mm thick sapphire window for infrared radiation access. The probing light passes through an optical path length d_{opt} = 30 mm. The 10 sensor node have been exposed to varying levels of temperature, humidity, and methane concentrations at the same time and in the same environment. Figure 1 shows the variability between different units. To correct the slope, one needs another calibration measurement.

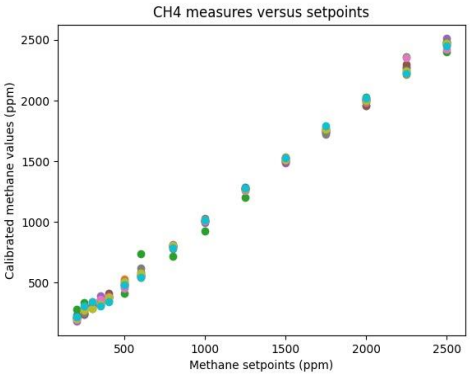

Figure 1: Sensitivity response for 10 sensing nodes at different concentration levels.

Figure 2 shows the corresponding errors in prediction for methane for the different models. The error in prediction can be as high as 1750 ppm, while the error when the calibration for the specific sensor is used remains in the order of tens of ppm.

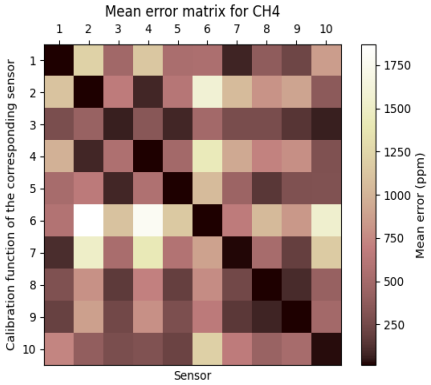

Figure 2: Error in prediction when the calibration models are applied to different sensing nodes.

The cross-sensitivity to temperature and humidity is shown in Figure 3 which highiights de dominance of the temperature coss-sensitivity. Finally, we evaluated the methane calibration models when transferred directly to the other units. In this scenario, the error in the predictions has an average of 1200 ppm.

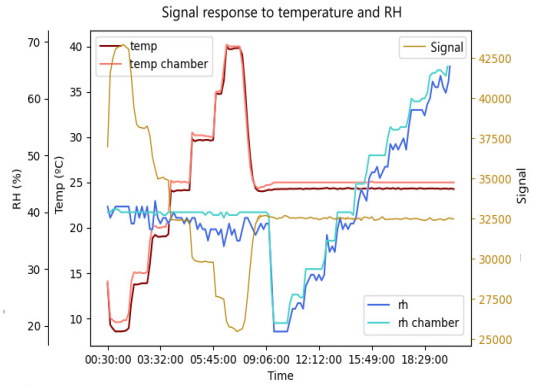

Figure 3: Sensing node exposed to different levels of humidity and temperature.

On the other hand, when performing a singular calibration for each unit the mean error decreases to 25 ppm. When the model incorporates calibration measurements from different sensing units, performing a multi-unit calibration, the average error is 400 ppm, which is a significant decrease with respect the use of models build with different units.

Discussion and Conclusions

In this contribution the development of sensing networks for methane leakage detection based on stationary, indirect photoacoustic spectroscopy is presented. While results of individual calibrations perfom with high accuracy, their cost is not affordable for the deployment of a dense network of sensors. Therefore, the possible to build a multi-unit calibration is demonstrated. This strategy is cost-effective and the performance decay is acceptable for the rapid detection of methane leakages.

References

[1] C. E. Kemp, A. P. Ravikumar, and A. R. Brandt, “Comparing Natural Gas Leakage Detection Technologies Using an Open-Source "Virtual Gas Field" Simulator,” Environmental science & technology, vol. 50, no. 8, pp. 4546–4553, 2016

[2] Dennis D. Baldocchi, Bruce B. Hicks, Tilden P. Meyers, “Measuring Biosphere-Atmosphere Exchanges of Biologically Related Gases with Micrometeorological Methods,” Ecology, vol. 69, no. 5, pp. 1331–1340, 1988.

[3] G. R. Gutierrez, L. Vogel, A. O. Perez, and S. Palzer, “Leakage Detection Using Low-Cost, Wireless Sensor Networks,” in 2022 IEEE Sensors, Dallas, TX, USA, 2022, pp. 1–4.

[4] V. Wittstock, L. Scholz, B. Bierer, A. O. Perez, J. Wöllenstein, and S. Palzer, “Design of a LED-based sensor for monitoring the lower explosion limit of methane,” Sensors and Actuators B: Chemical, vol. 247, pp. 930–939, 2017, doi: 10.1016/j.snb.2017.03.086.

DOI 10.5162/EUROSENSORSXXXVI/PT10.206

Design and Implementation of a Piezoelectric Energy Harvesting System Embedded in a Composite Sandwich Panel

Alkım ADSIZ[1], Bilsay SUMER[1], Mehmet N. BALCI[1]

[1] Mechanical Engineering Department Hacettepe University, Ankara Türkiye,

alkim1998@gmail.com ; alkim.adsiz@hacettepe.edu.tr

Summary:

Piezoelectric energy harvesting (PEH) appears as a prominent field, as it helps to provide enough energy to run small electronics or MEMS. Contemporary patents on PEH systems for aerospace applications, mainly focus on different design geometries or location of PEH on the host structure. In this study a novel combination of piezoelectric harvesters and composite panels are proposed. Series of piezoelectric harvesters are embedded into the cell structure of a composite sandwich panel. The system is expected to provide enough power to run structural health monitoring sensors of an aircraft.

Keywords: Piezoelectric energy harvesting (PEH), Smart materials, Composite sandwich structures, Aerospace.

Background, Motivation and Objective

Almost all type of systems, whether electronic or mechanical, are subjected to either electrical or mechanical inputs such as voltage, current force, motion and vibration, etc. Systems such as aeronautical vehicles, suffer mechanical vibrations with various frequencies. This work proposes a novel method for harvesting ambient mechanical energy with the help of piezoelectric energy harvesters embedded into the cells of a composite sandwich panel, which is a widely used constructing material in aerospace applications. Since the PEH system is shielded by a closed envelope, it is less prone to adverse environmental effects such as fatigue or corrosion. Another advantage is that the system's power output can be closely monitored to detect the changes in mechanical response, by which the system becomes its own sensor. Similar studies have been put forward to detect cracks with piezo layers [1]. As a result of multiple PEH existing on system, broadband energy absorption is possible, when each harvester is purposefully manufactured to be sensitive to resonant frequencies. Thus, the proposed method has a great potential to become the primary power source for aerospace sensor applications.

The objective of this study is to develop new type of embedded energy harvesters to be utilized in composite sandwich panels. Computational studies are carried out using ANSYS APDL [2]. A physical model will be built to conduct experimental studies. Results generated by ANSYS and those obtained by experiments are compared. Parametric studies are conducted to give the optimum power output.

Description of the System

The system (see Fig.1) is a combination of sandwich structure and piezoelectric energy harvesters. Sandwich structures are made out of various materials such as aluminum, carbon and glass fibers etc. Various harvester geometries were developed to be sensitive to different orientation of vibration. Hence, it can be different from what is shown in Fig.1. Moreover, the harvesters can be tuned for ambient frequencies by changing the beam length and tip mass. Detailed diagram of working principle is shown in (see Fig. 2.).

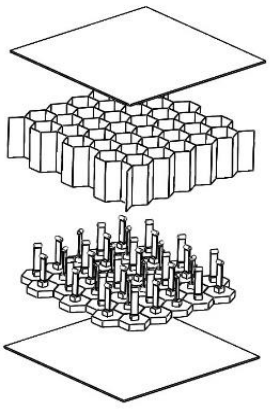

Fig. 1. Exploded view of the system

While the system is shaken by environmental vibrations, a phase difference occurs between

the movement of sandwich panel and harvester tip masses. This difference is then harvested by the newly developed PEH and results in an electrical energy.

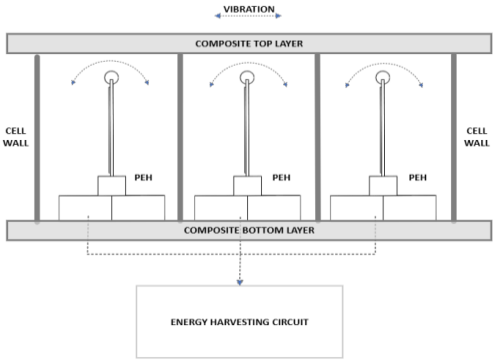

Fig. 2. 2D diagram & working principle

Results

1. Modal shapes of Sandwich Panel

First study is to simulate the physical elements under working condition. For the sake of repeatability and fastness of the simulation, an ANSYS APDL code was developed that can virtually create any sandwich panel with arbitrarily varying dimensions. Aluminum honeycomb sandwich panel with specified dimensions (30x40x16 mm) is parametrically created by the code. First four mode shapes & modal frequencies of the mentioned panel are computed and depicted below in (see Fig. 3.).

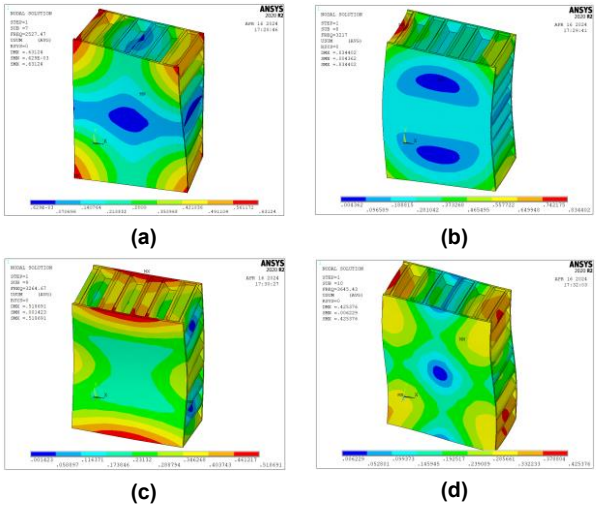

(a) (b) (c) (d)

Fig. 3. Modal analysis of a 30x40x16 aluminum sandwich panel (first 4 modes respectively, a)2527.47Hz, b)3217.00Hz, c)3264.67Hz, d)3645.43Hz)

2. Single PEH modal and harmonic analysis

A single piezoelectric unimorph energy harvester of the newly developed PEH system was modelled (see Fig. 4a.). Node displacements at dominant mode was found using modal analysis (see Fig. 4b.) and nodes with highest electrical potential can be seen as red on top of the piezoelectric layer (see Fig. 4c.). Harmonic analysis between 0-2 kHz ramped input, of the PEH shows a peak in electric potential (see Fig. 4d.) when the system is excited at the base (hexagonal body) with its natural frequency (1472 Hz).

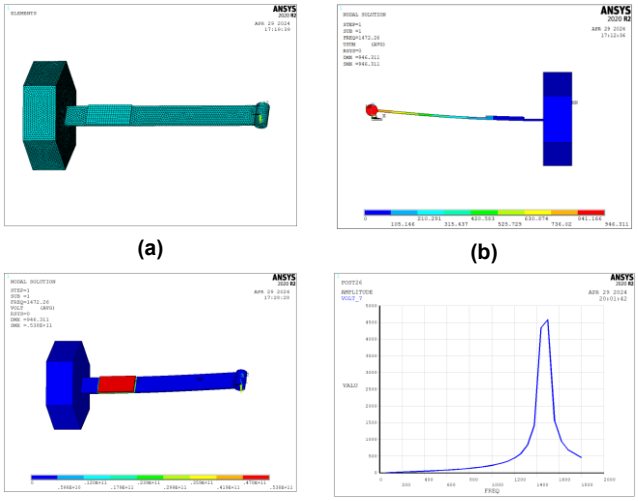

(a) (b) (c) (d)

Fig. 4.Harmonic analysis of a dimensionally scaled piezo harvester a)Elemental view of single PEH, b)First mode displacements, c)Electric potential, d)Harmonic voltage response

References

[1] J.B. Ihn, F.K. Chang, Detection and monitoring of hidden fatigue crack growth using a built-in piezoelectric sensor/actuator network I Diagn, (2004) Smart Mater Struct, 13, 609–620

[2] ANSYS, ANSYS Theory Reference for the Mechanical APDL and Mechanical Applications, (2009) release 12.0. Cannonsburg PA, USA: ANSYS Inc.

DOI 10.5162/EUROSENSORSXXXVI/PT10.227

Multifunctional polarizing microscope system- Classification silicosis tissue and collagen film

Chia-Ling Chiang[1], Lukas Jyuhn Hsiarn Lee[2,3], Chii-Wann Lin[4]
[1] Graduate Institute of Biomedical Electronics and Bioinformatics, National Taiwan University, Taipei 106319, Taiwan, R.O.C.
[2] National Institute of Environmental Health Sciences, National Health Research Institutes, Miaoli 350, Taiwan, R.O.C.
[3]Institute of Environmental and Occupational Health Sciences, National Taiwan University, Taipei 106319, Taiwan, R.O.C.
[4] Department of Biomedical Engineering, National Taiwan University, Taipei 106319, Taiwan, R.O.C.

cwlinx@ntu.edu.tw

Summary:
This study proposes a multifunctional microscope system composed of linear polarizers and CMOS polarization camera featuring different polarization directions especially. After that, we applied pathological tissue samples from patients with silicosis and collagen film as an example. According to preliminary results, it can clearly observe the arrangement of connective tissue in both tissue and crystalline particles in lymph node tissue with silicosis. Afterwards, outcomes are not only analyzed also classified by Image J and Python. The purpose is to assort different tissue in order to enhance diagnostic accuracy as a quantitative data method.

Keywords: Polarizer, CMOS, Silicosis, Lymph node, Collagen film

Background

Workers exposed to large amounts of silica particles in occupational environments for a long time are at a higher risk of developing silicosis. The main reason is that the presence of silanol (SiOH) groups on the surface of silica particles which can form hydrogen bonds with oxygen and nitrogen groups in biological cell membranes. This interaction may lead to the loss of membrane structure, lysosomal leakage, and tissue damage, resulting in inflammation of respiratory system tissues, pulmonary fibrosis, and sclerosis. In severe cases, it can lead to a decline in respiratory function, making it an irreversible lung disease and even death [1, 2]. However, despite strict regulations and management efforts, it still has 1.7 million workers approximately that is exposed to silicosis annually in the United States and other worldwide [3]. Moreover, although polarizing microscopes can display birefringent crystalline silica particles, sometimes the birefringent crystals observed within nodules are the result of inhaled silicate particles mixed with silica dust [2].

In this study, the multifunctional microscope system we proposed are not only installation of polarizers but also utilization CMOS polarizing cameras with different polarization directions on the fluorescence microscope. In addition to polarization function, each unit consists of four pixels composed of linear polarization in different four directions: 0°, 45°, 90°, and 135° for the camera in this system. Compared to traditional polarizing microscopes, the multifunctional microscope can measure physical properties which conventional imaging can not detect, such as classifying chemical isomers, analyzing stress and strain, and even enhancing contrast [4, 5]. Therefore, through measurements provided by this system, it is expected that silicosis tissue images captured at different polarization angles can distinguish from other tissues by different crystal structures and structure arrangement, aiming to quantify data and improve future diagnostic capabilities.

Material and Method

Polarized light microscope system

The original fluorescence microscope system (Olympus BX51) was modified by installing two linear polarizers, serving as the polarizer and analyzer, respectively. Due to the light source being a halogen lamp (350 to 1100 nm), polarizers with higher transmittance in the visible light spectrum were selected as the installation components. In the system configuration, it includes the following components in sequence: light source, polarizer, condenser, specimen,

objective lens, analyzer, and eyepieces. In order to observe crystal variations, a 360-degree rotating mount was installed on the polarizer to change the polarization direction additionally. Furthermore, the specimen was connected to a touch screen keypad to control movement more precisely compared to manual adjustment. It allows for more accurate positioning of samples within the field of view. Subsequently, CMOS cameras and traditional EMCCD cameras were installed above the microscope separately. Finally, captured images were processed and analyzed by Image J and python.

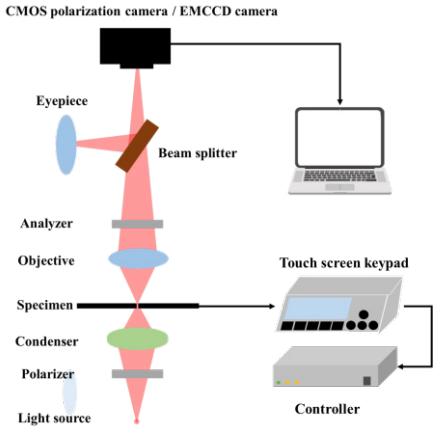

Fig. 1. Construction of polarized light microscope system.

Sample preparation

Because of oil attached on unused slides, it's difficult for the tissue samples to adhere on the surface and also to affect tissue observation. Therefore, we are able to washed it away on the surface of the glass slide with acetone first. After then, through isopropyl alcohol, it can remove the oil and the acetone remaining on the surface. Lastly, utilizing DI water is to rinse it for final cleaning. During the process, an ultrasonic vibrator is used to vibrate for 6 minutes. When replacing to the next solution, it will be rinsed with a large amount of DI water first to wash away the remaining solution on the surface of slides and then blow dry with nitrogen. After cleaning is completed, we flatted the tissue sample with DI water and covered it with a coverslip to complete the preparation.

Preliminary Results

After preparing the lymph node tissue sample from a patient with silicosis, it was placed under a polarized light microscope system for observation, as shown in the Fig. 2. Under orthogonal polarization, the arrangement in different direction of connective tissue and structure in both tissue as well as crystalline particles in Lymph node can be clearly observed through the eyepiece. Subsequently, EMCCD cameras were used to capture a series of 15 images with an exposure time of 0.15 seconds per each at 100 times magnification. Before images come out, it's significant to remove background to improve the signal-to-noise ratio for analysis of the crystalline particles. From the results depicted in the Fig 3., after setting the scale with Image J, the crystalline particles were distinguished from the background through thresholding methods. Furthermore, there are the total of 16 particles was counted as well as an average area of 9.093 nm^2 were calculated within the specified area.

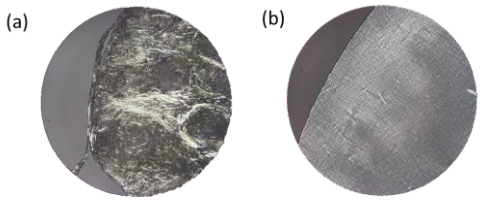

Fig. 2. The orthogonal polarized light image in a microscope: (a) Lymph node tissue (X100) (b) Collagen film (X100).

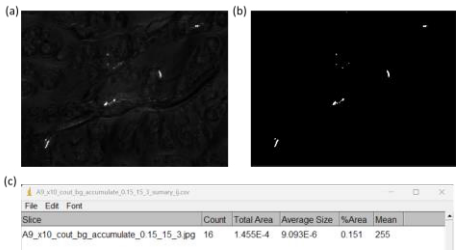

Fig. 3. The images are processed and analyzed by image J: (a) Before processing (b) After processing (C) Particle count and area summation.

References

[1] C. R. Thomas and T. R. Kelley, "A brief review of silicosis in the United States," Environmental health insights, vol. 4, p. EHI. S4628, 2010.

[2] M. I. Greenberg, J. Waksman, and J. Curtis, "Silicosis: a review," Disease-a-Month, vol. 53, no. 8, pp. 394-416, 2007.

[3] X. Liu, Q. Jiang, P. Wu, L. Han, and P. Zhou, "Global incidence, prevalence and disease burden of silicosis: 30 years' overview and forecasted trends," BMC Public Health, vol. 23, no. 1, p. 1366, 2023.

[4] X.-F. He and T. Dalsa, "Polarization-based imaging: Basics and benefits," Photon. Spectra, 2016.

[5] A. G. Andreou and Z. K. Kalayjian, "Polarization imaging: principles and integrated polarimeters," IEEE Sensors journal, vol. 2, no. 6, pp. 566-576, 2002.

[6] R. Oldenbourg, "Polarized light microscopy: principles and practice," Cold Spring Harbor Protocols, vol. 2013, no. 11, p. pdb. top078600, 2013

DOI 10.5162/EUROSENSORSXXXVI/PT10.237

Electrochemical Impedance Spectroscopy of Lithium-ion Battery Cells under Different Load Conditions

Khaled Ibrahim[1,2], Farhan Farooq[1], Silvester Sabathiel[1], Günter Hofer[3], Alexander Bergmann[2], Rudolf Heer[1]
[1] Silicon Austria Labs, Graz, 8010, Austria
[2] Institute of Electrical Measurement and Sensor Systems, Graz University of Technology, Graz, 8010, Austria
[3] Infineon Technologies, Graz, 8020, Austria

khaled.ibrahim@silicon-austria.com

Summary:
This paper analyzes the Electrochemical Impedance Spectroscopy (EIS) of a lithium-ion (Li-ion) battery cell under different load conditions and explores the corresponding equivalent circuit. The results analyze the EIS spectra at different State of Charge (SoC) levels and illustrate the changes in the electrical parameters. This study highlights the variations occurring during Li-ion battery discharge, which can serve as a basis for real-time EIS monitoring.

Keywords: Electrochemical impedance spectroscopy, SoC, lithium-ion, equivalent circuit

Title

Electrochemical Impedance Spectroscopy of Lithium-ion Battery Cells under Different Load Conditions.

Headlines

Investigating the applicability of real-time monitoring of electrochemical impedance spectroscopy of lithium-ion battery cells under different load conditions.

Background, Motivation an Objective

Electrochemical Impedance Spectroscopy (EIS) is a method of choice used to study the properties of linear time invariant electrochemical systems [1]. EIS works by applying an excitation current or voltage signal over a frequency range to the investigated system and measuring the resulting voltage or current. The derived transfer function represents the internal impedance of the battery cell and can be interpreted as an electric circuit composed of several elements.

EIS is used to analyze Lithium-ion (Li-ion) battery cells in an equilibrium state and under laboratory conditions. A rest period following a charge or discharge cycle is commonly implemented. Different rest periods will yield in different impedance spectra. Similarly, varying temperature values will lead to different results. For this reason, controlled measurement conditions are needed within the same EIS experiments.

Embedded EIS solutions allow impedance measurements using miniaturized and cost efficient devices. Integrating these chips into Battery Management System (BMS) enhances the performance and provides insightful information about the battery cell during real-time operation. Nevertheless, due to the characteristics of Li-ion battery cells and the connected load, it remains ambiguous which measurement conditions can be used for accurate real-time EIS measurements. Additionally, a reasonable frequency range must be used to be feasible for fast measurements (performing EIS at a single frequency of 1 mHz requires a time period of at least 16.7 minutes).

The main objectives of this paper are to investigate the applicability of real-time EIS of a Li-ion battery cell during operation under different load conditions and analyze the equivalent circuit parameters.

Description of the New Method or System

The experiment was conducted on a lithium-ion LG 18650-MJ1 battery cell that was connected to the BCS6402 battery discharger with the aim of measuring and analyzing the EIS spectra at different load conditions. The battery cell was continuously discharged, while EIS was performed at certain State of Charge (SoC) levels using an embedded EIS development board from Infineon technologies within the measurement frequency range of 7800 Hz to 1 Hz.

Results

To investigate the impact of the load on the impedance spectrum, an EIS measurement was conducted without and with a load while discharging at a rate of 0.02C. As shown in Fig. 1, the impedance spectrum changes in the high-frequency range, while only minor variations occurred in the frequency range of interest (558 Hz to1 Hz), which can be neglected in high ohmic Li-ion battery cells.

During battery discharge, electrons flow through the external circuit while ions move between electrodes through the electrolyte. Performing real-time EIS at different SoCs during battery discharge is expected to result in observables changes in the equivalent circuit parameters, including the ohmic resistance, double layer capacitance, charge transfer resistance and diffusion process as depicted in Fig. 2. The obtained impedance spectra at 95% and 65% SoC while discharging at different rates of 0.2, 0.5 and 1C is shown in Fig. 3.

Due to the parallel load connected to the battery cell, higher discharge currents are expected to result in lower total ohmic resistance, which can be extrapolated from the intersection of the Nyquist plot with the x-axis. However, due to the increased internal temperature in higher currents, the ohmic resistance of the battery decreases [2], which can be seen at 1C discharge rate.

Double layer capacitance results from the electrode electrolyte interface. At high discharge current density, the rapid movement of ions and current leads to a lower effective double layer capacitance [3]. This is because of the difficulty of ions to migrate quickly.

Charge transfer resistance represents the resistance of electrons transfer between an electrode and electrolyte. At high currents, the effective charge transfer resistance becomes smaller, following the Butler-Volmer equation [4].

During battery discharge, the movement of active species create a concentration gradient. At high and low SoCs concentration gradient becomes high, and this results in fast diffusion. As the battery discharges, the concentration gradient decreases and slows down the diffusion process.

This paper illustrates the EIS equivalent circuit parameters of a Li-ion battery cell while discharging under different load conditions. It highlights the difference if EIS is taken under laboratory conditions after a relaxation time and could be used as a basis for integrating EIS into BMS. Considering the fact that a full-range EIS measurement requires a period of approx. 2.5 minutes, the obtained real-time EIS spectrum might be misleading due to the rapid change in the SoC at high discharge currents. However, performing fast EIS at single frequency points could be considered in real-time EIS measurements.

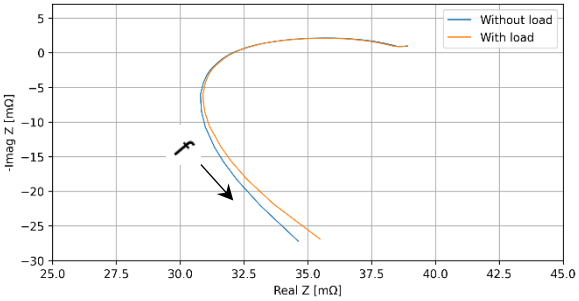

Fig. 1. Impedance spectrum without and with a load.

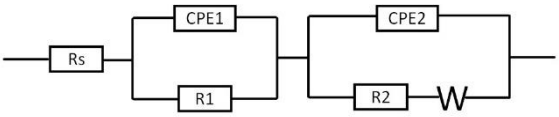

Fig. 2. Equivalent circuit representing the impedance spectrum.

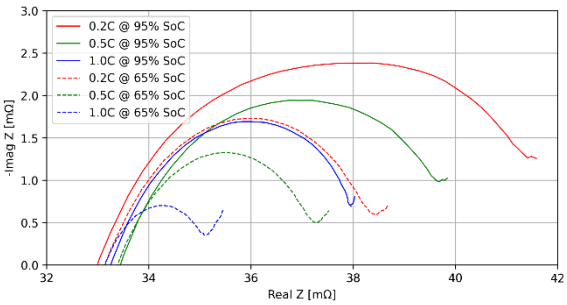

Fig. 3. Impedance spectra at 95% and 65% SoC .

References

[1] A. Ch. Lazanas and M. I. Prodromidis, “Electrochemical Impedance Spectroscopy–A Tutorial,” *ACS Meas. Sci. Au*, vol. 3, no. 3, pp. 162–193, Jun. 2023.

[2] L. H. J. Raijmakers, D. L. Danilov, J. P. M. van Lammeren, M. J. G. Lammers, and P. H. L. Notten, “Sensorless battery temperature measurements based on electrochemical impedance spectroscopy,” *Journal of Power Sources*, vol. 247, pp. 539–544, Feb. 2014.

[3] S. Shiraishi, “Chapter 27 - Electric Double Layer Capacitors,” in *Carbon Alloys*, E. Yasuda, M. Inagaki, K. Kaneko, M. Endo, A. Oya, and Y. Tanabe, Eds., Oxford: Elsevier Science, 2003, pp. 447–457..

[4] L. Stolz, M. Winter, and J. Kasnatscheew, “Practical relevance of charge transfer resistance at the Li metal electrode|electrolyte interface in batteries?,” *J Solid State Electrochem*, Jan. 2024.

DOI 10.5162/EUROSENSORSXXXVI/PT10.249

Experimental Evaluation of Thermoelectric Generators for Indoor Autonomous Sensors

Mohamad Ridwan, Manel Gasulla, Ferran Reverter
Dept.Electronic Eng., Universitat Politècnica de Catalunya, Castelldefels (Barcelona), Spain

ferran.reverter@upc.edu

Summary:
This work aims to identify potential indoor thermal energy sources and assess the feasibility of using a Thermo-Electric Generator (TEG) to generate electrical energy for powering indoor autonomous sensors. A commercial small TEG (4×4 cm^2) was tested with two heatsinks of different dimensions and at several values of temperature difference (ΔT) between the thermal source and the surrounding environment, so as to determine the amount of power available. The highest power outputs achieved by the TEG were 1.83 mW and 33.0 mW with the small and large heatsinks, respectively, at ΔT = 40°C, which are suitable to power most sensor nodes.

Keywords: Autonomous sensor, energy harvesting, thermoelectric generator, indoor applications, maximum power point.

Introduction

In the era of Internet of Things (IoT), many sensor nodes are deployed to collect data from, for example, the industry 4.0. In the coming future, it is foreseen that half of these sensors will be located indoors [1]. One of the main challenges right now is finding suitable ways to power these sensors, especially in places where it is hard or costly to wire them to the electrical grid. While batteries are usually employed, these have some limitations such as limited energy capacity, environmental challenges, shorter lifespan, and maintenance issues [2]. An attractive alternative to power these sensors autonomously is by harvesting energy from the environment, such as from sunlight, vibrations, radio frequency, and heat [3]. In such cases, the corresponding energy harvester must work close to the maximum power point (MPP) so as to leverage the available energy.

In order to harvest thermal energy, a Thermo-Electric Generator (TEG) is generally employed. A TEG is a solid-state device (and, hence, it operates silently without any moving parts [4]) composed of p-type and n-type semiconductors which are connected electrically in series and thermally in parallel. The resulting output power of a TEG depends on the temperature difference between its hot side and cold side.

This work has two main objectives: (1) identifying indoor thermal sources to power a sensor, and (2) characterization of a TEG at specific temperature differences provided by the previous thermal sources, with the goal of quantifying the available output power and assessing the feasibility of powering sensor nodes.

Indoor thermal sources

Several indoor sources of thermal energy have been investigated, such as hot water pipes, various types of lamps, a laptop charger, and a window frame. RTD thermal sensors (Labfacility DM-314) were employed to measure the temperature of each source and the ambient, with the data recorded by a Data Acquisition System (Keysight DAQ970A). Tab. 1 shows the resulting values of temperature difference (ΔT) between the heat sources and the ambient temperature.

Tab. 1: Temperature difference obtained by several indoor thermal sources.

Thermal Energy Source	ΔT (°C)
Hot pipe	40
Compact Fluorescent Lamp (CFL)	25
Linear Fluorescent Lamp (FL)	29
LED lamp	11
Laptop charger	27
Window frame	13

The objects indicated in Tab. 1 cause the specified ΔT when they are turned on. When those are turned off, the temperature steadily drops until it reaches the ambient temperature. As for the window frame, it undergoes such a ΔT when it is exposed to sunlight. In lamps and

chargers, the optimal location for a high ΔT is near the electronics block that control those. The maximum ΔT observed was 40 ºC for a hot pipe of the heating conditioning system of the building.

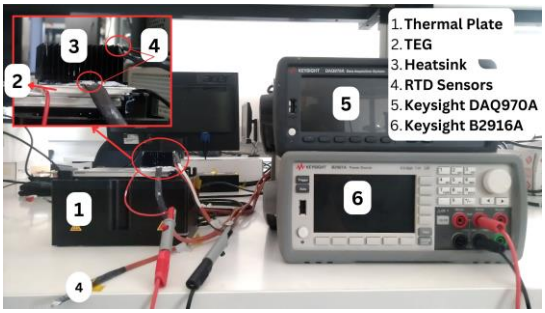

Fig. 1. Experimental setup

TEG in-lab characterization

In order to evaluate the power that can be extracted from the ΔT indicated in Tab. 1, a small commercial TEG of 4 × 4 cm² (EURECA TEG1-40-40-10/100) was in-lab characterized using the setup shown in Fig. 1. This TEG was heated on a thermal plate (QInstruments ColdPlate 2016-0110) and a heatsink was attached on the other (cold) side. The test was conducted at a room temperature of 23-24 °C, and ΔT was set by the thermal plate. Two heatsinks with different size were tested: a) heatsink #1 (Spreadfast SFH4001-21L) with 40 × 40 × 21 mm, and b) heatsink #2 (FischerElektronik SK-92-100 SA) with 100 × 100 × 40 mm. For each testing condition, the current-voltage characteristic of the TEG was extracted using a source and measure unit (Keysight B2961A), whereas thermal measurements (including the temperature at the hot and cold sides of the TEG) were carried out again using RTDs connected to the DAQ.

The experimental results are shown in Fig. 2 (for heatsink #1) and Tab. 2 (for both heatsinks), including the measured temperature difference (ΔT_{TEG}) between the two sides of the TEG. Accordingly, higher values of ΔT generate higher values of ΔT_{TEG}, and these are higher for heatsink #2 thanks to its larger dimensions. The power generated approximately increased proportionally to $(\Delta T_{TEG})^2$. The TEG with heatsink #1 produced a maximum power (P_{max}) of 1.83 mW at ΔT = 40°C, whereas it was 33.02 mW with heatsink #2. The corresponding power density is 0.11 mW/cm² and 2.06 mW/cm² for heatsinks #1 and #2, respectively. The experiment demonstrates that a larger heatsink results in a higher output power from the TEG, since this helps to decrease the temperature at the cold side and thus increases ΔT_{TEG}. This is, however, with the limitation that more space is required for the heatsink.

The power levels in Fig. 2 and Tab. 2 seem to be sufficient to power IoT sensor nodes, as the average power consumption of such sensors can be typically around 1 mW [2]. To generate 1 mW, $\Delta T \approx 30$ °C is required with heatsink #1, whereas ΔT lower than 10 °C is needed with heatsink #2, which can be obtained using the objects tested and reported in Tab. 1.

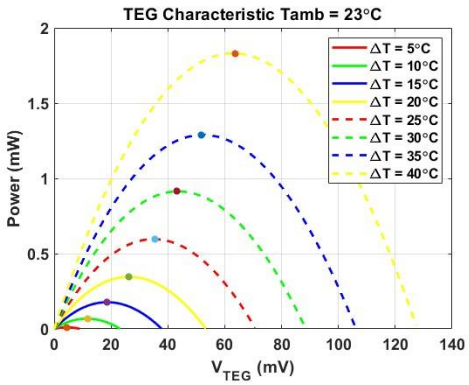

Fig. 2. Power-voltage characteristic of the TEG using heatsink #1.

Tab. 2: Maximum power at the TEG output for different values of ΔT and for two different heatsinks.

ΔT (°C)	TEG – heatsink #1		TEG – heatsink #2	
	ΔT_{TEG} (°C)	P_{max} (mW)	ΔT_{TEG} (°C)	P_{max} (mW)
5	1.20	0.011	2.05	0.55
10	1.83	0.068	4.17	2.09
15	2.25	0.18	5.84	4.20
20	2.90	0.35	7.95	7.12
25	3.65	0.60	9.84	12.00
30	4.44	0.91	12.09	17.96
35	5.21	1.29	14.30	24.80
40	6.15	1.83	16.50	33.02

References

[1] I. Mathews, S. N. Kantareddy, T. Buonassisi, and I. M. Peters, “Technology and Market Perspective for Indoor Photovoltaic Cells,” *Joule*, vol. 3, no. 6, pp. 1415–1426, Jun. 2019, doi: 10.1016/j.joule.2019.03.026.

[2] V. Pecunia, L. G. Occhipinti, and R. L. Z. Hoye, “Emerging Indoor Photovoltaic Technologies for Sustainable Internet of Things,” *Adv. Energy Mater.*, vol. 11, no. 29, p. 2100698, Aug. 2021, doi: 10.1002/aenm.202100698.

[3] S. Singh, “Environmental Energy Harvesting Techniques to Power Standalone IoT-Equipped Sensor and Its Application in 5G Communication,” *Emerg. Sci. J.*, vol. 4, pp. 116–126, Nov. 2021, doi: 10.28991/esj-2021-SP1-08.

[4] R. Aridi, J. Faraj, S. Ali, T. Lemenand, and M. Khaled, “Thermoelectric Power Generators: State-of-the-Art, Heat Recovery Method, and Challenges,” *Electricity*, vol. 2, no. 3, pp. 359–386, Sep. 2021, doi: 10.3390/electricity2030022.

Study of the Linearity of Low-Area Photovoltaic Cells for Indoor Autonomous Sensors

Bernat Martinez, Mohamad Ridwan, Manel Gasulla, Ferran Reverter
Dept.Electronic Eng., Universitat Politècnica de Catalunya, Castelldefels (Barcelona), Spain

ferran.reverter@upc.edu

Summary:
In the field of energy harvesting for autonomous sensors located indoors, this work analyses the linearity of low-area photovoltaic (PV) cells of different technology while subjected to different levels of illuminance coming from either artificial or natural sources. For indoor artificial lighting (to be precise, cold LED), the PV technologies under test show a linear response, except for the monocrystalline technology. However, for indoor natural light, only PV cells belonging to the III-V technology show a linear response. Monocrystalline PV cells show an increasing quadratic response, whereas amorphous and organic PV cells have a decreasing quadratic response. Accordingly, the most appropriate technology to leverage the indoor energy coming from the natural light is the monocrystalline.

Keywords: Autonomous sensor, energy harvesting, photovoltaic cells, indoor applications, maximum power point.

Introduction

Billions of wireless sensors are expected to be installed in the coming decade [1] using technological ecosystems such as the *internet of things*. In addition, almost half of these sensors will be installed indoors [1], which is the scenario of interest here. For example, most of the sensor nodes related to the *Industry 4.0* will be located indoors. However, the installation and interconnection of this massive number of sensor nodes motivates several technological challenges. One of these challenges is the power supply [2] of the sensor nodes, which is the focus of this work.

The most appropriate power-supply solution is the use of an energy harvester, which powers the sensor node by collecting energy from the environment. In comparison with primary batteries, an energy harvester is a more sustainable solution with less maintenance costs, especially for hard-to-reach locations [2]. Among the different energy harvesting domains, here we focus on the optical since it provides the highest electrical power density [3]. Optical energy harvesters rely on photovoltaic (PV) cells, which are commercially available in different dimensions and technologies. For tiny autonomous sensor nodes, PV cells are expected to have a low area (e.g., around 10 cm^2 or even lower) so as not to increase the dimensions of the node. As for the technology, monocrystalline and polycrystalline technologies are mainly recommended for outdoor applications, in which the optical energy comes from the sun. However, other technologies with a spectral sensitivity more adapted to the visible light (such as amorphous and organic technologies) are, in principle, suggested for indoor applications. The use of PV cells for outdoor applications has been extensively evaluated in the literature in the last decades. Nevertheless, its use for indoor applications is relatively new and the design of the complete system is more challenging since the energy available is much lower.

In the previous context, this work aims to study the linearity of different PV cell technologies while subjected to different levels of artificial and natural light available indoors, with the final aim to extract guidelines for the selection of the most appropriate technology.

Materials and Method

The study of linearity has been carried out for the commercial low-area PV cells of different technology (monocrystalline silicon, amorphous silicon, organic, and III-V type) summarized in Tab. 1. Two testing scenarios were considered: 1) scenario #1 under artificial lighting from 100 to 1000 lux of cold LED, and 2) scenario #2 under natural (sun) light from 1000 to 10000 lux; such levels of illuminance (both artificial and natural) are typically found indoors. The cold LED was reproduced by a spectrally tunable light source (Asensetek Light Cube) [4], whereas the sun light was emulated by a AAA

Tab. 1: Features of the commercial PV cells selected in this study

Ref.	Technology	Manufacturer	Model	Active area (cm^2)	Substrate
MonoC	Monocrystalline	AnySolar	IXOLAR KX0B141K06TF	8.77	Non-flexible
Am1	Amorphous	Panasonic	AM-1454	10.94	Non-flexible
Org1	Organic	Epishine	LEH3_50x20_6_10	10.00	Flexible
III-V	III-V type	Lightricity	EXL2-1V50	2.15	Non-flexible

solar simulator (Scientech SciSun-150). The temperature of the cells was kept at 25ºC using a thermoelectric cold/hot plate (Teca AHP-301CPV). The applied level of illuminance was monitored by a spectroradiometer (Avantes AvaSpec-ULS2048CL-EVO). For each testing condition, the current-voltage characteristic of each PV cell was measured through a source and measure unit (Agilent B2901A) and, then, the maximum power point (MPP) was extracted [4]. For a fair comparison between the four PV cells, the power related to MPP was divided by the corresponding PV-cell area (see Tab. 1) to have the power density at MPP.

Experimental results and discussion

Figs. 1 and 2 show the experimental power density at MPP versus the illuminance for scenarios #1 and #2, respectively. In both figures, the power density is normalized to the value obtained at the minimum illuminance (100 lux in Fig. 1 and 1000 lux in Fig. 2).

From Fig. 1, three technologies (Am1, Org1, III-V) show a linear response with respect to the illuminance. However, the MonoC cell shows an increasing quadratic response. Note that an increase of 10 of the input illuminance generates an increase of 28 in the output power.

As for Fig. 2, only the III-V technology shows a linear response versus the illuminance. Similar to Fig. 1, the MonoC cell shows an increasing quadratic response, but the Am1 and Org1 cells have a decreasing quadratic response. Here, an increase of 10 of the input illuminance brings about an increase of 15 in the output power for the MonoC cell, but only 6 and 5 for the Org1 and Am1 cells, respectively.

Such a quadratic behavior leads to a high efficiency at 10000 lux in the MonoC cell (17 %), but a low value in the Am1 and Org 1 cells (3% and 5%, respectively). The efficiency at 10000 lux of the III-V cell is 22%, but with a significant cost limitation. Therefore, amorphous and organic technologies are not recommended to leverage the peaks of optical power coming from the sun in rooms with outside windows. In such conditions, the most appropriate PV cell technology seems to be the monocrystalline.

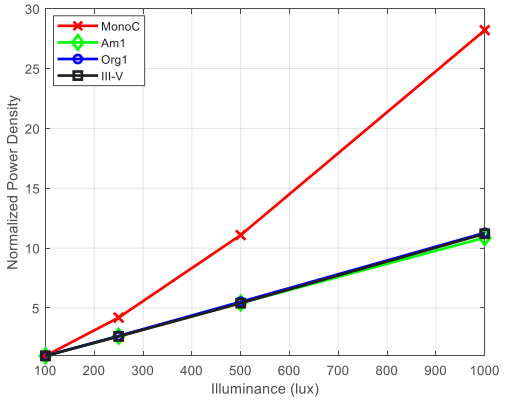

Fig. 1. Normalized power density versus illuminance of cold LED at 25ºC for different PV technologies.

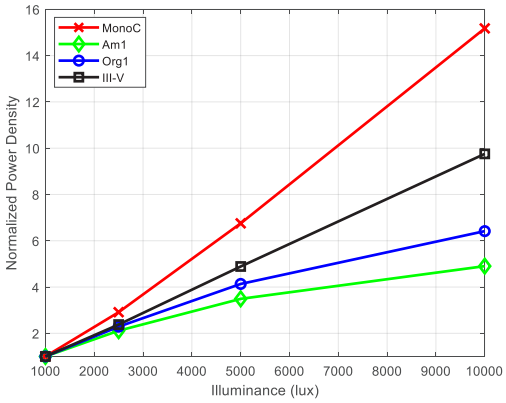

Fig. 2. Normalized power density versus illuminance of solar light at 25ºC for different PV technologies.

References

[1] I. Mathews, S. N. Kantareddy, T. Buonassisi, and I. M. Peters, Technology and Market Perspective for Indoor Photovoltaic Cells, *Joule* 3 (6), 1415–1426 (2019).

[2] V. Pecunia, L. G. Occhipinti, and R. L. Z. Hoye, Emerging Indoor Photovoltaic Technologies for Sustainable Internet of Things, *Adv. Energy Mater.* 11 (29), 2100698 (2021).

[3] A. Chatterjee *et al.*, Powering internet-of-things from ambient energy: a review, *Journal of Physics: Energy* 5, 022001 (2023).

[4] E. Ferré, M. Gasulla, and F. Reverter, Comparative analysis of low-power PV cells of different technologies under different types of indoor artificial lighting, in Proc. *IEEE – I2MTC 2024* (accepted).

DOI 10.5162/EUROSENSORSXXXVI/OT1.5

The Optimal Planform of a Cantilever Unimorph Piezoelectric Vibrating Energy Harvester (PVEH), with a Device-Layer Edge Block

Eliya Salman[1], *Sahar Lustig*[1], *David Elata*[1]
[1] *Technion – Israel Institute of Technology, Faculty of Mechanical Engineering, Haifa, 32000, Israel*

elata@technion.ac.il

Summary:
We consider the planform of a cantilever piezoelectric vibrating energy harvester (PVEH), that has an edge block which is patterned *only* in the device layer. We derive an analytic expression of the planform, which ensures an optimal performance of the cantilever PVEH. The contours of the optimal planform are described by Bessel functions, and the predictive capabilities of our new model are demonstrated by the good agreement with finite elements simulations.

Keywords: Piezoelectric unimorph, energy harvesting, vibrating cantilever, uniform strain, uniform curvature.

Background, Motivation and Objective

The optimal performance of a cantilever piezoelectric vibrating energy harvester (PVEH), is achieved when the axial strain in the piezoelectric layer, is uniform. Technology dictates the construction and thickness of the unimorph, but its planform is a design choice which makes optimization possible.

In a recent paper [1] we considered a PVEH with a massive edge block that extended into the handle layer. The inertia of this edge block dominated the vibration response of the structure. We showed that for such a massive edge block the optimal planform of the PVEH is a *trapeze*. The same conclusion was presented in many previous studies which were based on experiments, simulations, or a combination of both (e.g. [2],[3]). However, our work was the first rigorous analysis of the of the problem, and we presented an explicit functional form of the optimal trapeze planform [1]. That model was the first ever to offer predictive capabilities.

In contrast to those devices, there is a different class of PVEHs in which the edge block is patterned *only* in the device layer (e.g. Fig. 1), and does not extend into the underlaying handle layer. In this case, the inertia of the beam is as important as the inertia of the edge block.

In the present study we show that the optimal planform of a cantilever PVEH with a *device-layer* edge block, is *not* a trapeze with straight contours, but rather it is a planform with curved contours described by *Bessel* functions. We validate or model and demonstrate its predictive capabilities by using finite elements simulations.

Modelling – Analytic derivation

Figure 1 presents a schematic illustration of the PVEH. The beam has a length L, a uniform thickness h, and a rectangular cross-section with width $w(x)$, that changes from the clamped edge at $x=0$ to the far edge at $x=L$. It is assumed that the Euler-Bernoulli beam theory is applicable. An edge block which is patterned in the device layer is connected to the far edge (i.e. $x=L$), and has a mass m_L and a moment of inertia I_L. The moment of inertia refers to the z axis, and it is given relative to the center point of the edge cross-section (i.e. $x=L$, $y=z=0$).

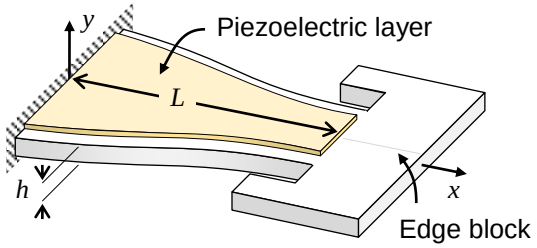

Fig. 1. PVEH with a device-layer edge block.

Within the context of the Euler-Bernoulli beam theory, we consider a steady state vibration of the cantilever in the form $y(x,t)=Y(x)\cdot T(t)$, where $Y(x)$ is the mode shape of the transverse deflection. The aim of the present study is to determine the functional form of $w(x)$ such that the axial strain on the top surface is uniform

$$\varepsilon_{xx}(x,y,z=h/2)=-\frac{d^2Y(x)}{dx^2}\frac{h}{2}=\bar{\varepsilon} \quad (1)$$

The governing equation that determines the out-of-plane displacement $y(x,t)$, is given by

$$\rho h w(x)\frac{\partial^2 y(t,x)}{\partial t^2}=-E\tilde{I}_{yy}\frac{\partial^2}{\partial x^2}\left(w(x)\frac{\partial^2 y(t,x)}{\partial x^2}\right) \quad (2)$$

where ρ is the density of the elastic material and E is the Young modulus, and $\tilde{I}_{yy}=h^3/12$.

Extracting $Y(x)$ from eq. (1) and substituting it into eq. (2), yields the differential equation

$$\frac{d^2w(x)}{dx^2}-\frac{\rho h}{2E\tilde{I}_{yy}}\omega^2x^2w(x)=0 \quad (3)$$

Equation (3) gives the optimal planform for a uniform strain over the top surface of the PVEH

$$w(x)=a_1\sqrt{x}\cdot I_{0.25}(\beta)+a_2\sqrt{x}\cdot K_{0.25}(\beta) \quad (4)$$

Here $\beta=x^2\omega\sqrt{\rho h/8E\tilde{I}_{yy}}$, $I_{0.25}$ and $K_{0.25}$ are modified *Bessel* functions, and the constants a_1 and a_2 are determined from the boundary conditions related to the resultant shear force and bending moment at $x=L$.

Finite Elements Simulations

With energy harvesting applications in mind, we consider cantilever beams made from single-crystalline silicon (SCS) using silicon on insulator (SOI) wafers technology [3]. Specifically, the beam and the edge block are patterned in the device-layer of the wafer. We consider beams that are along the (110) orientation of the anisotropic SCS where E_{xx}=169.7 GPa, and typical values of h=10 μm, L=2000 μm and a vibration frequency of ω=30,000 Rad/s (4.774 kHz). All edge-blocks are rectangular, with width w_{EB}=200 μm, and lengths L_{EB}=100, 200, 300 and 400 μm.

The eigenfrequency of the cantilever beam with a device-layer edge block was simulated using the COMSOL™ 6.0 finite elements code [4]. The *nonuniformity*, $S_{\varepsilon_{xx}}$, of the axial strain ε_{xx}, over the top surface of the cantilever, is computed by

$$S_{\varepsilon_{xx}}=\sqrt{\int_{x=0}^{L}\varepsilon_{xx}^{\,2}w(x)dx}\Big/\int_{x=0}^{L}|\varepsilon_{xx}|w(x)dx-1 \quad (5)$$

For a uniform strain, the nonuniformity is identically zero, $S_{\varepsilon_{xx}}$=0.

Table 1 presents the results for the different edge block lengths, L_{EB}. The strain nonuniformities are rather small. For perspective, we consider a non-optimal trapezoidal cantilever beam, with the same widths at the clamped and the far edge, as in the third case in table 1 (L_{EB}=300 μm). Figure 2 compares the strain distribution over the top surface for the optimal planform, and for the non-optimal trapezoidal planform. The strain over the top surface of the optimal beam (Fig. 2 bottom) is more uniform by a factor of ~50 relative to that of the trapezoidal beam (Fig. 2 top).

Tab. 1: The results of the eigenfrequency simulations for different edge blocks lengths

L_{EB} μm	Rel error of ω_n [%]	Nonuniformity $S_{\varepsilon_{xx}}$
100	0.023	$2.5851\cdot10^{-5}$
200	0.151	$8.7729\cdot10^{-5}$
300	0.435	$3.0367\cdot10^{-4}$
400	1.001	$9.8769\cdot10^{-4}$

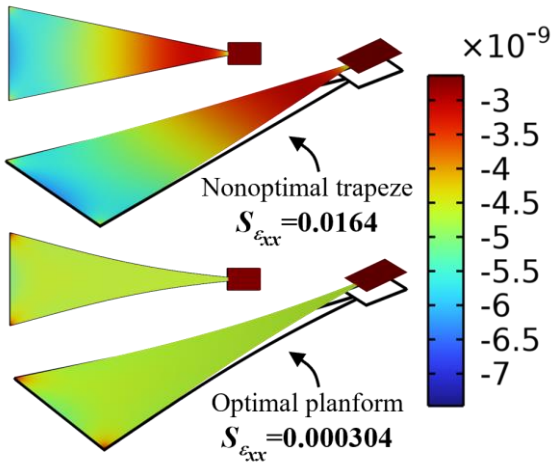

Fig. 2. Comparison of the strain distribution over the top surface between the optimal planform (bottom) and the trapezoidal planform (top).

This validates the predictive capabilities of the new model in Eq. (4).

Acknowledgement: This work was supported by the Israel Science Foundation, Grant 1820/22**.**

References

[1] E. Salman, et al., "On the optimal planform of a cantilever unimorph piezoelectric vibrating energy harvester," Smart Mater. Struct., **33**(3), 35029, 2024, doi: 10.1088/1361-665X/ad28d0.

[2] E. Halvorsen and T. Dong, "Analysis of tapered beam piezoelectric energy harvesters," PowerMEMS 2008, Sendai, 2008, pp. 241–244.

[3] Y. Jia and A. A. Seshia, "Five topologies of cantilever-based MEMS piezoelectric vibration energy harvesters: a numerical and experimental comparison," Microsyst. Technol., **22**(12), 2841–2852, Dec. 2016, doi:10.1007/s00542-015-2599-z.

[4] COMSOL, www.comsol.com., COMSOL AB, Stockholm, Sweden.

DOI 10.5162/EUROSENSORSXXXVI/OT5.201

Odour Classification and Concentration Estimation with a Chemical Sensor Array on a Drone

A.Vidal[1], J.Alonso-Valdesueiro[1,2], A.Benegiamo[1], J.Burgues[1], K.Karachristos[1], L. Terren[3], S. Doñate[3], A. Gutiérrez-Gálvez[2] S. Marco[1,2]
[1] Signal and Information Processing for Sensing Systems, Institute for Bioengineering of Catalonia, The Barcelona Institute of Science and Technology, Baldiri Reixac 10-12, 08028 Barcelona, Spain,
[2] Department of Electronics and Biomedical Engineering, Universitat de Barcelona, Martí i Franquès 1, 08028 Barcelona, Spain,
[3] Depuración de Aguas del Mediterráneo, Av. Benjamín Franklin 21, 46980 Paterna, Spain

avidal@ibecbarcelona.eu

Summary:
We present an approach to improve the accuracy of odor concentration prediction in wastewater treatment plants using drones equipped with electronic noses. Source specific regression models are more accurate than models calibrated on all the data. Therefore, we could leverage these source-specific models to perform better predictions by integrating a source classification engine before odor prediction,. In the scenario explored, the improvement is limited by the source classification accuracy.

Keywords: Environmental monitoring, electronic nose, drone, odour quantification, source classification

Background, Motivation an Objective

In a previous proposal, we suggested using a drone equipped with an Instrumental Odour Monitoring System (IOMS) to measure odour levels in real-time in a wastewater treatment plant (WWTP). The system includes a complete signal and data processing workflow that estimates the odour concentration based on EN13725.

Wastewater treatment plants have various sources of odour such as bioreactors, settlers, desanders, etc. However, it is difficult to determine the exact source that is producing the odour. These sources have diverse chemical profiles that could potentially provide information about the odour origin. Therefore, the classification of odour sources is an important aspect of odour monitoring.

In our previous work, we presented a single prediction model that incorporated data from all the odor sources. However, in this work, we propose an alternative method that involves using source-specific calibration models. To implement this approach, we have included an odor source classification model in our new workflow.

Description of the New Method or System

The dataset used in this exploration was acquired in the Molina de Segura WWTP. The measurement campaign and machine learning development strategy has been previously described. The dataset contains 40 measurements carried out along in month in summer 2020. The dataset contains measurements carried out in the vicinity of four different odour sources, namely: Settler (m1), Biological (m2), Chimney(m3) and Desander (m4).

The new data processing workflow comprises two key modelling steps: source classification and odour concentration quantification.

To quantify the odour, Partial Least Squares (PLS) regression and feature selection via interval-PLS is performed as described in earlier research [2]. The difference here is that in addition to the global model (mg) including all the sources we have learned source-specific odour prediction models (m1 to m4)

To classify the sources, a random forest classifier is used. A significant feature of the classifier is the possibility to defer source label assignment, when the classification confidence is low. If the classification confidence is high, source

specific calibration models are used, otherwise the global calibration model is used.

Results

Table 1 describes the results for the general model, table 2 assuming perfect knowledge of the emitting source, and table 3 and figure 1, describe the results for the final workflow.

The best results are found when the odour source is previously known, but unfortunately this goal cannot be achieved in practice in our scenario.

The best predictive performance was obtained when 60% of the samples were predicted with the general model and 40% of the samples were predicted with class specific models. Of this 40%, 80% were correctly classified.

The final proposal only marginally improves the results of the general model.

Illustrations, Graphs, and Photographs

Tab.1: Summary of the predictions for the general model, s1 to s4 correspond to the sources Settler, Biological, Chimney and Desander, respectively. T is the total prediction. Bias, Std and RMSE are expressed as factors. Corr. Is correlation.

	s1	s2	s3	s4	T
Bias	1.29	0.89	0.99	0.90	1.00
Std.	1.71	2.00	2.71	1.36	2.00
RMSE	1.76	1.96	2.56	1.36	1.94
Corr.	0.91	0.84	0.83	0.96	0.86

Tab.2: Summary of the predictions for the source-specific models with perfect sources classification.

	s1	s2	s3	s4	T
Bias	0.94	0.96	0.94	0.98	0.96
Std.	1.33	1.78	2.22	1.16	1.68
RMSE	1.27	1.64	2.11	1.13	1.67
Corr.	0.97	0.89	0.90	0.99	0.

Tab.3: Summary of the predictions for the models determined by the classifier output.

	s1	s2	s3	s4	T
Bias	1.19	0.80	1.03	0.87	0.96
Std.	1.69	1.99	2.42	1.30	1.90
RMSE	1.69	2.00	2.32	1.33	1.89
Corr.	0.91	0.83	0.87	0.97	0.88

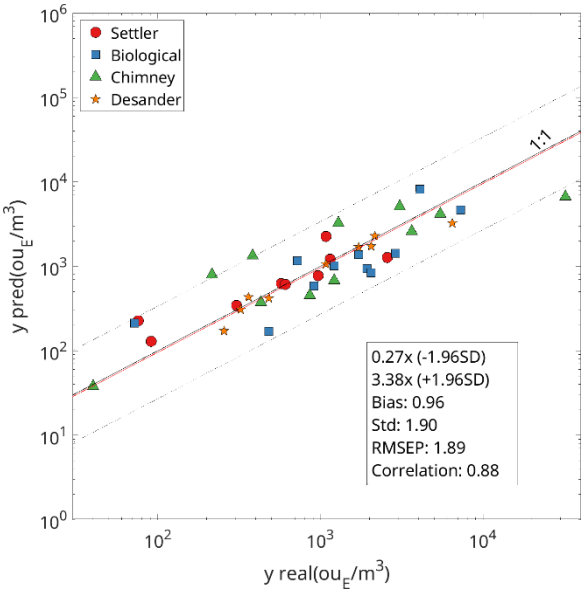

Fig. 1. Predicted odour plotted against real odour concentrations for the models determined by the classifier.

References

[1] J. Burgués, S. Doñate, M.D. Esclapez, L. Saúco, S. Marco, Characterization of odour emissions in a wastewater treatment plant using a drone-based chemical sensor system, *Science of The Total Environment* 846 (2022); doi: 10.1016/j.scitotenv.2022.157290

[2] A. Benegiamo, J. Burgués, J. Alonso-Valdesueiro, B.J. Lotesoriere, L. Terrén, L. Sauco, M.D. Esclapez, S. Doáte, A. Gutiérrez-Gálvez, S. Marco, Optimization of a Drone-Based System for Instrumental Odor Monitoring Using Feature Selection, *MDPI Proceedings* 97, 109 (2024); doi: 10.3390/proceedings2024097109